science for a changing world

The 2006 Eruption of Augustine Volcano, Alaska

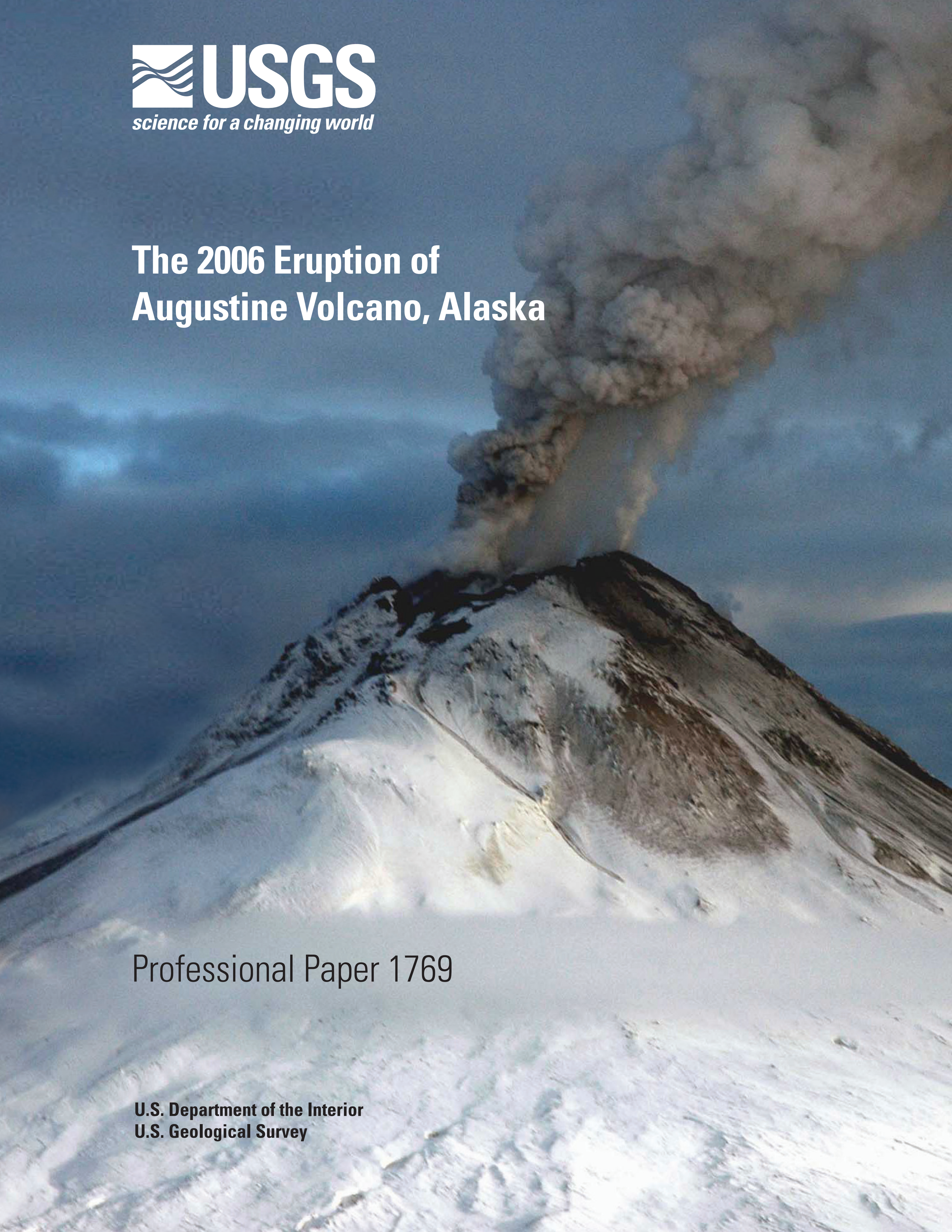

Professional Paper 1769

U.S. Department of the Interior
U.S. Geological Survey

COVER

The west side of Augustine Volcano on January 12, 2006, with minor ash plume in progress. Ash and lahar deposits from explosions on January 11 are visible on volcano's flanks. The original USGS/AVO photograph by Game McGimsey is shown below.

The 2006 Eruption of Augustine Volcano, Alaska

Edited by John A. Power, Michelle L. Coombs, and Jeffrey T. Freymueller

Professional Paper 1769

U.S. Department of the Interior
U.S. Geological Survey

U.S. Department of the Interior
KEN SALAZAR, Secretary

U.S. Geological Survey
Marcia K. McNutt, Director

U.S. Geological Survey, Reston, Virginia: 2010

This report and any updates to it are available online at:
http://pubs.usgs.gov/pp/1769/

For product and ordering information:
World Wide Web: http://www.usgs.gov/pubprod
Telephone: 1-888-ASK-USGS (1-888-275-8747)

For more information on the USGS—the Federal source for science about the Earth,
its natural and living resources, natural hazards, and the environment:
World Wide Web: http://www.usgs.gov
Telephone: 1-888-ASK-USGS (1-888-275-8747)

Suggested citation: Power, J.A., Coombs, M.L., and Freymueller, J.T., eds., 2010, The 2006 eruption of Augustine Volcano, Alaska: U.S. Geological Survey Professional Paper 1769, 667 p., 1 plate, scale 1:20,000, DVD-ROM.

Congress Cataloging-in-Publication Data

The 2006 eruption of Augustine Volcano, Alaska / edited by John A. Power, Michelle L. Coombs, and Jeffrey T. Freymueller.
p. cm. -- (Professional paper ; 1769)
ISBN 978-1-4113-2981-2 (alk. paper)
1. Augustine Volcano (Alaska)--Eruption, 2006. 2. Volcanism--Alaska--Augustine Volcano. I. Power, John A. II. Coombs, Michelle L. (Michelle Lynn) III. Freymueller, Jeffrey T.
QE523.A87A14 2010
551.2109798'3--dc22

2010040422

Foreword

The 1986 explosive eruption of Augustine Volcano, Alaska, prompted the creation of the Alaska Volcano Observatory (AVO), a cooperative program of the U.S. Geological Survey (USGS), the University of Alaska Fairbanks Geophysical Institute, and the Alaska Division of Geological and Geophysical Surveys. Since then, this effective long-term partnership has led the way in monitoring Alaskan volcanoes, communicating the hazards associated with volcanic activity, and furthering our knowledge of volcanic processes at work in Alaska. The unrest at Augustine that began in 2005 and culminated in eruption in 2006 showcased the advancement of monitoring technology over the past two decades. Such developments, including broadband seismometers, continuous GPS receivers, infrared imagery, remote web cameras, atmospheric pressure sensors, and digital data transmission, greatly improved our observations and understanding of the processes driving the 2006 eruption of this island volcano. In addition, this was the first Alaskan eruption that the public could track in real time via the Internet, as seismic data and Webcam images were available to followers all over the world.

To ensure that public officials, key government agencies, affected industries, the news media, and the general public were well informed and able to take appropriate actions to deal with the hazards associated with the reawakening volcano, AVO did not work alone. Other scientists from the USGS Volcano Hazards Program provided their time and expertise. NOAA's West Coast Alaska Tsunami Warning Center, the National Weather Service, the Federal Aviation Administration, the Department of Homeland Security, and the EarthScope/Plate Boundary Observatory also contributed significantly to the effective response to the 2006 eruption of Augustine.

The scientific response to this eruption involved an even larger pool of talent that included researchers from collaborating government agencies, universities, and private research institutions, as well as contributions from citizens in south-central Alaska who collected ash samples and provided visual observations and photographs. The result of these efforts is a comprehensive picture of Augustine as a volcanic system—magma generation deep in the crust; magma mixing and ascent in the shallow crust and volcanic conduit; pyroclastic flows, lahars, and lava that greatly altered the landscape of Augustine Island; and eruptive plumes that deposited ash in south-central Alaska and traveled hundreds of kilometers downwind.

The hazard-communication protocols and scientific insights developed at Augustine in 2006 were quickly applied at explosive eruptions of Okmok Volcano (2008), Kasatochi Volcano (2008), and Redoubt Volcano (2009), Alaska. This quick succession of explosive eruptions in the Aleutian Arc highlights the need for programs that provide both long-term surveillance and warnings of the hazards presented by active volcanoes, as well as increase our knowledge of the underlying physical processes so that future eruption forecasts can be more accurate. Although these eruptions all occurred far from major population centers, each presented a serious hazard because of the far-reaching effects of airborne volcanic ash.

The unprecedented impacts of volcanic ash on air travel in Europe from the 2010 eruption of Eyjafjallajökull Volcano in Iceland serves as a further reminder of the importance of understanding and communicating the hazards associated with explosive volcanism. This collection of papers studying the 2006 eruption of Augustine Volcano will serve as an important reference for scientists responding to future volcanic unrest, whether in Alaska or anywhere else where people's lives can be placed in harm's way when volcanoes awake.

Marcia McNutt

Director
U.S. Geological Survey

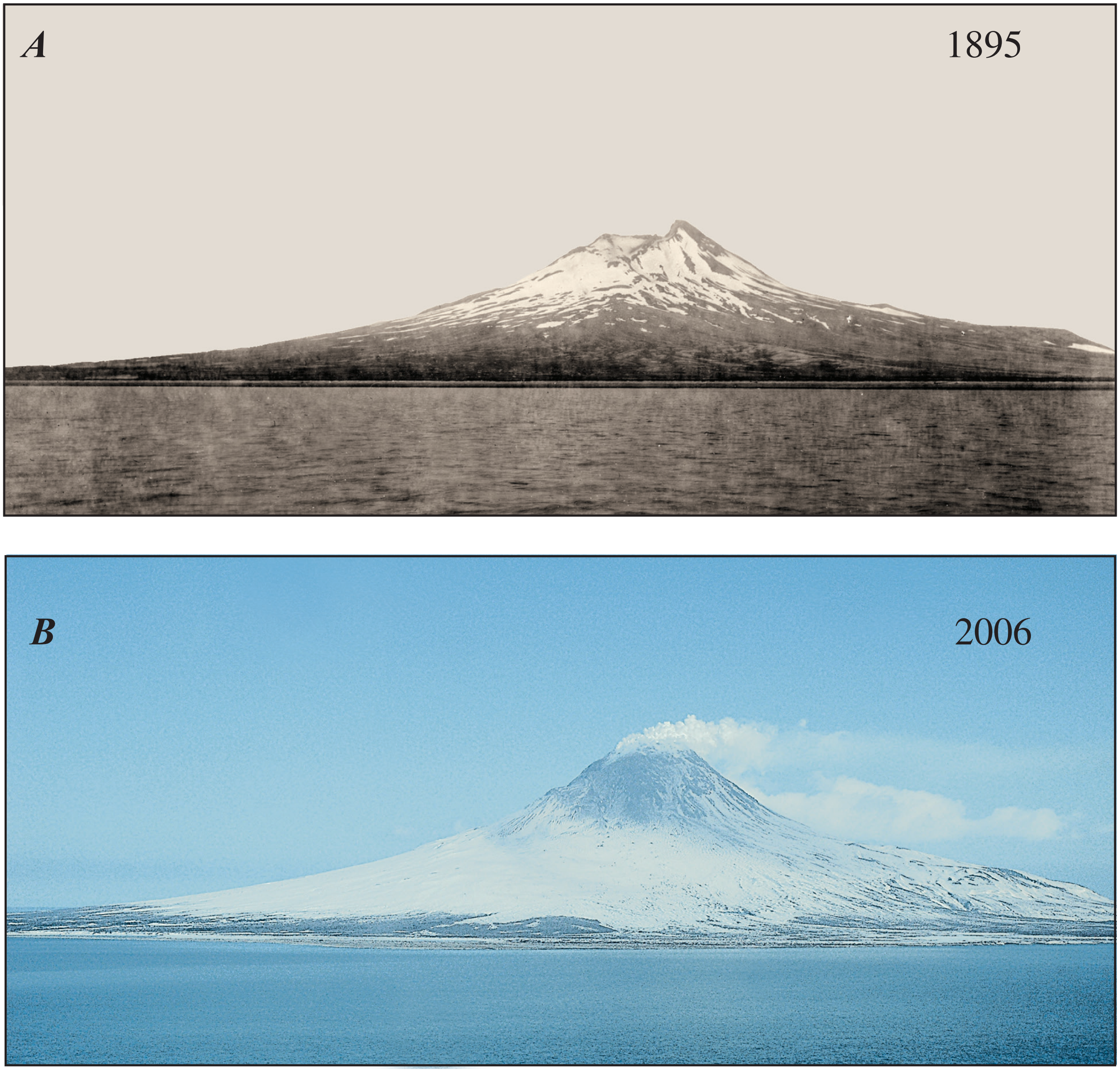

Two views of the southwest side of Augustine Volcano showing changes in summit morphology over a 111-year period. *A*, Top image shows the Augustine volcanic cone taken from a ship in 1895 (USGS photo by C.W. Purington). *B*, A similar image taken from an airplane flying at an altitude of roughly 500 feet at approximately the same position on March 29, 2006 (AVO photo by Dan Cervelli).

Preface

Augustine Volcano, the most historically active volcano in Alaska's Cook Inlet region, again showed signs of life in April 2005. Escalating seismic unrest, ground deformation, and gas emissions culminated in an eruption from January 11 to mid-March of 2006, the fifth major eruption in 75 years. The eruption began with a series of 13 short-lived blasts over 20 days that sent pyroclastic flows; snow, rock, and ice avalanches; and lahars down the volcano's snow clad flanks; ash clouds drifted hundreds of kilometers downwind. Punctuated explosive activity gave way to effusion of lava and emplacement of thick block-and-ash flows on the volcano's north flank that continued through mid-February. In mid-March renewed extrusion resulted in the building of a new, higher summit lava dome and two blocky lava flows on the north and northeast flanks of the cone. The eruption resulted in ash fall on many south-central Alaskan communities and disrupted air traffic in the region.

Augustine's frequent eruptions and relatively easy access have long drawn volcanologists to study the accumulation, ascent, and eruption of andesitic to dacitic magma. Studies of the most recent activity before 2006, in 1976 and 1986, revealed that the volcano lately produces explosive eruptions that are preceded by months of unrest and injection of new magma into a storage region in the upper several kilometers of the crust. Each of these eruptions then followed a similar progression from explosive to effusive behavior over several months. Petrologic and geophysical observations suggest that these three eruptions were triggered by similar magma mixing events and that the subsequent ascent and eruption of magma was governed by processes that were roughly constant from one eruption to the next. Geologic studies of the island show that in the more distant past parts of Augustine's edifice have failed repeatedly, resulting in debris avalanches that entered the sea and, at least once, in 1883, caused a tsunami that hit surrounding Cook Inlet coastlines. Such edifice failures and resultant local tsunamis should be expected in the future.

Recognition of Augustine's frequent activity and hazardous nature led to the installation of a network of telemetered seismometers beginning in 1971, the establishment of a geodetic network in 1988, and the installation of other new instrumentation such as pressure sensors, broadband seismometers, and cameras by the Alaska Volcano Observatory (AVO), and the selection of Augustine for geodetic instrumentation through the EarthScope/Plate Boundary Observatory program in 2004. In addition, remote sensing techniques, such as airborne thermal imaging and the advanced spaceborne thermal emission and reflection radiometer (ASTER), provided novel and often critical information as the 2006 eruption progressed. The combination of a long-term seismic network and an array of new monitoring techniques has provided a breadth and depth of understanding of Augustine's most recent activity that was not possible in the past.

This volume contains 28 chapters reporting on a diverse suite of new scientific observations and investigations that were motivated by the 2006 eruption. Understanding the magmatic processes that drive eruptions, identifying eruptive events, tracking the movement of ash clouds, and communicating the resultant hazards to other government agencies and the public are all critical tasks for AVO, and chapters touch upon all of these topics. One goal in this compilation is to synthesize the diverse information into as complete an understanding of the magmatic and eruptive processes as possible.

An equally important goal is to provide a framework for diagnosing periods of unrest and formulating forecasts of eruptions that will certainly take place at Augustine in the future. This latter goal is especially important, as Augustine's frequent eruptive activity suggests that another eruption can be expected within the next several decades. Consequently, the investigations in this volume are intended to provide both a means to better forecast future eruptive episodes and also an opportunity to formulate and test future hypotheses for magmatic and eruptive processes. Future eruptions may follow a course similar to those observed in 1976, 1986, and 2006. However, a major perturbation that upsets conditions within the magmatic system could occur, owing perhaps to the rise of a much larger or different parental magma or to a large edifice failure similar to the 1883 sector collapse. In such events, the comprehensive study of past eruptions will provide data critical to assessing the current state of the magmatic system.

In assembling this volume we have sought as consistent and accurate a portrayal of the 2006 eruption as possible. We have asked all authors to refer to the same basic eruption chronology, unless their observations and data require alternative explanations. Naturally, not all techniques or methodologies produce a completely consistent set of observations, nor do the precise conclusions in every paper support one another. We have grouped chapters on the basis of discipline. Papers that focus on specific techniques, methodology, or instrumentation are placed throughout the volume where they best fit with others that rely on their results.

We gratefully acknowledge the contributions of many reviewers and editorial assistance from Jim Hendley, Peter Stauffer, George Havach, Judy Weathers, Manuel Nathenson, Jan Zigler, and many others.

John A. Power, Michelle L. Coombs, and Jeffrey T. Freymueller

Contents

Chapters

Seismology

Geology of the 2006 Eruption

Other Geologic Investigations

Petrology and Geochemistry

Geodesy

Remote Sensing and Volcanic Emissions

Information Management

Note on Geographic Names on Augustine Island

Few place names on Augustine Island are formally recognized by the U.S. Board on Geographic Names (http://geonames.usgs.gov/). All place names associated with Augustine are informal with the exception of Burr Point, Augustine Creek, Augustine Island, and Augustine Volcano.

With the exception of the place names noted above, place names on Augustine Island are unofficial and only have capitalization for clarity. Within U.S. Geological Survey Professional Paper 1769 efforts have been made to consistently use place names on Augustine Island. The use of erroneous and unofficial names for Augustine Volcano—Mount Augustine and Mount Saint Augustine—has not been permitted except in historical quotations.

The map below shows many of the place names, both official and unofficial, used on Augustine Island.

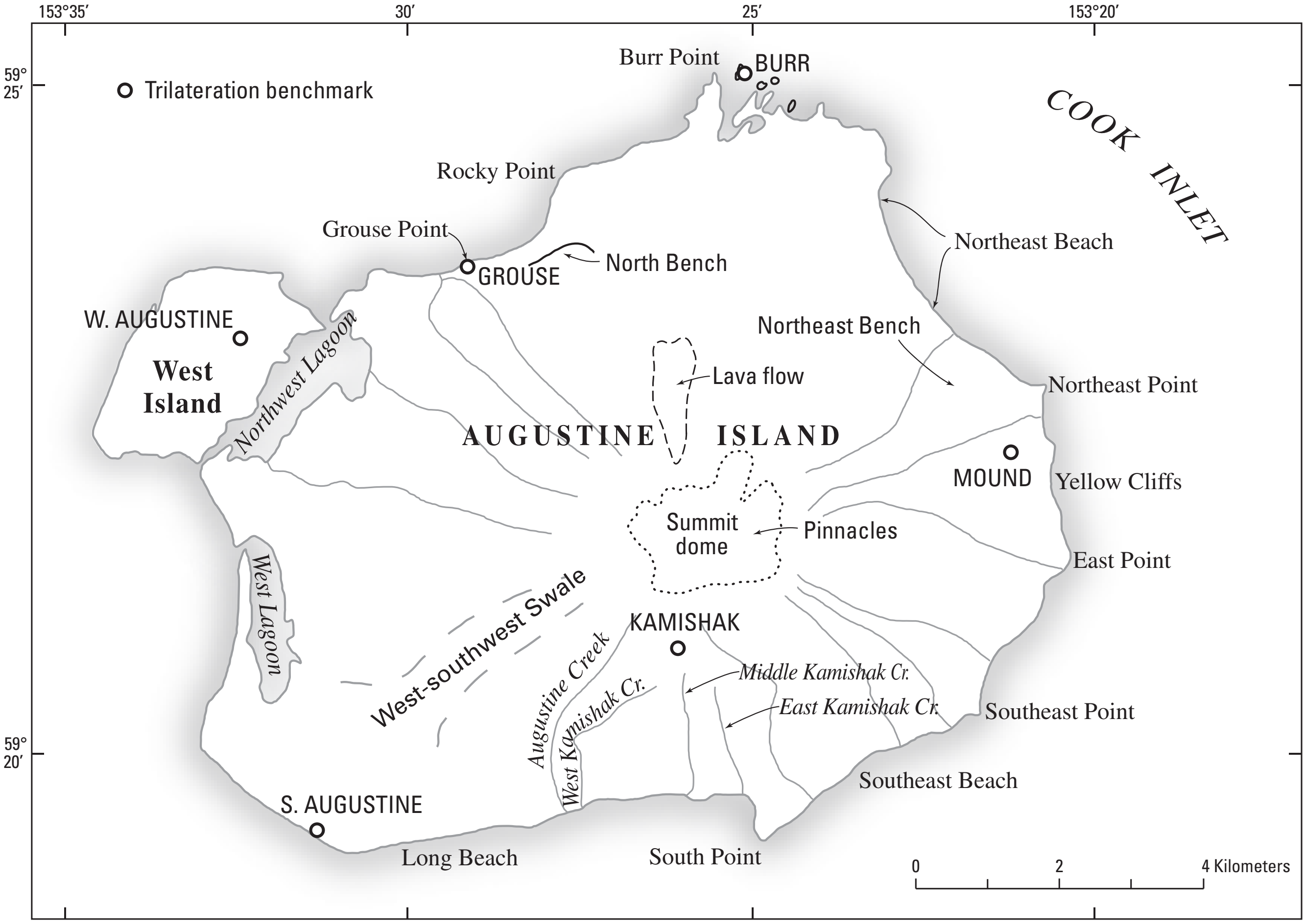

NOTE: All places names associated with Augustine are informal with the exception of Burr Point, Augustine Creek, Augustine Island, and Augustine Volcano. From Waitt, R.B., and Begét, J.E., 2009, Volcanic processes and geology of Augustine Volcano, Alaska: U.S. Geological Survey Professional Paper 1762 (http://pubs.usgs.gov/pp/1762/).

Seismology

Steam and minor ash plume rising above the summit of Augustine Volcano on January 12, 2006. View from the northwest Alaska Volcano Observatory photo by Game McGimsey.

The 2006 Eruption of Augustine Volcano, Alaska
Power, J.A., Coombs, M.L., and Freymueller, J.T., editors
U.S. Geological Survey Professional Paper 1769

Chapter 1

Seismic Observations of Augustine Volcano, 1970–2007

By John A. Power[1] and Douglas J. Lalla[2]

Abstract

Seismicity at Augustine Volcano in south-central Alaska was monitored continuously between 1970 and 2007. Seismic instrumentation on the volcano has varied from one to two short-period instruments in the early 1970s to a complex network comprising 8 to 10 short-period, 6 broadband, and 1 strong-motion instrument in 2006. Since seismic monitoring began, the volcano has erupted four times; a relatively minor eruption in 1971 and three major eruptions in 1976, 1986, and 2006. Each of the major eruptions was preceded by 9 to 10 months of escalating volcano-tectonic (VT) earthquake activity that began near sea level. The major eruptions are characterized seismically by explosive eruptions, rock avalanches, lahars, and periods of small repetitive low-frequency seismic events often called drumbeats that are associated with periods of lava effusion, and they all followed a similar pattern, beginning with an explosive onset that was followed by several months of discontinuous effusive activity.

Earthquake hypocenters were observed to move upward from near sea level toward the volcano's summit over a roughly 9-month period before the 1976 and 1986 eruptions. The 1976 eruption was preceded by a small number of earthquakes that ranged in depth from 2 to 5 km below sea level. Earthquakes in this depth range were also observed following the 2006 eruption. The evolution of earthquake hypocenters associated with the three major eruptions, in conjunction with other supporting geophysical and geological observations, suggests that the Augustine magmatic system consists of a deeper magma source area at about 3.5 to 5 km below sea level and a shallower system of cracks near sea level where volatiles and magma may temporally reside as they ascend to the surface. The strong similarity in seismicity and character of the 1976, 1986, and 2006 eruptions suggests that the processes responsible for magma generation, rise, and eruption at Augustine Volcano have been roughly constant since the early 1970s.

Introduction

Continuous seismic monitoring of Augustine Volcano began in the summer of 1970 and has continued to the present. During this 38-year period Augustine has experienced a minor eruptive event in 1971 and three major eruptions in 1976, 1986, and 2006, as well as long periods of relative seismic quiescence characterized by low-level earthquake activity. The major eruptions were all preceded by roughly 9 months of increased volcano-tectonic (VT) earthquake activity and were characterized by an explosive onset lasting several days to weeks that was followed by several months of episodic effusive activity. The eruptions are characterized by complex sequences of seismic events involving VT and long-period (LP) events, as well as seismic signals from explosions, pyroclastic flows, lahars, rock falls and avalanches, and small shallow repetitive earthquakes (see "Augustine Seismicity" section for definitions). The three major eruptions were remarkably similar in terms of the character of eruptive style, the sequence of eruptive events, and the character of associated seismicity. The similarities in seismic activity and eruptive behavior during these three eruptions suggests that the processes that govern production, ascent, and eruption of magma at Augustine have remained roughly constant or changed only slowly over the 38-year period of instrumental data available for this volcano.

As a result of the volcano's frequent eruptive activity, the associated volcanic hazards, and proximity to communities surrounding Cook Inlet, Augustine has a relatively long history of geologic investigation and seismic monitoring for an Aleutian arc volcano. Augustine's frequent eruptive activity, coupled with magmas recently ranging in composition from high-silica andesite (57 weight percent SiO_2) to dacite (64 weight percent SiO_2), make this volcano an excellent location to study the seismic expression of the processes that govern

---

[1] Alaska Volcano Observatory, U.S. Geological Survey, 4200 University Drive, Anchorage, AK 99508.

[2] 5106 Wesleyan Drive, Anchorage, AK 99508.

and accompany the accumulation, ascent, and eruption of higher viscosity magmas that are typical of explosive volcanism in a convergent margin setting.

In this paper we review the long-term seismic observations of Augustine Volcano between 1970 and 2007 and develop a conceptual model of the subsurface magmatic system. We begin with a review of the seismic instrumentation deployed on and around Augustine Island as a function of time. We then discuss the characteristics of seismicity observed during quiescent, precursory, and eruptive periods. This characterization relies principally on seismic measurements, such as the earthquake locations, magnitudes, waveform character, and durations of seismic signals associated with explosion events and lava effusion. We then develop detailed seismic chronologies of the activity surrounding the 1976, 1986, and 2006 eruptions. We offer a volcanological interpretation of the patterns of observed seismicity in combination with associated observations reported by other workers. We conclude with a discussion of the role that seismic observations played in forecasting the 2006 eruptions and make recommendations for evaluating future episodes of unrest through seismic investigations of Augustine Volcano.

Background

Augustine Volcano is a 1,200-m-high stratovolcano located on a small (8 x 11 km) island roughly 280 km southwest of Anchorage, Alaska (fig. 1). Augustine Volcano consists of a central complex of summit lava domes and flows surrounded by an apron of pyroclastic, lahar, avalanche, and ash deposits. The volcano is frequently active, with major eruptions recorded in 1883, 1935, 1963–64, 1976, 1986, and 2006. Minor eruptive events were reported in 1812, 1885, 1908, 1944, and 1971. The large eruptions are characterized by an explosive onset followed by the quieter effusion of lava. The three most recent eruptions in 1976, 1986, and 2006 had explosive onsets lasting from 4 to 18 days and included numerous individual vulcanian explosions that produced large ash plumes reaching altitudes of 10–15 km. Pyroclastic flows generated during these events swept down the flanks of the volcano, often reaching the surrounding waters of Cook Inlet. The quieter effusion of magma that generally followed the explosive onsets formed summit lava domes and/or short blocky flows that moved down the steep upper portions of the volcanic cone. Effusive activity typically occurred episodically over a period of 2 to 6 months and was often accompanied by block and ash flows produced when portions of the growing lava dome and flows became oversteepened and failed. Estimated eruptive volumes for the 1976, 1986, and 2006 eruptions are 0.39 km^3 (Kienle and Swanson, 1985), 0.10 km^3 (Holasek and Rose, 1991), and 0.12 km^3 (Coombs and others, this volume), respectively.

Geologic deposits on Augustine Island suggest that the present volcanic cone began to form more than 40,000 years ago (Waythomas and Waitt, 1998). Deposits from at least 13 major debris avalanches younger than 2,500 years are exposed on the sea cliffs surrounding Augustine Island, and they indicate that the Augustine cone is subject to frequent Bezymianny-style collapses similar to that of Mount St. Helens in 1980 (Gorshkov, 1959; Siebert and others, 1995). The most recent collapse and debris avalanche occurred during the 1883 eruption and generated a small tsunami in southern Cook Inlet (Waythomas and Waitt, 1998). Augustine's eruptive history during the Holocene is described by Waitt and Begét (2009).

Recent Augustine magmas are compositionally heterogeneous, with whole rock compositions ranging from basaltic andesites to dacites (56–64 weight percent SiO_2) (Johnston, 1978; Daley, 1986; Harris, 1994; Roman and others, 2006; Larsen and others, this volume). Roman and others (2006) suggest that the compositional heterogeneity of magmas erupted in 1986 resulted from the mixing of a cooler dacitic magma (residual from the 1976 eruption) and a newly injected more mafic magma. Progressive homogenization was not observed. Roman and others (2006) proposed that the mixing event took place in a network of dikes extending from roughly 2 to 5 km depth that prevented progressive homogenization throughout the 1986 eruption. Larsen and others (this volume) suggest the 2006 eruption was triggered by a similar mixing event that occurred at 3.5 to 5 km below mean sea level (b.m.s.l.)

In 1975, Augustine Volcano was the target of an extensive geophysical investigation that included temperature and heat flow measurements (Kienle and others, 1979), active and passive seismic investigations (Pearson, 1977), and an aeromagnetic survey (Barrett, 1978). The results of these investigations are summarized by Kienle and others (1979). The active seismic experiment involved the firing of 10 chemical shots that were recorded on 14 temporary, as well as the 5 permanent seismic stations. Data from this field experiment combined with data from exploratory wells drilled in southern Cook Inlet and a short seismic refraction line along Augustine's north shore were used to determine a three-dimensional velocity structure of the volcano (Kienle and others, 1979). The elements of this model are described in detail by Lalla and Power (this volume).

Augustine has also been the focus of a long-term program to monitor ground deformation. Between 1986 and 1989 a trilateration network was established that consisted of 19 benchmarks and 30 slope distances measured with an electronic distance measurement (EDM) device and zenith angles measured at six instrumentation stations (Power and Iwatsubo, 1998). This network was partially remeasured using the global positioning system (GPS) in 1992, 1993, 1994, 1995, and 1996. A complete reoccupation of the network with the inclusion of two benchmarks on the western shore of Cook Inlet was completed in 2000 (Pauk and others, 2001). A network of three telemetered single frequency continuous GPS (CGPS) receivers was established on the island in 1992 (Dzurisin and others, 1994), and a dual frequency receiver was added in 2000. These surveys and instruments indicated that the Augustine edifice was stable and not deforming above the precision of the measurements between 1986 and 2000. A portion of the 1986 summit lava dome was found to be subsiding at roughly 8 cm per year, however. This movement was attributed to a landslide block that formed the northern portion of the 1986 lava dome (Pauk and others, 2001). Synthetic aperture radar (InSAR) measurements of the volcano between 1992 and 2005 also indicate that the broader edifice has inflated during this period (Lee and others, this volume). In 2004 a network of five CGPS receivers was installed on the island as part of the National Science Foundation funded EarthScope program (Pauk and others, this volume).

Seismic Instrumentation, Recording and Analysis

Seismometers have been in operation on Augustine Island since 1970 (Harlow, 1971), with only minor gaps in data resulting from station and telemetry failures. A summary of seismic stations operated on Augustine Island between 1970 and 2007 is contained in table 1. The first permanent seismometer, AU1, was installed on the north flank of Augustine Volcano in 1970. By 1972 seismic instrumentation on the island had expanded to a five-station network capable of calculating standard earthquake hypocenters and magnitudes (fig. 2*A*). A number of other seismic stations (OPT, CKK, HOM, CDD, MMN) were installed surrounding southern Cook Inlet in the early 1970s to monitor regional earthquake activity (fig. 1) (Kienle and Swanson, 1983). All of these stations were 1-Hz short-period instruments that used standard analog telemetry. Unfortunately, all stations on Augustine Island failed in late December 1975 as a result of heavy winter storms and did not record the final month of the 1976 eruption's precursory seismicity. Three of these stations were repaired in February 1976, and a network of new stations was established in 1978.

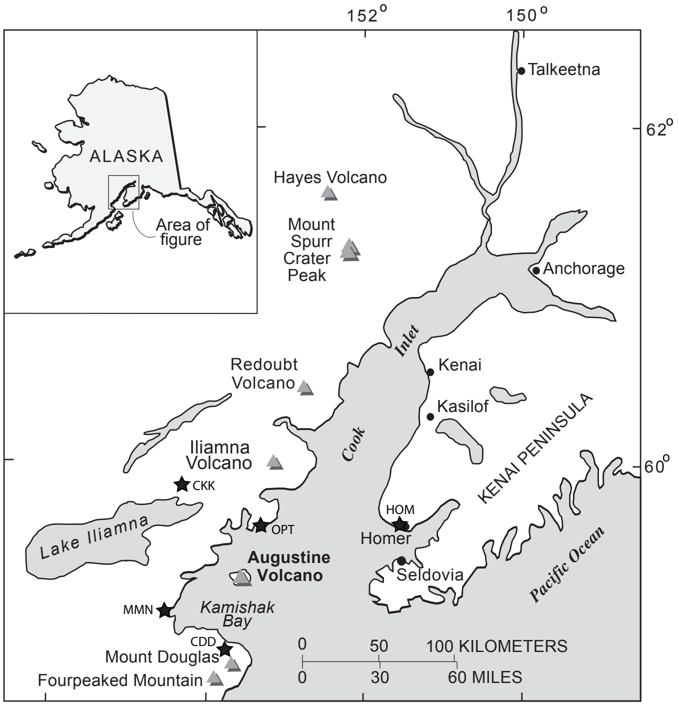

Figure 1. Map showing the location of Augustine Volcano relative to other volcanoes and to population centers in the Cook Inlet region of Alaska. Stars indicate locations of seismic stations CKK, OPT, MMN, CDD, and HOM.

The new four-station network established in 1978 (fig. 2*B*) operated through the 1986 eruption. Station AUT was added to the network on March 22, 1986, just 4 days before the 1986 eruption began (Power, 1988). No seismic stations were destroyed or disabled by volcanic activity in 1986.

Following the 1986 eruption the Augustine seismic network was reconfigured initially with five stations in 1987 and then eventually expanded to nine permanent short-period stations in the early 1990s (table 1). Most of these new stations were placed surrounding the 1986 summit lava dome to track shallow microearthquake activity (fig. 2*C*). A broadband seismometer, AUB, was initially co-located with station AUL in 1995. In 1998 the broadband components were renamed to be part of AUL (table 1).

The 2006 eruption disabled or destroyed stations AUS, AUR, AUP, AUH and AUL (fig. 2*C*). New stations AUSE and AUNW were installed on February 10 and March 30, 2006, respectively, to augment the impaired network, and station AUH was repaired on August 7. AUL and AUP were reestablished on September 4 and 6, 2006, respectively. A strong-motion instrument, AU20, was deployed on the island on January 9, 2006, and replaced by AU22 on September 1, 2006. A six-station temporary network of broadband seismometers, AU10 through AU15, was installed on Augustine Island (fig. 2*C*) in December of 2005 in response to increasing earthquake activity (Power and others, 2006). Three of these instruments operated throughout the 2006 eruption. Station AU12 operated until 0329 Alaska Standard Time (AKST) on January 30, 2006, when it was overrun by a pyroclastic flow, and station AU11 stopped recording data on February 11 as a result of water damage to the seismometer. Station AU10 failed as a result of water damage and did not return any useable data (table 1).

From 1970 through 1985, data from each of the Augustine Island seismic stations was telemetered to Homer, Alaska (fig. 1) and recorded on 16-mm photographic film. Film was read back on a Geotech 6585 film viewer that allows the arrival times from seismograms to be read at a scale of 1 s/cm. The primary limitation of this system is that individual events can be difficult to recognize during intense periods of earthquake or eruptive activity when adjacent traces overlap on the film. Starting in January 1986 the signals were relayed by leased telephone circuits to the Geophysical Institute in Fairbanks and were recorded on photographic film until April 1, 1989. A variety of specialized digital recording systems were used to track the seismic activity during the 1986 Augustine eruption (Power, 1988). Beginning on July 1, 1988, the data were digitally recorded on a number of computerized acquisition systems at the Geophysical Institute. In October 1989, AVO began to record Augustine data on an RSAM system (Endo and Murray, 1991) and intermittently on an event-detected IASPEI system (Lee and others, 1988). On January 1, 1994, the AVO expanded the number of channels on the IASPEI system and began to consistently record event-detected data at 100 samples per second (Jolly and others, 1996). An Earthworm acquisition system replaced the IASPEI system on March 1, 2002, and AVO began to maintain both an event-detected and a continuous archive of seismic data (Dixon and others, 2004).

From 1972 through December 1975, all earthquakes that had identifiable P-arrivals on four or more stations in the Augustine network were located. A total of 678 earthquakes were located during this period. From July 1985 through March 1986, 421 hypocenters were calculated, which is roughly twelve percent of the total number of events that were estimated to have occurred. The selected subset is thought to be representative of the entire population of earthquakes from this interval (Power, 1988). Since 1993 we have relied on the computerized acquisition systems to identify locatable earthquakes. When the detection algorithm identified several shocks closely spaced in time, hypocenters were calculated for all possible earthquakes based on a manual review of the event detected data. From 1993 through 2007, AVO cataloged 3,866 earthquakes at Augustine Island. The details of these locations can be found in a series of annual reports; the most recent is compiled by Dixon and Stihler (2009). From January 1976 to July 1985 and April 1986 to January 1993, hypocenters were not routinely calculated at Augustine Volcano (fig. 3).

From 1989 to the present, events detected by the various AVO seismic acquisition systems were processed using the interactive analysis program XPICK (Robinson, 1990) and the earthquake location program HYPOELLIPSE (Lahr, 1999) in a manner similar to that described by Lahr and others (1994). All detected earthquakes with more than three P and two S phases and with standard hypocentral errors less than 15 km were processed and saved in the AVO earthquake catalog (Dixon and Stihler, 2009). Located events were classified as VT, LP, shore-ice events, or unknown based on the time-domain appearance of the velocity seismogram as viewed on a computer screen. Of the of 3,866 located shocks, AVO classified 3,795 as VT earthquakes, 28 as LP events, and 43 as shore- or sea-ice events between 1993 and the end of 2007. Earthquakes with a P- and S-wave separation of more than 5 seconds on Augustine Island stations were assumed to come from a source other than the volcano and were not located.

We use two location techniques to calculate earthquake hypocenters for this study. The first uses the program HYPOELLIPSE (Lahr, 1999) in a similar fashion to the standard AVO earthquake catalog (Dixon and others, 2008). In both location techniques, hypocentral depths are referenced to sea level, with negative depths reflecting height above mean sea level (a.m.s.l.). For this study we use a one-dimensional

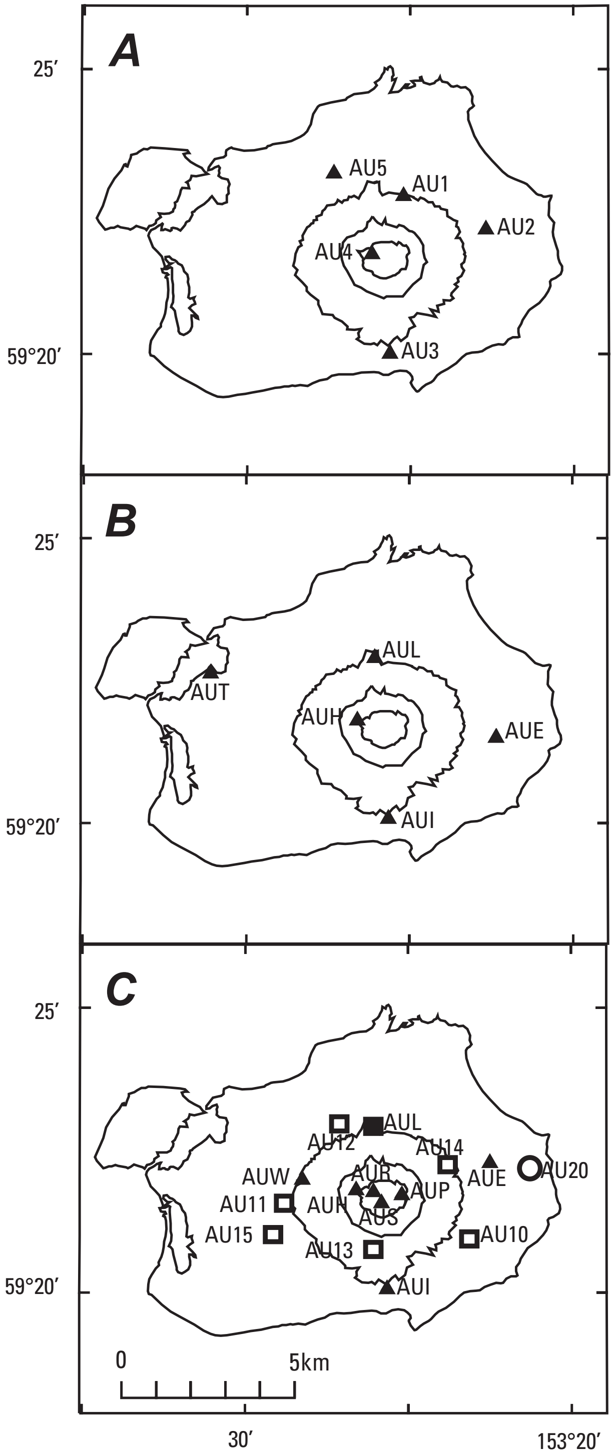

Figure 2. Maps showing the locations of seismic stations on Augustine Volcano before (*A*) the 1976 eruption, (*B*) the 1986 eruption, and (*C*) the 2006 eruption. Solid triangles represent short-period stations, solid squares represent permanent broadband sensors, open squares are temporary broadband stations deployed in late 2005, and the open circle is a strong motion instrument deployed in early 2006. Sea-level, 1,000-ft, 2,000-ft, and 3,000-ft contours are shown in map view.

Table 1. Seismic stations operated on Augustine Island between 1971 and 2007.

Station	North Latitude[1]	West Longitude[1]	Elevation (m)	Installation Date	Termination Date
AU1	59 22.39	153 25.23	508	08/01/1970	01/01/1976
AU2[2]	59 22.22	153 22.68	195	06/15/1971	01/01/1976
AU3	59 20.05	153 25.62	282	1972	04/06/1978
AU4	unknown	unknown	unknown	1972	07/1974
AU4[3]	59 21.79	153 26.19	890	07/1974	01/01/1976
AU5	59 23.19	153 27.35	152	1972	01/01/1976
AUI[4]	59 20.11	153 25.66	293	04/06/1978	current
AUH[5]	59 21.83	153 26.59	890	12/01/1978	current
AUL[6]	59 22.937	153 26.142	360	08/27/1978	current
AUE	59 21.531	153 22.365	172	10/29/1980	10/01/1988
AUE[7]	59 22.309	153 22.50	168	10/01/1988	current
AUP[8]	59 21.805	153 25.210	1033	06/26/1988	current
AUS[9]	59 21.599	153 25.840	1226	09/01/1990	01/11/2006
AUW	59 22.205	153 28.249	276	107/01/986	current
AUC	59 21.596	153 25.469	1175	09/13/1995	12/27/2000
AUR[9]	59 21.766	153 25.876	1204	11/01/1995	01/11/2006
AUB[10]	59 22.937	153 26.142	360	12/21/1995	09/28/1998
AUSE	59 20.481	153 23.850	152	02/10/2006	current
AUNW	59 22.694	153 28.609	160	03/30/2006	current
AU10[11]	59 20.974	153 23.126	219	12/20/2005	12/20/2005
AU11	59 21.576	153 28.818	234	12/20/2005	02/11/2006
AU12[12]	59 23.009	153 27.114	210	12/20/2005	01/30/2006
AU13	59 20.781	153 26.046	518	12/20/2005	05/30/2006
AU14	59 22.268	153 23.811	303	12/21/2005	08/07/2006
AU15	59 21.042	153 29.134	168	12/21/2005	08/10/2006
AU20	59 22.216	153 21.245	102	01/01/2006	08/31/2006
AU22	59 22.247	153 21.301	105	09/01/2006	current

[1] Datum is NAD27; numbers are in degrees and decimal minutes.

[2] Station had a single horizontal component of unknown orientation.

[3] Station relocated in July 1974, but name retained.

[4] Horizontal components added in 1987.

[5] Station destroyed by explosion on January 27, 2006, repaired August 7, 2006.

[6] Station destroyed by explosion on January 27, 2006, reinstalled on September 4, 2006.

[7] Station relocated on October 1, 1988, but name retained.

[8] Station destroyed by explosion on January 13, 2006, reinstalled on September 6, 2006.

[9] Station destroyed by explosion on December 15, 2006.

[10] Broadband station that replaces short-period station AUL on September 28, 1998.

[11] Station did not function properly and returned no useful data.

[12] Station overrun by a pyroclastic flow on January 30, 2007, data recovered from seismometer on August 15, 2006.

velocity model with six horizontal layers with boundaries at depths of −1.2, −0.7, 0.0, 1.0, 9.0, and 44.0 km. The top of the model at –1.2 km depth corresponds roughly with the summit of the volcano. The respective P-wave velocity for each layer is 2.3, 2.6, 3.4, 5.1, 6.3 and 8.0 km/s. These layer boundaries and velocities were determined using the results of the 1975 active source seismic experiment (Kienle and others, 1979) and were found to minimize residuals in a number of test runs of HYPOELLIPSE. For the precursory seismic sequences of the 1976, 1986, and 2006 eruptions we have then relocated the hypocenters using the two-dimensional ray tracing procedure described by Lalla and Power (this volume). This relocation technique uses the three-dimensional velocity model derived by Kienle and others (1979) for Augustine Island and station corrections calculated from the 1975 active source seismic experiment (Lalla and Power, this volume). This technique calculates theoretical traveltimes from grid points with a 0.25-km grid spacing embedded within the Augustine velocity structure and assigns the hypocenter to the grid point that most closely matches the observed arrival times. This technique accounts for the topography of the volcanic edifice when calculating traveltimes and allows hypocenters to be located above sea level. An evaluation of the accuracy of hypocenter determination using this technique indicates that hypocenters can be resolved within 0.25 km for shocks located above sea level and within 0.5 km for shocks located from sea level to 2 km b.m.s.l. (Lalla and Power, this volume). We have chosen this relocation technique for this study as it can be applied in a similar manner to the seismic data collected by both the analog and digital acquisition systems in use during the 1976, 1986, and 2006 eruptions of Augustine. Additionally, this relocation technique provides a means to determine absolute rather than relative locations. Deshon and others (this volume) studied earthquake families using waveform cross correlation techniques between 1993 and 2006. They found multiple earthquake families that occurred between 1993 and 2006

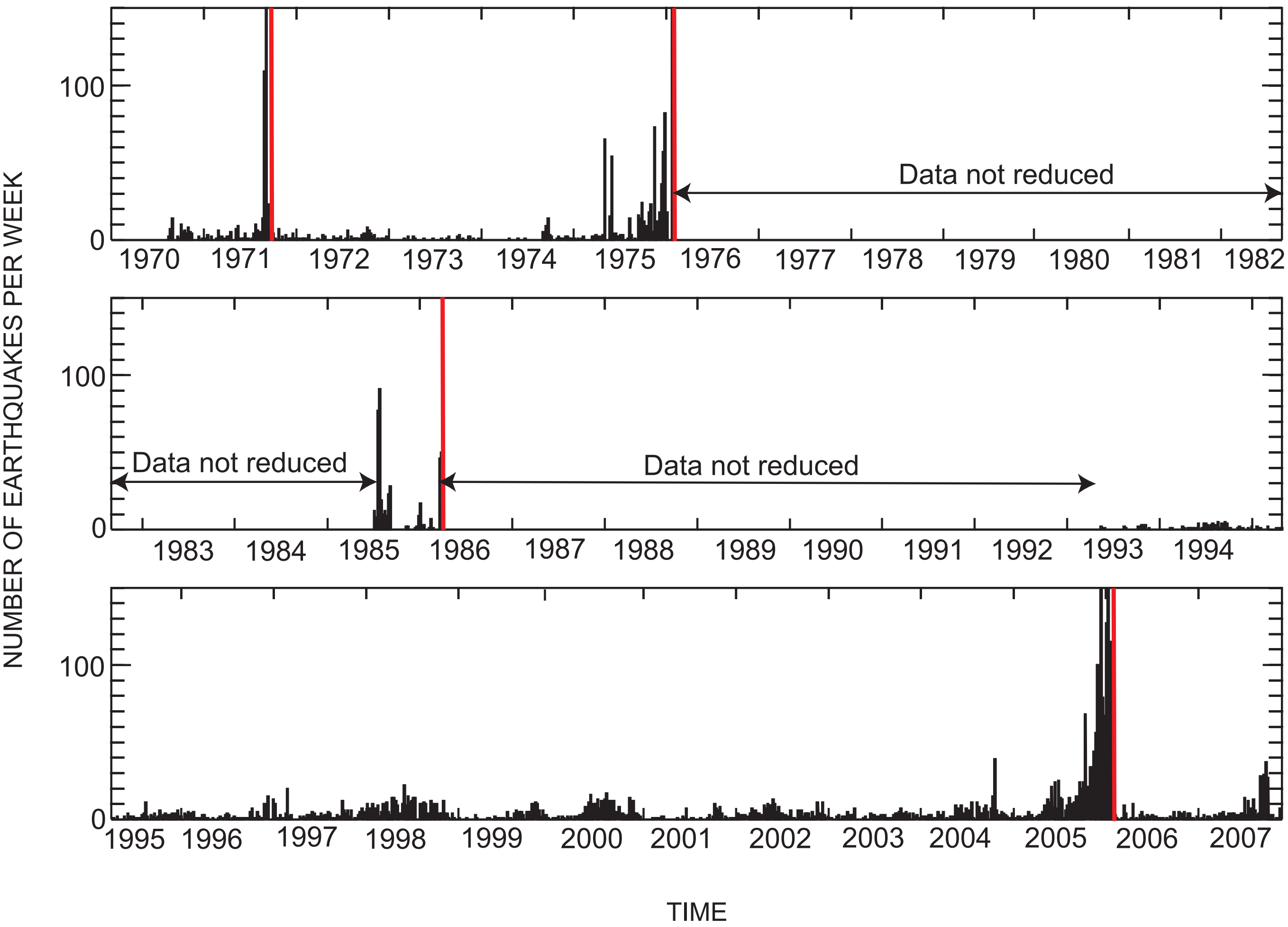

Figure 3. Histograms of the number of earthquakes located at Augustine Volcano per week between 1970 and 2007. Before installation of the full network in 1972 (table 1), data simply reflect number of earthquakes detected. Periods when earthquakes were not routinely located (January 1976 to July 1985 and March 1986 to May 1993) are noted. Red lines correspond to onsets of eruptions in 1971, 1976, 1986, and 2006.

and identified several families that occurred at progressively shallower depths in the weeks prior to the onset of eruptive activity in 2006.

Earthquake magnitudes at Augustine were calculated using several methodologies during the period of this study. From 1970 through 1976 a coda magnitude scale was used for earthquakes located beneath the central volcanic edifice, above 0.25 km a.m.s.l. For earthquakes at greater depth or those with hypocenters located away from the central edifice a local magnitude (M_L) was calculated using frequency-amplitude measurements in the manner described by Lahr (1999). This methodology was adopted to overcome strong attenuation affects observed for earthquakes with deeper hypocenters (Lalla and Kienle, 1978). For larger earthquakes that clipped all local stations on Augustine Island during this period, local magnitudes were determined at station CKK (fig. 1) assuming a hypocentral depth of sea level. Since 1985 we use frequency-amplitude measurements to calculate M_L using HYPOELLIPSE (Lahr, 1999). These methodologies were chosen to provide the most reliable magnitude information possible given the data available during the respective time period. During intereruptive periods, the largest earthquakes at Augustine generally do not exceed magnitude 1.2. The largest earthquakes recorded at Augustine during the period of this study reached magnitude 2.75 and occurred on January 22 and 23, 1976, in a 22-hour sequence that accompanied the onset of explosive activity in 1976 (fig. 4). A study of *b* values for Augustine earthquakes between 1993 and 2007 is given by Jacobs and McNutt (this volume).

Augustine Seismicity

The dominant seismic activity seen at Augustine Volcano between 1970 and 2007 are small VT earthquakes. These events generally have impulsive to emergent P arrivals and

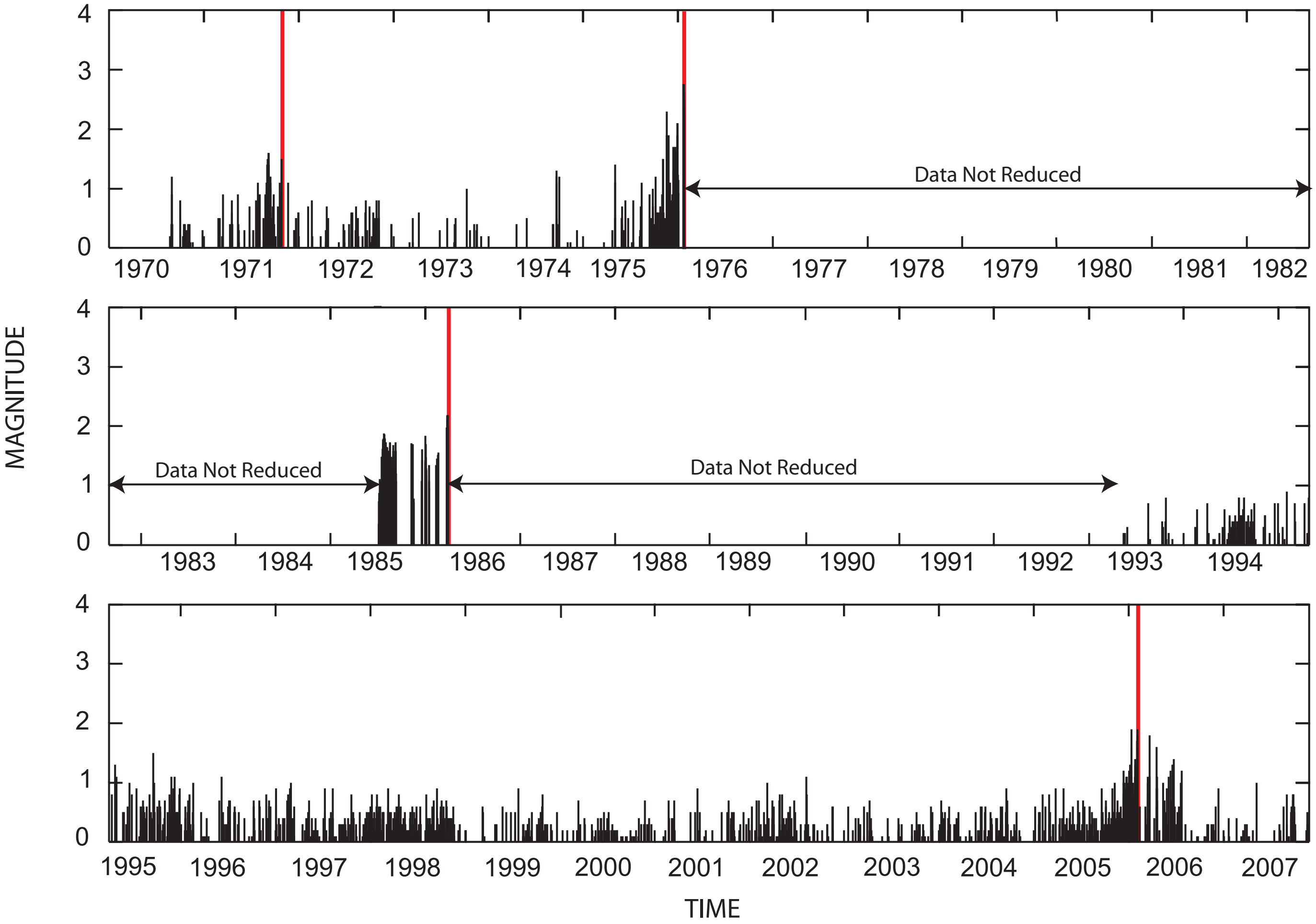

Figure 4. Summary of the magnitudes of detected earthquakes located at Augustine Volcano between 1970 and 2007. Magnitudes that are greater than magnitude (M_L) 0.0 are shown as individual vertical lines. Periods when earthquakes were not routinely located (January 1976 to July 1985 and March 1986 to May 1993) are noted. Red lines correspond to onsets of eruptions in 1971, 1976, 1986, and 2006.

poorly defined S arrivals and a broad spectrum with significant energy between 1 and 15 Hz (fig. 5*A*). At Augustine, waveforms from these earthquakes have well-defined phases on stations located high on the volcanic edifice, and the waveforms degrade rapidly on stations located on the pyroclastic apron (fig. 6). During intereruptive periods epicenters of these earthquakes generally occur within 1 to 2 km of the volcano's summit and range in depth from 1 km b.m.s.l. to 1.2 km a.m.s.l. (the volcano's summit). Infrequently, small VT earthquakes also occur on the south and north flanks of the volcano (fig. 7). Deshon and others (this volume) found that only 30 to 40 percent of located earthquakes occurred in event clusters, or earthquake families, between 1993 and 2006, suggesting that VT earthquake activity is widely distributed throughout the Augustine cone during this period.

At Augustine, LP events are comparatively rare; their occurrence is generally restricted to periods surrounding eruptive episodes. These events usually have emergent to poorly developed phases and have a strong peak frequency near 2 Hz (fig. 5*B*). Well-recorded LP events locate within 1 to 2 km of the volcano's summit at depths of sea level or above. At Augustine we also see a variety of waveforms that have a mix or range of frequencies similar to the hybrid events described by Lahr and others (1994). In this report we do not attempt to classify events as hybrids. Studies of event classifications during the 2006 eruption are given by Buurman and West (this volume) and Jacobs and McNutt (this volume).

Several times during the 1986 and 2006 eruptions, we recorded sequences of small repetitive regularly spaced events that often had similar waveforms. These earthquakes can occur at rates that range from 1 event every few minutes to as high as 8 to 10 events per minute or possibly higher. Similar small repetitive events have been reported at numerous volcanoes, typically during the effusive eruption of magma that ranges from high-silica andesite to dacite in composition. These volcanoes include Mount Usu, Japan (Okada and others, 1981), Mount St. Helens (Fremont and Malone, 1987; Moran and others, 2008; Thelen and others, 2008), Mount Redoubt (Power and others, 1994), Guagua Pichincha, Ecuador (Villagomez, 2000), and Soufriere Hills Volcano, Montserrat (Rowe and others, 2004). As a result of the repetitive character of these earthquakes they have recently been termed "drumbeats" at Mount St. Helens (Moran and others, 2008). At Augustine, drumbeat earthquakes typically have poorly defined phases and fairly narrow spectra, with most energy concentrated between 1 and 6 Hz (fig. 5*C*).

Seismic signals generated by explosive eruptions at Augustine generally have emergent onsets, extended high-amplitude codas, and fairly broad spectrums with peak frequencies near 2 to 3 Hz (fig. 5*D*). Explosive eruptions generally are quite powerful and register well on distant stations such as OPT and CKK (fig. 1). At Augustine, explosive eruptions are often accompanied by seismic signals associated with pyroclastic flows and lahars. These signals generally have a broad spectrum and can be very strong on individual stations on various quadrants of the volcano. A parametric study of explosive eruptions at Augustine in 2006 has been prepared by McNutt and others, (this volume).

Seismic signals from rock avalanches or rockfalls observed at Augustine are generally emergent and have a broad spectrum with energy between 1 and 6 Hz (fig. 5*E*). These signals are most prevalent when the lava dome and associated flows are actively growing and shedding material down the steep upper flanks of the volcano.

A unique type of low-frequency seismic event generated at Augustine results from the interaction of shore–fast sea ice and the ocean tides. During periods of cold winter weather (−15 to −30° C or 5 to −20° F), low frequency seismic events with emergent waveforms, a distinct lack of identifiable phases, and extended codas are often observed. The dominant frequency of these events is generally between 1 and 5 Hz (fig. 5*F*). The largest amplitudes occur on the stations closest to the shoreline and the seismic waves generally do not propagate well enough to be identified on stations high on the volcanic edifice or on the opposite side of the island. Between 1993 and 2007 we have observed these events being generated on all quadrants of the island, although they seem to be most often observed at station AUI (fig. 2*B*), suggesting a frequently active source area along the southern shoreline. We have visited the island when these events were occurring in February 1993 and March 2007 and have noted large accumulations of sea ice along the island's coastline. Mauk and Kienle (1973) found that events with these characteristics were most common during the ocean tide high, although they attributed them to volcanic activity. Because we only observe these events during periods of very cold weather, we believe they most likely reflect the breakage or movement of shore fast sea ice in response to the changing ocean tides in Cook Inlet. A similar explanation was advanced by Lalla and Kienle (1980).

Eruption Chronologies

In this section we describe the sequence of seismic events that accompanied the minor eruption in 1971 and the major eruptions in 1976, 1986, and 2006. For these chronologies we combine seismic information with visual, geological, and geophysical observations of the volcano to provide as much context for the seismic observations as possible. We focus on the periods from the time when seismicity first began to increase to the time when unrest ceased following the eruption. These periods are August 30, 1971, to December 21, 1971; May 2, 1975, to April 24, 1976; July 5, 1985, to September 10, 1986; and April 30, 2005, to March 18, 2006. The number of located earthquakes and the reported periods of eruptive activity for the 1976, 1986, and 2006 eruptions are shown on a comparative time scale in figure 8. In this paper the times of specific events are referenced to either Alaska Standard Time (AKST) or Alaska Daylight Time (AKDT). To convert to UTC before January 1, 1983, subtract 10 hours

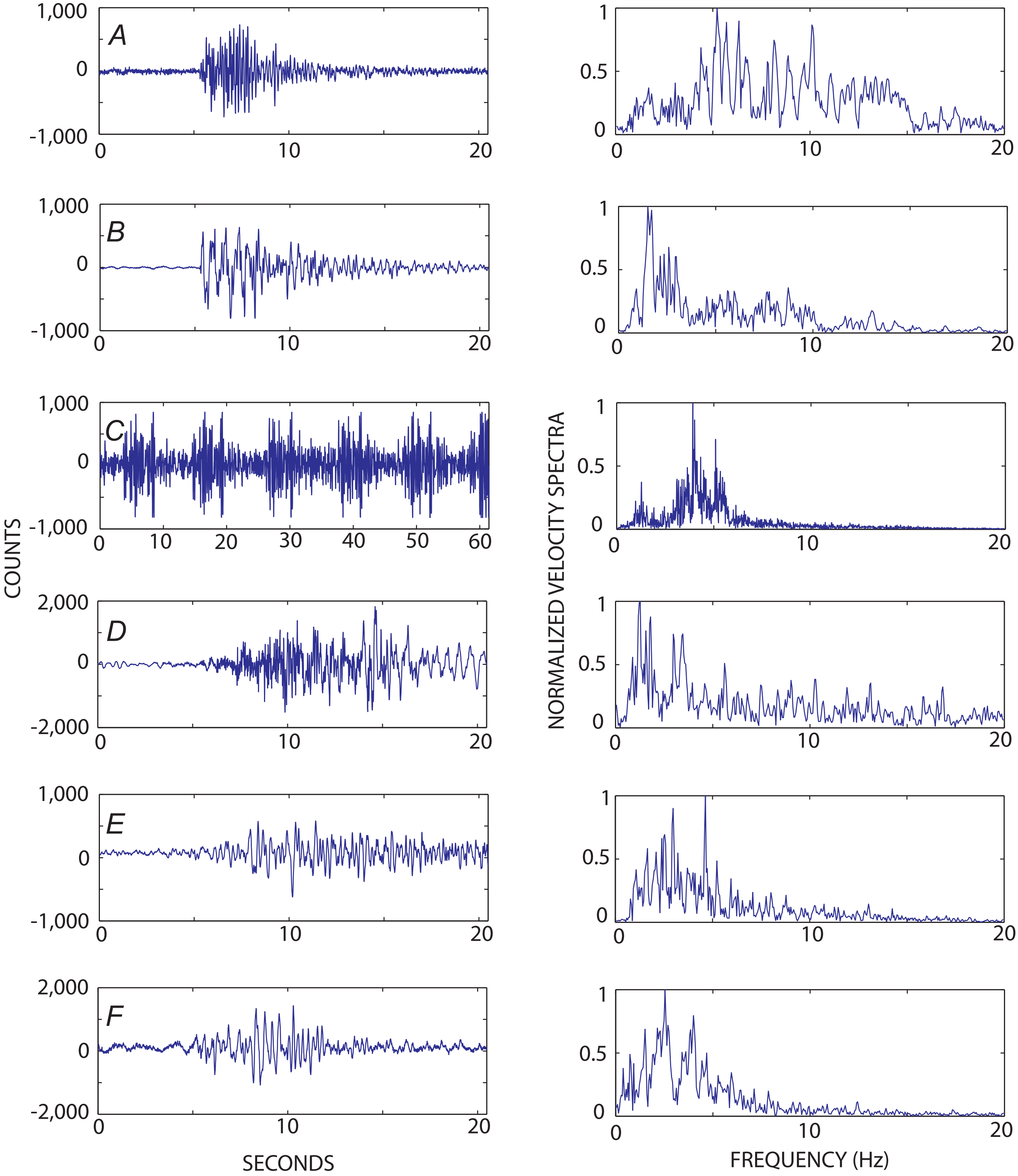

Figure 5. Waveforms and normalized velocity spectra of typical seismic events recorded at Augustine Volcano. Individual events represent, (*A*) volcano-tectonic earthquake at station AUH on May 26, 2005, 1601 AKST, $M_L = 0.2$, Z = 0.98 km a.m.s.l., station; (*B*) long-period event at station AUH on October 10, 2005, 0410 AKST, ML = 0.2, Z = 0.48 km a.m.s.l.; (*C*) drumbeats at station AUW on March 8, 2006, 1500 AKST; (*D*) explosion recorded at station AU13 on January 11, 2006, at 0514; (*E*) Rockfall on station AUE May 26, 2006, 0006 AKST; (*F*) ice event seen at station AUI on January 10, 2005, 1948 AKST. Spectra were calculated using a 20.48 second sample, except for the drumbeat earthquakes shown in panel *C*, which uses a 61.44-second sample.

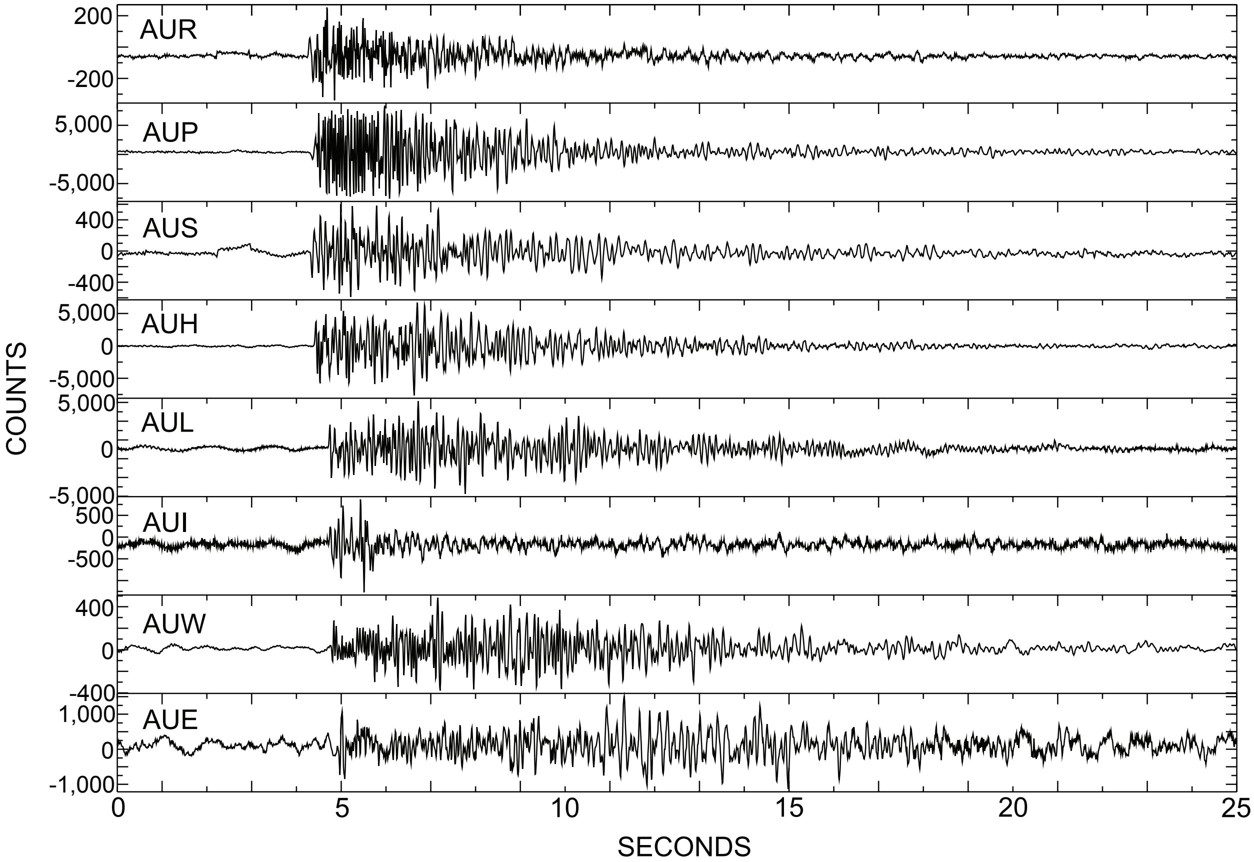

Figure 6. Velocity waveforms of a volcano-tectonic earthquake with magnitude (M_L) 0.1 that occurred on October 10, 2005, at 0037 UTC at a depth of 0.22 km a.m.s.l. beneath the summit of Augustine Volcano as recorded on various seismic stations on Augustine Island.

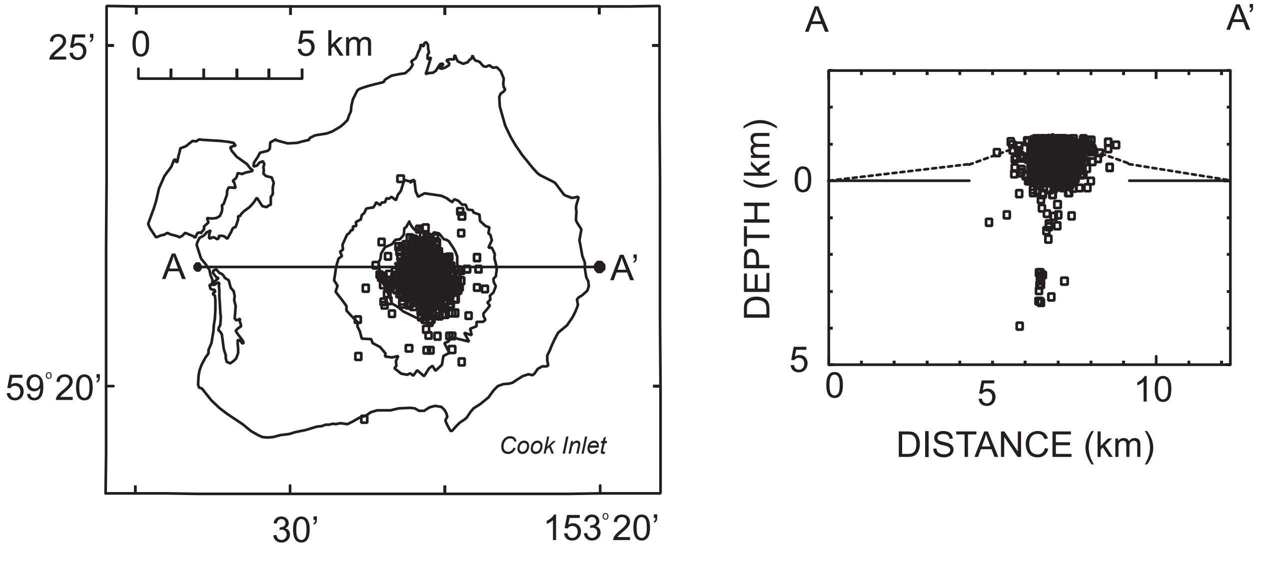

Figure 7. Map and west-east cross section (A to A') showing earthquake hypocenters at Augustine Volcano between 1993 and 2007. Only hypocenters with standard horizontal and vertical errors of less than 5 km are shown. Sea level, 1,000-ft and 2,000-ft contours are shown in map view. Dotted line in cross section represents approximate surface elevation along cross section A–A'. The hypocenters between 2 and 4 km depth all occurred between March 15 and August 16, 2006, following the end of the 2006 eruption.

from AKST and 9 hours from AKDT. After January 1, 1983, subtract 9 hours AKST and 8 hours from AKDT.

To provide a consistent measure of earthquake activity during these precursory seismic sequences we have relocated many earthquakes with the 2-dimensional ray tracing algorithm described by Lalla and Power (this volume). This was not possible for the 1971 eruption, because only two stations were operating on the volcano at that time. Histograms of the number of relocated earthquakes per day during the precursory sequences of the 1976, 1986, and 2006 eruptions are shown in figure 9. Relocated earthquake hypocenters for each precursory period are shown in map and east-west cross section in figure 10, and plots of focal depth versus time are shown in figure 11. Seismic events such as explosive eruptions, rock avalanches, and pyroclastic flows are more difficult to describe because the seismic stations operating on the volcano and the

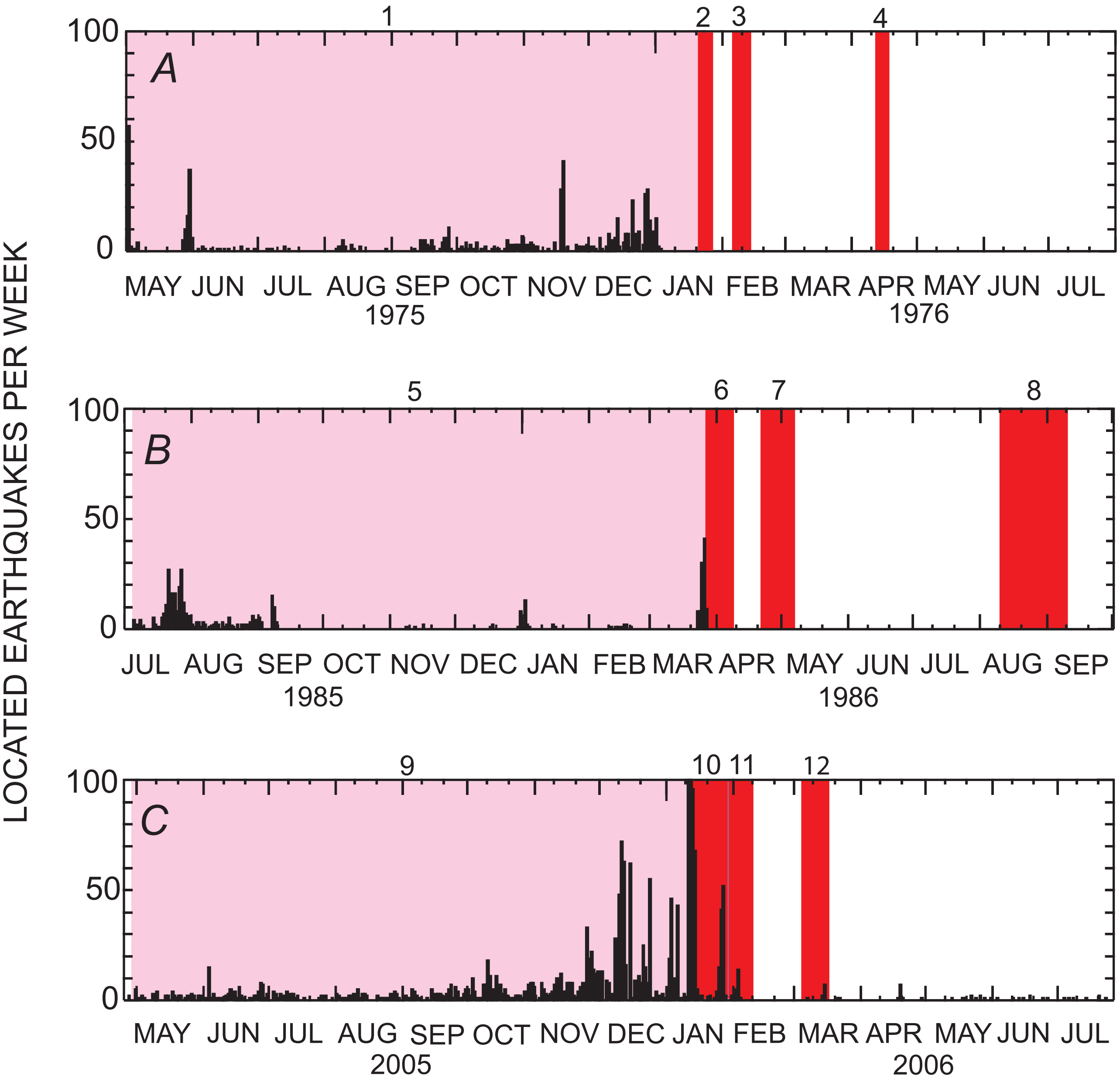

Figure 8. Comparative time lines of the eruptive phases of (*A*) 1976, (*B*) 1986, and (*C*) 2006 eruptions based on histograms of the number of located earthquakes each week. Pink shading corresponds to precursory periods, and red shading corresponds to eruptive periods. Numbers correspond to: 1, 1976 precursory phase; 2, the first 1976 explosive phase; 3, the second 1976 explosive phase; 4, 1976 effusive phase; 5, 1986 precursory phase; 6, 1986 explosive phase; 7, 1986 initial dome building phase; 8, 1986 second dome building phase; 9, 2006 precursory phase; 10, 2006 explosive phase; 11, 2006 continuous phase; and 12, 2006 effusive phase.

resolution of the recording media changed drastically between 1970 and 2007. For earlier time periods we rely on descriptions developed by Reeder and Lahr (1987) for the 1976 eruption and Power (1988) for the 1986 eruption.

The 1971 Eruption

On August 30, 1971, an intense earthquake swarm began that lasted until September 6, 1971 (fig. 3). These earthquakes had broad-spectrum VT waveforms and were of much larger magnitude than those previously recorded at Augustine. During the peak in activity between September 2 and 4, more than 300 identifiable earthquakes per day were recorded on station AU1. Seismic records from AU1 and AU2 on September 6 show the high level of VT earthquake activity recorded during this swarm (fig. 12). A photograph taken by Austin Post of the volcano on September 3, 1971, shows vigorous steaming on the east side of the volcano's summit (Kienle and Swanson, 1985). Smaller earthquake swarms were recorded November 28–30 and December 19–21, 1971 (fig. 3).

On October 7, 1971, a fishing boat 38 km north of the volcano reported a small ash eruption and red glow from the summit. This report coincides with a 2 hour period of volcanic tremor recorded on October 7 and 8 between 2300 and 100 (AKDT) (Kienle and Swanson, 1985). No information exists on the extent or type of eruptive products that may have been produced by this event. The red glow reported by

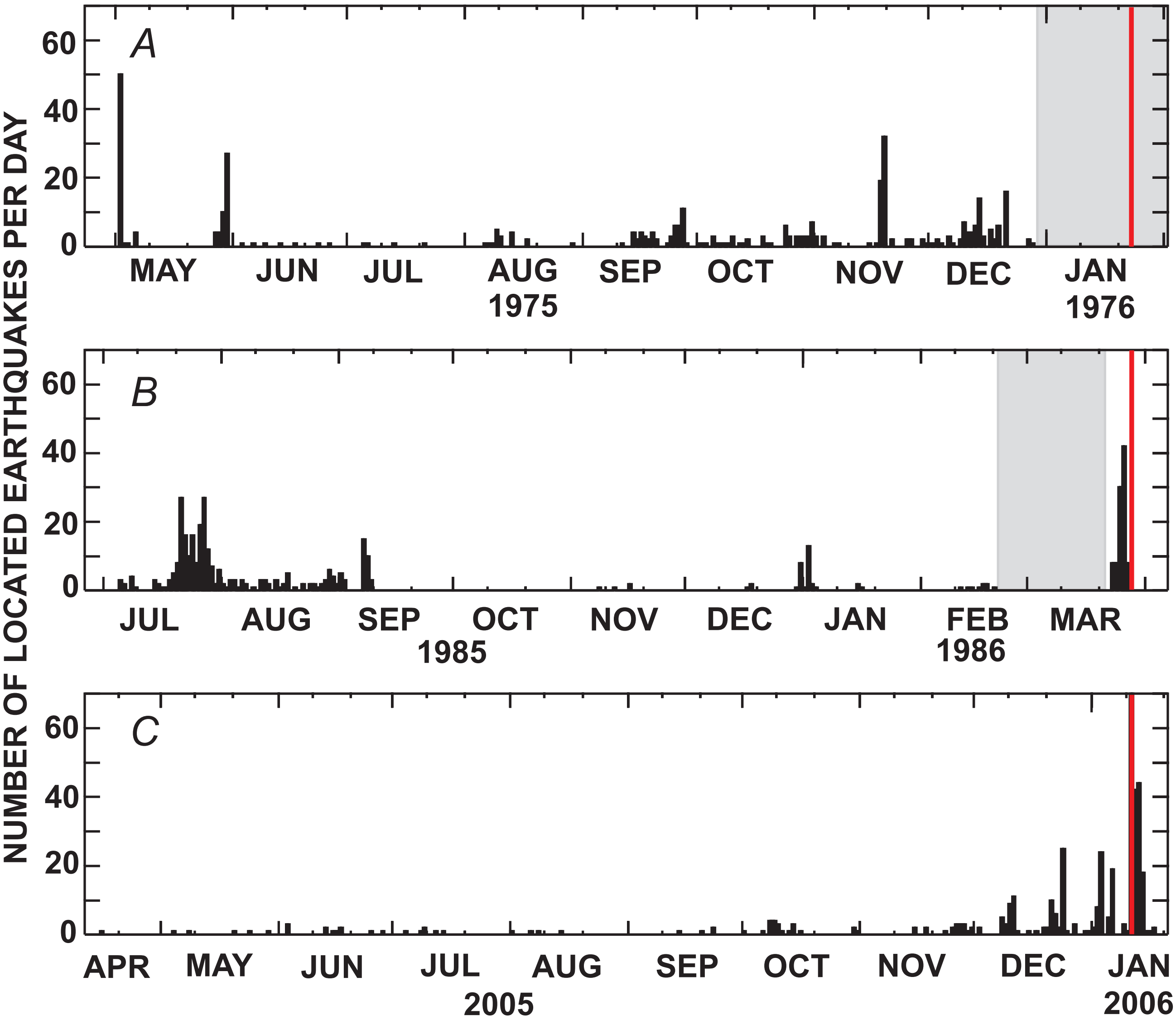

Figure 9. Histograms showing the number of relocated earthquakes that occurred before the (*A*) 1976, (*B*) 1986, and (*C*) 2006 eruptions of Augustine Volcano. The time periods when the Augustine seismic network was not operating sufficiently to relocate earthquakes are shown in gray. Red lines correspond to the onset of explosive events in the 1976, 1986, and 2006 eruptions.

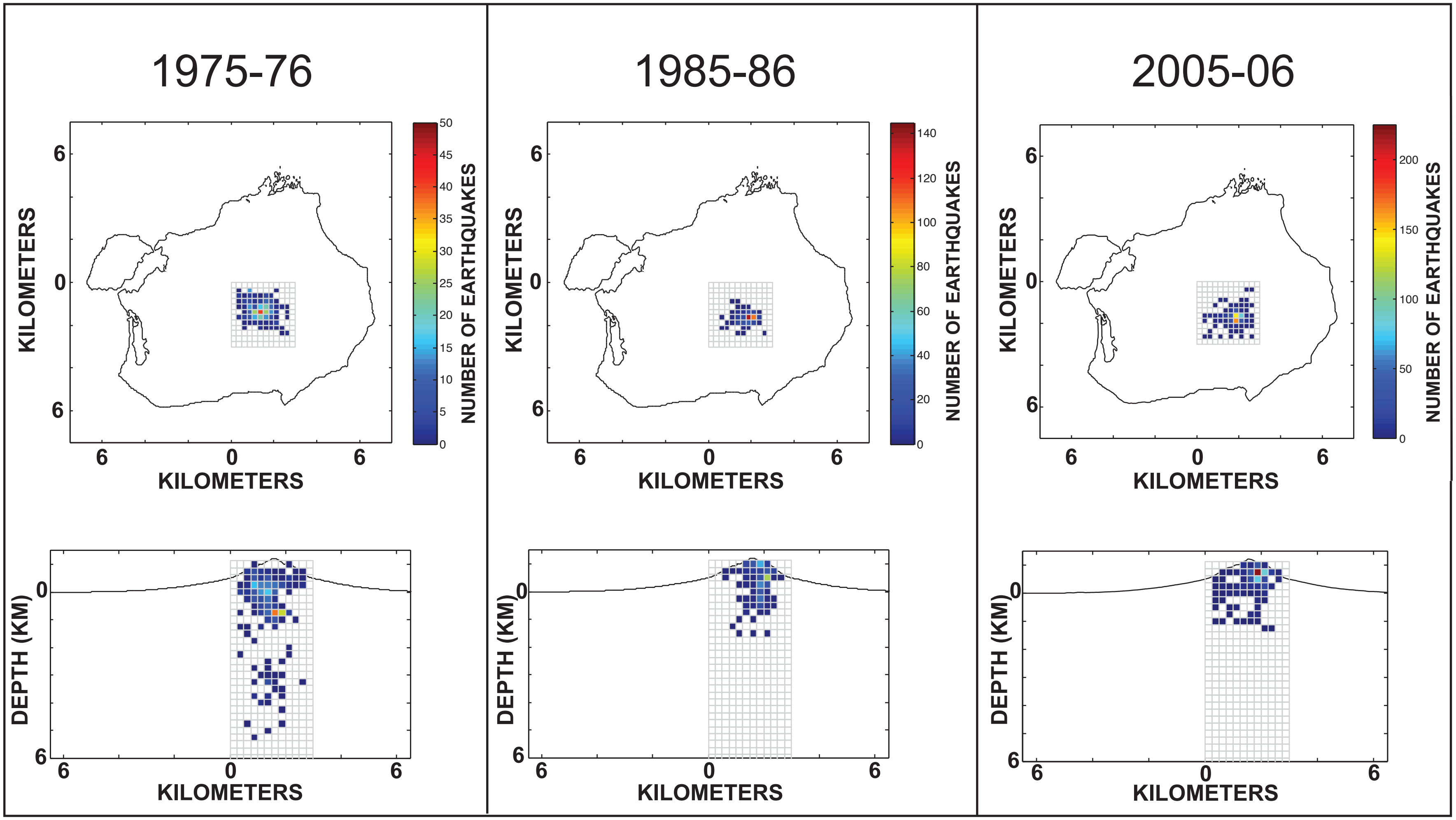

Figure 10. Map and east-west cross sections of relocated earthquakes at Augustine Volcano during precursory phases of the 1976, 1986, and 2006 eruptions. Color scales indicate the number of earthquakes located in each grid square.

the fishing boat suggests that it represents more than a simple phreatic explosion, perhaps mild explosive activity and a small lava extrusion near the volcano's summit.

The 1976 Eruption

Seismic activity associated with the 1976 eruption of Augustine Volcano was closely observed by the five stations on the island (fig. 2*A*) and the additional stations surrounding southern Cook Inlet (fig. 1). Unfortunately, all the stations on the island failed in early December 1975 as a result of severe winter weather (Johnston, 1978). However, station CKK on the Alaska Peninsula (fig. 1) operated at an unusually high gain and provided a means of tracking earthquakes at Augustine Volcano as small as magnitude (M_L) 0.25. The 1976 eruption consisted of four distinct phases based on the character of seismic activity and eruptive behavior. For this discussion we define the phases as follows:

1. Precursory phase (May 2, 1975, to January 23, 1976).
2. Explosive phase (January 22 to 25, 1976).
3. Second explosive phase (February 6 to 14, 1976).
4. Effusive phase (April 13 to 18, 1976).

These time periods were selected on the basis of descriptions of seismicity and eruptive activity provided by Reeder and Lahr (1987), Kienle and Shaw (1977), and Kienle and Swanson (1985).

Precursory Phase—May 2, 1975, to January 22, 1976

The precursory phase began with a pronounced swarm of VT earthquakes on May 2, 1975 (fig. 8). These shocks had impulsive arrivals and well-defined phases compared to most Augustine earthquakes. Relocated hypocenters clustered near sea level, and the largest magnitude was 1.4. This swarm quickly died off, with the last locatable event occurring on May 6, 1975. The volcano was then seismically quiet until May 27, when a second pronounced swarm of earthquakes began. This swarm consisted of 67 earthquakes large enough to be relocated (fig. 9), and the largest event had a magnitude of 0.7 (fig. 4). Seismicity following this swarm continued at a new higher rate of 5 to 10 relocated events per month. On September 14 the rate of seismicity climbed to a higher rate of tens of earthquakes located each month. This rate climbed again in late November to 100 to 200 events per month

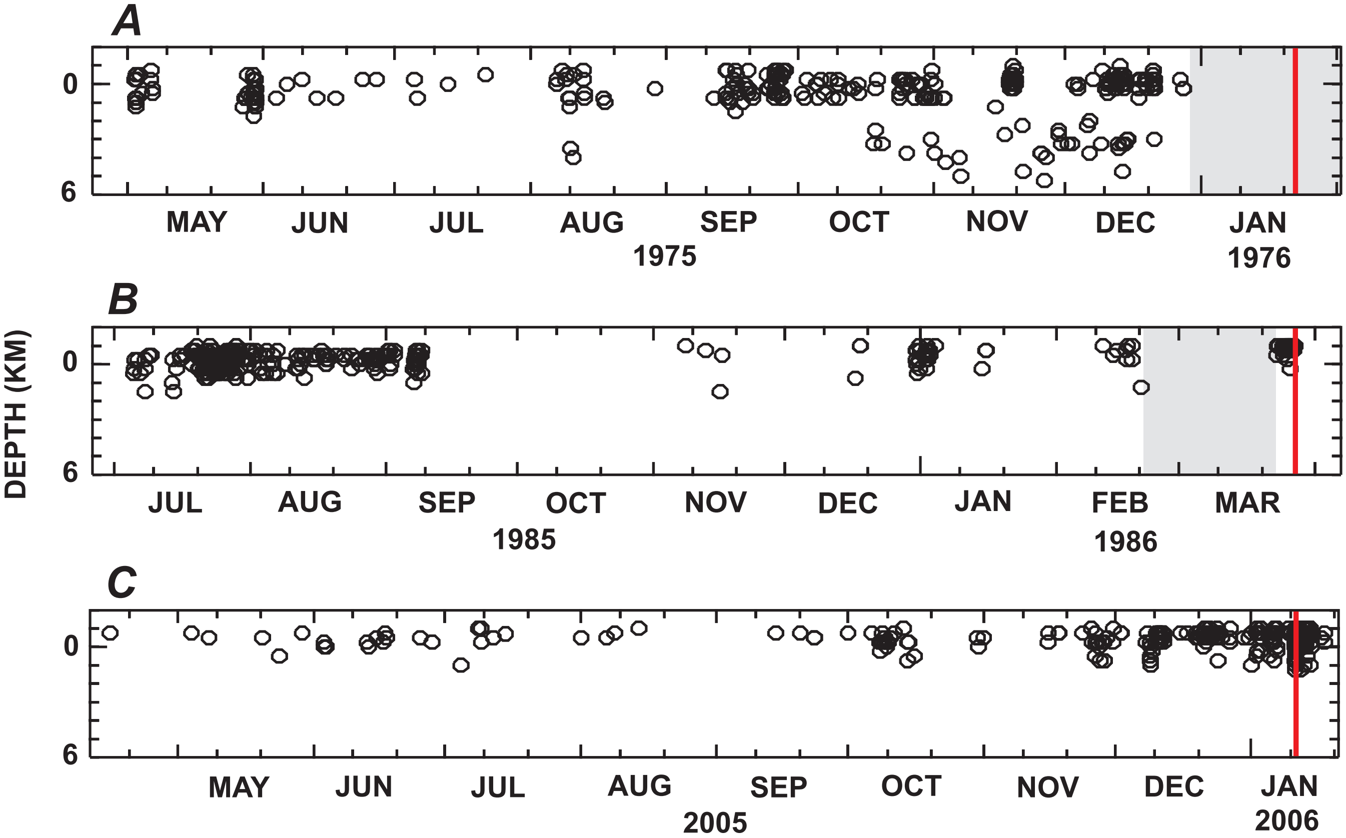

Figure 11. Plots of focal depth versus time for earthquakes relocated during the precursory phases of the (*A*) 1976, (*B*) 1986, and (*C*) 2006 eruptions of Augustine Volcano. The time periods when the Augustine seismic network was not operating sufficiently to relocate earthquakes are shown in gray. Red lines correspond to the onset of major explosive events in 1976, 1986, and 2006.

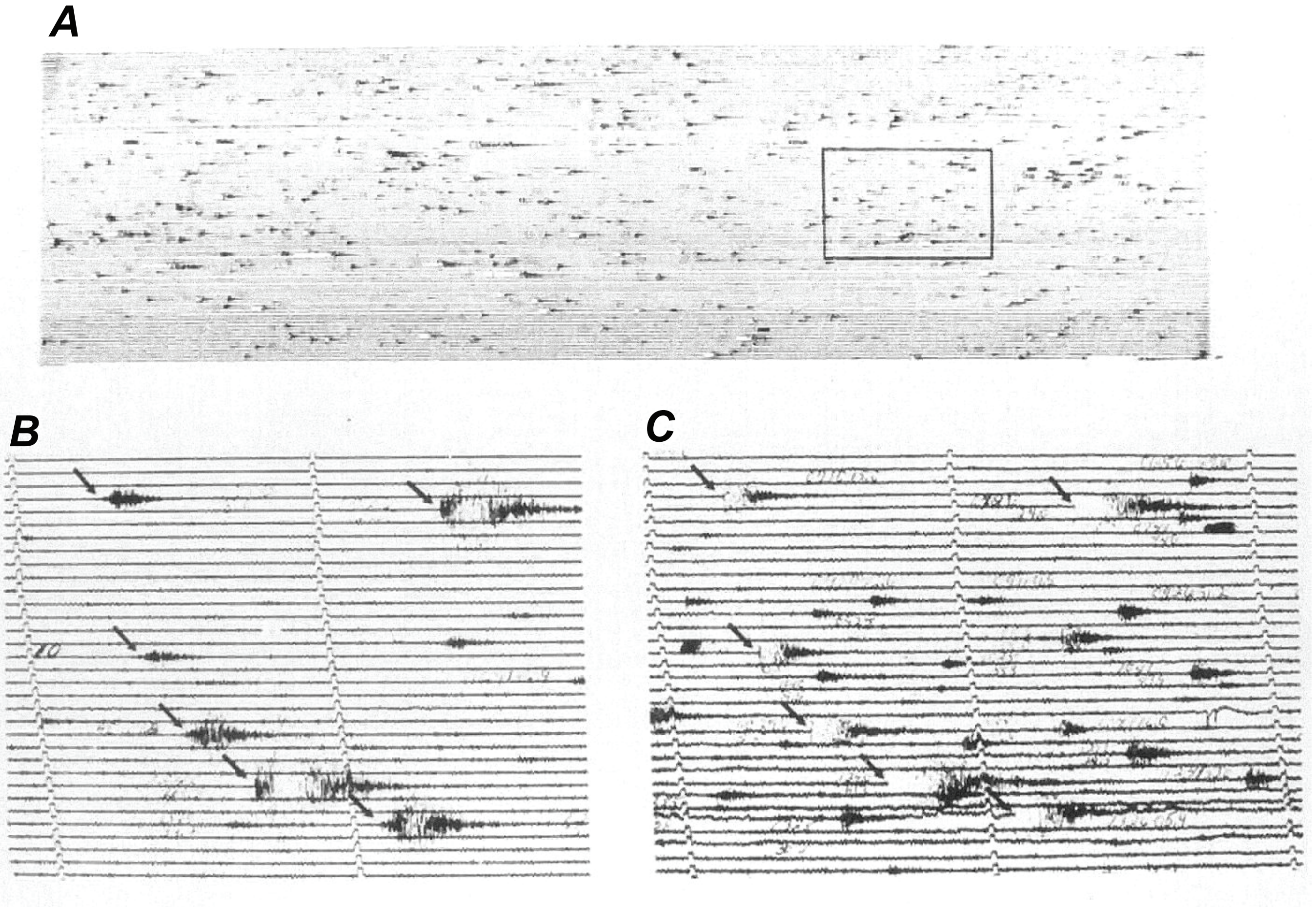

Figure 12. Drum records showing the character of earthquake activity prior to the 1971 eruption of Augustine Volcano. *A*, 24-hour drum record from seismic station AU1 on September 6, 1971. Small box in *A* denotes time periods shown in *B* and *C* on stations AU2 and AU1, respectively. Time marks represent 1 minute intervals.

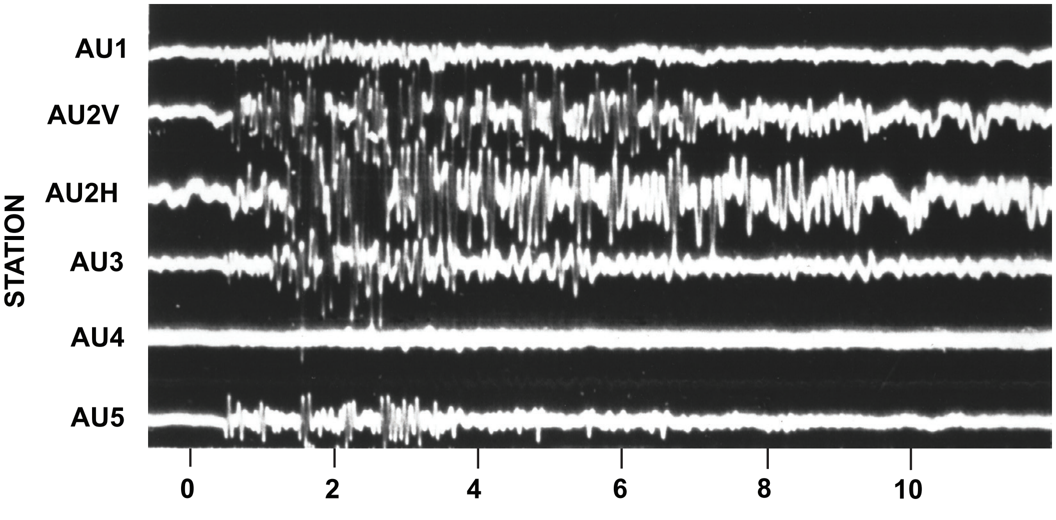

Central Event, Z=3.00km, M_L = -0.3
(Oct. 31 1975, 09:19 U.T.)

Figure 13. Seismograms from various seismic stations on Augustine Island of a magnitude (M_L) –0.3 earthquake located at a depth of 3 km below sea level on October 30, 1975 at 2319 AKST. Note small amplitudes observed at station AU4 (fig. 2*A*), which is near the summit, compared with other stations that are located on the flanks of the volcanic edifice. Stations AU2H and AU2V represent the horizontal and vertical components of station AU2, respectively.

(fig. 3). This high rate of earthquake activity continued until the network failed on December 22, 1975.

On August 10, earthquakes with hypocentral depths ranging from 2.75 to 5.25 km b.m.s.l. began to occur. Two of these deeper events were located on August 10 and 29, and additional events were located between October 18 and December 21, 1975 (fig. 11). The waveforms of these earthquakes have well-defined P and S phases and broader frequency content typical of VT earthquakes (fig. 13). Earthquakes in this depth range were found to have characteristically higher amplitudes on the flank stations such as AU2 and AU3 and lower amplitudes on the higher station AU4 (fig. 2*A*). This is the opposite of relative amplitudes observed for earthquakes with hypocentral depths of 1 km b.m.s.l. and above. Magnitudes of the deeper events ranged from −2.0 to 1.3. Increased steaming and fumorolic activity was reported by Johnston (1978) beginning in October of 1975.

Initial Explosive Phase—January 22 to 25, 1976

The 1976 eruption of Augustine began with a large explosion at 1759 AKST on January 22 which produced an ash plume that rose to 14 km a.m.s.l. (Kienle and Shaw, 1977; Reeder and Lahr, 1987). This explosion initiated a 22-hour-long sequence of more than 668 earthquakes that ranged in magnitude from 1.6 to 2.75 as determined by amplitude measurements on station CKK (fig. 1) located on the Alaska Peninsula. The rate and magnitudes of earthquakes recorded at station CKK and the times of explosive eruptions reported by Kienle and Shaw (1977) are shown in figure 14. This energetic swarm is the most vigorous recorded at Augustine Volcano between 1970 and 2007. The swarm was most intense between 0300 and 0600 AKST and was declining in intensity when the larger explosive events occurred (fig. 14). The explosive eruptions on January 23, 1976, as described by Kienle and Shaw (1977) were clearly the most powerful observed at Augustine during the 38 years of this study.

Kienle and Shaw (1977) report 12 additional Augustine explosions between 0353 on January 23 and 0457 AKST on January 27 that produced detectible infrasonic signals in Fairbanks. Reported plume heights for these explosions ranged from 6 to 12 km a.m.s.l. Reeder and Lahr (1987) report the occurrence of "large tremors" at station CKK associated with all 12 of these explosions. They report the occurrence of 22 additional "small tremors" recorded at station CKK between January 22 and 25 that may represent smaller explosions. Ashfall from these eruptions covered many areas surrounding Cook Inlet including Anchorage, Kenai, Homer, Seldovia, and Iliamna (Johnston, 1978).

The strong explosions in January 1976 removed a significant portion of the summit lava dome emplaced at the end of the 1964 eruption, leaving a crater that was estimated to be 200 m deep (Johnston, 1978). On the basis of coordinates of benchmarks located on the remnant crater rim (Power and Iwatsubo, 1998), we estimate the size of this crater to be roughly 550 by 350 m.

Second Explosive Phase—February 6 to 14, 1976

Eruptive activity resumed at 1444 AKST on February 6 with a powerful seismic signal recorded on station CKK. Activity continued at a sustained rate through February 14. Larger seismic signals were recorded late February 8 (Reeder and Lahr, 1987, figure 22). This phase of the eruption again produced large plumes that deposited ash on communities on the Kenai Peninsula, as well as numerous block-and-ash flows that moved down the north side of the volcano (Johnston,

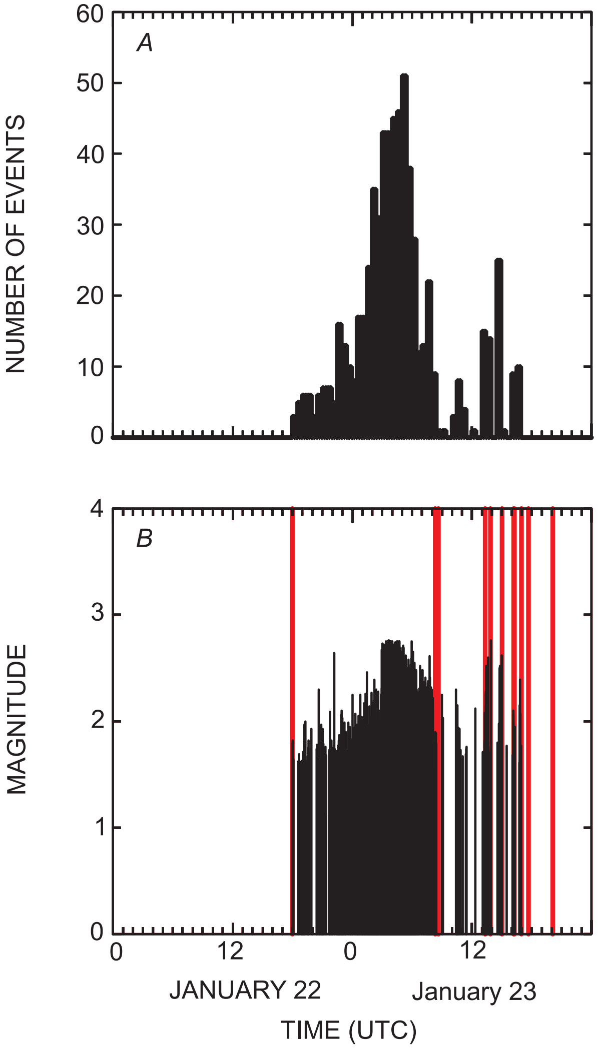

Figure 14. Time history of earthquake occurrence, magnitude, and explosive eruptions at Augustine Volcano on January 22 and 23, 1976. *A*, Number of earthquakes detected at station CKK during each 30-minute period. *B*, Each vertical line represents the magnitude of one earthquake as determined at station CKK. Red lines indicate times of explosive eruptions reported by Kienle and Shaw (1977). Time is referenced to UTC; to convert to AKST subtract 10 hours.

1978). Kienle and Swanson (1985) report that a new lava dome within the summit crater was first observed on February 12, 1976.

Effusive Phase—April 13 to 18, 1976

Seismic activity consisting of small tremors and shallow earthquakes resumed on April 13 and continued through April 18 (Reeder and Lahr, 1987, figure 24). Kienle and Swanson (1985) report that three seismic stations were reestablished on the island in February and these recorded numerous signals associated with block and ash flows that continued until April 24.

The 1986 Eruption

The 1986 eruption was well observed seismically by the network of four to five stations that was operating on the volcano throughout this eruption (fig. 2*B*). Descriptions of the 1986 eruption based on observations from individuals in the vicinity of the volcano, radar, observational overflights, satellite photographs, and a qualitative analysis of the seismic record were prepared by Yount and others (1987) and Swanson and Kienle (1988). A more detailed discussion of the seismic activity associated with the 1986 eruption was prepared by Power (1988).

Power (1988) divided the eruption into four phases based on the character of seismic activity and eruptive activity as follows:

1. Precursory phase (July 5, 1985 to March 26, 1986).
2. Explosive phase (March 26 to April 8, 1986).
3. Initial dome-building phase (April 21 to May 7, 1986).
4. Second dome-building phase (August 10 to September 10, 1986).

The character of seismicity changes dramatically from the precursory to the eruptive phase, and there are also significant differences among the remaining eruptive phases.

Precursory Phase—July 5, 1985 to March 26, 1986

The precursory phase to the 1986 consisted of several distinct swarms separated by long periods of seismic quiescence (Power, 1988). This phase began with a very energetic swarm of VT earthquakes that started on July 5, 1985, and continued until September 9, 1985. Relocated hypocenters in this swarm appear to have begun at depths of 0.2 to 0.4 km b.m.s.l. and quickly migrated to depths of 0.1 to 0.5 km a.m.s.l. The largest earthquake had a magnitude of 1.5. The swarm reached maximum intensity in late July 1985 (fig. 8).

Following this swarm the volcano went through a period of seismic quiescence from roughly September 10 to December 18. No other unusual behavior of the volcano was noted (Yount and others, 1987; Power, 1988). A small increase in the number of earthquakes began on December 18. This increase culminated in a short but intense swarm from December 31, 1985 to January 2, 1986. A magnitude 1.3 (M_L) earthquake on January 1 was the largest event of this period. Except for a small increase in mid-January, the volcano then remained relatively quiet until February 10 (fig. 8).

On February 10, 1986, the number of earthquakes increased an order of magnitude to tens of events per day. Unfortunately, on February 20 station AUI (fig. 2*B*) failed and earthquakes could not be located until it was repaired on March 22. To track seismicity during this period Power, (1988, figure 21) counted earthquakes from helicorder records of station AUH that were larger than M_L 0.25. Although, the number of events fluctuated greatly from day to day, the overall level of seismicity did not drop from this level until after the eruption. Earthquake activity during this period consisted of highly clustered bursts with 20 to 100 earthquakes occurring in a period of one to four hours. Earthquake activity of this character has been referred to as spasmodic bursts by Hill and others (1990). Figure 15 shows a helicorder record from station AUH illustrating a typical spasmodic burst on March 17, 1986. Individual spasmodic bursts can be separated by as much as 24 to 48 hours of relative quiescence. This increase in seismicity, coupled with reports of increased steaming, prompted the U.S. Geological Survey in Anchorage to make a series of observational overflights on February 22 and 28, and March 14 and 21. Increased fumarolic activity and snow melt were observed on successive flights (Yount and others, 1987).

A second order-of-magnitude increase in the seismicity rate to over 100 earthquakes per day greater than M_L 0.25 occurred on March 22. A ground party visited the volcano on this day to repair station AUI and to install station AUT. Vigorous steaming in the summit area and a strong sulfur smell downwind from the volcano were observed. The repair of station AUI allowed us to locate earthquakes again (fig. 9). Hypocentral depths of relocated earthquakes between March 22 and March 26 all cluster at 0.75 and 1.0 km a.m.s.l. (fig. 11). Late on March 24, a number of spasmodic bursts occurred that raised the rate of earthquake occurrence even higher (fig. 16). The largest events recorded during the 1986 eruption of Augustine Volcano occurred on March 26 and 27 and ranged in magnitude from 1.3 to 2.1 (fig. 4). Seismic signals with waveforms that resemble explosion events began to appear at 0957 AKST on March 26 (Power, 1988) (fig. 16). Power (1988) reported an upward migration of average hypocentral depth from 0.21 to 0.82 km a.m.s.l. during the precursory phase.

Explosive Phase—March 26 to April 8, 1986

The start of the eruption on March 26 marked a dramatic change in the character of the seismicity. However, analysis of this period is difficult because the film and helicorder records are saturated by the high levels of seismic activity. Before the

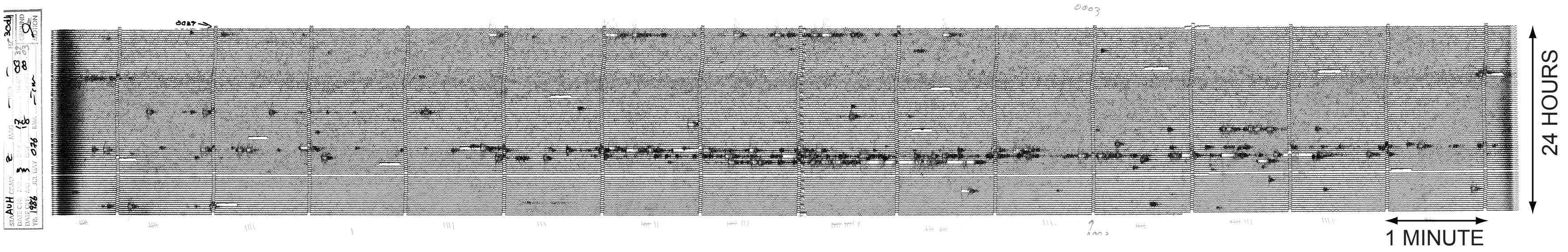

Figure 15. Drum record from seismic station AUH for March 17, 1986, showing a prominent spasmodic burst of earthquake activity composed of more than 75 earthquakes between 0630 and 0845 AKST. Note relative quiescence before and after spasmodic burst.

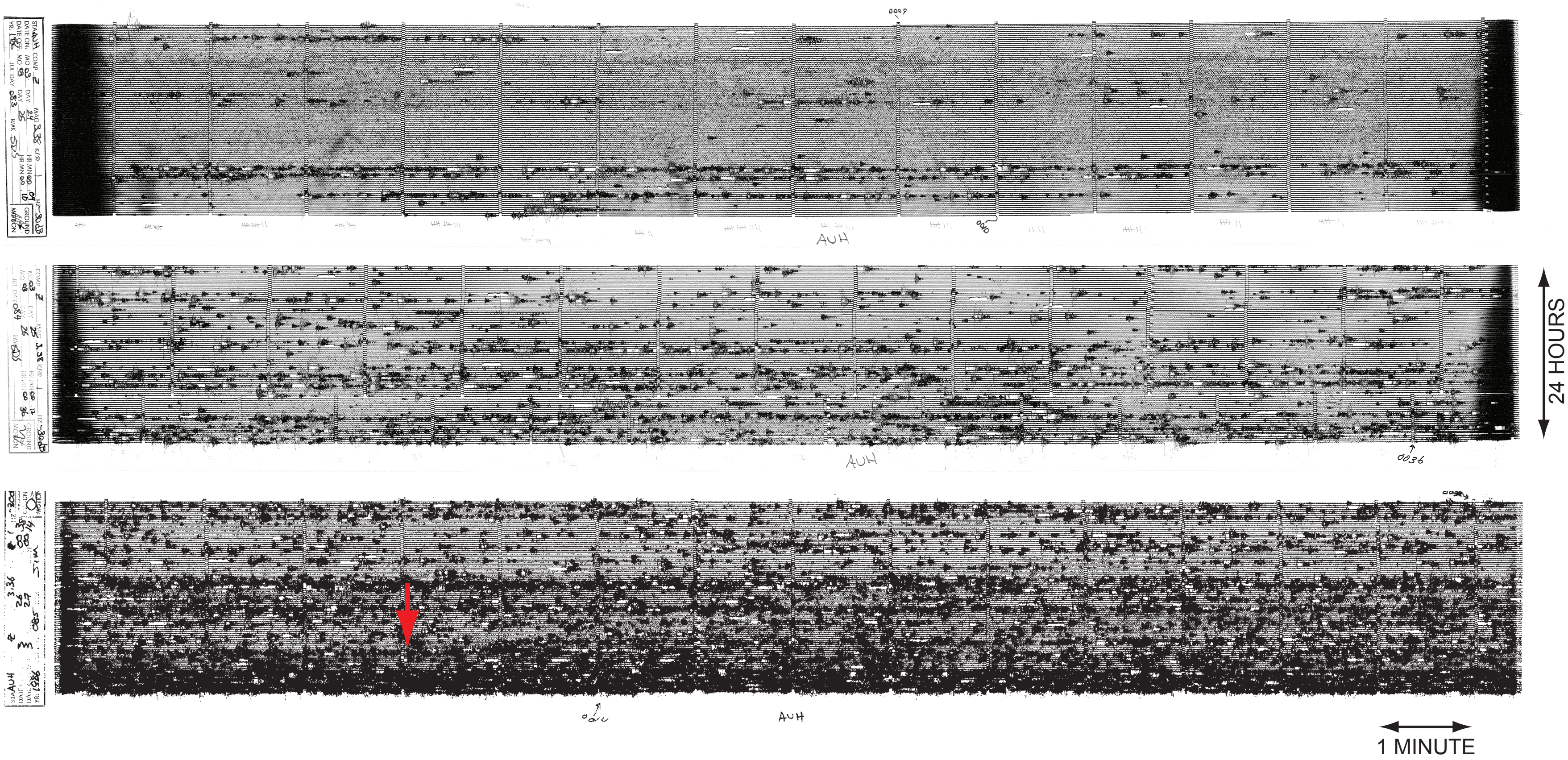

Figure 16. Drum records from seismic station AUH (fig. 2*B*) for March 24 through March 26, 1986, showing the strong buildup in earthquake activity before the onset of explosive activity in 1986. The red arrow notes the approximate onset of explosive activity at 0957 AKST on March 26, 1986.

explosive phase of the eruption, the seismic record is dominated by small VT earthquakes, generally of magnitude less than 1.3. Beginning at 0957 AKST on March 26 small explosions began to be interspersed with the earthquake signals. By 1711 AKST these explosions became strong enough to be recorded at station OPT, 25 km to the north of Augustine Volcano (fig. 1). As these explosion events began to increase in both amplitude and duration, the number of earthquakes began to diminish. By 0335 AKST on March 27 VT earthquakes were only occurring 5 to 10 minutes before the explosion events. Finally, by 1023 AKST on March 27 explosion events were taking place with no preceding earthquake activity. This sequence of intermixed earthquakes and explosions suggests that the Augustine vent opened rather slowly in 1986. This phase of the eruption produced widespread tephra throughout south-central Alaska and pyroclastic flows and lahars on Augustine Island (Yount and others, 1987).

To determine the relative size and rate of occurrence of explosions, Power (1988, figure 22) measured the onset and duration of the seismic signal at station OPT (fig. 1). These data show the relative intensity of explosive activity during this phase. The duration of individual events and the intensity of explosive activity increased slowly to a maximum on March 28 and then slowly decreased until March 31. At 0955 AKST on March 31 the largest single explosion occurred; the duration of this event was greater than 13 minutes at station OPT (Power, 1988). This explosion produced an eruption column that rose to more than 12 km above sea level, and spread ash over a wide area to the east of the volcano. Small explosions were also observed at OPT through April 4, and explosion events continued to be recorded on the island stations through April 8. Observations of these explosions, plume heights, and trajectories are discussed by Yount and others (1987). In addition to explosions, many events which could be related to pyroclastic flows and rock avalanches were also recorded during this phase.

Initial Dome Building Phase—April 21 to May 7, 1986

During this phase of the eruption a new lava dome was emplaced on the volcano's summit and a small lava flow moved down the upper northeast face of the volcano. Seismic activity was dominated by the occurrence of small repetitive earthquakes or drumbeats (Power, 1988, figure 29). A detailed description of observations of the volcano during this phase of the eruption is given by Yount and others (1987).

Drumbeat earthquakes first became apparent as a small increase above background noise at station AUH (fig. 2*B*) on April 21. By roughly 2000 AKST on April 21 the earthquakes were visible on helicorder records on all stations on the volcano and the signals from individual earthquakes began to run together, forming a continuous disturbance. To quantify this activity, Power (1988; figure 28) made hourly measurements of the signal amplitude on develocorder film on station AUH and identified periods when the signal was continuous or composed of identifiable discrete events. These measurements indicate that the drumbeat earthquakes increased in amplitude from April 22 to 27, then rapidly declined and disappeared completely by April 30. A second but less energetic period of drumbeats occurred from May 2 to 6 (Power, 1988). During this second period of drumbeats, individual events could be identified within the signal. On April 25 the approximate frequency of the signal was determined to be between 3 and 4 Hz.

Second Dome-Building Phase—August 10 to September 10, 1986

During this phase, dome building activity resumed and a peleean spine developed on the volcano's summit (Swanson and Kienle, 1988). This eruptive phase began about August 10, when Power (1988) reports that the number of avalanche signals began to increase gradually. Most of these signals were generated as small portions of the actively growing lava dome sloughed off the north side of the volcano's summit, forming pyroclastic flows (Kienle and Swanson, 1985). The seismic record became saturated with these signals on August 20. A count of surface events remained high until roughly September 10 (Power, 1988; figure 25). No associated increase in earthquake activity was noted (Power, 1988).

The 2006 Eruption

The 2006 eruption of Augustine Volcano received a much higher degree of monitoring and observation than earlier eruptions in 1971, 1976, and 1986. In addition to the increased seismic instrumentation (fig. 2*C*), a network of six continuous GPS receivers (CGPS) had been installed on the volcano by the Alaska Volcano Observatory (AVO) and EarthScope's Plate Boundary Observatory (PBO) (Pauk and others, this volume). Once unrest began, AVO deployed six temporary broadband seismometers, a strong-motion seismometer (AU20) (table 1), and five additional temporary CGPS (Cervelli and others, this volume) on the volcano. AVO also began a series of overflights to make visual observations, measure volcanic gas (McGee and others, this volume), and obtain thermal imagery (Wessels and others, this volume). AVO also deployed time-lapse and Web cameras (Paskievitch and others, this volume), and took high-resolution aerial photographs (Coombs and others, this volume). Researchers from the University of Alaska Fairbanks deployed a low-light camera in Homer, Alaska (Sentmen and others, this volume), and researchers from the New Mexico Institute of Mining and Technology deployed a lightning detection system (Thomas and others, this volume). Subsequent investigations of the deposits from the 2006 eruption are described by Coombs and others, (this volume), Vallance and others, (this volume), Larsen and others, (this volume), and Wallace and others (this volume).

The 2006 eruption of Augustine, like the 1976 and 1986 eruptions, consisted of four distinct phases defined by the character of seismicity, geophysical unrest, and eruptive activity, which are described below. The time periods for these phases are:

1. Precursory phase (April 30, 2005 to January 11, 2006).
2. Explosive phase (January 11 to 28, 2006).
3. Continuous phase (January 28 to February 10, 2006).
4. Effusive phase (March 3 to 16, 2006).

The number of located earthquakes per week, approximate times of phreatic and magmatic explosions, RSAM values from station AU13, ground deformation, measured SO_2 output, erupted volume, and the time periods of the four eruptive phases are summarized in figure 17.

Precursory Phase—April 30, 2005 to January 11, 2006

The precursory phase began as a slow, steady increase in microearthquake activity beneath the volcano on April 30, 2005. These earthquakes were all classified as VT earthquakes during standard AVO processing (Dixon and others, 2008). An earlier swarm in October of 2004 (fig. 3) developed seismicity rates that exceeded any observed since the 1986 eruption; however, the six-month-long period of quiescence between this swarm and April 30, 2005, makes any connection to the 2006 eruption uncertain. The number of located VT earthquakes slowly increased from an average of one to two per day in May 2005 to five to six per day in October 2005 to 15 per day in mid-December 2005 (fig. 3). Relocated hypocenters had average depths generally between 0.1 and 0.6 km a.m.s.l. between April and December of 2005. These hypocentral depths are shallower than those observed during the initial precursory stages of both the 1976 and 1986 eruptions (fig. 11). In July 2005, geodetic baselines measured by the CGPS receivers began to lengthen, showing a clear radial pattern indicative of a pressurization source beneath the volcano's summit near sea level (Cervelli and others, 2006).

On November 17 there was a clear offset in the GPS data (fig. 17) that Cervelli and others (2006) attribute to the onset of the upward propagation of magma or associated volatiles in a dikelike structure. This was followed on December 2 by the onset of a series of small phreatic explosions that were clearly recorded on the Augustine seismic network. The largest of these explosions occurred on December 10, 12, and 15. An observational overflight on December 12 revealed vigorous steaming from the summit area, a new vigorous fumarole on the summit's southern side at roughly 3,600 feet elevation, and a light dusting of ash on the volcano's southern flanks. A strong plume of steam and

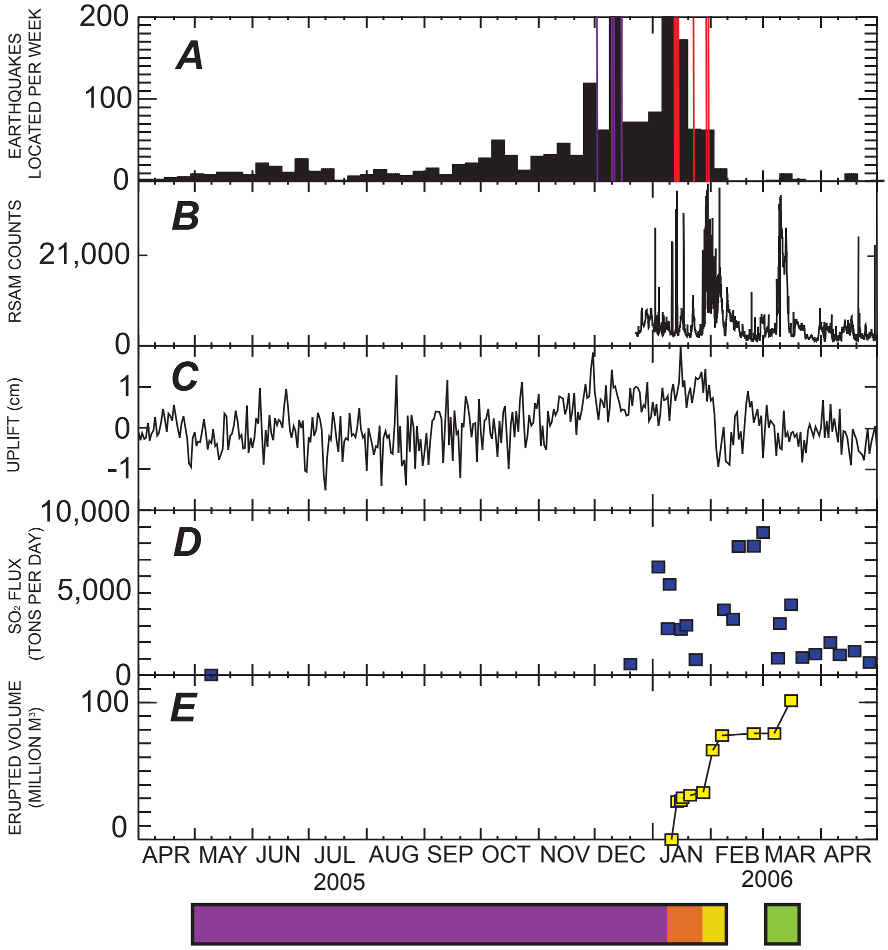

Figure 17. Summary of the 2006 eruption that shows (*A*) the number of earthquakes located each day, (*B*) the hourly RSAM record from station AU13, (*C*) the displacement measured between GPS stations A59 and AV02 (Cervelli and others, this volume), (*D*) the measured SO_2 flux (McGee and others, this volume), and (*E*) the erupted volume determined by Coombs and others (this volume). Purple and red lines in *A* correspond to approximate times of phreatic and magmatic explosions, respectively. Colors in bar at base of figure (purple, orange, yellow, and green) correspond to the precursory, explosive, continuous and effusive phases, respectively. Gap in bar represents hiatus in eruptive activity.

gas extended to the southeast. The explosion on December 15 disabled seismic stations AUS and AUR, the two highest seismic stations (fig. 2*C*). The ash was sampled on December 20 and was found to be a mix of weathered and glassy particles; the latter appear to be remobilized 1986 tephra (Wallace and others, this volume). Measurements of SO_2 flux on December 20, 2005, and January 4 and 9, 2006, returned values of 660, 6,700, and 2,800 tons per day, respectively (McGee and others, this volume).

Between December 12, 2005, and January 10, 2006, seismicity rates were strongly elevated, with more than 420 earthquakes located by the AVO (Dixon and others, 2008). Much of this activity occurred in spasmodic bursts similar to those observed before the 1986 eruption (fig. 15). Jacobs and McNutt (this volume) determined a *b* value of 1.85 for earthquakes during this period. Relocated hypocenters continued to cluster between 0.4 and 0.8 km a.m.s.l. On the basis of geodetic data, Cervelli and others (2006) suggest that magma and/or volatiles continued to move to progressively shallower depths within the Augustine edifice during this period.

On January 10 at roughly 1535 AKST, a 13-hour long swarm of VT earthquakes began that would culminate in two large explosions at 0444 and 0512 AKST on January 11, marking the onset of the explosive phase of the eruption (fig. 18). AVO would eventually locate more than 300 earthquakes during this swarm. Relocated hypocenters cluster beneath the volcano's summit at depths of 0.5 to 1.0 km a.m.s.l. The swarm began slowly, with locatable earthquakes occurring roughly every 2 minutes and magnitudes smaller than 1.0 (fig. 9). The seismicity rate peaked twice during the swarm at roughly 1800 January 10 and 0200 AKST January 11, and the magnitudes of located events also followed a similar progression (fig. 19).

Explosive Phase—January 11 to January 28, 2006

The two explosions on January 11 produced ash plumes, reported by the U.S. National Weather Service (NWS) to have reached heights greater than 9 km a.m.s.l. that moved slowly to the north and northeast (Bailey and others, this volume). Ash sampled on January 12 was primarily dense or weathered fragments, suggesting the involvement of little or no juvenile magma (Wallace and others, this volume). Over the next 36 hours, several sequences of drumbeat earthquakes occurred at rates as high as three to four per minute. Each of these sequences of drumbeats lasted 2 to 3 hours (fig. 18). These earthquakes suggest that magma may have begun to move within the shallow portions of the Augustine edifice, possibly forming a new lava dome if material reached the surface.

Explosive activity resumed on January 13 with a series of six powerful explosions that occurred at 0424, 0847, 1122, 1640, 1858 on January 13 and 0014 AKST on January 14 (fig. 18). The first explosion destroyed the seismometer at AUP (fig. 2*C*). Plumes reached altitudes of 14 km a.m.s.l. and deposited traces of ash on southern Kenai Peninsula communities. Ash from these eruptions was more heterogeneous than that from the January 11 explosions and contained dense particles as well as fresh glass shards, indicating the eruption of new magma (Wallace and others, this volume). Satellite imagery tracked these plumes as they moved eastward and disrupted commercial airline traffic to and from Alaska (Bailey and others, this volume). These explosions opened a new vent in the top of the 1986 lava dome that was estimated to be roughly 100 by 200 m in diameter (Coombs and others, this volume).

A January 16 overflight revealed a small new lava dome at the summit partially filling the new crater. An explosive eruption at 0758 AKST on January 17 sent ash to 13 km a.m.s.l. in a plume that moved westward. This explosion left a 20- to 30-meter-diameter crater in the new dome and produced ballistic fields on the volcano's western flanks (Coombs and others, this volume; Wallace and others, this volume; Schneider and others, 2006).

The eruptions of January 13–17 generated pyroclastic flows, snow avalanches, and lahars that moved down most flanks of the volcano. The January 17 explosion was followed by roughly 9 days of relative seismic quiescence. Brief periods of drumbeat earthquakes occurred throughout this period, and lava again filled the new crater and formed a small lava flow that moved to the east (Coombs and others, this volume; Vallance and others, this volume).

Explosive activity resumed on January 27 with two explosions at 2024 and 2337 and two on January 28 at 0204 and 0742 AKST (fig. 20) that generated ash plumes to heights of 9 km a.m.s.l. Ash moved southward and fell in trace amounts on Kodiak Island (Bailey and others, this volume; Wallace and others, this volume). The explosion at 2024 AKST on January 27 generated the largest single pyroclastic flow of the eruption, which moved down the north flank of the volcano (Coombs and others, this volume; Vallance and others, this volume). This explosion destroyed seismic stations AUH and AUL on the west and north flanks of the volcano. Destruction of these two final stations on the upper flanks of the volcano compromised AVO's ability to assign reliable hypocentral depths to earthquakes in near real-time.

Continuous Phase—January 28 to February 10, 2006

The volcano entered a period of more continuous eruptive activity starting at about 1430 AKST on January 28, 2006, with a roughly 2-hour period of volcanic tremor (fig. 20) that was accompanied by a significant ash plume that reached 9 km a.m.s.l. (Wallace and others, this volume). This phase of the eruption was characterized by continuous lower level ash production that gradually transitioned to the effusion of lava. Early in this phase the volcano erupted a more silicic magma (62.5 weight percent SiO_2) that formed a rubbly dome atop the remnants of the 1986 dome. By early February the composition of erupted magma had shifted back to a more andestic composition that formed a short lava flow that moved a short distance down the volcano's north side (Coombs and others, this volume).

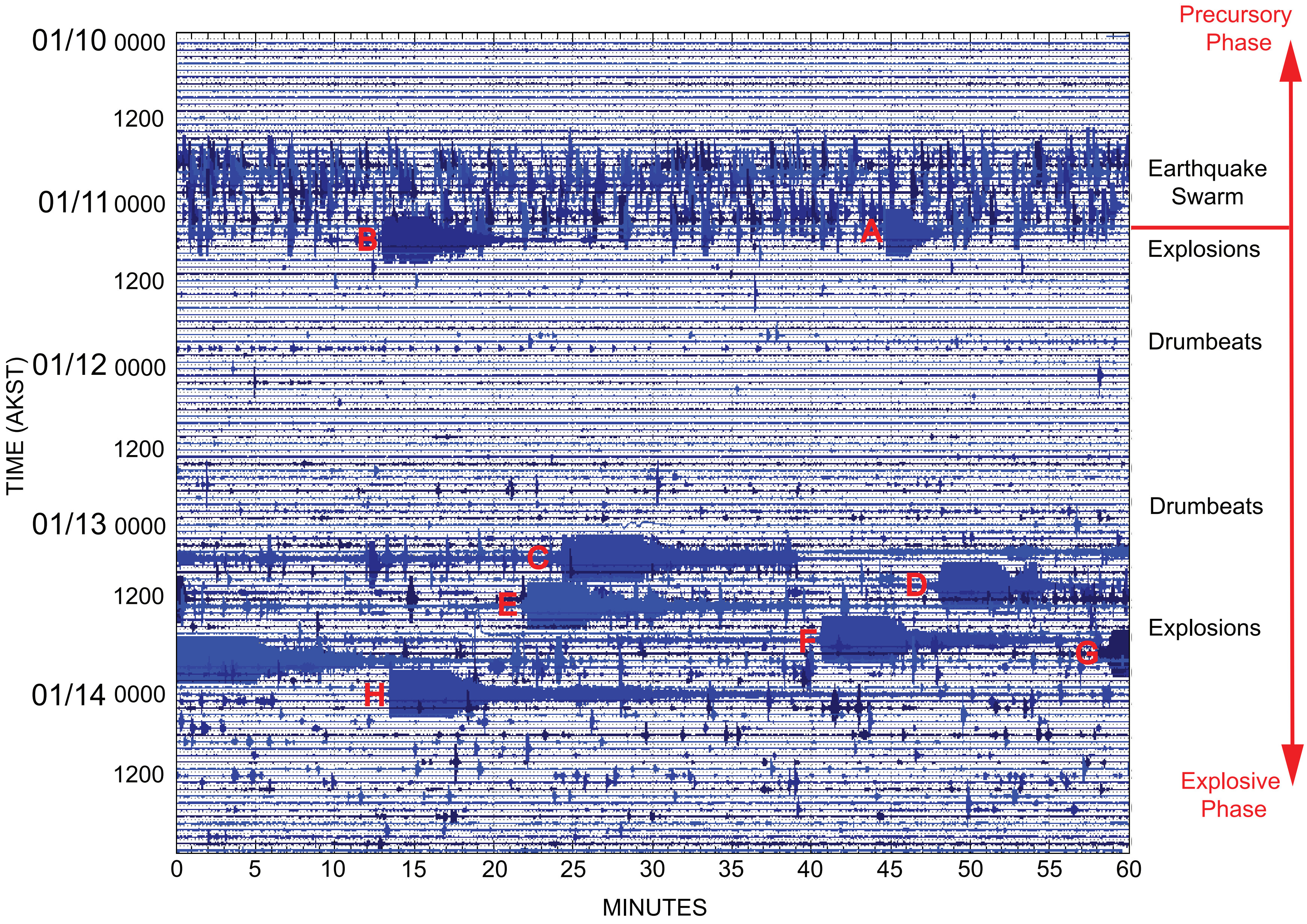

Figure 18. A 5-day velocity seismic record from station AU13 that shows the precursory earthquake swarm on January 11, 2006, the first eight explosions on January 11, 13, and 14, and the intervening periods of drumbeat earthquakes. Labeled events are A, explosion at 0444 AKST on January 11; B, explosion at 0512 AKST on January 11; C, explosion at 0424 AKST on January 13; D, explosion at 0847 AKST on January 13; E, Explosion at 1122 AKST on January 13; F, explosion at 1640 AKST on January 13; G, explosion at 1858 AKST on January 13; H, explosion at 0014 AKST on January 14.

At approximately 2200 AKST on January 28, the seismic network began to detect numerous signals associated with rock falls and block-and-ash flows generated by small failures of the growing lava dome and flows, cascading down the volcano's northern flanks (fig. 20). These signals generally have emergent onsets, extended codas, and a broad spectrum between 1 and 10 to 15 Hz. Numerous LP events are also observed during this time. Automatic event classification by Buurman and West (this volume) indicates that most seismic events had a lower frequency content or LP character during this phase of the eruption. One of these flows swept over seismic station AU12 at 0329 AKST on January 30, 2006, destroying the station's batteries. Fortunately, the seismometer and internally recorded data were recovered on August 11, 2006. Signals from rockfalls and small pyroclastic flows, as well as individual shallow LP events, declined markedly on February 3 at about 1500 AKST and then gradually decreased through the remainder of this phase.

Data from the remaining CGPS stations indicated that the volcano reversed its long inflationary trend on January 28 and began a sharp deflation that continued until 10 February. Modeling suggests the locus of deflation was at about 3.5 km b.m.s.l. (Cervelli and others, this volume).

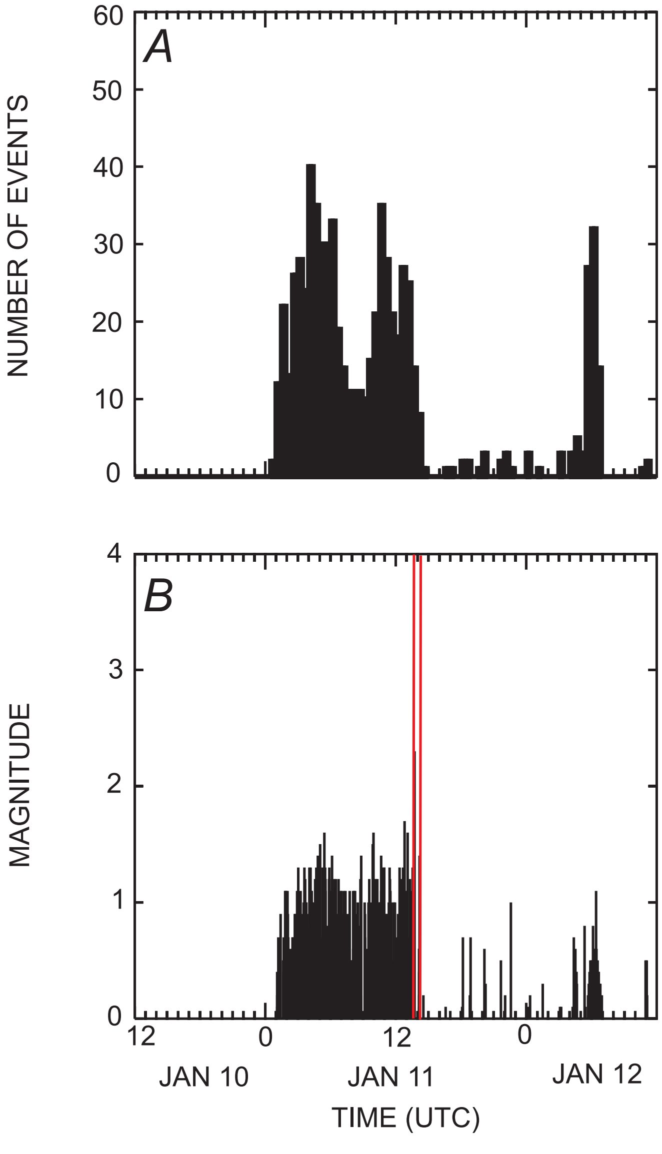

Figure 19. Time history of earthquake occurrence, magnitude, and explosive eruptions on January 10 through 12, 2006. *A,* Number of earthquakes located in each 30-minute period. *B*, Each vertical line represents the magnitude of one located earthquake. Red lines indicate times of explosive eruptions. Time is referenced to UTC; to convert to AKST subtract 9 hours.

Effusive Phase—March 8 to16, 2006

Following the end of the continuous phase, the volcano then entered a period of relative seismic quiescence that continued until March 3, 2006. This period is characterized by only an occasional rockfall signal. Visual observations of the volcano indicate that the period from February 10 to March 3 represents a cessation in eruptive activity. Geodetic data indicate that the volcano slowly inflated between February 10 and March 1 and then entered an 11-day period of deflation between March 1 and 12, 2006. The strength of this signal on the remaining CGPS instruments was not sufficient to accurately model a source depth for this episode of deflation (Cervelli and others, this volume).

On March 3 the number of rockfalls seen on the remaining seismic stations began to slowly increase. This activity peaked on March 6 and early on March 7. Starting on March 8, small repetitive drumbeat-style seismic events began to slowly emerge from the seismic background. The rate and size of the drumbeat events waxed and waned several times before forming a nearly continuous signal late on March 8 (fig. 21). Between 0500 and 2000 AKST on March 8 the rate of individual drumbeat events varied from two to as many as six per minute. After 2000 AKST on March 8, the events were occurring so rapidly (eight or more per minute) that they formed a continuous signal and it is no longer possible to distinguish individual events. RSAM records from station AU13 indicate that the amplitude of the continuous signal reached a maximum late on March 10 (fig. 17). This continuous signal lasted until about 1200 AKST on March 13 when the amplitude began a slow decline and individual events could again be distinguished occurring at a rate of about 5 per minute. The rate of events slowly declined, and by roughly 1200 AKST on March 16 they could no longer be identified.

Lava extrusion at the summit increased markedly in association with these drumbeat events, and two blocky lava flows moved down the north and northeastern flanks. Observations indicate that the effusion of lava had stopped by mid-March. The estimated volume of erupted material during this phase is 23 million cubic meters (Coombs and others, this volume).

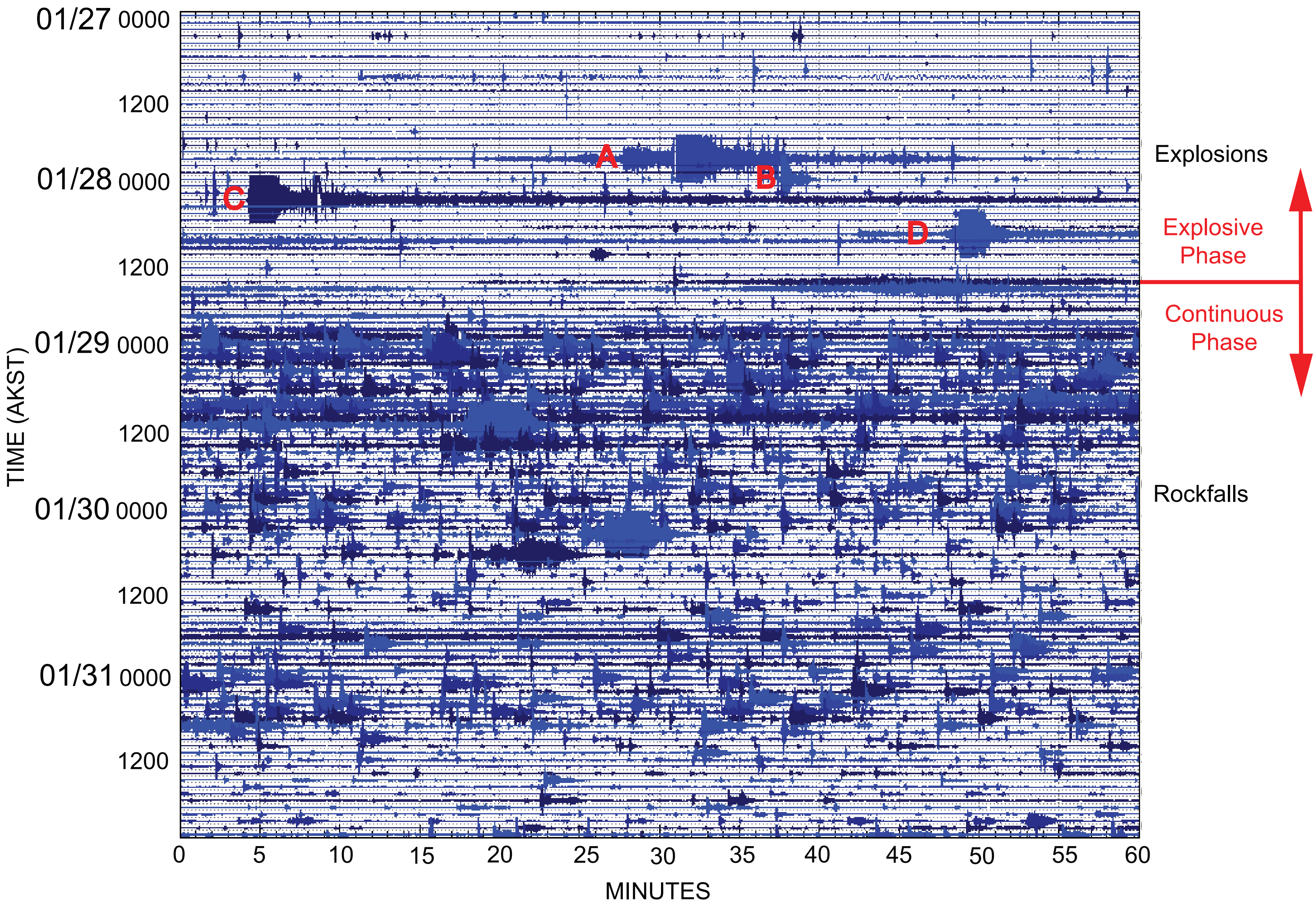

Figure 20. A 5-day velocity seismic record from station AU13 that shows the transition from the explosive to the continuous phase of the 2006 eruption. Labeled events are A, explosion at 2024 AKST on January 27; B, explosion at 2337 AKST on January 27, C, explosion at 0204 AKST on January 28; and D, explosion at 0742 on January 28, 2006.

Posteruptive Seismicity

On March 15, 2006, two earthquakes were located beneath the summit with hypocentral depths of 2.8 and 2.4 km b.m.s.l. Earthquakes with hypocenters between 2.3 and 3.75 km b.m.s.l. continued at a low rate until mid-August, by which time 18 shocks at this depth had been identified. These earthquakes had well-defined phases and a broad spectrum between 2 and 15 Hz, typical of VT earthquakes that represent a brittle failure source. To accurately locate these shocks we incorporated S-phases from the horizontal components of stations AU13, AU14, and AU15 (fig. 2*C*). Deshon and others (this volume) found that 11 of these earthquakes formed a single family suggestive of a common source, while the remaining 7 shocks had unique waveforms. These were the first earthquakes identified with hypocenters in this depth range at Augustine since December 1975. A representative waveform and a time history of these deeper earthquakes are shown in figure 22.

The seismic signals from rockfalls and the number of locatable earthquakes continued to decline throughout the summer of 2006. Small fluctuations in the rate of shallow VT earthquakes continued at Augustine throughout 2007 (figs. 3 and 4). These were generally small magnitude earthquakes that were most visible on station AUH. A pronounced increase in locatable VT earthquakes occurred between July and October, 2007 (fig. 3). Magnitudes of these earthquakes were less than 1.0 (fig. 4).

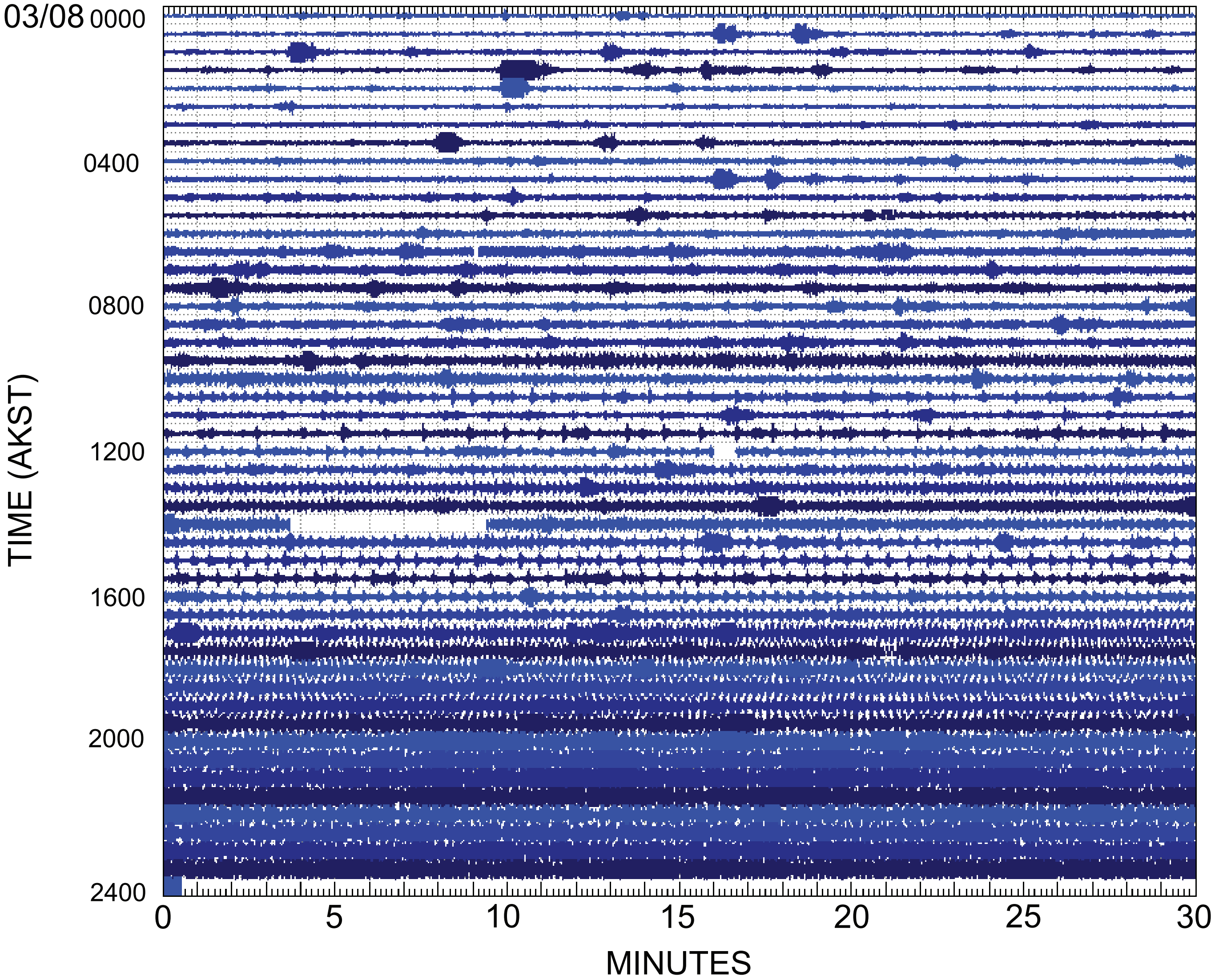

Figure 21. Velocity seismic record from station AUW on March 8 showing the onset of drumbeat earthquakes during the 2006 eruption. The rate and size of individual events changes several times until they form a nearly continuous signal at roughly 2330 AKST on March 8, 2006.

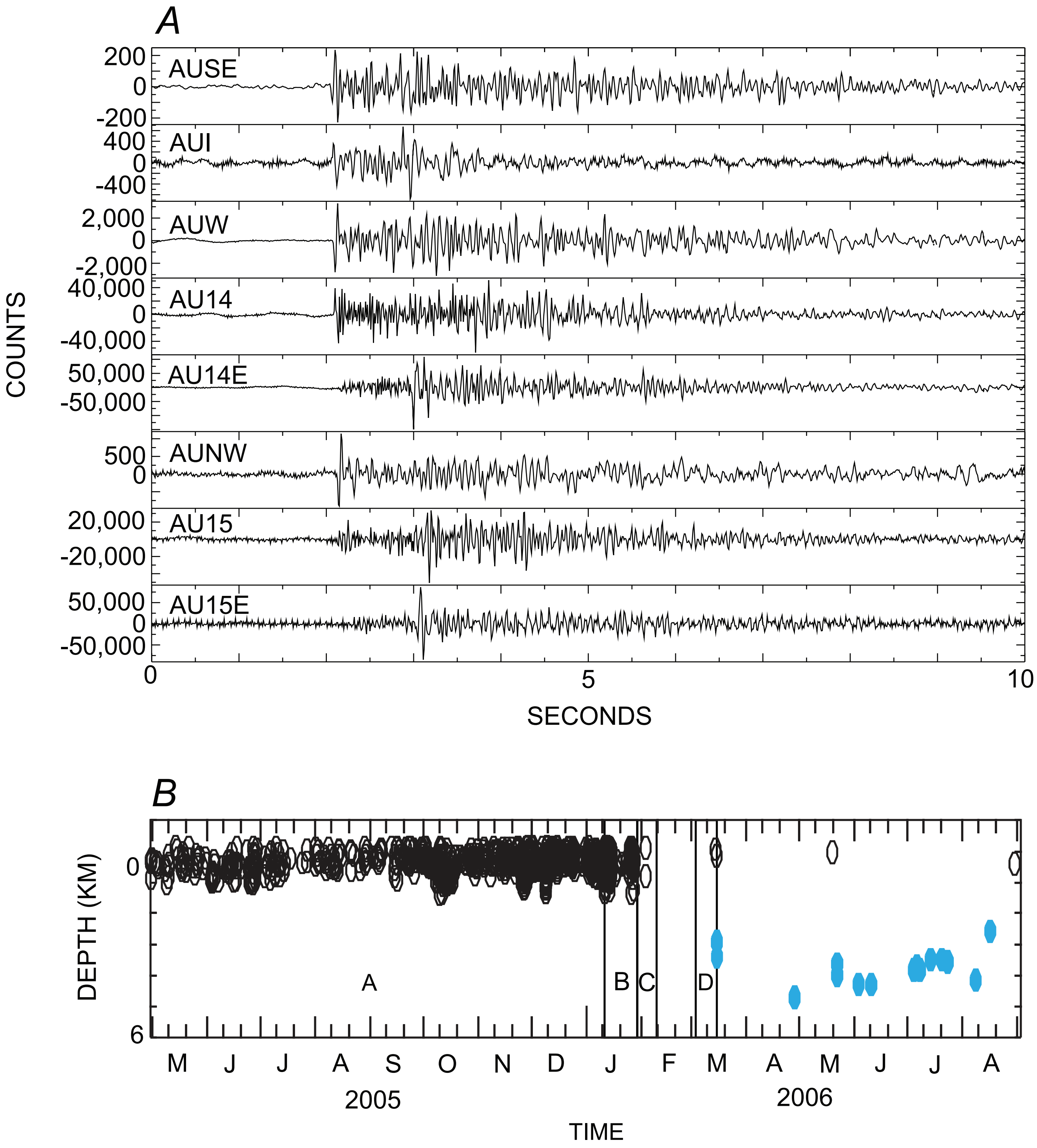

Figure 22. Representative waveform and plot of earthquake focal depth versus time, highlighting the occurrence of earthquakes between 2 and 5 km depth during the 2006 eruption sequence. *A*, Waveform of a magnitude 0.2 earthquake located at 3.55 km depth b.m.s.l. under the summit of Augustine on July 6, 2006. Individual station names are shown at left, east-west horizontal components are noted by "E" suffix. *B*, Plot of time versus focal depth showing the time history of the deeper earthquakes, noted by blue symbols, that followed the 2006 eruption. Labels A, B, C, and D note the precursory, explosive, continuous, and effusive phases of the 2006 eruption.

Discussion and Interpretation

This section relates the observed seismicity to the structure and subsurface configuration of the Augustine magmatic system and to the magmatic processes during the 1971, 1976, 1986, and 2006 eruptive sequences as well as the intervening quiescent periods. We will use the seismic patterns, waveform characteristics, and earthquake locations to infer both the geometry of the Augustine magmatic system and the evolution of the system during the three major eruptions. This discussion relies principally on the seismic record from 1970 through 2007 and secondarily on geophysical, geological, and visual observations reported by other authors.

Quiescent Periods

We think that the small shallow VT earthquakes most commonly seen at Augustine Volcano during quiescent periods, such as 1972 to 1975 and 1993 to 2004, represent small-scale adjustments within the upper portions of the volcanic edifice and summit dome complex. Deshon and others (this volume) find that only 30 to 40 percent of these earthquakes have similar waveforms, suggesting that seismicity is well distributed throughout the cone during quiescent periods. The stress regime responsible for the generation of these earthquakes is perhaps either thermal contraction of the cooling lava dome or gravitational slumping of the summit dome complex. Geodetic data from 1986 to 2000 indicate that portions of the summit dome complex can subside as much as 8 cm per year (Pauk and others, 2001). This process is relatively steady state, as evidenced by the relatively constant rate of VT earthquake activity observed between 1993 and 2004 (fig. 3).

Magmatic System Geometry

We think that the magmatic system beneath Augustine Volcano consists of a magma storage or source zone between 3.5 and 5 km b.m.s.l. that is connected by a largely aseismic conduit system to a shallower system of cracks that is centered near sea level. This shallower system roughly corresponds to the area where most earthquakes are located during the early precursory seismic sequences and may extend from as much as 0.9 km b.m.s.l. to several hundred m a.m.s.l. This shallower system of cracks is perhaps connected to the surface by a system of interconnected conduits or cracks that coalesce to a single north-south-trending dike at the volcano's summit. An idealized sketch of the inferred components of the Augustine magmatic system is shown in figure 23.

The deeper magma source area is only poorly defined seismically by the small number of earthquakes between 2 and 5 km b.m.s.l. that occurred in 1975 before the 1976 eruption (figs. 10 and 11) and following the 2006 eruption (figs. 7, 11 and 22). We speculate that the 1975 hypocenters most logically lie above the magma source zone, because they occurred before the 1976 eruption, and may reflect

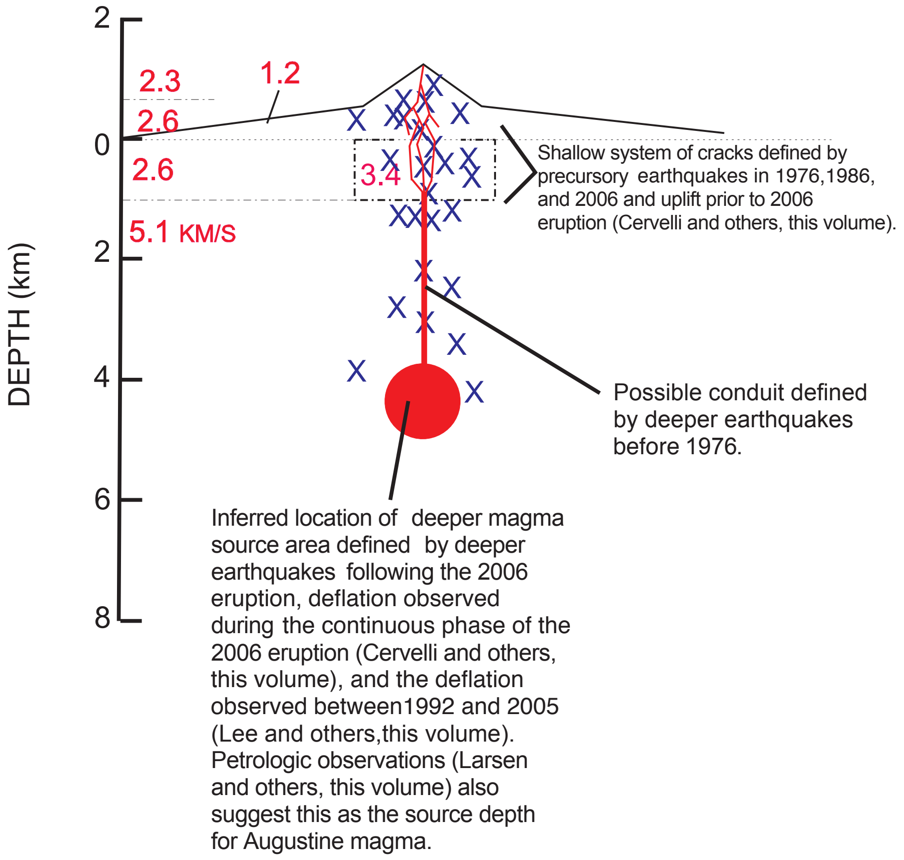

Shallow system of cracks defined by precursory earthquakes in 1976,1986, and 2006 and uplift prior to 2006 eruption (Cervelli and others, this volume).

Possible conduit defined by deeper earthquakes before 1976.

Inferred location of deeper magma source area defined by deeper earthquakes following the 2006 eruption, deflation observed during the continuous phase of the 2006 eruption (Cervelli and others, this volume), and the deflation observed between1992 and 2005 (Lee and others,this volume). Petrologic observations (Larsen and others, this volume) also suggest this as the source depth for Augustine magma.

Figure 23. Inferred cross section of the Augustine Volcano magmatic system based on seismic and supporting geophysical information. Principal components of the system are a shallow system of cracks that may extend from depths of 0.9 km below sea level to a few hundred meters above sea level, a deeper magma source area at 3.5 to 5.0 km depth, and a possible conduit defined by deeper earthquake hypocenters observed in 1975 and 2006. Xs note areas of VT earthquake hypocenters. P-wave seismic velocities determined by Kienle and others (1979) are shown on the left and beneath the volcano.

the upward movement of magma and associated volatiles along a conduit system or magma pathway. The 1976 eruption was both more explosive and more voluminous than the 1986 or 2006 eruptions. Perhaps the deeper precursory earthquakes in 1975 reflect the ascent of either a greater volume of magma or a more volatile rich and consequently more explosive magma. We have no compelling explanation for the lack of earthquakes in this 2-to-5-km depth range before the 1986 and 2006 eruptions. The 2006 precursory sequence was much more closely monitored than either the 1976 or 1986 precursory phases (fig. 2) and we located many more earthquakes in 2005 and 2006 than before either the 1976 or 1986 eruptions. On the basis of the appearance of deeper earthquakes' waveforms in 1975 and 2006 (figs. 12 and 22) and the increased station coverage in 2006 (fig. 2*C*), we think the lack of observed activity in this depth range before the 1986 and 2006 eruptions is not a reflection of network aperture, station geometry, or preferential data acquisition or processing. Consequently we suggest it is most likely that earthquakes in this depth range did not occur before either the 1986 or 2006 eruption.

The deeper earthquakes at 2 to 5 km b.m.s.l. that followed the 2006 eruption most likely reflect a stress response to the removal of magma from this area (fig. 22). Earthquakes at mid to upper crustal depths are often observed to begin beneath a volcanic edifice following the onset of eruptive activity. Such a stress response has been observed at numerous volcanoes, including Mount St. Helens, Washington (Weaver and others, 1981), Redoubt Volcano, Alaska (Power and others, 1994), and Mount Pinatubo, Philippines (Mori and others, 1996). The small numbers and magnitudes of these deeper (2 to 5 km b.m.s.l.) VT earthquakes may be a reflection of a smaller change in stress or strain rate associated with the more frequently active magma system at Augustine. Additional support for this source zone comes from the synthetic-aperture radar (InSAR) measurements from 1992 through 2005 that suggest the presence of a relatively subtle inflationary source at roughly 2 to 4 km depth (Lee and others, this volume) and the deflationary pressure source at 3.5-km depth that was active during the continuous phase of the 2006 eruption (Cervelli and others, this volume). Taking these observations together, we suggest that the magma source zone might most logically lie at 3.5 to 5.0 km depth. This depth is also consistent with petrologic evidence that suggests the source zone at 4 to 6 km depth b.m.s.l. for magmas erupted in 2006 (Larsen and others, this volume). Similar earthquakes in this depth range would not have been located following the 1976 eruption, because only three stations were operating during this period (table 1). Earthquakes in this depth range could easily have been missed following the 1986 eruption, when the network was relatively sparse and the data were recorded on photographic film.

We think the shallower system of cracks likely extends from about 0.9 km b.m.s.l. to a few hundred m a.m.s.l. and is the source zone for most of the VT earthquakes located at Augustine during precursory periods (figs. 7, 10 and 11). The concentration of earthquake hypocenters at this depth range may in part be governed by changes in the density that would accompany the P-wave velocity boundaries observed at 0.9 km b.m.s.l. and sea level. These changes in P-wave velocity are thought to reflect changes from zeolitized sediments to intrusive volcanic rocks beneath the Augustine cone (Kienle and others, 1979). These changes in density and lithology may cause magma and associated volatiles to pause in this area on their rise to the surface. This area of high earthquake activity is coincident with the inflation source modeled by Cervelli and others (this volume) that was active during the 2006 precursory phase.

We find no seismic expression of the deeper inflationary source at 7 to 12 km b.m.s.l. modeled by Lee and others (this volume). The only possible seismic expression of the Augustine magmatic system at mid- to lower-crustal depths is a single magnitude (M_L) 1.5 LP event at 26-km depth that occurred on April 15, 2008 (Dixon and Stihler, 2009).

Magmatic System Activation

Seismicity prior to the 1976, 1986, and 2006 eruptions all began within 0.5 km of sea level. We believe the onset of this seismic activity likely reflects the arrival of magmatic volatiles into the shallow system of cracks (fig. 23). The onset of seismic activity in this depth range began roughly 9 months before all three major eruptions and suggests that the processes that allow volatiles to accumulate in this area were active on a similar time scale before all three major eruptions. Confirmation of this interpretation comes from the uplift observed near sea level beneath the volcano's summit starting in July 2005 (Cervelli and others, 2006). The only seismic expression of movement of magma from greater depths are the shocks between 2 and 5 km depth below sea level that occurred between August and December 1975 (fig. 11) and between March and August 2006 (fig. 22).

As the system of cracks near sea level progressively pressurized, it likely forced some volatiles into the upper portions of the Augustine edifice. This is the process we suspect is responsible for the upward migration of hypocenters reported before the 1976 (Lalla and Kienle, 1980) and 1986 (Power, 1988) eruptions. Confirmation of this process comes from the progressive shallowing of the pressure source revealed by geodetic data between November 2005 and January 11, 2006 (fig. 17), reported by Cervelli and others (this volume). Additionally, increased fumorolic activity was reported 1 to 3 months before the 1976, 1986, and 2006 eruptions. All of these observations suggest that magmatic volatiles had moved upward through the Augustine cone in the months prior to each major eruption.

While the upward migration of earthquake hypocenters is expected, confirmed observations of this phenomenon are somewhat rare. This is perhaps more a reflection of deficiencies of volcano seismic networks, seismic velocity models, and processing methodology than an absence of physical process. The upward propagation of earthquake hypocenters has been reported at Mount Etna, Italy (Castellano and others, 1993), Mount Pinatubo (Harlow and others, 1995), Mount St. Helens (Moran and others, 2008; Thelen and others, 2008), and elsewhere. Propagating earthquake hypocenters have also often been observed associated with the intrusion of dikes in Hawaii (Klein and others, 1987). To examine this phenomenon at Augustine we use the methodology developed by Miller and others (2004) to track the progression of earthquake hypocenters driven by the migration of CO_2 in fold and thrust belts. First we smoothed our relocated hypocenter depths by calculating a 10-point running average of hypocentral depths similar to a convolution with a rectangular window or boxcar filter in the manner described by Oppenheim and Schafer (1975). We then calculated a best fit line to the relocated hypocenters of the precursory sequences of the 1976, 1986, and 2006 eruptions. The resultant data, best fit line, and linear correlation coefficient for each earthquake sequence are shown in figure 24. This analysis suggests that hypocenters moved upwards at a rate of approximately 1 km/yr before the 1976 and 1986 eruptions. A similar long-term upward progression of hypocenters was not observed during the 2006 precursory phase. This result is not unexpected, because the relocated earthquake depths in the 2006 precursory sequence began at a shallower level than in either the 1976 or 1986 precursory sequences (fig. 11). However, we do observe a short-term upward progression in hypocentral depth from 0.2 to 0.6 km a.m.s.l. between December 8 and 12, 2005 (fig. 24). A similar best-fit line for relocated hypocenters on these 4 days has a linear correlation coefficient of 0.9442 and a slope corresponding to 56 km/yr (150 m/d). Deshon and others (this volume) also found that earthquakes migrated upwards at this time on the basis of differential traveltimes measured between summit and flank stations. Geodetic data also indicate that magma and associated volatiles migrated upward between November 17, 2005, and January 10, 2006 (Cervelli and others, 2006). We note that a similar short-term upward migration in hypocenters may have occurred during the 1986 precursory phase between December 30, 1985 and January 1, 1986, when hypocenters migrated upwards from 0.2 to 0.6 km a.m.s.l. (fig. 24). The varying time scales (months and days) of these observed upward migrations suggests that separate physical processes or different conduit geometries may be responsible for generating the earthquake activity.

We did not observe any significant seismic activity under the flanks of the volcano throughout the period of this study, including the precursory sequences of the1976, 1986, or 2006 eruptions (fig. 10). Throughout the 38-year period of this study only a relatively small number of earthquakes were located under the volcano's flanks at distances of 3 to 10 km from the summit vent (fig. 7). This suggests that magma can

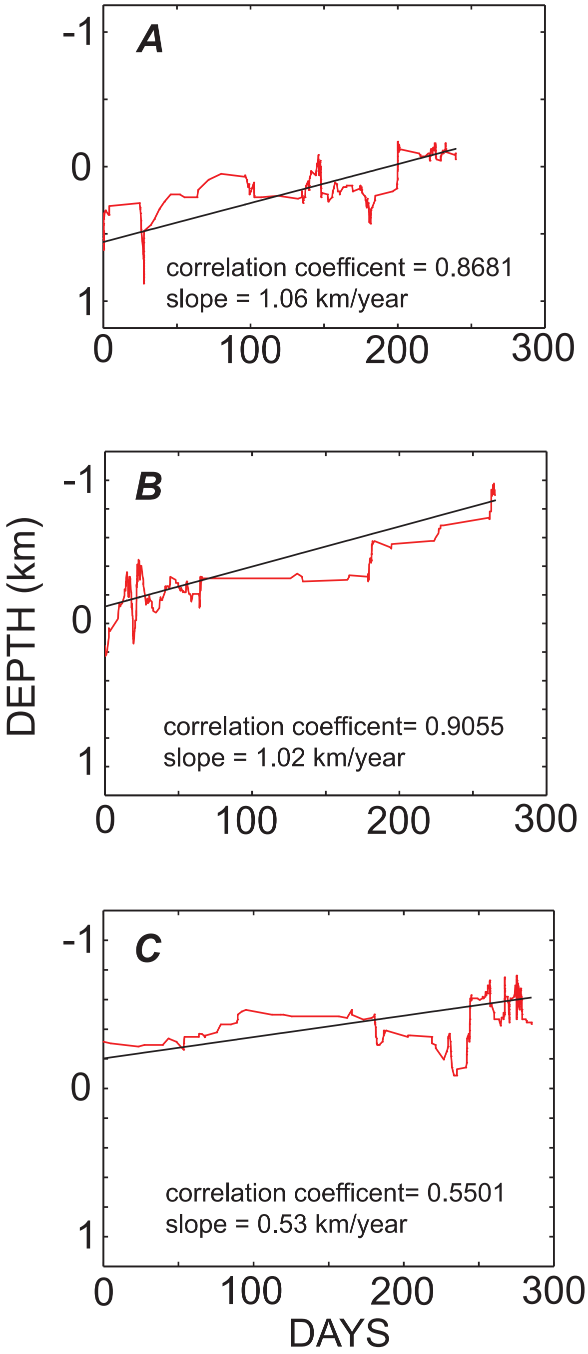

Figure 24. Smoothed hypocentral depths for relocated earthquakes (red lines) under the summit of Augustine Volcano from *(A)* May 2 to December 22, 1975, (*B*) July 4, 1985 to March 26, 1986, and (*C*) April 30, 2005 to January 11, 2006, plotted against the number of days in each sequence. These time periods correspond to the precursory seismic sequences for the 1976, 1986, and 2006 eruptions. Black lines represent least-squares fit to each set of hypocenters. Correlation coefficient and apparent rate of upward propagation of hypocentral depth are shown in each plot. The earthquake hypocenters in 2006 begin at shallower depth, and the resultant fit for the 2006 data (*C*) is poor.

move and erupt at Augustine without significantly stressing the surrounding crust. However, Fisher and others (this volume) did notice an increase in earthquake activity 25 km northeast of Augustine Island in the 6 months prior to the onset of the 2006 eruption and suggest that these earthquakes were triggered by magmatic processes at Augustine Volcano.

Eruption Initiation

The initial vent opening or onset of explosive activity appears to vary a great deal between the 1976, 1986, and 2006 eruptions. The onset of explosive activity in 1976 was extremely energetic seismically and was accompanied by a series of several hundred earthquakes on January 22 and 23, 1976 with larger magnitudes ($M_{L\max} \sim 2.75$) than any observed at Augustine between 1970 and 2007 (fig. 4). The most intense period of earthquake activity preceded the largest explosive eruptions reported by Kienle and Shaw (1977) by more than three hours (fig. 14). In contrast, explosive activity in 1986 was preceded by 3 days of increasing earthquake activity (fig. 16). The 1986 explosive sequence began with relatively small explosions that increased in size over 2 days (Power, 1988, fig. 22). Explosive activity in 2006 was immediately preceded by a 12-hour-long VT swarm (fig. 18) with a maximum magnitude of 1.6 (fig. 20), which is smaller than reported magnitudes of earthquakes that immediately preceded eruptions in 1976 or 1986 (figs. 4, 13).

The observed differences in the magnitudes and durations of earthquake swarms immediately preceding the three major eruptions suggest that the final ascent of magma and associated volatiles occurred differently in 1976, 1986, and 2006. The size of earthquakes does seem to scale roughly with the size of explosions and the amount of modification to the volcano's summit.

Drumbeat Events

The appearance of small, repetitive low- to medium-frequency seismic events or drumbeats at Augustine is very similar to seismicity often observed during effusive eruptions at Mount St. Helens (Moran and others, 2008; Thelen and others, 2008), Redoubt Volcano in Alaska (Power and others, 1994), Usu Volcano in Japan (Okada and others, 1981), Soufriere Hills Volcano in Montserrat (Rowe and others, 2004) and elsewhere. Often events with these frequency characteristics are referred to as hybrids (Lahr and others, 1994). The source mechanism of drumbeat seismicity has been the subject of vigorous research since their recent appearance at Soufriere Hills Volcano and Mount St. Helens. Proposed source models for drumbeat-style seismicity include a pressure transient in a fluid filled crack (Chouet, 1996; Waite and others, 2008), resonance of a fluid within a crack or conduit initiated by a stick-slip event within the magma (Neuberg and others, 2006), and stick-slip along the conduit magma interface (Iverson and others, 2006, Harrington and Brodsky, 2007; Iverson, 2009). It is not possible to fully characterize the source of repetitive events or drumbeats at Augustine given the observations and analysis presented here. However, the repeated occurrence of drumbeat seismicity during several eruptive events at Augustine allows us make some inferences about their source and significance.

Drumbeat-style seismicity was observed at Augustine associated with active periods of lava extrusion during both the initial dome building phase of the 1986 eruption (Power, 1988) and during the effusive phase of the 2006 eruption (fig. 21). In each case the drumbeats quickly coalesced into a continuous high-amplitude signal that persisted for roughly 8 days in both 1986 and 2006. At the end of each episode the high-amplitude signal slowly diminished until individual events could again be distinguished and then slowly faded into the normal seismic background. The initial dome building phase of the 1986 eruption had a second pulse of drumbeat seismicity that consisted only of discrete events and continued for 5 days. This second episode followed a 2 day hiatus in drumbeat activity (Power, 1988). In each of these cases of drumbeat style seismicity, the effusion of magma was actively occurring at the summit, building a lava dome.

Short episodes of drumbeat earthquakes lasting several hours were also observed briefly on January 11 and 12 during the early portions of the explosive phase of the 2006 eruption (fig. 18). These drumbeats provide some constraint on the source depth because they occur before many of the seismic stations were destroyed and we can determine their hypocentral depth relatively well. Relocated hypocenters using the 2D relocation method of Lalla and Power (this volume) suggest depths of 0.25 to 0.5 km a.m.s.l., while Deshon and others (this volume) have determined that a depth of 0.2 km a.m.s.l. or shallower for these events. The strongest sequence occurred between 2036 and 2206 AKST, and Buurman (2009) found these events to consist of a single family of events whose source migrates roughly 20 m over 1.5 hours.

The occurrence of repetitive events or drumbeats on January 11 and 12, 2006 suggests that magma may have reached the surface and a small lava dome may have begun to form as early as January 11. Unfortunately, insufficient visual observations of the summit of the volcano between January 11 and 13 do not allow us to confirm that new magma reached the surface at this time (Wessels and others, this volume). However, the strongest drumbeats begin at about 2036 AKST on January 11, which corresponds with the end of shallow deformation of the summit area. This change in deformation has been attributed to the possible onset of lava extrusion (Cervelli and others, this volume). Further, the deposits from the early explosions on January 13 contain a high percentage of dense low-silica andesite clasts, suggesting that these explosions may have partially removed new dome material (Vallance and others, this volume). The most likely explanation for these observations is that a new lava dome possibly began to form as early as late on January 11, 2006, in association with this sequence of drumbeats. Alternatively, these early drumbeats may only reflect the shallow movement of magma that may not have reached the surface.

During the effusive phase of the 2006 eruption, roughly 23 million m^3 of low-silica andesite (57 weight percent SiO_2) was erupted (Coombs and others, this volume). The average rate of extrusion during the 8 day period of drumbeat activity, assuming that magma effusion is restricted to periods when drumbeats are occurring, is roughly 33 m^3/s. We note that this extrusion rate exceeds the reported rates for Mount St. Helens in November 2004 through March 2005 of 4 to 5 m^3/s (Shilling and others, 2008) when drumbeat events were occurring at rates of 0.3 to 3 per minute (Moran and others, 2008). The rate of magma extrusion and drumbeat events (3 to 6 per minute) at Augustine greatly exceed the rates at Mount St. Helens, suggesting that the rate of drumbeat events may reflect the extrusion rate of magma. Unfortunately, the calculations of erupted volume at Augustine lack the temporal resolution to establish a specific relationship between magma flux and drumbeat rate and size. The drumbeats at Mount St. Helens occurred while lava was actively forming large peleean spines that were coated with fault gouge (Iverson and others, 2006). At Augustine there were no observations of notable fault gauge or spine development during the effusive phase of the 2006 eruption, suggesting that these are not required for generating drumbeat seismicity. No obvious periods of drumbeat activity were observed during the continuous phase of the 2006 eruption when magma with composition of 62.5 weight percent SiO_2 was dominant (Coombs and others, this volume). Oddly, magma erupted during the 2006 continuous phase at Augustine most closely matches the 65 weight percent SiO_2 of magma erupted at Mount St. Helens (Pallister and others, 2008) in 2004 when drumbeats were prevalent. This suggests that the occurrence of drumbeat style seismic events is not simply related to the magma's composition.

At the start of the 2006 effusive phase, drumbeats were observed to increase discontinuously in both rate and amplitude over a 16-hour period (fig. 21). At the end of the effusive phase drumbeats slowly decreased in rate and size between March 13 and 16. During most of this phase, the drumbeats formed a continuous high-amplitude signal that clipped many of the short-period stations on the island. Visual observations of the growing lava dome suggest that the high-amplitude drumbeat signal roughly corresponds to the period of maximum extrusion rate (Coombs and others, this volume; Wessels and others, this volume). These observations suggest that the rate and amplitude of drumbeats at Augustine in at least the 2006 effusive phase may correspond to the rate of magma extrusion.

It is also apparent from observations of the 2006 eruption of Augustine that lava domes can be emplaced on the summit without the occurrence of drumbeats. This was the case for the small dome observed on January 16, 2006 (Coombs and others, this volume). This dome was emplaced while stations as close as AUH (fig. 2*C*) were in operation without identifiable drumbeat seismicity. This indicates that magma of similar composition can move at shallow depths without accompanying drumbeat seismicity.

Observations of Augustine drumbeat-style seismicity suggest that its source is associated with the shallow movement of magma. The source is likely a complex process governed by a number of variables, such as the extrusion rate, ascent rate, gas content, compressibility and rigidity of magma as it moves at shallow depth. The best estimations of hypocentral depth suggest that drumbeats take place at 0.2 to 0.5 km a.m.s.l. These depths suggest that the actual source is within the Augustine cone and is not associated with a specific process related to the effusion of magma or formation of a lava dome at the volcano's summit. At Augustine the shallow movement of magma is closely associated temporally with the effusion of lava and emplacement of a lava dome at the summit of the volcano. The absence of obvious fault gauge or peleean spines at the summit of Augustine, as was observed at Mount St. Helens during drumbeat seismicity (Iverson, 2008; Moore and others, 2008) would lead us to prefer the models of Waite and others, (2008) or Neuberg and others (2006) for the source of Augustine drumbeats. At Augustine this style of seismicity is closely associated with effusion of magma at the summit.

Eruption Forecasting

In this section, we review the role that seismic observations played in formulating eruption forecasts and public warnings and the factors that influenced our interpretations during the 2006 eruption sequence, and we provide recommendations for evaluating future episodes of seismic unrest at Augustine Volcano. Neal and others (this volume) provide a detailed account of the specific warnings issued by AVO and the communication protocols used to disseminate the warnings, while Adleman and others (this volume) describe how AVO communicated with the news media and general public during the 2006 eruption. The forecasting strategy used by AVO relied on the synthesis of data from a number of different monitoring techniques, which include seismic (hypocenters, seismicity rate, RSAM, continuous spectral measurements, and waveform characteristics), visual observations, satellite observations, gas-flux measurements, and CGPS data. These observational data streams were supplemented by well-developed chronological information on the two most recent eruptions in 1976 (Johnston, 1978; Swanson and Kienle, 1985; Reeder and Lahr, 1987) and 1986 (Yount and others 1987; Power, 1988; Kienle and Swanson, 1988). The most important information for forecasting in 2006 was that the progression of unrest and eruptive events in 1976 and 1986 were strikingly similar. Both the 1976 and 1986 eruptions were preceded by roughly 9 months of slowly escalating VT earthquake activity. Each of these eruptions consisted of an initial explosive phase followed by two additional periods of eruptive activity characterized by milder explosive eruptions and effusive activity (fig. 8). Although the overall progression of seismic activity and eruptive events during the 1976 and 1986 eruptions were similar, there are notable differences that were considered in developing forecasts of the 2006 eruption. The most important differences were that the 1976 eruption was much more voluminous than the 1986 eruption, the 1976 precursory seismic sequence contained earthquakes with hypocenters in the 2 to 5 km depth range while the 1986 eruption did not, and the 1976 eruption progressed to completion much faster than the 1986 eruption (fig. 8).

The long-term AVO seismic monitoring program allowed us to identify the initial increase in VT earthquake activity and heighten our surveillance of the volcano as the shocks were occurring in the spring of 2005. Long-term seismic monitoring (fig. 3) allowed us to recognize that the initial subtle increase was significant, even though the early portions of the 2006 precursory seismicity were milder than either the 1976 or 1986 sequences (figs. 3, 4, 8). The prominent earthquake swam in October 2004 had a much shorter duration than the seismic increase in the spring of 2005.

This early identification of increased seismicity focused our attention on Augustine and allowed us to identify the uplift that began in July 2005 (Cervelli and others, 2006) at an early stage. Continued increases in both seismicity and uplift (fig. 17) provided a strong basis for the first public warning of possible renewed eruptive activity on November 29, 2005 when AVO moved the color code to yellow (Neal and others, this volume). Although some uncertainty persisted at this time about the eventuality of an eruption, the color code change positioned AVO to respond to the further escalations in unrest that were to follow shortly.

The continued increases in seismicity rate and geodetic uplift, combined with the phreatic explosions in early to mid December, the greatly increased fumorolic activity, opening of extensional cracks on the volcano's summit, and the greatly increased gas flux (McGee and others, this volume), served only to focus more of our attention on Augustine. During this period we greatly intensified our monitoring of Augustine by adding broadband seismometers, temporary CGPS receivers, time lapse cameras, Web cams (Paskievitch and others, this volume), and a pressure sensor (Petersen and others, 2006). In hindsight much of this equipment should have been deployed on the volcano earlier in the precursory phase when snow cover would have been lighter and we could have benefited from longer daylight hours.

The energetic earthquake swarm that began late on January 10 (fig. 18) was an unequivocal sign that eruptive activity should be expected in the short term. The level-of-concern color code was raised to orange at 2105 AKST on January 10, and AVO began 24-hour monitoring in both the Anchorage and Fairbanks offices. Although it was recognized on January 10 that the 2006 swarm had a more sudden onset than the earthquake swarm that immediately preceded eruptive activity in 1986 (compare figures 15 and 17). Unfortunately no warning was issued immediately following the first explosive event at 0444 AKST on January 11. The waveform of this explosion resembles a large VT earthquake in the short-period velocity record (fig. 18), and the relatively small amount of ash generated by this explosion only produced a short radar return (Schneider and others, 2006). The waveform of the second explosion at 0512 was much less ambiguous, and the level-of-concern color code was raised to red at 0550 AKST.

Following the onset of explosive activity on January 11, careful monitoring of seismic activity, along with radar and satellite imagery, allowed AVO to issue warnings of explosive eruptions on January 13, 14, 17, 27, and 28, often within seconds of the explosion's onset (Neal and others this volume). Further warnings were issued during the later phases of the eruption, again often formulated on the basis of the similar patterns in eruption progression observed during the 1976 and 1986 eruptions. The onset of drumbeat earthquakes on March 8 was especially noteworthy, because we were immediately able to associate this seismic activity with renewed lava extrusion. AVO lowered the level-of-concern color code from orange to yellow on April 28 and from yellow to green on August 9, 2006 (Neal and others, this volume).

A significant problem during the 2006 eruption was that all telemetered seismic and CGPS instruments near the volcano's summit and on the north side of the volcano were eventually destroyed by eruptive activity. This made it impossible to reliably calculate earthquake hypocentral depths in near-real time and track deformation of the upper portions of the edifice. To some extent, station loss is unavoidable; however, if stations had been operating high on the south and east flank of the volcano in 2006 these stations would likely have survived the eruption. In future years we recommend installing telemetered stations in locations near the site of AU13 and similar higher locations on all quadrants of the volcano. Ideally these seismometers would be three-component instruments.

In evaluating future episodes of unrest at Augustine, the following observations should be considered:

1. The 1976, 1986, and 2006 eruptions were all preceded by roughly 9 months of slowly escalating earthquake activity (figs. 3, 8) and hypocentral depths were observed to migrate slowly upward before the 1976 and 1986 eruptions (fig. 24). Shorter term upward migrations were also observed before the 1986 and 2006 eruptions.

2. Each of the three major eruptions began explosively and was followed by several months of discontinuous effusive activity. Although the overall character of each major eruption was similar, they progressed to completion on different time scales. The total duration of eruptive activity from beginning to end was approximately 85, 178, and 67 days for the 1976, 1986, and 2006, eruptions respectively (fig. 8).

3. Historical reports (Davidson, 1884; Coats, 1950; Detterman, 1968; Johnston and Detterman, 1979), as well as the geologic record (Waythomas and Waitt, 1998), indicate

that past eruptions show more variability in eruptive size and duration than we have seen in 1976, 1986, and 2006.

4. Smaller eruptions similar to that seen in 1971 should also be expected, and the period of precursory activity may be shorter than what was observed in 1976, 1986, and 2006.

5. Earthquakes at 2 to 5 km depth b.m.s.l. preceded the more explosive onset of the 1976 eruption (fig. 11). Procedures should be developed to closely monitor earthquake activity in this depth range.

6. The duration and size of earthquakes over the 24 to 48 hours immediately preceding the eruption's explosive onset in 1976, 1986, and 2006 showed great variability. Such variability in the onset of explosive activity should be expected in future eruptions.

7. Drumbeat seismicity was observed during the initial dome-building phase of the 1986 eruption and during the effusive phase of the 2006 eruption, when new magma was being actively extruded at the volcano's summit. Drumbeats were also observed during several brief periods of the explosive phase of the 2006 eruption. However, drumbeats were not observed in association with active lava extrusion during the second dome-building phase of the 1986 eruption or several periods of the 2006 eruption. Drumbeats should be taken as a strong indicator that magma is moving at shallow depth within the edifice and is likely forming a lava dome at the summit.

Summary and Conclusions

This paper summarizes the primary observations of seismic activity at Augustine Volcano between 1970 and 2007. During this period, Augustine Volcano experienced one minor and three major eruptions. Judging from the spatial and temporal development of earthquake hypocenters in association with a minor eruptive event in 1971 and three major eruptions in 1976, 1986, and 2006, we suggest that the subsurface magmatic system consists of a source region between 3.5 and 5 km depth b.m.s.l., and a system of cracks near sea level where magma and magmatic volatiles pause as they ascend to the surface. The position of these cracks may be controlled by density contrasts associated with rock types that are observed in changing P-wave velocities. These two magma storage areas are perhaps connected by a system of dikes or conduits that also extend to the surface.

The last three major eruptions at Augustine were all preceded by roughly 9 months of seismic activity. Hypocenters were observed to migrate upwards before the 1976 and 1986 eruptions over the length of the precursory period. However, before the 2006 eruption hypocenters began at a shallower depth, and a longer term upward migration was not observed. Relocated earthquake hypocenters and continuous geodetic data tracked a shorter term upward progression late in the precursory phase of the 2006 eruption (Cervelli and others, 2006; Cervelli and others, this volume). Each of these eruptions also followed a similar progression from explosive to effusive activity, although the time from onset to completion of eruptive activity varied considerably. Petrologic evidence also suggests that the magma-mixing events thought to have triggered the 1976, 1986, and 2006 eruptions involved magmas of similar composition. This overall similarity suggests that the physical processes responsible for the accumulation, rise, and eruption of magma at Augustine are roughly constant or change only slowly with time. If conditions do not change, future eruptions of Augustine might be expected to follow a similar pattern.

Acknowledgments

In compiling a long-term study of seismicity such as this we have relied on the hard work of many individuals over nearly a 40-year period. We gratefully acknowledge the early contributions of Jurgen Kienle, John Davies, Robert Forbes, Chris Pearson, Elliot Endo, Hans Pulpan, Dave Stone, and David Harlow. Many individuals, including Steve Estes, Guy Tytgat, John Benevento, Kaye Lawson, John Paskievitch, Ed Clark, John Lahr, and Tom Murray, managed to keep the Augustine seismic instrumentation and various acquisition systems operational over long periods of time. Scott Stihler, Jim Dixon, Tom Parker, and many others assisted with processing and archiving seismic data from 1993 through 2007. During the preparation of this manuscript we had useful conversations with Matt Haney, Phil Dawson, Bernard Chouet, Seth Moran, Greg Waite, Scott Stihler, Jim Dixon, Heather Deshon, Cliff Thurber, Helena Buurman, Katherine Jacobs, Stephanie Prejean, Mike West, Steve McNutt, Peter Cervelli, Michelle Coombs, Dave Schneider, Kristi Wallace, Tom Murray, Christina Neal, Kate Bull, Jessica Larsen, Game McGimsey, and many others. Peter Cervelli and Matt Haney provided extra assistance and guidance in preparing figures 10 and 24. We benefited from formal reviews of the text and figures by Diana Roman, Fred Klein, and Jeff Freymueller.

References Cited

Adleman, J.N., Cameron, C.E., Snedigar, S.F., Neal, C.A., and Wallace, K.L., 2010, Public outreach and communications of the Alaska Volcano Observatory during the 2005–2006 eruption of Augustine Volcano, *in* Power, J.A., Coombs, M.L., and Freymueller, J.T., eds., The 2006 eruption of Augustine Volcano, Alaska: U.S. Geological Survey Professional Paper 1769 (this volume).

Bailey, J.E., Dean, K.G., Dehn, J., and Webley, P.W., 2010, Integrated satellite observations of the 2006 eruption of Augustine Volcano, *in* Power, J.A., Coombs, M.L., and Freymueller, J.T., eds., The 2006 eruption of Augustine Volcano, Alaska: U.S. Geological Survey Professional Paper 1769 (this volume).

Barrett, S.A., 1978, A three-dimensional magnetic model of Augustine Volcano: University of Alaska Fairbanks, M.S. thesis, 175 p.

Buurman, H.M., 2009, Seismicity preceding volcanic explosions during the 2006 eruption of Augustine Volcano: University of Alaska Fairbanks, M.S. thesis, 85 p.

Buurman, H., and West, M.E., 2010, Seismic precursors to volcanic explosions during the 2006 eruption of Augustine Volcano, *in* Power, J.A., Coombs, M.L., and Freymueller, J.T., eds., The 2006 eruption of Augustine Volcano, Alaska: U.S. Geological Survey Professional Paper 1769 (this volume).

Castello, M., Ferrucci, F., Godano, C., Imposa, S., and Milano G., 1993, Upwards migration of seismic foci; a forerunner of the 1989 eruption of Mt. Etna (Italy): Bulletin of Volcanology, v. 55, p. 35–361.

Cervelli, P.F., Fournier, T., Freymueller, J.T., and Power, J.A., 2006, Ground deformation associated with the precursory unrest and early phases of the January 2006 eruption of Augustine Volcano, Alaska: Geophysical Research Letters, v. 33, doi: 10.1029/2006GL027219.

Cervelli, P.F., Fournier, T.J., Freymueller, J.T., Power, J.A., Lisowski, M., and Pauk, B.A., 2010, Geodetic constraints on magma movement and withdrawal during the 2006 eruption of Augustine Volcano, *in* Power, J.A., Coombs, M.L., and Freymueller, J.T., eds., The 2006 eruption of Augustine Volcano, Alaska: U.S. Geological Survey Professional Paper 1769 (this volume).

Chouet, B.A., 1996, Long-period seismicity; its source and use in eruption forecasting: Nature, v. 380, p. 309–316.

Coats, R.R., 1950, Volcanic activity in the Aleutian Arc: U.S. Geological Survey Bulletin, 974-B, p. 35–49.

Coombs, M.L., Bull, K.F., Vallance, J.W., Schneider, D.J., Thoms, E.E., Wessels, R.L., and McGimsey, R.G., 2010, Timing, distribution, and volume of proximal products of the 2006 eruption of Augustine Volcano, *in* Power, J.A., Coombs, M.L., and Freymueller, J.T., eds., The 2006 eruption of Augustine Volcano, Alaska: U.S. Geological Survey Professional Paper 1769 (this volume).

Daley, E.E., 1986, Petrology, geochemistry, and the evolution of magmas from Augustine Volcano, Alaska: University of Alaska Fairbanks, M.S. thesis 106 p.

Davidson, G., 1884, Notes on the volcanic eruption of Mount St. Augustine, Alaska, October 6, 1883: Science, v. 3, p. 186–189.

Detterman, R.L., 1968, Recent volcanic activity on Augustine Island, Alaska: U.S. Geological Survey Professional Paper 600-C, p. 126–129.

DeShon, H.R., Thurber, C.H., and Power, J.A., 2010, Earthquake waveform similarity and evolution at Augustine Volcano from 1993 to 2006, *in* Power, J.A., Coombs, M.L., and Freymueller, J.T., eds., The 2006 eruption of Augustine Volcano, Alaska: U.S. Geological Survey Professional Paper 1769 (this volume).

Dixon, J.P., Power, J.A., and Stihler, S.D., 2004, A comparison of seismic event detection with IASPEI and Earthworm acquisition systems at Alaskan volcanoes: Seismological Research Letters, v. 26, no. 2., p. 168–176.

Dixon, J.P., Stihler, S.D., Power, J.A., and Searcey, C., 2008, Catalog of earthquake hypocenters at Alaskan Volcanoes; January 1 through December 31, 2006: U.S. Geological Survey Data Series 326, 78 p.

Dixon, J.P., and Stihler, S.D., 2009, Catalog of earthquake hypocenters at Alaskan Volcanoes: January 1 through December 31, 2008: U.S. Geological Survey Data Series 467, 88 p.

Dzurisin, D., Iwatsubo, E.Y., Kleinman, J.W., Murray, T.L., Power, J.A., Paskievitch, J.F.,1994, Deformation monitoring at Augustine Volcano, AK: Eos, (American Geophysical Union Transactions), v. 75, abs. p. 166.

Endo, E.T., and Murray, T.L., 1991, Real-time seismic amplitude measurement (RSAM); a volcano monitoring and prediction tool: Bulletin of Volcanology, v. 53, p. 533–545.

Fisher, M.A., Ruppert, N.A., White, R.A., Sliter, R.W., and Wong, F.L., 2010, Distal volcano-tectonic seismicity near Augustine Volcano, *in* Power, J.A., Coombs, M.L., and Freymueller, J.T., eds., The 2006 eruption of Augustine Volcano, Alaska: U.S. Geological Survey Professional Paper 1769 (this volume).

Fremont, M., and Malone, S.D., 1987, High precision relative locations of earthquakes at Mount St. Helens, Washington: Journal of Geophysical Research, v. 92, p. 10233–10236.

Gorshkov, G., 1959, Gigantic eruption of the volcano Bezymianny: Bulletin of Volcanology, v. 21, p. 77–109.

Harlow, D.H., 1971, Volcanic earthquakes: Dartmouth College, M.A. thesis, 66 p.

Harlow, D.H., Power, J.A., Laguerta, E.P., Ambubuyog, G., White, R.A., and Hoblitt, R.P., 1995, Precursory seismicity and forecasting of the June 15, 1991 eruption of Mount Pinatubo, *in* Newhall, C.G., and Punongbuyan, R.S., eds., Fire and Mud, eruptions and lahars of Mount Pinatubo, Philippines: University of Washington Press, p. 258–306.

Harrington, R.M., and Brodsky, E.E., 2007, Volcanic hybrid earthquakes that are brittle-failure events: Geophysical Research Letters, v. 34, L06308, doi:10.1029/2006GL028714.

Harris, G.W., 1994, The petrology and petrography of lava from the 1986 eruption of Augustine Volcano: University of Alaska Fairbanks, M.S. thesis, 131 p.

Hill, D.P., Ellsworth, W.L., Johnston, M.J.S., Langbein, J.O., Oppenheimer, D.P., Pitt, P.A., Reasenberg, P.A., Sorey, M.L., and McNutt, S.R., 1990, The 1989 earthquake swarm beneath Mammoth Mountain, California; an initial look at the 4 May through 30 September activity: Bulletin Seismological Society of America, v. 80, p. 325–339.

Holasek, R.E., and Rose, W., 1991, Anatomy of 1986 Augustine Volcano eruptions as recorded by multispectral image processing of digital AVHRR weather satellite data: Bulletin of Volcanology, v. 53, p. 420–435.

Iverson, R.M., 2008, Dynamics of seismogenic volcanic extrusion resisted by a solid surface plug, Mount St. Helens, 2004–2005, *in* Sherrod, D.R., Scott, W.E., and Stauffer, P.H., eds, A volcano rekindled; the renewed eruption of Mount St. Helens, 2004–2006: U.S. Geological Survey Professional Paper 1750, p. 425–460.

Iverson, R.M., Dzurisin, D., Gardner, C.A., Gerlach, T.M., LaHusen, R.G., Lisowski, M., Major, J.J., Malone, S.D., Messerich, J.A., Moran, J.C., Pallister, J.S., Qamar, A., Schilling, S.P., and Vallance, J.W., 2006, Dynamics of seismogenic volcanic extrusion at Mount St. Helens in 2004–2005: Nature, v. 444, p. 439–443.

Jacobs, K.M., and McNutt, S.R., 2010, Using seismic *b*-values to interpret seismicity rates and physical processes during the preeruptive earthquake swarm at Augustine Volcano 2005–2006, *in* Power, J.A., Coombs, M.L., and Freymueller, J.T., eds., The 2006 eruption of Augustine Volcano, Alaska: U.S. Geological Survey Professional Paper 1769 (this volume).

Johnston, D.A., 1978, Volatiles, magma mixing, and the mechanism of eruptions of Augustine Volcano, Alaska: University of Washington, Ph. D. dissertation, 177 p.

Johnston, D.A., and Detterman, R.L., 1979, Revision of the recent eruptive history of Augustine Volcano; elimination of the “1902 eruption”: U.S. Geological Survey Circular, 804-B, p. 80–84.

Jolly, A.D., Power, J.A., Stihler, S.D., Rao. L., Davidson, G., Paskievitch J.F., Estes, S., and Lahr, J.C., 1996, Catalog of earthquake hypocenters for Augustine, Redoubt, Iliamna, and Mount Spurr volcanoes, Alaska; January 1, 1991–December 31, 1993: U.S. Geological Survey Open-file Report 96-007, 89 p.

Kienle, J., and Shaw, G.E., 1977, Plume dynamics, thermal energy and long distance transport of vulcanian eruption clouds from Augustine Volcano, Alaska: Journal of Volcanology and Geothermal Research, v. 6, p. 139–164.

Kienle, J., Lalla, D.J., Pearson, C.F., and Barrett, S.A., 1979, Search for shallow magma accumulations at Augustine Volcano: University of Alaska Fairbanks, Geophysical Institute, Final Report to U.S. Department of Energy, 157 p.

Kienle, J., and Swanson, S.E., 1983, Volcanism in the eastern Aleutian Arc; late quaternary and Holocene centers, tectonic setting and petrology; Journal of Volcanology and Geothermal Research, v. 17, p 393–432.

Kienle, J., and Swanson, S.E., 1985, Volcanic hazards from future eruptions of Augustine Volcano, Alaska: Geophysical Institute, University of Alaska Fairbanks, Rep. UAG R-275, 2nd ed., 122 p.

Klein, F.W., Koyanagi, R.Y., Nakata, J.S., and Tanigawa, W.R., 1987, The seismicity of Kilauea’s magma system, *in* Decker, R.W., Wright, T.L., and Stauffer, P.H., eds., U.S. Geological Survey Professional Paper 1350, p. 1019–1186.

Lalla, D.J., and Kienle, J., 1978, Evolution of seismicity at Augustine Volcano, 1970 to 1976 eruption: Geological Society of America, Abstracts With Programs, v. 10, p. 113.

Lalla, D.J., and Kienle, J., 1980, Problems in volcanic seismology on Augustine Volcano, Alaska: Eos (American Geophysical Union Tranactions), v. 61 p. 68.

Lalla, D.J., and Power, J.A., 2010, A two-step procedure for calculating earthquake hypocenters at Augustine Volcano, *in* Power, J.A., Coombs, M.L., and Freymueller, J.T., eds., The 2006 eruption of Augustine Volcano, Alaska: U.S. Geological Survey Professional Paper 1769 (this volume).

Lahr, J.C., 1999, HYPOELLIPSE; A computer program for determining local earthquake hypocentral parameters, magnitude and first motion pattern: U.S. Geological Survey Open-File Report 99-361, 48 p.

Lahr, J.C., Chouet, B.C., Stephens, C.D., Power, J.A., and Page, R.A., 1994, Earthquake classification, location and error analysis in a volcanic environment; implications for the magamatic system of the 1989–1990 eruptions of Redoubt Volcano, Alaska: Journal of Volcanology and Geothermal Research, v. 62, p. 137–151.

Larsen, J.F., Nye, C.J., Coombs, M.L., Tilman, M., Izbekov, P., and Cameron, C., 2010, Petrology and geochemistry of the 2006 eruption of Augustine Volcano, *in* Power, J.A., Coombs, M.L., and Freymueller, J.T., eds., The 2006 eruption of Augustine Volcano, Alaska: U.S. Geological Survey Professional Paper 1769 (this volume).

Lee, C.-W., Lu, Z., Jung, H.-S., Won, J.-S., and Dzurisin, D., 2010, Surface deformation of Augustine Volcano, 1992–2005, from multiple-interferogram processing using a refined small baseline subset (SBAS) interferometric synthetic aperture radar (InSAR) approach, *in* Power, J.A., Coombs, M.L., and Freymueller, J.T., eds., The 2006 eruption of Augustine Volcano, Alaska: U.S. Geological Survey Professional Paper 1769 (this volume).

Lee, W.H.K., Tottingham, D.M., and Ellis, J.O., 1988, A PC-based seismic data acquisition and processing system: U.S. Geological Survey Open-file Report 88-751, 31 p.

Mauk, F.J., and Kienle, J., 1973, Microearthquake triggering at St. Augustine Volcano, Alaska, triggered by earth tides: Science, v. 182, p. 386–389.

McGee, K.A., Doukas, M.P., McGimsey, R.G., Neal, C.A., and Wessels, R.L., 2010, Emission of SO_2, CO_2, and H_2S from Augustine Volcano, 2002–2006, *in* Power, J.A., Coombs, M.L., and Freymueller, J.T., eds., The 2006 eruption of Augustine Volcano, Alaska: U.S. Geological Survey Professional Paper 1769 (this volume).

McNutt, S.R., Tytgat, G., Estes, S.A., and Stihler, S.D., 2010, A parametric study of the January 2006 explosive eruptions of Augustine Volcano, using seismic, infrasonic, and lightning data, *in* Power, J.A., Coombs, M.L., and Freymueller, J.T., eds., The 2006 eruption of Augustine Volcano, Alaska: U.S. Geological Survey Professional Paper 1769 (this volume).

Miller, S.A., Colletti, C., Chlaraluce, L., Cocco, M., Barchi, M., and Kaus, B.J.P., 2004, Aftershocks driven by a high pressure CO_2 source at depth: Nature, v. 427, p. 724–727.

Moore, P.L., Iverson, N.R., and Iverson, R.M., 2008, Frictional properties of the Mount St. Helens Gouge, *in* Sherrod, D.R., Scott, W.E., and Stauffer, P.H., eds, A volcano rekindled; the renewed eruption of Mount St. Helens, 2004–2006: U.S. Geological Survey Professional Paper 1750, p. 415–424.

Moran, S.C., Malone, SD., Qamar, A.I., Thelen, W., Wright, A.K.,and Caplan-Auerbach, J., 2008, Seismicity associated with renewed dome-building at Mount St. Helens, 2004–2005, *in* Sherrod, D.R., Scott, W.E., and Stauffer, P.H., eds, A volcano rekindled; the renewed eruption of Mount St. Helens, 2004–2006: U.S. Geological Survey Professional Paper 1750, p. 27–60.

Mori, J., White, R.A., Harlow, D.H., Okubo, P., Power, J.A., Hoblitt, R.P., Laguerta, E., Lanuza, A., and Bautista, B., 1996, Volcanic earthquakes following the 1991 climactic eruption of Mount Pinatubo; strong seismicity during a waning eruption, *in* Newhall, C.G., and Punongbayan, R.S., eds, Fire and Mud, Eruptions and Lahars of Mount Pinatubo, Philippines: University of Washington Press, p. 339–350.

Neal, C.A., Murray, T.L., Power, J.A, Adleman, J.N., Whitmore, P.M., and Osiensky, J.M., 2010, Hazard information management, interagency coordination, and impacts of the 2005–2006 eruption of Augustine Volcano, *in* Power, J.A., Coombs, M.L., and Freymueller, J.T., eds., The 2006 eruption of Augustine Volcano, Alaska: U.S. Geological Survey Professional Paper 1769 (this volume).

Neuberg, J.W., Tuffen, H., Collier, L., Green, D., Powell, T., and Dingwell, D., 2006, The trigger mechanism of low-frequency earthquakes on Montserrat: Journal of Volcanology and Geothermal Research, v. 154, p. 37–50.

Okada, H., Watanabe, H., Yamashita, H., and Yokoyama, I., 1981, Seismologcal signifigance of the 1977–1978 eruptions and magma intrusion process of Usu Volcano, Hokkaido: Journal of Volcanology and Geothermal Research, v. 9, p. 311–334.

Oppenheim, A.V., and Schafer, R.W., 1975, Digital signal processing, Englewood Cliffs, New Jersey, Prentice Hall, 278 p.

Pallister, J.S., Thornber, C.R., Cashman, K.V., Clynne, M.A., Lowers, H.A., Mandeville, C.W., Brownfield, I.K., and Meaker G.P., 2008, Petrology of the 2004–2006 Mount St. Helens Lava Dome—implications for magmatic plumbing and eruption triggering, *in* Sherrod, D.R., Scott, W.E., and Stauffer, P.H., eds, A volcano rekindled; the renewed eruption of Mount St. Helens, 2004–2006: U.S. Geological Survey Professional Paper 1750, p. 647–702.

Paskievitch, J., Read, C., and Parker, T., 2010, Remote telemetered and time-lapse cameras at Augustine Volcano, *in* Power, J.A., Coombs, M.L., and Freymueller, J.T., eds., The 2006 eruption of Augustine Volcano, Alaska: U.S. Geological Survey Professional Paper 1769 (this volume).

Pauk, B.A., Power, J.A., Lisowski, M., Dzurisin, D., Iwatsubo, E.Y., and Melbourne, T., 2001, Global positioning system (GPS) survey of Augustine Volcano, Alaska, August 3-8, 2000; Data processing, geodetic coordinates and comparison with prior geodetic surveys: U.S. Geological Survey Open-File Report 01-99, 20 p.

Pauk, B.A., Jackson, M., Feaux, K., Mencin, D., and Bohnenstiehl, K., 2010, The Plate Boundary Observatory permanent global positioning system network on Augustine Volcano before and after the 2006 eruption, *in* Power, J.A., Coombs, M.L., and Freymueller, J.T., eds., The 2006 eruption of Augustine Volcano, Alaska: U.S. Geological Survey Professional Paper 1769 (this volume).

Pearson, C.F., 1977, Seismic refraction study of Augustine Volcano: University of Alaska Fairbanks, M.S. thesis, 131 p.

Petersen, T., De Angelis, S., Tytgat, G., and McNutt, S.R., 2006, Local infrasound observations of large ash explosions at Augustine Volcano, Alaska, during January 11–28, 2006: Geophysical Research Letters, v. 33 , doi 10.1029/2006GL026491.

Power, J.A., (1988), Seismicity associated with the 1986 eruption of Augustine Volcano, Alaska: University of Alaska Fairbanks, M.S. thesis, 142 p.

Power, J.A., and Iwatsubo E.Y., 1998, Measurements of slope distances and zenith angles at Augustine Volcano, Alaska, 1986, 1988, and 1989: U.S. Geological Survey Open-File Report 98-145, 17 p.

Power, J.A., Lahr, J.C., Page, R.A., Chouet, B.A., Stephens, C.D., Harlow, D.H., Murray, T.L., and Davies, J.N., 1994, Seismic evolution of the 1989–1990 eruption sequence of Redoubt Volcano, Alaska: Journal of Volcanology and Geothermal Research, v. 62, p. 69–94.

Power, J.A., Nye, C.J., Coombs, M.L., Wessels, R.L., Cervelli, P.F., Dehn, J., Wallace, K.L., Freymueller, J.T., and Doukas, M.P., 2006, The reawakening of Alaska's Augustine Volcano: Eos (American Geophysical Union Transactions), v. 87, p. 373, 377.

Reeder, J.W., and Lahr, J.C., 1987, Seismological aspects of the 1976 eruptions of Augustine Volcano, Alaska: U.S. Geological Survey Bulletin 1768, 32 p.

Robinson, M., 1990, XPICK users manual, version 2.7: Seismology Lab, Geophysical Institute, University of Alaska Fairbanks, 93 p.

Roman, D.C., Cashman, K.V., Gardner, C.A., Wallace P.J., and Donovan, J.J., 2006, Storage and interaction of compositionally heterogeneous magmas from the 1986 eruption of Augustine Volcano, Alaska: Bulletin of Volcanology, v. 68, p. 240–254, doi10.1007/s00445-005-003-z.

Rowe, C.A., Thurber, C.H., and White, R.A., 2004, Dome growth behavior at Soufriere Hills Volcano, Montserrat, revealed by relocation of volcanic event swarms, 1995–1996: Journal of Volcanology and Geothermal Research, v. 134, p. 199–221.

Schneider, D.J., Scott, C., Wood J., and Hall T., 2006, NEXRAD weather radar observations of the 2006 Augustine volcanic eruption clouds: Eos (American Geophysical Union Transactions) v. 87, abs. V51C-1686.

Sentman, D.D., McNutt, S.R., Stenbaek-Nielsen, H.C., Tytgat, G., and DeRoin, N., 2010, Imaging observations of thermal emissions from Augustine Volcano using a small astronomical camera, *in* Power, J.A., Coombs, M.L., and Freymueller, J.T., eds., The 2006 eruption of Augustine Volcano, Alaska: U.S. Geological Survey Professional Paper 1769 (this volume).

Shilling, S.P., Thompson, R.A., Messerich, J.A., and Iwatsubo, E.Y., 2008, Use of digitial aerophotogrammetry to determine rates of lava dome growth, Mount St. Helens, Washington, 2004–2005, *in* Sherrod, D.R., Scott, W.E., and Stauffer, P.H., eds, A volcano rekindled; the renewed eruption of Mount St. Helens, 2004–2006: U.S. Geological Survey Professional Paper 1750, p. 145–167.

Siebert, L., Beget, J.E., and Glicken, H., 1995, The 1883 and late-prehistoric eruptions of Augustine Volcano, Alaska: Journal of Volcanology and Geothermal Research, v. 66, p. 367–395.

Swanson, S.E., and Kienle, J., 1988, The 1986 eruption of Mount St. Augustine; Field test of a hazard evaluation: Journal of Geophysical Research v. 93, p. 4500–4520.

Thelen, W.A., Crosson, R.S., and Creager, K.C., 2008, Absolute and relative locations of earthquakes at Mount St. Helens, Washington using continuous data: implications for magmatic processes, *in* Sherrod, D.R., Scott, W.E., and Stauffer, P.H., eds, A volcano rekindled; the renewed eruption of Mount St. Helens, 2004–2006: U.S. Geological Survey Professional Paper 1750, p. 71–96.

Thomas, R.J., McNutt, S.R., Krehbiel, P.R., Rison, W., Aulich, G., Edens, H.E., Tytgat, G, and Clark, E., 2010, Lightning and electrical activity during the 2006 eruption of Augustine Volcano, *in* Power, J.A., Coombs, M.L., and Freymueller, J.T., eds., The 2006 eruption of Augustine Volcano, Alaska: U.S. Geological Survey Professional Paper 1769 (this volume).

Vallance, J.W., Bull, K.F., and Coombs, M.L., 2010, Pyroclastic flows, lahars, and mixed avalanches generated during the 2006 eruption of Augustine Volcano, *in* Power, J.A., Coombs, M.L., and Freymueller, J.T., eds., The 2006 eruption of Augustine Volcano, Alaska: U.S. Geological Survey Professional Paper 1769 (this volume).

Villagomez, D., 2000, Sismicidad del volcan Guagua Pichincha 1998–1999: Quito, Ecuador, Escuela Politecnica Nacional, M.S. thesis.

Waite, G.P., Chouet, B.A. and Dawson P.B., 2008, Eruption dynamics at Mount St. Helens imaged from broadband seismic waveforms; Interaction of the shallow magmatic and hydrothermal systems: Journal of Geophysical Research, v. 113, B02305, doi:10.1029/2007JB005259.

Waitt, R.B., and Begét, J.E., 2009, Volcanic processes and geology of Augustine Volcano, Alaska: U.S. Geological Survey Professional Paper 1762, 78 p., 2 map plates [http://pubs.usgs.gov/pp/1762/].

Wallace, K.L., Neal, C.A., and McGimsey, R.G., 2010, Timing, distribution, and character of tephra fall from the 2005–2006 eruption of Augustine Volcano, *in* Power, J.A.,

Coombs, M.L., and Freymueller, J.T., eds., The 2006 eruption of Augustine Volcano, Alaska: U.S. Geological Survey Professional Paper 1769 (this volume).

Waythomas, C.F., and Waitt, R.B., 1998, Preliminmary volcano-hazard assessment for Augustine Volcano, Alaska, U.S. Geological Survey Open-File Report 98-106, 39 p.

Wessels, R.L., Coombs, M.L., Schneider, D.J., Dehn, J., and Ramsey, M.S., 2010, High-resolution satellite and airborne thermal infrared imaging of the 2006 eruption of Augustine Volcano, *in* Power, J.A., Coombs, M.L., and Freymueller, J.T., eds., The 2006 eruption of Augustine Volcano, Alaska: U.S. Geological Survey Professional Paper 1769 (this volume).

Weaver, C.S., Grant, W.C., Malone, S.D., and Endo, E.T., 1981, Post-May 18 seismicity; volcanic and tectonic applications, *in* Lipman, P.W., and Mullineaux, D.R., eds., The 1980 eruptions of Mount St. Helens, Washington: U.S. Geological Survey Professional Paper 1250, p. 109–122.

Yount, M.E., Miller, T.P., and Gamble, B.M., 1987, The 1986 eruptions of Augustine Volcano, Hazards and effects: U.S. Geological Survey Circular 998, p. 4–13.

The 2006 Eruption of Augustine Volcano, Alaska
Power, J.A., Coombs, M.L., and Freymueller, J.T., editors
U.S. Geological Survey Professional Paper 1769

Chapter 2

Seismic Precursors to Volcanic Explosions During the 2006 Eruption of Augustine Volcano

By Helena Buurman[1] and Michael E. West[1]

Abstract

The 2006 eruption of Augustine Volcano, Alaska, generated more than 3,500 earthquakes in a month-long time frame bracketing the most explosive period of activity. We examine two quantitative tools that, in retrospective analysis, were excellent indicators of imminent eruption. The first tool, referred to as the frequency index (*FI*), is based on a simple ratio of high- and low-frequency energy in an earthquake seismogram. It is a metric that allows us to quantify the differences between the canonical high-frequency, hybrid, and low-frequency volcanic earthquakes. *FI* values greater than −0.4 indicate earthquakes classically referred to as high-frequency or volcano-tectonic events. *FI* values less than −1.3 correspond to events usually referred to as low-frequency earthquakes. Because the *FI* is based on a ratio and not a spectral peak, hybrid earthquakes are successfully assigned *FI* values intermediate to these two classes. In this eruption, we find a remarkable correlation between events with *FI* less than −1.8 and explosive eruptions. The second tool we examine is based on repeating seismic waveforms identified through waveform cross-correlation. Although the vast majority of earthquakes during this eruption have unique waveforms, subsets of events exhibiting a high degree of similarity occur and are closely tied to explosive eruption events. Of the 13 large explosion events, seven were preceded by clusters of highly similar earthquakes. We apply the *FI* and correlation tools together to identify changes in high- and low-frequency earthquake occurrences and examine their relations to the precursory, explosive, and continuous phases of the eruption. We find that earthquakes that have low *FI* values and earthquakes exhibiting high degrees of similarity occur almost exclusively within hours of explosive eruptions and postulate that they occur as a result of the final ascent of magma in the volcanic edifice. Because neither of these methods requires analyst-reviewed earthquake locations, we believe that they have considerable potential as automated real-time volcano monitoring tools.

Introduction

Seismicity has long been one of the most commonly monitored aspects of active volcanoes. Different volcanic processes produce very different types of earthquakes, varying in waveform duration, onset, frequency content, and amplitude. Earthquakes with impulsive P and S arrivals and peak frequencies between 5 and 15 Hz, for example, are typically the result of brittle failure of rock within the volcanic edifice (McNutt, 1996). They often occur at high rates during episodes of volcanic unrest, although they are also part of the natural background seismicity found at volcanoes. Another type of earthquake routinely observed during episodes of volcanic activity has an emergent P arrival and often lacks a distinct S arrival. This type of earthquake is dominated by frequencies between 1 and 5 Hz, has little energy at frequencies greater than 15 Hz, and is thought to result from the resonance of fluid-filled cracks (Chouet, 1988). Numerous trigger mechanisms exist for such a process, and we refer to the summaries of Neuberg and others (2005) and Petersen (2007) for excellent overviews.

Certain volcanic processes can cause earthquakes to have remarkably similar waveform characteristics. For one waveform to appear the same as another it must originate in approximately the same place and from the same process. Nondestructive processes such as stick-slip movement along a fault or conduit or destructive mechanisms such as the incremental opening of cracks are possible sources for such earthquakes. The low-frequency resonant sources can be particularly rich in similar waveforms because of their inherently nondestructive source (for example, Stephens and Chouet, 2001; Petersen, 2007).

Perhaps the most basic metric for tracking volcanic seismicity is the overall rate of earthquakes. Eruptions are

---

[1] Alaska Volcano Observatory, Geophysical Institute, University of Alaska Fairbanks, 903 Koyukuk Drive, Fairbanks, AK 99775.

almost always preceded by some type of earthquake swarm. The swarm may last hours or months and may contain a variety of earthquake types or consist of just one style of event (Benoit and McNutt, 1996). The wide range of swarm characteristics reflects the wide range of processes thought to produce them. However, the nearly ubiquitous existence of precursory seismic swarms is one of the foundations of volcano monitoring.

Quantifying seismic activity is an effective method for inferring the level of unrest and the type of activity occurring at a volcano. This can be challenging in a real-time setting because the rate of seismic activity in a precursory swarm typically exceeds the rate at which events can be processed by any sort of analyst-reviewed process. Earthquakes are often classified manually, and this is usually based on the experience and interpretation of the analyst in subjective method that can lead to inconsistencies across or even within datasets (Langer and others, 2006). The manual review of earthquakes is impossible to accomplish in real time during rapid seismic sequences, even though assessing earthquake parameters such as frequency content is precisely what is needed in order to know whether or not such swarms are building towards an eruption.

We present a method for differentiating between earthquake types based on their frequency content. Our approach is simple and can be applied without user intervention. We apply this method to the explosive sequences of the 2006 eruption of Augustine Volcano, Alaska. The method is largely independent of earthquake locations and is robust to changes in seismic network coverage. The only assumption we make is that the seismic events are being generated by the volcano—a reasonable assumption given the high rates of seismicity during most eruptions. This is particularly relevant to Augustine, where the earthquakes are clustered together such that the first-order earthquake locations (which at some volcanoes exhibit a clear rise to the surface before eruption; for example, Harlow and others, 1994) provided limited information about the eruptive processes.

We also investigate patterns of repeating earthquakes and examine how they relate to eruptive behavior. The classification of seismic events combined with the identification of repeating earthquakes provides a different insight into the processes that occur at an erupting volcano. We show that an automated analysis of this type could provide key observations and even identify precursors to explosive activity.

Augustine Volcano

Augustine Volcano is a 10-km-wide island located in Cook Inlet between the Kenai Peninsula and Cape Douglas, 115 km from the town of Homer, in south-central Alaska. It has an historical eruptive history dating back to 1812 and erupted four

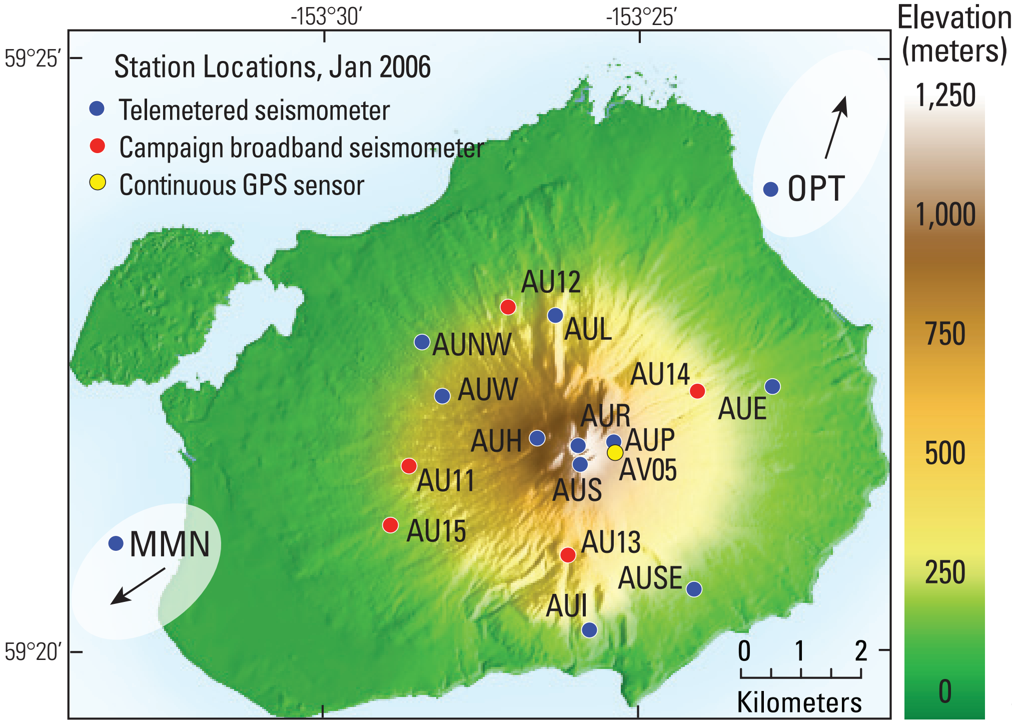

Figure 1. Locations of seismic stations on Augustine Island. Reference stations MMN and OPT used during the compilation of the catalog are located on the mainland; their directions are indicated.

times in the twentieth century alone, with the most recent eruption occurring in 1986 (Power and Lalla, this volume).

The 2006 eruption of Augustine began on January 11, following an 8.5-month period of precursory seismic activity (Jacobs and McNutt, this volume; Power and Lalla, this volume). An earthquake swarm occurred on January 10–11, 2006, which culminated in two phreatic explosions (Wallace and others, this volume) and heralded the onset of the explosive eruption sequence. On the basis of the character of unrest and the resultant eruptive deposits, Coombs and others (this volume) divide the eruption into several different phases. The explosive phase occurred between January 11 and January 28, during which time the eruptive activity was characterized by 2 largely phreatic and 11 magmatic explosions that generated ash plumes to heights greater than 9 km above sea level (asl) (Bailey and others, this volume), with repose periods between events lasting hours to days. These events recorded peak amplitudes greater than 20 Pa on the local pressure sensor located at station AUE (fig. 1), 3.5 km east of the volcano's summit. The explosions in the latter half of January were also strong enough to be recorded on the 153US infrasonic array at Fairbanks, 675 km north of Augustine (Wilson and others, 2006). A period of continuous eruptive activity (the continuous phase) began on January 28. This was characterized by a persistent ash plume up to 5 km asl (Bailey and others, this volume), produced by discrete but frequent (minutes to hours apart) minor explosions measuring less than 20 Pa at pressure sensor AUE. A gradual transition to effusive behavior followed, in which the small explosive events became fewer in number during the first week of February and the eruptive activity became dominated by dome growth with associated rockfalls and block and ash flows. Finally, a period of dome growth and lava flow (the effusive phase) between March 3 and March 16 brought the 2006 eruption sequence to a close.

The dataset used in this study spans the last 11 days of the precursory phase, which terminates with a vigorous seismic swarm of over 780 earthquakes, the entire explosive phase from January 11 to January 28, and the majority of the continuous phase from January 28 to February 6. By February 6 the seismic activity had begun to wane considerably and the volcano was moderately quiet until a short effusive dome-building phase occurred in early March 2006.

Data

Augustine was one of the more densely instrumented volcanoes in Alaska before 2006 as a result of its recent eruptive history and its proximity to settlements. The real-time seismic network on the island consisted of 10 short-period seismic stations at distances between 0 and 3.5 km from the summit and a broad-band seismometer 2.5 km from the summit. In late December 2005 the Alaska Volcano Observatory (AVO) deployed five campaign broad-band seismometers with on-site recording, as well as a telemetered strong motion sensor at a distance of 4.5 km. Over the course of the eruption, the five telemetered seismometers closest to the summit were destroyed, along with broad-band seismometer AU12. The loss of the summit seismic stations compromised AVO's ability to locate earthquakes during the latter portions of the eruption. The summit stations also provided the means with which to track the microseismicity occurring within the edifice, which was detectable only at those stations. Although not available in real time, the campaign broad-band data provided three-component records of high dynamic range with a flat response in the frequencies of interest. The 24-bit dynamic range allowed the entire eruption sequence to be recorded on scale.

The seismic data collected from the 2006 eruption of Augustine Volcano provide an excellent dataset for calibrating event classification schemes. A wide range of nonseismological observations complement this dataset, including deformation and visual records, as well as surface temperatures measured via satellite, all of which serve as independent verifications of volcanic processes observed in the seismic dataset. Perhaps most importantly, the eruption exhibited several types of activity, including a precursory earthquake swarm, vulcanian explosions, and sustained ash emission, in a 1-month time frame. This complexity provides the opportunity to benchmark tools against a variety of volcanic events in a single dataset.

Our analysis is based on a custom earthquake catalog. The analyst-reviewed earthquake catalog produced by AVO is limited to events that meet specific quality criteria (Dixon and others, 2008). For the current analysis we wished to include emergent earthquakes that cannot be located by traditional methods. We also wanted coverage of the final explosions and the transition into the continuous phase, even though the loss in summit stations compromised earthquake location during those periods. To accomplish this, we compiled a custom catalog of earthquakes for the period of time between January 1 and February 6. We scanned the full set of continuous waveforms and included in the catalog all earthquakes observed on a minimum of three stations including AU13, regardless of whether the trace was impulsive or emergent. Requiring a clear signal on station AU13 introduced a minor station bias in the data. In practice, however, there were few earthquakes visible away from the summit that were not well recorded on AU13. By requiring all arrivals to appear on one consistent station, we were able to catalog events by their arrival time at AU13 instead of the traditional method of cataloging events by their modeled origin time. This allowed us to analyze earthquakes that were not locatable, either because of poor station coverage or emergent onset. Of the 3,514 events in this catalog, 39 percent were included in the AVO analyst-reviewed catalog. This difference helped insulate the analysis from network changes and allowed a more comprehensive inclusion of earthquake types—at the notable expense of earthquake locations. We chose AU13 as our master station because it had the lowest signal-to-noise ratio of the campaign broadband stations and, unlike most of the telemetered stations located at similar distances, recorded continuously through the eruption. All broadband stations at Augustine were instrumented with Guralp CMG-6TD (30 s) seismometers recording at 100 Hz.

Teleseismic signals (including regional earthquakes) were identified by referring to mainland seismic stations OPT and MMN, situated at sufficiently great distances from Augustine Island so as not to record the volcanogenic signals, and were not included in the catalog.

Frequency Index Analysis

Method

The frequency content of an earthquake is a first-order metric with which to infer different source processes. The frequency with the greatest amplitude in the Fourier spectrum, the so-called dominant frequency, can be used as a general proxy for spectral content. Dominant frequency has been used in studies to characterize waveform types (for example, Latter, 1980; McNutt, 2002), but several shortcomings arise when using dominant frequency as a measure of the overall frequency content. Earthquakes with low signal-to-noise ratios are subject to low-frequency noise contamination (a particular issue for broadband data); the high-frequency earthquake shown in figure 2, for example, has a dominant frequency of 1.27 Hz, despite its considerable high-frequency content. The dominant frequency measure is also unable to identify earthquakes with bimodal frequency distributions, measuring only one peak in the spectra and therefore grouping it with other single-peaked events. This is a particular issue for hybrid-type earthquakes. Our early attempts to classify waveforms on the basis of dominant frequency were unsuccessful, in large part because hybrid events were arbitrarily grouped with either the high- or low-frequency groups, depending on which peak in the spectrum happened to be largest. These uncertainties associated with dominant frequency led us to seek a more robust metric for discriminating between different types of earthquake.

We develop the frequency index (*FI*) based on the ratio of energy in low and high frequency windows. Because the resulting measure spans many orders of magnitude, we use a base-ten logarithm to reduce the index to a simple number, typically between –3 and 1 for this dataset. The logarithm is intuitively appealing because waveforms with equal amounts of high and low energy (as defined by the frequency windows) have a frequency index of 0. A negative *FI* means the waveform is dominated by low-frequency energy, while a positive *FI* demonstrates a majority of energy in the high-frequency band.

We define the frequency index as

$$FI = \log_{10}\left(\frac{mean(A_{upper})}{mean(A_{lower})}\right), \qquad (1)$$

where A_{upper} are the spectral amplitudes across a band of high frequencies and A_{lower} are the spectral amplitudes measured across a lower range of frequencies. To calculate the *FI* in a consistent manner on thousands of waveforms, we use unfiltered waveforms with durations of 7 seconds: 1 second prior to the earthquake onset and 6 seconds after, ensuring that the high frequency P-wave onset is fully captured in the Fourier analysis. This is a sufficient time window over which to sample both the shorter duration, smaller magnitude earthquakes recorded, as well as the more emergent, lower frequency events. Linear trends and offsets are removed from the waveforms, and they are transformed to the frequency domain using a Tapered Fourier Transform. There is no need to correct for instrument response during this particular analysis, because the data were recorded on sensors with a flat response across our bandwidth of interest.

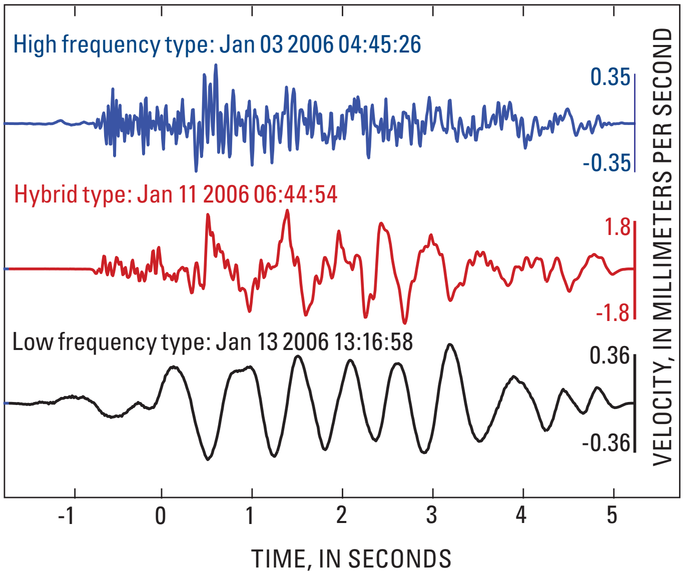

Figure 2. Selection of seismic waveforms from the “calibration set” used to translate between Frequency Index (*FI*) and the high-frequency, hybrid, and low-frequency earthquake classification. Waveforms were selected on the basis of visual criteria.

To determine suitable ranges for A_{lower} and A_{upper} we compiled a set of calibration waveforms. Using standard, if subjective, visual criteria, we selected high quality examples of three types of earthquake, based on the canonical high-frequency, low-frequency, and hybrid volcanic earthquake classification scheme (for example, Minikami, 1960; Lahr and others, 1994; McNutt, 1996). The high-frequency earthquakes contain energy up to 30 Hz; the low-frequency earthquakes contain a range of frequencies predominantly between 1 and 4 Hz; while the hybrid-type earthquakes sample both. Figure 2 shows example waveforms of high-frequency, hybrid and low-frequency type waveforms from this set. The frequency spectra for each event type were stacked to produce the spectra in figure 3*A*. The spectra were normalized to the area below each spectral curve prior

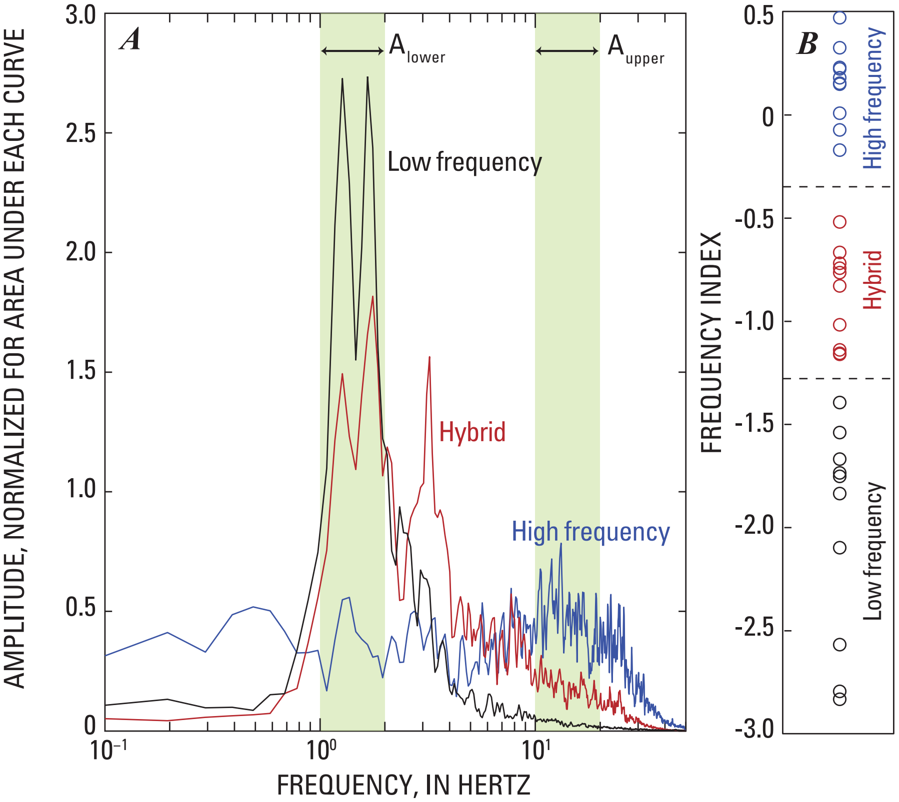

Figure 3. Frequency spectra and *FI* values for the "calibration set" of waveforms used to translate between Frequency Index (*FI*) and the high-frequency, hybrid, and low-frequency earthquake classification. *A*, Stacked frequency spectra of 10 high frequency, 10 low frequency and 10 hybrid "calibration waveforms," normalized for area beneath the curve. Ranges for A_{upper} and A_{lower} are displayed as shaded areas. *B*, *FI* values for each waveform, with dashed black lines indicating the half-distance between earthquake types.

to stacking. The intervals for A_{lower} and A_{upper} were defined across frequencies where the differences between the high-frequency, low-frequency and hybrid earthquake spectra were most pronounced: A_{lower} was attributed the range of 1-2 Hz, while A_{upper} was set to the range of 10-20 Hz, as shown in figure 3*A*. The *FI* values were calculated for the sample set and are shown in figure 3*B*. Although the frequency ranges in equation 1 are subjectively defined, the *FI* provides a repeatable quantitative measure of the frequency content inherent to the waveform. The calibration earthquakes provide an approximate translation between *FI* and the more traditional high-frequency, low-frequency, hybrid paradigm.

The high frequency, low frequency and hybrid groups fall within distinct *FI* limits, showing no overlap between groups, and exhibit an overall range of *FI* values between −2.9 and 0.5. Black dashed lines in figure 3*B* mark the half-distance between the group end-members at −0.4 for the transition from high frequency to hybrid earthquakes and at −1.3 for the transition from hybrid to low frequency earthquakes. The threshold for high frequency earthquakes is less than 0, which is not intuitive, since the 0 *FI* represents equal amplitudes at high and low frequencies. Indeed, the overall distribution of *FI* is biased towards the lower frequencies. There are two causes for this. The first is the greater attenuation of high frequencies with distance from the earthquake source. The second is the generally low signal-to-noise ratio of the high frequency earthquakes. This is due to the small magnitude of the seismicity (the largest located earthquake during the entire eruption had M_L 1.5, Dixon and others, 2008) and high levels of low-frequency noise resulting from the location of Augustine Island. These two factors tend to amplify the low frequency end of the spectrum. An examination of larger magnitude high-frequency earthquakes in other settings suggests that *FI* values of 1 and 2 should be common outside of this particular dataset.

FI Analysis for the Eruption Sequence

The distribution of *FI* values shows a distinct pattern with the eruptive phase (fig. 4). Before the swarm on January 10–11, the majority of events had significant amounts of high frequency energy as indicated by the *FI* values greater than −0.5, with rare events as low as −1.8. The earthquakes during the preeruptive swarm were different, exhibiting *FI* values between 0.6 and −1.7, with 80 percent between 0.2 and −0.8. These ranges indicate that the earthquakes still contain significant amounts of high frequency energy, but that lower frequencies are present too; less that 10 percent of the earthquakes show dominantly low frequency (below *FI* −1.3) energy content. After the first two explosions on January 11, the earthquakes shift to a lower *FI* , between −0.2 and −1.2, indicating that they are predominantly hybrid-type earthquakes. In the 12 hours before the first magmatic explosion on January 13 (Wallace and others, this volume), the *FI* range drops further to *FI* s of −0.5 to −1.6. In the hour prior to the first of the explosions on January 13, the *FI* drops as low as −2.9. Throughout

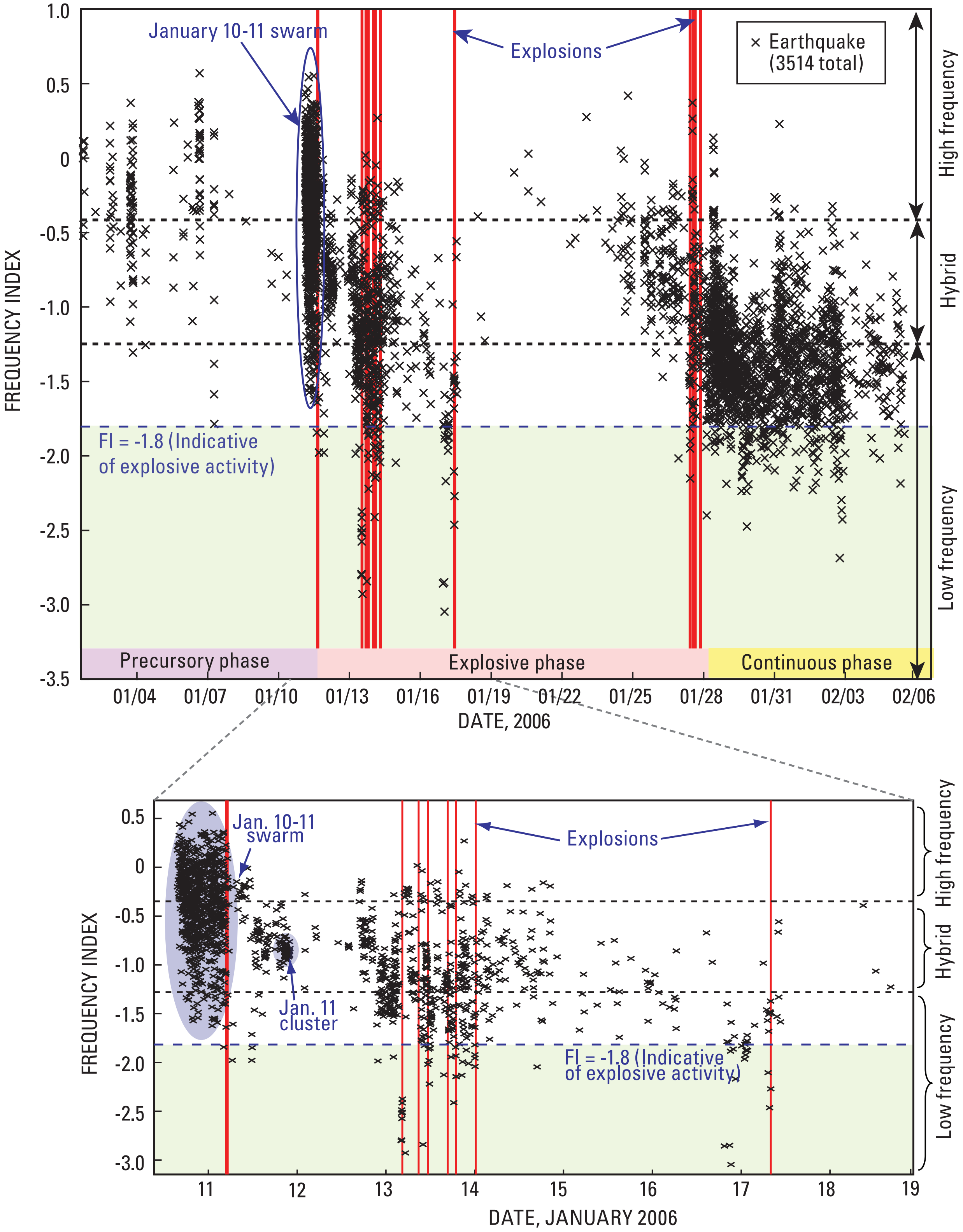

Figure 4. Distribution of Frequency Index (*FI*) with time at station AU13 for all earthquakes in the custom Augustine earthquake catalog. The *FI* range for the Augustine dataset is between 0.57 and –3.05. Explosions are marked with vertical red lines. *FI* = –1.8 (dashed line at the top of the shaded area) indicates the threshold *FI* for earthquakes as precursors to explosive eruptions. Translation to the traditional high-frequency, hybrid, and low-frequency classification scheme is marked by dashed black lines at *FI* –0.35 and *FI* –1.28.

the six explosions on January 13–14 the *FI* ranges from 0 to −2.9, with the majority of events between −0.7 and −2. Once the explosive activity ceases, the range diminishes somewhat, with most earthquakes falling within the *FI* range of −0.5 and −1.8, indicating hybrid and low frequency earthquake activity. A drop in *FI* is observed in the 12 hours prior to the explosion on January 17, with values as low as −3. After this explosion the seismicity decreases, and few events occur between January 17 and 25. Seismic activity resumes after January 25, and there is a systematic decline in the *FI* from 0.4 and −2 leading up to the magmatic explosions on January 27–28. Following the last of the 5 explosions on January 28, the *FI* remains low. The earthquake activity from January 28 through February 6 falls mostly between the *FI* values of −0.4 and −2.

Path and site effects can cause the frequency content of waveforms to vary significantly between stations. To verify the trends observed within the *FI* results, *FI* analysis was carried out at station AU15 located 3.5 km southwest of the edifice (fig. 1). The *FI* for these earthquakes was calculated using the same procedure described for the AU13 arrivals, with results shown in figure 5. The *FI* trends observed at station AU15 are similar to those found at station AU13, showing the same high *FI* values prior to the eruption sequence and a significant drop after the precursory swarm. The same association between low *FI* events and explosions is observed at AU15. In general, however, the upper *FI* values at AU15 are lower than those at AU13. Another difference between the *FI* at these stations is observed during the continuous phase. The majority of earthquakes at AU13 have *FI* values between −1 and −2, whereas the majority of events at station AU15 fall between −0.5 and −1.5, and the pronounced drop in *FI* seen at station AU13 after January 28 is scarcely evident at AU15. Strong wind can increase the *FI* of an earthquake, because it introduces high frequency noise into the spectrum and lowers the signal-to-noise ratio. It is possible that the poor weather conditions during the continuous phase had a greater effect on the signal-to-noise ratio at station AU15 than at AU13, given that the prevailing northwesterly wind direction affords minimal shelter to a site on the west of the island such as AU15. We consider wind noise to be one possibility for the 0.5 *FI* variation between these two stations.

Interpretation of Eruptive Sequence in Terms of *FI*

One of the most notable features of the eruption was the energetic swarm of earthquakes characterized by high *FI* values (up to 0.5) in the hours preceding the first explosive eruption on January 11. The predominance of high frequencies suggests that much of the energy was released by fracturing rock. We interpret this as the final opening of the conduit pathways to the surface, which facilitated the first of the explosions. The first two explosions were predominantly gaseous and contained little ash (Wallace and others, this volume),

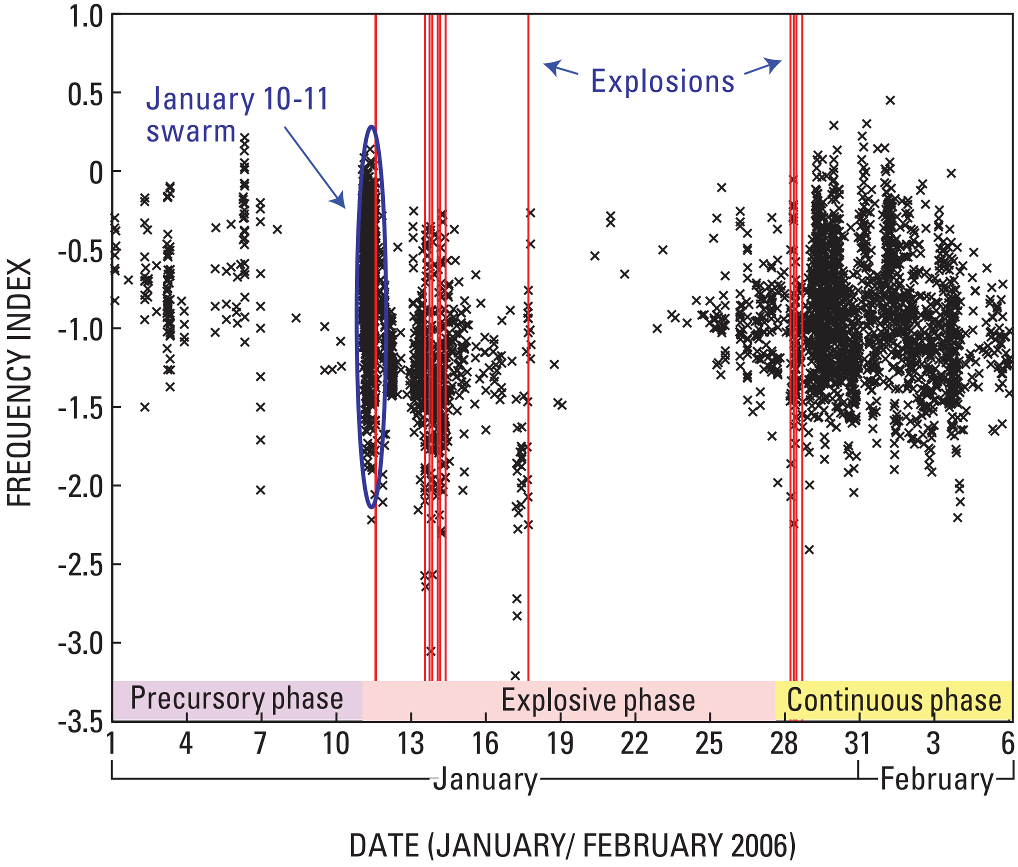

Figure 5. Frequency Index (*FI*) for the catalog recorded at station AU15. Explosions are marked with vertical red lines.

Table 1. Summary of earthquake clusters and *FI* associated with volcanic explosions at Augustine Volcano, Alaska, January 11-28, 2006.

[AKST, Alaska Standard Time; FI, Frequency Index]

Day, 2006	Time, AKST	Number of events in cluster prior to explosion	Length of cluster	Time between end of cluster and explosion	Maximum correlation within cluster	*FI* range of cluster	Number of events with *FI*<–1.8 since last explosion	Plume height, kilometers above sea level
Jan. 11	0444	<swarm>	-	13 min	-		1	9
Jan. 11[1]	0512	0	-	-	-		0	9
Jan. 13	0424	5	10 min	1 min	0.97	–2.35 -> -2.8	9	10
Jan. 13	0647	9	56 min	1 hr 17 min	0.96	–1.03 -> -1.3	2	>9
Jan. 13	1122	11	15 min	16 min	0.98	–0.93 -> -1.28	3	11
Jan. 13	1640	5	17 min	13 min	0.92	–1.07 -> -1.28	6	10
Jan. 13	1858	0	-	-	-		6	9
Jan. 14	0014	0	-	-			9	no data
Jan. 17	0758	6	37 min	6 hr 23 min	0.91	–1.78 -> -1.92	15	14
Jan. 27	2024	29	81 hr 13 min	9 hr 24 min	0.95	–0.5 -> -1.5	1	9
Jan. 27	2337	0	-	-	-		4	<3
Jan. 28	0204	0	-	-	-		0	8
Jan. 28	0742	0	-	-	-		0	8

[1] Disregarded because this explosion occurs within half an hour of the previous event.

suggesting that the high frequency fracturing preceding the eruption was driven by high-pressure gas moving ahead of the magma that followed in later eruptions. The precursory swarm on January 10-11 also contained a small number of events with *FI* as low as –1.6. These events are more consistent with a source generated from the migration of fluids. One possibility is that on January 10-11 magma within the Augustine edifice began to move slowly upwards. As the pressure on the magma decreased, additional water exsolved from the magma, creating a gas phase. This high-pressure gas phase migrated rapidly to the summit ahead of the magma, opening pathways and enabling magma to follow in the subsequent eruptive sequence.

These first two explosions were followed by a 2-day repose period, during which the average *FI* dropped to values between –0.2 and –1.2, with a notable 2-hour-long cluster of repeating earthquakes all with *FI* values near –0.9 (fig. 4). These hybrid and low frequency events were likely caused by the movements of magma into shallow levels of the edifice in anticipation of explosive eruption. The presence of hybrid earthquakes (*FI* –0.4 to –1.3)—and therefore some amount of high frequency energy—suggests that pathways to the surface were still not entirely open and brittle fracture continued as magma continued to force open conduits and/or squeeze through constrictions. The net effect, however, was to bring magma into shallow levels in the volcano. Cervelli and others (this volume) reach a similar conclusion, based on the deformation signals recorded at the summit, and suggest an upward propagating magma-filled crack near GPS station AV05 (fig. 1). Coombs and others (this volume) further propose that a small and relatively degassed lava dome effused on January 12, which was subsequently destroyed during the sequence of magmatic explosions on January 13–14.

FI as an Eruptive Precursor

Earthquakes with *FI* values lower than –1.8 are seen exclusively within 17 hours of the larger explosions in January 2006 and occur frequently during the continuous eruptive activity in late January and early February, diminishing in number with the gradual decline of explosive activity. Such a close association between explosions and low-*FI* earthquakes strongly suggests that these earthquakes are directly related to the explosive process. These results are summarized in table 1.

Low frequency earthquakes prior to eruption sequences are not unique to Augustine and have been observed in a variety of places, including Redoubt (for example, Chouet and others, 1994), Galeras (for example, Fischer and others, 1994), and Pinatubo (Harlow and others, 1994). The time scales over which these events occur vary between systems, ranging from hours to weeks, and are thought to depend on the amount of pressurization within the magmatic/hydrothermal system below the volcano (Chouet, 1996). The time scale of 17 hours at Augustine Volcano is similar to the build-up observed before the December 1989 eruption of Redoubt and is consistent with a system which has become pressurized.

The occurrence of low-*FI* earthquakes prior to explosive eruptions suggests that they are linked to the movement of magmatic fluids preceding extrusion. This is a significant observation from a monitoring perspective, as it presents a tool with which explosive eruption events might be anticipated. An empirical threshold of $FI < -1.8$ for this dataset, as indicated on figure 4, successfully anticipates explosive events or sequences. One earthquake with an *FI* of −2.1 occurred late on January 14, 17 hours after the final explosion of the January 13–14 eruptive sequence and did not occur as an explosion precursor. However its occurrence so soon after the powerful January 13–14 explosion sequence could mean that it was the final low-*FI* event from that sequence. Regardless, it is clear from table 1 that the limit of −1.8 never failed to indicate a pending explosion series, being successful for 10 of the 13 individual large explosions.

The Role of Attenuation

Because the *FI* analysis is based on waveform amplitude in different frequency bands, it will be influenced by attenuation effects. Seismic waves are diminished as a function of distance and frequency by a combination of intrinsic attenuation and scattering attenuation. The attenuating character of the Earth can be expressed through the quality factor *Q*, which is related to the seismic amplitude by

$$A(\omega, r) = A_0 r^{-n} \exp(-\omega r / 2Qv)\ , \qquad (2)$$

where $A(\omega, r)$ is the spectral amplitude as a function of angular frequency ω and distance r from the source (Aki and Richards, 1980). A_0 is the amplitude at the source, v is the propagation velocity, and r^{-n} is the geometric spreading factor, where n=1 for body waves and n= ½ for surface waves. To determine the influence of attenuation on *FI*, we combine equations 1 and 2. We simplify the system by approximating the lower and upper frequency ranges by their center (angular) frequencies, ϖ_{upper} and ϖ_{lower}:

$$FI(Q,r) = \log_{10}\left[\frac{A_{upper_0}\ r^{-n}\ exp(-\varpi_{upper} r/2Qv)}{A_{lower_0}\ r^{-n}\ exp(-\varpi_{lower} r/2Qv)}\right], \qquad (3)$$

$$FI(Q,r) = \log_{10}\left[\exp\left(-\frac{r}{2Qv}(\varpi_{upper} - \varpi_{lower})\right)\right] + \log_{10}\left[\frac{A_{upper_0}}{A_{lower_0}}\right], \qquad (4)$$

$$FI(Q,r) = \log_{10}\left[\exp\left(-\frac{r}{2Qv}(\varpi_{upper} - \varpi_{lower})\right)\right] + FI_0\ , \qquad (5)$$

where FI_0 is the *FI* at the source. The form of equation 5 is significant because it demonstrates that attenuation will reduce *FI* by a fixed term but will not change trends in the *FI* data coming from a single source region. In other words, if one is willing to assume an attenuation and velocity, *FI* can be corrected for distance by a static correction term. This result is shown in figure 6, where we consider the case when *FI* is 0 and vary the distance for different values of *Q*. *FI* decreases linearly with distance, and the effect is increasingly more pronounced at low *Q* values. In fact, this relation can be used in reverse to estimate attenuation directly using *FI* measured at a range of epicentral distances.

The above analysis makes several assumptions. We do not take into account the differential effect of attenuation within the frequency ranges specified by A_{upper} and A_{lower}. Since our frequency ranges are narrow, we approximate attenuation effects at the center frequencies across A_{upper} and A_{lower}, 15 and 1.5 Hz, respectively. The error introduced by this assumption is smaller than the variations introduced by an assumed *Q* value. We also assume a constant value of *Q*, contrary to the findings of studies of attenuation in other volcanic areas (such as Patanè and others, 1994), where *Q* is found to vary across orders of magnitude within single volcanic complexes.

Shortcomings of the *FI* Method

The Frequency Index technique worked well for the Augustine 2006 eruption, showing trends in seismicity that were otherwise difficult to quantify. Its success is largely due to the high-quality, close range dataset. The method would

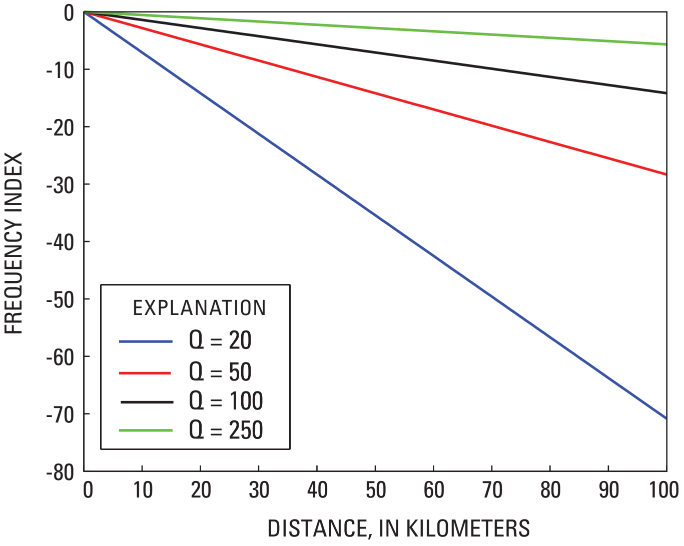

Figure 6. Frequency Index plotted against distance for different (fixed) values of the quality factor *Q*. The subsurface velocity was set to 1.3 km/s.

have been less successful at stations with poorer signal-to-noise ratios. The low-frequency bias evident in the model waveform set reflects this problem and indicates a fundamental challenge to quantifying the frequency content of small-amplitude seismic signals. It is possible that other datasets will be less contaminated by low-frequency noise than this dataset because the location of Augustine Island and the North Pacific wintertime storm conditions that prevailed during much of the eruption make for a seismically noisy environment. It is clear that site effects must be carefully considered when evaluating trends in *FI*, because they introduce an inherent bias within the *FI* calculation. This is demonstrated through the differences between figures 4 and 5 where station AU15, located in a particularly windy area of the island, yields much noisier data and lower values of *FI*.

Volcanic tremor could also influence the *FI* analysis. Our interval for A_{lower} (1–2 Hz) is within the common frequency range for volcanic tremor (for example, Gordeev, 1992), and it is possible that background tremor could add a low-frequency bias to the *FI*. Although potentially detrimental to the *FI* analysis, this may prove to be useful from a monitoring perspective. Volcanic tremor is often (although not always) associated with volcanic eruptions (Chouet, 1981), and an earthquake with a low *FI* due to tremor is also likely to be associated with a volcanic eruption. It therefore does not necessarily detract from the association between low *FI* and imminent eruption.

Repeating Earthquakes

Waveform similarity is another method for investigating trends in earthquake activity within large datasets. Recurring waveforms are significant because they are the product of earthquakes occurring in nearly the same place with the same mechanism. Not only do repeating events reveal the characteristic time of the seismogenic source, they can also be exploited for high-resolution mapping of the source volume. Stephens and Chouet (2001) and Green and Neuberg (2006) have used repeating low-frequency earthquakes to demonstrate that the sources of some low-frequency events are long lived, despite changes in a volcano's eruptive state. These events have been attributed to recurring interactions between magma and a fixed conduit geometry. Recurring high-frequency waveforms have been exploited by several authors to obtain precise relative relocations that define the timing and spatial extent of dike and fault structures within a volcanic edifice (for example, Got and others, 1994; Rowe and others, 2004; Thelen and others, 2008; DeShon and others, this volume). Here we explore the role of repeating earthquakes as precursors to explosive eruptions.

Method

We use cross-correlation to measure the similarity of waveforms in the event catalogue discussed above, again using station AU13. Focusing on a single station precludes the use of location techniques (see DeShon and others, this volume) but allows us to work with a more comprehensive catalog, improving time resolution and allowing us to extend the analysis into the latter portions of the eruption when all of the summit stations had been destroyed. Except for a handful of earthquakes at depths between 3.5 and 4.5 km, the located earthquakes all emanate from a relatively tight source region (Dixon and others, 2008; Power and Lalla, this volume), suggesting that the same is true for our more extensive catalog.

To calculate waveform cross-correlation, we extract a 6-second window of vertical component data beginning at the picked arrival time. Six seconds of data following the pick is sufficient to capture the largest amplitude sections of most waveforms (which dominate the cross-correlation) while minimizing the influence of background noise on short high-frequency waveforms. Changes in the window length of a few seconds showed only a minor influence on the correlation coefficients (not shown).

Each waveform in the dataset is correlated against all other waveforms using an algorithm tailored to large datasets using the newly developed waveform correlation toolbox for MATLAB (http://www.giseis.alaska.edu/Seis/EQ/tools/GISMO, accessed September 7, 2009). In the first step, all waveforms are transformed into the frequency domain. The first frequency-domain waveform is then multiplied against every other waveform, equivalent to convolution in the time domain. Exploiting the symmetry of the problem, the second waveform need only be multiplied by the third and subsequent waveforms, and so forth. This is equivalent to filling in the upper matrix triangle in figure 7 and completing the rest through a symmetry argument. The resulting cross-correlation series are transformed back to the time domain, where second-order polynomial interpolation is used to estimate the sub-sample maximum cross-correlation value. The maximum of the cross-correlation is normalized, following convention, to the scale of −1 to 1. The maximum value and its associated lag time are saved into n by n matrices, where n is the number of traces. Hereafter we refer to the normalized maximum of the cross-correlation function as simply the correlation value. The lag values are used to align the traces in time.

Figure 7 shows the similarity matrix for all events, chronologically left to right and top to bottom (not evenly spaced in time), with one pixel for each pair of waveforms. The matrix is symmetric with unity on the diagonal. Although figure 7 hardly does justice to the 10 million correlation values that form the matrix, it is clear that the majority of earthquakes throughout the eruption show little similarity. (Because we search for the optimum correlation lag times, even unrelated waveforms will often correlate at 0.5 or better.) Within this dataset, however, there are numerous clusters and time patterns with direct implications for volcanic processes (Buurman and West, 2006). The challenge is to mine the dataset in intuitive ways. We identify clusters using a hierarchical clustering method similar to that used by Rowe and others (2002). First we link all events on the basis of their correlations (fig. 8). Branches within the hierarchy are joined

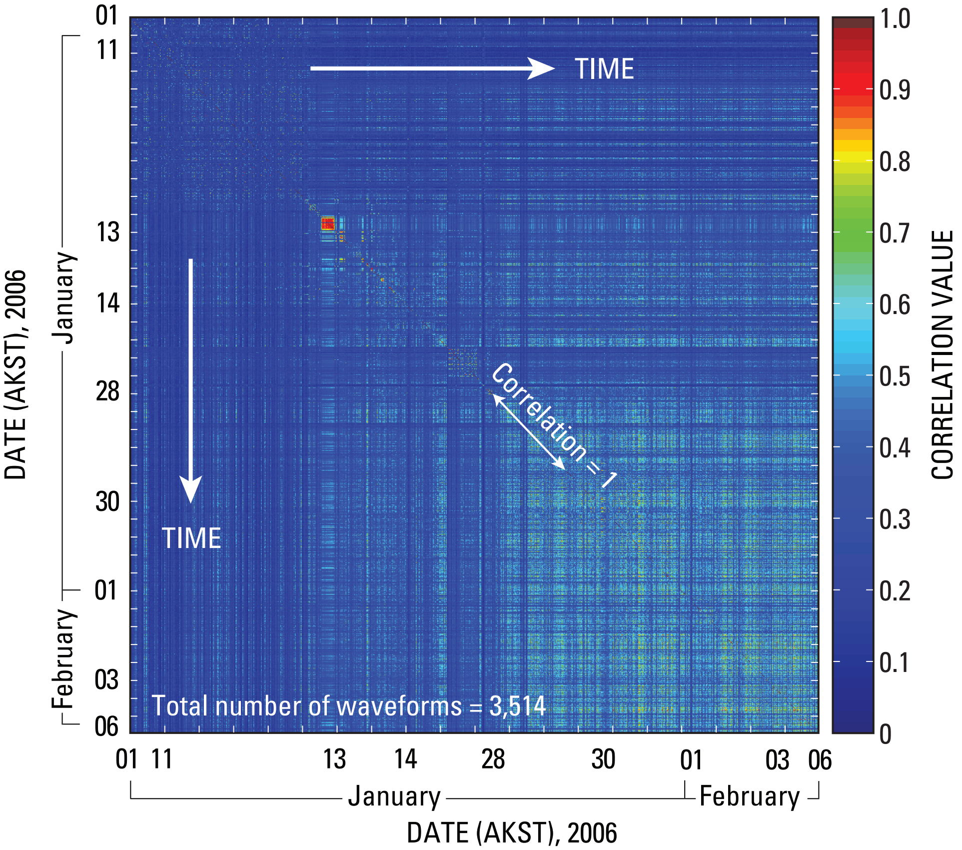

Figure 7. Correlation matrix for the entire Augustine 2006 catalog. Each point represents an earthquake correlation pair. The matrix is symmetric, with time progressing left to right and top to bottom. The correlations on the diagonal are equal to one as each waveform is auto correlated, although they appear muted because of the size of the matrix. The majority of cross-correlations in the dataset are poor, with values less than 0.6.

at nodes whose height is the mean correlation value between each pair of events spanning the two groups. That is,

$$C_{p,q} = \frac{1}{n_p n_q} \sum_{i=1}^{n_p} \sum_{j=1}^{n_q} C_{pi,qj}, \qquad (6)$$

where $C_{p,q}$ is the mean correlation between the nth events in groups p and q. These links may be between individual events or between clusters of events, depending solely on which linkage has the highest mean correlation. The formation of discrete clusters is then just a matter of selecting branches from the hierarchical cluster tree. Because the correlation value is influenced by the trace length, filter parameters, and frequency content of the waveforms, the choice of correlation threshold is somewhat arbitrary. Given the wide variety of earthquake types in our catalog, we choose a threshold of 0.8 based on visual inspection to define clusters in lieu of a more adaptive approach, such as that of Rowe and others (2002). The value 0.8 is on par with or somewhat higher than in comparable studies (Petersen, 2007; Green and Neuberg, 2006; Stephens and Chouet, 2001).

We refer to groups of similar waveforms as clusters. “Multiplet” and “clones” (for example, Frémont and Malone, 1987; Geller and Mueller, 1980; Thelen and others, 2008) are comparable terms. We prefer the term cluster because of the implied spatial proximity and avoid the term “swarm” because it suggests a similarity in time. We use cluster to indicate a

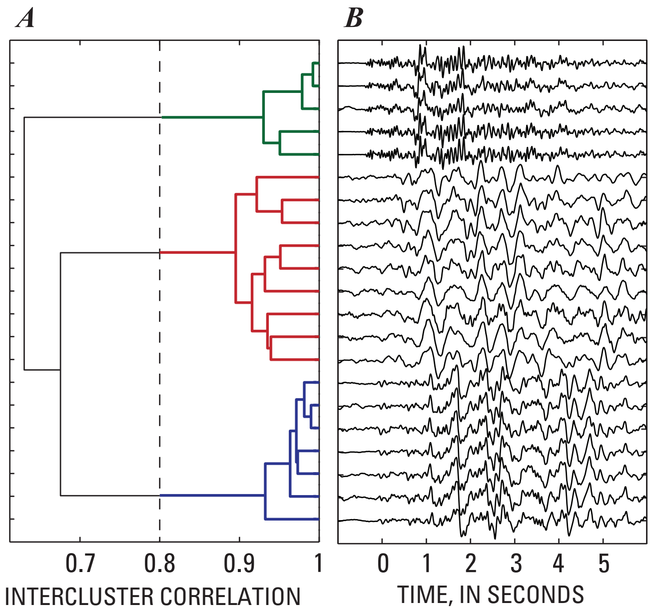

Figure 8. Illustration of the hierarchical clustering method used to group sample waveforms. *A*, The two most similar events are joined at a node, which yields a new correlation value. This value is then used to search the catalog for the next most similar event, pair, or group of events. Individual clusters are defined by assigning a minimum intercluster correlation value, indicated by the dashed line at 0.8. *B*, Waveforms corresponding to correlations in *A*.

similarity in waveform and, by extension, source location and mechanism. If a cluster occurs in a short period, it may also be a swarm, although this is not always the case.

In subsequent analyses we use a subset of data that includes the 40 largest clusters. This includes clusters of four or more events. By culling unrelated traces, trends not observed in figure 7 emerge as clear patterns that can be tied directly to different stages within the eruption (fig. 9*A*).

Clusters of Similar Events Before Explosive Eruptions

The most important pattern in the subset matrix is the presence of repeating events in the hours preceding explosive eruptions. More than half of the ash-producing explosions during the explosive phase were immediately preceded by small clusters of highly similar earthquakes ("precursory clusters"). The two phreatic explosions at the beginning of the explosive phase were closely spaced in time and occurred at the end of the seismic swarm, which itself contained several clusters of earthquakes, discussed later. The first four explosions in the sequence of six ash-producing events on January 13–14 were preceded by small clusters (5–11 events) of similar earthquakes. These clusters occurred in short periods of time, some lasting only 10 minutes (table 1), and all occurred within 2.5 hours of eruption. The explosion on January 17 was preceded by a cluster that occurred 7 hours prior to eruption. The last four eruptions of the explosive phase, which occur immediately prior to the transition to continuous activity, show different seismic precursors than the other large explosions; they are preceded by an 81-hour swarm of earthquakes, not all of which are as strikingly similar as the previous precursory clusters. These results are summarized in table 1.

The largest cluster occurred on January 11 within the space of 2 hours and contained 57 events with exceedingly high correlation values (fig. 9*D*). This cluster was followed by a smaller but more protracted cluster that ended only 14 minutes before the first of the ash-producing explosions of the explosive phase. Earthquakes in the second cluster also showed similarity (values greater than 0.7) with the largest cluster, suggesting that the two clusters were slight variations of the same mechanism.

The occurrence of repeating clusters immediately prior to explosions indicates that they represent either the mobilization of magma, the opening of conduits to the surface, or both. The interaction of magma with surrounding rock is well known to produce repeating events. This association is most convincing during periods of dome growth, when magma extrusion is observed at the surface accompanied by repeating event clusters (for example, Thelen and others, 2008; Green and Neuberg, 2006). The same patterns were observed during the March 2006 lava effusion at Augustine (not shown). Conduit opening prior to explosive eruptions is another viable option for the source of event clusters. In order for magma to erupt explosively, an open conduit to the surface is required. The magma ascent and gas exsolution that precedes explosions may well be responsible for creating (or reopening) such pathways to the surface (fig. 10). The progressive fracturing of a crack pathway, driven by high-pressure gas or fluid, is thought to be a mechanism for earthquake swarms (for example, Hill, 1977) and could produce nearly the same waveform. Although cracking is an inherently destructive process, a series of small progressive fractures on the same pathway would have the same mechanism and nearly the same seismic raypath. This would be an unlikely mechanism to explain many thousands of repeating events (for example, Petersen, 2007), but it is a more reasonable mechanism at Augustine, considering the modest size of the clusters preceding explosive eruptions.

Recurring Clusters

Figure 9*A* reveals a few occasions when a cluster of events pauses and resumes at a later time. A striking example of recurring clusters occurs on January 13 (fig. 9*E*). Two clustered swarms are separated by a gap of 3 hours but have events correlating as high as 0.9. This is seen by the high off-diagonal correlation values between the two swarms. These two small clusters occur immediately after explosions, suggesting that they are caused by posteruptive processes related to relaxation of eruptive stresses in the edifice. Alternatively, they may be related to a final release of gas or magma from the explosion.

Contemporaneous Groups of Repeating Events

Some clusters occur contemporaneously with other unrelated clusters. The repeating events in the preeruptive swarm on January 11 provide a good example. Within this group there are two main families of waveforms, referred to here as *A* and *B* (fig. 9*C*). The waveforms in group A contain significant amounts of high-frequency energy, indicated by their range in *FI* of −0.2 to −1.4. Waveforms in the B cluster have lower frequency content ($FI < -2.5$ for nine of the waveforms, with one outlier), although they also contain some portion of high-frequency content. Because both families occur during the same time period, the similarity matrix shows deceiving scatter when sorted chronologically (fig. 9*B*). The presence of two families, one rich in high frequencies, the other rich in low frequencies, demonstrates the coexistence of different seismic processes. Considering the vigor of this preeruptive swarm and its occurrence prior to the first explosive eruption, cluster A likely represents the brittle failure of rock caused by the incremental opening of cracks as a result of a new intrusion of fluids or gases in the shallow edifice. We attribute cluster *B*, rich in low-frequency energy, to resonances caused by this same movement of gas or fluid to shallow depths.

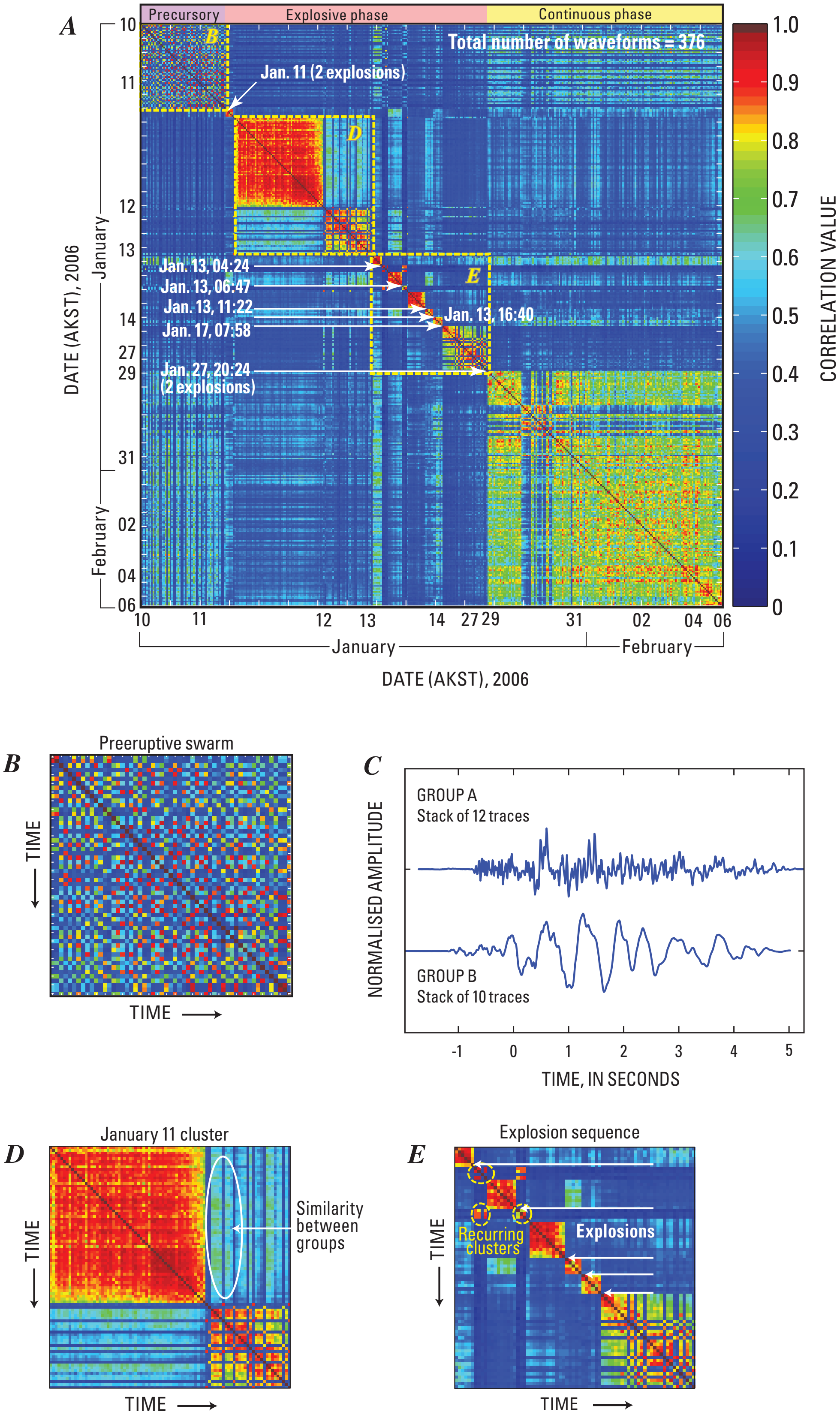

Figure 9. Refined correlation matrix (*A*), with sample waveforms (*C*), and enlarged sections of the matrix (*B, D, E*). *A*, Refined correlation matrix showing the 40 largest clusters. Explosions are marked with white arrows. Dashed yellow lines indicate enlarged areas (panels *B, D*, and *E*). *B*, Enlargement of the preeruptive swarm time period, showing disparate clusters of repeating events. *C*, Stacks of the two largest groups of waveforms present during the preeruptive swarm shown in *B*. *D*, Enlargement of the large clusters on January 11, containing correlation values as high as 0.97. E, Enlargement of the explosive phase, with recurring clusters circled. Explosions are marked with arrows.

Repeating Earthquakes During Continuous Eruptive Activity

The character of the repeating earthquakes changes with the transition to the continuously explosive phase on January 28, 2006. Whereas the earlier explosive phase was characterized by intermittent swarms of highly clustered events lasting minutes to hours, repeating events during the continuous phase are more variable but seem to follow one general waveform type. Our arbitrary correlation criterion of 0.8 groups these events into several small clusters. However, the subset similarity matrix (fig. 9*A*) suggests that there is one dominant cluster beginning on January 28 that extends beyond the end of our analysis on February 6 as seismicity began to taper significantly. This cluster is interspersed by a smaller cluster of 21 events on January 29 and 30.

Poor weather during much of the continuous phase prevented visual and satellite-based observations for all but the largest explosive events. The emergent broad-spectrum seismic data was at times enigmatic. In the absence of corroborating evidence it was challenging to separate how much of the seismicity represented rockfall activity on the new dome and how much was generated by the emplacement of new lava at the surface. Although both sources were surely present, the retrospective similarity analysis demonstrates that a subset of the events can be tied directly to magma extrusion. Rockfall events, including pyroclastic flows and avalanches, are inherently dissimilar because of their chaotic and destructive mechanism. The repeating sequence could be stick-slip behavior associated with dome growth, as has been documented in the 2004 Mount St. Helens sequence (Moran and others, 2008). However, the low frequency nature (fig. 4) of the events, combined with their registration at all on-island stations and on the pressure sensor at AUE (not shown), suggest that vulcanian explosions are a more plausible source. Indeed, as the number of explosions declined during early February (evident on the pressure sensor at AUE, not shown), so too did the number of repeating earthquakes.

Discussion

Combining *FI* Data and Correlation Data

In order to gain further insight into the seismic activity using the similarity matrix in figure 9*A* It is helpful to compare these results with the *FI* analysis. Table 1 presents the *FI* values of the clusters that occurred prior to explosions (“precursory clusters”), as well as listing the number of earthquakes with *FI* below −1.8 that occurred prior to each of the large explosion events. It is interesting to note that the very low *FI* earthquakes do not appear to occur in large clusters. Although events with *FI* below −1.8 show a unique correspondence to explosive eruptions (see section on “*FI* as an eruptive precursor”), they are a separate phenomenon from the repeating earthquakes. This suggests that they should be tracked independently and even that small numbers of very low *FI* events may have significant implications.

Not all explosions were preceded by precursory clusters or very low *FI* earthquakes. Almost all were preceded by one of the two, however. We disregard the second explosion of the sequence (table 1) because it occurs less than half an hour after the first. It is significant that 10 of the first 11 eruptions during the explosive phase were preceded by either repeating earthquakes or those with very low *FI*. Neither technique exhibits a significant change preceding the final two magmatic explosions of the explosive phase, which occurred immediately prior to the change to sustained eruptive activity. We suspect that by the time these explosions occurred, the volcano had already established a clear open conduit to the surface that allowed magma and gas to reach the surface without the constrictions present in early explosions. This suggests that both the frequency-based and correlation-based techniques (and likely all precursory seismic techniques) may perform better with initial eruptive activity than with ongoing repeat eruptions.

We hypothesize that both precursory clusters and very low *FI* earthquakes are associated with the movement of magma or, in some cases, gas. Specifically, we propose that the low frequency earthquakes are the result of the movement of magmatic fluids rising from the magma chamber (as proposed by Chouet, 1996), while the precursory hybrid clusters originate from the interaction between the advancing body of magmatic fluids and the brittle edifice (figure 10).

Although low frequency earthquakes and repeating earthquakes are commonly observed at volcanoes without eruption, the Augustine sequence provides unmistakable ground truth for these associations. By combining the two techniques, we see that although very low *FI* earthquakes can occur as precursory clusters, it is not generally the case and the two styles usually represent separate earthquakes.

Adaptations for Real-Time Use

The *FI* technique shows promise as an indicator of explosive magmatic eruptions. It is also a useful all-purpose tool for quantifying trends in seismicity. *FI* is particularly useful in tracking changes in large numbers of earthquakes where manual inspection of waveforms is quickly overwhelmed. Examples include the transition from explosive to continuous activity at Augustine, or the changes from high-frequency to hybrid and lower frequency events observed during the early stages of the 2004–8 Mount St. Helens dome building eruption (Moran and others, 2008). It provides a repeatable, quantifiable measure that is simple to calculate and faithfully reduces the overall frequency content of a waveform to a single parameter.

The correlation approach is similarly well suited to large datasets where the pattern matching required to identify repeating clusters of events is all but impossible without computational aids. Figure 7 provides an excellent example of how these rich correlation patterns in the Augustine sequence can be buried by high rates of scattered seismicity.

Both tools are readily adaptable to real-time use, and both techniques operate on short waveform segments encompassing a detected event but do not require event locations. This distinction is significant. A seismic event detection system is one of the most basic monitoring tools available at nearly all monitored volcanoes. Fully automated event locations, though existent, are still the exception at most volcanoes.

The *FI* parameter can be used in real time in its current form. All that is required is a real-time module to perform the trivial Fourier transform and ratio calculation and a database to store and track the progression of these values.

The correlation tool needs to be adapted slightly. In the analysis presented here, the complete seismic history of the eruption was already available, so that for a given moment in the eruption all events from the past and future could be used in the correlation. As a real-time tool, the correlation analysis must be limited to events that have already occurred. The easiest implementation would store the waveforms from detected events (or preferably store pointers to these waveforms in a continuous waveform archive). When a new event is detected, it would be correlated against other events in the recent past. This could include all events in a fixed time frame (say, 12 hours), or it may be more computationally appropriate to include a fixed number of events (say, the past 100 detected waveforms). The only significant challenge in implementing a real-time correlation tool is computational expense, although this could be minimized by storing the most recent waveforms in memory. Storing the Fast Fourier Transform of each waveform would be even more efficient. By correlating each incoming event against recent waveforms instead of the entire dataset, the resulting similarity matrix would be limited to a strip of data within n steps of the diagonal, where n is the number of recent events included in the correlation calculation. In many cases this may be sufficient to reveal the basic similarity patterns, as demonstrated by Umakoshi and others (2008). In the Augustine 2006 dataset, for example, most correlation patterns are fully revealed when only the previous 150 events are included.

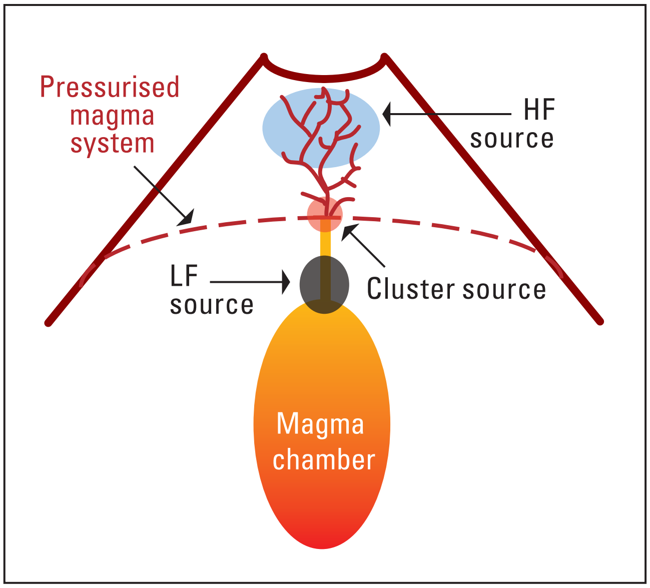

Figure 10. Schematic model showing the origins of high-frequency (HF) earthquakes, low-frequency (LF) earthquakes, and the (hybrid) clusters. Low-frequency earthquakes are generated by the movement of magmatic fluids, as proposed by Chouet (1996). Earthquake clusters have a tight source region, where both brittle fracture and fluid resonance occurs, at the head of the advancing body of magma. High-frequency earthquakes, such as those in the precursory swarm, are the result of the brittle fracture of rock in the edifice, where volatiles from the degassing body of magma break new pathways to the surface.

Both tools are simplistic in that they operate on single channels of data, though more comprehensive multichannel versions can be envisioned. The single-channel requirement makes them straightforward to implement, however, and given this simplicity we believe the frequency index and correlation tools can be readily incorporated into most processing systems. Although both tools have limitations and will not always be as insightful as they have proven for the Augustine 2006 eruption, we believe that they have the potential to become indispensable additions to the suite of seismic volcano monitoring tools.

Acknowledgments

We thank Stephanie Prejean and Rick Aster for their helpful comments and suggestions. We also thank John Power, Kate Bull, and Katie Jacobs for several useful discussions that also improved the manuscript.

References Cited

Aki, K., and Richards, P.G., 1980, Quantitative seismology: New York, W.H. Freeman, 700 p.

Bailey, J.E., Dean, K.G., Dehn, J., and Webley, P.W., 2010, Integrated satellite observations of the 2006 eruption of Augustine Volcano, *in* Power, J.A., Coombs, M.L., and Freymueller, J.T., eds., The 2006 eruption of Augustine Volcano, Alaska: U.S. Geological Survey Professional Paper 1769 (this volume).

Benoit, J.P., and McNutt, S.R., 1996, Global volcanic earthquake swarm database, 1979–1989: U.S. Geological Survey Open-File Report 96-0069, 333 p.

Buurman, H., and West, M., 2006, Integrated seismic observations of the 2006 eruption of Augustine Volcano: Eos

(American Geophysical Union Transactions), v. 87(52), Fall Meeting supp., abs V51C-1683

Cervelli, P.F., Fournier, T.J., Freymueller, J.T., Power, J.A., Lisowski, M., and Pauk, B.A., 2010, Geodetic constraints on magma movement and withdrawal during the 2006 eruption of Augustine Volcano, *in* Power, J.A., Coombs, M.L., and Freymueller, J.T., eds., The 2006 eruption of Augustine Volcano, Alaska: U.S. Geological Survey Professional Paper 1769 (this volume).

Chouet, B.A., 1981, Ground motion in the near field of a fluid-driven crack and its interpretation in the study of shallow volcanic tremor: Journal of Geophysical Research, v. 86, no. B7, p. 5985–6016.

Chouet, B.A., 1988, Resonance of a fluid-driven crack; radiation properties and implications for the source of long-period events and harmonic tremor: Journal of Geophysical Research, v. 93, p. 4375–4400.

Chouet, B.A., 1996, Long-period volcano seismicity; its source and use in eruption forecasting: Nature, v. 380, p. 309–316.

Chouet, B.A., Page, R.A., Stephens, C.D., Lahr, J.C. and Power, J.A., 1994, Precursory swarms of long-period events at Redoubt Volcano (1989–1990), Alaska—their origin and use as a forecasting tool: Journal of Volcanology and Geothermal Research, v. 62, p. 95–135.

Coombs, M.L., Bull, K.F., Vallance, J.W., Schneider, D.J., Thoms, E.E., Wessels, R.L., and McGimsey, R.G., 2010, Timing, distribution, and volume of proximal products of the 2006 eruption of Augustine Volcano, *in* Power, J.A., Coombs, M.L., and Freymueller, J.T., eds., The 2006 eruption of Augustine Volcano, Alaska: U.S. Geological Survey Professional Paper 1769 (this volume).

DeShon, H.R., Thurber, C.H., and Power, J.A., 2010, Earthquake waveform similarity and evolution at Augustine Volcano from 1993 to 2006, *in* Power, J.A., Coombs, M.L., and Freymueller, J.T., eds., The 2006 eruption of Augustine Volcano, Alaska: U.S. Geological Survey Professional Paper 1769 (this volume).

Dixon, J.P., Stihler, S.D., Power, J.A., and Searcy, C., 2008, Catalog of earthquake hypocenters at Alaskan volcanoes; January 1 through December 31, 2006: U.S. Geological Survey Data Series 326, 79 p. [http://pubs.usgs.gov/ds/326, accessed September 7, 2009].

Fischer, T.P., Morrissey, M.M., Calvache, M.L., Gomez, D., Torres, R., Stix, J., and Williams, S.N., 1994, Correlations between SO_2 flux and long-period seismicity at Galeras volcano: Nature, v. 368, p.135–137.

Frémont, M.J., and Malone, S.D., 1987, High precision relative locations of earthquakes at Mount St. Helens, Washington: Journal of Geophysical Research, v. 92, p. 10223–10236.

Geller, R.J., and Mueller, C.S., 1980, Four similar earthquakes in central California: Geophysical Research Letters, v. 7, p. 821–824.

Gordeev, E.I., 1992, Modeling of volcanic tremor wavefields: Journal of Volcanology and Geothermal Research, v. 51, p. 145–160.

Got, J.-L., Frechet, J., and Klein, F.W., 1994, Deep fault plane geometry inferred from multiplet relative relocation beneath the south flank of Kilauea: Journal of Geophysical Research, v. 99, p. 15375–15386.

Green, D.N., and Neuberg, J., 2006, Waveform classification of volcanic low-frequency earthquake swarms and its implication at Soufriere Hills Volcano, Montserrat: Journal of Volcanology and Geothermal Research, v. 153, p. 51–63.

Harlow, D.H., Power, J.A., Laguerta, E.P., Ambubuyog, G., White, R.A., and Hoblitt, R.P., 1994, Precursory seismicity and forecasting of the June 15, 1991, eruption of Mount Pinatubo, *in* Newhall, C.G., and Punongbayan, eds., Fire and mud; eruptions and lahars of Mount Pinatubo, Philippines: Philippine Institute of Volcanology and Seismology and University of Washington Press, p. 285–306.

Hill, D.P., 1977, A model for earthquake swarms: Journal of Geophysical Research, v. 82, no. 8, p. 1347–1352.

Jacobs, K.M., and McNutt, S.R., 2010, Using seismic *b*-values to interpret seismicity rates and physical processes during the preeruptive earthquake swarm at Augustine Volcano 2005–2006, *in* Power, J.A., Coombs, M.L., and Freymueller, J.T., eds., The 2006 eruption of Augustine Volcano, Alaska: U.S. Geological Survey Professional Paper 1769 (this volume).

Lahr, J.C., Page, R.A., Chouet, B.A., Stephens, C.D., Harlow, D.H., and others, 1994, Seismic evolution of the 1989-90 eruption sequence of Redoubt Volcano, Alaska: Journal of Volcanology and Geothermal Research, v. 62, p. 69–94.

Langer, H., Falsaperla, S., Powell, T., and Thompson, G., 2006, Automatic classification and a-posteriori analysis of seismic event identification at Soufriere Hills Volcano, Montserrat: Journal of Volcanology and Geothermal Research, v.153, p. 1–10.

Latter, J.H., 1980, Volcanic earthquakes and their relationship to eruptions at Ruapehu and Ngauruhoe volcanoes: Journal of Volcanology and Geothermal Research, v.9, p. 293–309.

Minikami, T., 1960, Earthquakes and crustal deformations originating from volcanic activities: Bulletin of the Earthquake Research Institute, v. 38, p. 497–544.

McNutt, S.R., 1996, Seismic monitoring and eruption forecasting of volcanoes; a review of the state-of-the-art and case histories, *in* Scarpa, R., and Tilling, R., eds., Monitoring and mitigation of volcano hazards: Berlin/Heidelberg, Springer-Verlag, p. 99–146.

McNutt, S.R., 2002, Volcano seismology and monitoring for eruptions, chap. 25 *of* Lee, W.H.K., Kanamori, H, Jennings, P.C., and Kisslinger, C., eds, International handbook of earthquake and engineering seismology: Academic Press, v. 81A.

Moran, S.C., Malone, S.D., Qamar, A.I., Thelen, W.A., Wright, A.K., and Caplan-Auerbach, J., 2008, Seismicity associated with renewed dome-building at Mount St Helens, 2004-2005, *in* Sherrod, D.R., Scott, W.E., and Stauffer, P.H., eds., A volcano rekindled; the renewed eruption of Mount St. Helens, 2004–2006: U.S. Geological Survey Professional Paper 1750, p.27–60.

Neuberg, J.W., Tuffen, H., Collier, L., Green, D., Powell, T., and Dingwell, D., 2005, The trigger mechanism of low-frequency earthquakes on Montserrat: Journal of Volcanology and Geothermal Research, v. 153, p. 37-50, doi: 10.1016/j.jvolgeores.2005.08.008.

Patanè, D., Ferrucci, F., and Gresta, S., 1994, Spectral features of microearthquakes in volcanic areas; attenuation in the crust and amplitude response on the site at Mt. Etna, Italy: Bulletin of the Seismological Society of America, v. 84, p. 1842–1860.

Petersen, T., 2007, Swarms of repeating long-period earthquakes at Shishaldin Volcano, Alaska, 2001–2004: Journal of Volcanology and Geothermal Research, v. 166, p. 177–192, doi:10.1016/j.volgeores.2007.07.014.

Power, J.A., and Lalla, D.J., 2010, Seismic observations of Augustine Volcano, 1970–2007, *in* Power, J.A., Coombs, M.L., and Freymueller, J.T., eds., The 2006 eruption of Augustine Volcano, Alaska: U.S. Geological Survey Professional Paper 1769 (this volume).

Rowe, C.A., Thurber, C.H., and White, R.A., 2004, Dome growth behavior at Soufriere Hills Volcano, Montserrat, revealed by relocation of volcanic event swarms, 1995–1996: Journal of Volcanology and Geothermal Research, v. 134, no. 3, p. 199–221.

Rowe, C.A., Aster, R.C., Borchers, B., and Young, C.J., 2002, An automative, adaptive algorithm for refining phase picks in large seismic data sets: Bulletin of the Seismological Society of America, v. 92, p. 1660–1674.

Stephens, C.D., and Chouet, B.A., 2001, Evolution of the December 14, 1989 precursory long-period event swarm at Redoubt Volcano, Alaska: Journal of Volcanology and Geothermal Research, v. 109, p. 133–148.

Thelen, W.A., Crosson, R.S., and Creager, K.C., 2008, Absolute and relative locations of earthquakes at Mount St. Helens, Washington, using continuous data; implications for magmatic processes, *in* Sherrod, D.R., Scott, W.E., and Stauffer, P.H., eds., A volcano rekindled; the renewed eruption of Mount St. Helens, 2004–2006: U.S. Geological Survey Professional Paper 1750, p.71–95.

Umakoshi, K., Takamura, N., Shinzato, N., Uchida, K., Matsuwo, N., and Shimizu, H., 2008, Seismicity associated with the 1991–1995 dome growth at Unzen Volcano, Japan: Journal of Volcanology and Geothermal Research, v. 175, p. 91–99.

Wallace, K.L., Neal, C.A., and McGimsey, R.G., 2010, Timing, distribution, and character of tephra fall from the 2005–2006 eruption of Augustine Volcano, *in* Power, J.A., Coombs, M.L., and Freymueller, J.T., eds., The 2006 eruption of Augustine Volcano, Alaska: U.S. Geological Survey Professional Paper 1769 (this volume).

Wilson, C.R., Olson, J.V., Szuberla, C.A.L., McNutt, S., Tytgat, G., and Drob, D.P., 2006, Infrasonic array observations at 153US of the 2006 Augustine Volcano eruptions: Inframatics, no. 13, p. 11–26.

The 2006 Eruption of Augustine Volcano, Alaska
Power, J.A., Coombs, M.L., and Freymueller, J.T., editors
U.S. Geological Survey Professional Paper 1769

Chapter 3

Using Seismic *b*-Values to Interpret Seismicity Rates and Physical Processes During the Preeruptive Earthquake Swarm at Augustine Volcano 2005–2006

By Katrina M. Jacobs[1] and Stephen R. McNutt[2]

Abstract

We use seismic *b*-values to explore physical processes during the Augustine Volcano 2005–6 preeruptive earthquake swarm. The preeruptive earthquake swarm was divided into two parts: the “long swarm,” which extended from April 30, 2005, to January 10, 2006; and the “short swarm,” which started 13 hours before the onset of explosive activity on January 11, 2006. Calculations of *b*-value for each of these swarms and for a background period were performed. The short swarm, directly preceding the eruption, had the lowest calculated *b*-value. In addition to the low value, the shape of the *b*-value plot for the short swarm appears to have two separate slopes, a shallower slope for magnitudes as great as 1.2 and a steeper slope for magnitudes greater than 1.2. Calculations of *b* were also run for three precursory deformation stages suggested by a separate investigation of deformation at Augustine Volcano. The highest *b*-value, found in stage 2, may indicate an increase in pore pressure and in thermal gradient, which matches the geodetic interpretation of a proposed dike intrusion. Finer resolution changes of *b* are explored through calculations of *b*-value versus time. An initial drop in *b*-value in late 2004 preceded the onset of increased seismicity. The temporal nature of this change and its timing are corroborated by atmospheric temperature data recorded on the summit of the volcano, which increased at approximately the same time. Stress at Augustine Volcano was also studied using 79 earthquakes that returned acceptable focal mechanisms between January 1, 2002, and January 10, 2006. These mechanisms and an attempted stress-tensor inversion imply that stresses within the Augustine edifice are highly variable and do not display a dominant faulting style. A population of high-frequency volcano-tectonic earthquakes during the short swarm is found to have accompanying very-long-period (20 seconds and greater) energy. Statistical analysis indicates that these earthquakes are a separate population of events. We interpret this population of earthquakes to represent a separate and distinct physical process that was not seen before the 13 hours preceding the eruption. The *b*-value time series also indicates that when changes in stress, pore pressure, and thermal gradient occur simultaneously, that stress effects dominate the observed *b*-value.

Introduction

The 2006 eruption of Augustine Volcano was preceded by 8 months of increased rates of volcano-tectonic (VT) earthquakes, similarly to previous eruptions in 1976 and 1986 (Power and Lalla, this volume). The eruption lasted from January 11 through mid-March, 2006, and was characterized by explosions, effusive activity, and pyroclastic flows. Only earthquakes that occurred before the onset of explosive activity on January 11 are examined here in hopes that we can gain insight about the sequence of processes that led up to the 2006 eruption. Study of this preeruptive period may provide better information for those monitoring future earthquake swarms at Augustine and other similar volcanoes. Although this study will focus on the earthquakes that occurred during the preeruptive earthquake swarm (April 30, 2005 to January 10, 2006), we also use Alaska Volcano Observatory (AVO) catalog data beginning in the year 2000 to establish background rates and a start date for the precursory swarm. A histogram showing

---

[1] School of Geography, Environment and Earth Sciences, Victoria University of Wellington, P.O. Box 600, Wellington, New Zealand.

[2] Alaska Volcano Observatory, University of Alaska Fairbanks Geophysical Institute, 903 Koyukuk Dr., Fairbanks, AK 99775.

located earthquakes per 30 days from January 1, 2000, through the January 11, 2006, eruptive activity can be seen in figure 1.

The concept of seismic *b*-values was first put forward by Ishimoto and Ida (1939) and was later recast in its more familiar form as the value of *b* in the Gutenberg and Richter relation, $\log N = a - bM$, where "N" is the cumulative number of events greater than or equal to magnitude "M", and "a" is an empirical constant (Ishimoto and Ida, 1939; Gutenberg and Richter, 1944). The *b*-value can also be thought of as a ratio of the number of small earthquakes to the number of larger earthquakes happening over a given period of time. Seismic *b*-values are often near one for tectonic areas and are found to be higher in volcanic areas (Bath, 1981; McNutt, 2005).

Seismic *b*-values have been shown to vary with several known physical parameters, including stress (Scholz, 1968), thermal gradient (Warren and Latham, 1970), pore pressure (Wyss, 1973), and fracture density (material heterogeneity) (Mogi, 1962). These physical parameters are likely to be affected by a variety of processes which are common at volcanoes. Given the links to these physical changes, investigating *b*-values has the potential to determine physical processes that are driving earthquake swarms.

Although *b*-values have been found to vary with four physical parameters, only three are considered here; material heterogeneity has been excluded from this study. Both Scholz (1968) and Warren and Latham (1970) suggest that some *b*-value changes initially thought to be due to material heterogeneity are in fact caused by stress differences or thermal gradient changes. Heterogeneity is often attributed to fixed rock properties, such as porosity or fracture density, and though it may vary slightly because of ongoing fracture formation and deformation, it is more likely to vary on long geologic time scales rather than short eruptive time scales (Zobin, 1979). Additionally, factors that make the material more heterogeneous, such as new fractures and injection of a magma body (fluid next to rock), are likely to produce transient signatures in the other three physical parameters.

Many *b*-values studies have been conducted at volcanoes. These investigations have covered both spatial mapping of *b*-values and temporal analyses. Spatial studies have identified small volumes of high *b*-values that have been interpreted as magma bodies (Wiemer and McNutt, 1997; Wiemer and others, 1998; Sanchez and others, 2004). At Long Valley caldera and at Martin and Mageik volcanoes significant temporal changes in *b*-value were observed during earthquake swarms (Wiemer and others, 1998; Jolly and McNutt, 1999). The small seismic volume at Augustine (fig. 2) makes it an ideal candidate for a temporal *b*-value study.

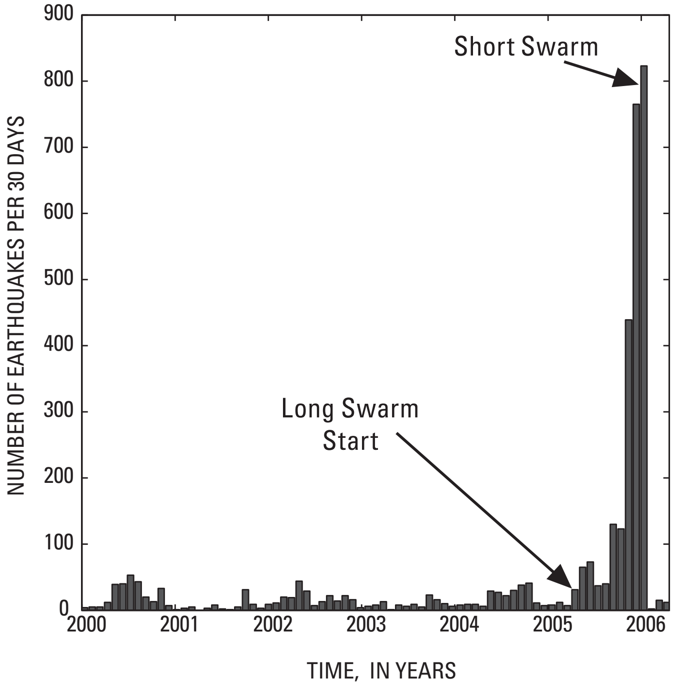

Figure 1. Histogram for located earthquakes per 30 days at Augustine Volcano from January 1, 2000, to January 11, 2006. Arrows point to the bins containing the start date of the long swarm (April 30, 2005) and the short swarm (January 10–11, 2006). Tick marks on the horizontal axis mark the beginning of each year.

Data

All located earthquakes at Augustine Volcano from 2000 through 2006 were selected from the AVO catalog. AVO maintains an earthquake catalog and publishes annual reports (for example, Dixon and others, 2008). The selected Augustine earthquake catalog has 2,945 located earthquakes between January 1, 2000, and the onset of the 2006 eruption on January 11, 2006. More than half (2,005) of the earthquakes are associated with the 2005–2006 preeruptive earthquake swarm. A rate histogram for the Augustine activity is shown in figure 1. Augustine earthquakes are located with an on-island seismic network that consists of 8 telemetered stations with 15 components (Dixon and others, 2008). Figure 2 shows a map of the island, its seismic instrumentation, and plots of the earthquake hypocenters selected from the AVO catalog. AVO catalog locations are determined using a one-dimensional six-layer velocity model derived from the model described by Lalla and Power (this volume). Processing is done using the XPICK seismic analysis software (Robinson, 1990) and the earthquake location program HYPOELLIPSE (Lahr, 1999). Magnitudes of completeness for Augustine Volcano ranged from 0.1 to -0.2 in 2005 (Dixon and others, 2008).

To use *b*-values to investigate temporal variations in physical processes we must assume, or demonstrate, that changes in *b*-value over time are meaningful. One potential problem is that if *b*-values are shown to change spatially, it may be difficult to determine whether they have also changed with time. The Augustine dataset presents us with a unique

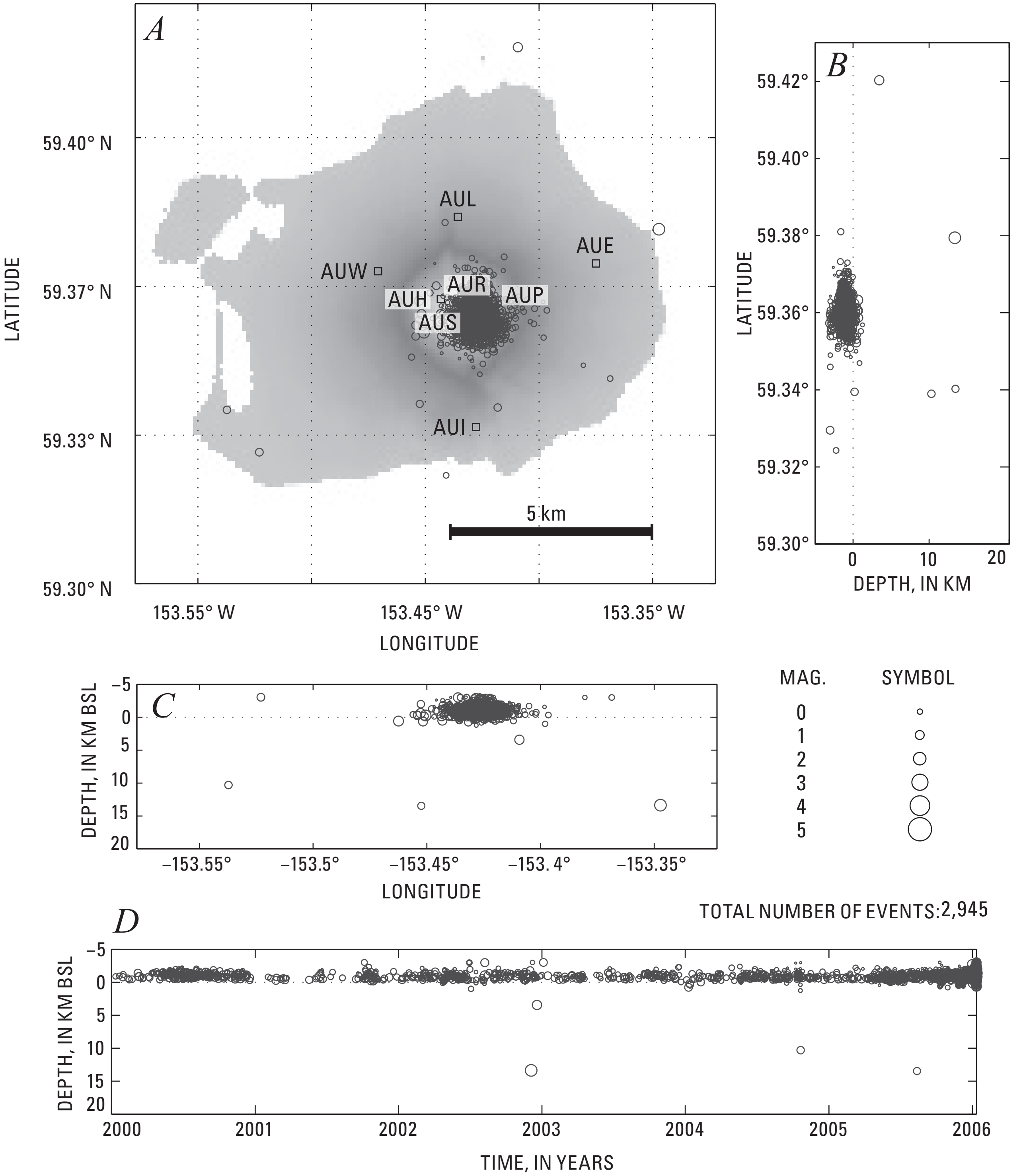

Figure 2. Summary plots of 2,945 earthquakes located by the Alaska Volcano Observatory near Augustine Volcano (shaded area is Augustine Island) from January 1, 2000, to January 11, 2006. Open circles show hypocenter locations. Hypocenters are scaled with magnitude (see scale). *A*, Earthquake epicenters in map view. *B* and *C*, north-south and east-west cross sections. *D*, Hypocenter focal depth plotted against time; a depth of 0 indicates sea level.

opportunity in this respect, because earthquakes located during the Augustine Volcano 2005–6 preeruptive swarm all occurred in a small seismic volume (fig. 2). The depth range for 95 percent of the earthquakes was confined to 0 to 2 km above sea level (asl), and depths appear to be constant over time. Despite the consistency, absolute depth control is poorly constrained and some earthquakes locate above the top of the volcano. In epicentral view the earthquakes span 1.5 km across the summit region. Some migration within this small volume is observed from late November 2005 to the onset of eruptive activity (DeShon and others, this volume; Power and Lalla, this volume). However, we believe that the seismic volume and the observed migration of events are small enough that we can consider the preeruptive swarm locations as essentially uniform in space.

The small seismic volume occupied by earthquakes at Augustine Volcano allows us to study the temporal evolution of *b*-values during the preeruptive earthquake swarm and compare our findings with information about temperature, pressure, and stress changes at Augustine. These other physical observations at the volcano will help to corroborate the temporal nature of observed *b*-value changes.

Methods

We first define a start date for the Augustine Volcano 2005–6 preeruptive earthquake swarm. Earthquake swarms are defined as increases in earthquake rates within a given volume over a relatively concentrated period of time without a single outstanding shock (Mogi, 1963). This is a rather loose definition and depends heavily on the opinions and perceptions of the reporter to define swarm durations. To lend a more quantitative element, we developed two algorithms, which used the daily number of located earthquakes to set a background rate and pick a swarm start date. We established the two algorithms to try to ensure that there was a real inflection or change at the selected point. Analysis of the years leading up to the 2005–6 activity was necessary to establish reliable background rates and give us a basis for determining change. A calendar year prior to the approximate onset of activity was used to establish background values used in each algorithm. Note that although only a single year is used to establish background rates in the algorithms, the earthquake rate at Augustine Volcano as seen in figures 1 and 2 appears to be relatively steady throughout the entire period from January 1, 2000, until the increase in activity in 2005. Late 2004 (October) is a possible exception to this statement; for details about this activity see Power and Lalla (this volume).

The first algorithm uses maximum daily event counts within a background period to establish a threshold for "increased activity." We call this method the largest-daily-count method (LDCM). In the case of Augustine all of these "counts" are located earthquakes, but the algorithm could potentially be used in places where earthquake locations are not possible. The second algorithm, the consecutive-days method (CDM), uses the low earthquake rate at Augustine Volcano to search for consecutive days with located earthquakes. Both the LDCM and CDM algorithms return a start date of April 30, 2005, for the beginning of the Augustine Volcano earthquake swarm. See appendix 1 for complete descriptions of the algorithms, flow chart diagrams, and additional details.

Using April 30, 2005, as the start date gives a total duration of 257 days for the preeruptive swarm. This long-building seismic swarm ultimately culminated in a very sharp increase in earthquake rate in the 13 hours directly preceding the eruption (Power and Lalla, this volume). For this paper we will term the 13-hour period of more energetic seismic activity on January 10–11, 2006, as the "short swarm" and refer to the swarm beginning April 30, 2005, as the "long swarm." This phenomenon of long and short swarms has been noted at many volcanoes (for both eruptive and non-eruptive swarm sequences), where either a long swarm, a short swarm, or both are present (Benoit and McNutt, 1996).

Calculations of *b*-value were carried out in ZMAP (Weimer, 2001). ZMAP is used to calculate a magnitude of completeness (M_c) for each *b*-value calculation, and only events above this threshold are used in the actual calculations (fig. 3). All *b*-values were determined using the maximum curvature method, which gives reasonable errors and is well suited for small earthquake catalogs and for temporal studies (Woessner and Wiemer, 2005). We also checked for station outages to ensure a uniform dataset. Although some station outages occur, we found no times when less than four seismometers were operating on Augustine Island. Four stations should generally be sufficient to determine consistent hypocenters and magnitudes (Lalla and Power, this volume).

To look for additional details, plots of *b*-value versus time were also generated using ZMAP (fig. 4). This calculation includes an automatic bootstrapping method to smooth the plot. A window size of 100 events with an overlap of 25 events was used to give the smallest time resolution possible. As with the standard *b*-value calculations, no cuts were made to the catalog, and the M_c was calculated for each time step.

Results

We found that the background (January 1, 2004–April 29, 2005) *b*-value was 1.51±0.1, the long swarm *b*-value was 1.26±0.04, and the short swarm *b*-value was 0.781±0.02 (fig. 3). A background calculation using all data between January 1, 2000, and April 29, 2005, yielded a *b*-value of 1.44±0.05, comparable to the background *b*-value which only uses data between January 1, 2004, and April 29, 2005. In addition to the low *b*-value for the short swarm, we also note the strange shape of its frequency-magnitude distribution curve (fig. 3*D*). The plot appears to have two separate slopes, a shallower slope for magnitudes up to 1.2 and a steeper slope for magnitudes greater than 1.2. The calculation of *b*-value with time shows an initial drop in *b*-value in mid-2004 and a dramatic rise and fall in the *b*-value associated with the occurrence of the short swarm (fig.4).

To investigate the relationship between seismicity and deformation, we calculated the *b*-value for each of the three global positioning system (GPS) deformation stages as outlined by Cervelli and others (2006) (fig. 5). For stage 1 (constant slow inflation from June 1, 2005, to November 17, 2005) a *b*-value of 1.31±0.06 was calculated. The calculation for stage 2 (increased inflation possibly due to dike intrusion, from November 17, 2005 to December 10, 2005) yielded a *b*-value of 1.85±0.1. Finally, stage 3 (constant from December 10, 2005 to January 11, 2006) gave a *b*-value of 1.18±0.05. Data from the short swarm on January 10–11, 2006, was left out of this *b*-value calculation for stage 3 because of the odd frequency-magnitude distribution (fig. 3D).

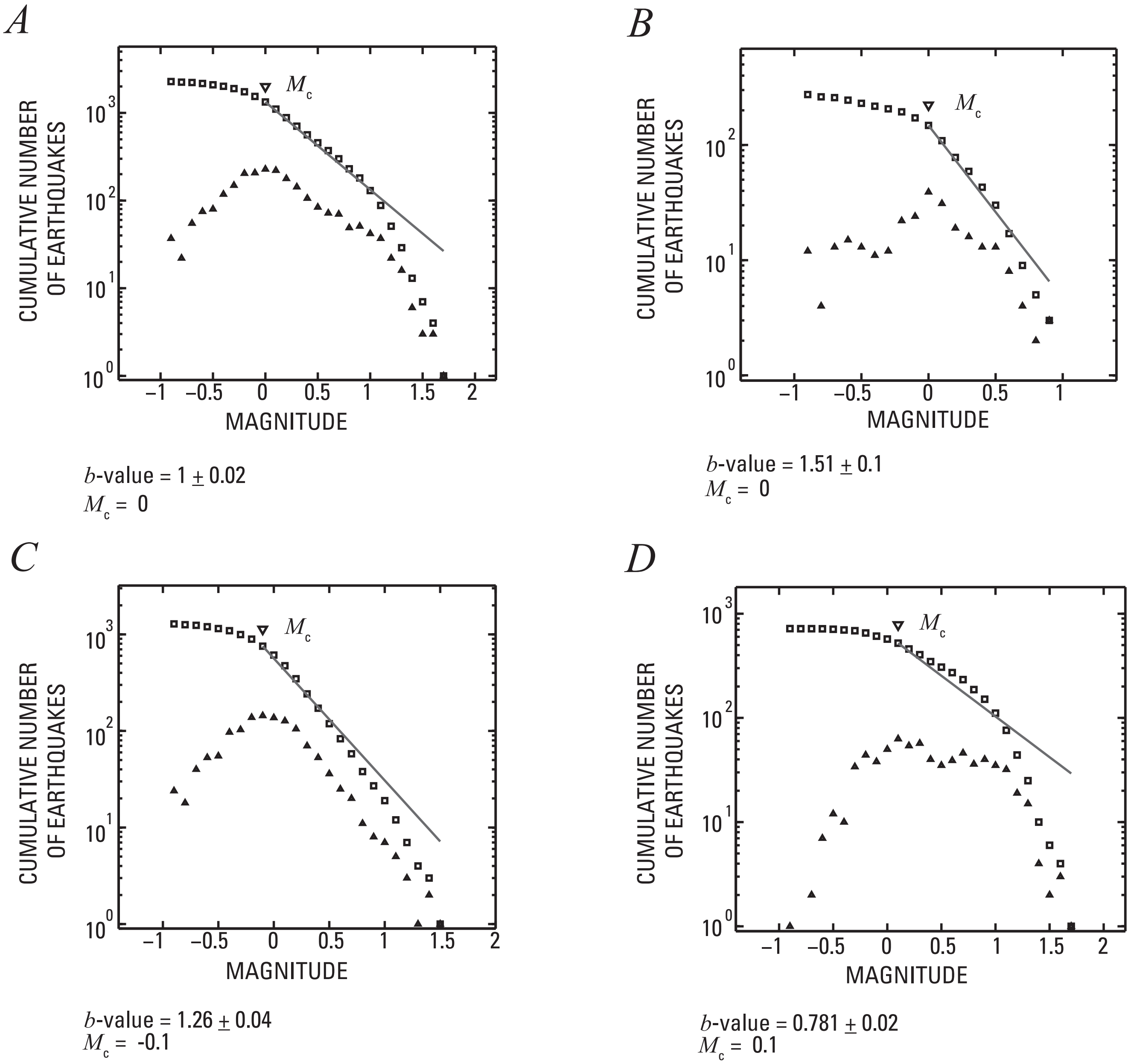

b-value = 1 ± 0.02
M_c = 0

b-value = 1.51 ± 0.1
M_c = 0

b-value = 1.26 ± 0.04
M_c = -0.1

b-value = 0.781 ± 0.02
M_c = 0.1

Figure 3. Cumulative frequency plots of Augustine earthquakes from January 1, 2000 to the initial eruption on January 11, 2006 with derived *b*-values. Triangles and squares show the number of earthquakes at each magnitude and the cumulative number of earthquakes, respectively. The magnitude of completeness (M_c) is shown by an inverted triangle; errors in *b*-value calculations reflect the 95-percent confidence interval of the maximum likelihood solution. *A*, The entire AVO earthquake catalog (January 1, 2000 to January 11, 2006). *B*, The background (January 1, 2000 to April 29, 2005). *C*, The long swarm (April 30, 2005 to January 10, 2006). *D*, The short swarm (13 hours prior to the initial eruption on January 11, 2006).

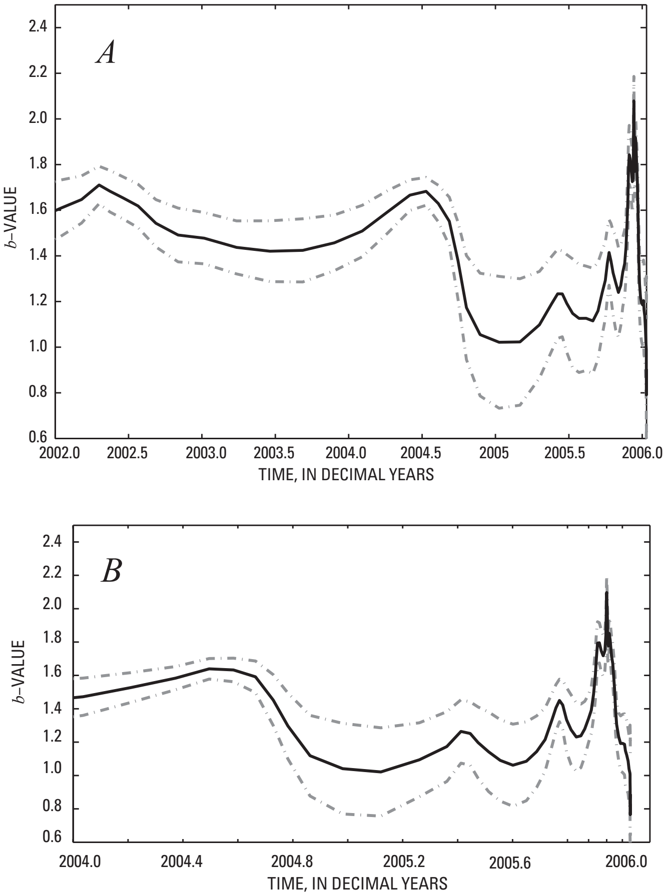

▲

Figure 4. Plots of *b*-value with time for Augustine earthquakes. *A*, For time interval 2002–6. The calculation uses a moving window of 100 earthquakes with an overlap of 25 events. The solid line is the calculated *b*-value, and the dashed lines indicate the 95-percent confidence interval of the maximum likelihood solution. *B*, Data for 2004–6 expanded for more detail.

▶

Figure 5. Results of *b*-value calculations for each precursory deformation stage outlined by Cervelli and others (2006). M_c is magnitude of completeness, and errors in *b*-value calculations reflect the 95-percent confidence interval of the maximum likelihood solution. *A*, Stage 1 (constant slow inflation from June 1, 2005, to November 17, 2005) *B*, Stage 2 (increased inflation possibly due to dike intrusion from November 17, 2005, to December 10, 2005) *C*, Stage 3 (continually increasing inflation from December 10, 2005, to January 11, 2006).

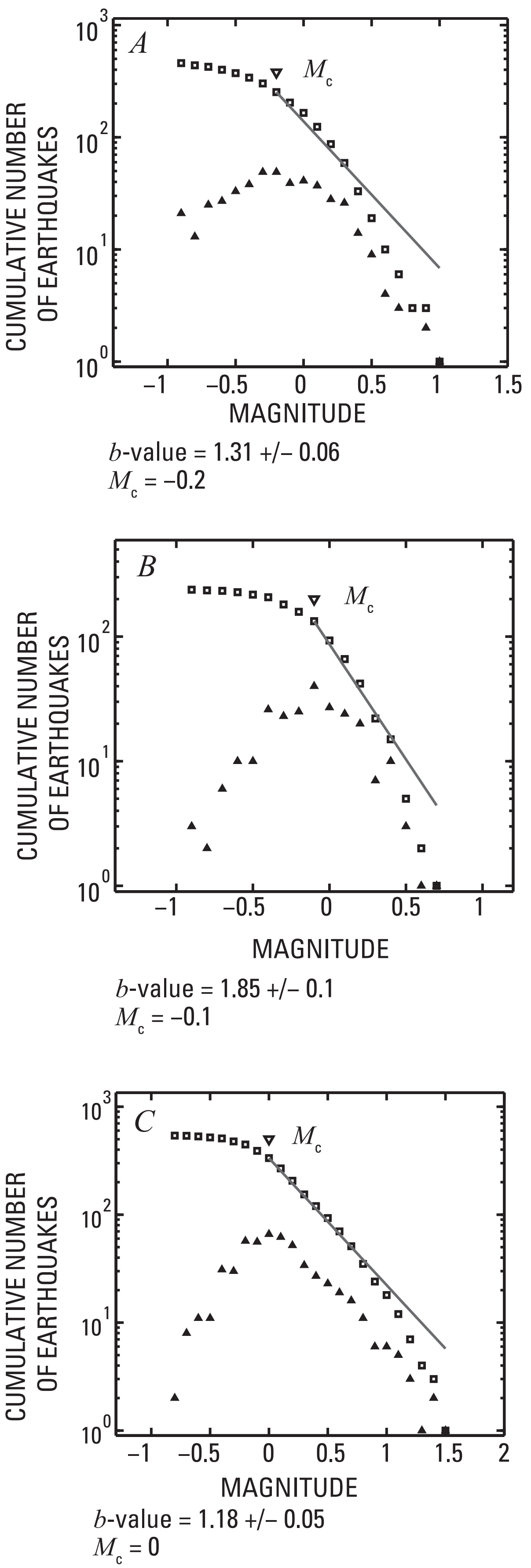

Discussion

Several physical processes could be associated with each part of an earthquake swarm. We expected to see an increase in stress in the surrounding region caused by pressurization of a deeper magma chamber during the long (building) swarm. This would lead to an overall decrease in the *b*-value. It was also expected that this would be followed by an increase in pore pressure and thermal gradient as the magma moved closer to the surface shortly before the eruption. These final changes would accompany the short swarm and cause an increase in the *b*-value above previous levels. These concepts are illustrated schematically in figure 6. Our results given earlier differ from this conceptual model. Neither the long swarm nor the short swarm shows an overall increase in *b*-value and it is the short swarm that has the lowest *b*-value of all the three periods. We will now examine these differences between our model and results by looking at the long and short swarms separately and then discussing our overall conclusions.

Long Swarm

We see in the plot of *b*-value versus time (fig. 4) that there is an initial drop in *b*-value in late 2004, but it precedes the actual seismic-swarm onset (April 30, 2005). A decrease in the *b*-value prior to the long swarm may explain why the long swarm does not have a *b*-value lower than the background period in the standard calculations. We will look to corroborate the timing of the *b*-value drop through correlation with other physical observations made at Augustine.

The *b*-values associated with the three precursory deformation stages help to identify some physical processes at work during the long swarm. The second stage of activity, from November 17, 2005, to December 10, 2005, has a higher *b*-value than the other two stages. Higher *b*-values are often associated with high thermal gradients and increases in pore pressure (Warren and Latham, 1970; Wyss 1973). At Augustine, the higher *b*-value could be explained as a result of pressurization that was caused by the inferred dike emplacement (Cervelli and others, 2006; Cervelli and others, this volume). An increase in pore pressure is likely to have occurred preceding the 75-km-long steam plume seen on December 12, 2005, in 250-m MODIS data (Bailey and others, this volume). The increase in *b*-value is also seen in figure 7, which shows the three deformation stages superimposed onto the plot of *b*-value with time. While the general trends in the *b*-value seem to correlate well, figure 7 also illustrates that they do not correlate exactly with the deformation changes, and there are additional changes in *b*-value that are not accompanied by any apparent changes in deformation.

Another physical observation at Augustine was an increase in temperature, at seismic station AUS (see fig. 2 for seismic-station locations). The hut at seismic station AUS contained a thermistor (LM335A thermocouple paired with a 3.3-kohm 5-percent resistor, manufactured by National Semiconductor) in the McVCO (a microcontroller-based frequency generator that replaces the voltage controlled oscillator (VCO) used in the analog telemetry of seismic data), which is used to test station health. The McVCO was located on a battery rack inside the AUS seismic hut, approximately 1.4 m off the ground. The LM335A works over a temperature range of –40 to 100°C and is accurate within 1°C. Temperature information from the thermistor was received with the calibration pulse, every 12 hours from late October 2000 through the eruption on January 11, 2006. No changes were made in the processing of this data from October 2000 through January 2006 when the AUS hut was destroyed (G. Tytgat, oral commun., 2006). Regional air temperature data from Homer, Iliamna, and Seldovia, courtesy of the Alaska Climate Data Center, and data from a National Oceanic and Atmospheric Administration (NOAA) weather station on Augustine Island

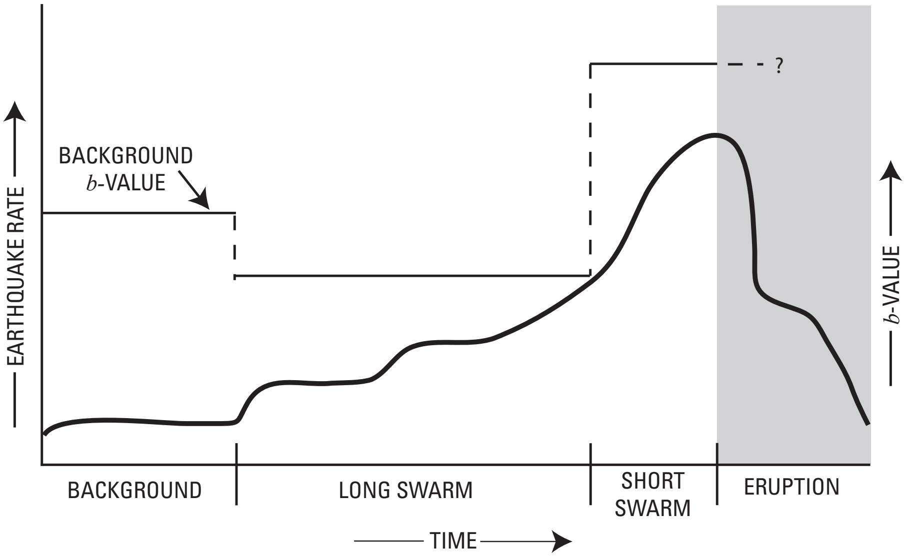

Figure 6. Schematic diagram illustrating how we expected the *b*-value to change over the course of the precursory earthquake swarm at Augustine Volcano. Curved line indicates the observed earthquake rate, and the straight horizontal lines indicate relative *b*-value changes expected for each part of the swarm activity.

were also processed for comparison with the recorded AUS temperatures.

The weather stations at Homer, Iliamna, Seldovia, and the Augustine NOAA station all gave temperatures that agreed with one another and varied systematically with the season. However, the changes seen at the AUS seismic hut differed from the others and are likely volcanic in origin. In figure 8 daily maximum temperatures from the three regional stations and the NOAA weather station on Augustine Island are plotted and overlain with weekly temperature averages from the AUS hut. Where data were unreported for a period, the average of the existing data within the 7-day period is shown instead. Periods where no data were reported are plotted as a zero value for both the regional stations and the AUS site. The long outage in AUS data in 2002 is a period when no data were received. Data were transmitted during the outage in 2004, but the temperature sensor did not report temperatures. These times do not correspond to the catalog-reported station outages (Dixon and others, 2008) and are more likely to be related to weather interference with the signal or a problem with the temperature sensor itself. Table 1 shows monthly average temperatures from January 2002 through January 2006. The monthly average shows a marked increase beginning in January 2005. A smaller increase of approximately 5°C is also seen in November and December 2004. This can also be seen in figure 9, where monthly averages of AUS hut temperatures from January 2002 through January 2006 are overlaid on the plot of *b*-values. Again, the monthly average shows a marked increase beginning in January 2005, and a smaller increase of approximately 5°C is also seen in November and December 2004.

Table 1. Monthly averaged temperatures at seismic station AUS on Augustine Volcano from January 2002 through January 2006.

[The value for January 2006 is only an average through January 11. All other values span the entire month. An asterisk indicates insufficient data to calculate the monthly average.]

	Average Temperature (°C)				
Month	**2002**	**2003**	**2004**	**2005**	**2006**
January	6.18	5.72	2.57	29.90	45.28
February	6.95	7.22	6.96	30.74	
March	5.74	2.83	1.55	35.75	
April	6.74	6.75	7.19	34.34	
May	4.31	8.82	11.00	28.35	
June	4.25	7.83	11.31	33.45	
July	*	13.51	15.04	39.03	
August	*	13.07	19.47	39.09	
September	6.96	8.78	12.09	33.39	
October	4.55	4.74	*	30.33	
November	5.28	3.87	13.70	24.26	
December	6.00	3.74	10.79	44.31	

An ASTER (advanced spaceborne thermal emission and reflection radiometer) image acquired on December 20, 2005, and the first FLIR (forward looking infrared radiometer) mission during the Augustine unrest on December 22, 2005, both revealed areas of warm, bare rock and active fumaroles. The FLIR observations recorded bare rock temperatures of 10°C and fumarole temperatures as high as 210°C (Wessels and others, this volume). These observations confirm that summit temperatures were

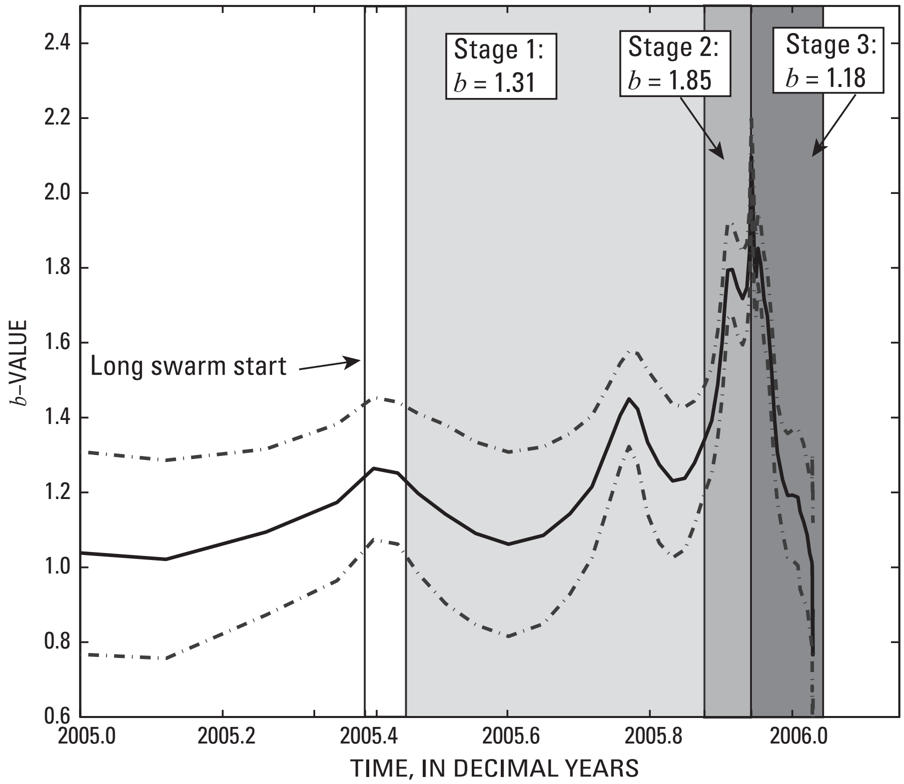

Figure 7. Plot of calculated *b*-value with respect to time for 2005–6, overlaid with shaded boxes indicating the periods of the long swarm and each of the three precursory deformation stages outlined in Cervelli and others (2006). The solid line is the calculated *b*-value, and the dashed lines indicate the 95-percent confidence interval of the maximum likelihood solution.

already elevated by late December. The AUS temperatures reported for those days were 44.6°C and 46.3°C, respectively. The consistency of data processing and a visit to the summit in December 2005 also provide evidence that this was a real thermal change (G. Tytgat and E. Clark, oral commun., 2006). The temperature change coincides with the initial *b*-value change in late 2004, which we see in our *b*-versus-time calculations. This change in *b*-value is possible evidence for a change in heat or fluid movement at depth at Augustine Volcano prior to the beginning of the seismic swarm.

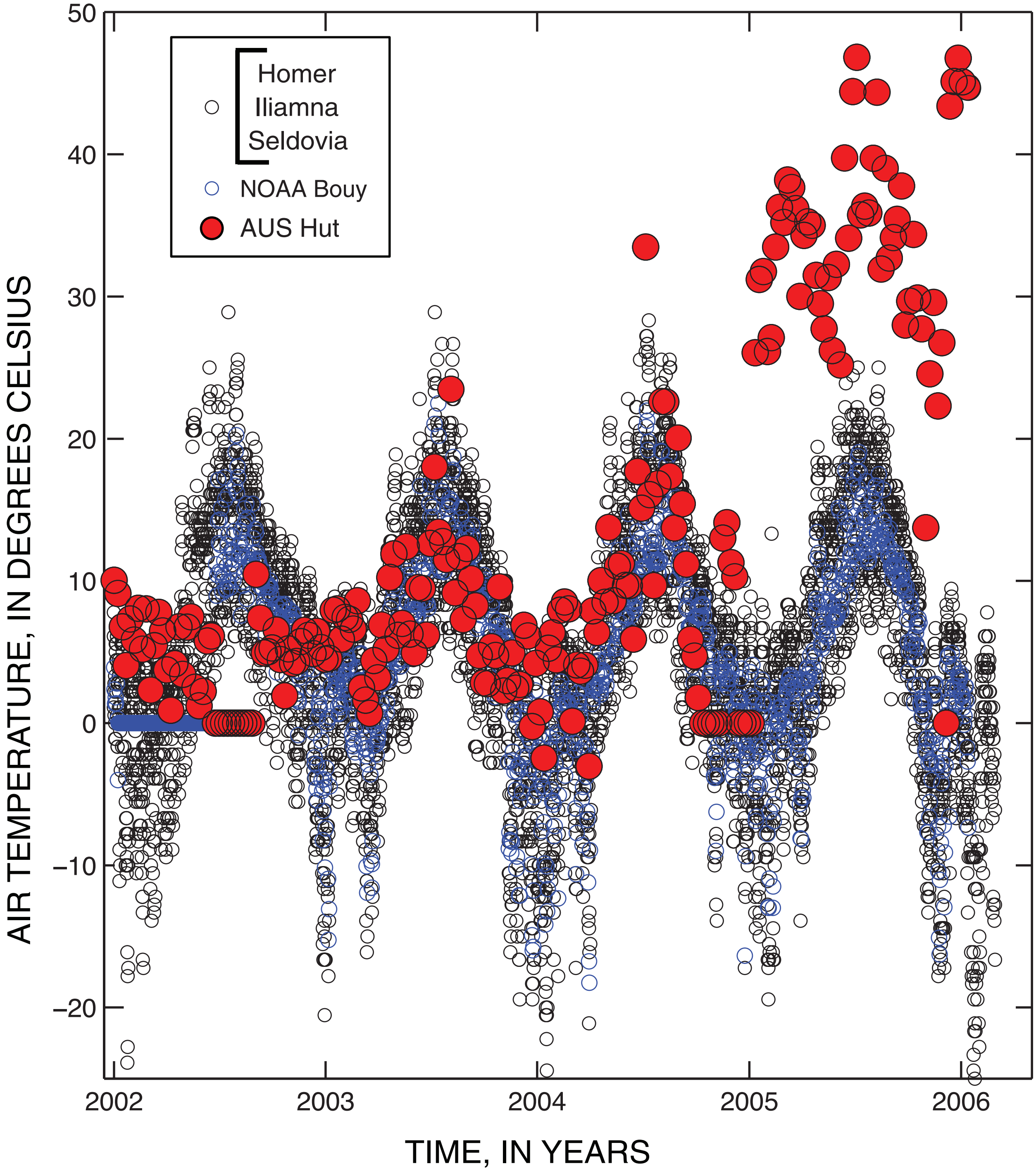

Figure 8. Plot of daily maximum air temperatures recorded in nearby communities (Homer, Iliamna, and Seldovia), at the Augustine Island NOAA weather station, and 7-day average temperatures from the seismic station AUS near the summit of Augustine Volcano. Tick marks on the horizontal axis mark the beginning of each year.

Given that the initial *b*-value decrease and temperature increase appear to be linked, we face the question, why does the *b*-value decrease? For *b*-value changes associated strictly with an increasing thermal gradient, the value of *b* should increase (Warren and Latham, 1970), the opposite of what we observe. We interpret this downward *b*-value trend to reflect an increase in stress throughout the seismic volume caused by the same physical process that is changing the thermal gradient. This suggests a possible influx of magma at depth or some other process that increases both thermal gradient and stress. Further support for a stress-induced *b*-value change is found in the slight time difference between the initial *b*-value change and the onset of the temperature increase seen in figure 9. A stress change would likely propagate instantaneously throughout the affected volume, whereas thermal (and pore pressure) effects take time to propagate through a volume of rock. Observing a stress change in *b*-values while we have evidence of thermal changes implies that stress effects dominate *b*-value observations when both parameters are changing simultaneously.

Because of the apparent importance of stress in overall *b*-value observations and past studies by Roman and others (2004), which suggest changes in stress tensors during periods of unrest and eruption, we undertook a study of focal mechanisms at Augustine. Determination of correct polarization of stations, normal or reversed, was made by looking at 37 large teleseisms from 2002 to 2006. *P*-wave polarities were then repicked for all located earthquakes for which at least six clear *P*-wave first motions were possible. Once the *P*-wave motions were repicked, the events were relocated using the same velocity model and processing steps as for the initial catalog locations (Dixon and others, 2008).

Focal mechanisms were computed for all earthquakes using FPFIT (Reasenberg and Oppenheimer, 1985). Solutions were judged acceptable if they had: a misfit of less than 0.15 (less than 15 percent of stations inconsistent with the preferred solutions); STDR (distribution around the hypocenter) ≥ 0.40; and an average uncertainty in strike, dip, and rake of ≤ 25°.

After applying this criteria, 79 out of 201 earthquakes returned acceptable focal-mechanism solutions. There were 19 events (out of 61 picked) with acceptable solutions from 2002 through 2004 and 60 events (out of 140 picked) from the long swarm (all events with acceptable solutions in 2005 occurred during the long swarm). Appendix 2 shows all 79 acceptable

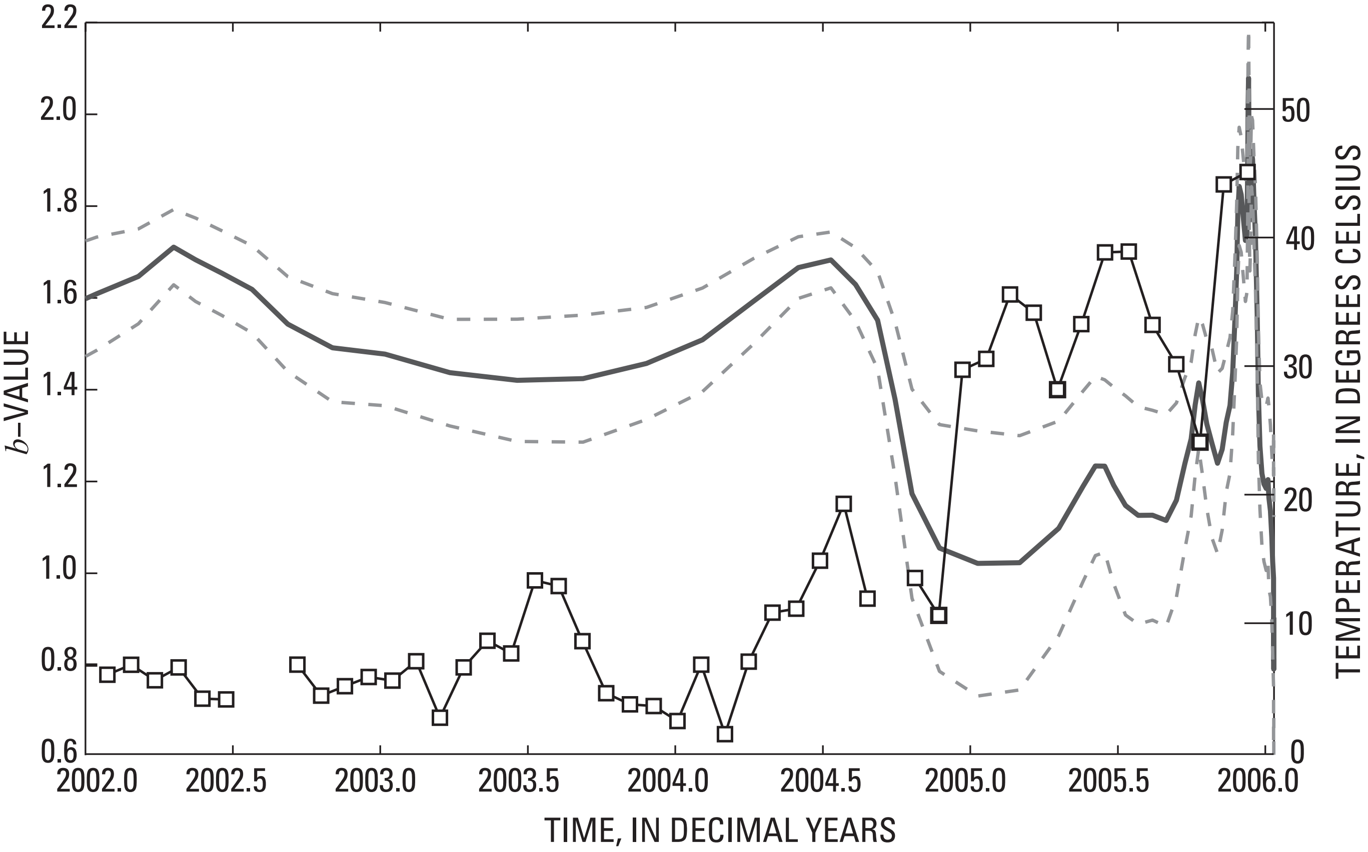

Figure 9. Plot of *b*-value with time from figure 4 (shown in boldline), overlaid with monthly average temperatures (as squares) from a thermistor at seismic station AUS. The *b*-value calculation uses a moving window of 100 earthquakes with an overlap of 25 events, and the dotted lines represent the 95-percent confidence interval of the maximum likelihood solution.

focal mechanisms. Stress tensor inversions were attempted in ZMAP for both the background data (2002 to 2004) and the long swarm (2005 through January 10, 2006) using the method of Michael (1987). The inversions had very high errors and do not display a dominant faulting style. The lack of any pattern or observable change in the focal mechanisms with time and the highly variable stress tensors agree with work by DeShon and others (this volume), which suggests no dominant faulting style or area within the Augustine Volcano seismic volume.

Short Swarm

In our conceptual model we expected the *b*-value of the short swarm to be the highest of all the time periods (fig. 6), and yet our results show that it is the lowest (fig. 3). We also see this low value in the calculation of *b*-value versus time, where there is a dramatic drop in *b*-value just before the eruption (fig. 4). We also note, however, that there is a strange bend or knee in the *b*-value curve (fig. 3*D*). This led us to question whether the low value was real and whether there was an “excess” of larger events occurring, or if this lower value was an artifact of a poor fit to a single distribution. Upon examining magnitudes with time, we find that the decrease in *b*-value leading into the eruption is real and appears to be caused by an increase in the number of $M_L \geq 1$ events (large earthquakes for Augustine) that occur in that time frame.

Having convinced ourselves that the observed low *b*-value for the short swarm is real, we look for ways to explain the observed knee in the frequency-magnitude distribution. Bends or knees like this one (fig. 3*D*) have been observed at other volcanoes, including Mount St. Helens (Qamar and others, 1983), Fernandina (Filson and others, 1973), and Usu (Okada and others, 1981; Okada 1983). At Fernandina the data are directly related to caldera collapse (Filson and others, 1973), so we will not seek comparisons with their conclusions. Okada and others (1981) outlined the appearance of odd frequency-magnitude plots at Usu and found that there were distinct earthquake families occurring in time. These earthquake families accounted for an unusually high number of earthquakes with similar magnitudes. Work by Buurman and West (this volume) and DeShon and others (this volume) indicates that earthquake families were occurring at Augustine from 1993 through 2006. Buurman and West (this volume) identified seven families on January 10–11, 2006, before the first eruption. Because only 41 out of 722 located earthquakes appear in the families on January 10–11, 2006, we conclude that earthquake families alone cannot explain the unusual shape of the frequency-magnitude plot.

The knee in the Mount St. Helens data corresponds to a group of earthquakes with magnitudes 4.5 and greater (Qamar and others, 1983). Low-frequency energy also accompanies many of the located earthquakes, and an increase in the low-to high-frequency amplitude ratio is observed leading up to the eruption. This has been interpreted as either the source of earthquakes becoming shallower or evidence of the magma chamber expanding (Qamar and others, 1983; Main, 1987).

A magnitude histogram for the short swarm is shown in figure 10. Most complete earthquake catalogs have a single normal-shaped distribution. The bell-shaped curve results from the lack of complete detection for magnitudes below the M_c and a similar reflected exponential decay of higher magnitudes resulting from decreasing frequency of occurrence. The histogram of the January 10–11, 2006, earthquakes is clearly not a single peaked bell-shaped curve and appears to be bimodal.

A separate study of very long period (VLP) energy was performed to investigate possible VLP energy associated with some of the high-frequency earthquakes during the short swarm, first observed by S. DeAngelis and J. Power (oral. commun., 2007). We looked for VLP signals during the short swarm (January 10–11, 2006) using data from temporary broadband stations AU11, AU12, AU13, AU14, and AU15 (for locations of these stations, see Power and Lalla, this volume). These seismometers were installed on Augustine Island in response to the increasing earthquake activity in December of 2005 and were not telemetered (Power and others, 2006). Initially we chose two different filters, a band pass filter from 0.01 to 0.2 Hz, and a second separate low pass filter of 0.05 Hz. The low pass filter

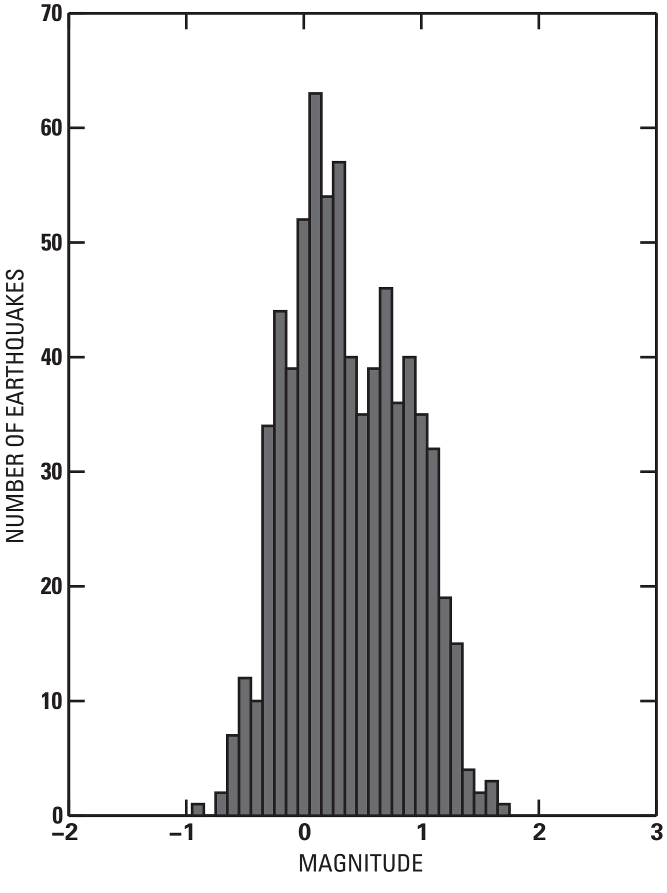

Figure 10. Histogram of magnitudes for located earthquakes at Augustine Volcano from the 13-hour short swarm on January 10–11, 2006.

of 0.05 Hz, corresponding to periods of 20 seconds and greater, showed the most consistent and largest amount of energy, and we chose that filter to examine all of the data.

To establish whether or not VLP energy was accompanying the high-frequency located earthquakes during the short swarm, we looked through continuous data at the time of each located earthquake, applied a 0.05 Hz low pass filter, and visually determined whether or not there was a pulse of VLP energy. No quantitative criteria were assigned for either amplitude or wavelength. Short-period stations AUP and AUW were used to verify the position of located earthquakes because the temporary broadband stations were not used for the location of earthquakes in the catalog. There were other long-period and VLP signals seen during this time frame, but no events without accompanying located high-frequency earthquakes were considered in this study. Figure 11 shows raw and filtered waveforms for several earthquakes at Augustine Volcano.

Using this method we found that 221 out of 722 located earthquakes during the short swarm had accompanying VLP energy. The events were separated according to this classification, and the individual properties of each group were examined. A magnitude histogram was created for each set of events, and these are plotted in figure 12. Both sets of events gave approximately normal distributions, indicating that they are complete populations of events. Furthermore, the two sets of events have notably different mean magnitudes. The smallest event without accompanying VLP energy is M_L 0.1, while the smallest event observed with VLP energy is M_L 0.9.

To test the significance of this apparent difference in mean magnitude, a Student t-test was run (Davis, 2002). This test examines the likelihood that two populations have come from a single parent population. The mean magnitude of the events with VLP energy was 0.91, and the mean magnitude of events without observed VLP energy was 0.16 (negative magnitudes

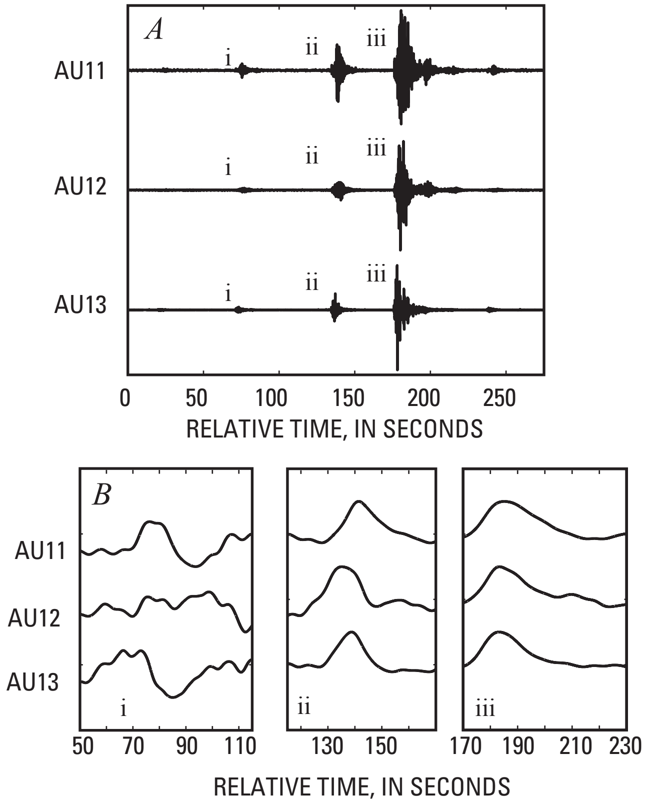

Figure 11. Waveforms for three located earthquakes at Augustine Volcano on January 10, 2006, as recorded on stations AU11, AU12, and AU13. The calculated origin time, depth, and magnitude are 19:48:58, 19:50:02, and 19:50:43 AKST; –0.57, –0.84, and –0.57 km below sea level; and 0.6, 0.6, and 1.4, respectively for the three earthquakes. *A,* Unfiltered waveforms at each station. *B,* Filtered waveforms around each earthquake that have been normalized to the maximum amplitude within the sample and low–pass filtered at 0.05 s for each station. Note that the first event shows no coherent VLP energy while the second and third events have significant VLP energy.

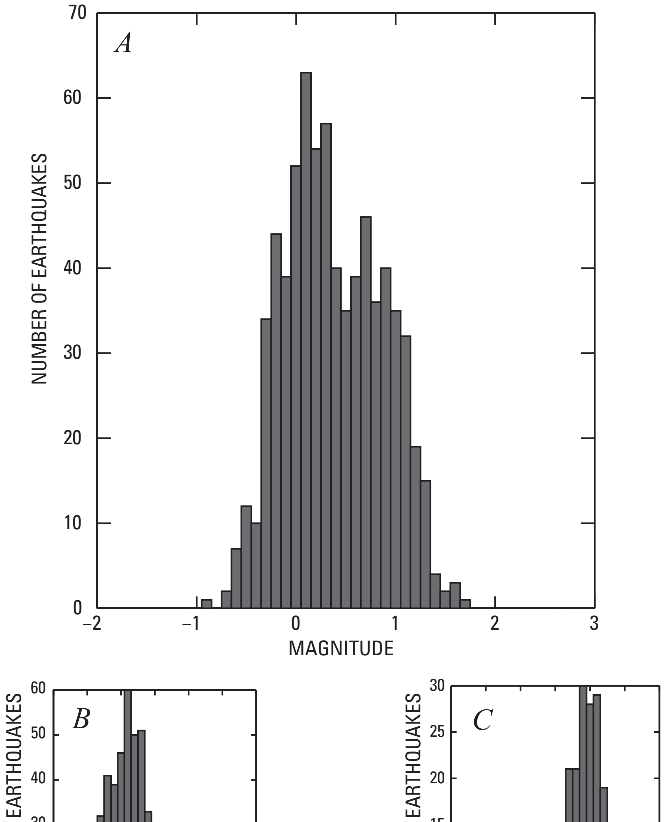

Figure 12. Magnitude histograms for (*A*) All events at Augustine Volcano during the short swarm (January 10–11, 2006), (*B*) Events with associated very long period energy, and (*C*) events without any associated very long period energy.

reduce the overall mean). The Student t-test produced a value of 26.3, well above the limit of 3.09 for a statistically significant difference between the means. Thus the two sets of earthquakes represent different parent populations.

To quantify the differences in energy implied by the differences in mean magnitude, we used ZMAP to calculate the cumulative moment for each earthquake population (fig. 13). The population with VLP energy has a moment of 1.01×10^{14} Nm, a factor of four larger than the cumulative seismic moment for the events without VLP energy (2.46×10^{13} Nm). The VLP events are also found to have more than half of the total moment for the entire seismic swarm and slightly more energy than all other earthquakes from January 1, 2000, through the January 11, 2006, eruption (9.49×10^{13} Nm).

Having observed that both events with and without VLP energy appear to have bell-shaped distributions (fig. 12), we note that the population without VLP energy represents earthquake activity on January 10–11, 2006, without the excess higher magnitude events that earlier made the observed magnitude histogram appear bimodal. The population with VLP energy, that has significantly higher magnitudes, corresponds to the $M \geq 1.0$ events that are seen to drive down the *b*-value for the short swarm. Essentially the population of VLP events is the "cause" of the bimodal magnitude histogram and of the associated low *b*-value for the short swarm.

The occurrence of VLP energy accompanying earthquakes and a bimodal *b*-value are in good agreement with the findings at Mount St. Helens (Qamar and others, 1983; Main, 1987), where both a bimodal frequency-magnitude distribution and the occurrence of lower frequency energy accompanying some of the recorded earthquakes were observed. Further comparison between these findings is ongoing.

The fact that the population of events without VLP energy has a similar M_c as the events in the long swarm suggests that the underlying process driving the long swarm continued during the short swarm and an additional population of earthquakes (those with VLP energy) was superimposed onto the existing seismicity trend. We believe that this is evidence of independent concurrent seismogenic processes at Augustine preceding the eruption. The fact that both sets of events appear to be happening in the same volume indicates that there is probably a difference in their mechanisms. Following Scholz (1968), we interpret the low *b*-values and larger event sizes of the VLP population to represent the formation of new fractures. The larger event size is required to accompany the low *b*-value because breaking rock, as opposed to failure along pre-existing fractures, requires much more energy.

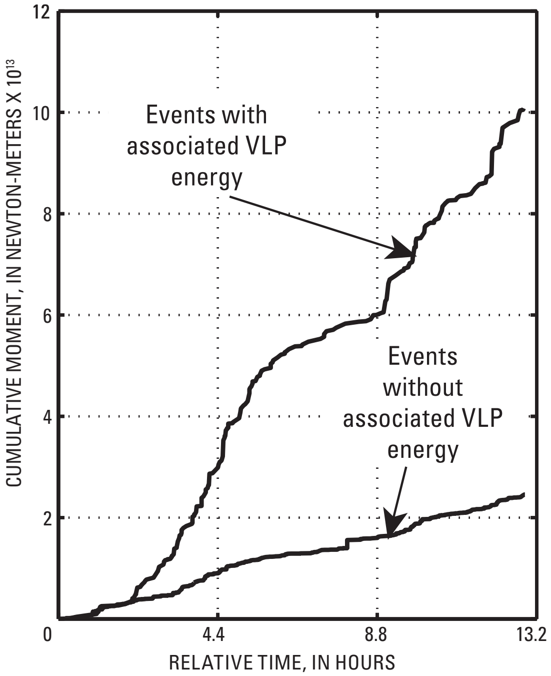

Figure 13. Cumulative seismic moment for earthquakes with and without associated very long period energy during the 13-hour short swarm on January 10–11, 2006. Time is shown in hours relative to the beginning of the short swarm at 1535 AKST on January 10.

A lull in earthquake rate is noted about 8 hours into the short swarm, and it appears in both populations of events (fig. 14). No major changes in depth or magnitude are seen in either population before or after the lull. Figure 15 shows several plots comparing the rate at which the two populations of events were occurring with time. We infer from the lack of change in either population that the individual processes causing each population of events did not change either. This indicates that the lull was not caused by a change in process and was probably the result of a mechanical, material, or thermal barrier present at Augustine Volcano.

Focal mechanisms were not attempted for the earthquakes during the short swarm. No clear stress tensor was produced from analysis of the background or long swarm, and so even if a stress tensor was produced from the short swarm, there would be no way to compare it to the preceding time periods.

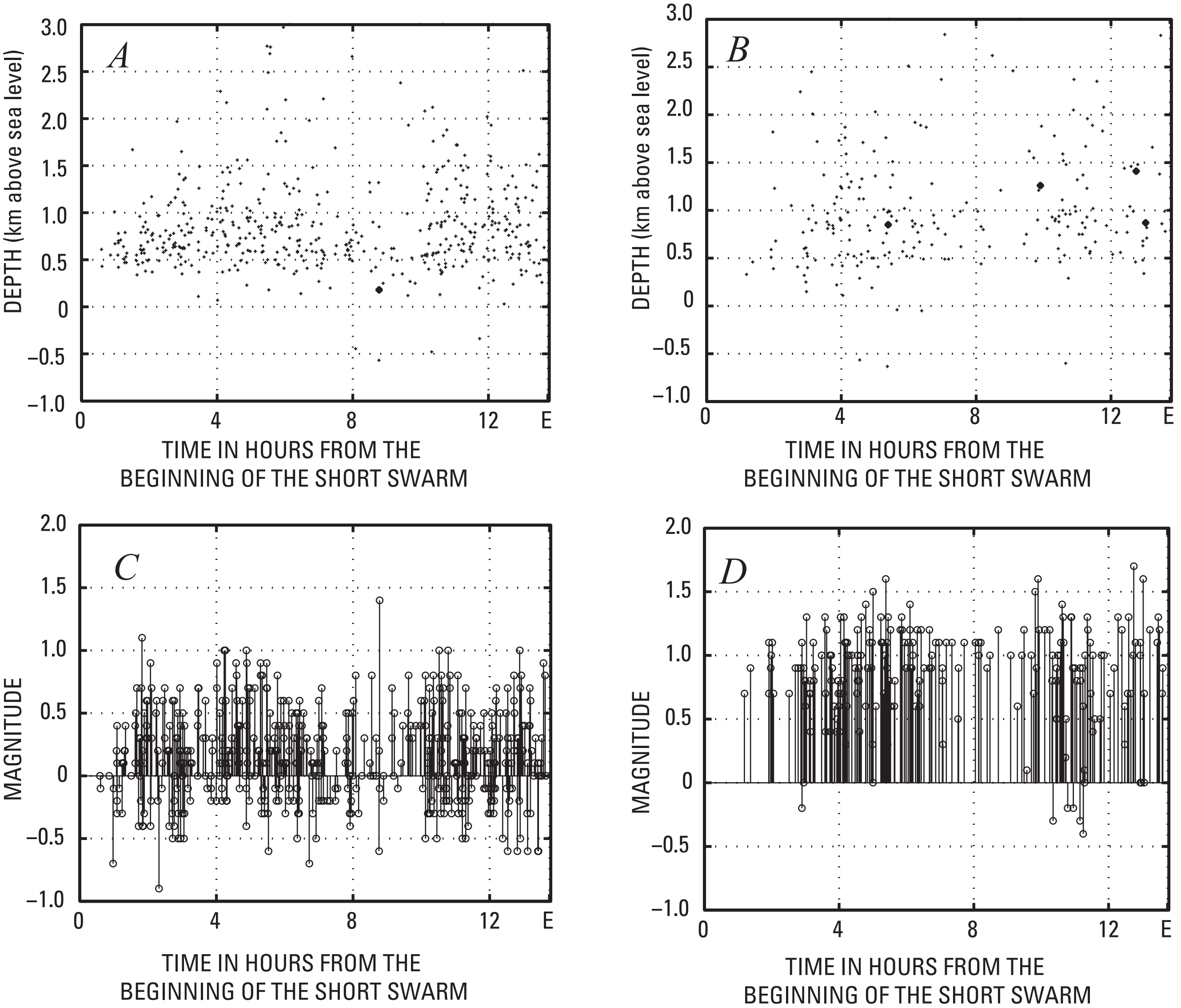

Figure 14. Plots of earthquake focal depth with time and of magnitude with time plots for events with very long period (VLP) energy (*A* and *C)* and without VLP energy (*B* and *D)*. The time axis reflects the time since the onset of the short swarm, taken to be at 1535 AKST on January 10, 2006. "E"marks the initiation of explosive activity.

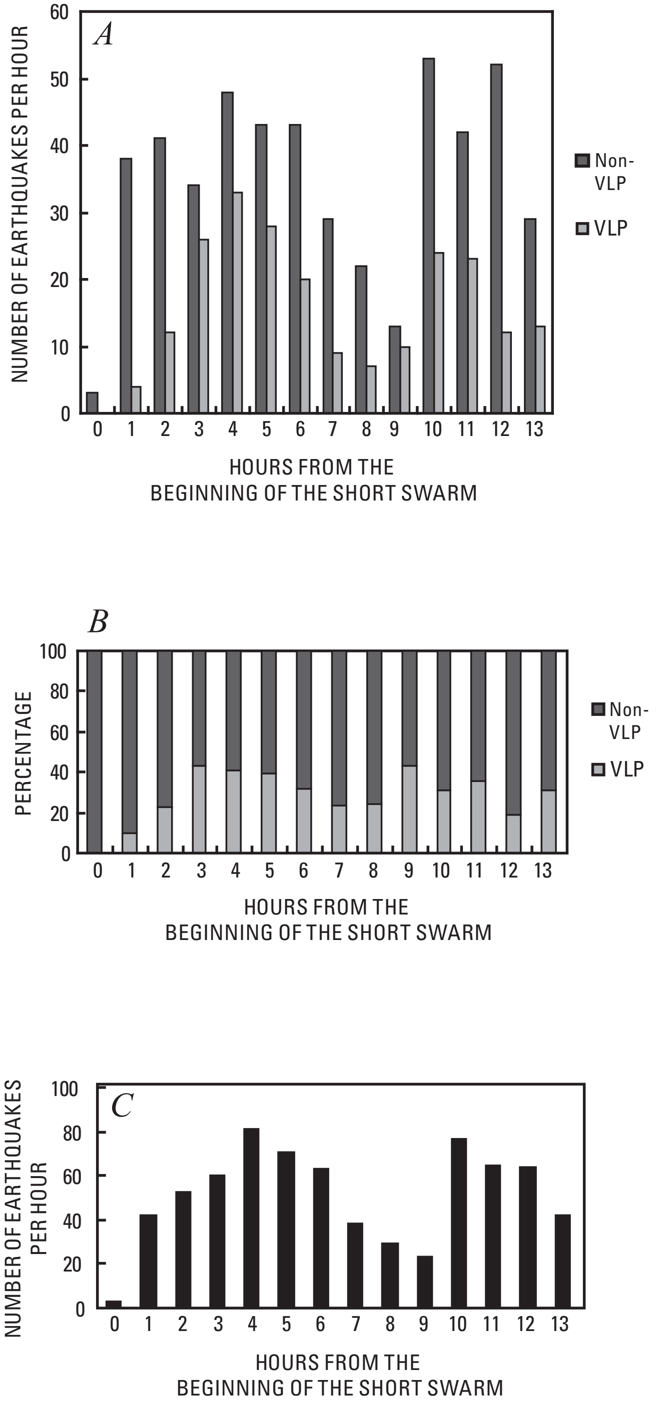

Figure 15. Summary plots the occurrence of earthquakes with very long period (VLP) and non-VLP energy during the 13-hour-long short swarm on January 10-11, 2006. *A*, histogram showing the number of earthquakes per hour with and without very-long-period energy. *B,* Percentage per hour of the two populations of earthquakes. *C,* Histogram showing the total number of earthquakes recorded per hour. Note that the total number of earthquakes in *C* tends to mirror the percentage of VLP events in *B* with a slight time delay.

Conclusions

We have been able to identify changes in *b*-value during the Augustine preeruptive earthquake swarm that we believe were caused by changes in thermal gradient, pore pressure, and stress. These changes have been substantiated through comparison with other physical observations at Augustine Volcano. Our observations in conjunction with temperatures recorded on Augustine Island suggest that when thermal-gradient and stress changes occur simultaneously, stress dominates the overall *b*-value observations. We have also been able to identify a unique set of high-frequency earthquakes that have associated VLP energy. These events are a complete and separate population from other high-frequency earthquakes occurring during the short swarm. The VLP events have significantly higher energy release than other earthquakes, and we believe that they may be the primary expression of magma moving towards the surface. We see preliminary evidence to suggest that *b*-value changes can precede other more obvious punctuations in activity, such as the onset of the seismic swarm. Changes in *b*-values can be used to corroborate other physical observations, such as the *b*-value changes that accompanied temperature changes or increased steaming before the large steam plume on December 12, 2005. These *b*-value changes may indicate that larger or deeper processes are occurring than can otherwise be observed. In this way *b*-value calculations can give us more information about the causes and physical process at work during earthquake swarms. Given these findings we suggest that systematic evaluation of *b*-values become a more regular part of monitoring efforts.

Acknowledgments

Thank you to Matt Haney, Seth Moran, and John Power for their reviews, which helped to shape this paper. We acknowledge the AVO staff, especially Scott Stihler, Guy Tytgat, Ed Clark, and Jim Dixon. During the course of this work we also had discussions with Mike West, Doug Christensen, Stephanie Prejean, Helena Buurman, Lea Burris, Celso Reyes, Matt Gardine, Nicole DeRoin, Tanja Peteresen, Silvio DeAngelis, and others.

References Cited

Bailey, J.E., Dean, K.G., Dehn, J., and Webely, P.W., 2010, Integrated satellite observations of the 2006 eruption of Augustine Volcano, *in* Power, J.A., Coombs, M.L., and Freymueller, J.T., eds., The 2006 eruption of Augustine Volcano, Alaska: U.S. Geological Survey Professional Paper 1769 (this volume).

Bath. M., 1981, Earthquake magnitude—recent research and current trends: Earth Science Review, v. 17, p. 315–98.

Benoit, J.P., and McNutt, S.R., 1996, Global volcanic earthquake swarm database, 1979–1989: U.S. Geological Survey Open-File Report 96-0069, 333 p.

Buurman, H., and West, M.E., 2010 Seismic precursors to volcanic explosions during the 2006 eruption of Augustine Volcano, *in* Power, J.A., Coombs, M.L., and Freymueller, J.T., eds., The 2006 eruption of Augustine Volcano, Alaska: U.S. Geological Survey Professional Paper 1769 (this volume).

Cervelli, P.F., Fournier, T.J., Freymueller, J.T., and Power, J.A., 2006, Ground deformation associated with the precursory unrest and early phases of the January 2006 eruption of Augustine Volcano, Alaska: Geophysical Research Letters, v. 33, doi: 10.1029/2006GL027219.

Cervelli, P.F., Fournier, T.J., Freymueller, J.T., Power, J.A., Lisowski, M., and Pauk, B.A., 2010, Geodetic constraints on magma movement and withdrawal during the 2006 eruption of Augustine Volcano, *in* Power, J.A., Coombs, M.L., and Freymueller, J.T., eds., The 2006 eruption of Augustine Volcano, Alaska: U.S. Geological Survey Professional Paper 1769 (this volume).

Davis, J.C., 2002, Statistics and data analysis in geology: New York, J. Wiley, p. 68–74.

DeShon, H.R., Thurber, C.H., and Power, J.A., 2010, Earthquake waveform similarity and evolution at Augustine Volcano from 1993 to 2006, *in* Power, J.A., Coombs, M.L., and Freymueller, J.T., eds., The 2006 eruption of Augustine Volcano, Alaska: U.S. Geological Survey Professional Paper 1769 (this volume).

Dixon, J.P., Stihler, S.D., Power, J.A., and Searcy, C., 2008, Catalog of earthquake hypocenters at Alaskan Volcanoes; January 1 through December 31, 2006: U.S. Geological Survey Data Series 326, 78 p.

Filson, J., Simkin, T., and Leu, L.-K., 1973, Seismicity of a caldera collapse—Galapagos Islands 1968: Journal of Geophysical Research, v. 34, p. 8591–8622.

Gutenberg, R., and Richter, C.F., 1944, Frequency of earthquakes in California: Bulletin of the Seismological Society of America, v. 34, p. 185–188.

Ishimoto, M., and Ida, K., 1939, Observations of earthquakes registered with the microseismograph constructed recently: Bulletin of the Earthquake Research Institute, University of Tokyo, v. 17, p. 443–478.

Jolly, A.D., and McNutt, S.R., 1999, Seismicity at the volcanoes of Katmai National Park, Alaska; July 1995–December 1997: Journal of Volcanology and Geothermal Research, v. 93, p. 173–190.

Lahr, J.C., 1999, HYPOELLIPSE; a computer program for determining local earthquake hypocentral parameters, magnitude, and first motion pattern (Y2K compliant version): U.S. Geological Survey Open-File Report 99-23, 48 p.

Lalla, D.J., and Power, J.A., 2010, A two-step procedure for calculating earthquake hypocenters at Augustine Volcano, *in* Power, J.A., Coombs, M.L., and Freymueller, J.T., eds., The 2006 eruption of Augustine Volcano, Alaska: U.S. Geological Survey Professional Paper 1769 (this volume).

Main, I., 1987, A characteristic earthquake model of the seismicity preceding the eruption of Mount St. Helens on 18 May 1980: Physics of the Earth and Planetary Interiors, v. 49, p. 283–293.

McNutt, S.R., 2005, A review of volcanic seismology: Annual Review of Earth and Planetary Science, v. 33, p. 461–491, doi: 10.1146/annurev.earth.33.092209.122459.

Michael, A.J., 1987, Use of focal mechanisms to determine stress; a control study: Journal of Geophysical Research, v. 92, p. 357–368.

Mogi, K., 1962, Magnitude-Frequency relation for elastic shocks accompanying fractures of various materials and some related problems in earthquakes (2nd paper): Bulletin Earthquake Research Institute, v. 40, p. 831–853.

Mogi, K., 1963, Some discussions on aftershocks, foreshocks and earthquake swarms, the fracture of a semi-infinite body caused by an inner stress origin and its relation to the earthquake phenomena (Third Paper): Bulletin of the Earthquake Research Institute-University of Tokyo, v. 41, p. 615–658.

Okada, Hm., Watanabe, H., Yamashita, H., and Yokoyama, I., 1981, Seismological significance of the 1977–1978 eruptions and the magma intrusion process of Usu volcano, Hokkaido: Journal of Volcanology and Geothermal Research, v. 9, p. 311–334.

Okada, Hm., 1983, Comparative study of earthquake swarms associated with major volcanic activities, *in* Shimozuru, D., and Yokoyama I., eds, Arc volcanism: physics and tectonics: Tokyo, TERRAPUB, p. 43–63.

Power, J.A., Nye, C.J., Coombs, M.L., Wessels, R.L., Cervelli, P.F., Dehn, J., Wallace, K.L., Freymueller, J.T., and Doukas, M.P., 2006, The reawakening of Alaska's Augustine Volcano: EOS (American Geophysical Union Transactions), v. 87, p. 373, 377.

Power, J.A., and Lalla, D.J., 2010, Seismic observations of Augustine Volcano, 1970–2007, *in* Power, J.A., Coombs, M.L., and Freymueller, J.T., eds., The 2006 eruption of Augustine Volcano, Alaska: U.S. Geological Survey Professional Paper 1769 (this volume).

Qamar, A., St. Lawrence, W., Moore, J.N., and Kendrick, G., 1983, Seismic signals preceding the explosive eruption of Mount St. Helens, Washington, on 18 May 1980: Bulletin of the Seismological Society of America, v. 73, p. 1797–1813.

Reasenberg, P., and Oppenheimer, D., 1985, FPFIT, FPPLOT, and FPPAGE; Fortran computer programs for calculating and displaying earthquake fault-plane solutions: U.S. Geological Survey Open-File Report 85-739, 25 p.

Robinson, M., 1990, XPICK users manual, version 2.7: Seismology Lab, Geophysical Institute, University of Alaska Fairbanks, 93 p.

Roman, D.C., Moran, S.C., Power, J.A., and Cashman, K.V., 2004, Temporal and spatial variation of local stress fields before and after the 1992 eruptions of Crater Peak vent, Mount Spurr Volcano, Alaska: Bulletin of the Seismological Society of America, v. 94, no. 6, p. 2366–2379.

Sanchez, J.J., McNutt, S.R., Power, J.A., and Wyss, M., 2004, Spatial variations In the frequency-magnitude distribution of earthquakes at Mount Pinatubo Volcano: Bulletin of the Seismological Society of America, v. 94, no. 2, p. 430–438.

Scholz, C.H., 1968, The frequency-magnitude relation of microfracturing in rock and its relation to earthquakes: Bulletin of the Seismological Society of America, v. 58, no. 1, p. 399–415.

Warren, N.W., and Latham, G.V., 1970, An experimental study of thermally induced microfracturing and its relation to volcanic seismicity: Journal of Geothermal Research, v. 75, no. 23, p. 4455–4464.

Wessels, R.L., Coombs, M.L., Schneider, D.J., Dehn, J., and Ramsey, M.S., 2010, High-resolution satellite and airborne thermal infrared imaging of the 2006 eruption of Augustine Volcano, *in* Power, J.A., Coombs, M.L., and Freymueller, J.T., eds., The 2006 eruption of Augustine Volcano, Alaska: U.S. Geological Survey Professional Paper 1769 (this volume).

Wiemer, S., 2001, A software package to analyze seismicity—ZMAP: Seismological Research Letters, v. 72, no. 2, p. 373–382.

Wiemer, S., and McNutt, S.R., 1997, Variations in the frequency-magnitude distribution with depth in two volcanic areas—Mount St. Helens, Washington, and Mt. Spurr, Alaska: Geophysical Research Letters, v. 24, no. 2, p. 189–192.

Wiemer, S., McNutt, S.R., and Wyss, M., 1998, Temporal and three-dimensional spatial analyses of the frequency-magnitude distribution near Long Valley Caldera, California: Geophysical Journal International, v. 134, p. 409–421.

Woessner, J., and Wiemer, S., 2005, Assessing the quality of earthquake catalogues; estimating the magnitude of completeness and its uncertainty: Bulletin of the Seismological Society of America, v. 95, no. 2, p. 684–698.

Wyss, M., 1973, Towards a physical understanding of the earthquake frequency distribution: Geophysical Journal of the Royal Astronomical Society, v. 31, p. 341–359.

Zobin, V., 1979, Variations of volcanic earthquake source parameters before volcanic eruptions: Journal of Volcanology and Geothermal Research, v. 6, p. 279–293.

Appendixes 1–2

Appendix 1. Start Date Algorithms

Algorithm Descriptions

Two algorithms were developed to quantitatively assign a start date for the Augustine 2005–6 preeruptive earthquake swarm. We call these algorithms the largest daily count method (LDCM), and the consecutive days method (CDM). Although the algorithms are written in a general format, they are tailored to Augustine Volcano. Each method requires a year of data to establish background rates. This period was chosen because earthquake rates at Augustine are generally steady for years at a time and the year–long period should eliminate any small seasonal or weather biases in the ability to locate earthquakes. Once the background rate has been established, we have a basis to look for increased rates of activity. Both algorithms assume that a swarm has already been detected; however, they could be run continuously on data with a moving background window to "search" for swarms. We use only located earthquakes in the algorithms; again, this is practical for Augustine, but isn't necessarily suitable for volcanoes where a large number of unlocated or long-period earthquakes occur. The CDM algorithm in particular is only suited to volcanoes with fairly low earthquake rates.

Both algorithms use the same initial background analysis to establish a trigger threshold for the selection of periods of increased activity or the occurrence of a swarm. We have chosen one–eighth of the total earthquakes from the previous year occurring in a period of 30 days as the trigger threshold for increased activity. The expected seismicity in an average 30-day period would be one–twelfth of the annual seismicity. Setting a threshold of one–eighth allows for monthly and seasonal variations within the yearly average, but also keeps the threshold low enough to detect small increases in rate. Later stages of the algorithms ensure that these initial triggers are not ordinary behavior. Once a trigger is found, another set of background calculations is performed on the 4 months prior to the beginning of the trigger to determine normal fluctuations in the earthquake rate.

The LDCM algorithm uses the daily number of located earthquakes. This is done by establishing another set of background criteria once a swarm is recognized. First the weekly average of the 4 months prior to the trigger is taken, and also the largest event count for a single day is found. These 4 months are then tested to see if there are any weeks within the 4 months that exceed three times the weekly average. If there is no week that exceeds three times the average in the 4 months, then the trigger period is searched for 7-day periods that exceed the weekly average. If a week is found within the trigger period that exceeds three times the weekly average, then the largest event count for that week is compared to the largest event count for the 4-month background. If there is a week that exceeds three times the weekly average of the previous 4 months and the highest daily event count in that week is equal to or exceeds the highest daily event count for the 4 months of background, then that day is taken as the swarm start date. Figure 17 is a flow chart diagram for the LDCM method.

Augustine Volcano has very low earthquake rates and many days without any located earthquakes. The CDM algorithm uses the number of consecutive days with located earthquakes as a second way to look for increased activity. Using the same initial trigger period as LDCM, we then define two more background parameters to search for the swarm start date. The first is the number of consecutive days with located earthquakes, and the second is the number of earthquakes found commonly within a short (1 to 5 days) span. For instance, at Augustine three earthquakes in 3 days is a common occurrence. The background period is analyzed to see how often this occurs and what the shortest time interval of reoccurrence is. Once this is established, the 30-day trigger period is searched for periods of time that meet the criteria of number of events in the shorter time frame. If the first instance found meets but does not exceed the number of earthquakes, then we look for another instance. If another instance is found, we look at the time interval between these instances and compare that to the occurrence information gathered from the background data. We continue searching for occurrences until one exceeds the thresholds of the background, or there are enough triggers in a short amount of time that we believe activity has increased, or activity returns to background for two weeks or more. Figure 18 is a flow chart diagram for the CDM method.

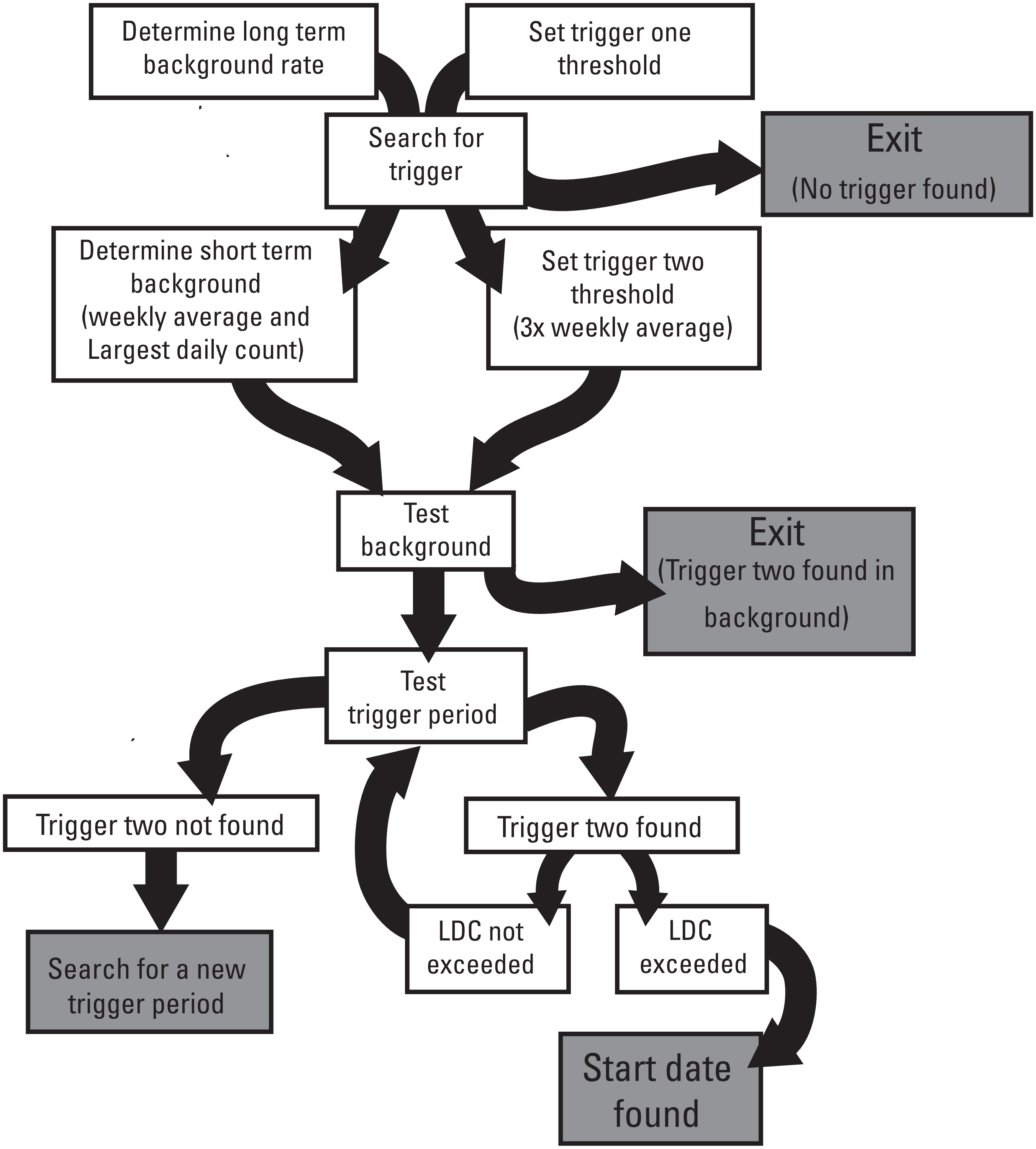

Figure 17. Flow–chart diagram illustrating the largest daily count method (LDCM) for swarm start–date determination.

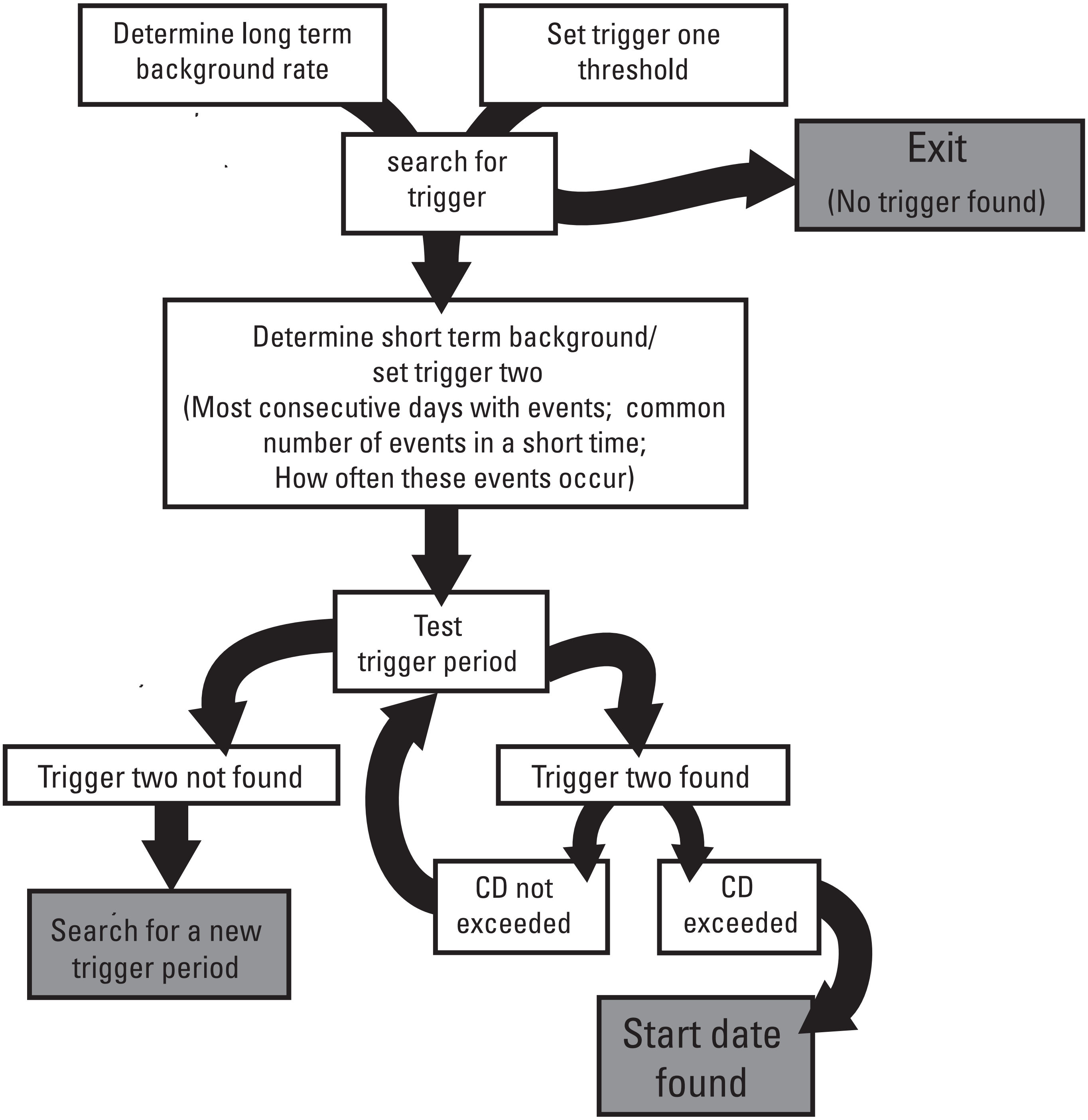

Figure 18. Flow–chart diagram illustrating the consecutive days method (CDM) for swarm start–date determination.

Results of LDCM and CDM Algorithms for the Augustine 2005–2006 Preeruptive Earthquake Swarm

Although the two algorithms use the same initial steps to classify earthquake activity as increased above background, they use unique secondary classifications to narrow down the start date. Both algorithms give a swarm start date of April 30, 2005. The detailed results for each step of the algorithms are given below.

Largest Daily Count Method

Define a reasonable background rate that is unbiased of previous swarms and annual weather phenomena:

- Calculate the previous calendar year's located earthquakes. Taking the average of an entire year's worth of data should eliminate most seasonal weather affects.
  Augustine: 238 located earthquakes total in 2004

Define a trigger to look for a swarm start date:

- Search for a 30-day period that exceeds 12.5 percent (1/8) of last year's earthquake total. Augustine: 238÷8 = 30 earthquakes
  Augustine: 4/14/2005–5/12/2005 = 31 earthquakes

If a trigger occurs, calculate the following data in order to define and test what is now taken to be the background seismicity rate:

- Take the weekly average for the 4 months prior to the 30 days of data in the trigger.
  Augustine: Two earthquakes per week

- Find the largest event count for a single day in those four months.
  Augustine: Three earthquakes in a single day

Test the background data calculated to see how representative the average daily located earthquake count is of the data:

- Search for weeks within the 4–month background period that exceed three times the weekly average calculated.
  Augustine: None

- If no week within the background period exceeds three times the weekly average of that period, then search for the first week in the 30-day trigger period that exceeds three times the background weekly average.

- If the weekly average and largest daily located earthquake counts are found to be unrepresentative of the time period, another method or calculation may be necessary.

Search the trigger period for deviations from the background averages:

- Search for the first week within the 30-day trigger period that exceeds three times the background weekly average.

  - If a week within the trigger period meets this criterion, find the largest daily earthquake count in that week.
    Augustine: Week of April 14th, six earthquakes, two in one day

- Compare this daily earthquake count to the largest daily earthquake count for the background period.

  - If the daily earthquake count for the trigger period week is less than the largest daily earthquake count for the background period, continue searching for another week that exceeds three times the weekly average and repeat as necessary.
    Augustine: Week of April 28th, nine earthquakes, five in one day

  - If the largest daily earthquake count for the trigger period is greater than or equal to the largest daily earthquake count for the background period, select that date as the start date.
    Augustine: Week of April 28th, nine earthquakes, five in one day (April 30th)
    Start Date: April 30th

Consecutive Days Method

Define a reasonable background rate that is unbiased of previous swarms and annual weather phenomena:

- Calculate the previous calendar year's located earthquakes. Taking the average of an entire year's worth of data should eliminate most seasonal weather affects.
  Augustine: 238 located earthquakes total in 2004

Define a trigger to look for a swarm start date:

- Search for a 30-day period that exceeds 12.5 percent (1/8) of last year's earthquake total.
  Augustine: 238÷8 = 30 earthquakes.Augustine: 4/14/2005-5/12/2005 = 31 earthquakes

If a trigger occurs, calculate the following data in order to define and test what is now taken to be the background seismicity rate:

- Define normal rates of continuous seismicity.
  - What is the longest string of consecutive days during normal activity?
    Augustine: 3 days
  - Find a value of consecutive days that is high, but occurs more than once.
    Augustine: 3 days (this is the longest string and occurs several times)
- Define normal numbers of earthquakes during the continuous seismicity.
  - Tally the highest number of events during these times.
    Augustine: Three earthquakes (in 3 days)
  - How often does this occur?
    Augustine: An average of every 13 days
  - What is the shortest time interval between occurrences?
    Augustine: One day (ranges to 30 days)

Search the trigger period for deviations from the background averages:

If there is a string of days that meets the consecutive day threshold or the events within a time threshold, look for a swarm.

- How many earthquakes are there?
- How does this compare to the normal number of earthquakes in a continuous period?
  Augustine triggers:
  April 14th: Three earthquakes, 3 days,
  Meets threshold
  April 18th: Three earthquakes, 2 days,
  Meets threshold
  ***April 24th: Three earthquakes, 1 day,**
  Meets threshold
  April 30th: Five earthquakes, 1 day,
  Exceeds threshold
  ***This is the shortest time between any three triggers in the background**
- Once a trigger is found that exceeds the threshold, this day (or the beginning of the set) is the swarm start date.

Start Date: April 30th

Appendix 2. Focal Mechanisms

Focal mechanisms were computed for all earthquakes using FPFIT (Reasenberg and Oppenheimer, 1985). Solutions were judged acceptable if they had: a misfit of less than 0.15 (less than 15 percent of stations inconsistent with the preferred solutions), STDR (distribution around the hypocenter) ≥ 0.40, and an average uncertainty in strike, dip, and rake of ≤ 25º. Below are 79 (out of 201) earthquakes that returned acceptable focal mechanisms. There were 19 events (out of 61 picked) with acceptable solutions from 2002 through 2004, and 60 events (out of 140 picked) from the long swarm (all events with acceptable solutions in 2005 occurred during the long swarm). If FPFIT returned two or more solutions for the same earthquake, we have retained the solution with the lowest combination of errors. Mechanisms are arranged with time starting from 2002 and getting later down each column and across each page.

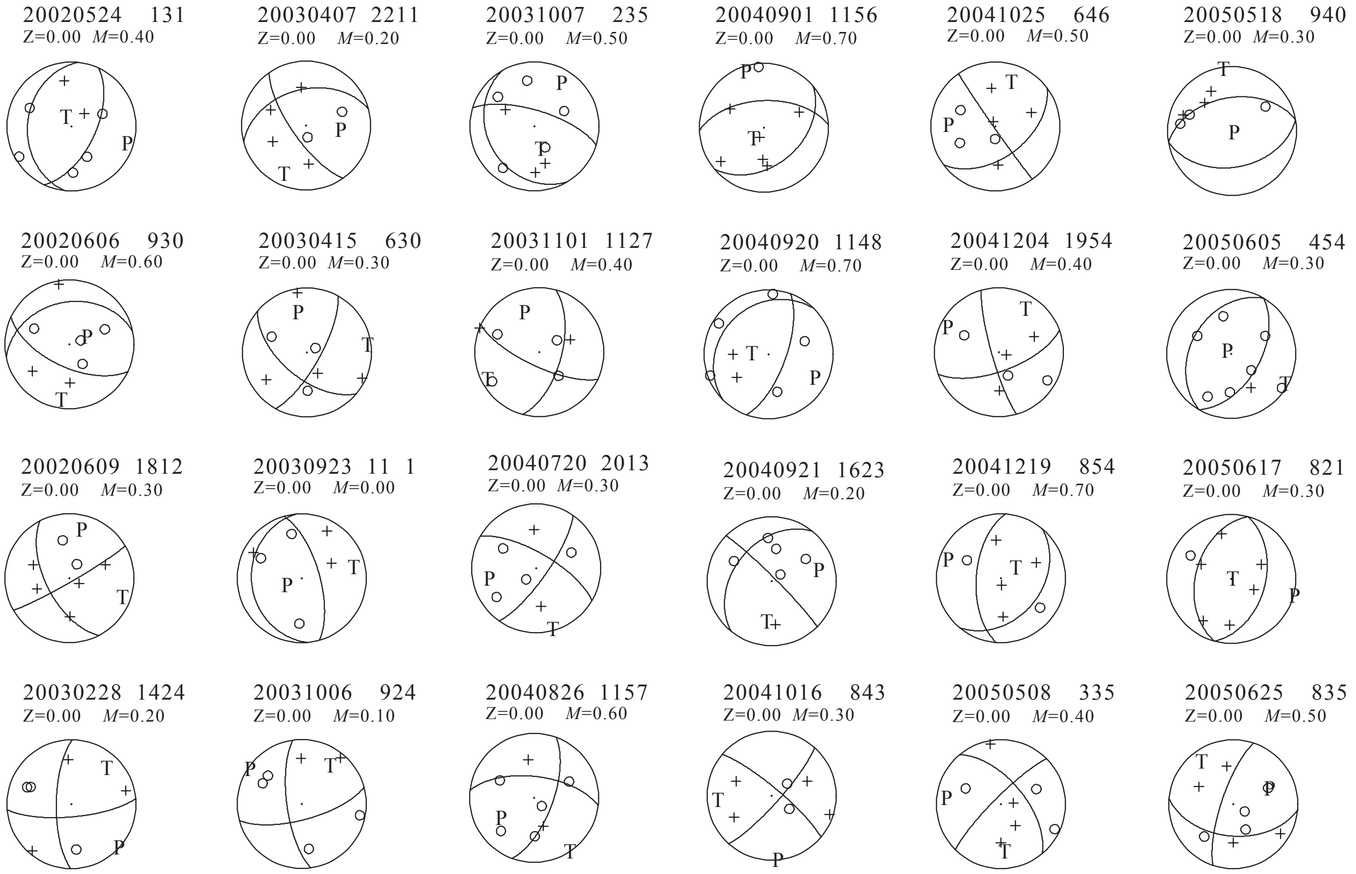

Fault-plane solutions for 79 earthquakes occurring at Augustine volcano from May 24, 2002 to January 6, 2006. P, compressional axis; T, tensional axis. Open circles correspond to dilatational (down) first motions, crosses to compressional (up) first motions. Each solution is coded for date and time (UTC) in this format: YYYYMMDD hhmm. Z, depth, in kilometers; *M*, magnitude.

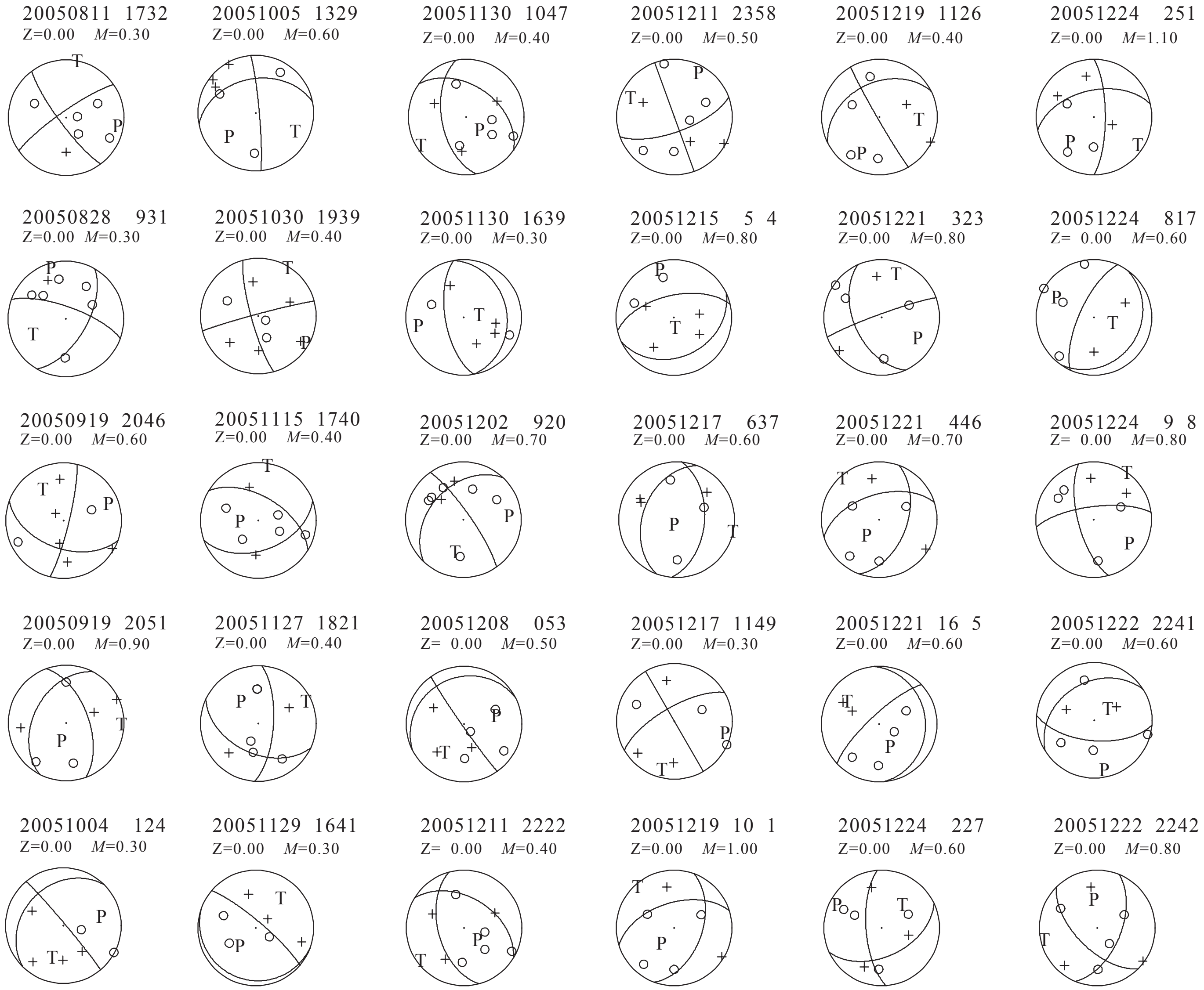
20050811 1732
Z=0.00 M=0.30
20051005 1329
Z=0.00 M=0.60
20051130 1047
Z=0.00 M=0.40
20051211 2358
Z=0.00 M=0.50
20051219 1126
Z=0.00 M=0.40
20051224 251
Z=0.00 M=1.10
20050828 931
Z=0.00 M=0.30
20051030 1939
Z=0.00 M=0.40
20051130 1639
Z=0.00 M=0.30
20051215 5 4
Z=0.00 M=0.80
20051221 323
Z=0.00 M=0.80
20051224 817
Z= 0.00 M=0.60
20050919 2046
Z=0.00 M=0.60
20051115 1740
Z=0.00 M=0.40
20051202 920
Z=0.00 M=0.70
20051217 637
Z=0.00 M=0.60
20051221 446
Z=0.00 M=0.70
20051224 9 8
Z= 0.00 M=0.80
20050919 2051
Z=0.00 M=0.90
20051127 1821
Z=0.00 M=0.40
20051208 053
Z= 0.00 M=0.50
20051217 1149
Z=0.00 M=0.30
20051221 16 5
Z=0.00 M=0.60
20051222 2241
Z=0.00 M=0.60
20051004 124
Z=0.00 M=0.30
20051129 1641
Z=0.00 M=0.30
20051211 2222
Z= 0.00 M=0.40
20051219 10 1
Z=0.00 M=1.00
20051224 227
Z=0.00 M=0.60
20051222 2242
Z=0.00 M=0.80

Continued.

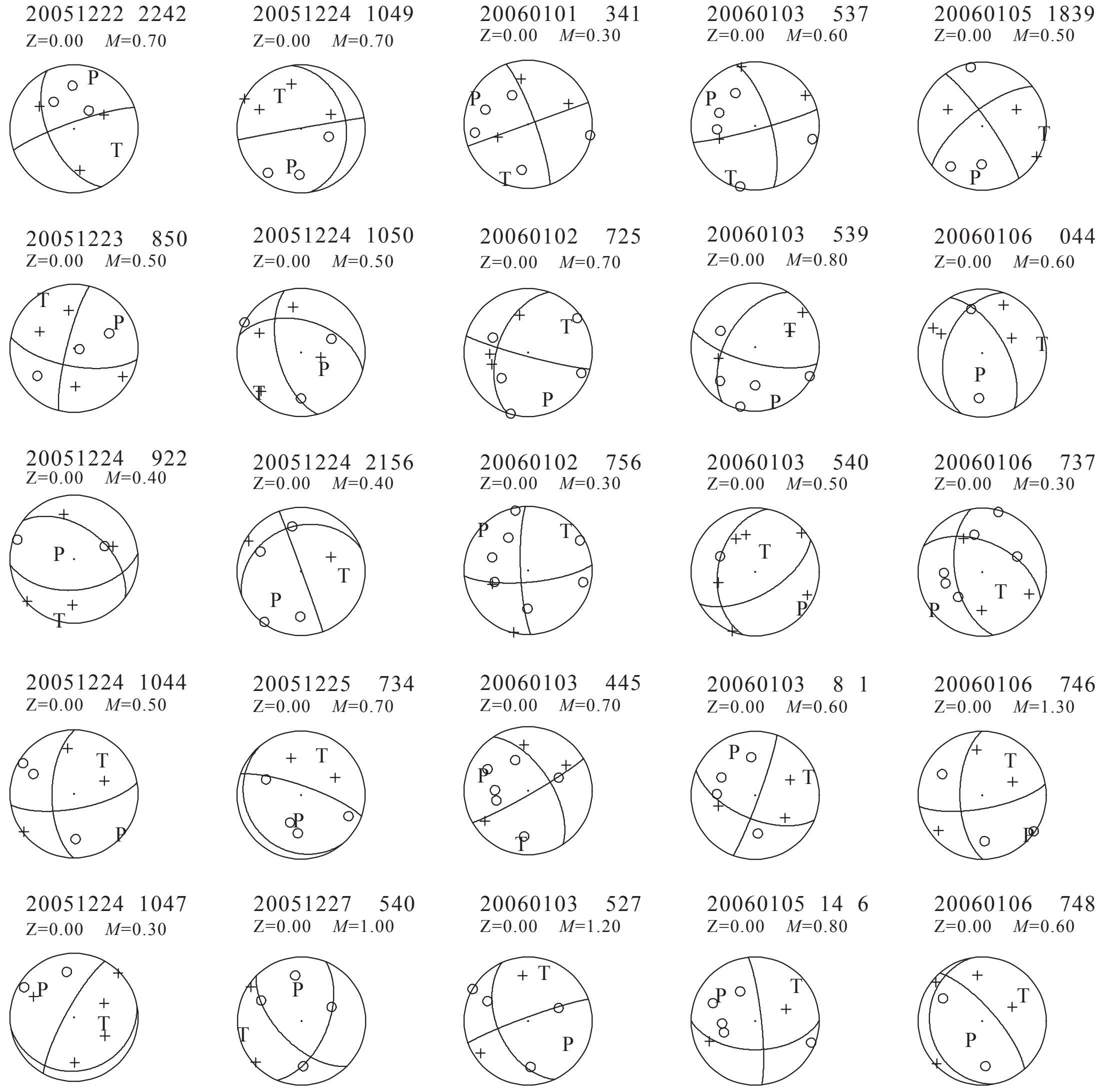
20051222 2242
Z=0.00 M=0.70
20051224 1049
Z=0.00 M=0.70
20060101 341
Z=0.00 M=0.30
20060103 537
Z=0.00 M=0.60
20060105 1839
Z=0.00 M=0.50
20051223 850
Z=0.00 M=0.50
20051224 1050
Z=0.00 M=0.50
20060102 725
Z=0.00 M=0.70
20060103 539
Z=0.00 M=0.80
20060106 044
Z=0.00 M=0.60
20051224 922
Z=0.00 M=0.40
20051224 2156
Z=0.00 M=0.40
20060102 756
Z=0.00 M=0.30
20060103 540
Z=0.00 M=0.50
20060106 737
Z=0.00 M=0.30
20051224 1044
Z=0.00 M=0.50
20051225 734
Z=0.00 M=0.70
20060103 445
Z=0.00 M=0.70
20060103 8 1
Z=0.00 M=0.60
20060106 746
Z=0.00 M=1.30
20051224 1047
Z=0.00 M=0.30
20051227 540
Z=0.00 M=1.00
20060103 527
Z=0.00 M=1.20
20060105 14 6
Z=0.00 M=0.80
20060106 748
Z=0.00 M=0.60
P
T

Continued.

This page intentionally left blank

The 2006 Eruption of Augustine Volcano, Alaska
Power, J.A., Coombs, M.L., and Freymueller, J.T., editors
U.S. Geological Survey Professional Paper 1769

Chapter 4

A Parametric Study of the January 2006 Explosive Eruptions of Augustine Volcano, Using Seismic, Infrasonic, and Lightning Data

By Stephen R. McNutt[1], Guy Tytgat[2], Steven A. Estes[1], and Scott D. Stihler[1]

Abstract

A series of 13 explosive eruptions occurred at Augustine Volcano, Alaska, from January 11–28, 2006. Each lasted 2.5 to 19 minutes and produced ash columns 3.8 to 13.5 km above mean sea level. We investigated various parameters to determine systematic trends, including durations, seismic amplitudes, frequency contents, signal characteristics, peak acoustic pressures, ash column heights, lightning occurrence, and lengths of pre-event and post-event quiescence. Individual tephra volumes are not known. There is no clear correlation between acoustic peak pressure and ash column height or between peak seismic amplitude and duration. However, several trends are evident. Two events, January 11 at 0444 AKST (1344 UTC) and January 27 at 2337 AKST (0837 UTC) are short (180 and 140 seconds) and have very impulsive onsets and high acoustic peak pressures of 93 and 105 Pa, as well as high peak seismic amplitudes. We interpret these to be mainly gas releases. Two of the largest events followed quiescent intervals of 3 days or longer: January 17 at 0758 AKST (1658 UTC), and January 27 at 2024 AKST (January 28 at 0524 UTC). These two events had reduced displacements (D_R) of 11.4 and 7.5 cm^2, respectively. Although these D_R values are typical for eruptions with ash columns to 9 to 14 km, most other D_R values of 1.6 to 3.6 cm^2 are low for the 7.0 to 10.5 km ash column heights observed. The combination of short durations, small D_R and high ash columns suggests that these events are highly explosive, in agreement with Vulcanian eruption type. Several events had long durations on individual seismic stations but not on others; we interpret these to represent pyroclastic or other flows passing near the affected stations so that tractions or momentum exchange from the cloud or flow adds energy to the ground only near those stations. The eruption on January 27 at 2024 AKST had more than 300 lightning flashes, whereas the following eruptions on January 28 at 0204 AKST and 0742 AKST had only 28 and 6 lightning flashes. The 2024 AKST eruption had a longer duration (1,180 versus <460 seconds), a higher ash column height (10.5 versus 7.0–7.2 km) and higher acoustic peak pressure (83 versus 66 and 24 Pa). The data suggest that the lightning-rich 2024 AKST eruption produced more tephra than the following eruptions, hence there were more charge carriers injected to the atmosphere. Seismic signals preceded the infrasound signals by 0 to 5 seconds with no obvious pattern in terms of the above groupings. The explosive eruption phase overlapped with the subsequent continuous phase by about 2 days. Parametric data may be useful to estimate eruption conditions in near real time.

Introduction

Following an 8.5-month period of precursory activity, Augustine Volcano began to erupt explosively on January 11, 2006 (Power and others, 2006). A series of 13 strong explosive eruptions occurred over the next 17 days, with most sending ash clouds to elevations of 10 km or more (table 1). New instrumentation added in December 2005 and January 2006 allows for a more comprehensive study of these eruptions than has previously been possible for explosive eruptions in Alaska. In particular, an infrasound pressure sensor located at AUE (fig. 1) recorded all 13 events on scale, temporary broadband seismometers remained on scale and complemented the permanent short-period network, and new lightning detection

---

[1] Alaska Volcano Observatory, Geophysical Institute, University of Alaska Fairbanks, Fairbanks, AK 99775.

[2] IRIS PASSCAL Instrument Center, New Mexico Tech, 100 East Road, Socorro, NM 87801.

equipment was installed on January 27, 2006, just before the last series of four strong explosive eruptions on January 27–28. This paper presents a systematic study of the 13 explosive eruptions, combining the new data to gain insights into processes contributing to observed variations in the explosivities of the eruptions, including plume heights, amounts of tephra, gas distribution, and electrical properties.

These new data (broadband seismic, infrasound, and lightning) are especially useful because for the 1976 and 1986 eruptions of Augustine Volcano only short-period seismic data were available. The seismic data for 1976 were recorded off island (Power and Lalla, this volume), and for 1986 only short-period data existed (Power, 1988). The short-period stations on the island in 2006 were all saturated (clipped), and several were damaged or destroyed by the eruptions, whereas the broadband stations remained on scale. Distant stations such as OPT (34 km north; fig. 1) remained on scale and provided a basis for comparisons. As will be shown, the new data streams provide many additional constraints on eruptive processes.

The 1976, 1986, and 2006 eruption sequences had remarkably similar precursory stages, which lasted 9, 9, and 8.5 months, respectively (Power and Lalla, this volume). The two previous eruption sequences began with explosive phases lasting 4 and 14 days, followed by effusive phases. This pattern was repeated in 2006; however, the explosive phase lasted 18 days.

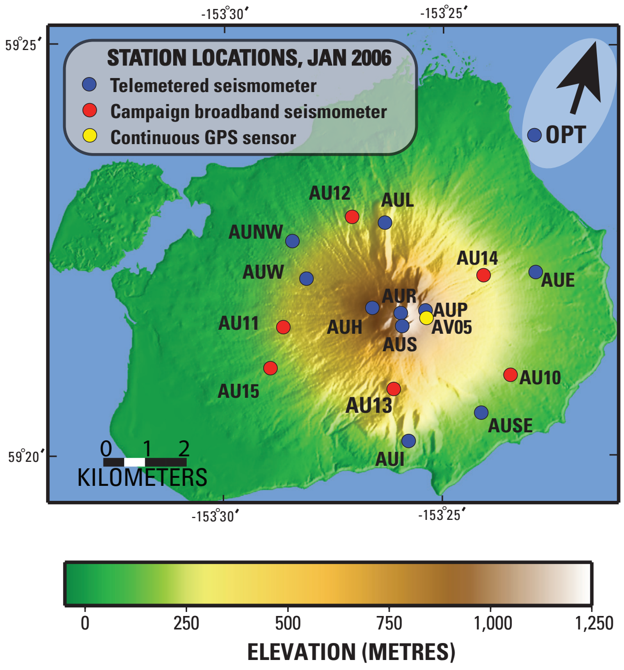

Figure 1. Map of seismic stations on Augustine Island. Stations shown have either short-period or temporary broadband seismometers. AUL has a permanent 3-component broadband station, and AUE has an infrasound sensor. Station OPT is on the Alaska mainland 34 km north of Augustine Volcano. (Image courtesy of H. Buurman.)

Augustine's Vulcanian eruptions are similar to eruptions at other volcanoes including Vulcano, Italy 1888–1890, Ngauruhoe, New Zealand 1975, Galeras, Colombia 1992–1993, Sakurajima, Japan 1985–1990, Asama, Japan 2004, and Montserrat, West Indies 1997 (Morrisey and Mastin, 2000; Ohminato and others, 2006; Druitt and others, 2002). A comparison is given in the discussion section of this paper, following presentation of the Augustine parameters.

Times in this paper are given in local time (Alaska Standard Time or AKST) followed by universal time (UTC) in parentheses where appropriate. At the time of the Augustine eruptions UTC was 9 hours ahead of local time; that is, 1200 (noon) AKST is equivalent to 2100 UTC.

Data and Methods

Seismic Data

The permanent seismic network on Augustine Island consisted of eight short-period stations and one broadband station (AUL; fig. 1). The short-period stations have a natural period of one second and use either Mark Products L4-C or Geotech S-13 vertical seismometers. The permanent broadband station uses a Guralp CMG-40T 3-component seismometer with a natural period of 30 seconds. Analog data from all short-period stations are telemetered to Homer, Alaska, by VHF radio, then by telephone and internet to the University of Alaska Fairbanks Geophysical Institute, where data are digitized at 100 Hz at 12-bit resolution. The broadband station is digitized on site at 100 samples per second and uses digital rather than analog radio telemetry. The permanent network was augmented by the addition of five temporary broadband stations that were recorded on site at 100 samples per second (fig. 1). All the short-period stations on the island were saturated (clipped) for all 13 of the large explosive eruptions. Station OPT, 33 km the north on the Alaskan mainland, is a short-period station that recorded all the events and remained on scale for all but one event (January 27 at 2337 AKST).

Seismic measurements include the duration and reduced displacement (D_R). Duration varies with the individual station used, and the gain, and distance. Because Augustine is a small island, all the local stations are close, within 5 km of the vent. All the short-period stations clipped during each of the 13 explosive eruptions. However, rather than being a problem, this actually afforded a convenient way to measure durations, which were estimated from the length of the continuously clipped (that is, strong) portion of the signal. This was measured from hard copies of seismograms at a standard scale of 600 seconds = 3.4 cm (figs. 2*A* and 2*B*; note the printed scale here is different). Several stations gave virtually identical durations, the most reliable being AUH and AUW. The closer station AUH gave preferred values early in the

Table 1. Parameters of the Augustine Volcano January 11–28, 2006, explosive eruptions.

[AKST, Alaska Standard Time; UTC, Universal Time; D_R, reduced displacement; OPT, Oil Point seismic station; I, impulsive; E, emergent]

Event Number	Date in 2006	Event Onset AKST (UTC)	Type	Pressure, in Pa	Duration: Acoustic, in seconds	Duration: Seismic, in seconds	D_R, in cm^2 OPT	Preceding Quiescence, in days	Number of lightning flashes	Plume Height, in km[1]
1	January 11	0444 (1344)	I	93	25	180	139	---	---	6.5
2	January 11	0512 (1412)	E	14	100	385	1.8	0.02	---	10.2
3	January 13	0424 (1324)	E	22	130	915	7.7	1.97	---	10.2
4	January 13	0847 (1747)	E	35	100	400	2.4	0.18	---	10.2
5	January 13	1122 (2022)	I	32	150	520	2.6	0.11	---	10.5
6	January 13 (January 14)	1640 (0140)	E	29	150	570	3.3	0.22	---	10.5
7	January 13 (January 14)	1858 (0358)	E	52	170	765	1.6	0.09	---	13.5
8	January 14	0014 (0914)	I	65	100	430	3.6	0.23	---	10.2
9	January 17	0758 (1658)	E + I	93	50	410	11.4	3.32	---	13.5
10	January 27 (January 28)	2024 (0524)	E + I	83	250	1180	7.5	10.52	365	10.5
11	January 27 (January 28)	2337 (0837)	I	105	20	140	178	0.13	1	3.8
12	January 28	0204 (1104)	I	66	150	460	2.9	0.10	28	7.2
13	January 28	0742 (1642)	E	24	160	240	2.1	0.24	6	7.0

[1] Schneider and others, 2006.

eruption sequence but was destroyed on January 27 and had to be replaced by others (for example AUE and AUI) using bootstrapping methods to yield durations. Some adjustments were necessary when pyroclastic or other flows (for example, lahars, rockfalls) passed near stations, because these added extra energy to the ground and prolonged the codas at the stations nearest to the flows (figs. 3*A* and 3*B*).

For the 1976 and 1986 eruptions of Augustine Volcano, the stations on the island either were not operational or were mostly clipped (Reeder and Lahr, 1987; Power, 1988). Station OPT, a single-component, 1-second vertical seismometer located 33 km north of the vent, was far enough away that the signals had attenuated and remained on scale. Thus data from OPT are useful for direct comparison between the 1986 and 2006 eruptions. We determined magnitudes for the explosive eruptions using OPT by forcing the origin to be at Augustine's vent and measuring the highest amplitude portion of the signal. The maximum values obtained were M_L=2.3 and 2.6, which agree well with the largest events during the 1976 eruption, which were M_L=2.3, although these were considered to be earthquakes occurring simultaneously with large tremors and were recorded at station CKK, 82 km to the northwest (Reeder and Lahr, 1987). The 2006 M_L values were then converted to D_R; both are measures of ground motion that use the same seismic measurements but different normalizations. D_R is peak-to-peak root mean square displacement multiplied by the square root of wavelength times distance (Fehler, 1983). For the 2006 events, we assumed surface wave propagation using

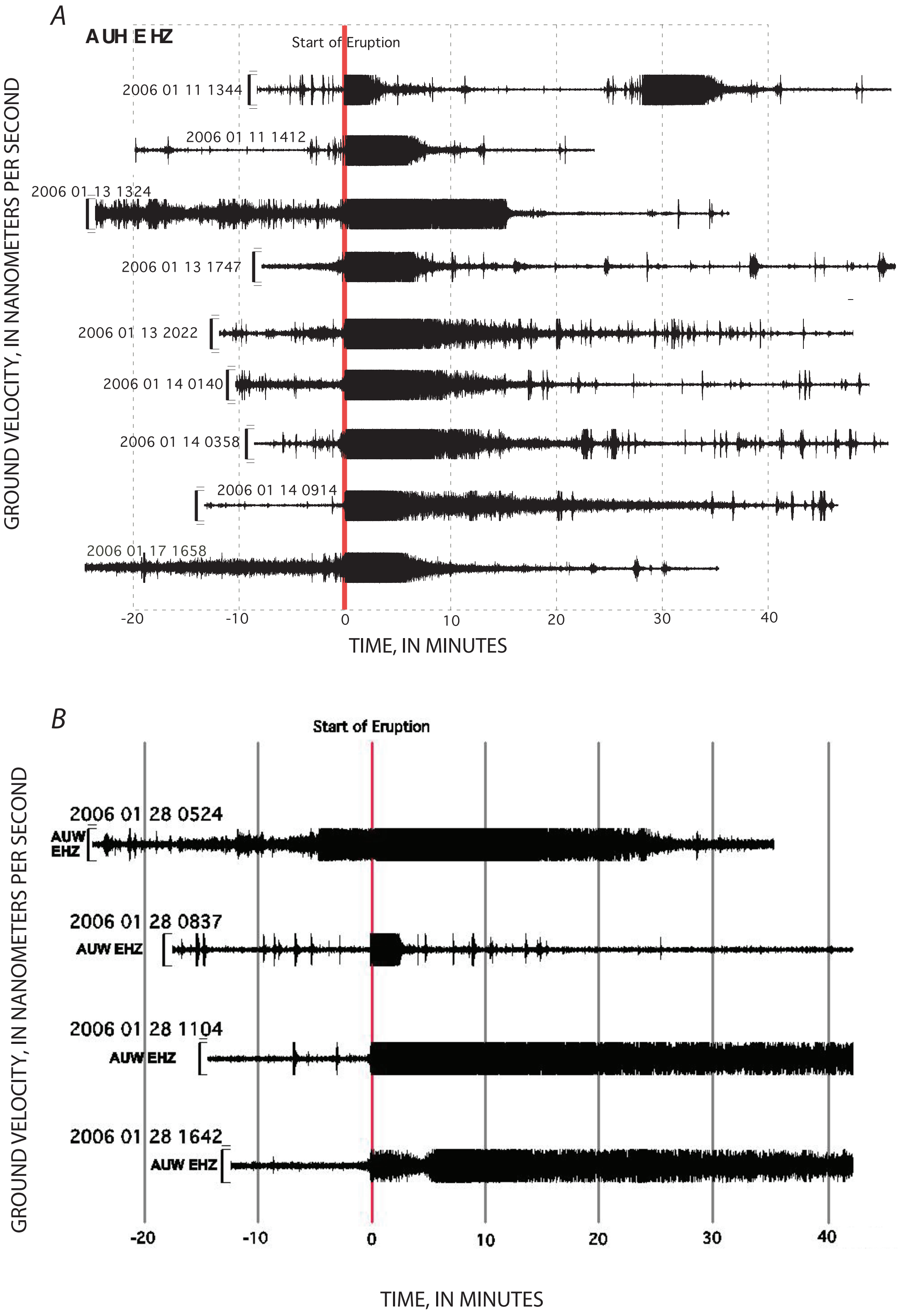

Figure 2. *A*, Seismograms (unfiltered) for the first 9 of 13 large explosive eruptions at Augustine Volcano in 2006. Data are from station AUH, which was destroyed on January 28, 2006. One hour of data is shown and the seismograms are aligned on the beginning of each explosive eruption. The durations of the clipped portion of the seismograms range from 3 to 15 minutes. *B*, Seismograms of the last 4 explosive eruptions. Data are from station AUW. Other features are as in part *A*. Time convention is YYYY MM DD HHMM. Times in UTC.

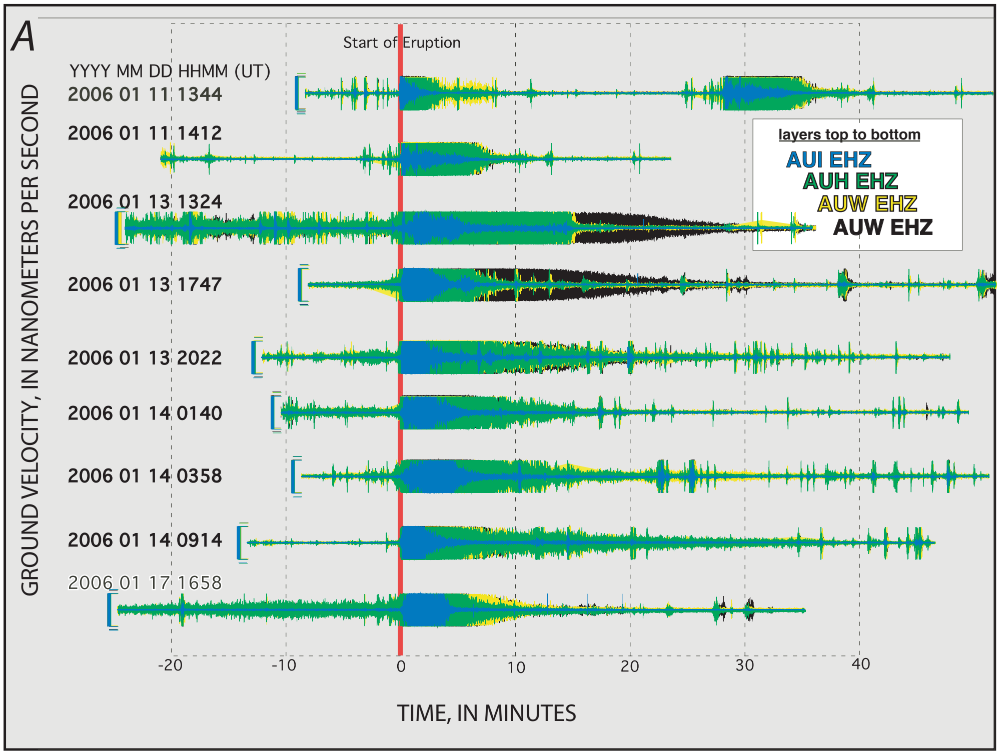

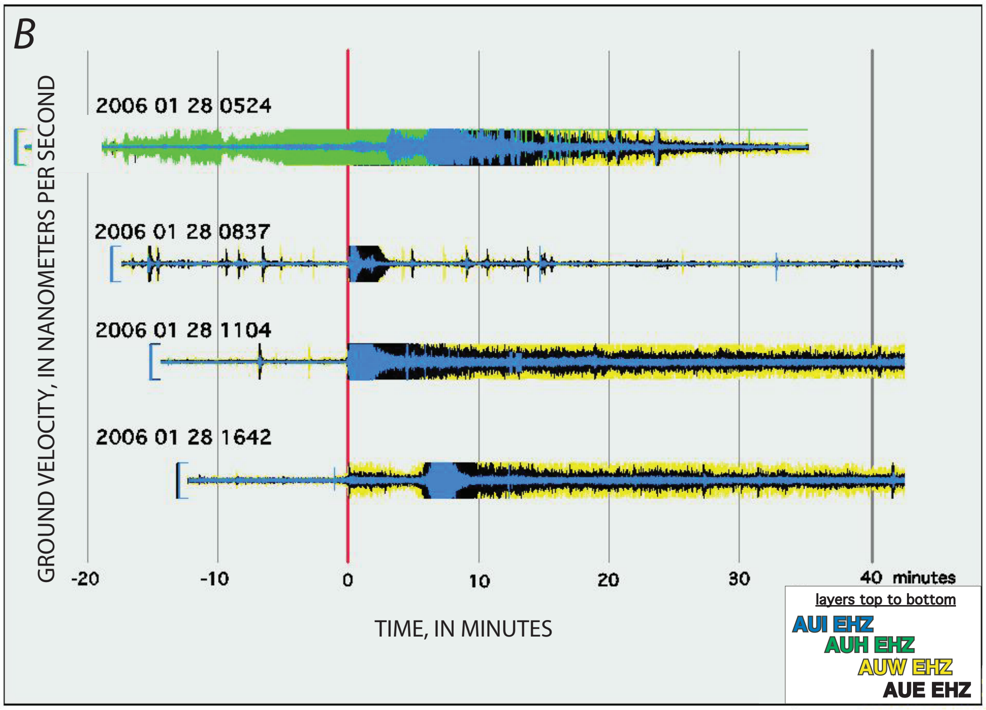

Figure 3. *A*, Overlaid seismograms for four stations (AUI, AUH, AUW, and AUE) on Augustine Island. Data are aligned on the beginning of each explosive eruption. Note that the codas for events 3 and 4 are much longer on station AUE than for the other stations, suggesting that pyroclastic or other flows passed near that station. *B*, Seismograms for four stations (AUI, AUH, AUE, and AUW) overlaid. Note that the colors and tiling are different than part A to better show the relative features of the different seismograms. Station AUH was destroyed during event 10 (top trace). EHZ is a code representing short-period seismic stations.

the same formulation, adjusted for differences in frequency content, as was used for the 1976 events to compare them with worldwide data (McNutt, 1994). The D_R values for the 2006 events are shown in table 1.

The D_R values computed here are systematically lower than those determined by van Manen and others (this volume). There are several reasons for this. Van Manen and others (this volume) used broadband stations on the island at close distances. Note that D_R corrects for geometrical spreading but does not correct for attenuation, so stations at distances of a few tens of km such as OPT generally give lower values than close stations. A clear example of this effect was observed for Pavlof Volcano (McNutt and others, 1991). A second effect is the choice of surface waves. Particle motions at many volcanoes show surface waves to be the most common component of tremor, so surface waves were assumed for Augustine Volcano. Further, the velocity of the high-amplitude portion of the signal at OPT is about 2 km/second, a value typical for surface waves. For the nearby broadband stations body waves may be more appropriate. Body waves always return higher values for D_R because of the way the formulations are set up (Fehler, 1983). A third factor is the narrow bandwidth of the short-period seismometer at station OPT; relatively high amplitude but very low frequency waves would not be visible. Finally, near-field terms may exist in the broadband data, which can be large near the source. Such waves would not appear in the OPT data. All these effects can give rise to quite different values for attempts to measure the same quantity using different stations. Because the purpose here is partly comparison with the previous eruptions, we used station OPT data as described above. The choice of other data may be more suitable for other purposes.

Broadband waveforms for all 13 explosive eruptions are shown in fig. 4*B* for temporary station AU14 (fig. 1). All seismograms are plotted at the same scale and the events are aligned on the start time to facilitate comparison.

Infrasound Data

A Chaparral Model 2.1 microphone was installed at AUE in early January 2006, and data were telemetered in the same manner as seismic data. This site has a direct distance of 3.2 km to Augustine Volcano's active vent (fig. 1). The laboratory calibrated pressure transducer system, consisting of the microphone, a voltage controlled oscillator (VCO) and a discriminator, has a flat response between 0.1 and 50 Hz and a linear response to pressures above 100 Pa. Both high-gain and low-gain channels were operated, with sensitivities of 0.171 and 0.0084 V/Pa, respectively (Petersen and others, 2006). The low gain channel remained on scale for all the explosive eruptions; peak values ranged from 14 to 105 Pa and are shown in table 1. A noise reduction system, consisting of eight microporous hoses spread out over a half circle, is connected to the microphone. Twelve of the large explosive eruptions were also recorded on the I53US infrasound array in Fairbanks, Alaska, 675 km north of Augustine (Olson and others, 2006). However, because atmospheric conditions varied so widely, it is not possible to use the I53US observations for comparative study of source processes (Olson and others, 2006). Thus, the discussion in this paper is mainly limited to the data from the local sensor, whose close distance of 3.2 km minimizes propagation effects.

For the infrasound data from station AUE (fig. 4*A*), durations were measured from the event onset to decay to the background (Petersen and others, 2006). These varied from 25 to 250 seconds (table 1). All the explosive eruptions remained on scale on the low gain channel, so maximum 0-peak (excess) pressures were measured directly from the waveforms. After the first event at 0444 AKST on January 11, with 93 Pa, the next ten events showed gradually increasing pressures from 14 Pa up to the maximum of 105 Pa at 2337 AKST on January 27 (Petersen and others, 2006). The next two events had lower pressures of 66 and 24 Pa and were followed by a continuous phase consisting of explosions with low pressures of 0.5 to 1 Pa occurring every few minutes for several days. These were only visible on the high-gain channel. Reduced pressures (Johnson 2000) may be obtained by multiplying the pressures by the distance to station AUE, which is 3.2 km. Only the 13 large explosions from January 11 to January 28 are considered in detail in this paper.

Infrasound waveforms for all 13 explosive eruptions are shown in fig. 4*A* for station AUE low-gain channel (fig. 1). All acoustigrams are plotted at the same scale and the events are aligned on the start time to facilitate comparison.

Lightning Data

Two New Mexico Tech Lightning Mapping Array (LMA) lightning detection stations were installed on January 27, 2006, in Homer and Anchor Point, 100 km east of Augustine Volcano (Thomas and others, 2007; Thomas and others, this volume). The stations record time of arrival of electromagnetic radiation in the unused channel 3 TV band (63 MHz) and constitute a minimal network capable of determining the azimuthal direction of impulsive radio emissions from electrical discharges (Thomas and others, 2004). The lightning stations detected both continuous electrical disturbances and lightning flashes in association with the last four explosive eruptions on January 27–28 (table 1) and with four stronger pulses on January 29–30 during the continuous phase. For the earlier eruptions (January 11–17), qualitative lightning reports were obtained from airline pilots, and two eruptions had data recorded by Bureau of Land Management (BLM) stations (Thomas and others, this volume).

The LMA stations recorded two main types of activity: lightning flashes and continuous electrical disturbances at the time of most vigorous eruption. We counted the number of discrete flashes associated with each of the eruptions on January 27–28 (table 1) and also measured the duration and peak radiated power of the continuous signals (Thomas and others, this volume). Because the lightning data were available only for the last four explosive eruptions, we can make only a few general conclusions about lightning.

Plume Heights and Quiescence Data

Two other parameters of interest are plume heights and the durations of preceding quiescence. Plume heights were determined from ground-based Nexrad Doppler radar measurements (Schneider and others, 2006) using data provided by the National Weather Service (NWS). Errors are discussed by Wallace and others (this volume). Resulting plume heights are shown in table 1. This method may not detect the diluted, uppermost parts of the plumes because the radar is tuned to see millimeter to centimeter sized particles; however, it provides an approximation that is consistent throughout the explosive eruption sequence. We measured the time interval between the start times of the events and show this in table 1 under the column labeled "preceding quiescence."

Results

This study compiles a set of measured parameters to describe and systematically compare the eruptions of Augustine Volcano in 2006. Once the parameters were measured, it became immediately obvious that the eruptions were not all the same, and that they fell into several clear groups. These are described and interpreted in this section. The infrasound pressure and D_R are shown in time sequence in figure 5. Because some of the explosive eruptions occurred closely spaced in time, the data appear bunched and are difficult to interpret. Thus, the same data are displayed in index order in figure 6. A comparison of the two figures allows for a complementary view of the data trends.

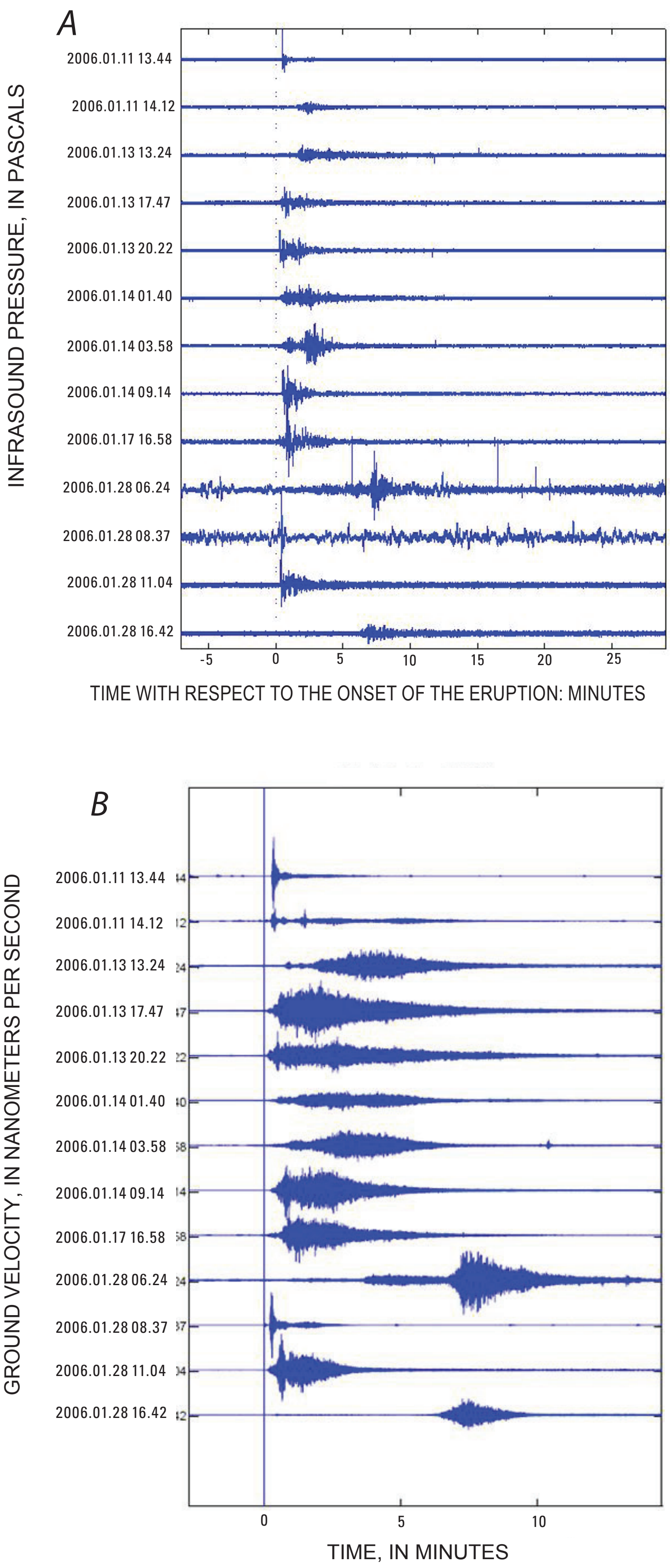

Figure 4. *A*, Acoustigrams of the 13 large explosive eruptions at Augustine Volcano in 2006. Data are from station AUE BDL (low gain). Thirty minutes of data are shown and the acoustigrams are aligned on the beginning of each explosive eruption (vertical dotted line). The durations of the strong portions of the signals range from 20 to 250 seconds. *B*, Seismograms of the 13 large explosive eruptions. Data are from broadband seismic station AU14 HHZ (vertical). Other features are as in part *A*. Times shown at left are UTC.

Short Strong Eruptions

The two shortest events were also two of the three events with the highest infrasound pressures and the two highest seismic amplitudes (table 1; figs. 4*A* and 4*B*). These were the first event on January 11 at 0444 AKST (event 1) and the January 27 event at 2337 AKST (event 11). These were quite short acoustically, only 20 to 25 seconds, whereas seismically they lasted 140 to 180 seconds. The periods of the highest amplitude seismic waveforms at OPT for each event were greater than 1 second each, longer than for any of the other events (the event at 0204 AKST on January 28 also had a long-period pulse near the onset, but this was not the highest amplitude pulse). Both events were very impulsive, with the initial pulse accounting for about 60 percent of the total energy of each event. Cumulative energy plots were used to make this estimate, as shown in figure 3 of Petersen and others (2006). Because they were strong, D_R=139 and 179 cm^2 (equivalent to M_L=2.25 and 2.55; both are measures of amplitude) one might suggest they were in some way the "biggest" of the eruptions. However, these two events appear to have produced the least amount of tephra. Event 11 had a plume only 3.8 km high that quickly dissipated, and event 1 mainly blew out old rock as it reamed out the vent. Its ash plume was the second smallest at 6.5 km high (Schneider and others, 2006). Photographs taken after the January 11 eruptions revealed small deposits near the summit and a few mixed avalanches or lahars. Observations and samples analyzed by Vallance and others (this volume), Wallace and others (this volume), and Coombs and others (this volume) suggest that little or no juvenile material was present in deposits from the January 11 eruptions. Taken together these observations suggest that these eruptions were gas rich and mainly erupted a large gas pocket or equivalent collection of gas charged magma.

Eruptions Preceded by 3 or More Days of Quiescence

Two of the eruptions followed inter-event quiescent periods of 3 days or more: January 17 at 0758 AKST (event 9) and January 27 at 2024 AKST (event 10). Both eruptions destroyed or partially destroyed new domes that had been emplaced during these quiescent intervals. The domes consisted of magma that had sat on the surface for some time and therefore lost much of its gas, forming a temporary plug. The new eruptions then pushed this material out of the way. Seismic data show that these two eruptions each had emergent onsets followed shortly by impulsive phases (Petersen and others, 2006; figure 4*A*); we suggest that the emergent part of the pressure record represents mostly old dome material being pushed out (gas poor) and that the impulsive phase of the pressure record represents the venting of a gas-rich parcel of magma that was previously

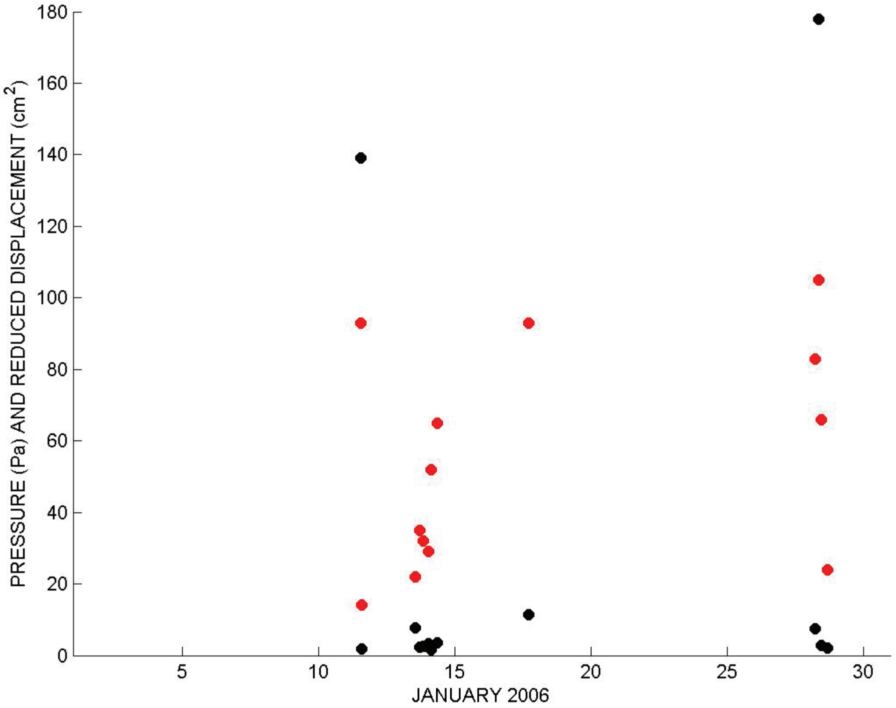

Figure 5. Acoustic peak pressure in Pa (red circles) and seismic reduced displacement in cm^2 (black circles) as a function of time for the 13 large explosive eruptions at Augustine Volcano in 2006.

beneath the dome. The eruptions produced the 3rd and 5th highest seismic amplitudes, the 2nd and 4th highest infrasound pressures (table 1; figs. 4*A* and 4*B*), and appear to be the two largest eruptions in terms of tephra production. The January 17 event was the only individual event to deposit significant tephra on land to the northwest of Cook Inlet, and the January 27 event produced a large pyroclastic flow, the Rocky Point flow (Coombs and others, this volume).

Low D_R but High Ash Column

Many of the eruptions shared the following characteristics: small D_R (1.6 to 3.6 cm^2), moderate infrasound pressures (14 to 66 Pa), a short time interval after the previous eruption (0.5 to 5.5 hours) and generally emergent signals on both seismic and infrasound data (table 1). These are the second event on January 11 at 0512 AKST (event 2), most of the events on January 13 and 14 (events 3 through 8) and the last two on January 28 (events 12 and 13). These events all had moderate durations of 100 to 170 seconds acoustically and 240 to 915 seconds seismically. Six of nine were emergent acoustically as determined by Petersen and others (2006), and the other three began with a weak impulsive phase that represented only about 15 percent of the total energy. The emergent character and moderate durations suggest that the gases are rather uniformly distributed in each batch of magma, so that the eruption is more of an intense "fizz" than a "pop." The data suggest that these are the most typical explosive eruption events and are most characteristic of the Vulcanian eruption style. The seismic and acoustic waveforms show some variation (figs. 4*A* and 4*B*), suggesting that although the events are similar, they are not identical to each other. Volcanic Explosivity Index (VEI; Newhall and Self, 1982) values of 2 to 3 would characterize these events, for which the plume heights were 7.0 to 13.5 km, but the volumes were small ($<2 \times 10^6$ m^3, Coombs and others, this volume). Preliminary acoustic modeling by Fernandes and others (2007) suggests exit velocities of 50 to 300 m/second and volume flux rates of 10^3 to 10^4 m^3/second.

Lightning and Duration

The four eruptions on January 27–28 differed dramatically in their electrical activity. The first produced 365 lightning flashes, the second 1 flash, and the next two 28 and 6 flashes (table 1). The ash plume heights were similar for events 10, 12, and 13, whereas the plume for event 11 was the smallest of any of the explosive eruptions. This was also the event with the highest infrasound pressure. These observations can be reconciled by inferring that event 11 was mostly gas with very little tephra, an inference confirmed by radar observations (Schneider and others, 2006). Of the other

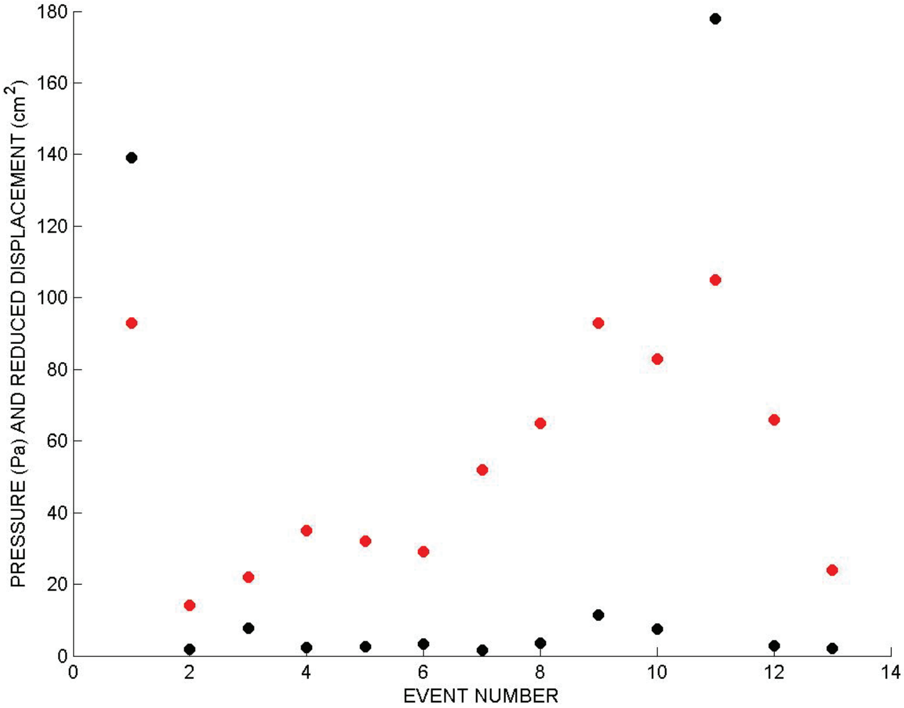

Figure 6. Acoustic peak pressure in Pa (red symbols) and seismic reduced displacement in cm^2 (black symbols) in index order for the 13 large explosive eruptions at Augustine Volcano in 2006.

parameters listed in table 1, the one that stands out as having the most direct correlation with the amount of lightning is the duration. This suggests that the tephra production is positively correlated with the duration, assuming that eruptions rates are similar. It also implies that the amount of tephra is proportional to the amount of lightning. The basic idea is that each tephra particle is a potential charge carrier, so the more particles, the higher total charge and greater potential to produce lightning. A detailed discussion of the lightning observations is given by Thomas and others (this volume).

End of Explosive Phase

An event that began on January 28 at 1430 AKST appears to be a transition event (fig. 7) between the period of discrete, moderate-large explosive events to nearly continuous, smaller explosions. It had smaller peak pressure (9 Pa) than any of the 13 explosive events and lasted much longer, about 1 hour 45 minutes compared to 15 minutes or less for the explosive events. After the transition event quiescence was observed for 6 hours, then at 1617 AKST on January 29 a series of small explosions (0.5 to 1 Pa) began to occur every few minutes for the next several days (fig. 7). A similar figure showing seismic data from station AU13 is given by Power and Lalla (this volume). Volcanic ash was observed in the air almost continuously starting at 1430 AKST on January 28 (Schneider and others, 2006) and lasting until February 2; this phase of the eruption is termed the continuous phase (Power and Lalla, this volume; Coombs and others, this volume). The continuous phase was punctuated by three larger events at 1119 AKST on January 29 (infrasound 13 Pa), and at 0328 AKST (13 Pa) and 0622 AKST (4.4 Pa) on January 30. These had durations of several minutes each and were accompanied by lightning (Thomas and others, this volume) but were all significantly smaller than all but one of the 13 numbered explosions. One may consider these events to be relatively large bursts of activity within the continuous phase. An alternative explanation is that these events were instead explosive eruptions (similar to the 13 numbered events), hence there was overlap rather than a clear separation between the explosive and continuous phases of the eruption.

Events Producing Pyroclastic Flows

Several of the 13 large explosive eruptions showed seismic evidence for the occurrence of pyroclastic or other flows, such as lahars or debris avalanches. These deposits have been described and mapped by Coombs and others (this volume) and Vallance and others (this volume). As shown in figure 3*A*, the events at 0424 AKST and 0847 AKST on January 13 had unusually long codas at station AUE (fig. 1). This suggests a primary part of the signal from the vent that appears on all stations, as well as a secondary part caused by pyroclastic material falling out of the cloud and transferring momentum to the ground near specific stations along the pyroclastic flow path, AUE in this case. Alternatively the extended codas may represent lahars, mixed avalanches, or other flow events that passed near the affected station, with tractions at their bases transferring seismic energy into the ground. Thus, the data suggest that the 0424 AKST and 0847 AKST eruptions (events 3 and 4) were accompanied by pyroclastic flows traveling to the east. Events 1, 9, and 10 showed slightly extended codas for station AUW (fig. 1) to the west, suggesting weak pyroclastic flows traveling to the west (figs. 3*A* and 3*B*). The last two events, numbers 12 and 13, had very long extended codas on station AUW (fig. 3*B*), suggesting sustained pyroclastic flows traveling to the west. The parameters concerning pyroclastic flows are summarized in table 2.

We also checked broadband data and radar data to confirm and to further elucidate these findings. The broadband data did not clip, so instead we see the primary signal from the eruption, followed by relative quiescence, and then an increase in signal level a few minutes later as the pyroclastic flow material applies tractions or transfers momentum near a particular station. The overall principle is the same, but the signals look different on the broadband stations as compared with the short-period stations. The broadband station parameters are also given in table 2. An example of the broadband data is shown in figure 8 for event 8. Here station AU12 (second from the top) shows a second signal pulse between 700 and 900 seconds that does not appear on other stations. This suggests that a pyroclastic or other flow travelled to the north-northwest (see fig. 1 for station locations). Coombs and others (this volume) and Vallance and others (this volume) used similar criteria, as well as spectrograms, to determine which eruptions produced various flow units. Some spectrograms showed higher frequencies for nearby flow events, in contrast to the lower frequencies of the more distant primary explosions. Similar observations were made by Zobin and others (2009) for Colima Volcano, Mexico.

Seismic and Infrasound Origin Times

The event times for the 13 explosive eruptions were assigned to the nearest minute based only on seismic data during the eruption response, mainly as a way to identify and keep track of the separate eruptions. Here we perform retrospective analyses of the origin times using both seismic and infrasound data. The measurements were made for the onset of seismic clipping to the nearest second on station AUH, AUE, or AUW (fig. 1). These are systematically late by about 1 second (the typical time from the onset to clipping), but the signal preceding the explosive eruptions was often contaminated by small earthquakes so the absolute onsets could not be uniformly determined. The acoustic onsets to the nearest second were determined by Petersen and others (2006) for station AUE BDL. Acoustic times for some subevents were determined by the authors. The seismic travel time is a few tenths of a second to station AUH because of the close distance of about 700 m, and assumed to be 1 second for AUE and AUW. The acoustic travel time is determined to be 10 seconds from detailed analysis of the 2337 AKST event on January 27, which had a very impulsive acoustic onset and also continuous electrical activity which began abruptly at the same time as the acoustic origin time (Thomas and others, this volume). Thus, we determined both seismic and acoustic origin times. These were generally not the same; a comparison (table 3) shows that they differ by 0 to 5 seconds, with the seismic origin time always earlier than the acoustic one. The time difference may be interpreted as a proxy for depth or as the time interval over which the final preeruptive processes occur. The measured time differences do not agree well with the groupings of events as given above (for example, short strong eruptions), although events 1 and 11 both share a seismic versus acoustic time difference of 4 seconds. Of the two events that followed quiescence (events 9 and 10), event 9 had a time difference of 0 seconds, which we interpret to represent an explosive source

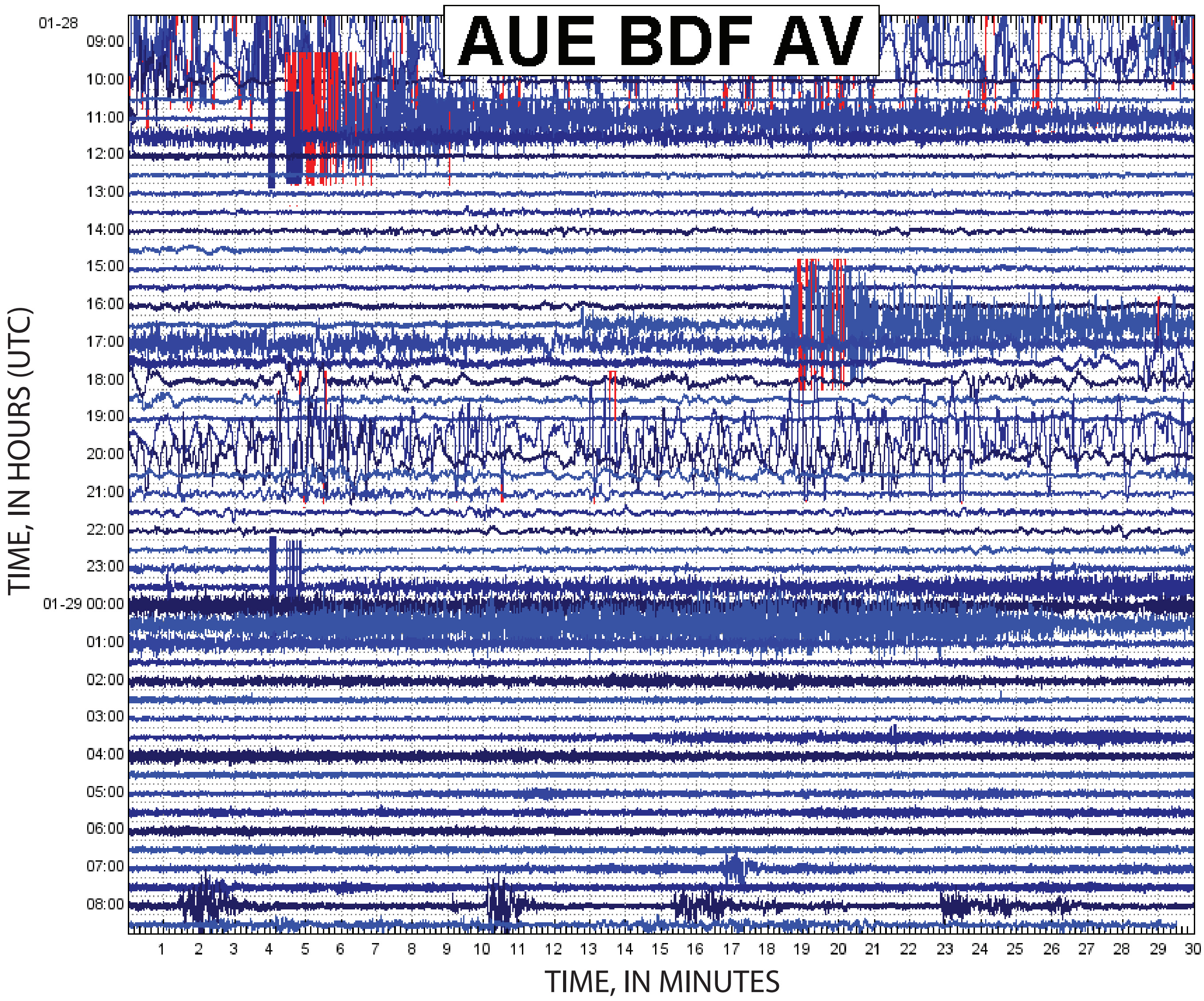

Figure 7. Acoustigram for eruptions at Augustine Volcano on January 28–29, 2006. Twenty-four hours of data are shown for acoustic station AUE BDF (high gain). Each line is 30 minutes. Events 12 (1104 UTC) and 13 (1642 and 1648 UTC) show partially clipped data in red and have codas about 45 minutes long. The event at 2330 UTC is a transitional event that lasts about 2 hours. Starting at 0717 UTC on January 29 are small discrete events occurring every few minutes that were characteristic of the continuous phase of the eruption (Coombs and others, this volume). Strong wind noise occurs from 0900 to 1000 UTC and from 1930 to 2030 UTC. AV is a code for stations maintained by the Alaska Volcano Observatory.

Table 2. Parameters of Augustine Volcano January 11–28, 2006, explosive eruptions showing evidence for pyroclastic flows.

[AKST, Alaska Standard Time; PF, pyroclastic flow; AUW, AU14, and others are seismic stations codes]

Event Number	Date in 2006	Event Onset AKST	Long Coda	Broadband Delayed Pulse	Seismic Station Destroyed	Interpretation
1	January 11	0444	AUW	---		Possible mixed avalanches
2	January 11	0512	---	---		---
3	January 13	0424	AUE	AU14	AUP	PF East
4	January 13	0847	AUE	AU12, AU13		PF East, North, South
5	January 13	1122	---	AU12		PF North
6	January 13	1640	---	AU14		PF East
7	January 13	1858	---	AU12		PF North
8	January 14	0014	---	AU12		PF North
9	January 17	0758	AUE, AUW	AU12, AU15		PF North, East, West, Southwest
10	January 27	2024	AUW	AU15	AUL, AUH	PF West, Southwest, North
11	January 27	2337	---	---		---
12	January 28	0204	AUW	---		PF West
13	January 28	0742	AUW	---		PF West

right at the surface, where the time difference for event 10 could not be determined because the seismic traces were already clipped when the largest phase occurred (table 3). The time differences for the largest group of events, characterized by low D_R and high ash columns (events 2, 3, 4, 5, 6, 7, 8, 12, and 13), spanned the range from 0 to 5 seconds. We note that all the events with a 5 second time difference fell in this group. The large time difference suggests a systematically deeper source or a prolonged initiation process for that group of explosive eruptions.

Discussion

The results, which divide the explosive eruptions into several groups based on common parameters, require a conceptual model of gas storage and release to explain the observations. An example of such a conceptual model is the schematic diagram shown in figure 9. The basic idea is that initially gases are uniformly distributed in the magma at depth. If the magma ascends relatively quickly, the gases remain uniformly distributed at the time of eruption (fig. 9*A*). The resulting eruption would then be expected to have an emergent onset and rather steady gas release throughout. This corresponds to the cases above with low D_R but high ash columns. A second scenario would be slow ascent of magma into a "leaky" system, so that most of the gases escape to the surroundings (fig. 9*B*). This is the scenario corresponding to the eruptions that follow three or more days of quiescence, and the domes that formed represent the accumulation of degassed magma. The third situation is the coalescence of gas into a large irregular pocket or a zone of gas charged magma (fig. 9*C*). This requires slow ascent of magma under sealed conditions so that the gas collects rather than escaping to the surroundings. The resulting eruption would be gas rich (or ash poor) and likely impulsive if the gas pocket ruptures quickly. The short strong eruptions correspond to this case.

This conceptual scheme allows us to use the eruption styles to "map" the pattern of gas distribution or storage underground for the times just before eruptions. Obviously this is a gross simplification; however, the basic elements are straightforward. The conceptual scheme also has testable elements: the deposits resulting from the eruptions may contain textural or other evidence to support the gas distribution hypotheses (Larsen and others, this volume; Coombs and others, this volume; Vallance and others, this volume). A diagram of the pre-eruption gas distribution based on the above scheme is shown in figure 10.

One major data gap is that we do not have high-quality measurements of the volumes of tephra for the various individual eruptions. Augustine is an island, so much of the fall deposits fell in the sea. Only the eruption on January 17

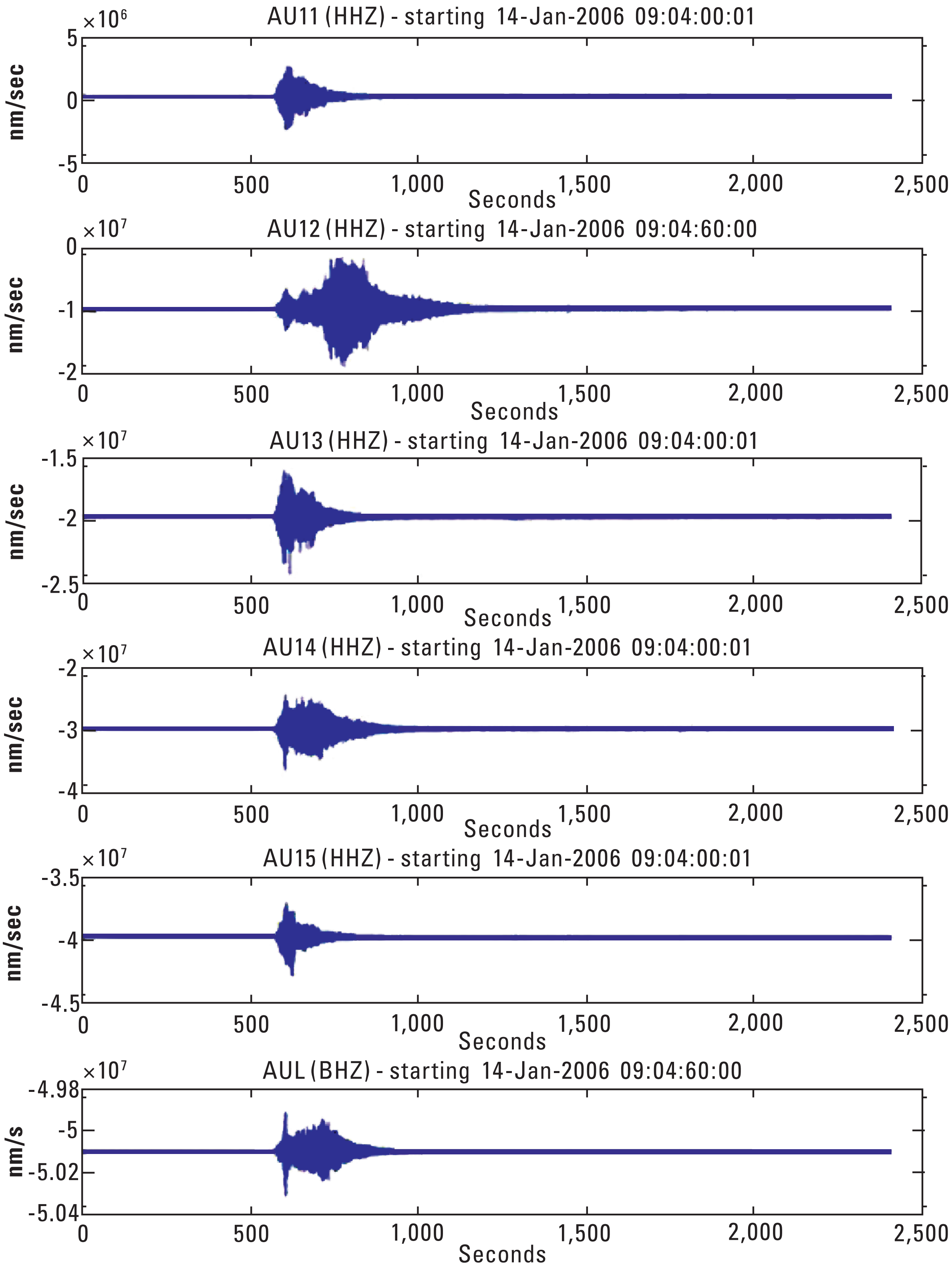

Figure 8. Broadband seismograms from all available stations for Augustine Volcano's January 14, 2006, explosive eruption at 0914 UTC (event 8). Data from the vertical component are shown. Note that the initial part of each trace is similar but that station AU12 (second from the top) shows a strong pulse from 700 to 900 seconds. This is interpreted to represent a pyroclastic flow or other flow event passing near that station only.

Table 3. Timing of seismic and infrasound onsets of Augustine Volcano January 11–28, 2006, explosive eruptions.

[AKST, Alaska Standard Time]

Event Number	Date in 2006	Event Onset AKST	Seismic Onset[1] AKST	Acoustic Onset[2] AKST	Seismic Origin Time[3] AKST	Acoustic Origin Time[4] AKST	Time Difference Seconds	Seismic Station Used
1	January 11	04:44	04:44:40	04:44:55	04:44:40	04:44:45	4	AUH
2	January 11	05:12	05:14:13	05:14:24	05:14:13	05:14:14	2	AUE
3	January 13	04:24	04:24:15	04:24:30	04:24:15	04:24:20	5	AUH
4	January 13	08:47	08:48:14	08:48:25	08:48:14	08:48:15	2	AUE
5	January 13	11:22	11:22:07	11:22:15	11:22:07	11:22:05	1	AUE
6	January 13	16:40	16:40:28	16:40:38	16:40:28	16:40:28	0	AUH
7	January 13	18:58	18:58:02	18:58:17	18:58:02	18:58:07	5	AUH[5]
8	January 14	00:14	00:13:22	00:13:37	00:13:22	00:13:27	5	AUH
9	January 17	07:58	07:58:19	07:58:28	07:58:18	07:58:18	0	AUE
10	January 27	[20:19][6]	20:19:45	---	---	---	---	AUH
		20:24	20:24:49	---	---	---	---	AUH
		[20:27]	20:27:42	---	---	---	---	AUE
		[20:31]	---[7]	20:31:05	---	20:30:55	---	---
11	January 27	23:37	23:37:34	23:37:47	23:37:33	23:37:37	4	AUE
12	January 28	02:04	02:04:15	02:04:26	02:04:14	02:04:16	2	AUE
13	January 28	07:42	07:42:29	07:42:43	07:42:28	07:42:33	5	AUE
		[07:48]	07:48:12	07:48:24	07:48:11	07:48:14	3	AUW

[1] Time of seismic trace clipping continuously.

[2] Acoustic onset time from Petersen and others, 2006.

[3] Seismic origin time assuming v = 3 km/sec (1 sec difference at AUE).

[4] Acoustic origin time assuming v = 320 m/sec (10 sec difference at AUE).

[5] Not clipped but significant pulse.

[6] Brackets [ ] indicate onset times of subevents.

[7] Seismic traces were already clipped so onsets could not be determined.

(event 9) produced a significant deposit on land (West side of Cook Inlet; Wallace and others, this volume) that could be measured sufficiently well to make volume estimates. The volume for this event, about 2 x 10^6 m^3, was then extrapolated from geologic data to make estimates of the total volume of tephra for all the eruptions. However, caution should be used in using extrapolated values because the variance is unknown. Another factor that is poorly known is the vent size and shape. Coombs and others (this volume) estimated the vent dimensions to be 30 by 45 m; assuming these as conduit dimensions yields drawdown depths of about 1.9 km for the eruptions of about 6 x 10^5 m^3 of tephra. Better estimates of these dimensions would help to infer the depths of each batch of magma that formed an eruption and would allow a depth scale to be added to figure 10. More data are needed here, and it is difficult to infer precise mechanisms without the individual volume estimates.

The approach used in this paper may be useful in terms of providing rapid feedback to improve future monitoring efforts at Augustine Volcano and elsewhere. The parameters are easy to measure, so they can be done in a few minutes during crises. They provide additional insight into factors such as likely ash production that are important for aviation safety. An additional benefit of the systematic study of parameters is that they may be combined to provide insight into other related questions. As an example, in figure 11 we plot durations as measured at

AUW (seismic), AUE BDL (infrasound), and on the I53US infrasound array in Fairbanks. The different symbols show which eruptions were accompanied by lightning (Thomas and others, this volume). It is clear that the eruptions that were of long duration both locally (AUE and AUW) and at distance (I53US) produced lightning, whereas the short ones at both did not (lower left of plots). The implication of this is that the longer the eruption, the more tephra is produced; each tephra particle is a potential charge carrier, so the more particles the higher the total charge available for lightning and other electrical phenomena (see also Thomas and others, this volume for additional discussion). From a monitoring perspective, these simple measurements may provide a rapid means of verifying the amount of tephra.

The four eruptions that occurred on January 27–28 were also the four for which we had instrumental data on lightning from the New Mexico Tech LMA stations (Thomas and others, this volume). Otherwise we would not have known the lightning occurred because no lightning was observed due to poor local weather, and further, the signals were not strong enough to show on the Bureau of Land Management (BLM) array in central Alaska. One factor that may have contributed to lightning production was a composition change that occurred approximately January 27 (Larsen and others, this volume; Coombs and others, this volume). The initial explosive eruptions produced mostly low-silica andesite, but for the January 27–28 eruptions the magma composition was dominantly high-silica andesite. The higher silica content may have contributed to greater lightning efficacy, but we cannot address this in detail with the limited data in hand. Another factor was that the January 27 eruption at 2031 AKST produced the largest pyroclastic flow unit, a 10.1 × 10^6 m^3 unit known as the Rocky Point flow (Coombs and others, this volume) that entered a pond on the north flank of Augustine Volcano (Begét, this volume). We speculate that interaction of the pyroclastic flow with the water in the pond may have created additional charged particles, but we cannot quantify this effect.

The parameters reported here do not permit us to comment on the terminations of the eruptions. Why were there six eruptions on January 13–14 a few hours apart instead of one larger one? Were these separate batches of magma? Did the eruptions stop when the gas-rich part had erupted? Did the vent partially close up or pinch off when the top-most

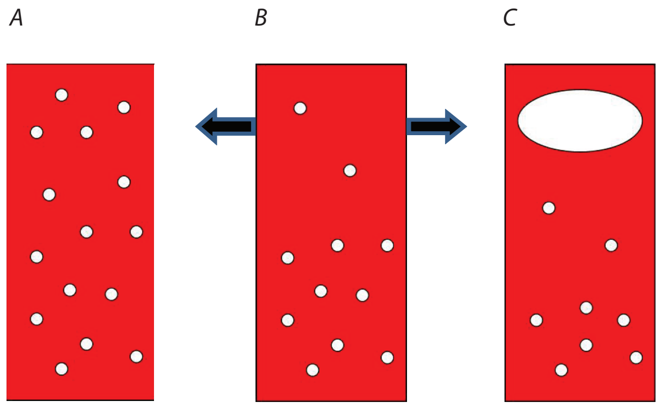

Figure 9. Schematic diagram of gas distribution in magma for three scenarios. *A*, Uniform gas distribution and rapid ascent. *B*, Slow ascent under leaky conditions; upper portion of column is gas poor. *C*, Slow ascent during sealed conditions; gas accumulates in a large bubble or irregular pocket or a gas-rich foam.

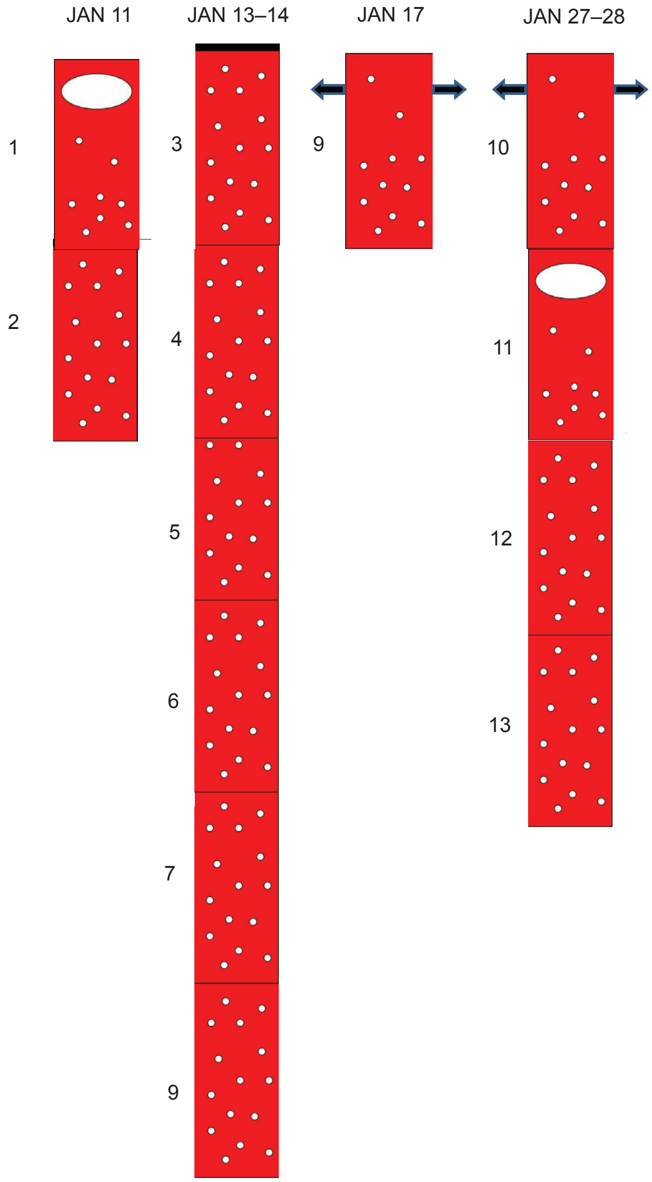

Figure 10. Schematic diagrams of gas distribution in the upper part of the conduit prior to Augustine Volcano's eruptions on January 11, 13–14, 17, and 27–28, 2006. These are "mapped" using the parameters and groupings of this paper to infer underground preeruptive conditions. Numbers to the left correspond the the event index number. The arrows represent gas loss to the surroundings.

material was removed? Some of the data reexamined may help to answer these questions, although they provide only indirect clues. For example the rates of decay of the seismic codas are variable. The coda decayed very abruptly for event 3 (see fig. 2*A*), suggesting possible pinching off of the conduit. The rates of decay were more gradual for most other events, some of which included complications such as small earthquakes in the coda. The codas for events 8, 12, and 13 were very long, suggesting a gradual loss of energy through an open conduit. The rates of decay as seen on broadband data (fig. 4*B*), however, were rather similar.

We briefly compare the Augustine explosive eruptions from 1976, 1986, and 2006. The durations of the largest events were remarkably similar: 11.83 minutes for 1976 (station CKK), 13.6 minutes for 1986, and 11 minutes for 2006 (both at OPT). The 1976 eruption had 13 large tremor events (the terminology used by Reeder and Lahr, 1987) versus 16 events with durations >2 minutes for 1986 (Power, 1988) and 13 large explosive events in 2006 (this paper). An infrasound array in Fairbanks (I53US and its predecessor) recorded 13 events in 1976 (Reeder and Lahr, 1987) and 12 in 2006 (Wilson and others, 2006); the array was not in operation in 1986. The first large explosion in 1976 was noted as being impulsive (Reeder and Lahr, 1987), similar to 2006 (event 1, this paper), whereas 1986 built up more gradually (fig. 22 of Power, 1988). The range of durations of the individual events also appears to be similar for all three eruptions. If one includes smaller events, such as the 35 small tremors in 1976 (Reeder and Lahr, 1987) and the 22+ events with durations between 1 and 2 minutes in 1986 (fig. 22 of Power, 1988)

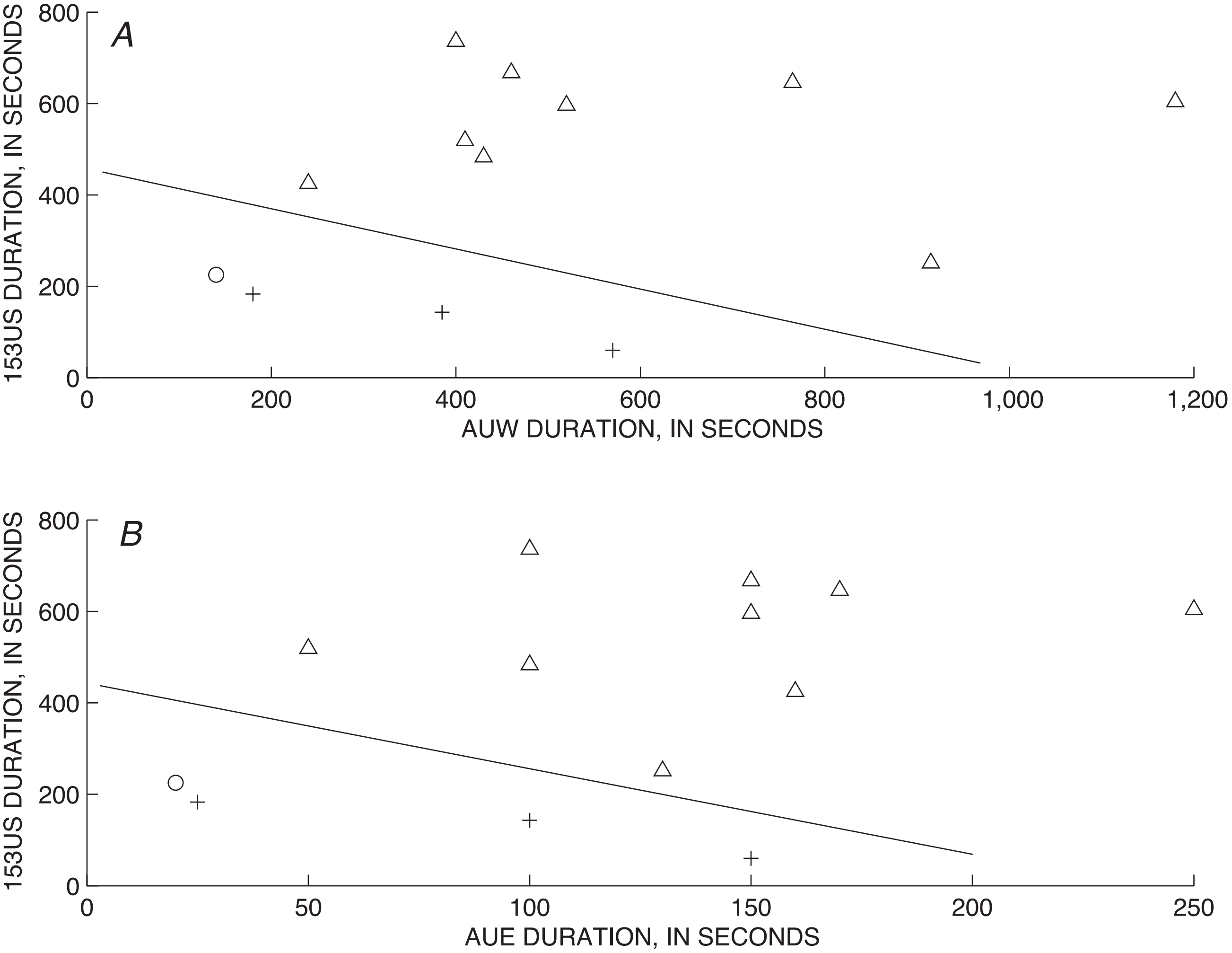

Figure 11. *A*, plot of I53US acoustic array duration (Wilson and others, 2006) versus AUW seismic duration for the 13 large explosive eruptions at Augustine Volcano in 2006. The triangles represent eruptions that were accompanied by lightning, and "+" symbols represent those with no reported lightning. *B*, I53US acoustic array duration versus AUE acoustic duration for the 13 large explosive eruptions. Symbols are as in part *A*. In both *A* and *B* a line is drawn from upper left to lower right to separate the eruptions that had lightning from those that did not. In both cases the eruptions with longer durations produced lightning. The point labeled "o" is event 11 which had only a single weak lightning flash.

then the two earlier eruptions have more events during the explosive phase. The 1976 explosive phase lasted just 4 days, the 1986 explosive phase lasted 14 days, and 2006 explosive phase lasted 18 days, suggesting that the rate of explosions was lowest in 2006. Otherwise the common parameters of the larger events of the three eruptions are quite similar, suggesting that the volcano has characteristic explosive behavior.

The Augustine explosive eruptions were similar to those at Asama (Ohminato and others, 2006), Montserrat (Druitt and other 2002), and Vulcano, Galeras, Ngauruhoe, and Sakurajima (Morrisey and Mastin, 2000) in terms of the strengths of the seismic and acoustic signals. However, there is significant variation in plume heights and volumes of ejecta. For the 2004 eruptions of Asama the infrasound signals ranged from 19 to 205 Pa as measured at a site 8 km away (these would be equivalent to 48 and 513 Pa at the 3.2 km distance of AUE). For Asama the seismic single force intensity was measured and eruption deposits were known for all five eruptions. The air shock intensity showed a positive correlation with the eruptions deposits, whereas the seismic force showed more variability. The differences in the parameters showed a similar spread to those for Augustine.

Vulcanian eruptions at Ngauruhoe, Galeras, and Sakurajima generally had ash plumes up to 4 to 5 km (Morrissey and Mastin, 2000). These most closely resemble the short strong eruptions (events 1 and 11) at Augustine, which had the lowest plume heights and inferred least amounts of ash. The other Augustine events most closely resemble those at Montserrat in terms of ash plume heights (3 to 15 km) and intervals between events (2.5 to 63 hours; Druitt and others, 2002). A full comparative study of these eruptions may be warranted.

Conclusions

Study of the major geophysical parameters of the 13 Augustine Volcano explosive eruptions from January 11–28, 2006, suggests that they fall into four main groups: (1) short strong eruptions (VEI=2), (2) events following quiescent intervals of 3 days or longer, (3) events with small D_R and high ash columns (low VEI=3), and (4) events with long durations and large amounts of tephra leading to high lightning production (high VEI=3). Systematic variations in gas storage and release are used to provide a conceptual basis for the differences in activity. New estimates of event origin times were based on seismic and acoustic data, and seismic evidence for pyroclastic or other flow events is presented. The various parameters are generally easy to measure, hence they could be used to make rapid measurements to aid crisis response. The diverse measurements made at Augustine are potentially useful for comparison with previous eruptions at other volcanoes; however, lack of data on tephra volumes for individual events leaves certain questions beyond reach. The Augustine eruptions are among the larger Vulcanian eruptions known to us and resemble some recent eruptions at Montserratt, 1995–99.

References Cited

Begét, J.E., 2010, Characterizing pyroclastic-flow interactions with snow and water using environmental magnetism at Augustine Volcano, *in* Power, J.A., Coombs, M.L., and Freymueller, J.T., eds., The 2006 eruption of Augustine Volcano, Alaska: U.S. Geological Survey Professional Paper 1769 (this volume).

Coombs, M.L., Bull, K.F., Vallance, J.W., Schneider, D.J., Thoms, E.E., Wessels, R.L., and McGimsey, R.G., 2010, Timing, distribution, and volume of proximal products of the 2006 eruption of Augustine Volcano, *in* Power, J.A., Coombs, M.L., and Freymueller, J.T., eds., The 2006 eruption of Augustine Volcano, Alaska: U.S. Geological Survey Professional Paper 1769 (this volume).

Druitt, T.H., Young, S.R., Baptie, B., Bonadonna, C., Calder, E.S., Clarke, A.B., Cole, P.D., Harford, C.L., Herd, R.A., Luckett, R., Ryan, G., and Voight, B., 2002, Episodes of cyclic Vulcanian explosive activity and fountain collapse at Soufriere Hills Volcano, Montserrat, *in* Druitt, T.H., and Kokelaar, P., eds., The eruption of Soufriere Hills Volcano, Montserratt, from 1995 to 1999: Geological Society London, Memoirs, p. 281–306.

Fehler, M., 1983, Observations of volcanic tremor at Mount St. Helens volcano: Journal of Geophysical Research, v. 88, p. 3476–3484.

Fernandes, J.J., Bellesiles, A.K., and Caplan-Auerbach, J., 2007, Estimates of gas flux from infrasonic signals at Augustine Volcano during the January 2006 eruption—Implications for eruption plume types [abs.]: Geological Society of America Cordilleran Section, 103rd annual mtg., paper no. 32-6.

Johnson, J.B., 2000, Interpretation of infrasound generated by erupting volcanoes and seismo-acoustic energy partitioning during Strombolian explosions: University of Washington, Seattle, Ph.D. dissertation.

Larsen, J.F., Nye, C.J., Coombs, M.L., Tilman, M., Izbekov, P., and Cameron, C., 2010, Petrology and geochemistry of the 2006 eruption of Augustine Volcano, *in* Power, J.A., Coombs, M.L., and Freymueller, J.T., eds., The 2006 eruption of Augustine Volcano, Alaska: U.S. Geological Survey Professional Paper 1769 (this volume).

McNutt, S.R., 1994, Volcanic tremor amplitude correlated with eruption explosivity and its potential use in determining ash hazards to aviation: U.S. Geological Survey Professional Paper 2047, p. 377–385.

McNutt, S.R., Miller, T., and Taber, J.J., 1991, Pavlof Volcano—seismological and geological evidence of increased explosivity during the 1986 eruptions: Bulletin of Volcanology, v. 53, p. 86–98.

Morrisey, M. and Mastin, L., 2000, Vulcanian Eruptions *in* Sigurdsson, H., B. Houghton, S.R. McNutt, H. Rymer, and J. Stix, eds. Encyclopedia of Volcanoes: San Diego, Calif., Academic Press, p. 463–475.

Newhall, C.G., and Self, S., 1982, Volcanic Explosivity Index (VEI)—An estimate of explosive magnitude for historical volcanism: Journal of Geophysical Research, v. 87, p. 1231–1238.

Ohminato, T., Takeo, M., Kumagai, H., Yamashina, T., Oikawa, J., Koyama, E., Tsuji, H., and Urabe, T., 2006, Vulcanian eruptions with dominant single force components observed during the Asama 2004 volcanic activity in Japan: Earth Planets Space, v. 58, p. 583–593.

Olson, J.V., Wilson, C.R., McNutt, S.R., and Tytgat G., 2006, Infrasonic wave observations of the January 2006 Augustine Volcano eruptions: Eos (American Geophysical Union Transactions), v. 87, abs. V51C-1685.

Petersen, T., De Angelis, S., Tytgat, G., and McNutt, S.R., 2006, Local infrasound observations of large ash explosions at Augustine Volcano, Alaska, during January 11–28, 2006: Geophysical Research Letters, v.33, L12303, doi:10.1029/2006GL026491.

Power, J.A., 1988, Seismicity associated with the 1986 eruption of Augustine Volcano Alaska: University of Alaska Fairbanks, M.S. Thesis, 142 p.

Power, J.A., and Lalla, D.J., 2010, Seismic observations of Augustine Volcano, 1970–2007, *in* Power, J.A., Coombs, M.L., and Freymueller, J.T., eds., The 2006 eruption of Augustine Volcano, Alaska: U.S. Geological Survey Professional Paper 1769 (this volume).

Power, J.A., Nye, C.J., Coombs, M.L., Wessels, R.L., Cervelli, P.F., Dehn, J., Wallace K.L., Freymueller, J.T., and Doukas, M.P., 2006, The reawakening of Alaska's Augustine Volcano: Eos (American Geophysical Union Transactions), v. 87, no. 37, p. 373, 377.

Reeder, J.W. and J.C. Lahr, 1987, Seismological aspects of the 1976 eruptions of Augustine Volcano, Alaska: U.S. Geological Survey Bulletin 1768, 32 p.

Schneider, D.J., Scott, C., Wood, J., and Hall T., 2006, NEXRAD weather radar observations of the 2006 Augustine volcanic clouds: Eos (American Geophysical Union Transactions), v. 87, abs. V51C-1686.

Thomas, R.J., Krehbiel, P.R., Rison, W., Hunyady, S.J., Winn, W.P., Hamlin, T., and Harlin, J., 2004, Accuracy of the lightning mapping array: Journal of Geophysical Research, v. 109, no. D14, D14207, doi: 10.1029/2004JD004549

Thomas, R.J., Krehbiel, P.R., Rison, W., Aulich, G., Edens, H., McNutt, S.R., Tytgat, G., and Clark, E., 2007, Electrical activity during the 2006 Mount St. Augustine volcanic eruptions: Science, v. 315, p. 1097.

Thomas, R.J., McNutt, S.R., Krehbiel, P.R., Rison, W., Aulich, G., Edens, H.E., Tytgat, G, and Clark, E., 2010, Lightning and electrical activity during the 2006 eruption of Augustine Volcano, *in* Power, J.A., Coombs, M.L., and Freymueller, J.T., eds., The 2006 eruption of Augustine Volcano, Alaska: U.S. Geological Survey Professional Paper 1769 (this volume).

Vallance, J.W., Bull, K.F., and Coombs, M.L., 2010, Pyroclastic flows, lahars, and mixed avalanches generated during the 2006 eruption of Augustine Volcano, *in* Power, J.A., Coombs, M.L., and Freymueller, J.T., eds., The 2006 eruption of Augustine Volcano, Alaska: U.S. Geological Survey Professional Paper 1769 (this volume).

van Manen, S.M., Dehn, J., West, M.E., Blake, S., and Rothery, D.A., 2010, The 2006 eruption of Augustine Volcano—Combined analyses of thermal satellite data and reduced displacement, *in* Power, J.A., Coombs, M.L., and Freymueller, J.T., eds., The 2006 eruption of Augustine Volcano, Alaska: U.S. Geological Survey Professional Paper 1769 (this volume).

Wallace, K.L., Neal, C.A., and McGimsey, R.G., 2010, Timing, distribution, and character of tephra fall from the 2005 –2006 eruption of Augustine Volcano, *in* Power, J.A., Coombs, M.L., and Freymueller, J.T., eds., The 2006 eruption of Augustine Volcano, Alaska: U.S. Geological Survey Professional Paper 1769 (this volume).

Wilson, C.R., Olson, J.V., Szuberla, C.A.L., McNutt, S.R., Tytgat, G., and Drob, D.P., 2006, Infrasonic array observations at I53US of the 2006 Augustine Volcano eruptions: Inframatics, March 15, 2006, 18 p.

Zobin, V.M., Plascencia, I., Reyes, G., and Navarro, C., 2009, The characteristics of seismic signals produced by lahars and pyroclastic flows—Volcan de Colima, Mexico: Journal of Volcanology and Geothermal Research, v. 179, p. 157–167.

The 2006 Eruption of Augustine Volcano, Alaska
Power, J.A., Coombs, M.L., and Freymueller, J.T., editors
U.S. Geological Survey Professional Paper 1769

Chapter 5

Earthquake Waveform Similarity and Evolution at Augustine Volcano from 1993 to 2006

By Heather R. DeShon[1], Clifford H. Thurber[2], and John A. Power[3]

Abstract

Temporal changes in waveform characteristics and earthquake locations associated with the 2006 Augustine eruption and preeruptive seismicity provide constraints on eruptive processes within the edifice. Volcano-tectonic earthquakes occur within the upper 1 to 2 km at Augustine between and during eruptive cycles, and we use the Alaska Volcano Observatory hypocenter and waveform catalog from 1993 to 2006 to constrain changes in event similarity and location over time. Waveform crosscorrelation with bispectrum verification improves the pick accuracy of the catalog data to yield better locations and allows for identification of families of similar earthquakes. Event waveform similarity is low at Augustine, with ~60 to 70 percent of events failing to form event families of more than 10 events. The remaining earthquakes form event families over multiple time scales. Events prior to the 2006 eruption exhibit a high degree of similarity over multiple years. Earthquakes recorded during the precursory and explosive phases of the 2006 eruption form swarms of similar earthquakes over periods of days or hours. Seismicity rate and event similarity decrease rapidly during the explosive and effusive eruption phases. The largest recorded swarms accompany reports of increased steaming and explosive eruptions at the summit. Relative relocation of some event families indicates upward migration of activity over time, consistent with magma transport by way of an ascending dike. Multiple regions of the edifice generate seismicity simultaneously, however, suggesting the edifice contains a network of fractures and/or dikes.

Introduction

Augustine Volcano is the youngest and historically most active volcano in the Cook Inlet region of Alaska. The edifice is composed primarily of andesitic material and forms a small island with a summit peak at 1.25 km above sea level. Past sector failures of the edifice have excited tsunamis in Cook Inlet. Major eruptions have taken place in 1883, 1935, 1963–64, 1976, 1986, and 2006, and these explosive eruptions created ash-rich plumes that posed significant hazard for overlying aircraft flight paths. The three most recent eruptions have followed similar eruptive sequences: (1) a precursory period of seismic unrest; (2) an explosive phase marked by one or more pyroclastic flow-generating eruptions; and (3) one or more dome-building effusive phases (Power, 1988; Power and Lalla, this volume). Most seismicity recorded at Augustine is volcano-tectonic (VT) in nature, with high-frequency P onsets indicative of shear failure in brittle material, and is confined to the upper 1 to 2 km of the edifice, with limited evidence for activity at 3 to 4 km below mean sea level (b.m.s.l.) (Kienle, 1987; Power, 1988; Power and Lalla, this volume). Low-frequency events associated with fluid processes are less common (Buurman and West, this volume). Magma transport during eruptive cycles at Augustine likely occurs through shallow dike propagation, with new eruptive cycles occurring as a result of an influx of juvenile magma at the base of the system (Cervelli and others, 2006; Roman and others, 2006).

Dike propagation at volcanoes frequently couples with increased rates of seismicity, and seismic monitoring provides useful early warning of major changes within volcanic systems (see McNutt, 2005, for a recent review). Because of the volcanic, seismic, and tsunami hazard posed by Augustine eruptions, the volcano has been seismically monitored since 1970. The Alaska Volcano Observatory (AVO) has maintained digital waveforms recorded by a network of five to eight short-period and broadband seismometers since 1993

---

[1] Center for Earthquake Research and Information, University of Memphis, 3890 Central Ave., Memphis, TN 38138.

[2] Dept. of Geoscience, University of Wisconsin-Madison, 1215 W. Dayton St., Madison, WI 53706.

[3] Alaska Volcano Observatory, U.S. Geological Survey, 4200 University Drive, Anchorage, AK 99508.

(fig. 1). Volcano seismic networks typically have few stations and marginal geographic coverage, and waveforms recorded at volcanoes are often noisy because of the complex interactions of tectonic and magmatic processes, wind, and poor site conditions. As a result, onset pick accuracy may be highly variable within a phase catalog. Routine catalog locations at Augustine exhibit a high degree of scatter within the shallow edifice that complicates interpretation of magmatic and hydrothermal processes. Scatter may be an artifact of location procedure or imprecise phase onset picks, or it may be a real feature of volcanic activity. Catalog earthquake locations at Augustine are calculated using analyst phase picks and an approximate, one-dimensional (1*D*) velocity model with station corrections developed for Augustine (Power, 1988). More than 3,800 events have been catalogued at Augustine from 1993 through 2006 (Dixon and others, 2008), and ~2,000 of these were related to the 2006 eruptive sequence (fig. 1).

Retrospective analyses of volcano seismic data using waveform crosscorrelation methods can provide insight into the relative similarity of waveforms in time and space, which in turn can reflect the underlying eruptive processes (for example, Got and others, 1994; Rubin and others, 1998; Battaglia and others, 2004; Rowe and others, 2004; DeShon and others, 2007). In this study, waveform crosscorrelation techniques are applied to the seismic event archive for Augustine Volcano extending from 1993 through December 2006. Identification of characteristic families of similar earthquakes provides a clearer picture of how seismicity evolves within the edifice before and during eruptive cycles at Augustine Volcano. We examine temporal changes in waveform characteristics associated with the 2006 Augustine eruption and preeruptive seismicity and identify families of similar earthquakes that occur at multiyear, multimonth, multiday, and multihour timescales. Relative location of selected event families associated with the precursory and explosive phases of the 2006 eruption provides insight into seismic and magmatic processes occurring at Augustine Volcano.

Method

Waveform Crosscorrelation

If two events are closely located in space and share similar source mechanisms, they should generate similar ground motions and be recorded as similar waveforms. Waveform crosscorrelation (CC) of two events recorded at the same station yields: (1) a maximum absolute value of the CC coefficient that varies between 0 and 1, where 1 represents a perfect waveform similarity; and (2) an associated relative time delay or lag

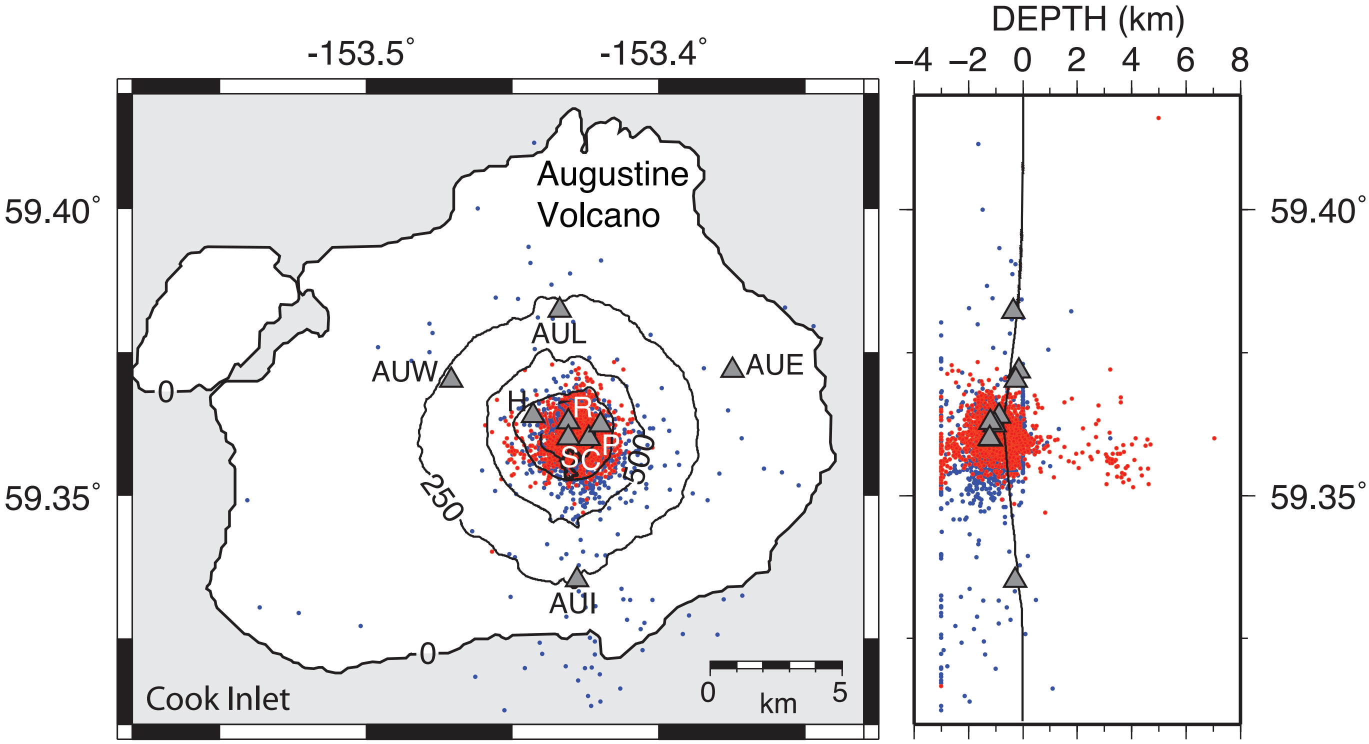

Figure 1. Map view and north-south oriented cross-section of Augustine Volcano. Contour interval is 250 m. Triangles are AVO seismic stations used for waveform crosscorrelation. The "AU" has been left off of the summit stations for drafting clarity. Blue dots are AVO catalog events occurring from 1993 to April 2005. Red dots are AVO catalog events occurring on and after April 2005.

reflecting the time shift necessary to best align the waveforms. High-quality time delay estimates can be identified by finding a threshold value for the CC coefficient that maximizes the number of correlated arrivals while minimizing the number of false-positive correlations (for example, Schaff and others, 2002). Correlation lag estimates can be used to correct inconsistent picks and revise absolute arrival times (for example, Dodge and others, 1995; Dodge, 1996; Shearer, 1998; Aster and Rowe, 2000; Rowe and others, 2002a). CC coefficients contain valuable information on event similarity and can be used to identify families of similar waveforms (Rowe and others, 2002a).

CC coefficients may be low if the underlying signals are not time-delayed similar waveforms, or if high levels of noise contaminate the underlying time-delayed signals. In the presence of correlated Gaussian noise, traditional CC methods may provide low coefficients for similar events, or high correlations with the estimated correlation lag driven by the correlated noise, rather than the signal of interest (Du and others, 2004). Correlated or partially correlated noise may result at individual stations because of a combination of constant predominant noise sources such as wind and site response effects. Bispectrum crosscorrelation (BCC), or CC in the third-order spectral domain, suppresses correlated Gaussian noise or low-skewness noise sources (Nikias and Raghuveer, 1987; Nikias and Pan, 1988; Yung and Ikelle, 1997) and can effectively identify the global CC time shift in cases where traditional methods fail because of correlated noise contamination. BCC produces time delay estimates consistent with traditional second-order spectral domain methods when noise is not correlated (Du and others, 2004).

The bispectrum crosscorrelation package for seismology (BCSEIS) verifies traditional CC time delay estimates by additionally computing a BCC lag prediction for filtered and unfiltered waveforms (Du and others, 2004). The use of BCSEIS with Augustine data closely follows the approach outlined for data from Redoubt Volcano, Alaska (DeShon and others, 2007). For Augustine data, the BCSEIS verification threshold was set to twice the sampling interval, and waveforms were filtered using a three pole, two pass, Butterworth bandpass filter with a low frequency corner at 1 Hz and a high frequency corner at 20 Hz. CC was performed using a window extending from 0.3 seconds before to 0.7 seconds following the P-wave arrival (fig. 2). This window was large enough to allow CC of the P-wave coda to identify similar families of earthquakes and incorporate large mispicks. The bulk of seismicity is small magnitude, near-summit events with high frequency P onsets and no discernable S-wave arrivals as recorded on the vertical component, short period summit stations. At the summit stations, the CC window may contain P and S wave information. We were primarily interested in identifying families of similar earthquakes, however, and crosscorrelation of P or P and S energy does not significantly bias our results.

Event Clustering and Pick Adjustments

We identified families of similar earthquakes using the verified CC coefficients and a dendrogram-based, hierarchical pair-group algorithm (Rowe, 2000; Rowe and others, 2002a). CC coefficients are used to fuse event pairs with high

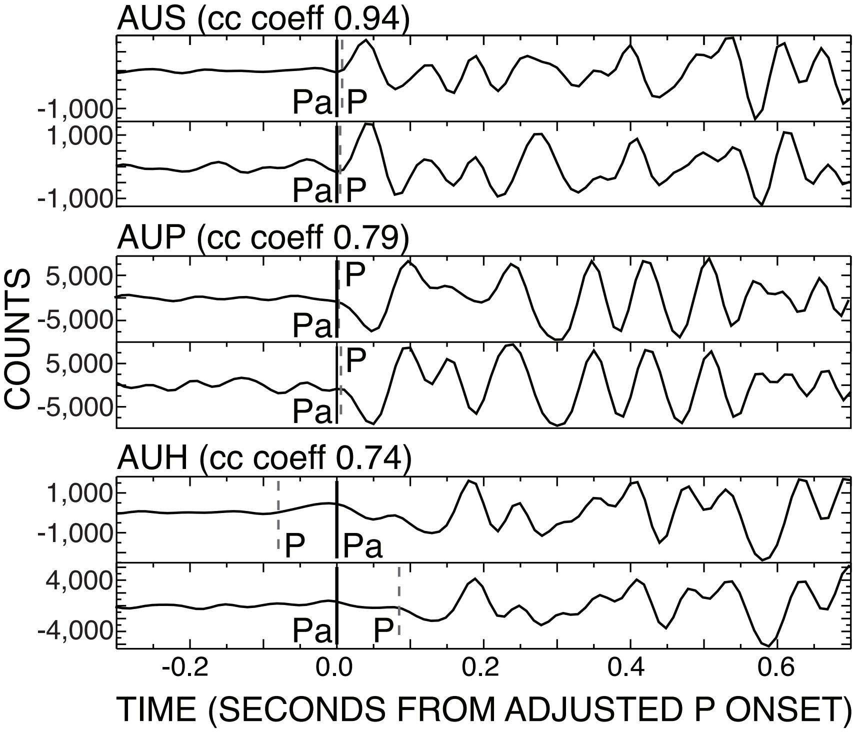

Figure 2. An example of bispectrum crosscorrelation package for seismology (BCSEIS) analysis for two Augustine earthquakes. The waveforms are aligned on the adjusted P onset (Pa) based on crosscorrelation (CC) and event clustering results. The original catalog P onset (P) is also marked. The associated CC coefficient for each event pair is shown next to the station name. Event pairs at each station with CC values ≥0.79 are automatically accepted for use with clustering techniques. Event pairs with CC values ≥0.30 are accepted if at least one other station reports a CC value ≥0.88 for the same data. For this event pair, CC coefficients and predicted lag estimates at AUS, AUP, and AUH would be accepted.

waveform similarity into clusters, and clustering is considered complete when a user-defined CC coefficient cutoff threshold is reached (see Rowe and others, 2002a, for further details). For the Augustine data, this threshold was set to 0.80. The set of time delays associated with each intracluster event pair, weighted by the associated standard deviation calculated during waveform CC, are inverted to solve for a set of phase onset corrections. Inversion is calculated using an iterative, conjugate gradient approach that minimizes the L1-norm misfit (Aster and Rowe, 2000; Rowe and others, 2002a).

We used the above process to solve for clusters or multiplets of highly similar waveforms at all stations within the Augustine network. Event pairs with BCC-verified CC values ≥0.79 were used during event clustering. Additionally, for a given event pair, if at least one station has a verified CC coefficient ≥0.88, then other stations need only have a verified CC coefficient ≥0.30 to also be included in the clustering analysis. Augustine events primarily separate into small clusters with fewer than six events, and approximately one-third of events do not get included in any cluster. This suggests that discrete, dissimilar earthquakes and/or noisy waveforms dominate the Augustine catalog. Visual analysis of clusters containing six or more events suggested that some could be combined to form larger clusters with similar, but not identical, waveforms. We combined like clusters and grew clusters by incorporating events that may have one or more verified and reported lag adjustments to other cluster members; these new events were confirmed as new cluster members by visual comparison. Clusters were then compared across the network to identify event families, or sets of events that generated similar waveforms at all stations (fig. 3). We interpret those families with ≥10 member events in this report.

Results

The seismic record at Augustine Volcano recorded from 1993 to 2005 is dominated by small-magnitude shallow edifice events occurring at rates as high as 54 events/month (fig. 4). Approximately 60 to 70 percent of recorded events are not associated with event families containing more than 10 earthquakes, based on waveform similarity measured by crosscorrelation. Waveform dissimilarity is the dominant feature of catalog seismicity. Waveform similarity, when present, increases with small accelerations in seismicity rate (fig. 4). The resulting families of similar earthquakes contain multiplets of temporally related events over short time scales (days and hours). The similarity of some of the sets of multiplets over longer periods of time (years and months) suggests that intrafamily clusters share source location and process and that some regions of the edifice may be reactivated.

Before the seismicity rate increase in April 2005, event families contain 10 to 20 events (fig. 4*A*), with similar waveforms separated in time by months to years. Figure 5 illustrates a typical event family extending from late 1998 to late 2000 (family S in fig. 4*A*). The family consists of 4 events in 1998, 5 events in 1999, and 10 events in 2000. Waveforms exhibit similarity in P onset, suggesting a similar location, source, and/or path, especially at summit stations AUP and AUH. Waveform similarity in the P coda at summit station AUR is not as high as at the other recording summit stations, which may be indicative of changes in path characteristics over time. As the seismicity rate increases during the early precursory stage in April 2005, event families occur over months and weeks rather than years (fig. 4*B*).

Family LM is an interesting example of both a long-term (year) and mid-term (month) time scale for waveform similarity. The family extends from 1997 through 1998 and reappears from 2004 through 2005 (figs. 4*A*, 4*B,* 6). The set of waveforms was originally identified as two separate clusters because of the opposite sign of the P onset at AUS (fig. 6); however, the seismometer at station AUS was replaced on September 19, 2003, at which point the orientation of the vertical channel was reversed. Waveforms in this family have a highly similar P onset on the summit stations but more variable P coda characteristics. Coda similarity is highest within the temporally related swarms that make up the family (fig. 6). The overall similarity of the waveforms suggests that the same region of the edifice was active throughout much of 1998 during a brief increase in seismicity rate and again during the precursory stages of the 2006 eruption (fig. 4*A*).

During November and December 2005, seismicity rate increases significantly, and the time scale of event similarity switches from years and months to weeks and days (fig. 4*C*). The average size of the families does not change significantly and consists of 10–20 events. Swarms of similar earthquakes occur over periods of hours and days followed by periods of quiescence. The same area of the edifice may reactivate days to weeks later, as illustrated by the time separation between events in families AI and AC (figs. 4*C*, 7). We also identified small swarms of highly similar events that appear to grade into one another over a period of days. This behavior is illustrated in figure 8 using families C, BC, and B, which occur during a period of increased seismicity from December 9 to 11, 2005 (fig. 4*C*). Individually, each family of ~15 events contains highly similar waveforms that occur over a period of hours. The P onset at each of the summit stations suggests a highly similar source process or location, but the P coda remains distinct between families (fig. 8). Over this same time period, events occur in other regions of the edifice, generating P onsets with opposite sign (fig. 9).

The shortest duration family consists of a swarm of ~70 similar earthquakes on January 11, 2006, from ~2000 to 2200 AKST (Alaska Standard Time) (family AD, fig. 4*C*). These events were recorded between the first two stages of explosive activity on January 11 and 13, 2006. Though these events are highly similar, the waveforms evolve over time, likely reflecting small changes in source process, source location, changes in path characteristics, or some combination of factors (fig. 10). Following this swarm, ~30 events with a similar high-frequency content but different onset and coda characteristics were recorded at the summit stations (family AH, figs. 4*C*,

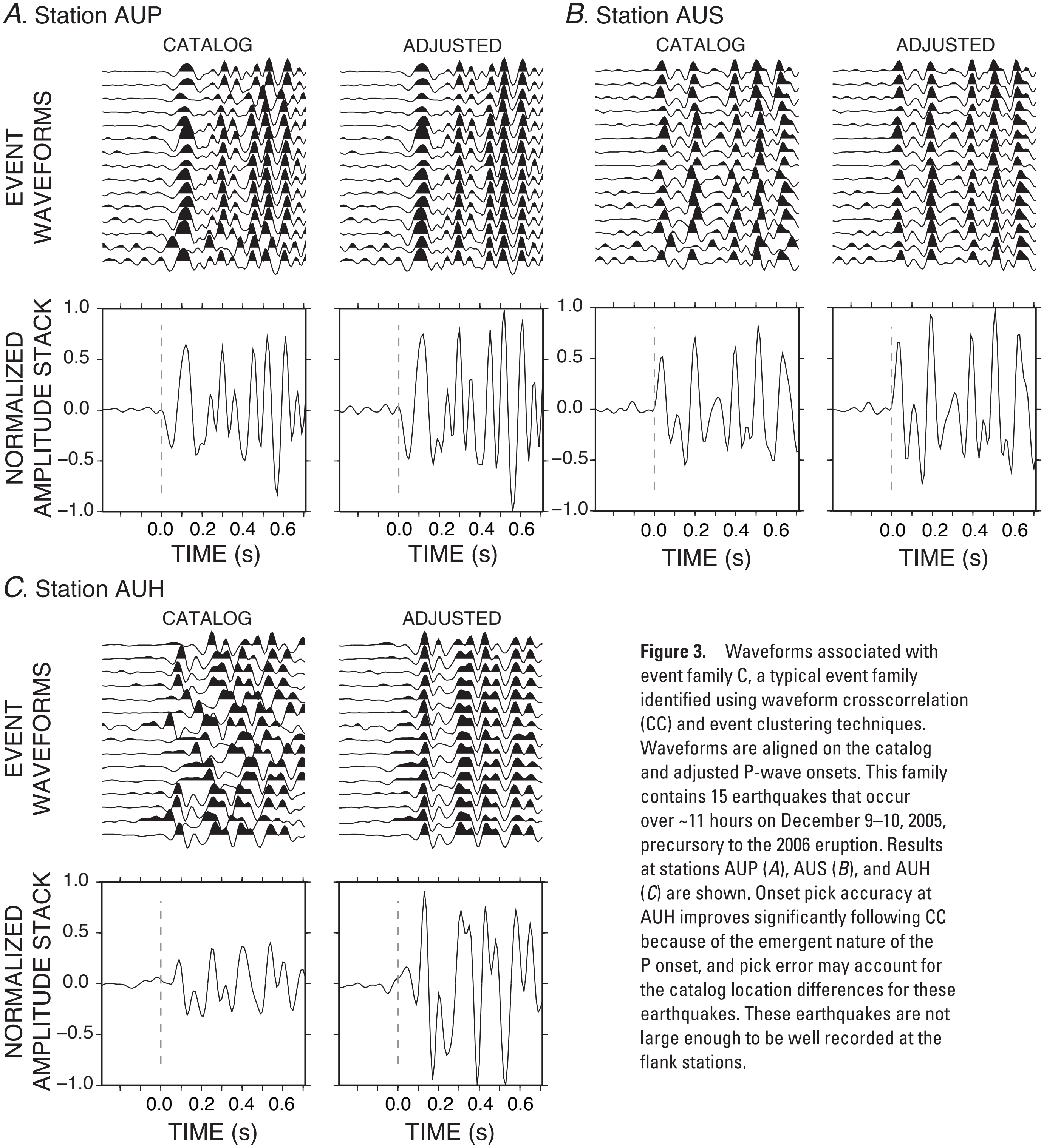

Figure 3. Waveforms associated with event family C, a typical event family identified using waveform crosscorrelation (CC) and event clustering techniques. Waveforms are aligned on the catalog and adjusted P-wave onsets. This family contains 15 earthquakes that occur over ~11 hours on December 9–10, 2005, precursory to the 2006 eruption. Results at stations AUP (*A*), AUS (*B*), and AUH (*C*) are shown. Onset pick accuracy at AUH improves significantly following CC because of the emergent nature of the P onset, and pick error may account for the catalog location differences for these earthquakes. These earthquakes are not large enough to be well recorded at the flank stations.

11). These events were not well recorded on the flank stations, however, so the catalog location quality is poor.

Events within each family exhibit waveform similarity that should correspond to spatial similarity, but catalog locations for events within individual families generally have a high degree of scatter. For example, family AD waveforms are linked by an average CC coefficient of 0.92 at station AUP, but the catalog depths for these events range from −3.0 to 0.0 km b.m.s.l. Events with identical source process and location should also exhibit identical differences in absolute arrival time between any two stations. This differential arrival time is independent of origin time but is sensitive to changes in path velocity over the time between earthquakes. For swarm activity over small time scales, we can assume the velocity along the path from earthquake to station does not change significantly, and we can use differential arrival times to prove colocation. We present an example of this process using family AD. We calculated the difference in absolute arrival time between summit station AUP and (1) summit station AUH; (2) flank station AUL; and (3) flank station AUW (fig. 12). These four stations exhibit high signal-to-noise ratio for events in family AD (fig. 10). We removed the median value of the differential times to find a time residual; residuals should be zero for colocated earthquakes. For family AD, the time residuals for each station-pair have a zero mean and scatter is small (fig. 12). The increased scatter in time residuals for AUP-AUL reflects the relatively poorer recording of these earthquakes at station AUL (fig. 10).

The mean differential arrival times for sets of station-pairs for each family contain information on relative locations between families. If families are separated in space, then the differential time median at any given station-pair should differ. In figure 13, we show the relationship between median differential times for station-pairs AUP-AUH, AUP-AUW, and AUP-AUL. Because of the assumption that path velocity does not vary over time, we show only event families with relatively short durations that occur during the 2006 Augustine eruption. Family AD, which occurred during the explosive phase, clearly separates from families A, B, BC, and C that occurred during the early precursory phase in November and December 2005 (fig. 13). The spatial similarity between the December 2005 events is consistent with the high degree

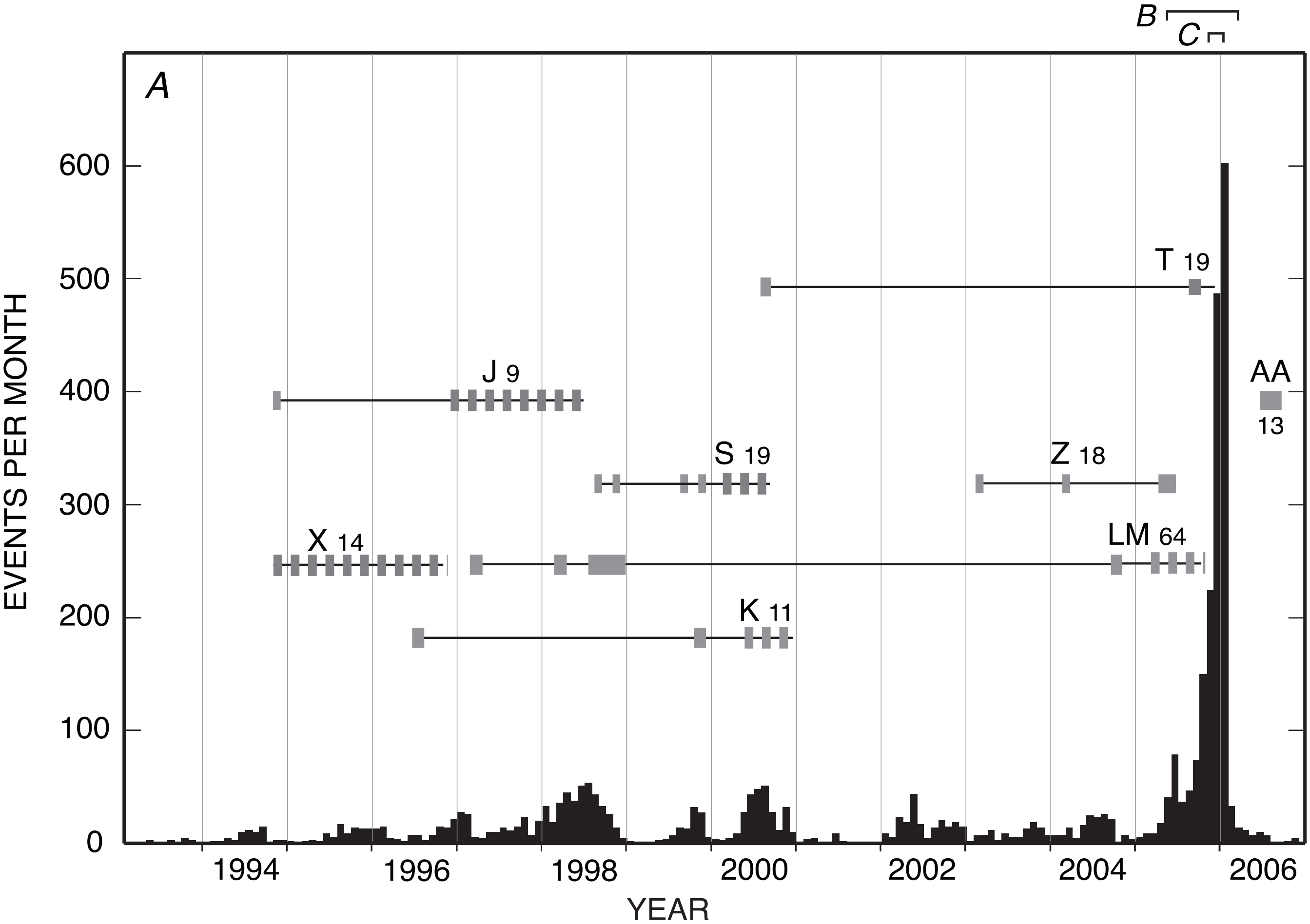

Figure 4. Seismicity rate and event families identified using the Augustine Alaska Volcano Observatory (AVO) catalog. On each panel, the histogram indicates seismicity rate over time and horizontal black lines indicate the extent in time of waveform families. Family names are indicated by letters and are followed by the number of member events. Solid squares represent time periods over which multiplets of earthquakes occur within each family. *A*, Histogram of the number of catalog earthquakes per month from 1993 to 2006. Event families with a time range on the month to year scale are shown. Bars indicate the time periods shown in panels *B* and *C*. *B*, Histogram of the number of catalog earthquakes per day during the 2006 eruption and precursory period. Seismicity rate decreases significantly following explosive eruptions in January 2006. Bar indicates the time period shown in panel *C*. *C*, Histogram of number of catalog earthquakes per day in November and December 2005, and in January 2006. Arrows mark periods of explosive, plume-forming eruptions. Black: first motion down at AUP. Gray: first motion up at AUP.

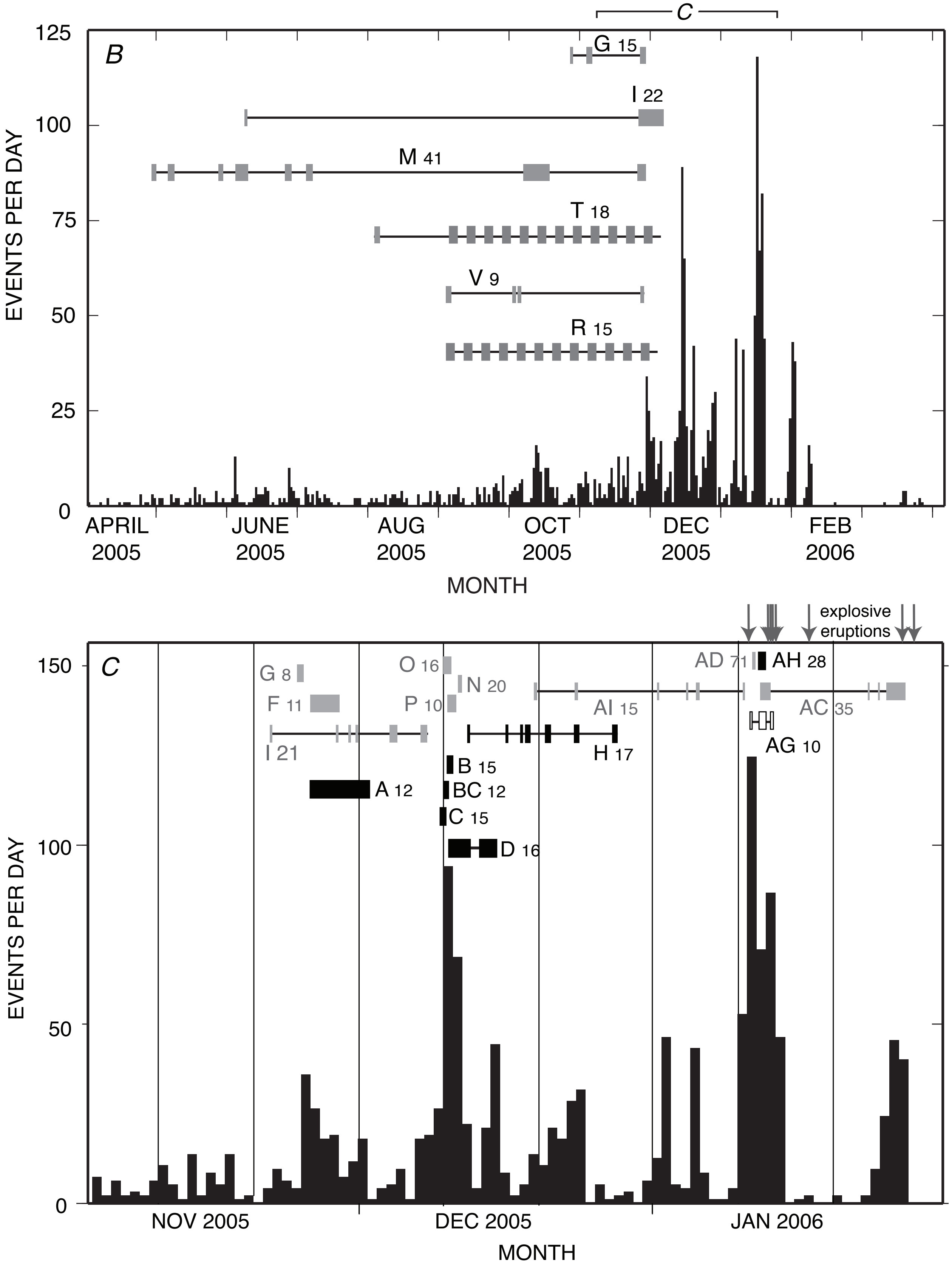

Figure 4.—Continued.

of intracluster waveform similarity between these clusters (fig. 8). On the basis of network geometry, the lower values for AUP-AUW and AUP-AUL for family AD likely indicate a shallower depth for these events relative to the other families. Shallow events should generate higher differential arrival times between summit and flank stations than events within the edifice near sea level because the sea level, events are actually closer to the flank stations than to the summit stations. Clusters O and N occur over the same period of time as families B, BC, and C but have opposite first motion polarity at AUP (fig. 9), and they appear separated in this diagram. This relationship suggests that multiple regions of the edifice can be simultaneously active.

We can further take advantage of the differential arrival-time medians for each cluster by inverting these data to solve for relative locations between families when families are well recorded on more than three stations. This location methodology is a variant of the method of hyperbolas (Milne, 1886) and the related equal-differential-time method (Zhou, 1994). To test this method, we relocated families A, B, and AD and used all station-pair combinations of summit stations AUP, AUS, and AUH and flank stations AUL and AUW. We solved for an initial cluster location by computing the misfit between the set of observed and calculated station-pair differential times. We solved for the location that minimizes the station-pair residuals, applying weighting to stabilize the inversion.

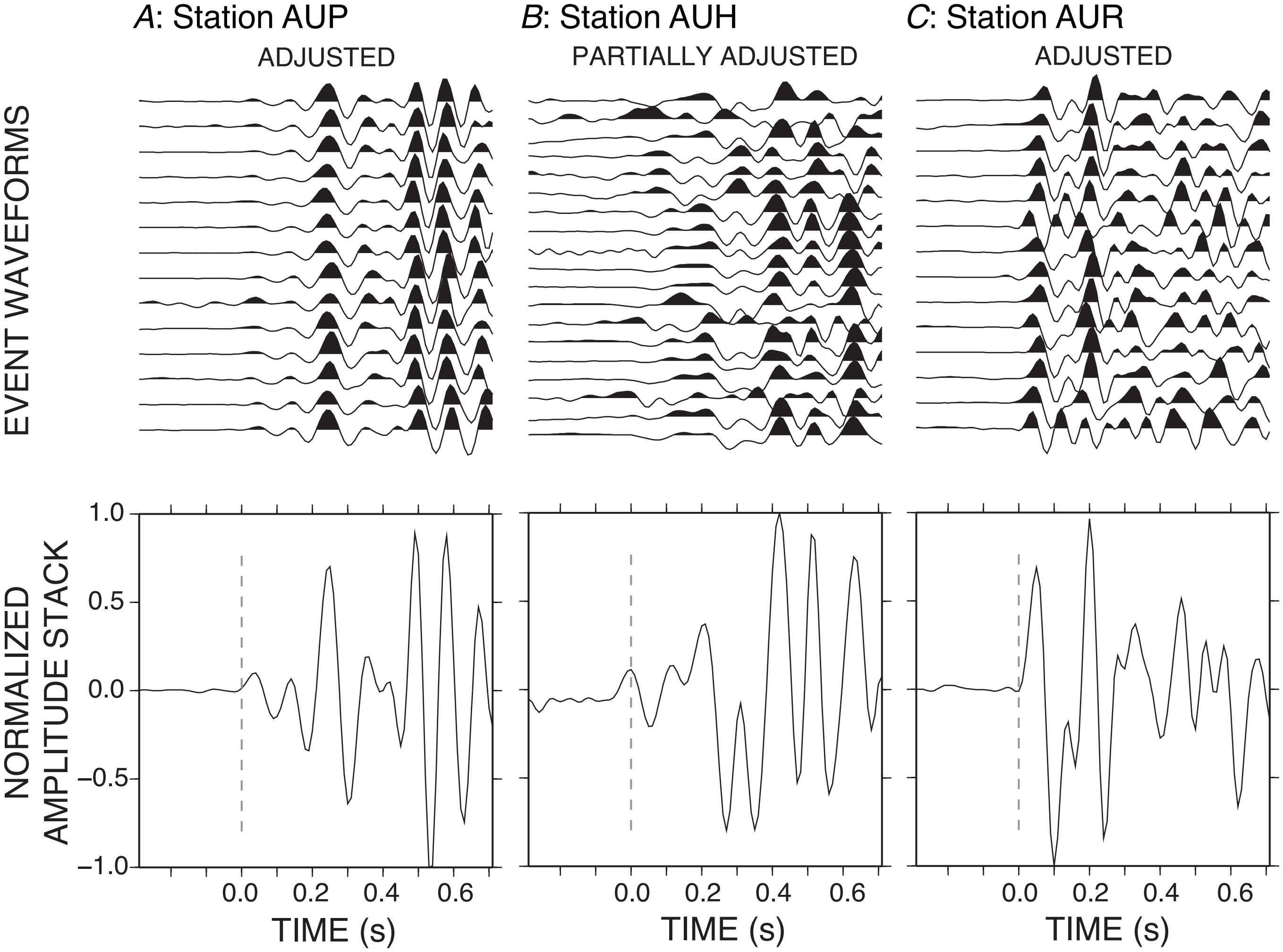

Figure 5. Waveforms and normalized amplitude stacks for event family S, which occur from June 22, 1998, through September 23, 2000 (see fig. 4*A* for full time extent), at stations AUP (*A*), AUH (*B*), and AUR (C). Waveforms are shown aligned on adjusted P onset and filtered between 1 and 20 HZ (upper panel) and as an normalized amplitude stack (lower panel). At all summit stations, such as the examples at AUP and AUR, the waveforms exhibit similarity in P onset, suggesting a similar location, source and path, but they are not identical. Because of the emergent nature of P onset at AUH, pick quality in the initial catalog was poor. The number of verified time delays between all possible event pairs was not sufficient for the inversion process to correctly adjust P onsets at this station.

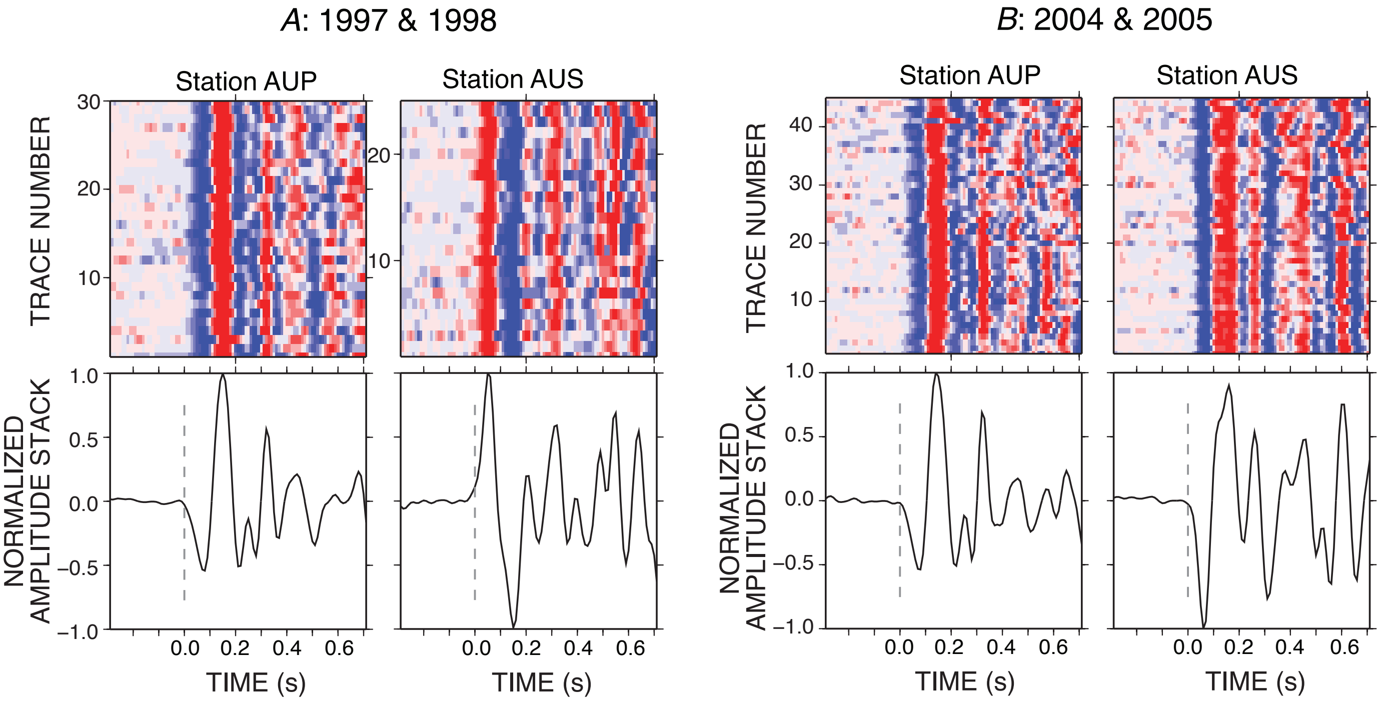

Figure 6. Waveforms for family LM recorded at summit stations AUP and AUS. A, Events from 1997 through 1998. B, Events from 2004 through 2005. Though the waveforms at AUS have different first motion P onsets, this reflects a change in vertical component orientation and not a change of source. Upper panels: Waveforms are visualized as wigglegrams (Rowe and others, 2002b), where red indicates positive and blue indicates negative normalized amplitude. Color intensity scales with normalized amplitude. Waveforms are aligned on the adjusted P onset and sorted by time (trace 1 being the earliest occurring event). Lower panels: Stack of amplitude normalized waveforms. The dashed line indicates P onset. Wigglegrams are used throughout this study to visualize families with more than 20 member events.

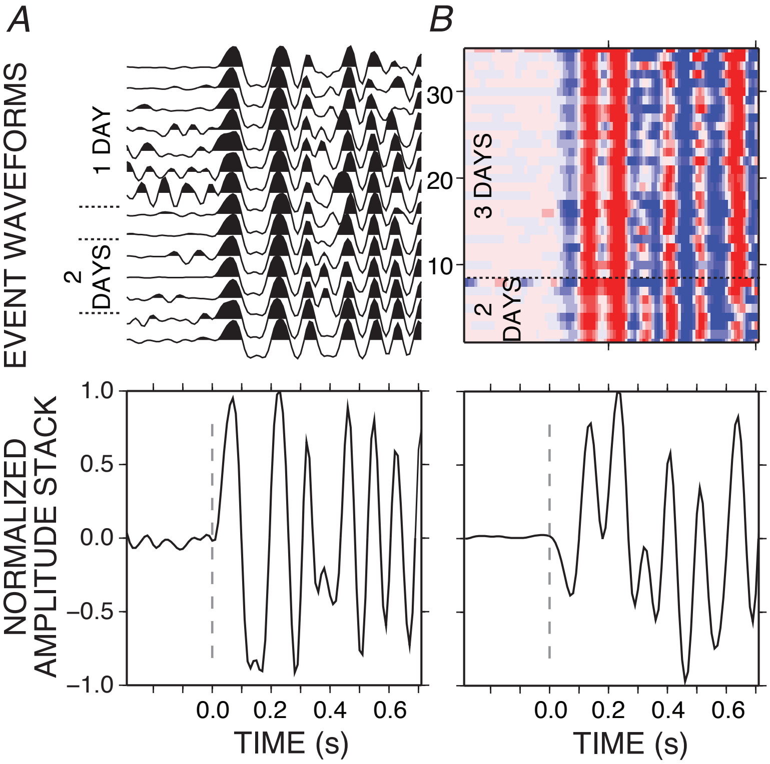

Figure 7. Waveforms and stacks for family AI at summit station AUP (*A*) and family AC at summit station AUH (*B*). Events making up these two families recur over multiple weeks (see fig. 4*B* for full time extent). Each family consists of subsets of single or multiplets of earthquakes that occur over much shorter time scales (one to three days), as noted by small dashed lines on the upper panel. Upper panels: Waveforms are aligned on the adjusted P onset and sorted by time. Family AC contains more than 30 events and is shown as a wigglegram. Lower panels: Stack of amplitude normalized waveforms. The dashed line indicates P onset.

Summit-to-summit times were assigned weight 1.0, and summit-to-flank and flank-to-flank stations were set to 0.02. We assumed a constant velocity half space of 3.5 km/s for P waves, which is slightly faster than the average edifice velocities in the 1D AVO velocity model for Augustine. Edifice velocities are poorly constrained at Augustine, however, and there is some evidence that edifice velocities may be as high as 4.4 km/s (Power, 1988). Families A and B are separated by ~100 m, but more significantly are located 400 m to the south, 200 m to the east, and 800 m deeper than family AD, which is associated with explosive eruptions.

Sumiejski and others (2009) extended this approach of using station-pair differential times to derive family locations for the 2006 Augustine eruption. They used the CC coefficients derived in this study for nine families (A, AC, AD, AH, B, BC, C, LM, and O) using all 36 Augustine station-pairs and incorporated a linear-gradient velocity model obtained from preliminary forward modeling of the data. They also calculated quality weights for each of the station-pair time differences and solved for location using both a grid search and a modified Geiger's method of iterative, reweighed least squares (see Sumiejski and others, 2009, for further information). The results indicated that family LM occurs at ~300 m b.m.s.l. Precursory activity A, B, BC, and C located at ~500 m above m.s.l. (a.m.s.l.), as does family AC that is associated in time with the explosive phase. Families AD and AH, also associated with the explosive phase, located near the Augustine summit at ~1,200 m a.m.s.l.

Deep events (below ~3 km b.m.s.l.) are fairly rare at Augustine. Fifty-four catalog events occur between 2.5 and 6 km b.m.s.l. at Augustine, and all but five of these occur in 2006. Power and Lalla (this volume) showed that all but 18 of these events are mislocated shallow earthquakes. Deep events at Augustine are not expected to be well recorded at summit stations (Lalla and Kienle, 1980), and most summit stations

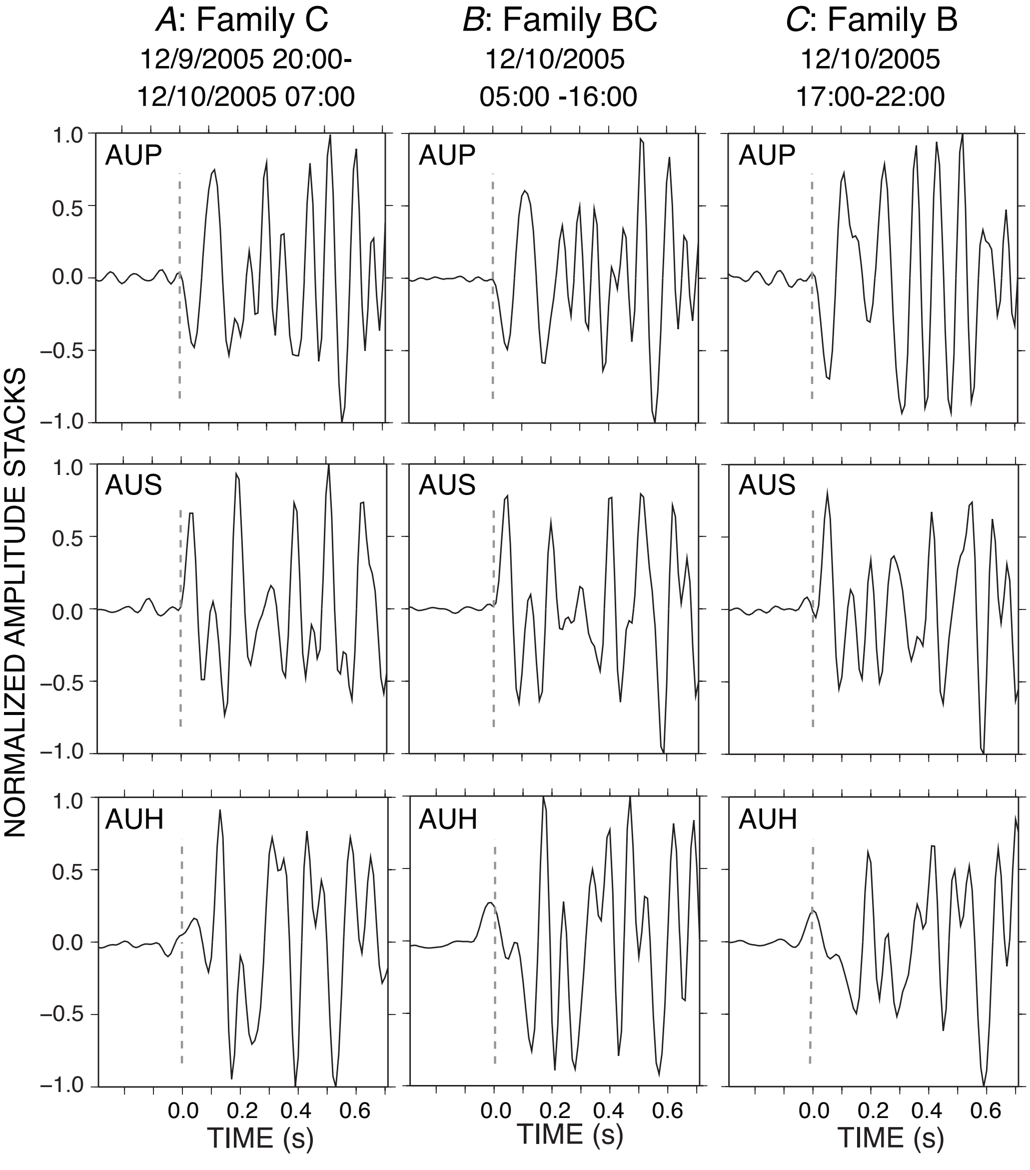

Figure 8. Normalized amplitude waveform stacks at stations AUP, AUS, and AUH aligned on adjusted P onset for event families C (*A*), BC (*B*), and B (*C*). These families occur consecutively in time during December 9–10, 2005, and the exact time extent of each is shown as date and hours AST. The event families are very similar in P onset and frequency content. Difference in P coda may be due to spatial migration or small changes in source mechanism. The mean centroid for each family is at ~ −0.68 km b.m.s.l.; the individual catalog hypocenter depth ranges are from −3 to 0 km b.m.s.l. The dashed line indicates P onset.

went offline following the explosive eruptions in January 2006. Of the remaining deep events, eleven of these events have fairly similar P onsets (fig. 14) and form event family AA (fig. 4*A*). The events occur throughout a 3-month period following the cessation of explosive activity. No deep seismicity was recorded during or following the 1986 Augustine eruption, although some activity was located at these depths before the 1976 eruption (Power and Lalla, this volume). Changes in network geometry between the 1976 and 1986 eruptions could account for this feature of the seismicity. Kienle (1987) interpreted seismicity occurrence at 3 to 4 km b.m.s.l. to be indicative of magma transport within or out of a storage body associated with the 1976 eruption. If a storage system is present at these depths and provided source material for the 2006 eruption, deep seismicity appears primarily linked to posteruptive processes.

Discussion

Seismic unrest prior to the 2006 eruption began as a steady increase in microearthquakes beneath the volcano, ranging from 1 to 2 events located in the AVO catalog per day in May of 2005 to 15 per day in mid-December. Over this period, continuous GPS (cGPS) sites located on the volcano flanks began to move away from one another in a radial manner, indicating inflation of the edifice. On November 17, 2005, the east-west baseline abruptly offset and motion at each station accelerated (Cervelli and others, 2006). On January 11, 2006, the eruption entered the explosive phase and generated the first of 13 explosive eruptions that continued throughout the month. During January 12–13, 2006, explosive eruptions ceased but seismicity rate reached a peak of 130 events/day (fig. 4*C*). At this time, a cGPS site located on the summit moved ~10 cm northeast. Six explosive eruptions commencing on January 13 and ending January 14, 2006, destroyed all summit seismic and cGPS stations. A large pyroclastic flow related to the January 28, 2006, explosive eruption buried the northernmost cGPS station and seismic stations AUL and AUH (fig. 1). Over February and March 2006, quieter magma effusion led to numerous pyroclastic flows, formation of a new lava dome, and magma flows on the north and northeast flanks. Seismicity rate returned to pre-2005 levels by late February 2006.

Cervelli and others (2006) modeled the Augustine cGPS data using an ascending dike source. They showed that the precursory-stage radial pattern recorded by the cGPS is consistent with an initial source with a top no higher than sea level. Mattia and others (2008) modeled the initial source as a vertical ellipsoid at ~300 m b.m.s.l. Summit cGPS data were well fit by a dike beginning to ascend on November 17 and reaching near the surface by mid-December 2005, likely coincident with increased edifice activity on December 9–11, 2005 (fig. 4*C*). The ascending dike likely did not breach the summit until the explosive eruption of January 13, 2006. The initial explosive eruption of January 11 contained no juvenile material, whereas the January 13 magmas were dominated by juvenile material (Wallace and others, this volume; Cervelli and others, 2006). This observation is consistent with the continuing motion recorded by the summit cGPS station through January 13, 2006.

The above model of the 2006 eruption is broadly consistent with a model for the 1986 eruption based on melt inclusion data (Roman and others, 2006). Roman and others (2006) found that the 1986 erupted magmas contained

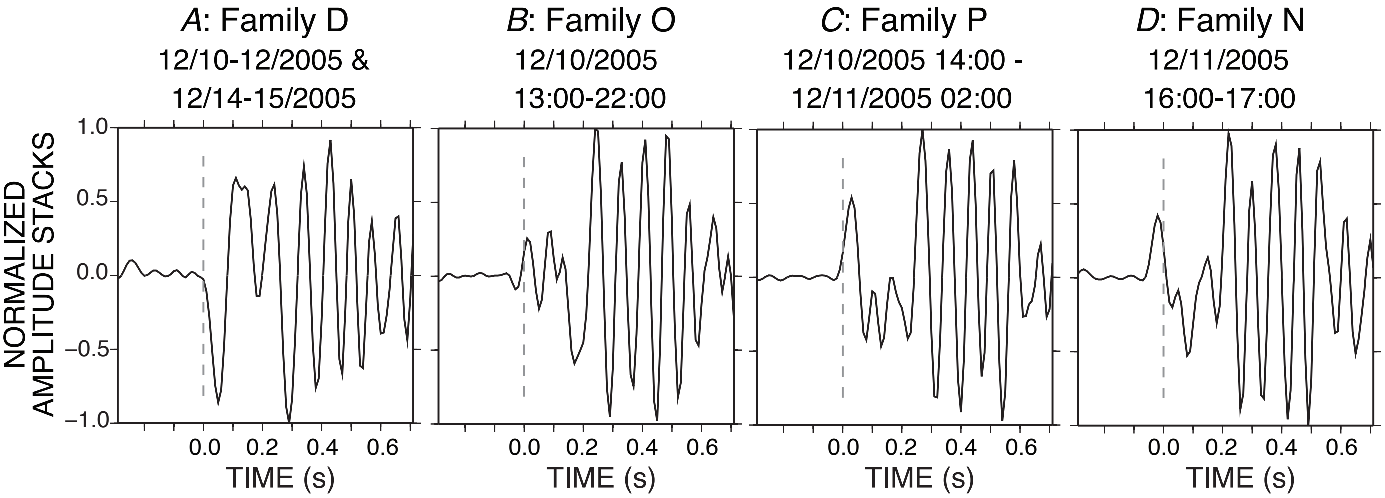

Figure 9. Normalized amplitude waveform stacks at station AUP for event families D (*A*), O (*B*), P (*C*), and N (*D*). These families occur from December 10 to 15, 2005, and hence overlap in time those shown in figure 8. Families O, P, and N have opposite first motion at AUP than either family D or families C, BC, and B (fig. 8). Similarly, the mean centroid of family D is –0.67 km b.m.s.l., much like that for the families shown in figure 8. Families O, P, and N have mean centroids of –0.62 km, –0.63 km, and –0.92 km b.m.s.l., respectively. This suggests that multiple regions of the edifice are generating volcano-tectonic earthquakes over the same temporal period. The time extent of each family is shown as date and hours AKST. The dashed line indicates P onset.

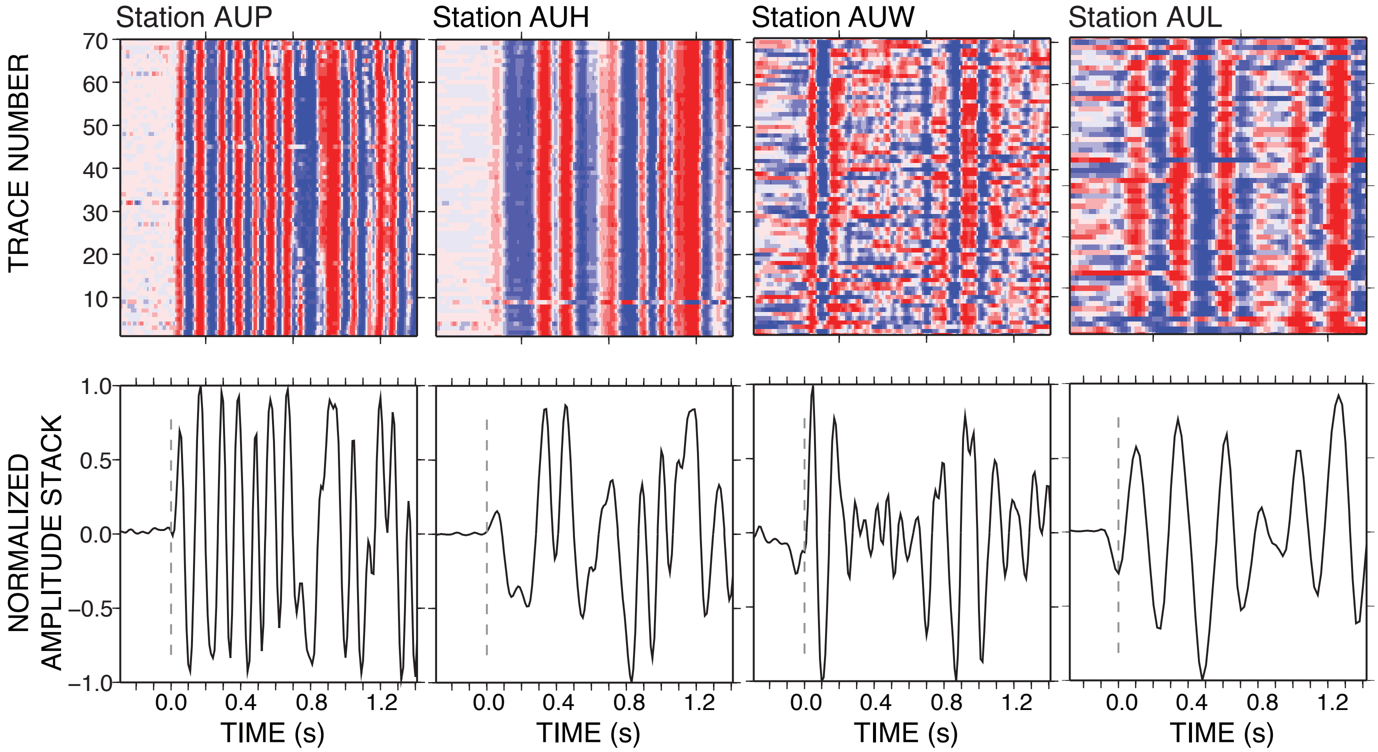

Figure 10. Wigglegrams and normalized amplitude waveform stacks for a swarm of ~70 earthquakes on January 11, 2006, which extended from ~2000 to 2200 AKST (family AD on fig. 4*C*). Waveforms are aligned on the adjusted P onset at summit stations AUP and AUH and at flank stations AUW and AUL. Though these events are highly similar, the waveform does evolve over time, likely reflecting small changes in source process or path. The dashed line indicates P onset.

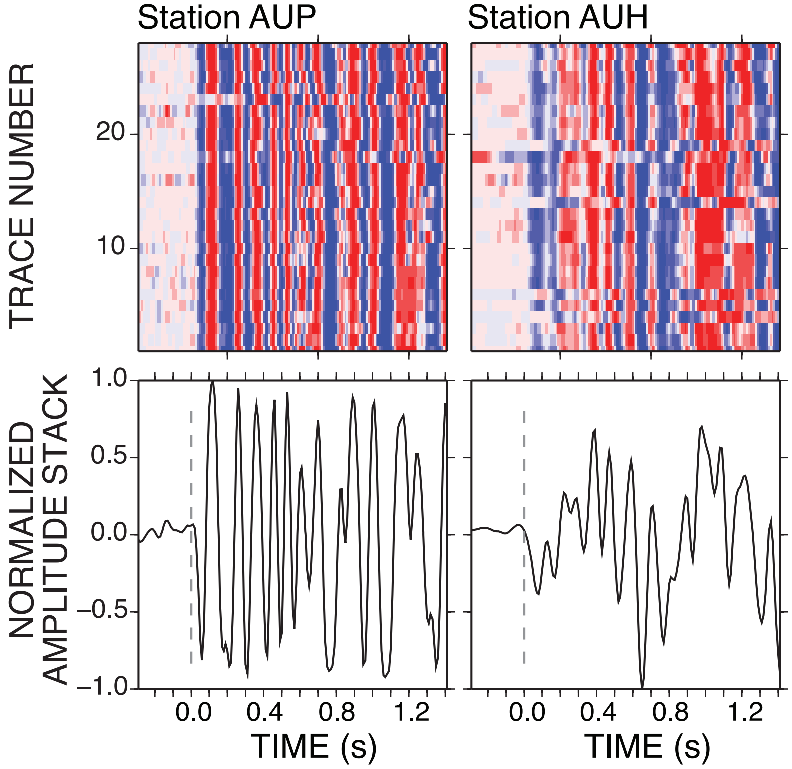

Figure 11. Wigglegrams and normalized amplitude waveform stacks for 28 similar earthquakes that occurred over a 13-hour period during the initial explosive stage (family AH on fig. 4*C*). Waveforms are aligned on the adjusted P onset at summit stations AUP and AUH. These events start to occur a few hours after the large swarm shown in figure 10 and contain the same overall frequency content of the larger swarm. However, first motion polarity is opposite. The dashed line indicates P onset.

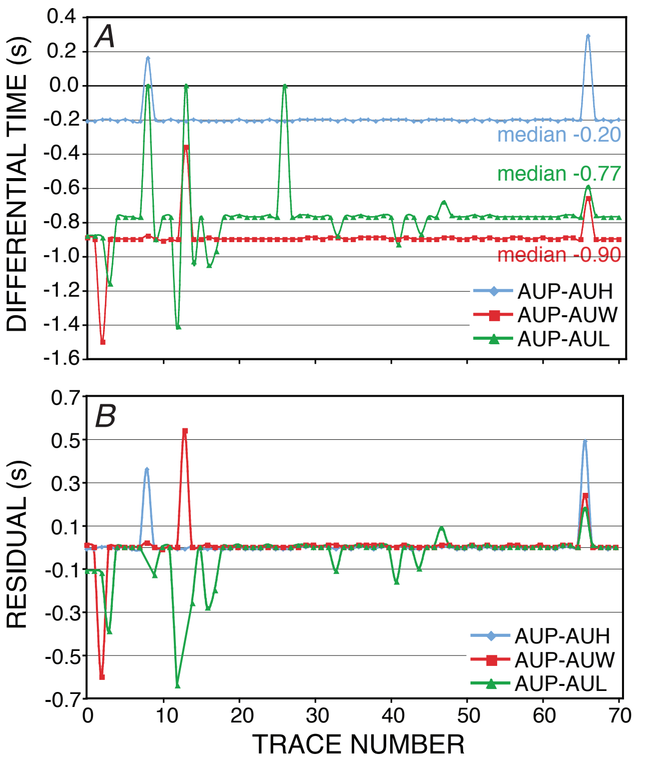

Figure 12. Collocated events should generate identical arrival-time differences at any two stations, as shown here for event family AD. *A*, Differential arrival times for 72 events in family AD indicate a very high degree of waveform similarity at stations AUP, AUH, AUW, and AUL. Differential times are calculated using the adjusted P-wave onset based on waveform crosscorrelation. The median value is noted. *B*, The residual time is calculated by removing the median for each station pair. The mean of the residuals for each station pair is 0.0 s, a strong indication that individual member events are collocated.

evidence for mixing between dacitic and more mafic source magma. Magma remained compositionally heterogeneous over the length of that eruption. They concluded that the 1986 eruption resulted from an injection of hot, mafic magma stored between 3 and 4 km b.m.s.l. This material mixed with more dacitic residual magma left in the edifice following the 1976 eruption. The source depth of 3 to 4 km is significantly deeper than the source constrained by cGPS modeling of the 2006 eruption, however. Both models suggest that magma storage and transport in the Augustine edifice takes place through a series of dikes, some of which are interconnected and some of which are not.

Volcano-tectonic (VT) seismicity caused by fluid and volatile transport is a commonly recorded feature of volcanoes before and during volcanic eruptions (for example, McNutt, 2005). Hill (1977) proposed that earthquake swarms result from the migration of fluids through a series of en echelon extension fractures linked to each other by small crack-tip shear fractures. Fracture mesh formation occurs within a constant stress field within a volume of rock, most favorably in materials with a high degree of heterogeneity and in the presence of low effective stress (Sibson, 1996), conditions likely to exist in a volcanic edifice. VT activity along the mesh

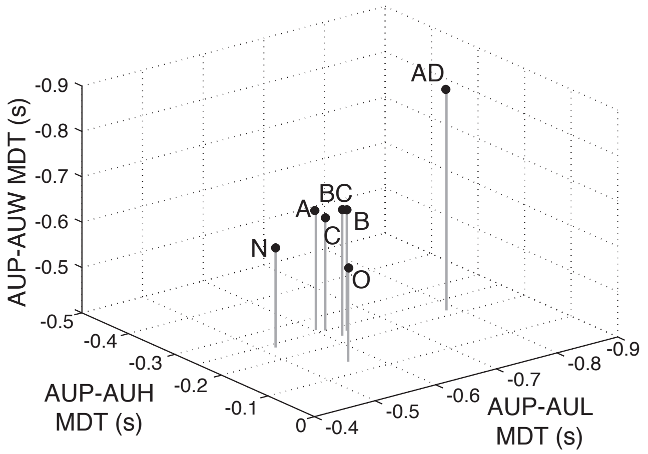

Figure 13. The median differential times (MDT) for a set of station-pairs for each family contain information on the relative location of event families in space. Here, the MDTs for station pairs AUP-AUH, AUP-AUL, and AUP-AUW are plotted for a number of well-recorded clusters occurring the 2006 eruption (see fig. 4*C* for family time ranges). On the basis of geometric arguments, family AD occurs higher in the edifice than the other families. Families C, BC, B, O, and N occur over the same period in early December but are not collocated on this diagram, indicating that multiple regions of the edifice can be simultaneously active.

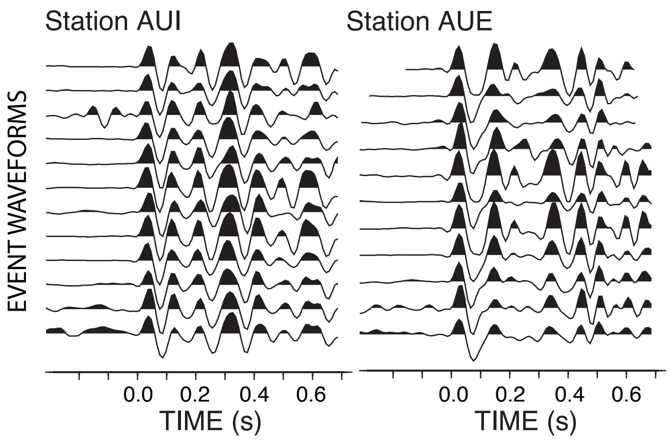

Figure 14. Waveforms for family AA, here shown at stations AUI and AUE, consist of deep earthquakes (~3 km b.m.s.l.) that occur from May through July 2006. All deep earthquakes in the AVO catalog occur in mid to late 2006. Only the flank stations recorded these earthquakes because of the timing.

of shear fractures could appear to be spatially and temporally variable (for example, Roman and Cashman, 2006), with small swarms of activity localizing on individual shears over shorter time scales. Magma transport through dike emplacement, as modeled for the 2006 Augustine eruption, can also generate VT swarms. Ukawa and Tsukahara (1996) suggested that VT swarm activity forms because of extension of wallrock ahead of a propagating dike tip. This model implies a spatial and temporal migration of seismicity in the direction of dike propagation. Roman (2005) showed that inflation of a dike would compress the surrounding wallrock and lead to generation of seismicity in a temporally and spatially random manner. Modeling suggests that seismicity caused by dike-tip propagation and by wallrock compression could be active at the same time (Roman and Cashman, 2006). Roman and Cashman (2006) compare seismicity and fault plane solutions at a number of volcanoes to each of the above models and conclude that at most compressive arc settings, the Roman (2005) and to a lesser extent the Hill (1977) model best explain recorded VT activity. Fracture mesh orientation would be controlled by the regional stress regime, while wallrock failure would reflect local perturbations to this regime. Well-constrained focal mechanism solutions can be used to distinguish between these two processes (Roman and Cashman, 2006).

Our observation that some waveforms repeat over multiple years suggests that in some regions of the edifice the VT source mechanism is nondestructive. Of the three models presented, this seems most consistent with the idea of shear failure along a fracture mesh. Volcanic edifices are fluid-rich and volatile-rich environments, and transport of materials within the edifice must constantly occur. Reported rates of fumoralic activity are fairly constant at Augustine. If transport does occur through a series of interconnected extension and shear fractures, periods of increased transport rate may lead to the periods of increased activity we identify as swarms making up individual event families. The mesh must evolve because of precipitation and mineralization within the fractures (Sibson, 1996). Seismicity not included in event families may be localized to shear fractures that form or reactivate variably in both space and time.

This interpretation does not preclude VT activity due to dike inflation or deflation within the edifice. If dikes are the primary magma transport and storage mechanism at Augustine, then wallrock adjustments due to volumetric changes in the existing dike complex may generate VT seismicity by locally perturbing the local stress field. Inflation may induce short-term compression in the surrounding wallrock and induce swarms of temporally and spatially related seismicity (Roman, 2005). Dike ascent during the precursory stage of the 2006 Augustine eruption is accompanied by increased seismicity rates (Cervelli and others, 2006; Mattia and others, 2008). If the ascending dike interacted with a preexisting dike network, as is posited for the 1986 Augustine eruption, then multiple dikes could have inflated or deflated over the course of the 2006 eruption. This may explain both the cloud-like pattern of dissimilar earthquakes that dominate the entire Augustine catalog and the swarms of highly similar waveforms generated during the 2006 eruption.

The largest identified swarms occurred as the ascending source dike reached near-surface elevations on December 9–11, 2005, and between explosive eruptions through January 2006 (fig. 4*C*). Locations of families identified during this period suggest that some seismicity generated over December 9–11, 2005, occurred ~700 to 800 m below the activity in January 2006 (this study; Sumiejski and others, 2009). We suggest that event families A, B, BC, and C are directly related to this ascending dike. All share similar waveform characteristics, such as frequency content and P onset sign (fig. 8), and the clusters are located very close to each other in space (fig. 13). However, we cannot distinguish if these swarms form because of failure along a propagating dike tip or within the surrounding wallrock during dike ascension. Cervelli and others (2006) and Mattia and others (2008) suggest that the ascending dike breaches the surface during the January 13, 2006, eruption. It is therefore likely that this dike causes the seismicity associated with the January 11 swarm (family AD). Seismicity occurring throughout the remainder of January is both related to summit activity (family AH) and to wallrock adjustments to changing pressures within the dike source at ~500 m a.m.s.l (family AC) (Sumiejski and others, 2009). Longer term magma storage may take place nearer ~300 m b.m.s.l. on the basis of modeling of cGPS data (for example, Mattia and others, 2008) recorded during the early precursory stage and the location of multiyear family LM (for example, Sumiejski and others, 2009).

Conclusions

Waveform similarity at Augustine volcano derived using waveform crosscorrelation techniques occurs over a number of time scales. Approximately 60 to 70 percent of volcano-tectonic events in the AVO catalog are not associated with event clusters containing more than 10 earthquakes. These events may be forming along shear fractures that form in conjunction with extension fractures and facilitate fluid movement within the volcanic edifice. Alternately, these events may reflect long-term wallrock failure caused by local stress perturbations associated with a series of interconnected storage dikes. Events forming families before the 2006 eruption exhibit a high degree of similarity over multiple years but generally consist of subsets of small temporally related swarms. These events would be consistent with either reactivation of shear fractures that form the fracture mesh systems or failure in wallrock near long-lived inflating or deflating dikes. Focal mechanisms would help distinguish between these two models.

Earthquakes recorded during the precursory phases of the 2006 eruption occur as swarms of similar earthquakes over periods of days or hours. The largest identified precursory swarms accompany reports of increased steaming and explosive eruptions at the summit, which are consistent with discrete dikes/sills opening to accommodate magma transport to the surface. Some event families appear directly associated with an ascending dike through late November and December 2006, but we cannot say whether these events occur along a propagating dike tip or within the surrounding wallrock without focal-mechanism data. Other event families clearly occur at the same time as dike ascension but occur throughout the volcanic edifice, suggesting that local stress perturbations activate a network of fractures or preexisting dikes. Combined with the generally low degree of event similarity at Augustine, the seismic results agree well with the hypothesis that magma transport and storage during eruptions involves numerous dikes located throughout the edifice (Roman and Cashman, 2006; Cervelli and others, this volume; Larsen and others, this volume; Power and Lalla, this volume).

Seismicity rate and event similarity decrease rapidly over the course of the 2006 eruption. The only family identified during the late eruptive and effusive phases contains relatively deep earthquakes between 3 and 5 km b.m.s.l. If the source dike for the 2006 eruption ascends from 0 km b.m.s.l. or deeper, these events may reflect posteruptive magma transport at the base of the Augustine magmatic system.

Acknowledgments

We thank James Dixon and the Alaska Volcano Observatory for access to waveform and pick data. Waveforms, shot locations and times, and parametric data from the active source experiment were obtained from the IRIS DMC. Stephanie Prejean provided helpful discussions. We thank Jeffery Freymueller, Charlotte Rowe, and Maurizio Battaglia for insightful reviews. Waveforms, picks, and crosscorrelation data reported in this study may be obtained by request through Heather DeShon. The material is based on research supported by NSF grant EAR-0409291 to Clifford Thurber.

References Cited

Aster, R.C., and Rowe, C.A., 2000, Automatic phase pick refinement and similar event association in large seismic datasets, *in* Thurber, C.H., and Rabinowitz, N., eds, Advances in seismic event location: Kluwer, Amsterdam, p. 231–263.

Battaglia, J., Thurber, C.H., Got, J.L., Rowe, C.H., and White, R.A, 2004, Precise relocation of earthquakes following the 15 June 1991 eruption of Mount Pinatubo, Philippines: Journal of Geophysical Research, v. 109, B07302, doi:10.1029/2003JB002959.

Buurman, H., and West, M.E., 2010, Seismic precursors to volcanic explosions during the 2006 eruption of Augustine Volcano, *in* Power, J.A., Coombs, M.L., and Freymueller, J.T., eds., The 2006 eruption of Augustine Volcano, Alaska: U.S. Geological Survey Professional Paper 1769 (this volume).

Cervelli, P.F., Fournier, T., Freymueller, J., and Power, J.A., 2006, Ground deformation associated with the precursory unrest and early phases of the January 2006 eruption of Augustine Volcano, Alaska: Geophysical Research Letters, v. 33, L18304, 10.1029/2006GL027219.

Cervelli, P.F., Fournier, T.J., Freymueller, J.T., Power, J.A., Lisowski, M., and Pauk, B.A., 2010, Geodetic constraints on magma movement and withdrawal during the 2006 eruption of Augustine Volcano, *in* Power, J.A., Coombs, M.L., and Freymueller, J.T., eds., The 2006 eruption of Augustine Volcano, Alaska: U.S. Geological Survey Professional Paper 1769 (this volume).

DeShon, H.R., Thurber, C.H., and Rowe, C., 2007, High-precision earthquake location and three-dimensional P wave velocity determination at Redoubt Volcano, Alaska: Journal of Geophysical Research, v. 112, B07312, doi:10.1029/2006JB004751.

Dixon, J.P., Stihler, S.D., Power, J.A., and Searcy, C., 2008, Catalog of earthquake hypocenters at Alaskan volcanoes; January 1 through December 31, 2006: U.S. Geological Survey Data Series 326, 78 p.

Dodge, D.A., 1996, Xadjust; a Matlab-based cross correlation analysis package: Seismological Research Letters, v. 67, p. 36.

Dodge, D.A., Beroza, G.C., and Ellsworth, W.L., 1995, Foreshock sequence of the 1992 Landers, California, earthquake and its implications for earthquake nucleation: Journal of Geophysical Research, v. 100, p. 9865–9880.

Du, W., Thurber, C.H., and Eberhart-Phillips, D., 2004, Earthquake relocation using cross correlation time delay estimates verified with the bispectrum method: Bulletin of the Seismological Society of America, v. 94, p. 856–866.

Got, J.L, Frechet, J., and Klein, F.W., 1994, Deep fault plane geometry inferred from multiplet relative relocation beneath the south flank of Kilauea: Journal of Geophysical Research, v. 99, p. 15375–15386.

Hill, D.P., 1977, A model for earthquake swarms: Journal of Geophysical Research, v. 82, p. 1347–1352.

Kienle, J., 1987, Mt. St. Augustine works, but how? [abs.]: Hawaii Symposium on How Volcanoes Work, Abstract Volume, p. 139.

Lalla, D.J., and Kienle, J., 1980, Problems in volcanic seismology on Augustine Volcano, Alaska [abs.]: Eos (Transactions American Geophysical Union), v. 61, p. 68.

Larsen, J.F., Nye, C.J., Coombs, M.L., Tilman, M., Izbekov, P., and Cameron, C., 2010, Petrology and geochemistry of the 2006 eruption of Augustine Volcano, *in* Power, J.A.,

Coombs, M.L., and Freymueller, J.T., eds., The 2006 eruption of Augustine Volcano, Alaska: U.S. Geological Survey Professional Paper 1769 (this volume).

Mattia, M., Palano, M., Aloisi, M., Bruno, V., and Bock, Y., 2008, High rate GPS data on active volcanoes; an application to the 2005-2006 Mt. Augustine (Alaska, USA) eruption: Terra Nova, v. 20, no. 2, p. 134–140.

McNutt, S.R., 2005, Volcanic seismology: Annual Reviews of Earth and Planetary Science, v. 33, p. 461–491.

Milne, J., 1886, Earthquakes and other earth movements: New York, D. Appleton and Company, 363 p.

Nikias, C.L., and Pan, R., 1988, Modeling of the 4th-order cumulants and phase estimation: Circuits Systems Signal Processing, v. 7, p. 291–325.

Nikias, C.L., and Raghuveer, M.R., 1987, Bispectrum estimation—a digital signal-processing framework: Proceedings of the IEEE, v. 75, p. 869–891.

Power, J.A., 1988, Seismicity associated with the 1986 eruption of Augustine Volcano, Alaska: Fairbanks, University of Alaska, M.S. thesis, 142 p.

Power, J.A., and Lalla, D.J., 2010, Seismic observations of Augustine Volcano, 1970–2007, *in* Power, J.A., Coombs, M.L., and Freymueller, J.T., eds., The 2006 eruption of Augustine Volcano, Alaska: U.S. Geological Survey Professional Paper 1769 (this volume).

Roman, D.C., 2005, Numerical models of volcanotectonic earthquake triggering on non-ideally oriented faults: Geophysical Research Letters, v. 32, L02304, doi:10.1029/2004GL021549.

Roman, D.C., and Cashman, K.V., 2006, The origin of volcano-tectonic earthquake swarms: Geology, v. 34, p. 457–460.

Roman, D.C., Cashman, K.V., Gardner, C.A., Wallace, P.J., and Donovan, J.J., 2006, Storage and interaction of compositionally heterogeneous magmas from the 1986 eruption of Augustine Volcano, Alaska: Bulletin of Volcanology, v. 68, p. 240–254, doi:10.1007/s00445-005-003-z.

Rowe, C.A., 2000, Correlation-based phase pick corrections and similar earthquake family identification in large seismic waveform catalogs: Socorro, New Mexico Institution of Mining & Technology, Ph.D. Thesis, 187 p.

Rowe, C.A., Aster, R.C., Borchers, B., and Young, C.J., 2002a, An automatic, adaptive algorithm for refining phase picks in large seismic datasets: Bulletin of the Seismological Society of America, v. 92, p. 1660–1674.

Rowe, C.A., Aster, R.C., Phillips, W.S., Borchers, B., Jones, R.H., and Fehler, M.C., 2002b, Using automated, high-precision repicking to improve delineation of microseismic structures at the Soultz geothermal reservoir: Pure and Applied Geophysics, v. 159, p. 563–596.

Rowe, C.A., Thurber, C.H., and White, R.A., 2004, Dome growth behavior at Soufriere Hills Volcano, Montserrat, revealed by relocation of volcanic event swarms, 1995-1996: Journal of Volcanology and Geothermal Research, v. 134, p. 199–221.

Rubin, A.M., Gillard, D., and Got, J.L., 1998, A reinterpretation of seismicity associated with the January 1983 dike intrusion at Kilauea Volcano, Hawaii: Journal of Geophysical Research, v. 103, p. 10003–10015.

Schaff, D.P., Bokelmann, G.H.R., Beroza, G.C., Waldhauser, F., and Ellsworth, W.L., 2002, High-resolution image of Calaveras Fault seismicity: Journal of Geophysical Research, v. 107, p. 2186, doi:10.1029/2001JB000633.

Shearer, P.M., 1998, Evidence from a cluster of small earthquakes for a fault at 18 km depth beneath Oak Ridge, southern California: Bulletin of the Seismological Society of America, v. 88, p. 1327–1336.

Sibson, R.H., 1996, Structural permeability of fluid-driven fault-fracture meshes: Journal of Structural Geology, v. 18, p. 1031–1042.

Sumiejski, L., Thurber, C., and DeShon, H.R., 2009, Relocation of eruption-related earthquake clusters at Augustine Volcano, Alaska, using station-pair differential times: Geophysical Journal International, v. 176, p. 1017–1022.

Ukawa, M., and Tsukahara, H., 1996, Earthquake swarms and dike intrusions off the east coast of Izu Peninsula, central Japan: Tectonophysics, v. 253, p. 285–303, doi:10.1016/0040-1951(95)00077-1.

Wallace, K.L., Neal, C.A., and McGimsey, R.G., 2010, Timing, distribution, and character of tephra fall from the 2005–2006 eruption of Augustine Volcano, *in* Power, J.A., Coombs, M.L., and Freymueller, J.T., eds., The 2006 eruption of Augustine Volcano, Alaska: U.S. Geological Survey Professional Paper 1769 (this volume).

Yung, S.K., and Ikelle, L.T., 1997, An example of seismic time picking by third-order bicoherence: Geophysics, v. 62, p. 1947–1952.

Zhou, H., 1994, Rapid three-dimensional hypocentral determination using a master station method, Journal of Geophysical Research: v. 99, p. 15439–15455.

The 2006 Eruption of Augustine Volcano, Alaska
Power, J.A., Coombs, M.L., and Freymueller, J.T., editors
U.S. Geological Survey Professional Paper 1769

Chapter 6

Distal Volcano-Tectonic Seismicity Near Augustine Volcano

Michael A. Fisher[1], Natalia A. Ruppert[2], Randall A. White[1], Ray W. Sliter[1], and Florence L. Wong[1]

Abstract

Clustered earthquakes located 25 km northeast of Augustine Volcano occurred more frequently beginning about 8 months before the volcano's explosive eruption in 2006. This increase in distal seismicity was contemporaneous with an increase in seismicity directly below the volcano's vent. Furthermore, the distal seismicity intensified penecontemporaneously with signals in geodetic data that appear to reveal a transition from magmatic inflation of the volcano to dike injection. Focal mechanisms for five events within the distal cluster show strike-slip-fault movement. Directly above the earthquake cluster, shallow (<5 km deep) folds and faults mapped using multichannel seismic-reflection data strike northeast, parallel to the regional structural grain. About 10 km northeast of Augustine Volcano, however, the Augustine-Seldovia arch, an important trans-basin feature, strikes west and intersects the northeast-striking structural zone. We propose that the fault causing the distal earthquake cluster strikes northwest, subparallel to the arch, and is a right-lateral strike-slip fault. Future earthquake monitoring might show whether increasing activity in the remote cluster can aid in making eruption forecasts.

Introduction

Augustine Volcano most recently erupted explosively during 2006, and intense shallow seismicity directly below the volcano's vent of the volcano preceded and accompanied this eruption (Cervelli and others, 2006, and this volume; Power and others, 2006). Contemporaneously with this volcanic and earthquake activity, seismicity occurred in a cluster located 25 km northeast of the volcano (figs. 1, 2). This distal seismicity ceased about 9 months after the eruption ended. On a worldwide basis, similar distal seismicity has occurred before many explosive eruptions (for example, White and Rowe, 2006). Thus, a future increase in distal seismicity near Augustine Volcano might help predict an eruption.

Regional Setting and Basin Structure

Augustine Volcano is part of the active magmatic arc associated with plate convergence at the Alaska-Aleutian subduction zone. The volcano lies within the southwestern part of the Cook Inlet forearc basin (fig. 1) and rests on a thick section of sedimentary and volcanic rocks that indicate protracted near-trench tectonics, including Late Triassic rocks that signal a transition from reef building far from volcanic sources to proximal magmatic-arc sedimentation (Wang and others, 1988), and thick Early Jurassic volcaniclastic rocks that record a vigorous volcanic arc near the Cook Inlet basin (Detterman and Hartsock, 1966; Fisher and Magoon, 1978). The Jurassic and Cretaceous batholiths exposed extensively along the northwest side of the Cook Inlet basin indicate active subduction during that period.

These plutonic rocks likely form the basement complex beneath the Cook Inlet basin, especially near Augustine Volcano. The basement complex might also include early Mesozoic oceanic crust, following from a tectonic analogy we draw between the Cook Inlet basin and the Great Valley of California, both of which are Mesozoic forearc basins. The Great Valley appears to be floored by oceanic crust, the distribution and structure of which is much debated (see summary cross sections in Constenius and others, 2000). The point is that the basement under Cook Inlet might have a complex structure.

We determined the upper-crustal structure near Augustine Volcano from a grid of multichannel seismic-reflection (MCS) lines collected by Western Geophysical, Inc., in 1975 (fig. 1). The data were obtained with an Aquapulse source, an array of six sleeve exploders in which propane and oxygen

---

[1] U.S. Geological Survey, 345 Middlefield Rd., Menlo Park, CA 92028.

[2] Geophysical Institute, University of Alaska Fairbanks, 903 Koyukuk Dr., Fairbanks, AK 99775.

were detonated to produce an acoustic pulse with reduced bubble oscillation. The survey ship employed two streamers—one 2,380 m long with 72 recording channels, and the other 184 m long with 12 channels designed to achieve a high spatial resolution.

MCS data reveal that the Iniskin structural zone strikes northeast through lower Cook Inlet (fig. 1). The structural zone is made up of reverse faults and faulted anticlines (fig. 3). The vertical component of offset along some faults amounts to 500 m. The total along-strike length of this zone is unknown but is at least 70 km. The MCS section in figure 3*C* shows the Iniskin structural zone extending southwestward to within about 10 km of Augustine Volcano (fig. 1). However, this zone's total southwestward extent remains unknown because the zone is not evident in Mesozoic rocks exposed on the northern part of the Alaska Peninsula, southwest of Augustine Volcano.

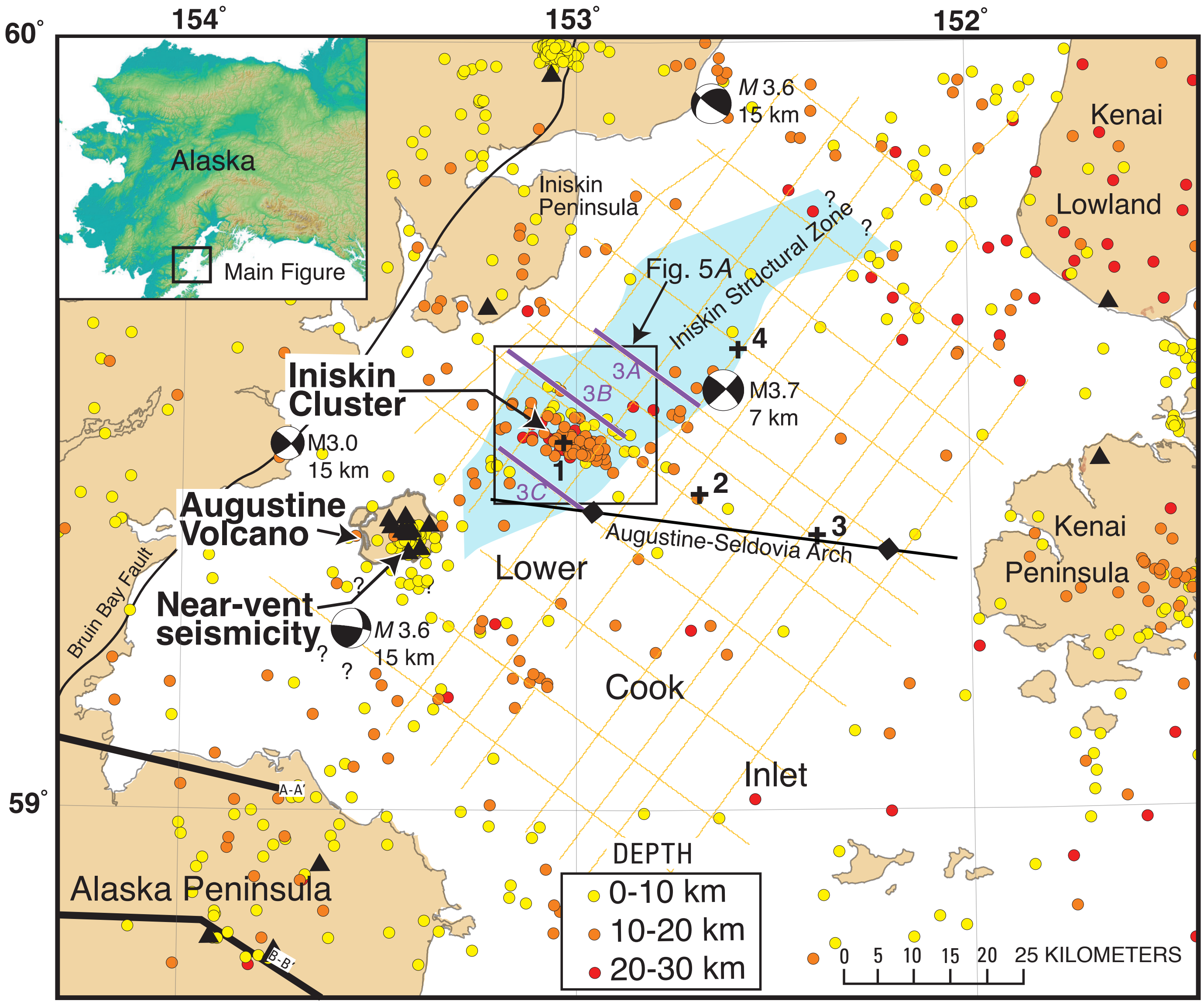

Figure 1. Map of Lower Cook Inlet, Alaska, showing the location of Augustine Volcano, the Iniskin earthquake cluster, and the Iniskin structural zone (blue area). Seismic events (colored dots) have not been relocated. Black rectangle on index map denotes area of relocated events in figure 5. Orange lines, show track lines of 1975 Western Geophysical, Inc., seismic-reflection survey; purple lines, multichannel seismic reflection sections shown in figure 3; Black lines labeled A-A′ and B-B′ indicate geologic cross sections by Detterman and Reed (1980) and Riehle and others (1993), respectively. Numbered black crosses show oil wells near Augustine Volcano: 1, Hawk #1; 2, Ibis #1; 3, South Arch #1; 4, COST #1. Earthquake epicenters are from the Alaska Earthquake Information Center (AEIC) catalog (1971-2006); earthquake focal mechanisms are lower-hemispheric projections. Black triangles show seismograph stations.

Geologic cross sections (A–A’, B–B’, fig. 1) from there show little-deformed, mainly flat lying rocks (Detterman and Reed, 1980; Riehle and others, 1993).

Folds and faults within the Cook Inlet basin strike consistently northeast (fig. 4). Northwest-striking structures are not evident in offshore areas, nor do such structures deform the major faults, such as the Bruin Bay Fault, that bound the basin on the northwest and southeast. The Iniskin structural zone strikes northeast, conforming to the regional structural grain.

The prime exception to the consistent northeastward strike is the westward strike of the Augustine-Seldovia arch, which extends across the basin to near Augustine Volcano (figs. 1 and 4). This arch is a fundamental feature of the Cook Inlet basin because it forms the south flank of the thick (7 km) accumulation of Cenozoic rocks north of the arch (for example Kirschner and Lyon, 1973). South of the arch, Cenozoic rocks are thin (<1 km thick) or absent (Fisher and Magoon, 1978). Evidently, the arch forms a trans-basin hinge that enabled rapid Cenozoic deepening of the northern part of the basin.

Seismicity

The regional seismicity of lower Cook Inlet, recorded in by the Alaska Earthquake Information Center (AEIC) catalog (1971–2006), is diffuse and reveals few patterns in map view (fig. 1), except in two areas of heightened activity. The first area encompasses abundant shallow earthquakes directly below the volcano’s vent. This seismicity was recorded by seismographs located on the volcano and on nearby parts of

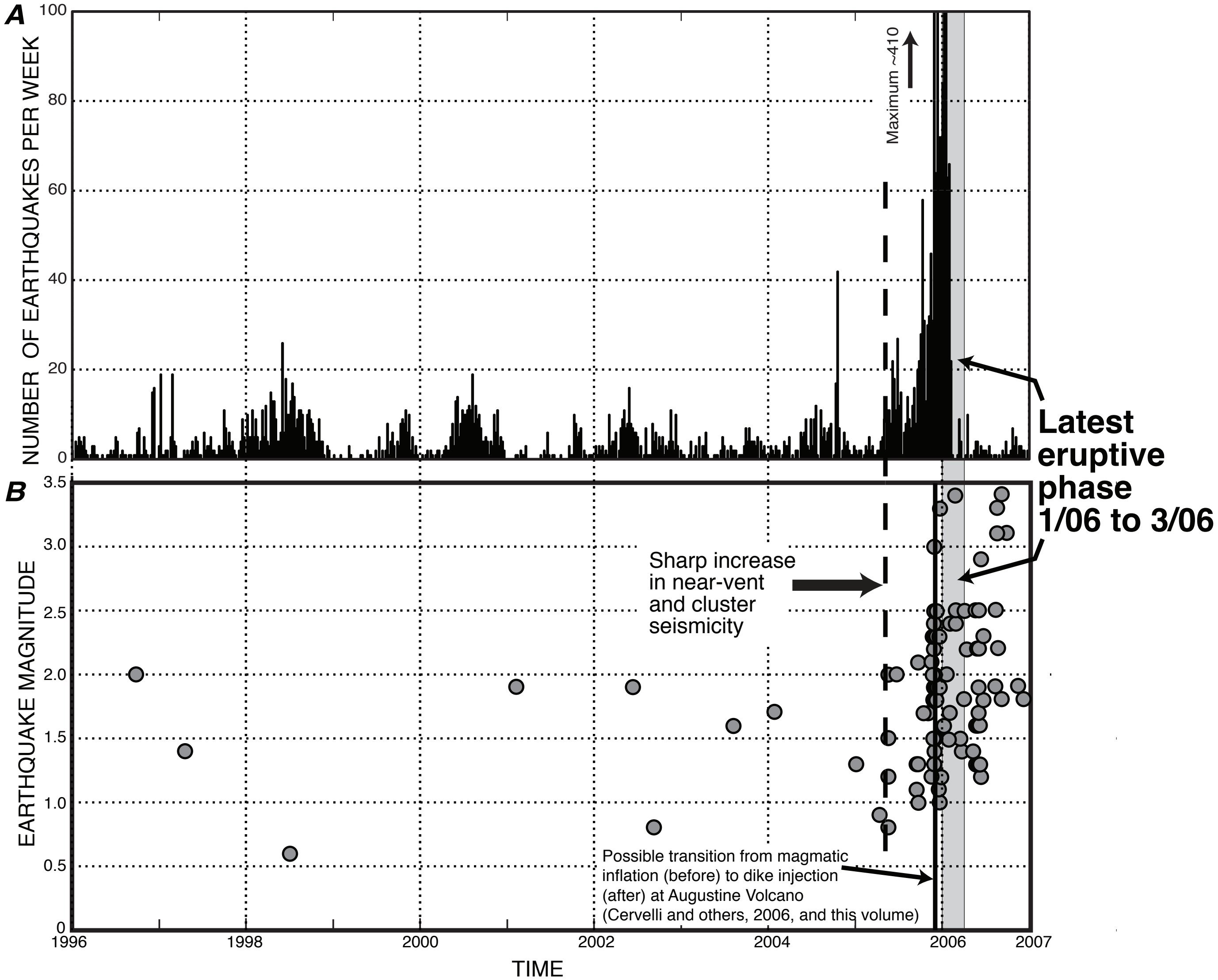

Figure 2. Earthquake activity over time at Augustine Volcano. *A*, near vent seismicity, *B*, seismicity within the Iniskin cluster. Cluster activity began about 8 months before the 2006 eruption and ended about 9 months afterward. Vertical dashed line denotes the abrupt increase in activity in late 2005.

the Alaska mainland. In general, near-vent earthquakes have very small magnitudes (*M*<=1.2). This activity has been attributed to volcanic processes because it is concentrated near sea level, directly below the volcanic vent. After 1996, near-vent seismicity oscillated between infrequent and moderately frequent until late 2005, when the frequency intensified to more than 100 events per week (fig. 2*A*).

The second area of heightened activity, which we call the Iniskin cluster, is located 25 km northeast of the volcano (fig. 1). Events making up this cluster were recorded by the Alaska regional seismic network; the nearest seismic stations are located on Augustine Volcano (fig. 1). Before we relocated the cluster events, their average horizontal and vertical location uncertainties were 3.6 and 4.1 km, respectively, at the 67 percent confidence level. In the worst case of the smallest events recorded by only a few stations, such uncertainties were as large as 10 km. Before being relocated, the group of epicenters was elongated northwest-southeast ward (fig. 1), but as we describe below, the relocated epicenters fill a compact area with a poorly expressed elongation.

Since 1996, near-vent earthquakes have numbered nearly 3,000 (Dixon and others, 2007), but only about 100 events have occurred within the Iniskin cluster. Cluster earthquakes were infrequent until mid-2005, when they became more frequent (fig. 2*B*). This increase in frequency occurred contemporaneously with the rapid rise in near-vent seismicity (compare figs. 2*A* and 2*B*), and both increases preceded by about 8 months the latest explosive eruption of Augustine Volcano. The level of earthquake activity within the Iniskin cluster remained relatively high throughout most of 2006, slowing only toward the end of the year. No events occurred in October and November, and only one in December.

An abrupt offset in geodetic data recorded during November 2006 indicates a change in the style of deformation at Augustine Volcano (Cervelli and others, 2006, and this volume). Before this offset, geodetic data most likely reveal magmatic inflation of the volcano, whereas afterward such data point to the onset of dike intrusion. The timing of this change in style of deformation coincides with a sharp increase in seismicity within the Iniskin cluster (fig. 2*B*).

To evaluate the detailed distribution of earthquakes within the Iniskin cluster, we relocated events, using the double-difference algorithm hypoDD (Waldhauser and

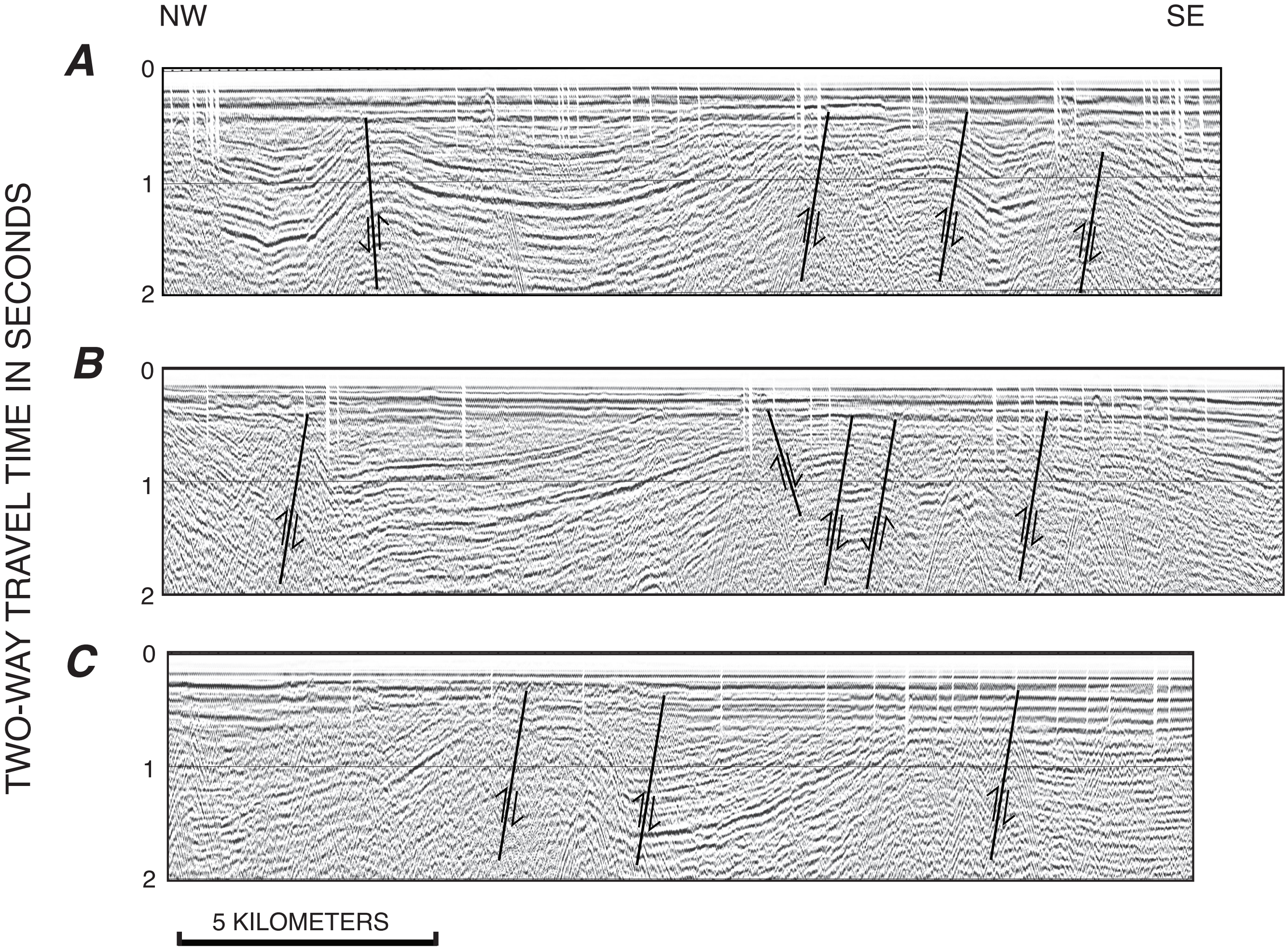

Figure 3. Multichannel seismic-reflection sections in lower Cook Inlet (fig. 1), collected with short survey streamer across the folds and faults of the Iniskin structural zone northeast of Augustine Volcano.

Ellsworth, 2000). Altogether, we relocated 108 events within 20 km of the center of the Iniskin cluster, using the catalog p- and s-wave arrivals and the standard plane-layer velocity model utilized by the AEIC for locating events in the study area (fig. 1). Because the number of events was small, we were able to use the singular-value decomposition approach, which is useful for working with small earthquake groupings because it provides information on the resolvability of hypocentral parameters and adequately represents location errors (Waldhauser, 2001). We allowed a maximum separation of 20 km between linked events and a maximum station distance of 300 km. The average offset between linked events was 4.6 km, and each event pair averaged 11 links.

The relocated events collapsed into a dense cluster less than 5 km across and from 11 to 16 km deep (figs. 5*B*–5*E*). The mean absolute location errors were 0.9 km horizontally and 1.2 km vertically, and the relative location accuracy between events was 32 m horizontally and 47 m vertically.

We calculated focal mechanisms for five events with magnitudes ranging from 3.1 to 3.4, using p-wave first motions and the program FPFIT (fig. 6) (Reasenberg and Oppenheimer, 1985). For all five events, the number of available first-motion picks ranged from 11 to 20; only one event had fewer than 15 picks. Regional stations in Cook Inlet provide good azimuthal coverage of the focal sphere. All mechanisms consistently indicate strike-slip faulting (fig. 5*A*). Although some uncertainity may remain in the focal-plane strike and dip estimates, the overall strike-slip sense of motion inferred from the five focal mechanisms is well constrained. By analyzing p-wave first motions for the events for which focal-mechanism data are available, we noted that earthquakes within the Iniskin cluster are spatially diverse but occupy a small volume and reflect a consistent mode of faulting.

Discussion

Strike of the Seismogenic Fault

Focal mechanisms for five earthquakes within the Iniskin cluster (fig. 5*A*) and for an M 3.7 event, 7 km deep and located northwest of the cluster along the Iniskin structural zone (fig. 1), all indicate that cluster seismicity results from strike-slip faulting. The main unresolved question is which nodal plane reveals the seismogenic fault.

One answer to this question is obtained from correlating nodal planes to the northeastward strike of the Iniskin structural zone (fig. 1). The northeast-striking nodal planes from all focal mechanisms closely parallel the strike of this zone, which, in turn parallels the regional structural grain of the basin (fig. 4). If this correlation is correct, then the cluster seismicity results from left-lateral oblique faulting. An important consideration in this analysis is that MCS data (for example fig. 3*C*), show the Iniskin structural zone extending southwestward from the Iniskin cluster, and so choosing the northeast-striking nodal plane relates the seismicity to a through going structure that connects the cluster with the volcano.

Alternatively, the northwest-striking nodal planes might be associated with one or more faults subparallel to the Augustine-Seldovia arch. About 10 km northeast of Augustine Volcano, this west-striking arch intersects the northeast-striking Iniskin structural zone (figs. 1, 4). As mentioned above in the section entitled “Regional Setting and Basin Structure,” this arch is the primary transverse structure within the southern part of the Cook Inlet basin. Although raw earthquake

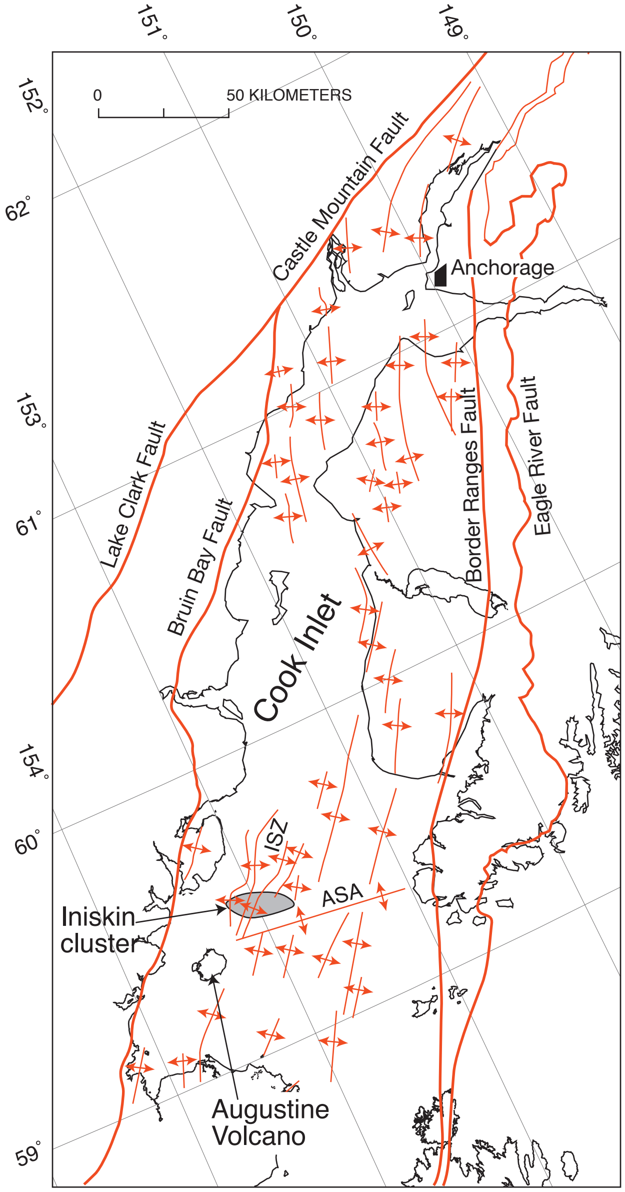

Figure 4. Map of geologic structures and major basin-bounding faults in the Cook Inlet basin. All features share a regional northeastward strike (Kirschner and Lyon, 1973; Magoon and others, 1976; Fisher and Magoon, 1978; Wilson and others, 1999; Haeussler and others, 2000). ISZ, Iniskin Structural Zone; ASA, Augustine-Seldovia Arch.

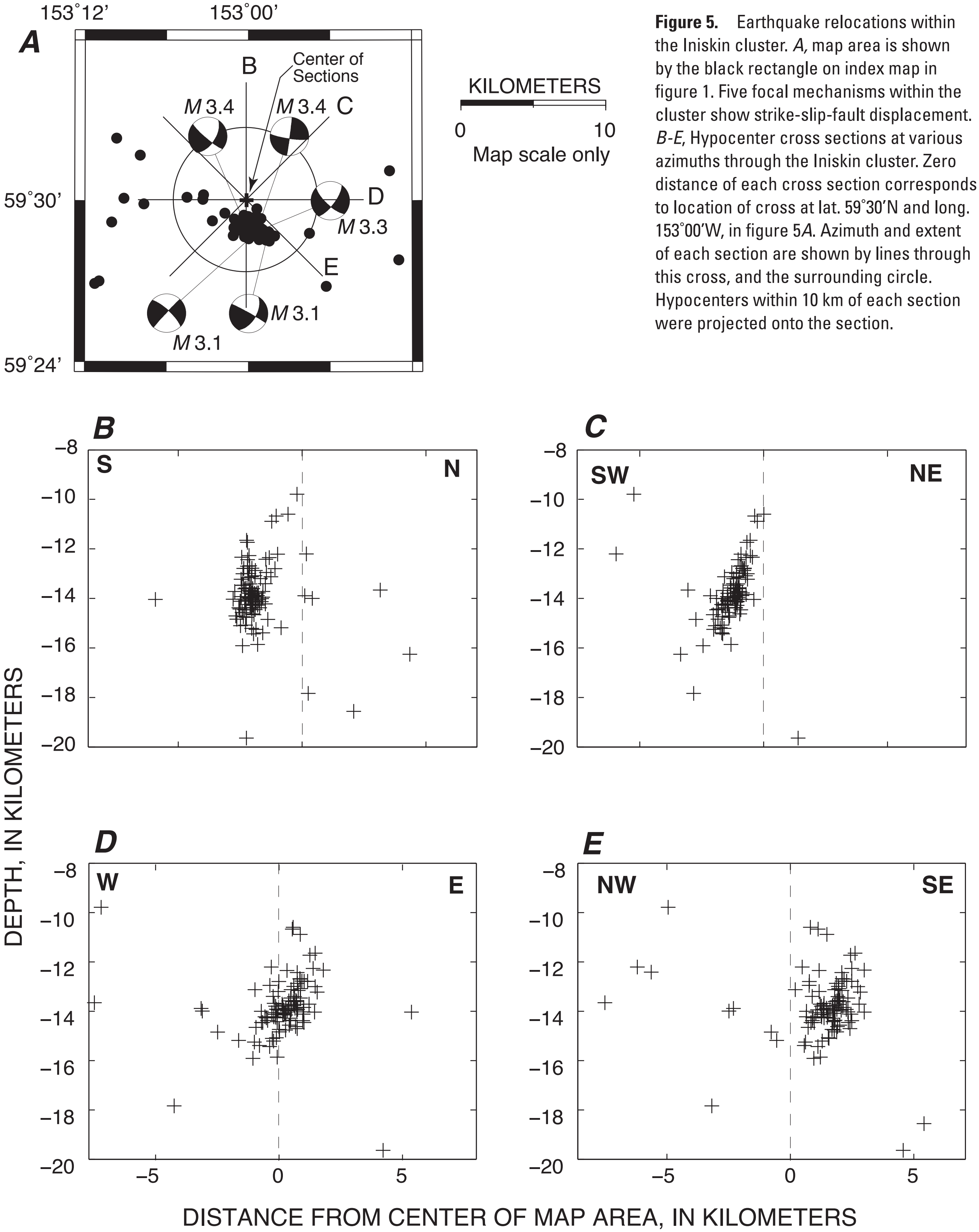

Figure 5. Earthquake relocations within the Iniskin cluster. *A,* map area is shown by the black rectangle on index map in figure 1. Five focal mechanisms within the cluster show strike-slip-fault displacement. *B-E*, Hypocenter cross sections at various azimuths through the Iniskin cluster. Zero distance of each cross section corresponds to location of cross at lat. 59°30′N and long. 153°00′W, in figure 5*A*. Azimuth and extent of each section are shown by lines through this cross, and the surrounding circle. Hypocenters within 10 km of each section were projected onto the section.

epicenters of events within the Iniskin cluster portray the cluster with a strong northwest-southeastward elongation (fig. 1), which seemingly fits this alternative answer, the relocated events form a dense central group with scattered outlying epicenters (fig. 5*A*). Overall, the relocated events show only a weak geographic elongation.

Of the four hypocenter cross sections in figure 5, the northwest-southeast cross section (fig. 5*C*) seems to be most nearly perpendicular to the earthquake cluster, indicating a northwest-striking right-lateral strike-slip fault sub parallel to the Augustine-Seldovia arch and perpendicular to the regional structural grain. Furthermore, regional stress determined from studies of earthquake activity at volcanoes near Augustine, notably Mounts Spurr, Iliamna, and Redoubt, indicate a northwestward direction of maximum principal stress (Jolly and others, 1994; Roman and others, 2004; Sanchez and others, 2004), suggesting that right-lateral strike-slip faults would strike northwest, at an angle of about 30˚ to the maximum stress direction. This northwestward direction of maximum principal stress agrees with the observations by Ruppert (2008), who used earthquake focal mechanisms from southern Alaska to calculate best-fitting stress tensors. Near Augustine Volcano, west- or northwest-striking strike-slip faults should predominate.

The ambiguity concerning the nodal plane partly arises because MCS data reveal the structure only of shallow (<7 km) crustal levels, because of limited seismic-source strength, whereas the relocated hypocenters in the Iniskin cluster range from 11 km to 16 km in depth. In comparison, near Augustine Volcano, the top of basement is about 10 km deep (see Fisher and Magoon, 1978, fig. 10). Thus, the seismicity appears to have originated within the basement complex below the Cook Inlet basin.

The northwest-striking nodal plane, then, may reveal a basement fault that could have originated as long ago as the early Mesozoic, the likely age of the basement complex. To produce the cluster seismicity, this fault would have been reactivated under the current stress regime as a right-lateral strike-slip fault.

Clearly, Augustine Volcano is situated at a complex structural crossroads. In our opinion, the Iniskin cluster most likely occurred along a northwest-striking right-lateral strike-slip fault associated with the trans basin Augustine-Seldovia arch. The fault might be a reactivated basement structure. The most troublesome aspect of this interpretation is that MCS data do not reveal a right-lateral transverse offset in the Iniskin structural zone directly above the Iniskin cluster.

Connection Between Seismicity and Volcanism

The close temporal association between abrupt increases in near-vent and cluster seismicity (figs. 2) and the fact that both increases preceded an explosive eruptive phase at Augustine Volcano by about 8 months suggest that magma flux and the seismogenic strike-slip fault are closely linked within the crustal stress field, as has been reported for other volcanoes. In fact, numerous studies of volcanic regions detail the close

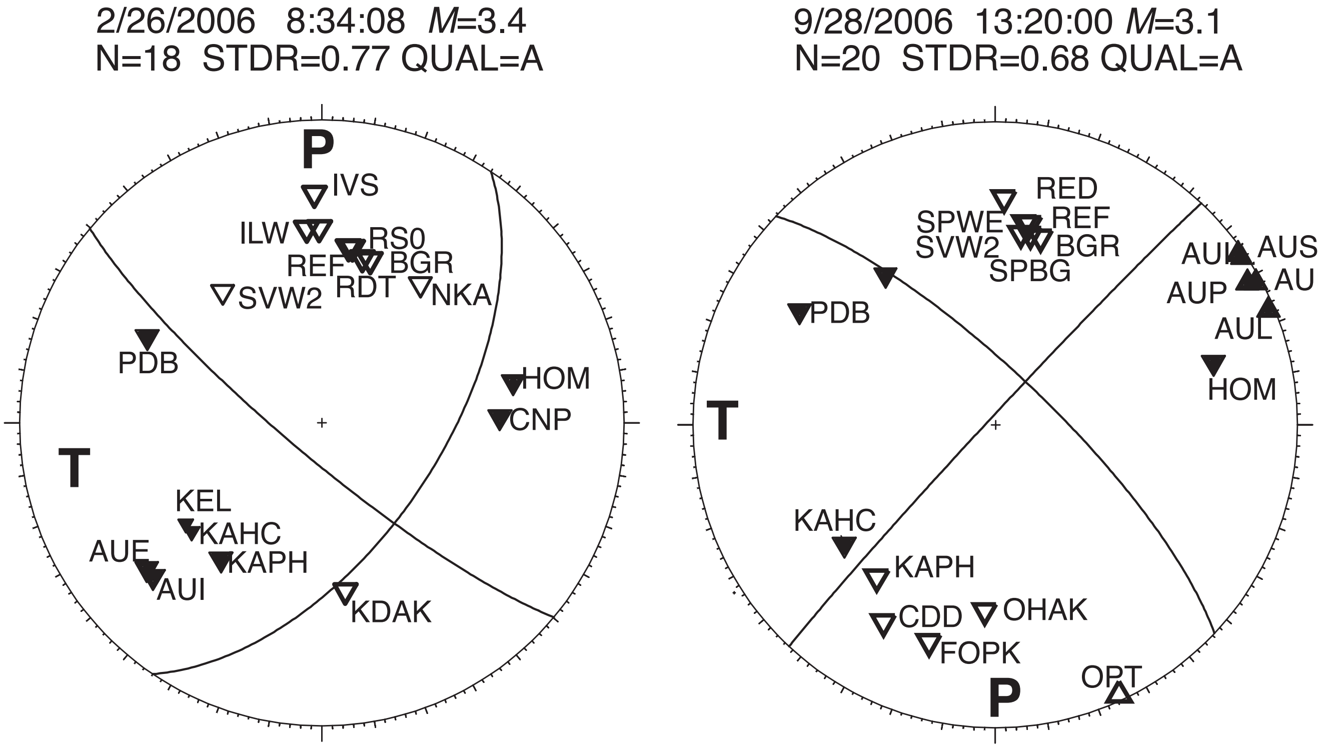

Figure 6. Two examples of p-wave first-motion focal mechanisms for events in the Iniskin cluster, both showing strike-slip motion.

coupling between earthquakes and volcanism and show that magmatic activity can trigger seismicity, and vice versa (Nostro and others, 1998; Hill and others, 2002; Toda and others, 2002; Feuillet and others, 2004; Diez and others, 2005; Manga and Brodsky, 2006; Parsons and others, 2006). Commonly, this triggering requires only subtle changes in Coulomb stress because the volcanic and earthquake systems are poised near critical points. White and Rowe (2006) compiled 25 examples from around the world in which distal earthquake clusters, such as the one we report on here, occurred from 2 to 30 km away from volcanoes just before they erupted. For example, Plinian eruptions of El Chichón (1982; Jimenez and others, 1999) and Mount Pinatubo (1991; Harlow and others, 1996) were preceded by distal earthquake swarms that began 2-26 months before cataclysmic eruptions. The ongoing eruption of South Soufriere Hills Volcano that began in 1995 was preceded by distal seismicity that occurred during the preceding 2 years (Aspinall and others, 1998). Thus, the distal volcano-tectonic seismicity we describe at Augustine Volcano conforms with observations worldwide.

Near Augustine Volcano, the coincident near-vent and distal seismicity appears to have occurred only once because no previous eruption of the volcano is known to have stimulated seismicity in the area of the Iniskin cluster. No candidate events are evident in the AEIC catalog. One possible reason for the dearth of earlier events is poor detection by the dispersed regional seismic network in Alaska before the 1990s. Another possible reason is that before 2005, shear stress within the asperity causing the Iniskin cluster had not attained near-critical values, and so volcanism before the 2006 eruption was an insufficient trigger. If so, then stress in the asperity causing the Iniskin cluster may need to rebuild after the 2006 seismicity. This conclusion bears critically on the use of distal seismicity, like the Iniskin cluster, to predict future eruptions at Augustine Volcano.

Conclusion

Clustered earthquakes located 25 km northeast of Augustine Volcano became more numerous over the 8 months just before the volcano’s 2006 explosive phase, and this seismicity abated within the 9 months after the eruption ceased. Focal mechanisms from events within the cluster reveal strike-slip faulting. We conclude that the earthquake cluster occurred along a northwest-striking right-lateral strike-slip fault because the cluster occurred near the trans-basin Augustine-Seldovia arch. The fault may be a reactivated basement structure. This interpreted fault strikes perpendicularly to a shallow structural zone, interpreted from MCS data, which includes reverse faults and anticlines. These structures, however, reveal no transverse offset. The clustered earthquakes near Augustine Volcano are similar to many examples of preeruption seismicity reported at volcanoes around the world. Recurrence of earthquake activity in or near the Iniskin cluster might be useful in predicting an imminent eruption of Augustine Volcano.

Acknowledgments

We thank the Geophysical Institute, University of Alaska Fairbanks and the Office of the Alaska State Seismologist for their support of part of this research. Reviews of the manuscript by Judith E. Fierstein and Thomas E. Moore of the U.S. Geological Survey, as well as two anonymous reviewers greatly improved this report.

References Cited

Aspinall, W.P., Miller, A.D., Lynch, L.L., Latchman, J.L., Stewart, R.C., White, R.A., and Power, J.A., 1998, Soufriere Hills eruption, Montserrat, 1995–1997; volcanic earthquake locations and fault plane solutions: Geophysical Research Letters, v. 25, p. 3397–3400.

Cervelli, P.F., Fournier, T.J., Freymueller, J.T., and Power, J.A., 2006, Ground deformation associated with the precursory unrest and early phases of the January 2006 eruption of Augustine Volcano, Alaska: Geophysical Research Letters, v. 33, doi:10.1029/2006GL027219, p. 5.

Cervelli, P.F., Fournier, T.J., Freymueller, J.T., Power, J.A., Lisowski, M., and Pauk, B.A., 2010, Geodetic constraints on magma movement and withdrawal during the 2006 eruption of Augustine Volcano, *in* Power, J.A., Coombs, M.L., and Freymueller, J.T., eds., The 2006 eruption of Augustine Volcano, Alaska: U.S. Geological Survey Professional Paper 1769 (this volume).

Constenius, K., Johnson, R.A., Dickinson, W.R., and Williams, T.A., 2000, Tectonic evolution of the Jurassic-Cretaceous Great Valley forearc, California; Implications for the Franciscan thrust-wedge hypothesis: Geological Society of America Bulletin, v. 112, p. 1703–1723.

DeShon, H.R., Thurber, C.H., and Rowe, C., 2007, High-precision earthquake location and three-dimensional P wave velocity determination at Redoubt Volcano, Alaska: Journal Geophysical Research, v. 112, doi:10.1029/2006JB004751, 24 p.

Detterman, R.L., and Reed, B.L., 1980, Stratigraphy, structure, and economic geology of the Iliamna Quadrangle, Alaska: U.S. Geological Survey Bulletin 1368-B, p. B1-B86, 81 sheet, scale 1:250,000.

Detterman, R.L., and Hartsock, J.K., 1966, Geology of the Iniskin-Tuxedni region, Alaska: U.S. Geological. Survey Professional Paper 512, p. 1–78.

Diez, M., La Femina, P.C., Connor, C.B., Strauch, W., and Tenorio, V., 2005, Evidence for static stress changes triggering the 1999 eruption of Cerro Negro Volcano, Nicaragua and regional aftershock sequences: Geophysical Research Letters, v. 32, doi:10.1029/2004GL021788, p. 4.

Dixon, J.P., Stihler, S.D., and Power, J.A., 2007, Catalog of earthquake hypocenters at Alaskan volcanoes: January 1 through December 31, 2006: U.S. Geological Survey Data Series 326, 79 p. Also available online at [http://pubs.usgs.gov/ds/367].

Feuillet, N., Nostro, C., Chiarabba, C., and Cocco, M., 2004, Coupling between earthquake swarms and volcanic unrest at the Alban Hills Volcano (central Italy) modeled through elastic stress transfer: Journal of Geophysical Research, v. 109, doi:10.1029/2003JB002419, p. 16.

Fisher, M.A., and Magoon, L.B., 1978, Geologic framework of lower Cook Inlet, Alaska: American Association of Petroleum Geologists Bulletin, v. 62, p. 373–402.

Haeussler, P.J., Bruhn, R.L., and Pratt, T.L., 2000, Potential seismic hazards and tectonics of the upper Cook Inlet basin, Alaska, based on analysis of Pliocene and younger deformation: Geological Society of America Bulletin, v. 112, p. 1414–1429.

Harlow, D.H., Power, J.A., Laguerta, E.P., Ambubuyog, G., White, R.A., and Hoblitt, R.P., 1996, Percursory seismicity and forecasting of the June 15, 1991, eruption of Mount Pinatubo, *in* Newhall, C.G., and Punongbayan, R.S., eds., Fire and mud; eruptions and lahars of Mount Pinatubo: Seattle, University of Washington Press, p. 285–306.

Hill, D.P., Pollitz, F., and Newhall, C., 2002, Earthquake-volcano interactions: Physics Today, v. 55, no. 11, p. 41–47.

Jimenez, Z., Espindola, V.H., and Espindola, J.M., 1999, Evolution of the seismic activity from the 1982 eruption of El Chinchon volcano, Chiapas, Mexico: Bulletin of Volcanology v. 61, p. 411–422.

Jolly, A.D., Page, R.A., and Power, J.A., 1994, Seismicity and stress in the vicinity of Mount Spurr volcano, south central Alaska: Journal of Geophysical Research v. 99, p. 15,305–15,318.

Kirschner, C.E., and Lyon, C.A., 1973, Stratigraphic and tectonic development of Cook Inlet petroleum province, *in* Pitcher, M.G., ed., Arctic Geology, American Association of Petroleum Geologists Memoir 19, p. 396–407.

Magoon, L.B., Adkison, W.L., and Egbert, R.M., 1976, Map showing geology, wildcat wells, Tertiary plant fossil locations, K-Ar dates, and petroleum operations, Cook Inlet area, Alaska: U.S. Geological Survey Miscelaneous Investigations I-1019, 3 sheets, scale 1:250, 000.

Manga, M., and Brodsky, E., 2006, Seismic triggering of eruptions in the far field; volcanoes and geysers: Annual Reviews of Earth Planetary Science, v. 34, p. 263–291.

Nostro, C., Stein, R.S., Cocco, M., Belardinelli, M.E., and Marzocchi, W., 1998, Two-way coupling between Vesuvius eruptions and southern Apennine earthquakes, Italy, by elastic stress transfer: Journal of Geophysical Research, v. 103, p. 24,487–424,504.

Parsons, T., Thompson, G.A., and Cogbill, A.H., 2006, Earthquake and volcano clustering via stress transfer at Yucca Mountain, Nevada: Geology, v. 34, p. 785–788.

Power, J.A., Nye, C.J., Coombs, M.L., Wessels, R.L., Cervelli, P.F., Dehn, J., Wallace, K.L., Freymueller, J.T., and Doukas, M.P., 2006, The reawakening of Alaska's Augustine volcano: Eos (American Geophysical Union Transactions), v. 87, no.37, p. 373, 377.

Reasenberg, P., and Oppenheimer D.H., 1985, FPFIT, FPPLOT, and FPPAGE; Fortran computer programs for calculating and displaying earthquake fault-plane solutions: U.S. Geological Survey Open File Report. 85-739, 37 p.

Riehle, J.R., Detterman, R.L., Yount, M.E., and Miller, J.W., 1993, Geologic map of the Mount Katmai Quadrangle and adjacent parts of the Naknek and Afognak Quadrangles, Alaska: U.S. Geological Survey Miscellaneous Investigations Series Map 2204, p. 1 sheet, scale 1:250,000.

Roman, D.C., Power, J.A., Moran, S.C., Cashman, K.V., Doukas, M.P., Neal, C.A., and Gerlach, T.M., 2004, Evidence for dike emplacement beneath Iliamna Volcano, Alaska in 1996: Journal of Volcanology and Geothermal Research, v. 130, p. 265–284.

Ruppert, N.A., 2008, Stress map for Alaska from earthquake focal mechanisms, *in* Freymueller, J.T., Haeussler, P.J., Wesson, R.L., and Ekstrom, G., eds., Active tectonics and seismic potential of Alaska: American Geophysical Union Monograph 179, p. 351–369.

Sanchez, J.J., Wyss, M., and McNutt, S.R., 2004, Temporal-spatial variations of stress at Redoubt volcano, Alaska, inferred from inversion of fault plane solutions: Journal of Volcanology and Geothermal Research, v. 130, p. 1–30.

Toda, S., Stein, R.S., and Sagiya, T., 2002, Evidence from the A.D. 2000 Izu Islands earthquake swarm that stressing rate governs seismicity: Nature, v. 419, p. 58–61.

Waldhauser, F., 2001, HypoDD – A program to compute double-difference hypocenter locations, U.S. Geological Survey Open-File Report 01-113, 25 p.

Waldhauser, F., and Ellsworth, W.L., 2000, A double-difference location algorithm: Method and application to the northern Hayward fault, California: Bulletin of the Seismological Society of America, v. 90, p. 1353–1368.

Wang, J., Newton, C.R., and Dunne, L., 1988, Late Triassic transition from biogenic to arc sedimentation on the Peninsular terrene—Puale Bay, Alaska Peninsula: Geological Society of America Bulletin, v. 100, p. 1466–1478.

White, R., and Rowe, C., 2006, Volcano-tectonic earthquake sequences near active volcanoes and their use in eruption forecasting [abs.]: Seismological Research Letters, v. 77, no. 2, p. 240.

Wilson, F.H., Detterman, R.L., and DuBois, G.D., 1999, Digital data for the geologic framework of the Alaska Peninsula, southwest Alaska, and the Alaska Peninsula terrane: U.S. Geological Survey Open-File Report 99-317 [http://wrgis.wr.usgs.gov/open-file/of99-317/].

The 2006 Eruption of Augustine Volcano, Alaska
Power, J.A., Coombs, M.L., and Freymueller, J.T., editors
U.S. Geological Survey Professional Paper 1769

Chapter 7

A Two-Step Procedure for Calculating Earthquake Hypocenters at Augustine Volcano

By Douglas J. Lalla[1] and John A. Power[2]

Abstract

This chapter describes a two-step technique for determining earthquake hypocenters at Augustine Volcano. The algorithm, which was originally developed in the mid-1970s, was designed both to overcome limitations in the standard earthquake-location programs available at the time and to take advantage of the detailed seismic-velocity information obtained at Augustine Volcano. Hypocenters are calculated on the basis of a two-dimensional (2D) ray-tracing procedure that accounts for in plane lateral discontinuities within the seismic velocity structure. This algorithm calculates the minimum P- and S-wave travel time between theoretical grid points embedded in the velocity structure to each station in the seismic network. Station corrections that account for the differences between the model and actual velocity structure are derived from a time-term analysis of the 1975 active-source seismic experiment. Each relocated hypocenter is assigned to the grid point with the lowest rms residual between observed and calculated arrival times. Statistical techniques are used to assess the effect of random errors in P-wave-arrival determination on hypocentral location. These tests suggest that the 2D ray-tracing procedure presented here is able to resolve earthquake hypocenter depths to within 0.25 km between the volcano's summit and sea level and within 0.5 km from sea level to depths of 2 km below sea level.

Introduction

Augustine Volcano is a 1,200-m-high stratovolcano on a small (8 by 11 km) island southeast of Anchorage, Alaska (fig. 1). The volcano consists of a complex of summit lava domes and flows surrounded by an apron of pyroclastic, lahar, avalanche, and ash deposits. The volcano is frequently active, with major eruptions recorded in 1883, 1935, 1963–64, 1976, 1986, and 2006 and minor eruptive events reported in 1812, 1885, 1908, 1944, and 1971. Because of its frequent eruptive activity and associated hazards and proximity to communities in south-central Alaska, Augustine Volcano has been continuously seismically monitored since 1970 (see Power and Lalla, this volume).

Earthquake activity at Augustine is dominated by volcano-tectonic earthquakes that occur within 1 km of sea level with local magnitudes (M_L) generally smaller than 1.2 (see Power and Lalla, this volume). During inter-eruptive periods, the Alaska Volcano Observatory (AVO) typically locates 100 to 200 small earthquakes each year at Augustine (Dixon and others, 2008). These small earthquakes generally have well-defined to emergent P-wave arrivals and poorly formed to emergent S-wave arrivals. Most earthquakes have P- and S-wave arrivals that are best defined at stations higher on the volcanic edifice, located on the central lava domes and flows, and degrade quickly at stations located closer to the coast on the apron of unconsolidated sedimentary deposits. Additionally, stations close to the island's shoreline are subject to large microseismic noise caused by ocean surf. A representative volcano-tectonic waveform is shown in figure 2. By the time of the 1976, 1986, and 2006 eruptions the volcano was monitored by networks of five, four, and eight permanent short-period seismometers, respectively (fig. 3).

Augustine Volcano was the target of an extensive active-source seismic experiment in 1975 that involved the detonation of 10 chemical explosions which were recorded at 14 temporary seismic stations, as well as at the five permanent stations operating on the island at the time. Data from this experiment were combined with the results from an earlier seismic refraction survey along the north shore of Augustine Island (Kienle and others, 1979) and with seismic-velocity

---

[1] 5106 Wesleyan Drive, Anchorage, AK 99508.

[2] Alaska Volcano Observatory, U.S. Geological Survey, 4210 University Drive, Anchorage, AK 99508.

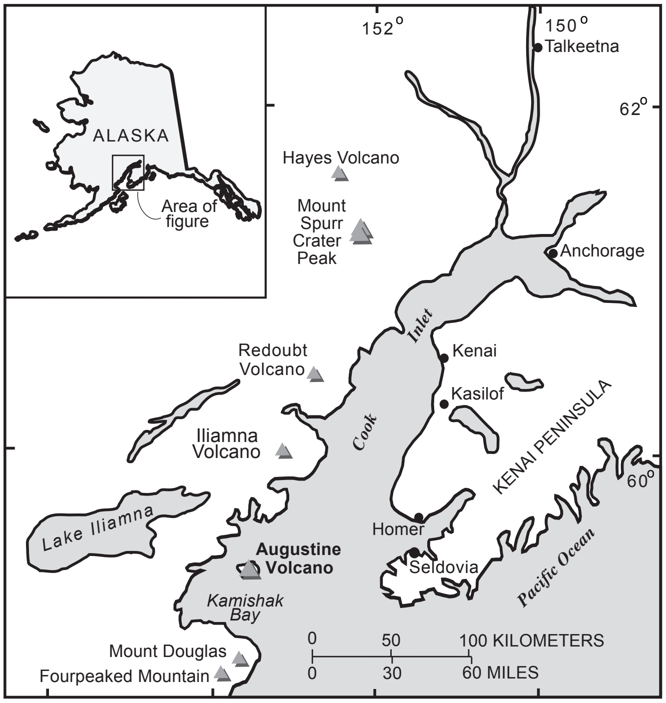

Figure 1. Map showing the Cook Inlet region of Alaska, location of Augustine Volcano, other nearby volcanoes and communities.

data from exploratory oil wells drilled in southern Cook Inlet to determine a three-dimensional (3D) seismic-velocity model of the volcano (fig. 4; Kienle and others, 1979).

Accurate calculation of earthquake hypocenters at Augustine Volcano is unusually difficult because of the high relative topography, the resulting large differences in the elevations of seismic stations, and the heterogeneity of Augustine's seismic-velocity structure. Early computerized earthquake-location algorithms such as HYPO71 (Lee and Lahr, 1971), HYPOINVERSE (Klein, 1978), and HYPOELLIPSE (Lahr, 1989), accounted for station elevations and horizontal changes in seismic-velocity structure through station corrections. Each of these algorithms assumed that the hypocenter was below the elevation of the lowest station. At such stratovolcanoes, as Augustine, this approach presented a serious limitation because topography dictates that many seismic stations are located near sea level and many earthquakes occur in the upper portions of the cone. To overcome this problem, more recent earthquake-location algorithms such as HYPOCENTER (Lienert and others, 1986) and HYPOELLIPSE (Lahr and others, 1994) allow a flat-layered seismic velocity model wherein the highest station can match the highest local topography and stations at lower elevation are embedded within the model. In these algorithms, raypaths and traveltimes are computed for the relative locations of source and receiver.

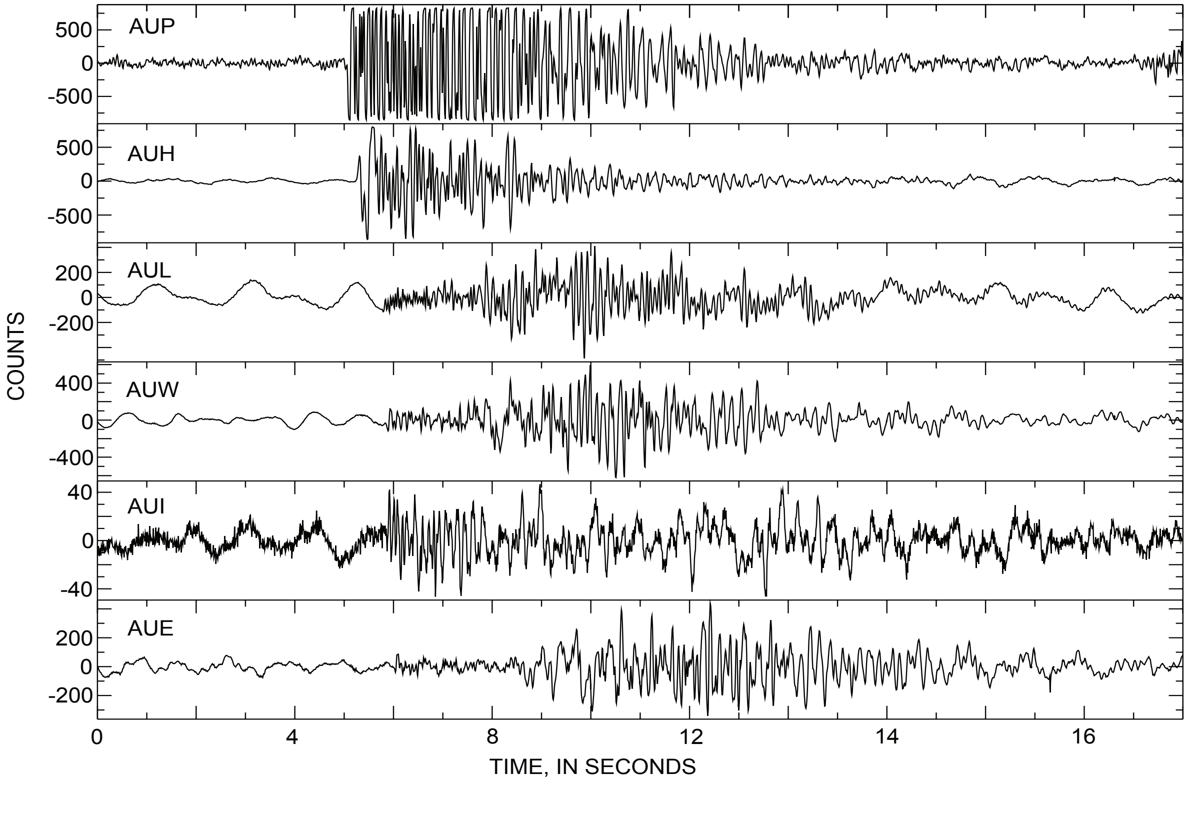

Figure 2. Volcano-Tectonic (VT) earthquake waveforms recorded at Augustine Volcano on January 3, 2006. Hypocenter was at a depth of 0.66 km a.m.s.l. and the local magnitude (M_L) was 0.6. See figure 3 for station locations.

To more accurately locate earthquakes at Augustine, we have developed a two-step procedure to calculate earthquake hypocenters for shocks that occur within a maximum radial distance of 3 km from the volcano's summit and between 1 km above mean sea level (a.m.s.l.) and 8 km below mean sea level (b.m.s.l). This procedure first uses a standard earthquake-location algorithm, such as HYPO71 or HYPOELLIPSE, to determine whether the shocks are occurring beneath the volcano's summit. Earthquakes that meet this criterion are then relocated by using a computer algorithm that calculates hypocenters within the 3D seismic-velocity model of Augustine Volcano shown in figure 4.

This algorithm, which was originally developed in the mid-1970s, was designed both to overcome limitations in the standard earthquake-location programs available at the time and to take advantage of the detailed seismic-velocity information at Augustine Volcano. The algorithm is based on a two-dimensional (2D) ray-tracing procedure that accounts for lateral discontinuities within the seismic-velocity structure. The algorithm calculates the minimum P- and S-wave traveltimes between theoretical grid points embedded in the velocity structure to each station in the seismic network. The grid is a 3 km by 3 km square centered on the summit of the volcano that extends from 1 km a.m.s.l. to 8 km b.m.s.l.; the spacing between grid points is 0.25 km in all three directions. The spatial extent of the grid is shown in figure 5. Station corrections derived from a time-term analysis (Scheidegger and Wilmore, 1957) of the 1975 active-source seismic experiment are applied to calculated traveltimes in order to account for discrepancies between the seismic-velocity model and the measured P-wave traveltime to each station. Each earthquake hypocenter is assigned to the grid point with the lowest residual between observed and calculated arrival times.

In this chapter, we describe details of the two-step hypocenter-relocation procedure and the algorithm that performs the 2D ray tracing and earthquake location within the Volcano's seismic-velocity structure. We also describe calculation of the travel time-terms and station corrections, using data from the 1975 active source seismic experiment. We then evaluate the precision and accuracy with which earthquakes can be located at Augustine with this technique by modeling the known sources of error. Finally, we compare the results of this algorithm with hypocenters calculated with the most recent version of HYPOELLIPSE (Lahr, 1999), using several station configurations.

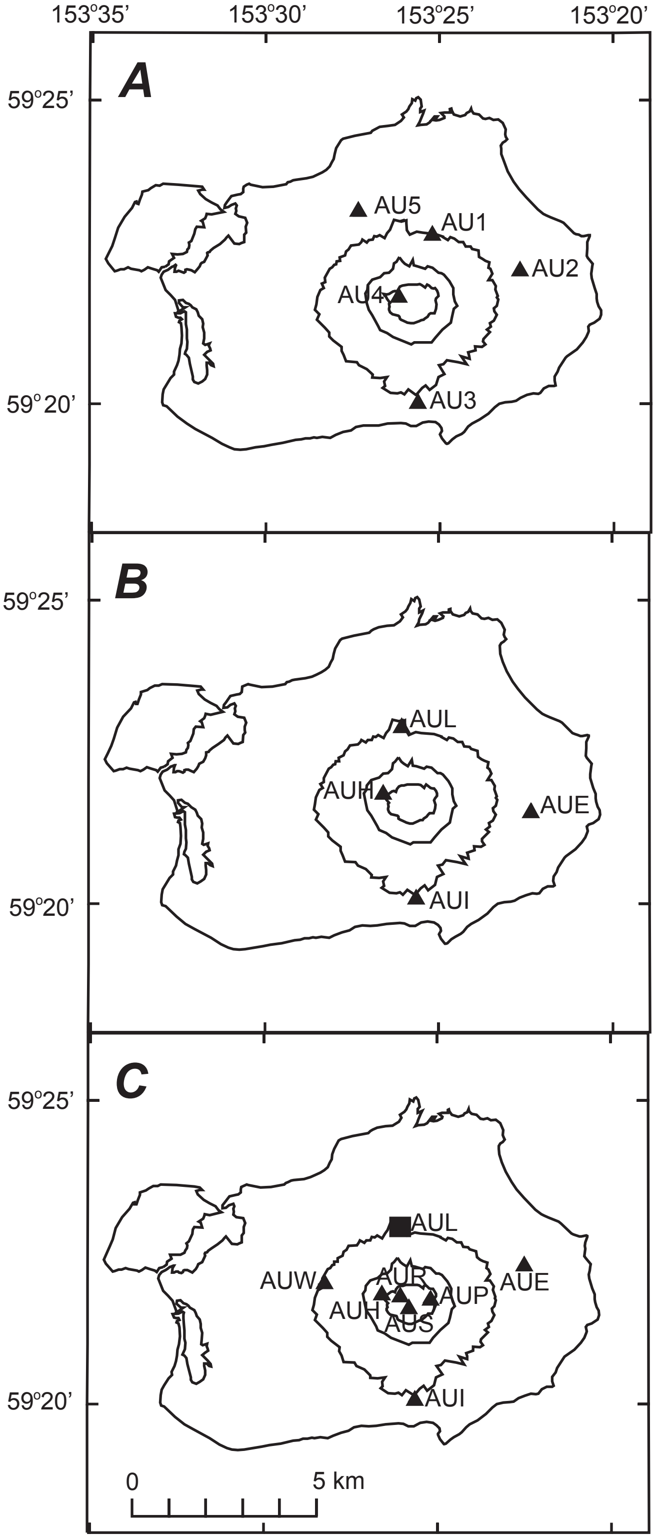

Figure 3. Map of Augustine Island, showing locations of short-period seismic stations on Augustine Volcano in *A*, 1975, *B*, 1985, and *C*, 2005. Triangles, short-period seismometers; squares broadband seismometers. Sea-level, 1,000-ft, 2,000-ft, and 3,000-ft contours are shown in map view.

Seismic-Velocity Model

In August 1975, Kienle and others (1979) conducted an active-source seismic experiment that involved the detonation of 10 chemical explosions on Augustine Island. These explosions were recorded by 14 temporary seismometers, as well as at four stations that were operating on the island as part of the permanent seismic network. The locations of shot points and

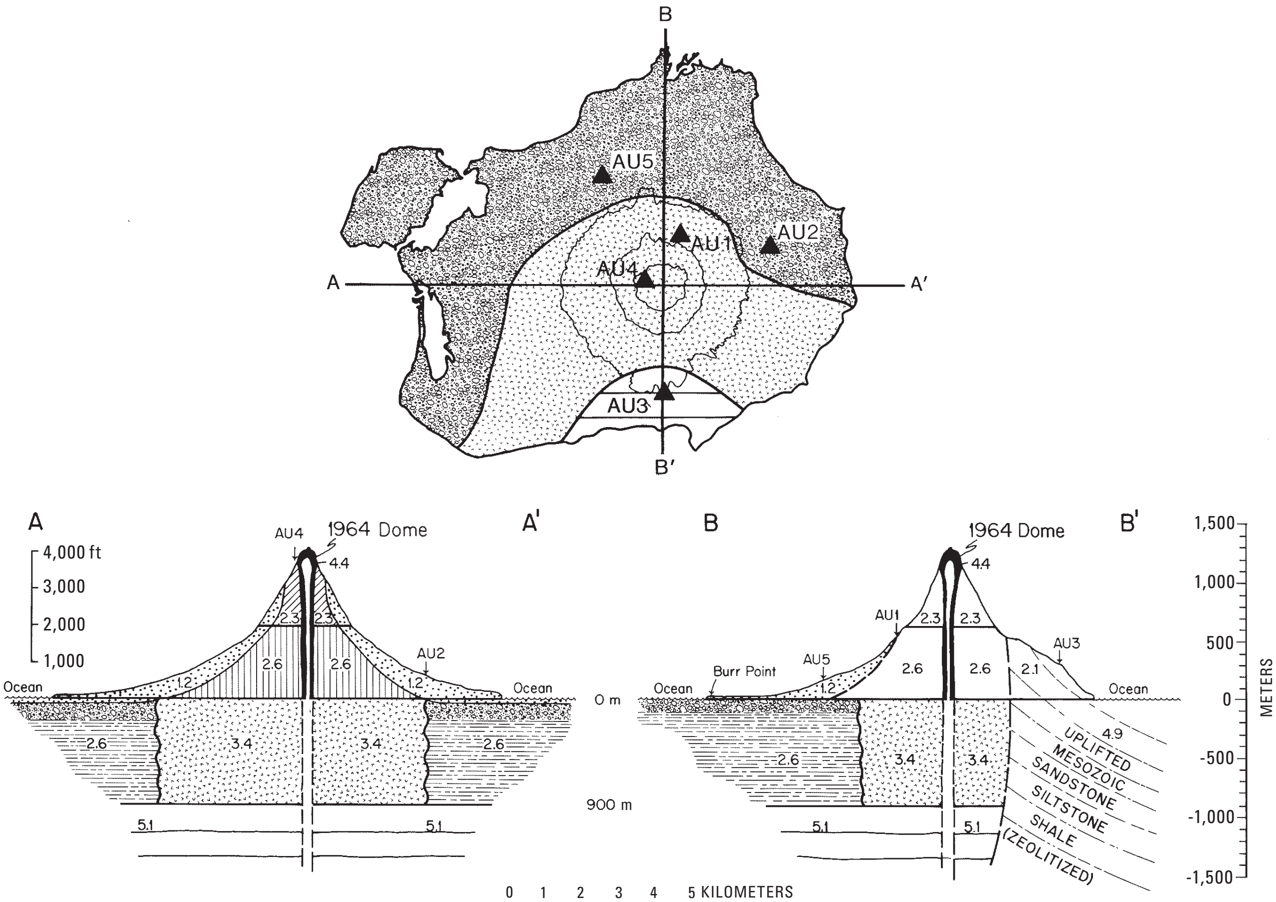

Figure 4. Map view and west-east and north-south cross sections illustrating generalized three-dimensional velocity model of Augustine Island (after Kienle and others, 1979). Map view of island shows velocity boundaries at sea-level (see fig. 3 for explanation of contour lines). Numbers represent seismic velocities in kilometers per second. Triangles note locations of seismic stations that operated in 1975.

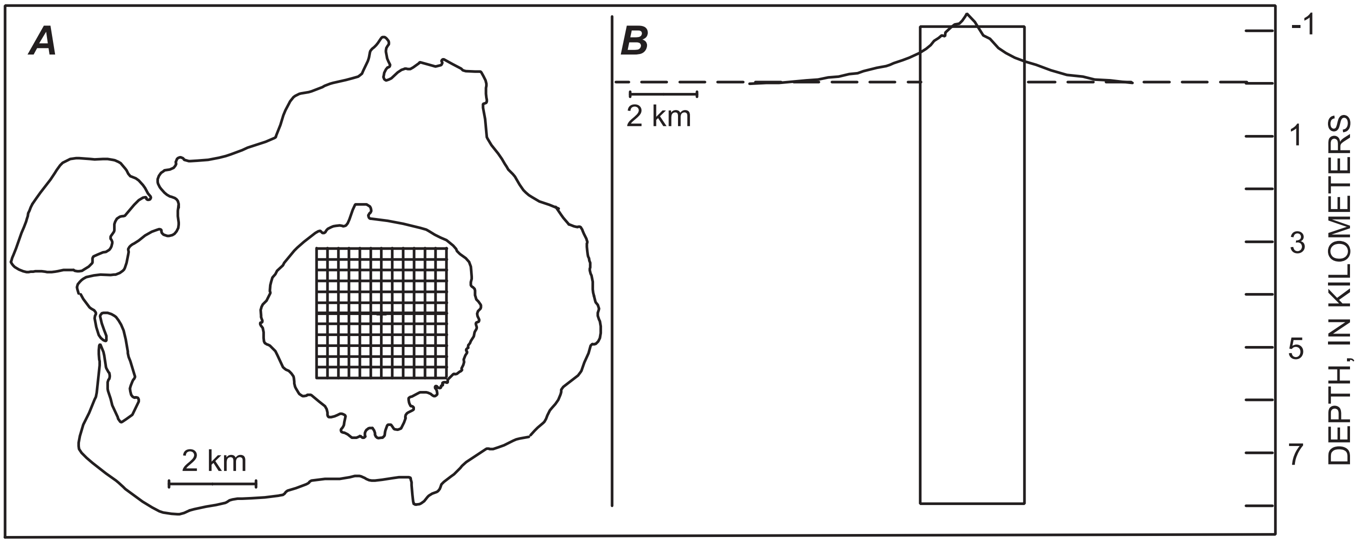

Figure 5. Map view and cross section of Augustine Volcano, showing *A,* the horizontal and *B*, vertical extent of the three-dimensional location grid in relation to volcano. Sea-level and 1,000-ft contour lines are shown in map view.

receivers are shown in figure 6. This combined network measured a total of 66 seismic rays that traversed all parts of the Island and the volcanic cone. These data provided the means to produce the 3D seismic-velocity structure shown in figure 4. An earlier 2D seismic-velocity model of Augustine Volcano was constructed by Pearson (1977), using the 1975 explosion data. A second, smaller active-source seismic experiment constructed in August 1995 measured similar seismic velocities on the volcanic cone (Clippard, 1998).

The major elements of the 3D seismic-velocity model are the cylindrical volcanic cone that comprises the central complex of lava domes and flows and has a P-wave velocity of 2.6 km/s between sea level and 600-m elevation. The seismic velocity decreases outward and upward to 2.3 km/s from 600-m elevation to the summit. The unconsolidated pyroclastic, avalanche, and lahar deposits that surround this central core have a P-wave velocity of 1.2 km/s. The layer between sea level and 0.90-km depth is laterally heterogeneous, increasing in seismic velocity from north to south across the island. The northern part of the island is underlain by a 2.6-km/s velocity layer that was interpreted as non-zeolitized sedimentary deposits. Beneath the central part of the volcano is a layer with a P-wave velocity of 3.4 km/s, perhaps consisting of interlaced volcanic dikes and sills. Near the south shore of the island, the zeolitized sedimentary deposits have been uplifted to near sea level, and in this area the seismic-velocity is 4.85 km/s. The southern part of the volcanic edifice to 600-m elevation is composed of uplifted sedimentary deposits with a P-wave velocity of 2.1 km/s. The stratum of the volcano beneath 0.90 km b.m.s.l. is modeled as a half-space with a P-wave velocity of 5.1 km/s. This layer is believed to represent zeolitized Lower Cretaceous sedimentary deposits (Detterman, 1973). The extent of each of these units is shown in figure 4. A detailed description of this model was presented by Kienle and others (1979).

Earthquake-Location Technique and Methodology

In the first step in calculating an earthquake hypocenter, we determine an initial location for each shock, using a standard algorithm, such as HYPO71 or HYPOELLIPSE with a flat-layered one-dimensional model, similar to the standard processing used to produce the AVO earthquake catalog (Dixon and others, 2008). We then remove earthquakes with hypocenters outside the location grid (fig. 5).

In the second step, we relocate the selected earthquakes, using the 2D ray-tracing procedure implemented by three computer programs written in the FORTRAN4 computer language. The programs are called TRAVEL, NORMAL and FASTM2; copies of them are contained on the DVD-ROM disc included with this volume (see appendix).

The program TRAVEL calculates traveltimes from all points in the three by 3 km by 3 km by 9 km grid to five seismic stations located on Augustine Island. To calculate the minimum traveltime between each grid point and each station, both the critical and refracted wave paths are considered. The minimum travel time from each grid point to each station is stored in a lookup table.

The program TRAVEL was originally coded to calculate traveltimes for the five stations in the 1976 Augustine seismic network. For this discussion, we refer to station names from the 1975 network (fig. 3*A*). To run with later network configurations, TRAVEL was modified with appropriate station coordinates and elevations. The reference elevation for this technique is sea level, with negative depths reflecting height above sea level.

The seismic-velocity model (fig. 4) is approximated as follows:

1. For stations AU5 and AU2, the contact between the 3.4 and the 2.6-km/s velocity zone (stippled area, fig. 4) is approximated by a circular arc with a radius of 2.2 km and a center at the volcano's summit (taken to be 59°21.65'N., 153°25.650' W.). Only within this layer, situated between sea level and 0.9-km depth, is a lateral velocity discontinuity allowed.
2. The volcanic cone is modeled as two bounded plane layers. From sea level to 600-m elevation the P-wave velocity is 2.6 km/s, and above 600-m elevation it is 2.3 km/s.
3. The seismic velocity model for rays traveling to station AU3 is considered to be a simple set of plane layers 2.1 km/s-velocity overlying a 3.4-km/s-velocity layer from sea level to 0.9-km depth.
4. Below 0.9 km b.m.s.l., a half space with a constant velocity of 5.1 km/s is assumed.
5. The central high-seismic-velocity conduit is assumed to affect only station AU4 and is modeled by applying a station correction that is proportional to the depth of the grid point below the station in the region between the summit and sea level. For grid points below sea level, the station correction is fixed at a maximum value of -0.1 s.

For homogenous plane-layered waves, we use the standard expressions to calculate traveltimes derived by many workers, such as Lee and Stewart (1981). For waves that meet a lateral discontinuity, the traveltime path is formulated for the specific ray path and seismic-velocity structure at Augustine.

The program NORMAL applies station corrections to the traveltime table and the calculated traveltimes are then normalized relative to station AU1 or its equivalent and stored in a second lookup table. To decrease the required computational time, this second lookup table is stored in binary rather than ASCII format.

The program FASTM2 performs a direct search of the traveltime lookup table and matches the normalized calculated traveltimes with normalized observed arrival times. Each earthquake hypocenter is then assigned to the grid point with the lowest value between the calculated and observed arrival times. The coordinates of this point are determined by a point to point search over all the grid points. Origin times are determined simultaneously in this process. This procedure considers both P- and S-wave arrival times, although the program is typically run without S-wave phases, which are difficult to determine at the vertical short-period stations on Augustine Island (fig. 2). The S-wave traveltime table is computed by assuming a constant V_p/V_S ratio of 1.78.

Station Corrections and Time-Term Analysis

To account for discrepancies between the actual and modeled traveltimes to individual seismic stations, we have applied traveltime corrections for the individual seismic stations that we use on Augustine Island. Station corrections are calculated by using a time-term analysis (Scheidegger and Wilmore, 1957) with observed traveltimes from the 1975 active-source seismic experiment (Kienle and others, 1979); the time terms are the observed traveltimes between the 5.1-km/s -velocity refractor (fig. 4) at the base of the 3D seismic-velocity model and each seismic station.

The time-term analysis for calculating station corrections relies on the following assumptions (Scheidegger and Wilmore, 1957): 1, the refractor velocity is uniform, 2, the refractor boundary is uniform and has negligible dip, and 3, the seismic-velocity structure of the overburden beneath any station is a function of only the depth normal to the refractor within the cone defined by the critically refracted waves. Under these assumptions, the traveltime between any two points s_i and s_j can be expressed by the following equation:

$$T_{ij} = d_i + d_j + \frac{L_{ij}}{V_r} \ , \qquad (1)$$

where T_{ij} is the traveltime between points s_i and s_j; d_i, d_j are the timeterms for points s_i and s_j, respectively; L_{ij} is the horizontal distance between points s_i and s_j, and V_r is the seismic-velocity of the refracting layer. The time-term is the summation of the total traveltime reduction needed for any number of plane layers above the refractor.

The part of the Augustine seismic-refraction dataset applicable to the time-term analysis consists of 31 critically refracted raypaths (fig. 6) and 15 unknown variables, which 14 are shot point or station time-terms and one is refractor slowness ($1/V_r$). One equation can be written for each shot point/receiver-site pair. Station 8 and shot point 4 occupied the same site in the 1975 active-source seismic experiment (Kienle and others, 1979). This station-shot point position overlap allows the system of equations to be solved uniquely for the unknown variables; without it, the system of equations could be solved only for relative time-terms.

The QR decomposition method of Lawson and Hanson, (1974) was used to solve this problem in a least-squares sense. We chose this method over formulating normal equations for two reasons: 1, solving the normal equations requires n^2 precision, whereas the QR decomposition method requires only n precision, so round-off errors are minimized; and 2, the QR decomposition method solves for a variable only if that column does not cause the condition number of the matrix to fall below the value allowed by consideration of the precision of the data, thus preventing problems associated with the precision of ill-conditioned matrices.

The standard deviation of each variable is estimated from the diagonal terms of the unscaled variance- covariance matrix and the residual solution vector. We assume that errors are additive and uncorrelated and have a consistent variance and that the mean is zero. The results of the time-term analysis are plotted in figure 6 and listed in table 1. The inversion yields a seismic velocity of the underlying refractor of 5.0±0.2 km/s, in agreement with the seismic velocity of 5.1±0.2 km/s calculated from the generalized model of Kienle and others (1979).

The station correction that we apply in the program NORMAL is the difference between the modeled traveltime from the 5.1 km/s -velocity refractor and the traveltime to the station calculated by time-term analysis. The station corrections thus account for discrepancies between the seismic-velocity model and the actual velocity structure beneath each station; we also increase the traveltime to account for the elevation of each station. Station corrections for all the stations used with the 2D earthquake-location algorithm are listed in table 2.

Implementation with 1976, 1986, and 2006 Seismic Networks

The Augustine seismic network has changed somewhat since this hypocenter-relocation procedure was originally formulated to locate earthquakes with the five-station network on the volcano in 1975 (see Power and Lalla, this volume). Some stations have been moved and renamed, and a number of stations were added to the network (fig. 3); stations AU4–AUH, AU3–AUI, AU2–AUE, and AU5–AUL have operated consistently since the early 1970s. This hypocenter- relocation procedure was used to determine earthquake hypocenters before the 1976 (Lalla and Kienle, 1978) and 1986 (Power, 1988) eruptions. During these periods, the Augustine seismic network consisted of five and four stations, respectively. This procedure has also been used to locate earthquakes before the 2006 eruptions of Augustine Volcano (see Power and Lalla, this volume).

Although many of the permanent stations on the island were located at shot-points or receiver sites used in the 1975 active-source seismic experiment (compare figs. 3 and 6), none of the 1975 shot-points and receiver sites was located at the exact position of stations AUI, AUL, or AU1; however, measurements were available for sites with equivalent positions with respect to major features of the seismic-velocity model (fig. 3). The time terms established for stations AU3, AU5, and R5 were used for stations AUI, AUL, and AU1, respectively (fig. 6). Additional travel time to compensate for changes in station elevation were added to each of these station corrections as needed.

For stations AU4 and AUH, a proportional correction was used to account for the effects of the 4.4-km/s-velocity central core of the volcano that extends from the summit to sea level (fig. 4). This correction makes a −0.025-s adjustment to each grid point for every 0.25 km the point is below the top of the model. A total correction of −0.1 s was applied to all grid points at sea level and below.

To relocate earthquakes in 2006, we observed that a four-station network provided hypocenters with the lowest average rms values. The four stations used were AUE, AUH, AUI and AUL (fig. 3*C*). We attempted to include stations AUP and AUW, using time-terms and station corrections from receivers

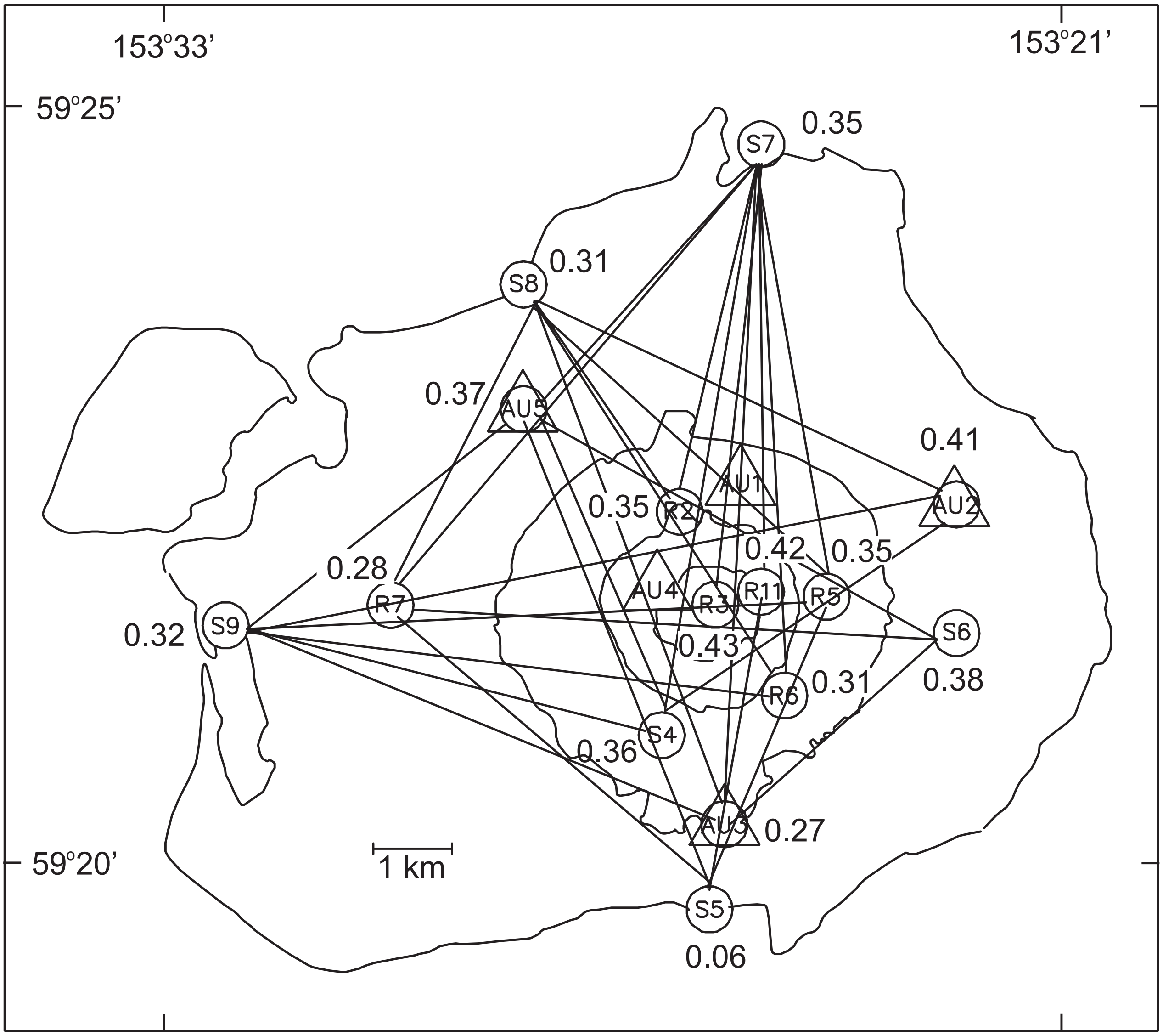

Figure 6. Map of Augustine Island showing locations of shot-points (S) and receiver sites (R) and time terms (numbers) from the 1975 active-source seismic experiment. Straight lines note ray paths used in calculation of time terms and stations corrections. Note that shot point 4 and receiver site 8 were collocated. Permanent short-period stations operating in 1975 are noted by triangles. Contour interval is 1,000 ft. Calculated time-terms are listed in table 1, and station corrections in table 2.

Table 1. Time-terms calculated for shot points and seismic stations.

Station	Time-term (s)	Standard deviation	Station elevation (km)
Shot point 4	0.36	0.04	0.00
Shot point 5	0.06	0.04	0.00
Shot point 6	0.38	0.04	0.17
Shot point 7	0.35	0.04	0.00
Shot point 8	0.31	0.04	0.00
Shot point 9	0.32	0.04	0.00
Station AU2	0.41	0.03	0.20
Station AU3	0.27	0.04	0.29
Station AU5	0.37	0.03	0.15
Station 2	0.35	0.04	0.68
Station 3	0.43	0.05	1.21
Station 5	0.35	0.03	0.50
Station 6	0.31	0.04	0.50
Station 7	0.28	0.04	0.15
Station 11	0.42	0.04	1.03

Table 2. Time-terms and station corrections.

Station	Time term	Model value	Station correction
AU1[1]	0.34	0.49	0.15
AU2	0.40	0.46	-0.06
AU3	0.28	0.21	-0.07
AU5	0.37	0.20	0.17
AUE[2]	0.27	0.31	-0.04
AUI[3]	0.38	0.43	-0.05
AUL	0.28	0.34	-0.06
AUE[4]	0.27	0.31	-0.06

[1] Time term from station S5 assumed, correction adjusted for elevation.

[2] Time term from station AU2 assumed, correction adjusted for elevation.

[3] Time term from station AU3 assumed, correction adjusted for elevation.

[4] Time term from station AU2 assumed, correction adjusted for elevation.

R7 and R11 (fig. 6), but this inclusion produced much greater average errors than in the four-station solutions. We also attempted to include station AUP, using the same proportional correction as for station AUH, but this inclusion also produced greater errors in test runs of the program. These results suggest that the parameterization of the seismic-velocity model by Kinele and others (1979) may not be accurate for stations at these locations. We did not attempt to expand the programs to include the other stations located on Augustine Island in 2005 and 2006 (fig. 3*C*).

Analysis of Error, Precision, and Accuracy

Our ability to determine earthquake hypocenters depends on our knowledge of the seismic-velocity structure of the Earth, the number and distribution of recording stations, and accurate measurement of the arrival times of seismic waves. A review of standard methods of determining earthquake hypocenters was presented by Lee and Stewart (1981). Earthquake-hypocenter determinations contain both systematic and random errors. Systematic errors result from errors in the velocity model, misidentification of phases, or timing errors and affect the accuracy of the hypocenter determination. The effects of systematic errors can be evaluated through controlled experiments, such as locating manmade explosions. Random errors result from errors in determining phase arrivals and affect the precision with which hypocenters can be calculated. The effects of random errors are generally estimated through the use of standard statistical techniques.

To estimate the effect of phase misidentification on the accuracy of earthquake locations at Augustine Volcano with the 2D ray-tracing procedure, we determined the precision with which we can measure P-wave arrivals. We then used a Monte Carlo simulation (Beck and Arnold, 1977) to evaluate our calculated hypocenters. The method consists of generating a population of synthetic arrival times for a given grid point within the location space calculated by the program TRAVEL. The initial arrivals for the “seed” event are taken from the traveltime lookup table, and a set of synthetic arrival times is generated by adding errors with a Gaussian distribution, a zero mean, and a standard deviation that corresponds to the precision with which we can determine P-wave arrivals for local earthquakes at the Augustine seismic stations. This method depends on the characteristics of the earthquakes, the individual stations in the seismic network, and the recording media used at the time of the earthquake.

To calculate the precision in measuring P-wave arrivals at each station, we measured the P-wave arrival times for groups of earthquakes located at Augustine a second time. The sum of the average difference between the two sets of P-wave arrivals and the associated standard deviation was taken to be an estimate of the precision of P-wave arrival determination at that station. Seismic data at Augustine were recorded on photographic film from 1970 to 1989 and digitally by various computerized acquisition systems after 1989 (see Power and Lalla, this volume). The average precision of P-wave-arrival determination was 0.034 s (Lalla and Kienle, 1980) at stations that operated in 1975 (fig. 3*A*), 0.06 s (Power, 1988) at the stations that operated in 1985 and 1986 (fig. 3*B*) and 0.02 s at the stations that operated in 2005, as determined by picking a set of 25 earthquakes that occurred in December of 2005 a second time. We believe that the improvement in precision in the 2005 data set reflects the higher-quality digitally recorded data and associated computerized analysis techniques.

To evaluate our ability to locate earthquakes at Augustine Volcano with the 2D ray-tracing procedure, we ran the Monte Carlo simulation with the stations used with this technique in the 1975, 1985 and 2005 networks (fig. 3) and allowed the average precision of P-wave-arrival determination to follow a Gaussian distribution centered at 0.02, 0.05, and 0.10 s, with seed events at 0.25-km intervals for grid points directly beneath the volcano’s summit to a depth of 7.75 km b.m.s.l.

These simulations allowed us to estimate the standard horizontal and vertical location errors that are typically referred to as ERZ and ERH. We define ERZ as

$$\mathrm{ERZ} = \sqrt{\sum_{1}^{n} \frac{(Z_i - \overline{Z})^2}{n-1}}\ , \tag{2}$$

where Z_i is the hypocentral depth, $\overline{Z}$ is the average hypocentral depth, and n is the number of hypocenters. ERH is calculated in the same way as ERZ, except that the horizontal rather than the vertical position is used. For each grid point, the estimated shift in ERZ and ERH represents the mean value of 100 test events, the results of which are summarized in figures 7 and 8. We also used this technique to estimate the expected shift in hypocentral depth for the networks operating in 1975, 1985–86 and 2005–6 (fig. 9).

We used these simulations to evaluate the shift in hypocenter position as a result of the changing array configuration in 1975. During 1975 five stations were operating on the island, four of which had temporary failures. For this evaluation, we ran these tests without phase readings from one of the stations in the 1975 network to simulate periods when the four stations were operational. Again, we ran these tests with a sample population of 100 test events for each grid point. The results of these simulations, showing the expected shifts in vertical and horizontal errors and in depth are summarized in figure 10.

These tests suggest that the 2D ray-tracing procedure presented here is able to resolve earthquake hypocenter depths to within 0.25 km for shocks located above sea level and within 0.5 km for shocks located between sea level and 2 km b.m.s.l. when the average network P-wave-arrival determination is 0.05 s. This result is similar to the precision estimates calculated for the 1975 (Lalla and Kienle) and 1985–86

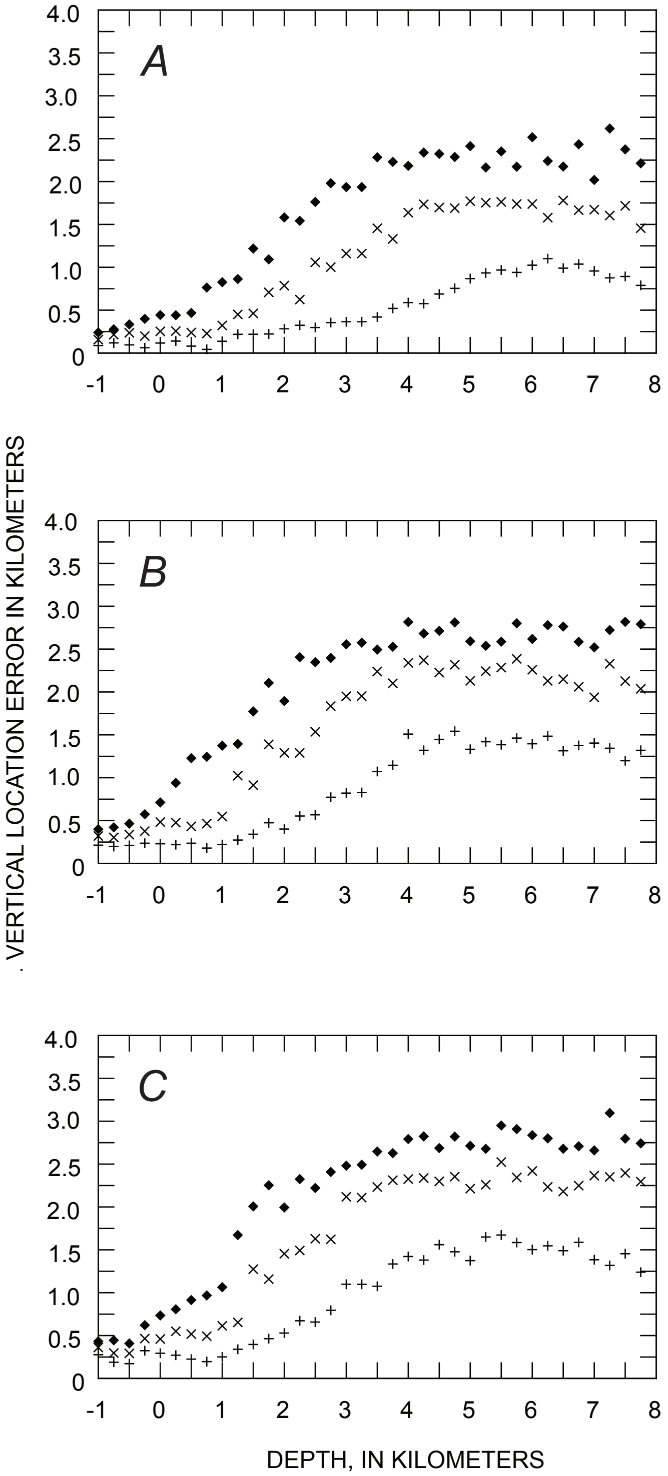

Figure 7. Simulated values of vertical location error (ERZ) based on three error levels of P-wave arrival determination for seismic networks used for the 2D ray tracing procedure in *A*, 1975, *B*, 1985–1986, and *C*, 2005–2006. The pluses, crosses, and diamonds, correspond to the 0.02-, 0.05- and 0.10-second P-wave reading errors, respectively. Each data point represents the mean ERZ for 100 simulated events.

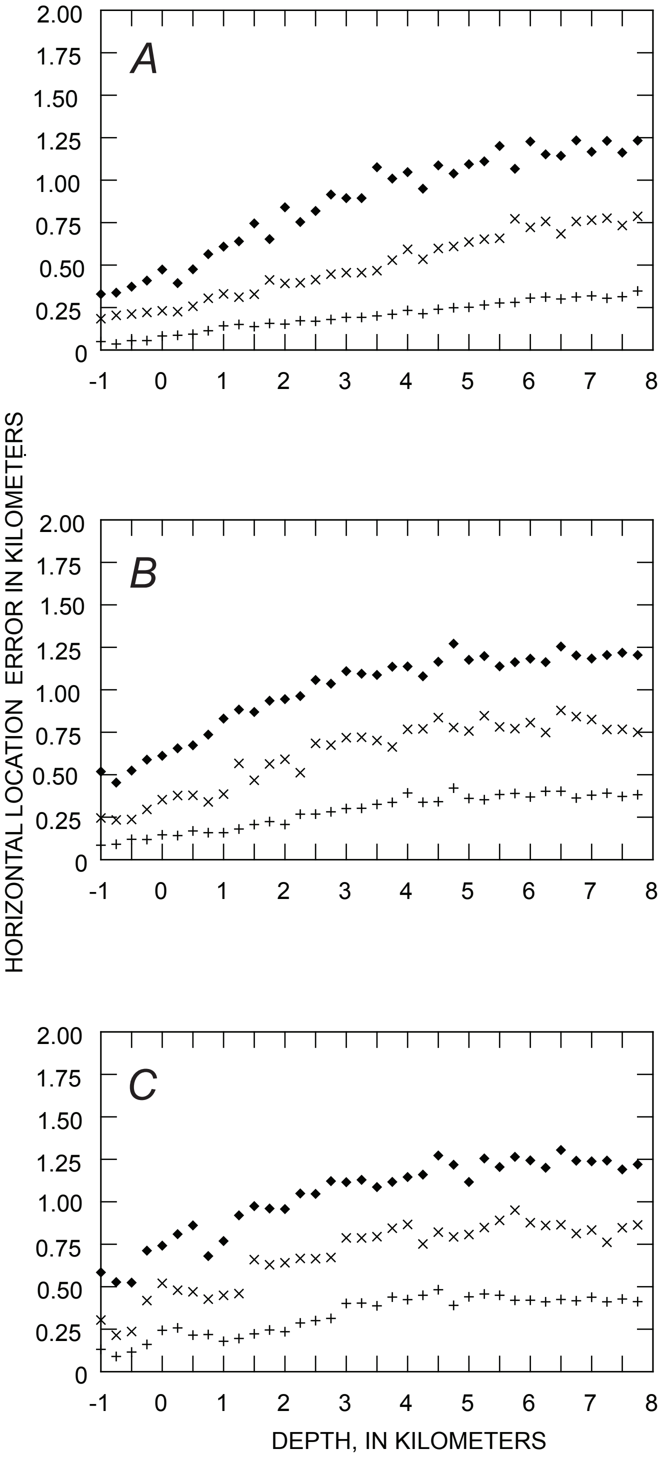

Figure 8. Simulated values of horizontal location error (ERH) based on three error levels of P-wave-arrival determination for seismic networks used for the 2D ray-tracing procedure in *A*, 1975, *B*, 1985–1986, and *C*, 2005–2006. The pluses, crosses, and diamonds, correspond to the 0.02-, 0.05-, and 0.10-second P-wave reading errors, respectively. Each data point represents the mean ERH for 100 simulated events.

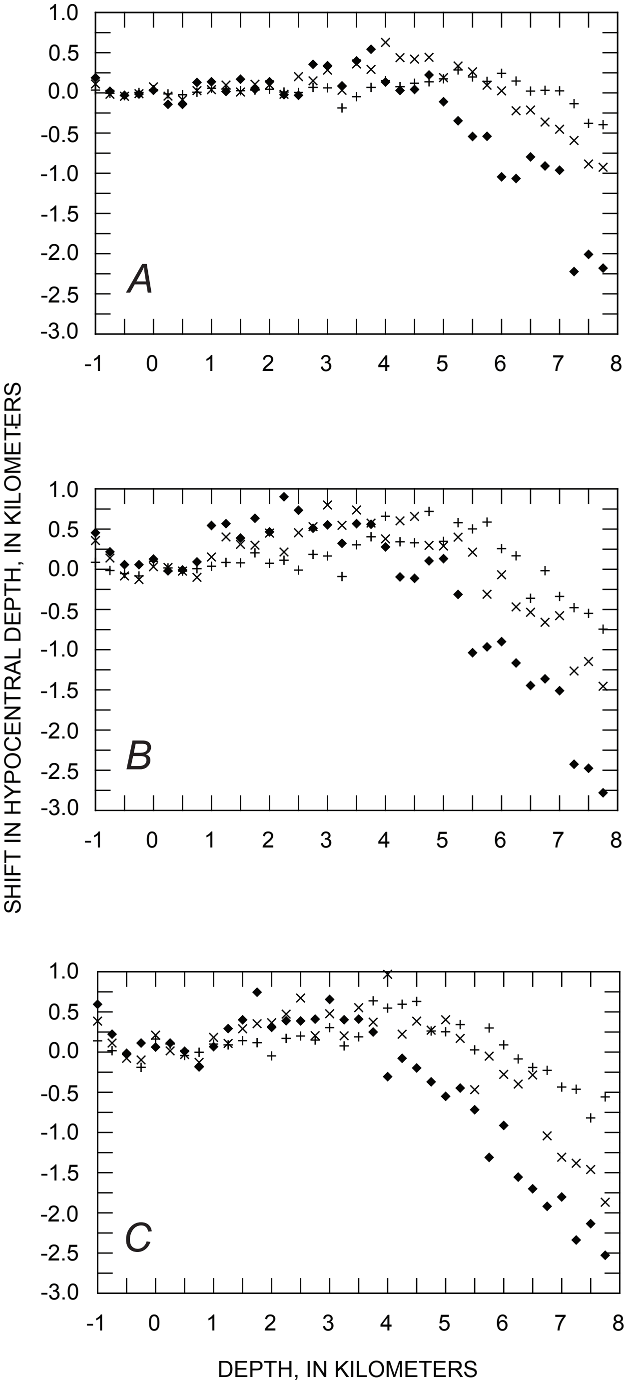

Figure 9. Simulated shifts in hypocentral depth based on three error levels of P-wave-arrival determination for seismic networks used for the 2D ray-tracing procedure in *A,* 1975, *B,* 1985–1986, and *C,* 2005–2006. The pluses, crosses, and diamonds correspond to the 0.02-, 0.05- and 0.10-second P-wave reading errors respectively. Every point represents the mean value of the shift in depth of 100 synthetic earthquake hypocenters.

(Power, 1988) networks, using the same statistical approach. These simulations also suggest that after 1993, when digital data allows us to determine P-wave-arrivals to within 0.02 s, that hypocentral depths can be determined to less than 0.25 km above sea level and less than 0.5 km above 2 km b.m.s.l. using a four-station network (figs. 7, 9, 10). The simulations for various four-station networks in 1975 plotted in figure 10 also indicate that a station high on the volcanic cone, such as station AU4 (fig. 3*A*) is critical for determining hypocentral depth. Changes in horizontal position for the same set of tests fig. 8) indicate an even smaller shift in calculated epicenter position as a result of our ability to determine P-wave arrivals. However, our ability to accurately determine earthquake depths rapidly diminishes below 3 km b.m.s.l.

The use of S-wave-phases was not considered in these simulations. We note that these uncertainties apply only for reading errors with a Gaussian shape.

Comparison with the Program HYPOELLIPSE

To further evaluate the accuracy of earthquake locations calculated with the 2D ray-tracing procedure, we located a subset of 30 well-recorded earthquakes that occurred between May 20 and December 10, 2005, with this technique and the program HYPOELLIPSE (Lahr, 1999), using two separate station configurations. For HYPOELLIPSE, we used a one-dimensional seismic-velocity model consisting of six horizontal layers with boundaries at depths of −1.2, −0.7, 0.0, 1.0, 9.0, and 44.0 km. The top of the model at 1.2 km a.m.s.l. corresponds approximately to the summit of the volcano. The respective P-wave velocities for each layer are 2.3, 2.6, 3.4, 5.1, 6.3, and 8.0 km/s. These layer boundaries and velocities, which were determined by using the results of the 1975 active-source seismic experiment (Kienle and others, 1979), were observed to minimize residuals in several test runs of HYPOELLIPSE. The station configurations used for HYPOELLIPSE were the entire permanent network in 2005 and a four-station network with only stations AUE, AUH, AUI, and AUL (fig. 3*C*), the same four stations used with the 2D ray-tracing procedure.

The average hypocentral depth and standard deviation for the 30 earthquakes sampled for each earthquake-location technique are listed in table 3, and calculated depths are compared in figure 11. These results suggest that hypocenters calculated with the 2D ray tracing procedure presented here yield earthquake depths by using P-wave-arrivals from four stations that are comparable to those calculated with HYPOELLIPSE by using the eight available stations of the 2005 network. The 2D relocations of our sample have a slightly higher standard deviation, indicating a greater scatter in depth. The run of HYPOELLIPSE with only four stations returns a deeper average depth and a higher standard deviation, suggesting that these hypocenters are not so reliable. These results indicate that the 2D relocations are preferable for periods when only

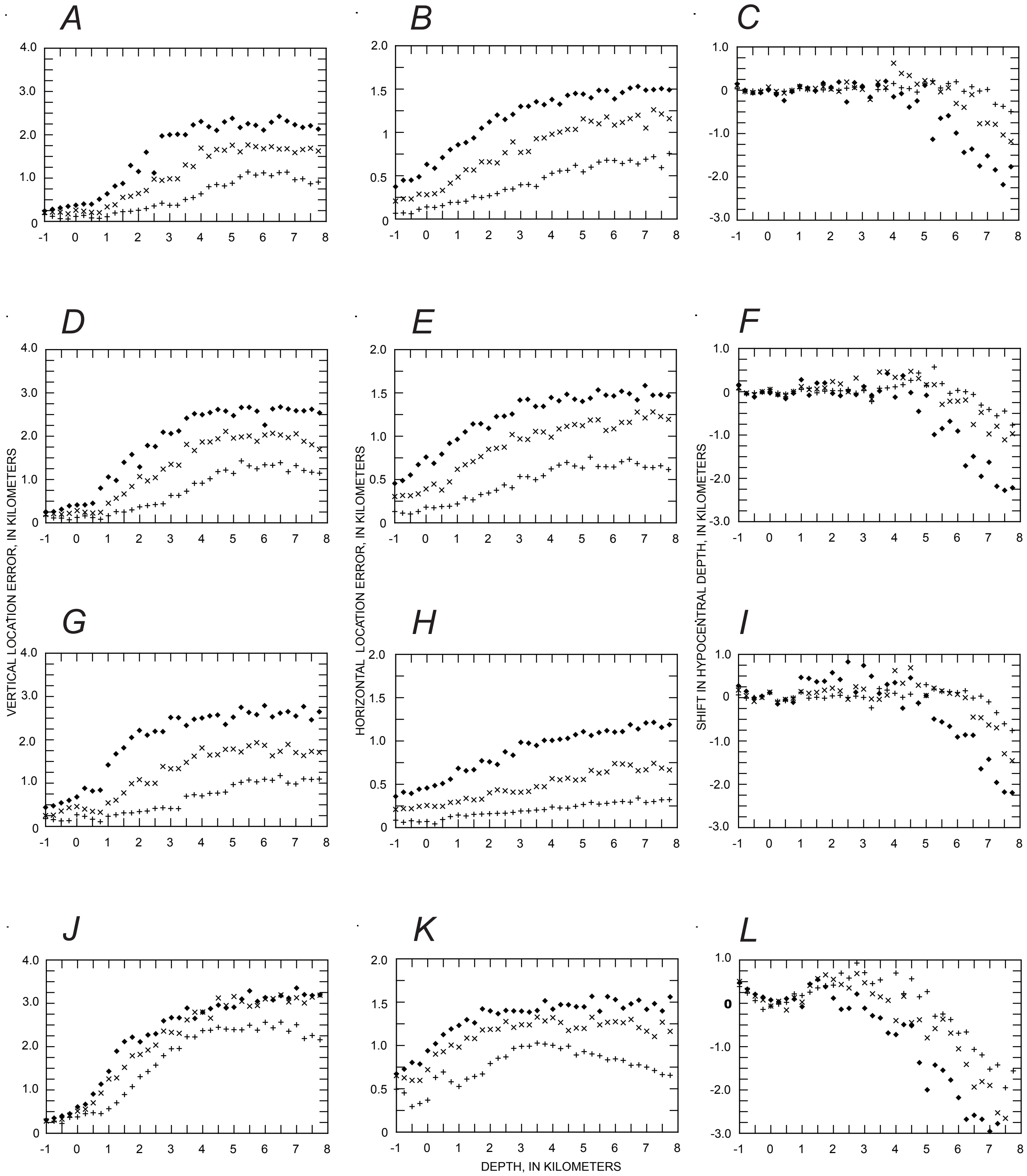

Figure 10. Simulated values of vertical location error (ERZ), horizontal location error (ERH), and shifts in hypocentral depth based on three error levels of P-wave arrival determination for various four station network configurations used to locate earthquakes on Augustine Island in 1975. The pluses, crosses, and diamonds correspond to the 0.02-, 0.05- and 0.10-second P-wave reading errors, respectively. Each data point represents the mean values for 100 synthetic earthquake hypocenters. *A–C*, correspond to hypocenters calculated without station AU2; *D–F,* to hypocenters calculated without station AU3; *G–I*, to hypocenters calculated without station AU4; and *J–L,* to hypocenters calculated without station AU5. See figure 3*A* for station locations.

four stations are operating on the volcano (fig. 11; table 3). The hypocenters calculated from HYPOELLIPSE might be improved further if station corrections were applied as described by Lahr and others (1994), which was not done for this comparison.

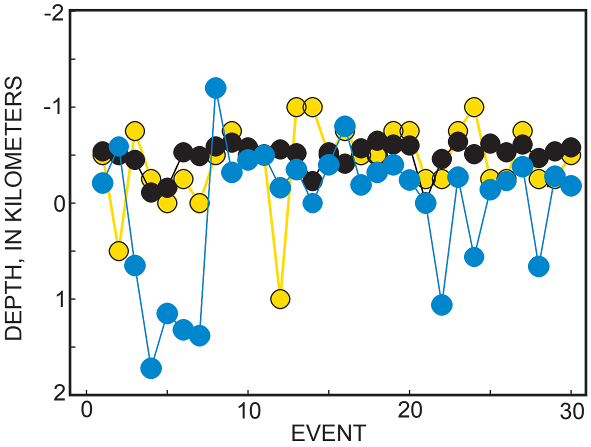

Figure 11. Comparison of earthquake hypocentral depths calculated with the 2D ray-tracing procedure and the program hypoellipse for a set of 30 earthquakes that occurred on Augustine Island in December of 2005. Black dots represent hypocentral depths calculated with the program hypoellipse, using the complete network in 2005; yellow dots represent hypocentral depths calculated with the 2D ray-tracing procedure; blue dots represent hypocentral depths calculated with the program hypoellipse, using only the same four stations used with the 2D ray-tracing procedure.

Summary and Conclusions

The two-step earthquake hypocenter-relocation procedure described here is able to resolve hypocentral depths to within 0.25 km for shocks that occur above sea level and to within 0.5 km for shocks above 2.0 km b.m.s.l. by using the seismic data collected at Augustine Volcano from 1972 to 2007. Hypocenters calculated with this procedure compare favorably with the results from the program HYPOELLIPSE, using the entire eight-station network present on Augustine Island in 2005. These results suggest that the two-step hypocenter-relocation procedure reliably calculates hypocenters at Augustine Volcano during periods when as few as four stations were operating on the island. Augustine Volcano was monitored by four- to five-station networks from 1972 to 1988 (see Power and Lalla, this volume). A study of comparative earthquake hypocenters at Augustine is presented by Power and Lalla (this volume).

Table 3. Hypocentral-depth comparisons.

Location technique	Average depth (km)	Standard deviation
Two-Dimensional ray-tracing procedure	–0.425	0.426
Hypoellipse (all stations)	–0.491	0.159
Hypoellipse (four stations)	0.0733	0.679

Several limitations are inherent in the 2D ray-tracing procedure presented here: 1, it allows for variation of seismic velocity in only two directions, and raypaths are strictly confined to the vertical plane that intersects the station and event location; 2, it takes into account only a simple box discontinuity located between sea level and 0.9 km b.m.s.l. and all other layers are considered to be homogenous and flat laying; 3, locations are not allowed to fall outside the average radius of the volcanic cone at the elevation of consideration; and 4, it can only be used to locate within 2.2 km of the volcano's summit (lat 59°21.65' N., long 153°25.69' W.). Earthquake hypocentral depths at Augustine calculated by using this technique with the seismic-velocity model of Kienle and others (1979) were found to be sensitive to a station located high on the volcanic edifice (fig. 10). Thus, the design of future networks should include several stations high on the Augustine cone, such as AUH, AUP, AUS, and AU4 (fig. 3). Ideally, these stations would have horizontal components, so that reliable S-wave readings could also be included in the hypocenter determination.

If this technique is to be used for future earthquake studies at Augustine, we recommend its expansion to include all available stations in the Augustine seismic network be evaluated. Should additional stations be added to the network, consideration should be given to placing these instruments at shot-points or receiver-sites used in the 1975 active source seismic experiment (fig. 6). Before this technique is used further, we recommend that the relative advantages of other hypocenter-relocation techniques, such as those described by Rowe and others (2004) and Deshon and others (this volume), should be carefully considered.

Acknowledgments

We thank Jurgen Kienle and Chris Pearson for useful discussions and insight into the Augustine seismic velocity structure. Diana Roman and Matt Haney provided helpful reviews of the manuscript.

References Cited

Beck J.V., and Arnold, K.J., 1979, Parameter estimation in science and engineering: New York, John Wiley and Sons, 499 p.

Clippard, J., 1998, Advances in seismic tomography with application to tunnel detection and volcano imaging: University of Alaska Fairbanks, Ph.D. dissertation, 298 p.

DeShon, H.R., Thurber, C.H., and Power, J.A., 2010, Earthquake waveform similarity and evolution at Augustine Volcano from 1993 to 2006, *in* Power, J.A., Coombs, M.L., and Freymueller, J.T., eds., The 2006 eruption of Augustine Volcano, Alaska: U.S. Geological Survey Professional Paper 1769 (this volume).

Detterman, R.L., 1973, Geologic map of the Iliamna B-2 quadrangle, Augustine Island, Alaska: U.S. Geological Survey Map GQ-1068.

Dixon, J.P., Stihler, S.D., Power, J.A., Tytgat, G., Estes, S., and McNutt, S.R., 2006, Catalog of earthquake hypocenters at Alaskan volcanoes: January 1 through December 31, 2005: U.S. Geological Survey Open-file Report 2006-1264, 78 p. [http://pubs.usgs.gov/of/2006/1264/].

Dixon, J.P., Stihler, S.D., Power, J.A., and Searcey, C., 2008, Catalog of earthquake hypocenters at Alaskan Volcanoes—January 1 through December 31, 2006: U.S. Geological Survey Data Series 326, 78 p.

Kienle, J., Lalla, D.J., Pearson, C.F., and Barrett, S.A., 1979, Search for shallow magma accumulations at Augustine volcano: Geophysical Institute, University of Alaska Fairbanks, final report to U.S. Department of Energy, 157 p.

Klein, F.W., 1978, Hypocenter location program HYPOINVERSE; part 1, Users guide to versions 1, 2, 3, and 4; part 2, Source listings and notes: U.S. Geological Survey Open-File Report 78-694, 114 p.

Lalla, D.J., and Kienle, J., 1978, Evolution of seismicity at Augustine Volcano, 1970 to 1976 eruption [abs.]: Geological Society of America, Abstracts with Programs, v. 10, p. 113.

Lalla, D.J., and Kienle, J., 1980, Problems in volcanic seismology on Augustine Volcano, Alaska [abs.]: Eos (American Geophysical Union Transactions), v. 61, p. 68.

Lawson, C.L., and Hansen, R.J., 1974, Solving least squares problems: Englewood Cliffs, N.J., Prentice-Hall, 340 p.

Lee, W.H.K., and Stewart, S.W., 1981, Principal and applications of microearthquake networks: New York, Academic Press, 340 p.

Lienert, B.R., Berg, E., Frazer, N. L., 1986, Hypocenter: an earthquake location method using centered, scaled, and adaptively damped least squares: Seismological Society of America Bulletin, v. 76, p. 771–783.

Pearson, C.F., 1977, Seismic refraction study of Augustine Volcano: Fairbanks, University of Alaska Fairbanks, M.S. thesis, 131 p.

Power, J.A., 1988, Seismicity associated with the 1986 eruption of Augustine Volcano, Alaska: Fairbanks, University of Alaska Fairbanks, M.S. thesis, 142 p.

Power, J.A., and Lalla, D.J., 2010, Seismic observations of Augustine Volcano, 1970–2007, *in* Power, J.A., Coombs, M.L., and Freymueller, J.T., eds., The 2006 eruption of Augustine Volcano, Alaska: U.S. Geological Survey Professional Paper 1769 (this volume).

Rowe, C.A., Thurber, C.H., and White, R.A., 2004, Dome growth behavior at Soufriere Hills Volcano, Montserrat, revealed by relocation of volcanic event swarms, 1995–1996: Journal of Volcanology and Geothermal Research, v. 134, p. 199–221.

Scheidegger, A.E., and Wilmore, P.L., 1957, The use of least squares method for the interpretation of data from seismic surveys: Geophysics, v. 22, p. 9–22.

Appendix 1. FORTRAN programs TRAVEL, NORMAL, and FAST configured for the 1975, 1985–86 and 2005–06 seismic networks at Augustine Volcano

This appendix contains the FORTRAN programs TRAVEL, NORMAL, and FAST configured for the 1975, 1985–86 and 2005–06 seismic networks at Augustine Volcano. These programs are contained on the DVD-ROM disc included with this volume.

Geology of the 2006 Eruption

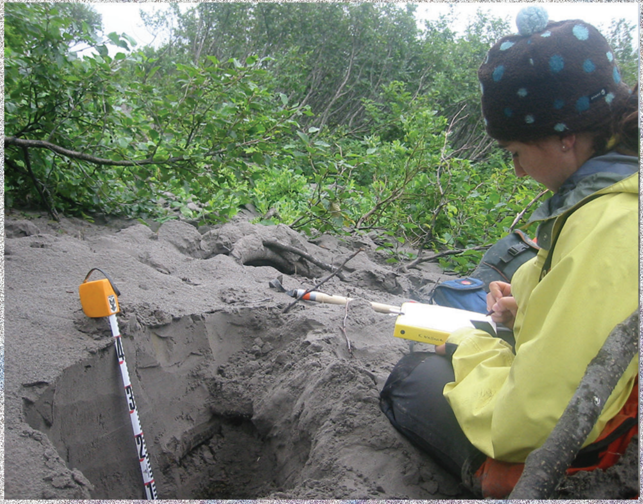

High-angle oblique aerial view, from the southeast, of Augustine Volcano's 2006 summit lava dome. Smooth collar around the south half of the dome is 2006 fall deposits that fill the 40-m-tall scarp formed during the 1976 eruption. Alaska Volcano Observatory photo taken May 13, 2006, by Cyrus Read.

The 2006 Eruption of Augustine Volcano, Alaska
Power, J.A., Coombs, M.L., and Freymueller, J.T., editors
U.S. Geological Survey Professional Paper 1769

Chapter 8

Timing, Distribution, and Volume of Proximal Products of the 2006 Eruption of Augustine Volcano

By Michelle L. Coombs[1], Katharine F. Bull[2], James W. Vallance[3], David J. Schneider[1], Evan E. Thoms[1], Rick L. Wessels[1], and Robert G. McGimsey[1]

Abstract

During and after the 2006 eruption of Augustine Volcano, we compiled a geologic map and chronology of new lava and flowage deposits using observational flights, oblique and aerial photography, infrared imaging, satellite data, and field investigations. After approximately 6 months of precursory activity, the explosive phase of the eruption commenced with two explosions on January 11, 2006 (events 1 and 2) that produced snow-rich avalanches; little or no juvenile magma was erupted. Seismicity suggests that a small lava dome may have extruded on January 12, but, if so, it was subsequently destroyed. A series of six explosions on January 13–14 (events 3–8) produced widespread but thin (0–30 cm) pyroclastic-current deposits on the upper flanks above 300 m altitude and lobate, 0.5- to 2-m-thick pyroclastic flows that traveled down most flanks of the volcano. Between January 14 and 17, a smooth lava lobe formed in the east half of the roughly 400-m-wide summit crater and was only partially covered by later deposits. An explosion on January 17 (event 9) opened a crater in the new lava dome and produced a ballistic fall deposit and pyroclastic flow on the southwest flank. During the interval from January 17 to 27, a rubbly lava dome effused. On January 27, explosive event 10 generated a pyroclastic current that left a deposit, rich in dense clasts, on the north-northwest flank. Immediately following the pyroclastic current, a voluminous 4.7-km-long pyroclastic flow swept down the north flank. Three more explosive blasts on January 27 and 28 produced unknown but likely minor on-island deposits. The cumulative volume of erupted material from the explosive phase, including domes, flows, and fall deposits (Wallace and others, this volume), was 30×10^6 m^3 dense-rock equivalent (DRE).

The continuous phase of the eruption (January 28 through February 10) began with a 4-day period of nearly continuous block-and-ash flows, which deposited small individual flow lobes that cumulatively formed fans to the north and northeast of the summit. A single larger pyroclastic flow on January 30 formed a braided deposit on the northwest flank. Roughly 9×10^6 m^3 (DRE) of magma erupted during this period. Around February 2, the magma flux rate waned and a northward lava flow effused and reached a length of approximately 900 m by February 10. Approximately 11×10^6 m^3 (DRE) of magma erupted during the second half of the continuous phase.

After a 23-day hiatus, lava effusion recommenced in early March (the effusive phase) and was accompanied by frequent (but volumetrically minor) block-and-ash flows. From March 7 to 14, extrusion increased markedly; two blocky lava-flow lobes, each tens of meters thick, moved down the north and northeast flank of the volcano; and a new summit lava dome grew to be ~70 m taller than the pre-2006 summit. This phase produced 26×10^6 m^3 (DRE) of lava. Active effusion had ceased about March 16, but, in April and May, three gravitational collapses from the west margin of the north lava flow produced additional block-and-ash flows. The basic sequence of the 2006 eruption closely matches that of eruptions in 1976 and 1986.

Introduction

The 2006 eruption of Augustine Volcano was monitored at an unprecedented level of detail for an Alaskan volcano. Precursory activity was detected by a network of seismic and GPS instruments, airborne gas measurements, and thermal and satellite data. As the eruption commenced in January of 2006, these tools were augmented by on-island remote cameras, helicopter-based thermal imaging, pressure sensors, and more. Despite the

---

[1] Alaska Volcano Observatory, U.S. Geological Survey, 4200 University Drive, Anchorage, AK 99508.

[2] Alaska Volcano Observatory, Alaska Division of Geological and Geophysical Surveys, 3354 College Road, Fairbanks, AK 99709.

[3] U.S. Geological Survey, Cascades Volcano Observatory, 1300 SE Cardinal Court, Vancouver, WA 98683.

volcano's remote location on Augustine Island, 115 km from Homer, Alaska, the Alaska Volcano Observatory (AVO) was able to follow closely the course of the eruption and correlate visual and thermal changes, geophysical signals, and eruptive deposits to gain a better understanding of the eruptive processes at work at this most active of Cook Inlet volcanoes.

The 2006 eruption unfolded in a series of three distinct phases (Power and others, 2006): an explosive phase of 17 days duration (January 11 to 28); a continuous phase of 13 days duration (January 28 to February 10); and an effusive phase of 13 days duration (March 3 to 16). The phases were distinguished by variations in eruptive style and magma composition (Larsen and others, this volume; Power and Lalla, this volume; Vallance and others, this volume; Wallace and others, this volume) and by corresponding deformation of the edifice (Cervelli and others, this volume). The overall sequence was similar to other historical eruptions of Augustine Volcano: beginning with an explosive onset, followed by lessening intensity, and finally concluding with an effusive phase (Power and others, 2006).

In this paper, we present a detailed chronology of the geologic events during the 2006 eruption, describing how and when on-island deposits (lava flows and domes and pyroclastic-flow, lahar, and avalanche deposits) were produced. The 2006 sequence was mostly determined as the eruption progressed, primarily from seismicity and numerous observational overflights, combined with aerial photographs, remotely operated on-island cameras, and satellite imagery. Continued analysis of the data generated during the eruption, as well as study of the stratigraphy of erupted deposits, has allowed us to further refine the timeline of events and their resulting deposits, sometimes deposit by deposit.

In addition to the chronology, we present a geologic map of the on-island deposits from the 2006 eruption (plate 1). The map was initially generated during the eruption but was greatly refined during a field campaign in the summer of 2006. Initiating the mapping as the eruption progressed allowed us to map the new deposits in a level of spatial and temporal detail not previously possible for the eruption of an Alaskan volcano. In some cases, we are able to distinguish deposits erupted during individual, minutes-long explosive events. Map units are introduced in the text in the order in which they were emplaced, and the Description of Map Units is found on the accompanying plate. Vallance and others (this volume) and Larsen and others (this volume) provide descriptions of the sedimentology and petrology, respectively, of the erupted products. The 2006 deposit map depicts sometimes ephemeral deposits and is meant to augment the more comprehensive geologic map of the island (Waitt and Béget, 2009).

Finally, we present volume estimates for individual deposits and combine these with our temporal framework to infer the time-eruptive volume progression of the eruption. In addition, component studies of the deposits reveal shifts in the composition of magmas feeding the eruption (Vallance and others, this volume) and, by combining component and volume data, we quantify the fluxes of two magmatic compositional end members. We show that the explosive phase produced pyroclastic flows initially rich in a low-silica andesite (57 weight percent SiO_2) that become progressively more silica rich and voluminous. The continuous-phase deposits, rich in high-silica andesite (62.5 weight percent SiO_2), are consistent with nearly continual spalling, degradation, and collapse of a rapidly growing summit lava dome. The effusive phase marked a change back to the low-silica andesite. These observations provide a framework within which we evaluate underlying magmatic processes that drove the eruption and show how eruptive style relates to magma flux.

Geologic Background

Augustine Volcano is an island volcano, located in upper Cook Inlet in south-central Alaska, that is part of the eastern Aleutian volcanic arc. Located 275 km southwest of Anchorage and 115 km west-southwest of Homer, Augustine Island is roughly circular, 9 km by 11 km in diameter, and Augustine Volcano reached an altitude of 1,260 m prior to the 2006 eruption. The volcano comprises a summit dome complex surrounded by an apron of pyroclastic and debris-avalanche deposits. On the south shoulder of the volcano, sedimentary rocks of the Jurassic Naknek Formation crop out from sea level to 400 m above sea level (asl) (Waitt and Béget, 2009).

The oldest known products of Augustine Volcano are late Pleistocene in age and comprise bedded hyaloclastite of olivine basalt and dense juvenile rhyolite (Johnston, 1978). Records of early to middle Holocene Augustine eruptions are scarce and limited to a few small tephra exposures on the south flank and some distal ashes with Augustine compositional affinities (Waitt and Béget, 2009). The late Holocene, prehistoric eruptive record is more complete and shows that Augustine often erupted explosively, producing sometimes thick tephra falls, an apron of flowage deposits, and an edifice consisting of overlapping lava domes and short lava flows (Waitt and Béget, 2009). In addition, the late Holocene has been marked by repeated edifice failures and debris avalanches, as recent as 1883 (Béget and Kienle, 1992). Augustine has erupted historically in 1883, 1935, 1964, 1976, and 1986, each time producing andesitic through dacitic fall deposits, pyroclastic flows, and lava domes.

The last several eruptions of Augustine Volcano have been remarkably similar in eruptive style and compositions of erupted material, and the 2006 eruption was no exception. In particular, the 2006 eruption followed a pattern similar to the 1976 eruption. After roughly 9 months of precursory seismicity, the 1976 eruption commenced on January 22 with 3 days of 13 explosive events, the first of which excavated a large crater at the summit that was 550 m by 350 m across and 200 m deep (Johnston, 1979; Swanson and Kienle, 1988; Power and Lalla, this volume). After a quiescent period of 12 days, the volcano then entered another, slightly less explosive phase from February 6 through 15, when it produced northward-directed, lithic-rich pyroclastic flows and, during the second half of this

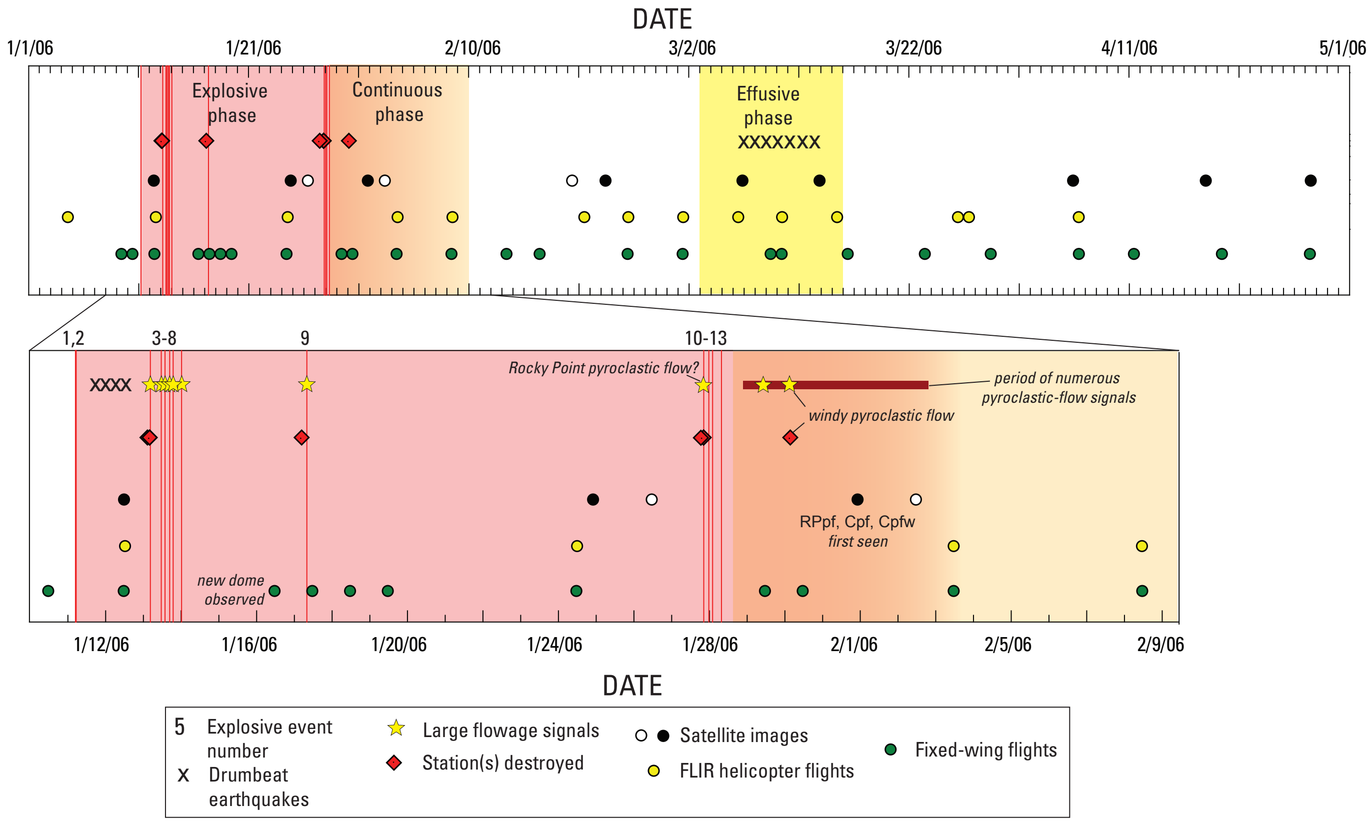

Figure 1. Timeline of eruptive events and observations during the 2006 eruption. Vertical red lines indicate timing of explosive-phase events 1–13. Timing of drumbeat earthquakes from Power and Lalla (this volume). For satellite images, open circles are Hyperion data, black circles are ASTER data (see Wessels and others, this volume, for details). Colored fields indicate the three eruptive phases defined in the text; transition from dark to light orange within continuous phase marks transition from pyroclastic-flow to lava-flow activity.

interval, a summit lava dome (Stith and others, 1977; Kamata and others, 1991). This phase resembled the 2006 continuous phase in the duration, progression, and character of the resulting deposits. After tapering effusive activity through February 1976, the final stage of the eruption occurred April 13 through 18 with expansion of the lava dome and shedding of accompanying block-and-ash flows (Johnston, 1978). The Kamata and others (1991, figs. 2, 3) map of the 1976 deposits mimics the distribution of the 2006 deposits.

The 1986 eruption sequence resembles the 1976 and 2006 sequences but with some distinct differences. The 1986 eruption also began with approximately 9 months of precursory, shallow seismicity, followed by a 12-day-long explosive phase marked by a series of discrete explosions (Power, 1988). After a 13-day lull, the first dome-building phase began and was marked by the effusion of a lava dome and short, steep northward lava flow and numerous small pyroclastic flows (Yount and others, 1987; Power, 1988). This period was followed by 3 months of quiet and then a final dome-building phase in August of 1986. This final phase was accompanied by the growth of a lava spine atop the new dome and emplacement of multiple pyroclastic flows.

Methods

Because of eruptive activity, field work on Augustine Island was limited throughout January and February 2006. Preliminary deposit maps were made using vertical and oblique aerial photos taken during observation flights, satellite imagery, and images acquired by remote on-island cameras (table 1; fig. 1). Because much of the eruption occurred in the winter, some deposits became covered by snow and were obscured in all images except those acquired immediately after emplacement. Those syn- and post-event images greatly aided the mapping process.

Photographs were taken with numerous digital cameras during field work, and observational and gas-measurement flights to and around Augustine Island that took place during the 2006 eruption. New deposits were often first observed and documented during such flights. At times, when vertical imagery was not also available, deposits would be roughly mapped using these oblique photos, and the exact locations would be refined when georeferenced imagery (orthophotos, for example) became available.

Table 1. List of observations and data used to compile deposit chronology.

[Main events shown in bold. For a complete list of flights, see Neal and others (this volume). For a complete list of satellite data and FLIR observations, see Wessels and others (this volume). For a complete list of low-light camera observations, see Sentman and others (this volume). Overflights and field work typically spanned over an hour or more and occurred around midday. Unit abbreviations are included in Observation column; for complete unit descriptions see plate 1]

Date	Time (AKST unless noted)	Image type or eruptive event	Observation	Comments
12/2/05		Overflight photographs		
12/12/05		Overflight photographs	Ash on surface; no flowage deposits	
12/20/05	12:37:00	ASTER daytime visual and thermal images	Two northeast-striking 250°C thermal features at summit	Thin clouds, but can see island
12/20/05		Overflight and fieldwork photographs	Snow-covered summit; ash seen on 12/12/2005 photos still visible below snow line; no flowage deposits	
12/22/05		Overflight and fieldwork photographs, FLIR	Snow-covered summit and flanks; no flowage deposits; some increased heat flow and fumarolic activity at summit with maximum temp. of at least 210°C	
1/4/06		Airphotos and orthophoto	Snow-covered flanks; no flowage deposits	
1/4/06		Overflight and fieldwork photos, FLIR	Snow-covered flanks; no flowage deposits; maximum summit fumarole temperature at least 390°C; overall heating of summit region	
1/10/06		Overflight photographs	Confirm that no flowage events are present	
1/11/06	**0444**	**Explosive event 1; beginning of explosive phase**		
1/11/06	**0512**	**Explosive event 2**		
1/11/06		Overflight photographs	First appearance of Exma on upper flanks	Lower flanks obscured by clouds
1/12/06	12:42:44	ASTER daytime VIS and thermal	Plume moving south	Mostly cloudy
1/12/06		Overflight and fieldwork photos, FLIR	Full extent of Exma from events 1 and 2 visible; ash from events 1 and 2 on north flank; low-level fluctuating ash emissions ongoing throughout day; new vent visible through 1986 dome, just south of 1986 spine	Better visibility than 1/11/2006
1/12/06		Burr Point camera photographs	Good views of north flank Exma	
1/13/06	**0424**	**Explosive event 3**		
1/13/06	**0847**	**Explosive event 4**		
1/13/06	0900	Burr Point camera photographs	Pyroclastic-flow-generated ash cloud on northeast and east flank; no active flows to north or northwest	Still rather dark. Cloud related to event 4
1/13/06	0915	Burr Point camera photographs	Coignimbrite cloud still present above northeast and east flanks; steaming, dark flow deposits are visible down north and northwest flanks	Significantly lighter than previous photo; flow deposits likely from event 3
1/13/06	0930 to 1115	Burr Point camera photographs	Ash cloud dissipates; steam rising from east flank is visible and it looks like most of the flows from event 4 flowed east	
1/13/06	0946	Mound camera photographs	Ash cloud mostly fills field of view; some sky visible in upper right (to the north)	
1/13/06	1032, 1039, 1106	Mound camera photographs	Ash plume rising straight up from vent; steam/ash rises from east flanks; some point-source steaming visible from surface of new flow(s)	
1/13/06	**1122**	**Explosive event 5**		

Table 1. List of observations and data used to compile deposit chronology.—Continued

Date	Time (AKST unless noted)	Image type or eruptive event	Observation	Comments
1/13/06	1130	Burr Point camera photographs	Plentiful ash billowing up from east flank, but also some ash/steam in foreground of photo on lower north flank; small Expf flow is seen making its way down the upper northwest flank	Five minutes after the end of event 5
1/13/06	1135	Mound camera photographs	Bushes visible in foreground, but rest of view is dark with gray airborne ash	
1/13/06	1145	Burr Point camera photographs	Dark ash cloud rising from summit and east flank; north flank has cleared and new dark Expf flows visible on upper north flank—one is still steaming, being emplaced? Newly steaming deposits low on north-northwest flank (lower right of photo)	
1/13/06	1206	Mound camera photographs	Ash rising from middle ground of image, plume above	
1/13/06	1428	Mound camera photographs	Nice views of new steaming flow deposits	
1/13/06	1630	Burr Point camera photographs	Plume, white in the last few images, appears to have become more ash rich and vigorous	
1/13/06	1638, 1640	Mound camera photographs	Image is darker, plume looks more ash rich	
1/13/06	**1640**	**Explosive event 6**		
1/13/06	1640 to 1714	Mound camera photographs	Series of dark images shows pyroclastic flow or surge coming toward camera	
1/13/06	1645	Burr Point camera photographs	Dark, billowing cloud rises from summit and east flank and covers east half of image; discrete pyroclastic flow descends just east of north lava flow; no flows on northwest flank	
1/13/06	1700 to 1715	Burr Point camera photographs	Ash from event 6 dissipates relatively quickly, only small plume from summit remains by 5:15	
1/13/06	**1858**	**Explosive event 7**		
1/13/06	unknown	Numerous satellite data sources	New vent visible in location of 1986 dome	
1/14/06	**0014**	**Explosive event 8**		
1/16/06		Overflight photographs	Summit has fresh snow; new lava dome visible (Exd1); many flank photos	Ash-covered unvegetated areas look deceptively like new flows
1/16/06	daytime	Mound camera photographs	New east flows visible underneath summit cloudcap	Camera view is now tilted
1/16/06		Numerous satellite data sources	Dome (Exd1) dimensions of 200 m by 160 m	
1/17/06	**0758**	**Explosive event 9**		
1/18/06		Overflight photographs	Entire island ash covered; ballistic blocks visible on upper south flank	Good lighting
1/21/06		Numerous satellite data sources	January 16 lava dome (Exd1) elongated; crater visible	
1/24/06		Aeromap airphotos	Good views of new Expf and Expct deposits on flank	Summit obscured by clouds
1/24/06		Overflight and fieldwork photographs, FLIR	Fresh snow on summit and flanks; light ash on southeast flank; dark, hot, steaming, levied flows on east, northeast, and north flanks; Exd1 visible on east part of summit, maximum temp of 140°C	Summit partially obscured by clouds/steaming
1/24/06	22:44:16	ASTER nighttime thermal	Thermal features at summit; weaker thermal features on flanks	Clear

Table 1. List of observations and data used to compile deposit chronology.—Continued

Date	Time (AKST unless noted)	Image type or eruptive event	Observation	Comments
1/26/06	12:03:15	Hyperion and ALI	Hot flowage deposits on northeast flank	Clear
1/27/06	**2024**	**Explosive event 10**		
1/27/06	**2337**	**Explosive event 11**		
1/28/06	**0204**	**Explosive event 12**		
1/28/06	**0742**	**Explosive event 13**		
1/28/06	1420	Mound camera photographs	Dark, billowing, ash-rich plume with white steam collar around its base above vent	
1/28/06	1429	Mound camera photographs	Plume looks slightly more energetic; ash raining to the south-southwest	
1/28/06	**1431**	**Explosive event 14; beginning of continuous phase**		
1/28/06	1418	Mound camera photographs	First sight of dark-gray ash in plume	
1/28/06	1431	Mound camera photographs	More ash falling; plume has bifurcated with second smaller arm rising more straight up; no flows are visible	
1/28/06	1436 to 1707	Mound camera photographs	Dark-gray plume present all afternoon until darkness falls; ash appears to rain to the south in all images	
1/29/06	1007 to 1015	Mound camera photographs	Thick billowing plume rises from summit and moves south; another ash cloud rises from north half of summit and moves down north flank	
1/29/06	1117	Strong (unnumbered) event		
1/29/06	1127	Homer camera photographs	Tall, wide plume visible above low clouds at top of image	
1/29/06	~1230	Overflight photographs	Island is ash covered and flows are steaming on west and north flanks	Photos from afar
1/29/06	1547 to 1642	Mound camera photographs	Images are starting to clear after being dark for most of the day; dark cloud seen moving south; blue sky in upper right (north); later in sequence cloud rises from north flank, then darkness sets in	
1/30/06	**0621**	**Strong (unnumbered) event**		
1/30/06		Overflight photographs	Views of plume from afar	No good island shots
1/30/06		Numerous satellite data sources	Two new lava lobes visible at summit (Exd2)	
1/31/06	22:50:44	ASTER nighttime thermal	RPpf and Cpfw visible; surface to east of RPpf obscured by plume	
2/2/06	11:53:18	Hyperion and ALI	Strong thermal features from dome at summit and block-and-ash flow down northeast flank	
2/3/06		Overflight and fieldwork photographs	White plume to 1,800 m asl; ash-rich plume rising from north flank	Volcano shrouded in clouds
2/3/06	**roughly 1200**	**Continuous-phase activity lessens**		
2/7/06		Numerous satellite data sources	900-m-long lava flow to north	
2/7/08	Night	Low-light camera in Homer	North flank pyroclastic-flow and lava activity	
2/8/06	0800 to 0830	Views from Homer	With binoculars, incandescent flows visible on north flank	

Table 1. List of observations and data used to compile deposit chronology.—Continued

Date	Time (AKST unless noted)	Image type or eruptive event	Observation	Comments
2/8/06	Morning	Mound camera photographs	Steaming (new dome?) at summit; grey (coignimbrite?) cloud on north flank	
2/8/06	midday	Overflight and fieldwork photographs, FLIR	Dark Cpf and RPpf flows on north flank in high contrast to fresh white snow; deposits range from 10 to 25°C with some bigger, hotter blocks	Summit obscured by lenticular cloud; first rock samples collected (from RPpf)
2/10/06		**Continuous phase ends; hiatus begins**		
2/16/06		Overflight photographs		Most of flanks obscured, but great summit views including dome
2/19/06	11:52:42	Hyperion satellite image	Smaller thermal feature at summit as compared to 2/2/06 image	
2/20/06		Overflight and fieldwork photographs; FLIR	Good views of Cpf, RPpf; visited deposits; Eflf dome and north flow visible especially in FLIR images	Rock samples collected from Exlh, Expf, Cpf; summit obscured somewhat by steaming and clouds
2/21/06		Airphotos and orthophoto	Good coverage of north-flank flow deposits	Summit is obscured by steam
2/22/06	12:37:03	ASTER daytime visual and thermal	Good views of flows	
2/24/06		Numerous satellite data sources	1,000-m-long lava flow to north	
2/24/06		Overflight and fieldwork photographs; FLIR	Excellent views of summit, including north lava flow	
3/1/06		Overflight and fieldwork photographs	No apparent changes since 2/24/06	
3/3/06		**Effusive phase begins**		
3/4/06		Mound camera photographs	Ash emissions	
3/5/06	nighttime	Low-light camera in Homer	Incandescence traveling down northeast slope	Probably associated with avalanching from lava dome
3/6/06	0517 to 0702	Burr Point camera photographs	Incandescence near the summit; no flows travel down flanks	
3/6/06	0621	Low-light camera in Homer	Incandescence traveling down northeast slope	
3/6/06		Fieldwork photographs	Active pyroclastic flow down northeast chute; north lava flow visible; northeast lava flow has not yet formed	Clear weather; excellent views
3/6/06	1417	Mound camera photograph	Pyroclastic flow moving down north flank	Coincident with 3-minute-long seismic signal
3/6/06	1616	Burr Point camera photographs	Small pyroclastic flow moving down northeast chute	
3/6/06	1947 to 2347	Burr Point camera photographs	Incandescence at summit and north and northeast flanks	Flows travel farther down flanks than during the morning of 3/6/06
3/6/06	22:39:02	ASTER nighttime thermal	Strong thermal anomalies at summit and north and northeast flanks	Light clouds
3/7/06	daylight hours	Mound camera photographs	All visible flanks covered in fresh ash	
3/7/06	daylight hours	Burr Point camera photographs	Ash emissions; north lava flow steaming; still no lava flow down northeast chute	Clear weather
3/8/06	1932 to 2002	Burr Point camera photographs	Incandescence at summit and north and northeast flanks	Clouds partially obscure lower flanks

Table 1. List of observations and data used to compile deposit chronology.—Continued

Date	Time (AKST unless noted)	Image type or eruptive event	Observation	Comments
3/9/06		Overflight photographs	Active block-and-ash flows from summit and northeast lava-flow front; northeast lava flow more active than north lava flow; entire northeast sector blanketed by light ash (coignimbrite)	Strong backlight on new deposits, unable to see how far northeast lava flow has progressed down chute
3/9/06	Evening/night	Burr Point camera photographs	Clear views of incandescent areas, including margins of northeast lava flow	
3/10/06		**Strongest effusive pulse begins**		
3/10/06	0828, 0830, 0859	Mound camera photographs	Block-and-ash flows moving down north and northeast flanks	
3/10/06		Overflight and fieldwork photographs; FLIR	Clear views of both north and northeast lava flows; active block-and-ash flows down east chute and from front of northeast lava flow	Excellent photos and FLIR shot of growing lava flows
3/13/06	Daytime	Burr Point camera photographs	Northeast flow has reached its final length	
3/13/06	22:45:18	ASTER nighttime thermal	Thermal data show extents of the north and northeast lava flows and delineate the hottest areas within them; match up well with low-light camera images from the same night	Clear
3/14/06	Early morning	Low-light camera in Homer	Incandescence, block-and-ash flows	
3/15/06		Fieldwork photographs; FLIR	Both north and northeast lava flows thickened and lengthened compared to 3/10/06; rockfall activity and ash emission diminished	Clear views
3/15/06		Mound camera photographs	Comparison between these and March 10 photos shows advance of northeast lava flow	
3/15/06		Strongest effusive pulse ends		
3/16/06		Overflight photographs	No major changes from last observation	Poor viewing conditions
3/22/06		Overflight photographs	No major changes from last observation	Clear views but images are mostly backlit
3/26/06		Overflight and fieldwork photographs; FLIR	No major changes from last observation; lava-flow fronts still hot, no significant temperature changes	
4/5/06	22:51:30	ASTER nighttime thermal	Summit and deposits still warm	Clear view
4/6/06		Overflight and fieldwork photographs; FLIR	Lava-flow fronts cooler; flow tops similar when compared to previous surveys; lava-flow dimensions unchanged; fumarole/vent atop dome very hot (650°C)	Fresh snow has covered many deposits
4/8/06	**1635 to 1708 AKDT**	**Two rockfall signals seen in seismic data**		
4/11/06		Overflight photographs	Small debris field on west side of north lava flow and narrow spokelike ash-fall deposit on northwest flank, both likely result of 4/8/06 rockfall(s)	
4/17/06	**1656 to 1732 AKDT**	**Rockfall signals seen in seismic data**		
4/18/06	~1430 AKDT	High-magnification photos from Homer	Intense steaming at summit and upper north flank	Photographs taken through binoculars by Dennis Anderson
4/19/06		Overflight photographs	Dark, sinuous debris deposit along west side of north lava flow (Pba) and spokelike ash-fall deposit on west flank	Both likely from April 17 rockfalls
4/27/06	12:37:30 AKDT	ASTER daytime visual and thermal		Partly cloudy with high cirrus clouds over east part of island

Table 1. List of observations and data used to compile deposit chronology.—Continued

Date	Time (AKST unless noted)	Image type or eruptive event	Observation	Comments
5/12/06		Airphotos	No changes	Good views of summit and flanks; no orthophoto made
5/13/06		Fieldwork photographs; FLIR	North-south linear trend of fumaroles and mineralization at summit; scarp along west side of north lava flow that fed April rock avalanches; images of all flowage deposits; summit vent cooled to 428°C	Clear summit views; rock sampling
5/16/06	22:45:16 AKDT	ASTER nighttime thermal	Summit and deposits still warm	Clear view
5/23/06		Overflight photographs	Good views of summit that show individual lava lobes	
5/26/06	**0106 to 0748 AKDT**	**Rockfall signals seen in seismic data**		
5/26/06		Mike Byerly photographs	Sequence of six photographs shows rock avalanche	Taken from boat north of island
5/26/06	0638, 0653, 0708 AKDT	Burr Point camera photographs	Two images: first just shows start of avalanche, second shows large ash cloud	
5/29/06	12:37:25 AKDT	ASTER daytime visual and thermal		Clear image
6/2/06		Overflight photographs	Dark debris deposits along west side of north lava flow	Likely from May 26 rock avalanches
7/12/06		Airphotos and orthophoto		Orthophoto used as base for 2006 geologic map (plate 1)
9/30/06	1630 AKDT	Citizen photographs from Homer	Strange, possibly meteoric cloud observed halfway down north flank	
10/1/06	**0750 to 0915 and 2116 to 2145 AKDT**	**Lahar(?) signals seen in seismic data**		
10/12/06		Overflight photographs	Pink, braided flow deposits atop lower parts of 2006 deposits on north flank	
10/15/06		Overflight photographs	Pink, braided flow deposits atop lower parts of 2006 deposits on north flank	

Commercial vertical aerial photography was obtained on several occasions throughout the eruption (table 1). Photographs from January 4, February 21, and July 12 were processed commercially to create orthophotos (fig. 2). Photos of the whole island were acquired at 1:36,000 scale, and during each flight a single flight line over the summit yielded photos at 1:12,000 scale. The digital orthophotos were produced at a resolution of 0.5 m/pixel. For features observed only on nonorthorectified photos, the vertical airphotos were digitally scanned at a high resolution, georeferenced to the January 4 base map, and optimized for the area of interest. Orthophoto base maps were supplemented by a 10-m-resolution digital elevation model (DEM) of the island generated in 1990.

Remote automated cameras provided time-stamped images of the volcano during the eruption (Paskievitch and others, this volume). Images from the cameras at the informally named “Mound” on the volcano’s east flank and at Burr Point at the northernmost coastline (fig. 3) often provided important information about event timing when no other data were available (figs. 4, 5).

Thermal imagery was obtained weekly or biweekly during the main phases of the eruption using Forward-Looking Infrared Radiometer (FLIR) cameras (Wessels and others, this volume). The primary FLIR unit is a gimbal-mounted camera that mounts to the underside of a helicopter. FLIR images were often useful in determining the outline of new features in low light or partially steamy conditions and also in making preliminary determinations of the character of deposits based on temperature. In addition, Advanced Spaceborne Thermal Emission and Reflection Radiometer (ASTER) and Hyperion satellite imagery provided emplacement timing and temperature information for certain deposits (Wessels and others, this volume).

We undertook a 3-week-long field campaign in August 2006, after the cessation of eruptive activity. During this time, we field checked deposits that had previously been mapped only from imagery; determined stratigraphic relations; collected samples for petrology, component studies, and grain-size analysis; and measured deposit thicknesses, where possible.

Before and during the eruption, numerous geophysical instruments were installed on the island by AVO, as well as by

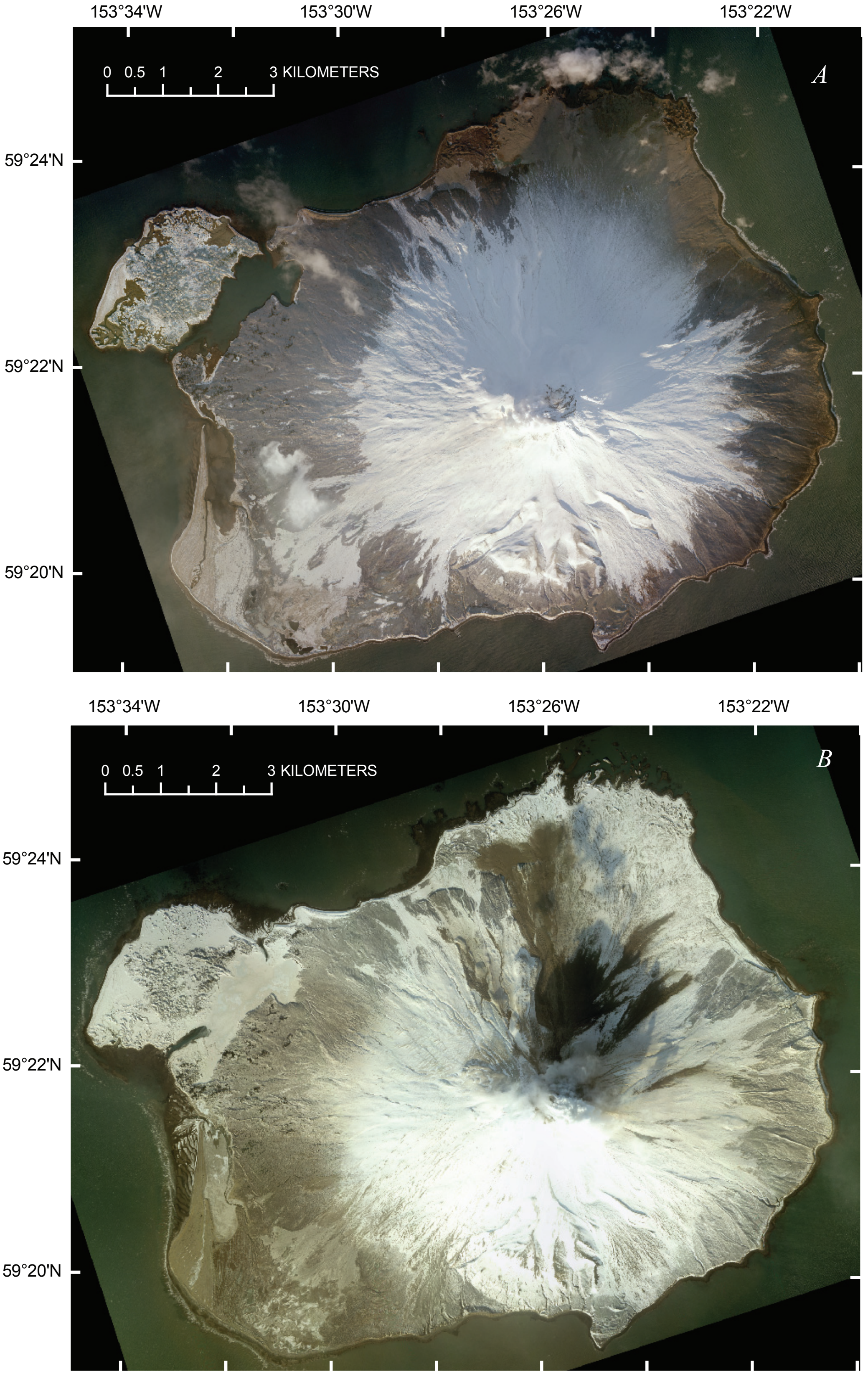

Figure 2. Orthophotographs of Augustine Island from *A*, January 4, 2006; *B*, February 22, 2006; and *C,* July 12, 2006. The projection is UTM Zone 5 and the datum is WGS 84.

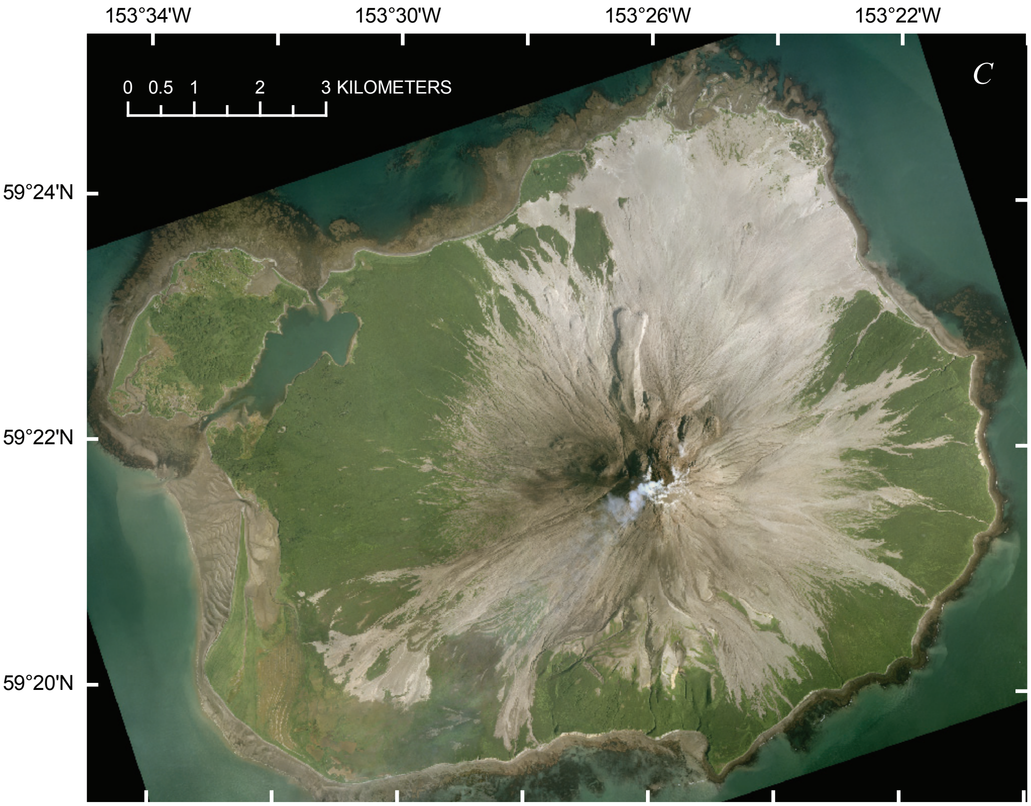

Figure 2.—Continued.

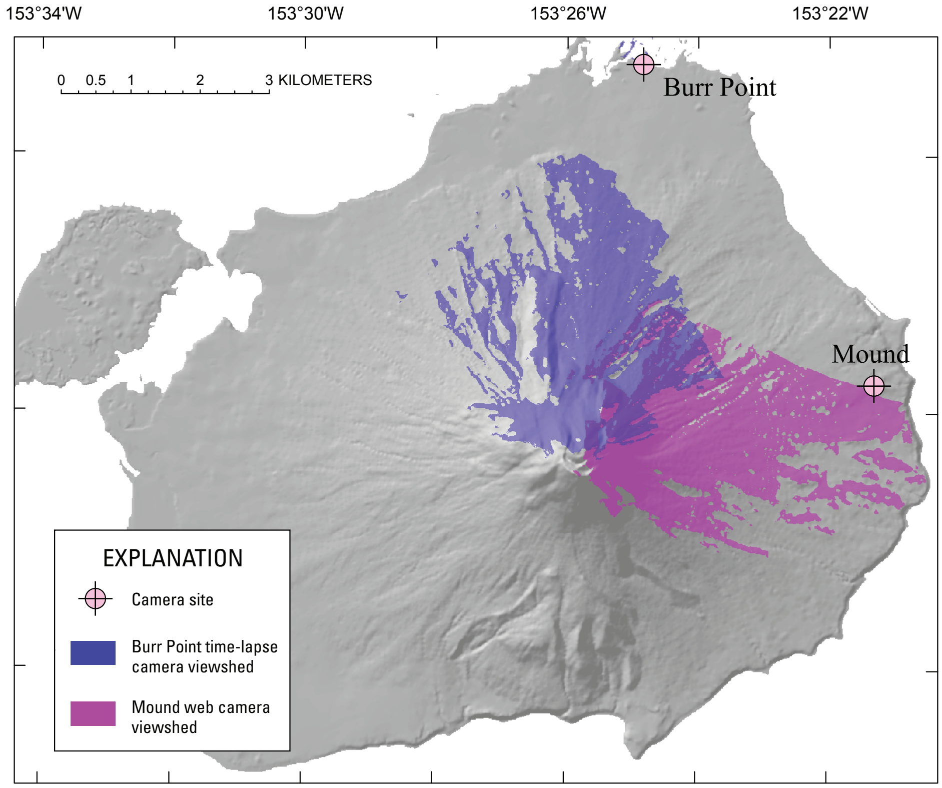

Figure 3. Shaded relief map showing location of on-island cameras and their viewsheds. Digital elevation model from 1990.

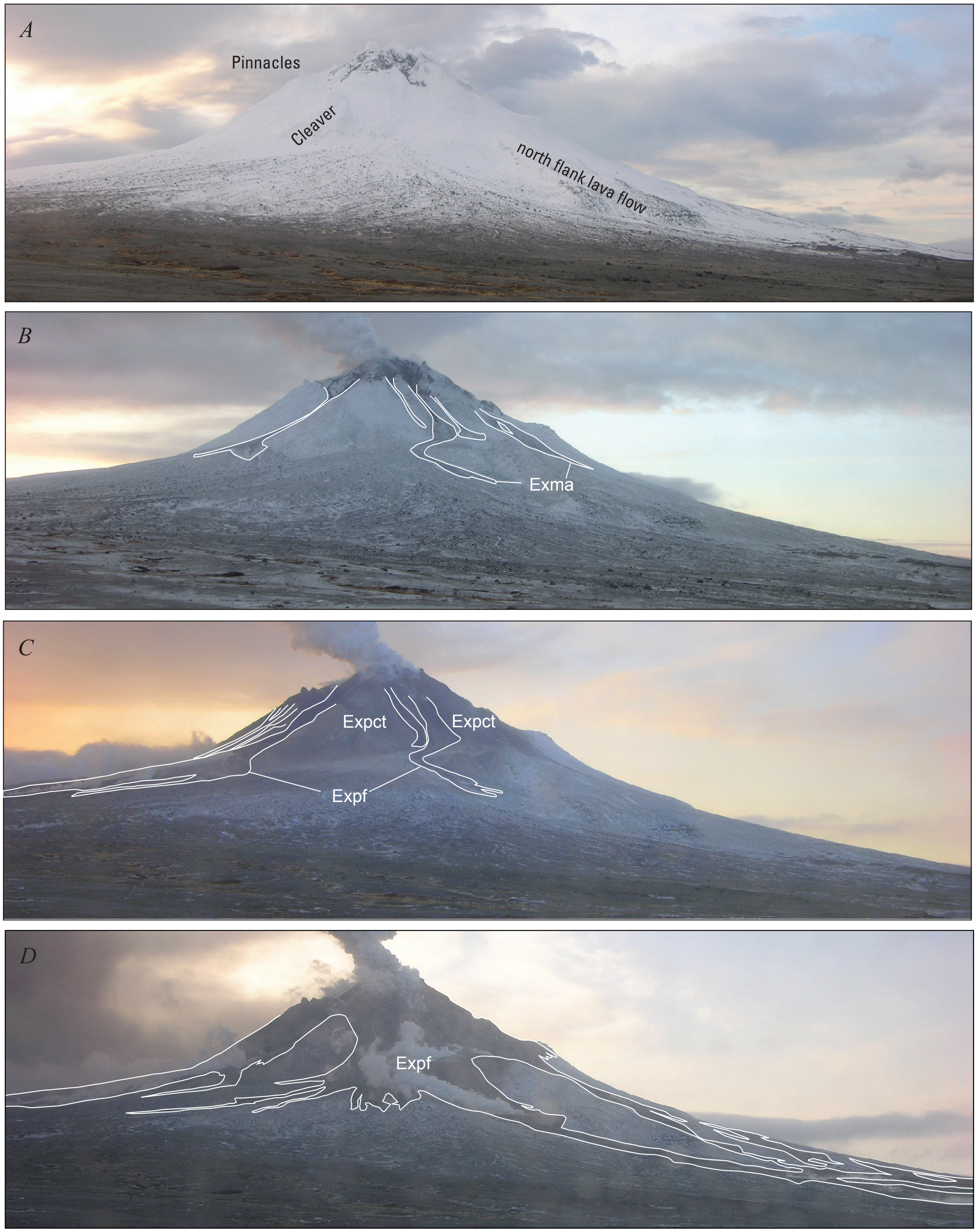

Figure 4. Views of the north flank of Augustine Volcano from the Burr Point time-lapse camera. All times are in AKST. *A,* 1100 January 5. *B,* 1030 January 12, 2006. Mixed-avalanche deposits formed during events 1 and 2 are outlined. *C,* 1045 January 13, 2006. Pyroclastic flow and current deposits (units Expf and Expct) emplaced during event 4 are outlined. *D,* 1200 January 13, 2006. Pyroclastic-flow deposits emplaced during event 5 are outlined. *E,* 1645 January 13, 2006. Ash cloud from event 6 pyroclastic flow is visible. *F,* January 14, 2006. Pyroclastic-flow deposits newly emplaced during events 7 and 8 are outlined. Other flows from these events may have followed drainages recently filled by previous flow events and, therefore, were not recognized. *G,* February 28, 2006. The Rocky Point pyroclastic-flow deposit (RPpf), pyroclastic-flow deposits (Cpf) from the continuous phase (January 28–31), and the north lava flow (Eflf), which began growing at the end of the continuous phase, are outlined. *H,* May 23, 2006. Lava flows (Eflf) and block-and-ash-flow deposits (Efba) are outlined.

Figure 4.—Continued.

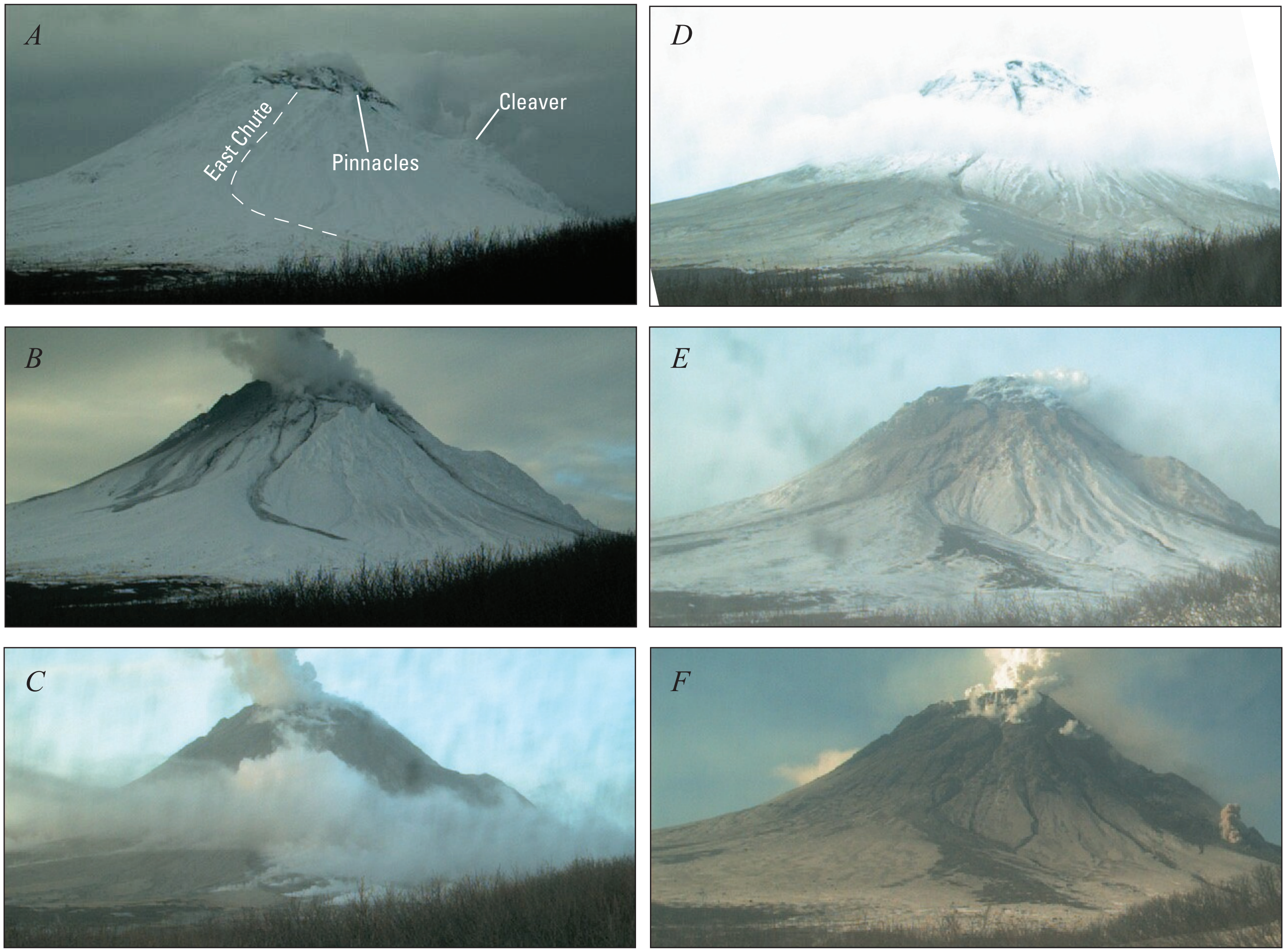

Figure 5. Views of the east flank of Augustine Volcano from the Mound web camera. *A,* January 9, 2006. *B,* January 12, 2006. Mixed-avalanche deposits from events 1 and 2 are visible. *C,* 1106 AKST January 13, 2006. Pyroclastic-flow deposits from events 3 and 4 are still steaming. *D,* January 16, 2006. Pyroclastic-flow and ash-fall deposits from events 3–8 blanket the lower flanks; the upper edifice is coated in new snow. *E,* February 8, 2006. The new steaming dome is visible at the summit. Thickest deposits from events 3 through 8 are still warm and snow-free in the east chute (left center) and on the southeast flank (bottom center). *F,* March 15, 2006. Summit dome has enlarged, and northeast lava flow has reached its final length; note small rockfall/block-and-ash flow at its toe.

the National Science Foundation Earthscope/Plate Boundary Observatory. These include a permanent network of short-period seismometers, a temporary network of broadband seismometers in place from December 20, 2006, to August 2006 (Power and Lalla, this volume), and a network of continuous GPS (CGPS) stations installed in 2004 (Pauk and others, this volume). CGPS provided information about edifice inflation and deflation (Cervelli and others, this volume), and the seismic network detected volcano-tectonic and long-period earthquakes, explosion signals, and emergent, cigar-shaped seismic signals associated with the movement of material over the ground surface (McNutt and others, this volume; Power and Lalla, this volume). The latter were particularly useful in the context of this study to help determine the emplacement locations of several flowage deposits. In addition to the invaluable data they provided while operational, the destruction of several stations recorded the timing of flow emplacement, making them almost as valuable in their demise.

While geophysical data are almost always recorded in UTC (Universal Time, Coordinated), we use Alaska Standard Time (AKST) throughout this paper unless noted, because it better correlates with the more common visual observations described herein. To convert AKST to UTC, add 9 hours. Alaska Daylight Time (AKDT), which is in effect annually after March 21, is 1 hour later than AKST. To convert AKDT to UTC, add eight hours.

Table 2. Explosive-phase events and associated flow behavior.

[Locations of seismic stations are shown on fig. 8]

Event No.	Date (2006)	Onset time (AKST)	Duration (mm:ss)[1]	Long coda[2]	Broadband delayed pulse[3]	Seismic station destroyed	Flow direction	Pyroclastic flow	Lahar	Mixed avalanche
1	1/11	0444	1:18	AUW			W			Upper flanks
2	1/11	0512	3:18	AUE	AU12, AU14		NW–E			Upper flanks
3	1/13	0424	11:00	AUE	AU14	AUP	ENE	Likely	Likely, to coast	Likely
4	1/13	0847	4:17	AUE	AU14		ENE	Confirmed, camera	Likely	Possible
5	1/13	1122	3:24	AUW	AU12		NNW	Confirmed, Burr Point camera	Likely, to coast	
				AUL			N	Confirmed, Burr Point camera	Likely, to coast	
				AUE	AU14		E	Confirmed, Mound camera	Likely, to coast	
6	1/13	1640	4:00	AUE	AU14		E,NE	Confirmed, Mound camera		
							N	Confirmed (small), Burr Point camera		
7	1/13	1858	3:00	AUW	AU12		NNW	Likely	Likely	
				AU14			NE	Likely	Likely	Probable
					AU13		SSW,SSE?	Likely	Likely	Likely
8	1/14	0014	3:00	AUW	AU12		NW	Likely	Likely	
				AUE	AU14		ENE	Likely	Likely	Probable, moderate
					AU13		SSW, SSE?	Likely	Likely, to coast	Likely, to coast
9	1/17	0758	4:11	AUE			ENE	Possible		
				AUW			WNW	Likely		
					AU12		NW	Likely		
					AU15		SW	Confirmed, overflight photos		
10	1/27	2024	9:00		AU12		WNW	Likely		
					AU14		E	Possible		
						AUL, AUH	N	Confirmed, large		
11	1/27	2337	1:02	AUE			E	Possible, small		
12	1/28	0204	2:06	AUW	AU12		N, WNW	Likely		
				AUE	AU14		E	Likely		
13	1/28	0742	3:00	AUW			N, WNW	Likely		

[1] Reported durations were measured at seismic station Oil Point, 30 km northeast of Augustine Volcano.

[2] Long coda indicates explosion/flow signals with extended durations that were detected at seismic station(s). Modified from McNutt and others (this volume).

[3] Broadband delayed pulse indicates that secondary, high frequency signals were detected on broadband seismometers after the initial signal.

Volcanic Activity And Resulting Deposits

Similar to recent eruptions of Augustine Volcano, the 2006 activity began with a series of short, discrete explosions, followed by an interval of nearly continuous but less energetic explosive activity that tapered to lava effusion. After a 3-week-long hiatus, effusive activity resumed in March to produce two lava flows. This sequence and the naming of three phases (explosive, continuous, and effusive) was generally established during the eruption and described in Power and others (2006) and only slightly refined here (fig. 1; table 1).

The Explosive Phase—January 11–28

Discrete explosive events, each several minutes long, occurred during a 17-day period from January 11 to January 28.

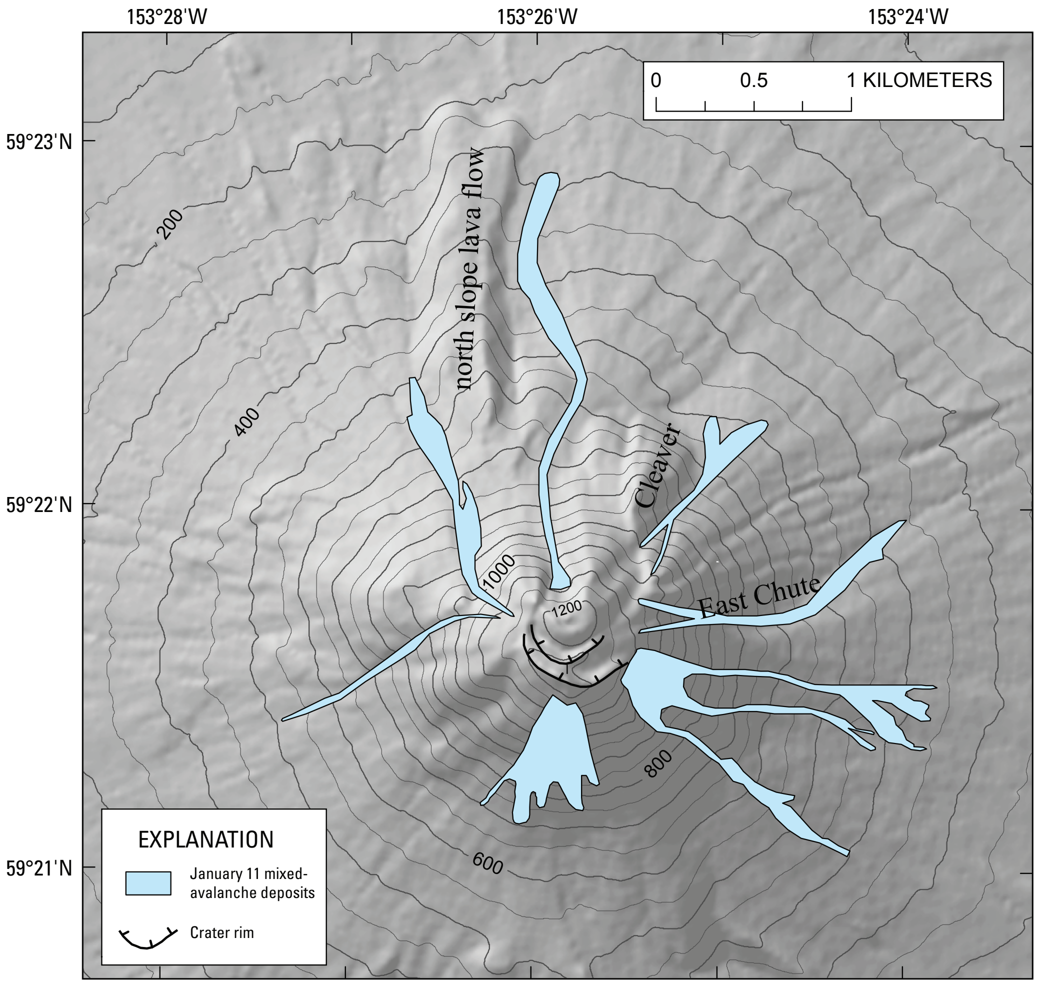

Figure 6. Map showing distribution of mixed-avalanche deposits that formed during explosive events 1 and 2 on January 11, 2006. These deposits were covered by later events; their locations are approximate. Contours show pre-2006 topography; contour interval is 50 m.

This time period is termed the "explosive phase" and individual events have been numbered 1 through 13 (Petersen and others, 2006; Power and others, 2006; table 1). Each event is best characterized by its seismic signal, which for many events records energy released during the initial ejection of material from the vent followed by ground shaking caused by movement of pyroclastic and other flows over the ground surface (McNutt and others, this volume). Aerial surveillance on January 12, 16, and 18; time-lapse photography; and seismicity constrain emplacement of pyroclastic flows during the sequence of explosive events. Seismic signals from stations downslope of flows or beside flow paths include 10–30-minute-long, high frequency, cigar-shaped codas and increase in amplitude on temporary broadband stations 10–20 minutes after explosions (table 2). Broadband stations downstream of flows show increased seismicity as much as 20 minutes after initial explosion signals. Such distinctive signals on instruments below or next to flows and their absence in other quadrants indicate pyroclastic-flow directions (McNutt and others, this volume). Between the explosive events, seismicity and visual observations show that lava effusion formed at least three small lava domes at the summit. In this section we describe the individual explosive events and their resulting deposits, as well as the lava domes effused during more quiescent intervals.

January 11: Explosive Events 1 and 2

At approximately 1530 AKST on January 10, a strong swarm of volcano-tectonic (VT) earthquakes began, culminating in two explosions at 0444 and 0512 AKST early in the morning of January 11 (table 1). These explosions, events 1 and 2, were 1 and 3 minutes long, respectively, as recorded seismically (table 2). They produced ash plumes that reached heights greater than 9 km asl and moved to the north and northeast of the volcano (Bailey and others, this volume; Schneider and others, 2006). Ash fragments sampled during on-island field work on January 12 are primarily dense or weathered, suggesting that these explosions did not release juvenile magma (Wallace and others, this volume).

An overflight of the volcano on the afternoon of January 11 revealed dark flowage deposits on the snow-covered upper south flank, but much of the rest of the volcano was hidden by clouds. An airplane volcanic gas flight, FLIR helicopter flight, and Burr Point time-lapse photographs on January 12 provided much clearer observations of the new deposits (table 1). Presumably all new deposits viewed on January 12 formed during the January 11 explosions.

The new deposits were present on most flanks of the volcano, extending as far as 2.5 km from the summit and reaching down to 300 m asl (figs. 4*B*, 5*B*, 6). Most were narrow and elongate, followed topographic lows, and ended in multiple lobate flow fronts (fig. 7). They were medium gray, and closer photographs reveal that they consisted of mixed snow, ice, and dark-colored debris; no steaming was observed (fig. 7*B*). Several had dark rills that suggest liquid water may have flowed down the central part of the deposits after the mixed snow and debris had come to rest. The flow deposits on the upper south flank appeared more snow rich than the others and formed a broad sheet rather than individual elongate lobes. None of the deposits appeared to have involved running water that flowed beyond the termini of the snow lobes. None of these deposits were sampled and essentially all were covered by subsequent flows on January 13, 14, and 17. Though not included on the deposit map, they appeared similar to later mixed-avalanche deposits of unit Exma (plate 1).

Seismic data provide some clues regarding flow emplacement during explosive events 1 and 2 (table 2). Each explosion registered as a seismic signal on all island seismometers, but some seismometers also recorded prolonged, broader spectrum waveforms after the actual explosions. These are interpreted to reflect the ground shaking caused by flow of rock and ice over the ground surface in the area near the particular seismometer. For event 1, a somewhat extended signal, or long coda, is evident at seismic station AUW on the west flank. For event 2, a long coda was recorded on seismic station AUE on the east flank. In addition, broadband seismometers AU12 and AU14 (on the northwest and northeast flanks, respectively) recorded delayed broad spectrum pulses after event 2, which likely record the passage of avalanches. These results suggest that most of the flows were emplaced during event 2.

January 11–12: Dome Growth?

In the 36 hours following events 1 and 2, several sequences of small, regularly spaced VT earthquakes, many with identical waveforms, were recorded at rates as high as 3 to 4 per minute and lasted for several hours (Power and Lalla, this volume). Similar earthquakes, often referred to as clones or drumbeats, have been associated with the emplacement of lava domes at other volcanoes, such as Mount St. Helens (Dzurisin and others, 2005). These earthquakes at Augustine suggest that the effusion of new lava may have begun late on January 11. In addition, subdaily CGPS solutions show that steady summit inflation ceased at roughly 1800 AKST on January 11; this is interpreted as the result of magma arriving at the surface and relieving pressure within the conduit (Cervelli and others, this volume, fig. 8).

Thermal and visual images acquired during a FLIR flight on January 12 revealed a new vent atop the 1986 dome at the volcano's summit, but no unambiguous new lava was observed (Wessels and others, this volume, fig. 6*D*). Later in the eruption, however, juvenile lava was observed without a distinctly strong thermal signature. There may, then, have been new lava at the surface on January 12, but it was not recognized thermally or it was visually hidden by ash and steam. If a dome did form, it was ephemeral and subsequently destroyed by blasts and/or partially covered by younger deposits. Abundant, dense, angular clasts in deposits from ensuing explosions may have been fragments of this ephemeral dome (Vallance and others, this volume).

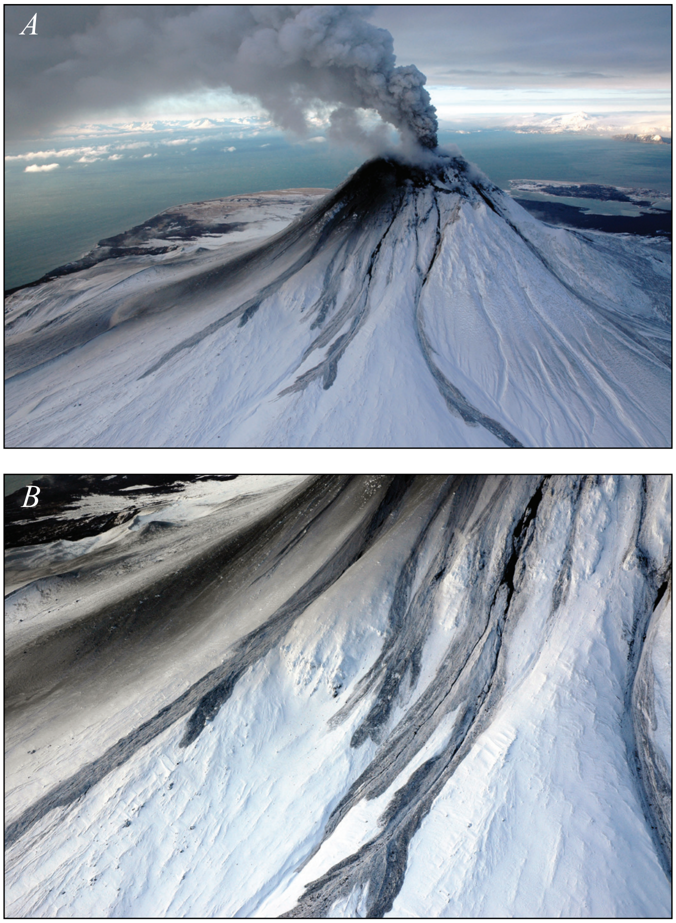

Figure 7. Oblique views of January 11, 2006, mixed-avalanche deposits. *A,* Mixed-avalanche deposits on the southeast and east flanks. View to the west. *B,* Detailed view of same deposits. Note streak of discolored snow at upper left that marks ash deposition. Photos by M.L. Coombs, January 12, 2006.

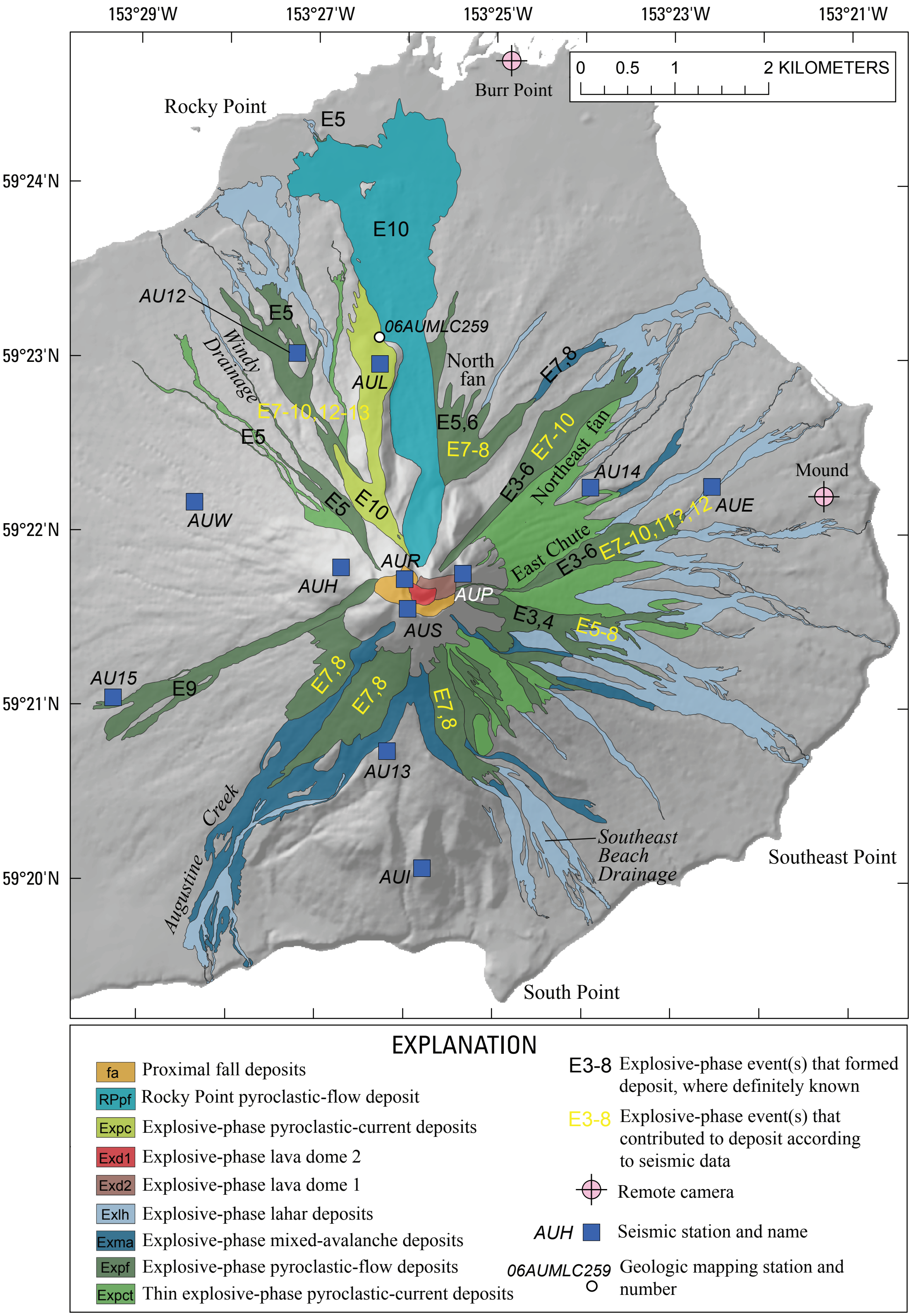

Figure 8. Map showing distribution of deposits from the explosive phase. Summit geophysical stations were destroyed during event 3. Station AUE recorded particularly strong seismic signals during events 3 and 4, thought to indicate that these events produced larger flows to the east (McNutt and others, this volume). Station AUL was destroyed during event 10, and debris from the station was found within a pyroclastic-flow deposit at station 06AUMLC259.

January 13 and 14: Explosive Events 3–8

A second series of six powerful explosions (events 3 through 8), ranging in duration from 3 to 11 minutes, occurred in a roughly 20-hour period between 0424 AKST January 13 and 0014 AKST January 14, as recorded by seismometers and an on-island pressure sensor (Petersen and others, 2006; Power and others, 2006; McNutt and others, this volume; Power and Lalla, this volume). The explosions produced ash plumes that reached altitudes of 14 km asl (Bailey and others, this volume) and deposited trace amounts of ash on the Kenai Peninsula communities of Homer and Port Graham (Wallace and others, this volume).

Explosive events 3 through 8 all resulted in the emplacement of hot pyroclastic deposits on most flanks of the volcano, which take two forms: thin (0–30 cm), laterally extensive (200–600 m wide by as much as 1.5 km long) sheets on the upper flanks, topped by farther-traveled coarse lobate flows (100 to 600 m wide by as much as 3 km long) (Vallance and others, this volume). These deposits have been mapped as two separate units: thin explosive-phase pyroclastic-current deposits (unit **Expct**) and explosive-phase pyroclastic-flow deposits (unit **Expf**), respectively (plate 1; fig. 8). Pyroclastic surges likely accompanied the explosions as well but the deposits were poorly preserved. In addition, the emplacement of pyroclastic flows on snow generated areally extensive mixed-avalanche deposits (unit **Exma**), lahars, and hyperconcentrated flows (unit **Exlh**; plate 1). These secondary deposits are described in detail in Vallance and others (this volume).

Some of the explosions that occurred on January 13 and 14 were photographed or bracketed by images from the Burr Point and Mound cameras (table 1), allowing us to link emplacement of some flows on the east and north flanks to individual events. The first overflight to the island after events 3–8 was on January 16 (fig. 9). Observers saw that the vegetation-free slopes of the volcano had been uniformly coated in brown ash-fall deposits; this coating somewhat obscured new flowage deposits. Closer inspection revealed that new flows had traveled down many slopes of the volcano and reached the coastline in several places (figs. 8, 9). Most followed tracks of earlier historic flows, but some, such as in the informally named Augustine Creek area (fig. 9*A*), destroyed vegetation. Later visits to the deposits revealed that pyroclastic flows had been limited to the upper two thirds of the edifice and that the flows that reached the coast were exclusively lahars and hyperconcentrated flows (fig. 8; Vallance and others, this volume).

Events 3 and 4

Events 3 and 4 occurred before sunrise on January 13 (0424 and 0847 AKST; table 1) and, thus, were not captured by the on-island cameras. The seismic signals for the two events lasted 11 and 4 minutes, respectively. Event 3 destroyed seismic station AUP and continuous GPS AV05 (collocated with AUP), located about 300 m from the volcano's summit (fig. 8). Both events produced the longest signal durations at short-period seismic station AUE, and the waveforms recorded there have codas indicative of pyroclastic flows (McNutt and others, this volume). Broadband station AU14 shows delayed seismic pulses during both events. These observations suggest that pyroclastic flows from the two events traveled predominantly to the east (fig. 8; table 2).

The event 3 seismic signal at station AUE was particularly long (>30 minutes) and was likely caused, in part, by lahars passing nearby, as well as by pyroclastic flows upslope (McNutt and others, this volume).

Due to darkness, no imagery is available to discriminate between flows emplaced during event 3 or event 4. The first image available after sunrise on the morning of January 13 from the Burr Point camera, at 0900 AKST, shows gray-brown ash clouds on the northeast and east flanks. Those ash clouds were the result of event 4, which began 13 minutes prior (table 1). A series of images from the Burr Point camera from 0915 to 1115 AKST show the ash clouds dissipating and new, fragmental steaming deposits on the northeast and east flanks (fig. 4*C*). No new discrete deposits were visible on the northwest flank, but the entire snow-covered upper northwest flank had been dirtied by either ash-fall deposits or thin surge or flow deposits. This blanket likely correlated to widespread pyroclastic-current deposits, recognized during August 2006 field work, that compose unit **Expct** (plate 1; fig. 8; Vallance and others, this volume). The results of events 3 and 4 on the south and west quadrants of the volcano are unknown but likely minor because of the absence of seismicity there.

Event 5

After a two-and-half-hour lull, event 5 began at 1122 AKST on January 13 and lasted for 3 minutes, 24 seconds. The first Burr Point image after this event, at 1130 AKST, showed an ash cloud rising from the summit and the east flank, while ash and steam shrouded the upper north flank (table 1). Steam and ash were visible rising from discrete tracks on the upper north and northwest flanks and along a single track on the lower north-northwest flank. By 1145 AKST, much of the ash and steam had cleared from the summit area, but a dark-gray cloud remained above the summit and east and southeast flanks. New discrete flow lobes were visible on the upper north and northwest flanks, as well as much farther down towards informally named Rocky Point (fig. 4*D*). A single flow was captured moving down the upper north flank. By 1200 AKST, the upper flanks were clear of steam and ash, though the lower east-southeast flank was still obscured in ash. Discrete flowage deposits were steaming on the upper north flank.

Seismicity during event 5 corroborates visual evidence. North and northwest of the volcano, stations AUL and AU12 both responded to flows during event 5 but not during earlier events. Because these were the first widespread pyroclastic flows of the sequence to flow north, they probably generated the lahars that moved downstream of the north fan and

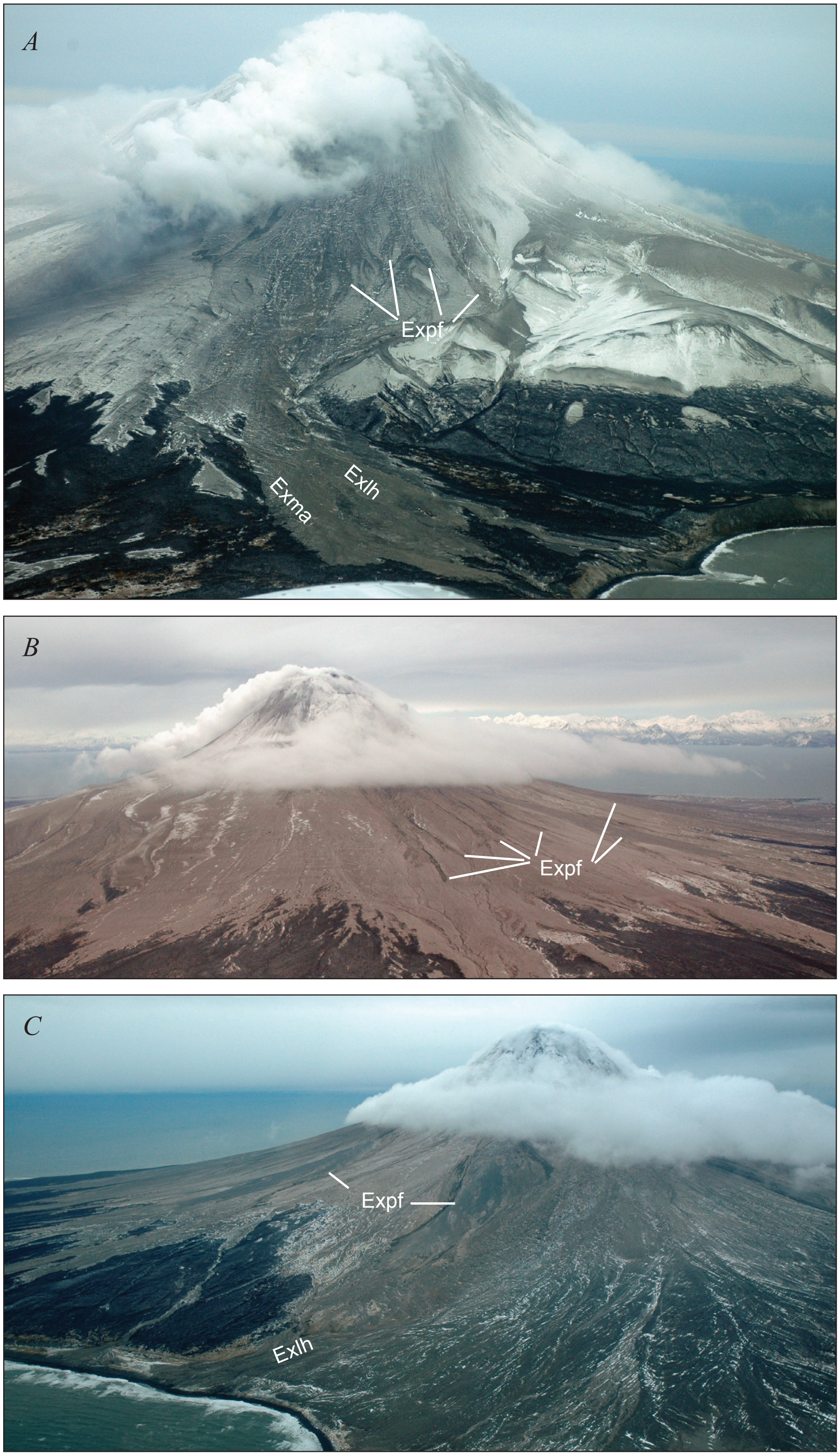

Figure 9. Explosive-phase deposits on the flanks of Augustine Volcano. *A,* Augustine Creek drainage, looking northeast. Lobate Expf, Exma, and Exlh deposits visible. *B,* View to the northwest. Vegetation-free slopes are covered in snow topped with ash fall. *C,* View to the southwest. Photos by R.G. McGimsey, January 16, 2006.

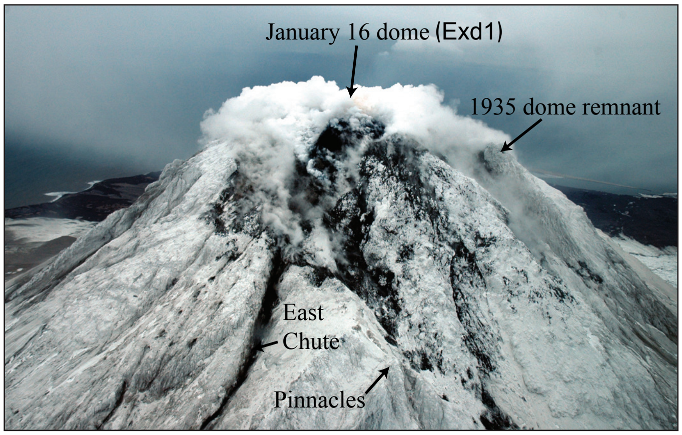

Figure 10. Oblique view of Augustine Volcano's summit showing the new lava dome (Exd1), January 16, 2006. View is to the southwest. This dome was later destroyed and/or buried by subsequent eruptive activity. Photo by R.G. McGimsey.

within informally named Windy Creek to the coast (fig. 8). The signal during event 5, in particular, could plausibly include lahars.

Event 6

A five-hour lull ensued, followed by event 6 that lasted from 1640 to 1644 AKST on January 13. An image taken from Burr Point at 1645 AKST shows a dark, billowing cloud rising from the east flank and a single pyroclastic flow traveling down the north flank just east of the north flank lava flow (fig. 4*E*). Photographs from Burr Point taken at 1715 and 1730 AKST show that flows on the north flank from event 6 all followed previous flow tracks; no new mappable areas are covered. A series of images from the Mound camera show a pyroclastic flow or surge descending the east flank toward the camera (table 1; fig. 5 of Paskievitch and others, this volume). As with previous events, we cannot visually determine the extent of flows from this event on the south or west flanks, but seismicity suggests that little material moved in those directions (table 2).

Events 7 and 8

Event 7 followed event 6 by 2 hours and lasted from 1858 to 1901 AKST on January 13, and event 8 started 5 hours later and lasted from 0014 to 0017 AKST on January 14. Neither of these events was captured by camera due to darkness. Dawn on January 14 brought overcast skies and clouds that obscured the mountain above approximately 500 m altitude. On the north flank, the Burr Point camera revealed only a couple of new flow deposits that must have formed during events 7 and 8 (fig. 4*F*).

Based on protracted seismic signals from instruments AU15, AU13, and AUI to the southwest and south of the volcano, pyroclastic flows and the mixed avalanches and lahars that they generated in Augustine Creek and informally named Southeast Beach Creek (fig. 8) most probably occurred during event 8.

January 16: Lava Lobe (unit Exd1)

Following event 8, the volcano entered a 3-day period of relative quiescence. Observers on a January 16 overflight discovered a dark lava lobe at the summit (fig. 10). Satellite images from the same day show that the lobe was roughly 200 m by 160 m and covered ~27,500 m^2; its thickness was unknown but can have been no more than a few tens of meters. It filled the crater that was likely formed during the explosions on January 13 and covered much of the 1986 dome. A satellite image from January 21 shows the same lobe, elongated to the east, but with a crater at the top. Dense, glassy ejecta, prominent in pyroclastic-flow deposits from event 9 on January 17, may be fragments of this dome (Vallance and others, this volume). The lobe likely reached its final size of roughly 275 m by 225 m by event 9 on January 17. Unlike the previous dome of January 11 and 12, no distinctive seismic signals accompanied its effusion (J. Power, oral commun., 2006).

This feature, explosive-phase dome 1 (unit Exd1; plate 1; fig. 8), was only partially covered by later effusion; a portion of it directly above the informally named East Chute remains exposed (fig. 11). It has a smooth surface, morphologically distinct from subsequent lava lobes. A single sample of the dome is low-silica andesite (57.5 weight percent SiO_2; Larsen and others, this volume).

January 17: Explosive Event 9

Approximately 80 hours after event 8, an 8-minute-long explosion, event 9, commenced in darkness at 0758 AKST on January 17 and sent an ash plume to 13 km asl that drifted to the west over the Alaska Peninsula (Power and others, 2006; Bailey and others, this volume).

Images from the Burr Point and Mound cameras from January 18 show that, if any fragmental flows from event 9 traveled down the north or east flanks, they followed the tracks of previous flows from events 3–8. An overflight on January 18, however, revealed a new flow deposit on the southwest flank (fig. 8). This flow traveled approximately 3.5 km from the summit, following a track previously developed by flows from the 1976 and 1964 eruptions (Waitt and Béget, 2009). Satellite images show that event 9 left a large crater in the new lava dome, and observers on the January 18 overflight noted a new field of ballistic blocks on the west and southwest side of the volcano extending to altitudes as low as 760 m (fig. 8). Data transmission from GPS station AV04 on the west flank stopped coincident with this explosion (fig. 8). The pyroclastic-flow deposit from event 9 is rich in dense, glassy clasts (Vallance and others, this volume) that are likely fragments of the new lava dome that had grown since January 14.

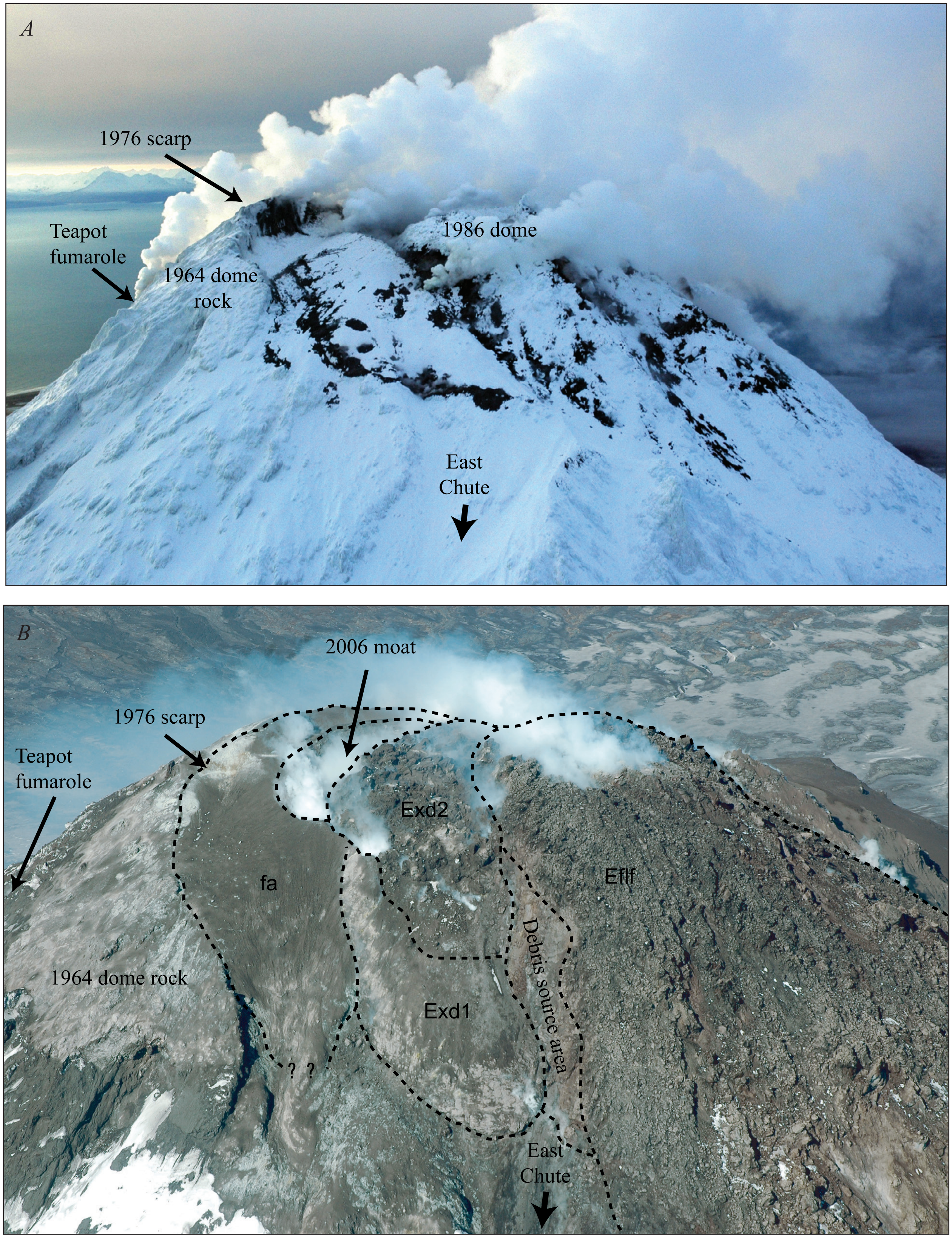

Figure 11. Oblique views of Augustine's summit before and after 2006 eruption. Views are to the west. *A,* Photo by K. Wallace, December 22, 2005. *B,* Photo by M.L. Coombs, May 13, 2006. The 2006 deposits are labeled as follows: Exd1, explosive-phase dome 1; Exd2, explosive-phase dome 2; Eflf, effusive-phase lava flows; fa, fall deposits.

Late January: Lava Effusion (unit Exd2)

Following event 9, Augustine Volcano remained seismically quiet for several days and an overflight on January 24 showed no new deposits on the flanks or changes at the summit. Satellite images from late January show that, at some time, most likely between events 9 and 10 (January 17 to 27), a new lava dome effused at the summit, partially covering explosive-phase lava dome 1 (fig. 8). The lobe is distinct from the earlier lava dome because it is lighter in color and its surface is much more rugged (fig. 11). Samples from this dome are high-silica andesite (62.3 to 63.1 weight percent SiO_2; Larsen and others, this volume). Explosive-phase lava dome 2 (unit **Exd2**) was likely partially destroyed during events 10–13 and was also later partially covered by effusive-phase lava. Therefore, its original extent is unknown. The portion of the dome that is still exposed lies within a moat formed by proximal 2006 fall deposits and is to the south of the new main summit dome that reached its final height during the effusive phase.

January 27 and 28: Explosive Events 10–13

After 10 days of relative quiescence, four explosions ensued in rapid succession: two on January 27 at 2024 and 2337 AKST (events 10 and 11) and two more on the morning of January 28 at 0204 and 0742 AKST (events 12 and 13). These all occurred at night and were initially detected seismically (Power and Lalla, this volume), and the resulting ash clouds were quickly detected by satellite images and radar (Bailey and others, this volume; Schneider and others, 2006). Event 10, the longest of the four at 9 minutes, sent an ash cloud to 10.5 km asl that drifted southeast. The other three ranged from 1 to 3 minutes in duration and sent ash clouds as high as 7.2 km (Schneider and others, 2006).

Because events 10 through 13 were at night, there were no visual or camera observations. The Burr Point camera was not in operation from January 23 to February 24, probably due to extreme weather conditions (Paskievitch and others, this volume). Observation overflights on January 29 and 30 found the island shrouded in ash during continuous-phase activity.

In the absence of visual observations of these events, seismicity and the destruction of geophysical stations provided clues about the accompanying activity. Event 10 destroyed station AUH, high on the volcano's west flank, 7 minutes after the beginning of the event and coincident with the strongest phase of the seismic signal recorded at broadband stations around the island. Event 10 also destroyed station AUL/AV03 near the toe of the prehistoric north flank lava flow (fig. 8). Unfortunately, the precise time of station AUL/AV03 destruction is unknown: the broadband seismometer at AUL had stopped sending data before the beginning of event 10, for unrelated reasons. The last data packet from GPS site AV03 was sent at 0459 AKST, however, 25 minutes before the start of the event (GPS data were transmitted on an hourly basis). Tellingly, pieces of the station were found within a new deposit below the north flank lava flow at locality 06AUMLC259 (fig. 8). This deposit is map unit **Expc** (explosive-phase pyroclastic-current deposits) and is mapped separately from other explosive-phase units due to its increased proportion of dense clasts and fines-deficient matrix (fig. 8; plate 1; Vallance and others, this volume). In addition to the different grain-size distribution, the deposit has a lithologic make-up that is transitional between earlier explosive-phase and later continuous-phase deposits—it contains low- and high-silica andesite in approximately equal proportions (Vallance and others, this volume).

In addition to the explosive-phase pyroclastic-current deposit mentioned above, there is evidence that event 10 also generated a second, larger pyroclastic flow. At the Oil Point reference seismic station, 30 km northeast of Augustine Volcano, the event seismic signal lasted 9 minutes (table 2), but its duration was minutes longer at several on-island stations and appears to record multiple flowage events (McNutt and others, this volume, fig. 4). The most plausible candidate to have also formed during event 10 is a 4.8-km-long pyroclastic-flow deposit on the north flank, first observed in an ASTER image from January 31 (Wessels and others, this volume) (fig. 4*G*; fig. 8). Named here the Rocky Point pyroclastic flow (unit **RPpf**; plate 1), it appears to have descended the north flank just east of the north flank lava flow before spreading out and filling in a small pond near the toe of the lava flow (Vallance and others, this volume). The deposit immediately overlies the explosive-phase pyroclastic-current deposits mentioned previously and immediately underlies the continuous-phase pyroclastic fan on the north flank. It is lithologically similar to continuous-phase deposits because it contains a high fraction of high-silica andesite clasts (Vallance and others, this volume).

While assigning the Rocky Point pyroclastic flow to event 10 is consistent with stratigraphy, the size of the deposit, the duration of the event 10 seismic signal, the airborne ash record from radar, and the lightning record all provide further evidence that link the two:

5. The Rocky Point pyroclastic flow is the single largest deposit of the eruption, with a volume of roughly 17×10^6 m^3 and a length of 4.8 km, thus we expect that the associated seismicity would be the longest flowage-derived signal during the time period when we know the flow was emplaced. Flow velocities of 5–10 m/s would require the emplacement of the flow over 8–16 minutes. For example, the smaller-volume, 3.7-km-long windy pyroclastic flow from the continuous phase (mapped as unit **Cpfw**) took roughly 7 minutes to come to rest. Between January 24, when observations show the Rocky Point flow to not be present, and the January 31 ASTER image, the longest flow/explosion signal recorded was during event 10.

6. During the continuous phase, the strongest ash signal detected by radar was from the windy pyroclastic flow, suggesting that

the much larger Rocky Point flow was not emplaced during the continuous phase (Schneider and others, 2006).

7. Event 10 produced the greatest number of lightning strikes between January 27 and the end of the eruption, the interval when a lightning-detection unit was operational (Thomas and others, this volume). The high number of lightning strikes can be the result of higher concentrations of airborne ash and/or the presence of additional steam, perhaps created as the Rocky Point pyroclastic flow entered the small pond (S. McNutt, written commun., 2007).

We have little information on the nature of flowage deposits produced during events 11–13 late on January 27 and early on January 28. Event 11 was very brief and it likely produced only minor deposits. The most energetic phases of events 12 and 13 lasted from 1 to 3 minutes, but the seismic signal had a long coda for event 12 at stations AUW and AUE and for event 13 at AUW, suggesting flows may have traveled east and northeast (McNutt and others, this volume). It seems likely that any pyroclastic-flow deposits from these two events are lithologically similar to the Rocky Point flow and to flows of the subsequent continuous phase.

The Continuous Phase—January 28–February 10

On the afternoon of January 28 at about 1430 AKST, 7 hours after event 13, Augustine Volcano entered a period of more continuous eruptive activity that lasted for 13 days. This period was characterized by (1) essentially continuous ash emission to heights of commonly less than 3,600 m asl, generating a variably ash rich plume, as recorded by satellite images and radar (Bailey and others, this volume; Schneider and others, 2006), (2) emplacement of pyroclastic flows on the north flanks of the volcano, as recorded by cigar-shaped seismic signals (Power and Lalla, this volume) and viewed in overflights, and (3) occasional larger seismic signals, thought to represent more explosive events, associated with ash clouds as high as 4,500–7,600 m asl. Ash fall was reported in Homer and Seldovia during this period (Wallace and others, this volume), 115 and 100 km east of the volcano, respectively. Activity waxed and waned during the continuous phase, as evidenced by variations in the number and duration of flow-related seismic events. The most vigorous activity ended on February 3 and was followed by steady effusion of a new lava dome and flow that lasted until approximately February 10. This entire interval from January 28 to February 10 is termed the “continuous phase” to distinguish it from the punctuated nature of the explosive phase.

January 28–February 3: Pyroclastic-Flow Emplacement

The early continuous phase resulted in a series of pyroclastic-flow deposits (units `Cpf`, `Cpc`, and `Cpfw`) on the north quadrant of the volcano (fig. 12; plate 1). These deposits cover an area of 4.9 km^2 and extend as far as 3.8 km from the summit. Several observation flights during the January 28 to February 3 interval provided information about the style of eruption (table 1), though observations of the volcano were hampered by airborne ash and poor weather. Additional evidence for timing of flow emplacement from this period is from seismicity, satellite images, and flow stratigraphy. The Burr Point time-lapse camera was not operational during the continuous phase, but the Mound camera provided several images of the activity during clear weather.

Seven hours after the four discrete explosive events on January 27 and 28 (events 10–13), seismometers recorded a roughly 2-hour period of volcanic tremor beginning at 1431 AKST on January 28. Starting at about 1418 AKST on January 28, coincident with (or slightly preceding) the increasing seismic tremor, Mound camera images revealed an ash-laden, vertically convecting plume that increased in vigor over the afternoon. Images show that no pyroclastic or debris flows or ash were deposited on the volcano’s north flank on January 28.

Beginning at 2200 AKST on January 28, seismic signals, at the rate of 5–10 per hour, first recorded the movement of pyroclastic flows down the flanks. The first visual evidence of flows on the north flank is from 1007 to 1015 AKST on January 29, when the Mound camera showed a thick billowing plume that rose from the summit and moved south and another ash cloud that rose from the north half of the summit and moved down the north flank (fig. 13).

A particularly strong seismic signal was recorded by the network starting at 1118 AKST on January 29. This emergent, broad-spectrum signal lasted for roughly 5 minutes and had the longest duration of any signal during the 13 hours since continuous activity began. Several lines of evidence suggest that it was caused by a large pyroclastic flow on the north flank. In web-camera images from Homer, the top of a wide ash cloud was visible above meteoric cloud tops from 1127 to 1137 AKST. Images from the Mound camera went dark starting at 1126 AKST, suggesting significant ash in the air. An observation flight on January 29 arrived in the vicinity of the island around 1230 AKST. Views of the volcano were hindered by broken clouds below and dense clouds above 2,100 or 2,400 m asl, but observers saw a plume from the summit vent that rose vertically and then turned southward, with ash visible to the south of the island. Observers also noted a prominent ash-and-steam cloud that rose from the upper north flank of the island (fig. 14*A*); the lower north flank was mostly obscured by clouds and ash. During the viewing period, this ash cloud dissipated, revealing discrete but widespread areas of steaming. A more diffuse, brown-gray cloud that drifted low above the coastline was plausibly a coignimbrite cloud. We cannot identify the exact deposit emplaced during this event, but it is likely one of the longer flow lobes on the north fan that extend down to 50–100 m asl (fig. 12).

For most of the rest of January 29, images from the Mound camera were dark, but by 1547 AKST the view cleared

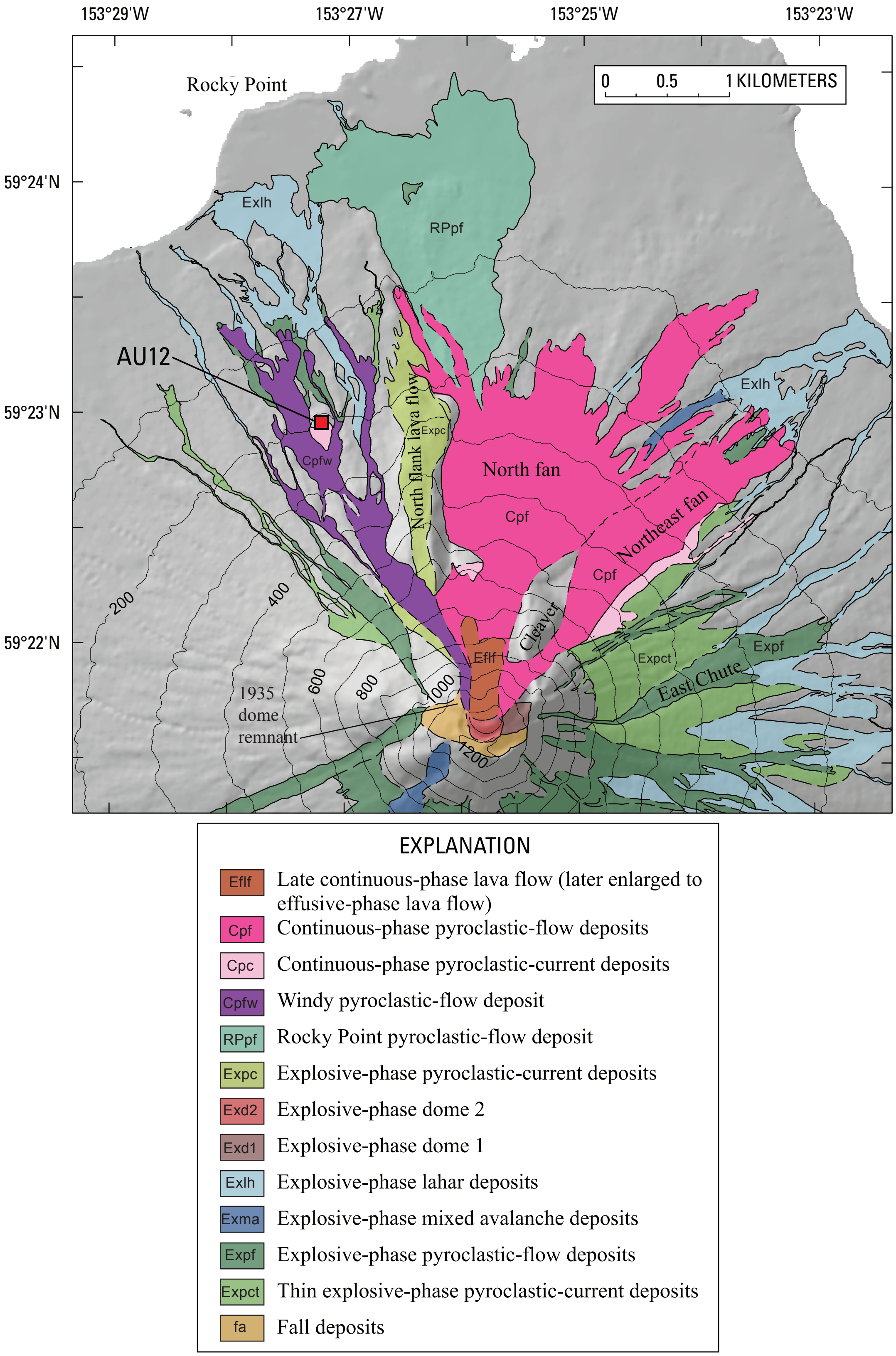

Figure 12. Map showing distribution of deposits at the end of the continuous phase (February 10, 2006). The location of broadband seismic station AU12, which was destroyed on January 30, 2006, is shown as a red square. Contours show pre-2006 topography; contour interval is 100 m.

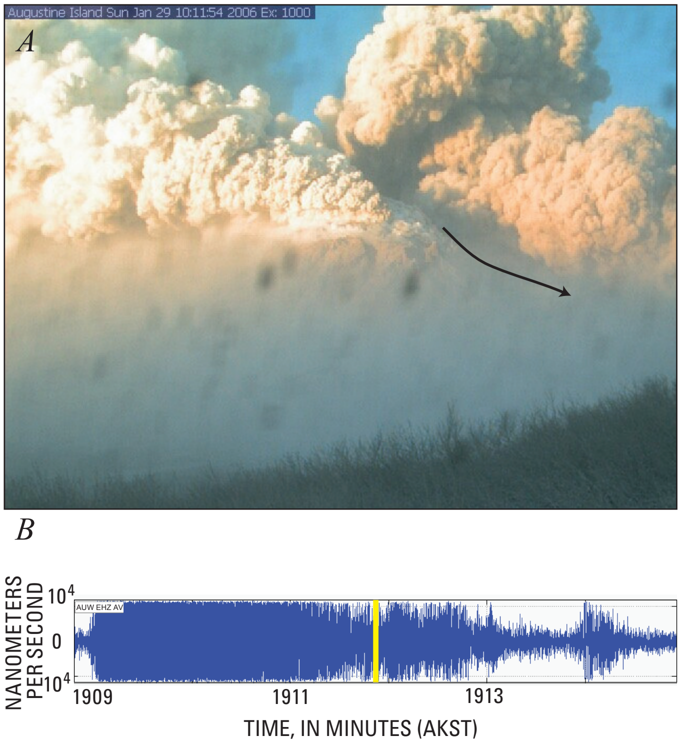

Figure 13. *A,* Mound web camera image from 10:11:54 AKST on January 29, 2006, showing intense steaming and likely ash emission from the summit and a small pyroclastic flow on the north flank (path shown by arrow). *B,* Seismic signal from station AUW showing small pyroclastic flow. Time that image was taken is shown by yellow line.

to show a dark cloud moving south and, in a single image, an ash cloud was visible rising from the north flank.

The destruction of a geophysical station recorded the passage of the single largest pyroclastic flow during the continuous phase. Campaign broadband seismic station AU12, on the northwest flank, was destroyed on January 30 at 0329 AKST (figs. 12, 15). We found the destroyed station at the edge of a pyroclastic-flow deposit in the summer of 2006. This braided deposit is named the windy pyroclastic flow deposit (unit Cpfw; plate 1) and is lithologically identical to other continuous-phase deposits (Vallance and others, this volume). Interestingly, AU12, which was 2.6 km from the summit, was destroyed approximately 4.5 minutes after the start of the flowage seismic signal, yielding an average flow rate of 9.6 m/s. During the 1976 eruption of Augustine Volcano, a series of time-stamped photographs recorded a pyroclastic flow that traveled at 50 m/s on the steep upper slopes and slowed to ~6 m/s as it reached the north coastline (Stith and others, 1977). The flowage seismic signal, which was no longer recorded by AU12 after its destruction, continues for approximately another 3 minutes on nearby broadband station AU11. If we assume that the flow traveled at the slower rate of 6 m/s for the rest of its course on the lower slopes of the volcano, it would have covered roughly 1.1 km in that time, for a total of 3.7 km. This is the exact length of the windy pyroclastic-flow deposit, suggesting that the entire flow was emplaced during this single flowage event. Radar data for this time interval shows the greatest ash signal seen during the continuous phase (Schneider and others, 2006), which is consistent with the idea that the windy pyroclastic flow was emplaced during a single, large event.

Smaller flowage signals continued to be recorded by the seismic network at a relatively high rate through February 3, though none were as large as the two on January 29 and 30. An overflight midday on January 30 revealed a dense vertical column rising from the summit vent to 4,900 m asl before drifting off as an ash cloud to the northeast for roughly 145 km (fig. 14*B*). The northern portion of the vertical eruption column and the tephra cloud moving to the northeast were brown gray and appeared more ash rich; the central, billowing part of the plume immediately above the vent was lighter colored. No fresh flowage deposits were identified in the southwest and southeast quadrants. An ashy haze that surrounded the slopes of the volcano, especially thick on the north flank, prevented views of the ground surface. During an observation flight on

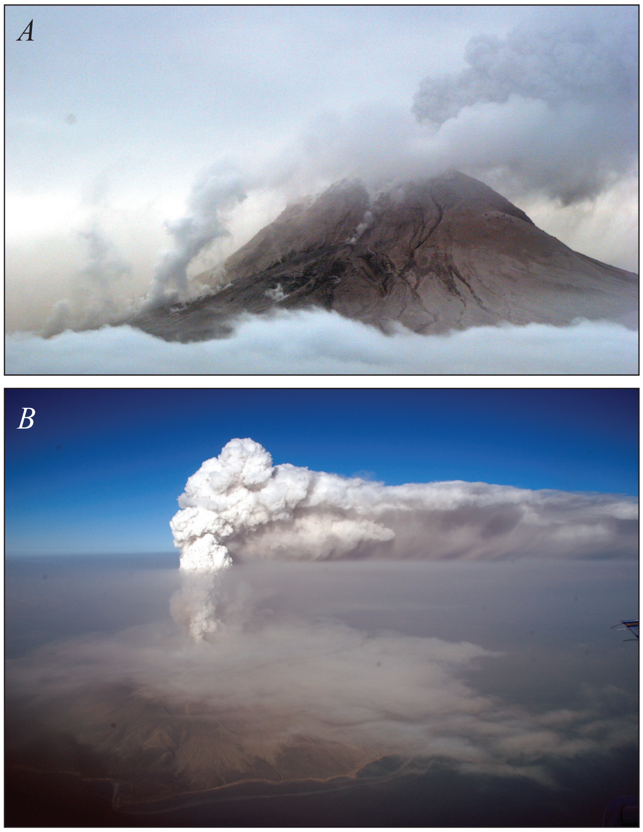

Figure 14. *A,* Photograph of the upper north flank of Augustine Volcano, taken by K. Wallace during January 29, 2006, overflight. Steaming flows are visible. *B,* Photograph of Augustine Island, looking north, taken by R.G. McGimsey during January 30, 2006, overflight.

February 3, the volcano was completely obscured by clouds, but observers saw an ash cloud above the volcano that reached to approximately 1,800 m asl. A brown plume was rising from high on the north flank.

Satellite images provided the first direct view of deposits of explosive events 10–13 and the early continuous phase (table 1). An ASTER image from January 31 showed the windy pyroclastic flow, the Rocky Point pyroclastic flow, and the north continuous-phase pyroclastic fan; much of the northeast flank was obscured in the image by a SO_2-rich plume (Wessels and others, this volume). A Hyperion satellite image from February 2 showed a strong thermal signature from the summit and a thin streak down the northeast chute; these were presumably a summit lava dome and a thin block-and-ash flow deposit (Wessels and others, this volume).

Observers first saw continuous-phase pyroclastic-flow deposits during a FLIR flight on February 8 (fig. 16). The deposits were dark and steaming, contrasting sharply with the surrounding snow-covered flanks. Numerous small pyroclastic flows constructed fans of fragmental debris on the north and northeast flanks. The fans resemble those from 1976 and 1986 eruptions in similar locations. On the northwest flank, the thickest portions of the windy pyroclastic-flow deposit (unit Cpfw) were visible as braided fingers; thinner and presumably cooler portions were obscured by new snow. Field work during August 2006 revealed that all continuous-phase deposits are light gray and poorly sorted and contain abundant, dense, large, high-silica-andesite blocks that resemble rocks of the second explosive-phase dome (Vallance and others, this volume).

February 3–10: Beginning of Lava Flow Effusion

The number of flow-related seismic signals tapered off over a period of 24 hours from roughly February 3 to February 4. Seismicity increased again over a 24-hour period on February 5. Beginning around February 3, the ash emission of the early continuous phase gave way to lava effusion that persisted through February 10, as evidenced by continued rockfall seismic signals, continued deflation as recorded in CGPS (Cervelli and others, this volume), persistent thermal anomalies in satellite data (Bailey and others, this volume), and incandescence at the summit and upper north flank viewed from Homer in early February (Sentman and others, this volume). Lava slowly or intermittently extruded from the summit area became unstable

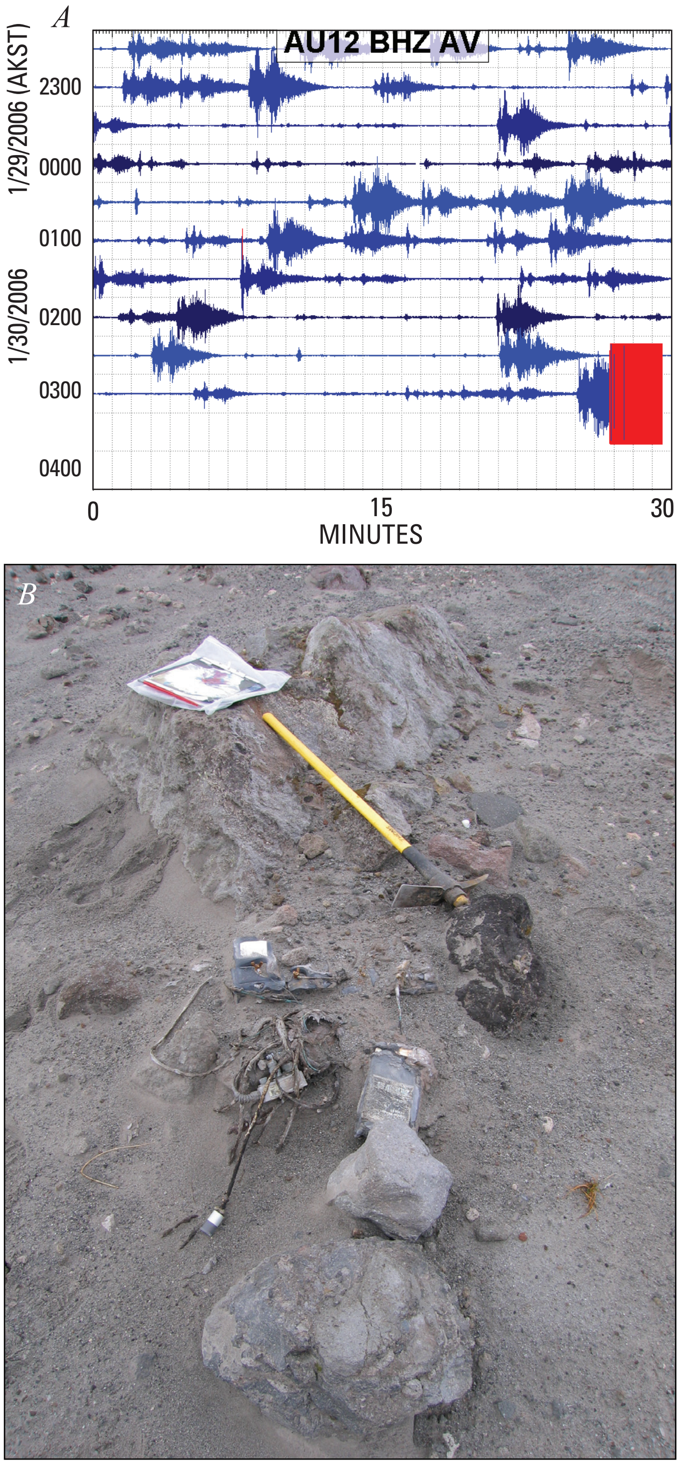

Figure 15. *A,* Seismic record showing a series of pyroclastic-flow signals recorded by campaign broadband seismometer AU12 on Augustine Volcano's northwest flank (see fig. 12 for location). The final flow signal ceased at 0329 AKST on January 30, 2006, when the station was overrun by the windy pyroclastic flow. Red rectangle indicates time period when signal strength exceeded the range of the instrument. *B,* Photograph of destroyed seismic station AU12. The data card was still intact and recorded that the station ceased operation on January 30 at 0329 AKST, presumably coincident with the emplacement of the windy pyroclastic flow. Larger boulders predate the 2006 eruption. The flow left only a thin deposit in this area but melted the station casing and much of the equipment. Flow direction was from top to bottom in the image. Adze is approximately 1 m long. Photo by M.L. Coombs, August 10, 2006.

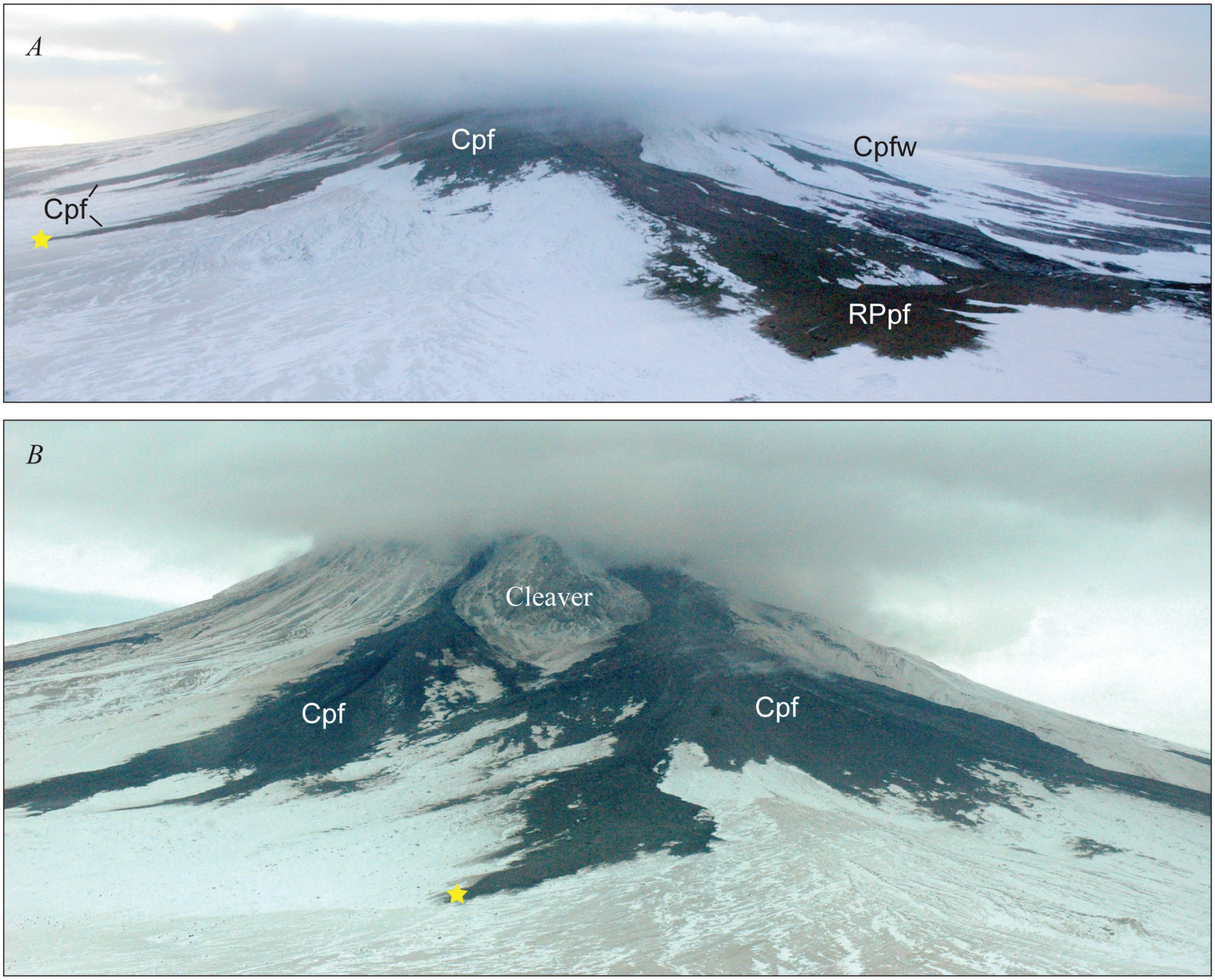

Figure 16 Photographs of continuous-phase pyroclastic-flow deposits, taken Feb 8, 2006. *A,* View towards south. *B,* View towards southwest. Star shows toe of the same flow deposit in both photos. Photos by M.L. Coombs.

and occasionally tumbled down the flanks as block-and-ash flows and rock falls. These events sometimes generated low-level ash clouds to altitudes of less than 3,000 m asl.

By February 7, satellite images showed that a multi-lobe lava flow had made its way down the north flank. It covered 215,000 m^2 and was roughly 900 m long by 300 m across. The lava progressed down a chute between the 1935 dome remnant and the informally named Cleaver (fig. 12). FLIR and visual observations on February 20 and 24 (Wessels and others, this volume) reveal that, by that time, the north lava flow was approximately 1,000 m long and that it extended from a new, dark, rubbly lava dome that covered the north half of Augustine's summit (fig. 4*F*). Given the lack of seismicity after February 10, we interpret that most of this growth occurred before then.

Eruptive Hiatus—February 10–March 3

During the period from February 10 to March 3, seismicity was low and no visual evidence exists to suggest that measurable volumes of magma were being erupted. FLIR flights on February 20 and 24 showed few changes had occurred at the summit (Wessels and others, this volume). However, several small explosions were recorded by seismic instruments and by the on-island pressure sensor (McNutt and others, this volume), and scattered rockfalls were recorded seismically. Periods of incandescence seen with the Homer low-light camera (Sentman and others, this volume) and with the Burr Point camera between February 15 and March 1 likely recorded the fracturing and spalling off of the lava-flow front.

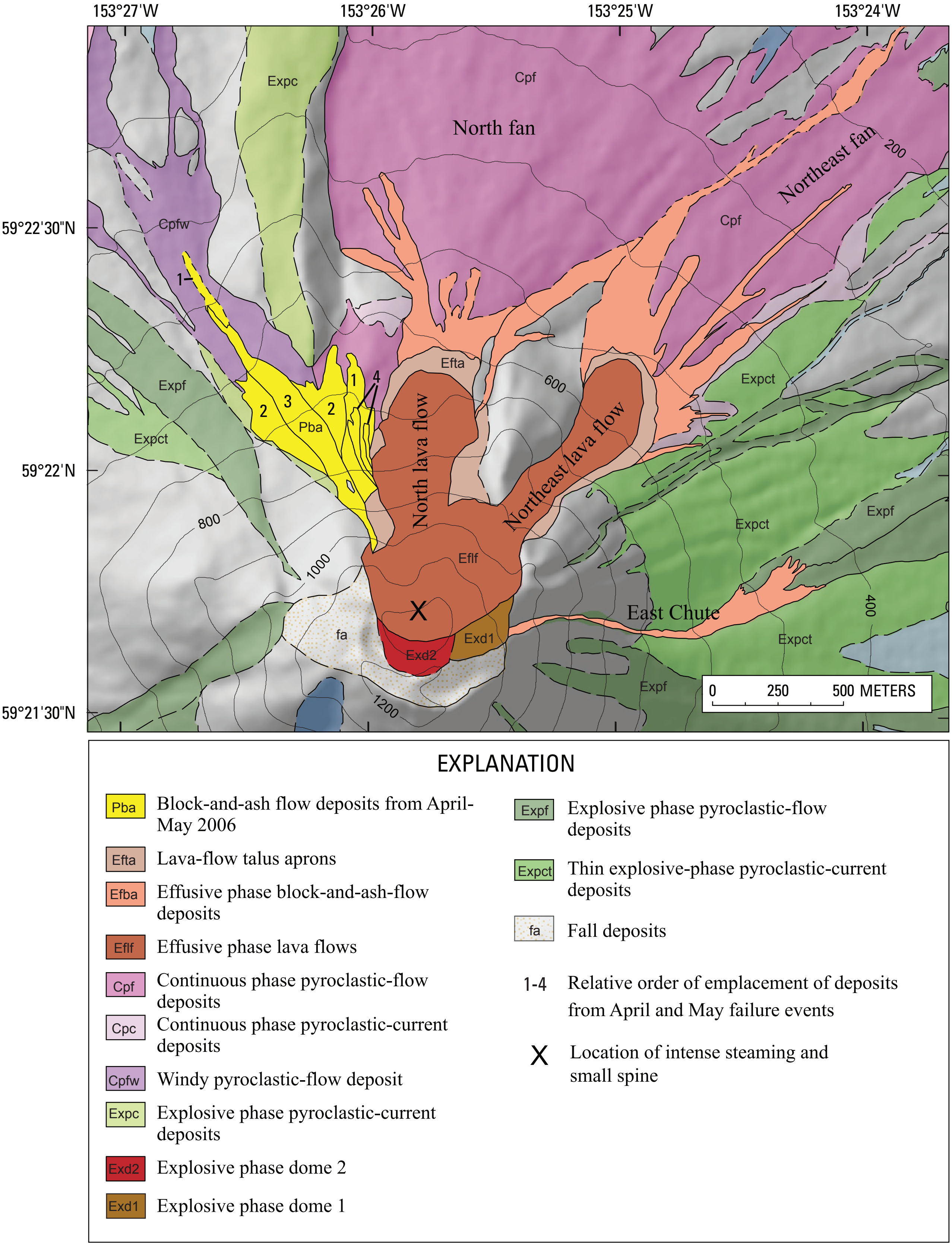

Figure 17. Map showing Augustine Volcano's summit region, highlighting deposits from the effusive phase (March 3–16, 2006) and after (April-May 2006). Contours show pre-2006 topography; contour interval is 100 m.

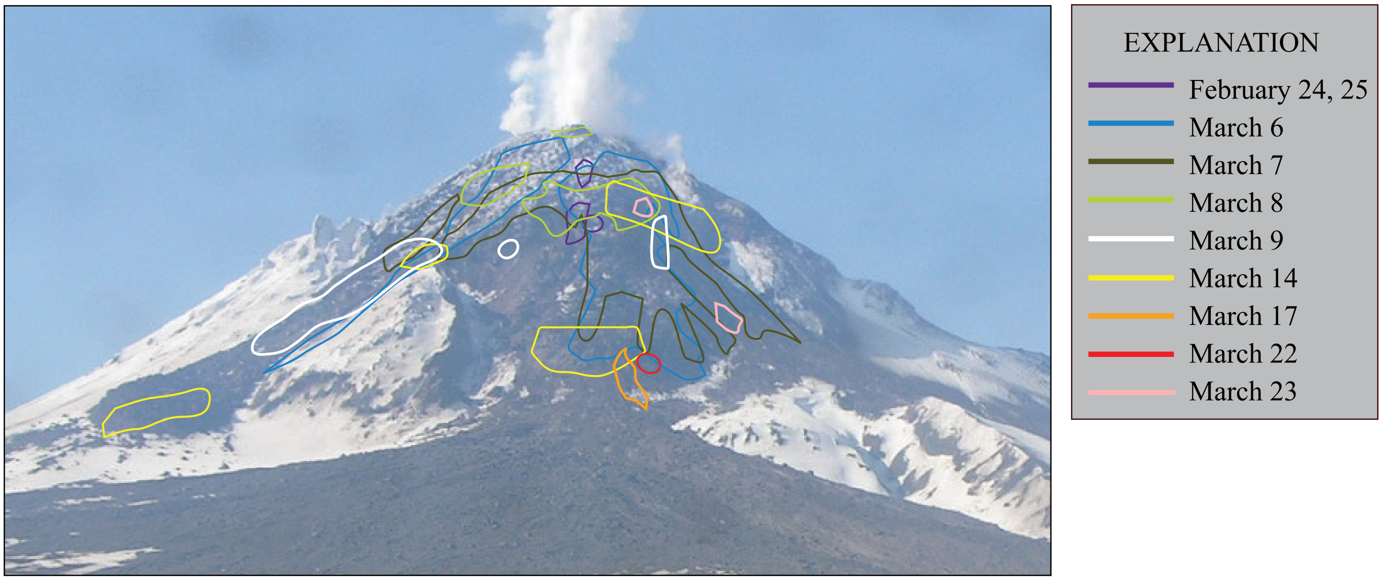

Figure 18. Photograph of the north flank of Augustine Volcano, taken from Burr Point time-lapse camera on May 13, 2006. Areas of incandescence, color-coded by day, are shown.

The Effusive Phase—March 3–16

After an apparent pause in eruptive activity throughout the latter half of February, Augustine Volcano resumed activity in March with the effusion of a larger summit dome, renewed growth of the north lava flow, and formation of a new lava flow down the northeast chute, all accompanied by vigorous block-and-ash flows (fig. 17; plate 1). In contrast to the continuous phase, clear weather and lesser amounts of airborne ash allowed thermal, visual, and satellite observations during this phase, which augmented seismic data. During this time, incandescent areas were observed at the summit and extending down the north flank; motion of incandescent blocks and/or flows was also observed. This activity was seen in nighttime images from the Homer camera, the low-light camera (also located in Homer; Sentman and others, this volume), and the Burr Point time-lapse camera (the Mound camera was not turned on at night due to power considerations; Paskievitch and others, this volume).

An increased number of rockfall seismic signals late in the evening of March 3 heralded the beginning of the effusive phase (Power and Lalla, this volume). On March 4, a series of small, localized ash emissions from the summit were captured with the Mound camera (table 1; fig. 5).

Observations of incandescence, though sometimes hampered by cloudy conditions, commenced during the night of March 5 and provided clues about the style of activity and growth of the lava flows and dome (fig. 18). Two types of incandescence were observed by Burr Point and Homer cameras. First, relatively stationary points and regions of incandescence represented exposed, hot parts of the growing lava dome or flows. Second, glowing streaks that moved downslope in subsequent, closely timed images (Sentman and others, this volume) represented block-and-ash flows shed from the summit dome and from the toes and flanks of the lava flows. These pyroclastic flows descended the north, northeast, and east chutes from the summit and were synchronous with seismic signals (DeRoin and others, 2007). Smaller streaks likely recorded incandescent rockfall or talus; such activity graded into larger block-and-ash flows.

On March 6, seismic vigor increased and clear daytime views revealed steaming and low-level ash emission that extended several hundred meters above the summit. Most of the steaming was on the north flank, and it appeared that the north lava flow that had effused during the end of the continuous phase was once again growing. No lava flow was visible in the northeast chute, although fresh, dark pyroclastic-flow deposits were visible, and a small pyroclastic flow was captured in motion at 1616 AKST by the Burr Point camera (table 1). Nighttime images showed that maximum incandescence occurred on March 6 and 7, when large swaths of the summit and upper north flank were glowing (fig. 18).

Seismicity quieted again for roughly 24 hours starting at 0600 AKST on March 7. Daytime views found no lava flow in the northeast chute on March 7 or 8. Starting at 0600 AKST on March 8, persistent, near-identical (drumbeat) earthquakes began to dominate the seismic signal (fig. 1; Power and Lalla, this volume). For 21 hours from 1730 AKST on March 8 to 1430 AKST on March 13, most on-island seismic stations received such strong signals that they were off the scale. By 1430 AKST on March 14, seismicity returned to pre-March 6 levels.

A lava flow was first observed within the northeast chute during an overflight on March 9. Observers also noted that pyroclastic-flow activity on March 9 was more prevalent to the northeast than to the north, suggesting active growth of the northeast lava flow during this time. That evening, nighttime cameras showed that the margin of the northeast lava flow was

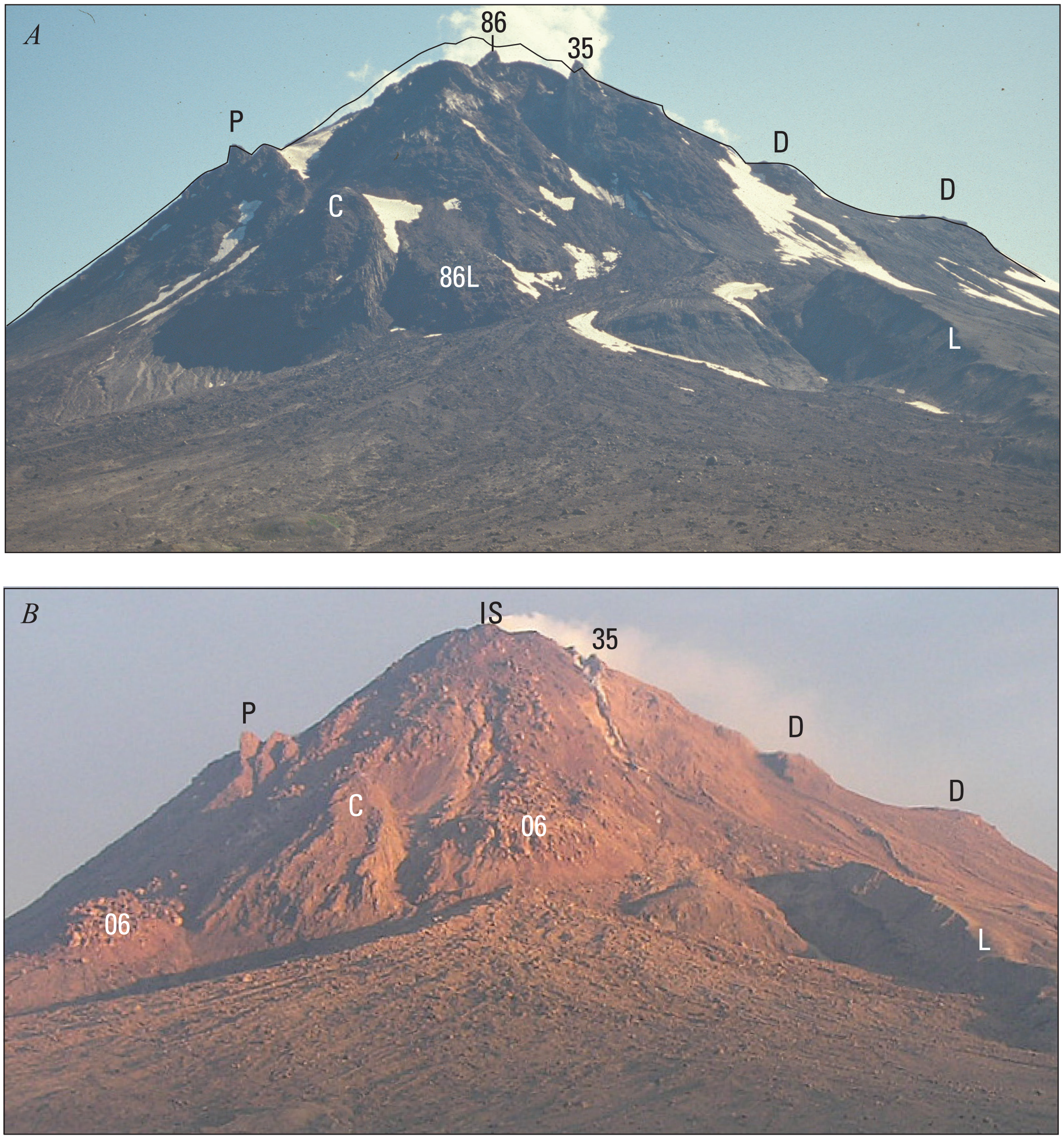

Figure 19. *A,* Augustine Volcano's edifice photographed from Burr Point to the north. Black line indicates edifice profile following the 2006 eruption. Photo by R.G. McGimsey, July 28, 1994. *B,* Augustine's edifice photographed from Burr Point time-lapse camera, July 24, 2006. P, Pinnacles (an old vent breccia; Swanson and Kienle, 1988); C, Cleaver; 86, 1986 lava spine; 35, 1935 dome remnant; D, prehistoric lava domes; 86L, lava flow from 1986 eruption; L, prehistoric north-flank lava flow; 06, lava flows from 2006 eruption; IS, incipient spine atop 2006 dome.

glowing. By March 14, areas of incandescence had moved down the slopes and marked the toes of the north and northeast lava flows (fig. 18).

Field crews flew to the island to acquire FLIR measurements twice during the effusive phase: on March 10 and March 15 (Wessels and others, this volume). Thermal images acquired on these dates delineate the new lava flows, whereas visual images were often partially obscured by steam, ash, and/or backlit conditions. On March 10, the new northeast lava flow was visible in thermal imagery and reached from the top of the new summit dome to the base of the Cleaver, for a total length of roughly 1,000 m. The north lava flow had also advanced from its position at the end of the continuous phase—it measured about 900 m from the summit to the toe. By March 15, the northeast flow had lengthened to about 1,300 m, while the north lava flow had advanced only slightly, if at all. Both flows, however, appeared to have thickened considerably at their toes between March 10 and 15; the toe of the northeast flow was 80 m high, and that of the north lava flow was 85 m.

After March 15, the summit dome and the two lava flows underwent few or no morphological changes, indicating that effusion had largely ceased by that date. Incandescence also decreased and was limited to the west margin of the north lava flow (fig. 18).

The lava flows (unit Eflf; fig. 17; plate 1) from the 2006 eruption are typical of andesitic block lava flows and have prominent lateral levees, blocky surfaces, and steep flow fronts. The north flow is roughly 700 m long from the base of the new dome, as much as 340 m wide, and 85 m thick at the toe. The northeast lava flow extends 900 m from the base of the new dome, is as much as 250 m across, and is 80 m thick at the toe. They are the most voluminous of any lava flows from recent eruptions of Augustine Volcano. The 1986 eruption resulted in a steep blocky flow that appeared to issue from the base of the dome (Swanson and Kienle, 1988); it descended the north summit region to an altitude of approximately 580 m asl (fig. 19*A*). The 2006 north lava flow covered essentially all of that flow and is about as long, but it is about 200 m wider (fig. 19*B*). The 2006 northeast lava flow filled the northeast gully to an altitude of 500 m asl. The two lava flows are essentially continuous with the new summit dome, which covered the north halves of the flow lobes emplaced in January, and filled the north half of the summit crater from the 1935 dome remnant on the west to the informally named Pinnacles to the east (fig. 11; fig. 19*B*). The new dome now forms the volcano's summit, approximately 70 m higher than it was before 2006.

Lava effusion was accompanied by numerous rockfalls and small block-and-ash flows that were detected seismically (DeRoin and others, 2007), observed during overflights, and photographed by cameras. The block-and-ash flows formed prominent, dark deposits (unit Efba) that sit atop the upper reaches of the continuous-phase pyroclastic flows of the north and northeast fans (fig. 17; plate 1). Unit Efba flows also traveled down the east chute. These poorly sorted deposits consist of clasts of mostly dense andesite in a fine-grained matrix (Vallance and others, this volume).

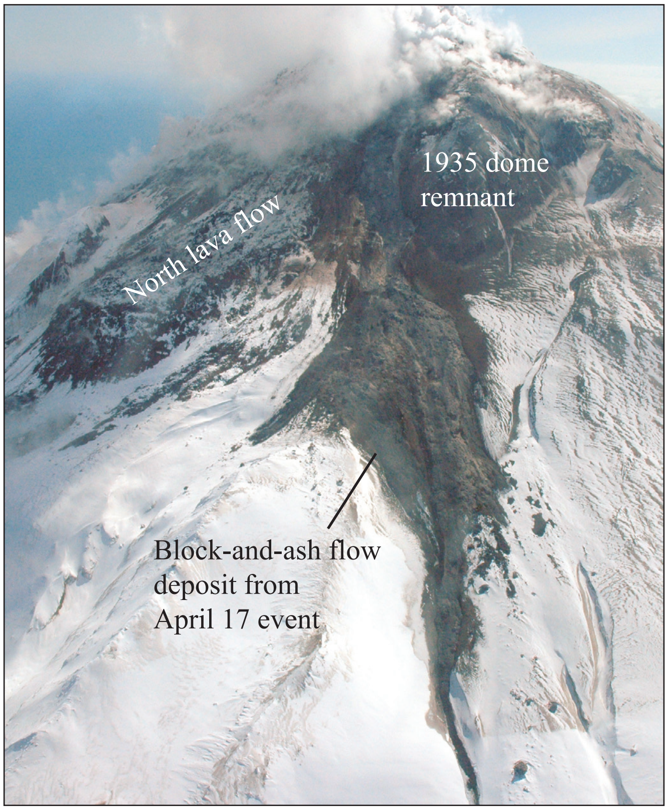

Figure 20. Photograph of Augustine Volcano's upper northwest flank, showing deposit from April 17 block-and-ash/rockfall event. Photo by R.G. McGimsey, April 19, 2006.

Figure 21. Photograph of Augustine Volcano's lower north flank, showing pink lahar deposits atop the 2006 Rocky Point pyroclastic-flow deposit. The lahars are thought to have occurred on October 1 and consist of remobilized fine-grained material from the 2006 eruptive deposits. Dark brown area at right of photo is pre-2006 surface. Field of view is approximately 500 m across. Photo by K.F. Bull, October 15, 2006.

Post-Eruption Activity—Rock Avalanches and Lahars

While eruption of juvenile magma apparently ceased by March 16, secondary activity involving the remobilization of 2006 eruptive deposits continued through October 2006.

Spring 2006 Rock Avalanches

On March 17 through 23, small, point-source incandescent areas were visible along the edges of the new lava flows. Rockfalls were recorded by seismic signals as often as a few times each day. Most signals recorded the downhill path of single, large boulders, as discovered in April when overflight observers saw a single boulder bounce down the west flank, marked the time, and found later that this activity correlated with a minute-long signal at nearby seismometer

AUW. Several longer, stronger seismic signals were found to correlate with larger rock-avalanche events.

The first rock-avalanche signals were detected on April 8. Between 1635 and 1708 AKDT, two bursts, 9 and 17 minutes long, were recorded seismically. Unfortunately, cloudy conditions at the time completely obscured the view from the Burr Point and Mound cameras. During a gas-monitoring flight on April 11, observers saw debris from the events (not present on an April 6 overflight) adjacent to the west margin of the north lava flow (table 1). The debris deposit extended almost as far downslope as the lava flow and had a total length of roughly 750 m. Large blocks—some steaming and some obviously cold—littered the area. A small lahar-like deposit extended downslope beyond the main debris field. Ash produced by this rock avalanche was carried by high winds across the northwest flank, leaving a radial, spoke-shaped deposit. Severely backlit conditions made it difficult to see the source area of the avalanche(s), but the axis of the deposit projected to a point below the summit dome. The deposit from this event was completely covered during subsequent activity, so it is not represented on the map (plate 1).

On April 17, a series of large flowage seismic signals, from 1656 to 1732 AKDT, were recorded by stations AUW, AUE, AUSE, and AUI. Elevated rockfall activity, recorded seismically, continued at a lesser rate until 0240 AKDT on the morning of April 18. Mound and Burr Point camera images from April 17 are obscured by clouds. During a gas-monitoring flight on April 19, observers saw a large amount of rock-avalanche debris on the volcano's northwest flank that had overrun the smaller debris field from April 8 (fig. 20). The main debris was not steaming, and they saw only a few hot blocks, mostly along the margin of the deposit. The distal end of the avalanche debris was incised and showed evidence of minor water flow. Backlit conditions once again prevented observations of the avalanche source area. The deposit was later partially covered by smaller rockfall events, but remnants of it are exposed and are shown on the deposit map as unit Pba (fig. 17; plate 1).

Rockfall activity increased again the night of May 25, leading to two particularly large flowage events on May 26 at 0106 and 0748 AKDT. The second event was the larger of the two and lasted approximately 5 minutes as recorded seismically. Unlike the previous avalanche events, the 0748 AKDT avalanche was photographed by both on-island cameras. Fortuitously, it was also photographed by M. Byerly aboard a boat approximately 5 km northeast of Augustine Island (table 1). Images from the three sources show that the rock avalanche was accompanied by an ash cloud that likely rose to 1 to 2 km above the summit and drifted to the south. An initial small ash puff was recorded along the flank of the lava flow at 0738 AKDT, then a light-gray cloud moved downslope along the west side of the north lava flow, growing in height as it flowed almost to the end of the north-slope lava flow. By ~0800 AKDT, the flowage event had ended but the cloud had diffused, increased in diameter, and drifted around to the south and west side of the summit.

Observers on a June 2 overflight saw the deposits and located the source area of the May 26 events as the upper west side of the northwest lava flow, where a line of fumaroles down the chute marked the breakaway surface. The debris overtopped the upper portion of the north flank lava flow before bifurcating down either side; somewhat more debris was directed along the west side of the lava flow. The debris overlies deposits from previous slides.

October 2006 Lahars

Several months after the cessation of eruptive activity, several small flowage events occurred, though these were different in nature than the spring rockfalls. On October 1, two pulses of seismicity were recorded from 0750 to 0915 (85 minutes) and 2116 to 2145 (29 minutes) AKDT. The signals were strongest on stations located on the east, north, and west flanks, and both were pulsatory with pulses from 2 to 10 minutes in duration (T. Petersen, written commun., 2006). These seismic signals had characteristics of surface clastic flows but persisted much longer than rockfall signals recorded previously.

On October 12 and 15, observers photographed new deposits on the lower north flank of the volcano (table 1). The new deposits were thin, braided, and obviously involved significant water in their emplacement (fig. 21). They were strikingly pinkish and light gray-colored, similar to pink ash-fall deposits associated with continuous-phase pyroclastic flow emplacement (Wallace and others, this volume). The largest of these October flow deposits was just south of the northeastern continuous-phase pyroclastic fan and reached the coastline. Others flowed atop Rocky Point and continuous-phase pyroclastic-flow deposits on the northwest flank, as well as on the west, south, and east sides. Where photographed on the north flank, new flows were most visible below a distinct break in slope at approximately 20 m asl. We believe that the observed lahar deposits correlate with the seismically detected events of October 1 and that they mostly involved remobilization of 2006 ash-fall deposits or matrix from continuous-phase pyroclastic-flow deposits. Deposits from these small-volume lahars are not shown on the 2006 geologic map (plate 1).

Volume Calculations

Methods

Using the geologic map, we have estimated the volumes of on-island erupted material from the eruptive phases of the 2006 Augustine Volcano activity (table 3; fig. 22). Most volumes were determined using the mapped areal extents of units and either estimating or measuring their thickness. Areas were measured from the time-slice maps (figs. 6, 8, 12, 17) to include buried deposits. The proximal, buried extents were either approximated or, where possible, mapped from imagery acquired during the eruption (for example, figs. 4

Table 3. Volume estimates for 2006 deposits.

[DRE, dense-rock equivalent; HSA, high-silica andesite; LSA, low-silica andesite]

Date (2006)	Deposit type (unit)	Deposit area (m^2)[1]	Deposit thickness (m)	Inflated eruptive volume (10^6 m^3)	Cumulative inflated erupted volume (10^6 m^3)[2]	Erupted volume (DRE; 10^6 m^3)	Cumulative erupted volume (DRE; 10^6 m^3)	Cumulative erupted HSA (DRE; 10^6 m^3)	Cumulative erupted LSA (DRE; 10^6 m^3)	Duration (hr:min:sec)	Magma flux (m^3/s)
					Explosive phase						
January 11	Mixed avalanches (Exma)	980,000	n/a	n/a	n/a	n/a	n/a	n/a	n/a		
January 12	Early, ephemeral lava dome	n/a	n/a	n/a	n/a	n/a	n/a	n/a	n/a		
January 13–14	Events 3–8, flows (Expf, Expct, Exma, Exlh)	16,570,000	various	7.39	7.4 (1.9)	4.4	4.4	1.3	3.2		
January 13–14	Events 3–8, fall[3]	n/a	n/a	20.30	27.7	7.7	12.1	3.5	8.6	00:28:41	7,050
January 14–16	Lava dome (Exd1)	30,000	30	0.82	28.5 (2.0)	0.7	12.9	3.7	9.1	59:43:00	3
January 16–17	Continued growth of Exd1	70,000	30	2.06	30.5 (2.1)	1.8	14.7	4.3	10.4	19:58:00	25
January 17	Event 9, flow (Expf)	610,000	0.3	0.18	30.7 (2.1)	0.1	14.8	4.3	10.5	00:04:11	
January 17	Event 9, fall[3]	n/a	n/a	1.73	32.5	0.7	15.5	4.5	11.0	100:00:00	3,100
January 17–27	Lava dome (Exd2)	60,000	0.15	1.89	34.3 (2.2)	1.7	17.2	5.9	11.3	150:00:00	3
January 27–28	Events 10–13, flows (RPpf, Expc)	3,870,000	various	16.90	51.2 (3.7)	10.1	27.3	14.1	13.2		
January 27–28	Events 10–13, fall[3]	n/a	n/a	6.26	57.5	2.4	29.7	15.0	14.7	00:15:08	13,800
					Continuous phase						
January 28–February 2	Flows (Cpf, Cpc, and Cpfw)	4,900,000	various	14.40	71.9 (5.2)	8.7	38.4	21.4	16.9	110:00:00	22
February 2–7	Lava flow (Eflf)	220,000	50	10.80	82.7 (6.1)	9.6	47.9	22.5	25.4		
February 7–10	Continued lava growth (Eflf)	30,000	50	1.50	84.2 (6.1)	1.3	49.3	22.6	26.6	192:00:00	16
					Effusive phase						
February 10–March 3	Hiatus	0	0	0.00	84.2 (6.1)	0.0	49.3	22.6	26.6		
March 3–16	Lava flow and dome (Eflf)	430,000	60	25.90	110.0 (8.9)	23.0	72.3	25.2	47.1		
March 6–16	Block and ash flows (Efba)	510,000	1	0.51	110.5 (8.9)	0.5	72.7	25.2	47.5	240:00:00	27

[1] Where referring to growing feature, like lava dome, deposit area refers to area of new growth only.

[2] Uncertainty estimate given in parentheses.

[3] Data from Wallace and others (this volume).

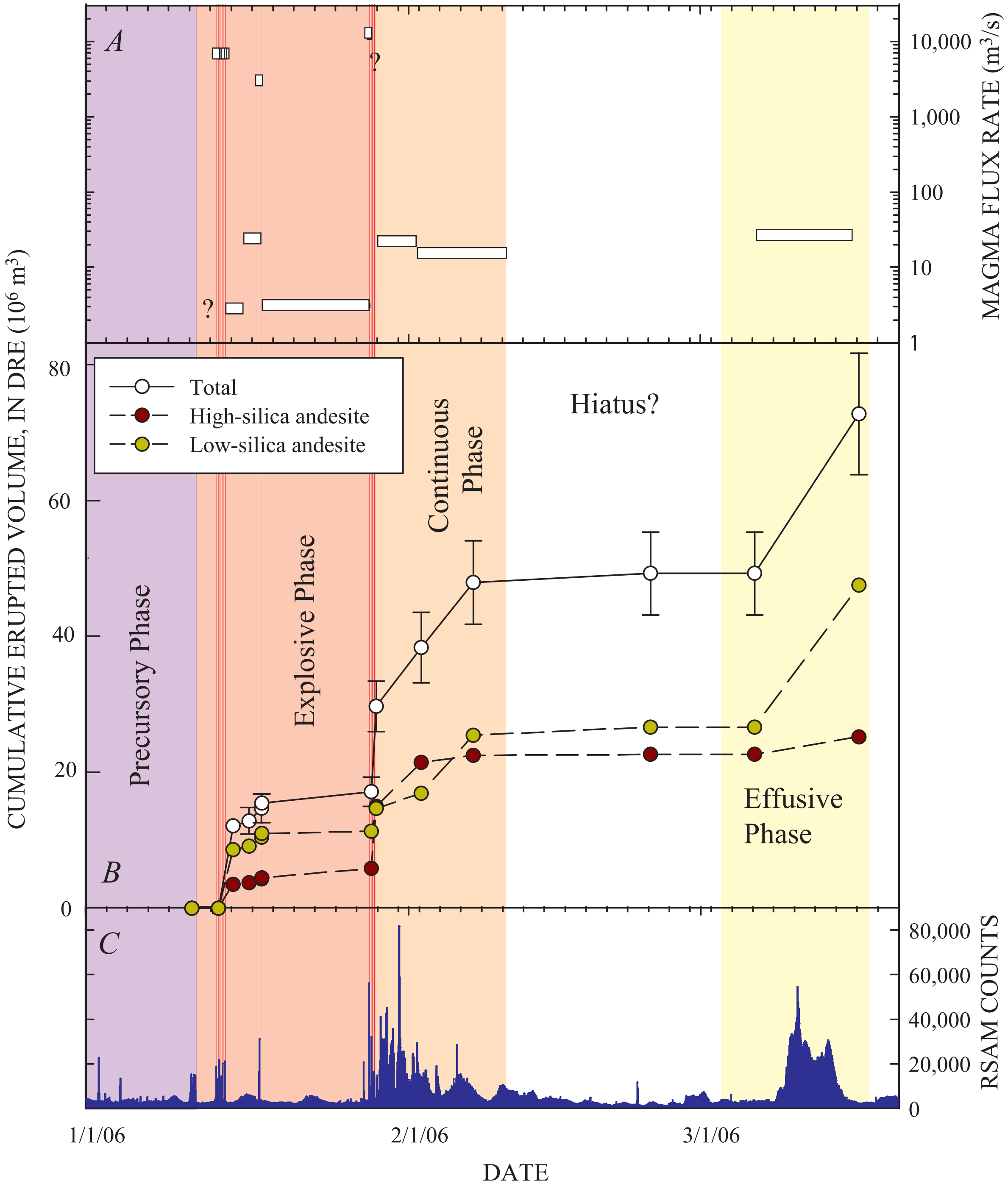

Figure 22. *A,* Magma flux rates (in dense-rock equivalent, or DRE) for intervals through the 2006 Augustine Volcano eruption. Flux rates plotted over red lines are for explosive events and have been calculated using the duration of the explosions; symbols have been enlarged for clarity. Flux rates that have been calculated for longer time periods are represented by bars. Note logarithmic scale. *B,* Cumulative erupted volume, in DRE, for the eruption. *C,* RSAM, or real-time seismic amplitude measurement, counts per day for Augustine station AU15. Explosive events 1–13 are shown as vertical red lines throughout *A*, *B*, and *C*.

and 5). Thicknesses of thinner pyroclastic-flow deposits were measured in the field (Vallance and others, this volume) and then averaged. The thicknesses of lava flows and domes were estimated or, where possible, measured from photographs and FLIR images (Wessels and others, this volume). For the continuous-phase and Rocky Point pyroclastic-flow deposits, volumes were calculated using digital terrain models (DTMs) generated by Aerometrics during the production of the orthophotos from January 4 and February 21, 2006. While these DTMs have unverified vertical accuracy, finding the difference of the two resulted in consistent volume gains over the mapped extents of the most voluminous pyroclastic flow deposits from late January and early February. Because field measurements of these deposits, many of which are several meters thick, were not possible in 2006, the values from the DTM differencing are presented here. Ash-fall volumes were calculated by Wallace and others (this volume) using the root-area method (Fierstein and Nathenson, 1992).

The main source of uncertainty in the calculations resides in the thickness measurements and/or estimates. These have propagated to the volumes and yield uncertainties of 25 to 50 percent. Inflated (erupted) volumes have been converted to dense-rock equivalent (DRE) using the following deposit/DRE ratios: 0.6 for fragmental flows, 0.9 for lava, and 0.4 for tephra-fall deposits.

Component analysis shows that each eruptive phase produced varying proportions of lithologic components (Vallance and others, this volume). Five dominant lithologies are low-silica andesite scoria; dense low-silica andesite; banded andesite; dense intermediate andesite; and high-silica andesite. We lump dense and scoriaceous low-silica andesite into a single compositional category and banded andesite and intermediate and high-silica andesite into another category to calculate volumetric estimates of two general compositional end members for each deposit (table 3). For lava flows, we assume they have the same proportions as block-and-ash flows shed from them; for domes, we assign composition based on the few of whole-rock analyses and surface appearance. Compositional ranges for the low- and high-silica andesite categories are 56 to 59 weight percent SiO_2 and 59 to 63 weight percent SiO_2, respectively (Larsen and others, this volume).

Results

The explosive phase produced about 14.7×10^6 m^3 as pyroclastic flows and 10.8 x10^6 m^3 as tephra fall (these and all subsequent values given as dense rock equivalent, or DRE; table 3). The first explosive-phase lava dome, effused from January 14–17, had a volume of roughly 2.5×10^6 m^3. The second dome, which effused between January 17 and 27, had a volume of roughly 1.7×10^6 m^3. The total volume produced during the explosive phase was 29.7×10^6 m^3. The largest single deposit of the eruption, the Rocky Point pyroclastic flow, erupted during event 10. During the explosive phase, low-silica and high-silica andesites were produced in nearly equal amounts, though during the first half of this phase, low-silica andesite dominated (fig. 22).

Combining volume estimates with eruption intervals allows us to calculate magma flux rates, which show three brief periods of rapid magma release that coincide with explosive events, as well as much lower flux rates during times of dome growth and lava effusion. Using a cumulative duration of events 3–8 of 28 minutes, 41 seconds yields a magma flux of 7,050 m^3/s (table 3; fig. 22). Event 9 lasted for 4 minutes, 11 seconds and yields a flux of 3,100 m^3/s (table 3). During events 10–13 on January 27 and 28, which cumulatively lasted 15 minutes, the calculated flux rate is roughly 14,000 m^3/s; this high rate corresponds with the eruption of the voluminous Rocky Point pyroclastic-flow deposit during event 10. The flux rates for the dome-building interval of January 14–17 and January 17–27 are much lower: 3–25 m^3/s and 3 m^3/s, respectively. If, however, explosive-phase lava dome 2 began growing later than January 17, the rate at which it effused could be much higher.

During the early continuous phase (January 28 through February 2), the volcano erupted 8.7×10^6 m^3 of magma in the form of pyroclastic-flow deposits. The volume of fallout tephra produced during this time is uncertain but was likely volumetrically minor (Wallace and others, this volume). As the vigor of the continuous phase waned, 9.6×10^6 m^3 of lava effused. Assuming continuous eruption during this period, the flux rate during the early continuous phase was 22 m^3/s and dropped to 16 m^3/s during its less vigorous second half. As shown by component studies (Vallance and others, this volume), the high-silica-andesite compositional end member dominated the first half of this phase, producing about three quarters, or 6.4×10^6 m^3, of the magma that fed the pyroclastic flows. The compositions of the lava flow and dome that effused during the second half of the continuous phase are less well known but, on the basis of appearance, are interpreted to be similar to that of the final lava flows—rich in low-silica andesite.

After an apparent hiatus from roughly February 10 through March 3, when no new magma was erupted, the effusive phase produced approximately 23.5×10^6 m^3 of lava and block-and-ash flows. Ash-fallout volumes were again likely minor during this interval (Wallace and others, this volume). This phase of the eruption was dominated by the low-silica-andesite end member, which accounted for roughly 20×10^6 m^3 of lava effused. The magma flux rate during the effusive phase was approximately 27 m^3/s, assuming constant effusion over this interval.

Eruptive Mechanisms During The 2006 Eruption

The 2006 and other recent eruptions of Augustine Volcano share similarities with other intermediate-composition, dome-building volcanoes worldwide. In general, however, Augustine seems to have briefer, more intense eruptive cycles compared to other dome-forming volcanoes, such as Mount St. Helens in Washington, Unzen volcano in Japan, Soufriere Hills volcano on Montserrat, or Santiaguito volcano in Guatemala, where eruption cycles typically last years (Rose, 1987; Swanson and Holcomb, 1990; Nakada and others, 1999; Kokelaar, 2002). We discuss the eruptive mechanisms responsible for the varying styles of the three eruptive phases of Augustine Volcano in 2006 and the corresponding activity in previous eruptions.

The Explosive Phase—Cyclic Vulcanian Explosions

The explosive phase of the 2006 eruption consisted of a series of discrete explosions, each minutes long, separated by periods of hours to days. Events 1 and 2 on January 11 produced cold mixed avalanches of snow, rock, and ice and fine-grained tephra-fall deposits that appear to contain little or no juvenile material (Wallace and others, this volume). We conclude that little or no magma had reached the shallow edifice and that the explosions were driven by ascending gases that had accumulated beneath the summit.

In contrast, events 3–13 produced ash-rich plumes, pyroclastic flows, and surges and resulting lahars and mixed avalanches that traveled far down all slopes of the volcano. Thus, the main magmatic eruption commenced on January 13. Pyroclastic-flow deposits from these events were not topographically confined and were likely formed during partial collapse of an eruptive column.

We were not able to calculate volumes for each individual event, but for those that we could, the volume varied dramatically. During event 9, the total volume erupted as both fall and flow deposits was ~0.8×10^6 m^3, whereas the volume of flow deposits from event 10 was 10×10^6 m^3 (both in DRE; table 3). For events 3 through 8, the total erupted volume was 12.1×10^6 m^3, which yields an average volume per event of roughly 2×10^6 m^3. For these events we calculate magma flux rates of 103 to 104 m^3/s. Because explosive events 11 through 13 were closely followed by the beginning of the continuous phase, volumes of deposits from these explosions are less well known.

Many of these characteristics are shared by other vulcanian explosions during previous eruptions of Augustine Volcano (Kienle and Shaw, 1979) and other andesitic volcanoes worldwide, including Soufriere Hills, Montserrat (Druitt and others, 2002); Mount Ngauruhoe, New Zealand (Nairn and Self, 1978); Lascar Volcano, Chile (Matthews and others, 1997); Mount Pinatubo, Philippines (Hoblitt and others, 1996); and Galeras Volcano, Columbia (Stix and others, 1997). Vulcanian explosions are attributed to two main mechanisms: either the interaction of magma with external water, or, as in the cases cited here, the sudden release of pressurized magma beneath a cooled or degassed lava cap (Self and others, 1979; Sparks, 1997; Stix and others, 1997; Morrissey and Mastin, 2000).

A consistent model that accounts for vulcanian explosions at other andesitic, dome-building volcanoes (Druitt and others, 2002) involves a shallow conduit filled with pressurized, vesicular magma, capped by degassed magma in the form of a lava dome or plug. As magma rises into the conduit from below and/or shallow crystallization causes vapor exsolution, increased conduit overpressure exceeds the strength of the cap (Sparks, 1997). At this point the cap is destroyed and a fragmentation wave descends into the conduit creating rapidly escalating conduit escape velocities and the formation of an ash-rich plume. The onset of the explosion is thought to be accompanied by a shock wave (Morrissey and Mastin, 2000). This phase is highly unstable and lasts seconds to minutes. Once the fragmentation wave reaches a level in the conduit where pressure is not great enough to drive fragmentation, the explosion greatly lessens in intensity or stops. Then the conduit refills, eventually leading to another degassed solid cap at the top, and the cycle repeats.

Only about half of the explosive events during the 2006 Augustine Volcano explosive phase had the impulsive acoustic waveforms that would result from the initial shock wave typical of vulcanian blasts (Petersen and others, 2006). The acoustic signal from event 1 was large and impulsive, consistent with this event acting as a vent clearing. The next impulsive event was event 5, which produced significant flows down the north flank. Events 8 through 12 were either impulsive or both emergent plus impulsive (Petersen and others, 2006). One explanation for the mix in waveforms is that some recorded partial failures of lava domes or plugs in addition to impulsive gas release.

By estimating the conduit dimension and erupted volume of each event, we can estimate the depth to which each explosion might have evacuated the conduit. We estimate the vent for the 2006 eruption to be roughly 30 by 45 m, elongate in the north-northwest–south-southeast direction, based on the location of an incipient spine atop the final dome (figs. 17, 19*B*); we assume the conduit will retain these dimensions. Events 3–8 each discharged approximately 2×10^6 m^3 of magma, which yields an average evacuation of the conduit to 1.9 km below the summit. If we have underestimated the dimension of the conduit and instead use a diameter of 50 m (similar to that of the 1986 spine), we calculate an average evacuation depth to 1 km. Such depths are consistent with those calculated for vulcanian explosions that occurred in 1997 at Soufriere Hills volcano, Montserrat (Druitt and others, 2002).

Event 10 was the largest of the explosive blasts, producing roughly 12.5×10^6 m^3 (DRE) of magma. Some of the material in the event 10 flow deposits is likely the destroyed portion of the explosive-phase dome 2. This dome had a volume of 1.7 x10^6 m^3 prior to event 10, and slightly less than half was destroyed during this event. Using a conservative estimate of 0.8 x10^6 m^3 as contributing to the volume of the event 10 flow deposits, juvenile magma erupted during this event would have been roughly 11.7 x10^6 m^3 (DRE). A distinct compositional shift, from predominantly low-silica andesite to predominantly high-silica andesite, occurred during event 10 between emplacement of the explosive-phase pyroclastic-current and Rocky Point pyroclastic-flow deposits (Vallance and others, this volume). Assuming that all of the juvenile magma was evacuated from a conduit with the dimensions above would result in a conduit length of over 11 km! Petrologic and geodetic evidence suggest, however, that the magma storage region that held the erupted high-silica andesite is located at a depth of roughly 5 km below the summit (Larsen and others, this volume; Cervelli and others, this volume), consistent with post-eruption earthquake hypocenters located at this depth (Power and Lalla, this volume). If this is accurate, event 10 likely evacuated the entire conduit and partially evacuated the magma storage region, whether the latter was a chamber, dike, sill, or crystal-mush zone. This is particularly intriguing given the compositional shift that occurred during this event and suggests that the low-silica andesite erupted during the first half of event 10 came from the conduit and that the high-silica andesite erupted during the second half of the event came predominantly from the magma storage region. This also suggests that this event may have cleared the way for the subsequent eruption of large volumes of high-silica andesite during the continuous phase.

An additional constraint on magma movement and withdrawal prior to and during the vulcanian blasts comes from GPS data that show a shallow inflationary source at sea level that was present from June through November of 2005 (Cervelli and others, 2006). Cervelli and others model this as the result of a point source near sea level that pressurized at a rate corresponding to 4×10^5 m^3/yr, or a volume change of 2×10^5 m^3 (Cervelli and others, 2006). This volume is an order of magnitude lower than material erupted during any one of the explosions, thus we suggest that this sea-level inflationary signal was caused by pressurization by magmatic gas, not magma. This pressurization may have been facilitated by the presence of the relatively impermeable zeolitized Naknek Formation near sea level beneath Augustine Volcano (Detterman and Reed, 1980). On November 17, following the 6-month-long signal, a much stronger inflationary signal began at the summit stations and lasted until January 12. The stronger signal has been modeled as the ascent of a north-south-trending dike from near sea level to the summit (Cervelli and others, 2006). Upward earthquake migration was detected in this depth range during the same time interval (DeShon and others, this volume; Power and Lalla, this volume). We suggest that this dike possessed a gas-filled tip that preceded new magma to the surface, culminating in the gas-rich but juvenile-magma-poor January 11 explosions. Magma then reached the surface on January 12 in the form of a lava dome; growing overpressure in the conduit caused vulcanian magmatic blasts to begin on January 13.

The Continuous Phase—Dome Growth and Collapse

The onset of the continuous phase heralded a distinct shift in eruptive style from the explosive phase. This phase was mainly characterized by pyroclastic-flow emplacement that tapered to lava effusion, but activity began the afternoon of January 28 with a two-hour-long period of volcanic tremor and accompanying ash emission. It was not until 2200 AKST the night of January 28 that the first flowage-type seismic signals were detected. Later observations, and discovery of a seismic station destroyed during this interval, revealed that each signal represented a pyroclastic flow of varying size. This activity continued until February 3, when slower effusion apparently led to the formation of a small lava flow.

By evaluating the volumes of erupted pyroclastic flows from this period, we can evaluate whether pyroclastic flows formed primarily as the result of a collapsing, preexisting dome or whether the dome was actively growing during this interval. The first half of the continuous phase produced more than 14×10^6 m^3 of erupted material (not DRE). A circular dome of this volume, if 40 m tall, would have a radius of ~340 m, which would more than cover the entire summit area. This indicates that pyroclastic flows during this period were not just the result of collapse of an existing lava dome but were instead occurring during active effusion and rapid collapse of a growing dome. Satellite imagery from the middle of this period shows that a roughly circular dome was present at the summit and that flows were initiating from its margins.

Similar activity has been recorded at other dome-forming volcanoes, notably Mount Merapi in Indonesia, Soufriere Hills in Montserrat, and Unzen in Japan. Often, periods of block-and-ash flow activity of this intensity are shorter, however, and thought to be due to collapse of a static dome. For example, on November 22, 1994, roughly 3×10^6 m^3 of block-and-ash flows formed over a 7-hour interval at Merapi when a portion of the summit lava dome collapsed (Abdurachman and others, 2000).

The continuous-phase activity is consistent with relatively high initial magma-flux rates that resulted in rapid effusion and almost continual collapse of a growing lava dome. The composition of this dome was predominantly high-silica andesite, unlike the low-silica-andesite-dominated explosive phase. As the dome grew, its margins became unstable and collapsed, forming classic, Merapi-style block-and-ash flows. Most of these traveled to the north and northeast of the summit, forming composite pyroclastic fans much like those formed during the 1976 and 1986 eruptions of the volcano. At least two larger pyroclastic flows, however, were emplaced early in the continuous phase, including the windy pyroclastic flow that erupted on January 30. These flows occurred when larger portions of the lava dome collapsed, or they reflect fluctuations in magma flux.

As magma flux at the conduit waned, lava that reached the surface remained intact to form a new dome and a short steep lava flow to the north. We did not sample the lava flow at this stage, but images from February show that debris from this lava tongue is much darker than underlying flowage deposits from earlier in the continuous phase, suggesting that the composition had perhaps transitioned to the low-silica andesite that erupted later in the effusive phase.

The Effusive Phase—Rapid Effusion of Lava and Block-and-Ash Flows

The flux rate calculated during the effusive-phase rate of ~27 m^3/s is quite high compared to other rates of lava effusion measured elsewhere. During periods of exogenous dome growth between 1980 and 1986, extrusion rates at Mount St. Helens varied from 1.4 to 40.3 m^3/s (Anderson and Fink, 1990), similar to or higher than the rates at Augustine Volcano. However, at Santiaguito in Guatemala, dome growth varied between periods of slow (0.16 m^3/s) and relatively fast (0.6–1.9 m^3/s) extrusion (Rose, 1987). At Mount Merapi in Indonesia, from 1984–1995, lava-dome effusion rates varied from 0.05 to 0.32 m^3/s, with an average long-term rate of 0.039 m^3/s (Siswowidjoyo and others, 1995). Thus, while effusion occurred over a short time period in March of 2006, the resulting volume was equivalent to that seen for domes/flows elsewhere erupted over much longer periods.

The block-and-ash flows during the effusive phase are much smaller in volume than flows from the continuous phase. They are similar to other classic deposits of this type seen at Unzen Volcano in Japan and elsewhere. At Unzen, Ui and others (1999) describe block-and-ash flows that occur when lava is actively flowing downslope, and the tensile strength of the deforming lava is exceeded by the pore pressure in the lava and the downslope tensional force. This causes a local explosion, often around a growing crack, and fragmentation is triggered at the lobe front—a likely explanation for the effusive-phase pyroclastic flows at Augustine Volcano.

The rock-avalanche events that occurred at Augustine Volcano in April and May, well after effusion had ceased, still resulted in observed ash clouds and block-and-ash-flow-type deposits. We suggest that these events resemble rockfall-induced block-and-ash flows that also occurred at Unzen (Ui and others, 1999). The steep slopes near Augustine's summit led to rock falls off the western edge of the still-hot north lava flow. As blocks of hot lava that retained high pore pressures hit the ground, they fragmented upon impact causing small block-and-ash flows. The rockfalls off the north lava flow occurred repeatedly from the same location, exposing fresh parts of the flow interior that had not been fully degassed. This may explain why each block-and-ash flow was somewhat bigger than the last.

Acknowledgments

We thank the entire staff of the Alaska Volcano Observatory (AVO) for their efforts during the 2006 Augustine eruption—without the detailed observations made by many, this paper would not have been possible. In particular, we are grateful for conversations with Peter Cervelli, Pavel Izbekov, Steve McNutt, Tina Neal, Chris Nye, John Power, Stephanie Prejean, and Kristi Wallace that helped us to refine our chronology of events and our ideas about eruptive mechanisms. Comments by Wes Hildreth, John Power, and in particular Tom Sisson improved the manuscript. We also thank the skilled helicopter and fixed-wing pilots who took us to the volcano despite often-challenging conditions. A special thanks to Cheryl Cameron and Seth Snedigar, who have made the AVO image database and other web-based tools that are so useful.

References Cited

Abdurachman, E.K., Bourdier, J.-L., and Voight, B., 2000, Nuées ardentés of 22 November 1994 at Merapi volcano, Java, Indonesia: Journal of Volcanology and Geothermal Research, v. 100, p. 345–361.

Anderson, S., and Fink, J.H., 1990, The development and distribution of lava textures at the Mount St. Helens dome, *in* Fink, J.H., ed., Lava flows and domes; emplacement mechanisms and hazard implications: Berlin, Springer-Verlag, International Association of Volcanology and Chemistry of the Earth's Interior, p. 25–46.

Bailey, J.E., Dean, K.G., Dehn, J., and Webley, P.W., 2010, Integrated satellite observations of the 2006 eruption of Augustine Volcano, *in* Power, J.A., Coombs, M.L., and Freymueller, J.T., eds., The 2006 eruption of Augustine Volcano, Alaska: U.S. Geological Survey Professional Paper 1769 (this volume).

Begét, J.E., and Kienle, J., 1992, Cyclic formation of debris avalanches at Mount St. Augustine volcano: Nature, v. 356, no. 6371, p. 701–704.

Cervelli, P.F., Fournier, T., Freymueller, J.T., and Power, J.A., 2006, Ground deformation associated with the precursory unrest and early phases of the January 2006 eruption of Augustine Volcano, Alaska: Geophysical Research Letters, v. 33, L18304, doi:10.1027/2006GL027219.

Cervelli, P.F., Fournier, T.J., Freymueller, J.T., Power, J.A., Lisowski, M., and Pauk, B.A., 2010, Geodetic constraints on magma movement and withdrawal during the 2006 eruption of Augustine Volcano, *in* Power, J.A., Coombs, M.L., and Freymueller, J.T., eds., The 2006 eruption of Augustine Volcano, Alaska: U.S. Geological Survey Professional Paper 1769 (this volume).

DeRoin, N., McNutt, S.R., Reyes, C., and Sentman, D.D., 2007, Rockfalls at Augustine Volcano, Alaska; 2003–2006: Eos Transactions of the American Geophysical Union, v. 88, S43–1038.

DeShon, H.R., Thurber, C.H., and Power, J.A., 2010, Earthquake waveform similarity and evolution at Augustine Volcano from 1993 to 2006, *in* Power, J.A., Coombs, M.L., and Freymueller, J.T., eds., The 2006 eruption of Augustine Volcano, Alaska: U.S. Geological Survey Professional Paper 1769 (this volume).

Detterman, R.L., and Reed, B.L., 1980, Stratigraphy, structure, and economic geology of the Iliamna quadrangle, Alaska: U.S. Geological Survey Bulletin 1368-B, 86 p, 1 sheet.

Druitt, T.H., Young, S.R., Baptie, B., Bonadonna, C., Calder, E.S., Clarke, A.B., Cole, P.D., Harford, C.L., Herd, R.A., Luckett, R., Ryan, G., and Voight, B., 2002, Episodes of cyclic Vulcanian explosive activity with fountain collapse at Soufriere Hills Volcano, Montserrat, *in* Druitt, T.H., and Kokelaar, B.P., eds., The Eruption of Soufriere Hills Volcano, Montserrat, from 1995 to 1999: London, The Geological Society, p. 281–306.

Dzurisin, D.J., Vallance, J.W., Gerlach, T.M., Moran, S.C., and Malone, S.D., 2005, Mount St. Helens reawakens: Eos (American Geophysical Union Transactions), v. 86, no. 3, p. 25, 29.

Fierstein, J., and Nathenson, M., 1992, Another look at the calculation of fallout tephra volumes: Bulletin of Volcanology, v. 54, p. 156–167.

Hoblitt, R.P., Wolfe, E.W., Scott, W.E., Couchman, M.R., Pallister, J.S., and Javier, D., 1996, The pre-climactic eruptions of Mount Pinatubo, June 1991, *in* Newhall, C.G., and Punongbayan, R.S., eds., Fire and Mud; eruptions and Lahars of Mount Pinatubo, Philippines: Seattle, University of Washington Press, p. 457–511.

Johnston, D.A., 1978, Volatiles, magma mixing, and the mechanism of eruption at Augustine Volcano, Alaska: University of Washington Ph.D. dissertation, 187 p.

Johnston, D.A., 1979, Onset of volcanism at Augustine Volcano, lower Cook Inlet, *in* Johnson, K.M. and Williams, J.R., Jr., eds., The United States Geological Survey in Alaska; accomplishments during 1978: U.S. Geological Survey Circular 0804-B, p. B78–B80.

Kamata, H., Johnston, D.A., and Waitt, R.B., 1991, Stratigraphy, chronology, and character of the 1976 pyroclastic eruption of Augustine Volcano, Alaska: Bulletin of Volcanology, v. 53, p. 407–409.

Kienle, J., and Shaw, G.E., 1979, Plume dynamics, thermal energy, and long-distance transport of vulcanian eruption clouds from Augustine Volcano, Alaska: Journal of Volcanology and Geothermal Research, v. 6, p. 139–164.

Kokelaar, B.P., 2002, Setting, chronology, and consequences of the eruption of Soufriere Hills Volcano, Montserrat (1995–1999), *in* Druitt, T.H., and Kokelaar, B.P., eds., The Eruption of Soufriere Hills Volcano, Montserrat, from 1995–1999: London, The Geological Society, p. 1–44.

Larsen, J.F., Nye, C.J., Coombs, M.L., Tilman, M., Izbekov, P., and Cameron, C., 2010, Petrology and geochemistry of the 2006 eruption of Augustine Volcano, *in* Power, J.A., Coombs, M.L., and Freymueller, J.T., eds., The 2006 eruption of Augustine Volcano, Alaska: U.S. Geological Survey Professional Paper 1769 (this volume).

Matthews, S.J., Gardeweg, M.C., and Sparks, R.S.J., 1997, The 1984–1996 cyclic activity of Lascar Volcano, northern Chile; cycles of dome growth, dome subsidence, degassing and explosive eruptions: Bulletin of Volcanology, v. 59, p. 72–82.

McNutt, S.R., Tytgat, G., Estes, S.A., and Stihler, S.D., 2010, A parametric study of the January 2006 explosive eruptions of Augustine Volcano, using seismic, infrasonic, and lightning data *in* Power, J.A., Coombs, M.L., and Freymueller, J.T., eds., The 2006 eruption of Augustine Volcano, Alaska: U.S. Geological Survey Professional Paper 1769 (this volume).

Morrissey, M.M., and Mastin, L.G., 2000, Vulcanian eruptions, *in* Sigurdsson, H., Houghton, B.F., McNutt, S.R., Rymer, H., and Stix, J., eds., Encyclopedia of volcanoes: San Diego, Academic Press, p. 463–475.

Nairn, I.A., and Self, S., 1978, Explosive avalanches and pyroclastic flows from Ngauruhoe 1975: Journal of Volcanology and Geothermal Research, v. 3, p. 39–60.

Nakada, S., Shimizu, H., and Ohta, K., 1999, Overview of the 1990–1995 eruption at Unzen Volcano: Journal of Volcanology and Geothermal Research, v. 89, p. 1–22.

Neal, C.A., Murray, T.L., Power, J.A., Adleman, J.N., Whitmore, P.M., and Osiensky, J.M., 2010, Hazard information management, interagency coordination and impacts of the 2005–2006 eruption of Augustine Volcano, *in* Power, J.A., Coombs, M.L., and Freymueller, J.T., eds., The 2006 eruption of Augustine Volcano, Alaska: U.S. Geological Survey Professional Paper 1769 (this volume).

Paskievitch, J., Read, C., and Parker, T., 2010, Remote telemetered and time-lapse cameras at Augustine Volcano, *in* Power, J.A., Coombs, M.L., and Freymueller, J.T., eds., The 2006 eruption of Augustine Volcano, Alaska: U.S. Geological Survey Professional Paper 1769 (this volume).

Pauk, B.A., Jackson, M., Feaux, K., Mencin, D., and Bohnenstiehl, K., 2010, The Plate Boundary Observatory permanent global positioning system network on Augustine Volcano before and after the 2006 eruption, *in* Power, J.A., Coombs, M.L., and Freymueller, J.T., eds., The 2006 eruption of Augustine Volcano, Alaska: U.S. Geological Survey Professional Paper 1769 (this volume).

Petersen, T., De Angelis, S., Tytgat, G., and McNutt, S.R., 2006, Local infrasound observations of large ash explosions at Augustine Volcano, Alaska, during January 11–28, 2006: Geophysical Research Letters, v. 33, L12303, doi:10.1029/2006GL026491.

Power, J., 1988, Seismicity associated with the 1986 eruption of Augustine Volcano, Alaska: Fairbanks, University of Alaska, unpub. M.S. thesis, 142 p.

Power, J.A., and Lalla, D.J., 2010, Seismic observations of Augustine Volcano, 1970–2007, *in* Power, J.A., Coombs, M.L., and Freymueller, J.T., eds., The 2006 eruption of Augustine Volcano, Alaska: U.S. Geological Survey Professional Paper 1769 (this volume).

Power, J.A., Nye, C.J., Coombs, M.L., Wessels, R.L., Cervelli, P.F., Dehn, J., Wallace, K.L., Freymueller, J.T., and Doukas, M.P., 2006, The reawakening of Alaska's Augustine Volcano: Eos (American Geophysical Union Transactions), v. 87, no. 37, p. 373, 377.

Rose, W.I., 1987, Volcanic activity at Santiaguito volcano, 1976–1984, *in* Fink, J.H., ed., The emplacement of silicic domes and lava flows: Boulder, Colo.,The Geological Society of America, p. 17–28.

Schneider, D.J., Scott, C., Wood J., and Hall T., 2006, NEXRAD weather radar observations of the 2006 Augustine volcanic eruption clouds: Eos (American Geophysical Union Transactions), v. 87, Abstract V51C–1686.

Self, S., Wilson, L., and Nairn, I.A., 1979, Vulcanian eruption mechanisms: Nature, v. 277, p. 440–443.

Sentman, D.D., McNutt, S.R., Stenbaek-Nielsen, H.C., Tytgat, G., and DeRoin, N., 2010, Imaging observations of thermal emissions from Augustine Volcano using a small astronomical camera, *in* Power, J.A., Coombs, M.L., and Freymueller, J.T., eds., The 2006 eruption of Augustine Volcano, Alaska: U.S. Geological Survey Professional Paper 1769 (this volume).

Siswowidjoyo, S., Suryo, I., and Yokoyama, I., 1995, Magma eruption rates of Merapi volcano, central Java, Indonesia during one century (1890–1992): Bulletin of Volcanology, v. 57, p. 111–116.

Sparks, R.S.J., 1997, Causes and consequences of pressurisation in lava dome eruptions: Earth and Planetary Science Letters, v. 150, p. 177–189.

Stith, J.L., Hobbs, P.V., and Radke, L.F., 1977, Observations of a nuee ardente from the St. Augustine Volcano: Geophysical Research Letters, v. 4, p. 259–262.

Stix, J., Torres, R.C., Narvaez, M.L., Cortes, G.P., Raigosa, J.A., Gomez, D.M., and Castonguay, R., 1997, A model of Vulcanian eruptions at Galeras Volcano, Columbia: Journal of Volcanology and Geothermal Research, v. 77, p. 285–304.

Swanson, D.A., and Holcomb, R.T., 1990, Regularities in growth of the Mount St. Helens dacite dome, 1980–1986, *in* Fink, J.H., ed., Lava flows and domes; emplacement mechanisms and hazard implications: Berlin, Springer-Verlag, International Association of Volcanology and Chemistry of the Earth's Interior, p. 3–24.

Swanson, S.E., and Kienle, J., 1988, The 1986 eruption of Mount St. Augustine; field test of a hazard evaluation: Journal of Geophysical Research, v. 93, p. 4500–4520.

Thomas, R.J., McNutt, S.R., Krehbiel, P.R., Rison, W., Aulich, G., Edens, H.E., Tytgat, G, and Clark, E., 2010, Lightning and electrical activity during the 2006 eruption of Augustine Volcano, *in* Power, J.A., Coombs, M.L., and Freymueller, J.T., eds., The 2006 eruption of Augustine Volcano, Alaska: U.S. Geological Survey Professional Paper 1769 (this volume).

Ui, T., Matsuwo, N., Sumita, M., and Fujinawa, A., 1999, Generation of block and ash flows during the 1990–1995 eruption of Unzen Volcano, Japan: Journal of Volcanology and Geothermal Research, v. 89, p. 123–138.

Vallance, J.W., Bull, K.F., and Coombs, M.L., 2010, Pyroclastic flows, lahars, and mixed avalanches generated during the 2006 eruption of Augustine Volcano, *in* Power, J.A., Coombs, M.L., and Freymueller, J.T., eds., The 2006 eruption of Augustine Volcano, Alaska: U.S. Geological Survey Professional Paper 1769 (this volume).

Waitt, R.B., and Begét, J.E., 2009, Volcanic processes and geology of Augustine Volcano, Alaska: U.S. Geological Survey Professional Paper 1762, 78 p., 2 map plates [http://pubs.usgs.gov/pp/1762/].

Wallace, K.L., Neal, C.A., and McGimsey, R.G., 2010, Timing, distribution, and character of tephra fall from the 2005–2006 eruption of Augustine Volcano, *in* Power, J.A., Coombs, M.L., and Freymueller, J.T., eds., The 2006 eruption of Augustine Volcano, Alaska: U.S. Geological Survey Professional Paper 1769 (this volume).

Wessels, R.L., Coombs, M.L., Schneider, D.J., Dehn, J., and Ramsey, M.S., 2010, High-resolution satellite and airborne thermal infrared imaging of the 2006 eruption of Augustine Volcano, *in* Power, J.A., Coombs, M.L., and Freymueller, J.T., eds., The 2006 eruption of Augustine Volcano, Alaska: U.S. Geological Survey Professional Paper 1769 (this volume).

Yount, E.M., Miller, T.P., and Gamble, B.M., 1987, The 1986 eruptions of Augustine Volcano, Alaska, hazards and effects, *in* Hamilton, T.D., and Galloway, J.P., eds., The United States Geological Survey in Alaska; accomplishments during 1986: U.S. Geological Survey Circular 0998, p. 4–13.

Chapter 9

Timing, Distribution, and Character of Tephra Fall from the 2005–2006 Eruption of Augustine Volcano

By Kristi L. Wallace[1], Christina A. Neal[1], and Robert G. McGimsey[1]

Abstract

The 2005–6 eruption of Augustine Volcano produced tephra-fall deposits during each of four eruptive phases. Late in the precursory phase (December 2005), small phreatic explosions produced small-volume, localized, mostly nonjuvenile tephra. The greatest volume of tephra was produced during the explosive phase (January 11–28, 2006) when 13 discrete Vulcanian explosions generated ash plumes between 4 and 14 km above mean sea level (asl). A succession of juvenile tephra with compositions from low-silica to high-silica andesite is consistent with the eruption of two distinct magmas, represented also by a low-silica andesite lava dome (January 13–16) followed by a high-silica andesite lave dome (January 17–27). On-island deposits of lapilli to coarse ash originated from discrete vent explosions, whereas fine-grained, massive deposits were elutriated from pyroclastic flows and rock falls. During the continuous phase (January 28–February 10, 2006), steady growth and subsequent collapses of a high-silica andesite lava dome caused continuous low-level ash emissions and resulting fine elutriate ash deposits. The emplacement of a summit lava dome and lava flows of low-silica andesite during the effusive phase (March 3–16, 2006) resulted in localized, fine-grained elutriated ash deposits from small block-and-ash flows off the steep-sided lava flows.

Mixing of two end-member magmas (low-silica and high-silica andesite) is evidenced by the overall similarities between tephra-fall and contemporaneous lava-dome and flow lithologies and by the chemical heterogeneity of matrix glass compositions of coarse lapilli and glass shards in the ash-size fraction throughout the 2005–6 eruption. A total mass of 2.2×10^{10} kg of tephra fell (bulk volume of 2.2×10^{7} m^3 and DRE volume of 8.5×10^{6} m^3) during the explosive phase, as calculated by extrapolation of mass data from a single Vulcanian blast on January 17. Total tephra-fall volume for the 2005–6 eruption is about an order of magnitude smaller than other historical eruptions from Augustine Volcano. Ash plumes of short duration and small volume caused no more than minor amounts (≤1 mm) of ash to fall on villages and towns in the lower Cook Inlet region, and thus little hazard was posed to local communities. The bulk of the ash fell into Cook Inlet. Monitoring by the Alaska Volcano Observatory during the eruption helped to prevent hazardous encounters of ash and aircraft.

Introduction

Augustine Volcano, in the eastern Aleutian arc, has erupted seven times since 1812 and is the most historically active volcano in south-central Alaska's Cook Inlet region (Miller and others, 1998; fig. 1). The most recent eruption in 2005–6 produced ash clouds and fall, pyroclastic flows, and lava domes and flows, similarly to recent eruptions in 1986 and 1976. Four distinct eruptive phases, defined on the basis of the various processes that occurred during the eruption, each generated some form of tephra-fall deposit during this most recent eruption. The four phases include the (1) precursory (April–December 2005), (2) explosive (January 11–28, 2006), (3) continuous (January 28–February 10, 2006), and (4) effusive (March 3–16, 2006) phases (Power and others, 2006). Documentation of tephra fall was challenging because the volcano is on a remote island and most of the tephra fell on water. The eruption occurred during the winter, so tephra deposits on land were subject to high winds and fallout on ephemeral snow. Because tephra volumes were small, tephra that fell onto nearby land surfaces (25–185 km away) comprised fine ash dustings that were mostly less than 1 mm thick and posed little hazard to local populations. Proximal deposits are complex and varied because of near-vent processes, including elutriation from pyroclastic flows and rockfalls and

---

[1] Alaska Volcano Observatory, U.S. Geological Survey, 4200 University Drive, Anchorage, AK 99508.

modification by reworking. Calculations of tephra-fall volume are based on mass data for an ash-fall deposit from a discrete plume on January 17, 2006. This was the only opportunity to accurately determine tephra-fall volume for a single event, because it was deposited on land and was quickly buried by snowfall, and thus we formulate total mass and volume for all fall deposits erupted during the explosive phase by extrapolation of these data.

This report describes the timing, distribution, character, mass, and origin of tephra-fall deposits from the 2005–6 eruption of Augustine and concludes with a discussion of their significance and hazards. Because most of the explosive events were not observed directly, we infer their origins from time-lapse photography, geophysical data, and deposit characteristics. Magmatic or hydrovolcanic explosions at the vent initiated some tephra falls, and dome collapses that formed pyroclastic flows or rockfalls, and generated fine-grained elutriate ash clouds initiated others. Regardless of origin, tephra plumes resulted from these events and at times extended hundreds of kilometers downwind.

Methods

We describe tephra-fall deposits in terms of (1) time of eruption, (2) distribution, (3) character, including thickness, particle size, composition (componentry and glass geochemistry), and preservation, (4) origin, and (5) mass, when known. Samples collected for this study are archived at the U.S. Geological Survey (USGS) Alaska Tephra Laboratory and Data Center at the Alaska Volcano Observatory (AVO) in Anchorage, Alaska.

Timing of Tephra Production

We adopt the sequence and naming of eruption phases of Power and others (2006) to describe the timing of the 2005–6 eruption. We use event numbers to reference individual explosions of the explosive phase (Vallance and others, this volume; Power and others, 2006; table1).

Tephra Distribution

Explosions that generated discrete plumes had distinct seismic signals (Power and Lalla, this volume; McNutt and others, this volume) that alerted AVO to collect plume data and tephra samples. Data collected include (1) estimation of plume height (from radar and/or pilot reports; Schneider and others, 2006), (2) seismic duration of explosive event (Power and Lalla, this volume), (3) direction of prevailing winds, (4) movement direction of plume in satellite and radar data (Bailey and others, this volume; Schneider and others, 2006), (5) ash-fall reports from nearby towns and villages, and (6) overflight photography. Timely access to these data facilitated tracking of individual plumes. During the continuous phase, secondary plumes of elutriated fine ash from pyroclastic flows and rockfalls were more complicated to track because their onset times and plume heights were difficult to constrain. Tephra fall into Cook Inlet could not be documented, so deposits too small to reach adjacent landmasses 25 km away are not reported here. Herein, the term “proximal” implies Augustine Island and “distal” implies any landmass off the island (that is, Alaska mainland, Kenai Peninsula, Kodiak Island).

Available satellite images and radar data allow reconstruction of plume trajectories (fig. 1) at the time of plume generation and transport, and they closely match the wind forecast data from the National Weather Service (NWS) and the National Atmospheric and Oceanic Administration (NOAA) (fig. 2). Our telephone network allowed people in towns and villages along the path of drifting plumes to report observations of ash clouds and tephra fall, although much of the tephra fall occurred in sparsely settled or uninhabited areas. Other papers in this volume present more detailed data on plume trajectories and distribution using various satellite data (Bailey and others, this volume; Webley and others, this volume). With one exception, we did not reconstruct deposit isopachs, because tephra fell over water or in remote, uninhabited areas and because some tephra lobes overlapped to form a single undifferentiated layer. Plume heights in text are all from radar data (Schneider and other, 2006, and data taken from poster by D.J. Schneider and others, 2006) for consistency and differ from pilot-reported heights, although both are shown in table 1.

Tephra Character

We characterize tephra-fall deposits in terms of thicknesses when known, particle size, composition (componentry and glass geochemistry), and preservation. We collected proximal tephra samples at 65 field stations in July–August 2006 and during brief visits to the island and affected regions while the eruption was in progress (fig. 3 and appendix 1). We deployed ash-collection buckets on Augustine in late December 2005 in an attempt to collect temporally constrained samples during times when it was unsafe to be on the island. The buckets were colocated with geophysical instruments to facilitate recovery during brief visits to the island throughout the eruption. Distal samples were collected during the eruption either during helicopter-based fieldwork or by local citizens upon request.

We use standard volcanic terminology to characterize particle size (Fisher, 1961; Schmid, 1981; Chough and Sohn, 1990). We did not perform quantitative particle-size analyses because distal sample quantities were insufficient and, in proximal samples, deposits were reworked owing to wind or melting of underlying snow. We constructed generalized stratigraphic sections to represent proximal fall deposits on all four quadrants of the island to show the relations between deposits eruption (fig. 4). Sections are derived from best preserved

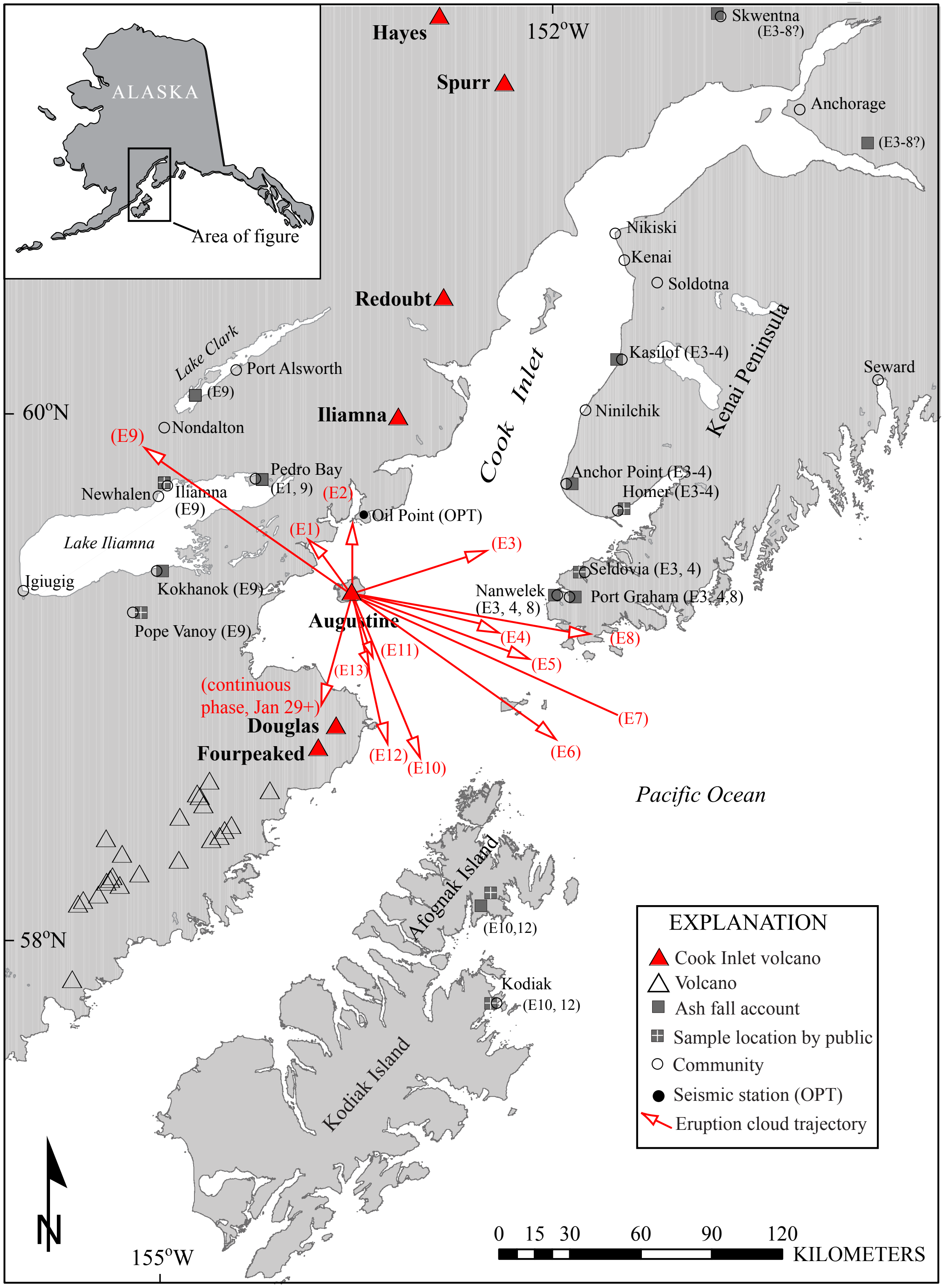

Figure 1. Map of south-central Alaska showing location of Augustine and other volcanoes, surrounding communities, ash-fall accounts, and ash-plume trajectories during the explosive and continuous phases of the 2005–6 eruption of Augustine. Plume trajectories are based on Nexrad radar data (data taken from poster of D.J. Schneider and others, 2006); E indicates explosive event number. Ash-fall accounts are eyewitness reports of ash fall. Such accounts are associated with event numbers but may fall off the path of the radar-derived plume trajectory, which indicates that shifting winds at different altitudes carried ash in those directions.

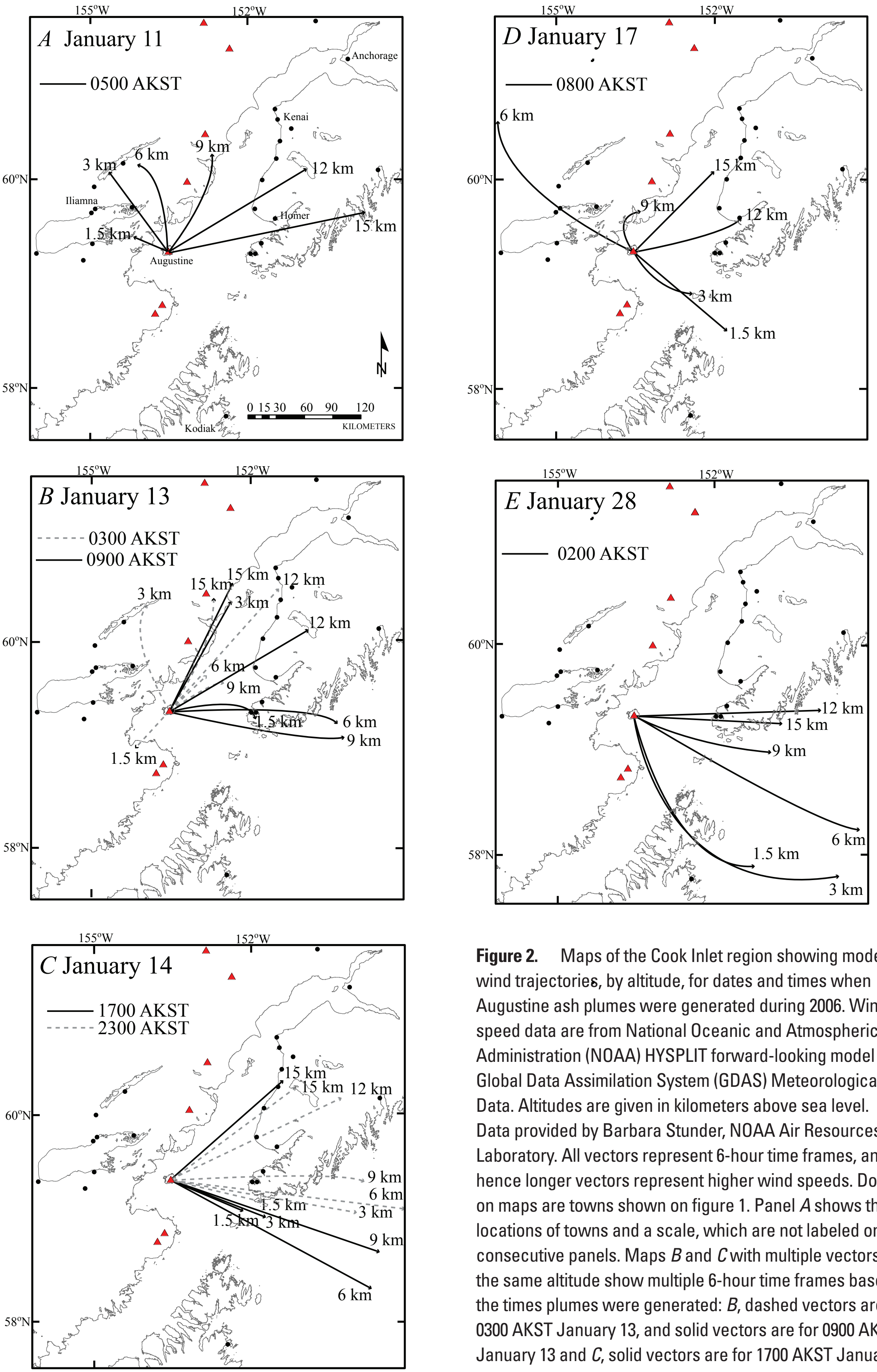

Figure 2. Maps of the Cook Inlet region showing modeled wind trajectories, by altitude, for dates and times when Augustine ash plumes were generated during 2006. Wind-speed data are from National Oceanic and Atmospheric Administration (NOAA) HYSPLIT forward-looking model and Global Data Assimilation System (GDAS) Meteorological Data. Altitudes are given in kilometers above sea level. Data provided by Barbara Stunder, NOAA Air Resources Laboratory. All vectors represent 6-hour time frames, and hence longer vectors represent higher wind speeds. Dots on maps are towns shown on figure 1. Panel *A* shows the locations of towns and a scale, which are not labeled on consecutive panels. Maps *B* and *C* with multiple vectors of the same altitude show multiple 6-hour time frames based on the times plumes were generated: *B*, dashed vectors are for 0300 AKST January 13, and solid vectors are for 0900 AKST January 13 and *C*, solid vectors are for 1700 AKST January 14 and dashed vectors are 2300 AKST January 14.

deposits protected by vegetation cover on the mid to lower flanks of the island.

Previous studies show that tephra from historical eruptions of Augustine have a range of glass compositions (for example, Kienle and Swanson, 1987; Johnston, 1978; Daley, 1986; and Roman and others, 2005). Therefore where possible, we use grain-discrete analysis of the glass fraction to help characterize the geochemistry of tephra deposits. Glass analyses were determined using a Cameca SX-50 electron microprobe at the University of Alaska Fairbanks Advanced Instrumentation Lab (table 2 and appendix 2). Analyses are of distal glass shards and of matrix glass of proximal lapilli. Brown, clear, and hybrid glass (mixture of brown and clear glass) identified throughout the eruption (fig. 5) posed some analytical challenges. Brown glass contains abundant microlites, while clear glass is mostly microlite free. Identifying pure glass pools in brown "glass" was challenging, and these data show significant scatter as a result. All glass analyses were filtered to eliminate the inclusion of mineral data (appendix 2), although the distinction between truly heterogeneous glass and scatter resulting from partial analysis of glass plus microlites is sometimes difficult to make. Larsen and others (this volume, their table 4) show glass analyses from tephra-fall deposits where they made a concerted effort to identify pure glass pools using backscatter imaging on the electron microprobe. For brevity, we pared down the hundreds of glass analyses that we performed to a summary of ranges of compositions listed by eruptive phase, event number, and lithology (table 2). Raw, filtered glass compositions are given in appendix 2.

We did component analyses using proximal, coarse-grained deposits and sorted clasts > 5mm into lithologies based on macroscopic appearance (table 3, fig. 5). The resulting lithologic types are the same as those used by researchers studying other proximal products from the eruption (Coombs and others, this volume; Vallance and others, this volume; Larsen and others, this volume). Component analyses are reported in percent of n clasts per sample.

Preservation of both distal and proximal tephra-fall deposits is discussed, because we think it is an important consideration for the future interpretation of these deposits as well as for the understanding of prehistoric tephra records, at least in this region. Eruption histories deciphered using Holocene tephrostratigraphic studies often show only minimum numbers of eruptions, because tephra-fall deposits are not always faithfully recorded in the geologic record (for example, Riehle, 1985; de Fontaine and others, 2007; Schiff and others, 2008). Thus, a discussion of preservation (or lack of) here is relevant to interpreting prehistoric tephra-fall records when direct observations were not made.

Tephra Origin

Multiple volcanic processes can generate ash clouds and ash fall—short-lived blasts, either magmatic or phreatic; sustained magmatic eruption; and elutriation of ash from pyroclastic flows. Integration of field observations and laboratory analyses of tephra-fall and other deposits of the 2005–6 eruption of Augustine is critical to interpreting the origins of the fall deposits. Close coordination with researchers who studied other aspects of the eruption (Coombs and others, this volume; Vallance and others, this volume; Larsen and others, this volume) allowed for consistent identification and characterization of all eruptive products. Evidence used to interpret deposit origin includes (1) duration of plume generation and plume height, (2) volume of fall deposits, (3) componentry of fragmental deposits, (4) contemporaneous volcanic activity, (5) seismicity, (6) acoustic signals, and (7) gas and steam emissions.

Tephra Mass

We used mass-per-unit-area sampling to calculate mass and volume of tephra fall. The mass per unit area (g/m^2) of a sample is the mass (g) of dried sample divided by the area (m^2) from which the sample was collected. These values were plotted on a base map, and contours of equal mass (isomass contours) were constructed. On the basis of our coarse sampling, we were able to draw four isomass contours: 10, 50, 100, and 10,000 g/m^2. Total mass of the tephra deposit was then calculated using the root-area method developed by Pyle (1989) and modified by Fierstein and Nathenson (1992) (table 4). This method accounts for the mass of tephra that fell beyond the most distal isomass contour (that is, 0 g/m^2). We calculate bulk and dense-rock-equivalent (DRE) deposit volume by assuming a bulk density of 1,000 kg/m^3 and a rock density of 2,600 kg/m^3, then dividing the total mass by these densities (Sarna-Wojcicki and others, 1981) (table 4). When calculating eruption rates (erupted mass/eruption duration), we use seismic duration at a distant station (32 km from Augustine; Power and Lalla, this volume) as a proxy for the length of time that a plume was generated (fig. 1).

We used mass per unit area, rather than deposit thickness, to calculate tephra-fall mass and volume, because individual deposits fell in place along with snow and subsequently were buried by snowfall. Modification by compaction does not alter results using this method (Scott and McGimsey, 1994). Tephra was collected from 10 sites of areas 0.04 to 0.25 m^2 (20×20 cm to 50×50 cm), depending on the amount of ash present. The tephra was preserved as a layer in the snowpack, which facilitated sampling the thin and sometimes diffuse deposit (fig. 6). Several snow pits were excavated at each sample site to expose the deposit and to select a representative sample location. Snow overlying the tephra deposit was shoveled away, a plastic measured-area template was placed on the deposit, and a trowel was used to trace out the measured area. The tephra deposit and some underlying snow were collected into large plastic, sealable bags using a trowel. In addition to tephra from the snowpack, one sample was collected on January 17 by a resident of the village of Iliamna, 90 km northwest of Augustine, who collected falling ash on a measured piece of aluminum foil.

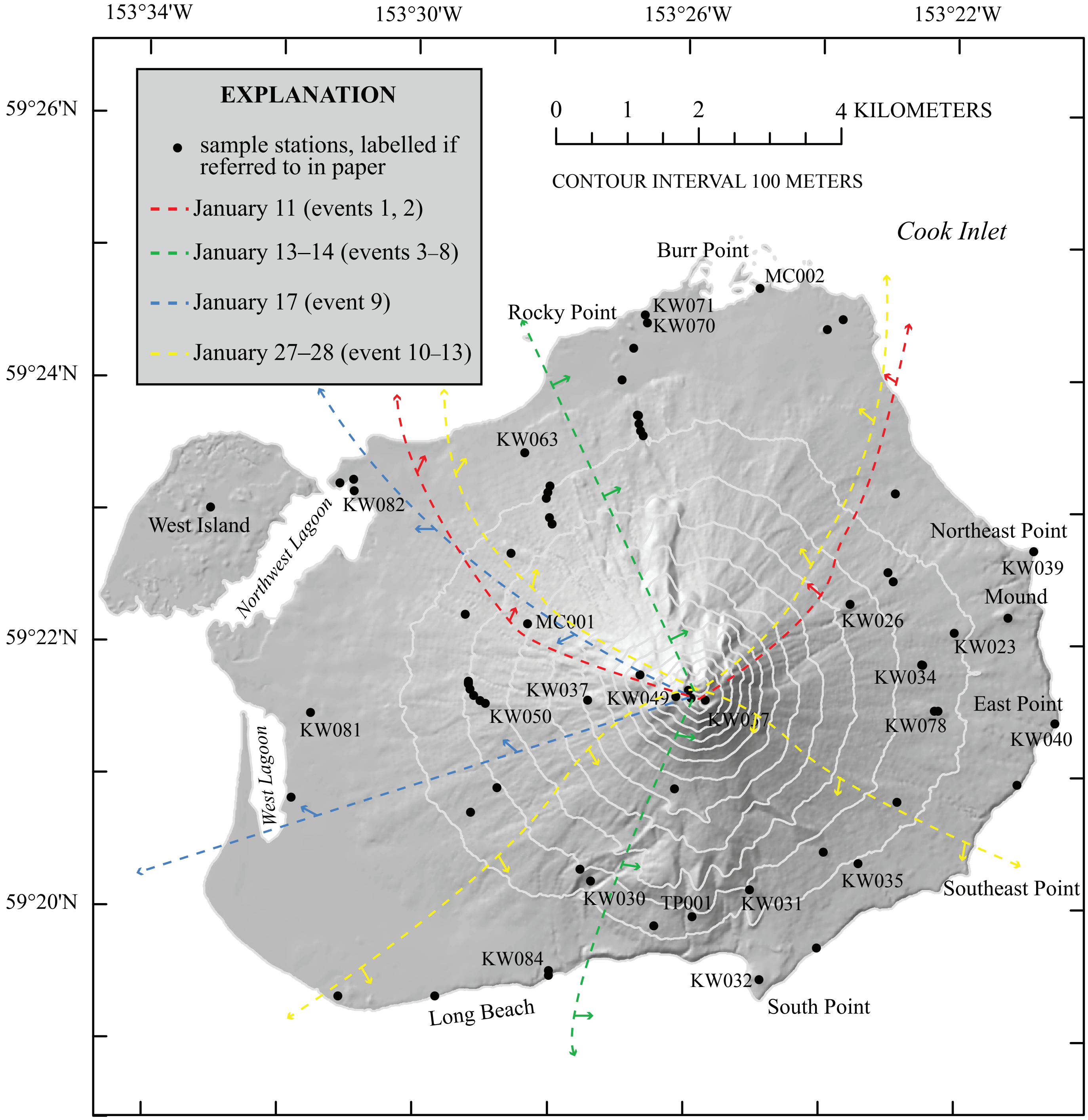

Figure 3. Shaded relief map of Augustine Island showing sample locations (black dots) for this study and dashed lines indicating the boundaries of ash-fall deposits from explosive events that occurred during the explosive phase of the 2005–6 eruption (January 11–28, 2006). Station names are shown for all samples referred to in the paper. Common geographic place names are shown though all except Burr Point are informal. Digital elevation model from 1990.

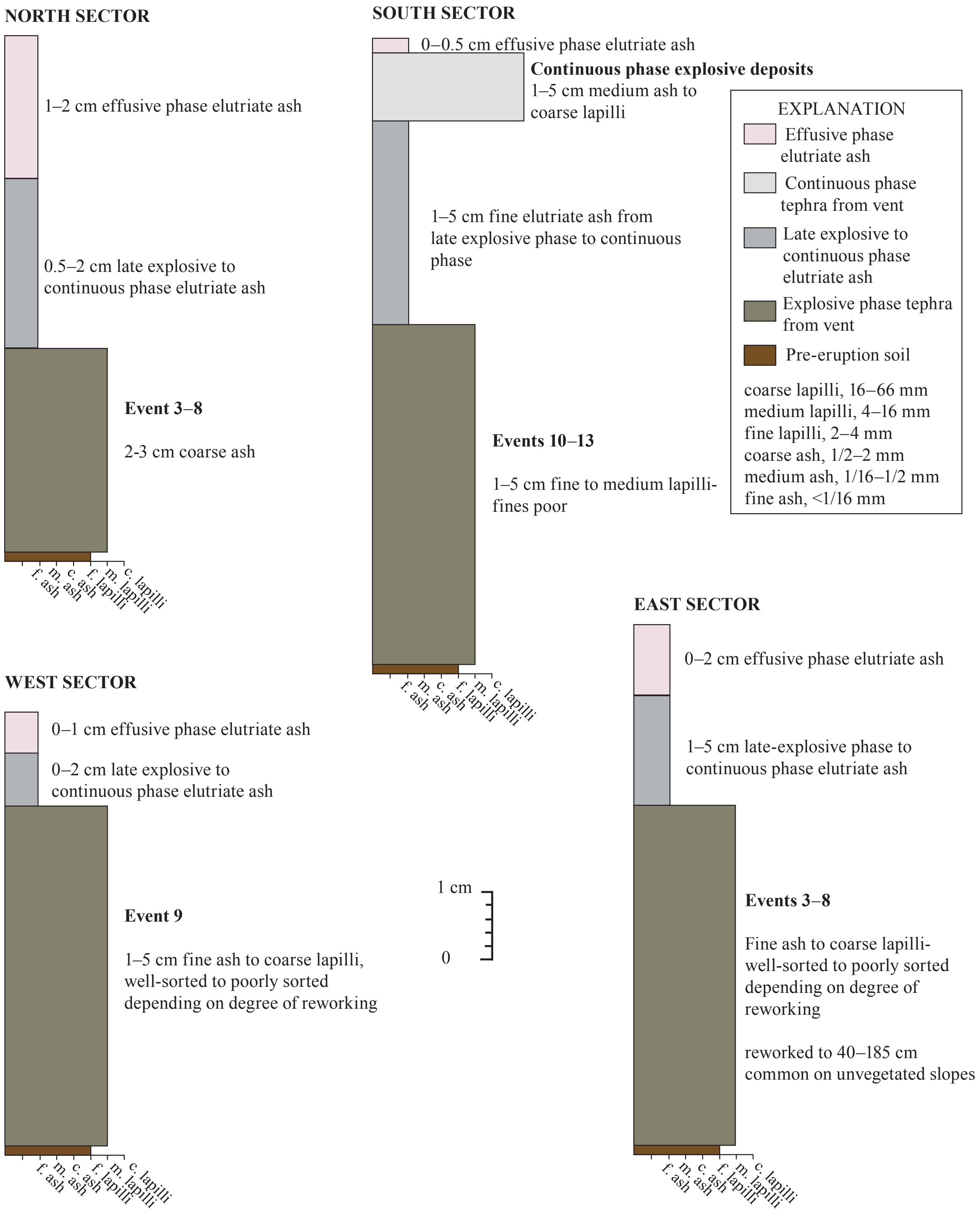

Figure 4. Generalized stratigraphic sections by volcano sectors, showing relations between and characteristics of proximal tephra-fall deposits from the explosive, continuous, and effusive phases of the 2005–6 eruption. Sections are derived from best preserved deposits in vegetated areas on the mid to lower slopes of the island.

Distribution, Character, and Origin of Tephra Deposits

In the following section, we describe in chronological order the tephra-fall deposits that formed during the four discrete phases of the 2005–6 eruption. For each phase, we describe the main eruptive phenomena, describe the resulting tephra deposits, and discuss the origin of tephra generated.

Precursory Phase Tephra Deposits (December 2005)

Distribution and Character of Precursory Phase Tephra

Following more than 7 months of increasing volcanic unrest in the form of seismicity and edifice inflation (Cervelli and others, this volume), several seismic signals suggested a series of small volcanic explosions at Augustine in mid-December. The three largest occurred on December 10, 12, and 15 (Power and others, 2006; Power and Lalla, this volume). Visual observations, radar, and satellite imagery failed to detect the ash plumes from these explosions because they were small or contained very little ash. Nonetheless, we were able to document resulting deposits during observation overflights and landings on the island within days of their occurrence.

A discontinuous, dark-colored dusting of fine to medium ash was observed on the island on December 12. This minor tephra-fall deposit was restricted to the southern sector of Augustine Island and nearby Cook Inlet. A sample collected on December 20 comprises both altered and fresh-looking, possibly juvenile, glass shards (fig. 3, sample TP001). The bulk of the deposit is fragments of altered rock and crystal fragments that are likely reworked older volcanic material.

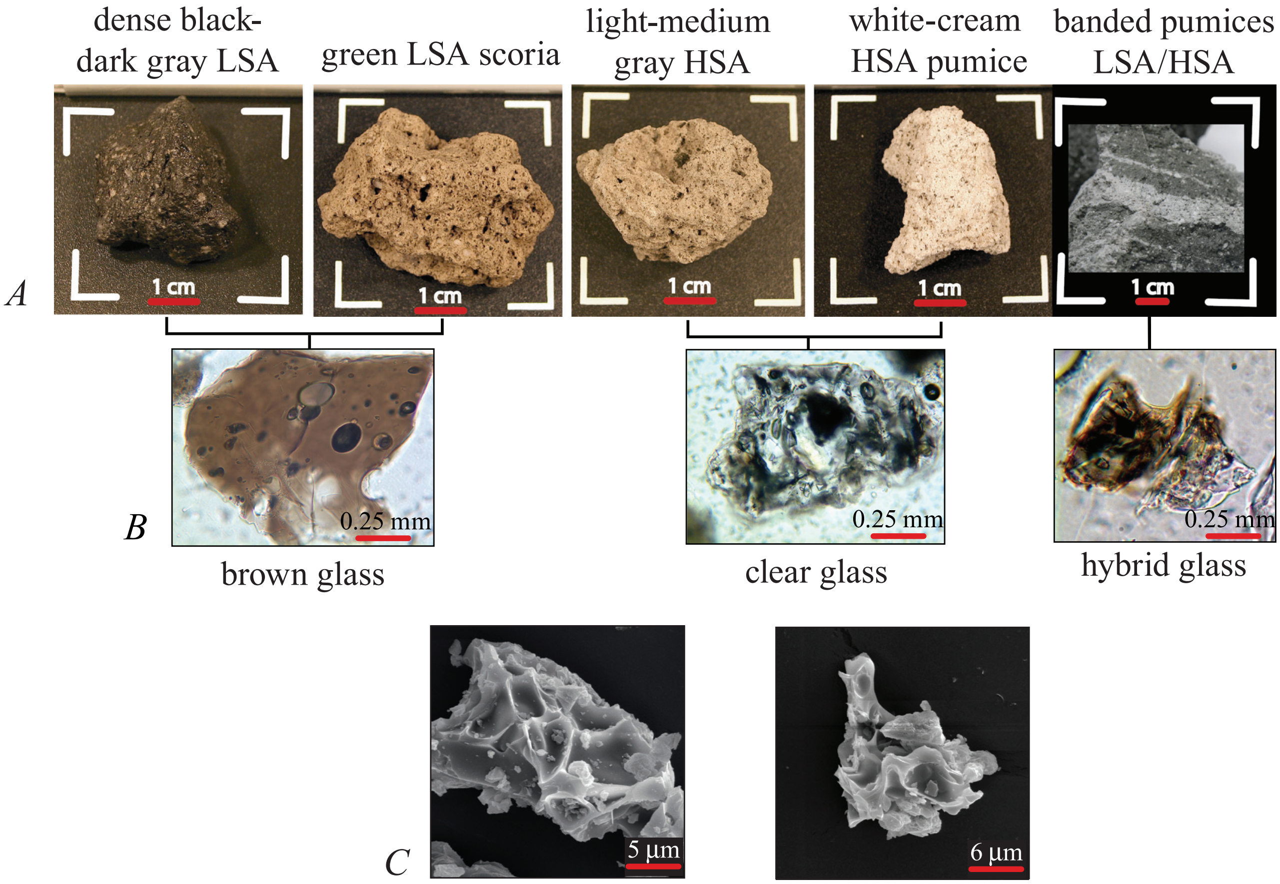

Figure 5. Photographs, photomicrographs, and SEM image of Augustine tephra. *A*, Photographs illustrating clast types erupted during the explosive phase, January 11–28, 2006. LSA, low silica andesite; HSA, high silica andesite. *B*, Transmitted-light photomicrographs illustrating glass phases, including brown, clear, and hybrid varieties. Typically, clear glass is associated with HSA magma and brown glass is associated with LSA magma, although most clasts contain a mixture of both magma compositions. *C*, Scanning electron microscope (SEM) image of vesicular ash particles erupted by Augustine Volcano on January 13, 2006. SEM photographs courtesy of Pavel Izbekov, University of Alaska Fairbanks.

Unaltered glass shards and pumice composed of both clear and brown glass show a range of SiO_2 between 73 and 77.5 wt. percent (table 2 and fig. 7). Reworking by high winds, deposition on snow cover and subsequent burial by younger tephra-fall deposits have now obliterated this deposit as a distinct entity from the geologic record.

Origin of Precursory Phase Tephra

Plumes that are not radar-reflective, the very small volume of deposits, and a lack of clear evidence of juvenile material, coupled with the presence of altered and clearly older lithic fragments, lead us to interpret these tephra deposits as being the result of phreatic explosions. Further evidence, such as impulsive, shallow seismicity suggestive of hydrothermal activity and a marked increase in gas and steam emissions above background levels at the volcano support this interpretation (Power and Lalla, this volume; Buurman and West, this volume; McGee and others, this volume).

Explosive Phase Tephra Deposits (January 11–28, 2006)

Distribution and Character of Explosive Phase Tephra

From January 11–28, a total of 13 discrete explosions sent ash plumes between 4 and 14 km asl and produced tephra fall downwind along several azimuths from the volcano (table 1, fig. 1). Strong seismicity associated with these events lasted 1–11 minutes (averaging 4 minutes; Power and Lalla, this volume) and closely matched the duration of plume generation. Plumes quickly detached from the vent and were distributed downwind (Bailey and others, this volume). The discrete and brief character of these explosions allowed us to discriminate individual ash clouds and to track their distribution using Nexrad radar (Schneider and others, 2006), satellite-image analysis (Bailey and others, this volume), and eyewitness reports. On January 11, 13, and 14, several plumes were generated within hours of one another (table 1) and subsequently coalesced. In such cases, individual ash clouds are poorly differentiated (Bailey and others, this volume). Minor amounts of tephra (1–3 mm) commonly fell between 25 and 185 km downwind from the volcano, and trace amounts (<0.5 mm) of fine ash were reported on one occasion as far as Castella, California, nearly 3,000 km southeast of Augustine.

Figure 6. Photograph showing measured-area sampling of an Augustine ash deposit (from January 17, 2006) preserved in the snow pack west of the volcano near Lake Iliamna. Photo by Christina Neal, March 10, 2006.

January 11, 2006 (Explosive Events 1 and 2)

Two explosions within 30 minutes, events 1 and 2, generated ash plumes to maximum heights of 6.5 and 10.2 km asl, respectively (Schneider and others, 2006). Radar data and satellite images show that the first of the two plumes traveled northwest, and ash fall was reported from villages surrounding Lake Iliamna, 25–80 km west and northwest of Augustine (fig. 1). Satellite images showed that the second ash plume traveled northeast over Cook Inlet, and no deposits were preserved.

On January 12, a field crew visited Augustine Island, and oblique aerial photographs taken that day show a dark-colored, distinct tephra deposit on the south flank and a less obvious dusting of ash on the snow-covered west and north flanks. Low-level ash emissions observed that day probably formed the dark spokelike fall deposit on the south, but we infer the ash on the west and north to have formed during events 1 and 2 (fig. 3). Observations suggested that the preexisting dome complex was partially destroyed during this explosion (Coombs and others, this volume). No tephra-deposit thicknesses were recorded. Samples collected from the west and north flanks of the volcano consist of coarse ash to lapilli with coatings of fine ash (table 3 and fig. 3, samples MC001 and MC002). The coarse fraction includes mainly gray, angular-to-subrounded, dense glassy-to-crystalline fragments and free crystal fragments. Orange, yellow, and red altered clasts of dense lava fragments are common. Vesicular particles are rare. We cannot determine whether the fresh-looking dense fragments are juvenile or recycled tephra or lava from previous eruptions.

A distal tephra-fall deposit, presumably from event 1, was sampled on March 10, 2006, 30 km northwest of Augustine. The deposit was dark colored and present as either a discrete 1–3 mm thick layer or distributed over a depth of 5 mm in the snow pack and underlying a fall deposit from event 9 (January 17) in this region (fig. 8). The event 1 deposit ranges from fine to coarse ash and contains a mixture of old-looking crystallized particles and fresh-looking unaltered clear, brown, and

Table 1. Summary of significant tephra-producing events of the 2005–2006 eruption of Augustine Volcano.

[Duration of seismic signal at station OPT is used as a proxy for duration of plume generation (Power and Lalla, this volume). Plume heights determined from Nexrad radar (data from poster of D.J. Schneider and others, 2006) and have error of ± 1.5 km (D.J. Schneider, oral commun., 2006); plume heights from pilot reports (PIREPs) are from the National Weather Service or Federal Aviation Administration. Plume direction based on satellite data (Bailey and others, this volume), National Oceanic and Atmospheric Administration HYSPLIT model forward trajectories, GDAS meteorological data, and eyewitness accounts. Maximum distance of tephra fall was from confirmed eyewitness reports or from Moderate Resolution Imaging Spectroradiometer (MODIS) satellite imagery. Observation of event: PIREP, pilot report; ph, overflight and fieldwork photograph; st, satellite images; web, web camera; tl, time-lapse camera; dep, photographs of deposits. Origin of tephra plume: vp, ash plume originating from vent; pf, ash cloud from elutriation of pyroclastic flow; rf, ash cloud from a rockfall event. Date of observation overflight for ease of identifying images in the Alaska Volcano Observatory image database (*http://www.avo.alaska.edu/images/*). nd, no data. All dates from 2006 unless noted.]

Event date, AKST (UTC)	Event no.	Event time, AKST	Seismic duration at OPT, min:sec	Plume height, in km asl	Plume height source	Plume direction	Maximum distance, in km	Observation of event	Origin of plume	Eye-witness account	Date of observation flight
Precursory Phase											
12/15/05	nd	nd	nd	nd	nd	nd	nd	dep	vp	F	12/20/05
Explosive phase											
1/11	1	4:44:00	01:18	6.5	radar	N, NE, NW	80	dep, st	vp	T	1/11, 1/12
1/11	2	5:12:00	03:18	10.2	radar	N, NW	80	dep, st	vp	T	1/11, 1/12
1/13	3	4:24:00	11:00	10.2	radar	E-SE	120	ph, st, dep	vp	T	1/16
1/13	4	8:47:00	04:17	10.2	Radar	E-SE	120	ph, st, dep, PIREP, web, tl	vp	T	1/16
				14-15	PIREP						
				16.0	PIREP						
1/13	5	11:22:00	03:24	10.5	radar	SE	120	ph, st, dep, PIREP, web, tl	vp	T	1/16
				16.0	PIREP						
1/13 *(01/14)*	6	16:40:00	04:00	10.5	radar	SE	120	ph, st, dep, PIREP, web, tl	vp	T	1/16
				9-11	PIREP						
1/13 *(01/14)*	7	18:58:00	03:00	13.5	radar	E SE	120	ph, st, dep	vp	T	1/16
1/14	8	0:14:00	03:00	10.2	radar	E SE	120	ph, st, dep	vp		1/16
1/17	9	7:58:00	04:11	13.5	Radar, PIREP	NW	140	ph, st, dep, PIREP	vp	T	1/18, 1/24
1/27 *(01/28)*	10	20:24:00	09:00	10.5	radar	SE	185	dep, st	vp	T	1/29, 1/30
1/27	11	23:37:21	01:02	3.8	radar	S SE	185	dep, st	vp	T	1/29, 1/30
1/28	12	2:04:13	02:06	7.2	radar	S SE	185	dep, st	vp	T	1/29, 1/30

1/28	13	7:42:00	03:00	7.2	radar	S SE	185	ph, st, dep, PIREP, web	vp	T	1/29, 1/30
					Continuous phase						
1/28	14	14:31:00	nd	3.8	radar		185	ph, st, dep, PIREP, web	vp, pf	T	1/29, 1/30
				8.0	PIREP						
				9.0	PIREP						
1/29	nd	11:17:00	05:30	7.2	radar	S SW	185	ph, st, dep, PIREP, tl	vp, pf	T	1/29, 1/30
				9.0	PIREP						
				15.0	PIREPs						
1/30	nd	3:25:00	02:04	7.2	radar	NE	160	ph, st, dep, PIREP	vp, pf	T	1/30, 2/3, 2/8
				4.0	radar						
1/30	nd	6:21:00	nd	7.2	radar	E NE	160	ph, st, dep	vp, pf		1/30, 2/3, 2/8
2/8/07			nd	nd	nd	N - local	nd	ph, web	pf	F	2/8
					Effusive phase						
3/4, 3/6, 3/7, 3/9, 3/10	nd	nd	nd	nd	nd	nd	85	ph, dep, web	rf, pf	T	3/6, 3/9, 3/10, 3/15

Table 2. Summary of groundmass glass average compositions for 2005–6 tephra from Augustine Volcano.

[All glass compositions determined using a Cameca SX-50 electron microprobe equipped with four wavelength-dispersive spectrometers and one energy-dispersive spectrometer at the University of Alaska Advanced Instrumentation Laboratory, Fairbanks, Alaska. Glasses analyzed using 15KeV, 10nA, and 10 micron-wide defocused beam. Oxide values given in weight percent and normalized to 100 percent anhydrous. Stdev, standard deviation; n, number of shards analyzed; GS, glass shard; MG, matrix glass from lapilli clast.]

Sample No.	SiO_2	TiO_2	Al_2O_3	FeO	MgO	CaO	Na_2O	K_2O	MnO	Cl	Total	Sample type
Precursory phase—December 2005												
clear glass-sample AT-703A.												GS
mean	76.96	0.26	13.30	1.46	0.28	2.07	3.85	1.71	nd	0.12	98.09	
stdev	0.62	0.33	0.90	0.76	0.22	0.68	1.23	0.85	nd	0.16		
n	7											
brown glass-sample AT-703B.												GS
mean	73.93	1.10	13.13	2.06	0.49	2.18	4.00	2.81	nd	0.27	97.69	
stdev	0.98	0.83	0.53	0.50	0.40	0.60	1.08	1.78	nd	0.09		
n	4											
Explosive phase—January 11, 2006, explosive events 1–2												
brown glass-samples AT-746, AT-769, AT-753, and AT-761.												GS
mean	65.56	0.96	16.44	4.22	1.68	4.78	4.68	1.54	nd	0.13	98.71	
stdev	0.89	0.32	0.48	0.52	0.61	0.70	0.33	0.23	nd	0.10		
n	5											
clear glass-samples AT-746, AT-769, and AT-761.												GS
Mean	77.09	0.23	12.38	1.57	0.22	1.84	4.51	2.01	nd	0.13	99.51	
stdev	0.88	0.17	0.38	0.37	0.10	0.67	0.32	1.18	nd	0.11		
n	9											
Explosive phase—January 13–14, 2006, explosive events 3–8												
dense low-silica andesite (DLSA)-samples AT-957B, AT-920A, and AT-967D.												MG
mean	68.16	0.84	15.27	3.55	0.80	4.10	5.01	2.00	0.05	0.23	99.81	
stdev	1.48	0.23	0.79	0.66	0.24	0.44	0.25	0.14	0.05	0.09		
n	11											
low-silica andesite scoria (LSAS)-samples AT-960A, AT920B, and AT-967A.												MG
mean	66.56	1.17	14.50	4.93	1.58	4.39	4.67	1.68	0.13	0.40	98.48	
stdev	1.02	0.16	0.57	1.04	0.27	0.36	0.39	0.10	0.05	0.13		
n	5											
high-silica andesite pumice (HSA)-sample AT-912D.												MG
mean	75.00	0.25	12.51	2.25	0.45	2.10	4.93	2.08	0.09	0.34	98.59	
stdev	0.53	0.13	0.45	0.71	0.04	0.11	0.32	0.06	0.03	0.13		
n	7											
Explosive phase —January 17, 2006, explosive event 9												
low-silica andesite scoria (LSAS)-samples AT-924A, AT-934A, AT905B, AT-943A, AT-949A.												MG
Mean	66.99	0.98	14.74	4.51	1.38	4.19	4.89	1.83	0.13	0.35	98.12	
stdev	1.59	0.20	1.10	0.63	0.22	1.13	0.39	0.49	0.10	0.12		
n	8											

Table 2. Summary of groundmass glass average compositions for 2005–2006 tephra from Augustine Volcano.—Continued

[All glass compositions determined using a Cameca SX-50 electron microprobe equipped with four wavelength-dispersive spectrometers and one energy-dispersive spectrometer at the University of Alaska Advanced Instrumentation Laboratory, Fairbanks, Alaska. Glasses analyzed using 15KeV, 10nA, and 10 micron-wide defocused beam. Oxide values given in weight percent and normalized to 100 percent anhydrous. Stdev, standard deviation; n, number of shards analyzed; GS, glass shard; MG, matrix glass from lapilli clasts.]

Sample No.	SiO_2	TiO_2	Al_2O_3	FeO	MgO	CaO	Na_2O	K_2O	MnO	Cl	Total	Sample type
Explosive phase—January 17, 2006, explosive event 9												
dense low-silica andesite (DLSA)-samples AT-940B , AT-923A, and AT-961B.												MG
mean	66.36	0.92	15.45	4.78	1.05	4.90	4.65	1.55	0.18	0.16	100.15	
stdev	1.21	0.16	1.01	0.71	0.23	0.55	0.24	0.20	0.09	0.06		
n	5											
high-silica andesite pumice (HSA)-samples AT-934B, AT-925C, AT-924C, and AT-961C.												MG
mean	74.42	0.47	12.34	2.36	0.41	2.10	5.23	2.25	0.07	0.34	100.38	
stdev	0.69	0.17	0.93	0.70	0.12	0.14	0.38	0.30	0.07	0.21		
n	6											
clear glass-samples AT-757, AT-759, AT-751, AT-744, AT-748, AT-767, AT-764, and AT-762.												GS
mean	76.25	0.47	12.36	1.89	0.33	1.45	4.03	3.07	nd	0.15	99.71	
stdev	0.91	0.38	0.71	0.34	0.20	0.75	0.62	1.48	nd	0.12		
n	13											
brown glass-samples AT-757, AT-759, AT-751, AT-744, AT-748, AT-767, and AT-762.												GS
mean	71.72	0.57	15.36	1.93	0.34	3.13	4.78	2.03	nd	0.15	99.12	
stdev	0.80	0.70	1.67	0.84	0.23	0.82	0.34	0.50	nd	0.15		
n	13											
Explosive phase —January 27–28, 2006, explosive events 10–13												
dense low-silica andesite (DLSA)-samples AT-932A, and AT-917A.												MG
mean	68.88	1.01	14.34	3.58	0.83	4.09	5.10	1.83	0.10	0.24	98.96	
stdev	4.00	0.66	0.81	2.61	0.89	0.58	0.06	0.18	0.14	0.17		
n	2											
high-silica andesite pumice (HSA)-sample AT-928A.												MG
mean	76.10	0.30	12.61	0.98	0.15	2.06	5.12	2.41	0.14	0.13	99.14	
stdev	0.20	0.02	0.66	0.42	0.01	0.09	0.35	0.19	0.10	0.11		
n	2											
clear glass-samples AT-733, AT-719, and AT-916.												GS
mean	75.30	0.26	13.29	1.11	0.31	1.93	4.98	2.61	0.06	0.18	100.04	
stdev	0.52	0.30	0.96	0.62	0.11	0.37	0.15	0.70	0.08	0.17		
n	3											
brown glass-sample AT-733.												GS
mean	69.28	0.60	15.88	2.79	0.85	4.09	4.52	1.72	0.03	0.24	98.80	
n	1											
Continuous phase—January 28–February 10												
clear glass-samples AT-770, AT-913, AT-909, and AT-953.												
Mean	76.04	0.50	12.52	1.63	0.32	1.76	4.60	2.35	0.12	0.21	99.68	GS

Table 2. Summary of groundmass glass average compositions for 2005–2006 tephra from Augustine Volcano.—Continued

[All glass compositions determined using a Cameca SX-50 electron microprobe equipped with four wavelength-dispersive spectrometers and one energy-dispersive spectrometer at the University of Alaska Advanced Instrumentation Laboratory, Fairbanks, Alaska. Glasses analyzed using 15KeV, 10nA, and 10 micron-wide defocused beam. Oxide values given in weight percent and normalized to 100 percent anhydrous. Stdev, standard deviation; n, number of shards analyzed; GS, glass shard; MG, matrix glass from lapilli clasts.]

Sample No.	SiO_2	TiO_2	Al_2O_3	FeO	MgO	CaO	Na_2O	K_2O	MnO	Cl	Total	Sample type
Continuous phase—January 28–February 10												
clear glass-samples AT-770, AT-913, AT-909, and AT-953.												
stdev	0.82	0.29	0.43	0.32	0.11	0.34	0.33	0.29	0.08	0.06		
n	21											
brown glass-samples AT-770, AT-909, and AT-953.												
mean	67.74	0.39	17.02	2.46	0.92	5.02	4.38	1.83	0.14	0.14	98.34	GS
stdev	1.72	0.36	1.51	0.95	0.41	1.19	0.82	0.81	0.02	0.17		
n	5											
Effusive phase—March 3–16												
clear glass-samples AT-915 and AT-919.												GS
mean	74.67	0.38	12.62	2.08	0.40	2.10	5.19	2.16	0.12	0.30	100.75	
stdev	0.36	0.07	0.09	0.19	0.07	0.13	0.21	0.10	0.05	0.08		
n	4											
brown glass-samples AT-915 and AT-919.												GS
mean	65.26	0.66	15.87	4.01	1.57	5.17	5.35	1.55	0.26	0.32	100.19	
stdev	0.94	0.04	0.08	0.50	0.82	0.47	0.53	0.19	0.10	0.16		
n	3											

hybrid glassy particles. Glass compositions range between 65–67 and 76–78 wt. percent silica (SiO_2) for brown and clear glass, respectively (table 2 and fig. 7).

Because of reworking by high winds, deposition onto snow, and subsequent burial by younger tephra-fall deposits, we recognized no primary exposures on the island following the eruption. Distal deposits are also not likely to be preserved in the geologic record owing to their small volume, deposition onto snowpack, and reworking by surface runoff.

January 13–14, 2006 (Explosive Events 3–8)

On January 13 and 14, six discrete explosions (events 3–8) produced ash plumes that reached between 10 and 13.5 km asl and that dispersed to the east-southeast (Schneider and others, 2006; fig. 1).

The Kenai Peninsula communities of Homer, Seldovia, Nanwelek, and Port Graham, 90–120 km downwind of Augustine, reported ash fall. In many cases ash fell with snow and snowflakes were particularly large and intricate, probably because of nucleation around ash particles (Adam Duran, oral commun., 2006). Ash from three or perhaps four of the six clouds fell entirely into Cook Inlet (events 5–7 and possibly event 3). In addition to ash fall on surrounding communities soon after these explosions, airborne ash clouds from the events took circuitous routes following high-level wind patterns. Back trajectories of the NOAA HYSPLIT wind-forecast model suggest that ash fell in northern California (January 16), communities on the southern Kenai Peninsula (January 17 and 19), Anchorage (January 19), and Palmer (January 31) because of recirculating plumes containing residual ash generated by explosive events of January 13–14.

We could not differentiate individual distal deposits from events 3–8 because they overlap and form a composite layer (table 1). The cumulative distal deposit was as much as 1 mm thick, gray-brown in color, and composed of fine to medium ash (table 3, fig. 9). Distal ash contains clear, brown, and hybrid glass shards.

Oblique aerial photographs of the island taken during a January 16 overflight show a continuous, distinctive dark-brown tephra deposit covering fresh snow on the north, east, and south flanks (fig. 3). In contrast, clean white snow on the west flank suggested little to no tephra deposition on that quadrant of the island. During August 2006, proximal ash-fall deposits from these events were chiefly preserved on the volcano's north, northeast, east, and southeast flanks but were most voluminous on the eastern sector of Augustine Island.

Except in a few locations where primary stratigraphy is preserved (fig. 3, station KW026), we are unable to differentiate proximal deposits from the six discrete explosions. Total deposit thicknesses range from 5 to 185 cm. Thicker accumulations (on the eastern flank, fig. 10*B,* and fig. 3, stations KW034, KW078) are clearly wind and water reworked, and 5 cm is a representative thickness value for proximal, primary deposits (table 3; fig 3, station KW023; fig. 10*A*). Proximal tephra consists of light-gray, fine ash to medium lapilli (table 3). Light-gray, well-sorted, fine-ash deposits were documented on the north flank, in addition to coarse-grained deposits. Together, these deposits contain the first clear evidence of juvenile material since the start of the eruption. Such evidence includes abundant fresh-looking, angular clasts, vesicular ash and lapilli, and unaltered glass

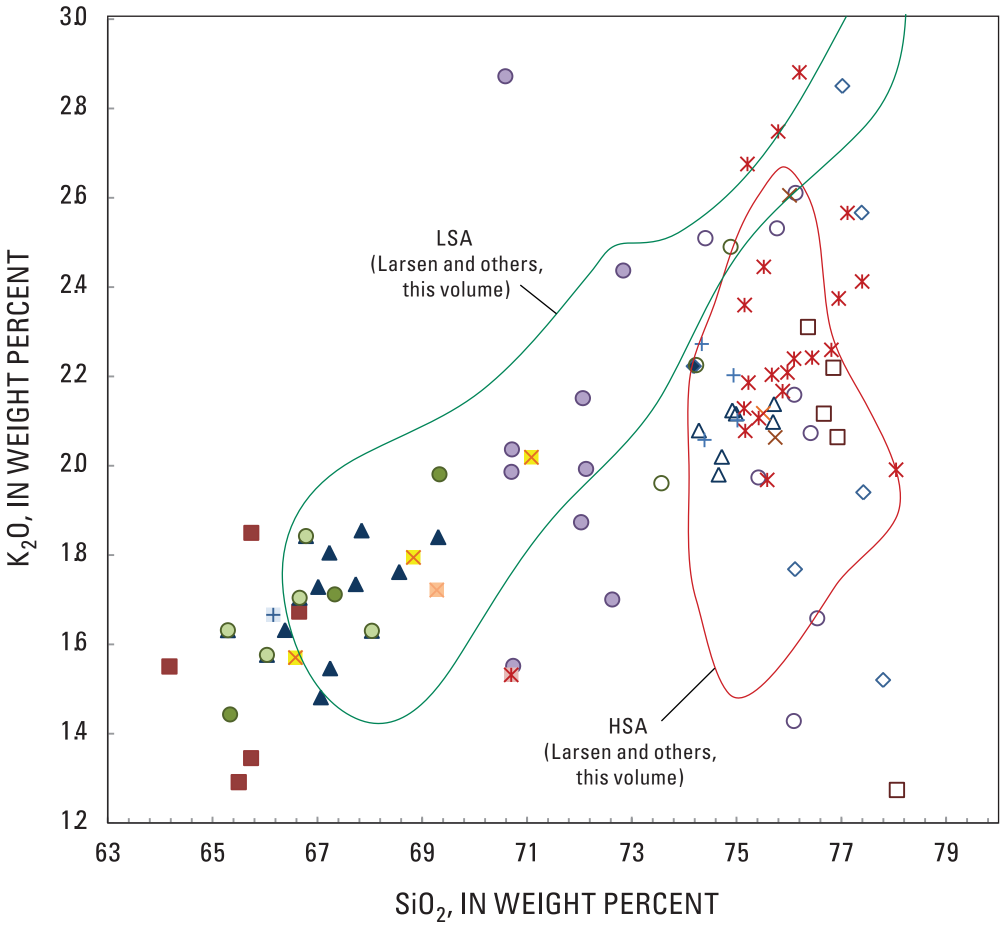

EXPLANATION

	Clear glass	Brown glass	DLSA	LSAS	HSA
Late Precursory Phase (Dec. 2005)	◇	◆			
Explosive Phase (Jan. 11)	□	■			
Explosive Phase (Jan. 13-14)			▲	▲	△
Explosive Phase (Jan. 17)	○	●	●	●	○
Explosive Phase (Jan. 27-28)	×	☒	☒		×
Continuous Phase (Jan. 28-Feb. 10)	✱	✱			
Effusive Phase (March 3-10)	+	+			

Figure 7. Plot of weight percent SiO_2 versus K_2O from microprobe analysis of groundmass (matrix) glass and glass shards for 2005–6 Augustine tephra-fall deposits. Data are separated by phase of eruption and by lithology. DLSA, dense low-silica andesite; LSAS, low-silica andesite scoria; HSA, high-silica andesite. Note that clear glass shards and HSA matrix glasses have more evolved and restricted compositions (74-78 wt. percent SiO_2), whereas brown glass shards and low-silica andesite matrix glasses have a wider range of compositions (64-74 wt. percent SiO_2). Low-silica andesite (LSA) and high-silica andesite (HSA) fields show matrix glass compositions of 2006 pyroclasts from Larsen and others (this volume).

Table 3. Summary of basic tephra-deposit characteristics for the 2005–6 eruption of Augustine Volcano.

[Maximum recorded thickness on Augustine Island (proximal thickness) was determined in July–August 2006, 6 months after the eruption ended. Maximum recorded thickness of tephra deposits on land surfaces off Augustine Island (distal thickness) was determined near the time of deposition. Bulk particle size for proximal tephra deposits uses volcanic terminology (Fisher, 1961; Schmid, 1981; Chough and Sohn, 1990): c, coarse; m, medium; f, fine. All distal deposits contain f. ash - m. ash. Componentry, in percent of clasts >5mm: HSA, high-silica andesite, gray–white pumices; DLSA, dense low-silica andesite, black–dark gray clasts; LSAS, low-silica andesite scoria; greenish-gray; banded clasts are typically pumiceous and contain gray and white/cream bands; LF, lithic fragments are nonjuvenile accidental clasts. n, number of clasts used to average componentry data; nd, no data. Componentry is from coarse-grained proximal deposits; no data from deposits with only fine-grained tephra.]

Eruption phase and date	Event no.	Max. proximal thickness, in cm	Max. distal thick-ness, in mm	Particle size range	HSA	DLSA	LSAS	Banded	LF	n
					Componentry					
Precursory Phase										
December 2005		0.2	0		nd	nd	nd	nd	nd	nd
Explosive Phase										
January 11, 2006	1–2	nd	3	f.ash–m. lapilli	nd	nd	nd	nd	nd	nd
January 13-14	3–8	180	1	f.ash–c. lapilli	26	22	41	2	9	475
January 17	9	1	3	f.ash–c. lapilli	35	32	20	2	11	977
January 27-28	10–13	5	1	f.ash–m. lapilli	52	18	8	8	14	215
Continuous Phase										
January 28-Feburary 10		5	1	f.ash–m. ash	60	13	6	13	8	195
Effusive Phase										
March 3-March 16		2	<1	f.ash	nd	nd	nd	nd	nd	nd

as determined by scanning electron microscopy (fig. 5). We identify four juvenile lithologies in the coarse-grained deposits (1) porphyritic, dense (black to dark gray), low-silica andesite (herein called dense low-silica andesite), (2) scoriaceous (greenish-gray), low-silica andesite (herein called low-silica andesite scoria), (3) porphyritic, pumiceous, high-silica andesite (light gray to white) (herein called high-silica andesite), and (4) banded clasts of varying textures and colors but predominantly pumiceous (fig. 5).

Componentry of undifferentiated fall deposits is 41 percent dense low-silica andesite, 22 percent low-silica andesite scoria, 26 percent high-silica andesite, 2 percent banded clasts, and 9 percent nonjuvenile lithic fragments (table 3). Glass compositions range from 66 to 69 wt. percent SiO_2 for low-silica andesite lapilli clasts and from 74 to 76 wt. percent SiO_2 for high-silica andesite (table 2 and fig. 7).

Deposits on exposed, nonvegetated slopes are most prone to reworking by wind and water (fig. 3, stations KW034, KW078, and fig. 10*B*). Deposits found in alder stands are largely unaffected by high winds and surface runoff, and outcrops of fine ash draped on branches were preserved some six months after deposition (fig. 3, station KW082, and fig. 10*C*). Figures 10*C*, *D* and *G* show only modest postdepositional modification resulting from slow melting of snow under and overlying the deposits. Distal tephra-fall deposits are not likely to be preserved in the geologic record, and certainly not as an identifiable discrete layer, because ash fall emplaced directly onto snow is remobilized during subsequent melting.

January 17, 2006 (Explosive Event 9)

Explosive event 9 on January 17 produced a plume as high as 13.5 km asl (Schneider and others, 2006) that dispersed to the west-northwest. Ash fall was first observed the same day by residents in villages surrounding Lake Iliamna, 50–120 km from Augustine (fig. 1). Observers described the deposit as a very thin dusting (<1 mm) of dark-colored ash. During field work in March 2006, the event 9 deposit formed a prominent and fairly continuous layer in the snowpack that ranged from a dark-colored discrete layer, 1–3 mm thick, to a disseminated layer over a depth of 0.5–3 cm within snow (fig. 8). Distal ash fall contains brown, fine to medium ash with clear, brown, and hybrid glass shards. Glass compositions are in the range of 71–73 and 75–77 wt. percent SiO_2 for brown and clear glass, respectively (table 2, and fig. 7).

Proximal tephra deposits from event 9 crop out on the western sector of the island (figs. 3, 4). Oblique aerial photographs of the island during an overflight of the volcano on January 17 show a distinct dark brown deposit on the western flank and in the area within 3 km of the summit. A new lava dome, first identified during an overflight on January 16, was partially destroyed by the January 17 explosion, leaving a large crater in the new dome (Coombs and others, this volume). Observers on an overflight on January 18 identified

Figure 8. Photograph showing two distal ash layers preserved in the snow pack, 40 km west-northwest of Augustine. The lower layer is from event 1 on January 11, 2006. Event 1 tephra was deposited onto snow cover and subsequently buried by more snow. The deposit is 1–3 mm thick in this region and either discrete (shown here) or disseminated over a zone 5 mm thick. The upper layer is from event 9 on January 17, 2006, and is 1–3 mm thick in this region and either discrete (shown here) or disseminated over a zone 0.5–3 cm thick. Black cap on marker is 5 cm. Photo by Kristi Wallace, March 10, 2009.

Figure 9. Photographs showing a dusting of ash on snow and a vehicle in Homer, Alaska on January 13, 2006. Photos courtesy of Michael Fairbanks.


elutriated ash-continuous phase
Jan 13-14 deposit
soil and
pre-2006 deposits
A
B
C
D
elutriated ash
lapilli fall
pre-2006
surface
E
effusive phase elutriated ash
block
January 17 explosion sequence
pre-2006 deposit
F
G

a ballistic field on the upper west flank, extending 760 m from the vent (fig. 3, station KW049, and fig. 11).

Proximal deposits observed in August 2006 range from 1 to 65 cm thick (4 and 1 km from the vent respectively) and include fine ash to coarse lapilli (fig. 3, stations KW082 and KW037, fig. 10*C*, *F*). Proximal deposits contain the same lithologies seen in deposits from events 3–8: (1) 32 percent dense low-silica andesite, (2) 20 percent low-silica andesite scoria, (3) 35 percent high-silica andesite, (4) 2 percent banded clasts, and (5) 11 percent nonjuvenile lithic fragments (table 3). Glass compositions range from 65 to 69 and from 74 to 75 wt. percent SiO_2 for low-silica andesite and high-silica andesite, respectively (table 2 and fig. 7).

The tephra deposit from this event is well preserved in alder stands low on the west flank of the island and in one primary, near-vent (1 km) deposit on a bench on the upper west flank (fig. 3, stations KW082 and KW037, fig. 10*C, F*). All other exposures on nonvegetated slopes are wind and water reworked.

January 27–28, 2006 (Explosive Events 10–13)

On January 27–28, four explosions produced ash plumes between 3 and 10.5 km asl (Schneider and others, 2006) and caused ash fall on Afognak and Kodiak Islands, as far as 185 km to the southeast and south-southwest of Augustine (fig. 1). Distal ash fall was reportedly minor, with less than 1 mm of accumulation on snow. Distal deposits contain brown, fine ash with clear, brown, and hybrid glass shards, and glass compositions range from 69 to 76 wt. percent SiO_2 (table 2 and fig. 7).

Direct observations of proximal tephra deposits from this time period were not possible immediately following their emplacement because of persistent airborne ash around the island during the continuous eruptive phase that began immediately after event 13. However, proximal deposits on the south flank are attributed to events 10–13, because those plumes were the only ones during the eruption that traveled in that direction. Proximal tephra deposits on the southern sector of the island are 1–5 cm thick and contain fine ash to medium lapilli (table 3; fig. 3, station KW032; fig. 4, and fig. 10*E*).

Componentry of these undifferentiated fall deposits is 18 percent dense low-silica andesite, 8 percent low-silica andesite scoria, 52 percent high-silica andesite, 8 percent banded clasts, and 14 percent lithic fragments (table 3). Glass compositions range from 66.5 to 72 wt. percent SiO_2 for low-silica andesite and from 76 to 77 wt. percent SiO_2 for high-silica andesite (table 2 and fig. 7). Proximal fall deposits on the north sector of the island are 1–5 cm thick, contain well-sorted, gray fine ash, and are considered to be elutriate from pyroclastic flows emplaced to the north on January 27 (fig. 3, station KW070, and fig. 4) (Coombs and others, this volume). Elutriate deposits from January 27–28 are indistinguishable from elutriate deposits from the continuous eruptive phase that immediately followed the emplacement of these deposits.

Origin of Explosive Phase Tephra

The explosive phase was characterized by discrete, short-duration (1–11 minutes) explosions that produced ash plumes with tops from 4 to 14 km asl (Schneider and others, 2006) and small-volume tephra deposits (table 1). Strong seismic (McNutt and others, this volume) and infrasonic (Peterson and others, 2006) signals accompanied individual explosions; the first explosive event was preceded by a series of volcano-tectonic earthquakes on January 10 and 11 (Buurman and West, this volume; Power and Lalla, this volume; Power and others, 2006). These observations suggest a Vulcanian-style eruption mechanism (Morressey and Mastin, 2000).

Despite the general similarity among the 13 events of the explosive phase, there are some important differences. Events 1 and 2 were relatively short (1:18 and 3:18 minutes) with impulsive seismic and infrasonic signals. Unlike later events, these generated only small-volume, mixed-rock-and-snow avalanches but no pyroclastic flows (Coombs and others,

◀ **Figure 10.** Photographs showing the condition and preservation of proximal tephra-fall deposits on Augustine Island from the 2005–6 eruption. *A*, Primary tephra deposit on the east flank with coarse ash to fine lapilli base from January 13–14 explosions capped by fine gray ash from the elutriation of pyroclastic flows and rockfalls, black cap on marker is 5 cm (fig. 3, KW023). *B,* Thick accumulation of wind and water reworked tephra from the January 13–14 explosions on the east flank; shovel is 60 cm long (fig. 3, KW034). *C*, Tephra preserved in an alder stand on the west flank, showing only minimal reworking; the deposit remains draped on tree branches after melting out from snow cover. Silver and orange markings on trowel handle are 1.5 cm each (fig.3, KW082). *D*, Fall deposit on the south flank, attributed to explosive events 10–13. Coarse lapilli clasts projecting out of fine-ash deposit (white arrows) indicate that fine ash deposits are thinner than maximum lapilli axes. Black cap on marker is 5 cm (fig 3, KW084). *E*, Lithic lapilli fall of low-silica andesite deposit (January 27–28 explosions) on the south coast of Augustine capped by fine elutriated ash from the continuous and effusive phases (fig. 3, KW032). *F*, Near vent exposure of January 17 tephra-fall deposit on the upper west flank, including a ballistic block; shovel is 60 cm long (fig. 3, KW037). *G,* Typical exposure of a tephra deposit overlying leaf litter and a well-defined organic layer in alder stands on Augustine Island. Pre-2006 tephra deposits underlie the organic horizon (fig. 3, KW063). All photos by Kristi Wallace, August 7, 2006.

this volume). Plumes from events 1 and 2 appear to have contained low concentrations of ash and only deposited very thin, localized tephra. Proximal deposits from these events are dominated by dense and altered material. Distal tephra deposits do contain glass with intermediate to silicic glass compositions. Because of the similar compositions of matrix glasses between juvenile 2006 tephra and that from the 1976 and 1986 eruptions, however, it is impossible to know if the analyzed shards are new 2006 material or recycled from previous eruptions. On the basis of other lines of evidence, we think that the glass in the distal January 11 ash may be recycled. This was also the case for ash from the 2004–5 eruption of Mount St. Helens, where clean glass in distal ash was determined to have derived from nonjuvenile sources (Rowe and others, 2008). Because events 1 and 2 contained little or no juvenile material, they were likely caused when gases at the top of the ascending magma body reached the surface (Larsen and others, this volume). Interestingly, event 11 on January 27 had a similar seismic signal (McNutt and others, this volume), a low ash signal in radar (Schneider and others, 2006), and may have formed by a similar process, although its deposits were not uniquely identified.

Vulcanian explosions of January 13–14 (events 3–8) generated plumes 10–16 km asl and column-collapse pyroclastic flows that spread radially on all sides of the volcano, as well as secondary lahars and mixed snow and rock avalanches (Vallance and others, this volume). Tephras from these events are dominated by low-silica andesite (63 percent), with lesser amounts of high-silica andesite, lithics, and banded clasts (table 3). The succession of six discrete explosive plumes within less than 24 hours suggests rapid ascent of magma to the surface. Following event 8, a low-silica andesite lava lobe effused at the summit (Coombs and others, this volume; Larsen and others, this volume).

On January 17, after a 3-day pause in explosive activity, a Vulcanian explosion (event 9) produced one of the highest

Figure 11. Photograph illustrating ballistic field near the summit of Augustine, upper west flank (fig.3, KW049). Fine ash generated from pyroclastic flows and rockfalls during the effusive phase drape ballistic blocks on the surface. New dome steaming in the background. Note circled figure for scale. Photo by Kristi Wallace, August 2006.

plumes of the eruption sequence (table 1). Like tephra from the January 13–14 events, event 9 tephra was predominantly low-silica andesite (52 percent), but deposits have slightly higher proportions of high-silica andesite compared to January 13–14 events (table 3). Low-silica andesite lapilli closely resemble the low-silica andesite of the new lava lobe in texture and composition (Coombs and others this volume; Larsen and others, this volume). The new lava dome probably sealed the vent and allowed pressure to build until it ruptured, and explosive decompression of gas-rich magma generated a vigorous plume.

Vulcanian explosions of January 27 and 28 (events 10–14) occurred after a 10-day hiatus in explosive events. Between January 17 and 27, a new high-silica lava-dome lobe grew at the summit (Coombs and others, this volume; Larsen and others, this volume). In coarse-grained fall deposits from events 10–13, high-silica andesite lithologies predominate (52 percent) and closely match the composition of the January 17–27 dome. Subordinate low-silica andesite is more commonly dense and black to dark gray rather than scoriacious (table 3). In addition to vent explosions that resulted in relatively coarse fall deposits, fine elutriated ash from large pyroclastic flows of January 27 (Coombs and others, this volume) fell on the north flank of the volcano. These fine-ash deposits are indistinguishable from continuous phase deposits (see below) in terms of predominance of high-silica andesite shards.

The succession of magma compositions throughout the explosive phase from low-silica to high-silica andesite, as shown in tephra-deposit componentry, is also seen in componentry of pyroclastic-flow deposits (Vallance and others, this volume). Petrological studies (Larsen and others, this volume; Webster and others, this volume) suggest that mixing between an old shallow (4–6 km below the surface) high-silica andesite magma and a deep, young mafic end member (basalt) produced the low-silica andesite that was predominantly erupted during the early explosive phase (January 13, 14, and 17). The high-silica andesite that predominated in the late explosive phase (January 27 and 28) was likely remobilized by the injection of the mafic magma, allowing it to rise to the surface (Larsen and others, this volume).

Continuous Phase Tephra Deposits (January 28–February 10, 2006)

Distribution and Character of Continuous Phase Tephra

The continuous phase of the eruption lasted from January 28 through February 10 and was characterized by constant low-level ash emissions from the summit vent (plume heights <4 km asl), emplacement of pyroclastic flows on the north flank that generated clouds of elutriate ash, and discrete explosions generating ash plumes between 3 and 7 km asl (Schneider and others, 2006). Persistent north winds dispersed ash to the south-southeast over this 2-week time period and ash fall occurred in communities on Afognak and Kodiak Islands, as far as 185 km from Augustine, on February 1 and 3 (fig. 1). Proximal tephra deposits blanketed all sectors of the volcano, but predominated on its northern flank.

Photographs taken during observational overflights on January 29 and 30 show a continuous plume of ash and steam rising from the summit of the volcano (fig. 12). The plume was light colored, which suggests low concentrations of ash compared to plumes of the explosive phase. Discrete explosions during this phase have durations and plume heights similar to those produced during the explosive phase (table 1), and we infer by analogy that such plumes contained higher concentrations of ash than at other times during this phase. Photographs taken on January 30 and February 3 show tephra fallout from two sources. The first is a plume extending downwind from the vertical eruption column rising from the summit vent (labeled A in fig. 12). The second is a cloud of elutriated ash generated during emplacement of pyroclastic flows on the north flank of the volcano (labeled B in fig. 12) (Coombs and others, this volume). This second ash cloud was distinctly brownish pink compared to the light gray, ash-poor plume originating at the vent. Observations of fall deposits on the island during overflights were hindered by the lack of visibility owing to the haze of suspended fine ash surrounding the erupting volcano.

Distal ash reportedly fell as a mixture of ash and snow during a snowstorm. Distal tephra deposits were light gray and contained minor amounts of ash. Cumulative ash fall on Kodiak Island was less than 1 mm thick. Distal samples contain brown, clear, and hybrid glass. Glass compositions range from 75 to 77 wt. percent SiO_2 for clear glass and from 66 to 69.5 wt percent SiO_2 for brown glass (table 2 and fig. 7).

Proximal fall deposits were widely distributed over Augustine Island. Coarse-grained tephra (lapilli) deposits, presumably originating from discrete explosions or from the continuous plume generated at the vent, are located mainly in the southern sector of the island where they overlie elutriate deposits (fig. 3, stations KW030 and KW032; fig. 4). Coarse tephra deposits range from 1 to 5 cm in thickness and contain 60 percent high-silica andesite, 13 percent dense low-silica andesite, 6 percent low-silica andesite scoria, 13 percent banded clasts, and 8 percent lithic fragments (table 3). Light gray fine ash associated with pyroclastic flows was deposited on all sectors of the volcano but is thickest (as much as 2 cm) on the north and south flanks (figs. 4 and 12). Elutriated fine ash deposits grade upward to overlying effusive phase deposits, which can be distinguished by their pale pinkish-orange color (figs. 12 and 13).

Origin of Continuous Phase Tephra

Steady extrusion of a high-silica andesite dome, numerous column- and dome-collapse pyroclastic flows and rock falls (Coombs and others, this volume), continuous low-level ash emissions (<4 km asl), and occasional discrete vent explosions characterized the continuous phase (January 28–Feburary 10, 2006). Seismicity during this time is consistent with steady magma ascent and extrusion at the surface (Power and Lalla, this volume). Discrete explosions produced plumes as high as 7.2 km asl and large pyroclastic flows (Coombs and others, this volume). Transient overpressures from sealing of the vent by high-silica andesite lava may have caused such bursts of energetic activity. High-silica andesite is the most common lithology in the fall deposits—consistent with explosive disruption of a high-silica andesite dome (table 2). Numerous continuous-phase pyroclastic flows generated low-level plumes of fine ash that drifted downwind and draped surroundings with fine-grained tephra deposits.

Continuous-phase fine-grained elutriated ash deposits contain a high proportion of clear glass shards, whose composition is consistent with the high-silica andesite dome and flows.

Effusive Phase Tephra Deposits (March 3–16, 2006)

Distribution and Character of Effusive Phase Tephra

On March 3, eruptive activity resumed after a brief hiatus (21 days) with the effusion of a low-silica andesite summit lava dome and lava flows that descended to the north and northeast, together with a coincidental increase in rock-fall activity (Coombs and others, this volume; Power and Lalla, this volume). Time-lapse photography and aerial observations revealed that elutriation of fine ash from rockfalls and small pyroclastic flows generated low-level ash clouds (<3 km asl). Fall deposits include localized fine ash on the north flank of

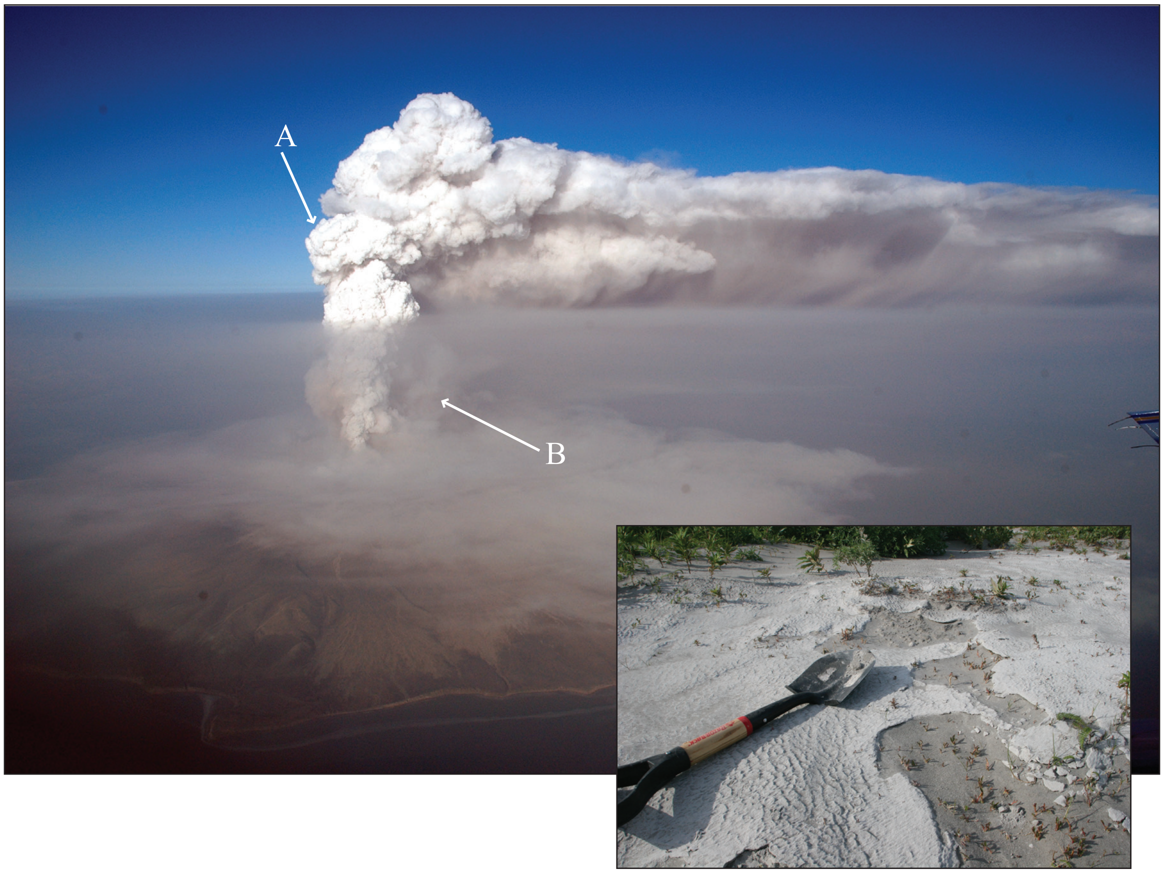

Figure 12. Photograph from an observation flight on January 30, 2006, showing tephra from two sources: *A*, a plume 10-15 km asl extending northeast from the vertical eruption column rising from the summit vent, and *B*, clouds of elutriated ash generated from newly emplaced pyroclastic flows on the north flank of the volcano. View from south. Photo by R.G. McGimsey. Inset photograph shows a typical exposure of a fine-ash deposit elutriated from pyroclastic flows on the north side of the island (fig.3-KW071). Shovel is 60 cm long. Photo by Kristi Wallace, August 6, 2006.

the volcano. Although radar or satellite imagery identified no significant ash clouds, on March 11 and 20, during a period of high easterly winds, minor ash fall was reported at the village of Pope Vanoy, near Lake Iliamna, 85 km west-northwest of Augustine (fig. 1).

Distal deposits were reportedly fine dustings of ash, clearly visible on fresh snow. A distal sample contains brown, clear (abundant), and hybrid glass shards. Glass compositions range from 68 to 78 wt. percent SiO_2 (appendix 2, sample AT-770). Proximal deposits are as much as 2 cm thick and contain fine, pinkish brown, well-sorted ash (fig. 13) with glass compositions ranging from 64 to 75 wt. percent SiO_2 (table 2 and fig. 7). Proximal tephra contains brown (abundant), clear, and hybrid glass shards. No explosions from the vent are thought to have occurred during this time.

Origin of Effusive Phase Tephra

Low-level plumes were generated from small pyroclastic flows and rock falls from the actively growing low-silica andesite lava dome and lava flows (Coombs and others, this volume; Power and Lalla, this volume). Tephra deposits are minor and were caused by the elutriation of fine ash from these small, gravitational collapses of the dome and from lava-flow fronts, either as minor rockfalls or block-and-ash flows. The pinkish brown color of elutriate ash deposits probably results from its more mafic composition (and higher proportion of brown glass shards) and possibly from oxidation. Clear, silicic glass shards, however, predominate in distal tephra deposits, which is inconsistent with the composition of the low-silica andesite dome being extruded during this time. Strong easterly winds reported during this interval likely remobilized unconsolidated fine material from the voluminous high-silica andesite pyroclastic-flow deposits on the north flank that were generated during the late explosive phase (Coombs and others, this volume) and carried it westward to the Iliamna area.

Mass of Select Tephra Deposits

Ideally, the total mass of tephra-fall deposits can be used to estimate the volume of magma that was explosively erupted and transported as ash clouds. Such data could not be obtained for all ash clouds generated during the Augustine 2005-6 eruption because of deposition (1) into Cook Inlet, (2) onto uninhabited and sparsely inhabited areas, and (3) of small volume, fine-grained ash onto seasonal snow pack and subsequent reworking. In addition, mixing of successive layers presented a problem for the six ash clouds generated on January 13 and 14, which fell onto land northeast of the volcano. Of the 13 tephras generated during the explosive phase, only that of January 17 was suitable for mass and volume calculation. Our estimates are based on 10 mass-per-unit-area measurements from this single deposit (figs. 14 and 15). On the basis of similarities in scale and assumed eruption mechanism to the other discrete ash clouds generated during the explosive phase, we use mass values from the January 17 deposit to extrapolate mass and volume values for the other events of the explosive phase (table 1 and 4). We do not estimate volumes of elutriated ash fall from pyroclastic flows.

The total mass for the January 17 tephra-fall deposit is estimated at 1.73×10^9 kg (fig. 14), with a bulk volume of 1.73×10^6 m^3 and a DRE volume of 6.65×10^5 m^3 (table 4). Total mass of tephra fall from the 13 discrete plumes generated during the explosive phase is calculated by multiplying the cumulative seismic duration by the mass eruption rate (calculated from the January 17 plume), which results in 2.2×10^{10} kg. Total bulk volume is 22×10^6 m^3 and total dense-rock equivalent (DRE) volume is 8.5×10^6 m^3 (table 4). These values are modest in comparison to tephra-fall volumes from previous historical eruptions of Augustine (Pyle, 2000; Venzke and others, 2002).

Significance and Hazards of Tephra-Fall Events

Although eruption parameters such as timing, magma composition, and total volume of erupted products for this eruption are much like those observed in past eruptions of Augustine, total vent explosion tephra-fall volume is about one order of magnitude smaller than estimates for the 1976 and 1986 eruptions (Pyle, 2000; Venzke and others, 2002). Historical eruptions of Augustine had a Volcanic Explosivity Index (VEI) of 4 (Venzke and others, 2002), but we assign the 2005–6 eruption a VEI of 3 on the basis of maximum plume height of 13.5 km (event 7 and 9). A VEI is typically weighted on both plume height and volume of tephra fall, but because of the overall lack of volume data for this eruption, we assign a VEI of 3 based on the explosion with the highest plume (L. Siebert, Smithsonian Institute, Global Volcanism Program, written commun., 2006). The 2005–6 eruption of Augustine produced about one order of magnitude less tephra fall than recent eruptions of Cook Inlet volcanoes Redoubt and Spurr (see, for example, Miller and others, 1998; Scott and McGimsey, 1994; McGimsey and others, 2001). Other volcanoes with similar Vulcanian-style eruption mechanisms, such as Unzen, Soufriere Hills, Vulcano, Ngauruhoe, Irazu, and Sakurajima, have tephra-fall volumes (individual events as well as cumulative over an eruptive episode) that are comparable within one order of magnitude (Bonnadonna and others, 2002; Herd and others, 2005; Venzke and others, 2002) to the 2005–6 eruption of Augustine.

Although the potential threat of ash fall was a significant concern during the eruption, the end result was that ash fall was not a significant problem in communities surrounding the volcano (fig. 1). Tephra fall was one of AVO's main concerns for surrounding communities, and the public mirrored these concerns through consultation of AVO's Web site and public communications (Adleman and others, this volume). Satellite imagery, NOAA HYSPLIT wind-model data, and ash-plume and fall modeling aided AVO in tracking and projecting ash-plume movement and, furthermore, assisted us in briefing the public about the likelihood and nature of tephra fall throughout the eruption. The only reports of health effects from ash fall were as a minor eye irritant on two occasions (aircraft encounters on January 14) and as a nose irritant on one occasion (January 17, Iliamna). Air-quality samplers of fine particulate matter (PM) operated by the Municipality of Anchorage (MOA) and the Department of Environmental Conservation (DEC) detected elevated levels of PM_{10} and $PM_{2.5}$ (<10 and 2.5 microns, respectively) in Anchorage, Soldotna, and Homer during the eruption. Nevertheless, fine particulate levels never exceeded Environment Protection Agency (EPA) air quality standards (fig. 16). Particles 10 microns (that is, PM_{10}) in diameter and smaller can be inhaled into the respiratory tract, where they can cause harm (C. Cahill, oral commun., 2006). On January 13, ash accumulation as thick as 1 mm in Homer probably exceeded the amounts for all other days when instruments were deployed. The small volumes of individual ash-fall deposits make it unlikely that ash caused environmental impacts to water supplies, and no such impacts were reported.

Figure 13. Photograph from an observation flight on March 6, 2006, showing generation of an ash cloud from a small block-and-ash flow associated with dome collapse during the effusive phase. Photo courtesy of Guy Tytgat. Inset photograph (fig.3, KW049) shows, (A), a fine pinkish-brown ash deposit associated with the effusive phase, (B), a fine gray oxidized ash deposit associated with the continuous phase, and (C), a coarse proximal tephra-fall deposit associated with the continuous phase. Both A and B were generated from pyroclastic flows, while C was generated from a vent explosion. Photo from the upper northwest flank of the volcano. Trowel is 25 cm long. Photo by Kristi Wallace, August 2006.

Table 4. Summary of mass and volume data for explosive-phase plumes from Augustine Volcano, January 11–28, 2006.

[Events 1 and 2 contain little juvenile material, so mass and volume calculations likely represent pre-2006 ejecta. Duration of seismic signal at distal seismic station Oil Point (OPT) (fig. 1; Power and Lalla, this volume) used as a proxy for time of plume generation. Mass of tephra fall is based on mass eruption rate for event 9 on January 17, 2006: 6.9×10^6 kg/sec. Bulk volume in cubic meters (m^3) calculated using a density of 1,000 kg/m^3. Dense-rock-equivalent (DRE) volume in cubic meters calculated using a density of 2,600 kg/m3.]

Event date, in AKST (UTC)	Event no.	Seismic duration at OPT, in min:sec	Mass, in 10^9 kg	Bulk volume, in 10^6 m^3	Dense-rock-equivalent volume, in 10^6 m^3
1/11/06	1	01:18	0.5	0.5	0.2
1/11/06	2	03:18	1.4	1.4	0.5
1/13/06	3	11:00	4.6	4.6	1.8
1/13/06	4	04:17	1.8	1.8	0.7
1/13/06	5	03:24	1.4	1.4	0.5
1/13/06 (01/14/06)	6	04:00	1.7	1.7	0.6
1/13/06 (01/14/06)	7	03:00	1.2	1.2	0.5
1/14/06	8	03:00	1.2	1.2	0.5
1/17/06	9	04:11	1.7	1.7	0.7
1/27/06 (01/28/06)	10	09:00	3.7	3.7	1.4
1/27/06	11	01:02	0.4	0.4	0.2
1/28/06	12	02:06	0.9	0.9	0.3
1/28/06	13	03:00	1.2	1.2	0.5
Total			**21.7**	**21.7**	**8.4**

Conclusions

Tephra fall from the 2005–6 eruption of Augustine occurred during each of four eruption phases. Phreatic explosions during the late precursory phase produced little ash fall and posed no hazard to local communities. Initial eruption of low-silica andesite mixed with subordinate high-silica andesite magma initiated a series of 13 discrete Vulcanian explosions during the explosive phase, which generated plumes from 4 to14 km asl and distributed ash 25–185 km from the volcano in all directions. Minor ash fall of ≤1 mm resulted and posed little hazard to local communities. The hazard to aviation was mitigated by monitoring efforts of the AVO and NWS. During the late explosive phase and continuous phase, a dome of high-silica andesite composition was extruded. Subsequent collapses of the dome generated voluminous pyroclastic flows (Coombs and other, this volume), which generated ash clouds (<4 km asl) by elutriation. The resulting tephra deposits are localized to and distributed all over the island (fig. 4). Tracking ash during this phase was hindered by the continuous, long-duration emission of fine-grained low-volume ash clouds. A return to the eruption predominantly of low-silica andesite magma during the effusive phase (Coombs and others, this volume) resulted in the emplacement of a dome and lava flows. Local ash fall associated with small collapses of the lava dome and lava flows was of limited extent and posed no hazard to local communities. Fall deposits from the 2005–6 eruption are not likely to be well-preserved in the geologic record on or off island, because of their small volume, deposition into Cook Inlet, and reworking by wind and water. Total eruption volume (Coombs and other, this volume) is comparable with past eruptions of Augustine, yet tephra-fall volumes are about an order of magnitude smaller because flowage deposits (pyroclastic flows, lava flows/domes, block and ash flows) make up the bulk of erupted products (Coombs and others, this volume). Magma heterogeneity observed throughout the eruption (fig. 7) in both whole-rock and glass compositions, and overall similarity to recent eruptions, will present challenges for future tephrostratigraphers aiming to distinguish among these and other deposits from Augustine.

Acknowledgments

We would like to thank the many residents of communities surrounding Augustine for their keen observations and sampling efforts made during this eruption. Many thanks to AVO staff for their samples and excellent, well-documented photography throughout the eruption. We thank Evan Thoms for his help with GIS map preparation. We thank Manny Nathenson for his significant contributions and helpful discussion of our mass and volume calculations. We thank Barbara Stunder of the National Weather Service for providing the HYSPLIT model, forward trajectories, and GDAS Meteorological Data shown in figure 2. We thank Rick Farrish for safely transporting us all over Augustine Island during our field campaign. We appreciate the opportunity to do fieldwork in the Iliamna region and thank the Iliamna region native councils and the National Park Service for access to this land. Special thanks to Judy Fierstein, James Vallance, and Michelle Coombs for their careful reviews and suggestions for revisions to this manuscript, which we think have increased its value significantly.

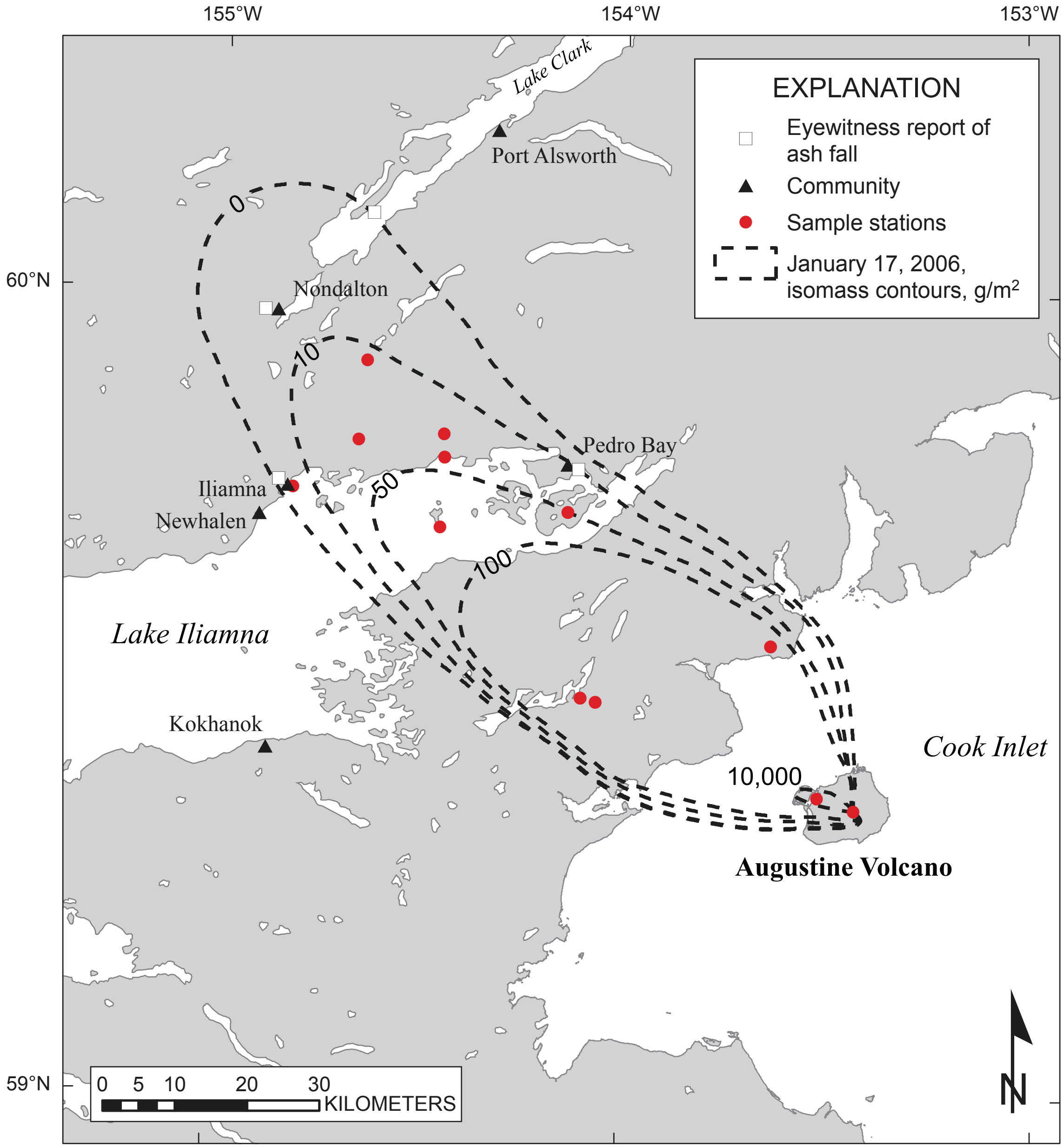

Figure 14. Isomass map of the tephra-fall deposit from Augustine on January 17, 2006. Contours represent lines of equal mass (g/m^2). Mass data were collected using measured-area sampling.

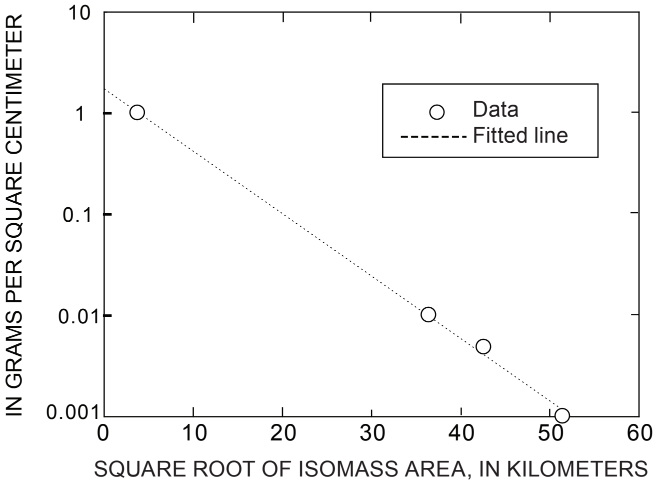

Figure 15. Plot showing mass per unit area (MPUA) versus the square root of isomass area for fall deposits from event 9 on January 17, 2006. The available data are well fitted by a single straight line for the calculation of total mass of the deposit. Tephra volume is calculated from the total mass of the deposit calculated using the root-area method (Pyle, 1989; Fierstein and Nathenson, 1992).

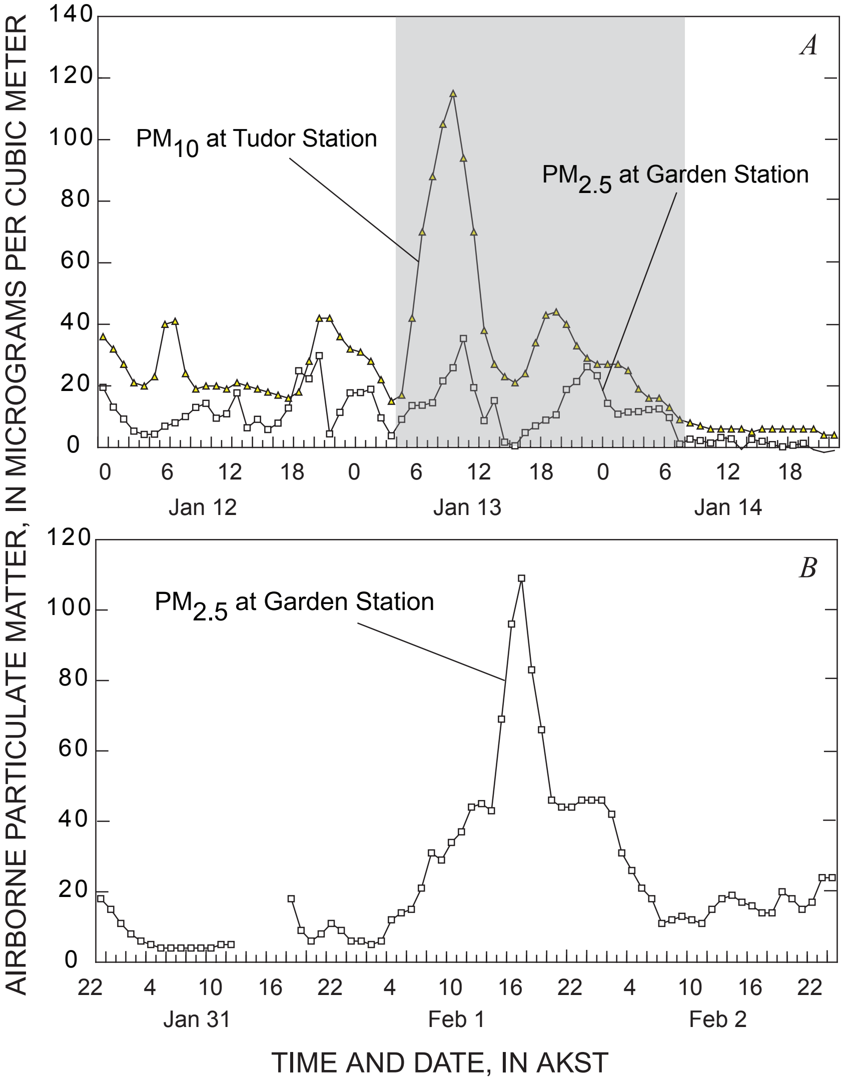

Figure 16. Plots showings airborne particulate matter (PM) in Anchorage, Alaska, on (*A*), January 12–14 and (*B*), January 31–February 2, 2006. Shaded area is the time frame when explosions occurred on January 13 and 14. PM levels however, did not exceed Environmental Protection Agency standards on these days. PM_{10}, aerodynamic diameter <10 microns; $PM_{2.5}$, aerodynamic diameter <2.5 microns. Tudor Station 3335 East Tudor Road; Garden Station, 3000 E 16th Street. Data provided by Steve Morris, Municipality of Anchorage, Environmental Services Division.

References Cited

Adleman, J.N., Cameron, C.E., Snedigar, S.F., Neal, C.A., and Wallace, K.L., 2010, Public outreach and communications of the Alaska Volcano Observatory during the 2005–2006 eruption of Augustine Volcano, *in* Power, J.A., Coombs, M.L., and Freymueller, J.T., eds., The 2006 eruption of Augustine Volcano, Alaska: U.S. Geological Survey Professional Paper 1769 (this volume).

Bailey, J.E., Dean, K.G., Dehn, J., and Webley, P.W., 2010, Integrated satellite observations of the 2006 eruption of Augustine Volcano, *in* Power, J.A., Coombs, M.L., and Freymueller, J.T., eds., The 2006 eruption of Augustine Volcano, Alaska: U.S. Geological Survey Professional Paper 1769 (this volume).

Bonnadonna, C., Mayberry, G., Calder, E.S., Sparks, R.S.J., Choux, C, Jackson, P., Lejeune, A., Loughlin, S., Norton, G, Rose, W., Ryan, G., and Young, S., 2002, Tephra fallout in the eruption of Soufriere Hills Volcano, Montserrat, *in* Druitt, T.H., and Kokelaar, B., eds., The eruption of Soufriere Hills Volcano, Montserrat, from 1995 to 1999: Geological Society of London Memoir, 21, p. 483–516.

Buurman, H., and West, M.E., 2010, Seismic precursors to volcanic explosions during the 2006 eruption of Augustine Volcano, *in* Power, J.A., Coombs, M.L., and Freymueller, J.T., eds., The 2006 eruption of Augustine Volcano, Alaska: U.S. Geological Survey Professional Paper 1769 (this volume).

Cahill, C.F., Cahill, T.A., Webley, P., Wallace, K.L., Dean, K.G., and Dehn, J., 2006, Size- and time-resolved composition of volcanic ash from Augustine Volcano, Alaska [abs.]: Eos (American Geophysical Union Transactions), v. 87, Fall meeting supp., abs. V22B-05.

Cervelli, P.F., Fournier, T.J., Freymueller, J.T., Power, J.A., Lisowski, M., and Pauk, B.A., 2010, Geodetic constraints on magma movement and withdrawal during the 2006 eruption of Augustine Volcano, *in* Power, J.A., Coombs, M.L., and Freymueller, J.T., eds., The 2006 eruption of Augustine Volcano, Alaska: U.S. Geological Survey Professional Paper 1769 (this volume).

Coombs, M.L., Bull, K.F., Vallance, J.W., Schneider, D.J., Thoms, E.E., Wessels, R.L., and McGimsey, R.G., 2010, Timing, distribution, and volume of proximal products of the 2006 eruption of Augustine Volcano, *in* Power, J.A., Coombs, M.L., and Freymueller, J.T., eds., The 2006 eruption of Augustine Volcano, Alaska: U.S. Geological Survey Professional Paper 1769 (this volume).

Chough, S.K., and Sohn, Y.K., 1990, Depositional mechanics and sequences of base surges, Songaskan tuff rings, Cheju Island, Korea: Sedimentology, v. 37, p. 1115–1135.

Daley, E.E., 1986, Petrology, geochemistry, and the evolution of lavas at Augustine Volcano, Alaska: Fairbanks, University of Alaska Fairbanks, MS thesis, 103 p.

de Fontaine, C.S., Kaufman, D.S., Anderson, R.S., Werner, A., Waythomas, C.F., and Brown, T.A., 2007, Late Quaternary distal tephra-fall deposits in lacustrine sediments, Kenai Peninsula, Alaska: Quaternary Research, v. 68, p. 64–78.

Fierstein, J., and Nathenson, M., 1992, Another look at calculation of fallout tephra volumes: Bulletin of Volcanology, v. 54, p. 156–167.

Fisher, R.V., 1961, Proposed classification of volcaniclastic sediments and rocks: Geological Society of America Bulletin, v. 72, p. 1409–1414.

Herd, R.A, Edmonds, M, and Bass, V.A., 2005, Catastrophic lava dome failure at Soufriere Hills Volcano, Montserrat, 12–13 July 2003: Journal of Volcanology and Geothermal Research, v. 148, p. 234–252.

Johnston, D.A., 1978, Volatiles, magma mixing and the mechanism of eruption of Augustine Volcano, Alaska: Seattle, University of Washington, Ph.D dissertation, 204 p.

Kienle, J., and Swanson, S. E., 1987, The 1986 activity of Mt. St. Augustine; volcanic hazards in the Cook Inlet Basin [abs.]: *in* Geologic Hazards Symposium, Alaska Geological Society Symposium Agenda and Abstracts, Anchorage, Alaska, May 12-15, 1987, unpaged.

Larsen, J.F., Nye, C.J., Coombs, M.L., Tilman, M., Izbekov, P., and Cameron, C., 2010, Petrology and geochemistry of the 2006 eruption of Augustine Volcano, *in* Power, J.A., Coombs, M.L., and Freymueller, J.T., eds., The 2006 eruption of Augustine Volcano, Alaska: U.S. Geological Survey Professional Paper 1769 (this volume).

McGee, K.A., Doukas, M.P., McGimsey, R.G., Neal, C.A., and Wessels, R.L., 2010, Emission of SO_2, CO_2 and H_2S from Augustine Volcano, 2002–2008, *in* Power, J.A., Coombs, M.L., and Freymueller, J.T., eds., The 2006 eruption of Augustine Volcano, Alaska: U.S. Geological Survey Professional Paper 1769 (this volume).

McGimsey, R.G., Neal, C.A., and Riley, C.M., 2001, Areal distribution, thickness, mass, volume, and grain size of tephra-fall deposits from the 1992 eruptions of Crater Peak Vent, Mt. Spurr volcano, Alaska: U.S. Geological Survey Open-File Report 01-0370, 38 p.

McNutt, S.R., Tytgat, G., Estes, S.A., and Stihler, S.D., 2010, A parametric study of the January 2006 explosive eruptions of Augustine Volcano using seismic, infrasound, and lightning data, *in* Power, J.A., Coombs, M.L., and Freymueller, J.T., eds., The 2006 eruption of Augustine Volcano, Alaska: U.S. Geological Survey Professional Paper 1769 (this volume).

Miller, T.P., McGimsey, R.G., Richter, D.H., Riehle, J.R., Nye, C.J., Yount, M.E., and Dumoulin, J.A., 1998, Catalog of the historically active volcanoes of Alaska: U.S. Geological Survey Open-File Report, 98-0582, 104 p.

Morrissey, M., and Mastin, L, 2000, Vulcanian eruptions, *in* Sigurdsson, H., Houghton, B.F., McNutt, S.R., Rymer, H., Stix, J., eds., Encyclopedia of volcanoes: Academic Press, p. 463–475.

Petersen, T., De Angelis, S., Tytgat, G., and McNutt, S., 2006, Local infrasound observations of the large ash explosions at Augustine Volcano, Alaska, during January 11–28, 2006: Geophysical Research Letters, v. 33, L12303, p. 1–5, doi: 10.1029/2006GL026491.

Power, J.A., Nye, C.J., Coombs, M.L., Wessels, R.L., Cervelli, P.F., Dehn, J., Wallace, K.L., Freymueller, J.T., and Doukas, M.P., 2006, The reawakening of Alaska's Augustine Volcano: Eos (American Geophysical Union Transactions), v. 87, no. 37, p. 373, 377.

Power, J.A., and Lalla, D.J., 2010, Seismic observations of Augustine Volcano, 1970–2007, *in* Power, J.A., Coombs, M.L., and Freymueller, J.T., eds., The 2006 eruption of Augustine Volcano, Alaska: U.S. Geological Survey Professional Paper 1769 (this volume).

Pyle, D.M., 1989, The thickness, volume, and grainsize of tephra-fall deposits: Bulletin of Volcanology, v. 51, p. 1–15.

Pyle, D.M., 2000, Sizes of volcanic eruptions, *in* Encyclopedia of volcanoes, Sigurdsson, H., Houghton, B.F., McNutt, S.R., Rymer, H., Stix, J., eds.: Academic Press, p. 263–269.

Riehle, J.R., 1985, A reconnaissance of the major Holocene tephra deposits in the upper Cook Inlet region, Alaska: Journal of Volcanology and Geothermal Research, v. 26, p. 37–74.

Roman, D.C., Cashman, K.V., Gardner, C.A., Wallace, P.J., and Donovan, J.J., 2005, Storage and interaction of compositionally heterogeneous magmas from the 1986 eruption of Augustine Volcano, Alaska: Bulletin of Volcanology, v. 68, p. 240–254, doi: 10.1007/s00445-005-0003-z.

Rowe, M.C., Thornber, C.R., and Kent, A.J.R., 2008, Identification and evolution of the juvenile component in 2004–2005 Mount St. Helens ash, *in* Sherrod, D.R., Scott, W.E., and Stauffer, P.H., eds. A volcano rekindled; The renewed eruption of Mount St. Helens, 2004–2006: U.S. Geological Survey Professional Paper 1750, p. 269–646.

Sarna-Wojcicki, A.M., Meyer, C.E., Woodward, M.J., and Lamothe, P.J., 1981, Composition of air-fall ash erupted on May 18, May 25, June 12, July 22, and August 7, *in* Lipman, P.W., and Mullineaux, D.R., eds., The 1980 eruptions of Mount St. Helens, Washington: U.S. Geological Survey Professional Paper 1250, p. 667.

Schmid, R. 1981, Descriptive nomenclature and classification of pyroclastic deposits and fragments; recommendations of the IUGS Subcommission on the Systematics of Igneous Rocks: Geology, v. 9, p. 41– 43.

Schiff, C.J., Kaufman, D.S., Wallace, K.L., Werner, A., Ku, T.L., 2008, Modeled tephra ages from lake sediments, base of Redoubt Volcano, Alaska: Quaternary Geochronology, v. 3, p. 56–67.

Schneider, D.J., Scott, C., Wood, J., and Hall, J., 2006, Nexrad weather radar observations of the 2006 Augustine volcanic eruption [abs.]: Eos (American Geophysical Union Transactions), v. 87, Fall meeting supp., abs. V51C-1686.

Scott, W.E., and McGimsey, R.G., 1994, Character, mass, distribution, and origin of tephra-fall deposits of the 1989–1990 eruption of Redoubt Volcano, south-central Alaska: Journal of Volcanology and Geothermal Research, v. 62, p. 251–272.

Vallance, J.W., Bull, K.F., and Coombs, M.L., 2010, Pyroclastic flows, lahars, and mixed avalanches generated during the 2006 eruption of Augustine Volcano, *in* Power, J.A., Coombs, M.L., and Freymueller, J.T., eds., The 2006 eruption of Augustine Volcano, Alaska: U.S. Geological Survey Professional Paper 1769 (this volume).

Venzke, E., Wunderman, R.W., McClelland, L., Simkin, T., Siebert, L., and Mayberry G., eds., 2002, Global Volcanism, 1968 to present: Smithsonian Institution, Global Volcanism Program Digital Information Series GVP-4 [http://www.volcano.si.edu/world/reports/, accessed on February 12, 2007].

Webley, P.W., Dean, K.G., Dehn, J., Bailey, J.E., and Peterson, R., 2010, Volcanic-ash dispersion modeling of the 2006 eruption of Augustine Volcano using the Puff model, *in* Power, J.A., Coombs, M.L., and Freymueller, J.T., eds., The 2006 eruption of Augustine Volcano, Alaska: U.S. Geological Survey Professional Paper 1769 (this volume).

Webster, J.D., Mandeville, C.W., Goldoff, B., Coombs, M.L., and Tappen, C., 2010, Augustine Volcano—The influence of volatile components in magmas erupted A.D. 2006 to 2,100 years before present, *in* Power, J.A., Coombs, M.L., and Freymueller, J.T., eds., The 2006 eruption of Augustine Volcano, Alaska: U.S. Geological Survey Professional Paper 1769 (this volume).

Appendix 1. Proximal Tephra Sample Station Locations on Augustine Island

Table 5. Proximal sample station locations on Augustine Island.

[All locations shown in datum WGS-1984; latitude and longitude are given in decimal degrees. The prefix "06AU" has been removed from all station names for brevity. PF, pyroclastic flow]

Station Name	Date Visited	Latitude	Longitude	Location Description
KLW020	7/31/2006	59.3857	-153.5154	NW Lagoon (south side west lands)
KLW021	7/31/2006	59.3872	-153.5156	NW Lagoon (south side west lands)
KLW022	7/31/2006	59.3867	-153.5190	NW Lagoon (south side west lands)
KLW023	8/1/2006	59.3683	-153.3670	1986 PF surface above Mound
KLW024	8/1/2006	59.3747	-153.3823	Northeast sector; south of seismic station AU14
KLW025	8/1/2006	59.3758	-153.3835	Feather edge of PF or lahar deposit
KLW026	8/1/2006	59.3718	-153.3929	Near ridge just below seismic station AU14
KLW027	8/1/2006	59.3469	-153.3810	Uphill of SE Point
KLW028	8/2/2006	59.3453	-153.4861	Reworked surge deposit in stressed alder
KLW029	8/2/2006	59.3382	-153.4591	Ridge south of Augustine Creek PF (tephra with abundant black dense juvenile clasts)
KLW030	8/2/2006	59.3367	-153.4565	Valley imediatly south of 06AUKW029
KLW031	8/2/2006	59.3358	-153.4173	Ridge south of AVO2/AV1
KLW032	8/2/2006	59.3244	-153.4147	South Point bluff
KLW033	8/2/2006	59.3484	-153.4797	Feather edge of SW PF finger (lower slopes);surges
KLW034	8/4/2006	59.3642	-153.3748	Near East Chute PF
KLW035	8/4/2006	59.3391	-153.3906	East Side
KLW036	8/4/2006	59.3999	-153.4494	Rocky Point PF
KLW037	8/4/2006	59.3628	-153.4446	Seismic station AUH
KLW038	8/4/2006	59.3284	-153.4006	SE coast near seal haul out (near South Point)
KLW039	8/5/2006	59.3786	-153.3475	NE Point Exactly
KLW040	8/5/2006	59.3569	-153.3420	East Point Bluff
KLW041	8/5/2006	59.3491	-153.3514	Between SE Point and S Point east of 2006 flowage deposits that enter the sea
KLW042	8/5/2006	59.3311	-153.4408	Between South Point and Augustine Creek PF
KLW043	8/5/2006	59.3221	-153.4947	Flats near West Lagoon
KLW044	8/5/2006	59.3471	-153.5305	West Lagoon
KLW045	8/5/2006	59.3835	-153.5509	West Island
KLW046	8/6/2006	59.3599	-153.4320	Summit-west
KLW047	8/6/2006	59.3596	-153.4285	Summit-east
KLW048	8/6/2006	59.3609	-153.4326	Summit-northwest side
KLW049	8/6/2006	59.3601	-153.4358	Ballistic field
KLW050	8/7/2006	59.3590	-153.4827	West side, upper alder stand
KLW051	8/7/2006	59.3594	-153.4840	West side transect
KLW052	8/7/2006	59.3600	-153.4856	West side transect
KLW053	8/7/2006	59.3608	-153.4865	West side transect
KLW054	8/7/2006	59.3615	-153.4869	West side transect
KLW055	8/7/2006	59.3616	-153.4869	West side transect
KLW056	8/7/2006	59.3618	-153.4870	West side transect
KLW057	8/7/2006	59.3702	-153.4879	West side transect

Table 5. Proximal sample station locations on Augustine Island.—Continued

[All locations shown in datum WGS-1984; latitude and longitude are given in decimal degrees. The prefix “06AU” has been removed from all station names for brevity. PF, pyroclastic flow]

Station Name	Date Visited	Latitude	Longitude	Location Description
KLW058	8/7/2006	59.3817	-153.4665	West side transect
KLW059	8/7/2006	59.3825	-153.4672	West side transect
KLW060	8/7/2006	59.3850	-153.4681	West side transect
KLW061	8/7/2006	59.3857	-153.4676	West side transect
KLW062	8/7/2006	59.3865	-153.4671	West side transect
KLW063	8/7/2006	59.3907	-153.4734	West side transect
KLW064	8/8/2006	59.3929	-153.4442	East side of ridge above Rocky Point PF
KLW065	8/8/2006	59.3935	-153.4449	West side of ridge above Rocky Point PF
KLW066	8/8/2006	59.3944	-153.4452	Ridge above Rocky Point PF, near surge
KLW067	8/8/2006	59.3955	-153.4457	Surge deposit western side of Rocky Point PF
KLW068	8/8/2006	59.3955	-153.4454	Surge deposit western side of Rocky Point PF
KLW069	8/8/2006	59.4040	-153.4467	Edge of Rocky Point PF, coastwise
KLW070	8/8/2006	59.4072	-153.4434	Just north of Rocky Point in hummocky topography
KLW071	8/8/2006	59.4081	-153.4438	Coastward of KW070 just north of Rocky Point
KLW072	8/8/2006	59.4077	-153.3949	Burr Point vicinity
KLW073	8/8/2006	59.4065	-153.3988	Burr Point vicinity
KLW074	8/8/2006	59.3858	-153.3818	North of NE Point where larger of 2006 lahars nears the coast
KLW075	8/9/2006	59.3405	-153.3991	East side near seismic station AUSE
KLW076	8/9/2006	59.3584	-153.3709	Upper Alder between East Point and SE Point, lahar visible to north
KLW077	8/9/2006	59.3584	-153.3719	Very near 06AUKW076
KLW078	8/9/2006	59.3642	-153.3751	East side; in high alder
KLW079	8/9/2006	59.3780	-153.4766	NW sector, west of Windy PF; in willow
KLW080	8/9/2006	59.3792	-159.4799	NW sector, west of Windy PF; in alder
KLW081	8/9/2006	59.3577	-153.5259	West sector, in low alder
KLW082	8/10/2006	59.3773	-153.5193	AVO field camp location
KW083	8/10/2006	59.3702	-153.3538	Benchmark Mound
KW084	9/25/2006	59.3254	-153.4667	SSW coast
KW085	9/25/2006	59.3248	-153.4667	SSW coastal bluff (prehistoric Augustine tephra fall)
TP001	12/20/2005	59.3486	-153.4216	Lower south flank
MC001	1/12/2006	59.3694	-153.4730	West flank of Augustine. Ash collection site AAW (seismic station AUW)
MC002	1/12/2006	59.4118	-153.4161	Burr Point. Ash collection site AAN

Appendix 2. Raw Electron Microprobe Geochemical Analyses of Glass from Augustine 2005–2006 Tephra

[This appendix appears only in the digital version of this work—in the DVD-ROM that accompanies the printed volume and as a separate file accompanying this chapter on the Web at: http://pubs.usgs.gov/pp/1769]

Table 6 is a Microsoft Excel file that contains the data used to derive table 2 and figure 7 after analyses were filtered to eliminate the inclusion of mineral data and other bad data points.

The 2006 Eruption of Augustine Volcano, Alaska
Power, J.A., Coombs, M.L., and Freymueller, J.T., editors
U.S. Geological Survey Professional Paper 1769

Chapter 10

Pyroclastic Flows, Lahars, and Mixed Avalanches Generated During the 2006 Eruption of Augustine Volcano

By James W. Vallance,[1] Katharine F. Bull,[2] and Michelle L. Coombs[3]

Abstract

Each of the three phases of the 2006 eruption at Augustine Volcano had a distinctive eruptive style and flowage deposits. From January 11 to 28, the explosive phase comprised short vulcanian eruptions that punctuated dome growth and produced volcanowide pyroclastic flows and more energetic hot currents whose mobility was influenced by efficient mixing with and vaporization of snow. Initially, hot flows moved across winter snowpack, eroding it to generate snow, water, and pyroclastic slurries that formed mixed avalanches and lahars, first eastward, then northward, and finally southward, but subsequent flows produced no lahars or mixed avalanches. During a large explosive event on January 27, disruption of a lava dome terminated the explosive phase and emplaced the largest pyroclastic flow of the 2006 eruption northward toward Rocky Point. From January 28 to February 10, activity during the continuous phase comprised rapid dome growth and frequent dome-collapse pyroclastic flows and a lava flow restricted to the north sector of the volcano. Then, after three weeks of inactivity, during the effusive phase of March 3 to 16, the volcano continued to extrude the lava flow, whose steep sides collapsed infrequently to produce block-and-ash flows.

The three eruptive phases were each unique not only in terms of eruptive style, but also in terms of the types and morphologies of deposits that were produced, and, in particular, of their lithologic components. Thus, during the explosive phase, low-silica andesite scoria predominated, and intermediate- and high-silica andesite were subordinate. During the continuous phase, the eruption shifted predominantly to high-silica andesite and, during the effusive phase, shifted again to dense low-silica andesite. Each rock type is present in the deposits of each eruptive phase and each flow type, and lithologic proportions are unique and consistent within the deposits that correspond to each eruptive phase.

The chief factors that influenced pyroclastic currents and the characteristics of their deposits were genesis, grain size, and flow surface. Column collapse from short-lived vulcanian blasts, dome collapses, and collapses of viscous lavas on steep slopes caused the pyroclastic currents documented in this study. Column-collapse flows during the explosive phase spread widely and probably were affected by vaporization of ingested snow where they overran snowpack. Such pyroclastic currents can erode substrates formed of snow or ice through a combination of mechanical and thermal processes at the bed, thus enhancing the spread of these flows across snowpack and generating mixed avalanches and lahars. Grain-size characteristics of these initial pyroclastic currents and overburden pressures at their bases favored thermal scour of snow and coeval fluidization. These flows scoured substrate snow and generated secondary slurry flows, whereas subsequent flows did not. Some secondary flows were wetter and more laharic than others. Where secondary flows were quite watery, recognizable mixed-avalanche deposits were small or insignificant, and lahars were predominant. Where such flows contained substantial amounts of snow, mixed-avalanche deposits blanketed medial reaches of valleys and formed extensive marginal terraces and axial islands in distal reaches. Flows that contained significant amounts of snow formed cogenetic mixed avalanches that slid across surfaces protected by snowpack, whereas water-rich axial lahars scoured channels.

Correlations of planimetric area (A) versus volume (V) for pyroclastic deposits with similar origins and characteristics exhibit linear trends, such that $A=cV^{2/3}$, where c is a constant for similar groups of flows. This relationship was tested and

---

[1] U.S. Geological Survey, Cascades Volcano Observatory, 1300 SE Cardinal Court, Vancouver, WA 98683.

[2] Alaska Volcano Observatory, Alaska Division of Geological and Geophysical Surveys, 3354 College Road, Fairbanks, AK 99709.

[3] Alaska Volcano Observatory, U.S. Geological Survey, 4200 University Drive, Anchorage, AK 99508.

calibrated for dome-collapse, column-collapse, and surgelike flows using area-volume data from this study and examples from Montserrat, Merapi, and Mount St. Helens. The ratio $A/V^{2/3} = c$ gives a dimensionless measure of mobility calibrated for each of these three types of flow. Surgelike flows are highly mobile, with $c \approx 520$; column-collapse flows have $c \approx 150$; and dome-collapse flows have $c \approx 35$, about that of simple rock avalanches. Such calibrated mobility factors have a potential use in volcano-hazard assessments.

Introduction

The 2006 eruption of Augustine Volcano spanned less than 4 months, yet the snowclad, unglaciated Alaskan island volcano erupted in a range of eruptive styles characterized by diverse deposit types, each with distinctive morphology, grain size, and lithologic composition. Within 3 months, three eruptive phases produced at least four lava domes and two lava flows, ranging in composition from low- to high-silica andesite (57.3–63.2 weight percent SiO_2; Larsen and others, this volume). During each eruptive phase, pyroclastic flows produced deposits with the same four predominant rock types; however, the flow deposits of each phase had distinctive morphology and proportions of lithologic components. Only the initial explosive phase generated lahars and mixed-rock-and-snow avalanches.

The morphology, lithologic composition, and areal extent of deposits were initially estimated during the eruption by utilizing onsite Web cameras, satellite imagery, aerial surveillance, and occasional field-based observations (Coombs and others, this volume). These early estimates provided important groundwork for later, field-based mapping, as well as for understanding the eruption chronology. Later field investigations revealed that the deposits were uniformly more abundant, widespread, and varied than suggested by preliminary estimates.

This chapter describes the flow deposits of the 2006 eruption of Augustine Volcano in terms of their morphology, lithologic composition, and sedimentology and discusses possible mechanisms for their flow generation and transport. Our study complements other chapters in this volume that discuss the eruption chronology, seismic interpretation of flow timing, tephra falls, and petrogenesis (Coombs and others, McNutt and others, Wallace and others, and Larsen and others). In particular, this chapter is a companion to that by Coombs and others, which presents a detailed chronology of the events that produced the on-island deposits, as well as a 1:20,000-scale map of the 2006 deposits. The detailed monitoring of Augustine Volcano enabled us to establish a fairly accurate chronology of flowage events (Coombs and others, McNutt and others, Power and Lalla, this volume), allowing us to show how composition and texture of erupted material and morphology of deposits changed during the course of the eruption. We show that lithologic components of clastic deposits, distinct in composition and texture, were produced throughout the eruption, though in proportions that varied systematically with eruptive phase and style. In addition, the distinctive morphologies and relations between pyroclastic-current, lahar, and mixed-avalanche deposits of the initial, explosive phase suggests that deposition on and incorporation of snow were primary controlling factors in the sheetlike morphology of the initial pyroclastic currents, the production of mixed avalanches, and the release of melted ice and snow to produce lahars.

Flowage Phenomena and Recognition of Their Deposits

"Pyroclastic current" is defined here as a general term meaning any pyroclastic density current, regardless of origin, mechanism of transport, or particle concentration. Genesis may be plume-column collapse, or fracturing and collapse of a dome or lava flow. A pyroclastic current is a hot mixture of rock (lithics, pumice, or both lithics and pumice), ash, and gas that flows rapidly away from its source. In this study, the high-solids-fraction end member of the pyroclastic-current spectrum is a pyroclastic flow, and the dilute end member is a pyroclastic surge. In pyroclastic currents, both dense and dilute, the fluid phase, gas, provides at least partial support for the particulate phase and lends such flows their mobility. We define "block-and-ash flows" as pyroclastic flows derived from fracturing and collapse of lava domes or lava flows.

A "lahar" is defined here as a rapidly flowing, gravity-driven mixture of rock debris and water from a volcano. A lahar event may include, in order of increasing proportion of water, debris-flow, hyperconcentrated-flow, and streamflow or flood phases, but the term "lahar" itself includes only sediment-rich debris flow and intermediate hyperconcentrated flows (Vallance, 2000). The fluid at least partly supports the solid particles in lahar flows.

We define volcanic "mixed avalanche" as a flow or avalanche of rock particles, water, and snow or ice in which snow and ice provide partial support for the solid particles. Such flows, variously termed "mixed avalanches" (Pierson, 1994) and "hybrid flows" (Waitt, 1995) are most common where pyroclastic currents sweep across the extensive snow and ice covering the flanks of a volcano. These phenomena are transitional between snow-rich avalanches and debris flow and commonly behave partly as sliding and partly as flowing mixtures. Waitt and others (1994) describe genetically related sequences of such flows generated by pyroclastic eruptions comprising initial relatively dry debris and snow flows, followed by debris-rich slushy flows and, finally, by watery laharic flows. We report similar sequences of pyroclastic currents, mixed avalanches, and lahars during the 2006 eruption of Augustine Volcano.

At Augustine deposits of pyroclastic flows and lahars are distinctive and commonly well preserved, whereas those of pyroclastic-currents emplaced on snow, mixed avalanches of snow and debris, and lahars that contained substantial snow are ephemeral and can be difficult to distinguish as little as

2 years after the 2006 eruption. Archetypal pyroclastic-flow deposits display coarse levees and digitate margins, and individual flow units are as thick as 2 m. Some more energetic flow deposits thicken to many meters on gentle axial slopes but may thin or be absent on steep slopes and commonly thin to a fine-grained featheredge at deposit margins. In contrast, lahar deposits at Augustine commonly comprise isolated blocks on scoured surfaces bounded by low-aspect blocky levees. Where they funnel into drainages, lahars leave scoured surfaces with faintly stratified deposits, as much as 2 m thick in favorable pockets. Both pyroclastic-current deposits emplaced on snow and mixed-avalanche deposits display soft irregular surfaces crisscrossed with cracks and have thin margins containing lapilli and blocks and commonly lack prominent levees, but ephemeral features like irregular surfaces and cracks disappear in a few years time. Each type of deposit commonly drapes large blocks and vegetation at its margins, suggesting flows that were of greater depth than thin remnants might suggest. These two types of deposit are more distinctive where the flows moved into vegetation. Pyroclastic currents stripped and singed vegetation above the snow level but left it unaffected below, whereas mixed avalanches broke exposed vegetation into uncharred stem and branch fragments but similarly preserved lush vegetation below the emplacement snow surface. In addition, mixed-avalanche deposits are emplaced downslope of cogenetic pyroclastic currents but commonly form genetically related marginal levees for lahars. In such cases, the marginal mixed-avalanche deposits form thick, poorly sorted fills with abundant scattered wood fragments, and the lahar deposits consist of scattered blocks and debris remnants on a scoured, axial channel surface that commonly has vegetation battered and bent over in the flow direction.

Geologic Background and Eruptive History

Augustine is an island volcano, approximately 8 by 11 km, in lower Cook Inlet, 280 km south-southwest of Anchorage, Alaska (fig. 1). The volcano, which is one of the more active volcanoes in Alaska, has had six major eruptions in the 2 centuries before 2006 (1812, 1883, 1935, 1963–64, 1976, 1986; Coats, 1950; Johnstone, 1978; Miller and others, 1998). It has a central vent and comprises a series of domes, lava flows, pyroclastic flows, and debris-avalanche deposits that overlie Jurassic and Cretaceous sedimentary rocks of the Naknek Formation exposed on the south side of the island (Dettermen and Reed, 1980; Waitt and Begét, 1996 and 2009). Johnston (1978) suggests that the onset of volcanism was during the Moosehorn glacial advance, 19.0–15.5 ka. Hummocky topography along the north coastline is evidence for numerous catastrophic collapses of the summit dome, the most recent of which, in 1883, generated a tsunami that reached the east shores of Cook Inlet (Begét and Kienle, 1992; Siebert and others, 1995; Begét and Kowalik, 2006; Waitt, this volume).

Recent historical eruptions of Augustine have followed sequences similar to that in 2006. Eruption sequences have typically begun with explosive activity that produced ash plumes to higher than 10 km above mean sea level (asl) and pyroclastic flows, followed by effusive activity that built lava domes and lava flows and caused block-and-ash flows (Kienle and Forbes, 1977; Johnston, 1978; Kienle and Swanson, 1985; Swanson and Kienle, 1988). Lavas and juvenile clasts have consistently been crystal-rich, vesicular to dense, two-pyroxene±amphibole±olivine, low- through high-silica andesite and dacite (56–64 weight percent SiO_2), with banded clasts of the same rock types (Johnston, 1978; Daley, 1986; Harris and others, 1987; Miller and others, 1998, p. 14).

The well-studied 1976 and 1986 eruptions of Augustine were particularly similar to the 2006 eruption in terms of sequence, deposit distributions, and magma compositions (Swanson and Kienle, 1988; Power and others, 2006; Coombs and others, this volume). Before the 1976 eruption, precursory seismic activity began in May 1975, and the volcano erupted explosively on January 22. Explosions continued for about 3 days, produced ash plumes as high as 14 km asl, and generated pyroclastic flows and lahars on all flanks of the volcano (Kienle and Forbes, 1977; Johnston, 1978). At least one of the pyroclastic flows burned and damaged a research station on the northern tip of the island, and another reached the sea to the east of there. Activity resumed on February 6, and the volcano erupted almost continuously until February 16. Pyroclastic flows also occurred during the continuous phase of ash emission. A lava dome emerged February 11–12. After a

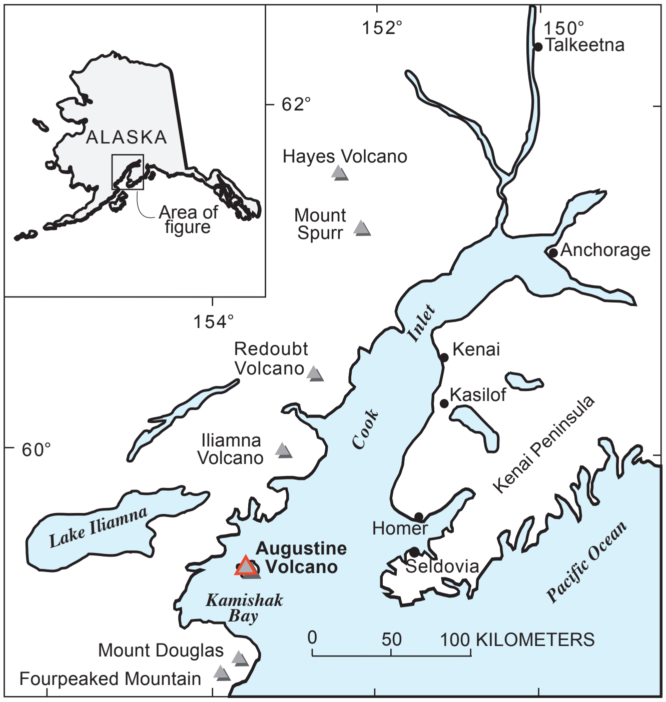

Figure 1. Index map of southern Alaska, showing location of Augustine Volcano in lower Cook Inlet.

repose period, renewed effusion occurred in August. The total volume of pyroclastic-flow deposits from the 1976 eruption was estimated at 0.05 km^3 (Kienle and Swanson, 1985).

Seismic activity precursory to the 1986 eruption began in July 1985, and the explosive phase began in late March 1986. Ash plumes rose as high as 12 km asl but, unlike during previous eruption, pyroclastic flows moved only northward, some reaching the sea (Swanson and Kienle, 1988). Ash reached surrounding communities, including Anchorage, March 27–31. During April 23–28, the continuous phase was marked by effusion and resulted in a short, blocky lava flow. Encroachment of the lava flow and a growing dome on steep slopes generated scattered block-and-ash flows. A 4-month repose followed the April activity. Renewed effusion August 30–31 accelerated dome growth and sent block-and-ash flows down the north flank of the volcano.

The 2006 Eruption Sequence

Slowly escalating, shallow seismicity (increasing from ~4–8 to 20–35 earthquakes per day) initiated precursory activity at Augustine in late April 2005 (Jacobs and McNutt, this volume; Power and Lalla, this volume). Seismicity increased through fall 2005. Inflation at the volcano began in midsummer 2005, marked by lengthening along a north-south baseline between stations located at 100 and 200 m asl, and continued at a steady rate until late November (Cervelli and others, 2006). Inflation reached a maximum by mid-December, suggesting intrusion of a northwest-striking dike at shallow levels (Cervelli and others, 2006; Cervelli and others, this volume). In mid-December, phreatic explosions produced a thin layer of ash on the winter snowpack within about 1 km of the vent (Power and others, 2006; Wallace and others, this volume). Small explosions continued through December.

From January to March 2006, distinct eruptive styles and deposits characterized each of the three eruptive phases (table 1). During the explosive phase, from January 11 to 28, 13 discrete vulcanian explosions, from 1 to 11 minutes in duration, initiated pyroclastic flows, and during quiescent intervals between explosions, three lava domes effused (Coombs and others, this volume). Initial pyroclastic currents of the explosive phase were widespread and deposited onto snow. Varying amounts of snow incorporated by the flows, or that underlay their still hot deposits, produced mixed avalanches and lahars (fig. 2*A*). Subsequent pyroclastic flows moved across previous deposits rather than snow and did not generate secondary flows (figs. 2*A*, 2*B*). None of the pyroclastic flows reached the sea, although near Rocky Point the last explosive-phase pyroclastic flow came within 100 m of the water (fig. 2*B*). During the continuous phase, from January 28 to February 10, continuous rapid effusion and nearly constant collapse of a high-silica-andesite lava dome punctuated by small explosions caused countless pyroclastic flows restricted to the north flank of the volcano (fig. 2*C*). After a pause in eruptive activity from February 10 to March 3, the effusive phase, from March 3 to March 16, generated blocky, dark-gray to black, low-silica andesite lava flows north and northeast of the summit and generated block-and-ash flows on steep flanks of the upper edifice (fig. 2*D*). After effusion ceased on March 16, the lava flows continued to shed rockfall and block-and-ash flows until at least late May. In October 2006, remobilization of pinkish-gray ash deposits during rainy weather resulted in water-rich lahar deposits, primarily on the north flank of the volcano (Coombs and others, this volume).

Methods

Field Methods

We conducted limited geologic fieldwork on Augustine Island (fig. 1) during the eruption and continued with more detailed investigations during 3 weeks in August 2006 and 1 week in July 2008. We noted pyroclastic-current, mixed-avalanche, and lahar deposits at more than 500 sites and collected 72 representative bulk samples for grain-size and lithologic analyses (table 2).[4] Where recognizable, distinct layers or facies present within each flow deposit were also sampled, and samples were taken at multiple sites along a longitudinal section of single flow units of at least two pyroclastic-flow deposits. As described below, all units contained clasts of multiple, distinct rock types, identifiable on the basis of color, morphology, and vesicularity. At 20 sites we performed “clast counts” to determine the proportions of various rock types within a given deposit. We conducted clast counts by picking a patch of ground at each site that contained at least 50 to 100 clasts, and counting the clasts that were 10 to 30 cm in diameter.

Methods for Analyzing Grain-Size Distributions

A total of 60 samples were submitted for grain-size analysis to the sediment-processing laboratory at the Cascades Volcano Observatory (table 3). All samples were sieved, using the visual-accumulation method, in one-ϕ intervals, from $-6\ \phi$ (32 mm diam) to $4\ \phi$ ($\geq$0.063 mm diam). Of the 60 samples, 17 samples had the fine-ash (<0.063 mm diam) portion analyzed on a Sedigraph to calculate the weight percentage of each size class between $5\ \phi$ and $10\ \phi$ (0.063 and 0.001 mm diam, respectively). Standard statistics for grain-size distributions were calculated for each bulk sample (table 4).

Methods for Analyzing Flow Components

Preliminary clast counts in the field were refined after grain-size analysis by performing lithologic analysis on representative size classes from explosive- and continuous-phase samples. Lithologic categories were initially defined in the

---

[4] Note that tables 2, 3, 4, 6 and 8 are grouped at the back of this chapter, after References Cited.

Table 1. Summary of 2006 eruption and resulting deposits at Augustine Volcano, Alaska.

[Phases, event dates and times, and unit names from Coombs and others (this volume). Seismic duration from McNutt and others (this volume). Plume height from Wallace and others (this volume). Units are defined in figure 2]

Phase	Event	Date (2006)	Time of onset (AST)	Seismic duration (mm:ss)	Plume height (km)	Units emplaced		Comments
						Lava flows and domes	Flowage deposits	
Explosive January 11–28	1	1/11	4:44	1:18	6.5		Mixed avalanches (Exma).	Mixed avalanches of rock and snow were observed after these initial explosions, but were later covered. No lahars were observed.
	2	1/11	5:12	3:18	10.2			
		1/12				Ephemeral dome		
	3	1/13	4:24	11:00	10.2		Pyroclastic flows and currents (Expct); mixed avalanches (Exma) and lahars (Exlh).	Most widespread pyroclastic currents (Expct); mixed avalanches (Exma) and lahars (Exlh) in the east sector occurred during this interval.
	4	1/13	8:47	4:17	10–16			
	5	1/13	11:22	3:24	10–16		Pyroclastic flows (Expf); mixed avalanche (Exma); lahar (Exlh).	Widespread pyroclastic flows (Expf); mixed avalanches (Exma) and lahars (Exlh) in the northern sector occurred during this interval. Thick pyroclastic flows with coarse levees (Expf) were common to the east and north.
	6	1/13	16:40	4:00	9–11			
	7	1/13	18:58	3:00	13.5		Pyroclastic flows (Expf); mixed avalanche (Exma); lahar (Exlh).	Widespread pyroclastic flows (Expf); mixed avalanches (Exma) and lahars (Exlh) in the south sector occurred during this interval. Thick pyroclastic flows with coarse levees (Expf) were likely on all flanks.
	8	1/14	0:14	3:00	10.2			
						Dome (Exd1)		
	9	1/17	7:58	4:11	13.5		Pyroclastic flows (Expf)	A pyroclastic flow (Expf) emplaced to the southwest, possibly other pyroclastic flows elsewhere.
						Dome (Exd2)		
	10	1/27	20:24	9:00	10.5		Pyroclastic current (Expc); Rocky Point pyroclastic flow (RPpf).	A pyroclastic current and the voluminous Rocky Point pyroclastic flow were emplaced to the north during this event. Transitional composition between other explosive-phase deposits (rich in scoriaceous low-silica andesite) and continuous-phase deposits (rich in high-silica andesite).
	11	1/27	23:37	1:02	3.8			Seismic signal indicates that this event was gas rich and mass poor.
	12	1/28	2:04	2:06	7.2			No observations of deposits from these events, but seismic signals suggest pyroclastic flows (McNutt and others, this volume).
	13	1/28	7:32	3:00	7–11			
Continuous January28– February 10	14	1/28	14:31	--	8–9		Pyroclastic flows and currents (Cpf, Cpc, Cpfw).	Thick, voluminous pyroclastic flows (Cpf, Cpfw, Cpc) were emplaced on the north flanks. High-silica andesite was predominant in deposits; scoriaceous low-silica andesite was rare. No lahar or mixed-avalanche deposits were emplaced. Lava flows began to effuse at the end of the continuous phase.
	--	1/29	11:17	--	--			
	--	1/30	--	--	--			
	--	2/3						
	--	2/10				Lava lobes		
Hiatus								
Effusive March 3–16	--	3/3				Lava flow (Eflf)	Block-and-ash flows (Efba).	Dark-gray to black block-and-ash flows, predominantly containing dense low-silica andesite, traveled 0.5 to 2 km beyond the north and northeast lava lobes, lava flows to the east and north fractured and collapsed. Rockfall formed talus aprons around lava-lobe fronts.
	--							
	--							
	--	3/16						

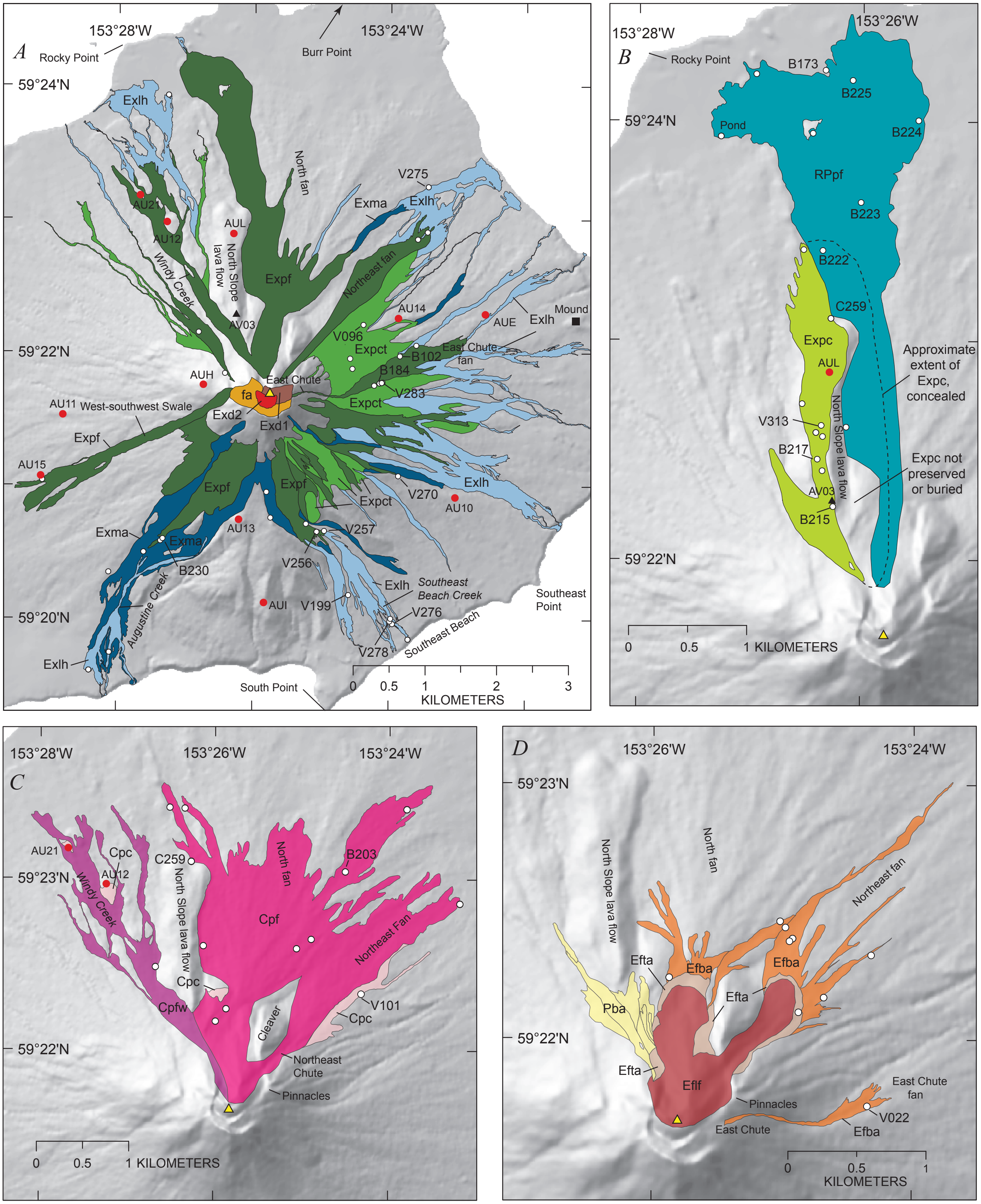

Figure 2. Time sequence of geologic maps of Augustine Volcano showing distribution of 2006 Augustine deposits and select sample locations (after Coombs and others, this volume). *A*, Explosive-phase deposits of events 1 through 9. *B*, Explosive-phase deposits of event 10. *C*, Continuous-phase deposits. *D*, Effusive-phase deposits. All place names associated with Augustine Volcano are informal except Augustine Creek, Augustine Island, and Burr Point.

EXPLANATION

	Unit	Name	Phase and event	Dates (2006)	Origin
🟨	Pba	Block-and-ash flow	Post-eruption	April and May	Collapse of lava flow, lines within indicate individual flow margins
			Effusive phase	March 3–16	
🟫	Efta	Talus from lava flow			Rockfall
🟥	Eflf	Lava flow			Effusion of lava
🟧	Efba	Block-and-ash flow			Collapse of lava flow
			Hiatus	Feb. 10–March 3	
			Continuous phase	Jan. 28–Feb. 10	
🟪	Cpfw	Windy Creek pyroclastic flow		January 30	Dome collapse
🟥	Cpf	Pyroclastic flow		January 28–30	Dome collapse
⬜	Cpc	Pyroclastic current, thin		January 28–30	Dome collapse
			Explosive phase	January 11–27	
🟧	fa	Fall deposits	Undifferentiated	January 13–27	Tephra and ballistic fallout
🟦	RPpf	Rocky Point pyroclastic flow	Event 10	January 27	Dome collapse, depressurization
🟩	Expc	Pyroclastic current	Event 10	January 27	Dome collapse, depressurization
🟥	Exd2	Lava dome 2	Event 9 to 10	January 17–27	Effusion of lava
🟫	Exd1	Lava dome 1	Event 8 to 9	January 14–17	Effusion of lava
🟩	Expf	Pyroclastic flow, coarse	Events 5–9	January 13–17	Column collapse
🟦	Exlh	Lahar	Events 3–8	January 13–14	Pyroclastic currents across snow
🟦	Exma	Mixed avalanche	Events 3–8	January 13–14	Pyroclastic currents across snow
🟩	Expct	Pyroclastic current, thin	Events 3–4	January 13–14	Column collapse

○ Sample site
● Seismic station
▲ GPS station
■ Remote-camera station
△ Summit, Augustine Volcano

field and later modified slightly after whole-rock compositional analysis and petrography (fig. 3; table 5). For a few samples, each size fraction was sorted into lithologic categories, and then clast populations for each rock type were counted and weighed (table 6). For most samples, however, we limited the lithologic analysis to the 4- and 8-mm size fractions.

2006 Flows and Flowage Deposits

Our results include emplacement chronology and detailed descriptions of the 2006 Augustine flowage deposits. We also summarize the detailed geologic mapping by Coombs and others (this volume). We use deposit characteristics, distribution, and timing to interpret emplacement and eruption mechanisms during each of the three eruptive phases.

Explosive-phase deposits include pyroclastic currents, lahars, and mixed avalanches on all flanks of the volcano. Pyroclastic deposits range from widely distributed, thin surge deposits to thick, lobate, flow deposits confined to drainages. In contrast, numerous pyroclastic flows of the continuous phase formed a thick fan restricted to the north side of the volcano and no lahars or mixed avalanches. Effusive-phase lava flows on steep slopes collapsed to form block-and-ash-flow deposits of limited extent north and east of the vent.

Explosive-Phase Deposits, January 11–28

The explosive phase comprised 13 discrete explosions, each lasting 1–11 minutes (table 1). Each explosion produced tephra plumes, and most explosions produced flowage deposits that together draped all flanks of the volcano. Flowage deposits included those emplaced by pyroclastic currents, lahars, and mixed avalanches.

Events 1 and 2, January 11: Vulcanian Explosions and Mixed Avalanches

Two explosions on January 11 cleared the vent, released plumes 6 to 9 km asl, deposited ash on the volcano's flanks, and produced small flowage deposits on the upper flanks of the volcano (table 1) (Schneider and others, 2006; Bailey and others, this volume). Seismicity suggests that the first short explosion was primarily a gas-release, vent-clearing event (McNutt and others, this volume). The second explosion probably produced the flowage deposits. After these explosions and before those of January 13, an ephemeral lava dome grew (table 1).

Alaska Volcano Observatory geologists on an overflight, plus Web- and fixed-camera images, documented mixed avalanches of rock and snow on the flanks of the volcano the afternoon after these explosions. Lobate deposits of the flows underlay upper drainages around the volcano (Coombs and others, this volume). The lobes were 50 to 300 m wide, confined to gullies, extended from 1 to 2 km down the flanks of the volcano from 300 to 700 m asl, and were at least several meters thick. Close examination of aerial photographs showed that the flows contained abundant snow, as well as rock debris. We observed little evidence of melting in the photographs; surface water was not released beyond the lobe fronts, although water rivulets formed on the flow surface. As a result, we infer that the flows were not particularly hot. These deposits were subsequently covered or destroyed by later events and so were not visited or sampled. Samples of the January 11 ash deposits contained altered, dense clasts and no juvenile material (Wallace and others, this volume). We therefore infer that these mixed-avalanche deposits contained little or no juvenile rock either.

Events 3 through 9, January 13–17: Widespread Pyroclastic Currents, Lahars, and Mixed-Avalanches

Seven explosions, five on January 13, one on January 14, and one on January 17, lasted 3–11 minutes. The explosions produced widespread pyroclastic currents, mixed avalanches, lahars, and tephra falls, and all deposits contained juvenile material (table 1, fig. 2*A*). The short duration of these events, their pyroclastic nature, and their seismic characteristics indicate that they were vulcanian. McNutt and others (this volume) infer that the short duration and the dominantly emergent characteristics of events 3–9 (table 1) indicate a moderately uniform distribution of gas within the magma as it exited the vent. The high proportions of vesicular, high- and low-silica andesite within pyroclastic products of the eruption are consistent with short-term, explosive release of gas-rich magma (fig. 4).

Figure 3. Photographs of clastic rock types ejected during 2006 eruption of Augustine Volcano, Alaska. *A*, Low-silica andesite scoria. *B*, Dense low-silica andesite. *C,* High-silica andesite, friable and vesicular with a cinderblock-like texture. *D,* Dense intermediate-silica andesite. *E*, Banded scoria with end members of high-silica andesite (HSA) and low-silica andesite scoria (LSAS).

Table 5. Rock types in flow deposits from the 2006 eruption of Augustine Volcano, Alaska.

Lithology (acronym)	Description	Vesicularity[1]
Low-silica andesite scoria (LSAS)	Reddish-brown to black vesicular porphyritic andesite with distinctive, pale- to olive-green rinds. Smaller lapilli are wholly olive green. Clasts commonly are cauliform. Abundant phenocrysts of plagioclase and less abundant pyroxene visible in hand specimen.	33±5
Dense low-silica andesite (DLSA)	Dark-gray to black, poorly vesicular andesite. Some groundmass is glassy, and clasts are commonly angular. Phenocrysts include plagioclase, clinopyroxene, and orthopyroxene. Some lapilli and blocks have breadcrust rinds.	20±4
High-silica andesite (HSA)	Light- to medium-gray, moderately vesicular, crystal-rich high-silica andesite. Phenocrysts include plagioclase, pyroxene, and amphibole. Clasts are lower in density than DLSA and commonly rounded owing to friable, cinderblock-like texture. Clast interiors may be variably oxidized.	37±8
High-silica andesite pumice (HSAP)	White to cream-colored porphyritic andesite, moderately to highly vesicular. Phenocrysts include plagioclase, pyroxene, and amphibole.	~42
Dense intermediate-silica andesite (DIA)	Light- to medium-gray, poorly vesicular porphyritic andesite. Some groundmass is glassy, and clasts are commonly angular.	22±3
Banded	Banded clasts; any combination of lithologies above.	39±9
Oxidized	Red, pink, orange, and yellow tinted clasts. Includes glassy, dense, vesicular clasts and crystals. May not all be juvenile.	Not determined
Crystals	Crystals, singly or in clots (with little to no groundmass attached; crystals more abundant than groundmass). Consistently present in the 2-mm and smaller size classes, increasing in proportion with decreasing size class.	Not applicable
High-silica inclusions[2]	Lavender patches and veinlets within HSA clasts in continuous-phase pyroclastic-flow deposits. In thin section, the patches are monocrystalline and polycrystalline masses in a groundmass of quartz, feldspar, clear glass, and vesicles. Masses are predominantly plagioclase (mostly sieve textured) but also include orthopyroxene and biotite. Micrographic textures are relatively common.	Not determined
Fine-grained gabbroic inclusions[2]	Salt-and-pepper, equigranular blocks or inclusions within dense low-silica andesite blocks of effusive-phase deposits. Crystals are ≤2 mm-diameter skeletal plagioclase, amphibole, and two-pyroxene.	Not determined

[1] As determined by point count by Larsen and others (this volume); errors are plus and minus 1σ.

[2] Lithology recognized in the field but not observed in the laboratory.

Explosive-Phase Pyroclastic Currents

Aerial reconnaissance on January 12, 16, and 18, time-lapse photographs, and seismic data constrain the emplacement of pyroclastic currents during the sequence of events 3 through 9 (table 1). Seismic signals from stations downslope of flows or beside flowpaths include 10–30-minute-long, cigar-shaped codas and increases in amplitude on temporary broadband stations 10–20 minutes after each explosion. Such distinctive signals on instruments below or next to flows, and their absence in other quadrants, delineate flowpaths (McNutt and others, this volume). Comparison of signals from instruments on all flanks of Augustine suggests that the longest-lasting flow occurred in a time-staggered sequence around the volcano. Signals indicating large flows were first recorded on east-side seismometers during events 3 through 5, on north-side seismometers during events 5 and 7, and on south-side seismometers during event 8 (Coombs and others, this volume; McNutt and others, this volume). Smaller flows occurred during the other events (table 1). Coombs and others (this volume), using time-lapse images from stations north and east of the volcano, report pyroclastic currents on the east and northeast flanks during events 4 and 5 and on the north flank during event 5 and smaller flows on the east and north flanks of the volcano after event 5. Aerial reconnaissance on January 16 indicated pyroclastic flowage deposits on all flanks of the volcano. An aerial survey revealed that an explosion on January 17 produced a pyroclastic flow on the Southwest flank, and seismicity suggests flows on the Northwest flank as well.

The deposits from these pyroclastic currents include two main types: a pyroclastic unit, typically 5 to 30 cm thick and widespread on the aprons of the volcano that is named the "thin, explosive-phase pyroclastic-current deposit" (map unit Expct); and an overlying unit, commonly 50–200 cm thick, lobate and with prominent blocky margins that is named the "explosive-phase pyroclastic-flow deposit" (map unit Expf) (fig. 2*A*).

The first voluminous pyroclastic currents to descend the volcano swept across steep, snow-covered slopes and spread widely on volcano aprons to form thin deposits (unit Expct, fig. 2*A*). These deposits blanket much of the upper slopes of the volcano down to about 300 m asl (fig. 2*A*)—a horizontal runout of 2 to 3 km and an elevation drop of 900 m. In August 2006, typical 5- to 30-cm-thick deposits commonly overlay snow but elsewhere thinned to a featheredge against pre-2006 surfaces to form complex tonguelike margins (fig. 5). Islands of pre-2006 deposits formed where this pyroclastic deposit lapped against gentle rises, ridges, and knolls.

Deposits of the first pyroclastic currents (unit Expct) commonly are poorly sorted, massive, and ungraded; however, near distal margins the deposits overlie graded and crudely bedded facies rich in dense clasts, as large as 1 m across. (fig. 6). Typical deposits have a bimodal size distribution with modes in lapilli- and ash-size and very fine ash components

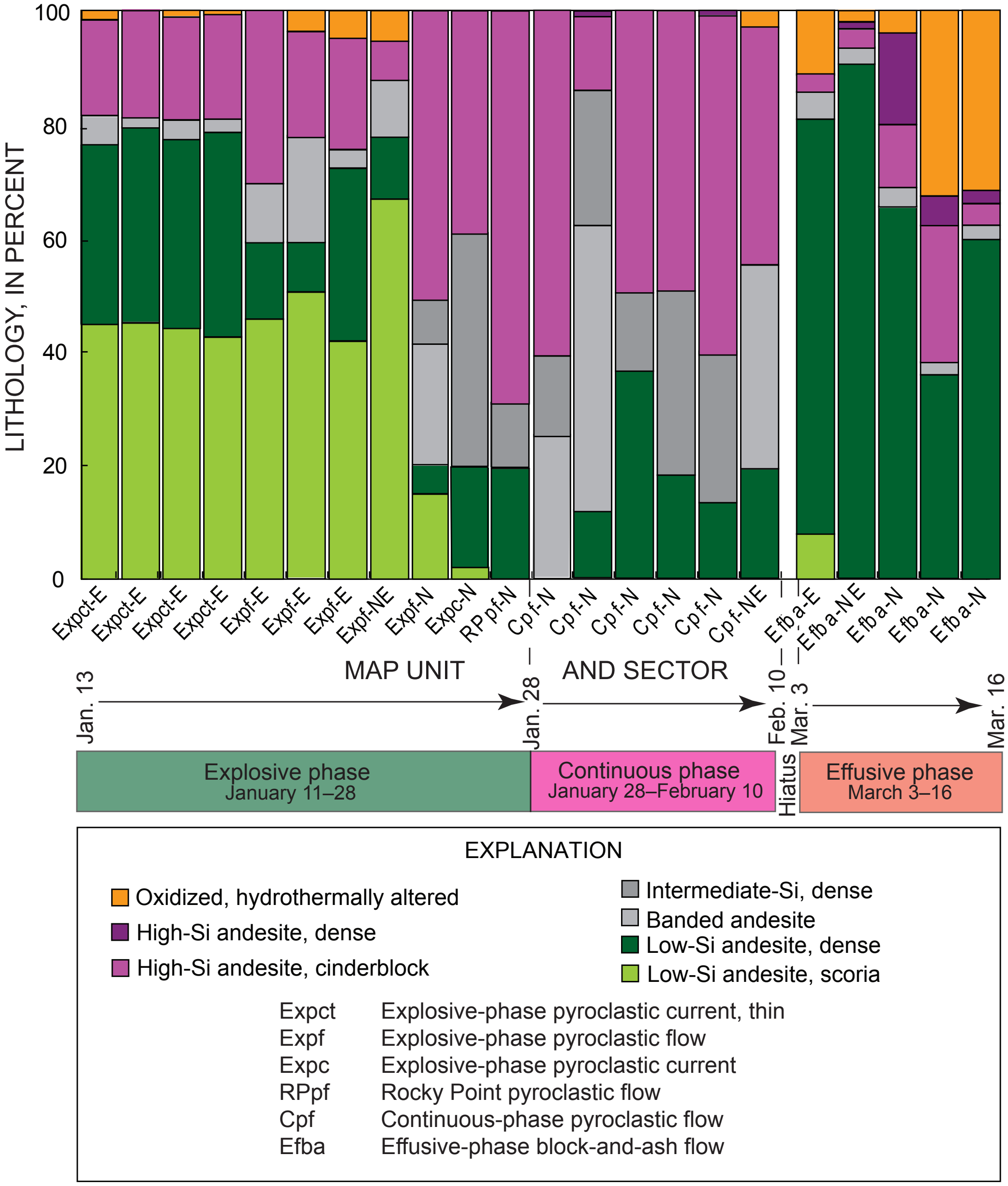

Figure 4. Plot of lithologic components versus flow type and quadrant for pyroclastic-current deposits, as determined by clast counts in the field (lithologies described in table 5).

ranging from 8 to 15 percent (figs. 6, 7). In contrast, basal stratified facies have stunted or absent lapilli-size modes and very fine ash components of less than 5 percent. Bedding within the fines-deficient facies nearly parallels bedding planes or dips at low angles toward source, and grading, if present, is inverse and coarse tailed (fig. 6). The stratified basal facies grades upward to the more common massive facies above within 1 or 2 cm.

After the initial widespread pyroclastic currents, multiple lobate pyroclastic flows (unit Expf), fig. 2*A*) funneled into valleys on all flanks of the volcano and produced deposits with archetypal morphology, including blocky, lobate margins and levees (fig. 8). The coarse pyroclastic-flow deposit (unit Expf) invariably overlies thin pyroclastic deposits (unit Expct) and thus postdates events 3 and 4 in drainages to the east and north and event 7 to the south and southwest. The largest flows moved as far as 3 to 4 km from source and typically moved farther along narrower valley axes than did initial widespread flows. The complex digitate margins of these distal flows thus now overlie pre-2006 surfaces (fig. 8). Deposit lobes are 5 to 30 m across and 1 to 2 m thick at distal or levee margins, although some thin toward their interiors and upslope to as little as 20 cm (fig. 9).

Coarse pyroclastic-flow lobes form overlapping sequences that indicate multiple episodes of deposition (fig. 9). Longitudinal cross sections of overlapping flow lobes indicate that subsequent flows plowed up and incorporated sediment from previous lobes even on gentle slopes. In adjacent areas, such lobes conformably overlie pre-2006 substrate with little evidence of erosion. Erosion of older 2006 pyroclastic-flow deposits by younger ones and an absence of such erosion on pre-2006 surfaces suggest that the older deposits remained somewhat fluid when subsequent flows inundated them.

The coarse pyroclastic-flow deposit (unit Expf, fig. 2) is poorly sorted, massive, and ungraded to inversely graded (fig. 9). Typical deposits have a bimodal size distribution, with lapilli and medium-to-coarse-ash modes (figs. 7, 9). Fine-grained basal layers may lack lapilli and blocks and have large fine-ash components. Inverse coarse-tail grading is common where blocks and large lapilli concentrate near the surface behind flow-lobe margins (fig. 9).

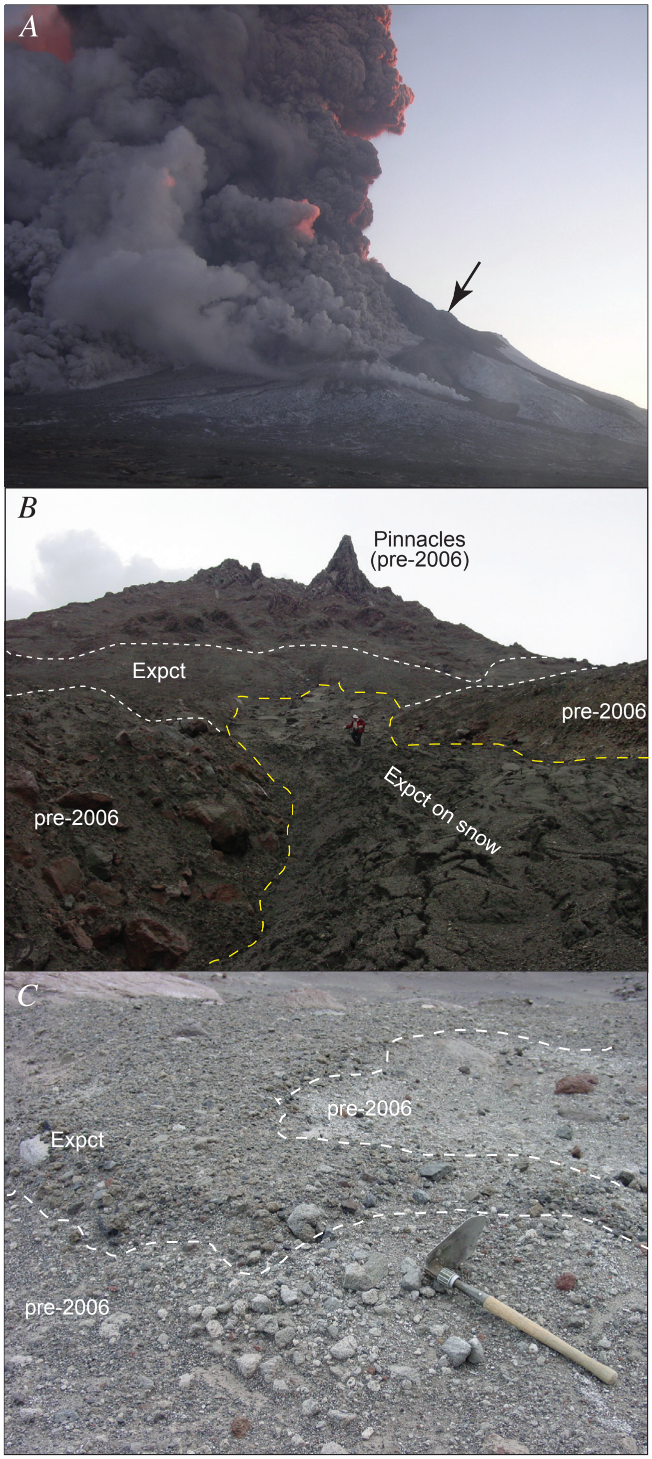

Figure 5. Photographs of thin explosive-phase pyroclastic-current deposit (unit Expct). *A*, Time-lapse photograph taken at 1645 AKST January 13, 2006, from Burr Point showing a pyroclastic current of event 6 moving down north slope of volcano toward camera. Arrow denotes blanket of debris already in place across the upper flanks, inferred to be unit Expct. *B*, Unit Expct deposit on east slope of volcano below Pinnacles (~1 km northeast of vent). Deposit is absent on steep, pre-2006 outcrops, including Pinnacles in background. In foreground, deposits in a gully were emplaced on snow. Later melting of snow caused deposits to become cracked and lumpy. *C*, Initial explosive-phase pyroclastic deposits (unit Expct) emplaced on pre-2006 moss- and lichen-covered surface, which was probably windswept of snow at time of deposition. Leading edge of 2006 flow is in middle of photograph. Flow drapes pre-2006 surface in a way typical of this deposit.

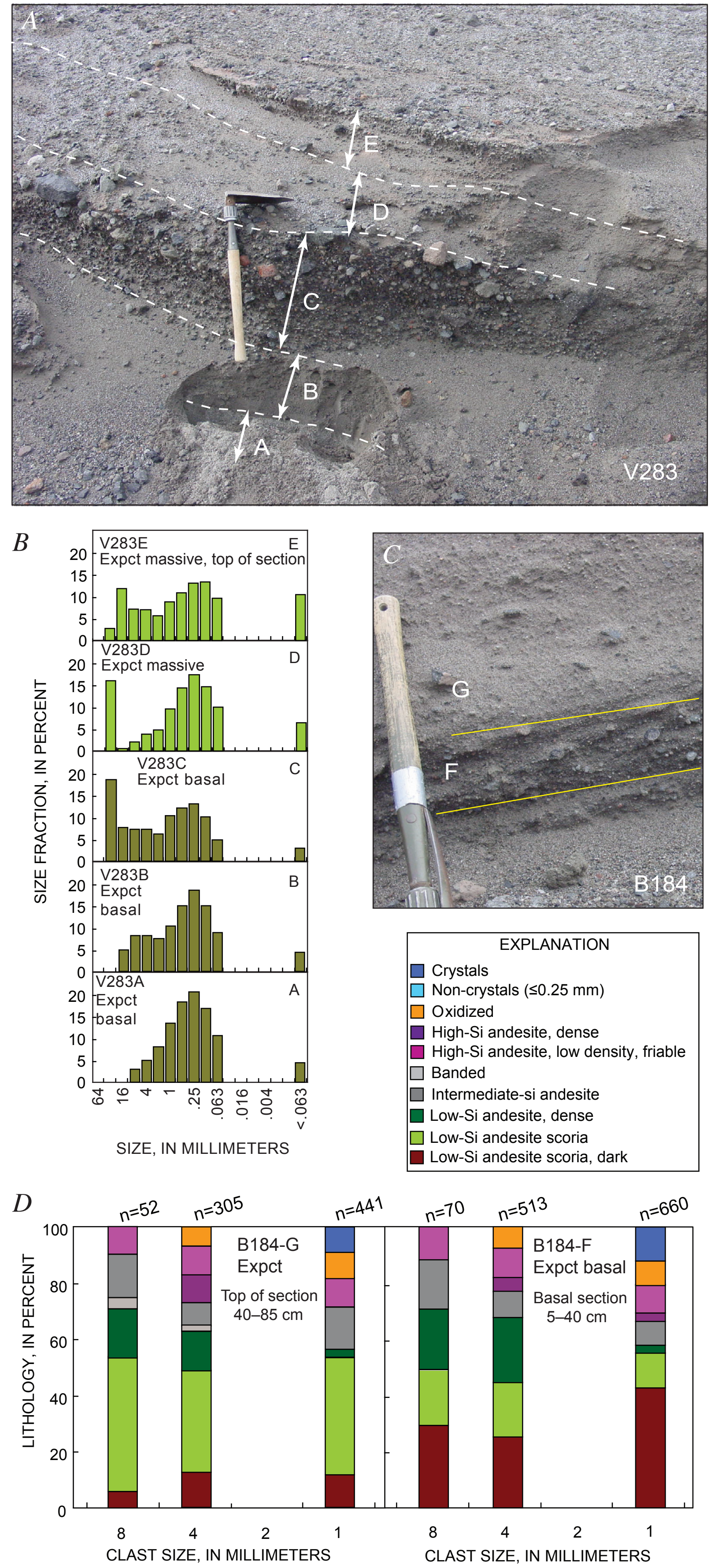

Figure 6. Basal stratified facies of thin explosive-phase pyroclastic-current deposit (unit Expct) on east flank of Augustine Volcano at station V283 (fig. 2*A*; table 3). *A,* Photograph of inversely graded, faintly stratified facies (layers A–C) overlain by ubiquitous, massive blanketing facies of deposit (layers D, E). Shovel is 50 cm long. *B,* Grain-size histograms of layers designated in figure 6A. *C,* Photograph of outcrop at station B184, approximately 50 m upslope of that shown in figure 6A, showing two 2006 layers on top of pre-2006 surface. Layer F is faintly crossbedded, and, like layers A through C at station V283, is friable. Layer G is typical blanketing facies of deposit. *D,* Plots of lithologic components of sample B184-F of basal facies and typical sample B184-G of deposit. Basal facies contains greater proportions of dark scoria and dense clasts than overlying deposit and other explosive-phase pyroclastic deposits. Sample locations are shown in figure 2*A* and table 2.

All pyroclastic deposits of the early explosive phase (events 3–9) contain similar proportions of lithologic components (figs. 4, 10; table 7). Low-silica andesite is the dominant rock type, and scoria is more common than dense rock (fig. 10). Subordinate rock types include high-silica andesite and dense, intermediate-silica andesite. Size- and density-segregation processes selectively sorted numerous blocks and lapilli of greenish-gray low-silica andesite scoria to the surface of pyroclastic flows as they slowed, lending deposits an easily distinguishable greenish gray hue. In fine-grained fractions, the three key constituents become more difficult to recognize, and we identify increasing proportions of phenocrysts (fig. 10).

Explosive-Phase Mixed Avalanches and Lahars

Mixed avalanches and lahars were generated by the first widespread pyroclastic currents (generally unit Expct) that moved across winter snowpack during events 3 through 8 on January 13 and 14; no such flows occurred thereafter. Aerial reconnaissance on January 12 and 16 constrains the emplacement of these flows. Flowline patterns along drainages are visible in oblique aerial photographs of January 16 but not in those of January 12. Scoured slopes and vegetation, as well as striations along northward-, eastward-, and southward-oriented streampaths, caused the patterns. These features were most conspicuous downslope of fresh pyroclastic-current deposits, and farther downstream in several drainages as far as the coast. Later observations showed that mixed-avalanche and lahar tracks caused the patterns (fig. 2*A*).

We infer that one or more of the six events on January 13–14 generated both mixed avalanches and lahars and, more specifically, that the first widespread pyroclastic currents to descend any particular valley during January 13–14 generated these flowage deposits (fig. 2*A*). Time-lapse photographs taken from the Mound camera (fig. 2*A*) suggest that east-side lahars had moved into several drainages downstream of the informally named East Chute during event 3 or 4 (Coombs and others, this volume, fig. 4*C*). Time-lapse photographs taken from Burr Point show fresh coarse pyroclastic-flow deposits (unit Expf) that descended the Northeast fan (fig. 2*A*; Coombs and others, this volume, figs. 5*C*, 5*D*). These pyroclastic-flow deposits overlap lahar deposits and one mixed-avalanche deposit, downstream along Northeast fan, suggesting that the

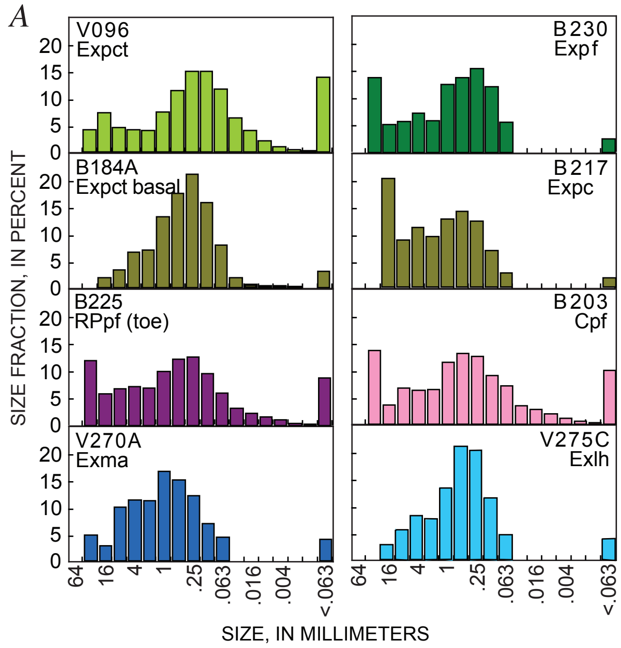

Expct	Explosive-phase thin pyroclastic current
Expct basal	Basal facies of unit Expct
Expf	Explosive-phase coarse pyroclastic flow
Exma	Explosive-phase mixed avalanche
Exlh	Explosive-phase lahar
Expc	Explosive-phase pyroclastic current, north flank
RPpf	Rocky Point pyroclastic flow
Cpf	Continuous-phase pyroclastic flow
Efba	Effusive-phase block-and-ash flow

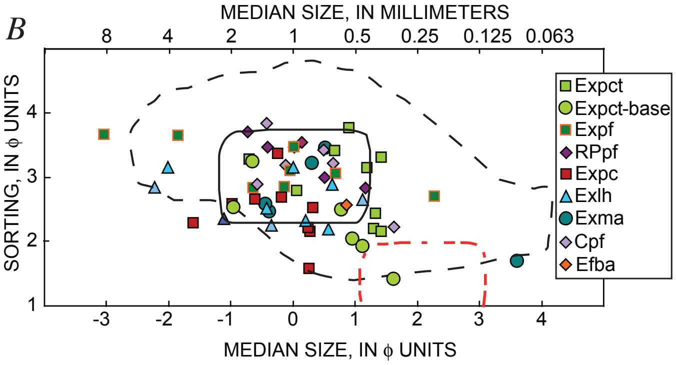

— — Field of 95 percent of pyroclastic-flow deposits (Sparks, 1976).

—— Redoubt Volcano proximal (<6 km) pyroclastic-flow deposits, (Gardner and others, 1994).

- - - Redoubt Volcano distal (6–10 km) pyroclastic-flow and pyroclastic-surge deposits (Gardner and others, 1994).

Figure 7. Summary of results from grain-size analyses of 2006 flowage deposits at Augustine Volcano. *A*, Histograms showing grain-size distribution of each clastic-flow type. Pyroclastic deposits with high fines content include deposits from initial thin, and subsequent coarse, explosive-phase pyroclastic deposits, the Rocky Point pyroclastic-flow deposit, and most continuous-phase pyroclastic-flow deposits. Some explosive-phase pyroclastic deposits are fines deficient. Bimodality with modes in lapilli and coarse-ash fractions, though present in some samples, is not conspicuous. *B,* Sorting versus median grain size for 2006 pyroclastic-flow deposits. Most samples fall within region of worldwide pyroclastic-flow deposits (dashed line; after Sparks, 1976) and 1989–90 proximal pyroclastic-flow deposits of Redoubt Volcano (solid line; after Gardner and others, 1994). Sample locations are shown in figure 2 and table 2; grain-size data are listed in tables 3 and 4.

lahar and mixed-avalanche deposits were emplaced during events 3 through 5.

Seismic signals provide further clues about the timing of lahar and mixed-avalanche emplacement (in this volume: Coombs and others; McNutt and others). Seismic stations adjacent to flowpaths recorded high-frequency, cigar-shaped codas following explosions, whereas other stations far from flowpaths recorded only explosion signals (McNutt and others, this volume). Broadband stations downstream of flows also showed increased seismicity as long as 20 minutes after initial explosion signals. The postexplosion timing and characteristics of these seismic signals suggest that they were produced by pyroclastic flows, mixed avalanches, and lahars that flowed toward the stations (Coombs and others, this volume). For example, station AUE, located between East Chute and Mound (fig. 2*A*) within about 100 m of a lahar path, recorded dominant, long-duration flowage signals, the longest of which lasted more than 30 minutes during event 3 and was partly caused by lahars passing near the station, rather than by pyroclastic flows upslope (McNutt and others, this volume). Stations AUE and AU14 also recorded signals consistent with flowage phenomena during events 4 and 5. The signal during event 5, in particular, could plausibly include lahars. Stations AUL and AU12 both recorded

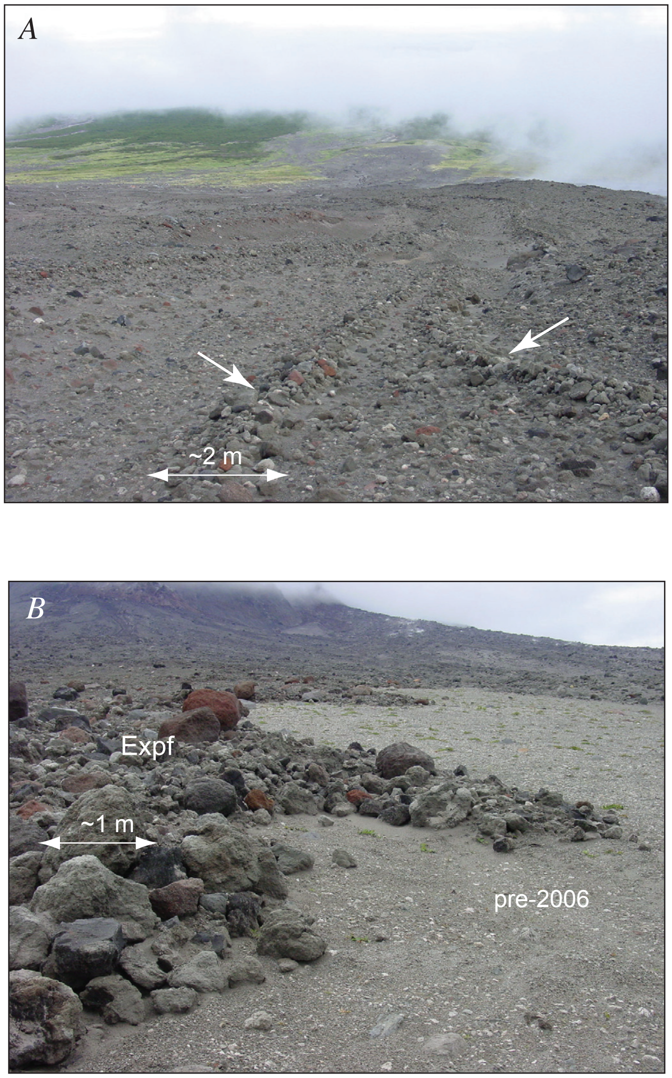

Figure 8. Photographs of coarse explosive-phase pyroclastic-flow deposits (unit Expf). *A,* Medial levees (arrows), approximately 50 cm high concentrate large lapilli and blocks and define margins of lobate deposits. *B*, Digitate, distal margin of coarse pyroclastic-flow deposit.

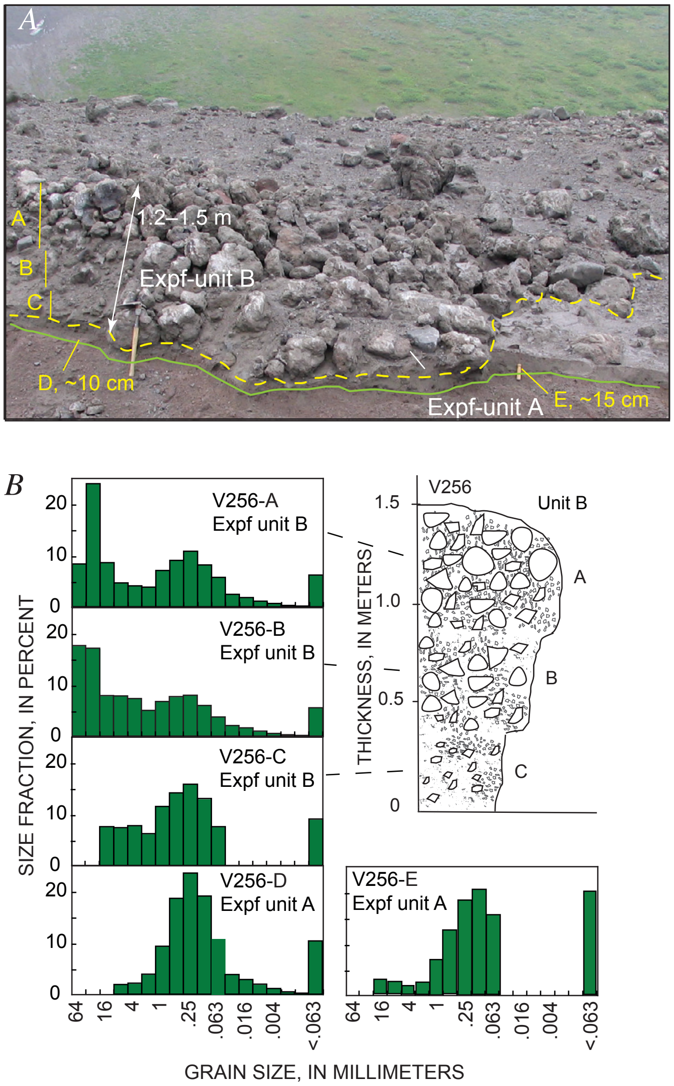

Figure 9. Overlapping explosive-phase pyroclastic-flow deposits (unit Expf) at station V256 (fig. 2*A*). *A*, Photograph showing distal margin of pyroclastic-flow unit B where it has overrun and partially eroded pyroclastic-flow unit A. Sampling sites are denoted in yellow as A through E. *B,* Unit B is inversely graded, as shown by histograms of grain-size distribution and by graphic log to right. Sample locations are shown in figure 2*A* and table 2.

flows during event 5 but not during earlier events. These deposits, which were the first widespread pyroclastic flows of the 2006 eruption, probably generated the lahars that moved downstream of North Fan and within Windy Creek drainage to the coast (fig. 2*A*). On the basis of the protracted seismic signals recorded at stations AU15, AU13, and AUI (fig. 2*A*), to the southwest and south of the volcano, pyroclastic flows and the mixed avalanches and lahars that they generated in Augustine Creek and Southeast Beach Creek probably occurred during event 8.

Mixed-Avalanche Deposits

Mixed-avalanche deposits (unit Exma) crop out south and east of the volcano, from upper slopes downstream as far as the coast, and extend from near the margins of some thin explosive-phase pyroclastic-flow deposits (fig. 2*A*). Mixed-avalanche deposits are most widespread in drainages on the southwest to southeast flanks of the volcano (fig. 2*A*). In the upper parts of Augustine Creek drainage, mixed-avalanche deposits occupy wide swaths of the valley, interrupted only by younger coarse pyroclastic-flow lobes (fig. 2*A*). In medial and distal reaches of valley systems, such as Augustine Creek, mixed-avalanche deposits crop out next to lahars (figs. 11–13). In areas where mixed-avalanche and lahar deposits mingle, the mixed-avalanche deposits occupy flow margins and commonly form islands surrounded by lahar deposits (fig. 13). On the east side of Augustine Island, mixed-avalanche deposits of more limited extent commonly are confined to upper-slope gullies and span a few minor drainages downslope (fig. 2*A*).

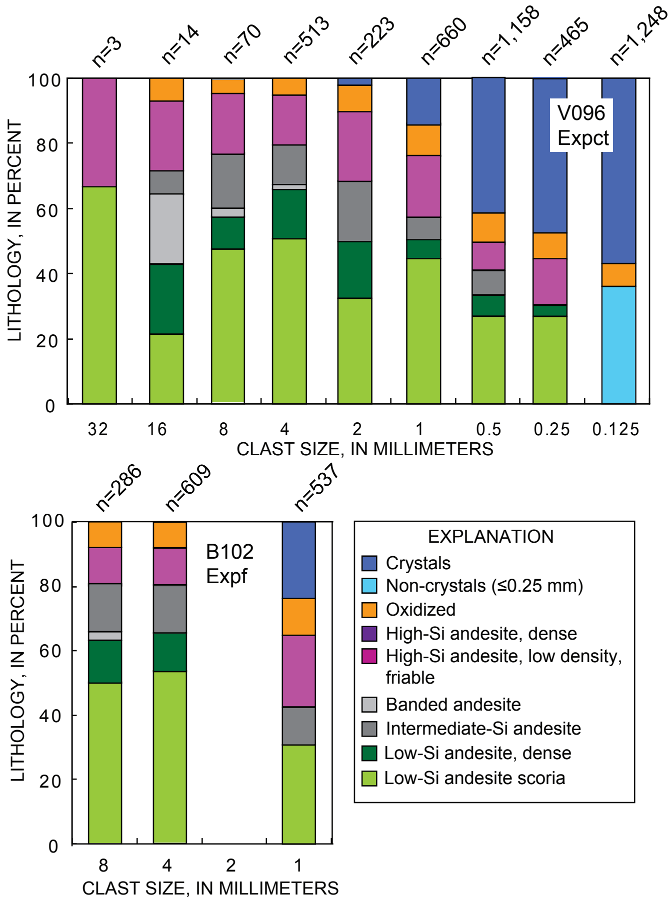

Figure 10. Plots showing lithologic components versus clast size for pyroclastic deposits of explosive-phase events 3 through 9. Above, initial explosive-phase pyroclastic deposit (unit Expct) and below, subsequent explosive-phase pyroclastic-flow deposit (unit Expf). Sample locations are shown in figure 2*A* and table 2.

Mixed-avalanche deposits have distinctive irregular surfaces crisscrossed with cracks. These cracks cut through the soft sediment that forms the deposits, and in August 2006, several months after the eruption, the cracks locally exposed snow. In protected, proximal reaches during August 2006, we observed that some deposits contained snow, some overlay snow, and others had distinctive, extremely uneven, lumpy surfaces due to the melting of both underlying and contained snow (figs. 11, 12). Along vegetated slopes at lower elevations, deposit surfaces were littered with uncharred alder and willow branches that had been broken to pieces and denuded small stems and twigs. Nearby such littered surfaces, deposit remnants were also scattered on top of large boulders and throughout patches of alder and willow whose upper branches were commonly denuded and broken but not charred. Apparently, the brush in mixed-avalanche paths was commonly buried and protected under snowpack when snow and debris mixtures slid across it. As a result, the vegetation, whose tops were generally clipped and destroyed, were irregularly draped with debris. Deposit margins, which are broadly lobate and do not form levees themselves, are common as levees of axial lahar flows (fig. 12).

The thickness of explosive-phase mixed-avalanche deposits ranges from 0.2 to 3 m and averages about 0.5 m. Poorly sorted, ungraded deposits typically have modes in gravel- and sand-size ranges (fig. 11). The deposits contain proportions of juvenile rock types similar to those of explosive-phase pyroclastic-flow debris. Locally, the lumpy surfaces are rich in fines (<0.063 mm diam) and cracked where snowmelt had pooled, collected the fines, and subsequently dried (fig. 11).

Lahar Deposits

Explosive-phase lahar deposits (unit Exlh) underlie the middle to lower parts of most drainages around the volcano, except those to the west (fig. 2*A*). Generally, lahar deposits are downstream of pyroclastic-flow deposits and adjacent to, or downstream of, mixed-avalanche deposits (figs. 2*A*, 13). Watery lahars and floods reached the coast on most flanks of the volcano (fig. 2*A*).

The variation in the areal extent of lahar inundation suggests a variation in water content among lahars. The most widespread lahar deposits are also those with characteristics most suggestive of high water content. The deposits

Table 7. Overview of lithologic components in key deposits of the three phases of the 2006 eruption of Augustine Volcano, Alaska.

[Phases, events, and units (after Coombs and others, this volume). Component values are 8-mm data averaged from table 6 and recalculated to 100 percent. Components are low-silica andesite scoria (LSAS), dense low-silica andesite (DLSA), dense intermediate-silica andesite (DIA), high-silica andesite (HSA), and mixtures (banded), defined in table 5. Units are defined in figure 2. Mixed-avalanche (Exma) and lahar (Exlh) data are not included in "Average for unit" column]

Phase date		Event	Unit(s) emplaced (map designation)		Lithologic components (in percent)																																												
			Lavas, lithology	Flowage deposits	Expct						Expf						Expct base (above) Expc (below)						RPpf						Exma (above) Exlh (below)						Cpf						Efba						Average for unit		
					LSAS	DLSA	DIA	Banded	HSA	Oxidized	LSAS	DLSA	DIA	Banded	HSA	Oxidized	LSAS	DLSA	DIA	Banded	HSA	Oxidized	LSAS	DLSA	DIA	Banded	HSA	Oxidized	LSAS	DLSA	DIA	Banded	HSA	Exotic[1]	LSAS	DLSA	DIA	Banded	HSA	Oxidized	LSAS	DLSA	DIA	Banded	HSA	Oxidized	LSA[2]	IA[3]	HSA
Explosive, January 11–28	1/11	1		Mixed avalanches (destroyed)																																													
		2																																															
	1/11–1/13		Ephemeral dome, LSA																																														
	1/13-1/14	3		Pyroclastic current, thin (Expct); mixed avalanche (Exma); lahar (Exlh)	45	16	14	4	16	6	Expf possible, no data						51	20	16	2	11	0							47	11	7	3	18	14													68	18	14
		4																																															
		5		Pyroclastic flow (Expf); mixed avalanche (Exma); lahar (Exlh)							62	11	10	2	11	4													41	19	14	1	16	9													75	13	12
		6																																															
		7																																															
		8																																															
	1/14–1/17		Dome (Exd1), LSA																																														
	1/17	9		Pyroclastic flow (Expf)							49	10	12	8	16	5																															62	21	17
	1/17–1/27		Dome (Exd2) HSA, IA																																														
	1/27	10		Pyroclastic current (Expc)													8	29	23	3	34	3																									38	27	35
				Rocky Point pyroclastic flow (RPpf)																			9	11	14	1	62	3																			21	15	64
	1/27–1/28	11		Pyroclastic flows? (buried)																																														
		12																																															
		13																																															
Continuous	1/28–2/3	14		Pyroclastic flow (Cpf, Cpfw, and Cpc)																															0	18	41	5	29	7							19	50	31
		--																																															
		--																																															
	2/3–2/10	--	Lava lobes, LSA																																														
		--																																														
Hiatus																																																	
Effusive	March 3–16		Lava flow (Ef1f); LSA	Block-and-ash flow (Elba)																																					9	63	9	0	4	15	85	10	5

[1] Oxidized + pumice.

[2] LSA = LSAS+DLSA.

[3] IA = DIA+banded.

downvalley of East Chute are the best examples of these water-rich flows (figs. 12*B*, 14*A*). On the east flank of the volcano, between about 500 and 100 m asl, long linear lahar levees, 2 to 10 m wide and about 20 cm high, consist of cobble and boulder accumulations littered with sand and silt. The levees trace along vegetated terraces and mossy surfaces upstream of the youngest explosive-phase coarse pyroclastic-flow deposit (unit Expf), toward their apparent source, the older, thin pyroclastic-current deposit (unit Expct; figs. 2*A*, 12). In between levees, large lahars were water rich and erosional. Boulders as large as 3 m in diameter, commonly of low-silica andesite scoria, dot eroded and scoured surfaces. In this scoured regime, willows and alders are commonly battered on their upstream sides, denuded, and bent downslope into bayonet-stick forms (fig. 14*A*). Downstream, levees lead into channels where the water-rich debris mixture flowed and deposited 30- to 100-cm-thick channel facies (fig. 14*B*). In outcrop, the channel facies has characteristics typical of transitional or hyperconcentrated-flow deposits, such as intermediate sorting, crude bedding, and both inverse and normal grading (fig. 14*B*). Where exposed, inversely graded strata underlie crudely stratified, normally graded sediment. In distal reaches, levees range in size and character from linear trains of scattered cobbles and boulders to boulder-cobble-rich accumulations, as thick as 50 cm.

Areally extensive lahar deposits commonly have margins bordered by mixed-avalanche deposits, suggesting

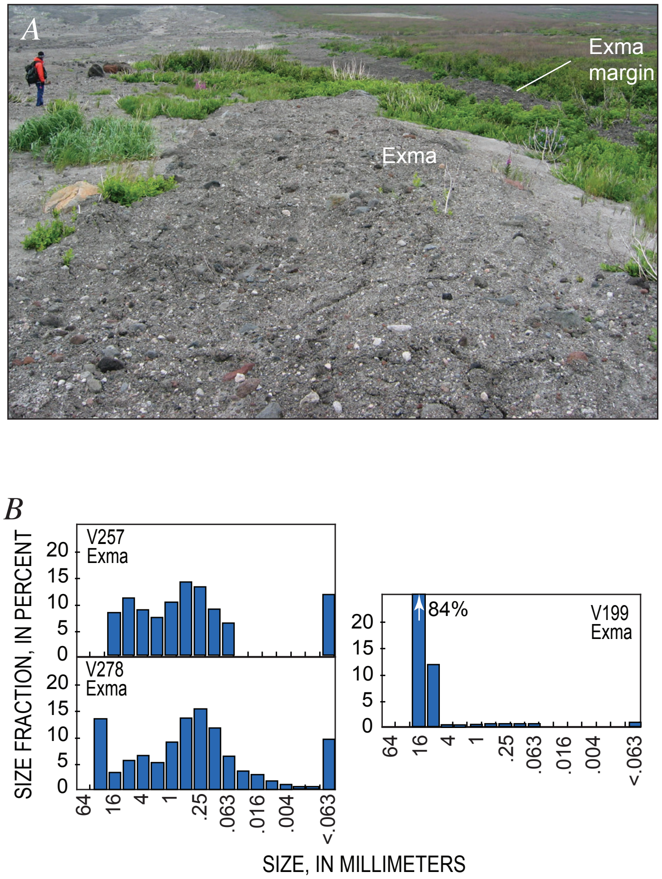

Figure 11. Photograph and grain-size plots of explosive-phase mixed-avalanche deposits (unit Exma). *A*, View downstream of mixed-avalanche deposit showing irregular, lumpy surface texture. Cracks formed after incorporated snow had melted, and wet, compacted fines had dried and contracted. Margin of deposit, cutting across upper right of photo, drapes vegetation. Apparently, much debris in this area was emplaced on top of snow that covered and protected vegetation, then melted into place, partly burying small alder trees. *B*, Histograms of grain-size distribution of mixed-avalanhce deposits, illustrating variability of size distribution. Sample locations are shown in figure 2*A* and table 2.

Figure 12. Photographs of lahar levees; view downstream. *A*, Boulders, cobbles, and sparse matrix that have accumulated along right margin of lahar. *B*, Mixed avalanche deposit (unit Exma) forms left-marginal levee-terrace, 2 m high, of lahar flow to right. Lahars denude alders and willows, forming bayonetlike stems that are battered and bent downstream. Green vegetation was protected from flow by burial under snow.

Figure 13. Photographs of explosive-phase lahar deposits. *A,* Aerial view down Augustine Creek on lower south-southwest flank of volcano, showing lahar deposit (unit Exhl; light-blue dashed outline and flow-direction arrows). Mixed-avalanche deposit (unit Exma) forms terraces lateral to, and islands within, lahar deposit. Lahar channels are scoured. *B,* Photograph of small-scale (~5 m across) lahar deposits. Lahar deposits in foreground (dashed lines) were generated by explosive-phase pyroclastic-flow deposit (unit Expf; solid lines) that came to rest on snow. *C,* Aerial view of bouldery mixed-avalanche and lahar deposits in Augustine Creek, bordering scoured lahar channels that cut seacliff. Lahar transport formed bouldery delta as far as 100 m offshore.

a genetic relation between these two types of deposit. South-southwest of the volcano, mixed-avalanche deposits are situated in intermediate valley reaches between source pyroclastic-flow deposits and lahars. Farther downstream, along intermediate to distal reaches of Augustine Creek, terraces of lumpy-surfaced mixed-avalanche deposits border lahar deposits rather than boulder-cobble levees (fig. 12*B*). In between these mixed-avalanche terraces are scoured lahar surfaces with scattered boulders, much like the scoured surfaces of the large lahars described above (fig. 12*A*). Downstream of the marginal mixed-avalanche deposits, boulder-cobble levees become evident. Near the coastline in Augustine Creek, bouldery mixed-avalanche and lahar deposits are situated on either side of a scoured channel incised in a low seacliff (fig. 13*C*). Lahars carried boulders as large as 1 m in diameter through the channel, and carried other boulders as far as 100 m into the ocean. We observed similar relations between mixed avalanches and lahars that moved to the coast along drainages on the south and southeast sides of the island.

The smallest-volume lahar deposits appear to have originated at the coarse margins of explosive-phase the pyroclastic-flow deposit (unit Expf, fig. 13*B*); fluid breakaways are visible at the toes and margins of some of the younger coarse pyroclastic-flow-deposit lobes. The lahar deposits, which are typically only few meters wide and no more than a few tens of meters long, have cobble-rich margins that become progressively less distinct with distance downslope (fig. 13*B*). These deposits are present where the pyroclastic flow deposit (unit Expf) evidently came to rest on top of snowpack.

The lithologic composition of lahar deposits (unit Exlh) is similar to that of explosive-phase pyroclastic currents (units Expct, Expf) and virtually identical to that of mixed-avalanche deposits (unit Exma). The greenish-gray, low-silica andesite scoria that is common in all explosive-phase deposits is also diagnostic in lahar deposits (tables 6, 7). A combination of size and density segregation has concentrated greater than 50 percent scoria in lahar-levee deposits. The channel facies of lahar deposits contain scoria proportions typical of other explosive-phase deposits, but also oxidized lithic clasts and pumice from pre-2006 deposits (table 6). These rock types are present in the lahars owing to progressive entrainment of sediment along the flowpath. At Augustine, lahar flowpaths rarely exceed 2 km in length, and so bulking factors in deposits are rarely much greater than 10 percent.

Grain-size characteristics of Augustine lahar deposits are similar to those of the transitional to hyperconcentrated flows documented at other volcanoes (Scott, 1988; Vallance, 2000). The sorting index ranges from 2.2 to 3.2, typical of transitional flows (table 2; Scott, 1988). The upper, crudely bedded deposits are moderately well sorted, have the finest mean grain size, and have grain-size distributions with a mode of about 0.5 mm (figs. 14*A*, 14*B*). Underlying, more massive deposits have the greatest proportions of coarse particles, the poorest sorting, and grain-size distributions with a weak bimodality (figs. 14*A*, 14*B*).

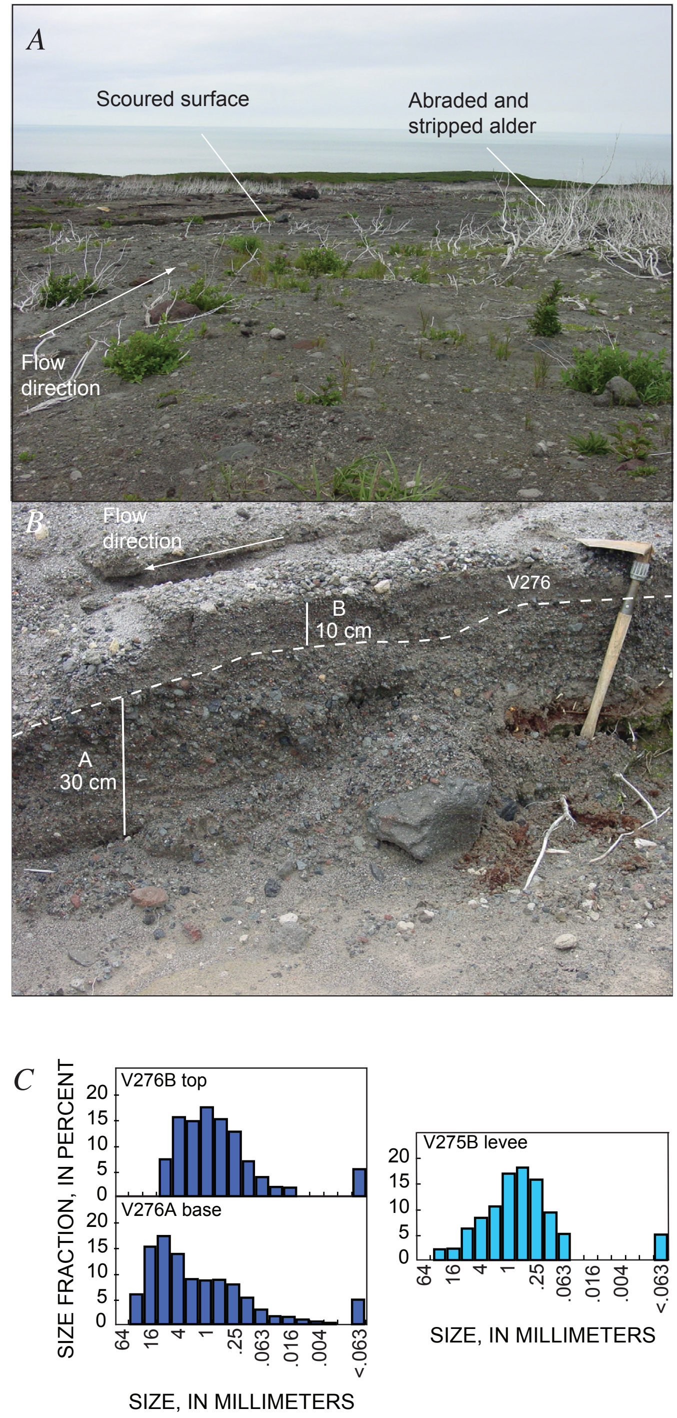

Figure 14. Photographs of scoured lahar surface (*A*) and nearby vertical section (*B*) at sample location V276, with histograms of deposit grain-size characteristics (*C*). *A*, Lahar surface is not only scoured but also displays willows and alders stripped of vegetation and bent in flow direction to form bayonetlike sticks. *B*, Normally graded lahar deposit where it funneled into distal channel and began to deposit its sediment load. Layer B is faintly stratified. Shovel is 50 cm long. *C*, Basal layer A contains a larger proportion of large clasts and also more fines than layer B. Nearby levee deposit (sample V275B) is relatively fines poor. Sample locations are shown in figure 2*A* and table 2.

Events 10 through 13, January 28–29: Pyroclastic Flows to the North and the Transition to the Continuous Phase

The 9-minute-long explosion of event 10 produced the largest-volume pyroclastic output of the explosive phase and sent pyroclastic currents northward. Events 11 through 13 either generated no pyroclastic currents or produced no deposits distinguishable from those of the subsequent continuous phase. Two distinctive pyroclastic currents occurred in rapid succession during event 10 (McNutt and others, this volume; Coombs and others, this volume). The first deposit contains large proportions of dense, nonvesicular andesite (unit **Expc**, fig. 2*B*). The second more widespread deposit, named the "Rocky Point pyroclastic flow," overlies the first deposit and covers an area of about 3 km^2 from the volcano's summit northward toward Rocky Point (unit **RPpf**, fig. 2*B*).

Stratigraphy, the destruction of monitoring devices, and the characteristics of seismic signals constrain the timing of the two large pyroclastic flows on the north flank to event 10. At 2024 AKST January 27, 2006 (0524 UTC, Jan. 28, 2006), a forceful blast destroyed seismic station AUL and GPS station AV03, both then located on the prehistoric North Slope lava flow (fig. 2*B*). Lithologically distinct pyroclastic deposits at these sites and battered fragments of the stations within deposits downstream (fig. 15*A*) shows that the initial flow (unit **Expc**) destroyed the stations. The Rocky Point pyroclastic flow overlies this pyroclastic-current deposit and underlies pyroclastic-flow deposits correlated to the continuous phase (unit **Cpf**; figs. 15*B*, 15*C*), suggesting that the flows occurred between 2024 AKST January 27 (event 10) and aerial observations midday on January 29 during the early part of the continuous phase. Coombs and others (this volume) infer that the Rocky Point flow occurred during event 10, on the basis of deposit size (largest of the 2006 eruption), the extent of the postexplosion seismic signal (~30 minutes), the relative size of the ash signal on radar (largest of the 2006 sequence, Schneider and others, 2006), and the number of lightning strikes (most recorded strikes during the 2006 eruption; Thomas and others, this volume). We accept their interpretation that the largest flow should correspond to an event with a long seismic coda, an ash-rich plume, and numerous lightning strikes. Event 10 is the only likely eruptive pulse during the time interval in question with these characteristics.

Explosive-Phase Pyroclastic-Current Deposit

The pyroclastic-current deposit (unit **Expc**) drapes the conspicuous North Slope lava flow (Waitt and Begét, 2009) and spills onto gentler slopes, a distance of 3.3 km northward from its source at the summit to its distal margin (fig. 2*B*). The limited distribution of this flowage deposit along the top of a ridge 50–100 m high is likely an artifact of the deposit's unknown extent: eastward, beneath pyroclastic-flow deposits of Rocky Point and the continuous phase; and westward, beneath younger deposits of the adjacent, upper-eastern Windy Creek drainage (figs. 2*B*, 2*C*). The thickness of the deposit varies. Along the steep eastern margin of the prominent lava flow, it is 20 to 150 cm thick; on the lava flow's western edge, it thins irregularly to zero, revealing patches of pre-2006 deposits. Under varying thicknesses of continuous-phase pyroclastic flow deposits (unit **Cpf**) and the Rocky Point pyroclastic-flow deposit (unit **RPpf**), it is 5 to 50 cm thick to the east (fig. 15). North to north-northwest of the North Slope lava flow, it thins to a few centimeters and extends downslope as irregular patches within tracts of alder. In this area, the alders are singed and stripped of leaves above 1 to 2 m above ground and unaffected below, suggesting that margins of the flow were gas rich and contained insufficient heat either to melt underlying snowpack fully or to burn vegetation. Snow melting during spring and summer thaw subsequently emplaced the patches.

Outcrops of the pyroclastic-current deposit commonly are inversely graded, massive to faintly bedded, and loose or friable (figs. 15, 16). Some parts appear to be ungraded, especially those overlain by and, possibly eroded by younger pyroclastic flows. Grain size ranges from fine ash to lapilli, has a mode in the coarse-ash-size fraction and, where coarser overall, has another faint mode in the lapilli-size fraction (fig. 16*C*).

The pyroclastic-current deposit is lithic rich and varies somewhat in the proportions of lithologic components intermediate between those of previous explosive-phase deposits and those of subsequent continuous-phase deposits (fig. 16*D*). Like previous pyroclastic deposits of the explosive phase, angular, dense, low- and intermediate-silica andesite clasts make up 25 to 50 percent of the rock types in the deposit. In contrast, however, the pyroclastic-current deposit contains greater proportions of high-silica andesite than all previous explosive-phase deposits (fig. 16; tables 6, 7).

The pyroclastic-current (unit **Expc**) and the Rocky Point (unit **RPpf**) deposits originated during the same 9-minute event, and so we considered their possible genetic relation but rejected that hypothesis for the following reasons. First, the pyroclastic-current deposit crops out in extensive areas where evidence of the Rocky Point pyroclastic flow is absent. Second, where the two deposits crop out together their contact is abrupt, sharp, and commonly erosionally unconformable. Third, grain-size characteristics of the two deposits differ where they overlap; for example, thin, fine-ash edges of the Rocky Point deposit overlie much coarser ash and lapilli deposits of the pyroclastic-current deposit (fig. 15*B*). These observations are inconsistent with a cogenetic origin, and so we conclude that these two units followed one another successively within a few minutes during event 10.

Explosive-Phase Rocky Point Pyroclastic Flow

The most voluminous and widespread pyroclastic flow of the 2006 eruption also occurred during event 10. The Rocky Point pyroclastic flow originated near the summit of the

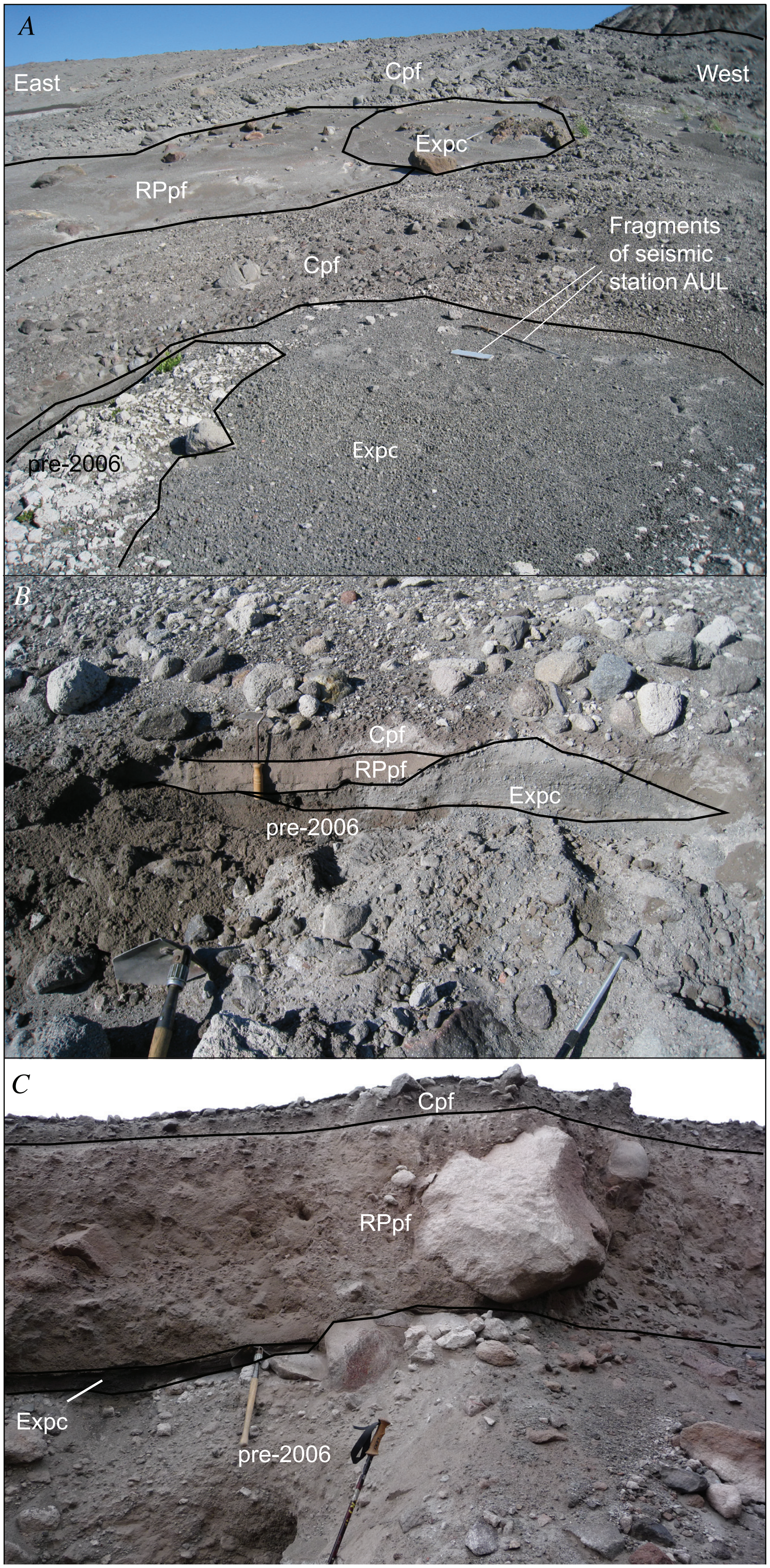

Figure 15. Photographs illustrating relations between 2006 explosive- and continuous-phase pyroclastic deposits on north flank of Augustine Volcano. *A,* Surface of pyroclastic-current deposit (unit Expc), oldest of 2006 deposits at this locality, with scattered fiberglass fragments, 40 and 90 cm long, from upslope seismic station AUL and GPS station AV03. Rocky Point pyroclastic-flow deposit (unit RPpf) thins from left to right (east to west) and disappears, whereas younger, continuous-phase pyroclastic-flow deposit (unit Cpf) drapes over and around gentle slopes. *B*, Thin, fine-grained Rocky Point deposit (unit RPpf) underlies continuous-phase pyroclastic-flow deposit (unit Cpf) and overlies friable, light-gray deposit (unit Expc). *C*, Rocky Point deposit (unit RPpf), 1 m thick, is in same stratigraphic position as in figure 15*B*.

volcano; traveled northward about 4 km, where a low ridge system, capped by a 50-m-high hill, divided the flow into two large and one small parts; and, finally, spread out to form several lobes across a nearly flat surface (figs. 2*B*, 17*C*). The flow moved just more than 5 km from its source and stopped less than 1 km from the shoreline near Rocky Point.

The Rocky Point pyroclastic-flow deposit (unit RPpf; fig. 2*B*) is distinctive, not only because of its size and distribution north of the volcano but also because of its physical characteristics. The deposit widens from about 0.3 to 1.8 km from south to north, averages 5 to 6 m in thickness, has maximum thicknesses of 10 to 15 m, and has a volume of about 1.6 × 10^7 m^3 (Coombs and others, this volume). Continuous-phase pyroclastic-flow lobes overlie proximal parts of the deposit (compare figs. 2*B*, 2*C*). Axial parts of the deposit thicken to as much as 15 m but thin to less than 1 m where the flow moved across steep slopes, locally revealing pre-2006 deposits on especially steep scarps. Narrow, blocky marginal terraces are present where a ridge to the west and a 50-m-high hill to the east funneled part of the flow (fig. 17*A*). The terraces, which apparently formed at ephemeral levels during the receding stage of the passing flow, are thus marginal relics of a fluid flow whose mass largely drained away and accreted downslope. Dozens of large blocks, 3 to10 m in diameter, dot the axial medial surfaces but are absent near lateral or distal deposit margins. Such blocks commonly have pyroclastic-debris aprons that ramp up on their stoss sides and streamline hollows on their lee sides (fig. 17*B*). Many blocks have patches of fine material, centimeters to a few tens of centimeters thick, with scattered lapilli and blocks perched on their tops (fig. 17*B*).

Along its eastern margin, the Rocky Point pyroclastic-flow deposit thins to a few centimeters and divides into numerous small tongues. These features were distinguishable in August 2006 from the subdued features of pre-2006 deposits only by the absence of moss and lichens. The western margin of the deposit is more readily delineated because there the flow lapped up on a prominent ridge, leaving behind not only deposits a few centimeters thick but also a fringe of scorched, broken, and denuded alders (fig. 17*A*).

Three distinct lobes of the Rocky Point pyroclastic-flow deposit fan across a flat surface north of an east-west ridgeline (fig. 17*C*). These lobes, which are about 10 m thick where flows debouched onto the plain, and thin to a few centimeters

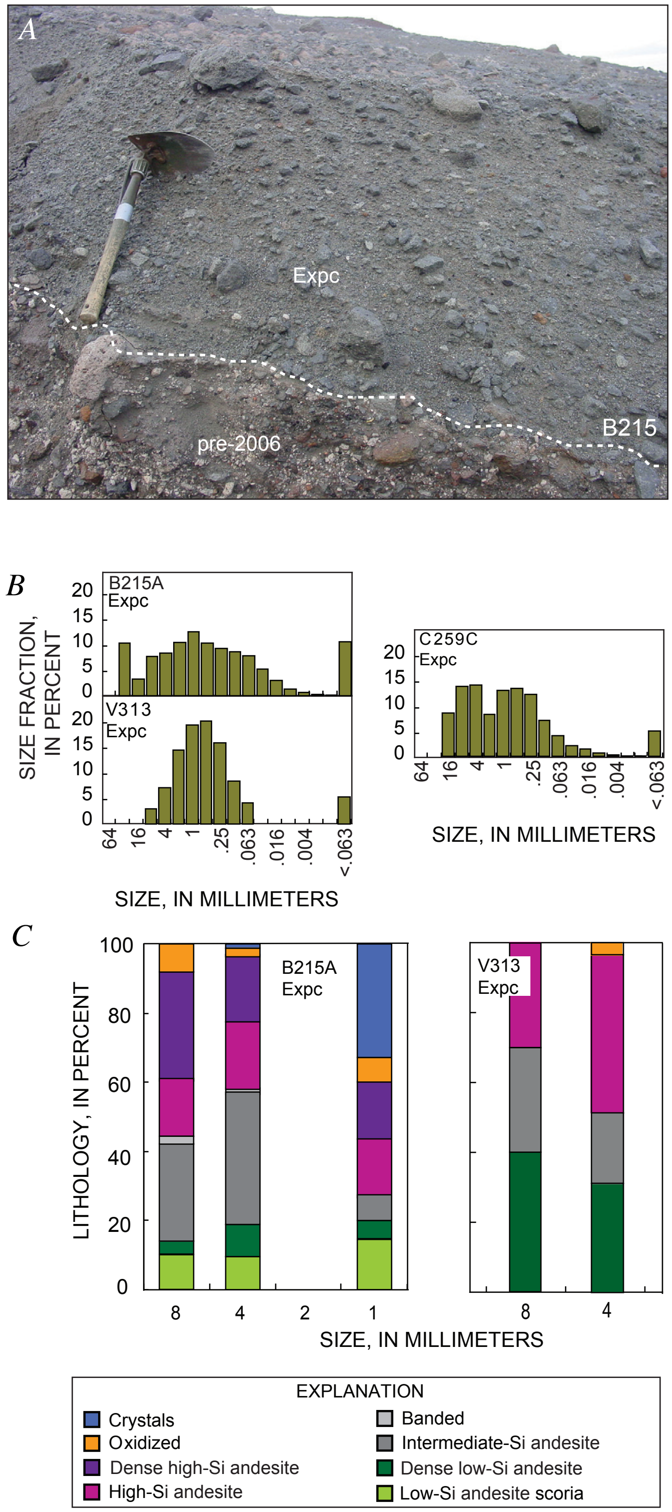

Figure 16. Explosive-phase pyroclastic-current deposit (unit Expc) on north-slope lava flow (fig. 2*A*). *A,* Photograph of cross section, 80 cm thick, from the site of samples V303 and B215 near GPS station AV03, destroyed during event 10. Shovel is 50 cm long. *B,* Grain-size distribution plots of deposits at site illustrated in figure 16*A* and at two other sites. Relatively high fines content of sample B215A is unlike that of other samples from this deposit. *C,* Plots of lithologic components of fines-poor deposit. Deposit is more like those of continuous phase than those of explosive phase and proportion of dense clasts is greater than in other deposits, suggesting a lithologic transition from explosive-phase to continuous-phase magma composition. Sample locations are shown in figure 2*A* and table 2.

near margins, coalesce to form nearly continuous deposit along about 1.8 km of the plain from east to west (fig. 17*C*). Lobes exhibit radiating systems of low ridges and swales. Like those Cole and others (2002) describe in large dome-collapse pyroclastic flows at Montserrat, these linear features parallel flow directions. In cross section, ridges have gentle slopes and broad axes spaced 5 to 20 m apart transverse to flow directions. Swales anastomose in the downflow direction, such that individual ridgelines are rarely traceable more than a few tens of meters. The large blocks that protrude 2 to 5 m above the surface are concentrated within thick axial parts of the lobes and poke through both ridges and swales described previously. These large blocks are absent where deposits thin and thus rarely appear within 100 m of lobe margins. Like the axial blocks upslope, such large blocks commonly preserve accumulations of fine matrix and lapilli, 5 to 20 cm thick, on their tops. Lobe margins thin to a few centimeters and commonly concentrate broken and slightly singed alder branches (figs. 18*A*, 18*B*).

As the westernmost lobe spread westward, it buried a shallow pond, resulting in several openwork depressions surrounded by accumulations of fine ash on the surface of the deposit where the pond had been. The interaction of hot pyroclastic debris and underlying water must have generated steam that migrated through the deposits, winnowing fine ash to form elutriation pipes. The openwork depressions are the surface manifestation of these elutriation pipes, which are not exposed in cross section.

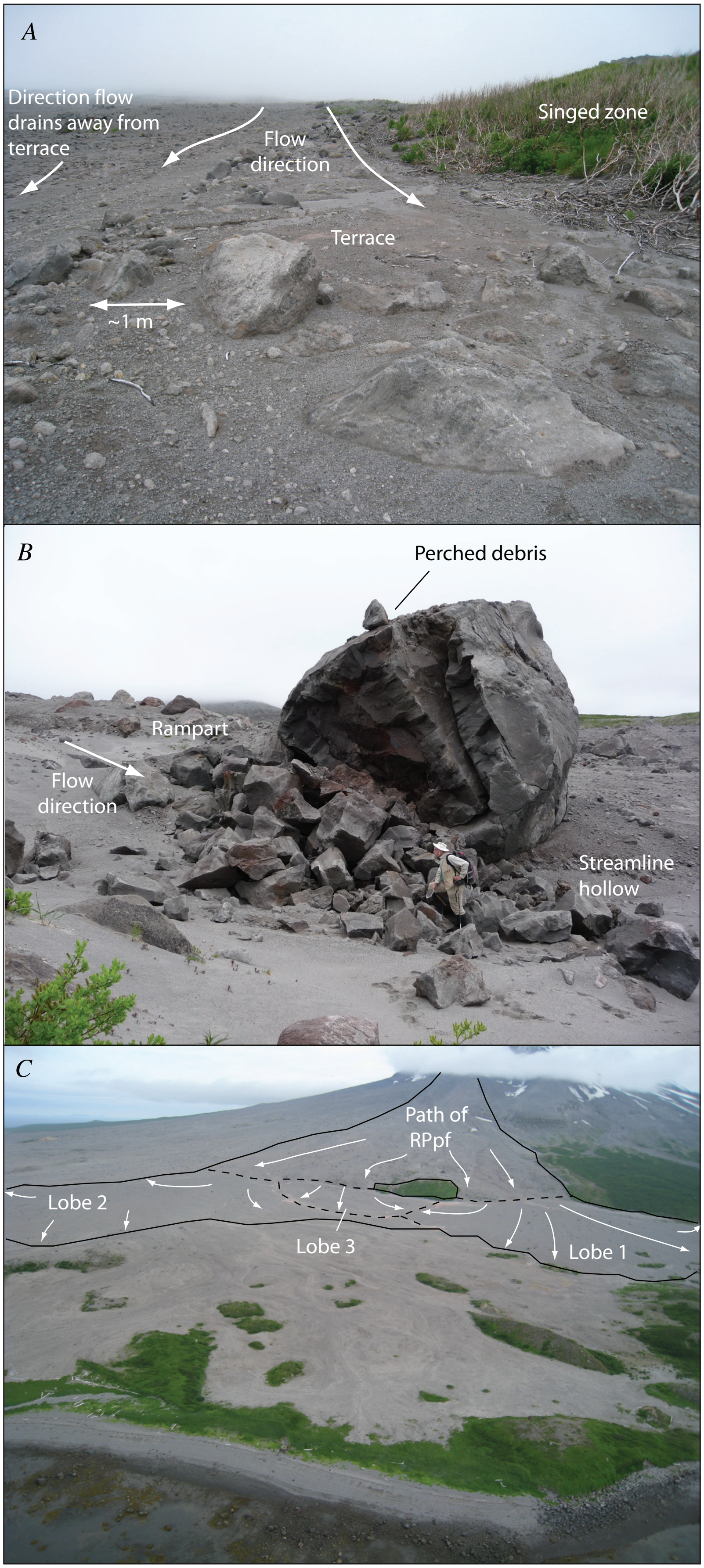

Figure 17. Photographs illustrating features of the Rocky Point pyroclastic-flow deposit (unit RPpf). *A,* Terrace formed shortly after peak flow, with subsequent channel drainaway during waning flow. *B*, Perched debris, debris rampart, and streamline hollow on this 8-m-high block suggest the following sequence: (1) flow was thick and energetic enough to move block 3 km into place; (2) subsequent flow was high enough over top of large block to leave debris; (3) waning flow formed a debris rampart and streamline hollow around block; and (4) highly fluid, waning flow drained downstream away from steep slopes, leaving thin deposits, locally less than 1 m thick. *C,* Flowpath illustrates approximate overall streamlines and three depositional lobes on low-lying apron north of volcano.

Thick fill deposits did not crop out by July 2008, intermediate ones have characteristics typical of pyroclastic flows, and thin ones have characteristics of surgelike flows. Deposits from about 0.3 to to more than 1 m thick are predominantly massive, though faintly inversely graded within their basal few centimeters (fig. 15*C*). Deposits not only thin toward lateral and distal margins but also fine (figs. 15*B*, 18*C*). Coarse deposits have modes in the coarse-ash to lapilli range, and fine marginal deposits have modes in the coarse-ash range (fig. 18*C*). Overall, the Rocky Point pyroclastic-flow deposit is relatively fines rich, containing 7 to 13 percent very fine ash, with the most fines rich parts at distal margins (fig. 18*C*).

The Rocky Point pyroclastic-flow deposit shows even more striking lithologic variations compared with earlier explosive-phase flows (units Expct and Expf) than does the coeval deposit (unit Expc). Friable high-silica andesite constitutes as much as 80 percent of clasts (excluding crystals) in most size classes, and low-silica andesite scoria generally less than 10 percent of the total (fig. 18*D*). White, high-silica andesite pumice is also a significant constituent, constituting as much as 20 percent of coarse to very coarse ash. Lapilli include significant proportions of both dense and scoriaceous low- to intermediate-silica andesite (fig. 18*D*).

Large blocks, 3 to 10 m in diameter, differ markedly in composition from lapilli and blocks smaller than about 1 m in diameter scattered on the surface of the deposit. The larger blocks that we examined consisted of uniform, intermediate-silica andesite or banded andesite. In contrast, in many areas, especially on distal fans, lapilli and smaller blocks at the surface consist predominantly of high-silica andesite. The huge blocks are probably too large to have been ejected from the vent during event 10, suggesting that this rock type originated by disruption of a dome that had grown between events 9 and 10. Smaller clasts carried on the surface to distal margins would have been emplaced last and therefore indicate the composition of the rock ejected from the vent during the last stages of event 10, after the capping domerock had been removed explosively. If these arguments are valid, event 10 disrupted a dome composed predominately of intermediate silica andesite, then tapped progressively deeper in the conduit and magma chamber to erupt high silica andesite, typical of late-stage event 10 and of the continuous-phase events that followed.

Continuous-Phase Deposits, January 28–February 10

The continuous phase began January 28 and lasted until February 10 (table 1). The first half of this phase, until about February 3, was marked by continuous emission of ash to heights below 4 km asl, punctuated by explosions that injected ash to 5 to 8 km asl (Schneider and others, 2006; Wallace and others, this volume). Direct observations of the volcano were hindered during this interval by poor weather and ashy haze, especially on the north flank (Coombs and others, this volume). Seismicity was dominated by flowage signals, which recorded the movement of pyroclastic flows down the north flanks (Power and Lalla, this volume). Fine, light-gray, massive ash deposits on the island likely represent elutriation from pyroclastic flows generated during this interval (Wallace and others, this volume). These observations, coupled with volume estimates (Coombs and others, this volume), suggest that rapid effusion of lava and dome collapse leading to numerous block-and-ash-flows dominated the early part of the continuous phase. From February 3 to 10, magma-flux rate waned, and a coherent lava flow and summit lava dome grew (Coombs and others, this volume).

The early part of the continuous phase generated pyroclastic-flow deposits (units Cpf and Cpfw) and thin pyroclastic-current deposits (unit Cpc, fig. 2*C*). Secondary flowage deposits, such as avalanches and lahars, were not identified. Lava effusion during the second half of the continuous phase probably generated small block-and-ash flows, but these were likely covered by, and indistinguishable from, subsequent effusive-phase block-and-ash flows.

Flow Morphology and General Characteristics

All pyroclastic-flow deposits of the continuous phase have similar composition, grain-size distribution, and outcrop characteristics but differ in morphology. Continuous-phase pyroclastic flows constitute thick, composite fans to the northeast and north of the summit (unit Cpf, fig. 2*C*). The Windy Creek pyroclastic-flow deposit (unit Cpfw, fig. 2*C*), however, is an anastomosing deposit on the northwest flank, which, on the basis of the timing of destruction of a seismometer on that flank (Coombs and others, this volume, fig. 15), we surmise was emplaced during a particularly large single-flow event. The continuous-phase pyroclastic current (unit Cpc) is a thin marginal facies emplaced coevally with the two pyroclastic-flow deposits described above. Unlike explosive-phase flows, continuous-phase flows were all restricted to the north quadrant of the volcano (fig. 2*C*).

The north and northeast fans of continuous-phase pyroclastic flows reach from the summit to about 100 m asl. Flows in the north fan traveled downslope between a cleaver and a prehistoric lava-dome remnant, and those in the northeast fan flowed down the Northeast Chute (fig. 2*C*). Prominent lateral-flow levees, rich in large blocks, define dozens of overlapping flow lobes, especially in the upper reaches of the fans (fig. 19*A*). The lower halves of these two fans spread out and overlap downslope of the cleaver. The lower edges consist predominantly of multiple, lobate fingers, as far as 4 km from the summit. Subdued levees define some flow margins, but elsewhere the distal lobes fan out with indistinct edges (fig. 19*B*). Although most flows traveled over unvegetated terrain, some lobes struck and singed alders near their termini. Comparison of digital terrain models of the volcano's edifice from before and after the continuous phase suggests that the two fans are as much as 20 m thick in their upper reaches (Coombs and others, this volume), whereas individual lobes are generally only as much as 2 m thick.

The Windy Creek pyroclastic flow (unit Cpfw, fig. 2*C*) was the only continuous-phase flow to travel northwestward; it fanned out over the northwest flank in a series of channels as it followed topographic lows over the somewhat-hummocky topography (fig. 19*C*), finally stopping about 50 m asl. The destruction of seismic station AU12 (fig. 2*C*) within its pathway pinpoints its emplacement at 03:24 AKST January 30 (Coombs and others, this volume). The deposit contains abundant blocks, as large as several meters across, that commonly form lateral levees alongside wide, flat-bottomed channels.

The thin pyroclastic-current deposit (unit Cpc, fig. 2*C*) is mapped in several locations as a featheredge facies of continuous-phase flows alongside margins of thicker flows, or where continuous-phase flows lap onto topographic highs. The deposit is generally less than 0.2 m thick and in some places consists only of scattered clasts of friable high-silica andesite atop the pre-2006 surface (Coombs and others, this volume, fig. 15).

Grain-size distributions in continuous-phase pyroclastic-flow deposits are similar to those in earlier pyroclastic-flow deposits, particularly the coarse explosive-phase deposits. Grain-size distribution in continuous-phase flow deposits is moderately bimodal, with modes in lapilli and medium-ash size classes (fig. 7*A*).

Continuous-Phase Compositions

The shift in eruptive style that began during event 10 continued during the continuous phase and corresponds with a shift in lithologic composition. As revealed in pebble counts and lithologic analysis, continuous-phase composition vary somewhat among individual deposits but generally the deposits are rich in high-silica andesite, dense intermediate-silica andesite, and banded clasts, with slightly less dense low-silica andesite and basically no low-silica andesite scoria (figs. 4, 19*D*; tables 6, 7).

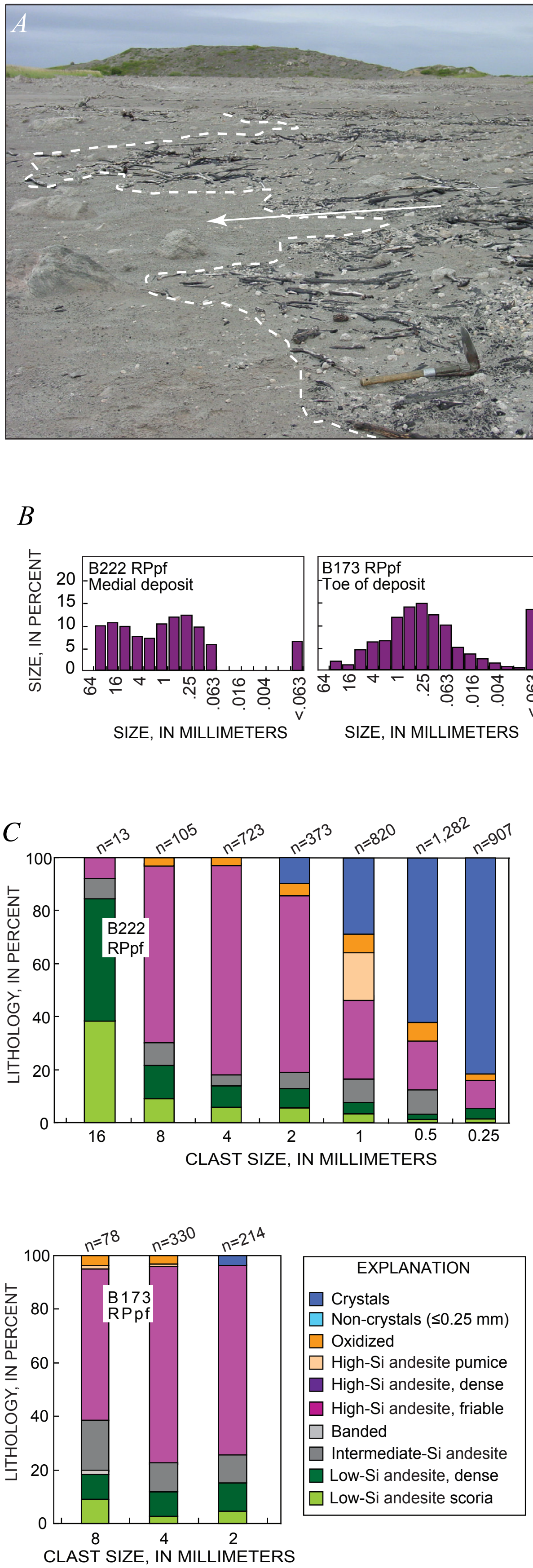

Figure 18. Rocky Point pyroclastic-flow deposit (unit RPpf), with grain-size characteristics and lithologic components. *A*, Photograph of distal-lobe margins marked by scorched willow branches and large lapilli (sample location B173). Arrow denotes the flow direction. Shovel is 50 cm long. *B*, Histograms of grain-size distribution of medial and distal deposit. Toe of deposit, which was not overlain by lobes of later flow pulses, is finer than more proximal deposits. *C*, Plots of lithologic components of the Rocky Point pyroclastic-flow deposit. Deposit contains abundant friable, high-silica andesite, a rock type also characteristic of subsequent continuous-phase deposits. Sample locations are shown in figure 2*B* and table 2.

The appearance of continuous-phase deposits shows the shift toward more silicic clast compositions: the deposits are characteristically pale brownish-pink to gray, lighter colored than the explosive- and effusive-phase deposits.

Effusive-Phase Deposits, March 3–16

The effusive phase began after an eruptive hiatus from about February 10 to March 3 (table 1). Whereas effusion of coherent lava lobes northward and northeastward began at the summit near the end of the continuous phase in early February, these lobes were enlarged during the effusive phase, and block-and-ash-flow deposits from February were buried by the products of March activity.

Effusion ultimately produced low-silica andesite in the form of a summit lava dome and two lava flows, descending northward and northeastward from the vent. As the lava emerged and became unstable, blocky material dislodged to form talus deposits, and caused rockfalls and gas release. The release of gas from the fragmenting lava generated block-and-ash flows that traveled down the north, northeast, and east flanks of the volcano (fig. 2*D*).

Talus Deposits

Aprons of rockfall deposits skirt the front of the northern and northeastern lava flows (unit Efta, fig. 2*D*). The deposits are highly oxidized, blocky, and unstable, and extend approximately 75 to 100 m beyond the lava flows (figs. 20*A*, 20*B*). These deposits were not sampled, owing to their instability and proximity to the oversteepened lava-flow fronts. We estimate the thickness of these talus aprons at 5 to 20 m.

Block-And-Ash-Flow Deposits

Block-and-ash flows were initiated from four areas: (1) the effusive-phase lava dome, (2) the front of the northern lava flow, (3) the front of the northeastern lava flow, and (4)

Figure 19. Photographs and lithogic components of continuous-phase pyroclastic-flow deposits (units Cpf and Cpfw). *A*, Continuous-phase deposit (unit Cpf) below effusive-phase lava flow (unit Eflf) on northeast flank of volcano. Thin, dark fingers of effusive-phase block-and-ash-flow deposit (unit Efba) sit atop overlapping, leveed lobes that compose deposit (unit Cpf). *B*, Distal toe of farthest-reaching part of deposit (unit Cpf) on north fan. Some distal parts of deposit lack levees and instead have featheredges. *C*, Windy Creek pyroclastic-flow deposit (unit Cpfw). Flow swept around and over topographic highs on northwest flank, with little deposition on steep lee slopes. *D*, Plot of lithologic components of deposit. Sample locations are shown in figure 2*C* and table 2.

the top and margin of the northeastern lava flow, which then traveled down East Chute (fig. 2*D*). The block-and-ash flows formed distinctive black, blocky, narrow tongues that are visible beyond the apron of varying and jumbled talus blocks (unit Efba, figs. 2*D*, 20*C*, 20*D*). The long, lobate deposits commonly have blocky levees. The northeastern block-and-ash-flow deposit is estimated to average 6 m in thickness, whereas the others average less than 3 m. Grain-size characteristics of this block-and-ash-flow deposit suggest concentrations of coarse lapilli and coarse ash and an absence of fine ash (fig. 2*E*).

Lithologic analyses indicate that effusive-phase pyroclastic-flow deposits contain significantly more low-silica andesite clasts than do either explosive- or continuous-phase deposits (figs. 4, 20*F*). Very few of these low-silica andesites are scoriaceous. The effusive-phase deposits also contain small to modest proportions of intermediate- and high-silica andesite (figs. 4, 20*F*). Hydrothermally altered and oxidized clasts are more common in effusive-phase block-and-ash-flow deposits than in the pyroclastic-flow deposits of other phases. Huge blocks of oxidized material, as large as several meters across, are common in outcrop.

Discussion

Lithologic Composition and the Three Eruptive Phases

Our field observations in August 2006 quickly revealed that the three eruptive phases were unique, not only in terms of style of volcanism, including associated seismicity, geodetic response, and ash emissions, but also in terms of the types and morphologies of deposits that were produced and, in particular, of their lithologic composition (fig. 4). Two important characteristics were revealed through lithologic analysis of the 2006 flowage deposits: (1) each lithology is present in the deposits of each eruptive phase and in each flow type, and (2) the lithologic proportions are unique to and consistent in the deposits of each eruptive phase.

Lithologic analysis reveals systematic changes in magma composition and clast texture during the 2006 Augustine eruption. Deposits of the three eruptive phases varied in composition and clast type, although a single rock type or group of rock types dominated each phase (figs. 4, 21, table 7). Thus, the explosive phase predominantly produced low-silica andesite, mostly as scoria, but also as 10–20 percent dense clasts; the continuous phase predominantly produced high-silica andesite and lesser intermediate-silica andesite and banded clasts, with clasts of all compositions varying in vesicularity; and the effusive phase produced an even higher proportion of low-silica andesite than the explosive phase, mostly as nonvesicular to sparsely vesicular clasts. Most clasts larger than 1 cm in diameter in effusive-phase block-and-ash flows are low-silica andesite (fig. 21).

Lithologic transitions coincided generally, but not exactly, with shifts in style of volcanism as marked by the three eruptive phases. Explosive-phase deposits of events 3 through 9 (Jan. 13–17) are lithologically similar, whereas event 10 (Jan. 28) yielded two flows whose lithologic composition differed from that of flows erupted earlier. The 9-minute explosion generated the pyroclastic-current that draped the north-slope lava flow and the voluminous Rocky Point pyroclastic flow, marking not only a transition from intermittent vulcanian explosions to continual dome collapses, but also a compositional transition within pyroclastic deposits from primarily scoriaceous, low-silica andesite to primarily friable, high-silica andesite (table 5). This compositional shift began the transition from the explosive to the continuous phase.

Disruption of two lava domes that had grown before event 10 (between Jan. 13 and 27) probably influenced the compositional shift, particularly in dense rock types, within event 10 pyroclastic deposits, but the tapping of a deeper, more silicic magma caused the most striking lithologic shift (figs. 4, 21, table 7; Larsen and others, this volume). The older dome (unit Exd1, fig. 2*A*), emplaced January 14–17, and shallow residual magma in the conduit are two possible sources of the dense, low-silica andesite clasts within the event-10 deposits, the pyroclastic current (unit Expc) and Rocky Point pyroclastic-flow (unit RPpf. A younger, explosive-phase lava dome (unit Exd2, figs. 2*A*, 21), composed of intermediate- to high-silica andesite and banded andesite, was extruded between events 9 and 10 (Jan. 17 and 27). Disruption of this younger dome may have generated the huge intermediate-silica andesite blocks within the Rocky Point pyroclastic flow and partly caused the increases in dense high-silica andesite within the deposits of both event 10 pyroclastic deposits. We conclude that pulverization of the domes caused increases in nonvesicular magma, resulting in inclusion of dense clasts in event 10 ejecta. Concentrations of more vesicular high-silica andesite within the Rocky Point pyroclastic-flow deposit, especially in distal areas and on the deposit surfaces, originated from the vent last and indicate the tapping of a deeper, more silicic magma body during event 10 that continued during the continuous phase (Larsen and others, this volume).

The proportions of low- to intermediate- to high-silica andesite in clastic deposits changed abruptly during event 10, at the start of the continuous phase, and again after the hiatus that preceded the effusive phase (figs. 4, 21). These trends heralded changes in eruption rate, magma composition, and gas content. During the explosive phase before event 10, proportions were about 70:15:15. During event 10 proportions showed a rapid change to 38:27:35 and then to 20:15:65. Subsequently, pyroclastic-flow deposits emplaced during the continuous phase contained no scoria, but enough dense low-silica andesite to change proportions to approximately 25:35:40. Probably, the magma had become sufficiently gas poor and had extruded slowly enough that no vesicular low-silica andesite ejecta formed, and fewer than a third of the ejecta were composed of dense, low-silica andesite. During

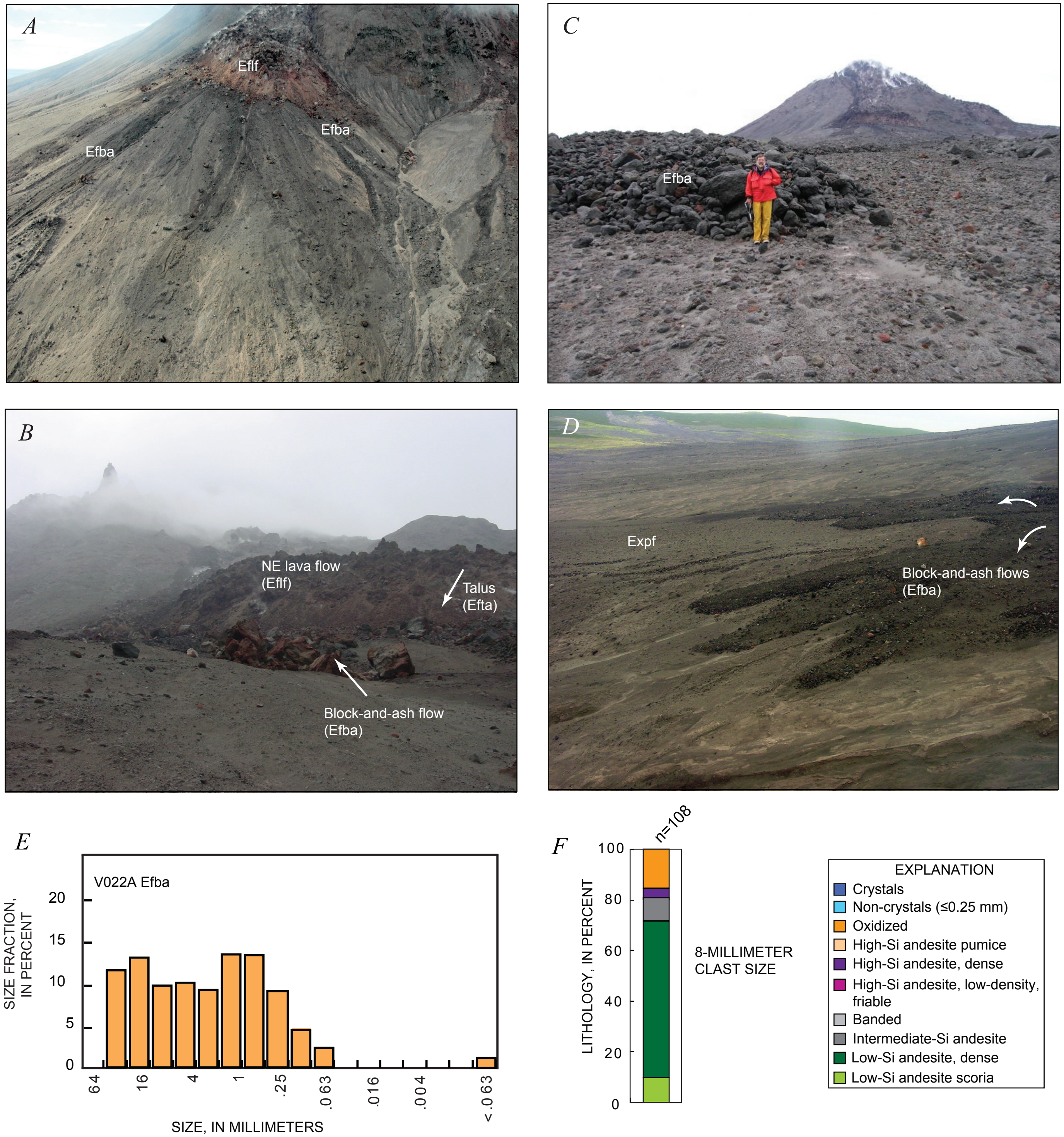

Figure 20. Photographs, plot of grain-size distribution, and lithologic components of effusive-phase block-and-ash-flow deposit (unit Efba). *A*, Aerial view south towards effusive-phase block-and-ash-flow deposit (unit Efba) and lava flow (unit Eflf). *B*, View of the northeast lava flow (unit Eflf), rockfall talus apron (unit Efta) below lava, and short block-and-ash-flow deposit (unit Efba). *C*, Distal margin of block-and-ash-flow deposits (unit Efba). *D*, Oblique aerial view of distinctive black block-and-ash-flow deposits in East Chute area. These deposits resulted from fracturing and collapse of parts of new lava flow. *E*, Grain-size distribution of block-and-ash-flow deposits. *F*, Plot of lithologic components of block-and-ash-flow deposit. Sample locations are shown in figure 2*D* and table 2.

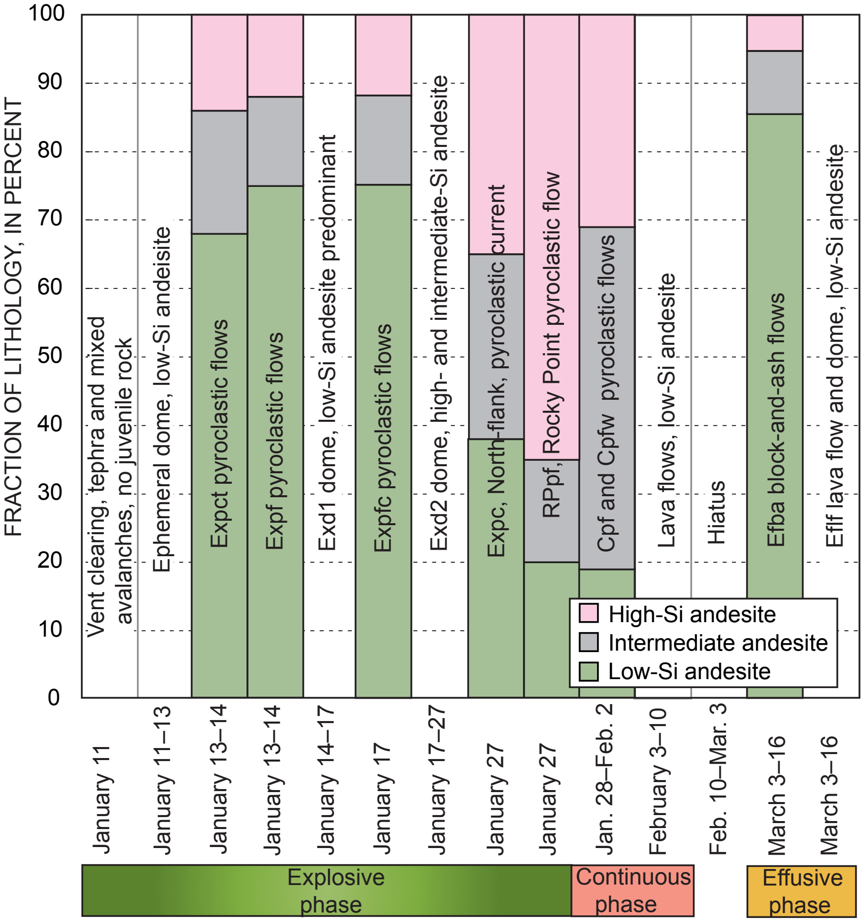

Figure 21. Plot summarizing chronologic changes in chief lithologic components in deposits of 2006 eruption of Augustine Volcano. Proportion of low-silica andesite, initially high, diminished at end of explosive phase and during continuous phase as proportion of intermediate- and high-silica andesite increased. These trends reverse from continuous phase to effusive phase. Low-silica andesite increased during the effusive phase and changed from being predominantly scoriaceous during the explosive phase, to predominantly dense during the effusive phase.

the continuous phase, proportions of both intermediate- and high-silica andesite increased significantly.

Banded clasts, which include any combination of compositions, most commonly compose bands of high- and low-silica andesite (table 4; Larsen and others, this volume). The proportions of banded clasts in the deposits varied widely but were largest in continuous-phase deposits (fig. 4), suggesting that mixing of low- and high-silica andesite magmas was common throughout the eruption but probably greatest during the continuous phase. Larsen and others (this volume), interpret the intermediate-silica andesite to be the product of complete mixing between high- and low-silica andesitic magmas.

Effusion of low-silica andesite lava began before the end of the continuous phase and continued during the effusive phase, producing block-and-ash flows predominantly composed of dense, low-silica andesite, sparse scoria, and about 13 percent high-silica andesite (figs. 4, 21, table 7). Larsen and others (this volume) suggest that the waning stages of the continuous and the effusive phase extruded the last dregs of eruptible high-silica andesite magma along with low-silica andesite lavas. High-silica andesite clasts in block-and-ash flows derive from inclusions of such material within the lava flow itself or from erosion and incorporation from underlying, continuous-phase pyroclastic-flow deposits.

Origin and Downslope Behavior of Pyroclastic Currents and Flows

During the 2006 eruption of Augustine Volcano, the chief factors that influenced pyroclastic-flow behavior and the nature of their deposits were genesis, grain size, and the characteristics of the surface over which they flowed. Column collapse from short-lived vulcanian blasts, dome collapse, and the collapse of viscous lavas on steep slopes caused the pyroclastic currents documented in this study.

Column-collapse flows during the explosive phase spread widely and probably were dilute and laterally mobile where they overran snowpack. Subsequent flows had similar fines content but were confined to drainages. This change in flow morphology occurred once previous pyroclastic flows had either melted the snowpack or coated the snow with layers of pyroclastic debris sufficiently thick to insulate new flows from the underlying snow. In contrast, the dome-collapse Rocky Point pyroclastic flow and the continuous-phase flows involved neither column collapse nor the influence of underlying snow. Only the Rocky Point pyroclastic flow, possibly because it was more voluminous and finer grained than subsequent flows, showed evidence of appreciable dilution as it moved. The dome failure that generated the large-volume

Rocky Point pyroclastic flow may have been deeper seated than subsequent dome-collapse flows, thereby unloading incompletely degassed lava that decompressed explosively to inflate the initial pyroclastic mass. The subsequent continuous-phase flows behaved as partially fluidized granular flows. In contrast, effusive-phase block-and-ash flows were caused exclusively by collapses of andesite lava-flow margins. These block-and-ash flows, though hot, were sufficiently coarse and permeable that gas escaped rapidly and lapilli and blocks were mostly supported by particle-to-particle contacts. These flows behaved basically as rock avalanches because their ash-and-gas mixture provided little fluidization to ameliorate their frictional-granular characteristics.

Formation of Levees and Digitate Margins During Pyroclastic-Flow Emplacement

Scoria-rich column-collapse flows of the explosive phase, dome-collapse flows of the continuous phase, and block-and-ash flows of the effusive phase all behaved similarly, regardless of their diverse origins, to produce deposits with coarse blocky levees and digitate distal margins, a morphology indicative of partially fluidized, granular flows with high solids fractions (fig. 22). Some of these pyroclastic flows may have been highly energetic on steep slopes near their source, but as they descended the volcano's slopes, hot particle and gas mixtures settled to form granular basal flows that moved across intermediate and gentler slopes of the volcano's apron. Overriding, elutriate ash clouds (fig. 5*A*) would have obscured basal granular flows. Once the pyroclastic flows began to decelerate, large, low-density particles began to migrate to the surfaces of the basal granular flows (figs. 9, 22*A*). The surface velocities of such granular flows are greater than those of propagating flow fronts; thus, particles at the surface migrate toward distal and lateral margins, where they accrete particle by particle, and then lag behind the moving flow to form levees (fig. 22*B*; for example, Lube and others, 2007). Fines-poor aggregations of outsize low-density particles that accrete at active flow fronts influence the behavior of the granular flow in two ways. First, because the largest particles in natural grainflows are commonly more angular than smaller ones, the coarse mixture at the front of flows may develop a greater Coulomb friction than in the finer following flows (Pouliquen and others, 1997). Second, coarse mixtures that form at flow margins are generally more permeable than finer interior flows. Because fluid, in this case gas, can more readily escape from the coarse and, therefore, permeable flow fronts than from the relatively less permeable ash-rich flows that follow, flows evolve Coulomb-friction-dominated perimeters that encompass fluidized or partially fluidized interiors, for example, in debris-flow systems (Iverson, 1997). More mobile debris that pushes a perimeter of less mobile debris results in unstable flow and the formation of large-particle-rich clefts and lobes at propagating flow fronts (Pouliquen and Vallance, 1999). When such partially fluidized, granular pyroclastic flows come to rest, they preserve clefts, lobes, and finger-shaped bifurcations as digitate deposit margins that are relics of granular-flow instabilities (fig. 22*A*).

A similar segregation process can occur with low-density particles and cause cleft-and-lobe structures. Vallance and Savage (2000) show that density segregation, though dependent on a different sorting mechanism than size segregation, is highly efficient in the upper parts of granular flows. Thus, if a flow contains large, low-density particles, such as pumice or scoria, these particles will migrate to the surface, where velocities are highest, and then move toward flow margins. If the perimeter thus formed is more frictional than the interior flow, a flow instability results, and the flow breaks into clefts and lobes. Again, the mechanism depends on the granular character of the flow; however, optimal density segregation occurs in more energetic granular flow than does optimal size segregation (Vallance, 1994; Vallance and Savage, 2000).

In such natural phenomena as pyroclastic flows, the granular material traps gas, which, if it cannot readily escape, partially supports the weight of the particles. The medium is then partially fluidized and thus flows more easily downslope. Pouliquen and Vallance (1999) modeled such flows in the laboratory by pouring aerated 500°C ash or sand down an inclined surface. The granular, sediment-rich basal avalanches control the behavior of these flows. Segregation of large, low-density particles that initially move upward and then toward flow fronts, as well as elutriation of small particles at flow fronts, ultimately forms coarse, permeable perimeters that are dominated by Coulomb friction (Pouliquen and Vallance, 1999). Consolidation of solids and entrapment of gas generate fines-rich flow interiors that are partially fluidized (Pouliquen and Vallance, 1999, fig. 7). As the flows slow and eventually come to rest, frictional contrasts with the bed—large at the flow perimeter and small in the fluid flow interior—cause flow instabilities that commonly result in digitate deposits similar to the flow fingers observed at Augustine Volcano in 2006 (fig. 22).

Behavior of Energetic Pyroclastic Currents—Implications for the Generation of Their Deposits

The initial pyroclastic-flow deposits of the explosive phase, and those from a vigorous dome collapse during event 10, share characteristics which indicate that they were energetic and diluted by gas ingestion as they moved. Such features include widespread, but thin, deposits; gradual thinning of deposits at lateral and distal margins and an absence of lateral or distal levees; the presence of large blocks in thick axial deposits and the absence of such blocks near margins; the presence of deposits on topographically high areas; evidence of vigorous elutriation, such as fines-deficient "lag" deposits and cogenetic fine marginal deposits; and temperatures insufficient to burn vegetation or completely melt underlying snow. On the basis of the deposits that these dilute, energetic flows produced, the most important processes are settling of large and dense blocks into thick, fluid axial parts

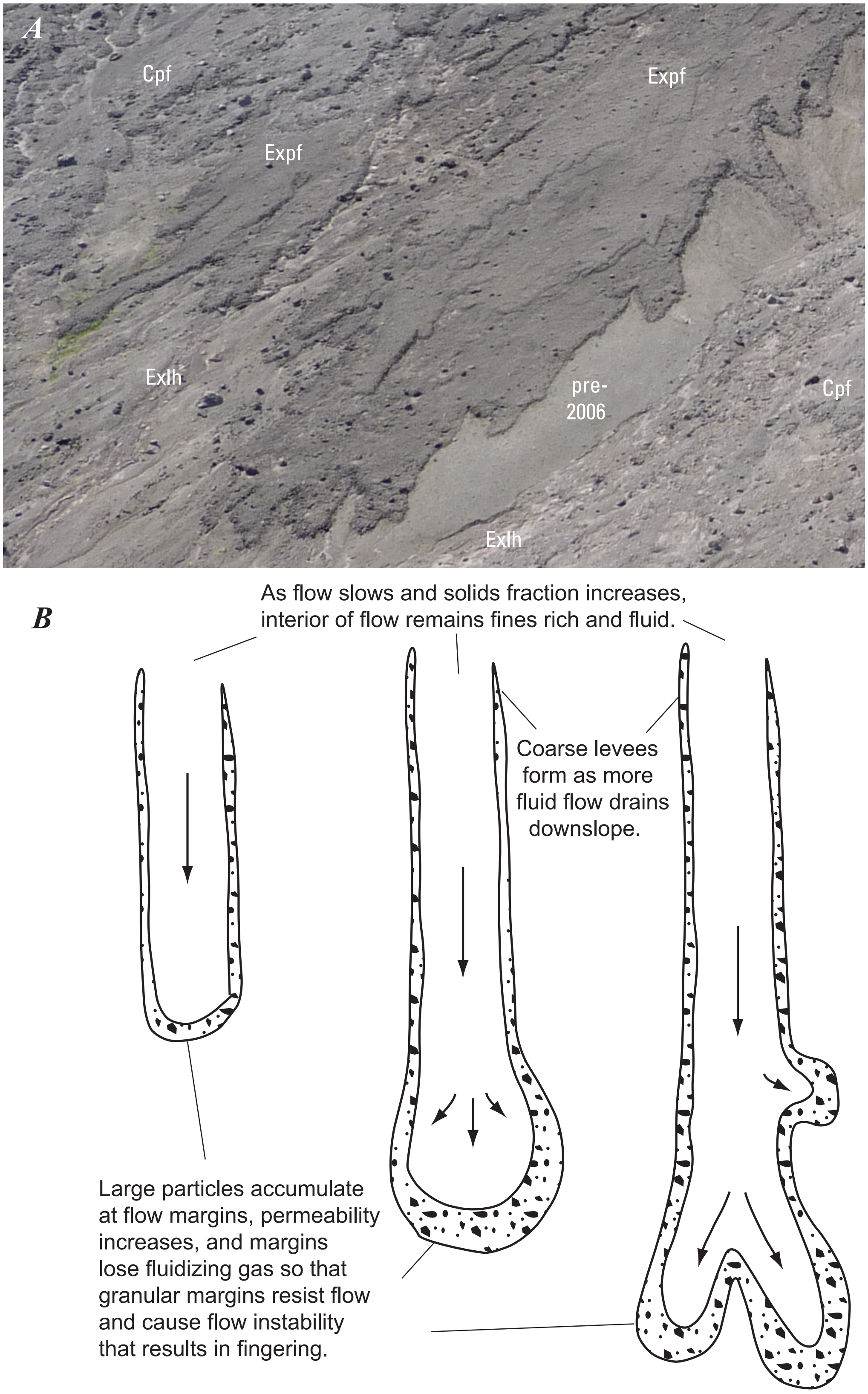

Figure 22. *A,* Oblique aerial photograph of part of northeast fan, showing coarse blocky digitate margins of explosive- and continuous-phase pyroclastic-flow deposits (units Expf and Cpf). *B*, Line drawing illustrating evolution of fingering in moving pyroclastic flow.

of the flow; elutriation of fine ash to form proximal lag facies and marginal fine surges, and a propensity to spread laterally, especially across snow-covered slopes. Each of the three types of explosive-phase deposit documented in this study exhibit some, but not all, of these features.

The Rocky Point pyroclastic flow originated as a large dome collapse that probably caused a sudden depressurization of deep-seated lava; it then evacuated the entire conduit and must have tapped into a magma "chamber" at 4- to 6-km depth. The collapse and decompressively vesiculated conduit magma generated a surge-like flow whose deposits fine and taper to thin margins, despite the enormous blocks contained in axial zones. The deposit shows notable drainaway features, such as stranded terraces (fig. 17*A*), matrix debris perched on blocks whose tops reach 8 m above the deposit surface (fig. 17*B*), and pre-2006 scarp surfaces that protrude through axial, meters-thick deposits lying on gentler slopes in adjacent areas. Cole and others (2002) described voluminous pyroclastic-flow deposits at Montserrat that originated from dome collapse and share many characteristics with the Rocky Point pyroclastic-flow deposit. For example, the Montserrat deposits also contain large blocks with matrix debris perched on their tops, indicating flow depths greater than local deposit thicknesses. Similarly, ridge-and-swale features, concentrations of low-density clasts, and tree fragments characterize distal zones. In the Rocky Point pyroclastic-flow deposit, we additionally noticed pyroclastic debris ramparts piled up on the stoss sides, and streamline hollows on the lee sides, of large blocks that had been grounded on steep slopes early in the depositional sequence (fig. 17*B*). Cole and others (2002, fig. 22) inferred that as these sheetlike flows decelerated, the upper parts of the flow drained downslope to form tapering, distal deposits with concentrations of low-density particles at their surface. On gently sloping fans, swales (inappropriately called furrows by Cole and others) are radially oriented parallel to flow but exhibit subordinate anastomosing patterns that divide and truncate the gently sloping ridges parallelling them. The large blocks are distributed 100 to 500 m inboard of the deposit margins situated both on ridges and in swales. We infer that the complex anastomosing swale patterns were paths followed by the most fluid pyroclastic debris as it drained away from material slightly more resistant to flow along ridges, while simultaneously following predominantly radial flow directions. On the basis of their characteristics, we concur with Cole and others (2002) that large dome-collapse pyroclastic flows like those at Montserrat and Rocky Point moved as a sheetlike body that drained away downslope, stranding huge blocks along slopes and fan apices. When it reached low-gradient slopes, the flow accreted incrementally at fan apices to form ~10-m-thick accumulations, and the overriding flow pushed downslope to produce fines-rich deposits, rich in low-density particles, that thin gradually toward distal margins.

The distribution and characteristics of the pyroclastic-current deposit (unit Expc, fig. 2*B*) suggest that it was the energetic product of laterally directed explosions at the beginning of event 10. Its deposit is similar to initial explosive-phase pyroclastic currents (unit Expct), but differs notably in its ubiquitous friability, mostly lacking fine matrix particles, and its distribution across the axis of a 50- to 100-m-high ridge. Even though it flowed across snowy slopes, the pyroclastic current did not generate lahars. The deposit at distal margins fines and tapers to thin edges. We infer that this deposit was emplaced by a surge-like flow because of its distribution on a high ridge and its lack of fine particles. Explosions directed northward at the beginning of event 10 probably initiated the pyroclastic current.

Initial pyroclastic flows of the explosive phase (unit Expct, fig. 2*A*) invariably flowed across snowpack, scoured it, and commonly came to rest on snow; thus, this underlying snow, rather than conditions at the vent, chiefly controlled both flow behavior and deposit characteristics (fig. 23). Deposits preserved on top of snow suggest that flows had cooled significantly to near-ambient temperatures during transit. This observation implies considerable heat transfer because pyroclasts exited the vent at temperatures in excess of the solidus temperature (Larsen and others, this volume). We infer that ingestion and vaporization of snow fluidized the flows so that the resulting deposits are widespread, commonly thin, and thin toward their lateral margins but do not fine there. Unlike the Rocky Point pyroclastic-flow deposit, these deposits rarely are more than 1 m and commonly only 10 to 20 cm thick (fig. 5*B*). Because the flows originated by column collapse of short-lived vulcanian plumes rather than by dome collapse, they did not carry outsize blocks. Blocks smaller than 1 m across are scattered across deposit surfaces, even near margins (fig. 5*C*). Where emplaced on windswept snow-free terrain, the deposits are smooth surfaced and thin toward margins. These deposits' distal margins rarely are preserved because distal parts of the deposits generated lahars and mixed avalanches. The evolution and behavior of these flows across snow are discussed in more detail below.

Behavior of Pyroclastic Flows Across Snow and the Evolution of Mixed Avalanches and Lahars

Theoretical analysis and experimental results by Walder (2000a,b) suggest a mechanism whereby initial pyroclastic flows can spread across snowpack and generate mixed avalanches and lahars. Pyroclastic flows can erode substrates formed of snow or ice through a combination of mechanical and thermal processes at the bed. Walder shows both theoretically (2000a) and experimentally (2000b) that thermal scour can effectively incorporate snow at the base of a pyroclastic flow. The fundamental cause of thermal scour is unstable fluidization of the pyroclast layer by a brief, intense burst of vapor at the instant when hot grains contact snow that involves vapor bubbling and particle convection which disrupt the snow surface (Walder, 2000b). The analysis shows that an upward flux of water vapor immediately upon pyroclastic-flow contact with snow can be great enough to fluidize the pyroclastic layer efficiently under the proper conditions. Those conditions are a function of emplacement temperature, overburden pressure or pyroclastic-flow thickness, and grain size, as illustrated in figures 24*A* and 24*B*. If vaporization is sufficient, hot pyroclastic material is efficiently mixed with underlying snow, and melting is enhanced. The tendency toward fluidization at the interface can enhance both the mobility of a pyroclastic flow and its ability to form slurries of snow, water, and pyroclastic material that may later coalesce and flow downstream. Increase in temperature and decrease in grain size favor fluidization at the interface, but the relation to overburden pressure is more complex. Overburden pressure at the interface enhances fluidization to a point where total load is too great and then suppresses the process (fig. 24*A*).

We can approximately constrain the overburden pressure P for Augustine flows by using deposit thickness, solids fraction, and rock density as proxies in calculating values for the actual flow, such that $P = \nu\rho_{\mathrm{rock}}gh$, where the solids fraction ν of the deposit is about 0.4 to 0.5, the density of the rock ρ_{rock}

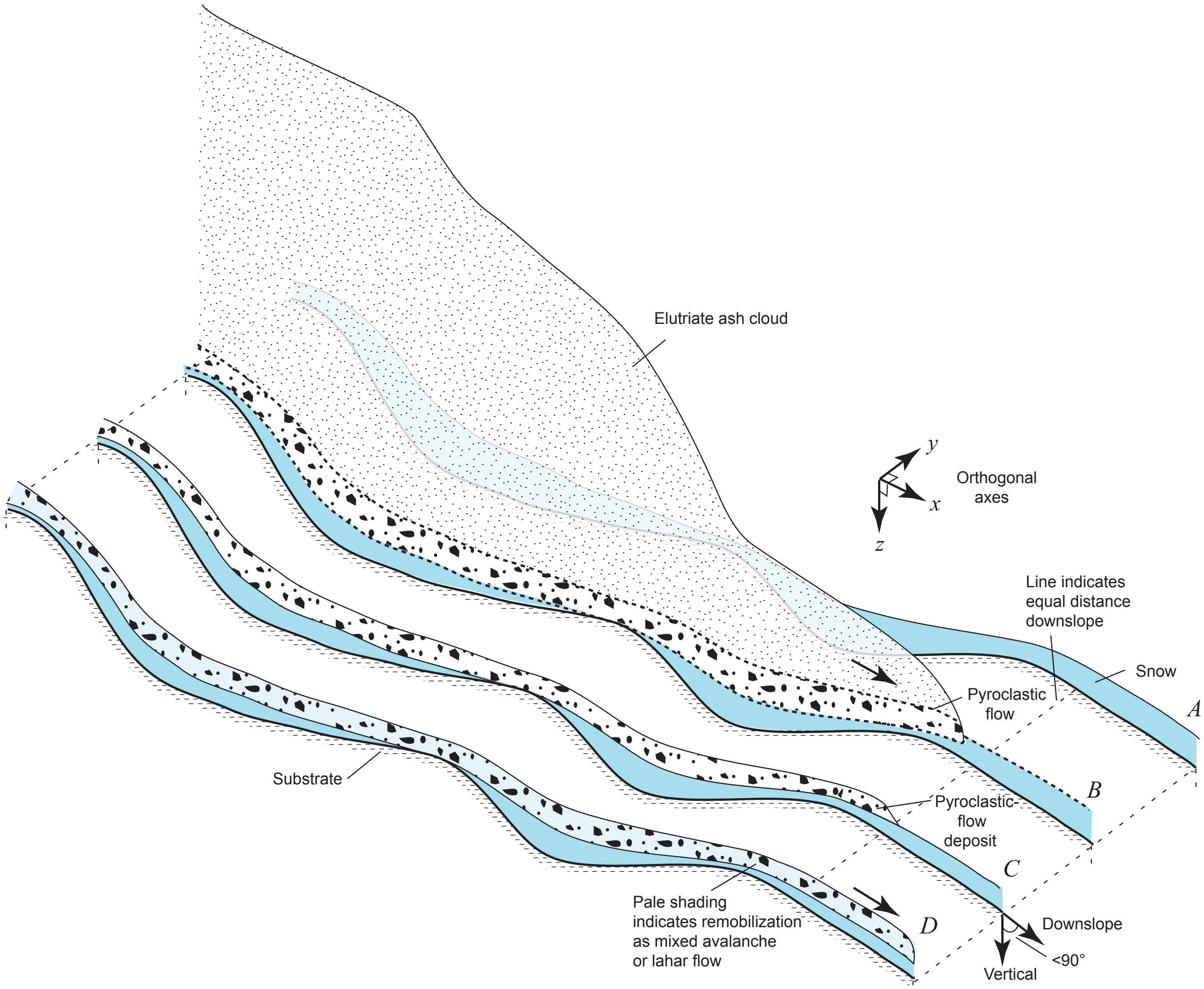

Figure 23. Schematic sketches of successive stages in the interaction of a pyroclastic flow with snow. *A,* Initial snow-covered slope. *B*, How a pyroclastic flow might move across snow, partially eroding and incorporating it. *C,* The pyroclastic flow stops briefly or decelerates almost to a stop. *D*, Finally, a mixture of snow, water, and pyroclastic debris begins to move and forms mixed avalanches (or lahars). Field evidence supports either sequence *A–B–D* or *A–B–C–D* but cannot distinguish whether pyroclastic flows come to a complete stop before initiating mixed avalanches or merely decelerates. Once in motion, mixed flows likely contain hot or warm pyroclastic debris, especially large particles, which can continue to convert snow to water through heat exchange, allowing the mixture to become progressively wetter with distance downstream.

is 1,600 to 2,600 kg/m^3, g is the gravitational constant, and h is the deposit thickness. Vaporization of snow dilutes moving flows, so that flow depth would have been greater than the thickness of deposits, but the solids fraction would probably have been correspondingly smaller, and so our simple calculation is not unreasonable. A further assumption is that the gas phase largely supports the pyroclasts, so that hydrostatic and total pressures are approximately equal. This assumption implies that the flow is fully fluidized—basal fluid pressure would diminish in the degree to which fluidization is partial. Our estimated P values for the initial thin pyroclastic current (unit Expct, fig. 2*A*) that initiated mixed-avalanche and lahar flows, using h = 0.1–0.2 m, are about a tenth (0.6–2.5 kPa) of those for subsequent flows; they appear to lie in the field where fluidization is favored (figs. 24*A*, 24*B*). The subsequent flows (unit Expf, fig. 2*A*) yield estimated overburden pressures that may fall in the field of suppressed fluidization where P = 8–20 kPa and h = 1–2 m (fig. 24*B*). Fine-grained pyroclastic flows are more apt to fluidize snow substrates than are coarse-grained flows—in fact, within reasonable, pyroclastic-flow temperature ranges of 300–800°C, grain size is a more important factor than temperature for inducing thermal scour (figs. 24*A*, 24*C*). Our grain-size data show that the initial thin pyroclastic current (unit Expct), which was generally finer grained than those that followed, falls in a field favorable to thermal scour of snow and coeval fluidization (fig. 24*C*). Lastly, we note that tephra-fall and pyroclastic debris from previous eruptions insulated underlying snow from subsequent flows (fig. 5*A*), greatly diminishing their facility for efficient thermal scour or fluidization.

Initial pyroclastic flows of the explosive phase invariably generated lahars and mixed avalanches, but some of these secondary flows were wetter and more laharic than others. Apparently, the resulting mixtures were sensitive to the available proportions of hot pyroclast material and snow. On the east side of the volcano, secondary flows were quite watery, and recognizable mixed-avalanche deposits are small or absent. In contrast, on the south side of the volcano, mixed-avalanche deposits predominate in medial reaches and form extensive marginal terraces and axial islands in distal reaches, as illustrated in Augustine Creek (figs. 2*A*, 13).

On the basis of field observations, our conception of how pyroclastic flows moving over snow generate slurries of snow, water, and pyroclastic material and how these mixtures behave downstream is illustrated in figures 23 and 25. Once a pyroclastic flow is in motion, it scours substrate snow thermally and mechanically, converting some snow to vapor and some to water. Our field data cannot constrain whether slurry mixtures begin to move while pyroclastic flows remain in motion (sequence *A–B–D*, fig. 23) or whether pyroclastic flows come to a complete stop, and then the wettest parts of slurries break away (sequence *A–B–C–D*, fig. 23)—each scenario is possible, given local conditions. We envision that moving slurries contain hot pyroclastic blocks and lapilli that transfer their heat more slowly than smaller particles and continue to melt remaining snow in slurries as they move. Thus, slurries that contain significant amounts of snow are likely to become progressively more water-rich downstream. The wettest parts of the slurries will be the most mobile, and such parts will coalesce where drainages join downstream. Flows that contain little snow will behave like lahars, segregating both large and low-density particles to their surfaces and margins and forming bouldery levees as they flow downstream (fig. 12*A*); however, those flows that contain significant amounts of snow will also segregate low-density snow toward their margins (fig. 25). By this process, mixtures that contain substantial

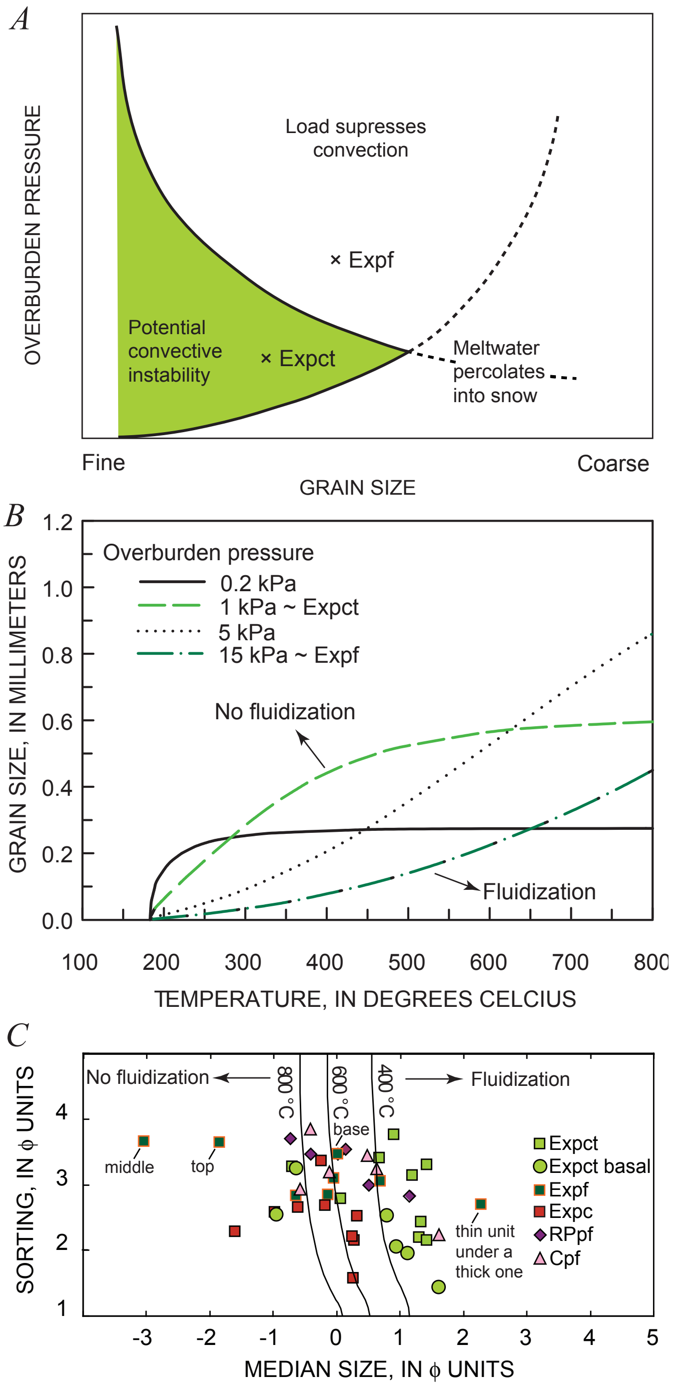

amounts of snow and move significant distances downstream can generate both snow-rich, marginal flows that slide across surfaces protected by snowpack, and water-rich axial flows that scour channels and are mainly laharic (fig. 25). The sliding marginal flows, like those in Augustine Creek (fig. 13*A*), preserve vegetation under snowpack, destroy exposed vegetation, and form marginal mixed-avalanche deposits that become draped over vegetation and are littered with shattered branches (figs. 11*A*, 12*A*). The cogenetic, water-rich axial flows scour their beds and leave trails of stripped vegetation and scattered boulders in their wakes (fig. 12*A*).

Relation Between Volume and Planimetric Area for Pyroclastic Flows and Surges—Implications Concerning Mobility

On the basis of simple dimensional analysis, we expect that planimetric area, *A*, will scale with deposit volume, *V*, to the two-thirds power for granular mass flows of similar origin with sudden onset. We see that $V = h_{ave}A$, where h_{ave} is the average deposit thickness. For lahars Iverson and others (1998) argued that $h_{ave} \approx \varepsilon A^{1/2}$, where ε is a constant and the deposits are dominantly tabular and thin relative to their lateral dimensions (that is, ε is a small constant). Substituting this approximation into the first equation gives the desired relation, $A = cV^{2/3}$, where c is a hypothetical constant, such that $c = \varepsilon^{-2/3}$ (Iverson and others, 1998). Iverson and others demonstrated the validity of this relation statistically by calibrating c with data from lahars. Dade and Huppert (1998) showed a similar relation to be true for debris avalanches, and Griswold and Iverson (2007) demonstrated such relations for nonvolcanic debris flows and rock avalanches. Finally, Calder and others (1999) and Widiwijayanti and others (2009) suggested such a relation for pyroclastic flows from the recent eruptions of Montserrat and Merapi.

◀ **Figure 24.** Plots that show how overburden pressure, temperature, and grain size influence potential for convective instability that favors erosion and entrainment of snow by pyroclastic flows moving across snowpack (from Walder, 2000b). *A*, Schematic plot of overburden pressure versus grain size, showing how decrease in grain size favors convective instability. Relation of overburden pressure to such instabilities is more complex. Increasing pressure increases likelihood of snow entrainment until load becomes too great and instability is suppressed. *B*, Isobaric plots of grain size versus temperature, showing field of snow fluidization and suppressed fluidization. We estimated likely overburden pressures of 2006 Augustine pyroclastic flows on their substrate by using explosive-phase-deposit parameters as proxies. Thus, pressure $P \approx \nu\rho gh$, where ν is solids fraction of deposit, ρ is rock density, g is gravitational constant, and h is deposit thickness. Such a calculation assumes that fluidizing gas supports weight of particles. Incomplete fluidization would diminish actual overburden pressure. Our estimated P values for initial thin pyroclastic-current deposit (unit Expct) that initiated mixed-avalanche and lahar flows are about a tenth of those for subsequent pyroclastic-flow deposits (unit Expf) and appear to lie in field where fluidization is favored. Subsequent flows yield estimated overburden pressures that may suppress fluidization. *C*, Isothermic boundaries between fluidization and its inverse on our sorting-versus-median-ϕ-size data for 2006 Augustine pyroclastic flows. Grain-size characteristics of initial flows (unit Expct) plot in field where fluidization is more likely than for those of subsequent flows.

We hypothesize here that log-log plots of planimetric area versus volume for pyroclastic-current deposits with similar origins and characteristics will fall along linear trends, such that $A = cV^{2/3}$, where c is a constant for similar groups of flows. To test and calibrate this relation, we analyzed trends in pyroclastic-current inundation data from Soufrière Hills Volcano, Montserrat (Calder and others, 1999; Druitt and others, 2002 a), Mount St. Helens in 1980 (Rowley and others, 1981), Merapi Volcano, Indonesia, in 2006 (Charbonnier and Gertisser, 2008), and Augustine Volcano in 2006 from this study (fig. 26*A*). We find considerable scatter among the data for pyroclastic-current deposits relative to those for lahars, rockfall avalanches, and volcanic debris avalanches (fig. 26*B*). Pyroclastic currents generally yield more widely varying data because such currents have diverse origins and behavior. Some currents, such as surges (Druitt and others, 2002a; Loughlin and others, 2002), are dilute and more mobile than others that are granular. Some currents have highly energetic origins at the vent, and others begin as simple gravitational collapses of domes and lava flows (Druitt and others, 2002b). Finally, some currents have a sudden onset, and others erupt continuously over significant time periods. In our analysis, we consider only currents that have a sudden onset, because the condition of continuous pyroclastic-current production violates the assumptions in the model presented here (Iverson and others, 1998). Our plot (fig. 26*A*) suggests grouping pyroclastic-currents into three flow types on the basis of mobility and, coincidentally, origin: (1) dome-collapse flows, (2) column-collapse flows, and (3) energetic surge-like flows. We obtain regression-line and two-thirds-slope correlations with large coefficients of determination, meaning positive correlations between planimetric area and deposit volume, for each flow types; however, we consider the correlation for the third type to be quite tentative because it includes only four data pairs (table 8). We tested whether best-fit regressions differ significantly from specified two-thirds-slope fits and observed that they do not differ significantly (table 8). In contrast, best-fit regressions do differ significantly from zero-slope fits for all three types, implying that the null hypothesis of no correlation between planimetric area and deposit volume must be rejected. Our statistical analyses of data for dome-collapse and column-collapse flows support our hypothesis that planimetric area *A* varies with $V^{2/3}$. We tentatively advance a similar relation for energetic surgelike flows but suggest that such a relation needs further testing with data.

The ratio $A/V^{2/3} = c$ gives a dimensionless measure of mobility calibrated for similar types of pyroclastic currents, and such calibrated mobility factors have a potential use in volcanic hazard assessments. Genesis, energy, and grain-size characteristics, all of which influence mobility among pyroclastic-currents, vary too widely for all flows to fall along similar trends (fig. 26*A*). As we might expect, surgelike flows are highly mobile and have a mobility factor of $c \approx 520$ that is greater than that of lahars, with $c \approx 200$ (fig. 26*B*; Iverson and others, 1998). The column-collapse flows studied here have a moderate mobility factor of $c \approx 150$, only slightly less than that

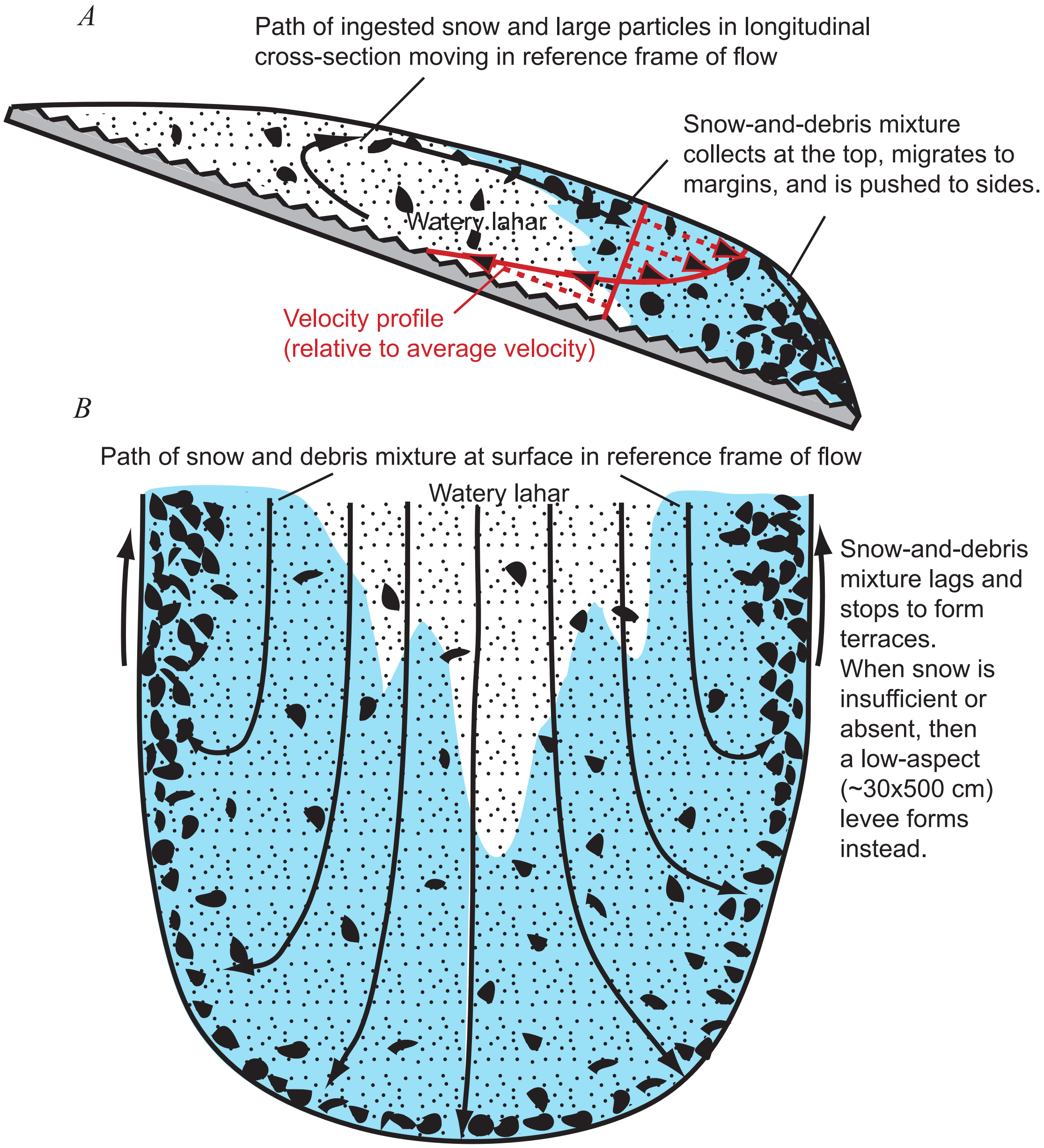

Figure 25. Schematic diagrams showing how simultaneous segregation of low-density snow and entrained coarse particles to surface of a mixed flow (simultaneous mixed avalanche and lahar) results in segregation of both snow and debris mixture to front (*A*) and margins (*B*) of flow. Whether such flows produce boulder-cobble levees or marginal mixed-avalanche deposits depends on amount of snow entrained at any particular time and place downstream while flow is in motion. Frame of reference advects downstream at average speed of flow (that is, at propagation velocity of flow front).

for lahars. Dome-collapse flows have a mobility factor of $c \approx 37$, a result similar to that of Widiwijayanti and others (2009), suggesting that they are no more mobile than volcanic debris avalanches and only slightly more mobile than nonvolcanic rockfall avalanches (fig. 26*B*). Mobilities of similar types of pyroclastic currents, as measured with our ratio $A/V^{2/3}$, yield more consistent results than H/L ratios, where H is the fall height and L is the runout distance (for example, Hayashi and Self, 1992; Calder and others, 1999). However, appropriate data are sparse, and our mobility relations could benefit by testing with additional data. Widiwijayanti and others (2009) present data illustrating the relation of cross-sectional area versus volume for dome-collapse flows and obtain the result: cross-sectional area = $0.05–0.1V^{2/3}$. Their data allow hazard zones for dome-collapse flows to be drawn in a consistent, repeatable way at any volcano, using the LAHARZ procedure of Iverson and others (1998). Cross-sectional areas for more energetic and dilute pyroclastic currents have proved difficult to measure, and data are needed to assess and calibrate the utility of the LAHARZ method for such flows. Indeed, mobile pyroclastic surges commonly accompany even the least mobile types of pyroclastic flow, such as those generated by the collapse of lava domes and flows.

Conclusions

The 2006 eruption of Augustine Volcano provided an opportunity to observe explosions, map and characterize pyroclastic and other flowage deposits, and test hypotheses concerning the origins and behavior of these flows. In particular, this study provided us with an unusual opportunity to observe the interaction of pyroclastic currents with winter snowpack. We summarize below our chief conclusions drawn from our data, and the methodologies that generated it.

1. Each of the three phases of the 2006 eruption had a distinctive style of volcanism and distinctive flowage deposits. The explosive phase comprised short vulcanian explosions that punctuated dome growth and produced pyroclastic currents on all flanks of the volcano. Initial pyroclastic currents spread widely across winter snowpack and generated slurries that coalesced to form mixed avalanches and lahars, whereas the final pyroclastic currents of the explosive phase involved explosive disruption and decompression of a lava dome. Continuous-phase activity consisted of rapid lava-dome growth and frequent dome-collapse pyroclastic flows restricted to the north sector of the volcano, followed by an andesite lava flow. After a 3-week pause, activity resumed with the extrusion of lava and a dome, accompanied by periodic block-and-ash flows, during the final, effusive phase of the eruption.

2. The three eruptive phases were unique—not just in terms of style of volcanism, including its associated seismicity, geodetic response, and ash emissions—but also in terms of the types and morphologies of deposits that were produced, and, in particular, of their basic lithologic components—low-, intermediate-, and high-silica andesite. Overall, during the three phases, lithologic compositions trended from low-silica andesite to high-silica andesite and back to low-silica andesite. However, each rock type is present in the deposits of each eruptive phase and each flow type.

3. The chief factors that influenced pyroclastic-current behavior and the morphology of their deposits were genesis, grain size, and the characteristics of the surfaces over which they flowed. Column collapse from short-lived vulcanian blasts, dome collapse, and the collapse of viscous lavas on steep slopes caused the pyroclastic flows documented in this study. Column-collapse flows during the explosive phase spread widely where they overran snowpack. Subsequent, similar flows were confined to drainages because previous pyroclastic currents had melted the snowpack, or coated it with ash or debris sufficient to insulate the later flows from the underlying snow. In contrast, later dome-collapse flows involved neither column collapse nor the influence of underlying snow. Because it was voluminous, the dome failure that generated the Rocky Point pyroclastic flow may have been sufficiently deep seated that unloading of incompletely degassed lava caused explosive decompression which initiated an energetic flow. High proportions of juvenile high-silica andesite within the deposits suggest that the Rocky Point explosion opened the conduit to the magma chamber and made way for continuous output of magma during the next phase. The subsequent, continuous-phase flows behaved as partially fluidized granular flows. Effusive-phase block-and-ash flows were caused exclusively by collapses of andesite lava flows.

4. Pyroclastic flows can erode and incorporate substrates formed of snow or ice through a combination of mechanical and thermal processes at the bed. Conversion of snow to vapor by hot pyroclast material fluidized such flows and thus enhanced their spread across snowpack and the resulting production of mixed avalanches and lahars. Walder's hypothesis (2000a,b) that thermal scour can effectively incorporate snow into a pyroclastic current, given proper pressure, temperature, and grain-size conditions at the pyroclastic layer's interface with substrate snow, is consistent with field observations during this study. Grain-size characteristics of initial pyroclastic flows, and estimates of overburden pressure at their base, are conditions that are favorable to thermal scour of snow and coeval fluidization. These flows scoured substrate snow and generated secondary slurry flows, whereas subsequent flows did not.

5. Initial pyroclastic flows of the explosive phase invariably generated lahars and mixed avalanches, but some of these secondary flows were wetter and more laharic than others. Where secondary flows were quite watery, mixed-avalanche

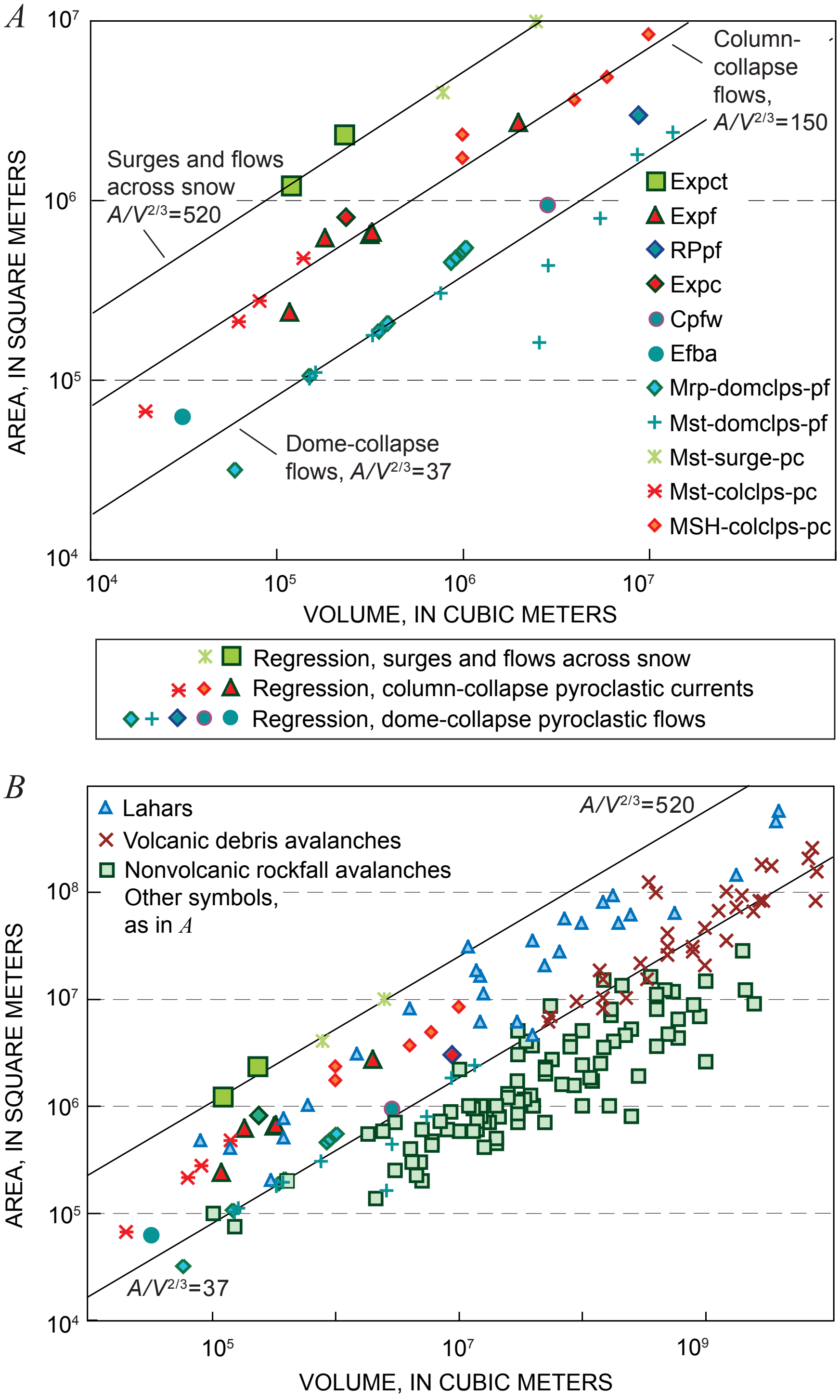

Figure 26. Plots of planimetric area versus volume for pyroclastic-current deposits of the 2006 eruption of Augustine Volcano relative to other pyroclastic currents, lahars, and debris avalanches. *A*, Augustine pyroclastic currents plotted with data of Charbonnier and Gertisser (2008) for Merapi pyroclastic currents (Mrp), of Calder and others (1999) for Montserrat currents (Mst), and of Rowley and others (1981) for Mount St. Helens currents (MSH). *B*, Area versus volume for worldwide occurrences of lahars (Iverson and others, 1998) and nonvolcanic debris flows and rock avalanches (Griswold and Iverson, 2007). Best fits to data of specified two-thirds-slope models are plotted in figure 26*A* for 21 dome-collapse flows, 14 column-collapse flows, and 4 surgelike flows. Same abbreviations for Augustine units as in figure 2; domclps-pf, dome-collapse pyroclastic flows; colcops-pc, column-collapse pyroclastic currents; and surge-pc, surgelike flows. Parameters and analysis of variance statistics for these models and for best-fit regression-line models are listed in table 8.

deposits were small or insignificant. Mixed-avalanche deposits that contained substantial snow blanketed medial reaches of valleys and had associated extensive marginal terraces and axial islands in distal reaches. Flows that incorporated significant amounts of snow formed cogenetic mixed avalanches that slid across surfaces protected by snowpack and water-rich axial lahars that scoured channels.

6. Plots of planimetric area (A) versus volume (V) for pyroclastic currents with similar origins and characteristics exhibit linear trends, such that $A = cV^{2/3}$ where c is a constant for similar types of flow. This relation was tested and calibrated for dome-collapse, column-collapse, and surgelike flows, using inundation-volume data from Montserrat (Calder and others, 1999), Mount St. Helens in 1980 (Rowley and others, 1981) and Augustine in 2006. The ratio $A/V^{2/3} = c$ gives a dimensionless measure of mobility, calibrated here for each of the three types of pyroclastic current. Energetic flows like surges are highly mobile and have an apparent dimensionless mobility factor of $c \approx 520$; column-collapse flows have a moderate mobility factor of $c \approx 150$; and dome-collapse flowss have an approximate mobility factor of $c \approx 35$, suggesting that these flows are not much more mobile than rock avalanches. Such calibrated mobility factors have a potential use in volcanic hazard assessments.

Acknowledgments

The entire staff of Alaska Volcano Observatory generously shared observations, ideas, and data that greatly helped us improve and refine this study. Numerous people set up and maintained the field camp during summer of 2006, without which this study would have been difficult or impossible. We especially thank Game McGimsey, Tina Neal, Evan Thoms, Cheryl Cameron, and Dan Jones for logistical field support. Our helicopter pilot, Rick Farrish transported us safely around the island, often in difficult conditions. Tim Druitt and Kristi Wallace provided careful reviews that helped us improve many defects in the manuscript.

References Cited

Bailey, J.E., Dean, K.G., Dehn, J., and Webley, P.W., 2010, Integrated satellite observations of the 2006 eruption of Augustine Volcano, *in* Power, J.A., Coombs, M.L., and Freymueller, J.T., eds., The 2006 eruption of Augustine Volcano, Alaska: U.S. Geological Survey Professional Paper 1769 (this volume).

Begét, J.E., and Kienle, J., 1992, Cyclic formation of debris avalanches at Mount St. Augustine volcano: Nature, v. 356, no. 6371, p. 701–704.

Begét, J.E., and Kowalik, Z., 2006, Confirmation and calibration of computer modeling of tsunamis produced by Augustine Volcano, Alaska: Science of Tsunami Hazards, v. 24, no. 4, p. 257–267.

Calder, E. S., Cole, P.D., Dade, W.B., Druitt, T.H., Hoblitt, R.P., Huppert, H.E., Ritchie, L., Sparks, R.S.J., and Young, S.R., 1999, Mobility of pyroclastic flows and surges at the Soufrière Hills Volcano, Montserrat: Geophysical Research Letters, v. 26, p. 537–540.

Cervelli, P.F., Fournier, T., Freymueller, J.T., and Power, J.A., 2006, Ground deformation associated with the precursory unrest and early phases of the January 2006 eruption of Augustine Volcano, Alaska: Geophysical Research Letters, v. 33, no. L18304, doi:10.1029/2006GL027219, p. 1–5.

Cervelli, P.F., Fournier, T.J., Freymueller, J.T., Power, J.A., Lisowski, M., and Pauk, B.A., 2010, Geodetic constraints on magma movement and withdrawal during the 2006 eruption of Augustine Volcano, Alaska, *in* Power, J.A., Coombs, M.L., and Freymueller, J.T., eds., The 2006 eruption of Augustine Volcano, Alaska: U.S. Geological Survey Professional Paper 1769 (this volume).

Charbonnier, S.J., and Gertisser, R., 2008, Field observations and surface characteristics of pristine block-and-ash flow deposits from the 2006 eruption of Merapi Volcano, Java, Indonesia: Journal of Volcanology and Geothermal Research, v. 177, p. 971–982.

Coats, R.R., 1950, Volcanic activity in the Aleutian Arc: U.S. Geological Survey Bulletin 974-B, p. 35–49.

Cole, P.D., Calder, E.S., Sparks, R.J.S., Clarke, A.B., Druitt, T.H., Young, S.R., Herd, R.A., Harford, C.L., and Norton, G.E., 2002, Deposits from dome-collapse and fountain-collapse pyroclastic flows at Soufrière Hills Volcano, Monserrat, *in* Druitt, T.H., and Kokelaar, B.P., eds., The eruption of Soufrière Hills Volcano, Montserrat, from 1995 to 1999: London Geological Society Memoirs, p. 231–262.

Coombs, M.L., Bull, K.F., Vallance, J.W., Schneider, D.J., Thoms, E.E., Wessels, R.L., and McGimsey, R.G., 2010, Timing, distribution, and volume of proximal products of the 2006 eruption of Augustine Volcano, Alaska, *in* Power, J.A., Coombs, M.L., and Freymueller, J.T., eds., The 2006 eruption of Augustine Volcano, Alaska: U.S. Geological Survey Professional Paper 1769 (this volume).

Dade, W.B., and Huppert, H.E., 1998, Long runout rockfalls: Geology, v. 26, p. 803–806.

Daley, E.E., 1986, Petrology, geochemistry, and the evolution of lavas at Augustine Volcano, Alaska: Fairbanks, University of Alaska, 106 p.

Dettermen, R.L., and Reed, B.L., 1980, Stratigraphy, structure, and economic geology of the Iliamna Quadrangle, Alaska: U.S. Geological Survey Bulletin 1368-B, 86 p.

Druitt, T.H., Calder, E.S., Cole, P.D., Hoblitt, R.P., Loughlin, S.C., Norton, G.E., Ritchie, L.J., Sparks, R.J.S., and Voight, B., 2002a, Small-volume, highly mobile pyroclastic flows formed by rapid sedimentation from pyroclastic surges at Soufrière Hills Volcano, Monserrat; an important hazard, *in* Druitt, T.H., and Kokelaar, B.P., eds., The eruption of Soufrière Hills Volcano, Monserrat, from 1995 to 1999: London Geological Society Memoirs, p. 263–279.

Druitt, T.H., Young, S.R., Baptie, B., Bonadonna, C., Calder, E.S., Clarke, A.B., Cole, P.D., Harford, C.L., Herd, R.A., Luckett, R., Ryan, G., and Voight, B., 2002b, Episodes of cyclic Vulcanian explosive activity with fountain collapse at Soufrière Hills Volcano, Montserrat, *in* Druitt, T.H., and Kokelaar, B.P., eds., The eruption of Soufrière Hills Volcano, Montserrat, from 1995 to 1999: London Geological Society Memoirs, p. 281–306.

Gardner, C.A., Neal, C. A., Waitt, R.B., and Janda, R.J., 1994, Proximal pyroclastic flow deposits from the 1989-1990 eruption of Redoubt Volcano, Alaska—stratigraphy, distribution, and physical characteristics: Journal of Volcanology and Geothermal Research, v. 62, p. 213–250.

Griswold, J.P., and Iverson, R.M., 2007, Mobility statistics and automated hazard mapping for debris flows and rock avalanches: U.S. Geological Survey Scientific Investigations Report 2007-5276, 49 p.

Harris, G.W., Swanson, S.E., and Nye, C.J., 1987, Comparative petrology and petrography of the 1976 and 1986 ejecta of Augustine Volcano [abs.]: Geological Society of America Abstracts with Programs, v. 19, p. 387.

Hayashi, J.N., and Self, S., 1992, A comparison of pyroclastic flow and debris avalanche mobility: Journal of Geophysical Research, v. 97, p. 9063–9071.

Iverson, R.M., 1997, The physics of debris flows: Reviews in geophysics, v. 35, p. 245–296.

Iverson, R.M., Schilling, S.P., and Vallance, J.W., 1998, Objective delineation of lahar-inundation hazard zones: Geological Society of America Bulletin, v. 110, p. 972–984.

Jacobs, K.M., and McNutt, S.R., 2010, Using seismic *b*-values to interpret seismicity rates and physical processes during the preeruptive earthquake swarm at Augustine Volcano 2005–2006, *in* Power, J.A., Coombs, M.L., and Freymueller, J.T., eds., The 2006 eruption of Augustine Volcano, Alaska: U.S. Geological Survey Professional Paper 1769 (this volume).

Johnston, D.A., 1978, Volatiles, magma mixing and the mechanism of eruption of Augustine Volcano, Alaska: Seattle, University of Washington, Ph.D. thesis, 204 p.

Kienle, J., and Forbes, R.B., 1977, Augustine—evolution of a volcano: Fairbanks, University of Alaska, Geophysical Institute Annual Report 1975–76, p. 26–48.

Kienle, J., and Swanson, S.E., 1985, Volcanic hazards from future eruptions of Augustine Volcano, Alaska: Geophysical Institute, University of Alaska Fairbanks, Rep. UAG R-275, 2nd ed., 122 p.

Larsen, J.F., Nye, C.J., Coombs, M.L., Tilman, M., Izbekov, P., and Cameron, C., 2010, Petrology and geochemistry of the 2006 eruption of Augustine Volcano, Alaska, *in* Power, J.A., Coombs, M.L., and Freymueller, J.T., eds., The 2006 eruption of Augustine Volcano, Alaska: U.S. Geological Survey Professional Paper 1769 (this volume).

Loughlin, S.C., Calder, E.S., Clarke, A.B., Cole, P.D., Luckett, R., Mangan, M.T., Pyle, D.M., Sparks, R.J.S., Voight, B., and Watts, R.B., 2002, Pyroclastic flows and surges generated by the 25 June 1997 dome collapse, Soufrière Hills Volcano, Montserrat, *in* Druitt, T.H., and Kokelaar, B.P., eds., The eruption of Soufrière Hills Volcano, Montserrat, from 1995 to 1999: London Geological Society Memoirs, p. 191–210.

Lube, G., Cronin, S.J., Platz, T., Freundt, A., Proctor, J., Henderson, C., and Sheridan, M.F., 2007, Flow and deposition of pyroclastic granular flows; a type example from the 1975 Ngauruhoe eruption, New Zealand: Journal of Volcanology and Geothermal Research, v. 161, p. 165–186.

McNutt, S.R., Tytgat, G., Estes, S.A., and Stihler, S.D., 2010, A parametric study of the January 2006 explosive eruptions of Augustine Volcano, Alaska, *in* Power, J.A., Coombs, M.L., and Freymueller, J.T., eds., The 2006 eruption of Augustine Volcano, Alaska: U.S. Geological Survey Professional Paper 1769 (this volume).

Miller, T.P., McGimsey, R.G., Richter, D.H., Riehle, J.R., Nye, C.J., Yount, M.E., and Dumoulin, J.A., 1998, Catalog of the historically active volcanoes of Alaska: U.S. Geological Survey Open-File Report 98-0582, 104 p.

Pierson, T.C., 1994, Volcanic mixed avalanches; a distinct eruption-triggered mass-flow process at snow-clad volcanoes: Geological Society of America Bulletin, v. 106, p. 1351–1358.

Pouliquen, O., Delour, J., and Savage, S.B., 1997, Fingering in granular flows: Nature, v. 386, p. 816–817.

Pouliquen, O., and Vallance, J.W., 1999, Segregation induced instabilities of granular fronts: Chaos, v. 9, p. 621–630.

Power, J.A., and Lalla, D.J., 2010, Seismic observations of Augustine Volcano, 1970–2007, *in* Power, J.A., Coombs, M.L., and Freymueller, J.T., eds., The 2006 eruption of Augustine Volcano, Alaska: U.S. Geological Survey Professional Paper 1769 (this volume).

Power, J.A., Nye, C.J., Coombs, M.L., Wessels, R.L., Cervelli, P.F., Dehn, J., Wallace, K.L., Freymueller, J.T., and Doukas, M.P., 2006, The reawakening of Alaska's Augustine

Volcano: Eos (American Geophysical Union Transactions), v. 87, no. 37, p. 373, 377.

Rowley, P.D., Kuntz, M.A., and McCleod, N.S., 1981, Pyroclastic-flow deposits, *in* Lipman, P.W., and Mullineaux, D.R., eds. The 1980 eruptions of Mount St. Helens: U.S. Geological Survey Professional Paper 1250, p. 489–512.

Schneider, D.J., Scott, C., Wood, J. and Hall, T., 2006, NEXRAD weather radar observation of the 2006 Augustine volcanic eruption clouds [abs.]: Eos (American Geophysical Union Transactions), v. 87, abstract V51C-1686.

Scott, K.M., 1988, Origins, behavior, and sedimentology of lahars and lahar-runout flows in the Toutle-Cowlitz River system: U.S. Geological Survey Professional Paper 1447-A, 78 p.

Siebert, L., Begét, J.E., and Glicken, H., 1995, The eruptive history of Augustine Volcano, Alaska: Journal of Volcanology and Geothermal Research, v. 66, no. 1, p. 367–395.

Sparks, R.S.J., 1976, Grain-size variations in ignimbrites and implications for the transport of pyroclastic flows: Sedimentology, v. 23, p. 147–188.

Swanson, S.E., and Kienle, J., 1988, The 1986 eruption of Mount St. Augustine; field test of a hazard evaluation: Journal of Geophysical Research, v. 93, no. 85, p. 4500–4520.

Thomas, R.J., McNutt, S.R., Krehbiel, P.R., Rison, W., Aulich, G., Edens, H.E., Tytgat, G, and Clark, E., 2010, Lightning and electrical activity during the 2006 eruption of Augustine Volcano, *in* Power, J.A., Coombs, M.L., and Freymueller, J.T., eds., The 2006 eruption of Augustine Volcano, Alaska: U.S. Geological Survey Professional Paper 1769 (this volume).

Vallance, J.W., 1994, Experimental and field studies related to the behavior of granular mass flows and the characteristic of their deposits: Houghton, Michigan Technological University, Ph.D.dissertation, 197 p.

Vallance, J.W., 2000, Lahars, *in* Sigurdsson, H., Houghton, B.F., McNutt, S.R., Rymer, H., and Stix, J., eds., Encyclopedia of volcanoes: San Diego, Calif., Academic Press, p. 601–616.

Vallance, J.W., and Savage, S.B., 2000, Particle segregation in granular flows down chutes, *in* Rosato, A.D., and Blackmore, D.L., eds. Segregation in granular flows: Dordrecht, Kluwer, p. 31–51.

Waitt, R.B., 1995, Hybrid wet flows formed by hot pyroclasts interacting with snow during the 1992 erupton of Crater Peak, Mount Spurr Volcano, Alaska, *in* Kieth, T.E.C., ed., U.S. Geological Survey Bulletin 2139, p. 107–118.

Waitt, R.B., 2010, Ejecta and landslides from Augustine Volcano before 2006, *in* Power, J.A., Coombs, M.L., and Freymueller, J.T., eds., The 2006 eruption of Augustine Volcano, Alaska: U.S. Geological Survey Professional Paper 1769 (this volume).

Waitt, R.B., and Begét, J.E., 1996, Provisional geologic map of Augustine Volcano, Alaska: U.S. Geological Survey Open-File Report 96-0516, 44 p.

Waitt, R.B., and Begét, J.E., 2009, Volcanic processes and geology of Mount Augustine, Alaska: U.S. Geological Survey Professional Paper 1762, 78 p.

Waitt, R.B., Gardner, C.A., Pierson, T.C., Major, J.J., and Neal, C. A., 1994, Unusual ice diamicts emplaced during the December 15, 1989 eruption of Redoubt Volcano, Alaska: Journal of Volcanology and Geothermal Research, v. 62, p. 409–428.

Walder. J.S., 2000a, Pyroclast/snow interactions and thermally driven slurry formation; part 1, theory for monodisperse grain beds: Bulletin of Volcanology, v. 62, p. 105–118.

Walder. J.S., 2000b, Pyroclast/snow interactions and thermally driven slurry formation; part 2, experiments and theoretical extension to polydisperse tephra: Bulletin of Volcanology, v. 62, p. 119–129.

Wallace, K., Neal, C.A., and McGimsey, R.G., 2010, Timing, distribution and character of tephra fall from the 2005-2006 eruption of Augustine Volcano, Alaska, *in* Power, J.A., Coombs, M.L., and Freymueller, J.T., eds., The 2006 eruption of Augustine Volcano, Alaska: U.S. Geological Survey Professional Paper 1769 (this volume).

Widiwijayanti, C., Voight, B., Hidayat, D., and Schilling, S.P., 2009, Objective delineation of areas at risk from block-and-ash pyroclastic flows and surges: Bulletin of Volcanology, v. 71, p. 687–703, doi:10.1007/s00445-008-0254-6.

Table 2. Samples taken and analyses performed for pyroclastic-flow, lahar, and mixed-avalanche deposis of the 2006 eruption of Augustine Volcano, Alaska.

[Samples are sorted by event and sector]

Sample Number	Latitude (decimal degrees)	Longitude (decimal degrees)	Sector 1=ESE-ENE 2=NE-WNW 3=SSE-SW	Unit	Phase	Emplacement Date	Event	Sample Type	Grain size	Sedi-graph	Com po nen try
V021A	59.366	-153.410	1	Expct	Explosive	1/13/06	3-4	Bulk	X		
V033A	59.368	-153.394	1	Expct	Explosive	1/13/06	3-4	Bulk	X		X
V096	59.371	-153.407	1	Expct	Explosive	1/14/06	3-4, 6-7	Bulk	X	X	X
V281A	59.363	-153.404	1	Expct	Explosive	1/13/06	3-4	Bulk	X		
V281B	59.363	-153.404	1	Expct	Explosive	1/13/06	3-4	Bulk	X		
V283A	59.363	-153.402	1	Expct basal	Explosive	1/13/06	3-4	Bulk	X		
V283B	59.363	-153.402	1	Expct basal	Explosive	1/13/06	3-4	Bulk	X		
V283C	59.363	-153.402	1	Expct basal	Explosive	1/13/06	3-4	Bulk	X		
V283D	59.363	-153.402	1	Expct top	Explosive	1/13/06	3-4	Bulk	X		
V283E	59.363	-153.402	1	Expct top	Explosive	1/13/06	3-4	Bulk	X		
V330	59.367	-153.382	1	Exlh	Explosive	1/13/06	3-4	Bulk	X		
B096A	59.366	-153.410	1	Expct	Explosive	1/13/06	3-4	Bulk			
B096B	59.366	-153.410	1	Expct	Explosive	1/13/06	3-4	Hand-picked juvenile clasts			
B106	59.365	-153.409	1	Expf	Explosive	1/13/06	3-4	Bulk	X		X
B184A	59.363	-153.403	1	Expct	Explosive	1/13/06	3-4	Bulk	X	X	X
B184B	59.363	-153.403	1	Expct	Explosive	1/13/06	3-4	Bulk	X	X	X
B184C	59.363	-153.403	1	Expct	Explosive	1/13/06	3-4	Bulk	X		
B102	59.346	-153.429	1	Expf	Explosive	1/13-14/06	3-7	Bulk	X		X
C120	59.351	-153.406	3	Expct	Explosive	1/13-14/06	3-8	Bulk	X		
V117	59.369	-153.447	2	Expf	Explosive	1/13/06	5	Bulk	X		
B176	59.404	-153.449	2	Expf	Explosive	1/13-14/06	5	Bulk	X	X	
V270A	59.384	-153.399	2	Exma	Explosive	1/13-14/06?	7?	Bulk	X		
V270B	59.384	-153.399	2	Exlh	Explosive	1/13-14/06	7	Bulk	X		
V272	59.386	-153.397	2	Exlh	Explosive	1/13-14/06	7	Bulk	X		
V275A	59.387	-153.391	2	Exlh	Explosive	1/13-14/06	7	Bulk	X		X
V275B	59.387	-153.391	2	Exlh	Explosive	1/13-14/06	7	Bulk	X		X
V275C	59.387	-153.391	2	Exlh	Explosive	1/13-14/06	7	Bulk	X		
V237	59.388	-153.385	2	Exlh	Explosive	1/14/06	7	Bulk	X		
V258	59.366	-153.398	3	Exma	Explosive	1/13-14/06	7	Bulk	X		
V199	59.336	-153.410	3	Exma	Explosive	1/14/06	8	Bulk	X		
V256A	59.344	-153.418	3	Expf-top	Explosive	1/14/06	8	Bulk	X	X	
V256B	59.344	-153.418	3	Expf-mid	Explosive	1/14/06	8	Bulk	X	X	
V256C	59.344	-153.418	3	Expf-base	Explosive	1/14/06	8	Bulk	X		
V256D	59.344	-153.418	3	Expf-base	Explosive	1/14/06	8	Bulk	X	X	
V256E	59.344	-153.418	3	Expf	Explosive	1/14/06	8	Bulk	X		
V257	59.344	-153.416	3	Exma	Explosive	1/14/06	8	Bulk	X		
V264	59.345	-153.420	3	Expf-reworked	Explosive	1/13-14/06	8	Bulk			

Table 2. Samples taken and analyses performed for pyroclastic-flow, lahar, and mixed-avalanche deposis of the 2006 eruption of Augustine Volcano, Alaska.—Continued

[Samples are sorted by event and sector]

Sample Number	Latitude (decimal degrees)	Longitude (decimal degrees)	Sector 1=ESE-ENE 2=NE-WNW 3=SSE-SW	Unit	Phase	Emplacement Date	Event	Sample Type	Grain size	Sedigraph	Componentry
V276A	59.333	-153.399	3	Exlh-base	Explosive	1/13-14/06	8	Bulk	X	X	X
V276B	59.333	-153.399	3	Exlh-top	Explosive	1/13-14/06	8	Bulk	X	X	
V278	59.333	-153.400	3	Exma	Explosive	1/13-14/06	8	Bulk	X	X	X
V280	59.333	-153.400	3	Exlh	Explosive	1/13-14/06	8	Bulk	X		
B230	59.343	-153.455	3	Expf	Explosive	1/13-14/06	8	Bulk	X		X
C025A	59.329	-153.468	3	Exlh	Explosive	1/13-14/06	8	Bulk			
B129	59.360	-153.436	3	Expf	Explosive	1/17/09	9	Bulk			
V254	59.350	-153.487	3	Expf	Explosive	1/17/06	9	Bulk	X		
V019	59.352	-153.477	2	Expf	Explosive	1/17/06	9	Bulk	X		X
V297	59.386	-153.442	2	Expc	Explosive	1/27/06	10	Bulk	X		
V311	59.376	-153.439	2	Expc	Explosive	1/27/06	10	Bulk			
V312A	59.376	-153.440	2	Expc	Explosive	1/27/06	10	Bulk	X		
V312B	59.376	-153.440	2	Expc	Explosive	1/27/06	10	Bulk	X		
V312C	59.376	-153.440	2	Expc	Explosive	1/27/06	10	Bulk			
V312D	59.376	-153.440	2	Expc	Explosive	1/27/06	10	Bulk	X		
V313	59.377	-153.439	2	Expc	Explosive	1/27/06	10	Bulk	X		X
V315	59.379	-153.442	2	Expc	Explosive	1/27/06	10	Bulk	X		
B215A	59.371	-153.437	2	Expc	Explosive	1/27/06	10	Bulk	X	X	X
B216	59.373	-153.439	2	Expc	Explosive	1/27/06	10	Bulk	X		
B217	59.374	-153.440	2	Expc	Explosive	1/27/06	10	Bulk	X		
C259C	59.385	-153.438	2	Expc	Explosive	1/27/06	10	Bulk	X	X	X
B173	59.404	-153.439	2	RPpf	Explosive	1/27/06	10	Bulk	X	X	X
B222	59.390	-153.439	2	RPpf	Explosive	1/27/06	10	Bulk	X		X
B223	59.394	-153.434	2	RPpf	Explosive	1/27/06	10	Bulk	X		
B224	59.400	-153.425	2	RPpf	Explosive	1/27/06	10	Bulk	X	X	
B225	59.403	-153.435	2	RPpf	Explosive	1/27/06	10	Bulk	X	X	
C259B	59.385	-153.438	2	RPpf	Explosive	1/27/06	10	Bulk	X		
B218	59.377	-153.436	2	Cpf	Continuous	>1/27/2006	>14	Bulk	X		
V224	59.383	-153.395	2	Cpf	Continuous	>1/28/06	>14	Bulk	X		
LC259A	59.385	-153.438	2	Cpf	Continuous	>1/28/06	>14	Bulk	X	X	
B143	59.369	-153.446	2	Cpf	Continuous	>1/28/06	>14	Hand-picked juvenile clasts			
B149A	59.371	-153.432	2	Cpf	Continuous	>1/28/06	>14	Hand-picked juvenile clasts			
B155A	59.376	-153.429	2	Cpf	Continuous	>1/28/06	>14	Bulk			
B203	59.384	-153.409	2	Cpf	Continuous	>1/28/06	>14	Bulk	X	X	X
V101	59.372	-153.405	2	Cpc	Continuous	>1/28/06	>14	Bulk	X		X
C294	59.375	-153.445	2	Cpfw	Continuous	1/30/06	Windy	Bulk	X		
V022A	59.363	-153.405	1	Efba	Effusive	3/3-16/06	>14	Bulk	X		X

Table 3. Grain-size distribution for samples of clastic-flow deposits of the 2006 eruption of Augustine Volcano, Alaska.

[Samples sorted by map unit[1]. Data are obtained by sieve analysis and given in weight percent. Data for grain sizes <0.063 mm obtained by sedigraph. Fine-ash totals from sedigraph-measured smaples are calculated from sedigraph data, not weighed. All samples analyzed at the Cascades Volcano Observatory]

Sample Number	Unit	31.5 mm	16.0 mm	8.0 mm	4.0 mm	2.0 mm	1.0 mm	0.50 mm	0.25 mm	0.125 mm	0.063 mm	Fine ash (<0.063 mm)	31 µm	16 µm	8 µm	4 µm	2 µm	1 µm
V021A	Expct	0.0	5.4	10.0	7.1	4.7	8.8	11.4	14.6	15.6	10.2	12.2						
V033A	Expct	16.4	9.0	8.0	7.9	6.0	9.8	11.3	12.4	9.4	4.9	4.9						
V096	Expct	4.2	7.4	4.6	4.2	4.0	7.5	11.5	15.1	15.1	11.8	14.0	6.3	4.0	2.1	1.0	0.4	0.2
V281A	Expct	0.0	0.0	2.2	2.6	6.3	12.4	18.3	19.1	19.1	12.9	6.9						
V315	Expct	2.5	10.9	9.5	9.4	6.8	10.0	13.9	15.6	12.2	6.6	2.5						
V283D	Expct	16.0	0.6	2.1	3.9	4.9	9.6	14.4	17.4	14.7	10.0	6.4						
V283E	Expct	2.8	11.7	7.1	6.9	5.6	8.8	10.8	13.0	13.3	9.6	10.3						
V283A	Expct-basal	0.0	0.0	3.0	4.9	8.1	13.4	18.2	20.6	16.8	10.6	4.4						
V283B	Expct-basal	0.0	4.9	8.0	8.0	7.5	10.3	14.9	18.4	14.9	8.7	4.3						
V283C	Expct-basal	18.5	7.6	7.2	7.2	6.1	10.4	12.1	13.1	10.0	4.8	3.0						
B184A	Expct	0.0	1.9	3.4	6.7	7.2	13.6	18.0	21.6	16.3	8.1	3.2	1.9	0.6	0.3	0.2	0.1	0.0
B184B	Expct	1.9	2.7	3.0	5.1	6.0	9.9	15.1	19.5	18.1	11.0	7.7	3.9	1.7	1.0	0.7	0.3	0.2
B184C	Expct	0.0	0.0	0.3	1.0	3.2	10.5	19.1	26.1	24.1	11.9	4.0						
C120	Expct	0.0	3.9	21.6	16.5	7.7	8.3	11.6	12.8	9.1	5.0	3.6						
V117	Expf	7.7	14.0	8.4	8.0	8.3	11.0	13.9	14.5	9.1	3.7	1.3						
B102	Expf	3.8	9.1	10.3	9.1	8.7	10.6	13.2	14.6	10.2	5.5	4.8						
B176	Expf	0.0	1.3	3.5	5.5	7.5	10.8	15.6	19.7	18.7	10.9	6.3	2.6	1.5	1.1	0.7	0.3	0.1
V256A	Expf-top	23.8	8.5	4.6	4.1	3.8	7.0	9.0	10.7	8.1	5.7	6.2	2.4	1.8	1.1	0.6	0.2	0.1
V256B	Expf-middle	17.0	7.8	7.8	7.2	5.0	6.7	7.6	7.9	6.0	3.7	5.5	2.0	1.6	1.0	0.5	0.2	0.1
V256C	Expf-base	0.0	7.5	7.4	7.7	6.2	11.5	14.1	15.8	13.1	7.6	9.0						
V256D	Expf-base	0.0	0.0	1.9	2.1	3.9	9.3	18.6	23.5	19.0	10.8	10.3	3.8	2.8	2.0	1.1	0.5	0.2
V256E	Expf	0.0	2.3	1.8	1.3	1.8	6.6	12.2	18.4	20.4	15.3	19.9						
V019	ExPf	2.5	3.6	4.0	6.3	9.5	13.7	15.6	14.4	12.3	8.0	10.1						
B230	Expf	13.9	5.1	5.8	7.2	5.9	12.6	13.9	15.4	12.1	5.5	2.6						
V237	Exlh	3.1	5.6	9.2	11.8	11.8	14.8	15.3	13.0	8.0	3.7	3.7						
V270B	Exlh	0.0	7.8	12.2	10.8	8.2	11.0	12.0	12.0	9.5	6.5	10.0						
V275B	Exlh	2.1	2.2	6.3	8.3	10.5	17.1	18.2	15.8	9.4	5.1	5.0						
V275C	Exlh	0.0	2.8	5.8	8.1	7.7	13.6	21.0	20.4	11.7	4.8	4.1						
V280	Exlh	0.0	16.8	22.0	11.2	6.3	7.6	8.6	9.5	7.0	5.1	5.8						
V330	Exlh	0.0	4.0	8.4	9.1	8.6	11.9	12.8	14.9	14.3	9.4	6.5						

V276A	Exlh-hcf	5.9	15.3	17.5	13.9	8.9	8.7	8.8	7.9	5.2	2.9	4.8	1.6	1.4	1.0	0.5	0.2	0.1
V276B	Exlh-hcf	0.0	0.4	7.3	15.7	14.8	17.5	15.2	12.7	6.9	3.8	5.3	1.8	1.7	1.0	0.5	0.2	0.1
V272	Exlh-hcf	0.0	3.6	4.4	5.0	5.7	12.8	16.5	17.0	15.1	10.7	9.2						
V275A	Exlh-hcf	0.0	3.2	16.8	17.7	13.8	12.9	12.0	10.2	6.4	3.4	3.6						
V199	Exma	0.0	84.1	11.9	0.2	0.2	0.4	0.6	0.6	0.6	0.6	0.8						
V257	Exma	0.0	8.2	11.1	8.8	7.2	10.3	14.2	13.3	9.0	6.2	11.7						
0V258	Exma	5.6	5.3	6.2	7.2	3.0	48.7	6.0	6.1	4.1	3.2	4.6						
V254	Exma	0.0	0.0	0.0	0.0	0.7	0.7	2.3	9.5	23.0	22.4	41.4						
V270A	Exma	4.8	2.9	10.0	11.4	11.3	16.8	15.2	12.2	7.0	4.5	4.0						
V278	Exma	13.5	3.2	5.5	6.4	5.1	9.1	13.6	15.4	11.8	6.3	9.6	3.6	2.8	1.7	0.9	0.3	0.3
V297	Expc	3.9	9.5	12.6	8.3	7.7	10.1	14.3	15.8	12.0	4.9	1.0						
V312A	Expc	0.0	1.0	6.8	9.8	8.8	18.2	20.4	16.1	10.4	5.0	3.5						
V312B	Expc	0.0	0.0	0.0	9.7	13.9	20.0	25.8	19.4	7.7	2.4	1.1						
V312C	Expc	0.0	0.0	16.4	29.0	11.2	10.7	8.8	9.1	7.6	4.3	2.9						
V313	Expc	0.0	0.0	3.0	7.3	14.9	19.9	20.6	16.2	8.6	4.2	5.4						
B215A	Expc	10.4	3.2	7.7	8.4	10.5	12.6	10.4	9.4	8.7	7.9	10.7	5.3	3.1	1.3	0.6	0.3	0.1
B216	Expc	2.5	8.3	5.6	6.7	8.4	13.2	17.0	18.5	13.0	6.1	0.8						
B217	Expc	0.0	20.3	8.8	11.1	9.5	12.7	14.2	12.3	6.8	2.7	1.7						
C259C	Expc	0.0	8.6	13.9	14.1	8.3	13.0	13.4	12.2	7.2	4.2	5.0	2.3	1.5	0.7	0.3	0.1	0.1
B173	RPpf	2.0	1.2	4.6	6.4	6.6	12.1	14.4	15.3	12.7	10.3	13.9	5.1	3.7	2.5	1.6	0.7	0.4
B222	RPpf	9.8	10.5	9.6	7.4	6.9	10.2	11.7	12.1	9.5	5.6	6.7						
B223	RPpf	17.1	9.6	7.2	7.1	6.5	9.8	10.8	10.5	7.6	5.7	8.1						
B224	RPpf	0.0	9.7	8.9	8.2	4.9	11.4	13.8	15.6	11.8	7.9	7.5	2.6	2.0	1.4	0.9	0.4	0.2
B225	RPpf	12.2	6.0	6.9	7.3	7.1	10.2	12.4	12.8	9.7	6.1	8.9	3.2	2.4	1.6	1.1	0.5	0.3
C259B	RPpf	0.0	0.0	1.9	5.1	6.1	8.5	15.0	21.7	21.3	14.3	6.1						
B218	Cpf	2.7	10.5	6.1	8.1	10.6	13.4	14.1	12.0	8.4	6.4	7.4						
B203	Cpf	13.6	3.5	6.8	6.3	6.4	11.4	13.2	12.6	9.0	7.0	9.9	3.4	2.7	1.9	1.0	0.6	0.2
C259A	Cpf	10.2	10.9	8.4	7.5	8.4	11.5	13.9	14.2	9.6	4.0	1.3	0.7	0.2	0.2	0.1	0.0	0.0
V224	Cpf	9.7	1.5	3.8	5.9	8.3	11.7	14.4	14.9	12.3	9.9	7.8						
C294	Cpf	24.9	7.6	4.0	4.0	5.5	7.4	10.5	11.2	10.0	8.3	6.5						
V101	Cpc	6.8	9.4	5.2	5.4	5.7	11.2	13.4	15.2	12.9	8.5	6.3						
V022A	Efba	11.7	13.4	10.0	10.6	9.7	14.1	14.0	9.0	4.6	1.8	1.2						

---

[1] Map units defined in figure 2. Expct, Explosive-phase pyroclastic-current deposit, thin; Expf, pyroclastic-flow deposit; Expc, pyroclastic-current deposit; Exlh, lahar deposit (hcf,hyperconcentrated flow deposit); Exma, mixed-avalanche deposit; RPpf, Rocky Point pyroclastic-flow deposit; Cpf, Continuous-phase pyroclastic-flow deposit; Cpfw, pyroclastic-flow of Windy Creek; Cpc, pyroclastic-current deposit; Efba, Effusive-phase block-and-ash-flow deposit.

Table 4. Statistics of grain-size analyses for samples of pyroclastic-flow, lahar, and mixed-avalanche deposits from the 2006 eruption of Augustine Volcano, Alaska.

[All values in phi units. Statistics calculated by using software courtesy of Sebastien Dartevelle, Los Alamos National Laboratories. Units defined in figure 2]

Sample	Unit	Mean	Median	Sorting	Mode	Skewness	Kurtosis
V021A	Expct	0.60	1.19	3.14	2.5	-0.16	0.96
V033A	Expct	-1.14	-0.70	3.27	-5.5	-0.11	0.70
V096	Expct	0.72	1.42	3.31	1.5	-0.25	1.08
V281A	Expct	1.38	1.42	2.15	2.5	0.05	1.23
V315	Expct	-0.42	0.07	2.78	1.5	-0.20	0.75
V283D	Expct	-0.36	0.91	3.76	1.5	-0.30	1.22
V283E	Expct	0.08	0.68	3.41	2.5	-0.13	0.85
V283A	Expct-basal	1.01	1.12	1.94	1.5	-0.12	0.97
V283B	Expct-basal	0.31	0.78	2.52	1.5	-0.24	0.87
V283C	Expct-basal	-1.24	-0.64	3.23	-5.5	-0.17	0.67
B184A	Expct-basal	0.73	0.96	2.04	1.5	-0.18	1.03
B184B	Expct-basal	1.05	1.33	2.44	1.5	-0.20	1.18
B184C	Expct-basal	1.56	1.61	1.43	1.5	-0.06	0.94
V117	Expf	-1.07	-0.64	2.83	1.5	-0.16	0.70
B102	Expf	-0.48	-0.14	2.84	1.5	-0.13	0.79
B176	Expf	1.06	1.30	2.20	1.5	-0.16	1.05
V256A	Expf-top	-1.66	-1.85	3.64	-5.5	0.12	0.64
V256B	Expf-mid	-2.41	-3.04	3.65	-6.5	0.28	0.71
V256D	Expf-base	-0.48	0.02	3.46	1.5	-0.12	0.89
V256E	Expf	2.83	2.28	2.70	2.5	0.09	1.28
B230	Expf	-0.77	-0.04	3.09	1.5	-0.27	0.80
V019	Expf	1.34	1.64	2.07	3.5	-0.28	0.94
V256C	Expf-base	0.30	0.70	3.05	1.5	-0.09	1.07
V297	Expc	-0.60	-0.18	2.69	1.5	-0.19	0.71
V312A	Expc	0.11	0.27	2.15	0.5	-0.08	1.04
V312B	Expc-base	0.15	0.26	1.58	0.5	-0.08	0.97
V312C	Expc-top	-0.92	-1.60	2.29	-2.5	0.42	0.82
V313	Expc	0.30	0.25	2.21	0.5	0.18	1.34
B215A	Expc	-0.20	-0.24	3.36	-0.5	0.01	0.91
B216	Expc	-0.16	0.33	2.53	1.5	-0.27	0.93
B217	Expc	-1.24	-0.97	2.58	-4.5	-0.04	0.68
C120	Expc	-0.75	-0.95	2.53	-3.5	0.16	0.69
C259C	Expc	-0.67	-0.60	2.65	-2.5	0.03	0.83
B173	RPpf	1.07	1.17	2.82	1.5	-0.02	1.10
B222	RPpf	-0.75	-0.41	3.47	1.5	-0.02	0.89
B223	RPpf	-1.05	-0.73	3.70	-5.5	0.02	0.81
B224	RPpf	0.05	0.51	2.99	1.5	-0.14	0.88
B225	RPpf	-0.48	0.02	3.46	1.5	-0.12	0.89
V022A	Efba	0.46	0.78	2.55	3.5	-0.22	0.86
V237	Exlh	-0.56	-0.42	2.51	0.5	-0.05	0.91
V270B	Exlh	-0.09	0.00	3.16	-3.5	0.06	0.91
V275B	Exlh	0.07	0.20	2.34	0.5	-0.06	1.06
V275C	Exlh	0.27	0.57	2.20	0.5	-0.17	1.09
V280	Exlh	-1.27	-2.01	3.16	-3.5	0.43	0.88
V330	Exlh	0.34	0.64	2.88	1.5	-0.04	1.01
V276A	Exlh-hcf[1]	-1.65	-2.23	2.85	-3.5	0.32	0.86
V276B	Exlh-hcf[1]	-0.27	-0.34	2.25	-0.5	0.13	0.96
V272	Exlh-hcf[1]	1.00	1.12	2.65	1.5	-0.03	1.28
V275A	Exlh-hcf[1]	-0.88	-1.12	2.35	-2.5	0.20	0.84
V199	Exma	-4.40	-4.49	0.43	-4.5	0.47	3.34
V257	Exma	0.09	0.31	3.21	0.5	0.00	0.93
V258	Exma	-0.74	-0.38	2.47	-0.5	-0.15	2.21
V254	Exma	3.91	3.61	1.69	5.5	0.12	0.56
V270A	Exma	-0.55	-0.43	2.58	-0.5	-0.06	0.99
V278	Exma	-0.23	0.53	3.45	1.5	-0.22	0.93
B218	Cpf	-0.32	-0.11	3.18	0.5	0.02	1.08
B203	Cpf	-0.35	0.14	3.54	-5.5	-0.12	0.92
C259A	Cpf	-1.04	-0.58	2.89	1.5	-0.18	0.72
V224	Cpc	0.34	0.65	3.22	1.5	-0.11	1.23
C259B	RPpf	1.42	1.62	2.22	1.5	-0.06	1.36
C294	Cpfw	-1.00	-0.43	3.84	-5.5	-0.06	0.68
V101	Cpc	-0.22	0.49	3.42	1.5	-0.17	1.01

[1] Hyperconcentrated-flow lahars

Table 6. Lithologic components in pyroclastic-current, lahar, and mixed-avalanche samples from the 2006 eruption of Augustine Volcano, Alaska.

[All values in weight percent. Components: low-silica andesite scoria (LSAS), dense low-silica andesite (DLSA), dense intermediate-silica andesite (DIA), high-silica andesite (HSA), high-silica andesite pumice (HSAP), and mixtures (banded) and defined in table 5. Phases and units (after Coombs and others, this volume), are defined in figure 2]

Sample	Unit[1]	Event	Size[2] (mm)	Clasts counted[3]	LSAS	DLSA	DIA	Banded	HSA	HSAP	Oxidized	Crystals	Non-crystals
V033A	Expct	3–4	8	171	43.9	22.2	10.5	2.3	13.5	0.0	7.6	0.0	0.0
			4	395	43.3	22.8	11.1	1.8	14.7	0.0	6.3	0.0	0.0
			1	509	46.8	6.3	10.8	0.0	13.9	1.6	5.7	14.9	0.0
V096	Expct	3–4	32	3	66.7	0.0	0.0	0.0	33.3	0.0	0.0	0.0	0.0
			16	14	21.4	21.4	7.1	21.4	21.4	0.0	7.1	0.0	0.0
			8	70	47.1	10.0	17.1	2.9	18.6	0.0	4.3	0.0	0.0
			4	513	50.5	15.2	12.3	1.6	15.4	0.0	5.1	0.0	0.0
			2	223	32.3	17.0	18.8	0.0	21.5	0.0	8.1	2.2	0.0
			1	660	44.7	5.9	6.1	0.0	18.8	0.0	10.2	14.4	0.0
			0.5	1,158	26.2	6.4	7.0	0.0	8.7	0.2	9.9	41.7	0.0
			0.25	465	26.5	3.7	0.0	0.0	13.8	0.0	8.2	48.0	0.0
			0.125	1,248	0.0	0	0	0	0.0	0.0	7.3	56.7	36.0
Average	Expct	--	--	--	40.8	10.9	8.4	6.0	17.6	0.1	6.6	14.8	3.0
B184A	Expct basal	3–4	8	51	49.0	21.6	17.6	0.0	11.8	0.0	0.0	0.0	0.0
			4	728	44.2	23.2	9.5	0.3	15.7	0.1	7.0	0.0	0.0
			1	744	55.2	2.8	8.5	0.0	12.6	0.0	8.9	12.0	0.0
B184B	Expct basal	3–4	8	52	53.8	17.3	15.4	3.8	9.6	0.0	0.0	0.0	0.0
			4	305	48.9	13.8	8.2	1.6	20.0	0.7	6.9	0.0	0.0
			1	441	53.3	2.9	14.7	0.2	10.4	0.0	9.3	9.1	0.0
Average	Expct basal	--	--	--	50.7	13.6	12.3	1.0	13.4	0.2	5.3	3.5	0.0
B102	Expf	3–7	8	286	50.0	13.3	14.7	2.1	11.9	0.0	8.0	0.0	0.0
			4	609	53.5	11.8	14.4	0.0	11.2	0.8	8.2	0.0	0.0
			1	537	30.9	1.5	11.0	0.0	21.4	0.0	11.4	23.8	0.0
B230	Expf	8	8	72	73.6	8.3	5.6	2.8	9.7	0.0	0.0	0.0	0.0
			4	703	56.8	5.3	16.4	0.1	15.4	2.4	3.7	0.0	0.0
V019	Expf	9	8	147	48.3	9.5	12.2	7.5	17	0	5.4	0	0.0
Average	Expf	--	--	--	53.0	8.0	12.4	13.0	13.9	0.8	6.3	--	0.0
V278	Exma	8	8	76	47.4	10.5	6.6	2.6	18.4	9.2	5.3	0.0	0.0
			4	649	47.8	10.9	12.3	1.7	13.3	2.2	11.9	0.0	0.0
V275A	Exlh	7	8	138	40.6	29.7	7.2	0.0	12.3	0.0	10.1	0.0	0.0
			4	705	38.2	15.5	14.6	0.0	20.4	0.0	11.3	0.0	0.0
			1	344	39.0	0.3	9.0	--	19.5	0.0	13.1	19.2	0.0
V275B	Exlh-levee	7	8	131	58.8	11.5	5.3	0.8	19.1	0.0	4.6	0.0	0.0
			4	352	53.7	9.9	10.5	0.3	17.0	0.0	8.5	0.0	0.0
			1	671	31.0	2.5	6.7	0.0	20.0	0.0	14.2	25.6	0.0

Table 6. Lithologic components in pyroclastic-current, lahar, and mixed-avalanche samples from the 2006 eruption of Augustine Volcano, Alaska.—Continued

[All values in weight percent. Components: low-silica andesite scoria (LSAS), dense low-silica andesite (DLSA), dense intermediate-silica andesite (DIA), high-silica andesite (HSA), high-silica andesite pumice (HSAP), and mixtures (banded) and defined in table 5. Phases and units (after Coombs and others, this volume), are defined in figure 2]

Sample	Unit[1]	Event	Size[2] (mm)	Clasts counted[3]	LSAS	DLSA	DIA	Banded	HSA	HSAP	Oxidized	Crystals	Non-crystals
V276A	Exlh	8	8	250	24.0	17.2	29.6	1.2	15.6	0.0	12.4	0.0	0.0
			4	327	38.8	15.9	15.9	0.9	15.9	0.0	12.5	0.0	0.0
			1	402	43.0	3.7	10.9	0.0	12.9	0.0	15.2	14.2	0.0
Average	Exlh	--	--	--	42.0	11.6	11.7	0.9	16.8	1.0	10.8	5.4	0.0
B215A	Expc	10	8	114	9.6	3.5	28.1	1.8	48.2	0.0	8.8	0.0	0.0
			4	959	9.7	9.2	38.5	0.0	39.0	0.0	2.5	1.1	0.0
			1	808	14.5	5.3	7.3	0.0	32.9	0.0	7.1	32.9	0.0
C259C	Expc	10	8	279	13.6	44.4	9.7	6.8	24.0	0.0	1.4	0.0	0.0
			4	2,080	35.3	39.3	9.8	1.2	11.4	0.0	2.9	0.0	0.0
V313	Expc	10	8	10	0.0	40.0	30.0	0.0	30.0	0.0	0.0	0.0	0.0
			4	179	0.0	29.6	20.1	0.6	44.1	1.7	3.9	0.0	0.0
Average	Expc	--	--	--	11.8	24.5	20.5	1.7	32.8	0.2	3.8	4.9	0.0
B173	RPpf	10	8	78	9.0	9.0	19.2	1.3	56.4	1.3	3.8	0.0	0.0
			4	330	2.4	9.1	10.6	0.0	73.9	0.9	3.0	0.0	0.0
			2	214	4.2	10.7	9.8	0.0	71.5	0.0	0.5	3.3	0.0
B222	RPpf	10	32	2	0.0	100.0	0.0	0.0	0.0	0.0	0.0	0.0	0.0
			16	13	38.5	46.2	7.7	0.0	7.7	0.0	0.0	0.0	0.0
			8	105	8.6	12.4	8.6	0.0	67.6	0.0	2.9	0.0	0.0
			4	723	5.8	7.9	3.3	0.0	79.8	0.0	3.0	0.1	0.0
			2	373	5.4	6.7	5.9	0.3	67.6	0.0	4.6	9.7	0.0
			1	820	2.7	3.9	8.3	0.0	31.7	18.0	7.0	28.4	0.0
			0.5	1282	0.9	1.6	9.2	0.0	19.6	0.0	6.9	61.8	0.0
			0.25	907	0.7	4.0	0.0	0.0	11.1	0.0	2.5	81.7	0.0
Average	RPpf				7.1	19.2	7.5	0.2	44.3	2.2	3.1	16.8	0.0
B203	Cpf	≥14	8	95	0.0	33.7	31.6	0.0	28.4	0.0	6.3	0.0	0.0
			4	641	0.0	42.6	7.2	0.0	46.6	0.0	3.6	0.0	0.0
V101	Cpc	≥14	8	73	0.0	1.4	50.7	11.0	28.8	0.0	8.2	0.0	0.0
			4	589	0.0	4.9	40.6	0.2	45.7	0.0	8.7	0.0	0.0
Average	Cpf				0.0	20.6	32.5	2.8	37.4	0.0	6.7	0.0	0.0
V22A	Efba		8	108	9.0	63.1	9.0	0.0	3.6	0.0	15.3	0.0	0.0

[1] Units after Coombs and others (this volume), same as in table 1.

[2] Size is defined as particles remaining on sieve indicated; for larger size classes (≥1.0 mm), grains were sorted by using a hand lens and binocular microscope, and commonly the lithologic differences were best determined by using wetted clasts (which represented the most common field conditions). Clast-type groups were then dried, counted, weighed, and normalized to 100 percent. For smaller size classes (≤0.50 mm), sorting was done by using a single paintbrush hair under a binocular microscope. Clast types were sorted by lithology or oxidation for most size classes. The samples whose small grains were sorted had them divided among crystals, noncrystals, and oxidation. Lithologies are described in table 3.

[3] Not all size classes were counted for all samples. Clasts from each size class were initially sorted from 32 mm to 0.125 mm to assess the similarity in clast-type proportions between size classes. The 4- and 8-mm size classes were deemed representative of the proportions of lithologies for many samples.

Table 8. Parameters and analysis-of-variance statistics for alternative linear models of log-transformed volume versus planimetric area for pyroclastic-current deposits worldwide and those from the 2006 eruption of Augustine Volcano, Alaska.

Variable	Best-fit regression	Specified 2/3 slope	Specified zero slope
	Dome-collapse pyroclastic flows		
Slope of line	0.659	0.667	0
Intercept of line at log *V*=0	1.612	1.5661 = log 37	5.530
Number of data pairs (N)	21	21	21
Residual degrees of freedom (DF)	19	20	20
Residual sum of squares (SS)	0.800	0.801	5.133
Residual mean square (MS)	0.042	0.042	0.257
Standard error of model (sigma)	0.205	0.200	0.507
Coefficient of determination (r^2)	0.844	0.844	0
F statistic comparison to best-fit regression	Not applicable	0.017	102.9
Null hypothesis	Not applicable	Accepted, 0.99-confidence level	Rejected
	Column-collapse pyroclastic currents		
Slope of line	0.736	0.667	0
Intercept of line at log *V*=0	1.779	2.1717 = log 150	5.943
Number of data pairs (N)	14	14	14
Residual degrees of freedom (DF)	12	13	13
Residual sum of squares (SS)	0.110	0.151	4.731
Residual mean square (MS)	0.009	0.012	0.364
Standard error of model (sigma)	0.095	0.108	0.603
Coefficient of determination (r^2)	0.977	0.968	0
F statistic comparison to best-fit regression	Not applicable	4.493	547.9
Null hypothesis	Not applicable	Accepted, 0.99-confidence level	Rejected
	Surge-like pyroclastic currents		
Slope of line	0.653	0.667	0
Intercept of line at log *V*=0	2.794	2.718 = log 520	6.509
Number of data pairs (N)	4	4	4
Residual degrees of freedom (DF)	2	3	3
Residual sum of squares (SS)	0.008	0.008	0.444
Residual mean square (MS)	0.004	0.003	0.148
Standard error of model (sigma)	0.064	0.053	0.385
Coefficient of determination (r^2)	0.981	0.981	0
F statistic comparison to best-fit regression	Not applicable	0.045	105.5
Null hypothesis	Not applicable	Accepted, 0.99-confidence level	Rejected

This page intentionally left blank

The 2006 Eruption of Augustine Volcano, Alaska
Power, J.A., Coombs, M.L., and Freymueller, J.T., editors
U.S. Geological Survey Professional Paper 1769

Chapter 11

Characterizing Pyroclastic-Flow Interactions with Snow and Water Using Environmental Magnetism at Augustine Volcano

By James E. Begét[1]

Abstract

In-place measurements of environmental magnetic susceptibility of pyroclastic flows, surges and lahars emplaced during the 2006 eruption of Augustine Volcano show that primary volume magnetic susceptibilities of pyroclastic materials decreased where the flows encountered water and steam. The Rocky Point pyroclastic flow, the largest flow of the eruption sequence, encountered a small pond near the north coast of Augustine Island where local interactions with water and steam caused susceptibilities to decrease from 1,084±128×10^{-5} SI to 615±114×10^{-5} SI. Ash produced during phreatic explosions and pyroclastic surges that crossed snow also produced deposits with reduced susceptibilities, while lahar deposits derived from pyroclastic flows showed even greater reductions in susceptibility (430±129×10^{-5} SI). The susceptibility reductions are probably largely attributable to oxidation of iron in magnetite and other minerals within the pyroclastic flows, although other physiochemical processes may play a role. Measurements of the magnetic properties of pyroclastic flows, surges, and lahar deposits can be a useful tool in understanding the processes that occur when pyroclastic flows encounter ice, snow, and water and interact with water and steam on the slopes of active volcanoes.

Introduction

The interactions that occur between pyroclastic flows and snow, ice, and water are of considerable interest to volcanologists because these processes sometimes generate floods and lahars that cause destruction and fatalities in areas far beyond the maximum extent of the pyroclastic flows themselves. For instance, the 1985 eruption at Nevado del Ruiz Volcano in the Andes Mountains of Colombia generated pyroclastic flows and surges that were restricted to the upper reaches of the volcano, far from any human habitation. However, the pyroclastic eruption melted snow and ice over part of the summit ice cap and generated devastating mudflows that traveled as far as 100 kilometers down stream valleys. These lahars traveled down the Río Lagunillas and caused an estimated 23,000 fatalities at the town of Armero, where local people had had little comprehension of the risks from the Ruiz eruption (Pierson and others, 1990).

The lahar and flood deposits produced by interactions between pyroclastic flows and glaciers, snowfields, and bodies of water have attracted much attention since the catastrophic Ruiz eruption. For instance, during the eruptions of Ruapehu Volcano in New Zealand in 1994–95 and 2005–6, interactions of pyroclastic material and snow became a focus of concern. Lahars that traveled downslope after explosive events at the summit were observed during emplacement, and their deposits were intensively studied (Cronin and others, 1997). Unfortunately, once again it proved difficult to observe and study active surges and pyroclastic flows and the processes that occur during their encounters with snow and ice, because the active vents are extremely hazardous to approach during eruptions, and because these kinds of eruptions and processes typically produce large clouds of ash, gas, and steam that hide the ground-level interactions. As a result, the processes involved in the generation of lahars and floods by pyroclastic flows are still poorly understood.

The 2006 eruption of Augustine Volcano provided an excellent opportunity to study pyroclastic-flow and surge deposits that had encountered ice, snow, and water, as well as associated lahar deposits resulting from those interactions. Comprehensive sedimentological and stratigraphic studies of the pyroclastic-flow and lahar deposits produced in 2006 at Augustine Volcano showed that such interactions were complex and varied. Some pyroclastic flows traveled across snowfields with little obvious effect on the sedimentology of

---

[1] Alaska Volcano Observatory, Department of Geology and Geophysics, University of Alaska Fairbanks, 900 Yukon Drive, Fairbanks, AK 99775.

the pyroclastic flow deposits, while others crossed areas of snow and were locally modified and transformed into mixed rock-and-snow avalanches, lahars, and water-rich floods (Vallance and others, this volume).

In this paper, we present tests of a new geophysical technique that we believe has great promise as a means to identify and characterize pyroclastic-flow and surge deposits that have interacted with snow, ice, and water. Environmental magnetism is the study of interactions between environmental processes and the magnetic properties of sediments (Evans and Heller, 2003). Studies of environmental magnetism often focus on changes in magnetic susceptibility, because this geophysical characteristic of sediments is relatively easily measured and has been shown to undergo significant changes in response to various environmental factors and depositional processes (Maher and Thompson, 1999). We have followed this approach and focused on magnetic susceptibility in this study.

Pyroclastic-flow deposits that have interacted with snow, ice, and water are good candidates for this kind of study, because the initial magnetic susceptibility of volcanic rocks and volcanic ash deposits produced by explosive eruptions elsewhere in Alaska have been shown to be relatively high, indicating the presence of abundant susceptible iron-bearing minerals (Begét and others, 1994). However, to our knowledge, no prior studies of the changes in magnetic susceptibility of pyroclastic deposits due to interactions with water and steam have ever been undertaken. Searches on Google Scholar and GeoRef found no record of scientific papers on this subject, and recent academic textbooks on environmental magnetism (Evans and Heller, 2003) and volcanology (Schmincke, 2004) contain no references to this kind of investigation.

This paper presents the results of several hundred measurements of magnetic susceptibility on fresh, in place, deposits of the 2006 pyroclastic flows on the flanks of Augustine Volcano, as well as measurements on more areally restricted surge and lahar deposits. The purpose of this paper is not to descriptively characterize the magnetic mineralogy and magnetic characteristics of the 2006 deposits, but to report on the initial development and field-testing of a new geophysical approach that can quickly and quantitatively characterize a key geophysical property of pyroclastic-flow deposits that records evidence of past interactions with water and snow.

2006 Pyroclastic Flows and Related Deposits on the North Flank of Augustine Island

The 3-month-long eruption at Augustine Volcano in 2006 involved a variety of different eruptive mechanisms and produced a wide array of pyroclastic and secondary deposits (Coombs and others, this volume; Vallance and others, this volume). Explosive activity began on January 11, 2006, and more than a dozen discrete Vulcanian blasts occurred in the next 20 days, generating ash fall, pyroclastic flows, mixed avalanches of snow, ice, and rock, and lahars. On January 28, the eruption moved into a more continuous eruptive phase as rapid effusion of lava led to vigorous block-and-ash-flows. A summit lava dome began to form in early February, and, after a pause from February 10 to March 2, two short, blocky lava flows were emplaced by late March. The initial period of explosions, lasting from January 11 to January 28, is referred to as the explosive phase, while eruptive events occurring from January 28 to February 10 are considered to be part of the continuous phase, and all subsequent activity is part of the effusive phase (Power and others, 2006; Coombs and others, this volume).

On January 27, 2006, near the end of the explosive phase, a discrete several-minute-long explosive event (event 10 in the nomenclature of Vallance and others, this volume) deposited the Rocky Point pyroclastic flow on the north flank of the volcano (fig. 1). This flow is the most voluminous of any single flow produced during the eruptive sequence, totalling 17 million m^3 (Coombs and others, this volume). It traveled almost to sea level on the north side of Augustine Island and buried earlier 2006 pyroclastic flows on the north flank of the volcano (fig. 2).

The distal portion of the Rocky Point pyroclastic flow nearly reached the coast, traveling over a small pond of water. The pond lay at 25 m above sea level (asl) and was approximately 50 m in diameter. The pond is partly surrounded by hummocks of the late 19th century Burr Point debris-avalanche deposit and the older Rocky Point debris-avalanche deposit (Begét and Kienle, 1992; Siebert and others, 1995) and likely was formed during one of these events. The 2006 Rocky Point pyroclastic flow completely filled the lake basin with pyroclastic debris. This pyroclastic flow also generated small, relatively dilute ash-cloud surges that traveled short distances beyond the lateral margins of the pyroclastic flow and singed alders and other vegetation around the former shoreline of the pond, leaving well-sorted sandy ash deposits.

The initial magmatic explosive events early in January that marked the beginning of the explosive phase occurred when Augustine Volcano was completely covered with winter snow. These explosions generated pumiceous pyroclastic flows, snow avalanches, and lahars that moved down all sides of the volcano (Vallance and others, this volume). By the time the Rocky Point pyroclastic flow was emplaced on January 28, much of the winter snowpack on the volcano had been removed or buried by the earlier pyroclastic flows. The snow was almost completely gone when block-and-ash flows, emplaced during the later continuous phase, subsequently buried the uppermost parts of the Rocky Point pyroclastic flow (Coombs and others, this volume).

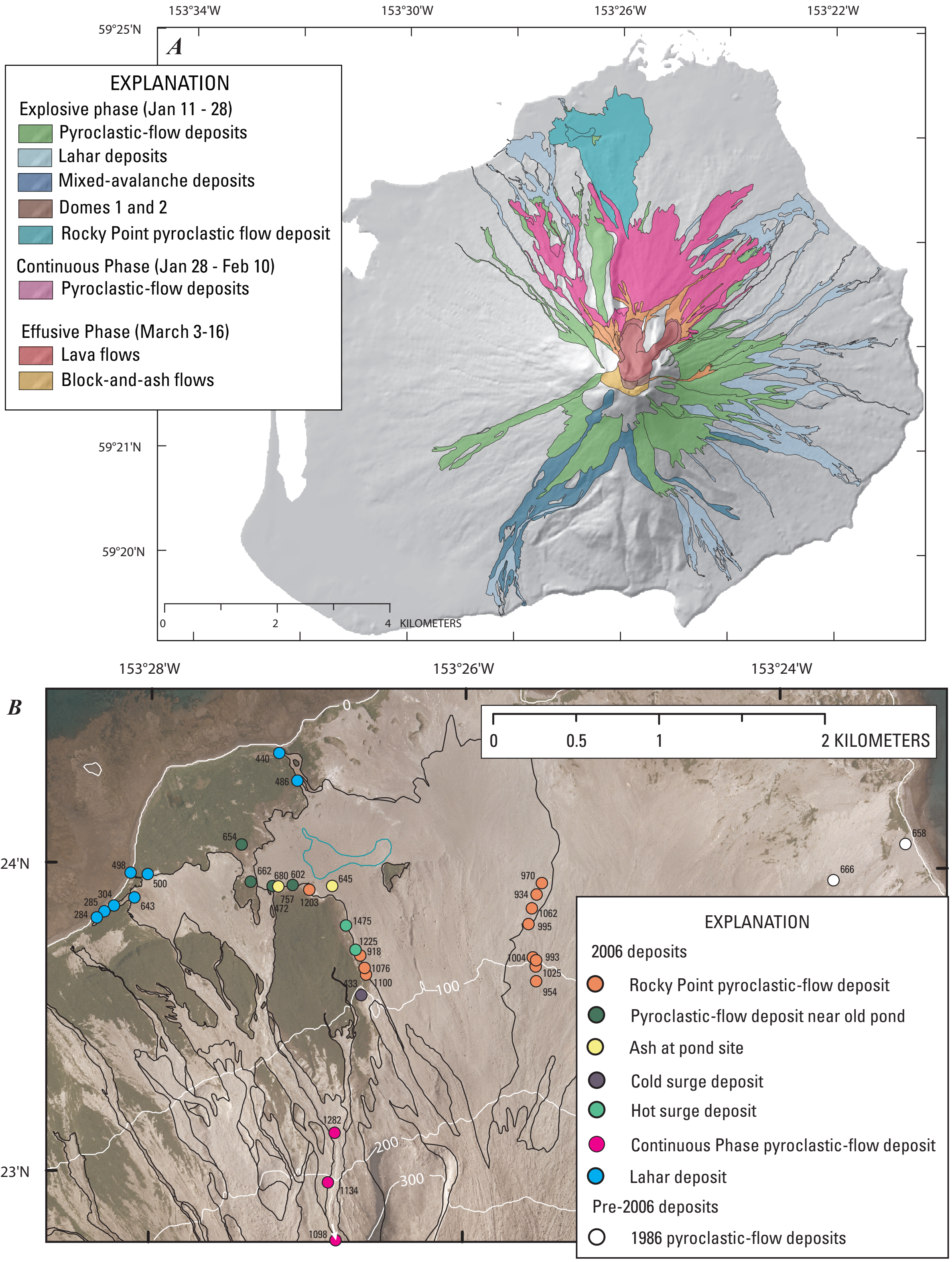

Figure 1. Generalized maps showing deposits from the 2006 eruption of Augustine Volcano on Augustine Island. *A,* Distribution of deposits from the 2006 eruption draped over shaded-relief map of Augustine Island, modified from Coombs and others (this volume). *B,* Sample locations for this study on the north flank of Augustine Volcano, overlain on an orthophoto taken July 12, 2006. Outlines of contiguous 2006 deposits are shown in black. The general outline of the small pond buried by the Rocky Point pyroclastic flow, as mapped in July 2006 by Begét, is shown in light blue, and100-m contours shown in white. Some 2006 deposits were sampled in fresh exposures in a small channel 170 m east of the region of contiguous flows and a few sites were sampled on 1986 pyroclastic flows (see text for detailed discussion).

Magnetic Susceptibility of Pyroclastic Flows, Surges and Lahars at Augustine Volcano

Augustine Volcano produced a wide range of pyroclastic deposits during the 2006 eruption. This study targets the Rocky Point pyroclastic flow deposit because it provides an almost ideal opportunity to test the hypothesis that measurements of magnetic susceptibility can provide a quantitative tool for identifying and characterizing pyroclastic deposits that have been in contact with snow, ice, and water. We also present some results from lahars, from pyroclastic flows on the north flank that were produced during the later continuous phase of the eruption and from 1986 Augustine pyroclastic flow deposits.

Magnetic susceptibility is a basic geophysical property of all rocks and sediments. Magnetic susceptibility can be measured on a mass, molar, or volume basis. It is determined by measuring the effect of an applied magnetic field of known strength on a sample. The ease of magnetization of the sample is a complex function of the concentration, size, shape, and mineralogy of magnetizable material in the sample. Most of the susceptibility signal in volcanic rocks typically reflects the presence of common ferromagnetic minerals, such as magnetite, hematite, and iron-titanium oxides, with a minor contribution from other ferromagnesian minerals that contain relatively small amounts of Fe^{2+}, Fe^{3+}, or Mn^{2+} such as olivine, amphiboles, and pyroxenes.

Field measurements of volume magnetic susceptibility of the 2006 deposits at Augustine Volcano were made with a Bartington MS2 susceptibility meter and an MS2F microprobe. A small amount of sample preparation, including the excavation of small pits, was done in this study to standardize the sampling process, but the volume magnetic susceptibility measurements themselves are nondestructive. When measuring volume susceptibility, the MS2 meter has a sensitivity of 2×10^{-6} SI, with a range from $1–9999\times10^{-5}$ SI, and a resolution of 2×10^{-6} SI in standard mode. The Bartington instrument has become an international standard for environmental susceptibility measurements and records data in dimensionless volume susceptibility units, which are multiplied by 10^{-5} to convert susceptibilities into SI units (Bartington Corporation, 2004).

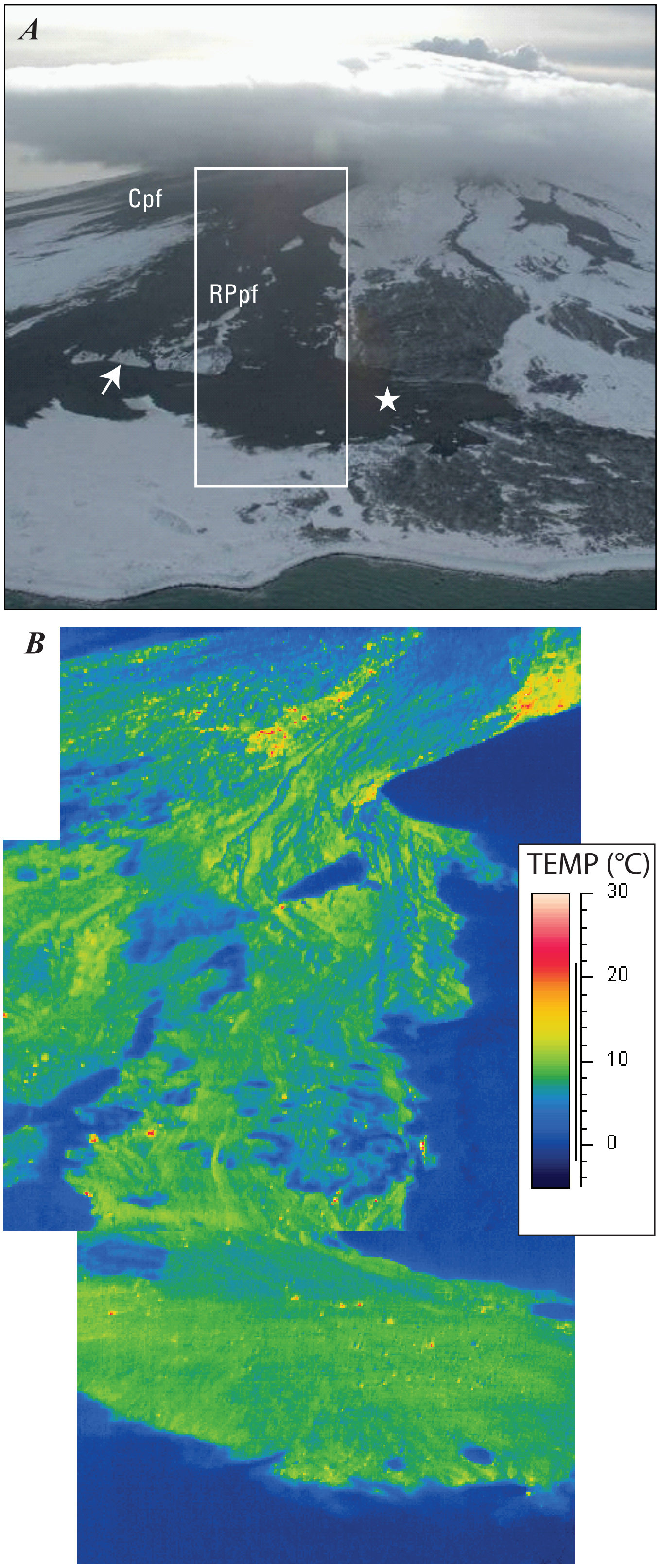

◄**Figure 2.** Views of recently emplaced pyroclastic flow deposits, February 8, 2006. *A,* Oblique aerial photograph of Augustine's north flank, showing the Rocky Point pyroclastic flow (RPpf) and the overlying Continuous Phase pyroclastic flow fan (Cpf). The Rocky Point flow was bifurcated by a low ridge (white arrow). Westernmost lobe of the Rocky Point flow crossed and filled in a small lake (star). Box shows approximate area of panel B. Photo by M. Coombs, USGS. *B,* Thermal infrared image mosaic showing close up of Rocky Point deposit. Images by D.J. Schneider, AVO.

The Bartington M2SF microprobe is designed for use in geologic studies. The probe has a diameter of 15 mm and measures volume susceptibility in a small region of the sample immediately beneath the probe. In order to take a measurement the probe is placed on the sample and activated. The instrument then applies a magnetic field and measures the sample response, with about 90 percent of the susceptibility signal coming from the upper few millimeters of the sample, where the magnetic field projected by the probe is strongest (fig. 3). The MS2F microprobe proved to be ideal for field studies of the pyroclastic-flow deposits because the knowledge that 90 percent of the susceptibility response is obtained from a restricted area within a few millimeters of the MS2F probe allows the operator to precisely control what the instrument is measuring, even in field settings. For this study the goal was to effectively measure the susceptibility of the matrix of pyroclastic-flow deposits, so the probe was placed directly on exposures of the well-sorted and finer grained pyroclastic flow matrix visible between clasts in the pyroclastic flow deposits. Voids or lithic clasts hidden beneath the surface of the area chosen for the matrix sampling have a negligible influence on volume susceptibility measurements, as long as they were buried more than approximately 2 cm below the surface, or if they were more than 1 cm away from the outside edges of the MS2F microprobe (fig. 3).

Several different sampling methods were tested during this study. Initially, shallow pits and trenches approximately 50 cm deep were excavated into the tops of pyroclastic flow deposits and into the sides of associated levees, and the MS2F microprobe was then inserted into the pit for the measurement. Subsequent measurements were taken on smoothed surfaces cut only a few centimeters into the surface of massive pyroclastic flow deposits and levees to expose the matrix of the deposits, and in some cases directly on the hardpan surface of indurated pyroclastic flow deposits. After each measurement, the surface was excavated to check if voids or blocks were present just below the surface of the prepared site. No significant differences in susceptibility were observed among any of the various sampling strategies as long as the excavations and natural surfaces measured were flat and smooth.

Component analysis of the 2006 pyroclastic flow deposits revealed that they contain several different lithologies and that the relative percentages of the different lithologies changed through the course of the 2006 eruption (Vallance and others, this volume). All of the magnetic susceptibility values discussed in this paper, unless specifically noted otherwise, are from the Rocky Point pyroclastic flow, which was erupted during a short time interval and has broadly similar proportions of lithic components throughout its extent (Vallance and others, this volume). The susceptibility of the two major lithic components in the Rocky Point pyroclastic-flow deposit was measured directly on representative lithic blocks and showed that different rock types produced during the 2006 eruption have dramatically different susceptibilities (table 1). Low-silica andesite scoria and dense clasts have susceptibilities between 1,200–1,700×10^{-5} SI, while friable and moderately vesicular high-silica andesite “cinderblock” clasts (Vallance and others, this volume) have volume susceptibilities of 700–1,200×10^{-5} SI. The Rocky Point pyroclastic flow deposit consists mainly of high-silica andesite, with clasts of low-silica andesite being present as a secondary component. The large difference in the susceptibility measured between the two principal lithologies suggests that the volume susceptibility of the pyroclastic flow will be strongly influenced by the relative proportion of these two major components within the deposit. Component analysis of different size fractions of the Rocky Point pyroclastic flow found that similar percentages of the major components were present from the coarsest to the finest grain sizes of the pyroclastic flow (Vallance and others, this volume), suggesting that susceptibility measurements of the matrix of the pyroclastic flow deposit are a good approximation of the susceptibility of the entire pyroclastic flow deposit.

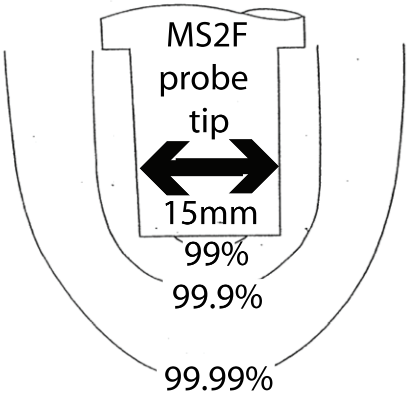

Figure 3. An isomagnetic field plot showing the rapid decrease in sensitivity of the M2SF field probe with distance from the tip of the instrument. The probe tip is 15 mm in diameter and has a maximum sensing distance of 15-20 mm, but the instrument is highly sensitive to the magnetic susceptibility of sample material just below and within a few millimeters of the center of the probe tip, so that 99% of the measured signal comes from material directly beneath the probe, and 99.9% of the signal is measured within a few millimeters of the probe. This property of the instrument makes it feasible to accurately measure the volume susceptibility of pyroclastic flow deposit matrices, as long as no voids or large lithic clasts are present within a few millimeters of the base of the probe. Figure modified from the Bartington M2S system operating manual (Bartington Corporation, 2004).

The Rocky Point pyroclastic flow traveled down the volcano’s north flank, where previous explosive events had deposited pyroclastic flows and cleared the surface of snow (Coombs and others, this volume; Vallance and others, this volume). Measurements taken from different places on the Rocky Point deposit yielded generally similar magnetic susceptibilities of 900–1,400×10^{-5} SI. The repeatability of the susceptibility measurements taken at each site was good, with values of one standard deviation from the mean typically falling no more then 10–20 percent from the average value for the entire group of susceptibility measurements. The

Table 1. Magnetic susceptibility measurements of the Rocky Point pyroclastic flow and associated deposits from the 2006 eruption of Augustine Volcano.

Station Number	Elevation (meters)	Latitude (north)	Longitude (west)	Magnetic suscepti-bility[1]	1σ [2]	N[3]	Deposit type
Rocky Point pyroclastic-flow deposit							
06AUJEB45	84	59.394	153.444	1100	63	10	PF[4] 1evee ridge with pink top
06AUJEB46	79	59.394	153.444	1076	82	9	PF body
06AUJEB47	76	59.395	153.444	918	83	5	Pink top in PF body
06AUJEB40	52	59.398	153.426	1062	83	4	PF body matrix
06AUJEB41	40	59.398	153.426	934	42	3	PF matrix
06AUJEB42	34	59.399	153.425	970	49	4	Flow terminus lobe
06AUJEB35	116	59.394	153.426	954	91	4	PF matrix
06AUJEB36	91	59.395	153.426	1025	1	5	PF matrix
06AUJEB37	88	59.395	153.426	1004	211	4	PF matrix
06AUJEB38	85	59.395	153.426	993	9	5	PF matrix
06AUJEB39	61	59.397	153.427	995	49	5	PF matrix
06AUJEB52	23	59.399	153.450	1203	30	6	PF matrix upslope of pond
06AUJEB40A	49	59.401	153.429	1240	119	6	Fines-depleted matrix
Rocky Point pyroclastic-flow deposit, in or adjacent to pond							
06AUJEBJA	30	59.399	153.454	472	43	5	Pink oxidized phreatic ash
06AUJEBJ	23	59.399	153.454	757	35	6	Pink oxidized PF matrix
06AUJEB51	23	59.399	153.448	645	84	6	Fine pink ash in collapse pit
06AUJEB51A	23	--	--	443	95	4	Fine pink ash in pond phreatic explosion pits
06AUJEB51B	23	59.399	153.456	662	49	8	PF matrix
06AUJEB51C	23	59.401	153.457	654	19	11	PF matrix, thin in bushes
06AlJ.JEB88	21	59.399	153.452	802	50	5	Pinkish PF in pond
06AUJEB89	19	59.399	153.452	602	37	7	Reddish oxidized PF in pond
06AUJEB90	14	59.399	153.453	680	24	5	Pink phreatic ash in pond
06AUJEB40B	46	59.3995	153.453[5]	907	55	6	Lower PF beside pond
06AUJEB40C	46	59.3995	153.453[5]	1200	14	2	PF around burned spruce
06AUJEB42A	30	--	59.399[5]	1299	25	5	PF 100 m from pond
Surge deposits associated with Rocky Point pyroclastic flow							
06AUJEB44	109	59.393	153.444	433	41	7	Cold surge
06AUJEB44A	101	59.3935	153.444[5]	1025	94	3	Distal ash cloud
06AUJEB44B	87	59.3935	153.444[5]	1166	127	6	Intermediate surge depos
06AUJEB48	71	59.395	153.445	1225	63	6	Proximal surge deposit
06AUJEB49	49	59.397	153.446	1475	308	4	Coarse proximal surge
06AUJEB51	23	59.399	153.448	1084	33	3	Ash cloud from surge
06AUJEB51A	14	59.3995	153.448[5]	827	45	3	Gray surge deposit
Continuous phase pyroclastic-flow deposit on northwest flank							
06AUJEB2	278	59.379	155.447	1098	8	2	PF matrix
06AUJEB2A	287	59.379	155.447	989	9	2	PF matrix
06AUJEB2B	314	59.379	155.447	1058	134	4	PF matrix
06AUJEB3	213	59.383	153.448	1134	30	2	PF matrix
06AUJEB4	170	59.385	153.447	1282	35	2	PF levee

Table 1. Magnetic susceptibility measurements of the Rocky Point pyroclastic flow and associated deposits from the 2006 eruption of Augustine Volcano.—Continued

Station Number	Elevation (meters)	Latitude (north)	Longitude (west)	Magnetic susceptibility[1]	1σ [2]	N[3]	Deposit type
2006 lahar deposits							
06AUJEB59	14	59.398	153.468	643	21	3	Lahar clasts
06AUJEB91	12	59.399	153.467	500	18	7	Lahar matrix
06AUJEB53	6	59.404	153.451	486	17	10	Lahar matrix
06AUJEB60	2	59.398	153.470	304	54	11	Lahar matrix
06AUJEB93	1	59.399	153.469	498	23	8	Lahar matrix
06AUJEB55	1	59.406	153.453	440	23	10	Lahar matrix
06AUJEB61	1	59.397	153.472	284	22	10	Lahar matrix
06AUJEB62	0.5	59.397	153.472	285	114	10	Lahar matrix
Individual clasts from 2006 pyroclastic-flow deposits							
06AUJEB45	84	59.394	153.444	1517	93	6	Low-silica andesite
06AUJEB35	116	59.394	153.426	1288	56	3	Low-silica andesite bomb
06AUJEB35	116	59.394	153.426	761	28	3	High-silica andesite
06AUJEB2A	287	59.379	155.447	1203	0	1	High-silica andesite
06AUJEB2A	287	59.379	155.447	989	9	2	Boulder in PF matrix
06AUJEB2B	314	59.379	155.447	1150	0	1	Prismatic boulder
1986 pyroclastic-flow deposits							
06AUJEB57	26	59.399	153.394	666	50	8	1986 PF
06AUJEB58	9	59.401	153.387	658	18	11	1986 PF matrix samples
06AUJEB58A	6	59.401	153.387	672	94	11	1986 PF matrix

[1] Reported magnetic susceptibility values are averages of N measurements.

[2] σ is the standard deviation of the averaged magnetic susceptibility measurements.

[3] N is the number of individual magnetic susceptibility measurements at each station.

[4] PF is an abbreviation for pyroclastic-flow deposit.

[5] Measurements made on traverses downhill from the first station in the series.

variation in the entire data set of susceptibility measurements for the Rocky Point pyroclastic flow deposit is somewhat larger (table 1), and is thought to reflect variations in the initial componentry of these deposits.

Susceptibility Measurements Along a Traverse at the Margin of the Rocky Point Pyroclastic Flow Deposit

The pyroclastic flow deposits emplaced in 2006 on the north side of Augustine Volcano partially buried a preexisting pyroclastic fan that has been developing since 1883 (Waitt and Begét, 2009). On the lower part of the pyroclastic fan, the Rocky Point pyroclastic flow deposit is bordered on its western edge by a much older lava flow. On its western margin against the lava flow, the Rocky Point pyroclastic flow developed flat terraces and a levee that could be traced for hundreds of meters downslope. Alder trees and soil buried by the Rocky Point pyroclastic flow were charred and incinerated, showing that the pyroclastic flow was hot in this area (fig. 4).

In order to better understand the sources of variation in magnetic susceptibility, measurements were made at eight separate sites during a 1-km-long traverse along the western margin of the Rocky Point pyroclastic flow (fig. 1). The averages of all of these measurements ranged from 937 to 1,061×10^{-5} SI, indicating that much less variability in magnetic susceptibility occurs in this particular region of the pyroclastic flow than was seen in the complete data set from the Rocky Point pyroclastic flow and the subsequent flows of the continuous phase (fig. 5). The small range of susceptibilities measured from this one part of the Rocky Point pyroclastic flow supports our suggestion that the susceptibility within the lithic components of each flow strongly influences the matrix magnetic susceptibility. The greater variability within the entire set of susceptibility measurements for the Rocky Point pyroclastic flow and later pyroclastic-flow deposits is therefore thought to reflect a small amount of variability in the relative abundances of the constituent components occurring through the entire pyroclastic flow (fig. 6).

Continuous-Phase Pyroclastic Flow Deposits

Measurements of magnetic susceptibility were also made on pyroclastic flow deposits produced during the continuous phase of the 2006 eruption (Coombs and others, this volume). Numerous block-and-ash flows, erupted from January 28 to February 10, are found on the upper parts of the pyroclastic fan on the north side of Augustine volcano, where they bury the slightly older Rocky Point pyroclastic flow deposit. Magnetic susceptibility measurements were made on continuous-phase pyroclastic flow deposits on both the east and west sides of the pyroclastic fan. These values ranged between 917×10^{-5} SI and 1,282×10^{-5} SI, similar to the susceptibility measurements made on the Rocky Point pyroclastic flow deposits. Studies of the lithic makeup of deposits of the continuous phase found mostly a mixture of high-silica andesite and intermediate andesite clasts and banded clasts, with only minor amounts of greenish porphyritic andesite. The measured susceptibilities in the continuous-phase pyroclastic flow

Figure 4. The 2006 Rocky Point pyroclastic flow traveled down the north side of Augustine Island and flowed into a small pond. Yellow rucksack is 80 cm tall.

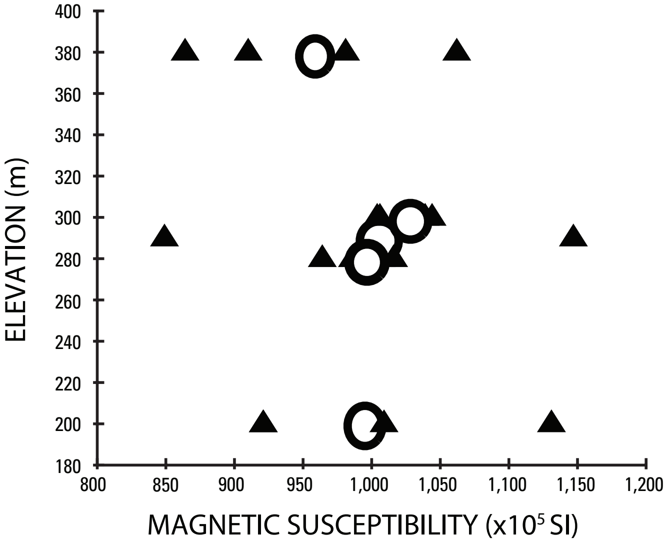

Figure 5. Magnetic susceptibility of the Rocky Point pyroclastic flow measured within a single channel along a 1.5-km-long traverse at five sites between 380 m and 200 m elevation. Multiple measurements were taken at each site. Triangles on the plot show the value of the individual magnetic susceptibility measurement, while large open circles show the mean value calculated for each site. The average susceptibilities were nearly identical at all sites along the traverse.

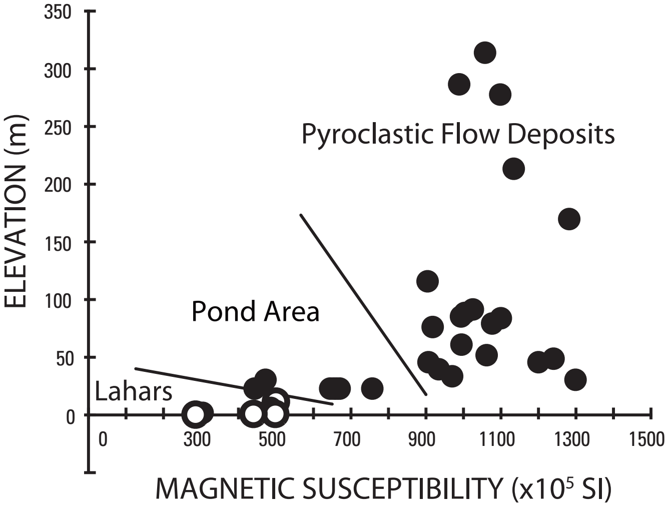

Figure 6. Average volume magnetic susceptibilities of 2006 Rocky Point pyroclastic flow deposits (solid circles), measured on the slopes above the pond site and at the pond site, and lahar deposits (open circles) measured in stream channels. The susceptibilities of the pyroclastic flow deposits in the former pond area were notably lower than those of other pyroclastic flow deposits, and lahar deposits were characterized by similarly low or even lower magnetic susceptibilities.

deposits probably reflect variations in the componentry of the deposits at different localities, just as was seen in the Rocky Point pyroclastic flow deposits.

Interaction of Rocky Point Pyroclastic-Flow Deposits with Water and Steam

The volume magnetic susceptibility of Rocky Point pyroclastic flow deposits decreased significantly where the Rocky Point flow encountered a small pond on the north side of Augustine Volcano (figs. 1, 2). As discussed above, the magnetic susceptibility of pyroclastic flow deposits determined at numerous sites above the pond ranged from ca. 900×10^{-5} SI to 1300×10^{-5} SI. A virtually identical range of susceptibility values was obtained from measurements on the Rocky Point pyroclastic flow deposits in areas immediately adjacent to the pond (table 1). For instance, at a site just 25 m from the pond, where the flow had partially buried alders and burned them (fig. 7), the averaged volume susceptibility of the Rocky Point pyroclastic flow deposit was 1203×10^{-5} SI. This value is indistinguishable from susceptibility measurements taken farther upslope and demonstrates that no significant changes were observed in the susceptibility of the pyroclastic flows as a result of travel distance or elevation loss anywhere throughout the Rocky Point pyroclastic flow deposit above the pond area (fig. 6).

The susceptibility of the Rocky Point pyroclastic flow deposit decreases abruptly where it encountered water at the pond site. During fieldwork in August 2006, the former pond site was found to be filled with the Rocky Point pyroclastic flow deposits but was still easily recognizable as a round, flat local depression in the deposit surface. While rootless fumaroles were rare within the Rocky Point pyroclastic deposit at lower elevations, several small rootless fumaroles were still active in this area, suggesting some moisture might still be present below the former pond surface (fig. 8).

The susceptibility values measured on the flow-deposit matrix around the pond basin ranged from 756×10^{-5} SI to 802×10^{-5} SI, or about 10 to 40 percent lower than the susceptibility of Rocky Point pyroclastic flow deposits or the later, continuous-phase pyroclastic flow deposits found higher on the north side of Augustine Volcano (table 1). The abrupt decrease in magnetic susceptibility observed in Rocky Point pyroclastic flow deposits filling the pond basin suggests that interactions between the hot pyroclastic flow and water and steam produced significant reductions in the initial susceptibility of the pyroclastic flow deposit.

Phreatic Ash and Other Deposits near the Pond

Multiple small craters in the surface of the pyroclastic flow deposits within the pond area, ranging from approximately 1 to 3 m in diameter (fig. 8), show that small phreatic explosions occurred in this area during or soon after the pyroclastic flows entered the pond. These explosion craters are mantled with as much as 10 cm of pink, silt-size ash derived from material elutriated from the 2006 pyroclastic flow

Figure 7. Photograph showing Rocky Point pyroclastic flow deposit on the north flank of Augustine Volcano. The presence of charred alders and soil in a lateral levee of the Rocky Point pyroclastic flow deposit 50 m from the pond area indicates that the flow was still hot when it reached the pond area. Rucksack in photo (indicated by arrow) is 0.8 m in length.

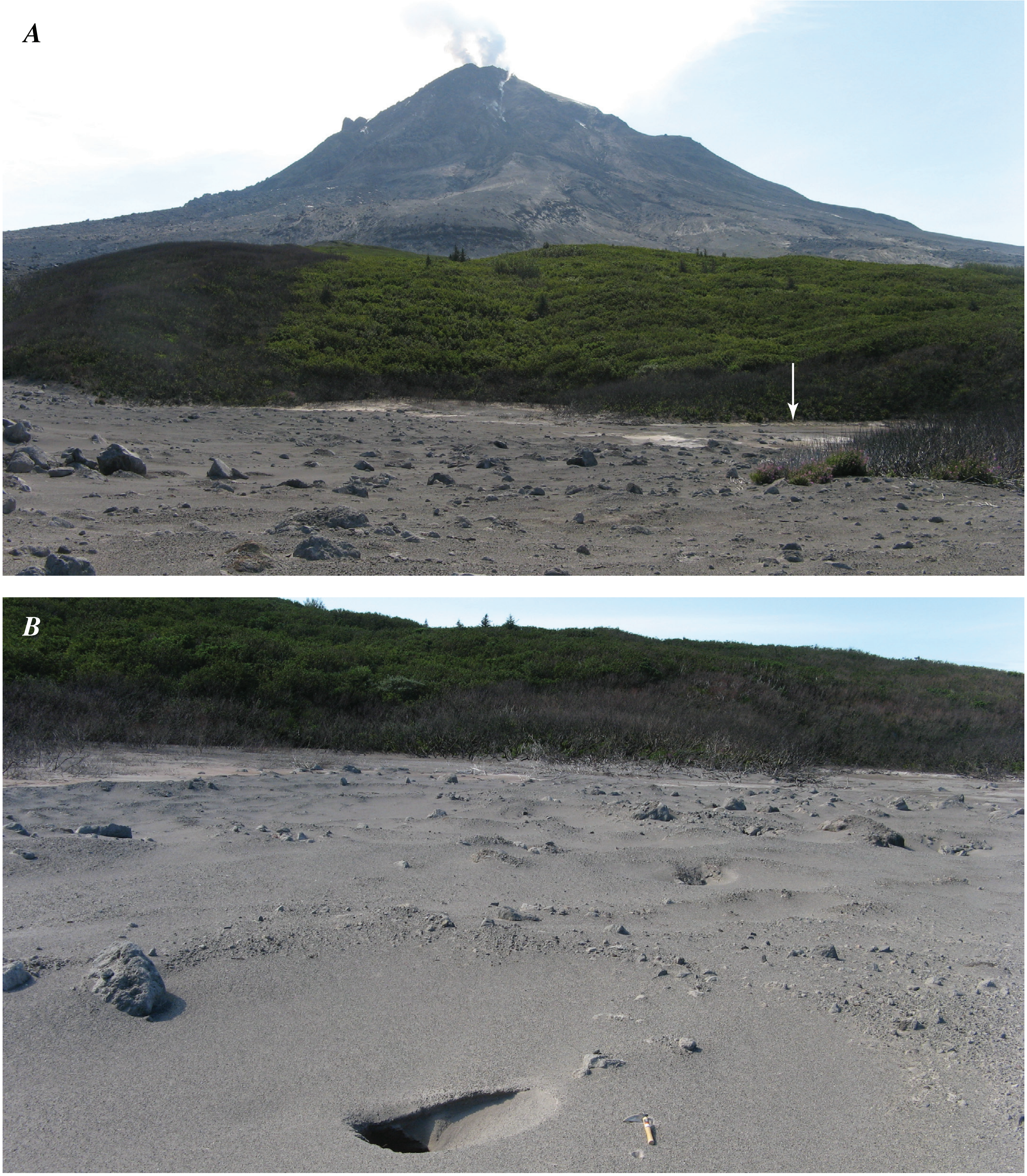

Figure. 8. Photographs of the Rocky Point pyroclastic flow. *A,* View looking south at the area of the pond filled by deposits of the 2006 Rocky Point pyroclastic flow. The Rocky Point pyroclastic flow traveled downslope alongside the ridge at the left of the image, and filled a pond (arrow) at the base of the ridge. Note the area of dead alders along the ridge caused by ash-cloud surges from the pyroclastic flows. Two traverses through the deposits left by the ash-cloud surges were made about 800 m upslope. *B,* Small phreatic explosion craters (pseudocraters) and rootless fumaroles within the pond area. The tool next to the rootless fumarole in the foreground is 28 cm long.

deposits. The magnetic susceptibility of this ash is 482×10^{-5} SI, a value 50 to 70 percent lower than that of the unaltered Rocky Point pyroclastic flow deposits outside the pond area. The low magnetic susceptibility of the phreatic ash deposits in the pond area provides additional evidence that interaction with water and steam can produce significant reductions in the magnetic susceptibility of pyroclastic flow deposits.

The secondary phreatic explosion craters probably formed during very shallow explosions caused by rapid superheating of steam that produced locally overpressured conditions (Shepherd and Sigurdsson, 1982; Sheridan and Wohletz, 1983; Schmincke, 2004). The phreatic ash generated in these explosions was probably originally part of the matrix of the pyroclastic flow that interacted with water and steam as the pyroclastic flow travelled into the pond. The ash underwent an additional period of interaction with steam during the phreatic explosion as local pockets of water flashed to steam and blasted out the small craters. The additional interaction with steam during the phreatic explosions may account for the markedly lower susceptibility of the phreatic ash when compared to the matrix of the Rocky Point pyroclastic flow deposits in the same area.

Vertical Profiles Cut into the 1986 Pyroclastic Flow Deposits

Magnetic susceptibility measurements reported on 2006 pyroclastic flow deposits are from the upper parts of flows and the top and flanks of flow levees. These pyroclastic flow deposits, even in distal areas, were at least 1 m thick and were still hot 4–7 months after the eruption, so that it was not possible to safely excavate a trench completely through a 2006 pyroclastic flow deposit during this study in order to make susceptibility measurements from the top to the bottom of a pyroclastic flow deposit.

Eroded sections through 1986 pyroclastic flow deposits were found in three places beyond the limits of the 2006 pyroclastic flow deposits. Susceptibility measurements were made at 10-cm intervals from the top to the bottom through the three different 1986 pyroclastic flow deposits in order to investigate the possible variations in susceptibility with depth within pyroclastic flows (fig. 1). No significant variations in susceptibility with depth were found in any of the three 1986 pyroclastic flow deposits we studied (fig. 9). This suggests that the susceptibility measurements made in shallow surface trenches excavated into pyroclastic flow deposits are reasonably representative of the magnetic susceptibility of the matrix of the entire pyroclastic flow at any given site.

The 1986 pyroclastic flow deposits were characterized by significantly lower susceptibilities than all the 2006 pyroclastic flow deposits above the pond area.The field setting of the 1986 pyroclastic flow deposits indicated they had not interacted with water (table 1). Light gray dacite clasts make up the main variety of lithic blocks found in the 1986 pyroclastic flows (Waitt and Begét, 2009; Roman and others, 2006), and susceptibility measurements showed that these blocks were characterized by lower susceptibilities than either of the major lithic components of the 2006 Rocky Point pyroclastic flow deposits. This finding is consistent with the hypothesis presented above that the volume susceptibility of a pyroclastic flow deposit matrix primarily reflects the susceptibility and relative abundance of its major lithic components.Because component analyses of the 2006 Augustine pyroclastic flow deposits showed that their fine-grained matrix material consisted of comminuted rock material derived from the major coarse-grained components (Vallance and others, this volume), the susceptibility measurements on the 1986 deposits comprise a rapid proxy measurement of their componentry. Therefore, the significant differences in susceptibility found between the 1986 and 2006 deposits are an indication that susceptibility data can be used to map and differentiate separate groups of pyroclastic flow deposits.

2006 Rocky Point Pyroclastic Surge Deposits

Magnetic susceptibility measurements of surge deposits that had decoupled from the Rocky Point pyroclastic flow and traveled up a slope adjacent to the main pyroclastic fan were made along two traverses spaced about 50 m apart at a site ca. 800 m inland and 175 m higher than the pond area. At this locality the surge had singed alders within a few meters of the western margin of the Rocky Point pyroclastic fan, but it was unable to burn alders after traveling 100 m and 20–30 m

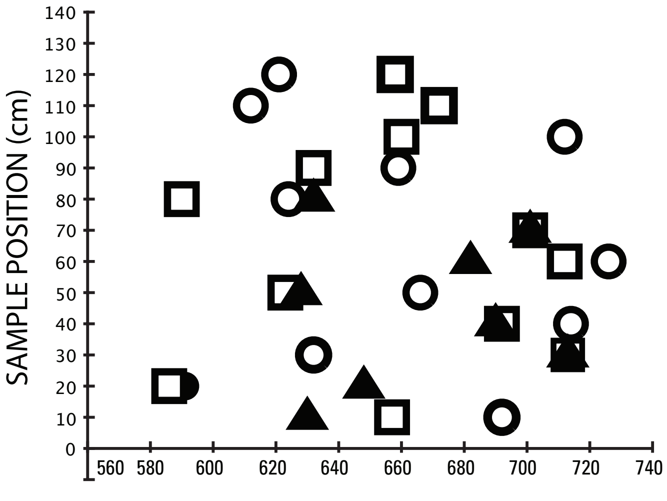

Figure 9. Vertical magnetic susceptibility profiles measured though three 1986 pyroclastic flow deposits.The measurements were taken at 10-cm intervals from the bottom to the top, with two flows (open circle and open square symbols) being ca. 1.3 m thick and one flow (solid triangle symbol) being ca. 1 m thick. No progressive changes or systematic pattern of susceptibility was noted in any of the three measured vertical profiles.Note that although the susceptibility measurements from each pyroclastic flow deposit showed small variations through the sections, the average susceptibilities (658×10^{-5} SI, 665×10^{-5} SI, and 671×10^{-5} SI) of the three 1986 flows were essentially identical.

higher up the slopes (table 1).These slopes were not affected by pyroclastic flows or floods before the Rocky Point eruptive event, and snow was probably present on these slopes and interacted with the pyroclastic surge as it traversed this slope up into the alder grove (Coombs and others, this volume). The ash-cloud surge deposits consisted of weakly bedded coarse sandy beds as much as 10 cm thick that thinned quickly and disappeared within 100 m of the western margin of the Rocky Point pyroclastic flow.

The susceptibility of the surge deposits immediately adjacent to the Rocky Point pyroclastic fan, in an area where the surge had burned alders, averaged 1,166×10^{-5} SI, while the average volume susceptibility of deposits from the same surge at higher elevations, where they had cooled enough to not singe alders, was only 433×10^{-5} SI. The observed decrease in susceptibility is greater then 60 percent, i.e. much larger than the decrease in susceptibility observed downslope, where the Rocky Point pyroclastic flow traveled into the pond. The rapid and significant decrease in susceptibility measured over short distances in the ash cloud surge deposits adjacent to the Rocky Point pyroclastic flow deposit shows that the magnetic characteristics of pyroclastic surge deposits can change very rapidly. This contrasts strongly with the susceptibility data from the pyroclastic flows themselves, which showed no progressive changes with travel distance.

2006 Lahar Deposits

Lahar deposits were preserved in several small stream channels downstream from the pyroclastic flow deposits on the north flank (figs. 1, 10). Repeat photography and field observations during the 2006 eruption indicate that these lahars formed during the earliest explosive phase, when low-silica andesite-rich pyroclastic flows produced widespread flooding and lahars that reached the north coast of Augustine Island (Coombs and others, this volume).

The thin lahar deposits are composed of silt- and sand-rich diamictons that form flat terraces along narrow stream channels that are often no more than 2 to 10 m wide. The deposits are all less than 1 m thick, and often only 20–30 cm thick, with porphyritic greenish andesite boulders and rounded cobbles being the primary coarse lithic component (fig. 10). The greenish andesite boulders in pyroclastic flows had high susceptibilities (table 1), but volume susceptibility measurements on the matrix of the lahar deposits were much lower, with values ranging from 284×10^{-5} SI to 643×10^{-5} SI (fig. 6). These susceptibility values measured on lahars are lower than those measured on any of the pyroclastic flow deposits except those deposited within the pond basin.There is some overlap between highest susceptibility values measured on the lahar deposits and the susceptibility values measured for Rocky Point pyroclastic flow and phreatic ash deposits at the pond, but the lowest susceptibility values for the lahars are notably lower than any of the pyroclastic flow deposits from the 2006 eruption.

Interpretation of the Magnetic Susceptibility Data

Magnetic susceptibility is a measure of the relative amounts of different kinds of magnetic minerals present in samples. The changes in magnetic susceptibility documented in this study where pyroclastic flows encountered water and snow therefore record changes in the characteristics of the magnetic minerals in the pyroclastic flow deposits (Evans and Heller, 2003). It is well known that environmental factors, such as soil development or hydrothermal activity, can cause the alteration

Figure 10. Photograph of thin, fine-grained lahar deposits preserved in small stream channels just downslope from the terminal zone of the Rocky Point pyroclastic flow deposits. Also shown is the Bartington MS2F microprobe used in this study. Entrenching tool handle is 40 cm long.

or destruction of the existing magnetic minerals and the generation of new magnetic minerals (Liu and others, 1999). An important finding of this study is that the magnetic susceptibility of pyroclastic flow and surge deposits erupted by Augustine Volcano in 2006 were reduced in areas where encounters with water, snow, and steam occurred. Water-mediated lahar deposits derived from the pyroclastic flows had still lower susceptibilities. Our finding that interactions with water caused susceptibility variations in 2006 pyroclastic flow and lahar deposits at Augustine Island suggest that measurement of magnetic susceptibility variations can provide a new tool for evaluating interactions between pyroclastic flows and water.

Pyroclastic flows typically contain collections of different lithologies or components. Our data show that the susceptibilities of pyroclastic flow deposits erupted at Augustine Volcano in 2006 are somewhat variable but are all higher than pyroclastic flow deposits erupted in 1986. This reflects the higher susceptibilities of the major lithologic components of the 2006 pyroclastic flows and demonstrates that different assemblages of pyroclastic flow deposits produced during separate eruptive events can be differentiated by their magnetic susceptibility. This finding suggests that magnetic susceptibility data may be a useful tool for differentiating and mapping pyroclastic deposits at active volcanoes.

The magnetic susceptibility of the 2006 pyroclastic flow deposits showed significant changes in two key areas. At the northwest margin of the 2006 pyroclastic fan, Rocky Point pyroclastic flows filled a small pond basin. The magnetic susceptibilities of the pyroclastic flow deposits were significantly lower within the infilled pond basin, where the flows encountered water and steam, than they were anywhere else in the pyroclastic fan. Similar reductions in susceptibility were also found in ash cloud surge deposits that had traveled across an area where snow covered the ground. Lahar deposits in stream channels downstream from the pyroclastic flow deposits showed even lower volume susceptibility values.

The observed reductions in magnetic susceptibility in these 2006 Augustine deposits may reflect several different geochemical processes, but most of the change is probably attributable to oxidation of the iron-bearing minerals caused by interactions between the hot pyroclastic flows and water and steam. Oxidation is an inevitable consequence of the exposure of hot pyroclastic rocks to water and steam. Generations of volcanologists have noted the creation of oxidized, hematite-rich zones at the tops of pyroclastic flows, known as “pink tops,” and applied this classic criterion to infer the past presence of heat and water (Ross and Smith, 1961; Hildreth, 1983; Tait and others, 1998). Oxidation of iron-bearing minerals from the ferrous to ferric state characteristically results in the production of mineral phases with lower magnetic susceptibility, and we believe this is the main cause of the susceptibility changes we have observed in the 2006 Augustine pyroclastic flow, surge, and lahar deposits that formed by interactions with water, snow, and steam. Other geochemical processes may also be playing a role, including partial disruptions and dislocations of the atomic structure of the ferro-magnesium minerals (Ishikawa, 1958).

Over long periods of time, weathering and soil development can also cause changes in the original susceptibility of sediments (Maher and Thompson, 1999; Singer and others, 1992), but the 2006 pyroclastic deposits at Augustine were only a few months old when this study was made, and so were far too young for weathering to have greatly affected them.

Did Density Fractionation Occur in the 2006 Augustine Pyroclastic Flows, Surges, and Lahars?

In addition to the effect of geochemical processes on magnetic susceptibility, some physical processes produce sorting of sediments and can alter magnetic susceptibility. For instance, the higher density of magnetic minerals causes them to preferentially settle out of wind-blown sediment and water-transported sediment (Begét, 2001; Oldfield, 1991, 1992; Begét and others, 1990; Begét and Hawkins, 1989).

Could pyroclastic flow processes play a role in creating the observed variations in magnetic susceptiblity at Augustine Volcano?As noted above, the highest group of susceptibility values measured on any of the volcaniclastic deposits came from the 2006 pyroclastic flow deposits. The volume susceptibility measurements from the matrix of these flow deposits showed some variability from flow to flow, probably reflecting differences in the mix of the initial lithic components of the numerous pyroclastic flows produced during this part of the eruption. However, when the susceptibility of one area of the Rocky Point pyroclastic flow deposit was measured at multiple sites along its western margin, the susceptibility of the deposit showed little change for hundreds of meters downslope, suggesting that the processes involved in the lateral transit and emplacement of the Rocky Point pyroclastic flow did not produce progressive susceptibility changes along its flow path.

The prevailing modern view is that pyroclastic flows are dominantly turbulent, although locally they may be characterized by laminar or even plug flow (Schmincke, 2004). The finding here that density sorting and depletion by fractionation of heavy magnetic minerals did not occur to any significant degree as the 2006 pyroclastic flows traveled downslope suggests that the flows were sufficiently turbulent during emplacement to suspend all of the fine-grained components and minimize the loss of heavy Fe-bearing minerals. This was true for samples measured in pyroclastic flow deposit channels, recording sedimentation from the base of flow deposits, from pyroclastic flow levees formed by “freezing” of marginal parts of the pyroclastic flows, and also from flat-surfaced pyroclastic fans and terminal lobes that may have undergone plug flow as they decelerated and stopped.

Regeneration and formation of new matrix material by clast-to-clast collisions as the pyroclastic flow travels downslope and produces a deposit along its path probably plays an important role in modulating downslope changes in magnetic susceptibilities in the 2006 pyroclastic flow deposits. The absence of any progressive change in susceptibility in the Rocky Point pyroclastic flow from the upper slopes to the lower slopes strongly suggests that either density fractionation of the heavier magnetic minerals did not occur to a significant extent during flow, or new magnetic minerals were continually being added to the matrix of the flows by comminution of larger particles.

In contrast, significant reductions in magnetic susceptibility were observed in 2006 surge deposits that traveled only about 100 m beyond the margin of the Rocky Point pyroclastic flow deposit. Surges are typically highly inflated and have much lower particle concentrations than block-and-ash flows, and they would be more likely to be affected by density fractionation. The rapid decrease in susceptibility observed in the local surge deposits formed in 2006 at Augustine Volcano likely reflects some oxidation and alteration of the ferromagnetic minerals produced as the heat of the surge produced water and steam from the underlying snow, but we also suspect that some significant amount of the reduction in susceptibility seen in the distal surge deposits reflects progressive fractionation and removal of the denser magnetic minerals from the turbulent and dilute surge ash cloud as it traveled away from its source in the main Rocky Point pyroclastic flow deposit.

The magnetic susceptibility of lahars found downslope from the Rocky Point pyroclastic flow deposits is lower than that of the hot pyroclastic deposits from which they were derived. Lahars generated during the 2006 Augustine eruption appear to have been mainly produced by interactions between pyroclastic flows and surges and the winter snowpack (Vallance and others, this volume). The sediment in the lahars was in direct and prolonged contact with water, and the low susceptibility of the lahars is thought to reflect sustained geochemical alteration and oxidation of the ferromagnetic minerals. It is possible that some loss of heavy minerals by density fractionation may also have occurred during lahar deposition, but we do not see any progressive evolution in the susceptibility of the lahar deposits with distance away from the pyroclastic flow margin, as occurred in the surge deposits. For this reason, we do not think that density fractionation was an important factor in the evolution of the magnetic susceptibility of the lahar deposits, and we attribute the lower magnetic susceptibility that characterizes these deposits to water-rock interaction as the pyroclastic flows encountered snow and water and transformed into lahars that traveled to the lower flanks of the volcano.

Acknowledgments

This study was supported by the Alaska Volcano Observatory and by a National Science Foundation grant to Begét. We gratefully acknowledge helpful reviews by John Hagstrum and John Power of the U.S. Geological Survey, and by Kate Bull of the Division of Geological and Geophysical Surveys of the State of Alaska. Michelle Coombs and Jim Vallance kindly introduced the author to the complexities of the 2006 Augustine pyroclastic flow deposits during fieldwork on Augustine Island, and Michelle Coombs helped the author with an early draft of the manuscript.

References

Bartington Corporation, 2004, Operation Manual for MS2 Magnetic Susceptibility System: 72 p.

Begét, J.E., 2001, Continuous late Quaternary proxy climate records from loess in Beringia: Quaternary Science Reviews, v. 20, p. 499–509.

Begét, J., and Hawkins, D., 1989, Influence of orbital parameters on Pleistocene loess deposition in central Alaska: Nature, v. 337, p. 151–153.

Begét, J. E., and Kienle, J. 1992, Cyclic formation of debris avalanches at Mt. St. Augustine volcano, Alaska: Nature, v. 356, p. 701–704.

Begét, J., Stone, D., and Hawkins, D., 1990, Paleoclimatic forcing of magnetic susceptibility variations recorded in central Alaskan loess: Geology v. 18, p. 40–43.

Begét, J. E., Stihler, S., and Stone, D. B., 1994, A 500 year long record of tephra falls from Redoubt Volcano and other volcanoes in upper Cook Inlet, Alaska: Journal of Volcanology and Geothermal Research, v. 62, p. 55–67

Coombs, M.L., Bull, K.F., Vallance, J.W., Schneider, D.J., Thoms, E.E., Wessels, R.L., and McGimsey, R.G., 2010, Timing, distribution, and volume of proximal products of the 2006 eruption of Augustine Volcano, *in* Power, J.A., Coombs, M.L., and Freymueller, J.T., eds., The 2006 eruption of Augustine Volcano, Alaska: U.S. Geological Survey Professional Paper 1769 (this volume).

Cronin, S.J., Hodgson, K.A., Neall, V.E., Palmer, A.S., and LeCointre, J.A., 1997, The 1995 Ruapehu lahars in relation to the late Holocene lahars of Whangaehu River, New Zealand: New Zealand Journal of Geology and Geophysics, v. 40, p. 507–520.

Evans, M.E. and Heller, F., 2003, Environmental Magnetism: principles and applications of environmagnetics: Amsterdam, Academic Press, 299 p.

Hildreth, W., 1983, The compositionally zoned eruption of 1912 in the Valley of Ten Thousand Smokes, Katmai National Park, Alaska: Journal of Volcanology and Geothermal Research, v. 18, p. 1–56.

Ishikawa, Y., 1958, An order-disorder transformation phenomenon in the $FeTiO_3$–Fe_2O_3 solid solution series: Journal of the Physics Society of Japan, v. 13, p. 828–837.

Liu, X.M., Hesse, P., Rolph, T. and Begét, J., 1999, Properties of magnetic mineralogy of Alaskan loess, evidence for pedogenesis: Quaternary International, v. 62, p. 93–102.

Maher, B., and Thompson, R., 1999. Quaternary climates, environments and magnetism: Cambridge University Press, 354 p.

Oldfield, F., 1991, Environmental magnetism, a personal perspective: Quaternary Science Review, v. 10, p. 73–85.

Oldfield, F., 1992, The source of fine-grained 'magnetite' in sediments: Holocene, v. 2, p. 180-182.

Pierson, T.C., Janda, R.J., Thouret, Jean-Claude, and Borrero, C.A., 1990, Perturbation and melting of snow and ice by the 13 November 1985 eruption of Nevado del Ruiz, Colombia, and consequent mobilization, flow, and deposition of lahars: Journal of Volcanology and Geothermal Research, v. 41, p. 17–66.

Power, J.A., Nye, C.J., Coombs, M.L., Wessels, R.L., Cervelli, P.F., Dehn, J., Wallace, K.L., Freymueller, J.T., and Doukas, M.P., 2006, The reawakening of Alaska's Augustine Volcano: Eos (American Geophysical Union Transactions), v. 87, no. 37, p. 373, 377.

Roman, D.C., Cashman, K.V., Gardner, C.A., Wallace, P.J., and Donovan, J.J., 2006, Storage and interaction of compositionally heterogeneous magmas from the 1986 eruption of Augustine Volcano, Alaska: Bulletin of Volcanology, v. 68, p. 240–254.

Ross, C.S., and Smith, R.L., 1961, Ash-flow tuffs, their origin, geologic relations and identitification: U.S. Geological Survey Professional Paper 366, 81 p.

Schmincke, H-U., 2004, Volcanism: Berlin, Springer Press, 324 p.

Shepherd, J.B., and Sigurdsson, H., 1982, Mechanism of the 1979 explosive eruption of Soufriere Volcano, St. Vincent: Journal of Volcanology and Geothermal Research, v. 13, p. 119–130.

Sheridan, M. and Wohletz, K.H., 1983, Hydrovolcanism, basic considerations and review: Journal of Volcanology and Geothermal Research, v. 17, p. 1–29.

Siebert, L., Begét, J., and Glicken, H., 1995, The 1883 and late-prehistoric eruptions of Augustine volcano, Alaska: Journal of Volcanology and Geothermal Research, v. 66, p. 367–396.

Singer, M.J., Fine, P., Verosub, K.L., and Chadwick, O.A., 1992, Time dependence of magnetic susceptibility on soil chronosequences on the California coast: Quaternary Research, v. 37, p. 323–332.

Tait, S., Thomas, R., Gardner, J., and Jaupart, C., 1998, Constraints on cooling rates and permeabilities of pumice in an explosive eruption jet from colour and magnetic mineralogy: Journal of Volcanology and Geothermal Research, v. 86, no. 1–4, p. 79–91.

Vallance, J.W., Bull, K.F., and Coombs, M.L., 2010, Pyroclastic flows, lahars, and mixed avalanches generated during the 2006 eruption of Augustine Volcano, *in* Power, J.A., Coombs, M.L., and Freymueller, J.T., eds., The 2006 eruption of Augustine Volcano, Alaska: U.S. Geological Survey Professional Paper 1769 (this volume).

Waitt, R.B. and Begét, J.E., 2009, Volcanic processes and geology of Augustine Volcano, Alaska: U.S. Geological Survey Professional Paper 1762, 78 p.

The 2006 Eruption of Augustine Volcano, Alaska
Power, J.A., Coombs, M.L., and Freymueller, J.T., editors
U.S. Geological Survey Professional Paper 1769

Chapter 12

Remote Telemetered and Time-Lapse Cameras at Augustine Volcano

By John Paskievitch[1], Cyrus Read[1], and Thomas Parker[1]

Abstract

Before and during the 2006 eruption of Augustine Volcano, the Alaska Volcano Observatory (AVO) installed a network of telemetered and nontelemetered cameras in Homer, Alaska, and on Augustine Island. On December 1, 2005, a network camera was installed at the Homer Field Station, a University of Alaska Fairbanks Geophysical Institute (UAF/GI) facility on a bluff near Homer, where telemetered Augustine data are received. The camera placed there provides observations of the volcano from a distance of 126 km (78 miles) in daylight hours during clear sky conditions. On January 9, 2006, a radio-telemetered network camera was installed on the lower eastern flank of the volcano at "Mound," 4.4 km (2.7 miles) from the summit. The proximity of this camera provided for near-field images of the volcano. A nontelemetered camera with onsite recording was installed 3.8 km (2.4 miles) north of the volcano's summit near Burr Point on December 17, 2005. This camera recorded high-resolution images at a rate of 4 images per hour through much of the eruptive sequence. A low-light camera was installed on February 8, 2006, at the Homer facility to augment the extreme low-light camera installed by the UAF/GI (Sentman and others, this volume). On September 10, 2006, a second radio-telemetered network camera was installed at Lagoon camp on the west side of Augustine Island, 5.4 km (3.3 miles) west-northwest of the summit. The installation of these camera systems proved valuable for assessing volcanic activity, determining ground hazards and on-island weather for visiting field teams, and deciphering depositional history after the eruption.

Introduction

Augustine Volcano, in lower Cook Inlet, is one of the most frequently active volcanoes in Alaska, recently erupting in 1976 and 1986 (Miller and others, 1998). Increased seismicity and deformation, starting in April 2005 and escalating in November 2005, indicated that the volcano was likely to become active once again (Power and others, 2006). Therefore, the Alaska Volcano Observatory (AVO) installed a network of telemetered and nontelemetered cameras in Homer, Alaska, and on Augustine Volcano (fig. 1) in anticipation of an eruption. These cameras, similar to ones previously installed by AVO to monitor Veniaminof and Spurr volcanoes, augmented telemetered geophysical data and provided frequent visual observations of this remote volcano. Images from the telemetered cameras were served over the Internet on AVO's Web site for internal and public use. This paper presents a description of the equipment and installation of these cameras, and a chronology of when they were operational. More detailed analysis of the images is presented in Coombs and others (this volume) and Vallance and others (this volume).

Chronology of the 2006 Eruption and Camera Installation

Beginning in mid-2005, AVO detected an increased number of earthquakes beneath Augustine's summit and evidence of inflation of the volcanic edifice (Power and others, 2006). Seismicity increased to higher levels in November 2005. Several phreatic explosions occurred in December 2005. On January 10, 2006, seismicity increased sharply, and this was followed on January 11 by two brief explosive eruptions. From January 13 through 28, 11 more discrete vulcanian blasts produced ash clouds that rose to 16 km above sea level (asl), pyroclastic flows, lahars, and avalanches on the island

---

[1] Alaska Volcano Observatory, U.S. Geological Survey, 4200 University Drive, Anchorage, AK 99508.

(the “explosive phase”). On January 28, the volcano entered a period of more continuous activity consisting of rapid lava effusion, block-and-ash flows, and ash emission (the “continuous phase”; Coombs and others, this volume). After a pause in activity from February 10 to March 3, activity resumed during the “effusive phase” as two lava flows and a new summit lava dome were emplaced, accompanied by many small block-and-ash flows from the growing lava bodies.

A network camera was installed at the Homer Field Station on December 1, 2005. A nontelemetered camera with onsite storage was installed on the north flank of the volcano near Burr Point on December 17, 2005. On January 9, 2006, AVO installed the first remote radio-telemetered network camera on Augustine Island east-northeast of the summit at a site informally known as “Mound,” just two days before the onset of the explosive phase. On February 8, 2006, a low-light camera and network video server were installed at the Homer Field Station. The final network camera was installed on the west side of Augustine Island at the informally named “Northwest Lagoon” on September 10, 2006. Daytime activity during all three phases of the eruption was mostly imaged by both the netcam at Mound and the nontelemetered camera at Burr Point, except when weather clouds or ash obscured the view The image records of both the telemetered and non telemetered

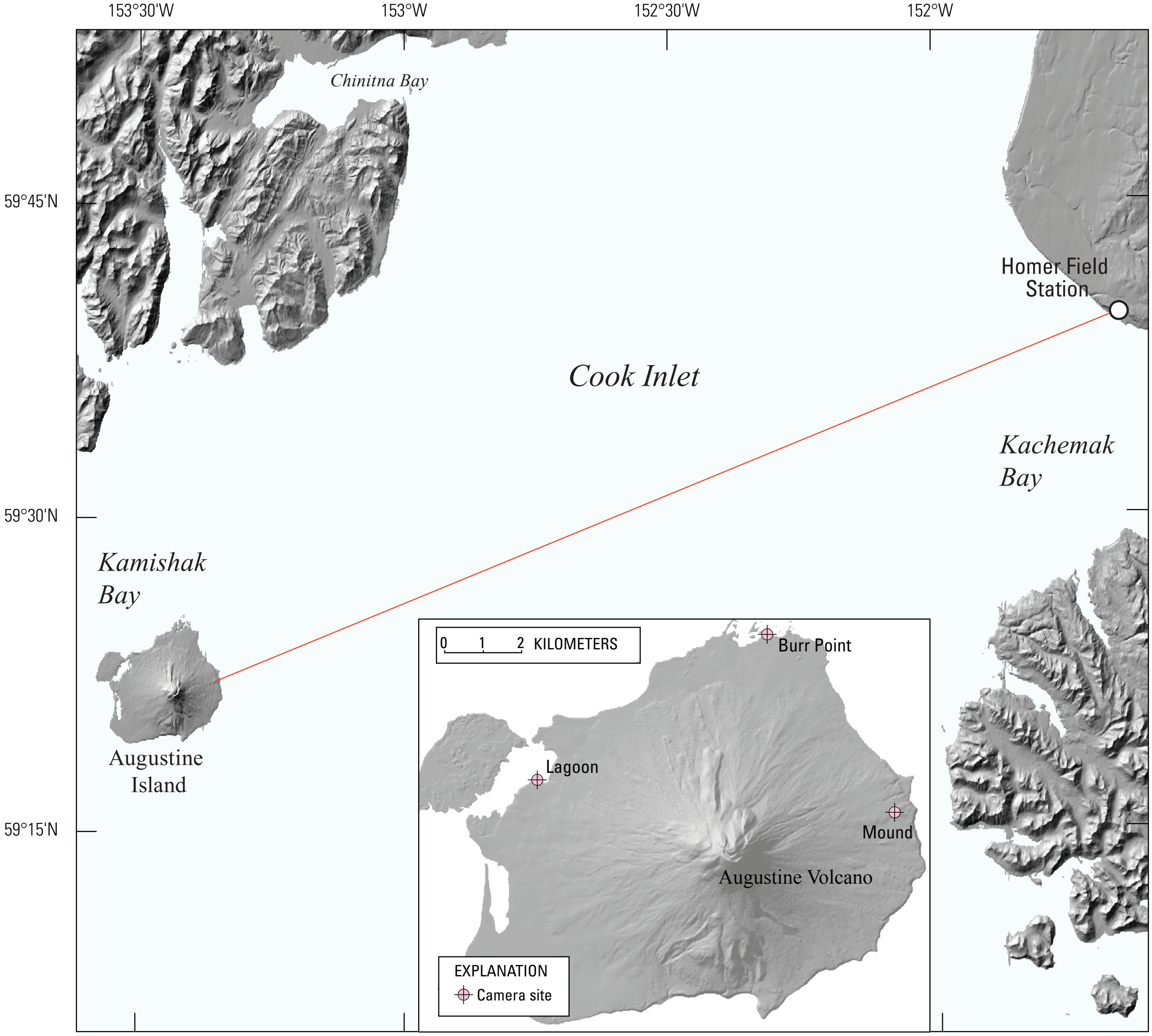

Figure 1. Map of lower Cook Inlet showing Augustine Island and telemetry path (in red) from the Mound camera back to the Homer Field Station. Inset map shows location of cameras on Augustine Island.

telemetered cameras were occasionally interrupted during parts of January and February as a result of various power problems, exceeding on-site recording capacity, and physical damage to the installations. Cameras located in Homer did not image any of the explosive activity because of poor visibility, but they did record much of the activity during the continuous and effusive phases of the eruption.

Cameras Used

A variety of cameras were used to establish the visual monitoring network (table 1). Stardot network cameras were used for telemetered daylight images. The Stardot Netcam MegaPixel is an IP networked camera (appendix 1). Its Web interface allows adjustment and control of various parameters, including those affecting image quality, date and time stamps, text overlays, security, file naming, and image transfer. Near-real-time images can be viewed remotely using http and automatically uploaded to designated servers using ftp.

A Watec 120N analog camera connected through a Stardot video server provided telemetered nighttime images. The Watec 120N is a monochrome low-light camera with sensitivity in the near-infrared (appendix 1). It was used in conjunction with a Watec 120N control box which allows for gain adjustment and image integration. Images from this camera were sampled and transmitted across a Stardot Ethernet-based video server (appendix 1).

A Nikon COOLPIX 8700 configured with a Harbortronics DigiSnap 2000 time-lapse control system was used to take time-lapse images and store them on-site. The Nikon COOLPIX 8700 is an 8 effective megapixel digital camera. The Harbortronics DigiSnap 2000 controls image sampling intervals, and a Harbortronics voltage regulator conditions the power needed by both the camera and DigiSnap 2000. This system was tested, packaged, and provided by the Hawaiian Volcano Observatory (HVO) and is further described in Orr and Hoblitt (2008). Vendor specifications for equipment used in this package are given in appendix 1.

Homer-based Network Camera

A Stardot Netcam MegaPixel camera was installed at the UAF/GI Homer facility on December 1, 2005. It is mounted on a window ledge inside the facility and aimed through a window at Augustine Island. The camera is fixed with a remotely controllable 8 mm to 48 mm motorized zoom lens. It is attached to the Homer-based UAF/GI network and is accessible through the Internet. It sends images at user-defined intervals to an ftp server at AVO facilities in Anchorage. Images were transferred at 5-minute intervals throughout the eruption.

The distance of this camera from the volcano (126 km, or 78 miles) allows for a broader field of view, useful for determining heights and lateral trends of plumes. However, darkness and cloud conditions between camera and target often prevented observation of the volcano, and none of the explosive events in January were imaged. This camera did provide useful images during the continuous and effusive phases of activity at times when clear skies coincided with daylight hours (fig. 2). More proximal cameras that require radio telemetry or onsite storage were decided upon to capture the potential eruptive activity.

Figure 2. Image of Augustine Volcano, 78 miles away, captured by the Homer Field Station netcam on December 1, 2005.

Mound Network Camera

A radio-telemetered Stardot Netcam MegaPixel camera was installed at Augustine Volcano at “Mound” on January 9, 2006, just before the onset of explosive activity. Mound is located on a small hill on the east side of the island at an elevation of about 100 m and 4.4 km from the summit. The camera is mounted within a Stardot enclosure attached to a solar panel mounting structure (fig. 3).

The equipment package (fig. 4) at Mound includes a Trimble NetRS GPS receiver for deformation monitoring, a RefTek ANSS-130 strong-motion accelerometer for seismic monitoring, the Stardot

Table 1. Summary of cameras installed during 2005 and 2006 to monitor Augustine Volcano.

Camera Name	Camera Used	Date of Initial Deployment	Lens Used	Operating Resolution (pixels)	Image Capture Frequency	Camera Outage/ Reduced Capture Rate
Homer Netcam	Stardot Netcam Megapixel	12/1/2005	8-48-mm motorized zoom lens	640×480	1 image every 5 minutes	None
Homer Low-Light Camera	Watec 120N	2/8/2006	n/a	758×494	1 image every 2 minutes	None
Mound Netcam	Stardot Netcam Megapixel	1/9/2006	8-mm zoom lens	640×480	2 images every 30 minutes	1/17/2006 – 2/21/2006: Frequency of image capture reduced during low visibility or darkness to save power.
Burr Point Time- Lapse Camera	Nikon COOLPIX 8700	12/17/2005	Built in Nikon lens	1,024×768 (in TV mode)	1 image every 15 minutes	1/23/06 – 2/24/06: Camera was removed from island for maintenance. 5/13/06: Camera ran out of battery.
Lagoon Netcam	Stardot Netcam	9/10/2006	8-mm zoom lens	320×240	2 images every 60 minutes	Occasional outages due to poor radio telemetry.

camera system, a serial-based power controller, a serial-to-Ethernet device server, and an Intuicom EB-1 wireless Ethernet bridge. All Ethernet devices are part of the Homer-based UAF/GI network and are linked to it using the Intuicom Ethernet Bridge (appendix 1).

The image interval of this camera was decided partly by bandwidth limitations, but mostly by power considerations. The combined power requirement of the equipment at Mound is nearly 12W, which is a heavy load for a small-scale solar power system during the winter months in Alaska. Power use had to be managed to stay within the limits of the reserve and recharge rate of the power system, which was done through a USGS-designed power controller (appendix 2). This is a device that reports site voltage and allows management of four independently controlled power ports through a terminal session. The camera was placed on a power port that is programmable for powering on at user-defined intervals and durations. The Mound camera was typically set to power on at 30-minute intervals for 5-minute durations. The camera was powered on for longer durations during periods of anticipated or actual eruptions. While powered on, the camera was set to transfer images at 2-minute intervals.

One of the advantages of a near-field camera is that it suffers far less obstruction from cloud and fog than a camera (in this comparison) placed 78 miles away in Homer. While the Homer camera failed to image any of January's explosive events, the Mound camera imaged most of them. The most impressive sequence imaged by the Mound camera was during an explosive event on January 13, between 16:35 and 16:45 AKST (fig. 5).

Low-light Camera

A Watec 120N low-light camera was installed at the UAF/GI Homer facility on February 8, 2006, which supplemented a small astronomical CCD camera (Sentman and others, this volume). The low light camera is mounted on a ledge inside the facility and aimed through a window at Augustine Volcano. It is attached to the Homer-based UAF/GI network by a video server. The video server is accessible through the Internet and sends images at user-defined intervals to an ftp server at AVO facilities in Anchorage. Images were transferred at 2-minute intervals through most of the eruption.

This camera allowed viewing of the volcano at night. It imaged much of the summit area activity during the effusive phase of the eruption (fig. 6).

Time-Lapse Camera

A stand-alone 8.0 megapixel Nikon COOLPIX 8700 digital camera system was installed on an old debris-flow deposit on the north side of the volcano at Burr Point on December 17, 2005. The camera enclosure housed the camera,

Figure 3. The Mound camera aimed at Augustine Volcano. The camera's housing has a protective debris- and snow-shedding shield of bent aluminum. The housing is attached to an Alaska Volcano Observatory (AVO) solar-panel mounting structure. AVO photo by M. Coombs, January 12, 2006.

intervalometer, and DC-DC inverter, and it had a lexan window plate through which images were captured. This box was attached to a larger fiberglass box that housed a 100A/hr lead-acid battery. The image interval of 15 minutes and image file size of approximately 600KB allowed for about 70 days of storage on a 4-gigabyte flash card.

The location of this camera allowed imaging of the north side of the volcano, where activity was focused during the continuous and effusive phases of the eruption. The camera captured much of the daylight eruptive activity in high resolution and allowed reconstruction of the sequence of events (Coombs and others, this volume; their fig. 4). In addition, incandescent lava and block-and-ash flows were often visible in nighttime images from this vantage during the effusive phase of the eruption (fig. 7; Coombs and others, this volume; their fig. 17).

Lagoon Camera

A Stardot Netcam system was installed on a wooden hut at the Northwest Lagoon base camp on the west side of Augustine Island on September 10, 2006. This camera used an existing Plate Boundary Observatory (PBO) Intuicom radio

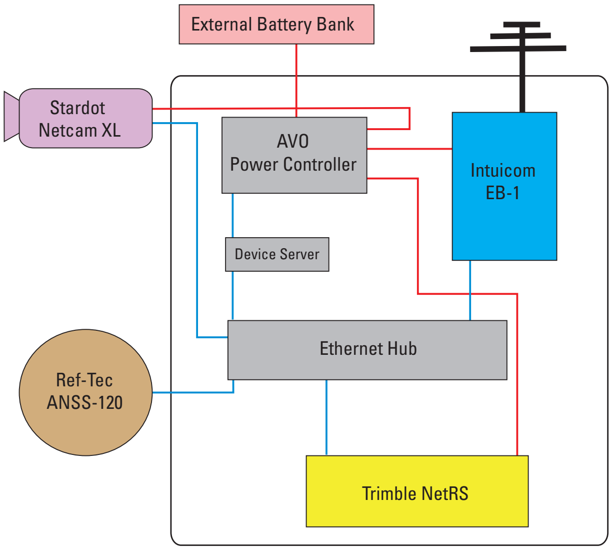

Figure 4. Block diagram of the Mound equipment package. Red lines indicate 12-volt DC power connections to the Alaska Volcano Observatory (AVO) power controller, while blue lines indicate data connections. The thin black line represents a Hardigg Storm Case iM2700, which houses electronic equipment.

network, as described in Pauk and others (this volume). The camera has an 8-mm lens. Image resolution was kept low, set to 320×240, and image upload interval was set to 2 images per hour in order not to impact bandwidth on the PBO network. Although this camera was not installed until after the eruptive activity, it was useful during post-eruption field operations (fig. 8) and is still operational in May 2010.

Image Handling

Images were uploaded from the individual devices to a file server at AVO in Anchorage. Image retention on the file server was limited to allow for frequent synchronization with upstream processing systems. The AVO internal Web server retrieved new images from the file server at a scheduled interval. Once on the

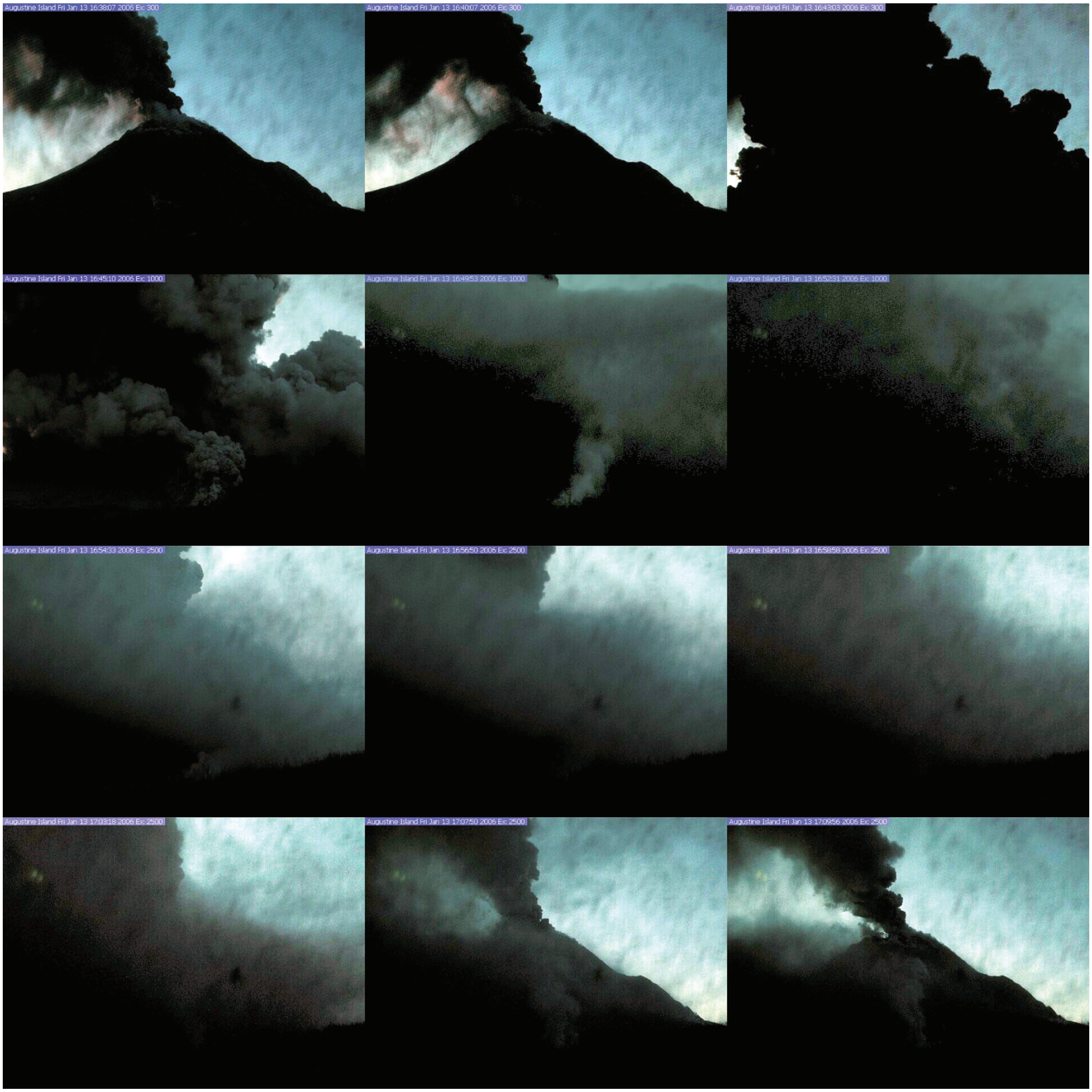

Figure 5. Augustine Volcano eruptive sequence as imaged by the Mound camera. Images cover from 16:38:07 to 17:09:56 AKST on January 13, 2006. The sequence of images is from left to right in each row and top to bottom in rows.

Figure 6. Nighttime image of a lava flow from Augustine Volcano, captured on February 8, 2006, from the Homer Field Station using the Watec 120N low-light camera. The outline of the volcano is seen with the lava dome visible on the right side of the summit. The light colored foreground is snow which has bright spots where moonlight is being reflected.

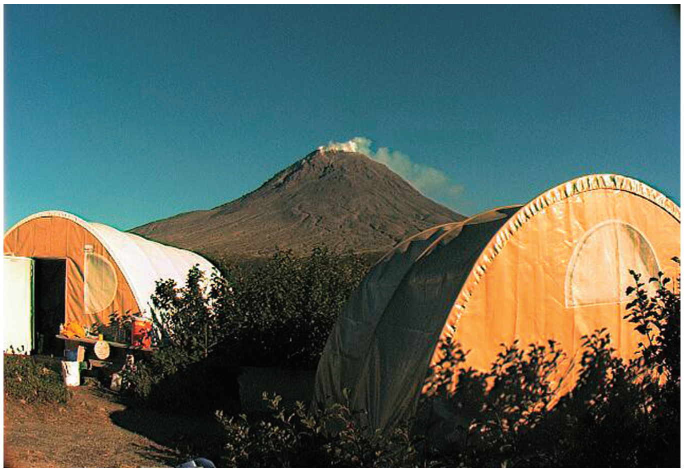

Figure 8. Image captured by the Lagoon camera during field operations on Augustine Island on September 12, 2006, showing an Alaska Volcano Observatory (AVO) base camp.

Figure 7. Image of Augustine Volcano captured by the Burr Point time-lapse camera at 1747 AKST on March 6, 2006, during the effusive phase of the eruption. Incandescence is from growing lava dome and lava flows on the volcano's north flank.

internal Web server, the images were sorted into directories by date for long-term storage and retrieval. A pointer to the most recent image from each camera was maintained to allow it to be downloaded from a static URL. Images were available on the internal Web server within 5 minutes of their acquisition. Rapid creation of simple animations from each camera was made possible by stitching together individual images into an AVI file encoded with MJPEG.

The AVO public Web server retrieved images from each camera's static URL on a set schedule. The public server only maintained the most recent image from each camera. Images were available on the server within 10 minutes of their acquisition.

Conclusions

The use of the Augustine remote camera systems established real-time visual observations of eruptions as a critical aspect of the AVO response. Near and far field cameras at multiple angles capable of imaging in all light conditions allows for critical hazard assessments, estimation of plume heights, accurate depositional chronology, and onsite weather/hazard assessments for field teams visiting an active volcano. The telemetered cameras are still operational as of May 2010 and AVO continues to use them as part of its monitoring repertoire.

References Cited

Coombs, M.L., Bull, K.F., Vallance, J.W., Schneider, D.J., Thoms, E.E., Wessels, R.L., and McGimsey, R.G., 2010, Timing, distribution, and volume of proximal products of the 2006 eruption of Augustine Volcano, *in* Power, J.A., Coombs, M.L., and Freymueller, J.T., eds., The 2006 eruption of Augustine Volcano, Alaska: U.S. Geological Survey Professional Paper 1769 (this volume).

Miller, T.P., McGimsey, R.G., Richter, D.H., Riehle, J.R., Nye, C.J., Yount, M.E., and Dumoulin, J.A., 1998, Catalog of the historically active volcanoes of Alaska: U.S. Geological Survey Open-File Report 98-582, 104 p.

Orr, T.R., and Hoblitt, R.P., 2008, A versatile time-lapse camera system developed by the Hawaiian Volcano Observatory for use at Kilauea Volcano, Hawai'i: U.S. Geological Survey Scientific Investigations Report 2008-5117, 8 p. [http://pubs.usgs.gov/sir/2008/5117/].

Pauk, B.A., Jackson, M., Feaux, K., Mencin, D., and Bohnenstiehl, K., 2010, The Plate Boundary Observatory permanent global positioning system network on Augustine Volcano before and after the 2006 eruption, *in* Power, J.A., Coombs, M.L., and Freymueller, J.T., eds., The 2006 eruption of Augustine Volcano, Alaska: U.S. Geological Survey Professional Paper 1769 (this volume).

Power, J.A., Nye, C.J., Coombs, M.L., Wessels, R.L., Cervelli, P.F., Dehn, J., Wallace, K.L., Freymueller, J.T., and Doukas, M.P., 2006, The reawakening of Alaska's Augustine Volcano: Eos (American Geophysical Union Transactions), v. 87, no. 37, p. 373, 377.

Sentman, D.D., McNutt, S.R., Stenbaek-Nielsen, H.C., Tytgat, G., and DeRoin, N., 2010, Imaging observations of thermal emissions from Augustine Volcano using a small astronomical camera, *in* Power, J.A., Coombs, M.L., and Freymueller, J.T., eds., The 2006 eruption of Augustine Volcano, Alaska: U.S. Geological Survey Professional Paper 1769 (this volume).

Vallance, J.W., Bull, K.F., and Coombs, M.L., 2010, Pyroclastic density currents, lahars, and mixed avalanches generated during the 2006 eruption of Augustine Volcano, *in* Power, J.A., Coombs, M.L., and Freymueller, J.T., eds., The 2006 eruption of Augustine Volcano, Alaska: U.S. Geological Survey Professional Paper 1769 (this volume).

Appendixes 1 and 2

Appendix 1. Product data sheets and manuals.

Equipment	Internet Link for Manual
Stardot Netcam MegaPixel	http://stardot-tech.com/netcam/netcam-brochure.pdf
Watec 120N	http://www.wateccameras.com/products.php?prod_id=124
Stardot video server	http://www.stardot.com/express6/specs.html
Nikon COOLPIX 8700	http://www.nikonusa.com/pdf/manuals/coolpix/CP8700_en.pdf
Harbortronics DigiSnap 2000	http://www.harbortronics.com/digisnap2000_manual.pdf
Harbortronics voltage regulator	http://www.harbortronics.com/detail.php?id=45
Intuicom EB-1	http://www.intuicom.com/www/datasheets/INT_EB1_Datasheet.pdf

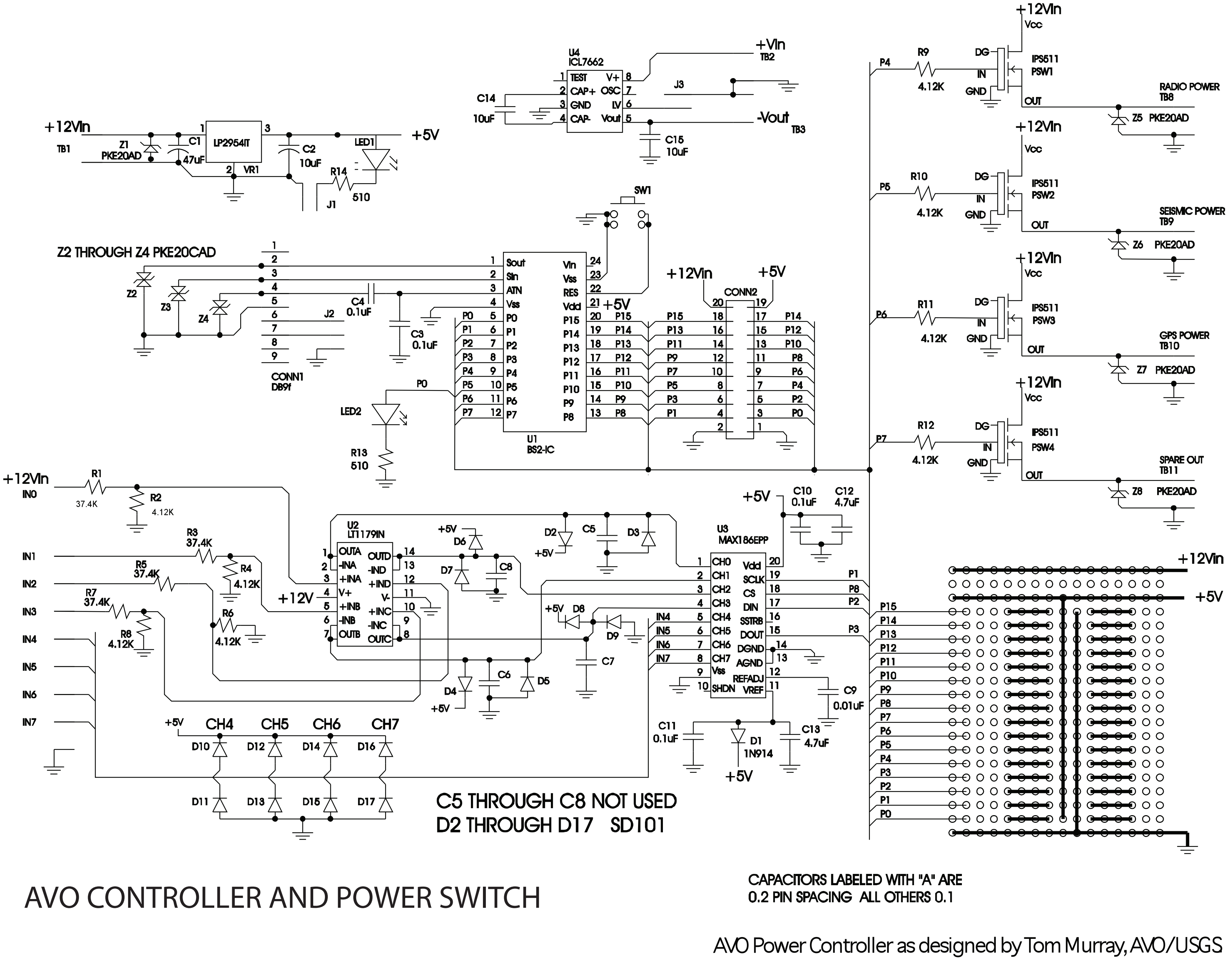

Appendix 2. Schematic of the Alaska Volcano Observatory (AVO) “Stamp” which allows remote power and timing control of devices.

]

Other Geologic Investigations

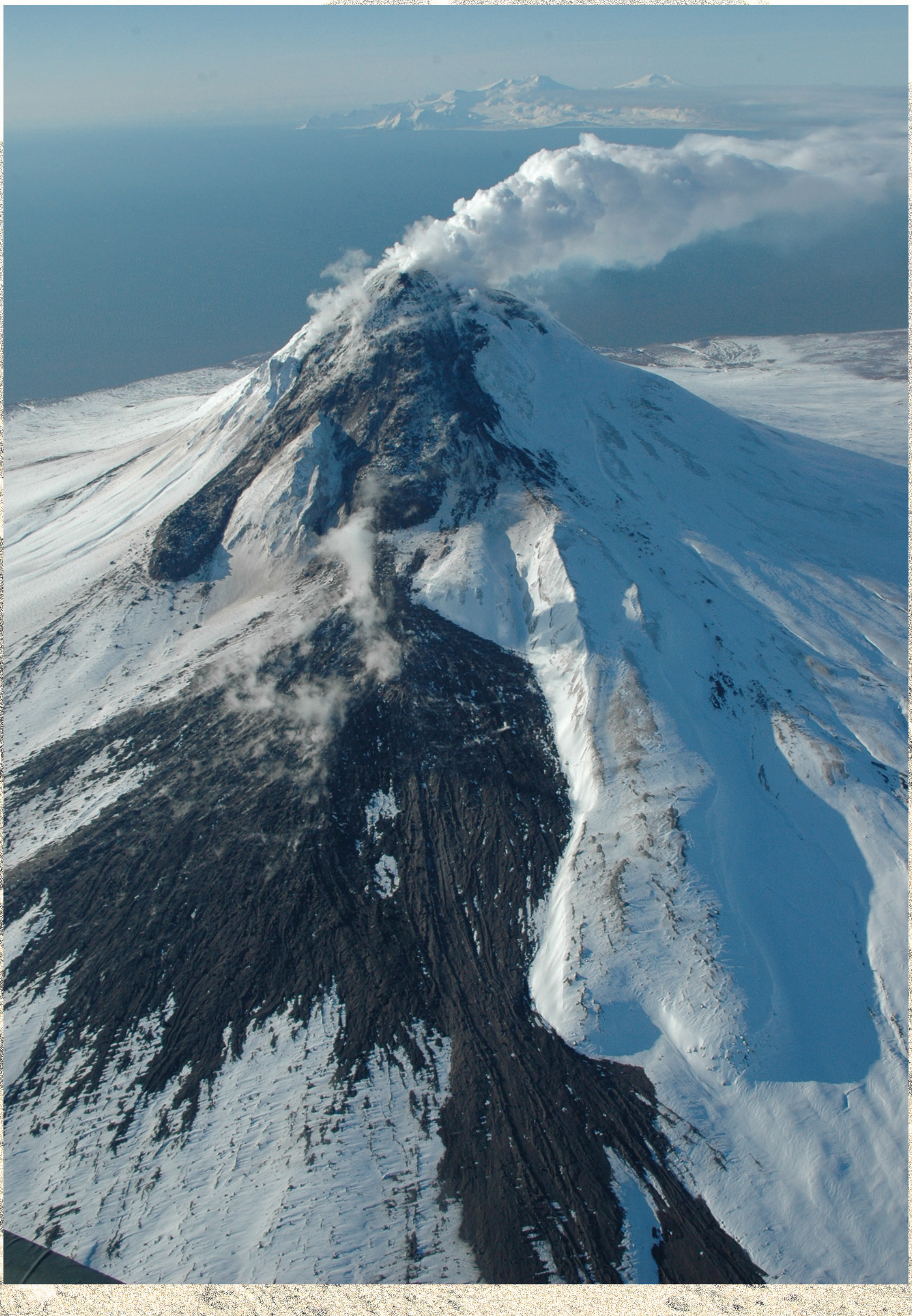

Oblique aerial view of the north side of Augustine Volcano on April 6, 2006, showing deposits from the 2006, eruption. A strong steam plume rises from the summit, and the northeast and north lava flows are visible on the upper parts of the edifice. Snow free area in foreground is hot pyroclastic deposits from the 2006 eruption. Alaska Volcano Observatory photo by R.G. McGimsey.

The 2006 Eruption of Augustine Volcano, Alaska
Power, J.A., Coombs, M.L., and Freymueller, J.T., editors
U.S. Geological Survey Professional Paper 1769

Chapter 13

Ejecta and Landslides from Augustine Volcano Before 2006

By Richard B. Waitt[1]

Abstract

A late Wisconsin volcano erupted onto the Jurassic-Cretaceous sedimentary bedrock of Augustine Island in lower Cook Inlet in Alaska. Olivine basalt interacting with water erupted explosively. Rhyolitic eruptive debris then swept down the south volcano flank while late Wisconsin glaciers from mountians on western mainland surrounded the island. Early to middle Holocene deposits probably erupted onto the island but are now largely buried. About 5,200, 3,750, 3,500, and 2,275 yr B.P. Augustine ash fell 70 to 110 km away.

Since about 2,300 yr B.P. several large eruptions deposited coarse-pumice fall beds on the volcano flanks; many smaller eruptions dropped sand and silt ash. The steep summit erupting viscous andesite domes has repeatedly collapsed into rocky avalanches that flowed into the sea. After a collapse, new domes rebuilt the summit. One to three avalanches shed east before about 2,100 yr B.P., two large ones swept east and southeast between about 2,100 and 1,700 yr B.P., and one shed east and east-northeast between 1,700 and 1,450 yr B.P. Others swept into the sea on the volcano's south, southwest, and north-northwest between about 1,450 and 1,100 yr B.P., and pyroclastic fans spread southeast and southwest. Pyroclastic flows and surges poured down the west and south flanks and a debris avalanche plowed into the western sea between about 1,000 and 750 yr B.P. A small debris avalanche shed south-southeast between about 750 and 390 yr B.P., and large lithic pyroclastic flows went southeast.

From about 390 to 200 yr B.P., three rocky avalanches swept down the west-northwest, north-northwest, and north flanks. The large West Island avalanche reached far beyond a former sea cliff and initiated a tsunami. Augustine's only conspicuous lava flow erupted on the north flank.

In October 1883 a debris avalanche plowed into the sea to form Burr Point on the north-northeast; then came ashfall, pyroclastic surge, and pyroclastic flows. Eruptions in 1935 and 1963–64 grew summit lava domes that shed coarse rubbly lithic pyroclastic flows down the southwest and south flanks. Eruptions in 1976 and 1986 grew domes that shed large pyroclastic flows northeast, north, and north-northwest.

The largest debris avalanches off Augustine sweep into the sea and radiate tsunami about lower Cook Inlet.

Introduction

Augustine's 2006 eruption embellished a mountain cone built by countless eruptions and mass-wastages over more than 15,000 years. This chapter summarizes pre-2006 surface geology detailed in a stratigraphic monograph and geologic map (Waitt and Begét, 2009). Like many other stratovolcanoes, Augustine has erupted repeatedly, sending pyroclastic flows down its flanks and depositing tephra near and far. Unusual about this cone is the rapidity with which domes build near the summit and then fail as debris avalanches. During the past two millennia or so Augustine has shed more than a dozen such rocky avalanches into the sea.

Setting and Rocks

Augustine Island, about 90 km^2, lies in southwestern Cook Inlet in southcentral Alaska (fig. 1*A*). Its nearly symmetrical mountain summit before 2006 peaked at 1,254 m (figs. 1*B*, 2). This island volcano lies along an active segment of the eastern Aleutian arc and 90–140 km above a seismic Benioff zone (Kienle and Swanson, 1983). The region's most explosive volcano, Augustine has erupted countless times since the end of the last ice age, including historical eruptions in 1812, 1883, 1935, 1963–64, 1976, 1986, and 2006.

Augustine's summit consists of many overlapping andesitic lava domes extruded intermittently over centuries. Most coastal cliffs expose diamicts comprising angular domerock cobbles and boulders, some as large as 4–12 m, all set in a

---

[1] U.S. Geological Survey, Cascades Volcano Observatory, 1300 SE Cardinal Court, Vancouver, WA 98683.

sandy matrix rich in very angular fragments. The surfaces of most diamicts are hummocky, many meters in relief. These deposits resemble the debris avalanche off Mount St. Helens in May 1980 (Voight and others, 1983; Glicken, 1998). That avalanche revealed the origin of hummocky, rocky diamicts at the bases of many other stratovolcanoes. Since the 1980s such landscape on Augustine's lower flanks has been interpreted as deposits of debris avalanches (Siebert and others, 1989, 1995; Begét and Kienle, 1992; Waitt and Begét, 1996, 2009).

Augustine's porphyritic andesite lava domes and flows range from dark gray to light gray to reddish (oxidized). Debris avalanches and lithic pyroclastic flows contain angular boulders and smaller fragments of this andesite. The ashy flows and coarse fall layers are rich in white to buff pumice. Rare inliers of fragmental olivine basalt lie on the volcano's south flank. Augustine rocks scatter chemically across the SiO_2 field of andesite (LeBas and Streckeisen, 1991), and glass-fraction analyses of prehistoric through 1996 pumice range from dacite to rhyolite. A few whole-rock analyses spill into the fields of basaltic andesite or low-silica dacite, but I call all these look-alikes andesite.

Augustine rocks have varied neither mineralogically nor chemically during the past few thousand years (Kienle and Swanson, 1985; Daley, 1986; Larsen and others, 2010). Each eruption seems to emit a similar suite of porphyritic andesite. For the 1976 eruption Johnston (1978) inferred that basalt

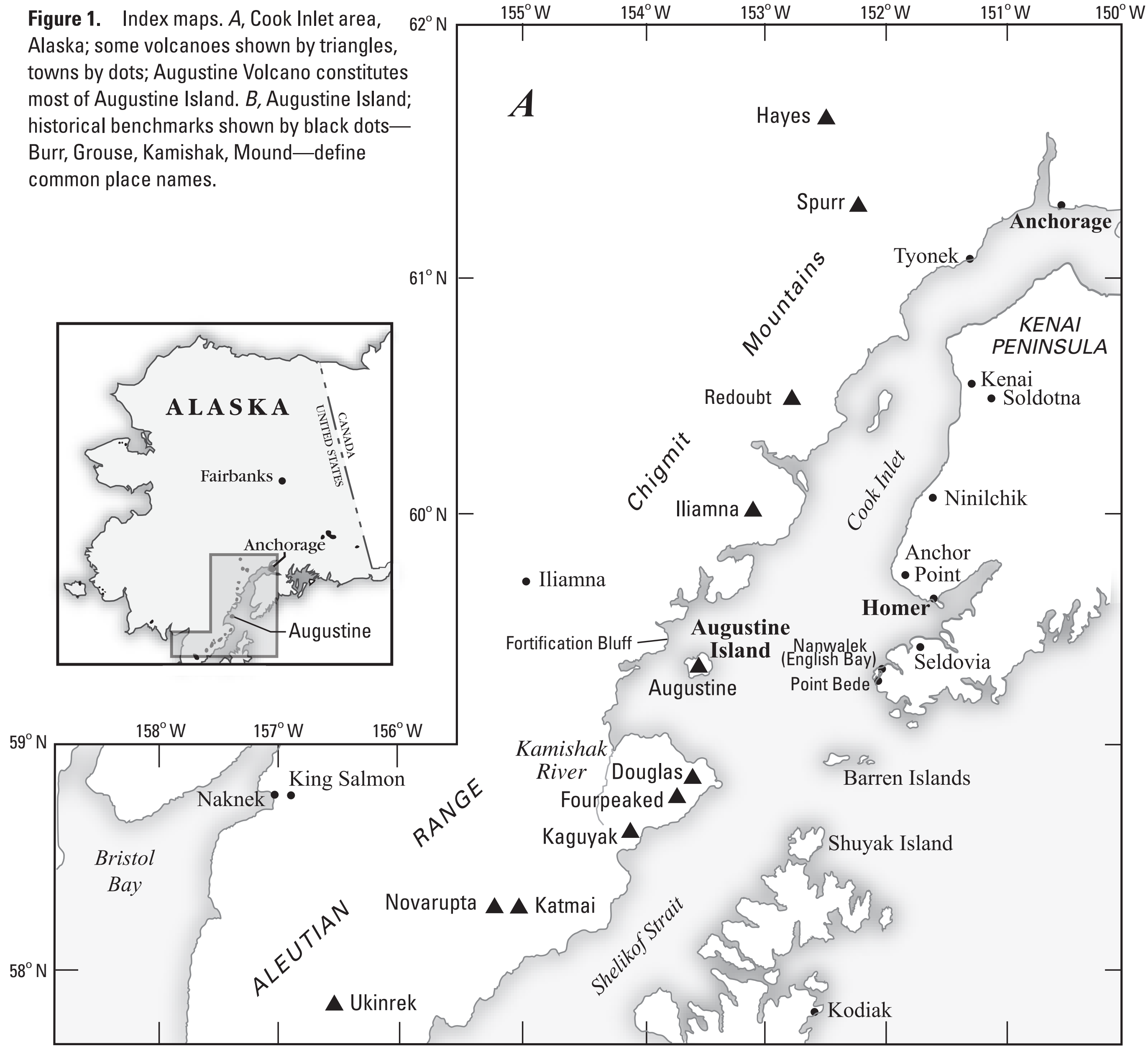

Figure 1. Index maps. *A*, Cook Inlet area, Alaska; some volcanoes shown by triangles, towns by dots; Augustine Volcano constitutes most of Augustine Island. *B*, Augustine Island; historical benchmarks shown by black dots—Burr, Grouse, Kamishak, Mound—define common place names.

magma intruded into a dacite chamber, the two partly mixing before erupting. Such magmas also mixed to trigger the 1986 and 2006 eruptions (Roman and others, 2006; Larsen and others, 2010). Variegated "mixed-magma" pumice also lies in the deposits of several prehistoric eruptions.

Chronology and Geomorphology

A few dozen radiocarbon dates from organic materials interbedded with tephra (fall deposits) on Augustine Island or at distal sites give limiting ages of the tephras (Waitt and Begét, 2009, table 2). Once bracketed by radiocarbon dates, a distinguishable tephra is a date by proxy.

Tephra blankets parts of Augustine's flanks and veneers mainland areas far downwind—eastward about 80 percent of the time. Stratigraphy on Augustine's east and southeast flanks shows six coarse pumiceous layers separated by layers of peat enclosing sand and silt ashes. In upward succession (fig. 3; table 1) the coarse tephras are G (2,100 yr B.P.), I (1,700 B.P.), H (1,500–1,400 B.P.), C (1,200–1,000 B.P.), M (750 B.P.), and B (390 yr B.P.). They are typically 10 to 80 cm thick along depositional axes and taper off laterally. The lower coarse tephras—G, I, H, and C—drifted east and southeast; tephra M drifted south and tephra B strongly northeast (Waitt and Begét, 2009, fig. 7). On Augustine's lower flanks large fragments in the coarse tephras are 1–5 cm in diameter. Between and atop these coarse tephras lie many sand-silt tephras of lesser eruptions including the seven historical ones from 1812 to 2006 (figs. 3, 4).

Table 1 includes the range of uncertainty in calendar ages if the raw radiocarbon dates were calibrated. Calibration does not much change discussion about the past 2,200 years, only adds a range of uncertainty. To keep text readable, dates remain in raw (uncalibrated) round numbers.

Geomorphic character suggests a deposit's origin and age. A deposit more vegetated than its otherwise identical neighbor must be older. Rocky debris fanning gently seaward must be much younger than its neighbor cut back to a high seacliff. A seacliff ceases to develop when a flow spreads beyond it and shifts the coast seaward. Seacliffs well back of Augustine's coasts tell of wave erosion arrested by new eruption deposits (fig. 5). Debris avalanches stand out from other

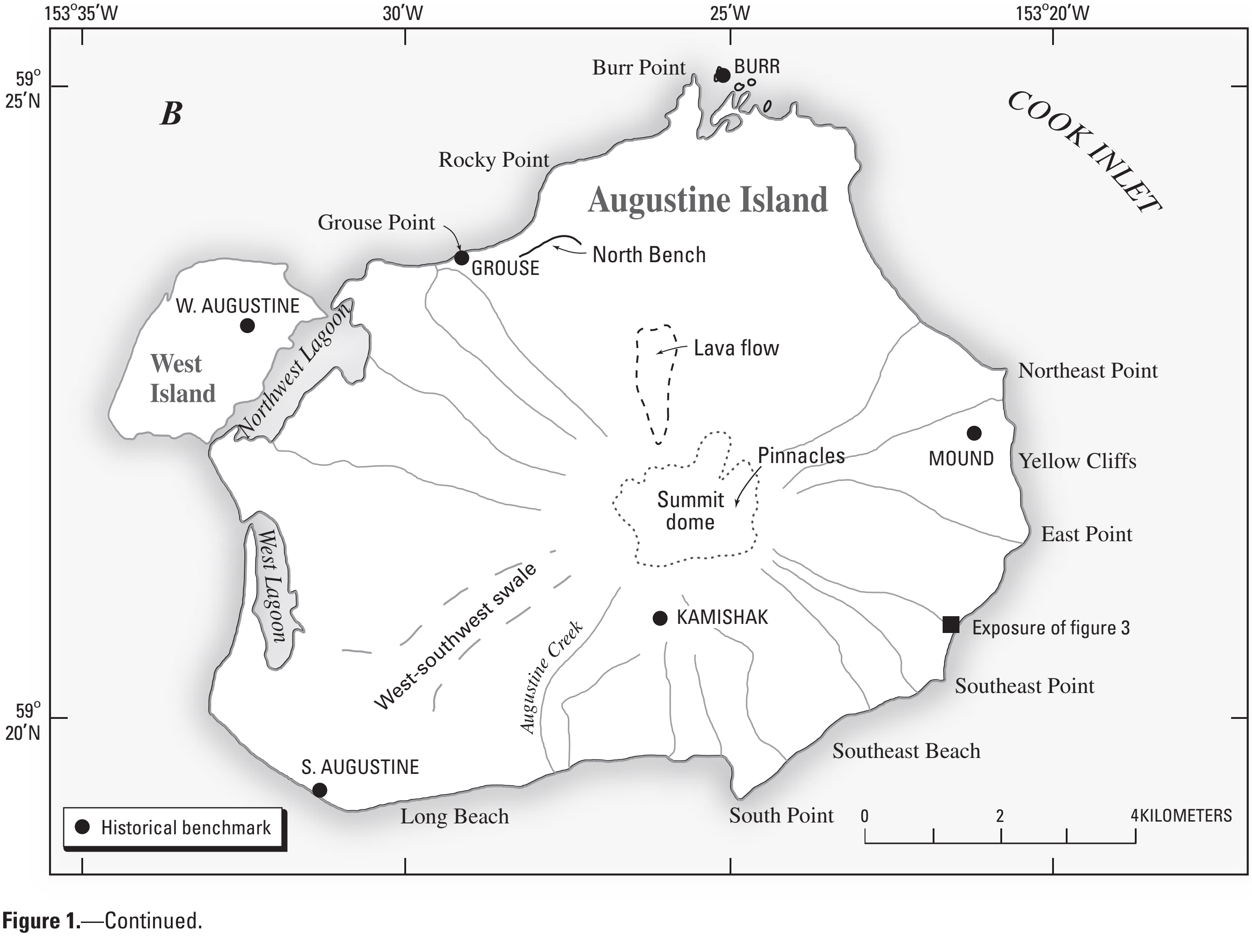

Figure 1.—Continued.

flow deposits by their huge angular dome-andesite boulders and topography of hummocks and depressions. Offshore of most of Augustine's avalanches, such hummocky topography also shows in bathymetric contours (fig. 6).

Mesozoic Rocks

Hard sedimentary bedrock reaching 400 m above the present south coast formed Augustine Island before the volcano existed (fig. 7). Fossils identify most of these hard layered rocks with the Upper Jurassic Naknek Formation (Detterman and Jones, 1974) on the western mainland (Detterman and Hartsock, 1966; Magoon and others, 1976). On Augustine Island the gently south-dipping Naknek comprises slope-forming siltstone to fine sandstone and cliff-forming sandstone. At higher altitudes, 350 to 400 m, friable sandstone and conglomerate contains *Inoceramus* and other fossils that correlate with the Upper Cretaceous Kaguyak Formation on mainland Cape Douglas to the south-southwest (Jones and Clark, 1973; Detterman and Jones, 1974). Cut by deep gullies, Mount Augustine's smooth and broad south slopes below 550 m are of this Jurassic-Cretaceous bedrock.

Pleistocene Deposits

A ridge 500 m long and 60 m high along the south coast consists of Naknek sandstone and overlying glacial deposits that crop out 200 m higher. Faults and open fissures riddle this coastal rock; bedding attitudes vary widely, their dips much steeper than in the upslope bedrock. This ridge is a Pleistocene block landslide that must have slid on seaward-dipping Naknek shale.

Diamicts containing striated pebbles to boulders of granite, diorite, gabbro, gneiss, greenstone, and chert crop out on the south flank. These unweathered exotic stones derive from the glaciated mountains along the west side of lower Cook Inlet probably during the late Wisconsin between 30,000 and 12,000 ^{14}C yr B.P. The stones as high as 290 m above sea level on Augustine, apparently the height to which glaciers spread across lower Cook Inlet during lowered sea levels

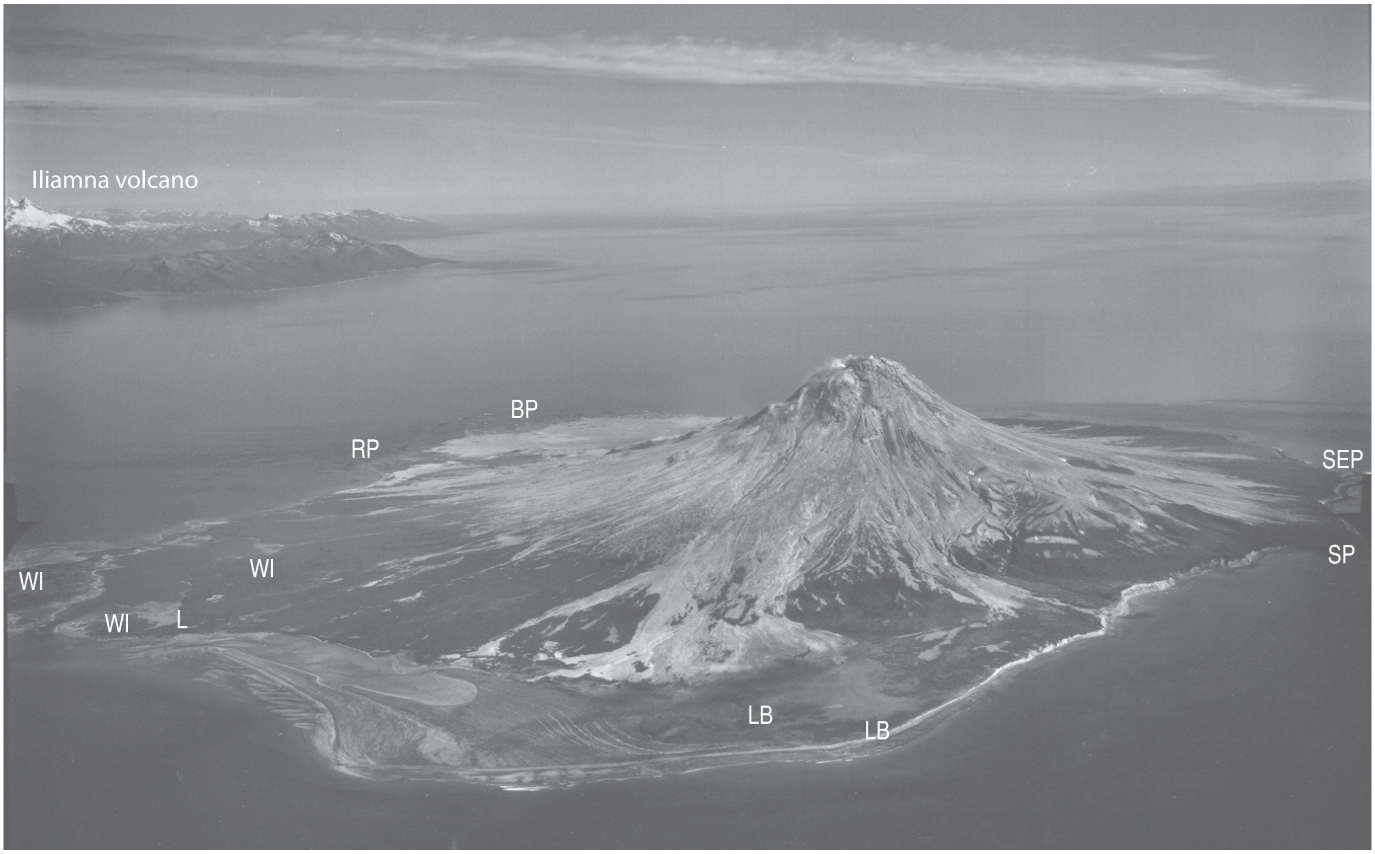

Figure 2. Oblique aerial view northeastward of Augustine Island and volcano. Much of vegetated (dark-toned) area of lower flanks is debris avalanches: BP, Burr Point; RP, Rocky Point; WI, West Island; L, Lagoon; SP, South Point; LB, Long Beach; SEP, Southeast Point. Light-toned areas are deposits of pyroclastic flows of 1963–64, 1976, and 1986 eruptions. The near point is built up over the last thousand years by seaward-accreting beach ridges capped by eolian sand. USGS photograph by Austin Post, August 25, 1987.

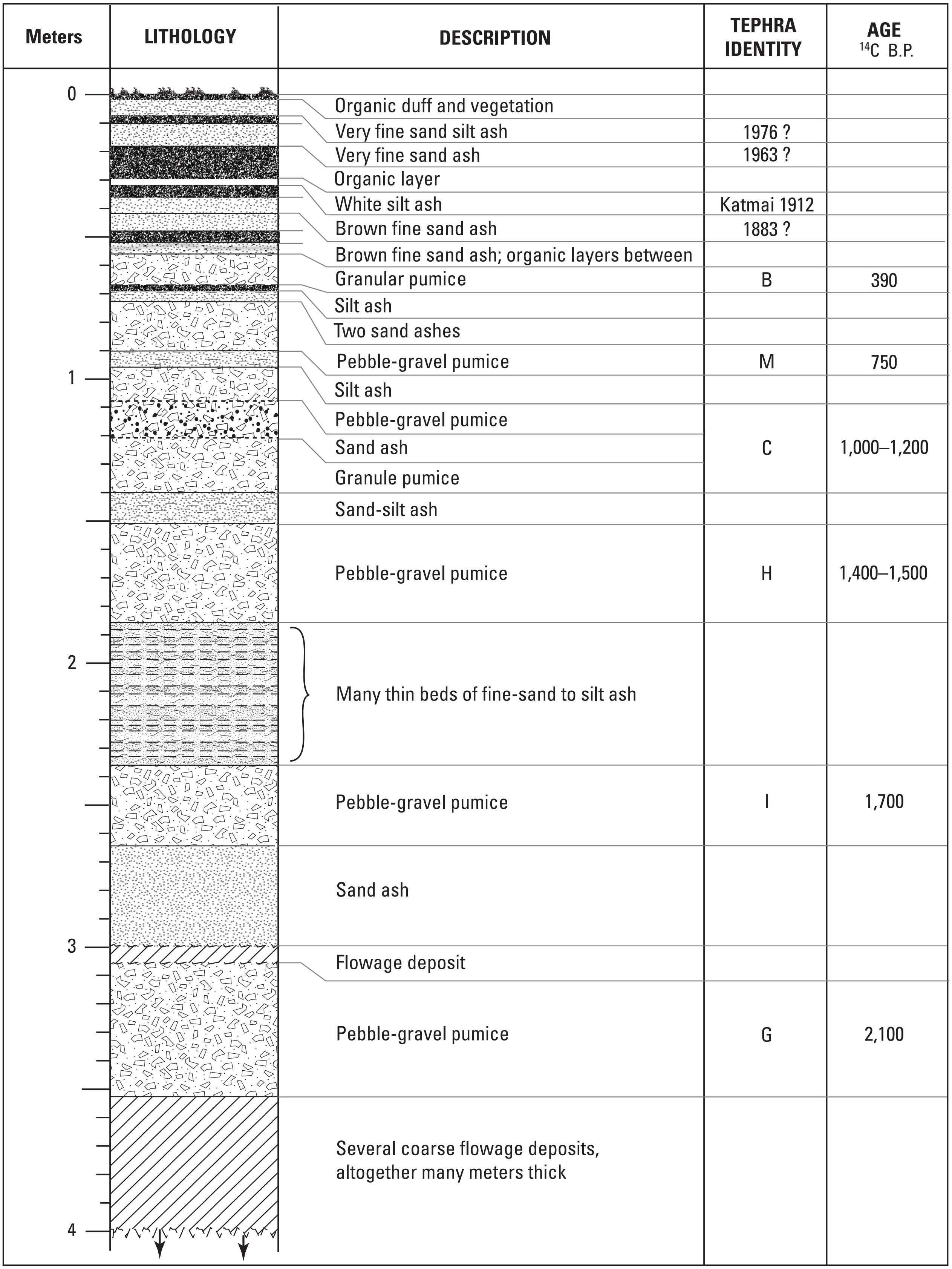

DESCRIPTION	TEPHRA IDENTITY	AGE ^{14}C B.P.
Organic duff and vegetation		
Very fine sand silt ash	1976 ?	
Very fine sand ash	1963 ?	
Organic layer		
White silt ash	Katmai 1912	
Brown fine sand ash	1883 ?	
Brown fine sand ash; organic layers between		
Granular pumice	B	390
Silt ash		
Two sand ashes		
Pebble-gravel pumice	M	750
Silt ash		
Pebble-gravel pumice	C	1,000–1,200
Sand ash		
Granule pumice		
Sand-silt ash		
Pebble-gravel pumice	H	1,400–1,500
Many thin beds of fine-sand to silt ash		
Pebble-gravel pumice	I	1,700
Sand ash		
Flowage deposit		
Pebble-gravel pumice	G	2,100
Several coarse flowage deposits, altogether many meters thick		

Figure 3. Tephra stratigraphy overlying flowage deposits on Augustine Island north of Southeast Point (fig. 2*B*). Flowage deposits below tephra G are each several meters thick. Radiocarbon ages are uncalibrated.

Table 1. Stratigraphy of coarse pumiceous "marker-bed" tephra layers and debris-avalanche deposits, Augustine Volcano.

Debris Avalanche	Tephra Layer	Approximate Age (^{14}C yr BP), or [AD]	Calibrated Age Range BP at 2σ confidence, or [AD]
Burr Point		[1883]	[1883]
Rocky Point			
West Island (incl. Grouse Pt.)			
• • • • • • • • • •	B	390	310–510
Southeast Beach			
• • • • • • • • • •	M	750	660–780
Lagoon			
• • • • • • • • • •	C	1,000–1,200	750–1,300
Long Beach			
South Point			
North Bench (may be older)			
• • • • • • • • • •	H	1,400–1,500	1,240–1,530
Northeast Point			
• • • • • • • • • •	I	1,700	1,530–1,700
Southeast Point			
Yellow Cliffs			
• • • • • • • • • •	G	2,100	1,990–2,150
East Point (perhaps comprises 3 separate avalanches)			

about 15,000 years ago (Hamilton and Thorson, 1983) and surrounded Augustine Island's mountain.

Augustine's south flank (fig. 7) exposes fragmental porphyritic olivine basalt and basaltic andesite, some beds cemented palagonite. Angular fragments scatter through low-angle cross beds containing 3- to 8-mm mud balls, and angular bombs have sagged 25 cm. Apparently these were water-propelled explosions, the beds emplaced wet. The upper 20 cm of this basaltic hyaloclastite is interlayered with the base of overlying rhyolitic tephra. So olivine basalt erupted from a south-flank vent while pumice erupted upslope, likely the summit.

Holocene Tephra, Flows, and Lava Domes

Sections high on Augustine's south side expose bedded deposits of pumiceous falls, lithic falls, and pumiceous pyroclastic flows. A peat layer halfway up one tall section dates to 2,160 yr B.P. Except on such inliers, deposits of early and middle Holocene eruptions on Augustine Island lie buried beneath younger eruptive debris. But on Shuyak Island 110 km southeast of Augustine (fig. 1*A*), two tephras chemically fingerprinted to Augustine date between 6,460 and 5,020 yr B.P., where a higher Augustine tephra dates to 3,620–3,360 yr B.P. (Waitt and Begét, 2009, plate 2). At Kamishak Creek 70 km southwest of Augustine Island, an Augustine-chemistry fall tephra dates between 3,850 and 3,660 yr B.P. (Riehle and others, 1998, fig. 8). A likely Augustine ash near Homer 110 km northeast of Augustine dates to about 2,275 yr B.P. Early to middle Holocene Augustine tephras lie on Fortification Bluff west-northwest of Augustine (Riehle and others, 1998; Waitt and Begét, 2009).

Gray porphyritic andesite forms Kamishak dome at altitude 513 m on Augustine's south flank (figs. 2, 7). Porphyritic andesite also forms domes F and P, knobs at 1,025 and 910 m on the upper northwest flank. West Island debris avalanche must have left a theater-shaped scar in this area, so domes F and P postdate about 370 yr B.P. but precede historical eruptions. Several overlapping prehistoric domes form the east and south sides of the summit cone. Several historical domes overlap this old dome rock. All-but-buried porphyritic andesite crops out here and there far below these domes, far enough down to be lava flows.

Prehistoric Late Holocene Deposits

Most of Augustine's lower-flank deposits are bouldery diamicts, each an unsorted mixture of angular clasts of summit-dome rock of all sizes, sand to enormous boulders. Most of them I infer as debris avalanches but a few as lithic pyroclastic flows. This summary piece skips soon from description (diamict) to interpretion (debris avalanche).

Between about 2,500 and 1,450 ^{14}C yr B.P.

A continuous high sea cliff between Southeast Point and Northeast Point exposes bouldery debris and intervening tephra that divide into at least four thick diamicts, probably debris avalanches.

East Point Debris Avalanches

The lowest of these four, East Point diamict beneath tephra G (table 1), forms the lower 13 m of this seacliff. Its angular andesite boulders as large as 5–7 m are set in a sand-gravel diamictic matrix of shattered andesite. A few prismatically jointed clasts must have been hot juvenile dome rocks. Fluvial deposits within the diamict section suggest it comprises two or three successive avalanches.

Yellow Cliffs Debris Avalanche

Overlying East Point debris avalanches and tephra G, a yellowish diamict 5–9 m thick forms the middle to upper part of the east-coast seacliff. Matrix and clasts as large as 3.5 m are strongly altered and soft, yet the deposit contains sporadic huge pods of scarcely altered andesite diamict. These unoxidized zones and this diamict's position sandwiched between unoxidized diamicts show that the alteration had occurred in the summit source area before landsliding.

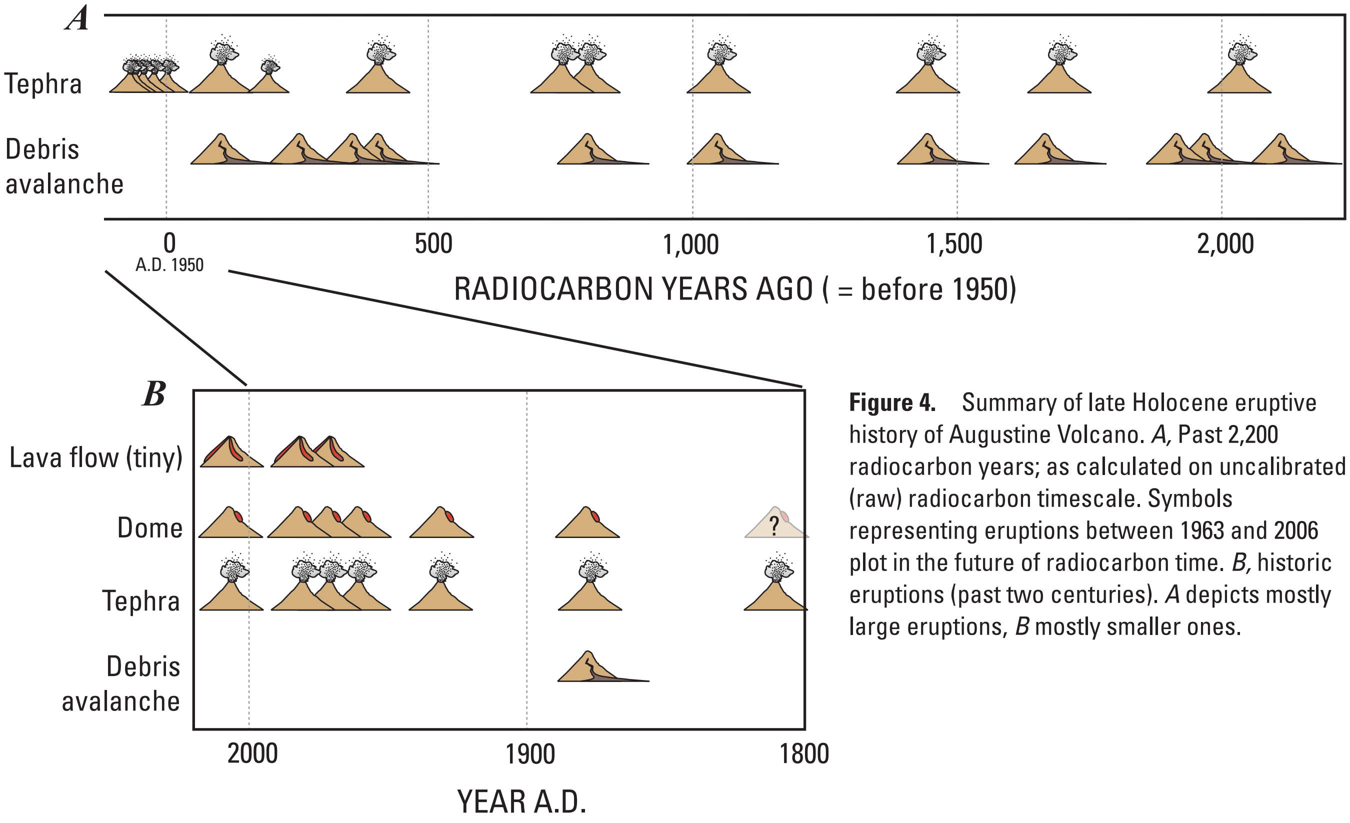

Figure 4. Summary of late Holocene eruptive history of Augustine Volcano. *A,* Past 2,200 radiocarbon years; as calculated on uncalibrated (raw) radiocarbon timescale. Symbols representing eruptions between 1963 and 2006 plot in the future of radiocarbon time. *B,* historic eruptions (past two centuries). *A* depicts mostly large eruptions, *B* mostly smaller ones.

Southeast Point and Northeast Point Debris Avalanches

Overlying Yellow Cliffs avalanche in the coastal cliff near Southeast Point, a diamict at least 8 m thick contains boulders as large as 4–7 m (fig. 8) and a scarcely altered matrix. This Southeast Point avalanche extends to Northeast Point where tephra I overlies it, overlain in turn by Northeast Point diamict (fig. 9).

Along the top of the east-coast cliff between tephras I and H, a coarse diamict at Northeast Point is as thick as 20 m, contains angular andesite boulders as large as 7 m (fig. 8), and traces up gullies to the base of the summit domes. Beneath mantling tephra and peat, the surface's sharp local relief is at least 6 m. By these properties it is clearly another rocky avalanche. In spots the diamict is strikingly monolithologic, every fragment very angular. A dome block 30 m long is more disaggregated than "jig-saw" blocks in the 1980 Mount St. Helens avalanche (Glicken, 1996). So immense a block could only have piggybacked atop an avalanche.

At Northeast Point the deposit crosses a coastwise scarp 650 m long and 30 m high (fig. 5), a seacliff cut back into the Yellow Cliffs and older avalanches. Northeast Point avalanche overrode and largely buried this scarp. Boulders as large as 5 m extend 600 m offshore. From there the sea has eroded this avalanche back to its present seacliff.

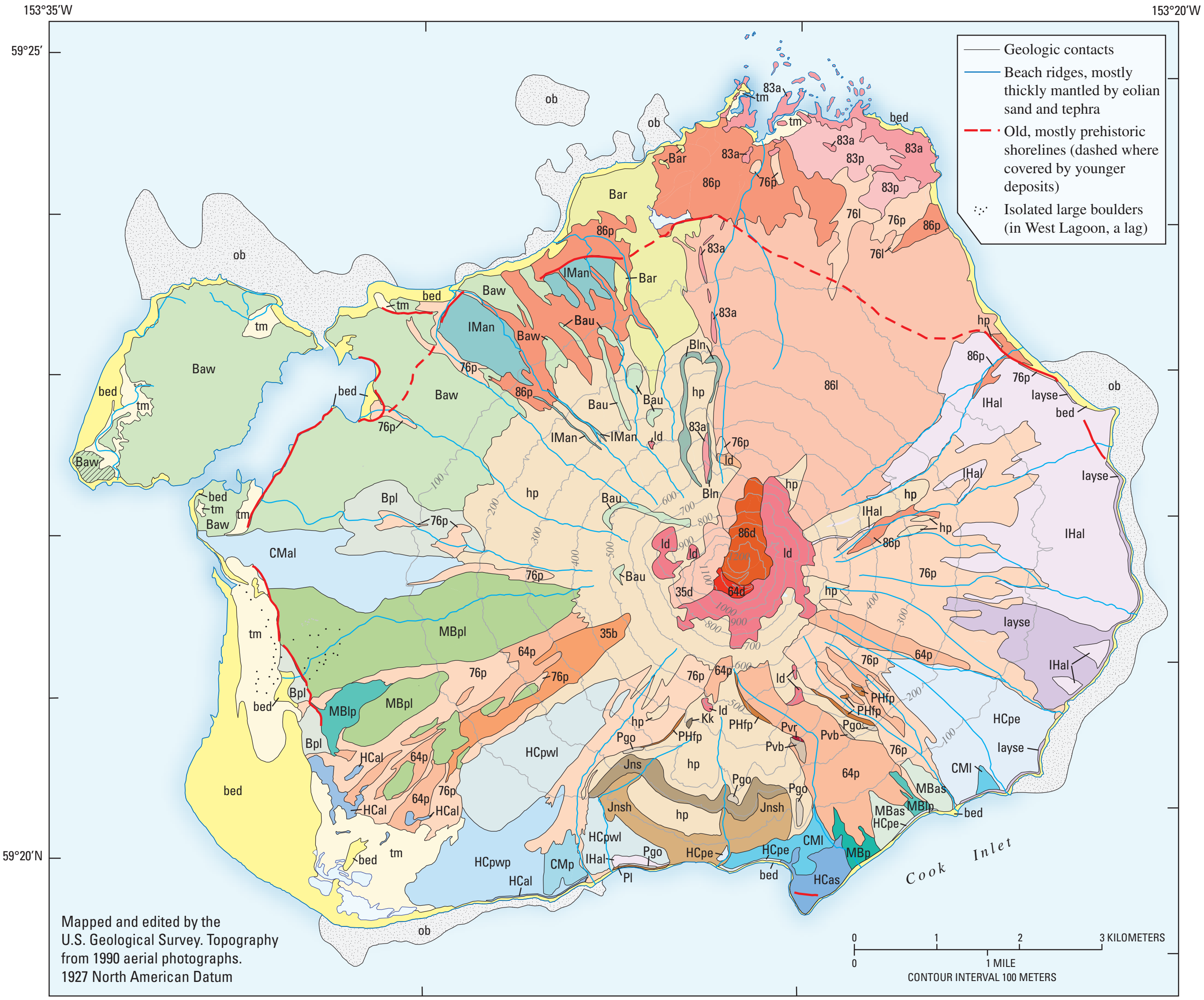

Figure 5. Pre-2006 geologic map of Augustine Island greatly simplified from Waitt and Begét (2009, plate 1). Ruled area of West Island is planed-off hummocks.

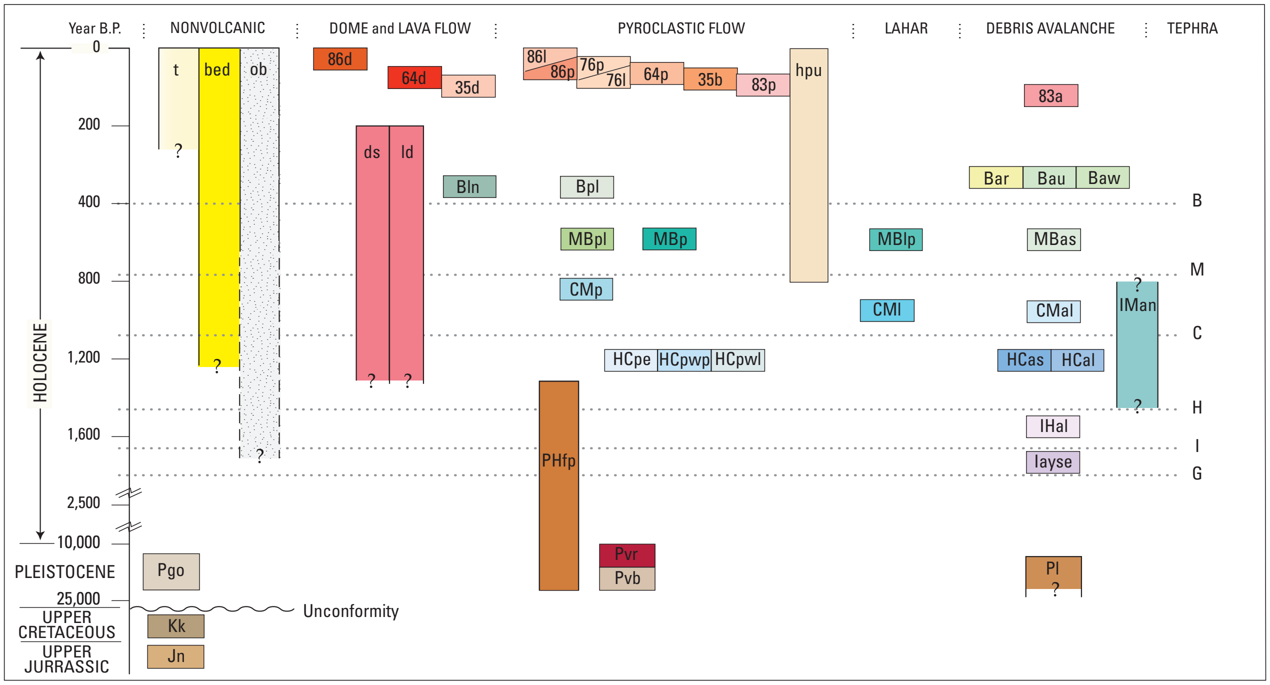

RECENT TO PREHISTORIC

tm	Tidal and marsh alluvium.
bed	**Beach and eolian deposits**—Loose medium to coarse sand in bodies parallel to coast.
ob	Offshore boulders

HISTORICAL ERUPTIONS

86dg	
86l 86p	1986 lava dome and agglutinate—Porphyritic andesite. 1986 lithic and pumiceous pyroclastic flow.
76l 76p	1976 lithic and pumicous pyroclastic flow.
64d	1963-64 Lava dome—Porphyritic andesite.
64p	1963-64 pyroclastic flow and lahar.
35d	1935 lava dome—Porphyritic andesite.
35b	1935 blocky rubble—Shed from summit dome.
83p	1883 pyroclastic flow and surge.
83a	1883 debris avalanche—Bouldery diamict.
hp	Pyroclastic flow, lahar, and fall deposits of historic and prehistoric eruptions.

PREHISTORIC

Younger than about 390 ^{14}C yr B.P.

Bln	North Slope lava flow—Massive porphyritic andesite.
Bar	Rocky Point debris avalanche—Bouldery nonsorted diamict.
Bpl	Lithic pyroclastic flow (or lahar?).
Bau	Undifferentiated small debris avalanches.
Baw	**West Island debris avalanche**—Bouldery diamict.

Between about 750 and 390 ^{14}C yr B.P.

Lithic pyroclastic-flow or lahar(?):

MBpl	Bouldery diamict of andesite, finely lobate and leveed.
MBp	Pyroclastic flow.
MBas	Southeast Beach debris avalanche—Bouldery diamict.
MBlp	Lahar or pyroclastic flow

Between about 1,100 and 750 ^{14}C yr B.P.

CMal	Lagoon debris avalanche—Bouldery diamict.
CMp	Pyroclastic flow.
CMl	Lithic pyroclastic flow (or lahar)—Cobble gravel to gravelly sand.

Between about 1,450 and 1,100 ^{14}C yr B.P.

IMan	North Bench debris avalanche—Bouldery diamict.
HCpe	**Southeast pyroclastic fan**—Boulders to gravelly sand.
	Southwest pyroclastic fan:
HCpwp	Pumiceous pyroclastic flow—Pumiceous gravelly sand.
HCpwl	Lithic pyroclastic flow—Cobble to boulder gravel.
HCas	South Point debris avalanche—Bouldery diamict of angular andesite fragments.
HCal	Long Beach debris avalanche—Bouldery diamict of angular fragments.

Between about 1,700 and 1,450 ^{14}C yr B.P.

IHal	Northeast Point debris avalanche and lahar—Bouldery diamict of andesite fragments and sandy gravel.

Between about 2,500 and 1,800 ^{14}C yr B.P.

layse	Yellow Cliffs, Southeast Point, and East Point debris avalanches—Bouldery diamicts of angular andesite fragments.

Lava domes (late(?) Holocene)

ds	Pre-1883 summit-dome complex—Porphyritic-andesite domes forming east crater rim and upper east and south flanks.
ld	Lava domes and flows —Inliers of porphyritic andesite. Includes Dome P on the northwest flank at altitude 910 m, Dome F on the northwest flank at altitude 1,025 m, Dome Kamishak on the south flank at altitude 513 m, and flatter inliers at levels 380–530 m on south and north flanks.

LATE PLEISTOCENE (TO HOLOCENE ?)

PHfp	Fall and pyroclastic flows—Interbedded pumiceous and lithic pyroclastic flows and pumiceous falls.

LATE(?) PLEISTOCENE

Pgo	Glacial deposits—Gravel veneer of diverse angular clasts of exotic diorite, granite, gneiss, gabbro, greenstone, limestone.
Pvr	Rhyolitic pumiceous beds.
Pvb	Basaltic hyaloclastite.
Pl	Block landslide—Sandstone and shale of Naknek Formation highly jointed and faulted, riddled with open fissures, apparently a displaced block derived upslope from unit Jn.

PREDATING AUGUSTINE VOLCANO

Kk	Kaguyak Formation (Upper Cretaceous)—Greenish fossiliferous sandstone and sandy pebble conglomerate.
Jn	**Naknek Formation (Upper Jurassic)—**Cliff-forming sandstone overlying siltstone with thin sandstone interbeds.

Between about 1,450 and 1,100 ^{14}C yr B.P.

Several bodies of coarse bouldery diamict lie along Augustine's lower southwest, south, and southeast slopes, capped by tephra C but not by H.

South Point and Long Beach Debris Avalanches

Jutting 600 m seaward from the south coast, South Point diamict is at least 30 m thick. Its hummocky surface 10 m in relief includes angular porphyritic-andesite clasts as large as 9 m—properties showing it's a debris avalanche. South Point being broader and reaching more seaward than Northeast Point suggests its relative youth. The capping tephra-and-peat sequence 1–2 m thick has the C tephra near its base, stratigraphically proving relative youth. Yet eroded back into a high cliff, this coarse avalanche is geomorphically older than the weakly cliffed avalanches around the west and north coasts.

Long Beach diamict sparsely exposed on the lower southwest flank forms a belt of hummocks beyond 1976 ashflows. Hummocks as much as 9 m high and 20 across—one mostly a 9-m boulder (fig. 10)—reveal the deposit as another coarse debris avalanche. Hummocks typically contain boulders as large as 6 m and are capped by tephra C. At low tide a large-boulder lag reaches half a kilometer off the south-southwest shore, and convoluted bathymetric contours reach farther (figs. 5, 6).

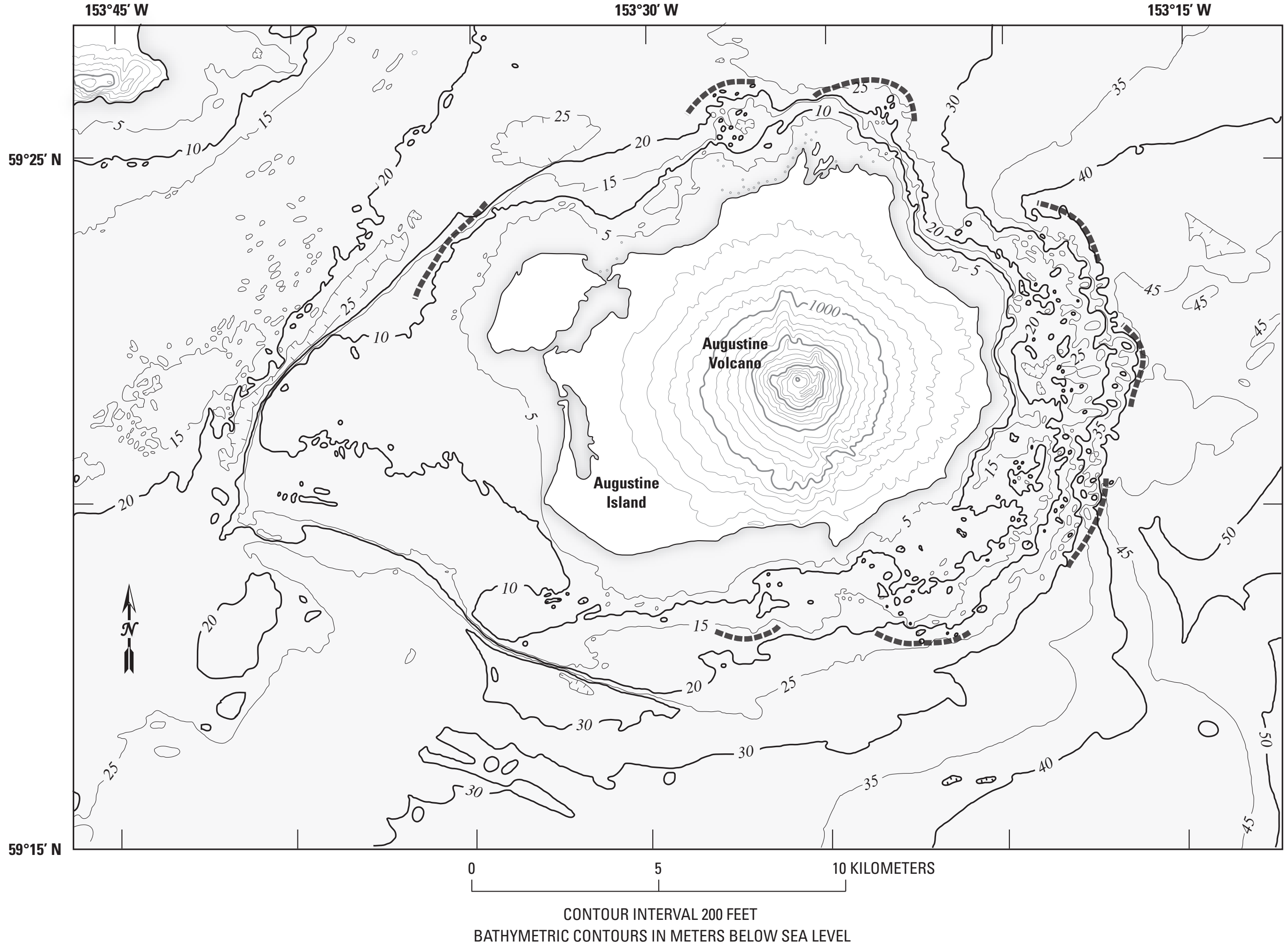

Figure 6. Conspicuously bumpy submarine topography revealing offshore distribution of debris avalanches. Heavy dashed line indicates approximate outer limits. The 200-ft (about 60 m) contours on Augustine Island and the 5-m contours of bathymetry are from U.S. Geological Survey 1:250,000 Iliamna quadrangle. Hummocky topography attributed to Augustine's debris avalanches extends to depth of 45 m and as far as 3.8 km off east coast and to depth of 25 m as far as 2.8 km off north coast. Farther areas of lumpy topography, such as 5–10 km west and northwest of West Island are from late Wisconsin glaciation or other nonvolcanic processes.

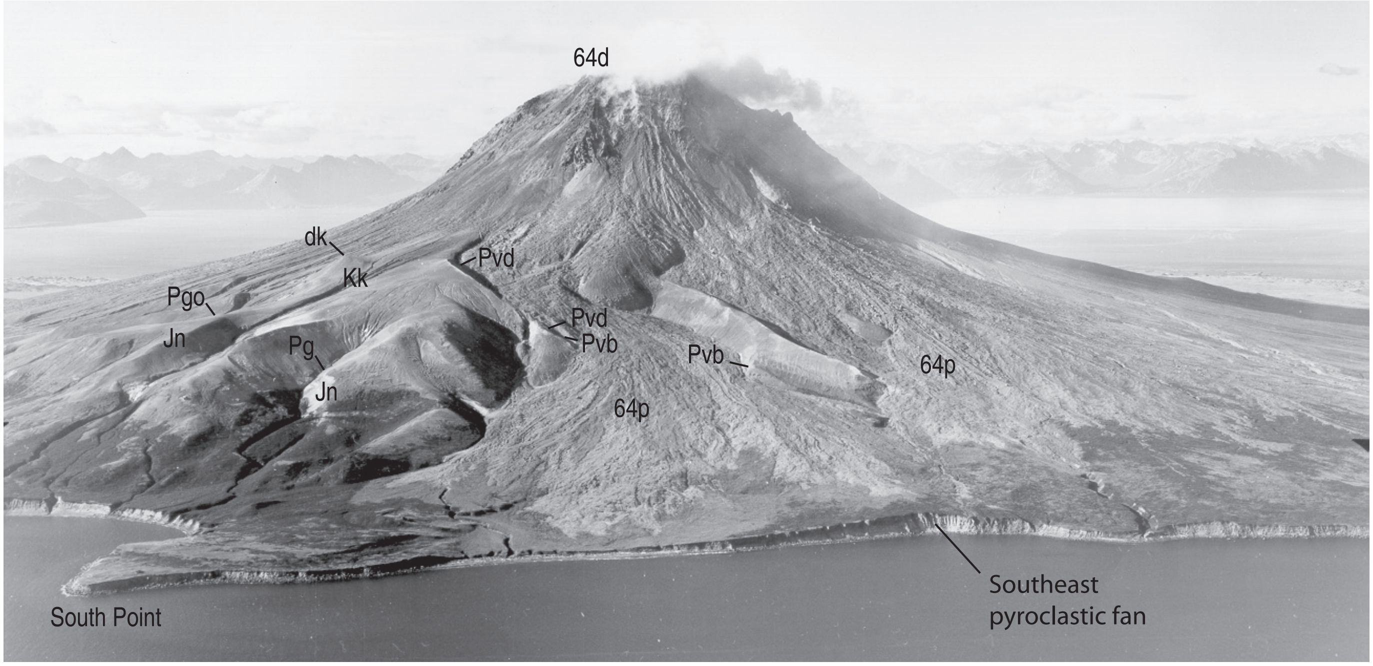

Figure 7. Oblique aerial view north-northwestward of Augustine Volcano. Most smooth, maturely dissected topography of south flank is Jurassic and Cretaceous bedrock (Jn, Kk) being gradually buried by Augustine's young cone and fall tephras. Shown are locations of Kamishak dome (dk) and Pleistocene deposits: basaltic hyaloclastite (Pvb), dacitic fall and flow deposits (Pvd), and glacial deposit (Pgo). Below 1964 dome (64d) are extensive coarse 1963–64 pyroclastic flows (64p). USGS photograph by Austin Post, September 3,1966.

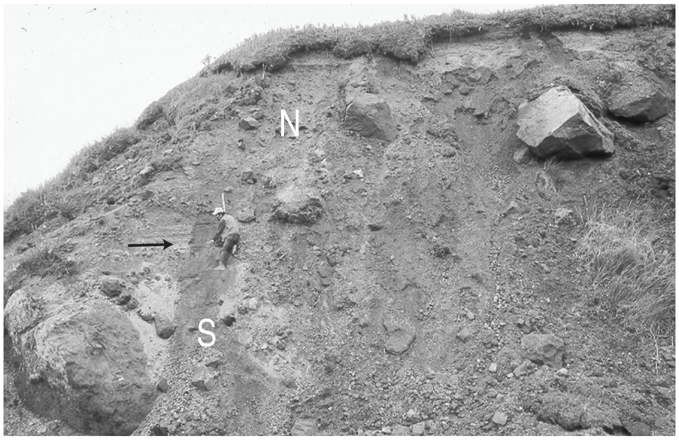

Figure 8. Bouldery Southeast Point debris avalanche (S) overlain by tephra I (small arrow at man), overlain in turn by bouldery Northeast Point debris avalanche (N), capped by tephra H and younger tephras and soils. East coast of Augustine Island.

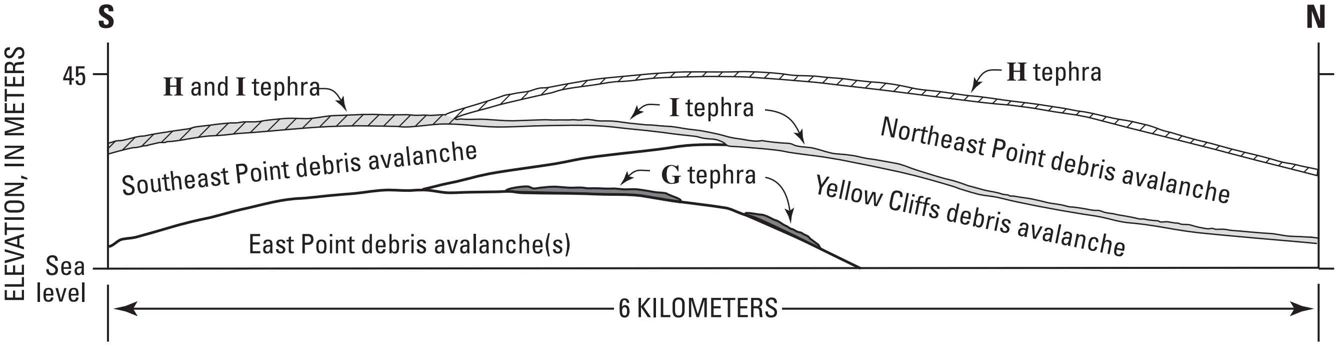

Figure 9. Schematic sketch of coastal cliffs along east side of Augustine Island showing stratigraphic relations of the four oldest debris avalanches and the three oldest coarse pumiceous-tephra marker beds: G, I, and H.

Southwest and Southeast Pyroclastic Fans

A steep angular-gravel fan on Augustine's southwest flank includes 6-m andesite boulders and is capped by tephra C. Many closely spaced levees and intricately lobate margins embellish its surface. These and other characteristics—it lacks hummocks—show it to be of lithic pyroclastic flows. In coastal cliffs a sandy pumiceous pyroclastic flow as thick as 16 m overlies the Long Beach avalanche. Pumice clasts concentrate in the oxidized upper 3 m, lithic clasts in the lower 10. One site reveals two such massive deposits—the lower 13 m thick and punctuated by openwork gas-escape pipes, the upper 4 m thick. Both flows followed the valley of Augustine Creek.

Pumiceous to lithic pyroclastic flows lie in the lower parts of the seacliff along Augustine's south-southeast coast. Numerous 6–9-m angular andesite boulders stud the surface upslope. Several closely paired levees trend downslope, curving into multilobate convex-downslope end ridges. Low in local relief, this deposit has the morphology of pyroclastic flow. The short distance (3 km) and steep slope (24°) from summit dome to deposit account for the huge blocks. It is roughly coeval with a lithic unit of southwest fan.

North Bench Debris Avalanche

At least 15 m thick, North Bench diamict comprises angular boulders as large as 5 m and its mildly hummocky topography has sparse local relief of 6 m. It is almost certainly another rocky avalanche. Pyroclastic flows and maybe tsunami overwash filled its lows and subdued its surface. A gently convex-seaward 23-m seacliff, the highest along Augustine's northwest coast, truncates the deposit. Younger deposits that descended intervening gullies and fanned along the coast isolated this cliff 400 m from the sea (fig. 5). North Bench avalanche is geomorphically much older than other northside avalanches.

Figure 10. Nine-meter megaclast of summit-dome porphyritic andesite forming a single hummock of Long Beach debris-avalanche deposit on lower southwest flank of Augustine Volcano.

Only the younger two coarse tephras lie on Augustine's northwest flank. In upslope gullies the avalanche is overlain by tephra B and younger ashes. Atop North Bench's seacliff, overlying strata are thin and only 1 or 2 ashes lie beneath the Katmai 1912 ash.

Between about 1,100 and 390 ^{14}C yr B.P.

Lagoon Debris Avalanche

Lagoon avalanche's sharp, hummocky local relief reaches 10 m and displays angular 3-m andesite boulders. Peat containing tephras M and B cap the highest coastal exposures and high hummocks inland. This avalanche apparently buried and rode beyond an older seacliff, perhaps the one truncating North Bench. Reaching 700 m seaward of this old cliff, Lagoon avalanche is only moderately cut back. Thus geomorphically it is fairly young. Hummocks below altitude 8 m along the coastal cliff are devoid of the M and B tephras. Water seems to have washed over these lower hummocks, stripping the tephras.

Pyroclastic Flow and Southeast Beach Avalanche

Atop a seacliff now isolated from the sea along the inner margin of West Lagoon is a 4-m bed of massive cobbly sand, apparently lithic pyroclastic flow, sandwiched between tephras B and M. This deposit formerly extended at least 300 m seaward, its legacy a lag of boulders as large as 2.5 m in West Lagoon. Waves must have eroded the deposit back, then to the west the long sand spit grew north, enclosing the lagoon. This low-relief deposit is marked upslope by intricately lobate termini and numerous levees containing large boulders, some with smaller stones piled behind. The levees and many small flow lobes reveal it as a lithic pyroclastic flow.

A bouldery diamict exposed in the upper part of the bluff along Southeast beach is studded with angular blocks as large as 2.5 m; lag boulders on the beach and in the surf zone reach 7 m. This small debris avalanche is sandwiched between tephras M and B.

Younger than about 390 ^{14}C yr B.P.

West Island Debris Avalanche

Separated from the northwest coast of Augustine Island by Northwest Lagoon (figs. 2, 5), West Island comprises a core of conical hummocks as high as 30 m (fig. 11*A*) covered in alder and scrub spruce, surrounded by lower hummocks, some cut by seacliffs. Angular andesite boulders on West Island reach 5 m and lie in brecciated matrix. A boulder field visibly reaches at least 1¼ km offshore, submarine hummocky topography twice that (fig. 6). West Island avalanche mantles the volcano's lower northwest flank with angular boulders as large as 4 m. But most of it swept as much as 5 km beyond a sea cliff cut 8 to 18 m high that had been Augustine's coast (fig. 5). Up from the coast, tephra M (or B?) underlies the avalanche. Hummocks and lows on West Island are overlain by peat containing five sand ashes, three beneath Katmai 1912 ash—but no tephra B. The avalanche dates to about 370 yr B.P. (table 1).

A hummocky diamict about Grouse Point consists of angular boulders that on the wave-winnowed beach reach 7 m. One hummock 12 m in diameter seems to be largely one block of shattered andesite. Boulders extend nearly a kilometer seaward, and bathymetric contours show it extends offshore another half kilometer. Grouse Point diamict is considerably younger than North Bench avalanche—whose truncating seacliff it crosses—and seems instead an arm of West Island avalanche.

Loose gravelly sand 10–30 cm thick and containing angular juvenile andesite overlies West Island diamict at several sites. It resembles the deposit of the May 1980 pyroclastic surge at Mount St. Helens (Waitt, 1981). Apparently the large West Island landslide unleashed a similar but smaller surge (Siebert and others, 1989; Waitt and Begét, 2009).

Some nearshore southwestern hummocks of West Island are beveled off, capped by openwork boulders, and incised by steep-sided channels (fig. 11*B*). Apparently water rushed over them as the avalanche plowed into the sea. Atop one such hummock three sand ashes underlie the 1912 Katmai ash: the hydraulic planing occurred with the West Island avalanche, not later.

Just south of West Island avalanche, low parts of Lagoon avalanche are also devoid of tephras M and B, areas oddly strewn by large boulders. West Island avalanche's crash into the sea evidently raised a water wave that swept over seaward parts of Lagoon avalanche. These waves may have washed over North Bench, causing the meager stratigraphy atop a deposit geomorphically old by its high, straight seacliff.

Rocky Point Debris Avalanche

A coarse diamict about Rocky Point (fig. 12) contains angular 5-m andesite boulders and sharp, hummocky topography as high as 15 m. At low tide this debris forms bouldery wave-beveled islands and shoals to 12 km offshore. Rocky Point bristles with scrub alder but not the dense spruce of West Island and seems younger. Capping the coarse diamict is a weakly oxidized soil and organic layer, an 1883(?) sand ash, and the white-silt 1912 Katmai ash. The lone ash layer beneath the Katmai ash also shows this deposit younger than West Island.

North Slope Lava Flow

A lava flow of porphyritic andesite or basaltic andesite on Augustine's middle north flank (figs. 5, 13) issued from below the base of the summit-dome complex and terminates 450 m lower. About 100 m thick, it is the only conspicuous lava flow on the island. It seems not covered by Rocky Point avalanche, but the west levee of the 1883 Burr Point avalanche overlies and postdates the lava flow. This stratigraphy and the flow's azimuth suggest it came late in the eruption that began with Rocky Point avalanche.

Beach and Eolian Deposits

Southwest Augustine Island comprises dozens of subparallel accreted beach ridges and overlying eolian deposits (figs. 2, 5). Landward ridges underlie tephra M, 70 cm of eolian sand, and Katmai 1912 ash. Seaward ridges underlie thinner eolian sand atop pebbly beach gravel. This wide platform reflects the delivery of voluminus sand to the south coast before tephra M—the thick deposits of southwest and southeast pyroclastic fans, which longshore currents then moved west. At the back of sandy beaches round the island lie coastwise ridges of eolian sand, some more than a kilometer long. They accumulated over centuries, shown by interbeds of peat and sand ash, the Katmai 1912 ash near the top.

Historical Deposits

Capt. James Cook named "Mount St. Augustine" in 1778: "This Mountain is . . . conical . . . and of a very considerable height" (Beaglehole, 1967). English, French, Spanish, and Russian commercial voyages preceded George Vancouver's 1794 coastal mapping including Augustine: "a lofty, uniform, conical mountain" (Lamb, 1984). The many early accounts mention an Augustine eruption only in 1812, when Chernobory (Mount Augustine) "burned" and mainland villagers couldn't reach the island (Doroshin, 1870). This cryptically suggests pumiceous flows swept into the sea. Doroshin's sketch (fig 13*A*) shows a fresh-looking northside subsummit dome.

1883 Eruption

Augustine's 1883 eruption is partly documented by contemporaneous accounts. On the 6th of October 1883, Mount Augustine (Chernoburoy) generated ash plumes and a tsunami experienced at English Bay 85 km east. The record book of the Alaska Commercial Company [ACC] (1883) at English Bay that day includes:

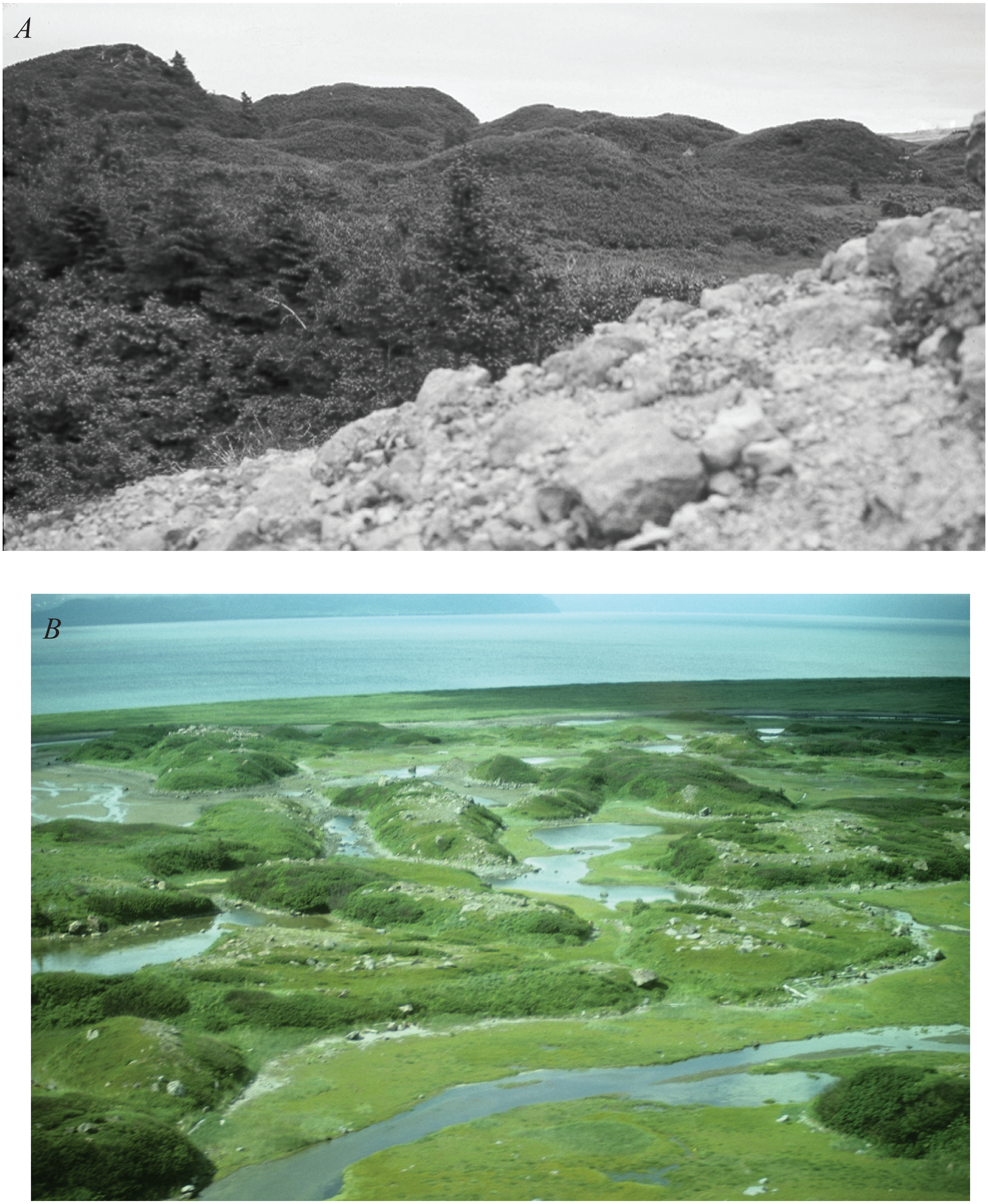

Figure 11. Views of West Island debris-avalanche hummocks at Augustine Island, Alaska. *A,* View southeastward of southwest side of central core of high conical hummocks of West Island avalanche. *B*, Near oblique-aerial view west of oddly planed-off hummocks on southwest part of West Island. I infer the modified hummocks and scabland-like channels between them to have been eroded by a water wave across this part of the West Island debris avalanche—a tsunami being born.

> *This Morning at 8.[15] o'clock 4 Tidal Waves flowed one following the other into the shore, the sea rising 20 feet above the usual Level. The air became black and foggy, and it began to thunder; it began to rain a finely Powdered Brimstone Ashes, which lasted for about 10 Minutes, and which covered all the parts of Land to a depth of over 1/4 of a inch, clearing up at 9 o'clock A.M. Cause of occurrence: Eruption of the active Volcano at the Island of Chonoborough. Rain of Ashes commencing again at 11. o'clock A.M. and lasting all day.* [simplified]

George Davidson, a 16-year veteran of mapping Alaska's coast, summarizes accounts of witnesses to Augustine's effects near English Bay (Davidson, 1884):

> *About eight o'clock on the morning of Oct. 6, 1883, parties at English Harbor heard a heavy report to windward. Dense volumes of smoke were rolling out of the summit of St. Augustin, moving north-eastward, and a column of white vapor arose from the sea near the island. Fine pumice-dust soon began to fall. About twentyfive minutes past eight A.M., a great 'earthquake wave' came like a wall of water. It carried off all the fishingboats from the point, and deluged the houses. Fortunately it was low water, or all of the people at the settlement must inevitably have been lost.* [simplified]

Davidson's eruption "smoke" from Augustine at about 8 o'clock concludes in the ACC logbook entry: ashfall at 11—three hours for the cloud to drift 85 km east-northeast to English Bay. A tide-gauge marigram at St. Paul (Kodiak) harbor also record an explosion and the tsunami of contemporary accounts. Superimposed on a tidal oscillation of 1.8 m are two high-frequency signals: an air-wave arrival at 8:31 a.m. and tsunami arrival at 11:00 (fig. 14). The air wave records an explosive eruption. At sound speed (about 331 m/s), it covers the 185 km air distance in about 9.3 minutes, implying eruption at Augustine about 8:22.

The volcano continued in intermittent eruption for months. In a late-1884 letter, Davidson reported that in June 1884 an ACC captain sailed past Augustine Island and saw:

> *From the summit a great slide over half a mile broad towards the rocky boat harbor on the north. Material had poured to the base of the mountain and filled the harbor.* [simplified]

Burr Point Debris Avalanche

Steep hummocks as high as 30 m about Burr Point (fig. 12) resemble the debris avalanche off Mount St. Helens in May 1980. A sharp levee of andesite blocks marks the avalanche's west margin. Brecciated andesite constitutes the hummocks, individual blocks to 5 and 10 m, one slab 25 m long, all in a matrix of pulverized andesite rich in very angular clasts. Several blocks of loose sintered spatter and fragile fall pumice rafted to the coast intact.

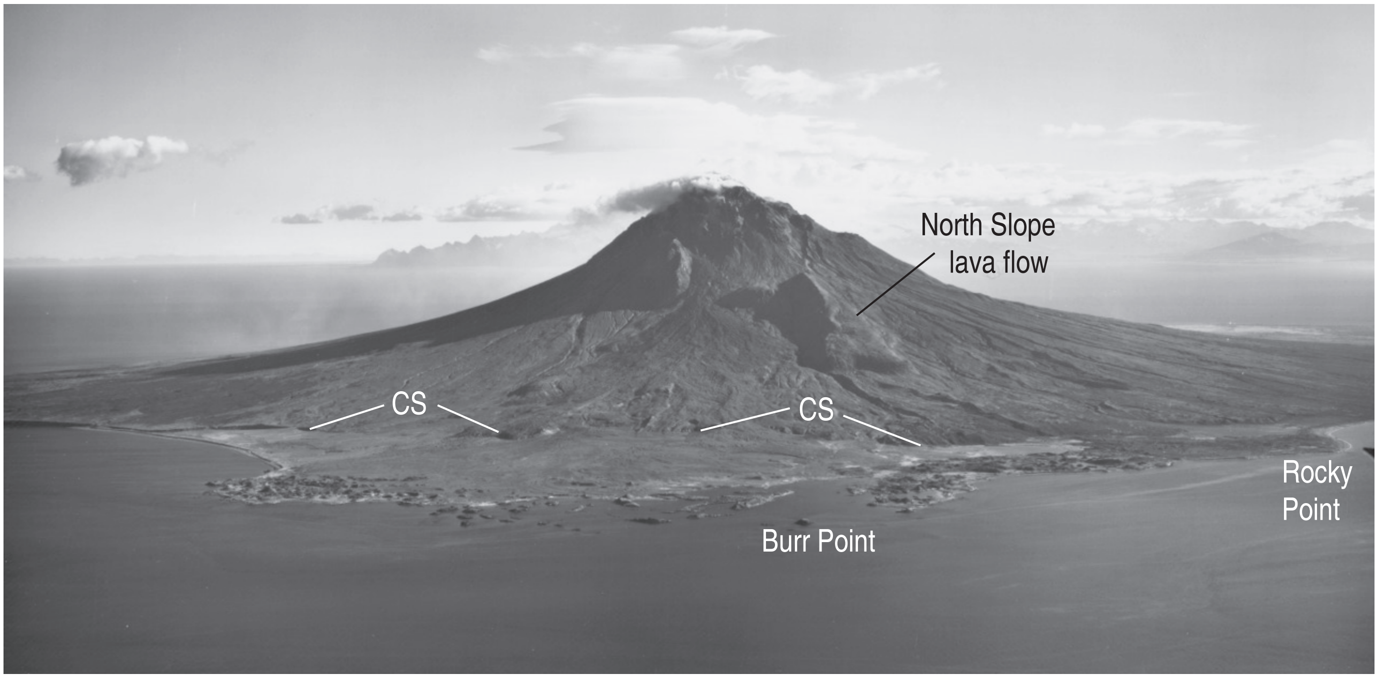

Figure 12. Distant oblique-aerial view of Augustine from the north showing hummocky deposit about Burr Point deposited by landslide in October 1883. This avalanche overrode the cliffed shoreline (CS) and entered the sea. Debris avalanche is in turn overlain by light-colored pyroclastic-flow debris of 1883, overlain upslope by small flows of 1935 and 1963–64. Smaller late-prehistoric Rocky Point avalanche lies just west (right). North Slope lava flow apparently erupted shortly after Rocky Point avalanche, long before Burr Point avalanche. Summit is 1964 dome. USGS photograph by Austin Post, September 3, 1966.

A former high seacliff on Augustine's north-northeast coast (figs. 5, 12) was overridden by the avalanche, which then plowed into the sea. Clear on 1960s' photographs, the cliff grows obscure as 1976 and 1986 pyroclastic flows bury the old scarp. Burr Point's islands extend to 2 ⅔ km, and submarine hummocks 4 km, beyond the old seacliff (fig. 6).

Its hummocks nearly devoid of vegetation and the many islands only meagerly carved back into seacliffs show Burr Point to be much younger than West Island. Rocky Point's thicker soil and offshore parts reduced to rocky shoals also show Burr Point's relative youth. Burr Point hummocks are overlain by soil containing the 1912 Katmai ash underlain by gray 1883 ash. Inland the gray ash is overlain by pyroclastic flow later in the 1883 eruption.

Coastal hummocks draped high above storm high water by mud containing exotic crystalline-rock pebbles enclose marine shells dating to 6,210–7,170 ^{14}C yr B.P. (fig. 15). To have scraped up such mud the avalanche must have plowed into the bay at high speed.

Pyroclastic Flow and Surge, and Lava Dome

Burr Point avalanche is buried upslope by laminated medium sand overlain by thick massive pebbly medium sand cut by openwork gravel pipes that had conveyed steam up from underlying wet mud. Pyroclastic surge apparently came after the avalanche. Then one or more hot pyroclastic flows filled a watery low behind the avalanche hummocks.

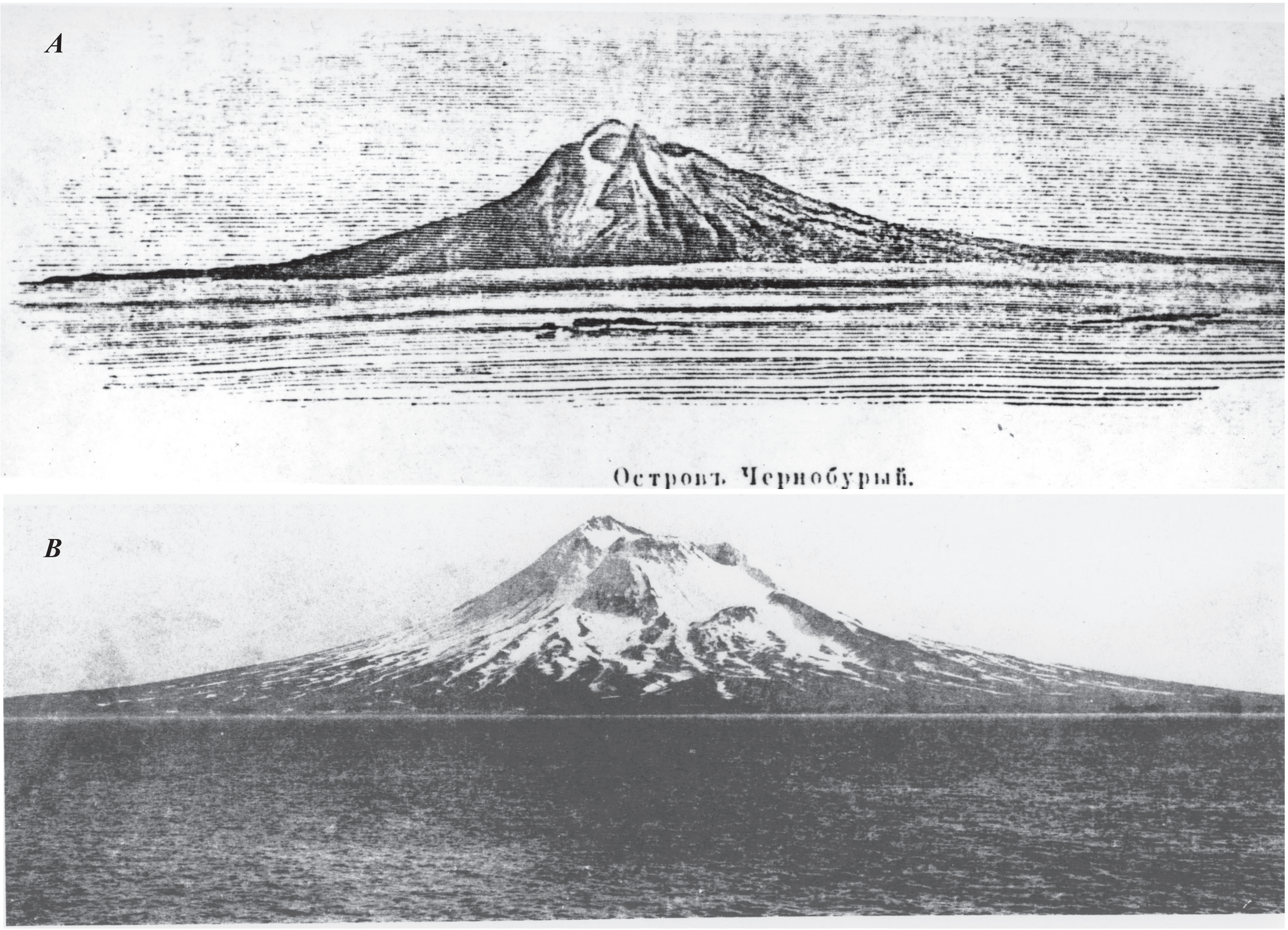

Figure 13. Augustine Volcano, Alaska, showing large-scale effects to summit area by 1883 eruption. *A*, Drawing by Doroshin (1870) showing spine, view from northeast. Bump on right horizon and downslope right of spine seems to be North Slope lava flow. Compared to later photographs, the northeast shoreline of Augustine shown here is less extended: Burr Point deposit does not yet exist. *B*, Photograph taken 1909 from similar northeast perspective by John Thwaites. Since 1870 the former spine and part of upper north flank disappeared, replaced by a large lava dome. Contrasting to Doroshin's drawing, Burr Point now exists.

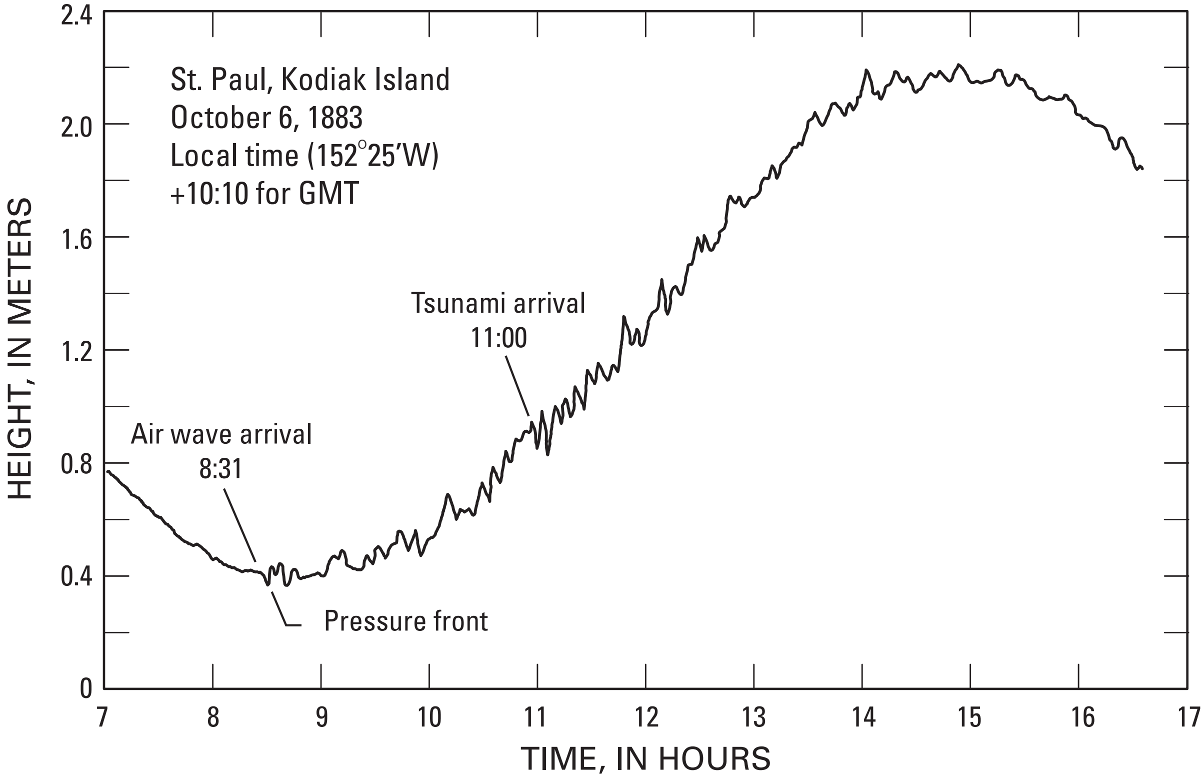

Figure 14. Tide-gauge marigram from St. Paul (Kodiak), Alaska, on October 6, 1883. It shows arrivals of wave train of air wave and of tsunami from Augustine, both superimposed on a tidal cycle of amplitude 1.8 m. Marigram from US Coast and Geodetic Survey archives (see Lander, 1996, p. 49 and fig. 16). The gauge was at Kodiak (St. Paul) Harbor at longitude 152°25′ W). Time is local sun time (before standardized time zones in 1884). For GMT add about 10 hours, 10 minutes. First motion in tide guage for air-pressure wave (depressing sea surface) is negative but for tsunami (raising sea surface) is positive. Lander (1996, figs. 48–90) shows many marigrams and interprets tsunami waves on them.

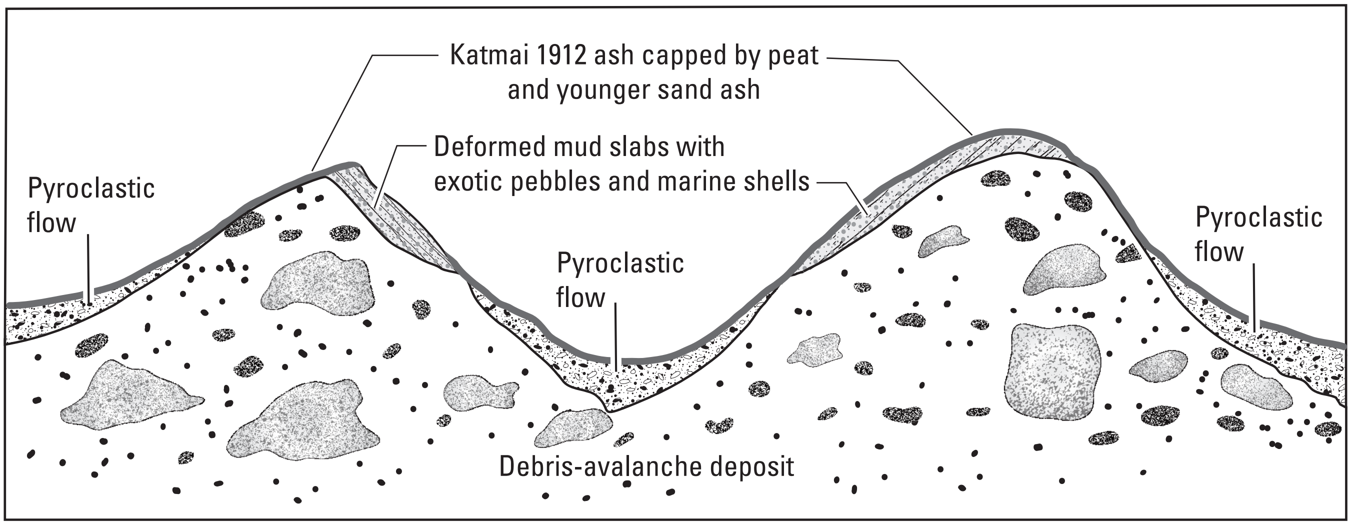

Figure 15. Schematic sketch of stratigraphic relations atop 1883 hummocks east of Burr Point. Bouldery debris avalanche is overlain by pyroclastic flow and by Katmai 1912 silt ash and younger sand ashes interlayered with peat. Deformed slabs (lined) of compact, fissile mud containing marine shells and rounded small pebbles of diverse exotic lithology drape over some hummocks. Marine shells (see explanation in text) from these slabs are radiocarbon dated at 6,210 and 7,170 yr B.P.

A broad lava dome that grew in the subsummit avalanche scar shows on photographs taken before 1963 (figs. 13*B*, 16). The 1883 crater still steamed profusely and rocks rolled off in 1895, as if the dome remained active (Becker, 1898). This dome disappeared beneath the 1976 lava dome.

1935 and 1963–64 Eruptions

Photographs from 1935 show a steaming dome draping west-southwest off the summit cone. Aerial photographs in the 1940s to 1960s and Bob Detterman's 1967 fieldwork also distinguish this dome. Rubble downslope contains angular boulders to 6 m where 1935 photos show light-toned debris recently shed from the dome. Remnants of the 1935 dome form a point just north-northwest of the summit (fig. 5).

From his 1967 visit, Detterman (1968) described the 1963–64 eruption, the summit dome steaming through 1966. The 1964 dome crowning the old summit complex drapes down to the south (figs. 5, 7). Downslope the bouldery andesite rubble includes clasts as large as 7 m on a debris fan whose intricate levees reveal emplacement by repeated lithic pyroclastic flows. Scattered large angular blocks lie in areas of 1964 ballistic fall denoted by Detterman (1968).

1976 and 1986 Eruptions

Augustine's 1976 eruption, better chronicled than earlier ones (Johnston, 1978; Kienle and Shaw, 1979), explosively shed pumiceous pyroclastic flows onto several flanks, especially north, in late January and early February. A large andesite summit dome emerged in February, grew rapidly in April, and tapered off into summer. It buried the 1883 dome and part of the 1935 dome. Its steep north edge repeatedly sloughed lithic pyroclastic flows.

North-flank 1976 pumiceous pyroclastic flows approached and reached the sea. Overlapping pumiceous flows end in intricately lobate marginal scarps and contain large pumice blocks and banded breadcrust bombs. Shed later from the growing dome, lithic flows with huge blocks but

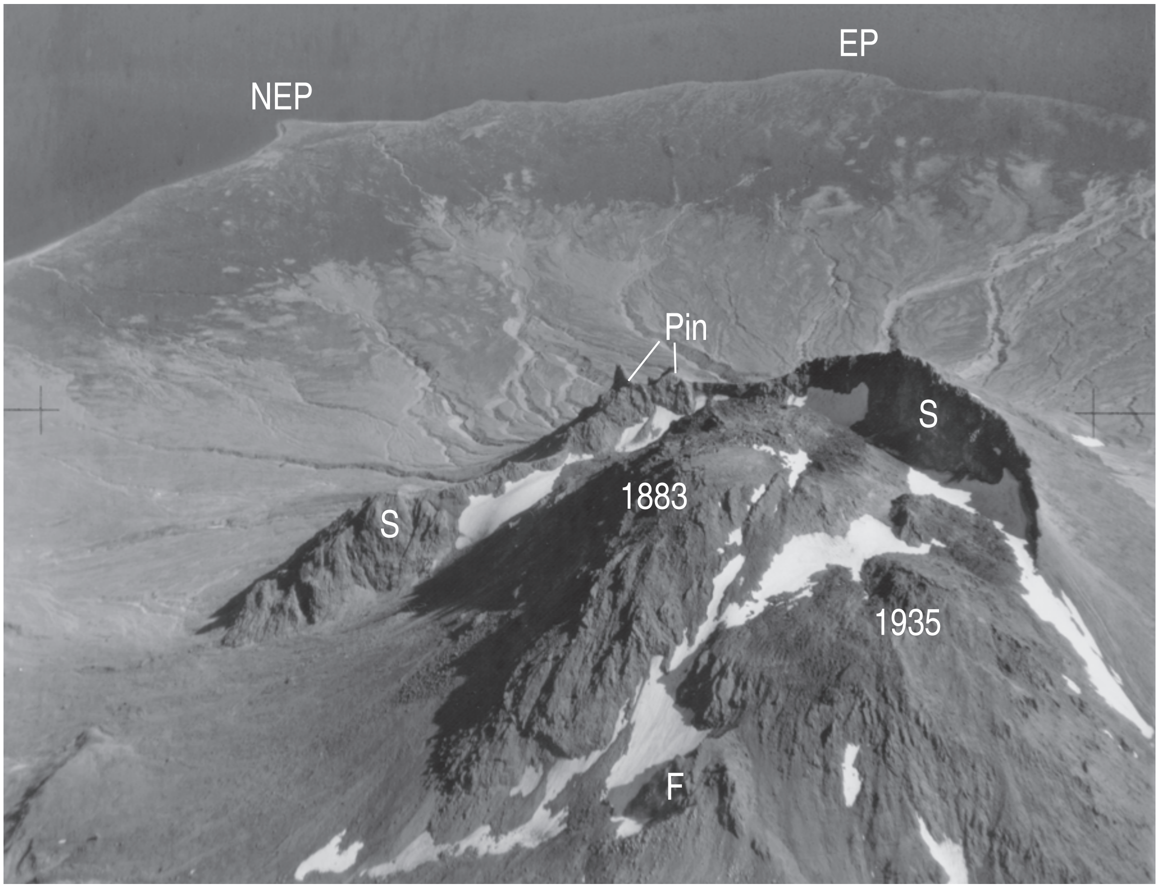

Figure 16. Oblique-aerial photograph eastward of Augustine Volcano before 1963–64 eruption showing 1883 and 1935 domes and prehistoric summit-dome complex (S) and dome F (dome P, below F, is out of shot). Arcuate scarp behind 1883 dome is scar left by 1883 landslide that cut into the composite summit dome including Pinnacles area (Pin). The coastal landmarks are Northeast Point (NEP) and East Point (EP). USGS photograph by Austin Post, August 24, 1960.

little pumice spread less far. Pumiceous flows also descended swales and gullies on other flanks across older fragmental debris, following some gullies nearly to the coast (fig. 5). A late-January surge reached Burr Point and offshore. It ripped into a research hut, inside burning mattresses and melting plastic, simulated in a lab oven at 500–700°C (Johnston, 1978; Kamata and others, 1991; Waitt and Begét, 2009).

Augustine's eruptions between late March and late August 1986 sent scores of pyroclastic flows down its north and northeast flanks. Some early pumiceous pyroclastic flows melted snow to transform into watery floods that left small bars of gravel and lags of boulders or graded down gullies into lahars. An andesite lava dome extruding near the summit incorporated the 1976 dome (fig. 17) (Yount and others, 1987; Swanson and Kienle, 1988). As the new dome grew between late April and late August, parts of it repeatedly collapsed to form small billowing pyroclastic flows that smeared coarse andesite rubble down the north and northeast flanks.

2006 Eruption

The 2006 eruption spewed small flows onto all flanks except the west (Vallance and others, this volume). On January 28, 2006, a pyroclastic flow of dense pumice swept down to the lower north flank and filled the shallow pond there. In winter 2006, a dome grew at the summit, filling the subsummit moat north of the 1986 dome and covering that dome and draping new stiff lava flows down the upper north and northeast flank. These and small lithic pyroclastic flows spalling from the lava flows expanded until the end of March 2006. Simplified here as figure 5, Waitt and Begét's (2009, plate 1) geologic map is as plotted before the 2006 eruption.

High-Energy Flows from an Island

Pyroclastic Density Current

Hot pyroclastic density currents (flows and surges) can move at 280 km/hr and cross water. Surges crossed water lethally during 1902 eruptions of Mont Pelée and La Soufrière and during 1911 and 1965 eruptions at Taal in the Philippines (Anderson and Flett, 1903; Moore and others, 1966; Blong, 1984; Scarth, 2002). Many ashy flows and surges of the last 2,200 years lie at Augustine's coast. Clearly they sweep into the sea from time to time.

Figure 17. View southward of 1986 dome and lava-flow tongue at its base. Photograph mid-July 1986 by Jürgen Kienle, University of Alaska Geophysical Institute.

A landslide taking a volcano's summit will depressurize intruding magma and hot groundwater. These can explode as at Mount St. Helens in May 1980 when the fountaining gas-rock mixture collapsed into a ground-hugging hot surge (Waitt, 1981). But of Augustine's 12 debris avalanches in the past 2,300 years, only West Island about 370 yr B.P. clearly includes a large ground surge.

Debris Avalanche

Augustine's many hummocky boulder diamicts around its coasts originated as debris avalanches from collapsing summit domes. Bulk volume of Burr Point avalanche beyond the former coast is about 0.25 km^3 and of West Island avalanche about 0.4 km^3. On southwest West Island, the planed-off hummocks and lag boulders record a great sweep of avalanche-displaced seawater. The mud slabs with marine shells draping hummocks at Burr Point show that the 1883 avalanche also crashed into the sea violently. Many earlier Augustine avalanches of similar volumes rode far seaward, indicating their high speed into seawater.

Tsunami

At least twelve debris avalanches off Mount Augustine in the past 2,300 years entered the sea, that in 1883 (Burr Point) generating witnessed tsunami. Many historical debris avalanches off alpine mountains or volcanoes have run into water fast enough to generate large waves on distant shorelines (Waitt and Begét, 2009, table 4). Augustine Island gives evidence that two of its debris avalanches initiated tsunami: West Island about 370 yr B.P. and Burr Point in 1883.

The shores of lower Cook Inlet bear sporadic and sparse evidence of tsunami. On the mainland north-northeast of Augustine, sand 2 m above high tide bearing beach cobbles and logs overlies 300-yr-B.P. Iliamna eruptive deposits, and trees rooted deeper show a tree-ring perturbation at A.D. 1883 (fig. 1*A*) (Anders and Begét, 1999). An apparent 1883 tsunami deposit crops out 1½ m above spring high tide on the sand spit that guards Nanwalek (English Bay) harbor. Overlying a brown soil, sand containing beach pebbles and cobbles washed upslope (fig. 18). Gray ash atop the pebbles is surely the ashfall from Augustine in October 1883 of the contemporary accounts. This is capped by the white Katmai ash of 1912 (Begét and Kowalik, 2006, fig. 5; Begét and others, 2008; Waitt and Begét, 2009).

Possible prehistoric tsunami deposits—beds of sand bearing rounded cobbles—lie within thick peat beds 5 m above high tide near Nanwalek and Seldovia (Begét and others, 2008). Enclosing peat dating to 1,620–1,650 yr B.P. approximately coincides with Augustine's Northeast Point debris avalanche (fig. 5; table 1). A likely tsunami deposit

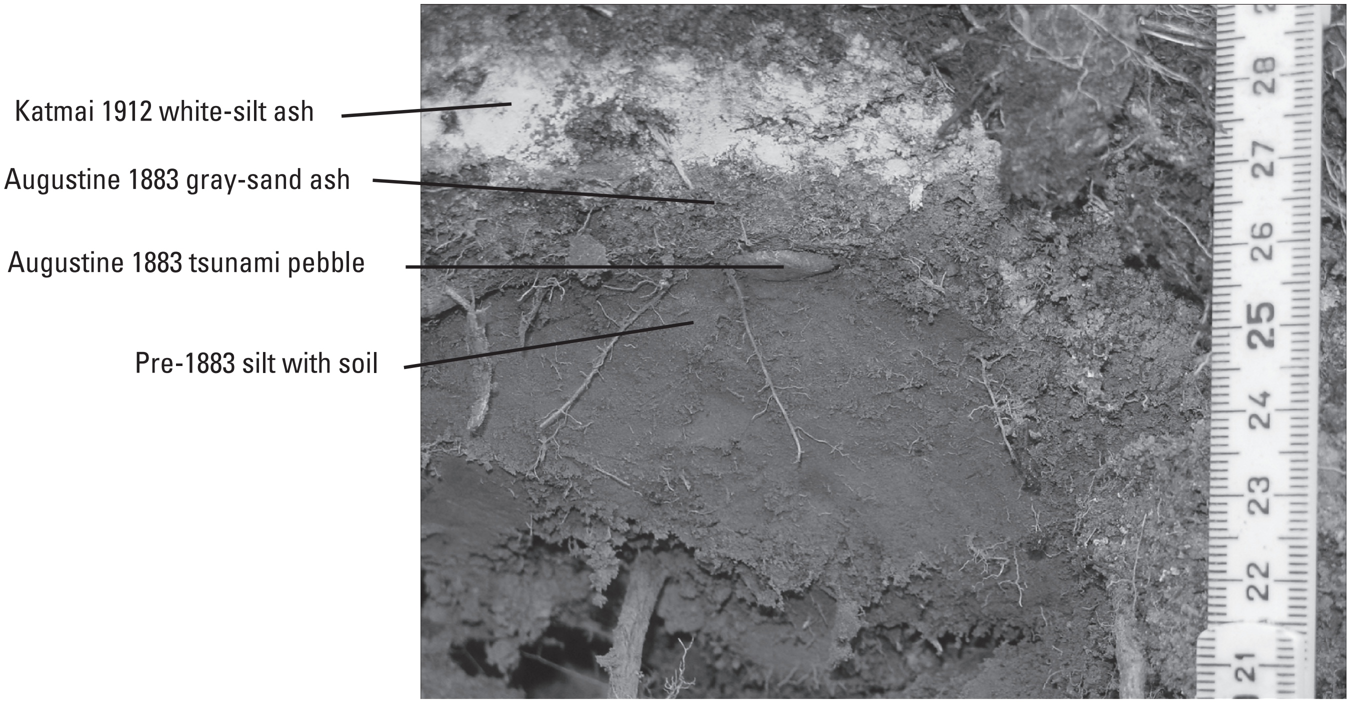

Figure 18. View of 1883 tsumani and ashfall deposits near Nanwalek (in 1883 English Bay). Overlying a brown soil are beach pebbles transported up to 1.5 meters above high-tide level, evidently by tsunami on October 6, 1883. Above the pebbles lies 1.5 cm of fine-sand ash, evidently of 1883 ashfall deposited October 6–7, 1883. Overying that is Katmai 1912 white-silt ash. Scale numbered in centimeters. Photograph by J.E. Begét, University of Alaska, Fairbanks. Begét and Kowalik (2006, fig. 5) show a different view of this stratigraphy.

lies at Point Bede on lower Kenai Peninsula (fig. 1*A*)—angular large boulders thrown 5–10 m back from a seacliff 1 to 2 m above high tide. Atop the boulders and beneath Katmai 1912 ash lie 2–4 sand-silt ashes, showing the boulders were cast up several centuries ago.

Summary

Augustine began erupting before or during the late Wisconsin. Several south-flank exposures reveal sporadic middle to late Holocene eruptions of pumiceous flows and coarse pumiceous tephra. Between 2,200 and 390 B.P., six eruptions deposited coarse-pumice tephra, an average one every 300–360 yr. Countless smaller eruptions deposited many thinner and finer ash layers.

The dominant style over time seems to be growth of steep summit domes, eventually truncated by collapse into a debris avalanche—one every 180–200 years average. Eruptions of coarse pumiceous tephra and significant pyroclastic flows average once every three centuries or so.

Augustine's late Holocene debris avalanches are many, but an attending Mount St. Helens-like surge seems rare. A surge deposit does overlie bits of West Island avalanche. Whether most debris avalanches came during or between eruptions is unclear. That some avalanches contain prismatically jointed andesite reveals hot rock in the summit dome at the time. But in only a few of the documented stratigraphic sections does a coarse tephra immediately overlie a debris avalanche. Spotty tephra G overlies nearly directly the uppermost of the East Point avalanches, tephra I overlies Southeast Point avalanche (fig. 9), and tephra C immediately overlies South Point avalanche. These suggest but by do not prove that the decapitations of the summit dome uncorked substantial eruptions. Apparently the 1883 avalanche immediately preceded eruptions of sand-sized tephra. An 1883-like avalanche was a worry just before the 2006 eruption. But no serious swelling appeared like that preceding the May 1980 landslide off Mount St. Helens.

The seven historical eruptions between 1812 and 2006 have yielded no tephras comparable to the six thick and coarse prehistoric pumiceous ones. Pumiceous flows on the north flank in the 1976 and 1986 eruptions did build fans as thick as some of those in prehistoric eruptions on other flanks.

The waves as high as 6 or 7 m at English Bay in October 1883 originated when a moderate-volume avalanche swept into the shallow sea. Augustine's summit has since grown back wider and taller than it was just before that slide. The 1883 avalanche occurred during a falling low tide in a sparsely populated region. Were a large debris avalanche off Augustine to plunge into the sea during intermediate or high tide, consequent tsunami in coastal areas of lower Cook Inlet would likely be larger and far more damaging.

References Cited

Alaska Commercial Company, 1883 [unpublished], Record Books for English Bay Station: Fairbanks, University of Alaska library Archives, Box 10 (May 15, 1883–July 1884).

Anders, A.M., and Begét, J.E., 1999, Giant landslides and coeval tsunamis in lower Cook Inlet, Alaska [abs.]: Geological Society of America Abstracts with Programs, v. 31, no. 7, p. A48

Anderson, T., and Flett, 1903, Report on the eruptions of the Soufrière in St. Vincent, and on a visit to Montagne Pelée in Martinique: Philosophical Transactions of the Royal Sociey of London, Ser. A, v. 200, p. 353–553.

Beaglehole, J.C., ed., 1967, The voyage of the *Resolution* and *Discovery* 1776–1780—The Journals of Captain James Cook on his Voyages of Discovery: Hakluyt Society, Cambridge University Press, 718 p.

Becker, G.F., 1898, Reconnaissance of the gold fields of southern Alaska, with some notes on general geology: U.S. Geological Survey 18th Annual Report, pt. 3, p. 28–58.

Begét, J.E., and Kienle, J., 1992, Cyclic formation of debris avalanches at Mount St. Augustine volcano: Nature, v. 356, p. 701–704.

Begét, J.E., and Kowalik, 2006, Confirmation and calibration of computer modeling of tsunamis produced by Augustine Volcano, Alaska: Science of Tsunami Hazards, v. 24, p. 257–266.

Begét, J.E., Gardner, C.A., and Davis, K., 2008, Volcanic tsunamis and prehistoric cultural transitions in Cook Inlet, Alaska: Journal of Volcanology and Geothermal Research, v. 176, p. 377–386.

Blong, R.J., 1984, Volcanic hazards—a sourcebook on the effects of eruptions: Sydney, Academic Press, 424 p.

Coombs, M.L., Bull, K.F., Vallance, J.W., Schneider, D.J., Thoms, E.E., Wessels, R.L., and McGimsey, R.G., 2010, Timing, distribution, and volume of proximal products of the 2006 eruption of Augustine Volcano, *in* Power, J.A., Coombs, M.L., and Freymueller, J.T., eds., The 2006 eruption of Augustine Volcano, Alaska: U.S. Geological Survey Professional Paper 1769 (this volume).

Daley, E.E., 1986, Petrology, geochemistry, and the evolution of magmas from Augustine volcano, Alaska: Fairbanks, University of Alaska, M.S. thesis, 69 p.

Davidson, G., 1884, Notes on the eruption of Mount St. Augustine, Alaska, October 6, 1883: Science, v. 3, no. 54, p. 186–189.

Detterman, R.L., 1968, Recent volcanic activity on Augustine Island, Alaska: U.S. Geological Survey Professional Paper 600-C, p. 126–129.

Detterman, R.L., and Hartsock, J.K., 1966, Geology of the Iniskin-Tuxedni region, Alaska: U.S. Geological Survey Professional Paper 512, 78 p. and geologic map, scale 1:63,360.

Detterman, R.L., and Jones, D.L., 1974, Mesozoic fossils from Augustine Island, Cook Inlet, Alaska: American Association of Petroleum Geologists Bulletin, v. 58, p. 868–870.

Doroshin, Petr, 1870, Some volcanoes, their eruptions, and earthquakes in the former Russian holdings in America: Verhandlungen der Russisch-Kaiserlichen Mineralogischen Gesellschaft zu St. Petersburg, Zweite Serie, Fünfter Rand, p. 25–44 (in Russian).

Glicken, H., 1996, Rockslide–debris avalanche of May 18, 1980, Mount St. Helens volcano, Washington: U.S. Geological Survey Open-File Report 96-677, 90 p.

Glicken, H., 1998, Rockslide–debris avalanche of May 18, 1980, Mount St. Helens volcano, Washington: Bulletin of the Geological Survey of Japan, v. 49, p. 55–106 and 10 map plates.

Hamilton, T.D., and Thorson, R.M., 1983, The Cordilleran ice sheet in Alaska, *in* Porter, S.C., ed., vol. 1, The late Pleistocene, *in* Wright, H.E., Jr., ed., Late Quaternary environments of the United States: Minneapolis, University of Minnesota Press, p. 38–52.

Johnston, D.A., 1978, Volatiles, magma mixing, and the mechanism of eruption of Augustine volcano, Alaska: Seattle, University of Washington, Ph.D. dissertation, 177 p.

Jones, D.L., and Clark, S.H.B., 1973, Upper Cretaceous (Maestrichtian) fossils from the Kenai-Chugach Mountains, Kodiak and Shumagin Islands, southern Alaska: U.S. Geological Survey Journal of Research, v. 1, 125–136.

Kamata, H., Johnson, D.A., and Waitt, R.B., 1991, Stratigraphy, chronology, and character of the 1976 pyroclastic eruption of Augustine volcano, Alaska: Bulletin of Volcanology, v. 53, p. 407–419.

Kienle, J. and Shaw, G.E., 1979, Plume dynamics, thermal energy, and long-distance transport of vulcanian eruption clouds from Augustine volcano, Alaska: Journal of Volcanology and Geothermal Research, v. 6, p. 139–164.

Kienle, J., and Swanson, S.E., 1983, Volcanism in the eastern Aleutian arc—late Quaternary and Holocene centers, tectonic setting and petrology: Journal of Volcanology and Geothermal Research, v. 17, p. 393–432.

Kienle, J., and Swanson, S.E., 1985, Volcanic hazards from future eruptions of Augustine volcano, Alaska: Fairbanks, University of Alaska Geophysical Institute, document R-275, 126 p. and map.

Lamb, W.K., ed., 1984, George Vancouver, A Voyage of Discovery to the North Pacific Ocean and round the world 1791–1795, v. 4: London, Hakluyt Society, no. 166.

Lander, J.F., 1996, Alaskan tsunamis 1737–1996: National Oceanographic and Atmospheric Administration (NOAA), National Geophysical Data Center (Boulder, Colo.), Geophysical Research Document 31, 195 p.

Larsen, J.F. Nye, C.J., Coombs, M.L., Tilman, M., Izbekov, P., and Cameron, C., 2010, Petrology and geochemistry of the 2006 eruption of Augustine Volcano, *in* Power, J.A., Coombs, M.L., and Freymueller, J.T., eds., The 2006 eruption of Augustine Volcano, Alaska: U.S. Geological Survey Professional Paper 1769 (this volume).

LeBas, M.J., and Streckeisen, R.W., 1991, The IUGS systematics of igneous rocks: Journal of the Geological Society of London, v. 148, p. 825–833.

Magoon, L.B., Adkison, W.L., and Egbert, R.M., 1976, Map showing geology, wildcat wells, Tertiary plant fossil localities, K-Ar age dates, and petroleum operations, Cook Inlet area, Alaska: U.S. Geological Survey Miscellaneous Investigations Series Map I-1019.

Moore, J.G., Kazuaki, N., and Alcaraz, A., 1966, The 1965 eruption of Taal volcano: Science, v. 151, p. 955–960.

Riehle, J.R., Waitt, R.B., Meyer, C.E., and Calk, L.C., 1998, Age of formation of Kaguyak Caldera, eastern Aleutian arc, Alaska, estimated by tephrochronology: U.S. Geological Survey Professional Paper 1595, p. 161–168.

Roman, D.C., Cashman, C.V., Gardner, C.A., Wallace, P.J., and Donovan, J.J., 2006, Storage and interaction of compositionally heterogeneous magmas from the 1986 eruption of Augustine Volcano, Alaska: Bulletin of Volcanology, v. 68, p. 240–254.

Scarth, A., 2002, La Catastrophe—the eruption of Mount Pelée, the worst volcanic disaster of the 20th century: Oxford University Press, 246 p.

Siebert, L., Glicken, H., and Kienle, J., 1989, Debris avalanches and lateral blasts at Mount St. Augustine volcano, Alaska: National Geographic Review, v. 5, p. 232–249.

Siebert, L., Begét, J.E., and Glicken, H., 1995, The 1883 and late-prehistoric eruptions of Augustine volcano, Alaska: Journal of Volcanology and Geothermal Research, v. 66, p. 367–395.

Swanson, S.E., and Kienle, J., 1988, The 1986 eruption of Mount St. Augustine—field test of a hazard evaluation: Journal of Geophysical Research, v. 93, p. 4500–4520.

Vallance, J.W., Bull, K.F., and Coombs, M.L., 2010, Pyroclastic flows, lahars, and mixed avalanches generated during the 2006 eruption of Augustine Volcano, *in* Power, J.A., Coombs, M.L., and Freymueller, J.T., eds., The 2006 eruption of Augustine Volcano, Alaska: U.S. Geological Survey Professional Paper 1769 (this volume).

Voight, B., Janda, R.J., Glicken, H., and Douglass, P.M., 1983, Nature and mechanics of the Mount St. Helens rockslide avalanche of 18 May 1980: Geotechnique, v. 33, p. 243–273.

Waitt, R.B., 1981, Devasting pyroclastic density flow and attendant air fall of May 18—stratigraphy and sedimentology of deposits, *in* Lipman, P.W., and Mullineaux, D.R., eds., The 1980 eruptions of Mount St. Helens, Washington: U.S. Geological Survey Professional Paper 1250, p. 439–458.

Waitt, R.B., and Begét, J.E., with contributions by Juergen Kienle, 1996, Provisional geologic map of Augustine Volcano, Alaska: U.S. Geological Survey Open-File Report 96-516, 44 p., map scale 1:25,000.

Waitt, R.B., and Begét, J.E., 2009, Volcanic processes and geology of Augustine Volcano, Alaska: U.S. Geological Survey Professional Paper 1762, 78 p. and 2 map plates.

Yount, M.E., Miller, T.P., and Gamble, B.M., 1987, The 1986 eruptions of Augustine Volcano, Alaska—hazards and effects: U.S. Geological Survey Circular 998, p. 4–13.

The 2006 Eruption of Augustine Volcano, Alaska
Power, J.A., Coombs, M.L., and Freymueller, J.T., editors
U.S. Geological Survey Professional Paper 1769

Chapter 14

Preliminary Slope-Stability Analysis of Augustine Volcano

By Mark E. Reid[1], Dianne L. Brien[1], and Christopher F. Waythomas[2]

Abstract

Augustine Volcano has been a prolific producer of large debris avalanches during the Holocene. Originating as landslides from the steep upper edifice, these avalanches typically slide into the surrounding ocean. At least one debris avalanche that occurred in 1883 during an eruption initiated a far-traveled tsunami. The possible occurrence of another edifice collapse and ensuing tsunami was a concern during the 2006 eruption of Augustine. To aid in hazard assessments, we have evaluated the slope stability of Augustine's edifice, using a quasi-three-dimensional, geotechnically based slope-stability model implemented in the computer program SCOOPS. We analyzed the effects of topography, variations in rock strength, and earthquake-induced strong ground motion on the relative stability of millions of potential large (>0.1 km^3 volume) slope failures throughout the edifice.

Preliminary results from pre-2006 topography provide three insights. First, the predicted stability of all parts of the upper edifice is approximately the same, suggesting an equal likelihood of slope failure, in agreement with geologic observations that debris avalanches have swept all sectors of the volcano. Second, the least stable (by a small amount) sector is on the east flank where a debris avalanche would flow into deeper ocean water and a resulting tsunami would be directed toward the southwestern part of the Kenai Peninsula. Third, most model scenarios predict stable edifice slopes, and only scenarios assuming extensive weak rocks and moderate to strong ground shaking predict potential large collapses. Because other transient triggering mechanisms, such as shallow magma intrusion, may be needed to instigate slope instability, monitoring ground deformation and seismicity could help short-term forecasting of impending edifice failure.

Introduction

Augustine Volcano, an island volcano near the mouth of Cook Inlet, Alaska (fig. 1) composed primarily of multiple lava domes, has produced a remarkable series of large debris avalanches over the past 3,500 years. These debris avalanches, believed to initiate as massive landslides emanating from the flanks or summit of the edifice (Siebert and others, 1989; Begét and Kienle, 1992; Siebert and others, 1995), typically travel into the surrounding ocean (Waythomas and Waitt, 1998; Waythomas and others, 2006). Previous investigators have hypothesized that tsunamis occur when debris avalanches enter the sea during eruptions of the volcano (Kienle and Swanson, 1985; Kienle and others, 1987; Begét and Kienle, 1992; Siebert and others, 1995; Begét and Kowalik, 2006; Begét and others, 2008). A debris avalanche generated during the 1883 eruption of Augustine is believed to have caused a tsunami that struck the village of English Bay (now called Nanwalek), about 80 km east of the volcano (Davidson, 1884; Kienle and others, 1987; Siebert and others, 1995; Lander, 1996). Augustine is one of the most historically active volcanoes in the eastern Aleutian Arc (Simkin and Siebert, 1994; Miller and others, 1998), and its renewed eruptive activity in 2006 prompted concerns about a potential edifice collapse and subsequent tsunami.

During the 2006 eruption of Augustine, we performed a preliminary slope-stability analysis of the upper edifice. Numerous factors can affect the potential instability of volcanic edifices (Voight and Elsworth, 1997), including steep slopes, weakened rocks, strong earthquake shaking, shallow magma intrusion, elevated pore-fluid pressures induced by rain or snowmelt infiltration, or thermal fluid pressurization from intruding magma (Reid, 2004). Most of these factors are poorly known at Augustine as well as at other volcanoes. The 1883 edifice collapse occurred early in an eruption, and geologic evidence indicates the West Island debris avalanche occurred during an earlier eruption about 450 yr B.P., but it is uncertain whether all previous large slope failures were associated with eruptions. Rather than speculate on a myriad of destabilization scenarios, our preliminary analysis focused on two controls that are better known at Augustine: stresses

---

[1] U.S. Geological Survey, 345 Middlefield Road, MS 910, Menlo Park, CA 94025.

[2] Alaska Volcano Observatory, U.S. Geological Survey, 4200 University Drive, Anchorage, AK 99508.

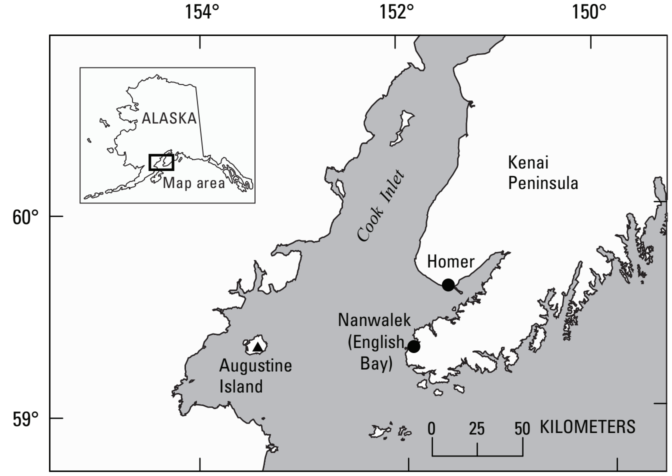

Figure 1. Southern Alaska, showing locations of Augustine Island, Cook Inlet, towns of Homer and Nanwalek (English Bay), and part of the Kenai Peninsula.

induced by topography and transient stresses created by strong ground motion during large earthquakes, in both of which rock strength strongly modulates potential slope instability. We used a quasi-three-dimensional (3D) geotechnical method implemented in the computer program SCOOPS (Reid and others, 2000) to perform our slope-stability assessments. We focused on potentially large (>0.1 km^3 volume) slope failures (landslides) affecting pre-2006 topography.

Herein we present a brief history of past debris avalanches from Augustine Volcano to provide a context for our slope-stability analyses, a short summary of our quasi-3D analytical approach, and the results for six plausible scenarios examining the effects of rock strength and earthquake-induced strong ground shaking at Augustine. Our preliminary analysis for each scenario indicates the relative stability of all parts of the upper edifice, the predicted least stable regions, and the volumes associated with potential slope failures.

History of Debris Avalanches at Augustine Volcano

Geologic studies on Augustine Island have identified and named at least 12 large debris-avalanche deposits on the flanks of the volcano that are younger than about 3,500 years (Waitt and others, 1996; Waitt and Begét, 2009; Waitt, this volume), each of which may have generated a tsunami when it flowed into Cook Inlet (Kienle and others, 1987; Begét and Kienle, 1992). Deposits of the West Island and Burr Point debris avalanches (fig. 2; table 1) possess the hummocky surface morphology, large megaclast blocks, and poorly sorted, fines-poor composition of similar deposits at Mount St. Helens (Siebert, 1984; Glicken, 1991). All of the large debris-avalanche deposits recognized on Augustine Volcano extend to the coast (Waitt and others, 1996; Waitt and Begét, 2009; Waitt, this volume) and typically are well exposed in seabluffs and gullies. Submerged hummocky topography offshore indicates that several of these debris avalanches traveled an additional 4 to 6 km across the sea floor.

Radiocarbon dating of buried soils associated with tephra and debris-avalanche deposits allowed Begét and Kienle (1992), Waitt and others (1996), and Waitt and Begét (2009) to propose a chronology for debris-avalanche formation at Augustine over the past 3,500 years (table 1). Their chronology is based on stratigraphic relations among dated tephra layers that are diagnostic enough in the field that they can be readily identified as stratigraphic markers. The stratigraphic relations of the debris-avalanche deposits to major tephra units can thus be used to establish age control on the debris-avalanche deposits. Other than the 1883 Burr Point deposit, no debris-avalanche deposits at Augustine have been directly dated, and it is unclear how many of these deposits are contemporaneous with major tephra units.

The spatial distribution of debris-avalanche deposits on Augustine Island indicates that debris avalanches have swept all sectors of the island in the past (fig. 2; table 1). At least five debris avalanches have occurred on the north and west flanks of the volcano, five on the east and south flanks, one on the northeast flank, and one on the southwest flank. The three most recent debris avalanches, including the 1883 Burr Point debris avalanche, postdate tephra B (about 478–257 yr B.P.) and have all been directed north-northwestward. Because of the approximately clockwise migration of slope failures around the edifice over the past several thousand years, some researchers have postulated an increased likelihood of future slope failure in the northeast sector (Siebert and Begét, 2006). The youngest debris avalanche on the southeast flank is recorded by the Southeast Beach debris-avalanche deposit (Waitt and Begét, 2009) which predates tephra B and postdates tephra M (about 709–478 yr B.P.).

Generalized physical descriptions of the debris-avalanche deposits at Augustine are presented by Waitt and others (1996) and Waitt and Begét (2009). Most of these deposits are composed of poorly sorted dacitic or andesitic rubble and silt- to boulder-size material. Megaclasts as large as 30 m across occur in some of the deposits; these clasts are intact pieces of former summit domes that were not disaggregated during downslope transport. Some of the clasts exhibit minor hydrothermal alteration, but only the Yellow Cliffs deposit (fig. 2) contains abundant material hydrothermally altered to clay. This debris-avalanche deposit is the only one at Augustine that records a flank collapse associated with pervasive alteration of the edifice.

Estimated volumes of the debris-avalanche deposits vary but most exceed 0.1 km^3. Siebert and others (1995) and Waitt and Begét (2009) estimated volumes for the debris-avalanche deposits on the north and west flanks of the volcano (table 1). The 1883 Burr Point debris-avalanche deposit has

Table 1. Characteristics of large debris-avalanche deposits on Augustine Island.

[Modified from Siebert and others (1995) and Waitt and Begét (2009). Composite stratigraphy includes debris-avalanche deposits and dated tephra deposits. Recalibrated radiocarbon ages (in years) bracketing tephras from Waythomas (2000)]

Composite stratigraphy	Map unit (fig. 2)	Sector of island affected	Volume of deposit (km^3)	Composition
Burr Point (A.D. 1883)	83a	North-northeast	0.25 to 0.3	Andesite, some alteration
Rocky Point	Bar	North	0.15	Andesite
West Island + Grouse Point	Baw, Bag	Northwest	0.3 to 0.5	Andesite, dacite
(257±18) Tephra B (478±27)				
Southeast Beach	MBas	Southeast		Andesite
(478±27) Tephra M (709±23)				
Lagoon	CMal	West		Andesite
(709±23) Tephra C (1,102±22)				
North Bench	IMan	North-northwest		Andesite
Long Beach	HCal	Southwest		Andesite
South Point	HCas	South		Andesite
(1,102±22) Tephra H (1,552±22)				
Northeast Point	IHa	Northeast		Andesite
(1,552±22) Tephra I (1,736±26)				
Southeast Point	GIays	Southeast		Unaltered
Yellow Cliffs	GIays	Southeast		Andesite, extensive alteration
(1,736±26) Tephra G (3,154±25)				
East Point	Ga	East		Andesite, some alteration

an estimated volume of 0.25 to 0.3 km^3; the missing volume of the edifice, resulting in a horseshoe-shaped crater, is about 0.24 km^3. Siebert and others (1995) suggested that multiple marginal levees and three depositional lobes resulted from an edifice failure which occurred in a retrogressive, closely timed process. The adjacent and underlying Rocky Point debris-avalanche deposit, which is only part exposed, has an estimated volume of 0.15 km^3, including its submarine extent. One of the largest edifice-failure events created the West Island debris-avalanche deposit, which has an approximate volume of 0.5 km^3. Older debris-avalanche deposits elsewhere on the island have patchy subaerial exposure, and most of them have submarine extents; volume estimates for these deposits are unavailable but probably range from 0.25 to 0.5 km^3.

Slope-Stability-Analysis Approach

To assess the future potential slope instability at Augustine Volcano, we use a quasi-3D, “method of columns” limit-equilibrium analysis that quantifies slope stability for different scenarios. Previously, we used this geotechnical approach to analyze the edifice stability at Mount St. Helens and Mount Rainier in Washington State (Reid and others, 2000; Reid and others, 2001) and at Volcán Casita in Nicaragua (Vallance and others, 2004), as well as on coastal bluffs in Seattle, Wash. (Brien and Reid, 2007). Our approach systematically searches the topography as defined by a digital elevation model (DEM) and computes the stability of millions of potential landslides affecting all parts of an edifice; these potential slope failures can encompass a wide range of depths and volumes. After this search is complete, every DEM gridpoint of interest will have been included in some potential landslides. The analysis results in maps portraying the relative stability of all parts of the edifice, the location of the overall least stable potential landslide, and the volumes of potential landslides. Our approach, implemented in the computer program SCOOPS, was detailed by Reid and others (2000) and is briefly described below.

At Augustine Volcano, we are interested in assessing the potential for massive flank collapse in places where the internal structure of the edifice is poorly known. For our analysis, we assumed arcuate potential failure surfaces. Although smaller rock failures are commonly controlled by local discontinuities, such as bedding or jointing surfaces, most large edifice collapses extend deep into the edifice, ignore smaller rock discontinuities, and create arcuate failure surfaces (Siebert, 1984; Voight and Elsworth, 1997). Potential failure surfaces composed of sections of a sphere represent the simplest 3D arcuate geometry unconstrained by internal discontinuities. We did not explicitly analyze the potential effects of internal discontinuities.

Each potential failure mass that we analyzed consists of a group of 3D vertical columns, as defined by the DEM, with a spherical failure surface at depth. Our method, which uses a 3D extension of Bishop’s simplified method for two-dimensional rotational failure (Bishop, 1955), can incorporate variable 3D rock properties, 3D pore-fluid-pressure distributions, and simplistic earthquake-shaking effects. The shear resistance of each potential failure mass is given by the

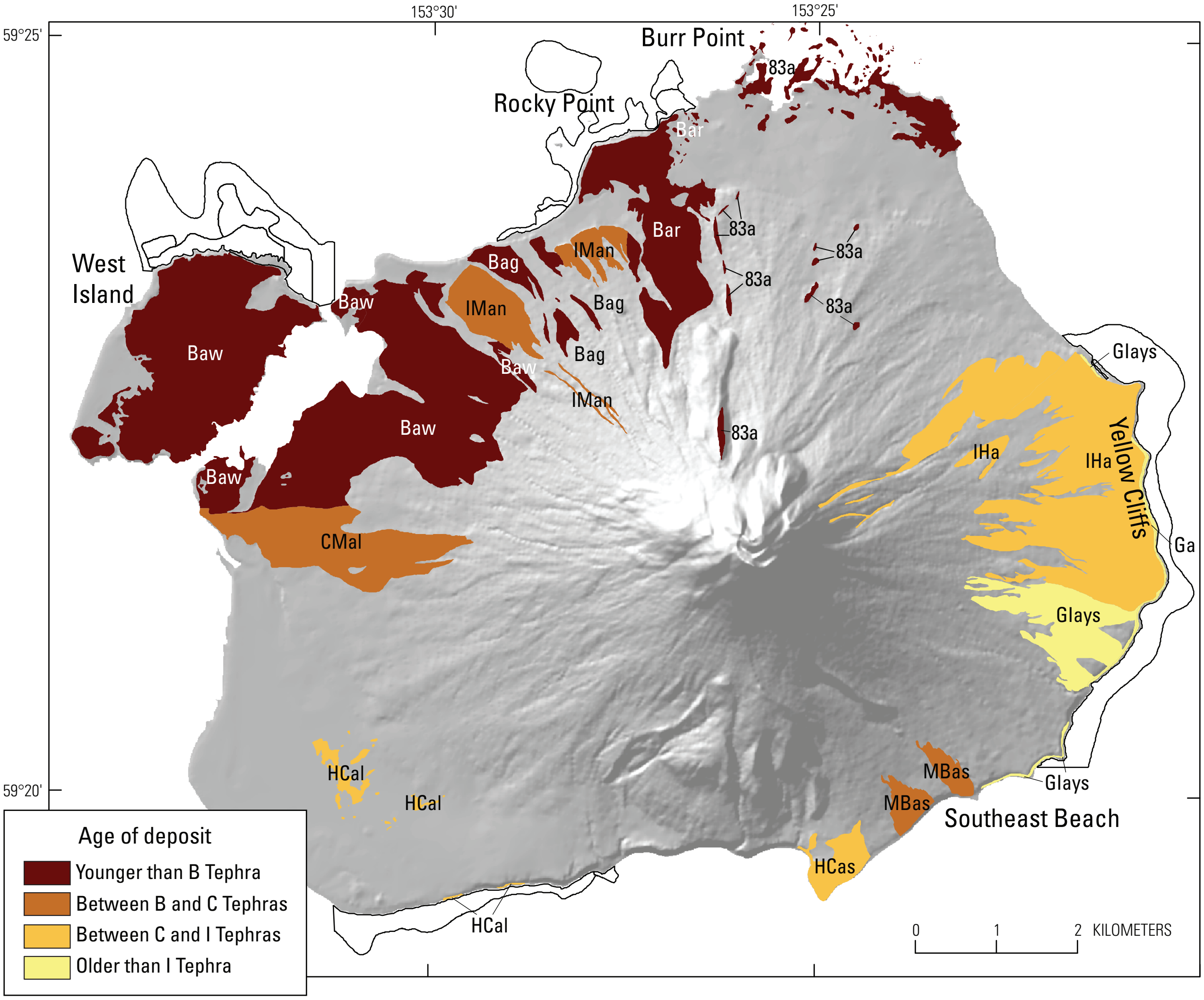

Figure 2. Augustine Island, showing distribution of large debris-avalanche deposits, grouped by age of separating tephra layers. Debris-avalanche unit names and mapped extent from Waitt and Begét (2009). Outlined areas nearshore show extent of some avalanche deposits. Debris-avalanche stratigraphy and tephra ages are listed in table 1. Except for Burr Point, local geographic names (for example, West Island, Rocky Point, Yellow Cliffs, and Southeast Beach) are informal. Shaded-relief image derived from U.S. Geological Survey 10-m digital elevation model (DEM) (unpub. data, 1990).

Coulomb-Terzaghi failure rule, $\tau = c + (\sigma_n - u)\tan\phi$, where c is the cohesion, σ_n is the total normal stress acting on the failure surface (a function of overlying rock weight), u is the pore-fluid pressure on the failure surface, and ϕ is the angle of internal friction. We compute a factor of safety, F, for each potential failure mass, using vertical-force equilibrium and rotational-moment equilibrium, as described by Reid and others (2000). Instability is reflected in F values <1.0; low F values indicate a propensity for collapse. This analysis accounts for the vertical stresses induced by topography and rock weight. We track the minimum F value affecting each DEM point and aggregate the results to produce factor-of-safety maps, as well as associated landslide volumes. If desired, destabilizing earthquake shaking can be incorporated as a pseudostatic horizontal force. Following the approach of Hungr (1987), this force is applied to the base of each vertical column in the potential failure mass (Reid and others, 2000).

Scenarios Analyzed for Augustine Volcano

For our preliminary slope-stability analysis, we need estimates of topography, rock properties (strengths and unit weights), and potential earthquake shaking. A water table at high elevations within the edifice could be destabilizing; such a condition appeared to facilitate the 1980 collapse of Mount St. Helens (Voight and others, 1983). However, little is known about groundwater conditions at Augustine. Given fractured, permeable rocks in a generic edifice, groundwater-flow modeling suggests that an elevated water table is unlikely (Hurwitz and others, 2003), although localized perched groundwater or fluids in cracks could contribute to future edifice instability. Here, we ignore the possible effects of shallow magma intrusion or elevated pore-fluid pressures. We are interested in larger edifice failures and therefore analyze the stability of potential failures only of volumes from 0.1 to 1.0 km^3.

The pre-2006 topography of Augustine Island is well known, defined by a 10-m DEM derived from a 1:25,000-scale map (U.S. Geological Survey, unpub. data, 1990). A shaded-relief image of this DEM portraying local slope at each DEM node is shown in figure 3. Topographic modifications caused by the 2006 eruption had a relatively minor effect on the overall edifice geometry (fig. 4) and would likely have only minor effects on our analysis. Because we calculate the slope stability of massive failures encompassing large parts of the edifice, we resampled the DEM at a 50-m grid spacing for computational efficiency. For accurate estimates of *F* value and volume, about 100 DEM columns are needed to define each potential failure mass. Our resampled DEM spacing provides about 400 columns within potential failure masses near the low end of our desired volume range (0.1 km^3). Our search region for slope-stability analysis is limited to steeper sides of the volcanic edifice. Within this search region, we analyze the stability of millions of potential failure masses for each scenario.

A primary control on slope stability is shear strength. Rock properties, such as strength and unit weight, can vary drastically both spatially and temporally within a volcanic edifice. Fresh massive lava flows may be mechanically strong whereas air-fall deposits may be weak; even visually similar rock types may have spatially varying mechanical properties. Progressive acid sulfate-argillic hydrothermal alteration can weaken rocks over time, possibly promoting slope instability (Lopez and Williams, 1993; Watters and others, 2000; Reid and others, 2001).

The upper, steep part of Augustine Volcano is composed primarily of fresh andesite and dacite lava domes (fig. 4) with little or no visible hydrothermal alteration (Waitt and others, 1996; Waitt and Begét, 2009). Visual inspection by the

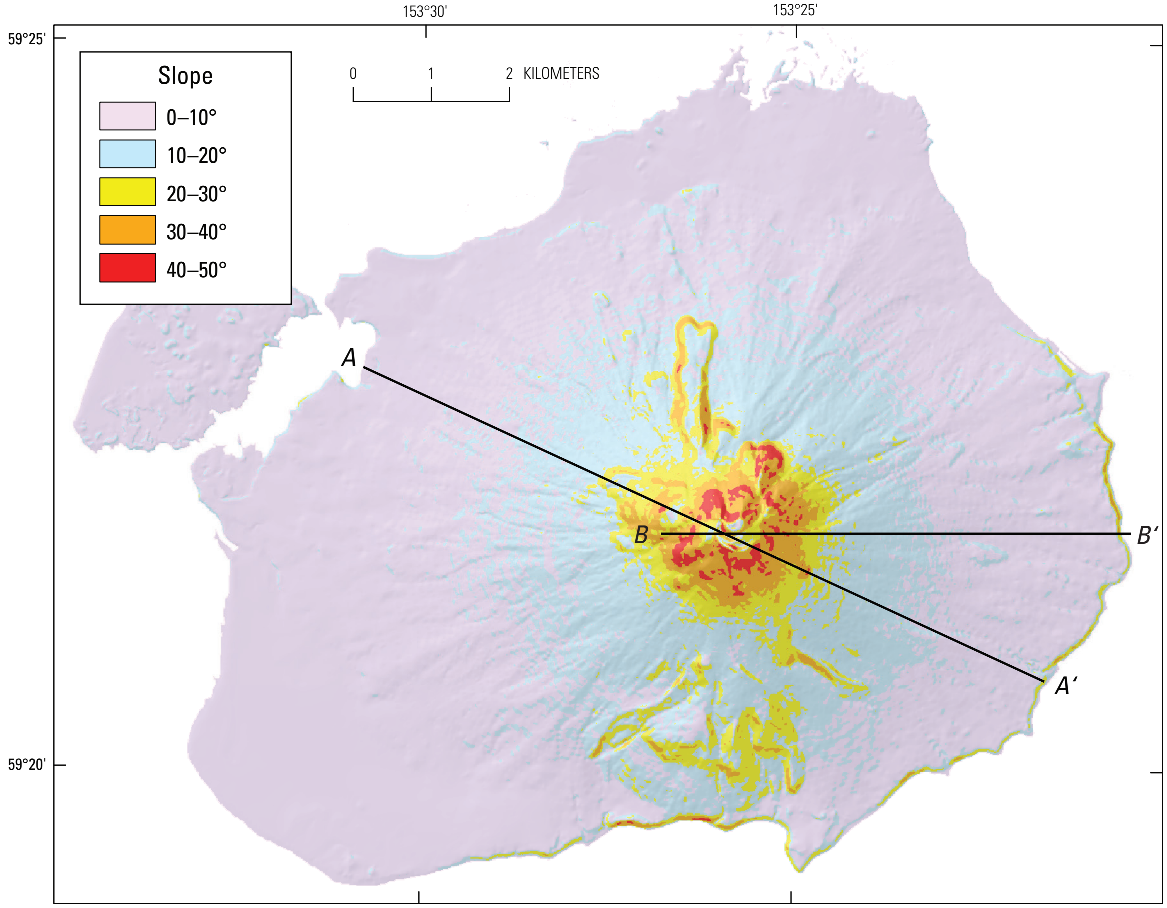

Figure 3. Augustine Island, showing slopes derived from unpublished U.S. Geological Survey (USGS) 10-m digital elevation model (DEM). Steepest slopes occur on upper edifice. Lines *A–A'* and *B–B'*, locations of cross sections in figures 4 and 7. Shaded-relief image derived from U.S. Geological Survey 10-m digital elevation model (DEM) (unpub. data, 1990).

first author of the upper domes in 1997 also revealed only localized alteration at fumaroles. Thus, the carapace of the modern Augustine edifice appears to lack widespread acid sulfate alteration. This style of alteration, present at Mount Rainier (Finn and others, 2001), can weaken rocks (Watters and others, 2000) and significantly reduce slope stability (Reid and others, 2001). The upper Augustine edifice, composed primarily of fresh dome rocks, is more nearly uniform than in the notable layering at some other stratovolcanoes. Although nearly all the debris-avalanche deposits derived from the Augustine edifice contain little altered rock, the Yellow Cliffs deposit does contain hydrothermally altered clay. Thus, more altered rocks may be present at depth within the edifice.

For our preliminary slope-stability analysis, we use two end-member scenarios, assuming uniform shear strength (defined by internal angle of friction and cohesion) and unit weight (table 2), representing strong rocks and relatively weak altered rocks. No direct measurements of strength or unit weight are known for Augustine Volcano dome rocks. Cohesion can play a crucial role in defining the volume and depth of a slope failure (Reid and others, 2000), but estimating the cohesion of rocks at depth within an edifice is difficult. Solid, dense igneous rocks can have a cohesion of 10,000 to 100,000 kPa, but highly altered rocks only 10 kPa. Using either surface-rock exposures or debris-avalanche deposits from volcanoes, other researchers have obtained a few measurements of cohesion and internal angle of friction, including at Mount St. Helens (Voight and others, 1983), Mounts Rainier and Hood (Watters and others, 2000), and Citlaltépetl (Zimbelman and others, 2004). We used these published strength values from volcanoes, as well as values determined for other igneous rocks (Jaeger and Cook, 1979; Hoek and Bray, 1981), to constrain our estimates of shear strength. Our end-member scenarios likely bracket values within the Augustine edifice, although Augustine dome rocks probably have properties closer to those of strong rocks (table 2). Rock properties likely vary within the Augustine edifice. Nevertheless, these end members illustrate the possible effects on slope instability.

Finally, we analyzed several scenarios involving large earthquakes. Augustine Island is subject to large tectonic earthquakes with probable ground motions much greater than those of local volcanic or volcano-tectonic origin. Other researchers have estimated probable peak ground accelerations (PGAs) throughout Alaska by combining frequency and magnitude estimates of earthquakes from potential sources with empirical relations for strong-ground-motion attenuation with distance from the source (Wesson and others, 2007). This method estimates strong ground motion for various probabilities of earthquake occurrence. In Alaska, the method takes into account fault sources, such as the Alaska-Aleutian megathrust, and the available seismic record (Wesson and others, 2007). Estimated PGA values are high in much of southern Alaska. From results derived for the Augustine Island region, we selected two PGA values to bracket potential moderate to large earthquakes at Augustine, where a PGA value of 0.35 *g* corresponds to about a 10-percent probability of exceedance in 50 years and a PGA value of 0.5 *g* corresponds to about a 2-percent probability of exceedance in 50 years. As discussed above, these estimated accelerations can be treated as a pseudostatic horizontal force in our analyses. We follow the approach that Voight and others (1983) applied at Mount St. Helens and use the same strength parameters in our ground-shaking scenarios as in our static scenarios. The combination of a static scenario and two ground-shaking scenarios for both strong and weak edifice rocks produces the six scenarios listed in table 2.

Results of Simulations

The minimum stabilities computed by using the program SCOOPS for the six scenarios listed in table 2 are mapped in figure 5, representing the lowest *F* values computed for any potential landslide encompassing each DEM node. Potential landslides with the lowest *F* values are defined as critical failures. The outline of the overall least stable potential landslide (out of about 20 million) computed for each scenario is also shown in figure 5. These results do not necessarily show complete failure masses, except for the overall minimum outlined in black, nor do they indicate that areas with similar *F* values will fail simultaneously. The computed volumes within the target range 0.1 to 1.0 km^3 associated with the least stable

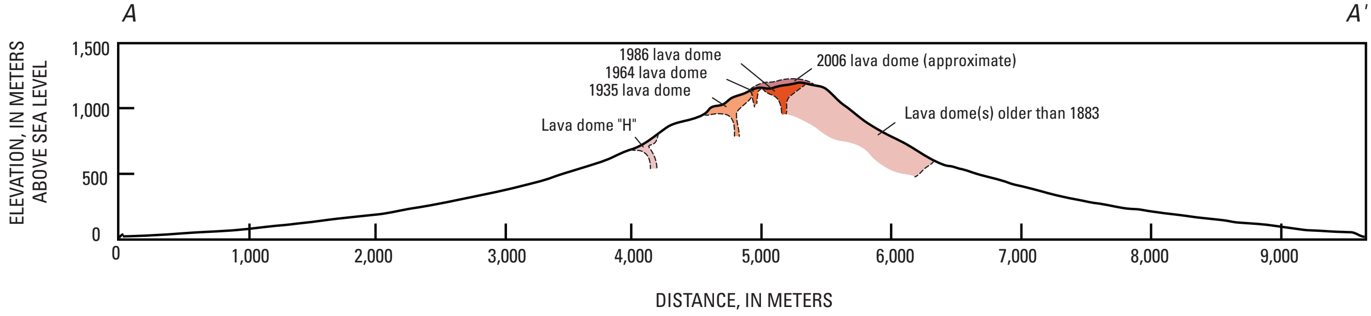

Figure 4. Geologic cross section *A–A′* through Augustine Volcano (see fig. 3 for location), showing dome rocks in upper edifice. Geologic units modified from Waitt and others (1996), with approximate location of 2006 dome added. No vertical exaggeration.

Table 2. Slope-stability scenarios analyzed for Augustine Volcano.

[*F*, factor of safety; PGA, peak ground acceleration]

Scenario	Input				Results	
	Friction angle (°)	Cohesion (kPa)	Unit weight (kN/m³)	Earthquake PGA (*g*)	Minimum *F*	Volume of minimum *F* mass (km³)
1	40	1,000	24	0	2.42	0.13
2	40	1,000	24	0.35	1.35	0.17
3	40	1,000	24	0.5	1.10	0.21
4	28	300	21	0	1.29	0.10
5	28	300	21	0.35	0.71	0.11
6	28	300	21	0.5	0.57	0.11

potential landslide (critical failure) at each DEM node are shown in figure 6. By selecting a point in figure 5, the associated volume can be determined in figure 6.

Variations in potential slope stability induced by differences in rock strength within the Augustine edifice are illustrated in figures 5*A* (uniformly strong rocks) and 5*D* (uniformly weak rocks). These results indicate that (1) a strong-rock edifice has much higher *F* values (min 2.42), whereas a weak-rock edifice has *F* values approaching 1, the limit of stability; (2) the predicted least stable potential landslide is on the upper east flank in both scenarios; and (3) most of the steep upper edifice has *F* values like those of the least stable mass in both scenarios. In these scenarios, potential large landslides have an approximately equal likelihood of initiating from any side of the edifice. Volumes associated with the least stable mass are close to the lower volume limit of 0.1 km^3 in both scenarios (figs. 6*A*, 6*D*).

The potentially destabilizing effects of earthquake ground shaking on the Augustine edifice are illustrated in figures 5*B*, 5*C*, 5*E*, and 5*F*. Given a uniformly strong edifice, moderate ground shaking (PGA value, 0.35 *g*) reduces the *F* value throughout the edifice (fig. 5*B*), but the pattern of stability is similar to that of the non-earthquake scenario (fig. 5*A*). In this scenario, the least stable potential landslide (*F* value, 1.35) is still on the east flank, and most of the upper edifice has similar *F* values. Strong ground shaking (PGA value, 0.5 *g*) further reduces the minimum *F* value almost to 1, and the predicted least stable mass is on the east flank. An interesting effect is shown by the increases in volume and depth associated with the least stable potential landslide (fig. 7; table 2): with strong rocks, the least stable volume increases from 0.13 km^3 with no shaking, through 0.17 km^3 with moderate shaking, to 0.21 km^3 with strong shaking.

Given a uniformly weak edifice, *F* values throughout the edifice also decrease with increasing ground shaking (compare figs. 5*D* through 5*F*). As with the strong-rock scenarios, the overall pattern of *F* values remains similar between scenarios. Much of the upper edifice has similar *F* values, and the least stable potential landslide is on the east flank. However, absolute *F* values are considerably lower, and computed minimum *F* values are well below 1 in both the moderate- and strong-ground shaking scenarios (figs. 5*E*, 5*F*; table 2). A pseudostatic-force analysis using peak ground accelerations often produces lower calculated *F* values; therefore, instability can be exaggerated (Seed, 1973; Chowdhury, 1978). In these weak-rock scenarios, all the computed volumes associated with the least stable potential landslides are close to the lower limit of 0.1 km^3, suggesting that our preset lower volume limit is controlling the predicted sizes of landslides, rather than are edifice geometry and material properties.

Discussion

The results of our simulations of Augustine edifice stability highlight the effects of topography in controlling the location of potential future slope instability. Large-volume failures integrate destabilizing effects over many DEM nodes. Thus, our maps of calculated slope stability (fig. 5) differ somewhat from a map of local slope at the DEM nodes (fig. 3). Large areas of steep local slope occur on the north and northwest flanks of the edifice (fig. 3), whereas our results indicate that the east flank is potentially the least stable. The relatively small north-northwest-facing theater at the current summit does not appear to exert a strong control on the location of potential large edifice failures. Our results also indicate that most of the steep, upper edifice has similar stabilities for a given scenario, as might be expected for a relatively symmetric cone. This result suggests that in the absence of locally destabilizing events, an approximately equal likelihood exists of a future slope failure affecting any sector of the volcano. Such results agree well with the observation that past debris avalanches have inundated all sectors of the island (Begét and Kienle, 1992; Waitt and Begét, 2009).

Most of the scenarios that we evaluated predict a stable edifice. Parts of the edifice are predicted to become unstable only in scenarios that involve extensive weak, possibly hydrothermally altered rocks and moderate to severe ground shaking. Because Augustine rock strengths are likely nearer those

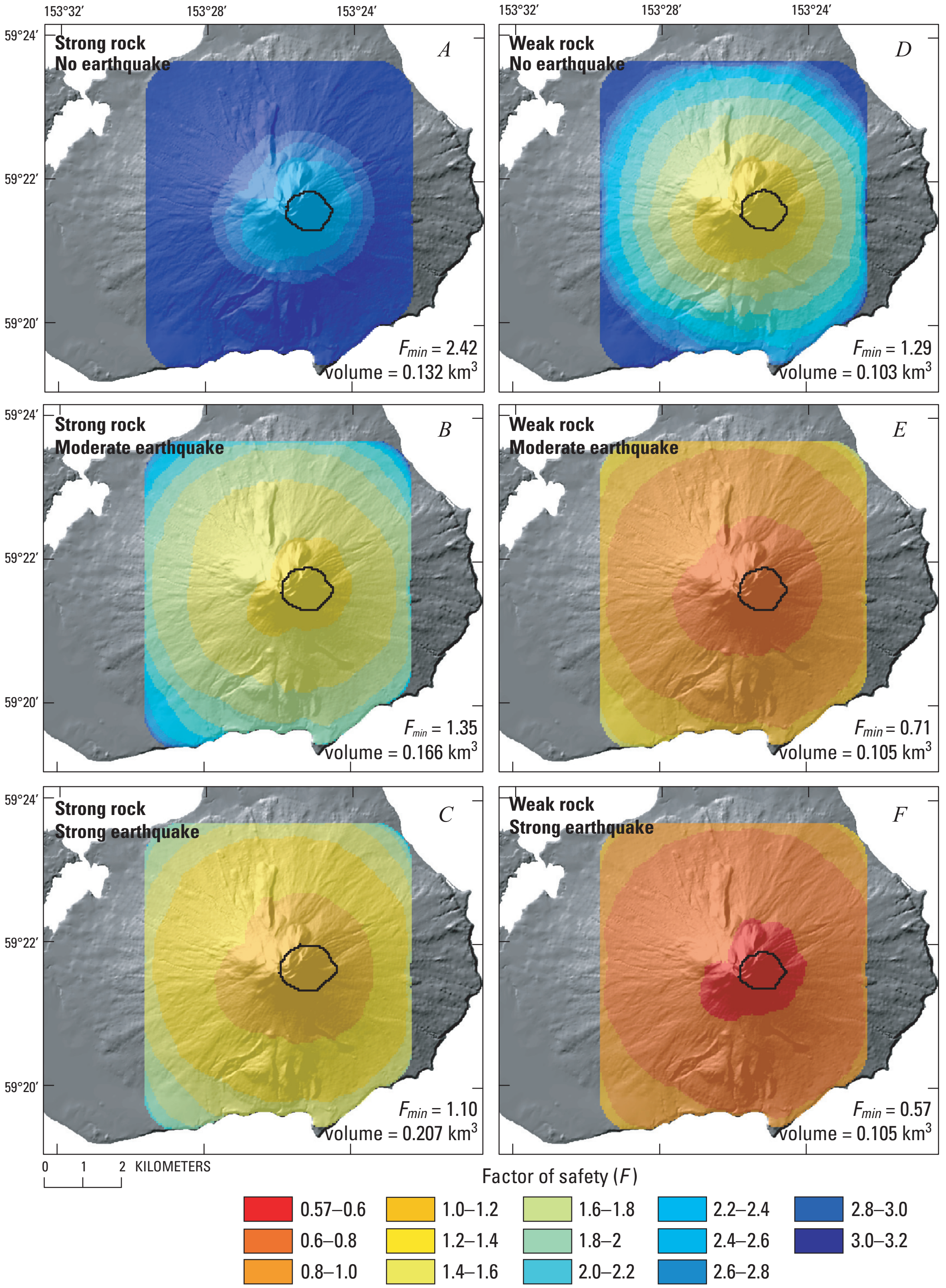

Figure 5. Augustine Volcano, showing computed slope stability of the edifice for six scenarios listed in table 2. Lowest computed factor of safety (*F*) for any potential landslide intersecting each digital elevation model (DEM) node (critical failure) is shown for area searched in our analysis. Warmer colors indicate lower stability; orange and red areas are potentially unstable. Black outline, area of predicted overall least stable potential landslide; minimum factor of safety (F_{min}) and volume associated with this potential landslide are denoted on each diagram. *A*, Scenario 1, with strong rock and no earthquake ground shaking. *B*, Scenario 2, with strong rock and moderate earthquake ground shaking. *C*, Scenario 3, with strong rock and strong earthquake ground shaking. *D*, Scenario 4, with weak rock and no earthquake ground shaking. *E*, Scenario 5, with weak rock and moderate earthquake ground shaking. *F*, Scenario 6, with weak rock and strong earthquake ground shaking. Shaded-relief image derived from U.S. Geological Survey 10-m digital elevation model (DEM) (unpub. data, 1990).

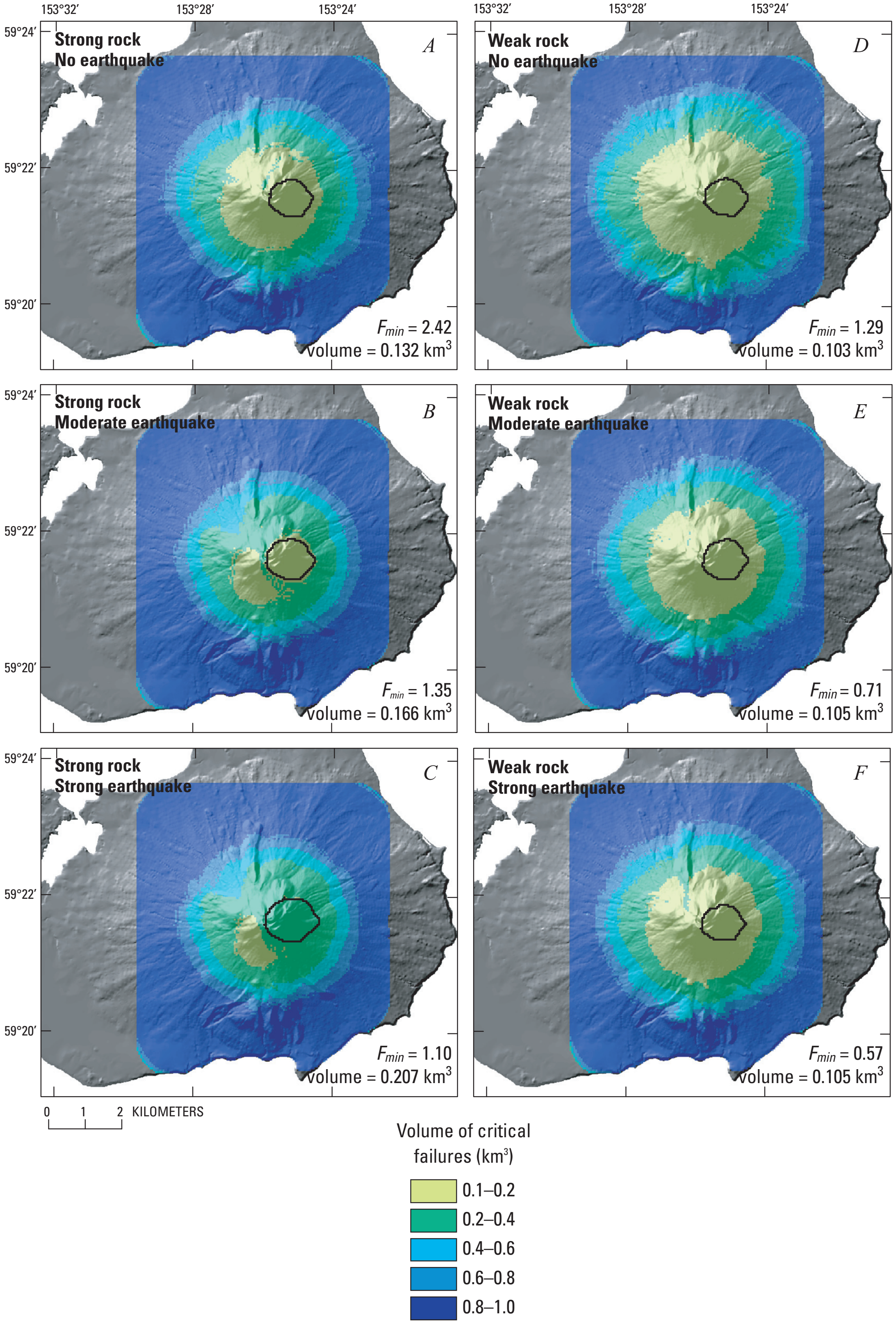

Figure 6. Augustine Volcano, showing potential landslide volumes associated with computed stability of critical failures shown in figure 5. Black outline, area of predicted least stable potential landslide. Six scenarios (*A-F*) shown are summarized in figure 5 and listed in table 2. Shaded-relief image derived from U.S. Geological Survey 10-m digital elevation model (DEM) (unpub. data, 1990). See figure 5 for explanation of abbreviations.

of strong rocks, our results suggest that the edifice is unlikely to undergo a massive landslide triggered solely by gravitational failure or a moderate earthquake. Even in scenarios with pervasive weak rocks, slopes are unlikely to fail by gravity alone (fig. *5D*), implying that additional triggering mechanisms, such as shallow magma intrusion, local oversteepening caused by deformation, and (or) thermal pressurization of pore fluids or gases, are needed to provoke massive collapse at Augustine Volcano.

Although predicted least stable landslide volumes in most of our scenarios are near the lower limit of 0.1 km^3, this analysis does not directly account for retrogressive failure, as occurred at Mount St. Helens in 1980 (Voight and others, 1983; Voight and Elsworth, 1997). At Mount St. Helens, a retrogressive style of collapse increased the failure volume from about 0.8 km^3 for the initial slide block to 2.3 km^3 for all three slide blocks (Voight and others, 1983; Reid and others, 2000). In addition, failed rock masses typically expand as they move downslope. At Mount St. Helens, the volume increased from 2.3 km^3 of source rock to about 2.8 km^3 of debris-avalanche deposit (Voight and others, 1983). At Augustine, both failure retrogression and dilation of debris could enlarge a debris avalanche from its initial failure volume. Stress changes in the subsurface induced by shallow magma intrusion or thermal pressurization could also instigate a larger initial landslide.

A future edifice collapse that produces a debris avalanche with a volume >0.1 km^3 would likely reach the ocean and could generate a tsunami. Our preliminary results suggest that the likelihood of collapse is nearly equal on all sides of the island, although the travel distance from source to coast varies around the island. However, our results indicate that the east flank is marginally less stable. Any avalanche from this flank would travel into deep water, which can enhance the formation of larger tsunamis (Waythomas and others, 2006). A tsunami generated on this side of the island would be directed more toward the southwestern part of the Kenai Peninsula (fig. 1) and the town of Homer (~110 km away) than would a tsunami initiated on the north (as in 1883) or west side of the island.

This preliminary slope-stability analysis focuses primarily on the effects of topography and earthquake shaking. It does not account for spatially varying rock properties within the edifice, the occurrence of such dynamic triggers as shallow magma intrusion or thermal pressurization, or potential retrogression of an initial failure into the edifice. Also, we did not evaluate possible changes in slope stability induced by new lava-dome growth during the 2006 eruption. Nevertheless, our results highlight potential failure locations, given reasonable assumptions about the Augustine edifice. With additional research, rock properties might be better defined, although determining them for rocks at potential failure depth deep within the edifice would be difficult. Possible dynamic triggering events might also be better modeled. Future instability at Augustine Volcano will likely be accompanied by volcanic unrest. Monitoring seismicity and ground deformation should aid in detecting shallow magma movement and may help in short-term forecasting of impending edifice failure.

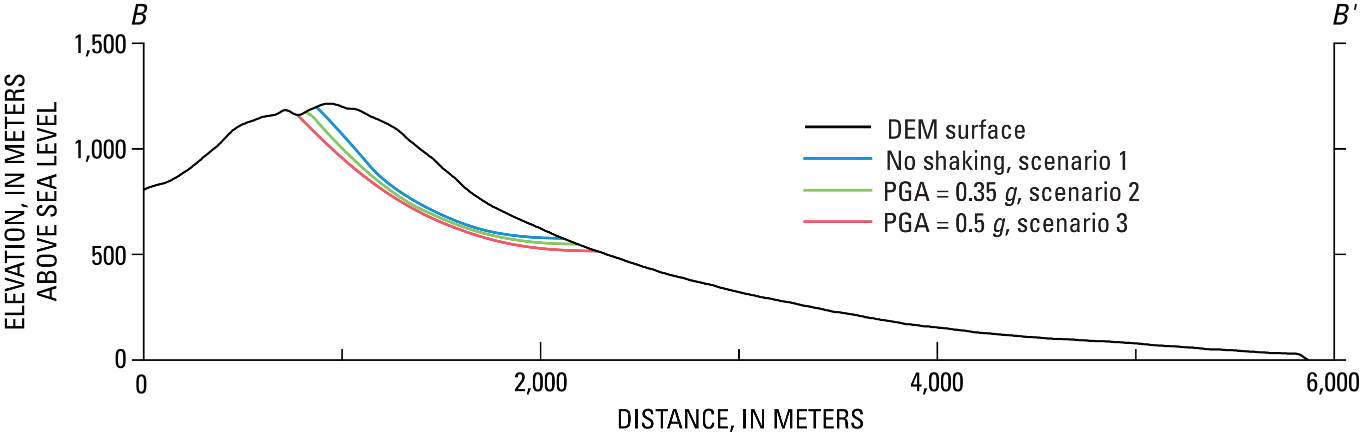

Figure 7. Cross section *B–B′* through Augustine Volcano (see figure 3 for location), showing predicted least stable potential landslide surfaces for scenarios 1 (no earthquake shaking), 2 (moderate ground shaking with peak ground acceleration = 0.35 *g*), and 3 (strong ground shaking with peak ground acceleration = 0.5 *g*), all with strong rocks. Volume of predicted least stable landslide increases with increasing strength of ground shaking (table 2). No vertical exaggeration. DEM, digital elevation model; PGA, peak ground acceleration.

References Cited

Begét, J.E., Gardner, C., and Davis, K., 2008, Volcanic tsunamis and prehistoric cultural transitions in Cook Inlet, Alaska: Journal of Volcanology and Geothermal Research, v. 176, p. 377–386.

Begét, J.E., and Kienle, J., 1992, Cyclic formation of debris avalanches at Mount St. Augustine volcano: Nature, v. 356, no. 6371, p. 701–704.

Begét, J.E., and Kowalik, Z., 2006, Confirmation and calibration of computer modeling of tsunamis produced by Augustine Volcano, Alaska: Science of Tsunami Hazards, v. 24, no. 4, p. 257–266.

Bishop, A.W., 1955, The use of slip circles in the stability analysis of slopes: Geotechnique, v. 5, p. 7–17.

Brien, D.L., and Reid, M.E., 2007, Modeling 3-D slope stability of coastal bluffs using 3-D ground-water flow, southwestern Seattle, Washington: U.S. Geological Survey Scientific Investigations Report 2007-5092, 54 p. [http://pubs.usgs.gov/sir/2007/5092/].

Chowdhury, R.N., 1978, Slope analysis: Amsterdam, Elsevier, v. 22, 423 p.

Davidson, G., 1884, Notes on the volcanic eruption of Mount Saint Augustine, Alaska, October 6, 1883: Science, v. 3, no. 54, p. 186–189.

Finn, C.A., Sisson, T.W., and Deszcz-Pan, M., 2001, Aerogeophysical measurements of collapse-prone hydrothermally altered zones at Mount Rainier volcano: Nature, v. 409, p. 600–603.

Glicken, H., 1991, Sedimentary architecture of large volcanic-debris avalanches, *in* Fisher, R.V., and Smith, G.A., eds., Sedimentation in volcanic settings: Santa Barbara, Calif., Society of Economic Paleontologists and Mineralogists, p. 99–106.

Hoek, E., and Bray, J.W., 1981, Rock slope engineering (3d ed.): London, Institute of Mining and Metallurgy, 358 p.

Hungr, O., 1987, An extension of Bishop's simplified method of slope stability analysis to three dimensions: Geotechnique, v. 37, no. 1, p. 113–117.

Hurwitz, S., Kipp, K.L., Ingebritsen, S.E., and Reid, M.E., 2003, Groundwater flow, heat transport, and water table position within volcanic edifices—Implications for volcanic processes in the Cascade Range: Journal of Geophysical Research, v. 108, no. B12, DOI: 10.1029/2003JB002565.

Jaeger, J.C., and Cook, N.G.W., 1979, Fundamentals of rock mechanics (3d ed.): New York, Chapman and Hall, 593 p.

Kienle, J., Kowalik, Z., and Murty, T.S., 1987, Tsunamis generated by eruptions from Mount St. Augustine volcano, Alaska: Science, v. 236, no. 4807, p. 1442–1447.

Kienle, J., and Swanson, S.E., 1985, Volcanic hazards from future eruptions of Augustine Volcano, Alaska (2d ed.): Fairbanks, University of Alaska, Geophysical Institute Report UAG-R 275, 122 p.

Lander, J.F., 1996, Tsunamis affecting Alaska: Boulder, Colo., U.S. National Oceanic and Atmospheric Administration, National Environmental Satellite Data and Information Service, National Geophysical Data Center, 195 p.

Lopez, D.L., and Williams, S.N., 1993, Catastrophic volcanic collapse; relation to hydrothermal processes: Science, v. 260, no. 5115, p. 1794–1796.

Miller, T.P., McGimsey, R.G., Richter, D.H., Riehle, J.R., Nye, C.J., Yount, M.E., and Dumoulin, J.A., 1998, Catalog of the historically active volcanoes of Alaska: U.S. Geological Survey Open-File Report 98-0582, p. 104.

Reid, M.E., 2004, Massive collapse of volcano edifices triggered by hydrothermal pressurization: Geology, v. 32, no. 5, p. 373–376.

Reid, M.E., Christian, S.B., and Brien, D.L., 2000, Gravitational stability of three-dimensional stratovolcano edifices: Journal of Geophysical Research, v. 105, no. B3, p. 6043–6056.

Reid, M.E., Sisson, T.W., and Brien, D.L., 2001, Volcano collapse promoted by hydrothermal alteration and edifice shape, Mount Rainier, Washington: Geology, v. 29, no. 9, p. 779–782.

Seed, H.B., 1973, Stability of earth and rockfill dams during earthquakes, *in* Hirshfeld, R.C., and Poulos, S.J., eds., Embankment-dam engineering: New York, Wiley and Sons, p. 239–269.

Siebert, L., 1984, Large volcanic debris avalanches; characteristics of source areas, deposits, and associated eruptions: Journal of Volcanology and Geothermal Research, v. 22, p. 163–197.

Siebert, L., and Begét, J.E., 2006, Two millennia of edifice instability at Augustine Volcano, Alaska and implications for future collapse: Eos, American Geophysical Union Transactions, v. 87, no. 52, fall meeting supp., abstract V51C-1692.

Siebert, L., Begét, J.E., and Glicken, H., 1995, The 1883 and late-prehistoric eruptions of Augustine volcano, Alaska: Journal of Volcanology and Geothermal Research, v. 66, p. 367–395.

Siebert, L., Glicken, H., and Kienle, J., 1989, Debris avalanches and lateral blasts at Mount St. Augustine volcano, Alaska: National Geographic Research, v. 5, no. 2, p. 232–249.

Simkin, T., and Siebert, L., 1994, Volcanoes of the world (2d ed.): Tucson, Ariz., Geoscience Press, 349 p.

Vallance, J.W., Schilling, S.P., Devoli, G., Reid, M.E., Howell, M.M., and Brien, D.L., 2004, Lahar hazards at Casita and San Cristóbal Volcanoes, Nicaragua: U.S. Geological Survey Open-File Report 2001-468, 18 p., 3 map plates.

Voight, B., and Elsworth, D., 1997, Failure of volcano slopes: Geotechnique, v. 47, no. 1, p. 1–31.

Voight, B., Janda, R.J., Glicken, H., and Douglass, P.M., 1983, Nature and mechanics of the Mount St. Helens rockslide-avalanche of 18 May 1980: Geotechnique, v. 33, p. 243–273.

Waitt, R.B., 2010, Ejecta and landslides from Augustine Volcano before 2006, *in* Power, J.A., Coombs, M.L., and Freymueller, J.T., eds., The 2006 eruption of Augustine Volcano, Alaska: U.S. Geological Survey Professional Paper 1769 (this volume).

Waitt, R.B., and Begét, J.E., 2009, Volcanic processes and geology of Augustine Volcano, Alaska: U.S. Geological Survey Professional Paper 1762, 78 p., 2 map plates, [http://pubs.usgs.gov/pp/1762].

Waitt, R.B., Begét, J.E., and Kienle, J., 1996, Provisional geologic map of Augustine Volcano, Alaska: U.S. Geological Survey Open-File Report 96-516, 44 p., 1 map plate.

Watters, R.J., Zimbelman, D.R., Bowman, S.D., and Crowley, J.K., 2000, Rock mass strength assessment and significance to edifice stability, Mount Rainier and Mount Hood, Cascade Range Volcanoes: Pure and Applied Geophysics, v. 157, p. 957–976.

Waythomas, C.F., 2000, Reevaluation of tsunami formation by debris avalanche at Augustine Volcano, Alaska: Pure and Applied Geophysics, v. 157, p. 1145–1188.

Waythomas, C.F., and Waitt, R.B., 1998, Preliminary volcano-hazard assessment for Augustine Volcano, Alaska: U.S. Geological Survey Open-File Report 98-0106, 39 p.

Waythomas, C.F., Watts, P., and Walder, J.S., 2006, Numerical simulation of tsunami generation by cold volcanic mass flows at Augustine Volcano, Alaska: Natural Hazards and Earth System Sciences, v. 6, p. 671–685.

Wesson, R.L., Boyd, O.S., Mueller, C.S., Bufe, C.G., Frankel, A.D., and Petersen, M.D., 2007, Revision of time-independent probabilistic seismic hazard maps for Alaska: U.S. Geological Survey Open-File Report 2007–1043, 33 p.

Zimbelman, D.R., Watters, R.J., Firth, I.R., Breit, G.N., and Carrasco-Núñez, G., 2004, Stratovolcano stability assessment methods and results from Citlaltépetl, Mexico: Bulletin of Volcanology, v. 66, no. 1, p. 66–79.

Petology and Geochemistry

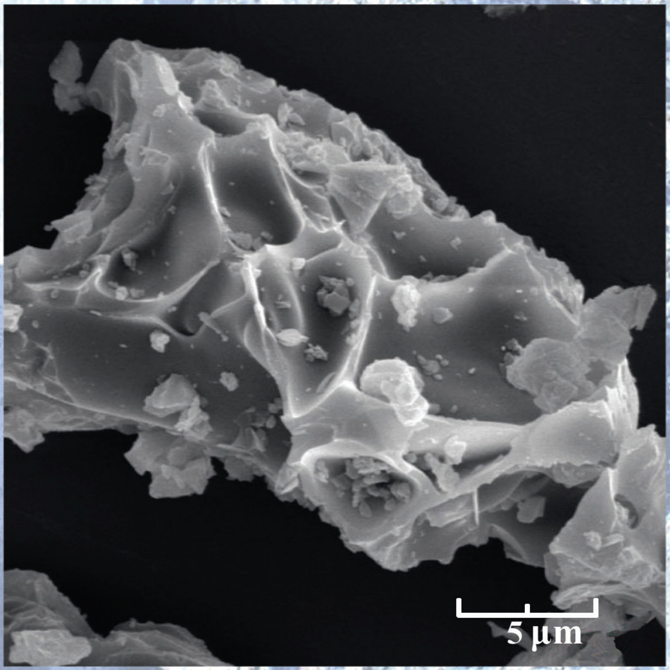

Oblique aerial photo, looking southeast, showing Augustine Volcano’s 2006 lava dome and northeast lava flow at the end of the 2006 eruption's effusive phase. Alaska Volcano Observatory photo taken March 15, 2006, by Tim Plucinski.

Chapter 15

Petrology and Geochemistry of the 2006 Eruption of Augustine Volcano

By Jessica F. Larsen[1], Christopher J. Nye[2], Michelle L. Coombs[3], Mariah Tilman[1], Pavel Izbekov[1], and Cheryl Cameron[2]

Abstract

Deposits from the 2006 eruption of Augustine Volcano, Alaska, record a complex history of magma mixing before and during the eruption. The eruption produced five major lithologies: low-silica andesite scoria (LSAS; 56.5 to 58.7 weight percent SiO_2), mostly during the initial explosive phase; high-silica andesite pumice (HSA; 62.2 to 63.3 weight percent SiO_2), prevalent during the continuous phase; dense low-silica andesite (DLSA; 56.4 to 59.3 weight percent SiO_2), predominantly during the late effusive phase; and dense intermediate andesite (DIA) and banded clasts, present throughout the eruption but most abundant in the continuous phase. The DIA and banded clasts have compositions that fall between and partially overlap the ranges noted above. All rock types are phenocryst-rich (36 to 44 volume percent), containing plagioclase, orthopyroxene, augite, Fe-Ti oxides, olivine, and rare amphibole, apatite, and anhydrite. Glasses from tephra and flow-deposit clasts range from 66 to nearly 80 weight percent SiO_2 and represent highly evolved melt relative to the bulk rock compositions. Fe-Ti oxides recorded f_{O_2}~2 log units above the Ni-NiO buffer and temperatures of 904±47°C and 838±14°C from LSAS and HSA samples, respectively, with the intermediate lithologies falling in the middle of these ranges. The dense low-silica andesite and scoria (collectively LSA) are compositionally nearly identical, and trace-element patterns show that the HSA is not the result of shallow crustal fractionation of the LSA. The petrological and geochemical data indicate that two-component magma mixing between the LSA and HSA caused the compositional spread in eruptive products. The phenocryst population in the LSA suggests that it represents a hybrid formed from the HSA and an unerupted, basaltic “replenishing” magma. On the basis of petrological and geophysical observations reported here and elsewhere in this volume, the HSA was stored as a crystal-rich mush with its top at ~5-km depth. An influx of basalt remobilized and partially mixed with a portion of the mush, forming the hybrid LSA. The lower viscosity LSA ascended towards the surface as a dike, erupting during the explosive phase in mid-January 2006. In late January, a large explosion produced the first significant volumes of HSA, followed by several days of rapid HSA effusion during the eruption’s continuous phase. After a three-week hiatus marked by elevated gas output, signifying an open system, degassed LSA erupted during the final, effusive phase. Consistency in eruptive styles and compositions suggests that the HSA magma body may have been similarly rejuvenated during the past several eruptions.

Introduction

Understanding the magmatic processes that drive eruptions is an integral component of volcano studies. Studying the deposits of recent, well-monitored eruptions allows us to place petrologic studies in a context that would be impossible for prehistoric or more poorly documented eruptions, thus yielding more insight into the link between what happens below the volcano’s surface and what comes out of the vent. Augustine Volcano, located in Cook Inlet in south-central Alaska, is one of the most active volcanoes in the Aleutian arc, with eight confirmed explosive eruptions in the past 200 years (Waythomas and Waitt, 1998). Because of the frequency of eruptions and the unique hazards that Augustine presents, understanding the processes that trigger eruptive events there is an important role of the Alaska Volcano Observatory (AVO). The consistent

---

[1] Alaska Volcano Observatory, Geophysical Institute, 903 Koyukuk Drive, University of Alaska, Fairbanks, AK 99775.

[2] Alaska Volcano Observatory, Alaska Division of Geological and Geophysical Surveys, 3354 College Road, Fairbanks, AK 99709.

[3] Alaska Volcano Observatory, U.S. Geological Survey, 4200 University Drive, Anchorage, AK 99508.

pattern of eruptions, in terms of precursory activity and eruptive style, combined with the increased amount of independent datasets for the 2006 eruption, makes Augustine suitable for cross-disciplinary studies of volcanic processes that can be applied to less well monitored volcanoes. The frequency of eruptions at Augustine also presents an excellent opportunity to compare petrologic data from the three most recent eruptions in 1976, 1986, and 2006.

Petrologists have long recognized that many products of subduction-zone volcanoes show evidence of magma mixing, and recent studies of historical and ongoing eruptions show that mixing is often temporally linked to magma's arrival at the earth's surface (for example, Coombs and others, 2000; Costa and Chakraborty, 2004; Izbekov and others, 2002; Murphy and others, 2000; Nakamura, 1995; Pallister and others, 1996). Understanding the process of magma mixing as a potential eruption trigger is important in the case of Augustine Volcano's most recent eruptions. Magmas erupted at Augustine in the 30 years prior to the 2006 eruption show clear evidence of magma mixing in the form of mingling (banded clasts) and hybridization at both macro and micro scales (Johnston, 1978; Roman and others, 2005). Both the 1976 and 1986 eruptions are thought to have been triggered by the injection of basaltic magma into a more silica-rich andesite/dacite magma body. Their whole-rock compositions are similar and limited in range between 56 to 64 weight percent SiO_2. The 1976 deposits include olivine and hornblende phenocrysts that appear to have grown in a mafic magma that was not found in the erupted material (Johnston, 1978). After the 1986 eruption, a better understanding of magma storage and transport at Augustine emerged from the increased quantity of geophysical and petrological data (Harris, 1994; Power, 1988; Roman and others, 2005). Roman and others (2005) suggest a model of interconnected dikes to explain how Augustine commonly produces mixed magmas but maintains a relatively narrow compositional range (56–64 weight percent SiO_2) throughout 200 years of historical activity, while also maintaining compositional heterogeneity throughout individual eruptive cycles.

The 2006 eruption of Augustine Volcano followed a sequence of events similar to those in 1976 and 1986. A precursory phase began April 30, 2005, and both seismicity and inflation of the edifice slowly increased over the next 7 months (Jacobs and McNutt, this volume; Cervelli and others, 2006). By mid-December 2005, earthquakes were occurring at a rate of 15 per day at a depth close to sea level, along with intermittent steam explosions, the largest of which were observed on December 10, 12, and 15 (Power and others, 2006). On January 11, 2006, seismometers recorded two explosions at Augustine, marking the onset of the explosive phase of the eruption. The explosive phase was dominated by a series of 13 discrete Vulcanian blasts that produced pyroclastic flows and ash fall rich in low-silica andesite scoria (Coombs and others, this volume; Vallance and others, this volume; Wallace and others, this volume; fig. 1). On January 28, Augustine entered a continuous eruptive phase dominated by low-level, ash-rich plumes and multiple pyroclastic flows, likely the result of rapid effusion and collapse of lava at the summit (Coombs and others, this volume; Wallace and others, this volume). Deposits from this phase include crystal-rich high-silica andesite and lesser amounts of banded clasts, dense intermediate andesite, and dense low-silica andesite (Vallance and others, this volume). After a hiatus in eruptive activity that lasted from February 10 to March 3, the eruption entered an effusive phase dominated by dome growth and the extrusion of rubbly lava flows accompanied by small-volume block-and-ash flows (Coombs and others, this volume). The effusive deposits contained primarily dense low-silica andesite and dense intermediate andesite (Vallance and others, this volume). The 2006 eruptive sequence ended on March 16, 2006, with the cessation of drumbeat earthquakes that accompanied the dome growth (Power and Lalla, this volume).

In this paper we present an overview of the petrography, petrology, and geochemistry of the products from the 2006 Augustine eruption. Our results are tied to the dominant lithologies erupted during each of the explosive, continuous, and effusive eruptive phases. We show that the eruptive products are the result of hybridization of an unerupted replenishing mafic magma, not seen in the eruption products in its pure, unmixed form, and a shallowly residing high-silica andesite body that was reinvigorated just before eruption. The data presented in this chapter are used in conjunction with companion studies on melt inclusion preeruptive volatile contents (Webster and others, this volume), geodetic constraints (Cervelli and others, this volume), and reaction-rim growth on olivines (Tilman, 2008), among others, to develop a model for the locations of magma storage and the timescales of magma movement before and during the different phases of the 2006 eruption. This model provides one explanation for the conveyor-belt-like similarity and frequency of historic Augustine eruptions.

Geological Setting

Augustine Volcano lies in the eastern Aleutian arc, approximately 80 km above the Wadati-Benioff zone (Syracuse and Abers, 2006). Volcanism in the eastern arc is caused by northwestward subduction of the Pacific Plate beneath the North American Plate at a rate of roughly 55 mm/yr (Kienle and Swanson, 1983).

The wholly Quaternary volcano sits atop crust of the Peninsular Terrane, thought to have amalgamated with nearby terranes prior to Late Jurassic time and accreted to North America in the mid-Cretaceous (Detterman and Reed, 1980). The terrane comprises Mesozoic marine and nonmarine sedimentary rocks of the Jurassic Naknek Formation, which crop out on the south flank of Augustine from sea level to 400 m above mean sea level (amsl). It is overlain by a thin veneer of friable sandstone and conglomerate of the Cretaceous Kaguyak Formation (Waitt, this volume). Seismic velocity studies suggest that these rocks have been uplifted on the south shoulder by faulting, and that lower-velocity sediments underlie the volcano on other sectors from sea level to ~900

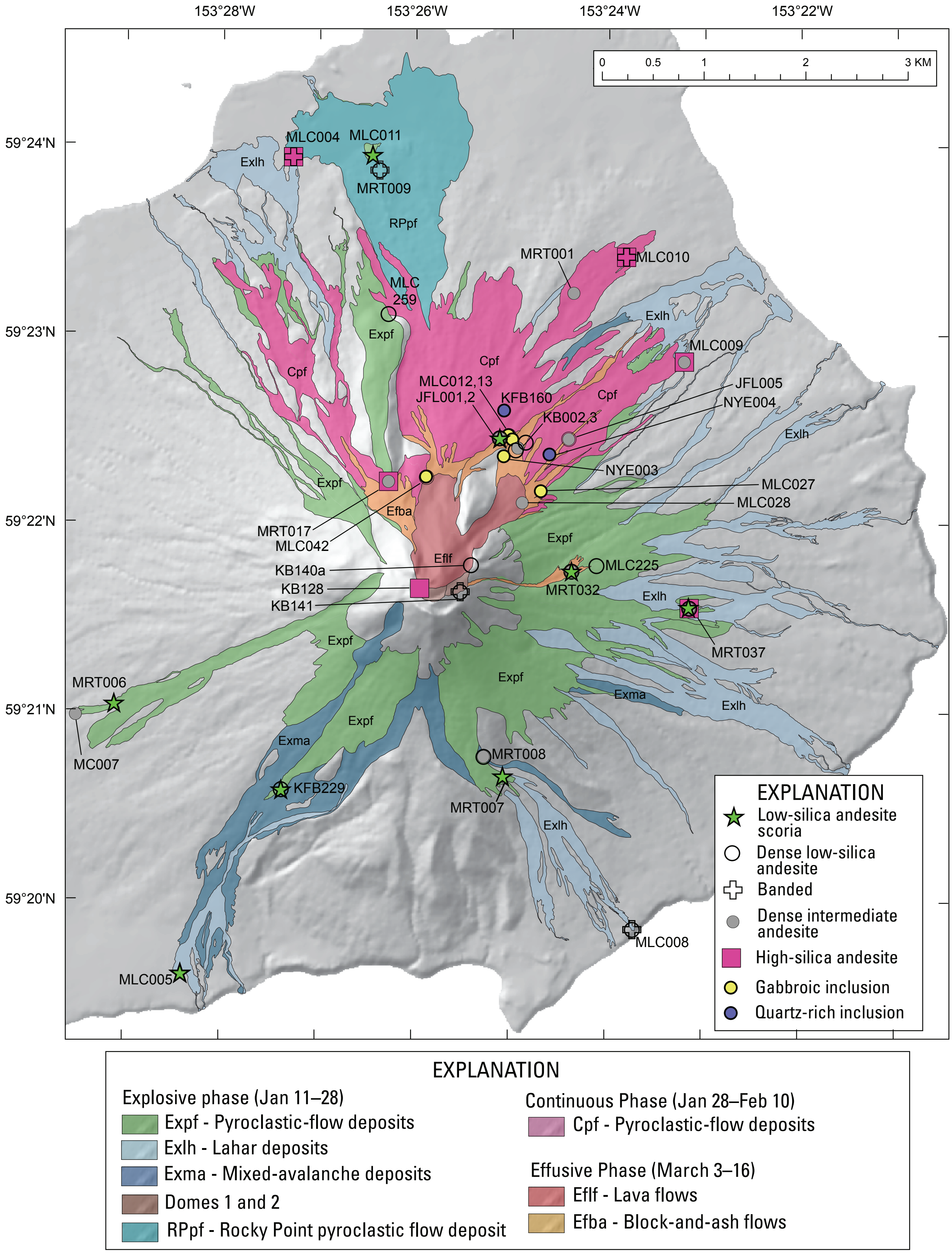

Figure 1. Map of Augustine Island showing deposits from the 2006 eruption and the location of samples used in this study. The 06AU- preface on sample locations is removed for clarity. Units simplified from Coombs and others (this volume).

m below mean sea level (bmsl) (Kienle and others, 1979). Beneath the summit, an intermediate-velocity region from sea level down to 900 m bmsl is interpreted as sedimentary strata that have been interlaced with volcanic dikes and sills (Kienle and others, 1979). High-velocity rocks everywhere underlie the volcano below 900 m bmsl, interpreted by Kienle and others as zeolitized Naknek Formation.

The oldest known products of Augustine Volcano are late Pleistocene in age (Johnston, 1978). They comprise poorly sorted bedded fragmental material, with clasts of olivine basalt as large as 20 cm in diameter, as well as radially fractured clasts of dense juvenile rhyolite. There is extensive palagonitization of the material and it appears to be the result of hyaloclastite eruption likely from a flank vent. The upper 20 cm is interlayered with the base of a rhyolitic tephra-fall deposit.

Records of early to middle Holocene Augustine eruptions are scarce and limited to the base of a few small tephra exposures on the south flank and some distal ashes with Augustine compositional affinities (Waitt, this volume). The late Holocene, prehistoric eruptive record is more complete, and shows that Augustine often erupted explosively, producing sometimes thick tephra falls, an apron of flowage deposits, and an edifice consisting of overlapping lava domes and short flows. In addition, repeated edifice failures and debris avalanches have marked the late Holocene record, with the most recent in 1883. Augustine has erupted historically in 1883, 1935, 1964, 1976, and 1986, each time producing andesitic through dacitic ash fall and pyroclastic flows.

Several lines of evidence have been used to argue that Augustine's subvolcanic plumbing system is immature and that it lacks a large, well-developed magma storage region, or "magma chamber." Recent eruptions have modest volumes (<0.5 km^3), thus involving small magma batches. Compositional heterogeneity is the norm and persisted throughout the 1986 eruption, suggesting that the eruption was not fed from a single magma storage region but instead by a system of small-volume dikes in the shallow subsurface, some of which contained residual magma from 1976 (Roman and others, 2005). Between eruptions, minimal edifice deformation and gas output have been observed (McGee and others, this volume; Power and others, 2006)

Despite the apparent absence of a large shallow magma body beneath Augustine, there are some indications of shallow-crustal magma storage and crystallization prior to previous eruptions. Seismicity prior to the 1976 eruption outlined a central, narrow plumbing system that reached from 8 km to the surface (Kienle and others, 1979). About half of Holocene eruptions produced magmas that contain hornblende, and Al-in-hornblende geobarometry from two Holocene fall units yields equilibrium pressures of 100 to 260 MPa, equivalent to depths between 3.5 and 9 km (Tappen and others, 2009). Melt inclusions in crystals within 1986 and prehistoric magmas contain wide ranges in both dissolved water and carbon dioxide, indicating crystallization at depths mostly between 8 km and several hundred meters bsl (Roman and others, 2005; Webster and others, this volume).

Sample Descriptions

Clasts within deposits of the 2006 eruption were initially separated into five major lithologic groups on the basis of hand-sample characteristics, primarily color and vesicularity (Vallance and others, this volume; fig. 2). Subsequent whole-rock analyses confirm the initial categories. The five lithologies are present in most deposits from the eruption, though in varying proportions. They are:

1. Low-silica andesite scoria (LSAS), almost exclusively erupted during the 2006 explosive phase, representing ~45 percent of the explosive-phase ejecta, with less than 3 percent appearing during the remainder of the eruption. LSAS clasts are moderately vesicular, with black to reddish-brown cores and olive-green to light-gray rinds.

2. High-silica andesite (HSA), most abundant in continuous-phase deposits but also present in explosive-phase ejecta. The most evolved whole-rock, matrix glass, and mineral compositions of 2006 ejecta belong to the HSA, which accounts for >5 to 30 percent of clasts within explosive-phase units, approximately 80 percent of continuous-phase deposits, and <10 percent of effusive phase deposits (Vallance and others, this volume). HSA mostly occurs as rounded, crystal-rich, slightly friable clasts that are light to dark gray, moderately vesicular, and often colored by oxidation.

3. Dense intermediate andesite (DIA), erupted during all eruptive phases but most prevalent in deposits of the continuous-phase. This lithology was originally identified in the field by its medium-grey color and makes up approximately 10 percent of explosive-phase ejecta and a third of continuous-phase ejecta (Vallance and others, this volume). We note, however, that some DIA clasts, especially in the explosive phase, may be accidental lithics of pre-2006 dome lavas. DIA is found as rounded to angular, medium to light gray, poorly to nonvesicular clasts, or as lava.

4. Dense low-silica andesite (DLSA), which composes the effusive-phase lava flows and is present throughout the eruption products in varying proportions as clasts in flow and fall deposits. DLSA makes up 8 to 25 percent of the deposits from the explosive and continuous phases and ~60 percent of effusive-phase deposits (Vallance and others, this volume). It is dark gray to black, poorly to nonvesicular, and commonly forms angular clasts, some of which have breadcrust rinds.

5. Banded clasts are any combination of the above colors and texture that show distinct to diffuse banding. They are found throughout the eruption but are most prevalent during the continuous phase.

In addition to these five major lithologies, crystal-rich, fine-grained gabbroic (FGGI) and quartz-rich inclusions were

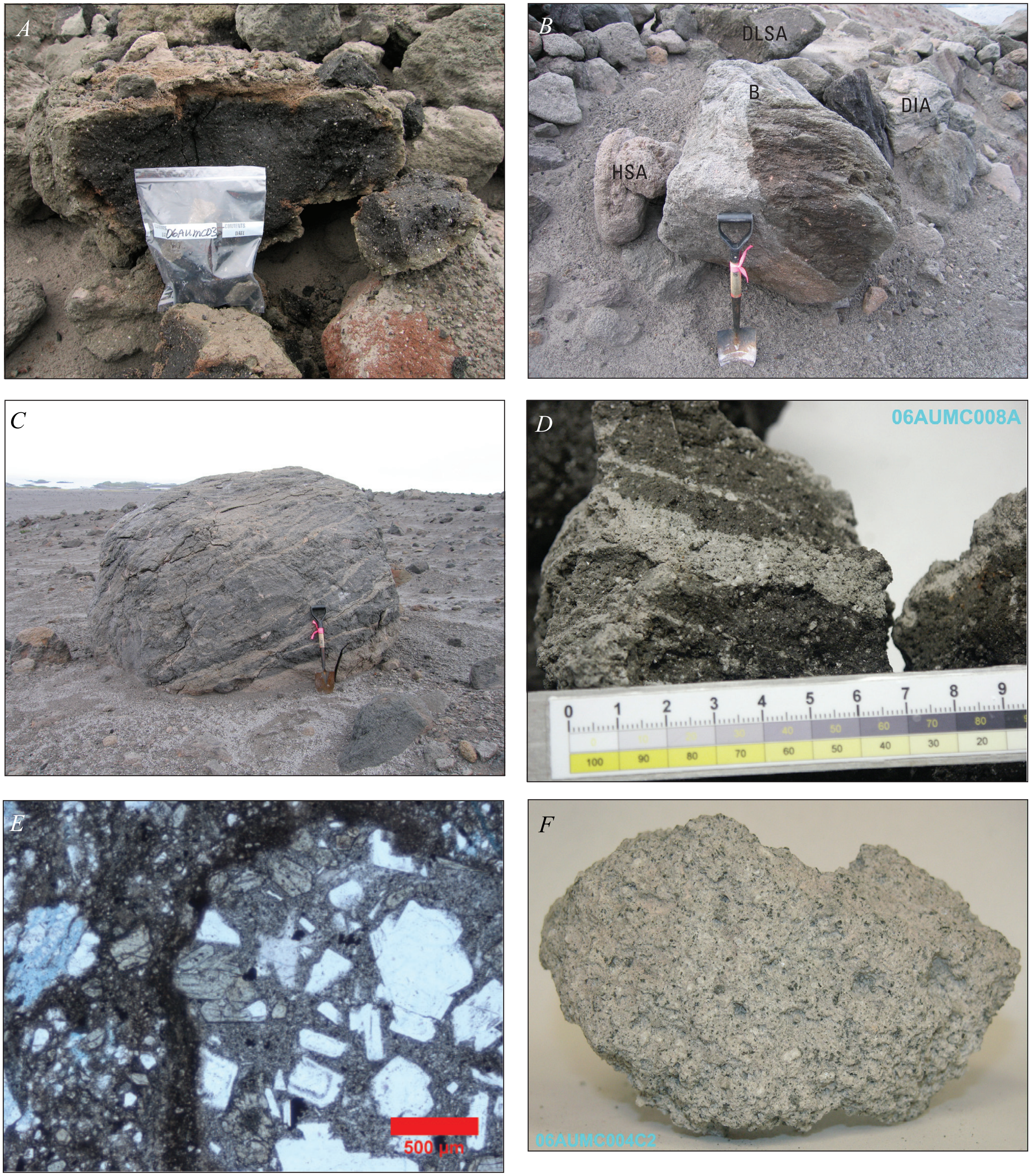

Figure 2. Photographs depicting typical occurrences and major lithologies of deposits from the 2006 Augustine eruption. *A,* Broken clast of low-silica andesite scoria with olive green rind and black interior, within an explosive-phase pyroclastic-flow deposit. Sample site 06AUMLC035. *B,* Continuous-phase pyroclastic-flow deposit containing high-silica andesite (HSA), dense intermediate andesite (DIA), dense low-silica andesite (DLSA), and banded (B) clasts. *C,* Large banded boulder found in Rocky Point pyroclastic-flow deposit from late in the explosive phase. *D,* Interior of banded clast 06AUMC008a, collected from an explosive-phase pyroclastic-flow deposit, showing distinct bands of high- and low-silica andesite. Scale is in centimeters. *E,* Transmitted-light photomicrograph showing crystal-rich and crystal-poor regions of sample 06AUMC007b from the January 13–14 low-silica andesite scoria. *F,* High-silica andesite sample 06AUMC004c2.

sampled from the continuous- and effusive-phase deposits (fig. 3). Fine-grained gabbroic inclusions are salt and pepper in color, nearly holocrystalline, and finely vesicular. They are almost exclusively found as inclusions within DLSA lavas of the effusive phase. Quartz-rich inclusions were found in continuous-phase deposits as light gray or salt-and-pepper bands or pods in larger andesite clasts.

Samples were collected by AVO scientists during the course of the eruption on January 12 and 24, February 8 and 20, and May 13 and after the eruption during August 2006. A geologic map of the 2006 deposits (Coombs and others, this volume) was used to determine sampling localities in order to collect samples from as many of the eruptive events as possible (fig. 1). For each eruptive unit, we collected samples of the multiple lithologies present in most deposits (table 1 and appendix 1). In addition to 2006 samples, we collected samples from a Pleistocene outcrop on the south flank of the island that contains coevally erupted hyaloclastite and pumice (Waitt, this volume), and some clasts from 1976 and 1986 pyroclastic flows for whole-rock analysis.

Analytical Methods

Major and trace element compositions of 70 samples from the 2006 eruption were determined at the Washington State University (WSU) Geoanalytical Laboratory using XRF and ICP-MS techniques (table 2 and appendix 3).[4] Samples were cleaned in deionized water, dried for several days at less than 100^{o}C, partially crushed to pea-sized or smaller grains, and then sent to WSU for analysis. x-ray fluorescence and ICP-MS analyses were conducted following the methods outlined in Johnson and others (1999) and Knaack and others (1994), respectively. All intensity values were concatenated and reduced using a single calibration file to reduce interbatch analytical variations.

Petrographic analysis consisted of documentation of the groundmass and phenocryst types and textures and point-count analyses of thin sections. At least five thin sections for each of the five main lithologic types were counted for modal analyses. Point counts were conducted using an automated stage with a minimum of 1,000 points per slide, including void space. Normalized percentages were calculated after removing void counts.

Phenocryst, microlite, and groundmass-glass compositions were determined at the University of Alaska Fairbanks (UAF) Advanced Instrumentation Lab (AIL) using a Cameca SX-50 electron microprobe equipped with four wavelength-dispersive spectrometers and one energy-dispersive spectrometer. Phenocryst phases were analyzed for major elements using a 15-KeV, 10-nA focused beam and standard ZAF corrections. Glasses were analyzed using a 15-KeV,

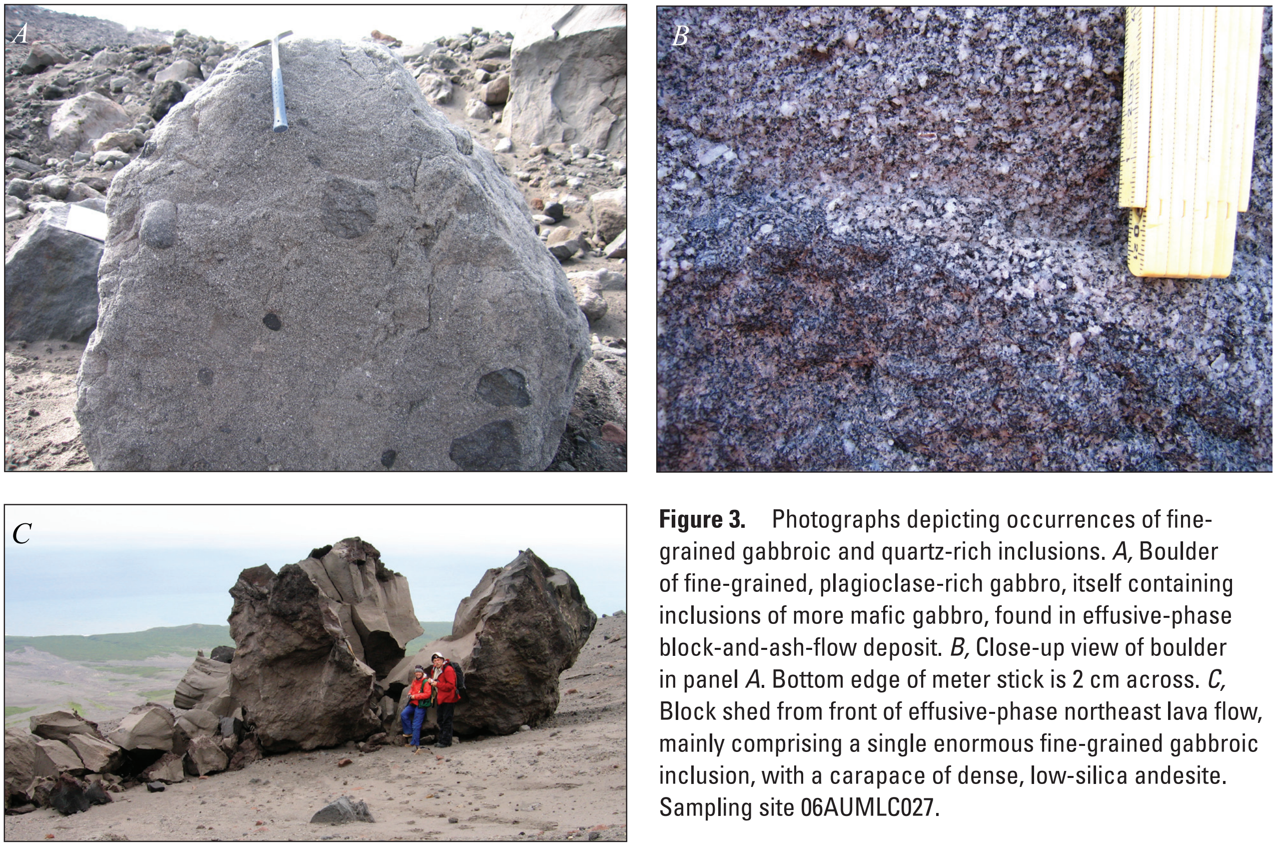

Figure 3. Photographs depicting occurrences of fine-grained gabbroic and quartz-rich inclusions. *A,* Boulder of fine-grained, plagioclase-rich gabbro, itself containing inclusions of more mafic gabbro, found in effusive-phase block-and-ash-flow deposit. *B,* Close-up view of boulder in panel *A*. Bottom edge of meter stick is 2 cm across. *C,* Block shed from front of effusive-phase northeast lava flow, mainly comprising a single enormous fine-grained gabbroic inclusion, with a carapace of dense, low-silica andesite. Sampling site 06AUMLC027.

---

[4] Note that tables 2 through 8 are at the back of this chapter.

Table 1. Samples of Augustine Volcano 2006 eruptive products used in this study, sorted by eruptive unit and lithologic type.

[Unit names are defined by Coombs and others (this volume). On our figure 1, Expf, Expc, and Expct are lumped into Expf and Cpf and Cpfw are lumped into Cpf for simplicity. In addition, the appendix contains new major and trace element data for 2 samples from the 1883(?) lava flow; 3 samples from 1964 pyroclastic flows; 5 samples from 1976 pyroclastic flows; 11 samples from 1986 pyroclastic flows; 5 samples from early Holocene pumice fall and bombs; 8 juvenile clasts from the late Pleistocene basalt/basaltic andesite hyaloclastite; 3 dense juvenile rhyolite clasts from within the hyaloclastite; and 3 rhyolite pumice clasts from the fall unit directly overlying the hyaloclastite. The prefix "06AU" has been removed from all sample names for brevity. (#) indicates that the sample was analyzed for major and trace elements]

Deposit dates	Phase	Unit	Low-silica andesite scoria	Dense low-silica andesite	Banded	Dense intermediate andesite	High Silica Andesite	Inclusion
Jan 13–14 (E5–8)	Explosive	Expct, Expf	MRT037c#	MRT037b# MRT037f# MRT037a		MRT037e#		MRT037d# (low-K)
Jan 13–14 (E3–8)			MC005a# MC005c.p3# MC005c.p4# MC005c.p5# MC008b.p1# MC008b.p2# KFB229a# MRT007b#	MC008b.p3# KFB229b# MRT008a#	MC005c.p1# MC008a.f# MC008a.m# MC005c.p2	MC008b.l1# MRT008b#	MC005c.p2# (pumice)	
Jan 17 (E9)		Expf	MC007c#			MRT006#		
Jan 21		Exd1		KB141b#	KB141a			
Jan 22–28		Exd2					JWV059a# KFB128a#	
Jan 27 (E10)		Expc		MLC259e# MLC225#				
		RPpf	MRT009b# MC011a#		MC004c3m# MC004c3 MRT009c		MC004a MC004c1# MC004c2#	
Jan 28–Feb 4	Continuous	Cpf			MC010p2# MC010p3m# MC010p3	MC009l1# MRT001b#	MC009p1# MC009p2# MC010p1#	NYE004# (high-Si) KFB160# (high-Si)
		Cpfw				MRT017a#	MRT017b#	
March 3–16	Effusive	Eflf		KB140B# MLC042b# MLC057#		MLC028#		MLC042a# (gabbroic)
		Efba	JFL001e# MRT032c#	JFL001d# JFL001f# JFL002# JFL005b# KB003# MC012b# MRT032a# NYE001#		JFL001b# JFL005a# KB002A# KB002B# KB002C# MRT032b#		MC012a# (gabbroic) MC013a# (gabbroic) MC027a# (gabbroic) NYE003# (gabbroic)

10-nA, 10-micron-wide defocused beam and a routine to minimize Na loss. Comenditic glass standard KN-18 was routinely analyzed during glass analyses to monitor instrument drift.

Fe-Ti oxide grains were separated from crushed samples of the major lithologies using a magnet. Grain mounts of the separated oxides were polished and touching ilmenite-titanomagnetite pairs without obvious disequilibrium textures or exsolution lamellae were analyzed by microprobe. Analyses consisted of core to rim transects, in 3-micron increments across each grain, with anomalously high Si analyses removed because of possible interference with glass. The analyses showed no significant change in composition from core to rim, so the values for each oxide were averaged. The pairs were subjected to the Bacon and Hirschman (1988) equilibrium test, and those found to be in equilibrium were run through QUILF (Andersen and others, 1993) to determine the temperature and oxygen fugacity (f_{O_2}). As discussed below, the high f_{O_2} of the magmas is outside of the calibration for the QUILF algorithm (Evans and others, 2006; Lattard and others, 2005); thus temperatures presented herein have been adjusted downward by 30°C (Rutherford and Devine, 1996).

Results

Petrography

Eruptive products of the 2006 eruption are typical of andesite and dacite produced by convergent-margin volcanoes worldwide: they are porphyritic, variably vesicular, and have glassy to microlite-rich groundmasses. The 2006 magmas contained phenocrysts of, in order of decreasing abundance, plagioclase, augite, orthopyroxene, Fe-Ti oxides, olivine, and rare amphibole, apatite, anhydrite, quartz, and biotite. (fig. 4; table 2). Amphibole is rare within all major lithologies. Apatite and anhydrite are present in less than 0.6 volume percent in all lithologies, and apatite exists mainly as inclusions within plagioclase. Biotite, quartz, significant anhydrite, and abundant amphibole are present only within the FGGI minor lithology. Plagioclase is the most abundant mineral phase by far, averaging from 27 to 32 volume percent in the major lithologies.

All rock types are phenocryst-rich, with LSAS, DLSA, DIA, and banded samples ranging from 36 to 40 volume percent phenocrysts in terms of average values (table 2), though we note that individual samples may lie outside this range (appendix 2). Two fine-grained gabbroic inclusions have an average of 74 volume percent phenocrysts.

Of the five major lithologies, high-silica andesite samples are the richest in phenocrysts. From point-count analysis of seven HSA samples, we found an average of 45 volume percent crystals, with a standard deviation of 7 volume percent. Interestingly, three replicate point-count analyses of a single HSA thin section yielded results of 40 to 57 volume percent, an unexpectedly high range (appendix 2). (Replicate analyses of LSAS and DLSA samples yielded ranges within a few volume percent.) In addition, we noted that hand specimens of HSA appeared particularly crystal-rich. To further assess HSA phenocryst content, we use a mass balance approach. If we perform a linear least squares, mass balance regression of the phenocryst compositions determined by electron microprobe (see section on Phase Descriptions and Compositions below), using their modal percentages from the point counts against the whole rock compositions to derive the volume percent of glass in the groundmass, we find that the point-count modes yield significant mismatches in Si, Mg, Fe, and Ca. In contrast, when glass content is reduced from 55 to 46 volume percent and other phenocrysts are increased proportionally, we obtain a better fit in the mass balance calculation. We suggest that the disparity between the point-count and mass balance methods for the high-silica andesite is a result of assigning groundmass glass to points where the glass may account for less than the total thickness of the thin section. Thus the actual crystallinity of the high-silica andesite magma is likely closer to 55 volume percent.

All lithologies are variably vesicular, even those described as relatively dense, and range from 16 to 45 volume percent porosity. Average vesicularities for the major lithologies are 37.3 volume percent for HSA, 38.7 volume percent for banded, 33.6 volume percent for LSAS, 22.1 volume percent for DIA, and 19.8 volume percent for DLSA (fig. 5, table 2). Void spaces are commonly irregularly shaped and variably sized, from sub-mm size to more than 10 mm.

Both DLSA and LSAS have dark gray to brown groundmasses, dominated by abundant microlites and containing very little residual glass (<1 volume percent by point counts; figs. 5, 6*A*, *B*). In contrast, HSA pumice clasts have groundmass composed almost wholly of clear, microlite-free glass that often forms finely stretched filaments (fig. 6*C*). These filaments and bubble voids are often stretched or aligned in one orientation. Based on normalized point-count totals, the HSA contains an average of 51.7 volume percent glass and 1.4 volume percent microlite-rich groundmass (fig. 5). The DIA and banded clasts contain a mix of both groundmass textures, averaging 10.6 and 37.8 volume percent glass and 51.5 and 37.8 volume percent microlite-rich groundmass in the DIA and banded clasts respectively.

The major lithologies, especially LSAS, all show some glomerophenocrystic plagioclase, pyroxene, olivine, or symplectite olivine. The FGGI minor lithology contains notable pervasive skeletal plagioclase crystals, with a more equigranular texture than that observed in the major lithologies. Quartz-rich inclusions are marked by polycrystalline plagioclase and quartz masses as large as several mm in diameter, surrounded by a microlitic groundmass of quartz, plagioclase, orthopyroxene, and glass. Patches of granophyric texture are present. Graphic textures in plagioclase, hornblende, orthopyroxene, and clinopyroxene are occasionally present in samples from the major lithologies.

Diffuse to sharp banding representing various stages of magma-mingling and hybridization is evident in Augustine deposits at all scales, from large boulders to micro-scale textures seen in thin section (fig. 2*B* to 2*E*). Heterogeneity is also observed from deposits from each phase of the eruption, in variations in glass color (tan to colorless), phenocryst abundances (appendix 2), and disequilibrium textures.

Whole-Rock Compositions

Systematic differences in whole-rock composition among the products of the 2006 eruption mirror the macroscopic differences first identified among lithologies in the field. Lavas and pyroclasts from the 2006 eruption range from 56.5 to 63.2 weight percent SiO_2, fully spanning the andesite range and extending slightly into both the basaltic-andesite and dacite fields (fig. 7; table 3). For simplicity we refer to them all as andesite. The samples range from 0.7 to 1.1 weight percent K_2O and straddle the low-K to medium-K boundary, which is low by comparison with other Aleutian arc lavas, but not with convergent margin lavas worldwide (Gill, 1981). Analyzed LSAS samples range from 56.5 to 58.7 weight percent SiO_2 and DLSA from 56.4 to 59.3 weight percent SiO_2. HSA samples span 62.2 to 63.3 weight percent SiO_2, though all but one sample cluster near 62.2 weight percent. DIA and banded samples fall between and partially overlap these ranges. Fine-grained gabbroic inclusions (FGGI) range from 54.5 to 57 weight percent SiO_2 and fall along a lower K_2O trend in comparison to other 2006 samples. A single sample, initially identified as HSA in the field, falls along this low-K trend as well and is termed “low-K HSA” (fig. 7). Two quartz-rich inclusions have 73 and 76.3 weight percent SiO_2 and 2.2 to 3.0 weight percent K_2O, which is much higher than other Augustine samples.

Major- and trace-element abundances in 2006 samples plot along linear trends on silica variation diagrams, except for inclusions and the low-K HSA sample (figs. 8, 9). For example, the R-squared value of a linear fit to the K_2O versus SiO_2 plot shown in fig. 7 is 0.99. Slight deviations from the linear trend exist at the mafic end in MgO and especially Cr. In Cr, the linear array appears to split from the most mafic LSAS towards increasing silica. Cr values for the majority of LSAS and about half of DLSA fall 10 to 20 ppm below the dominant array defined by HSA, DIA, banded, and some DLSA (fig. 9). At the silicic end, HSA samples have, for certain trace elements (for example, La and Nd), a larger and extend over a range that appears to fall outside the tight linear array formed by the rest of the 2006 rocks (fig. 9). Interestingly, the deviations appear to correlate with time

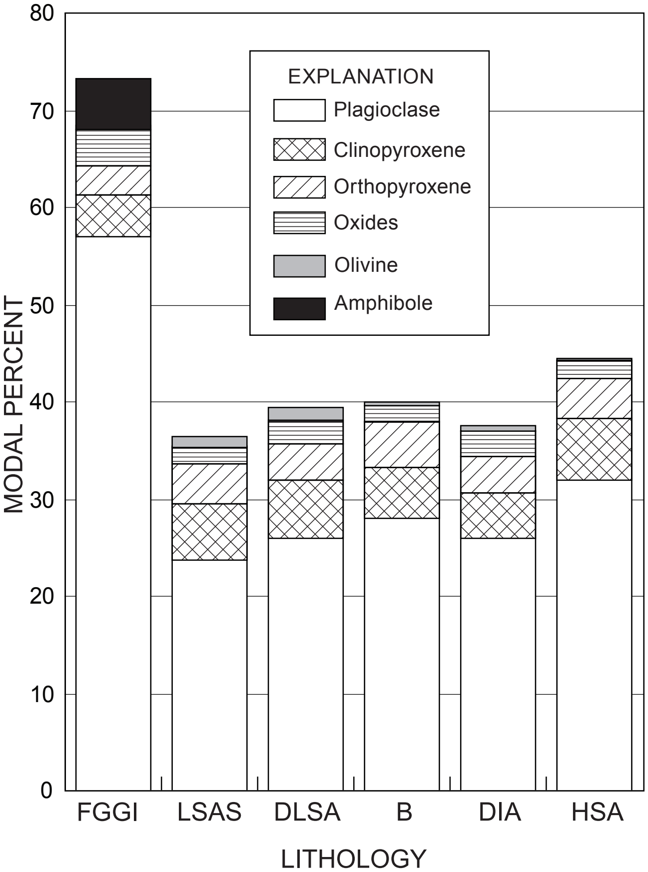

Figure 4. Modal percents of major and minor phenocryst phases in Augustine 2006 eruption deposits. HSA is high-silica andesite, DIA is dense intermediate andesite, B is banded, DLSA is dense low-silica andesite, LSAS is low-silica andesite scoria, and FGGI is fine-grained gabbroic inclusions. Modal percents are averages from point counts of at least 1,000 points per slide, normalized after removing void space counts. Groundmass percentages make up the balance to 100 percent. Oxides include all opaque minerals.

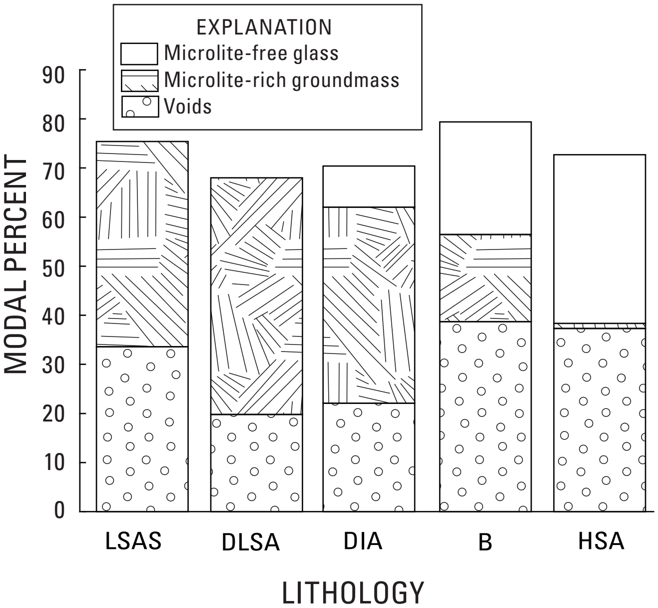

Figure 5. Average modal percentages of groundmass textures and void space (that is, vesicularity) for the five major lithologies from the Augustine 2006 eruption. Abbreviations as in figure 4.

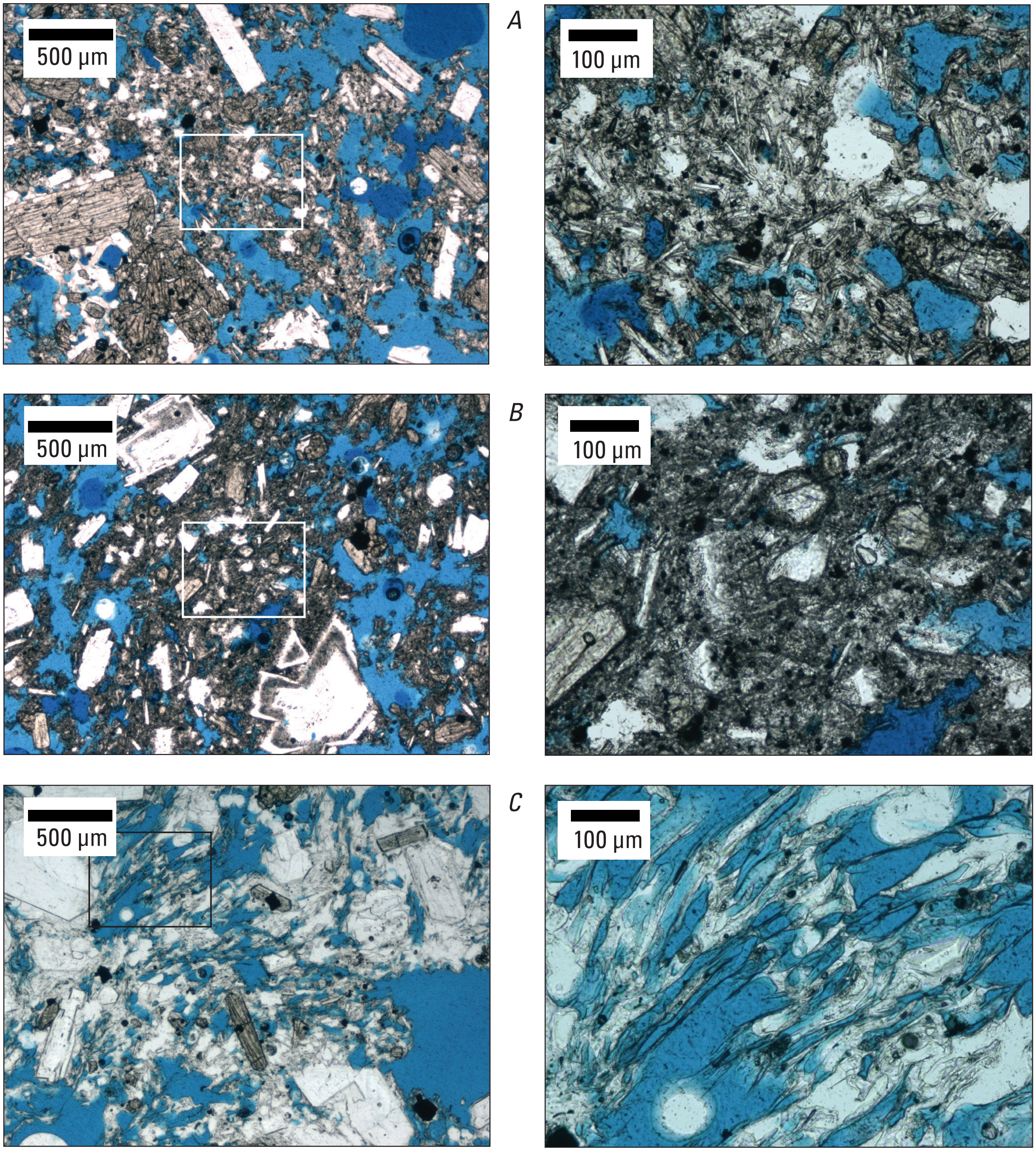

Figure 6. Transmitted-light photomicrographs showing groundmass textures of major Augustine 2006 lithologies. All samples have been impregnated with blue epoxy. Boxes in left-hand panels indicate regions that are enlarged in right-hand panels. *A,* Microlite-rich groundmass from sample 06AUMRT007b (low-silica andesite scoria) erupted during the explosive phase. *B,* Microlite-rich groundmass from sample 06AUMRT001b (dense low-silica andesite) erupted during the continuous phase. *C,* Nearly microlite-free clear glass from sample 06AUMC009p1 (high-silica andesite) erupted during the continuous phase.

of eruption: all explosive-phase low-silica andesites fall along the low-Cr trend, and all low-Nd high-silica andesites were erupted during the explosive phase.

To emphasize small trace-element differences within the 2006 ejecta suite, we have normalized their compositions to an average LSAS composition (fig. 10). This normalization scheme is preferred here because we focus on the changes across the 2006 eruption products only, rather than a broader comparison between different volcanic systems or across different tectonic settings. Normalization to the most primitive magma erupted allows us to look in greater detail at the relationships of the 2006 products to one another within the single eruption sequence. Trace element values for DLSA and LSAS samples are very similar (fig. 10*A, B*). HSA samples show elevated concentrations of large ion lithophiles (LILE), the U, Th, Pb group, and HFSE (Zr, Hf, Nb, Ta) and lower concentrations of compatible trace metals relative to the LSA samples. HREE (Eu through Lu) concentrations in the HSA are similar to those of LSAS and DLSA samples, whereas LREE (La through Sm) show a progressively greater enrichment with decreasing atomic number (fig. 10*C*). DIA and banded trace-element concentrations span a range bracketed by HSA and LSA (fig. 10*D*). Lower silica gabbroic inclusions show marginally higher concentrations of MREE and lower concentrations of LILE, HFSE, and Th, U, and Pb compared with LSA and HSA samples (fig. 10*E*). Gabbroic inclusions are also unusual in their lower concentrations of transition metals, despite their lower SiO_2 content. Two silicic inclusions are off the predominant range, and have very high concentrations of MREE, HREE, and some (but not all) of the LILE.

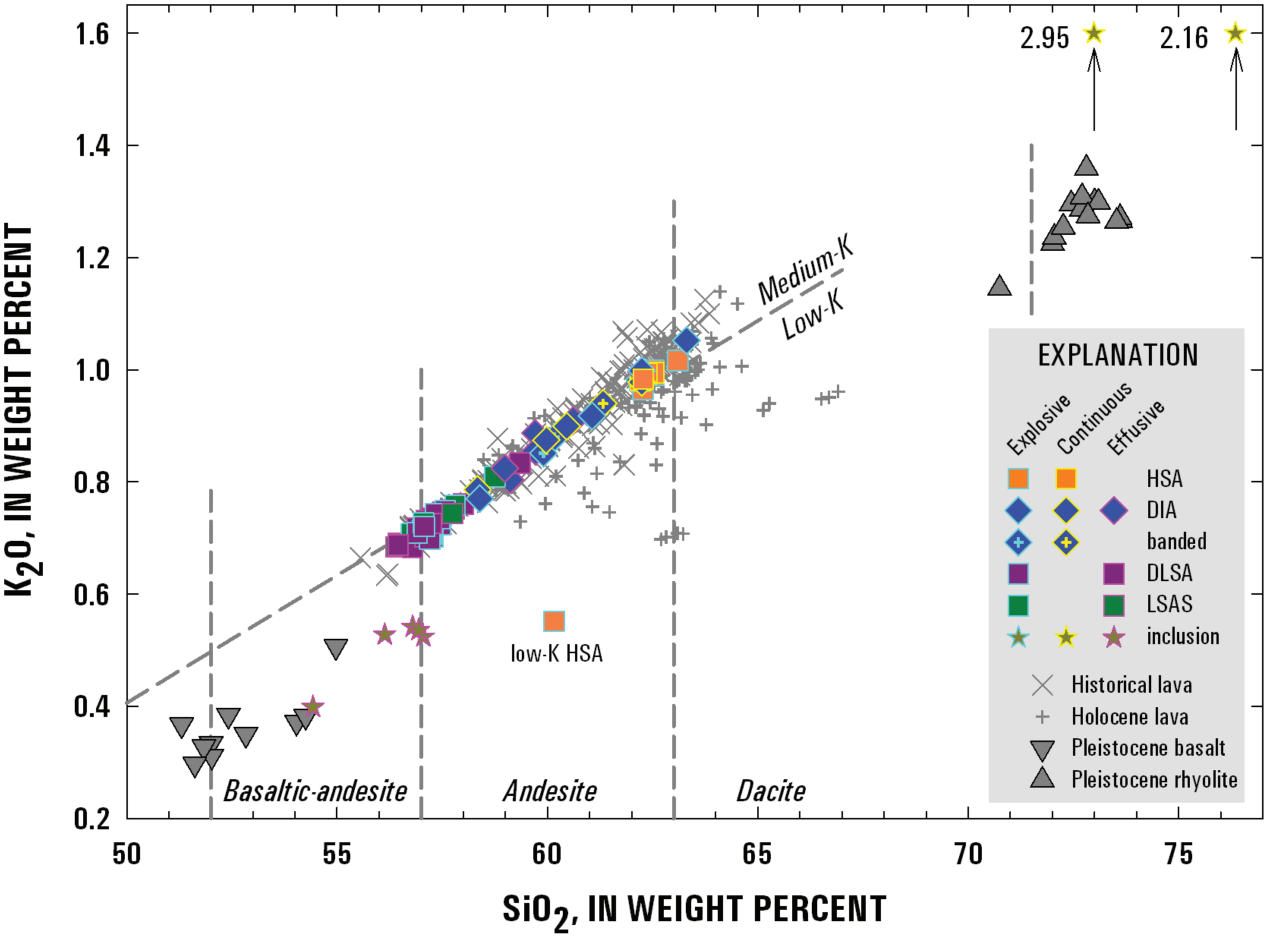

Figure 7. K_2O-silica variation diagram of Augustine whole-rock samples from Pleistocene to present. All 2006 data, and some of the pre-2006 historical, Holocene, Pleistocene basaltic rock, and Pleistocene rhyolite data are from this study; additional data are from Roman and others (2005), Daley (1986), Johnson and others (1996), C. Gardner (unpublished), C. Nye and J. Begét (unpublished), and K. Wallace (unpublished). Diagonal line shows boundary between low-K and medium-K andesites of Gill (1981). Vertical compositional boundaries from LeMaitre (1991).

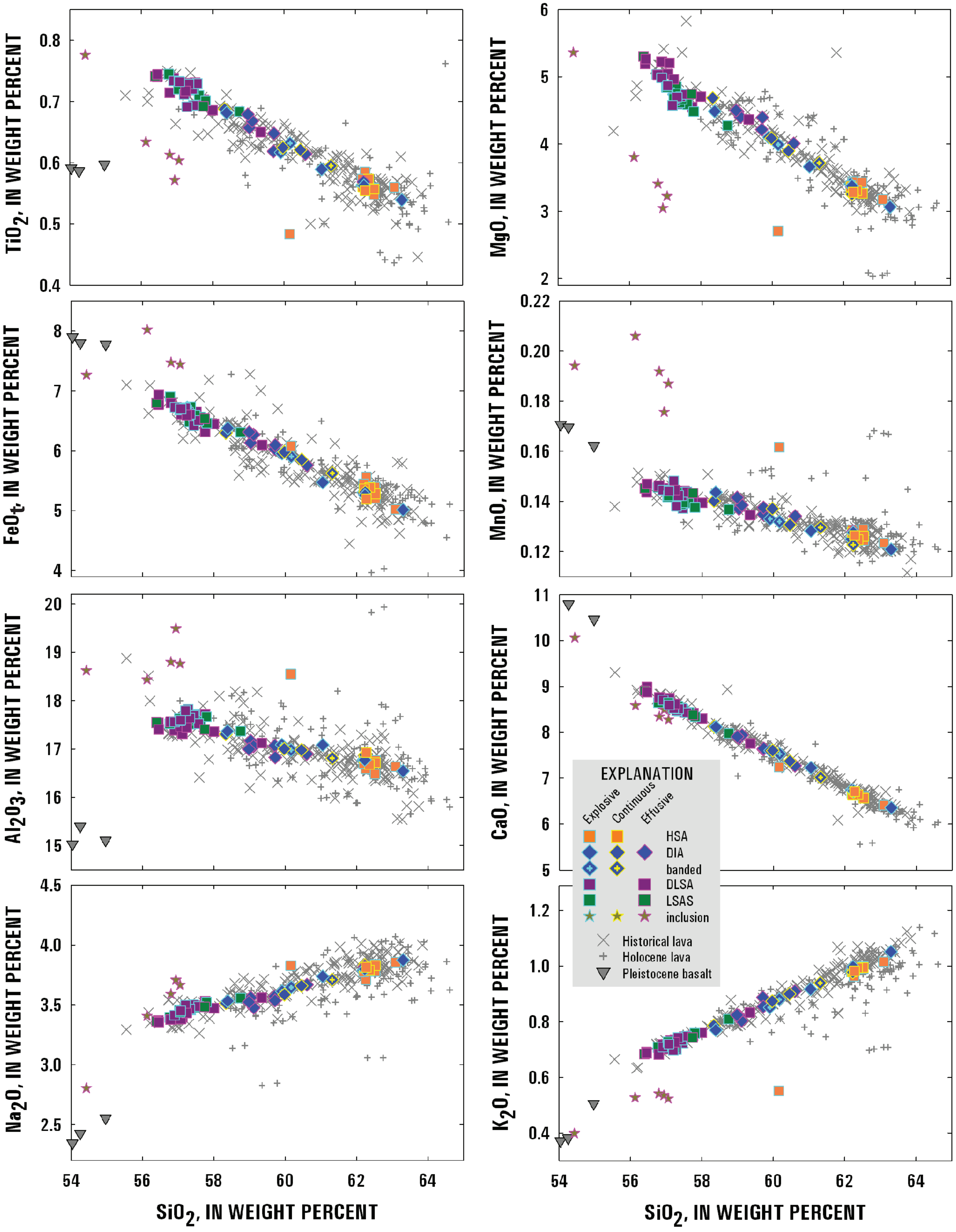

Figure 8. Major-element silica variation diagrams for Augustine 2006 samples (excluding quartz-rich inclusions). Data sources for pre-2006 samples are the same as for figure 7. FeO_t is total iron analyzed as FeO.

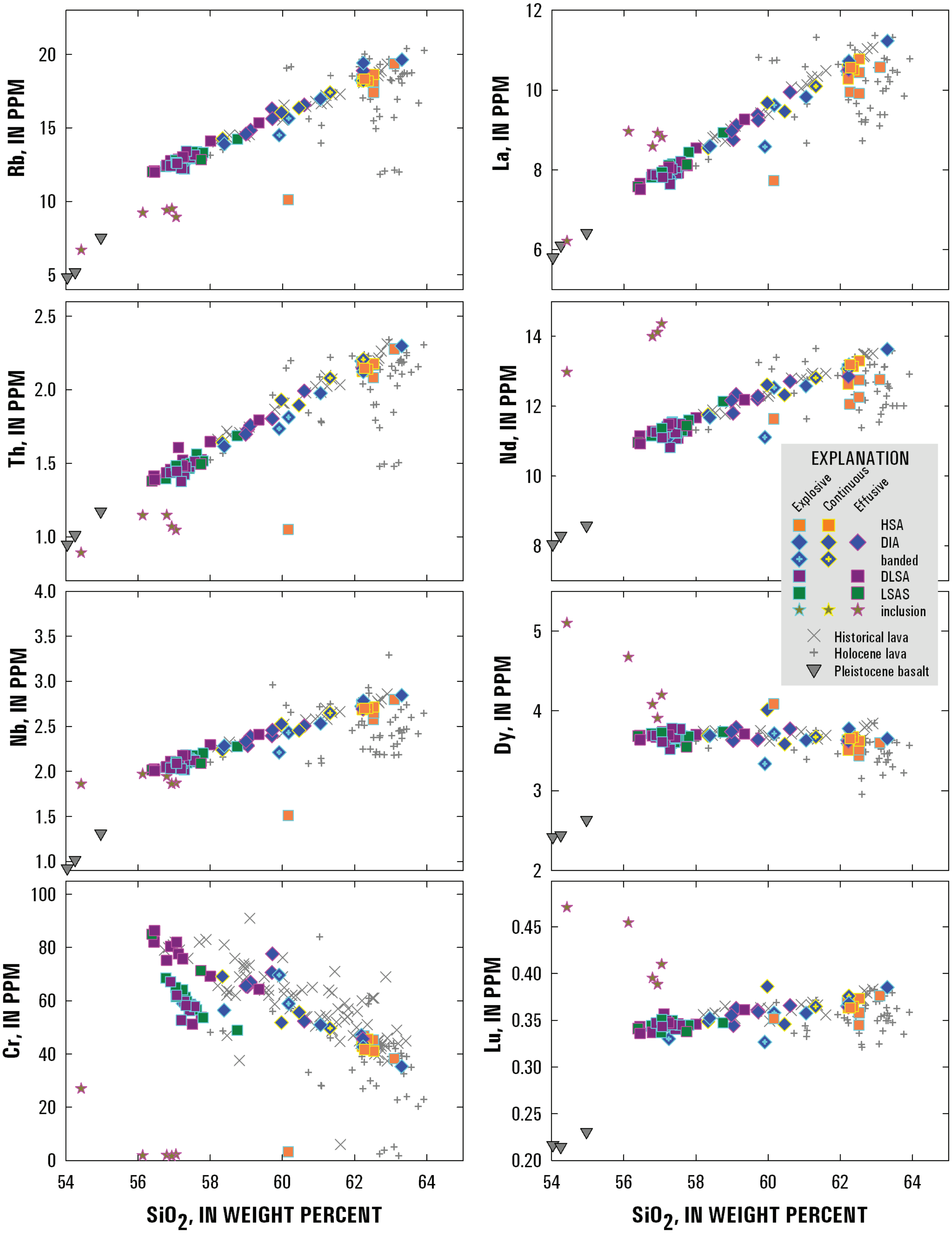

Figure 9. Trace-element silica variation diagrams for 2006 samples (excluding quartz-rich inclusions). Data sources for pre-2006 samples are the same as for figure 7.

Compositional Trends, Pleistocene to Present

The overwhelming majority of all analyzed samples from Augustine span 56 to 64 weight percent SiO_2, similar to the range of compositions produced in 2006 (fig. 7). Eruption products from 2006 yield trends on major and trace-element variation diagrams that broadly overlap those shown by products of Holocene and especially historical eruptions of the volcano, though 2006 samples are less dispersed about the linear trend than those erupted before 2006 (figs. 7 to 9).

In comparison with the 2006 eruptive products, other samples from historical eruptions are similar (figs. 7 to 9), yet tend to be slightly elevated in K_2O and Na_2O, especially at the high-silica end. Late Holocene (prehistoric) samples have compositions that are broadly similar to historical lavas, yet they extend to significantly lower middle and heavy REE abundances (fig. 10*F*).

The only known Augustine products to fall outside the basaltic-andesite-to-dacite spectrum are from the only Pleistocene outcrop on the island, which exposes rhyolitic pumice (71 to 74 weight percent SiO_2) and basaltic hyaloclastite (51 to 55 weight percent SiO_2), apparently erupted coevally (Plank and others, 2006; Waitt, this volume). Both mafic and silicic samples from this deposit fall along a lower K_2O trend than those from Holocene Augustine eruptions (fig. 7). Compared to typical Augustine products, the Pleistocene basalts have lower concentrations of all REE, LILE, and HFSE (fig. 10*F*). The rhyolites are higher in LILE, LREE, U, Th, and Pb, but their concentrations of MREE and HREE are dramatically lower than the andesites and are about as low as seen in the coerupted basalts.

Phase Descriptions and Compositions

Here we present an overview of the main phases found within rocks from the 2006 eruption. Phase compositions are illustrated in plots, and representative analyses are given in tables 3 to 6. The complete datasets for olivine, oxides, and pyroxenes are given in Tilman (2008). The full glass and plagioclase datasets are presented in electronic supplementary appendix 3 and 4, respectively.

Groundmass Glass

We analyzed matrix (groundmass) glass from most lithologies found within pyroclastic and lava flow deposits, as well as in tephra samples from January 13, 14 and 17 and the 1986 eruption (table 4; fig. 11). The high concentrations of plagioclase, pyroxene, and oxide microlites in the groundmasses, especially of the more mafic samples, made glass analysis difficult. During probe sessions, we identified glass pools within microlite-rich samples using a combination of backscattered electron images (BSE) and reflected light, but the results of some analyses indicate that the beam was at least partially on crystal(s) in addition to glass. Clearly anomalous analyses were deleted from the dataset presented here, though some analytical scatter is still likely the result of the electron beam hitting other phases. In contrast to the microlite-rich low-silica andesites, the groundmass of more silicic lithologies, comprising glass in the HSA pumice and lighter bands in banded clasts, is relatively microlite-poor, making it easier to find clean glass to analyze. This contrast resulted in an overrepresentation of silicic samples within our groundmass-glass dataset.

The entire glass dataset spans a range of SiO_2 contents from 66 to nearly 80 weight percent; matrix glasses from tephra and flow-deposit clasts span a similar range (fig. 11). All groundmass glass analyses represent melt that has evolved significantly away from the bulk rock compositions, reflecting the relatively crystal-rich nature of the 2006 eruption products. Within this range, however, the groundmass glass compositions show more than one simple trend, as a function of lithology and timing of deposition.

On an SiO_2-K_2O variation diagram, low-silica andesite scoria glasses from the explosive phase form a linear but discontinuous trend that includes dacitic (66 to 73 weight percent SiO_2) and rhyolitic (76 to 78 weight percent SiO_2) compositions (fig. 11). These glasses show a trend of steadily increasing K_2O with SiO_2, from ~1.5 to 3.0 weight percent K_2O between 66 and 78 weight percent SiO_2. Although "normal" groundmass glass within the low-silica andesite clasts shows a gap between 74 and 76.6 weight percent SiO_2, glass pools from within a plagioclase-rich clot in the LSAS span this range and fall along the same trend as other LSAS glasses. Dense low-silica andesite clasts have glass compositions similar to the low-silica end of the LSAS range.

Glasses from HSA clasts and the lighter portions of banded clasts all form a tight cluster on variation diagrams, with most of these glasses ranging from 74 to 77 weight percent SiO_2. Interestingly, these glasses have 1.5 to 2.6 weight percent K_2O, and fall slightly below the trend found in the low-silica andesite groundmass glass analyses (fig. 11). For other oxides, higher silica clasts generally fall along the same trend as the lower silica lithologies (not shown). The compositions of this group of samples do not vary with eruptive phase (table 4).

The few glass analyses from dense intermediate andesite clasts either fall into the low-silica end of the LSAS trend or in the HSA-dominated cluster.

The single low-K HSA clast contains rhyolitic glass with correspondingly low K_2O, from 1.1 to 1.6 weight percent (fig. 11). This sample also has the most silica-rich glasses analyzed, ranging from 76.7 to 79.7 weight percent. These glasses are not obviously different from other 2006 glasses in the abundances of other oxides. Groundmass glass from two fine-grained gabbroic inclusions trend toward these low values of K_2O, and partially overlap with HSA glasses (fig. 11).

Glass analyses from a distal tephra sample collected from an early explosion on January 13, 2006, follow the same trend as LSAS clasts. Lapilli clast samples from proximal tephras emplaced on January 13 through 17 were sorted according to lithologies assigned to flow samples (Wallace and others, this volume); glasses from these clasts fall along the same compositional trends as those from flow-deposit clasts (appendix 4).

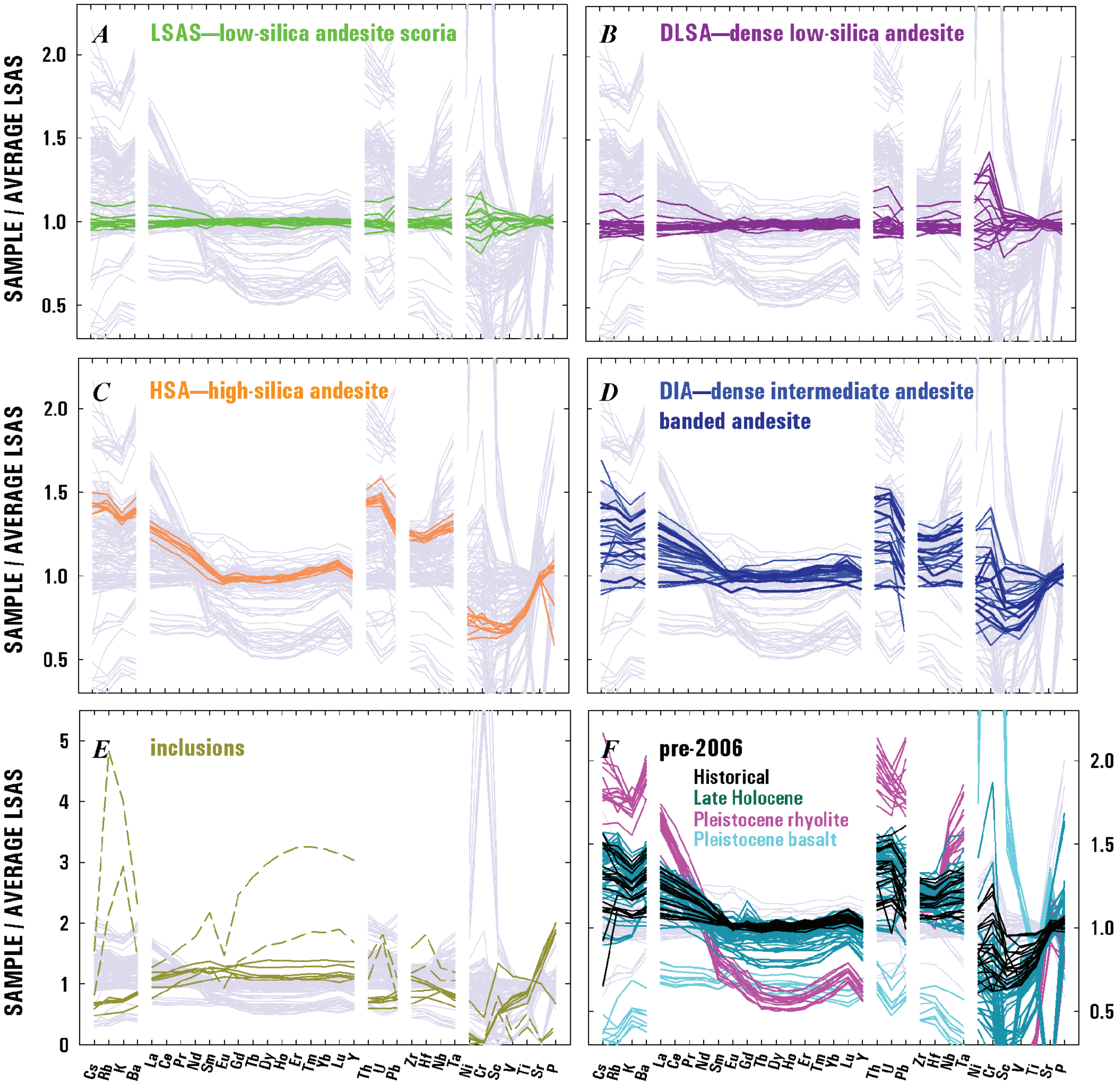

Figure 10. Incompatible-element variation diagrams showing trace-element abundances for 2006 and pre-2006 Augustine samples, normalized to the average composition of 2006 low-silica andesite scoria. Thin gray lines show the entire suite of measurements, and the colored lines in each panel show data highlighted for individual lithologies and ages. *A*, Low-silica andesite scoria. *B*, Dense low-silica andesite. *C*, High-silica andesite. *D*, Dense intermediate andesite and banded. *E*, Fine-grained gabbroic inclusions and low-K high-silica andesite (solid lines), and quartz-rich inclusions (dashed lines). *F*, Pre-2006 Augustine samples. Data are from this study, C. Nye and J. Begét (unpublished), and K. Wallace (unpublished).

Plagioclase

Plagioclase is the dominant mineral phase in the major lithologies with 24 to 32 volume percent phenocrysts and as much as 47 volume percent microlites in the groundmass (fig. 4; table 2). Phenocrysts are generally euhedral and tabular and range from 0.2 to 8.0 mm in size. In contrast, fine-grained gabbroic inclusions contain as much as 64 volume percent plagioclase. The FGGI phenocrysts have coarsely sieved interiors, showing extensive dissolution.

Five distinctive types of plagioclase phenocrysts are recognized in the major lithologies of the 2006 Augustine eruption on the basis of texture and composition. Type 1 plagioclases are texturally homogeneous, oscillatory zoned, have subtle compositional variations (fig. 12*A*), and are almost exclusively found within high-silica andesite pumices. They are optically clear with rare subtle dissolution surfaces, and contain almost no glass and mineral inclusions. Electron probe microanalysis (EPMA) profiles show fine oscillations superimposed on a weakly reverse compositional trend from An_{48} in the cores to An_{54} at the rims (fig. 12*A*). Type 2 plagioclases are oscillatory-zoned, with as much as 20 mole percent anorthite compositional variations across the zones (fig. 12*B*). Despite textural similarity to Type 1, Type 2 phenocrysts are characterized by larger chemical variations. Their EPMA profiles show abrupt jumps in An content corresponding to calcic zones at major dissolution surfaces. Each jump shows the same asymmetrical rim-ward pattern: an An_{48-54} plateau truncated by a dissolution surface, a sudden increase in An content as much as 80 mole percent, and a gradual return to the An_{48-54} plateau. Isolated glass inclusions and acicular microlites of ortho- and clinopyroxene are also abundant near dissolution surfaces. Large phenocrysts usually contain 2-3 major dissolution surfaces and associated jumps in An content. Type 2 plagioclases are present in all lithologies, although they are more common in high-silica andesite as compared to more mafic products of the 2006 eruption. Type 3 plagioclases are sub- to anhedral and are made up of oscillatory-zoned cores, surrounded by An_{70-90} rims with a distinctive texture formed by a network of profuse, interconnected inclusions of glass and microlites, commonly referred to as resorption rims, sieved texture, or "dusty zones" (Browne and others, 2006; Nakamura and Shimikata, 1998; Tsuchiyama, 1985). Type 3 cores are typically similar to those of Types 1 and 2, though larger Type 3 crystals may have more calcic cores. The resorption rims have the same principle characteristics as the calcic zones in Type 2 plagioclases, but they have higher An content (as much as 90 mole percent), more inclusions and are greater in width (fig. 12*C*). The proportions of glass and mineral inclusions in the resorption rims decrease conspicuously toward the boundary with the groundmass. Interestingly, glass inclusions

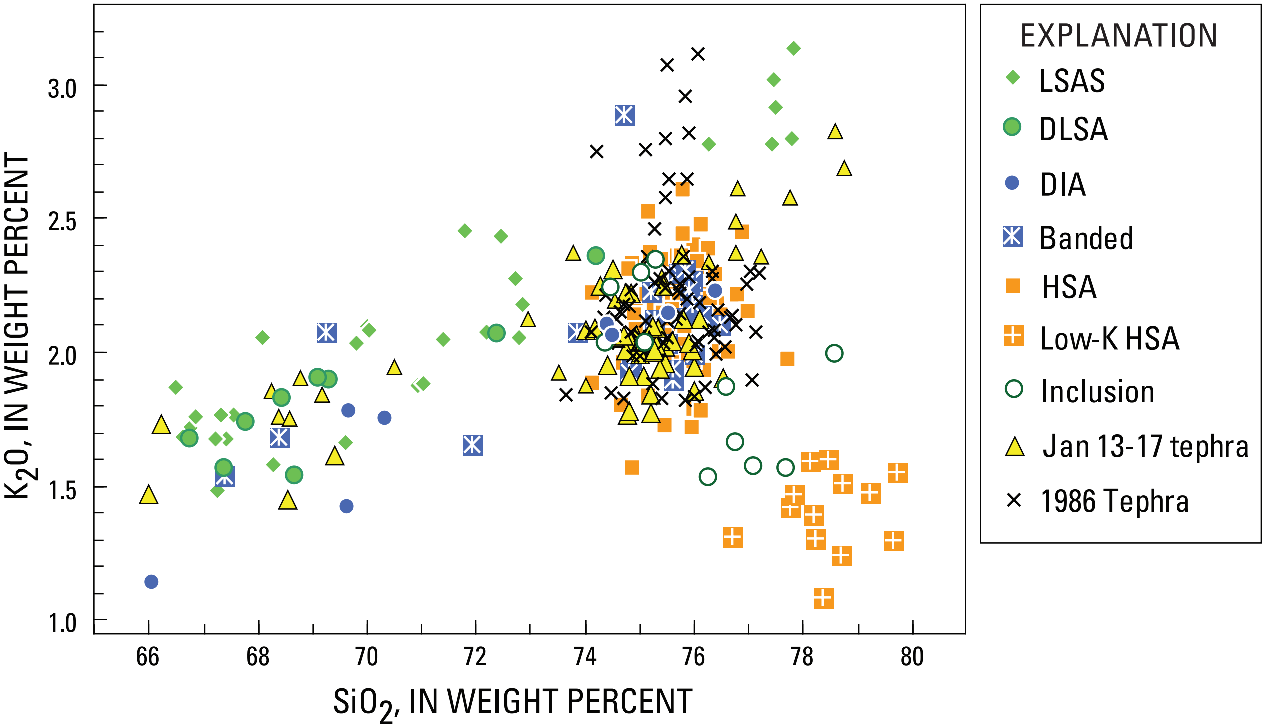

Figure 11. Groundmass-glass analyses from the Augustine 2006 lithologies, compared with select analyses from 2006 tephra fall deposits from the January 13–14 and January 17 explosions. Also plotted for comparison are analyses from 1986 tephras (P. Izbekov, unpublished data).

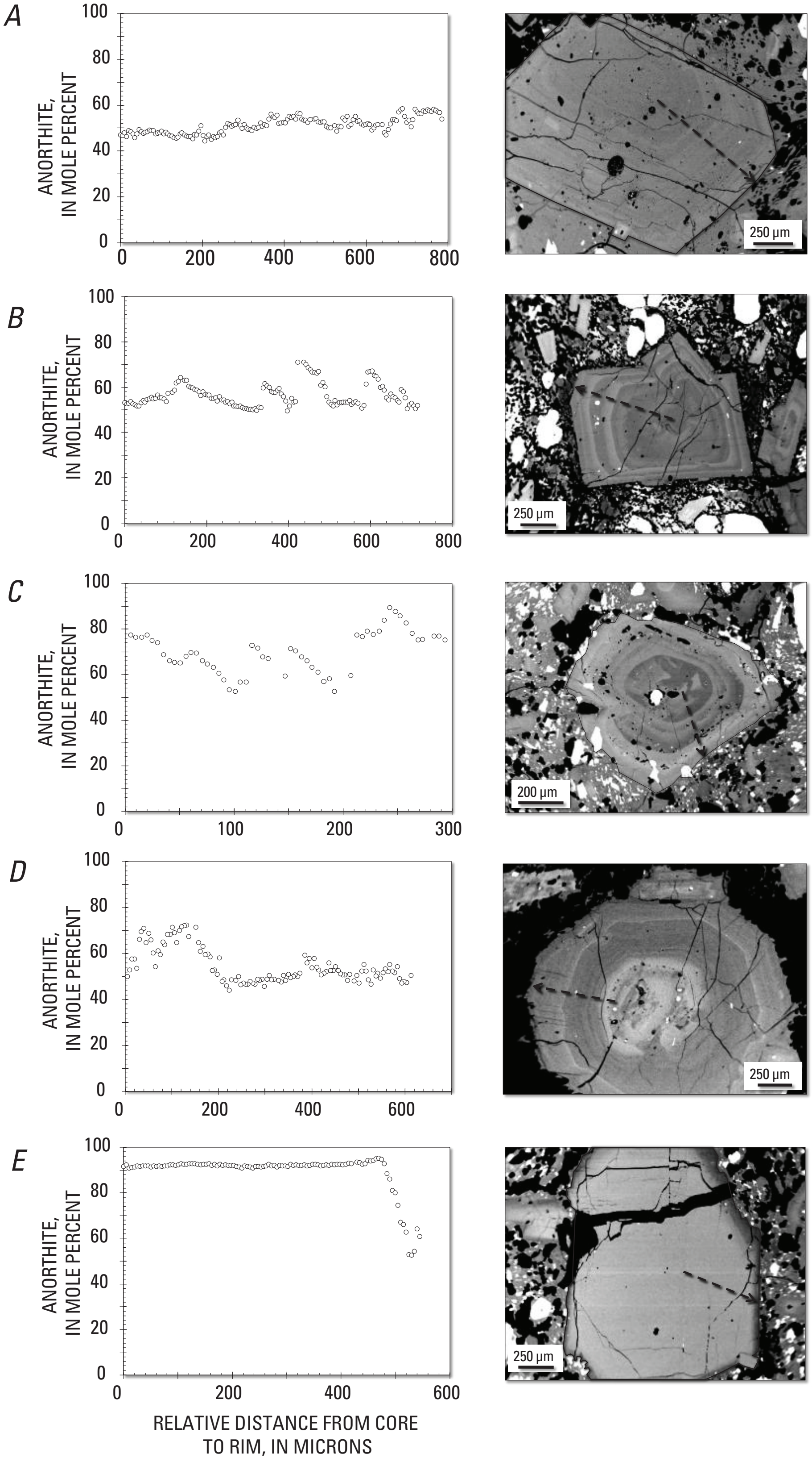

Figure 12. Back-scattered electron (BSE) images and corresponding profiles showing anorthite content of five major plagioclase phenocryst types identified in 2006 eruption deposits.

in the resorption rims are often vesicular. Type 3 plagioclases are present in all lithologies, although in high-silica andesite the resorption rim is surrounded by an oscillatory-zoned rim 10-150 microns wide, whereas in low-silica andesites the resorption rim contacts groundmass, with $An_{65\text{-}75}$ composition at the contact. Type 4 plagioclases are compositionally and texturally heterogeneous, with calcic cores surrounded by oscillatory-zoned rims (fig. 12*D*). The cores commonly contain inclusions of glass and microlites, as well as patches of $An_{48\text{-}54}$ plagioclase. The composition of cores reaches An_{90} and overlaps with the composition of resorption rims in Type 3 plagioclases. Type 4 plagioclase crystals have oscillatory rims that overlap in composition with Type 1 phenocrysts. Type 4 plagioclases are found predominantly in high-silica andesite. Type 5 plagioclase phenocrysts consist of euhedral, compositionally and texturally homogeneous $An_{92\text{-}94}$ cores surrounded by oscillatory-zoned rims (fig. 12*E*). Type 5 plagioclases are rare, but found in all lithologies. Widths of the outermost oscillatory-zoned rims in high-silica andesites often exceed 150 to 200 micron, whereas in low-silica andesites they are significantly narrower (20–30 microns).

All major lithologies are characterized by similar ranges of phenocryst compositions of $An_{45\text{-}90}$, with a primary mode at ~An_{54} (fig. 13). The second mode at >90 mole percent in compositions of DLSA phenocrysts is due to the large number of Type 5 plagioclase analyses (fig. 13*D*). Plagioclase microlites have the same composition as the outermost rims of phenocrysts in all lithologies. Composition of microlites in HSA and DIA are nearly the same ($An_{50\text{-}54}$ and $An_{50\text{-}55}$, respectively) and overlap with the composition of the Type 1 phenocrysts. Compositions of microlites in LSAS and DLSA are $An_{57\text{-}73}$ and $An_{64\text{-}77}$, respectively, which both overlap considerably with the composition of calcic zones in Type 2 plagioclases, as well as of resorption rims in Type 3 plagioclases. Textural and compositional characteristics of plagioclases from products of the 2006 eruption are the same as those in products of 1964, 1976, and 1986 eruptions. For example, Type 2 oscillatory-zoned plagioclases from all four eruptions show impressive similarity of their EPMA profiles characterized by the "plateau" composition at $An_{48\text{-}54}$ (fig. 14).

Pyroxenes

Although both are present in all lithologies, clinopyroxene (average 5.6 volume percent) is slightly more abundant than orthopyroxene (4.7 volume percent on average; fig. 4, table 2). Pyroxene phenocrysts are generally unzoned, although orthopyroxene is often rimmed with clinopyroxene, which is particularly common in LSA lithologies. Orthopyroxene phenocrysts from all lithologies have an average composition of $Wo_2En_{65}Fs_{32}$ (fig. 15, table 5). High-Ca pyroxene phenocrysts are predominantly augite to diopside, with an average composition $Wo_{44}En_{41}Fs_{14}$. Pyroxene phenocrysts are typically tabular and less than 1 mm in length, but some phenocrysts as large as 5 mm were observed, especially in low-silica andesites.

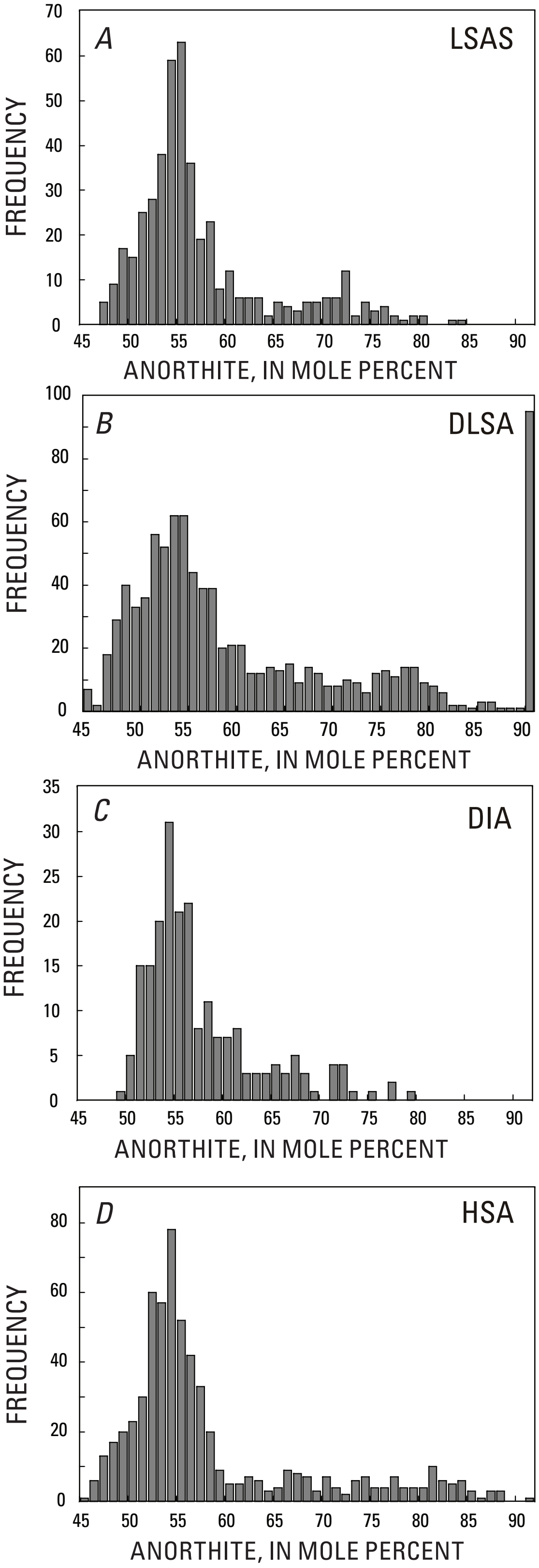

Figure 13. Histograms showing frequency versus anorthite content for spot analyses on plagioclase phenocrysts from the four major lithologies in 2006 eruption deposits. Abbreviations as in figure 4.

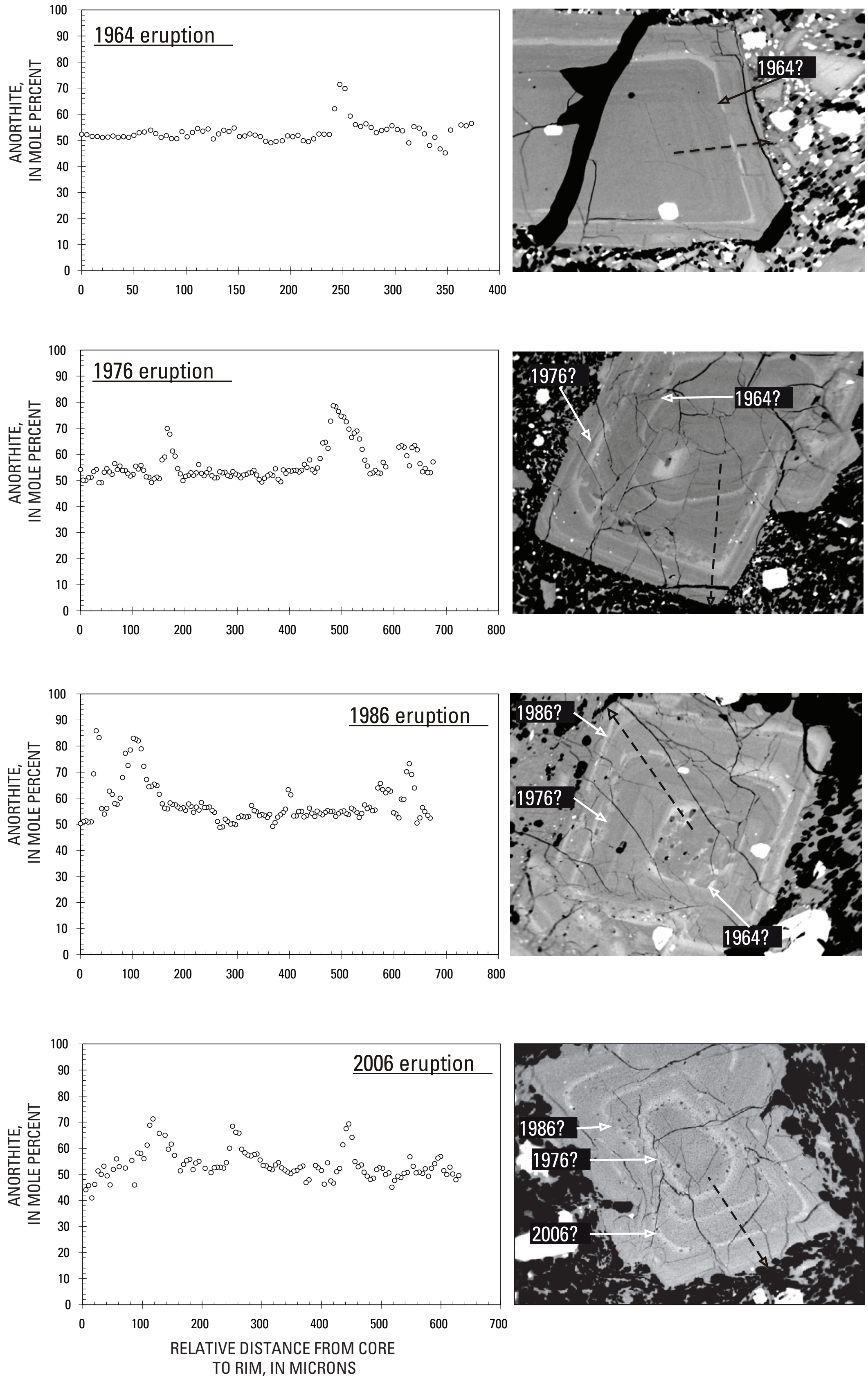

Figure 14. Back-scattered electron (BSE) images and anorthite-content profiles for representative plagioclase phenocrysts from the last four Augustine eruptions.

Orthopyroxene and clinopyroxene are both present in the 2006 deposits as microlites in the groundmass, and orthopyroxene is found in reaction rims on olivine. The compositions of the groundmass and rim pyroxenes are the same as the phenocrysts (fig. 15). Mg numbers range from 0.67 to 0.74 for orthopyroxene and 0.73 to 0.85 for clinopyroxene.

Fe-Ti Oxides and Geothermometry

All lithologies contain Fe-Ti oxides both in the groundmass and as inclusions in phenocrysts and reaction rims. Chromite is also present as inclusions in olivine phenocrysts. Fe-Ti oxides in the groundmass are commonly euhedral, less than 30 microns in width, and the pairs analyzed for this study are unzoned; often ilmenite and magnetite are present as touching pairs (fig. 16). Oxides present as inclusions in other minerals are almost always anhedral and are as large as 1 mm. DLSA clasts contain predominantly titanomagnetite, which often exhibits ilmenite exsolution lamellae. Ilmenite phenocrysts are rare in this lithology. The other lithologies also contain predominantly titanomagnetite, yet have more abundant ilmenite than DLSA.

Touching pairs in grain mounts used for geothermometry were groundmass grains as opposed to anhedral grains found as mineral inclusions. The f_{O_2} recorded by oxide pairs in 2006 Augustine magmas is approximately 2 log units above the Ni-NiO buffer (NNO), roughly equivalent to the rhenium-rhenium oxide (RRO) buffer (fig. 17). In investigating Mount Pinatubo magma, Rutherford and Devine (1996) experimentally confirmed that the QUILF algorithm overestimates temperatures by 30±5°C in magma with f_{O_2} near RRO

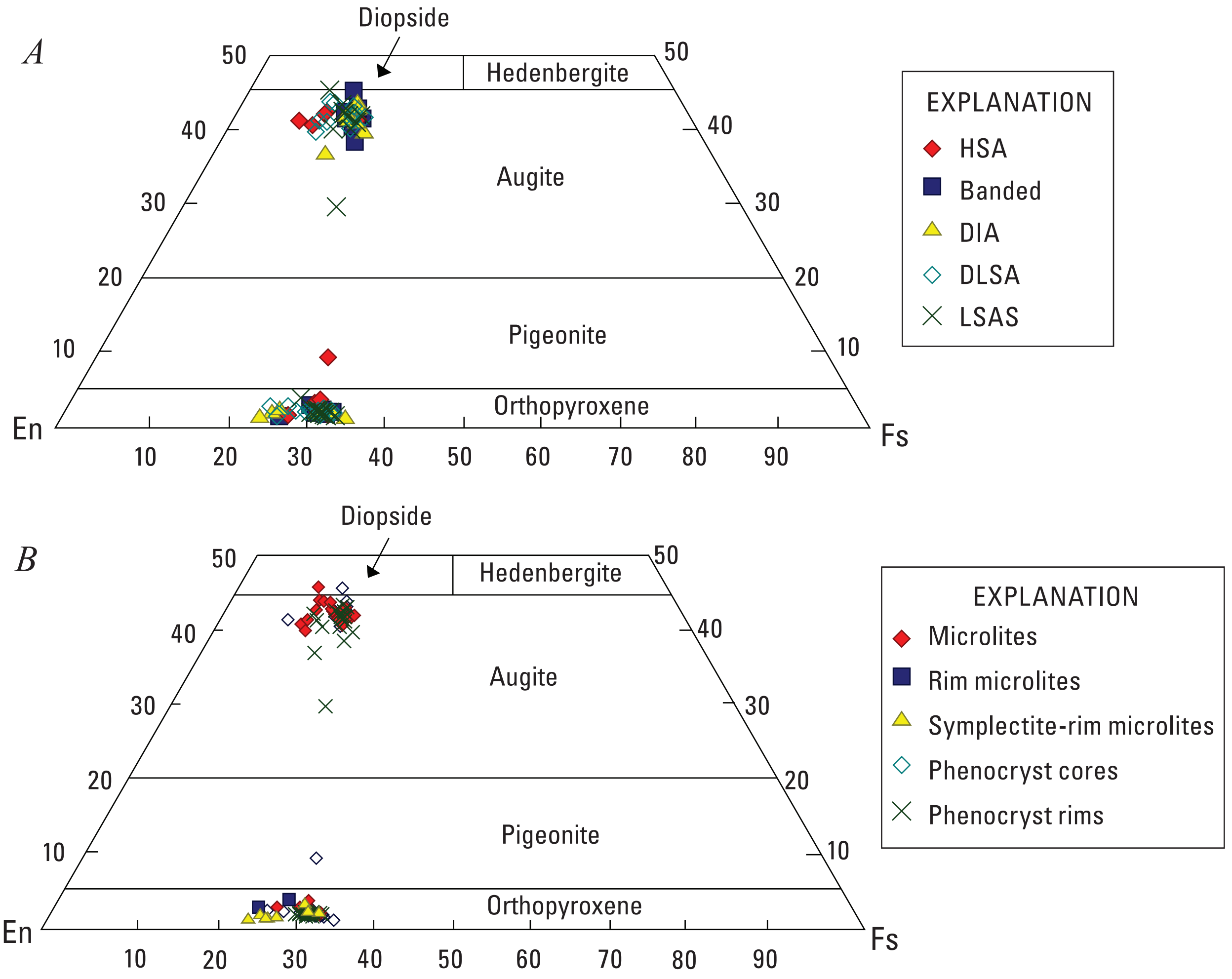

Figure 15. Classification diagram for pyroxene phenocrysts and microlites from the 2006 Augustine eruption. The apices of the ternary diagram represent 100 mol % of each pyroxene component as follows: En-enstatite, Fs-ferrosilite, and the top apex (not shown) represents wollastonite (Wo). Symbols represent single point analyses from rim and core of individual phenocrysts. Abbreviation of lithologic types as in figure 4: *A*, Pyroxenes sorted by lithology. *B*, Pyroxenes sorted by type. Rim pyroxene indicates pyroxenes found in the pyroxene-rimmed olivines. Symplectite pyroxene indicates pyroxenes found either in a symplectic olivine reaction rim or a symplectic pseudomorph.

because this is outside the limits of the calibration of Andersen and others (1993). Calculating the temperatures using other geothermometer algorithms (for example, Ghiorso and Evans, 2008), regardless of the method used to estimate the mol fractions of ulvospinel and ilmenite (for example, Stormer, 1983), all result in overestimations of the temperature, relative to the findings of Rutherford and Devine (1996). Thus, the temperature estimates included here have been decreased by 30°C from the original QUILF estimate.

Results using the QUILF algorithm (Andersen and others, 1993) indicate that LSAS was erupted at temperatures from 825 to 968°C (average of 904°C, one standard deviation of 47°C, n = 12) and HSA from 811 to 868°C (average of 838°C, one standard deviation of 14°C, n = 20; table 6 and fig. 17). Oxide pairs from banded and DIA clasts yield temperatures from 819 to 840°C and 829 to 853°C, respectively. A single oxide pair from a dense low-silica andesite sample yielded a temperature of 920°C. Oxide temperatures are consistent within each lithology type, but the HSA, banded, and DIA show a narrower range of temperatures, which are generally lower than those estimated for the low-silica andesites.

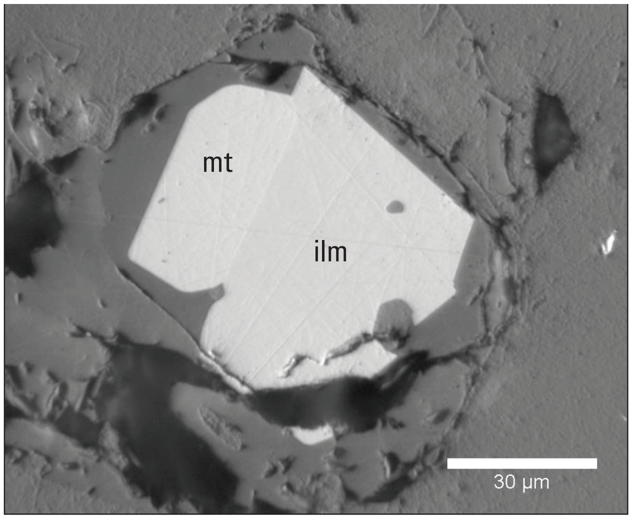

Figure 16. Back-scattered electron image of touching magnetite-ilmenite pair separated from groundmass of high-silica andesite sample 06AUMLC004c1.

Olivine

Olivine phenocrysts are present in all lithologies but are most abundant in the low-silica andesites, with 1.3 volume percent in DLSA and 1.0 volume percent in LSAS samples (fig. 4; table 2).

There are four main textural variations in the olivine phenocrysts. Type 1 are sub–to euhedral phenocrysts with no reaction rims (fig. 18*A*). They have core compositions that average 84 mole percent forsterite component (Fo_{84}) and are unzoned except for 5-10 micron, Fe-enriched (Fo_{73}) rims (table 7).

Type 2 olivines are sub- to anhedral phenocrysts that are resorbed and usually have thin (< 50 microns) reaction rims composed of orthopyroxene microlites (fig. 18*B*). Type 2 olivines are generally unzoned and have an average composition of Fo_{84}.

Type 3 olivines are subhedral with rims that consist of two concentric zones (fig. 18*C*). Inner rims can be as much as 500 microns thick, but average ~100 microns, and consist of fine-grained intergrowths of orthopyroxene and magnetite, commonly called a symplectite. This portion of the rim appears opaque in transmitted light, but the intergrowth texture is clearly visible in BSE images and x-ray maps. Outer rims are 50 microns thick, on average, and consist of orthopyroxene microlites. Some symplectite pseudomorphs after olivine are also present, and these are surrounded by orthopyroxene rims (fig. 18*D*). Orthopyroxenes in all rims have an average composition of $Wo_2En_{70}Fs_{28}$ (table 5), similar to the compositions of the phenocrysts and microlites. The titanomagnetite in the symplectite rims has approximately the same FeO, Al_2O_3, MnO, and MgO content and generally less TiO_2 and more Cr_2O_3 than in the titanomagnetite phenocrysts (table 6). Large (>600 micron) Type 3 olivines are normally zoned, with core compositions of ~Fo_{84} and rim compositions of ~Fo_{74}. Smaller Type 3 olivine crystals (<300 micron) are unzoned and have compositions that average Fo_{74}. Although HSA samples have the lowest percentages of olivine, those that are present are mostly Type 3.

Type 4 olivines are characterized by hopper and swallowtail habits (fig. 18*E* and 18*F*). They are often rimmed by thin jackets of orthopyroxene and occasionally by symplectite. Type 4 olivines are generally unzoned and have an average composition of Fo_{84}. They are most common in DLSA.

Amphibole

Amphibole is rare in all major lithologies and is unevenly distributed among different samples, with several grains in some thin sections and none in others, even within a single lithology. Rare amphibole phenocrysts in the low-silica and intermediate andesites have average lengths of 350 microns, are anhedral, and are typically surrounded by fine-grained reaction rims 40 to 100 microns thick (fig. 19*A*), composed of plagioclase, orthopyroxene, and oxides. In addition, pseudomorphs of amphibole, with the same mineralogy and texture as the reaction rims, are found in these lithologies, suggesting that amphiboles were once more abundant. Amphibole phenocrysts found in HSA clasts are sub- to euhedral, rarely surrounded by reaction rims, and larger than those in the more mafic rocks, with average lengths of ~600 microns (fig. 19*B*). Fine-grained gabbroic inclusions contain the highest modal abundances of amphibole, ranging to 10 volume percent. Amphiboles in this lithology are 0.6 to 2 mm in size, subhedral to anhedral, with plentiful reentrants and melt or plagioclase inclusions (fig. 19*C*). Analysis of a handful of grains from all lithologies yields compositions that straddle divisions between edenite, pargasite, hornblende, and tschermakite (table 8).

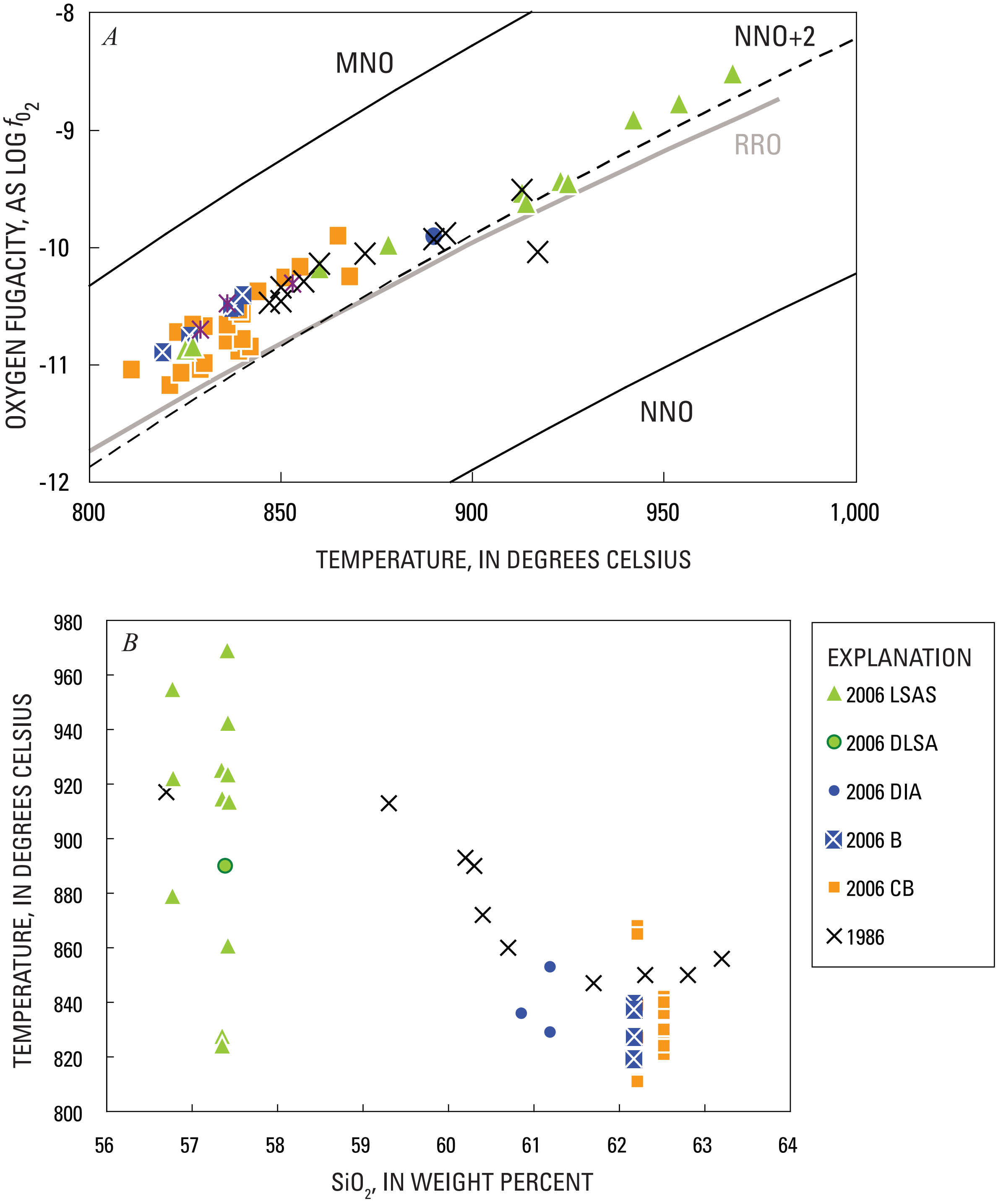

Figure 17. Temperature-composition relations of Augustine magmas and eruption products. *A*, Temperature and f_{O_2} for Augustine magmas as estimated from Fe-Ti oxide pairs. Rhenium-rhenium oxide (RRO) buffer was calculated using Pownceby and O'Neill's (1994) equation calibrated from 850-1250 K. *B*, Whole-rock SiO_2 content versus temperature. Abbreviations as in figure 4. 1986 data are taken from Roman and others (2005) and are averages of sample sets representing various rock types erupted during the explosive phase of the 1986 eruption. Temperature and oxygen fugacity for 2006 and 1986 samples calculated using QUILF (Andersen and others, 1993), with temperatures subsequently decreased by 30°C to account for overestimation at high oxygen fugacity (Rutherford and Devine, 1996).

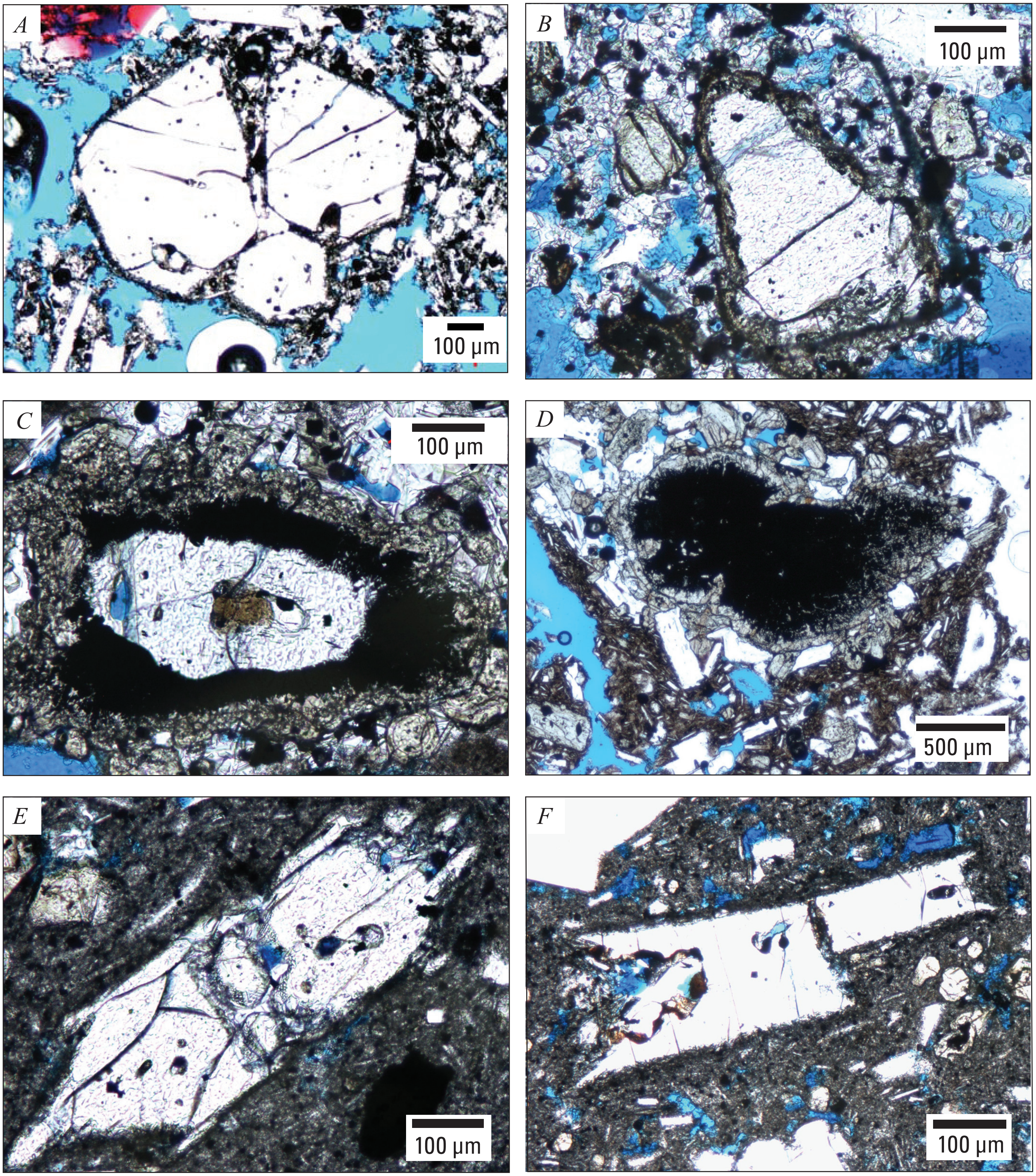

Figure 18. Olivine textures found in Augustine 2006 eruption deposits. All images are transmitted-light photomicrographs. *A*, Euhedral, unrimmed olivine from sample 06AUMC008a. *B*, Anhedral, pyroxene-rimmed olivine from sample 06AUKB002a. *C*, Symplectite-rimmed olivine from sample 06AUKB003. *D,* Symplectite olivine pseudomorph from sample 06AUMC008b.p3. *E*, Hopper olivine from sample 06AUKB003. *F,* Hopper olivine from sample 06AUMC005c.p3.

Accessory Minerals

Apatite is present throughout all lithologies, with the LSAand HSA containing greater modal abundances and the fine-grained gabbroic inclusions notably less (appendix 1). It consists of fine, needle-shaped crystals that are slightly green in plane polarized light. Crystals range in size from 6 to 200 microns and are most commonly found within larger plagioclase and clinopyroxene crystals, although some samples show fine apatite needles within the groundmass as well. Apatite inclusions are present in plagioclase with all textures, including "clean," melt-inclusion-rich, and coarsely sieved. Apatite needles in plagioclase, although not possessing a discernible orientation, preferentially occupy one or more oscillating zones within the plagioclase.

Anhydrite is a rare accessory mineral in these samples and is only found in a handful of thin sections and only within the banded, low-silica andesite scoria and fine-grained gabbroic intrusive lithologies. It is more abundant in the fine-grained gabbroic inclusions, but is still rare, with each thin section having only a couple of anhydrite crystals. Anhydrite was not found in samples collected after May 2006, but this is probably because of the extreme scarcity of anhydrite crystals and not a result of a change in crystal distribution. Primary

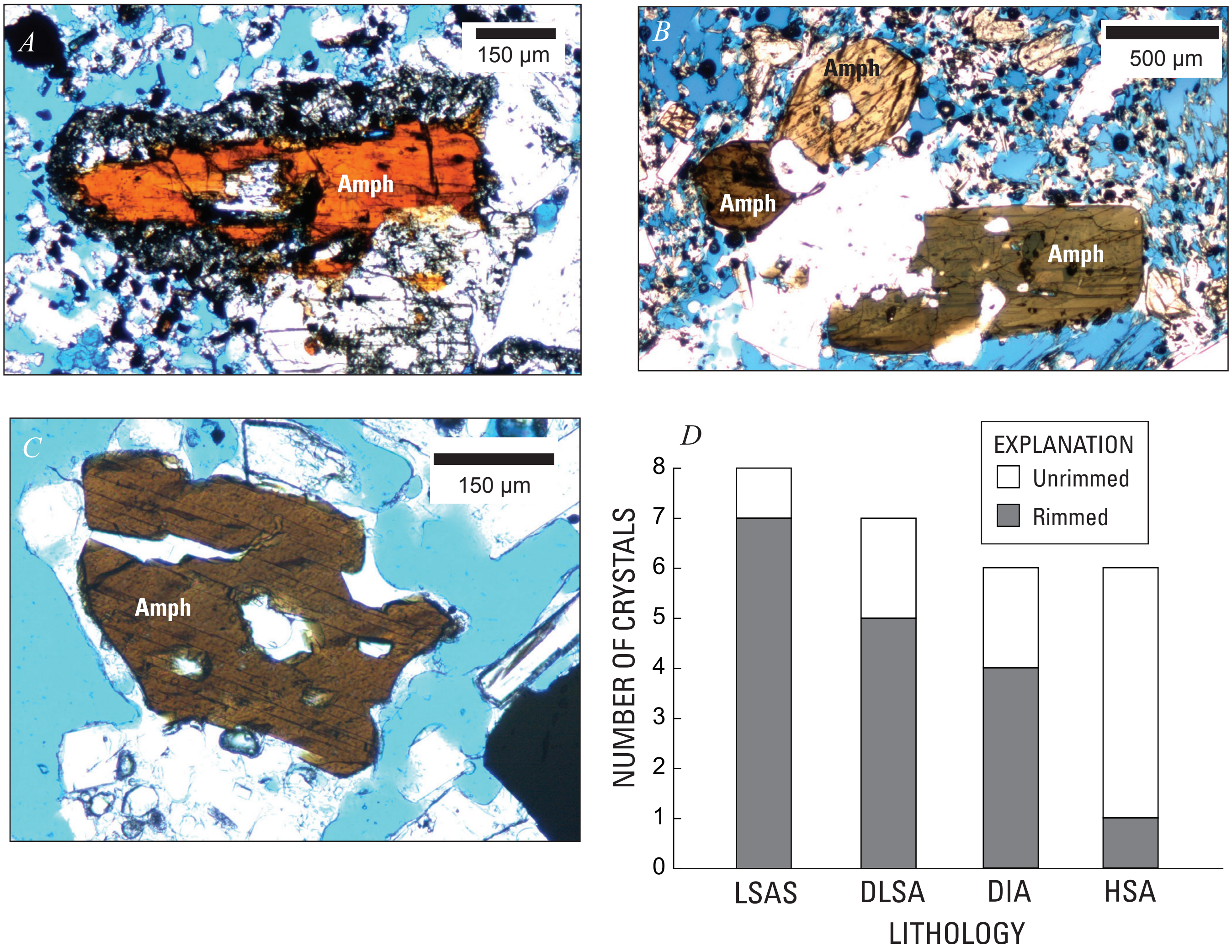

Figure 19. Transmitted-light photomicrographs and histogram of amphibole phenocrysts found in Augustine 2006 eruption deposits. *A*, Fine-grained reaction rim around amphibole phenocryst in DIA sample 06AUKB002a, collected from effusive-phase block-and-ash-flow deposit. *B*, Cluster of unrimmed, euhedral amphiboles from high-silica andesite sample 06AUMC004c, collected from Rocky Point pyroclastic-flow deposit. *C*, Resorbed phenocryst from gabbroic-inclusion sample 06AUMC013a, collected from effusive-phase block-and-ash-flow deposit. *D*, Histogram showing occurrence of rimmed and unrimmed amphibole in samples from the major lithologies of the 2006 eruption. Abbreviations are as in figure 4.

anhydrite crystals range from 200 to 600 microns long, are subrounded, and have a thin, dark-colored, fine-grained rim.

Discussion

Source and Origin of Erupted Magmas

The dominant geochemical signature of the 2006 Augustine magmas lies in the linear array of major oxides and trace elements, which is consistent with two-component magma mixing (figs. 7 to 10). The trends observed in the 2006 deposits mirror closely those observed from the historical Augustine eruptions and a significant proportion of Holocene magmas as well. The simplest explanation is that two-component mixing between the low-silica and high-silica andesites before and during the 2006 eruption creates the tight linear array in major and trace elements. However, complexities in petrogenesis of the LSA and HSA endmembers exist, and these will be discussed below.

High-Silica Andesite—Reinvigorated Resident of Shallow-Crustal Body

Several lines of evidence help place constraints on HSA storage conditions. Fe-Ti oxide geothermometry indicates that the high-silica andesite was stored at 838±14°C before eruption. Petrological results, including melt inclusion analyses (Webster and others, this volume), indicate that the HSA was stored at a depth of approximately 4 to 6 km below the surface. The presence of amphibole phenocrysts indicates that the magma resided at a depth equivalent to water pressures above amphibole stability. While the stability of amphibole has not been experimentally determined for this particular composition, we can look to other experimental studies on similar whole-rock compositions for comparison. Phase equilibrium experiments showed that amphibole was stable in the andesite (63.4 weight percent SiO_2) erupted in 1989–90 from Redoubt Volcano at pressures above 100 MPa from 850 to 875°C (Browne and Gardner, 2006). This is equivalent to depths equal to or greater than 3 to 4 km. The maximum dissolved water concentration measured in melt inclusions within high-silica andesite pyroxenes was 4 weight percent (with CO_2 below detection), equivalent to a pressure of 100 MPa (Webster and others, this volume).

Geophysical signals associated with the 2006 eruption are consistent with petrologic findings. Approximately 20 earthquakes, which occurred after the eruption in 2006 ended, were located beneath the summit at a depth of 4 km (Power and Lalla, this volume). One explanation for these post eruption events is that they occurred in response to pressure reduction after magma withdrawal and eruption from this depth. The majority of the high-silica andesite was erupted during the continuous phase, temporally coincident with a marked deflationary signal seen in the geodetic data. This signal has been modeled as being the result of a pressure decrease of a cylindrical body whose top is approximately 5 km below the surface (Cervelli and others, this volume).

It is likely that the HSA resided in this shallow-level reservoir for decades prior to eruption. The composition and phase assemblage of the 2006 high-silica andesite closely resemble those of the silicic end member of the 1976 and 1986 eruptions. For example, equilibrium plagioclase compositions in the host magma remained the same throughout the four most recent eruptions (1964, 1976, 1986, and 2006). This indicates relatively constant melt composition, temperature, and water pressure in the shallow-level host reservoir since at least 1964. For example, Type 2 oscillatory-zoned plagioclases from all four eruptions show impressive similarity of their EPMA profiles characterized by the “plateau” composition at An_{48-54} (fig. 14). Increasing numbers of high-An “spikes” with each subsequent eruption suggest that some individual crystals may record multiple recharge events linked to these eruptions. Despite evidence for repeated recharge and magma mixing during each of these eruptions, the host magma has not changed significantly in composition. Also, the HSA phenocryst assemblage (table 2) shows less evidence of reaction and disequilibrium than the mixed, intermediate, and low-silica andesites. For example, fewer than than 10 percent of HSA plagioclases show visible resorption. This implies that if the shallow reservoir persists as a convecting liquid + crystal magma, then its volume must be large relative to newly arriving magma. On the other hand, if it persists as a largely solid crystal mush, then it is possible that during each eruption newly arrived magma “carves off” and mixes with only a portion of the mush.

Although the majority of chemical variations within the 2006 sample suite reflect two-component mixing, there is some deviation from the mixing trend for some trace elements, particularly the LREE. The 2006 HSA samples that diverge most from the mixing trend were erupted during the explosive phase and have LREE compositions similar to prehistoric Holocene lavas. They also diverge in composition from the pre-2006 historical lavas, which are similar to the majority of the 2006 lavas. If this difference is not simply an artifact of a limited dataset, then some of the HSA may be remobilized from a portion of the subvolcanic system, which is at least hundreds of years old. If material this old was erupted, we expect that it represents remobilized crystal mush and did not originate from a persistent liquid + crystal magma. This model is the best that fits both petrological and geophysical data available at this time.

Although the model for the HSA as derived from a crystal mush at 4 to 6 km fits the petrology and geophysical observations, the origins of the crystal mush itself are less well understood. It is tempting to assume that it is derived primarily by fractional crystallization of low-silica andesite remaining in the crust from previous eruptions. However, the trace-element data (fig. 9) argue against this in three ways. First, concentrations of REE heavier than Eu are the same as in the 2006 low-silica andesite. Crystallization at ~100 MPa in these andesites is dominated by plagioclase, and because REE are incompatible, plagioclase crystallization should result in increased REE concentrations in the melt. At other Aleutian volcanoes, crystallization through the andesite and dacite range produces such increases (for example, Finney and others, 2008; Jicha and Singer, 2006). Second, concentrations of other incompatible elements, such as LILE, HFSE, and HPE only increase by 30–50 percent , which is less than half of the increase in other Aleutian andesite systems. Third, Cr and Ni concentrations, although lower than in the LSA, are still much higher than almost all other Aleutian andesites (Nye and others, 2008) and too high to reflect extensive fractional crystallization. The crystals are expected to be relatively depleted in incompatible elements and enriched in compatible elements compared to their host liquids, and a mixture of mush-plus-liquid could have a bulk composition similar to these andesites. Other petrogenetic paths can be imagined, such as production of HSA much deeper, where the pyroxene/plagioclase ratio of precipitating crystals is much higher, but these are less plausible.

Low-Silica Andesite Scoria and Dense Low-Silica Andesite—Similar Heterogeneous Hybrid Magmas

The two low-silica andesites are very similar in terms of bulk-rock composition, mineralogy, and mineral texture, and for most elements form a tight geochemical group that anchors the mafic end of the mixing array that is the dominant geochemical feature of 2006 lavas. LSAS and DLSA both contain reacted crystals, and plagioclase shows the largest degrees of disequilibrium, with roughly 30 percent of plagioclase phenocrysts in the LSA having sieved textures typical of Type 3 plagioclases described above. Elsewhere in 2006 ejecta, these plagioclase phenocrysts are in apparent textural equilibrium only in the HSA samples. Equilibrium plagioclase in the low-silica andesites have An-rich cores and less calcic rims. The composition of microlites and outermost rims of phenocrysts varies from An_{57} to An_{77}, correlating with the large variability of matrix glass compositions (fig. 11). Most likely this is due to rapid crystallization in response to two simultaneous syneruptive processes: (1) decompression (degassing) crystallization and (2) assimilation of the colder host magma.

An important feature of the LSAS erupted in 2006 is the presence of chromite-bearing Fo_{84} olivine and $An_{92\text{-}94}$ plagioclase crystals. In combination with the strongly reacted plagioclase, those phases likely represent xenocrysts. Thus, the LSAS and DLSA are interpreted to be hybrid magmas, with strongly reacted plagioclase crystals representing xenocrysts derived from the LSA and with chromite-bearing olivine crystals and anorthite derived from a more mafic cryptic magma.

The range in temperatures recorded by Fe-Ti oxide microlites in the low-silica andesite scoria is consistent with a mixing origin for this magma. Temperatures range from 825°C, the temperature for the high-silica andesite body, to as high as ~970°C. Because small, unzoned groundmass crystals recorded these temperatures, we interpret the large temperature range to reflect postmixing conditions in the hybrid low-silica andesite magma. These grains either grew during or after mixing, or else they were small enough to undergo diffusive reequilibration. The highest temperature of 970°C may approach that of the injected, unerupted mafic end member.

The most significant, although still small, compositional differences between the dense and scoriaceous low-silica andesites are in Cr, Ni, and to a lesser extent Mg. The majority of LSAS samples, and about half of the DLSA samples have Cr concentrations of 50 to 70 ppm and fall below the dominant mixing array (fig. 9). The low-silica andesite, which anchors the mafic end of the mixing array, is dominantly DLSA and has 75 to 86 ppm Cr. The fact that many low-silica andesite samples fall below the mixing array, yet contain the signature reacted, An-poor, plagioclase crystals we infer to have been acquired during mixing, suggests that these low-Cr low-silica andesites acquired their low-Cr signatures after mixing. Point-count data are neither sufficiently precise nor numerous enough to rigorously constrain this model. However, they provide qualitative support, because the samples with the lowest whole-rock Cr have the lowest modal proportion of mafic phenocrysts and the highest Cr samples have the highest proportion. If the LSA was vertically heterogeneous as it tunneled through the HSA body (for example, Bergantz and Breidenthal, 2001), the top portion could have been relatively gas-rich and crystal-poor relative to the base, because of in-place phase segregation. The first-erupted, gas-rich and relatively crystal-poor LSA would thus have lower Cr, while the lower portion remained to further mix and degas in the HSA body and retained a higher proportion of its phenocrysts during segregation as the LSA dike tunneled through the HSA body.

Unerupted, Mafic End Member

If the low-silica andesites are hybrids, then it is axiomatic that a more mafic magma was present but did not erupt. Influxes of unerupted high-alumina basalt were also invoked to explain the spectrum of magmas erupted during the 1976 and 1986 eruptions, through mixing with a dacite to form the hybrid, low-silica andesites that were the most mafic composition erupted in both cases (Johnston, 1978; Roman and others, 2005). The most mafic magma erupted in 2006 closely resembles the low-silica andesites erupted in 1976 and 1986. We concur with the previous studies and suggest that similar processes were operating in 2006. However, no good candidates for the pure mafic mixing end member exist in the geologic record at Augustine. The only known basalt on Augustine, which erupted in the late Pleistocene, has major and trace element abundances that fall far off the mixing trend of the 2006 ejecta (figs. 7 to 10). Thus, there is no natural analog at Augustine for the replenishing basalt to use in models to constrain the proportion that hybridized to form the LSA. Projection of the 2006 trend to lower silica contents indicates overlap between potential end members and analyzed Aleutian magmas between ~49 and ~53 weight percent silica (not shown in our plots). We suggest that the mafic end member falls within this compositional range, and could perhaps be further constrained by systematic compositional analysis of plagioclase populations within the LSA.

Evidence from other eruptions also shows that the erupted mafic end member must itself be the hybrid result of mixing, such as Lassen 1915 (Clynne, 1999), Miyakejima 1983 (Kuritani and others, 2003), and Hokkaido-Komagatake 1929 (Takeuchi and Nakamura, 2001). Also, in 1996 at Karymsky Volcano in Kamchatka, basalt and andesite erupted simultaneously from two vents. The andesite contained calcic plagioclase that derived from the basalt, but no other signs of mixing, indicating that hybridization was complete and occurred within two months (Izbekov and others, 2002). A similar process at Augustine could have yielded andesite that shows little beyond xenocrysts to reveal its hybridized origin. Hildreth (2007) notes that in the Cascades basaltic lavas are rare, or unknown, at the major polygenetic centers, although common at surrounding monogenetic centers. He infers this basic observation to require that there are efficient filters, perhaps in the form of mush columns, beneath polygenetic volcanoes such as Augustine. In summary, mafic replenishing magmas that do not erupt in their pure form, without hybridization, seem to be the rule, rather than the exception.

Dense Intermediate Andesite and Banded Clasts—Products of Syneruptive Mixing

Compositions and mineral assemblages of DIA are intermediate between HSA and LSA, and discrete domains in banded clasts comprise both end members. The DIA resulted from relatively complete hybridization of the LSA and HSA, whereas banded clasts preserve macroscopic heterogeneity. Because the DIA is most prevalent in the continuous phase, it is likely that mixing was initiated just before the onset of the 2006 eruption and that during the interval between January 17 and 28 mixing between the HSA and LSA was ongoing. Presumably the mixed magma was nearly exhausted during the continuous phase because LSA was the dominant product of the effusive phase.

Fine-Grained Gabbroic and Quartz-Rich Inclusions—Chamber Rind and Frozen Interstitial Liquids?

The fine-grained gabbroic inclusions and low-K HSA samples are both low in incompatible elements (figs. 9, 10), suggesting that they are crystal residua. However, low Cr, Ni, and MgO, high Al_2O_3, and mineral modes from the point-count data all show that the inclusions are plagioclase dominated, suggesting that if they are crystal residua, they formed under conditions where plagioclase crystallization was favored over clinopyroxene. The dominance of plagioclase, coupled with the presence of amphibole, suggests crystallization at mid-crustal depths. The highly evolved, low-K matrix glasses in these lithologies indicate that perhaps any matrix melt that evolved during crystallization was stripped away and that they subsequently remelted to form the evolved, low-K glasses (fig. 11). Perhaps they represent cumulate material that was remelted/mobilized during heating and magma mixing accompanying replenishment. This agrees with Harris (1994), who recognized that magma plumbing beneath Augustine Volcano in 1986 was perhaps more complex than previous workers thought, suggesting the mixing of three distinct magmas: residual 1976 magma, newly injected mafic magma, and partially crystallized chamber ‘rind’ material.

Quartz-rich inclusions have mineralogy and trace-element abundances (fig. 10) radically different from the gabbroic inclusions and must have a different origin. They may be hypabyssal plutonic rocks entrained in and partially melted by young Augustine magmas. Subsequently, the new melt fraction crystallized upon cooling and/or transport to the surface, resulting in the vesicular, fine grained groundmass aggregate of quartz, feldspar, orthopyroxene, and glass. It is unknown from where in the subsurface plumbing system these inclusions were entrained, but their relative abundance in deposits of the continuous phase indicate that they had to have come from depths less than or equal to the high-silica andesite magma body. Differential movement between partial melts and relict crystals likely accounts for drastic alterations in bulk composition from that of the parent magma.

Magma Mixing Processes and Timing

Constraints from Plagioclase Phenocrysts

As discussed in the sections above, there is evidence that two-stage mixing took place before the 2006 eruption, creating the hybrid LSA (mixing event 1) and DIA (mixing event 2) magmas. One way to track magma mixing is through the abundant disequilibrium phenocryst textures observed in the 2006 samples. Perhaps the most complex array of disequilibrium textures is found in the plagioclase phenocrysts (table 9). Just before the mixing events, HSA magma contained Types 1, 2, and 4 plagioclase phenocrysts. Type 1 phenocrysts had uniform compositions of An_{40-50} and had grown entirely in the HSA with no evidence for disequilibrium. Type 2 plagioclases were similar, but more anorthitic spikes and associated resorption zones recorded previous rapid disequilibrium events. Type 4 phenocrysts had more calcic cores with thick overgrowths that suggested that they had been inherited from some previous, more mafic magma. The basaltic end member contained anorthitic, Type 5 plagioclase.

During mixing event 1, efficient mixing between the HSA and basalt formed the hybrid LSA. The new LSA thus contained crystals from both parents—Type 5 from the basalt

Table 9. Sources and mixing paths for plagioclase and olivine types from Augustine 2006 eruptive products.

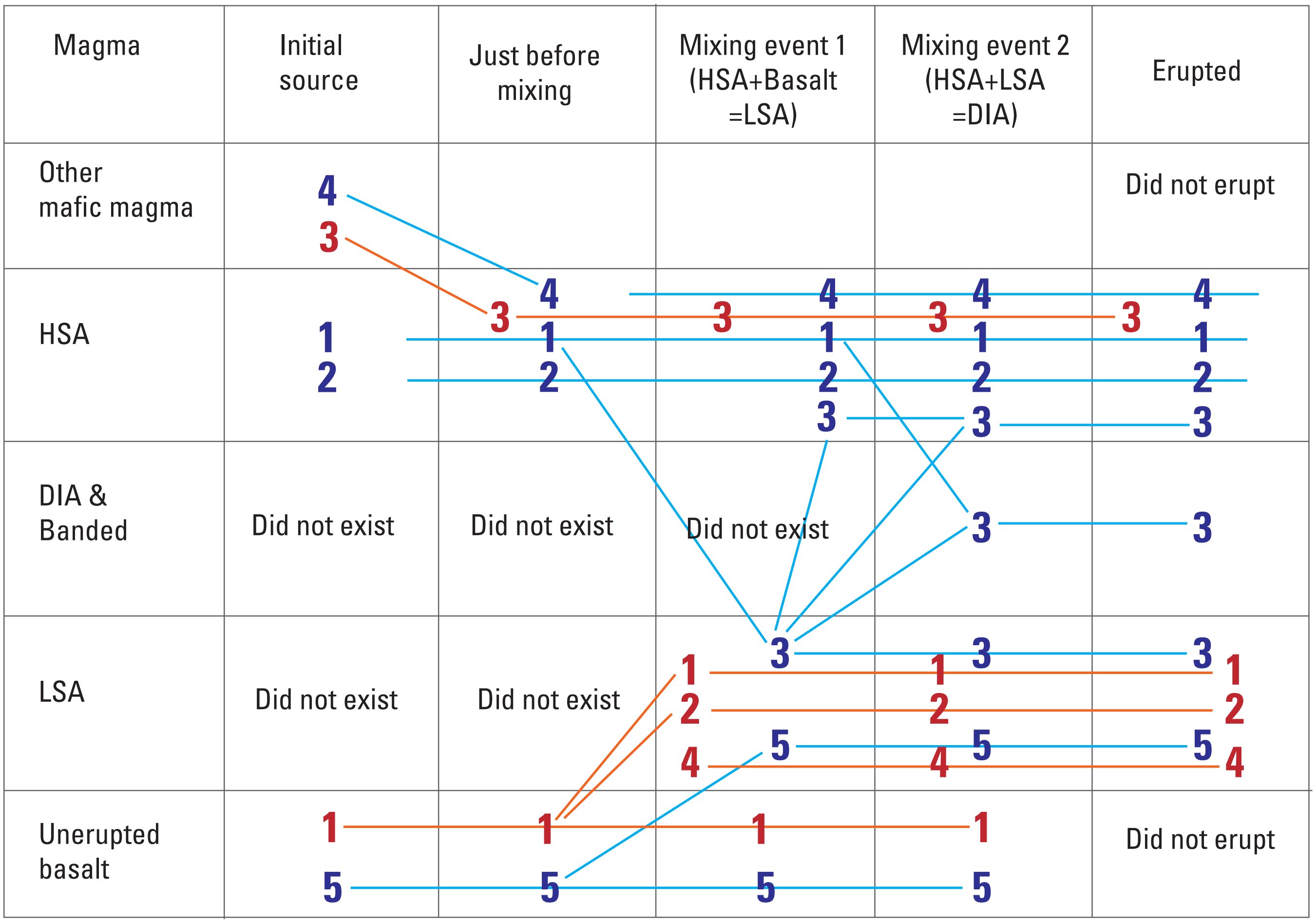

Magma	Initial source	Just before mixing	Mixing event 1 (HSA+Basalt =LSA)	Mixing event 2 (HSA+LSA =DIA)	Erupted
Other mafic magma	4 3				Did not erupt
HSA	1 2	4 3 1 2	4 3 3 1 2 3	4 3 3 1 2 3	4 3 3 1 2 3
DIA & Banded	Did not exist	Did not exist	Did not exist	3	3
LSA	Did not exist	Did not exist	3 1 2 5 4	3 1 2 5 4	3 1 2 5 4
Unerupted basalt	1 5	1 5	1 5	1 5	Did not erupt

Plagioclase

Type 1: Clean, relatively unzoned, $An_{40\text{-}50}$

Type 2: Clean, $An_{40\text{-}50}$ with spikes to An_{75}

Type 3: $An_{40\text{-}50}$ cores with dusty zones and An_{80} spikes

Type 4: An_{70} cores with unzoned $An_{40\text{-}50}$ rims

Type 5: $An_{92\text{-}94}$ cores and thin more sodic rims

Olivine

Type 1: No reaction rim, narrow zoning profile

Type 2: Thin px reaction rim

Type 3: Thick symplectite rim

Type 4: Hopper and swallowtail

and mostly Type 1 from the HSA. These Type 1 crystals, and Types 2 and 4 to a lesser extent, underwent heating and chemical disequilibrium in their new host, leading to dissolution (sieved) zones around the relatively sodic cores. These became Type 3 plagioclase. Some Type 3 plagioclase likely mixed directly back into the HSA during this time period.

During mixing event 2, high-silica andesite and low-silica andesite mixed to form DIA and banded lithologies. This likely occurred predominantly between the end of the explosive phase (January 17) and the beginning of the continuous phase (January 28). The newly formed intermediate andesite incorporated mostly Type 3 plagioclase from the LSA and Type 1 plagioclase from the HSA, the latter of which likely underwent resorption in the somewhat hotter intermediate magma, creating additional Type 3 plagioclase. During this time, some Type 3 plagioclase mixed back into the HSA, as evidenced by some Type 3 crystals with sodic overgrowths that were found in HSA samples.

The clean, sodic rims on Type 3 plagioclase can be used to estimate timing between mixing events and eruption. Rims range in thickness from 10 to 150 microns. Recent estimates of rim growth rates on anorthite seed crystals in rhyodacitic melt range from 3×10^{-10} cm/s to 60×10^{-10} cm/s (Larsen, 2005). These rates yield times of 2 to 40 days for a 10 micron rim and 30 to 560 days for a 150 micron rim. This time range likely encompasses both mixing events described above.

Olivine Reaction Rims and Magma Mixing Time Scales

Another clue about the timing of magma mixing relative to eruption may be found in olivine phenocrysts. Type 3 olivines have pyroxene-magnetite symplectite rims as much as 500 microns thick. These crystals are strongly normally zoned, with Fo_{84} cores and Fo_{74} rims. The wide zoning pattern and thick rims suggest that these have been present and reacting in their current host for long periods of time, probably years to decades (Tilman, 2008). We suggest that these crystals were inherited by the HSA from a mafic magma not related to the 2006 eruption, much like Type 4 plagioclase (table 9). Type 3 olivines are also present in samples from the 1986 eruption and were noted by Johnston (1978) in samples from the 1976 eruption, indicating residence in the HSA mush for at least 30 years. Type 2 olivines have much narrower, pyroxene-only rims and range from Fo_{87} to Fo_{80}, with much narrower zonation in the olivine towards the rim, if present. Similar thin rims of orthopyroxene have been shown to form on olivine xenocrysts when they are introduced into a more silicic magma during magma mixing events (Coombs and Gardner, 2004). Rims on Type 2 olivine in the 2006 rocks range from 10 to 40 microns. The rim growth rate calibrated by Coombs and Gardner (2004) is parabolic, and thus by squaring the average rim width, a linear rate of rim growth with time for a similar melt composition and temperature yields 1.02 micron^2/hr. Applying this rate to the Augustine olivine rims indicates that the olivine crystals were introduced into a new host 4 to 64 days before eruptive quenching. A potentially important difference between their experiments and the Augustine magmas, however, is f_{O_2}. The Coombs and Gardner (2004) experiments were run at an oxygen fugacity of ~Ni-NiO, whereas the 2006 Augustine magmas had an oxygen fugacity of closer to Re-ReO_2 (RRO). Tilman (2008) ran a series of two experiments at this f_{O_2} and obtained a faster rim growth rate. While these results are preliminary, they suggest even shorter times between mixing and eruption, of approximately 12 days for a 40 micron rim. The short duration required to form the thin pyroxene rims from the experiments indicates that they could have formed either during mixing event 1, as olivine was transferred from basalt to andesite, or during mixing event 2, as olivine passed from low-silica andesite to intermediate or high-silica andesite.

Type 4 olivines, with hopper morphologies, are extremely rare in the HSA and uncommon in the mixed and mingled banded and dense intermediate andesite samples. They are similar to hopper olivines observed in the 1976 and 1986 deposits (Harris, 1994; Johnston, 1978). Because many of the hopper grains have a resorption surface that is surrounded by pyroxene growth, the hopper olivines probably grew before mixing event 2. The hopper shape reflects rapid cooling (Faure and others, 2003), and perhaps those olivines originated during mixing event 1 as a result of cooling of the replenishing basalt when it mixed with the cooler HSA (table 9). Following this, mixing event 2 resulted in resorption and pyroxene rim formation during introduction to the HSA.

Groundmass Evolution and Amphibole Reactions During Ascent, Heating, and Cooling

Because of the extreme variations in eruptive style and flux between the three phases of the 2006 eruption (Coombs and others, this volume), one might expect the eruptive products to reflect variations in ascent rate as well. Each discrete Vulcanian blast of the explosive phase was the result of sudden conduit depressurization, emptying the conduit catastrophically of roughly 2×10^6 m^3 of magma until equilibrium was reestablished (Coombs and others, this volume). The continuous phase saw steady ascent of magma from ~5 km depth to the surface. Magma that fed the lava flows of the effusive phase was presumably more degassed and ascended more slowly. Many recent studies have shown that the ascent history of magma will strongly affect the growth of microlites in the groundmass, because decompression drives water from the melt and stabilizes solid phases (for example, Cashman and Blundy, 2000; Geschwind and Rutherford, 1995; Hammer and others, 1999; Hammer and Rutherford, 2002). As microlites grow in the groundmass, the residual melt, and quenched glass, become more evolved. Thus, as a result of the changing ascent rates noted above for the 2006 eruption, we expect to see differences in microlite growth reflected in the groundmass glasses (fig. 11).

In addition to the speed and continuity of the ascent path, magma composition and temperature will affect microlite growth. For example, groundmass microlite content increased systematically with decreasing silica content in andesites and dacites from the 1953 to 1974 eruption of Trident Volcano, even in eruptive units with identical ascent paths (Coombs and others, 2000). Each phase of the 2006 Augustine eruption produced nearly the full range of magmatic compositions, though in widely varying proportions (Vallance and others, this volume). To test whether variations in microlite content and groundmass glass composition are functions of bulk composition, ascent rate, or both, we look at glass compositions and qualitatively at groundmass crystallinity in samples of all lithologies from all three phases.

Groundmass Glasses in the LSA

Low-silica andesite scoria contains microlite-rich groundmass and residual glass that varies widely in composition (fig. 11). This large range exists despite a relatively constant bulk-rock composition and phenocryst assemblage, indicating that the compositional variations reflect changes in microlite content. January 13 tephra follows a similar pattern, and thus these glasses probably evolved the same way. Could the compositional range of the LSAS and early tephra glasses reflect magma mixing instead of late-stage decompression crystallization? If this were the case, one would expect the evolved end of this trend to overlap with matrix glasses from the silicic endmember of the eruption, represented by HSA and the light colored regions in the banded clasts. Instead, the HSA and related samples have glasses that cluster at a lower silica content than the most evolved LSAS and have K_2O contents that place them slightly below the LSAS trend. This suggests that the LSAS matrix-glass trend is not the result of mixing of melt phases between the two end members and that instead the groundmass glass trend is driven by decompression-induced crystallization.

The most evolved LSAS and tephra glasses range to 78.7 weight percent SiO_2, and some quartz was detected in the groundmass using semiquantitative EPMA. The highly evolved melt in the presence of quartz resulted from extensive groundmass crystallization and equilibration at very shallow depths (Cashman and Blundy, 2000). Plotting these evolved glass compositions on a projected quartz-albite-anorthoclase ternary diagram yields equilibration pressures of 25 MPa, equivalent to a depth of about 1 km. Interestingly, one-atmosphere experiments on natural Augustine pumice consistently yielded melt silica contents of 76±1 weight percent (Brugger and others, 2003). Those authors suggest that such magmas only reach more silicic groundmass melt compositions during high degrees of effective undercooling. This is likely the case at Augustine. The wide range in groundmass glass composition in LSAS samples could have resulted from magma parcels being evacuated from a variety of pressures/depths within the conduit during a single explosion (for example, Clarke and others, 2007).

Low-Silica Andesite Amphibole Reaction Rims

Very few amphibole phenocrysts were found in the LSAS, but those that were identified invariably have reaction rims, indicating breakdown of this hydrous phase at some pressure lower than its stability field, either during slow ascent or during a stalling-out period on its way to the surface (Rutherford and Hill, 1993). We suggest that LSAS amphibole reaction rims grew as this magma slowly broke its way to the surface before the eruption (see section A Magmatic Model for Augustine 2006, below). Applying rates of amphibole breakdown determined experimentally in dacites from Redoubt and Mount St Helens, we can estimate a time scale over which the rims likely formed in the Augustine magma, with a few caveats. The average bulk composition of the LSA is lower in silica content than either the Redoubt or St. Helens dacites, while the groundmass glasses range from similar (>76 weight percent) to lower in SiO_2 (~66 weight percent; Browne and Gardner, 2006; Rutherford and Hill, 1993). The temperatures of the LSA are generally hotter than those used in the Redoubt amphibole breakdown experiments (840°C; Browne and Gardner, 2006), while those employed by Rutherford and Hill are more similar to the average temperatures of all LSA oxides analyzed (860 to 900°C, fig. 17). Because temperature appears to have a great influence on amphibole reaction rates during decompression (Browne and Gardner, 2006), it is probably more appropriate here to apply the rates constrained by Rutherford and Hill (1993), despite the differences in bulk and groundmass glass compositions. Thus, the 40-to-100-micron thick rims observed in the LSA indicate that this magma spent ~20 to 57 days outside the amphibole stability field, at shallower depths than about 4 km. Given the first signs of phreatic explosions starting on December 10, and the first explosive phase of the eruption January 12, the range of thicknesses observed in the amphibole breakdown rims indicate initiation of ascent of the LSA magma sometime near mid-November 2005, which correlates very well with geodetic observations as described below.

Alternatively, rimmed amphibole crystals found in low-silica andesite may have derived from another magma, perhaps the high-silica andesite. If this was the case, reaction rims may have formed as the amphibole underwent heating (Browne and Gardner, 2006). Additional analyses of amphibole compositions would further constrain this possibility.

Groundmass Glass Compositions in the HSA

In contrast to the LSA, the high-silica andesite groundmass is nearly microlite-free and has very consistent groundmass glass compositions, for both the explosive and continuous phases. This is true even for HSA samples found in the same deposit as LSAS with microlite-choked groundmass. The HSA did not undergo extensive decompression-induced crystallization during ascent. Because HSA clasts erupted coevally with LSAS, these parcels of magma must have had the same ascent histories. The lack of microlite growth in the HSA is likely to the result of a combination of a more silicic starting composition, which would increase viscosity and inhibit crystal nucleation and growth, and the fact that HSA was likely heated immediately before eruption by mixing, slightly "superheating" the melt phase.

A Magmatic Model for Augustine 2006

Here we combine our petrologic data and conclusions with other geophysical and geologic evidence to construct a model of magma storage, mixing, and movement before and during the 2006 Augustine eruption. In addition to explaining the observations and events of 2006, any feasible model should also address the consistency in eruptive style and composition of the last several Augustine eruptions, which suggests a common, repeatable mechanism.

Several months before the beginning of the eruption, volatile-rich basalt rose through a hot, ductile mid-crustal pathway and intersected the crystal-rich HSA body, probably at a depth of 4–6 km bsl (fig. 20*A*). Evidence from melt inclusion analyses from 2006, 1986, and prehistoric samples (Webster and others, this volume) indicate maximum entrapment pressures of 160 to 200 MPa in rhyolitic inclusions in plagioclase, which indicates maximum depths of about 6 to 8 km for the HSA body, including the estimate from 1986 inclusions. Ascent of the basalt was not detected seismically, but small volcano-tectonic earthquakes began near sea level directly below Augustine's summit in late April 2005 (Jacobs and McNutt, this volume; Power and Lalla, this volume), and a similarly located weak inflationary source was detected by continuous GPS starting in the summer of 2005 (Cervelli and others, this volume; Cervelli and others, 2006). This zone of geophysical unrest coincides with a region of low to medium seismic velocities interpreted to be dome material overlying sediments interlaced with dikes and sills; these sit atop zeolitized sedimentary strata below 0.9 km bsl (Kienle and others, 1979). We suggest that the shallow unrest resulted from pressurization of the volcanic edifice by gases exsolved from the basalt as it ascended, intersected the HSA, cooled, and crystallized. The total volume change for a modeled point source near sea level is roughly 2×10^5 m^3 (Cervelli and others, 2006), about 2.5 orders of magnitude less than the total erupted volume in 2006 (Coombs and others, this volume).

The introduction of wet basalt into the HSA body first partially reheated the HSA body, lowering its crystal content. The rate of heating of a silicic magma body by a newly introduced hotter body will depend on their size and geometry, but it can take hundreds of days to heat the silicic magma by tens of degrees (Snyder, 2000). Next, the basalt and a newly rejuvenated portion of the HSA body hybridized to form the erupted LSA. This process was likely aided by vesiculation of the basalt as it cooled and crystallized (Huppert and others, 1982; Thomas and others, 1993), causing density instability and convective overturn. The heating of the HSA and hybridization were probably coeval. The homogeneous composition of the LSA indicates that hybridization was thorough, and if it began at the onset of geophysical unrest, it was quick, taking 6 months or less.

A portion of the hybrid LSA then rose through the upper, crystal-rich portion of the HSA body. Whether it took the form of a dike or diapir is unknown and depends on the crystallinity (and thus rigidity) of the HSA body. The LSA then propagated as a dike into the dacite-porphyry crust above the HSA body and ascended toward the surface during the late precursory phase (fig. 20*B*). The LSA was apparently able to initiate dike formation because of its lower viscosity, whereas the crystal-rich HSA was not able to do so. This scenario of a newly arrived, less viscous magma creating a pathway for a resident, crystal-rich magma was proposed by Pallister and others (1996) for the eruption of Mount Pinatubo. Since then, this model has also been applied to the eruption of the Yunokuchi Pumice, Akagi, Japan (Umino and Horio, 1998) and the 1929 eruption of Komagatake volcano, Japan (Takeuchi and Nakamura, 2001). At Komagatake, it was shown that dike propagation of a less viscous mixed andesite magma could occur at a chamber overpressure of only 8 MPa, whereas unrealistically high overpressures would have been required to propagate a dike of the more viscous, crystal-rich silicic magma resident in the chamber.

The exact timing of LSA dike initiation is not known, but GPS data place some constraints on the dike's movement. Edifice-inflation rates increased on November 18, 2005, and GPS data are consistent with propagation of a small dike from 1.25 km depth to the surface between November 18 and January 11 (Cervelli and others, 2006; fig. 20*B*). The upward movement of such a dike at greater depths would not be detected by the Augustine GPS network (P. Cervelli, oral communication, 2008), so it is not known exactly when the dike started its ascent from the HSA body. Modeled dike ascent rates are not constant, and they slow from 100 m/hour around November 25. An offset occurred in the GPS time series on November 17, at a similar time as the appearance of new cracks at the summit of Augustine. This event could point towards the initiation of the rise of the dike just before the edifice inflation rate accelerated on November 18. If we also compare with the preliminary estimates of LSA ascent timescale from the amphibole reaction rims described above, rise of the LSA dike from a depth of ~4 km starting November 17 would indicate that the quickest rising magma would reach the surface around December 7, which is close to the time of the first of the observed phreatic explosions, and the slowest would reach the surface the week of January 12, marking the onset of the explosive phase of the eruption.

Phreatic explosions, increased SO_2 output, and heating of the edifice in December 2005 (McGee and others, this volume; Power and others, 2006; Wessels and others, this volume) all suggest that significant gas had accumulated at the tip of the LSA dike and that some made it to the surface ahead of the LSA magma. A strong swarm of VT earthquakes on January 10–11 likely recorded the final opening of the dike to the surface, but two explosions on January 11 contained little or no juvenile magma (Wallace and others, this volume), and deformation recorded by a summit GPS station continued unabated through these events, suggesting that not much magma was evacuated from the edifice (Cervelli and others, this volume).

LSA magma likely reached the surface on January 12 in the form of a small ephemeral lava dome, recorded by drumbeat earthquakes that signify lava effusion (Power and Lalla, this volume). Vulcanian blasts on January 13, 14, and 17 each drained the conduit to a depth of roughly 2 km below the surface (Coombs and others, this volume; fig. 20C), and produced dominantly LSA deposits, but including a small percentage of HSA as well (Vallance and others, this volume). In between explosions, the conduit refilled with LSA and minor amounts of HSA from the top of the rejuvenated magma body. Explosions were driven by overpressure in the conduit that developed below a degassed lava/magma cap, similar to those seen at Soufriere Hills Volcano, Montserrat (Druitt and others, 2002). The range in LSA groundmass glass compositions indicates that some LSA underwent extensive decompression-driven groundmass crystallization before eruption, likely during storage in the shallow portions of the conduit before explosive release. The continuation of the inflationary trend throughout January indicated that gas pressurization in the shallow subsurface continued throughout this period (Cervelli and others, this volume).

The presence of some HSA in explosive-phase deposits indicates that mixing occurred during the upward passage of the LSA through the HSA body, and/or some HSA was drawn into the dike during LSA ascent. Interestingly, the final, effusive phase of the 2006 eruption was also dominated by LSA,

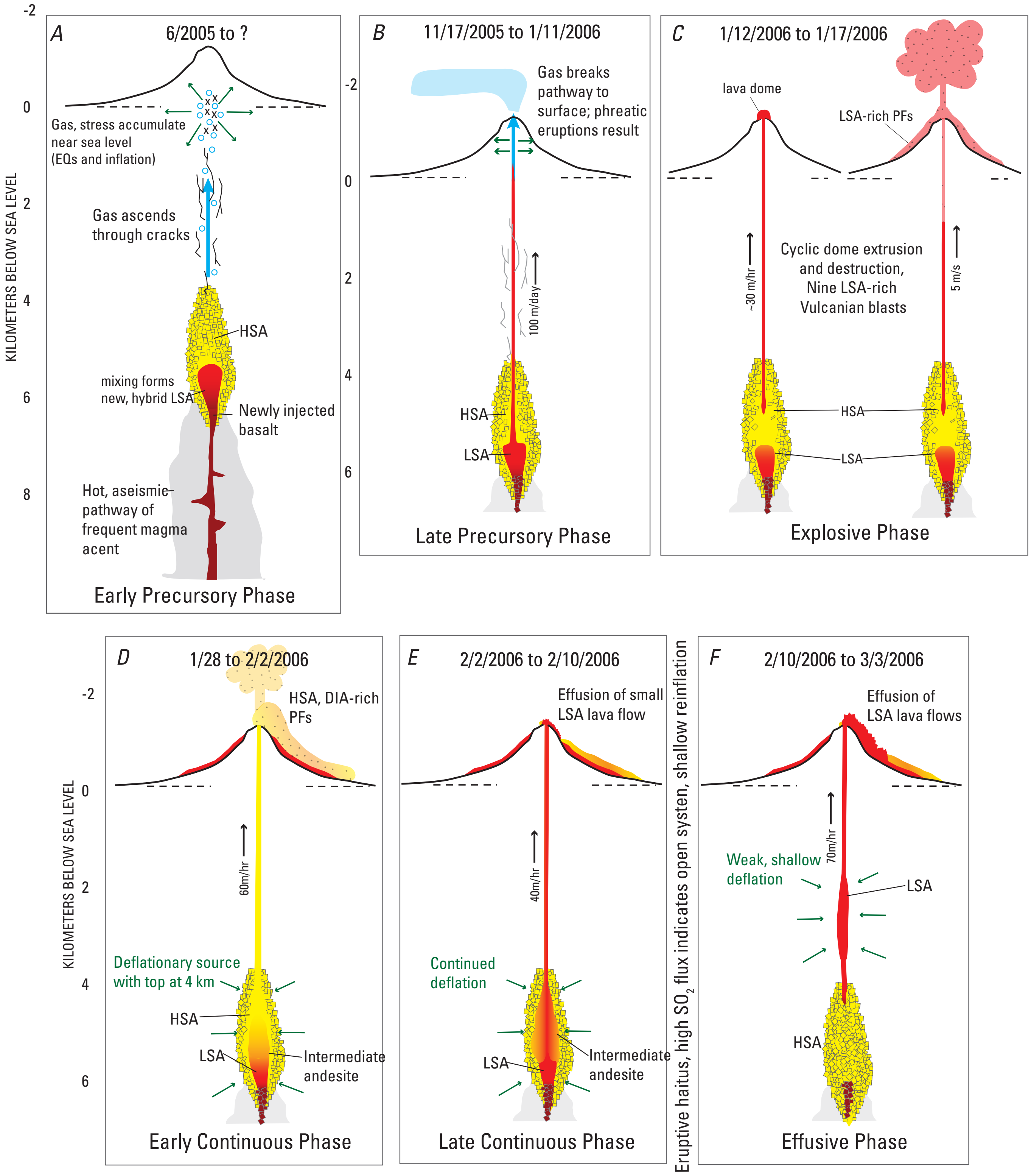

Figure 20. Schematic depiction of magma configuration and events for six time periods before and during the 2006 eruption. HSA is high-silica andesite, DIA is dense intermediate andesite, LSA is low-silica andesite, PF denotes pyroclastic flows.

indicating that in this case, not all of the hybrid andesite was erupted during the initial phase, but that instead some remained at the base of the HSA magma body. It is also clear that during the period between January 17 and 27, continued mixing between LSA and HSA created the more thoroughly mixed intermediate andesite that erupted during the continuous phase.

Slow effusion of a lava dome occurred from January 17 through 27. An explosion on January 27 destroyed this new dome and produced the largest single deposit of the 2006 eruption: about 20 million m^3 of predominantly HSA formed the Rocky Point pyroclastic flow (Coombs and others, this volume; Vallance and others, this volume). This event marked a distinct shift in the dominant composition of erupted material, likely coinciding with exhaustion of the LSA “slug” that made its way through the resident HSA and initially drove the eruption. Whereas earlier explosions were fed only from the conduit, the January 27 explosive event undoubtedly tapped the resident magma body. This is consistent with the fact that for the first time during the eruption, GPS signals record a deep deflation (>4 km depth) that begins around January 27 and continues through February 10 (Cervelli and others, this volume).

Following the explosive eruption of HSA on January 27, ascent and effusion of predominantly HSA occurred for the next several days (Coombs and others, this volume; fig. 20*D*). Little or no LSA was erupted during this interval, but HSA was accompanied by effusion of banded and DIA magmas (Vallance and others, this volume). We interpret this interval as the evacuation of the rejuvenated portion of the resident HSA body through an open conduit from ~5 km to the surface. Ascent rates were high enough for the groundmass to remain microlite-free, though this could also have resulted from the recent heating of the HSA by the LSA.

During the waning of the continuous phase, mass flux continued to be quite high as the north lava flow effused (fig. 20*E*). Eruptable HSA had been exhausted and mostly intermediate andesite was erupted. The deflationary trend overlaps this period, as well as the earlier continuous phase.

During the eruptive pause from February 10 to March 3, high SO_2 emission rates suggested that the system was open and that relatively shallow magma was degassing (McGee and others, this volume). Weak, shallow inflation during this period (Cervelli and others, this volume) is interpreted to have been caused by magma accumulation, somewhere between the HSA body and the surface. This relatively degassed, dense LSA must have been present at the base of the HSA magma body and ascended after the HSA was exhausted.

During the effusive phase, from March 3 through 16, degassed LSA ascended and erupted in the form of two lava flows and a new summit dome (fig. 20*F*). The DLSA brought with it numerous inclusions of fine-grained gabbro, chunks of crystallized portions of the plumbing system.

The 2006 Augustine Eruption in Context

The range in whole-rock compositions of deposits from the 2006 eruption matches that of the historical and most Holocene samples, essentially spanning the andesite range (fig. 7). Basalt and rhyolite erupted coevally in the late Pleistocene but have not erupted since (Waitt and Begét, 2009; J.E. Begét, oral communication). Those rocks fall along a lower K trend compared to historical lavas, including those from 2006. Prehistoric Holocene lavas span a limited SiO_2 range but fall along an intermediate K trend relative to Pleistocene and historical samples. Similarly, many trace-element arrays formed by 2006 and other historical magmas on variation diagrams are elevated in relation to those formed by the Pleistocene basalt and rhyolite. Similar temporal systematics (that is, progressive increase in highly incompatible elements at a given SiO_2 level) have been seen at nearby Redoubt volcano (Begét and Nye, 1994). The differences between the Pleistocene basalt and rhyolite and modern lavas mean that these exact compositions are not appropriate for modeling the modern Augustine magmatic system. However, they do suggest that similar magmas may exist in the modern Augustine system, even if they have not erupted during the Holocene.

Holocene Augustine lavas have high concentrations of compatible transition metals (Mg, Cr, Ni, Fe), and high molar Mg/(Mg+Fe) (Mg#) and dramatically low concentrations of all incompatible trace elements (including LIL, U, Th, Pb, REE, and HFSE) relative to other Aleutian lavas of similar SiO_2 content (fig. 21). Augustine magmas do not follow the liquid line of descent typical of most Aleutian volcanoes where basaltic parental magmas evolve to andesite and dacite accompanied by a steady increase in incompatible elements and decrease in compatible transition metals. Within the andesite range at Augustine the most highly incompatible elements only increase by about 50 percent, and MREE and HREE have constant concentrations (fig. 10). Over similar SiO_2 ranges at other Aleutian volcanoes all incompatible elements (including HREE) increase, with the most incompatible increasing by 200–300 percent (for example, Aniakchak; Dreher and others, 2005; C.J. Nye and others, unpublished data). There are several possible reasons for the low rate of increase of incompatible elements at Augustine, including (a) high crystal/liquid distribution coefficients associated with the high silica content of the groundmass; (b) high effective bulk partition coefficients during crystallization at high pressure, where the ratio of pyroxene ± amphibole to plagioclase is higher; (c) whole-rock concentrations of incompatible elements reflecting a large amount of crystal accumulation; or (d) these magmas being primitive high-Mg# andesites (Kelemen and others, 2003 and 2004), rather than highly evolved fractionates. Possibilities (c) and (d) are also at least qualitatively consistent with the high concentrations of compatible elements in these lavas.

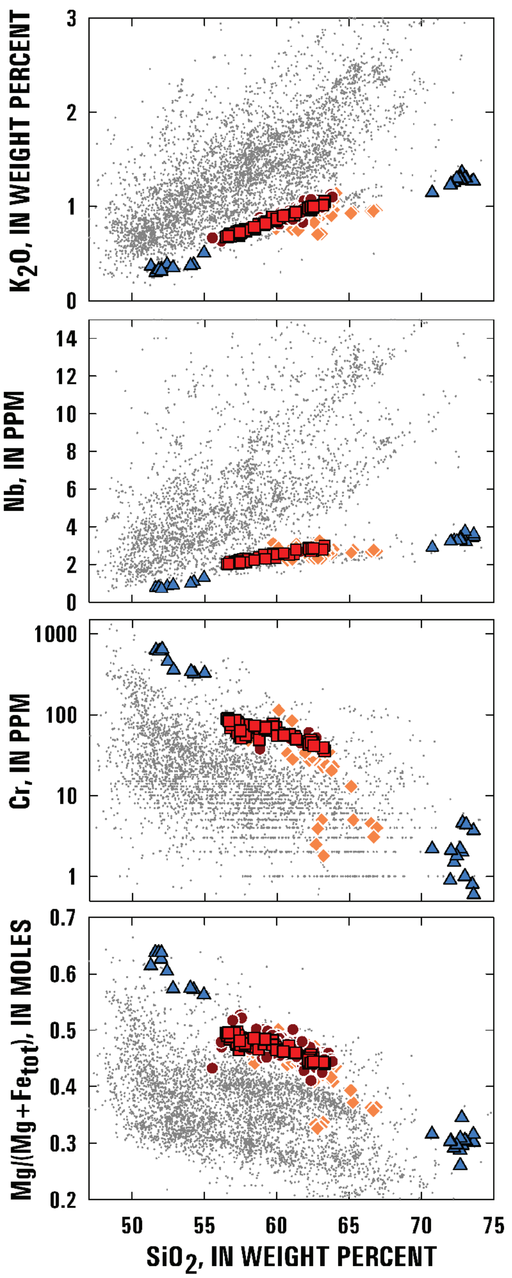

Figure 21. Comparison of Augustine magmas with other Aleutian arc magmas. Augustine magmas are different from the majority of Aleutian magmas in having relatively high Mg# (molar Mg/(Mg+Fe)) and compatible transition metals Cr (shown), as well as Ni and Mg (not shown), as well as low concentrations of incompatible elements, such as K and Nb (shown). The low concentrations of incompatible elements reflect relatively less enrichment with increasing silica in addition to lower-than-average initial concentrations of many incompatible elements. Colored symbols are Augustine lavas (red squares, 2006; dark red circles, pre-2006 historical; orange diamonds, prehistoric late Holocene; blue triangles, late Pleistocene). Gray dots are all other Aleutian analyses from the open literature and unpublished Alaska Volcano Observatory analyses.

It is beyond the scope of this paper to evaluate the above hypotheses. It is our intention instead to point out that Augustine magmas are quite distinct from typical Aleutian magmas, particularly those from the central arc. Trace element concentrations in minerals would be useful in constraining the mineral/melt distribution coefficients during crystallization, thus further constraining petrogenesis. Emphasis on phenocryst mineralogy and petrology in this study shows that especially the low-silica magmas, which erupted, are hybrids requiring the presence of an even lower-silica magma. Thus possibility (d), that these are simply primitive andesites, appears too simple an explanation.

Acknowledgments

It takes an observatory to document an eruption and our understanding of the 2006 eruption of Augustine would not be nearly as complete without the efforts of the entire staff of the Alaska Volcano Observatory. In addition, we thank Jim Webster, Charlie Mandeville, Peter Cervelli, John Power, and Jeff Freymueller for insightful discussion regarding the Augustine magmatic system. Charlie Bacon, Brandon Browne, and Jeff Freymueller provided critical reviews that helped to improve the manuscript. This work was funded by the U.S. Geological Survey's Volcano Hazards Program.

References Cited

Brugger, C.R., Johnston, D.A., and Cashman, K.V., 2003, Phase relations in silicic systems at one-atmosphere pressure: Contributions to Mineralogy and Petrology, v. 146, p. 356–369.

Cashman, K.V., and Blundy, J., 2000, Degassing and crystallization of ascending andesite and dacite: Philosophical Transactions of the Royal Society, v. 358, p. 1487–1513.

Cervelli, P.F., Fournier, T.J., Freymueller, J.T., Power, J.A., Lisowski, M., and Pauk, B.A., 2010, Geodetic constraints on magma movement and withdrawal during the 2006 eruption of Augustine Volcano, *in* Power, J.A., Coombs, M.L., and Freymueller, J.T., eds., The 2006 eruption of Augustine Volcano, Alaska: U.S. Geological Survey Professional Paper 1769 (this volume).

Cervelli, P.F., Fournier, T., Freymueller, J.T., and Power, J.A., 2006, Ground deformation associated with the precursory unrest and early phases of the January 2006 eruption of Augustine Volcano, Alaska: Geophysical Research Letters, doi: 10.1027/2006GL027219.

Clarke, A.B., Stephens, S., Teasdale, R., Sparks, R.S.J., and Diller, K., 2007, Petrologic constraints on the decompression history of magma prior to Vulcanian explosions at the Soufriere Hills Volcano, Montserrat: Journal of Volcanology and Geothermal Research, v. 161, p. 261–274.

Clynne, M.A., 1999, A complex magma mixing origin for rocks erupted in 1915, Lassen Peak, California: Journal of Petrology, v. 40, p. 105–132.

Coombs, M.L., and Gardner, J.E., 2004, Reaction rim growth on olivine in silicic melts—implications for magma mixing: American Mineralogist, v. 89, no. 5–6, p. 748–759.

Coombs, M.L., Eichelberger, J.C., and Rutherford, M.J., 2000, Magma storage and mixing conditions for the 1953-1974 eruptions of Southwest Trident volcano, Katmai National Park, Alaska: Contributions to Mineralogy and Petrology, v. 140, no. 1, p. 99–118.

Coombs, M.L., Bull, K.F., Vallance, J.W., Schneider, D.J., Thoms, E.E., Wessels, R.L., and McGimsey, R.G., 2010, Timing, distribution, and volume of proximal products of the 2006 eruption of Augustine Volcano, *in* Power, J.A., Coombs, M.L., and Freymueller, J.T., eds., The 2006 eruption of Augustine Volcano, Alaska: U.S. Geological Survey Professional Paper 1769 (this volume).

Costa, F., and Chakraborty, S., 2004, Decadal time gaps between mafic intrusion and silicic eruption obtained from chemical zoning patterns in olivine: Earth and Planetary Science Letters, v. 227, p. 517–530.

Daley, E.E., 1986, Petrology, geochemistry, and the evolution of magmas from Augustine Volcano, Alaska: University of Alaska Fairbanks, unpublished M.S. thesis, 103 p.

Detterman, R.L., and Reed, B.L., 1980, Stratigraphy, structure, and economic geology of the Iliamna Quadrangle, Alaska: U.S. Geological Survey Bulletin, 1368-B, 86 p.

Dreher, S.T., Eichelberger, J.C., and Larsen, J.F., 2005, The petrology and geochemistry of the Aniakchak caldera-forming ignimbrite, Aleutian Arc, Alaska: Journal of Petrology, v. 46, p. 1747–1768.

Druitt, T.H., Young, S.R., Baptie, B., Bonadonna, C., Calder, E.S., Clarke, A.B., Cole, P.D., Harford, C.L., Herd, R.A., Luckett, R., Ryan, G., and Voight, B., 2002, Episodes of cyclic Vulcanian explosive activity with fountain collapse at Soufriere Hills Volcano, Montserrat, *in* Druitt, T.H., and Kokelaar, B.P., eds., The eruption of Soufriere Hills Volcano, Montserrat, from 1995 to 1999: London, The Geological Society, p. 281–306.

Evans, B.W., Scaillet, B., and Kuehner, S.M., 2006, Experimental determination of coexisting iron-titanium oxides in the systems FeTiAlO, FeTiAlMgO, FeTiAlMnO, and FeTiAlMgMnO at 800 and 900°C, 1–4 kbar, and relatively high oxygen fugacity: Contributions to Mineralogy and Petrology, v. 152, p. 149–167.

Faure, F., Trolliard, G., Nicollet, C., and Montel, J.-M., 2003, A developmental model of olivine morphology as a function of the cooling rate and the degree of undercooling: Contributions to Mineralogy and Petrology, v. 145, p. 251–263.

Finney, B., Turner, S., Hawkesworth, C., Larsen, J.F., MNye, C., George, R., Bindeman, I., and Eichelberger, J.C., 2008, Magmatic differentiation at an island-arc caldera—Okmok Volcano, Aleutian Islands, Alaska: Journal of Petrology, v. 49, no. 857–884.

Geschwind, C.H., and Rutherford, M.J., 1995, Crystallization of microlites during magma ascent—The fluid mechanics of the 108086 eruptions at Mount St. Helens: Bulletin of Volcanology, v. 57, p. 356–370.

Ghiorso, M.S., and Evans, B.W., 2008, Thermodynamics of rhombohedral oxide solid solutions and a revision of the Fe-Ti two-oxide geothermometer and oxygen-barometer: American Journal of Science, v. 308, p. 957–1039.

Gill, J.B., 1981, Orogenic andesites and plate tectonics: Springer-Verlag, Berlin, 370 p.

Hammer, J.E., and Rutherford, M.J., 2002, An experimental study of the kinetics of decompression-induced crystallization in silicic melt: Journal of Geophysical Research, v. 107, p. 148–227.

Hammer, J.E., Cashman, K.V., Hoblitt, R.P., and Newman, S., 1999, Degassing and microlite crystallization during preclimactic events of the 1991 eruption of Mount Pinatubo, Philippines: Bulletin of Volcanology, v. 60, p. 335–380.

Harris, G.W., 1994, The petrology and petrography of lava from the 1986 eruption of Augustine volcano: University of Alaska Fairbanks unpublished M.S. thesis, Fairbanks, AK, 131 p.

Hildreth, E.W., 2007, Quaternary Magmatism in the Cascades—Geologic Perspectives: U.S. Geological Survey Professional Paper 1744, 136 p.

Huppert, H.E., Sparks, R.S.J., and Turner, J.S., 1982, Effects of volatiles on mixing in calc-alkaline magma systems: Nature, v. 297, p. 554–557.

Izbekov, P., Eichelberger, J.C., Patino, L.C., Vogel, T.A., and Ivanov, B.V., 2002, Calcic cores of plagioclase phenocrysts in andesite from Karymsky volcano—evidence for rapid introduction by basaltic replenishment: Geology, v. 30, p. 799–802.

Jacobs, K.M., and McNutt, S.R., 2010, Using seismic *b*-values to interpret seismicity rates and physical processes during the preeruptive earthquake swarm at Augustine Volcano 2005–2006, *in* Power, J.A., Coombs, M.L., and Freymueller, J.T., eds., The 2006 eruption of Augustine Volcano, Alaska: U.S. Geological Survey Professional Paper 1769 (this volume).

Jicha, B.R., and Singer, B.S., 2006, Volcanic history and magmatic evolution of Seguam Island, Aleutian Island arc, Alaska: Geological Soceity of America Bulletin, v. 118, p. 805–822.

Johnson, K.E., Strong, D.F., Harmon, R.S., Richardson, J. M., and Moorbath, S., 1996, Isotope and trace element geochemistry of Augustine volcano, Alaska—implications for magmatic evolution: Journal of Petrology, v. 37, p. 95–115.

Johnson, D.M., Hooper, P.R., and Conrey, R.M., 1999, XRF analysis of rocks and minerals for major and trace elements on a single low dilution Li-tetraborate fused bead: Advances in x-ray Analysis, v. 41, p. 843–867.

Johnston, D.A., 1978, Volatiles, magma mixing, and the mechanism of eruption at Augustine volcano, Alaska: University of Washington Ph.D. dissertation, 187 p., 20 plates.

Kelemen, P.B., Yogodzinski, G.M., and Scholl, D.W., 2003, Along strike variation in the Aleutian Island arc—genesis of high Mg# andesite and implications for continental crust, *in* Eiler, J., ed., Inside the Subduction Factory, American Geophysical Union Monograph 138, p. 1–54.

Kelemen, P.B., Hanghoj, K., and Greene, A.R., 2004, One view of the geochemistry of subduction-related magmatic arcs, with an emphasis on primitive andesite and the lower crust, *in* Rudnick, R.L., ed., The crust: Elsevier Ltd., p. 593–659.

Kienle, J., and Swanson, S.E., 1983, Volcanism in the eastern Aleutian Arc—late Quaternary and Holocene centers, tectonic setting and petrology: Journal of Volcanology and Geothermal Research, v. 17, no. 1-4, p. 393–432.

Kienle, J., Lalla, D.J., Pearson, C.F., and Barrett, S. A., 1979, Search for shallow magma accumulations at Augustine volcano: University of Alaska Fairbanks Geophysical Institute Final Report to U.S. Dept. of Energy, Washington D.C. 157 p.

Knaack, C., Cornelius, S.B., and Hooper, P.R., 1994, Trace element analyses of rocks and minerals by ICP-MS: Open File Report, Department of Geology, Washington State University [http://www.wsu.edu/~geolab/].

Kuritani, T., Yokoyama, T., Kobayashi, K., and Nakamura, E., 2003, Shift and rotation of composition trends by magma mixing—1983 eruption at Miyakejima Volcano, Japan: Journal of Petrology, v. 44, p. 1895–1916.

Larsen, J.F., 2005, Experimental study of plagioclase rim growth around anorthite seed crystals in rhyodacitic melt: American Mineralogist, v. 90, p. 417–427.

Lattard, D., Sauerzapf, U., and Kasemann, M., 2005, New calibration data for the Fe-Ti oxide thermo-oxybarometers from experiments in the Fe-Ti-O system at 1 bar, 1,000–1,300^{o}C and a large range of oxygen fugacities: Contributions to Mineralogy and Petrology, v. 149, p. 735–754.

LeMaitre, R.W., 1991, A classification of igneous rocks and glossary of terms: Oxford, Blackwell Scientific Publications, 193 p.

McGee, K.A., Doukas, M.P., McGimsey, R.G., Neal, C.A., and Wessels, R.L., 2010, Emission of SO_2, CO_2 and H_2S from Augustine Volcano, 2002–2008, *in* Power, J.A., Coombs, M.L., and Freymueller, J.T., eds., The 2006 eruption of Augustine Volcano, Alaska: U.S. Geological Survey Professional Paper 1769 (this volume).

Murphy, M.D., Sparks, R.S.J., Barclay, J., Carroll, M.R., and Brewer, T.S., 2000, Remobilization of andesite magma by intrusion of mafic magma at the Soufriere Hills Volcano, Montserrat, West Indies: Journal of Petrology, v. 41, p. 21–42.

Nakamura, M., 1995, Continuous mixing of crystal mush and replenished magma in the ongoing Unzen eruption: Geology, v. 23, p. 807–810.

Nakamura, M., and Shimikata, S., 1998, Kinetic constraints on the mode of magma mixing and ascent in the 1991 Unzen eruption: Earth and Planetary Science Letters, v. 161, p. 119–133.

Nye, C., Coombs, M.L., Larsen, J.F., Izbekov, P., Tilman, M., and Cameron, C., 2008, Augustine Volcano—Mg-, Cr-, and Ni-rich; LILE, REE, and HFSE-poor: Geochimica et Cosmochimica Acta, v. 72, p. A692.

Pallister, J.S., Hoblitt, R.P., Meeker, G.P., Knight, R.J., and Siems, D.F., 1996, Magma mixing at Mount Pinatubo—petrographic and chemical evidence from the 1991 deposits, *in* Newhall, C.G., and Punonhbayan, R., eds., Fire and mud—eruptions and lahars of Mount Pinatubo: Seattle, University of Washington Press, p. 687–731.

Plank, T., Zimmer, M.M., Hauri, E.H., and Nye, C.J., 2006, The Augustine basalt: Eos (American Geophysical Union Transactions), Fall Meeting Supplement, v. 87, abs. V42B-06.

Power, J.A., 1988, Seismicity associated with the 1986 eruption of Augustine Volcano, Alaska: University of Alaska Fairbanks, unpublished M.S. thesis, 142 p.

Power, J.A., and Lalla, D.J., 2010, Seismic observations of Augustine Volcano, 1970–2007, *in* Power, J.A., Coombs, M.L., and Freymueller, J.T., eds., The 2006 eruption of Augustine Volcano, Alaska: U.S. Geological Survey Professional Paper 1769 (this volume).

Power, J.A., Nye, C.J., Coombs, M.L., Wessels, R.L., Cervelli, P.F., Dehn, J., Wallace, K.L., Freymueller, J.T., and Doukas, M.P., 2006, The reawakening of Alaska's Augustine Volcano: Eos (American Geophysical Union Transactions), v. 87, no. 37, p. 373, 377.

Pownceby, M.I., and O'Neill, H.St.C 1994, Thermodynamic data from redox reactions at high temperatures. IV. Calibration of the Re-ReO_2 oxygen buffer from EMF and NiO+Ni-Pd redox sensor measurements: Contributions to Mineralogy and Petrology, v. 118, p. 130–137.

Roman, D.C., Cashman, K.V., Gardner, C.A., Wallace, P., and Donovan, J., 2005, Storage and interaction of compositionally heterogeneous magmas from the 1986 eruption of Augustine Volcano, Alaska: Bulletin of Volcanology, v. 68, p. 240–254.

Rutherford, M.J., and Devine, J.D., 1996, Preeruption pressure-temperature conditions and volatiles in the 1991 dacitic magma of Mount Pinatubo, *in* Newhall, C.G., and Punongbayan, R.S., eds., Fire and Mud—eruptions and lahars of Mount Pinatubo, Philippines: Seattle, University of Washington Press, p. 751–766.

Rutherford, M.J., and Hill, P.M., 1993, Magma ascent rates from amphibole breakdown—an experimental study applied to the 1980-1986 Mount St. Helens eruptions: Journal of Geophysical Research, v. 98, p. 19667–19685.

Snyder, D., 2000, Thermal effects of the intrusion of basaltic magma into a more silicic magma chamber and implications for eruption triggering: Earth and Planetary Science Letters, v. 175, p. 257–273.

Stormer, J.C., 1983, The effects of recalculation on estimates of temperature and oxygen fugacity from analyses of multicomponent iron-titanium oxides: American Mineralogist, v. 68, p. 586–594.

Syracuse, E.M., and Abers, G.A., 2006, Global compilation of variations in slab depth beneath arc volcanoes and implications: Geochemistry, Geophysics, Geosystems, v. 7, no. 5, p. Q05017, doi:05010.01029/02005GC001045.

Takeuchi, S., and Nakamura, M., 2001, Role of precursory less-viscous mixed magma in the eruption of phenocryst-rich magma—evidence from the Hokkaido-Komagatake 1929 eruption: Bulletin of Volcanology, v. 63, p. 365–376.

Tappen, C.M., Webster, J.D., Mandeville, C.W., and Roderick, D., 2009, Petrology and geochemistry of prehistoric pumice fall eruptions (2100–1000 a.B.P.) at Mt. St. Augustine Volcano, Alaska: Journal of Volcanology and Geothermal Research, v. 183, p. 42–62.

Thomas, N., Tait, S., and Koyaguchi, T., 1993, Mixing of stratified liquids by the motion of gas bubbles—application to magma mixing: Earth and Planetary Science Letters, v. 115, p. 161–175.

Tilman, M.R., 2008, An investigation of symplectite-rimmed olivine and magmatic processes during the 2006 eruption of Augustine Volcano, Alaska: University of Alaska Fairbanks, unpublished M.S. thesis, 166 p.

Tsuchiyama, A., 1985, Dissolution kinetics of plagioclase in the melt of the system diopside-albite-anorthite and origin of dusty plagioclase in andesites: Contributions to Mineralogy and Petrology, v. 89, p. 1–16.

Umino, S., and Horio, A., 1998, Multistage magma mixing revealed in phenocryst zoning of the Yunokuchi Pumice, Akagi Volcano, Japan: Journal of Petrology, v. 39, p. 101–124.

Vallance, J.W., Bull, K.F., and Coombs, M.L., 2010, Pyroclastic flows, lahars, and mixed avalanches generated during the 2006 eruption of Augustine Volcano, *in* Power, J.A., Coombs, M.L., and Freymueller, J.T., eds., The 2006 eruption of Augustine Volcano, Alaska: U.S. Geological Survey Professional Paper 1769 (this volume).

Waitt, R.B., and Begét, J.E., 2009, Volcanic processes and geology of Augustine Volcano, Alaska: U.S. Geological Survey Professional Paper 1762, 78 p., 2 map plates [http://pubs.usgs.gov/pp/1762/].

Waitt, R.B., 2010, Ejecta and landslides from Augustine Volcano before 2006, *in* Power, J.A., Coombs, M.L., and Freymueller, J.T., eds., The 2006 eruption of Augustine Volcano, Alaska: U.S. Geological Survey Professional Paper 1769 (this volume).

Wallace, K.L., Neal, C.A., and McGimsey, R.G., 2010, Timing, distribution, and character of tephra fall from the 2005–2006 eruption of Augustine Volcano, *in* Power, J.A., Coombs, M.L., and Freymueller, J.T., eds., The 2006 eruption of Augustine Volcano, Alaska: U.S. Geological Survey Professional Paper 1769 (this volume).

Waythomas, C.F., and Waitt, R.B., 1998, Preliminary volcano-hazard assessment for Augustine Volcano, Alaska: U.S. Geological Survey Open-File Report 98-0106, 39 p., 1 plate, scale unknown.

Webster, J.D., Mandeville, C.W., Goldoff, B., Coombs, M.L., and Tappen, C., 2010, Augustine Volcano—The influence of volatile components in magmas erupted A.D. 2006 to 2,100 years before present, *in* Power, J.A., Coombs, M.L., and Freymueller, J.T., eds., The 2006 eruption of Augustine Volcano, Alaska: U.S. Geological Survey Professional Paper 1769 (this volume).

Wessels, R.L., Coombs, M.L., Schneider, D.J., Dehn, J., and Ramsey, M.S., 2010, High-resolution satellite and airborne thermal infrared imaging of the 2006 eruption of Augustine Volcano, *in* Power, J.A., Coombs, M.L., and Freymueller, J.T., eds., The 2006 eruption of Augustine Volcano, Alaska: U.S. Geological Survey Professional Paper 1769 (this volume).

Tables 2–8

Table 2. Summary of modal abundances for Augustine 2006 lithologies as determined by point counting.

[Each value is average of n samples within each lithology, in volume percent; one standard deviation is given in parentheses. All values, except for void space, are calculated on a void-free basis. At least, 1,000 points were counted for all samples. LSAS, low-silica andesite scoria; DLSA, dense low-silica andesite; DIA, dense intermediate andesite; FGGI, fine-grained gabbroic inclusions. n.p., not present]

	LSAS	**DLSA**	**DIA**	**Banded**	**HSA**	**FGGI**
Plagioclase	23.7 (3.1)	25.9 (3.4)	25.9 (7.0)	28.1 (6.2)	31.9 (5.2)	56.9 (10.6)
Clinopyroxene	5.8 (3.1)	6.1 (2.3)	4.8 (2.9)	5.2 (1.5)	6.4 (3.2)	4.3 (3.6)
Orthopyroxene	4.0 (1.4)	3.7 (1.0)	3.6 (1.8)	4.7 (1.3)	4.1 (1.5)	3.1 (0.2)
Opaques	1.8 (0.9)	2.4 (1.8)	2.6 (3.0)	1.6 (0.7)	1.8 (0.5)	3.8 (0.7)
Olivine	1.1 (0.9)	1.3 (0.4)	0.6 (0.5)	0.3 (0.3)	0.2 (0.2)	n.p.
Amphibole	n.p.	0.0 (0.1)	n.p.	0.0 (0.1)	0.1 (0.1)	6.1 (5.2)
Apatite	n.p.	n.p.	n.p.	0.0 (0.1)	0.0 (0.1)	n.p.
Anhydrite	0.0 (0.1)	n.p.	n.p.	0.0 (0.1)	n.p.	0.0 (0.1)
Total phenocrysts	36.7 (4.9)	39.5 (3.4)	37.7 (10.4)	40.0 (6.5)	44.8 (7.2)	73.6 (11.9)
Crystalline groundmass	63.1 (5.0)	60.2 (3.7)	51.5 (29.3)	21.6 (24.7)	1.2 (1.5)	0.1 (0.1)
Glass	0.1 (0.2)	0.0 (0.1)	10.7 (23.4)	38.3 (26.0)	53.9 (6.5)	26.3 (12.0)
Voids	33.4 (5.3)	19.8 (4.0)	22.1 (3.4)	38.7 (9.5)	37.4 (7.9)	29.8 (2.9)
n	12	7	5	8	7	2

Table 3. Representative whole-rock compositions of Augustine 2006 eruptive products.

[The prefix “06AU” has been truncated from all sample IDs. Total iron (FeO_t) as FeO]

Phase	**Explosive**				**Continuous**		**Effusive**		
Map unit	**ExPfc**	**RPpf**	**ExPfc**	**RPpf**	**Cpf**	**Cpf**	**EfLf**	**Efba**	**EfLf**
Lithology	**DLSA**	**LSAS**	**DIA**	**HSA**	**DIA**	**HSA**	**DLSA**	**DIA**	**DIA**
Sample ID	**MRT037f**	**MRT009b**	**MRT037e**	**MC004c1**	**MRT017a**	**MRT017b**	**MLC057**	**KB002C**	**MLC028**
Major elements measured by XRF in weight percent normalized to 100. LOI not determined. Total is original analytical total.									
SiO_2	57.07	57.20	58.39	62.52	59.97	62.27	57.07	59.11	62.23
TiO_2	0.732	0.711	0.682	0.558	0.625	0.555	0.729	0.668	0.569
Al_2O_3	17.59	17.79	17.37	16.48	17.00	16.92	17.46	17.05	16.77
FeO_t	6.70	6.71	6.38	5.39	5.98	5.19	6.60	6.27	5.26
MnO	0.144	0.148	0.144	0.129	0.137	0.126	0.143	0.139	0.128
MgO	4.87	4.57	4.49	3.43	4.09	3.28	5.04	4.40	3.37
CaO	8.59	8.52	8.11	6.58	7.60	6.71	8.74	7.94	6.73
Na_2O	3.45	3.50	3.53	3.78	3.59	3.81	3.38	3.48	3.82
K_2O	0.720	0.697	0.770	0.999	0.875	0.983	0.702	0.804	0.996
P_2O_5	0.125	0.141	0.134	0.137	0.133	0.139	0.127	0.134	0.134
Total	98.76	99.13	99.05	100.34	98.60	99.43	98.42	99.73	98.66
Trace elements measured by XRF, in ppm.									
Ni	28.6	24.3	26.0	19.9	26.5	18.7	35.9	32.2	20.6
Cr	62.0	52.7	56.5	45.3	51.8	41.7	82.0	67.0	45.7
Sc	26.4	23.2	23.0	17.7	21.3	17.3	26.6	23.0	17.5
V	204	194	186	134	164	131	203	179	139
Ba	306	303	340	457	386	443	301	356	435
Rb	12.5	12.6	13.8	19.4	16.0	19.6	12.6	14.5	19.7
Sr	324	342	328	321	320	329	319	318	323
Zr	86	86	91	114	102	107	85	96	107
Y	20.9	20.6	21.1	20.9	22.8	20.3	20.1	19.6	21.0
Nb	2.2	1.5	2.3	3.0	2.7	1.9	1.2	2.1	2.0
Ga	17.3	18.2	17.3	14.9	17.1	15.3	16.4	17.2	17.5
Cu	36.3	35.2	33.7	24.3	31.5	17.3	18.2	25.2	22.5
Zn	65.7	63.7	64.7	60.1	61.2	58.1	61.0	57.1	56.4
Trace elements measured by ICPMS, in ppm.									
La	7.81	7.90	8.60	9.92	9.68	10.56	7.83	9.12	10.51
Ce	17.40	17.57	18.94	21.22	21.11	22.66	17.40	20.07	22.50
Pr	2.474	2.503	2.653	2.860	2.893	3.024	2.485	2.802	3.021
Nd	11.10	11.41	11.68	12.26	12.61	13.19	11.14	12.34	12.85
Sm	2.900	3.034	3.106	3.042	3.205	3.198	2.945	3.211	3.184
Eu	1.003	1.019	1.012	0.903	1.006	1.001	1.001	1.020	0.965
Gd	3.306	3.349	3.309	3.072	3.505	3.366	3.301	3.439	3.285
Tb	0.576	0.580	0.579	0.539	0.614	0.573	0.575	0.590	0.576
Dy	3.614	3.697	3.691	3.438	4.016	3.653	3.737	3.794	3.621
Ho	0.766	0.776	0.770	0.718	0.852	0.765	0.767	0.799	0.763
Er	2.141	2.202	2.210	2.067	2.414	2.166	2.145	2.278	2.205
Tm	0.328	0.332	0.335	0.319	0.362	0.340	0.329	0.351	0.332
Yb	2.111	2.152	2.165	2.084	2.394	2.180	2.128	2.244	2.204
Lu	0.344	0.350	0.352	0.345	0.386	0.363	0.344	0.363	0.364

Table 3. Representative whole-rock compositions of Augustine 2006 eruptive products.—Continued

[The prefix “06AU” has been truncated from all sample IDs. Total iron (FeO_t) as FeO]

Phase	Explosive				Continuous		Effusive		
Map unit	ExPfc	RPpf	ExPfc	RPpf	Cpf	Cpf	EfLf	Efba	EfLf
Lithology	DLSA	LSAS	DIA	HSA	DIA	HSA	DLSA	DIA	DIA
Sample ID	MRT037f	MRT009b	MRT037e	MC004c1	MRT017a	MRT017b	MLC057	KB002C	MLC028
Trace elements measured by ICPMS, in ppm.									
Ba	305	296	337	415	381	439	299	356	440
Th	1.446	1.376	1.615	2.082	1.930	2.144	1.454	1.757	2.143
Nb	2.088	2.028	2.286	2.576	2.526	2.702	2.056	2.387	2.693
Y	19.87	20.42	20.17	19.20	22.24	20.32	19.60	20.71	20.47
Hf	2.388	2.303	2.560	2.837	2.742	2.937	2.341	2.676	2.998
Ta	0.145	0.147	0.159	0.187	0.180	0.193	0.145	0.168	0.192
U	0.582	0.561	0.661	0.847	0.796	0.886	0.585	0.732	0.909
Pb	1.897	1.855	2.125	2.503	2.352	2.686	2.037	1.351	2.648
Rb	12.59	12.25	13.91	17.40	16.07	18.32	12.42	14.83	18.90
Cs	0.284	0.267	0.314	0.415	0.362	0.400	0.272	0.332	0.412
Sr	319	337	325	288	316	327	313	318	322
Sc	24.35	23.39	22.28	15.65	20.16	16.31	25.20	22.71	16.39
Zr	80.8	81.9	87.1	98.8	97.6	103.6	80.2	92.7	104.0

Table 4. Groundmass glass average compositions of Augustine 2006 eruptive products by lithology and sample.

[Sample lithology acronyms are as noted in text. FeO_t—All Fe analyzed as FeO. Analyses reported are normalized to 100% volatile-free. Original totals are reported. n denotes the total number of analyses averaged to give the reported glass compositions. Numbers in parentheses are the standard deviations from the averaged analyses (n total from each thin section)]

Sample-	06AUMC005c	06AUMRT037c	06AUMC007c	06AUMRT009b	06AUMRT037b	06AUMC008a
	LSAS	LSAS	LSAS	DLSA	DLSA	Banded
SiO_2	71.16 (1.57)	77.38 (0.52)	67.48 (1.02)	70.04 (2.07)	68.98 (2.70)	69.25
TiO_2	0.97 (0.29)	0.37 (0.05)	1.17 (0.19)	1.13 (0.12)	0.65 (0.28)	1.33
Al_2O_3	13.72 (0.92)	11.90 (0.28)	14.33 (0.37)	13.77 (0.72)	15.16 (1.30)	13.88
FeO_t	4.03 (0.46)	1.71 (0.19)	5.38 (0.66)	4.04 (0.31)	3.54 (0.69)	4.04
MnO	0.12 (0.07)	0.07 (0.08)	0.17 (0.10)	0.01 (0.00)	0.05 (0.03)	0.07
MgO	0.90 (0.11)	0.37 (0.05)	1.40 (0.21)	0.74 (0.12)	0.64 (0.19)	0.57
CaO	3.13 (0.49)	1.30 (0.18)	4.05 (0.25)	3.37 (0.89)	4.14 (1.07)	3.39
Na_2O	3.37 (0.42)	3.90 (0.12)	3.65 (0.23)	4.21 (0.57)	4.65 (0.59)	4.65
K_2O	2.06 (0.24)	2.90 (0.14)	1.76 (0.18)	1.93 (0.13)	1.80 (0.30)	2.08
P_2O_5	0.23 (0.08)	0.02 (0.04)	0.30 (0.05)	0.46 (0.36)	0.19 (0.08)	0.36
Cl	0.30 (0.08)	0.07 (0.02)	0.31 (0.03)	0.29 (0.03)	0.20 (0.07)	0.38
Totals	99.15	100.18	100.02	100.30	98.53	98.56
n	13	6	11	3	6	1

Table 4. Groundmass glass average compositions of Augustine 2006 eruptive products by lithology and sample.—Continued

[Sample lithology acronyms are as noted in text. FeO_t—All Fe analyzed as FeO. Analyses reported are normalized to 100% volatile-free. Original totals are reported. n denotes the total number of analyses averaged to give the reported glass compositions. Numbers in parentheses are the standard deviations from the averaged analyses (n total from each thin section)]

Sample	06AUMC005c	06AUMRT017a	06AUMRT037e	06AUKFB128	06AUMC004a	06AUMRT017b
	Banded	DIA	DIA	HSA	HSA	HSA
SiO_2	75.54 (0.61)	72.07 (3.65)	69.68	75.70 (0.42)	75.73 (0.68)	75.52 (0.51)
TiO_2	0.38 (0.13)	0.39 (0.12)	0.26	0.43 (0.19)	0.45 (0.18)	0.33 (0.13)
Al_2O_3	12.57 (0.29)	14.23 (1.78)	15.49	12.86 (0.16)	12.85 (0.39)	12.96 (0.34)
FeO_t	1.89 (0.16)	2.52 (0.72)	2.90	1.91 (0.11)	2.05 (0.18)	2.02 (0.16)
MnO	0.07 (0.07)	0.16 (0.08)	0.09	0.05 (0.04)	0.08 (0.08)	0.06 (0.03)
MgO	0.46 (0.13)	0.84 (0.49)	0.58	0.41 (0.04)	0.42 (0.06)	0.41 (0.04)
CaO	2.08 (0.24)	3.51 (1.18)	3.83	2.10 (0.13)	2.08 (0.06)	2.11 (0.17)
Na_2O	4.46 (0.33)	4.08 (0.95)	4.79	4.10 (0.19)	3.83 (0.38)	4.16 (0.16)
K_2O	2.10 (0.13)	1.83 (0.39)	1.78	2.12 (0.10)	2.16 (0.22)	2.07 (0.13)
P_2O_5	0.07 (0.04)	0.12 (0.07)	0.18	0.07 (0.05)	0.08 (0.03)	0.09 (0.03)
Cl	0.39 (0.07)	0.27 (0.07)	0.43	0.25 (0.07)	0.26 (0.06)	0.28 (0.07)
Totals	99.82	99.95	100.12	99.51	99.42	99.21
n	19	7	1	30	52	9

Sample	06AUKFB128	06AUMC004a	06AUMRT017b	06AUMC009p1
	HSA	HSA	HSA	HSA
SiO_2	75.70 (0.42)	75.73 (0.68)	75.52 (0.51)	75.34 (0.25)
TiO_2	0.43 (0.19)	0.45 (0.18)	0.33 (0.13)	0.28 (0.15)
Al_2O_3	12.86 (0.16)	12.85 (0.39)	12.96 (0.34)	12.80 (0.26)
FeO_t	1.91 (0.11)	2.05 (0.18)	2.02 (0.16)	1.83 (0.09)
MnO	0.05 (0.04)	0.08 (0.08)	0.06 (0.03)	0.09 (0.06)
MgO	0.41 (0.04)	0.42 (0.06)	0.41 (0.04)	0.36 (0.03)
CaO	2.10 (0.13)	2.08 (0.06)	2.11 (0.17)	2.03 (0.14)
Na_2O	4.10 (0.19)	3.83 (0.38)	4.16 (0.16)	4.69 (0.20)
K_2O	2.12 (0.10)	2.16 (0.22)	2.07 (0.13)	2.07 (0.06)
P_2O_5	0.07 (0.05)	0.08 (0.03)	0.09 (0.03)	0.09 (0.05)
Cl	0.25 (0.07)	0.26 (0.06)	0.28 (0.07)	0.42 (0.07)
Totals	99.51	99.42	99.21	99.50
n	30	52	9	5

Table 5. Representative pyroxene phenocryst compositions

[Acronyms of sample lithologies are as noted in the text. FeO_t – All Fe analyzed as FeO. Mole fractions of the wollastonite (Wo), enstatite (En), and ferrosilite (Fs) pyroxene quadrilateral components. Mg# is molar Mg /(Mg+Fe). n is the number of individual analyses averaged to provide representative data. Numbers in parentheses are standard deviations about the average representative analyses]

[Core compositions]

	LSAS Opx	LSAS Cpx	DLSA Opx	DLSA Cpx	DIA Opx	DIA Cpx
SiO_2	53.29 (0.72)	52.39 (0.57)	53.33 (0.10)	51.64 (0.26)	52.69 (0.36)	52.10 (0.18)
TiO_2	0.12 (0.03)	0.29 (0.14)	0.16 (0.03)	0.33 (0.13)	0.14 (0.03)	0.26 (0.08)
Al_2O_3	0.80 (0.16)	1.46 (0.45)	0.85 (0.03)	1.78 (0.22)	1.36 (0.70)	1.26 (0.16)
FeO_t	19.81 (0.15)	9.16 (0.64)	20.22 (0.45)	9.01 (0.10)	19.45 (2.43)	8.92 (0.28)
MnO	0.71 (0.05)	0.40 (0.16)	0.76 (0.04)	0.35 (0.09)	0.77 (0.36)	0.52 (0.03)
MgO	23.95 (0.36)	14.76 (0.27)	24.32 (0.23)	14.77 (0.13)	24.46 (1.61)	14.56 (0.20)
CaO	1.05 (0.11)	21.93 (0.27)	1.16 (0.25)	21.39 (1.36)	0.99 (0.34)	23.10 (0.15)
Na_2O	0.04 (0.01)	0.35 (0.06)	0.04 (0.05)	0.35 (0.06)	0.02 (0.03)	0.36 (0.02)
Totals	99.76	100.74	100.84	99.61	99.89	101.05
Wo	2	43	2	43	2	45
En	66	41	66	41	67	40
Fs	32	15	32	15	31	15
Mg #	0.68	0.74	0.68	0.75	0.69	0.75
n	5	3	3	2	3	2

	Banded Opx	Banded Cpx	HSA Opx	HSA Cpx
SiO_2	53.57 (0.39)	51.27 (2.74)	52.68 (0.83)	51.54
TiO_2	0.17 (0.02)	0.63 (0.63)	0.20 (0.04)	0.48
Al_2O_3	0.73 (0.13)	3.29 (3.17)	0.94 (0.15)	4.27
FeO_t	20.01 (0.49)	8.44 (0.72)	19.69 (1.34)	5
MnO	0.71 (0.04)	0.33 (0.13)	0.74 (0.18)	0.05
MgO	24.06 (0.24)	14.60 (0.85)	23.45 (0.79)	16.43
CaO	1.07 (0.09)	22.16 (0.30)	2.33 (2.38)	20.58
Na_2O	0.02 (0.02)	0.28 (0.04)	0.04 (0.06)	0.2
Totals	100.33	101.00	100.06	98.54
Wo	2	45	5	43.11
En	66	41	64	47.88
Fs	32	14	31	8.28
Mg #	0.68	0.76	0.68	0.85
n	4	4	3	1

Table 5. Representative pyroxene phenocryst compositions.—Continued

[Acronyms of sample lithologies are as noted in the text. FeO_t—All Fe analyzed as FeO. Mole fractions of the wollastonite (Wo), enstatite (En), and ferrosilite (Fs) pyroxene quadrilateral components. Mg# is molar Mg /(Mg+Fe). n is the number of individual analyses averaged to provide representative data. Numbers in parentheses are standard deviations about the average representative analyses]

[Rim compositions]

	LSAS Opx rim	LSAS Cpx rim 1	LSAS Cpx rim 2	DLSA Opx rim 1	DLSA Opx rim 2	DLSA Cpx rim	DIA Opx rim 1
SiO_2	53.75 (0.49)	50.44 (1.14)	53.96	53.04 (0.04)	49.06	51.48 (0.15)	53.21 (0.35)
TiO_2	0.15 (0.04)	0.75 (0.21)	0.18	0.16 (0.04)	0.75	0.30 (0.10)	0.16 (0.00)
Al_2O_3	0.84 (0.07)	4.41 (1.15)	1.49	0.80 (0.07)	5.11	1.62 (0.19)	0.79 (0.01)
FeO_t	19.49 (0.61)	8.52 (0.98)	19.07	19.31 (0.81)	7.03	9.15 (0.15)	20.32 (0.64)
MnO	0.65 (0.02)	0.12 (0.04)	0.61	0.67 (0.05)	0.17	0.37 (0.01)	0.78 (0.04)
MgO	24.18 (0.15)	15.06 (0.62)	23.95	24.40 (0.55)	15.28	14.97 (0.11)	24.37 (0.59)
CaO	1.06 (0.06)	20.40 (0.11)	1.26	1.10 (0.01)	20.52	21.94 (0.13)	1.07 (0.14)
Na_2O	0.01 (0.01)	0.24 (0.06)	0.23	0.03 (0.02)	0.27	0.35 (0.01)	0.01 (0.01)
Totals	100.13	99.92	100.75	99.48	98.2	100.15	100.70
Wo	2	42	3	2	42.87	43	2
En	67	43	66	67	44.42	41	66
Fs	31	14	31	31	11.67	15	32
Mg #	0.69	0.76	0.69	0.69	0.79	0.75	0.68
n	5	2	1	2	1	2	2

	DIA Opx rim 2	DIA Cpx rim	Banded Opx rim 1	Banded Opx rim 2	Banded Cpx rim	HSA Opx rim 1	HSA Opx rim 2	HSA Cpx rim
SiO_2	51.99	51.71 (0.74)	53.41 (0.74)	52.33	51.68 (1.70)	53.47 (0.23)	52.86	50.88
TiO_2	0.35	0.68 (0.01)	0.16 (0.03)	0.36	0.51 (0.34)	0.18 (0.02)	0.24	0.42
Al_2O_3	2.17	2.26 (0.39)	0.78 (0.19)	1.25	2.56 (1.44)	0.74 (0.06)	1.35	3.7
FeO_t	8.88	9.84 (0.74)	20.46 (0.35)	8.16	9.36 (0.57)	19.96 (0.22)	9.00	6.78
MnO	0.25	0.37 (0.13)	0.65 (0.05)	0.37	0.26 (0.06)	0.75 (0.15)	0.36	0.21
MgO	17.43	14.55 (0.07)	24.09 (0.45)	15.01	14.79 (0.40)	24.22 (0.11)	14.96	15.96
CaO	19.84	20.80 (0.37)	1.16 (0.11)	22.23	21.55 (1.22)	1.08 (0.10)	21.91	22.04
Na_2O	0.28	0.36 (0.03)	0.00 (0.00)	0.33	0.34 (0.05)	0.03 (0.04)	0.32	0.22
Totals	101.19	100.57	100.73	100.04	101.04	100.41	101.00	100.22
Wo	38	42	2	44.15	43	2	43.32	44.02
En	47	41	66	41.49	41	66	41.18	44.36
Fs	14	16	32	13.16	15	32	14.37	10.82
Mg #	0.78	0.73	0.68	0.77	0.74	0.69	0.75	0.81
n	1	2	3	1	4	2	1	1

Table 6. Representative Fe-Ti oxide pair analyses, temperatures, and oxygen fugacities from Augustine 2006 eruptive products.

[All analyses are averages of multiple points on individual grains; 1 standard deviation is in parentheses. Four select pairs from each lithology were chosen to represent the range of compositions, temperatures, and oxygen fugacities calculated from the oxide probe data. FeO_t is total Fe calculated to FeO. n is the number of analyses per grain. Temperature and oxygen fugacity (f_{O_2}) calculated using QUILF (Andersen and others, 1993) and then decreased by 30 degrees °C because the QUILF algorithm overestimates temperatures by 30 °C in magma with oxygen fugacity RRO (Rutherford and Devine, 1996)]

[HSA lithology]

	06AUMC010p1		**06AUMC010p1**		**06AUMC010p1**		**06AUMC010p1**		**06AUMC005cp1**		**06AUMC005cp1**		**06AUMC005cp1**		**06AUMC005cp1**	
	HSA		**HSA**		**HSA**		**HSA**		**Banded**		**Banded**		**Banded**		**Banded**	
Ti-magnetite																
	Pair 2a		Pair 3		Pair 5		Pair 8		Pair 1a		Pair 2		Pair 4		Pair 5	
TiO_2	8.05	(0.30)	7.12	(0.49)	7.54	(0.47)	7.68	(0.67)	7.28	(0.53)	7.34	(0.45)	7.37	(0.22)	7.28	(0.53)
Al_2O_3	2.36	(0.14)	2.19	(0.09)	2.07	(0.06)	2.00	(0.10)	2.00	(0.09)	2.04	(0.07)	1.99	(0.08)	2.00	(0.09)
FeO_t	81.17	(0.97)	82.08	(0.92)	80.12	(0.75)	82.87	(1.62)	82.17	(2.15)	81.26	(1.30)	82.57	(0.45)	82.17	(2.15)
MnO	0.42	(0.11)	0.47	(0.07)	0.41	(0.08)	0.45	(0.10)	0.43	(0.11)	0.42	(0.11)	0.40	(0.11)	0.43	(0.11)
MgO	1.95	(0.09)	1.80	(1.80)	1.72	(0.06)	1.70	(0.05)	1.59	(0.04)	1.61	(0.04)	1.55	(0.05)	1.59	(0.04)
Cr_2O_3	0.24	(0.05)	0.28	(0.07)	0.28	(0.04)	0.24	(0.06)	0.27	(0.03)	0.29	(0.04)	0.27	(0.05)	0.27	(0.03)
SiO_2	0.07	(0.01)	0.11	(0.11)	0.11	(0.04)	0.08	(0.02)	0.08	(0.04)	0.05	(0.03)	0.04	(0.05)	0.08	(0.04)
Total	94.26		94.05		92.31		95.02		98.32		93.01		94.19		92.47	
n	4		7		9		11		15		9		9		11	
Ilmenite																
TiO_2	35.15	(1.95)	33.58	(3.44)	33.19	(2.15)	31.14	(1.74)	34.03	(1.65)	33.22	(2.48)	32.75	(1.97)	34.03	(1.65)
Al_2O_3	0.43	(0.02)	0.40	(0.121)	0.39	(0.39)	0.40	(0.04)	0.36	(0.04)	0.37	(0.03)	0.37	(0.04)	0.36	(0.04)
FeO_t	59.23	(1.12)	59.18	(1.41)	58.35	(0.52	60.69	(1.28)	58.66	(1.47)	60.86	(0.94)	60.02	(0.36)	58.66	(1.47)
MnO	0.26	(0.06)	0.33	(0.05)	0.27	(0.03)	0.28	(0.05)	0.27	(0.08)	0.29	(0.11)	0.27	(0.10)	0.27	(0.08)
MgO	2.03	(0.03)	1.92	(0.11)	1.79	(0.04)	1.60	(0.05)	1.77	(0.07)	1.58	(0.08)	1.63	(0.04)	1.77	(0.07)
Cr_2O_3	0.12	(0.06)	0.10	(0.05)	0.09	(0.03)	0.11	(0.07)	0.08	(0.07)	0.12	(0.05)	0.10	(0.04)	0.08	(0.07)
SiO_2	0.01	(0.02)	0.03	(0.04)	0.01	(0.01)	0.07	(0.07)	0.04	(0.04)	0.04	(0.09)	0.01	(0.02)	0.04	(0.04)
Total	97.23		95.54		94.09		94.28		95.21		96.48		95.14		94.13	
n	3		7		6		8		5		11		13		5	
T (°C)	840		823		839		855		826		837		838		840	
log f_{O_2}	-10.57		-10.72		-10.53		-10.16		-10.75		-10.51		-10.50		-10.40	

Table 6. Representative Fe-Ti oxide pair analyses, temperatures, and oxygen fugacities from Augustine 2006 eruptive products.—Continued

[All analyses are averages of multiple points on individual grains; 1 standard deviation is in parentheses. Four select pairs from each lithology were chosen to represent the range of compositions, temperatures, and oxygen fugacities calculated from the oxide probe data. FeO_t is total Fe calculated to FeO. n is the number of analyses per grain. Temperature and oxygen fugacity (f_{O_2}) calculated using QUILF (Andersen and others, 1993) and then decreased by 30 degrees °C because the QUILF algorithm overestimates temperatures by 30 °C in magma with oxygen fugacity RRO (Rutherford and Devine, 1996)]

[DIA and DLA lithologies]

	06AUMRT006		**06AUMRT006**		**06AUJFL001b**		**06AUMRT009b**		**06AUMC008bp1**		**06AUMC008bp1**		**06AUMC008bp1**		**06AUMC005cp5**	
	DIA		**DIA**		**DIA**		**DLSA**		**LSAS**		**LSAS**		**LSAS**		**LSAS**	
Ti-magnetite	DIA Pair 1		Pair 3		Pair 1		Pair 1		Pair 1		Pair 3		Pair 6		Pair 4	
TiO_2	8.31	(1.00)	7.54	(0.75)	7.22	(0.43)	10.19	(0.93)	7.73	(0.35)	8.01	(1.06)	11.33	(1.57)	10.40	(1.15)
Al_2O_3	2.18	(0.08)	1.88	(0.21)	2.06	(0.08)	2.11	(0.06)	1.92	(0.10)	2.25	(0.06)	3.20	(0.27)	3.33	(0.13)
FeO_t	81.39	(1.20)	81.22	(0.63)	82.52	(0.79)	80.05	(1.27)	81.72	(1.23)	81.55	(0.95)	76.54	(0.65)	78.72	(0.65)
MnO	0.42	(0.13)	0.43	(0.08)	0.43	(0.07)	0.43	(0.07)	0.40	(0.40)	0.43	(0.09)	0.41	(0.07)	0.36	(0.07)
MgO	2.09	(0.09)	1.94	(0.14)	1.73	(0.04)	2.55	(0.09)	2.00	(0.05)	2.09	(0.08)	2.77	(0.25)	3.05	(0.13)
Cr_2O_3	0.27	(0.04)	0.22	(0.02)	0.30	(0.06)	0.30	(0.04)	0.29	(0.05)	0.31	(0.07)	0.12	(0.02)	0.18	(0.07)
SiO_2	0.29	(0.06)	0.50	(0.36)	0.51	(0.19)	0.27	(0.07)	0.05	(0.02)	0.04	(0.04)	0.11	(0.03)	0.13	(0.20)
Total	94.96		93.72		94.77		95.90		94.10		94.69		94.48		96.16	
n	15		6		14		14		11		5		5		6	
Ilmenite																
TiO_2	34.11	(1.95)	34.88	(2.01)	32.29	(2.06)	35.36	(1.54)	36.38	(2.68)	36.34	(1.25)	36.01	(0.73)	30.82	(5.10)
Al_2O_3	0.44	(0.04)	0.36	(0.04)	0.38	(0.05)	0.52	(0.08)	0.49	(0.21)	0.41	(0.04)	0.63	(0.03)	0.91	(0.51)
FeO_t	59.86	(0.97)	59.37	(0.91)	60.45	(1.20)	58.37	(1.13)	57.60	(2.23)	57.46	(0.66)	59.34	(0.48)	60.62	(3.68)
MnO	0.26	(0.08)	0.28	(0.07)	0.24	(0.10)	0.25	(0.04)	0.26	(0.10)	0.32	(0.06)	0.18	(0.07)	0.23	(0.12)
MgO	2.05	(0.08)	1.96	(0.06)	1.77	(0.14)	2.37	(0.16)	2.41	(0.14)	2.20	(0.09)	2.56	(0.05)	2.95	(0.33)
Cr_2O_3	0.11	(0.04)	0.10	(0.06)	0.11	(0.04)	0.12	(0.03)	0.06	(0.05)	0.11	(0.06)	0.12	(0.02)	0.12	(0.04)
SiO_2	0.12	(0.16)	0.18	(0.11)	0.46	(0.24)	0.17	(0.05)	0.05	(0.08)	0.02	(0.02)	0.01	(0.01)	0.03	(0.02)
Total	96.95		97.12		95.70		97.17		97.24		96.86		98.85		95.68	
n	13		13		16		7		9		6		4		4	
T (°C)	853		829		836		890		825		827		925		968	
log f_{0_2}	-10.31		-10.70		-10.48		-9.91		-10.87		-10.84		-9.45		-8.51	

Table 7. Representative olivine analyses from Augustine 2006 eruptive products.

[Each analysis is representative of one point from core or rim of olivine crystal. Relative error is less than 1 % on each analysis. Texture refers to symplectite rimmed (Symplectite), euhedral unrimmed (Euhedral), pyroxene rimmed (Px rimmed), and hopper (Hopper) olivine respectively. FeO_t is total Fe calculated as Fe^{2+}. Fo is mole percent forsterite content. Mg# is mols Mg divided by total mols of Mg, Fe^{2+}, and Fe^{3+}]

	HSA		**Banded**		**Banded**		**DIA**		**DIA**	
Sample ID	06AUMRT017b		06AUMRT037a		06AUMC008a		06AUJFL001b		06AUJFL001b	
Texture	Symplectite		Symplectite		Euhedral		Symplectite		Px rimmed	
	Core	Rim	Core	Rim	Core	Rim	Core	Rim	Core	Rim
SiO_2	39.22	38.25	38.42	37.75	39.24	39.40	39.64	38.06	40.42	40.26
TiO_2	0.03	0.01	0.02	0.00	0.04	0.04	0.02	0.05	0.01	0.01
Cr_2O_3	0.01	0.02	0.00	0.00	0.03	0.11	0.01	0.00	0.00	0.05
FeOt	17.33	22.01	20.74	21.18	15.09	14.80	20.20	23.05	13.70	13.71
MnO	0.37	0.36	0.36	0.46	0.20	0.22	0.44	0.50	0.27	0.05
MgO	44.54	40.58	39.68	40.12	43.70	43.36	40.14	38.78	46.97	46.28
CaO	0.13	0.05	0.06	0.09	0.15	0.11	0.07	0.06	0.16	0.18
Total	101.78	101.48	99.44	99.76	98.45	98.05	100.54	100.68	101.76	100.62
Fo	81.77	76.38	77.02	76.76	83.58	83.73	77.60	74.58	85.70	85.71
Mg#	0.82	0.77	0.77	0.77	0.84	0.84	0.78	0.75	0.86	0.86

	DLSA		**DLSA**		**DLSA**		**LSAS**		**LSAS**	
Sample ID	06AUMRT032a		06AUMRT032a		06AUMC008bp3		06AUJFL001e		06AUMC008bp1	
Texture	Euhedral		Hopper		Symplectite		Px rimmed		Euhedral	
	Core	Rim	Core	Rim	Core	Rim	Core	Rim	Core	Rim
SiO_2	40.31	41.00	39.13	38.73	40.21	39.42	39.24	38.45	39.81	38.91
TiO_2	0.00	0.00	0.03	0.00	0.00	0.02	0.02	0.00	0.10	0.02
Cr_2O_3	0.03	0.03	0.03	0.04	0.00	0.03	0.01	0.03	0.04	0.05
FeOt	13.06	13.22	16.02	19.17	21.45	20.41	14.42	15.16	15.76	18.74
MnO	0.12	0.23	0.27	0.39	0.45	0.30	0.28	0.18	0.20	0.37
MgO	46.89	46.04	45.73	43.14	37.97	38.30	46.47	45.30	43.20	40.49
CaO	0.18	0.18	0.17	0.15	0.05	0.06	0.16	0.16	0.17	0.19
Total	100.89	100.98	101.60	101.87	100.14	98.54	100.82	99.49	99.29	98.77
Fo	86.38	85.92	83.34	79.72	75.54	76.72	84.92	84.03	82.82	79.07
Mg#	0.86	0.86	0.84	0.80	0.76	0.77	0.85	0.84	0.83	0.79

Table 8. Representative amphibole phenocryst compositions from Augustine 2006 eruptive products.

[Sample lithology acronyms are as noted in the text. One standard deviation is in parentheses. FeO_t is total Fe calculated as Fe^{2+}. Compositions are averages of n points on a single phenocryst]

	06AUMC004cp1	06aujfl001b	06aumrt032b	06aumrt037e	06aumrt037c	06aumc013a
	HSA	DIA	DIA	DIA	LSAS	FGGI
SiO_2	45.52 (0.61)	42.74 (0.42)	45.84 (0.22)	45.90	44.28 (0.17)	45.00 (0.80)
TiO_2	2.03 (0.48)	2.10 (0.63)	1.48 (0.33)	1.81	1.44 (0.12)	1.52 (0.62)
Al_2O_3	8.15 (0.17)	12.09 (0.19)	8.63 (0.11)	9.21	9.31 (0.21)	9.26 (0.52)
FeO_t	11.63 (0.28)	10.97 (0.36)	12.64 (0.38)	12.70	13.00 (0.33)	12.08 (0.41)
MnO	0.25 (0.04)	0.18 (0.06)	0.37 (0.14)	0.37	0.44 (0.09)	0.38 (0.11)
MgO	15.68 (0.15)	14.89 (0.07)	14.91 (0.18)	14.91	14.77 (0.29)	15.14 (0.29)
CaO	11.83 (0.63)	12.17 (0.56)	12.86 (0.38)	12.29	11.15 (0.85)	12.75 (0.10)
K_2O	0.15 (0.02)	0.24 (0.01)	0.12 (0.02)	0.22	0.17 (0.03)	0.11 (0.04)
Na_2O	1.77 (0.21)	2.30 (0.19)	1.64 (0.05)	1.74	1.78 (0.07)	1.79 (0.15)
Cl	0.06 (0.04)	0.05 (0.04)	0.07 (0.4)	0.06	0.06 (0.01)	0.08 (0.02)
Total	97.08 (1.09)	97.73 (0.72)	98.56 (0.82)	99.22	96.38 (1.61)	98.10 (0.69)
n	4	5	4	1	3	4

Appendixes 1–5. Additional Descriptions and Compositional Data for Samples Used in This Study

Appendix 1. Samples of Augustine Volcano 2006 eruptive products used in this study, sorted by eruptive unit and lithologic type.

[This appendix appears only in the digital version of this work—in the DVD-ROM that accompanies the printed volume and as a separate file accompanying this chapter on the Web at http://pubs.usgs.gov/pp/1769]

This table lists samples of Augustine Volcano 2006 eruptive products used in this study. The samples are sorted by eruptive unit and lithologic type.

Appendix 2. Modal Mineralogy and Point Count Data for the Augustine Eruptive Lithologies.

[This appendix appears only in the digital version of this work—in the DVD-ROM that accompanies the printed volume and as a separate file accompanying this chapter on the Web at http://pubs.usgs.gov/pp/1769]

This table presents the modal mineralogy data, determined from 1,000 point counts from thin sections of each lithology. These data form the basis for the average modal mineralogy data presented in table 2 and figure 4.

Appendix 3. Augustine Whole-Rock Geochemical Analyses.

[This appendix appears only in the digital version of this work—in the DVD-ROM that accompanies the printed volume and as a separate file accompanying this chapter on the Web at http://pubs.usgs.gov/pp/1769]

This appendix includes data collected by the Washington State University Geoanalytical Laboratory for the Alaska Volcano Observatory. The data include analyses from 2006 Augustine eruptive products, as well as pre-2006 historical, and early Holocene and Pleistocene samples.

Appendix 4. Groundmass Glass Electron Microprobe Analyses from Augustine 2006 Samples used in this Study.

[This appendix appears only in the digital version of this work—in the DVD-ROM that accompanies the printed volume and as a separate file accompanying this chapter on the Web at http://pubs.usgs.gov/pp/1769]

This appendix includes glass compositional analyses from several major lithologies form the 2006 eruptive products. It also includes glass data from tephra samples from December 24, 2005 and January 13, 14, and 17,2006. Tephra analyses from 1986 samples are also included for comparison. The data included in this appendix is also plotted in figure 11 in the text.

Appendix 5. Representative Electron Microprobe Analyses of Plagioclase Phenocrysts in Augustine 2006 Samples used in this Study.

[This appendix appears only in the digital version of this work—in the DVD-ROM that accompanies the printed volume and as a separate file accompanying this chapter on the Web at http://pubs.usgs.gov/pp/1769]

The electron microprobe analyses presented here represent the core to rim transects shown in figure 12 of the text.

The 2006 Eruption of Augustine Volcano, Alaska
Power, J.A., Coombs, M.L., and Freymueller, J.T., editors
U.S. Geological Survey Professional Paper 1769

Chapter 16

Augustine Volcano—The Influence of Volatile Components in Magmas Erupted A.D. 2006 to 2,100 Years Before Present

By James D. Webster[1], Charles W. Mandeville[1], Beth Goldoff[1], Michelle L. Coombs[2], and Christine Tappen[3]

Abstract

The petrology and geochemistry of 2006 eruptive products of Augustine Volcano, Alaska, have been investigated through analyses of whole-rock samples, phenocrysts, silicate melt inclusions, and matrix glasses to constrain processes of magma evolution, eruption, and degassing. Particular attention was directed toward the concentrations and geochemical relationships involving the magmatic volatile components H_2O, CO_2, S, and Cl. The analytical results for 2006 samples have been integrated with data for samples of Pleistocene basalt, prehistoric andesites, and 1986 andesites from Augustine to provide a broad view of volatile behavior in Augustine magmas. The observation of generally similar geochemical features for this range of eruptions indicates that magmatic and volatile degassing processes have been relatively consistent during the past 2,100 years.

Augustine andesites range from low-silica to high-silica compositions and contain phenocrysts of plagioclase, orthopyroxene, and clinopyroxene, with lesser olivine, amphiboles, iron-titanium oxides, and apatite. The groundmass varies from strongly crystallized and/or oxidized to comparatively clear, microlite-poor vesicular glass. Coexisting iron-titanium oxides of 2006 rock samples, which are generally consistent with those of prior eruptive materials, indicate f_{O_2} values of approximately NNO+1.5 to NNO+2.5 and oxide crystallization temperatures of 835 to 1,052°C.

The compositions of matrix and melt-inclusion glasses range from rhyodacite to rhyolite and show relationships that reflect magma evolution involving fractional crystallization and multiple stages of mingling and/or mixing. In particular, melt inclusions of low-silica andesites express mixing of magmas with more widely varying compositions, than do melt inclusions of high-silica andesites and dacites. The melt inclusions of 2006, 1986, and prehistoric andesites contain moderate to high concentrations of H_2O and Cl and lesser CO_2 and SO_2. Comparing the abundances of H_2O, CO_2, and Cl in these melt inclusions with experimentally established volatile solubilities for felsic melts indicates that the 2006 and prehistoric samples are most consistent with the ascent of fluid-saturated magmas containing 1 weight percent of H_2O-enriched vapor under closed-system conditions and that pressures of volatile phase exsolution range from 150 to less than 20 MPa. This closed-system behavior was maintained to quite shallow depths prior to eruption, and this pressure range is consistent with constraints derived from 2006 geodetic measurements indicating magma storage and crystallization at 4 to 6 km and upwards to near-surface depths. The magmatic fluids were relatively oxidizing and included H_2O-enriched and HCl-, H_2S-, S_2-, and $SO_2 \pm CO_2$-bearing vapors; hydrosaline aqueous liquids largely enriched in Cl^-, SO_4^{2-}, alkalis, and H_2O; and moderately saline, H_2O-poor liquids containing Cl^-, SO_4^{2-}, and alkali elements.

Introduction

The diverse 2006 eruptive activities of Augustine Volcano, Alaska, included pyroclastic flows; explosive injection of glassy juvenile ash, rock fragments, and gases into the troposphere and lower stratosphere; and lahars, lava flows, dome-forming extrusions, associated block-and-ash flows, and small phreatic explosions (Power and others, 2006; Vallance and others, this volume; McGee and others, this volume; and other contributions to this volume). The estimated total volume of 2006 eruptive materials is approximately 73 million

---

[1] Department of Earth and Planetary Sciences, American Museum of Natural History, Central Park West at 79th St., New York, NY 10024-5192.

[2] Alaska Volcano Observatory, U.S. Geological Survey, 4200 University Drive, Anchorage, AK 99508.

[3] 251 Pleasant Street, New London, NH 03257.

m^3 (dense-rock equivalent, or DRE; Coombs and others, this volume). The compositions of the erupted magmas, based on whole-rock data, range from basaltic andesite to dacite, though high- through low-silica andesitic magmas were dominant (Larsen and others, this volume; Vallance and others, this volume). Analyses of groundmass glasses establish the maximum in the range in silica content of the most chemically evolved melts as >79 weight percent (Izbekov and others, 2006; Larsen and others, this volume).

Knowledge of the silica content of the eruptive products is important, because the concentration of SiO_2 controls the physical properties of magma, through melt polymerization, which exerts a strong control on eruptive behavior of volcanoes. In this regard, the 2006 Augustine magma compositions changed from (1) dominantly low-SiO_2 andesitic scoria during the January explosive phase, to (2) dominantly high-SiO_2 andesite during a continuous phase of rapid lava effusion in late January and early February, to (3) dense low- and intermediate-SiO_2 andesites during the final, effusive phase in March (Coombs and others, this volume; Vallance and others, this volume; Larsen and others, this volume). Concurrently, the phases of eruptive activities ranged from (1) a series of Vulcanian explosions that produced ash plumes and pyroclastic flows, lahars, and mixed snow and rock avalanches during the explosive phase, to (2) continuous eruption of ash plumes and pyroclastic flows, to (3) an intervening eruptive pause, to (4) late-stage, dome growth and emission of lava flows during the effusive phase.

Magmatic volatile components also control eruptive activities and magmatic processes because they influence: melt viscosity and magma rheology, rates of component diffusion through melts, the thermal stability of aluminosilicate melts and minerals, and the exsolution of fluids. The manner of fluid exsolution exerts a strong control on styles of volcanic eruption and on the compositions and textures of eruptive materials. Thus, it is important to establish the compositions of melt and coexisting magmatic fluids during magma evolution, pre- and syn-eruptive fluid exsolution, and subsequent post-eruptive degassing at Augustine Volcano.

During volcanic activity preceding 2006, Augustine erupted magmas that were variably enriched in the magmatic volatile components H_2O, CO_2, S, and Cl. This observation is well demonstrated from extensive investigations of the 1976 and 1986 eruptions. Johnston's (1978, 1979) analyses of materials erupted in 1976, for example, measured elevated Cl concentrations (0.3 to 0.6 weight percent) in silicate melt inclusions and estimated preeruptive H_2O concentrations to have averaged 6.5 ± 1.5 weight percent. The former study also concluded that some melts erupted in 1976 were saturated in a Cl- and H_2O-rich fluid. Roman and others (2006) studied 1986 eruptive materials, and measured the abundances of H_2O, CO_2, Cl, and SO_3 in melt inclusions. This study also determined that magma mixing processes continued during magma ascent, based on relationships involving H_2O, K_2O, and SiO_2 in the melt-inclusion data. Recent research on materials erupted in prehistoric time has determined highly variable enrichments of magmatic H_2O and Cl (Tappen and others, 2009) and evidence of preeruptive volatile phase saturation of some fractions of these ancient magmas (Webster and others, 2006).

The objectives of this investigation are to determine the petrologic characteristics, major-element compositions, and abundance of volatile components of silicate melt inclusions and matrix glasses representing magmas erupted in A.D. 2006 and those erupted in prehistoric time (for example, 2,100, 1,700, 1,400, and 1,000 years before present) and more recently (A.D. 1986). The petrology and geochemistry of 2006 eruptive products are addressed in more detail by Larsen and others (this volume). We have integrated compositional data for 238 melt inclusions and 42 analyses of matrix glasses to illuminate relationships between the volatile components and processes of magma evolution, magmatic volatile phase exsolution, and ensuing processes of volcanic eruption at Augustine Volcano.

We refer to fluids and/or volatile phases, in this chapter, to include all noncrystalline, polycomponent phases, but this terminology does not bear on silicate melts that also are fluids by this definition. Relatively low-density, volatile component-enriched phases are denoted vapor, and higher density phases are referred to as liquid. The low-density phases are commonly dominated by H_2O and/or CO_2, and higher-density liquids are most commonly enriched in H_2O and electrolytes and may also involve molten sulfides. We refer to electrolyte-enriched fluids as saline, and the relatively dense fluids that are dominated by aluminosilicate constituents are addressed as melts.

Samples Investigated

This investigation reports petrologic and petrographic descriptions and compositional data for nine rock samples collected from 2006 tephra, dome, pyroclastic-flow, and lahar units (collected in February and August of 2006); a pumice sample from a 1986 pyroclastic-flow deposit; and a sample of Pleistocene basalt (table 1; appendix I). The 2006 samples include high- and low-silica andesites representing magma erupted during the three phases of the 2006 eruption: the explosive, continuous, and concluding effusive phase.

Our 1986 sample (AVO 208) was collected from a broad pyroclastic-flow deposit on the north flank of the volcano during the summer of 2003 (table 1). The porphyritic olivine basalt (RBW91A137) was found as a juvenile clast in the mid-section of a 10-m thick hyaloclastite outcrop on the volcano's south flank, and was collected there in 1991 by Dr. Richard B. Waitt (U.S. Geological Survey). This singular basalt outcrop contains ≤18 cm-wide, rounded to subangular, porphyritic olivine basalt clasts in a palagonite matrix and is presumably Pleistocene in age (Waitt and Begét, 2009).

The data resulting from the investigation of these samples are compared with results from Tappen and others (2009) of similar research on five samples of prehistoric fall deposits (tephra units C1 (AVO 201), C2 (AVO 202), H (AVO 204),

Table 1. Descriptions and collection localities for rock samples from Augustine Volcano, Alaska.

Rock Sample	Unit	Age of Eruption	Sample Type	Sample Location
RBW91A137	Juvenile clast-bearing hyaloclastite	Pleistocene[1]	Porphyritic olivine basalt	South flank of volcano
AVO 201	Lower C1 tephra	≈ 1,000 yr B.P.	Light-gray pumiceous tephra	Near South Point
AVO 202	Lower C2 tephra	≈ 1,000 yr B.P.	Light-gray pumiceous tephra	Near South Point
AVO 203	Tephra I	≈ 1,700 yr B.P.	Light-gray pumiceous tephra	Yellow Cliffs
AVO 204	Tephra H	≈ 1,400 yr B.P.	Light-gray pumiceous tephra	Between SE Point and East Point
AVO 205	Tephra G	≈ 2,100 yr B.P.	Light-gray pumiceous tephra	Near NE Point
AVO 208	Pyroclastic flow	A.D. 1986	Pumiceous tephra	North slope of volcano
06AUMC010.p1	Pyroclastic flow	A.D. 2006	High-silica andesite	NNE of crater
06AUMC008B.p1A	Lahar	A.D. 2006	Low-silica andesite scoria; banded	SSE coast of island
06AUMC005c.p5A	Lahar	A.D. 2006	Low-silica andesite scoria	SSW coast of island
06AUCWM007	Pyroclastic flow	A.D. 2006	Low-silica andesite scoria	N slope near crater rim
06AUCWM012	Block and ash flow	A.D. 2006	High-silica andesite	N slope near crater rim
06AUCWM014	Block and ash flow	A.D. 2006	Dense low-silica andesite	N slope near crater rim
06AUJW001	Dome extrusion	A.D. 2006	Oxidized, dense low-silica andesite	Crater rim
06AUJW004	Pyroclastic flow	A.D. 2006	Dense low-silica andesite	N slope near crater rim
06AUJW010	Block and ash flow	A.D. 2006	Dense low-silica andesite	N slope near crater rim

[1] Basalt estimated to have formed during Pleistocene eruption (Waitt and Begét, 2009).

I (AVO 203), G (AVO 205), using the nomenclature of Waitt and Begét, 2009), and with samples from the 1986 eruption studied by Roman and others (2006). Details on sample localities, petrology, and geochemistry for the prehistoric tephra samples are included therein.

Methods

Sample Preparation

Phenocrysts, silicate melt inclusions, and matrix glasses were analyzed in polished thin sections and in grain mounts prepared by gently crushing the rocks, picking individual phases, and mounting these phases on glass slides with epoxy. Three to five polished thin sections were prepared from each of the 2006 samples and studied petrographically.

The great majority of silicate melt inclusions in these samples are, as described below, vitreous and free of daughter crystals, but most melt inclusions hosted by clinopyroxene of the basalt sample (RBW91A137) are partially crystallized so they were re-fused to glass by heating mineral separates of melt inclusion-bearing, clinopyroxene phenocrysts at 1,100 to 1,150°C for 4 to 6 hours in open crucibles at one atmosphere.

Electron Microprobe Analysis

Electron microprobe analyses (EPMA) of glass and minerals were conducted with a Cameca SX-100 at the American Museum of Natural History (AMNH). Pyroxene, amphibole, and plagioclase phenocrysts, as well as glass in melt inclusions and in groundmass were analyzed for SiO_2, Al_2O_3, Na_2O, K_2O, CaO, FeO, MnO, TiO_2, MgO, F, P_2O_5, Cl, and S using wavelength-dispersive techniques at 15 KeV. We used a 2-nA beam current to analyze Na_2O, K_2O, FeO, SiO_2, and F, and a 10-nA beam current to analyze all other elements. The peak counting times for Na_2O, K_2O, SiO_2, and F were 20 seconds; for FeO were 20 to 30 seconds; for Al_2O_3, CaO, MnO, TiO_2, and MgO were 30 seconds; and for P_2O_5, Cl, and S were 40 to 60 seconds. Standards for S, Cl, and F were $BaSO_4$, scapolite, and synthetic MgF_2, respectively. The major- and trace-element concentrations of internal "standard" glasses (a felsic peralkaline obsidian and a natural topaz rhyolite reference glass that are generally similar in composition to that of the glasses of this study) were also determined to monitor analytical accuracy and instrumental drift. The 1-σ analytical precision for the glass analyses has been estimated from 26 analyses of the obsidian (conducted during five analytical sessions spanning a one-year period and given here in relative percent): 0.7 for SiO_2, 1 for Al_2O_3, 3 for K_2O, 4 for Cl, 5 for Na_2O, 8 for CaO, 10 for FeO, 30 for F and TiO_2, and 60 for MnO. The abundances of MgO, S, and P_2O_5 are <0.005 weight percent in this obsidian and hence unrepresentative of the melt-inclusion compositions, so their 1-σ precisions were estimated from melt-inclusion data from individual samples to be ≤8, 25, and 25 relative percent, respectively.

To minimize Na and K migration during glass analyses, these constituents were analyzed with a 2-nA beam current during the first pass and the melt inclusions and areas of matrix glass were moved constantly under a defocused beam. We also used a subcounting (time zero intercept) routine for some Na analyses in melt inclusions from low-silica andesite. The stability of the Na and K signals for glass analyses reported in this study was confirmed by conducting 3 successive analyses on the same area of glass of randomly selected samples. Most melt-inclusion and matrix-glass analyses utilized an 8-µm electron-beam diameter, but a 4-µm beam diameter was required for some analyses of matrix glasses to avoid vesicles and microlites. Additionally, the small size and paucity of crystal-free melt inclusions in sample 06AUJW001 demanded the use of a 2-µm beam diameter for analysis on a stationary point on the melt inclusion, but the glass was moved under the beam during analysis.

Pairs of adjoining titanomagnetite and ilmenite grains were analyzed for Al_2O_3, FeO, MnO, TiO_2, and MgO with the electron beam set at 40 nA, 15-Kev, and with a 1-µm beam diameter. All elements were counted for 30 seconds at the peak position. Major- and trace-element concentrations of minerals were verified on magnetite and ilmenite standards.

Infrared Spectroscopic Analyses of Glasses

Dissolved H_2O and CO_2 concentrations in the glass of melt inclusions were measured by Fourier Transform Infrared (FTIR) spectroscopy utilizing techniques described by Newman and others (1986) and Mandeville and others (2002) that are summarized here. Room-temperature infrared (IR) spectroscopic measurements on melt inclusions of prehistoric and 1986 samples were conducted in transmittance mode using a Nicolet 20SXB FTIR spectrometer attached to a Spectra Tech IR Plan microscope at the AMNH. IR spectra were collected over the mid-IR to near-IR regions using a KBr beam splitter, MCT/A detector, globar source, and 1,000 scans with a spectral resolution of 4 cm^{-1}. More recent transmission FTIR analyses of melt inclusions in 2006 samples were performed with a Thermo Electron Nexus 670 spectrometer interfaced with a Continuum IR microscope at the AMNH utilizing a KBr beam splitter, MCT/A detector, globar source, and 200 to 400 scans with 4 cm^{-1} spectral resolution. For all analyses, the IR objective and spectrometer were purged with dry nitrogen at a rate of 15 liters/minute.

The melt inclusion and matrix glasses were analyzed 3 to 4 times each, and the total dissolved H_2O and CO_2 concentrations in these glasses were determined from the intensity of IR bands at 4,500 cm^{-1} (hydroxyl OH^-) and 5,200 cm^{-1} (molecular H_2O) and 2,350 cm^{-1} (CO_2). The reported H_2O concentrations refer to total H_2O. The thicknesses of the doubly polished, melt inclusion-bearing phenocryst wafers were measured 8 to 10 times using a Mitutoyo digimatic indicator which has a precision of $\pm$2 µm. The 1-σ precision for H_2O and CO_2 analyses of these glasses is estimated as 0.1 and 0.02 weight percent, respectively.

Results

Description of the Rock Samples

All of the prehistoric tephra, 1986, and 2006 rock samples are porphyritic and contain phenocrysts of plagioclase, orthopyroxene, and clinopyroxene with plagioclase dominant; the abundance of orthopyroxene is subequal to or exceeds that of clinopyroxene. Most samples also contain minor to trace phenocrystic olivine and amphibole, and the accessory phases include apatite and Fe-Ti oxides. Larsen and others (this volume) report that all 2006 rocks that they examined contain 36 to 44 volume percent phenocrysts, and Tappen and others (2009) observed 30 to 40 volume percent phenocrysts in the prehistoric tephra. The groundmass materials are vesicular and vitreous to strongly devitrified. All rocks contain trace to abundant microlites. The Pleistocene olivine basalt (RBW91A137) is porphyritic and contains 0.2 to 11 volume percent plagioclase (An_{74-91}), 12.2 to 14.2 volume percent clinopyroxene ($Wo_{35-42}En_{48-53}Fs_{5-11}$) 3.5 to 6.5 volume percent olivine ($Fa_{13-22}Fo_{77-88}$), 1.7 volume percent amphibole (Mg numbers of 63-73), and trace amounts of orthopyroxene ($Wo_2En_{66}Fs_{32}$) (Daley, 1986; C. Tappen, unpublished data). Additional petrographic details for all samples are provided in the appendix and by Tappen and others (2009).

The whole-rock compositions for three of these samples were determined and are reported in table 2. The other six samples were not analyzed, but given their textural and mineral-chemical characteristics that are described below, we determine that most are low- to high-silica andesites on the basis of comparisons with sample descriptions and analyses from Larsen and others (this volume).

Phenocrysts

Plagioclase

Plagioclase occurs as phenocrysts and microphenocrysts, and individual crystals appear twinned, broken, rounded,

Table 2. Bulk compositions of whole-rock samples, Augustine Volcano, Alaska

[Major to trace elements (including Ni-Zn) measured by X-ray fluorescence and all other trace elements by inductively coupled plasma mass spectroscopy at Washington State University]

Rock Sample	06AUMC005c.p5	06AUMC008b.p1	06AUMC010.p1
(wt percent)			
SiO_2	57.42	57.35	62.61
Al_2O_3	17.67	17.52	16.81
TiO_2	0.72	0.72	0.56
MgO	4.61	4.75	3.36
CaO	8.51	8.46	6.64
MnO	0.14	0.14	0.13
FeO[1]	6.58	6.73	5.36
Na_2O	3.48	3.46	3.81
K_2O	0.74	0.74	0.98
P_2O_5	0.13	0.13	0.14
TOTAL	99.61	99.11	98.87
(ppm)			
Ni	28	28	24
Cr	56	60	43
V	195	195	130
Ga	17	17	17
Cu	36	36	20
Zn	61	63	57
La	8.21	8.21	10.36
Ce	17.22	17.28	20.98
Pr	2.28	2.31	2.66
Nd	10.55	10.76	11.77
Sm	3.05	3.08	3.13
Eu	1.02	1.00	0.97
Gd	3.32	3.30	3.24
Tb	0.57	0.58	0.56
Dy	3.61	6.71	3.51
Ho	0.78	0.79	0.76
Er	2.15	2.25	2.19
Tm	0.33	0.33	0.33
Yb	2.11	2.16	2.19
Lu	0.34	0.35	0.36
Ba	314	313	427
Th	1.46	1.49	2.12
Nb	2.26	2.21	2.83
Y	20.84	21.38	21.39
Hf	2.43	2.51	2.98
Ta	0.16	0.16	0.20
U	0.55	0.58	0.81
Pb	2.15	1.94	2.50
Rb	13.0	13.0	18.2
Cs	0.30	0.29	0.40
Sr	319	320	312
Sc	24.9	26.1	20.3
Zr	83	83	104

[1] All iron reported as FeO.

or euhedral. Plagioclase is also a dominant component of glomeroporphyritic aggregates containing orthopyroxene and clinopyroxene ± Fe-Ti oxides. These multiphase clots have been observed previously in the products of other eruptions by Johnson (1986) and Tappen and others (2009) and may represent breakdown of amphibole and pyroxene or remobilized phenocrysts from earlier magmas. Most plagioclase crystals range from 0.05 to 3.5 mm in length, but a few rare phenocrysts are as large as 4.8 mm in length. Plagioclase phenocrysts exhibit a variety of internal textural features including: simple normal and reverse zoning, simple oscillatory zoning, oscillatory zoning with complex internal resorption-growth boundaries and/or as rims, and other oscillatory zoned phenocrysts contain coarse sieve textures in cores. Although most are characterized by simple oscillatory zoning; more rarely, plagioclase phenocrysts are composed of coarsely sieved cores surrounded by growth boundaries that are both oscillatory in composition and appear complexly resorbed. Melt inclusions, inclusions of orthopyroxene microlites, and oxide inclusions occur within these compositional resorption-growth boundaries. Other growth zones contain dusty material that is texturally reminiscent of crystallized groundmass.

Plagioclase phenocrysts and microphenocrysts from seven 2006 samples range from andesine to bytownite (An_{36-82}; table 3). Larsen and others (this volume) provide a detailed analysis of plagioclase petrography, geochemistry, and crystallization history for 2006 samples.

Pyroxenes

Orthopyroxene is more abundant than clinopyroxene in most samples. Pyroxenes typically have subhedral to euhedral crystal morphologies, but some grains are distinctly rounded. Most pyroxene phenocrysts are not zoned.

Orthopyroxene phenocrysts are typically larger than clinopyroxene phenocrysts. The former exhibit lengths as large as 1.8 mm while most are <1.2 mm in length. Orthopyroxene phenocrysts in three 2006 samples are hypersthene with $Wo_{1-3}En_{64-76}Fs_{21-33}$ and Mg numbers of 66-78 (table 4). Clinopyroxene occurs as subhedral to euhedral crystals with most phenocrysts ranging from 0.05 to 1 mm in length. A few rare phenocrysts are up to 2 mm in length. Clinopyroxene phenocrysts in three 2006 samples are augitic with $Wo_{44-45}En_{41-47}Fs_{7-14}$ and Mg numbers of 74 to 87. Most phenocrysts contain ≤2 weight percent Al_2O_3, but some contain nearly 5 weight percent Al_2O_3.

Iron-titanium oxides

Ilmenite and titanomagnetite occur as phenocrysts, microphenocrysts, and microlites in the groundmass, and as inclusions in other phenocrysts of these samples. The oxides are subhedral to anhedral, and some are as large as 0.5 mm in length although most are ≤0.3 mm long. All but two of the samples contain both oxides in physical contact with one another, and most exhibit little to no visible evidence of exsolution.

The composition of ilmenite in four 2006 samples ranges from X_{ilm} 0.50 to 0.72 and the corresponding titanomagnetite compositions range from X_{usp} 0.21 to 0.48 (calculated with QUILF of Andersen and others, 1993, and evaluated by Bacon and Hirshmann, 1988). Estimated equilibration temperatures and oxygen fugacities (f_{O_2}), based on the compositions of coexisting oxide minerals, are reported in table 5. We note that because of the elevated f_{O_2} of these magmas, which are outside of the acceptable calibration range for the QUILF algorithm (Evans and others, 2006; Lattard and others, 2005), we reduced the temperatures determined with QUILF and reported in the figures and tables by 30°C (Rutherford and Devine, 1996). This approach is consistent with that of Larsen and others (this volume).

Amphibole

Approximately one-half of the 2006 samples studied contain rare amphibole, and sample 06AUJW001 contains several volume percent amphibole. Most of the rare amphibole phenocrysts are subhedral and rounded, and some crystals are embayed. Of the amphiboles observed in these samples, roughly half of the crystals show either reaction rims or rim alteration, and the other half are devoid of evidence of mineral replacement of amphibole rims. Some amphibole occurs as inclusions in other silicate minerals.

Analyzed amphiboles contain from 45.4 to 49.4 weight percent SiO_2, 6.2 to 9.4 weight percent Al_2O_3, 14.8 to 15.9 weight percent MgO, and 11.4 to 13.0 weight percent FeO (table 6). The TiO_2 content ranges from 1.0 to 2.4 weight percent, and total alkalis vary from 1.3 to 2.3 weight percent. Na_2O and K_2O exhibit negative correlations with the SiO_2 contents of amphibole (table 6). All 2006 amphiboles analyzed in this study are identified as magnesio-hornblende based on the classification of Leake (1997) and Hawthorne and Oberti (2007). Chlorine concentrations range from 0.06 to 0.09 weight percent with the highest value occurring in the core of an iron-rich crystal that is zoned with respect to Mg, Ti, Ca, F and Cl (table 6). Fluorine concentrations in 2006 amphiboles vary widely from below detection (<0.02 weight percent) to 0.47 weight percent in the rim of this zoned crystal (table 6). One amphibole from a dense, intermediate-silica andesite scoria clast (06AUJFL001b; Larsen and others, this volume, their table 8) erupted during the continuous phase (January 28 to February 10, 2006) contains 42.8 weight percent SiO_2, 14.9 weight percent MgO, 10.96 weight percent FeO, 2.3 weight percent Na_2O, 9.9 weight percent CaO, and 0.05 weight percent Cl as well as elevated Al_2O_3 (for example, 11.4 weight percent) slightly extending the range of compositions determined for 2006 samples.

Olivine

Olivine is a very minor phase in most of the 2006 rocks studied. It typically occurs as small rounded, subhedral, embayed, and altered grains generally <0.6 mm in diameter. The typical form of alteration involves oxidation along rims

Table 3. Compositions of plagioclase in 2006 rock samples of Augustine Volcano, Alaska.

[Electron microprobe analyses (wt percent) of representative plagioclase phenocrysts from seven rock samples]

Rock Sample	**06AU JW004**	**06AU JW004**	**06AU JW010**	**06AU JW010**	**06AU CWM007**	**06AU CWM007**	**06AU CWM012**	**06AU CWM012**	**06AU MC005**	**06AU MC005**	**06AU MC008**	**06AU MC008**	**06AU MC010**	**06AU MC010**
Composition	Anorthitic	Albitic	Anorthitic	Albitic	Anorthitic	Albitic	Anorthitic	Subequal An-Ab	Anorthitic	Subequal An-Ab	Anorthitic	Albitic	Anorthitic	Albitic
SiO_2	48.20	55.02	51.16	57.50	51.55	58.36	47.64	54.26	52.48	56.69	48.84	60.86	54.12	56.60
Al_2O_3	33.28	29.50	31.74	26.95	30.59	26.89	33.63	28.52	30.62	27.80	31.49	23.88	29.91	27.28
TiO_2	0.01	0.00	0.00	0.01	0.03	0.07	0.04	0.03	0.00	0.05	0.00	0.03	0.02	0.00
MgO	0.04	0.02	0.03	0.08	0.04	0.03	0.02	0.04	0.01	0.00	0.06	0.04	0.02	0.03
CaO	16.38	9.77	14.30	8.99	13.48	9.00	16.80	10.93	13.21	10.33	16.24	7.20	12.70	9.62
MnO	0.02	0.00	0.03	0.00	0.00	0.00	0.04	0.00	0.07	0.00	0.03	0.00	0.05	0.00
FeO	0.47	0.23	0.40	0.38	0.52	0.29	0.41	0.49	0.38	0.05	0.79	0.87	0.33	0.29
Na_2O	2.33	7.07	3.50	5.57	3.54	5.86	1.99	5.99	3.90	5.68	2.42	6.93	4.04	6.20
K_2O	0.02	0.12	0.05	0.18	0.10	0.15	0.07	0.11	0.08	0.14	0.06	0.42	0.07	0.19
TOTAL	100.75	101.73	101.21	99.66	99.85	100.64	100.63	100.37	100.74	100.74	99.93	100.23	101.26	100.21
Chemical Formula														
Si	2.20	2.45	2.30	2.58	2.35	2.59	2.18	2.45	2.37	2.52	2.25	2.71	2.42	2.54
Al	1.79	1.55	1.69	1.43	1.64	1.41	1.81	1.52	1.63	1.46	1.71	1.25	1.57	1.44
Ti	0.00	0.00	0.00	0.00	0.00	0.00	0.00	0.00	0.00	0.00	0.00	0.00	0.00	0.00
Mg	0.00	0.00	0.00	0.01	0.00	0.00	0.00	0.00	0.00	0.00	0.00	0.00	0.00	0.00
Ca	0.08	0.47	0.69	0.43	0.66	0.43	0.82	0.53	0.64	0.49	0.80	0.34	0.61	0.46
Mn	0.00	0.00	0.00	0.00	0.00	0.00	0.00	0.00	0.00	0.00	0.00	0.00	0.00	0.00
Fe	0.02	0.01	0.02	0.01	0.02	0.01	0.02	0.02	0.01	0.02	0.03	0.03	0.01	0.01
Na	0.21	0.61	0.31	0.48	0.31	0.50	0.18	0.52	0.34	0.49	0.22	0.60	0.35	0.54
K	0.00	0.01	0.00	0.01	0.01	0.01	0.00	0.01	0.00	0.01	0.00	0.02	0.00	0.01
End Members														
An	79.44	43.03	69.11	46.62	67.39	45.50	82.02	49.91	64.88	49.73	78.49	35.58	63.21	45.67
Ab	20.45	56.34	30.60	52.26	32.02	53.60	17.58	49.49	34.65	49.47	21.16	61.95	36.38	53.26
Or	0.12	0.63	0.29	1.11	0.60	0.90	0.41	0.60	0.47	0.80	0.35	2.47	0.41	1.07

[1] FeO represents all iron.

Table 4. Compositions of pyroxenes in 2006 rock samples of Augustine Volcano, Alaska.

[Electron microprobe analyses (wt. percent) of representative orthopyroxene (opx) and clinopyroxene (cpx) phenocrysts from three rock samples. Original iron analysis was determined as FeO and is reported herein separately as Fe_2O_3 and FeO. Chemical formula and end members computed with PRBDATNT (Harlow and others, 2006)]

Rock Sample	06AUM C008b.p1a	06AUM C008b. p1a	06AUM-C008b.p1a	06AUM-C008b.p1a	06AUJ W001	06AUJ W001	06AUJ W001	06AUJ W001	06AUC WM012	06AUC-WM012	06AUC-WM012	06AUC WM012
Mineral	Opx	Opx	Cpx	Cpx	Opx	Opx	Cpx	Cpx	Opx	Cpx	Cpx	Cpx
SiO_2	52.75	53.66	50.02	51.08	53.21	53.57	52.31	52.83	53.23	53.00	52.84	52.37
TiO_2	0.24	0.32	0.08	0.43	0.20	0.17	0.24	0.32	0.05	0.34	0.31	0.25
Al_2O_3	0.83	1.44	4.85	2.16	1.14	0.82	1.29	1.49	0.62	1.59	1.54	1.28
Fe_2O_3	0.81	4.54	2.31	2.32	0.17	0.00	1.86	0.95	0.00	2.23	0.33	0.70
FeO	20.15	12.38	4.14	7.25	18.73	20.71	6.93	8.62	19.65	6.80	8.60	7.36
MnO	0.75	0.49	0.18	0.39	0.57	0.74	0.34	0.33	1.08	0.35	0.30	0.31
MgO	22.63	25.66	15.80	14.10	24.16	23.13	14.58	14.36	23.02	14.46	14.43	14.91
CaO	1.70	1.39	20.95	21.16	1.13	1.10	21.51	21.19	0.89	21.17	21.22	21.26
Na_2O	0.01	0.07	0.26	0.34	0.00	0.03	0.42	0.36	0.07	0.78	0.35	0.29
K_2O	0.00	0.04	0.01	0.00	0.00	0.00	0.02	0.04	0.01	0.00	0.02	0.00
TOTAL	99.87	99.99	98.60	99.23	99.31	100.27	99.50	100.49	98.62	100.72	99.94	98.73
						Chemical Formula						
Si	1.96	1.94	1.85	1.92	1.97	1.98	1.95	1.96	1.99	1.95	1.97	1.97
Al_{IV}[1]	0.04	0.06	0.15	0.08	0.03	0.02	0.05	0.04	0.01	0.05	0.03	0.03
Al	0.00		0.06	0.02	0.02	0.01	0.01	0.02	0.02	0.02	0.03	0.02
Ti	0.01	0.01	0.02	0.01	0.01	0.01	0.01	0.01	0.00	0.01	0.01	0.01
Fe^{3+}	0.02	0.12	0.06	0.07	0.01	0.00	0.05	0.03	0.00	0.06	0.01	0.02
Fe^{2+}	0.63	0.37	0.13	0.23	0.58	0.64	0.22	0.27	0.62	0.21	0.27	0.23
Mn	0.02	0.02	0.01	0.01	0.02	0.02	0.01	0.01	0.03	0.01	0.01	0.01
Mg	1.26	1.38	0.87	0.79	1.33	1.27	0.81	0.79	1.28	0.79	0.80	0.83
Ca	0.07	0.05	0.83	0.85	0.05	0.04	0.86	0.84	0.04	0.84	0.85	0.86
Na	0.00	0.01	0.02	0.03	0.00	0.00	0.03	0.03	0.01	0.06	0.03	0.02
K	0.00	0.002	0.00	0.00	0.00	0.00	0.00	0.00	0.00	0.00	0.00	0.00
Mg numbers[2]	66	78	87	77	69	66	78	74	66	78	74	78
						End Members						
En	64.39	76.35	47.62	42.25	68.08	65.06	43.01	41.72	66.36	43.15	41.80	43.44
Fs	32.12	20.66	7.00	12.19	29.62	32.69	11.44	14.03	31.78	11.41	14.00	12.03
Wo	3.49	2.98	45.38	45.56	2.30	2.25	45.55	44.25	1.86	45.43	44.20	44.53

[1] Tetrahedrally coordinated aluminum.

[2] Mg numbers = 100x(cations Mg/(cations Mg + cations Fe^{2+})). Data are based on analyses of 4 orthopyroxene and 5 clinopyroxene phenocrysts from sample 06AUMC008b.p1a, 4 orthopyroxene and 4 clinopyroxene phenocrysts from sample 06AUJW001, and 6 orthopyroxene and 5 clinopyroxene phenocrysts from sample 06AUCWM012.

Table 5. Compositions of iron-titanium oxide minerals in 2006 samples of Augustine Volcano, Alaska.

[Electron microprobe analyses (wt percent) of representative ilmenite (ilm) and titanomagnetite (usp = ulvospinel) grains. FeO represents all iron]

Rock Sample	06AUM C008	06AUM C008	06AUC WM007	06AUC-WM007	06AUC WM012	06AUC-WM012	06AU JW004	06AUJ W004
Mineral	Ilm	Usp	Ilm	Usp	Ilm	Usp	Ilm	Usp
Oxide (wt percent)								
TiO_2	33.28	12.00	33.69	12.84	35.41	7.99	36.12	9.29
Al_2O_3	0.61	2.92	0.37	1.67	0.41	2.01	0.44	1.98
FeO	58.99	76.74	57.03	78.03	61.86	85.24	61.26	83.69
MnO	0.17	0.35	0.26	0.44	0.32	0.47	0.29	0.44
MgO	2.64	3.23	1.96	2.14	1.88	1.74	1.95	1.94
TOTAL	95.79	95.58	93.45	95.46	100.03	97.83	100.18	97.70
X_{usp}[1]	-	0.376	-	0.374	-	0.221	-	0.258
X_{ilm}[1]	0.642	-	0.619	-	0.627	-	0.627	-
Av. T (°C)[2]	960±55		977±39		845±7		875±29	
Log fo_2[3]	-9.01±0.8		-8.75±0.6		-10.47±0.1		-10.05±.04	
DFMQ[4]	2.0±0.1		2.0±0.3		2.5±0.1		2.3±0.1	
No. of pairs analyzed	10		8		7		8	

[1] Cation assignment based on Stormer (1983). Ulvospinel = usp.

[2] Av. T (°C) = average temperature in °C calculated with QUILF from Andersen and others (1993); data also evaluated using methods of Bacon and Hirshmann (1988), and corrected by reducing temperatures by 30°C given that the range in fo_2 exceeds that of the useful range for QUILF; see text for discussion.

[3] Log fo_2 calculated with QUILF from Andersen and others (1993).

[4] DFMQ = number of log units from the fayalite-magnetite-quartz buffer based on Chou (1978).

and along internal cracks. Representative compositions of olivine phenocrysts in 2006 rocks are reported in table 7 of Larsen and others (this volume).

Groundmass

The groundmass of these samples varies from strongly crystallized and/or oxidized to comparatively clear, microlite-poor vesicular glass. Typically, the high-silica rocks contain trace microlites in the groundmass. For example, samples 06AUJW001, 06AUMC008, 06AUCWM007, and 06AUCWM014 contain relatively fresh matrix glass. Conversely, the low-silica rock samples contain a felty, microlite-rich groundmass. The matrix glasses of these samples are dacitic to rhyolitic in bulk composition. The matrix glasses from these samples also contain a range of volatile component abundances; H_2O varies from 0.09 to 0.12 weight percent, and CO_2 is not observed at the 30-ppm limit of detection. The compositions of the matrix glasses are generally consistent with those of the corresponding melt inclusions except that the former generally contain less H_2O, Cl, and S (table 7).

Description of the Melt Inclusions of the 2006, 1986, and Pleistocene Basalt Samples

Silicate Melt Inclusions in the 2006 Samples

Melt inclusions occur in plagioclase, orthopyroxene, clinopyroxene, amphibole, and apatite. Most of these inclusions contain one or more vapor and/or glass-contraction bubbles and are partially crystallized to completely vitreous; the glass appears colorless to light pink or brown in color. The melt inclusions range from <1 to >100 microns in diameter, but most are <50 microns in size.

We focused our investigation on melt inclusions in plagioclase and pyroxene phenocrysts. The 131 melt inclusions in 2006 samples analyzed for this study were unheated

Table 6. Compositions of amphiboles in 2006 rock samples of Augustine Volcano, Alaska.

[Electron microprobe analyses (wt percent) of representative amphibole phenocrysts in two rock samples. Amphiboles not zoned chemically]

Rock Sample	06AUMC008	06AUMC008	06AUMC008	06AUMC008	06AUMC008	06AUMC008	06AUJW001	06AUJW001	06AUJW001	06AUJW001
SiO_2	45.36	47.23	46.84	46.97	47.55	48.08	48.44	47.84	47.09	49.44
TiO_2	2.43	1.63	1.53	1.51	1.62	1.49	1.53	1.30	0.97	1.36
Al_2O_3	9.45	7.69	7.12	7.07	7.12	7.11	6.86	7.31	8.41	6.22
FeO[1]	12.08	11.37	12.21	11.97	11.67	12.08	11.49	12.66	12.99	11.95
MnO	0.22	0.32	0.35	0.35	0.37	0.32	0.37	0.54	0.59	0.39
MgO	15.08	15.38	15.65	15.50	15.55	15.65	15.75	15.25	14.77	15.93
CaO	11.38	11.09	11.19	11.20	11.17	11.15	11.19	10.87	10.01	11.18
Na_2O	2.10	1.49	1.50	1.39	1.50	1.48	1.31	1.22	1.41	1.29
K_2O	0.23	0.13	0.10	0.11	0.16	0.11	0.09	0.08	0.11	0.11
S	b.d.	0.01	0.01	0.01	0.01	b.d.[2]	0.01	b.d.	b.d.	b.d.
F	0.07	0.17	b.d.	b.d.	0.23	b.d.	0.04	0.47	0.07	0.17
Cl	0.07	0.06	0.06	0.07	0.07	0.08	0.06	0.06	0.09	0.08
O=F,Cl	0.05	0.09	0.02	0.02	0.12	0.02	0.03	0.23	0.05	0.10
TOTAL	98.49	96.60	96.56	96.17	97.05	97.58	97.16	97.59	96.55	98.13
Chemical Formula										
T-Site Si^{+4}	6.58	6.93	6.84	6.89	6.97	6.98	7.05	6.96	6.94	7.14
T-Site $^{V}Al^{+3}$	1.42	1.07	1.16	1.11	1.03	1.02	0.95	1.05	1.06	0.86
C-Site $^{I}Al^{+3}$	0.20	0.26	0.06	0.11	0.20	0.20	0.22	0.21	0.40	0.20
C-Site Ti^{+4}	0.27	0.18	0.17	0.17	0.18	0.16	0.17	0.14	0.11	0.15
C-Site Fe^{+3}	0.09	0.02	0.47	0.37	0.03	0.09	0.02	0.29	0.03	0.01
C-Site Fe^{+2}	1.38	1.37	1.02	1.10	1.41	1.38	1.38	1.25	1.57	1.43
C-Site Mn^{+2}	0.03	0.04	0.04	0.04	0.05	0.04	0.05	0.07	0.07	0.05
C-Site Mg^{+2}	3.26	3.37	3.41	3.39	3.40	3.39	3.42	3.31	3.24	3.43
B-Site Ca^{+2}	1.77	1.74	1.75	1.76	1.75	1.73	1.75	1.69	1.58	1.73
B-Site Na^{+}	0.01	0.01	0.08	0.06	0.00	0.02	0.00	0.05	0.00	0.01
A-Site Na^{+}	0.58	0.41	0.35	0.33	0.43	0.40	0.37	0.30	0.40	0.35
A-Site K^{+}	0.04	0.03	0.02	0.02	0.03	0.02	0.02	0.01	0.02	0.02
TOTAL	15.62	15.44	15.37	15.36	15.46	15.42	15.38	15.31	15.42	15.37
Mineral	mghb[3]	mghb	mghb	mghb	mghb	mghb	mghb	mghb	mghb	mghb

and naturally vitreous. We strove to locate and analyze melt inclusions in the periphery of plagioclase and pyroxene phenocrysts, as they are more likely to represent newer (that is, 2006) magma, but we also studied randomly located melt inclusions in these phenocrysts. Melt inclusions are most abundant in plagioclase, and some of the plagioclase-hosted inclusions occur in compositionally zoned boundary layers that are aligned parallel to the crystallographic growth planes of the host mineral; these boundary layers appear mottled when viewed petrographically with crossed nichols in transmitted light. Prior research has suggested that such patchy or sieve-textured zones form during heating and resorption events (Bacon and others, 1992; Lowenstern, 1995; Browne and others, 2006; Blundy and Cashman, 2001, 2005; Tappen and others, 2009). A small number of the melt inclusions analyzed were located in these resorption-growth boundary

Table 6. Compositions of amphiboles in 2006 rock samples of Augustine Volcano, Alaska. —Continued

[Electron microprobe analyses (wt percent) of representative amphibole phenocrysts in two rock samples. Amphiboles not zoned chemically]

Rock Sample	06AUJW001	06AUJW001	06AUJW001	06AUJW001	06AUJW001	06AUJW001	06AUJW001	06AUJW001	06AUJW001
SiO_2	49.35	48.50	48.51	46.94	46.18	47.22	48.78	48.44	49.11
TiO_2	1.35	1.35	1.23	1.01	1.07	1.15	1.14	1.23	1.36
Al_2O_3	7.28	7.20	7.16	8.52	8.90	8.55	7.00	7.13	6.18
FeO[1]	13.12	12.77	12.52	13.51	13.58	13.05	12.78	12.88	11.88
MnO	0.47	0.52	0.51	0.55	0.52	0.58	0.54	0.52	0.43
MgO	14.92	15.13	15.16	14.71	14.57	14.63	15.41	15.18	15.75
CaO	10.49	10.74	10.65	10.19	9.89	10.20	10.62	10.60	11.02
Na_2O	1.48	1.25	1.14	1.47	1.40	1.32	1.31	1.35	1.12
K_2O	0.11	0.11	0.13	0.12	0.12	0.10	0.09	0.18	0.11
S	0.01	b.d.	b.d.	b.d.	0.01	b.d.	b.d.	0.01	0.01
F	0.23	0.40	0.26	b.d.	0.20	0.06	0.26	0.11	0.15
Cl	0.06	0.07	0.07	0.05	0.07	0.07	0.07	0.07	0.06
O=F,Cl	0.12	0.20	0.14	0.01	0.11	0.04	0.14	0.07	0.08
TOTAL	98.89	98.06	97.36	97.07	96.50	96.95	98.04	97.73	97.18
Chemical Formula									
T-Site Si^{+4}	7.09	7.05	7.08	6.86	6.80	6.92	7.08	7.05	7.15
T-Site $^{V}Al^{+3}$	0.91	0.95	0.92	1.14	1.20	1.08	0.92	0.95	0.85
C-Site $^{I}Al^{+3}$	0.33	0.28	0.31	0.33	0.34	0.40	0.27	0.28	0.21
C-Site Ti^{+4}	0.15	0.15	0.14	0.11	0.12	0.13	0.12	0.14	0.15
C-Site Fe^{+3}	0.01	0.01	0.01	0.22	0.03	0.06	0.02	0.01	0.02
C-Site Fe^{+2}	1.57	1.55	1.52	1.44	1.37	1.55	1.54	1.56	1.43
C-Site Mn^{+2}	0.06	0.06	0.06	0.07	0.07	0.07	0.07	0.07	0.05
C-Site Mg^{+2}	3.20	3.28	3.30	3.21	3.20	3.20	3.33	3.30	3.42
B-Site Ca^{+2}	1.62	1.67	1.67	1.60	1.56	1.60	1.65	1.65	1.72
B-Site Na^{+}	0.08	0.00	0.01	0.04	0.05	0.01	0.00	0.01	0.01
A-Site Na^{+}	0.34	0.35	0.32	0.38	0.35	0.37	0.37	0.37	0.31
A-Site K^{+}	0.02	0.02	0.03	0.02	0.02	0.02	0.02	0.03	0.02
TOTAL	15.35	15.37	15.34	15.40	15.37	15.39	15.39	15.40	15.33
Mineral	mghb	mghb	mghb	mghb	mghb	mghb	mghb	mghb	mghb

[1]FeO represents all iron. [2]Below detection limit = b.d. [3]Mghb=magnesiohornblende.

layers, but the compositions of these inclusions show no systematic differences with those trapped in other portions of plagioclase. We avoided analysis of melt inclusions located in the patchy-mottled sieve-textured cores of plagioclase phenocrysts. Melt inclusions in pyroxene do not typically occur within compositional boundaries, because most pyroxene phenocrysts are more homogeneous than the corresponding plagioclase phenocrysts for individual samples. We also avoided melt inclusions that contain crystals, lay along cracks, or those that contain multiple or excessively large vapor and/or glass-contraction bubbles that are indicative of leakage after entrapment.

The silicate melt inclusions of these samples are dacitic to rhyolitic in bulk composition (table 7). Melt inclusions from 2006 samples contain 0.4 to 6 weight percent CaO, 0.8 to 5 weight percent FeO, and 0.2 to 2.0 weight percent MgO.

Table 7. Average compositions of silicate melt inclusions and matrix glass of rock samples from Augustine Volcano, Alaska.

[Major to trace elements in matrix glass (mat gl) and representative melt inclusions (MI) hosted by plagioclase (plag), clinopyroxene (cpx), or orthopyroxene (opx) determined by electron microprobe; H_2O and CO_2 measured by fourier-transform infrared spectroscopy]

Rock Sample	06AUMC 005c.p5 plag MI	06AUM-C008b. p1 plag MI	06AUM-C008b. p1 mat gl	06AUM C010. p1 plag MI	06AUJ W001 mat gl	06AU JW004 plag MI	06AUJ W004 mat gl	06AUC-WM007 plag MI	06AUC-WM007 mat gl	06AUJ W010 plag MI	06AUC-WM012 plag MI	06AUC-WM014 mat gl	AVO208 (1986) plag MI[1]	1986 plag and cpx MI[2]	Prehistoric MI[3]	Prehistoric mat gl[3]	RB-W91A137 cpx MI
(wt. percent)																	
SiO_2	70.17± 2.23	69.90± 2.56	71.19± 3.18	72.17± 1.91	73.76± 1.04	72.56± 1.52	74.30± 2.04	73.44± 1.89	75.86± 2.69	75.69± 0.86	73.26± 1.25	65.34± 3.43	71.86± 1.45	72.96± 1.25	72.63± 1.56	75.39± 2.20	54.92± 1.54
Al_2O_3	13.54± 1.21	13.69± 1.52	13.26± 2.67	12.13± 0.70	12.61± 0.23	12.26± 0.46	12.14± 0.72	12.04± 0.55	13.10± 3.44	11.77± 0.67	11.50± 0.57	15.68± 1.38	12.19± 0.19	12.57± 0.42	12.38± 0.61	12.93± 0.48	14.61± 0.73
TiO_2	0.39± 0.28	0.40± 0.24	0.59± 0.42	0.26± 0.10	0.36± 0.04	0.29± 0.16	0.39± 0.14	0.30± 0.20	0.43± 0.17	0.27± 0.15	0.37± 0.09	0.96± 0.10	0.35± 0.11	0.26± 0.08	0.19± 0.08	0.33± 0.07	0.62± 0.11
MgO	0.54± 0.34	0.72± 0.35	0.51± 0.26	0.35± 0.15	0.36± 0.05	0.52± 0.16	0.24± 0.13	0.41± 0.24	0.25± 0.20	0.44± 0.09	0.60± 0.11	0.46± 0.12	0.47± 0.08	0.17± 0.05	0.36± 0.12	0.49± 0.14	5.89± 0.91
CaO	2.81± 0.84	3.21± 0.95	2.99± 1.46	1.79± 0.45	1.93± 0.14	1.87± 0.24	1.69± 0.99	1.81± 0.32	1.71± 1.40	1.78± 0.20	1.70± 0.30	1.85± 0.55	1.92± 0.12	2.11± 0.14	2.04± 0.25	2.38± 0.44	10.33± 1.59
MnO	0.09± 0.04	0.08± 0.05	0.09± 0.09	0.11± 0.09	0.05± 0.02	0.08± 0.06	0.04± 0.02	0.04± 0.06	0.05± 0.07	0.09± 0.06	0.06± 0.06	0.06± 0.02	0.06± 0.03	n.a.[5]	0.06± 0.03	0.06± 0.03	0.16± 0.03
FeO[4]	2.85± 1.43	2.97± 1.02	3.95± 2.11	1.59± 0.27	1.68± 0.26	2.07± 0.61	1.92± 0.64	1.84± 0.87	1.52± 0.40	1.85± 0.50	2.47± 0.30	4.77± 0.93	2.00± 0.33	1.84± 0.32	1.59± 0.52	1.82± 0.29	6.86± 1.13
Na_2O	4.56± 0.51	4.55± 0.83	4.09± 2.05	3.86± 0.42	4.39± 0.11	4.85± 0.93	4.24± 0.24	5.50± 0.87	4.28± 0.91	5.21± 0.45	3.91± 0.59	04.43± 0.18	3.80± 0.31	3.82± 0.28	4.10± 0.33	4.23± 0.27	2.04± 0.50
K_2O	1.72± 0.16	1.82± 0.27	2.26± 0.38	2.14± 0.56	2.19± 0.08	2.23± 0.20	2.62± 0.37	2.20± 0.30	2.72± 0.62	2.52± 0.28	2.27± 0.25	1.48± 0.18	2.03± 0.06	1.80± 0.21	1.61± 0.27	1.84± 0.21	0.61± 0.12
P_2O_5	0.11± 0.11	0.10± 0.08	0.14± 0.15	0.05± 0.02	0.05± 0.01	0.05± 0.03	0.07± 0.01	0.08± 0.06	0.07± 0.02	0.06± 0.04	0.07± 0.03	0.30± 0.06	0.07± 0.03	n.a.	0.05± 0.02	0.06± 0.03	0.15± 0.03
S	0.02± 0.01	0.02± 0.02	0.01± 0.01	0.02± 0.01	0.01± 0.01	0.02± 0.03	0.00± 0.01	0.02± 0.01	0.01± 0.01	0.01± 0.01	0.02± 0.01	b.d.[6]	0.02± 0.01	0.02± 0.01	0.02± 0.01	0.01± 0.01	0.23± 0.11
Cl	0.36± 0.03	0.38± 0.12	0.33± 0.24	0.44± 0.13	0.23± 0.02	0.45± 0.14	0.26± 0.08	0.41± 0.12	0.20± 0.05	0.43± 0.06	0.56± 0.15	0.35± 0.02	0.44± 0.07	0.29± 0.06	0.31± 0.06	0.32± 0.03	0.30± 0.04
F	0.02± 0.02	0.03± 0.03	0.03± 0.04	0.03± 0.06	0.03± 0.04	0.03± 0.06	0.03± 0.03	0.06± 0.09	0.15± 0.02	0.03± 0.03	0.06± 0.08	0.02± 0.02	0.03± 0.04	n.a.	0.02± 0.03	0.03± 0.05	0.03± 0.04
TOTAL	97.18	97.88	100.63	94.76	98.68	97.00	97.94	97.96	101.00	100.15	96.91	95.76	95.30	96.02	95.38	99.88	97.26
Number of analyses	13	54	6	23	9	14	6	8	6	6	13	3	14	8	79	18	6
CO_2	<0.003	n.a.	n.a.	<0.003	<0.003	<0.003	n.a.	n.a.	n.a.	n.a.	<0.003	n.a.	n.a.	0.011± 0.007	0.009± 0.033	n.a.	n.a.
H_2O	4.1 ± 0.01	n.a.	n.a.	3.08 ± 1.30	0.01	1.70 ± 0.56	n.a.	n.a.	n.a.	n.a.	3.16 ± 0.14	n.a.	2.58 ± 0.98	3.46 ± 1.92	4.19 ± 1.82	n.a.	n.a.

[1] Data of this study. [2] Data of Roman and others (2006). [3] Data of Tappen and others (2009) for melt inclusions hosted by plagioclase, pyroxene, and amphibole. [4] All iron reported as FeO. [5] Constituent not analyzed. [6] Constituent below detection limit; matrix glass analyses for 06AUCWM014 may have included iron-titanium oxides in groundmass glass.

Silicate Melt Inclusions in the 1986 Sample

The silicate melt inclusions from sample AVO 208 are rhyolitic in composition and are somewhat more chemically evolved than some melt inclusions of the 2006 samples. The melt inclusions contain less cafemic constituents than those in 2006 rocks; the concentrations of CaO, FeO, and MgO in the former range from 1.8 to 2.1, 1.5 to 2.4, and 0.3 to 0.6 weight percent, respectively. Water was measured in several of these melt inclusions, and the average concentration is 2.6 weight percent. Sulfur varies from 0.02 to 0.04 weight percent and Cl from 0.38 to 0.51 weight percent, respectively.

Silicate Melt Inclusions in the Basalt

The clinopyroxene-hosted silicate melt inclusions in the basalt sample (RBW91A137) are basaltic-andesite to andesitic in composition. Water was not measured directly in these melt inclusions, but the apparent H_2O concentration of most of these reheated melt inclusions varies from 2 to 4 weight percent using the volatile-by-difference method. These estimated H_2O concentrations could be lower than those in the melt at the time of entrapment due to diffusive loss of H_2 and H_2O out the melt inclusions during reheating and refusion. Sulfur varies from 0.08 to 0.36 and Cl from 0.27 to 0.37 weight percent, respectively.

What do the Melt Inclusion Compositions Represent?

Some silicate melt inclusions are influenced by syn- and post-entrapment processes that modify their compositions and render them nonrepresentative of the bulk melt at the time of entrapment (Lowenstern, 1995; Danyushevsky and others, 2000; Anderson, 2003, Bodnar and Student, 2006). Melt-inclusion compositions may be modified, for example, by host crystallization after entrapment, because post-entrapment crystallization of plagioclase on melt inclusion-host wall contacts increases the SiO_2, FeO, MgO, and K_2O contents and simultaneously reduces the abundances of Al_2O_3, CaO, and Na_2O in the residual melt of the inclusion. Neither the plagioclase- or pyroxene-hosted melt inclusions of this study exhibit trends indicative of this process.

Melt-inclusion glass may also be modified by leakage or post-entrapment diffusive re-equilibration. Consequently, we analyzed no melt inclusions on cracks and the felsic melt inclusions did not require re-fusion to glass prior to analysis, so we consider the abundances of volatile components to represent those of the local melt at the time or entrapment. It is conceivable that H_2O was partially exchanged between bulk magma and entrapped melt after entrapment, through the diffusion of H_2 through the host phenocrysts (Roedder, 1984; Massare and others, 2002), but we cannot constrain the potential consequences of this process. As noted previously, however, the pyroxene-hosted basaltic-andesite melt inclusions were refused and quenched to glass prior to analysis, and their compositions are likely to reflect some diffusive loss of H_2O.

The average compositions of the felsic melt inclusions of 2006 high-silica andesites are equivalent, at the 1-σ level of confidence, with their corresponding areas of matrix glass except for differences in the volatile-components H_2O, S, and Cl. This observation is important as it indicates that the compositions of the late-stage aliquots of melt that quenched to form matrix glass and melt entrapped in growing plagioclase and pyroxene were alike, and, thus, the melt inclusions are compositionally representative of the late-stage melts of 2006 magmas.

Compositional Relationships Involving Melt Inclusions in the Basalt, 1986, and 2006 Samples

The integration of these melt inclusion data sets provides important insights into the evolution of 2006 and earlier Augustine magmas. The differentiation of relatively primitive to residual rhyolitic melts caused the alkalis to increase in abundance and to exhibit increased dispersion in the highly felsic melts. For example, the melt inclusions in 2006 eruptive materials that were analyzed contain higher alkali contents than the melt inclusions from prehistoric tephra. The whole-rock data detail the overall trend.

Before proceeding, we note that detailed analysis and interpretation of the Pleistocene basalts (Larsen and others, this volume) show them to be geochemically distinct from all younger, historic eruptive materials of Augustine Volcano; the geochemical trends characterizing Pleistocene basalts are inconsistent with those of younger volcanic rocks. The former rocks exhibit trends that are lower in K_2O and related large-ion lithophile trace elements; rare-earth elements (REE); and the high-field strength elements Zr, Hf, Nb, and Ta than those of rocks representing historic eruptions. Therefore, in the figures (fig. 1) and discussion that follow, we include data from whole-rock samples and melt inclusions of the Pleistocene basalts in order to provide some constraints on the geochemistry of relatively primitive Augustine magmas, even though the compositions of these older basaltic magmas may be geochemically distinct from the younger basaltic magmas that are not yet well constrained.

The compositions of melt inclusions and matrix glasses exhibit geochemical trends that reflect processes of magma evolution. Magmatic differentiation, for example, is accompanied by decreasing concentrations of alkaline earth elements and increasing abundances of alkali elements in residual fractions of melt. Plots of CaO and MgO versus Na_2O and K_2O in the integrated data sets for Augustine rocks show two distinct relationships (fig. 2). One correlation (that is, mixing trend 1) involves the melt inclusions, groundmass glasses, and some whole-rock data of predominantly low-silica rock samples that is best fit with a linear trend expressing the consequences of magma evolution dominated by hybridization. Although the melt inclusions of the Pleistocene basalt (RBW91A137) may be geochemically distinct from younger basaltic magmas of Augustine Volcano, we interpret the mixing line to be directed toward their compositions because (1) this trend is consistent with the abundances of nonvolatile components in whole-rock samples, and (2) we have no other constraints at this time.

The second correlation (that is, mixing trend 2, fig. 2) is also best fit with a linear curve, but in this case the trend involves either small reductions in alkaline earth concentrations with increasing alkali abundances or no statistically significant change in CaO and MgO (figs. 2*A*, 2*B*, 2*C*). Many of the melt inclusions that contain less K_2O and Na_2O, represented by the second trend, also contain lower FeO and TiO_2 concentrations. This second trend characterizes the geochemistry of melt-inclusion and matrix glasses from dacitic and high-silica andesitic rock samples of prehistoric, 1986, and 2006 eruptions, and it includes glasses from some 2006 low-silica andesites. Given its linear nature, we interpret it to reflect magma evolution also dominated by magma mixing and/or mingling, but of two relatively silicic end members.

The chemical evolution of magmas can be expressed with the Larsen Index ([(SiO_2x0.333)+(K_2O)]-(CaO+FeO+Mg)) on a weight percent basis; Carmichael and others, 1974). We have applied this index to the Augustine melt-inclusion data in order to interpret the behavior of P, S, and Cl. Phosphorus, for example, shows significant dispersion in the integrated data sets (fig. 3*A*). The highest P values occur in dacitic to rhyodacitic melt inclusions. In addition, the P concentrations of all of these relatively felsic melt inclusions decrease from values as high as 0.35 weight percent to values near zero as their compositions vary from dacite to rhyolite. Relative to P, the S concentrations of all dacitic to rhyolitic melt inclusions show somewhat less dispersion and range from 100 to 700 ppm (fig. 3*B*), and this range is similar to that determined for felsic melt inclusions in 1976 magmas (100 to 500 ppm S; Johnston, 1978). Chlorine also exhibits significant dispersion in the dacitic to rhyodacitic melt inclusions, as it varies from 0.1 to nearly 0.8 weight percent (fig. 3C). This range is consistent with the 0.3 to 0.6 weight percent Cl determined in melt inclusions of 1976 rocks by Johnston (1978) and the 0.22 to 0.37 weight percent Cl in 1986 melt inclusions studied by Roman and others (2006).

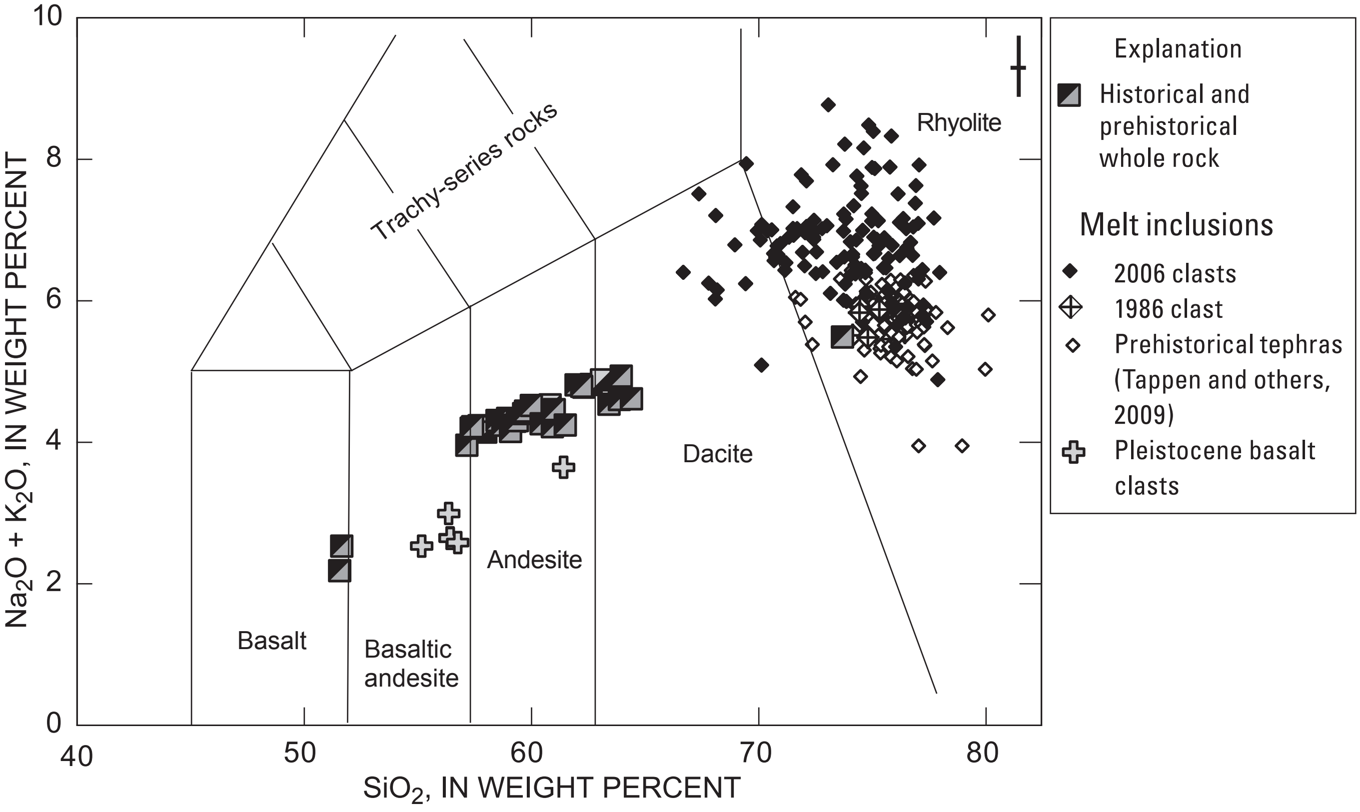

Figure 1. Plot of the relation between concentrations of total alkali elements and silica in Augustine Volcano whole-rock samples (Keinle and Forbes, 1976; Daley, 1986; Larsen and others, this volume) (black and gray squares) and silicate melt inclusions from 2006 rock samples (see text and appendix for descriptions) (black diamonds), prehistoric tephra (open diamonds), 1986 tephra (gridded diamonds), and reheated andesitic melt inclusions from Pleistocene basalt (filled crosses). Data reflect magma evolution and are reported on an anhydrous basis with analytical totals normalized to 100 weight percent. Representative and relative 1-σ precision for melt-inclusion analyses shown in upper right corner. Rock fields after Le Bas and others (1986).

It is noteworthy that the S contents of all felsic melt inclusions are distinctly less than those of the basaltic-andesite melt inclusions of the Pleistocene basalt. Moreover, the presence of 0.08 to 0.36 weight percent S and 0.27 to 0.37 weight percent Cl in these basaltic-andesite melt inclusions (from sample RBW91A137) is consistent with those of basaltic melt inclusions hosted by Fo_{80-85} olivine phenocrysts of Augustine basalt (Johnston, 1978; Zimmer and others, 2004). The latter inclusions contain 0.24 to 0.45 weight percent S and 0.3 to 0.6 weight percent Cl, as well as H_2O concentrations approaching 5 weight percent. Interestingly, these abundances of volatile components in mafic to intermediate-silica content melt inclusions are also consistent with observations made from other mafic, subduction-related magmas. Wade and others (2006), for example, determined that high-Al basaltic liquids from Arenal Volcano contained up to 4 weight percent H_2O, >0.2 weight percent S, and approximately 0.15 weight percent Cl. Straub and Layne (2003) measured 0.7 to 0.9 weight percent Cl and also estimated up to 10 weight percent H_2O in andesitic melt inclusions of volcanic rocks from the Izu arc. Gurenko and others (2005) found 0.04 to 0.29 weight percent S in basaltic-andesite melt inclusions from Chikurachki volcano, Russia. Moreover, Anderson (1982) reports that up to 0.33 weight percent S occurs in rehomogenized melt inclusions of such magmas on a world-wide basis; just as Wallace (2005) notes that these volatile abundances are consistent with those recorded for other subduction-related volcanic systems.

The integrated 2006-, 1986-, and prehistoric-sample melt-inclusion data exhibit no distinct relationships involving CO_2 and magma differentiation, because the CO_2 abundances of most melt inclusions are below the limit of detection. The inclusions do, however, contain widely ranging abundances of H_2O (fig. 4). The H_2O concentrations of the melt inclusions from 2006 samples range from 1.2 to 4.7 weight percent, range from approximately 2 to 6 weight percent for the 1986 samples (that is, ours and those of Roman and others, 2006), and range from approximately 2 to 8 weight percent for melt inclusions of prehistoric samples. These data have been plotted, for comparison, relative to the computed H_2O and CO_2 concentrations of vapor-saturated rhyolitic melt at pressures of 20 to 400 MPa (200 to 4,000 bars) and temperatures of 900 to 1,000°C. Plots like these provide key constraints on pressures of melt and magmatic fluid equilibration as addressed below.

Discussion

Magma Evolution at Augustine During the Past 2,100 Years

Outcrops at Augustine are dominated by andesite and dacite (Waitt and Begét, 2009); basaltic and basaltic-andesite rocks are rare at the surface. This skewed compositional distribution of volcanic rocks indicates that the more primitive mafic magmas feeding this volcano differentiate significantly before eruption. Prior research concluded that magma mixing/mingling is crucial to the evolution of Augustine magmas and that the geochemical features of this process are overprinted by crystal fractionation, assimilation, and fluid exsolution. Johnston (1978) was one of the first to articulate this after systematic analysis of 1976 eruptive products. He surmised that fluid-saturated, residual dacitic melt mixed with fluid-undersaturated basaltic melt, and that extensive crystallization occurred afterward within the resulting mixed products. In a recent study of the compositionally heterogeneous materials of the 1986 eruption, Roman and others (2006) determined that some batches of erupted magma reflect mixing in the shallow crust of newly arrived, comparatively mafic magma with compositionally evolved magma that was residual from the 1976 eruption. They also concluded that some 1986 material represents juvenile magma that evolved without mixing. More complex mixing processes for 1986 magmas were called upon by Harris (1994) and Johnson and others (1996). In this three-component scenario, relatively new magma mixed with magma residual from the 1976 eruption and with partially crystallized residual “rind” material that was low in K_2O and very low in related incompatible elements (Larsen and others, this volume).

Other research has interpreted evidence of a stronger role of fractional crystallization. Daley (1986) argued from analyses of prehistoric, 1935, 1963–64, and 1976 eruptive materials, that andesitic magmas formed by crystal fractionation of parental basaltic magmas at comparatively high pressures, and this process was followed by subsequent fractionation of andesitic liquid to dacitic compositions by low-pressure crystallization. To Daley (1986), magma mixing had only minor effects on magma evolution. Moreover, Johnson and others (1996) concluded that closed-system crystal fractionation was the dominant evolutionary process for some 1976 magmas, even though their interpretation of oxygen isotopic characteristics of whole-rock data was consistent with magma mixing. More recent research (Tappen and others, 2009) on tephra from 4 prehistoric eruptions reveals that crystal fractionation was dominant even though the phenocrysts also provide ample evidence of mixed and/or mingled magmas. Given the extent of prior research on processes of magma differentiation in 1986 and older magmas, we focus herein on processes reflected in 2006 rocks in the following discussion, but we also compare these results with those bearing on prior eruptions to provide a broad context for processes of magma evolution at Augustine Volcano (fig. 5).

Mixing and/or Mingling in 2006 Magmas

The 2006 eruptive materials afford ample evidence of magma hybridization. During our field work and that of others in the summer of 2006 (Vallance and others, this volume; Larsen and others, this volume; Tilman, 2008), a large variety of banded rocks, that are definitive evidence of incomplete mixing of magmas of differing compositions, was observed (fig. 6). In addition, hand sample 06AUMC008B.p1A exhibits light- and intermediate-gray banding on a smaller scale. The

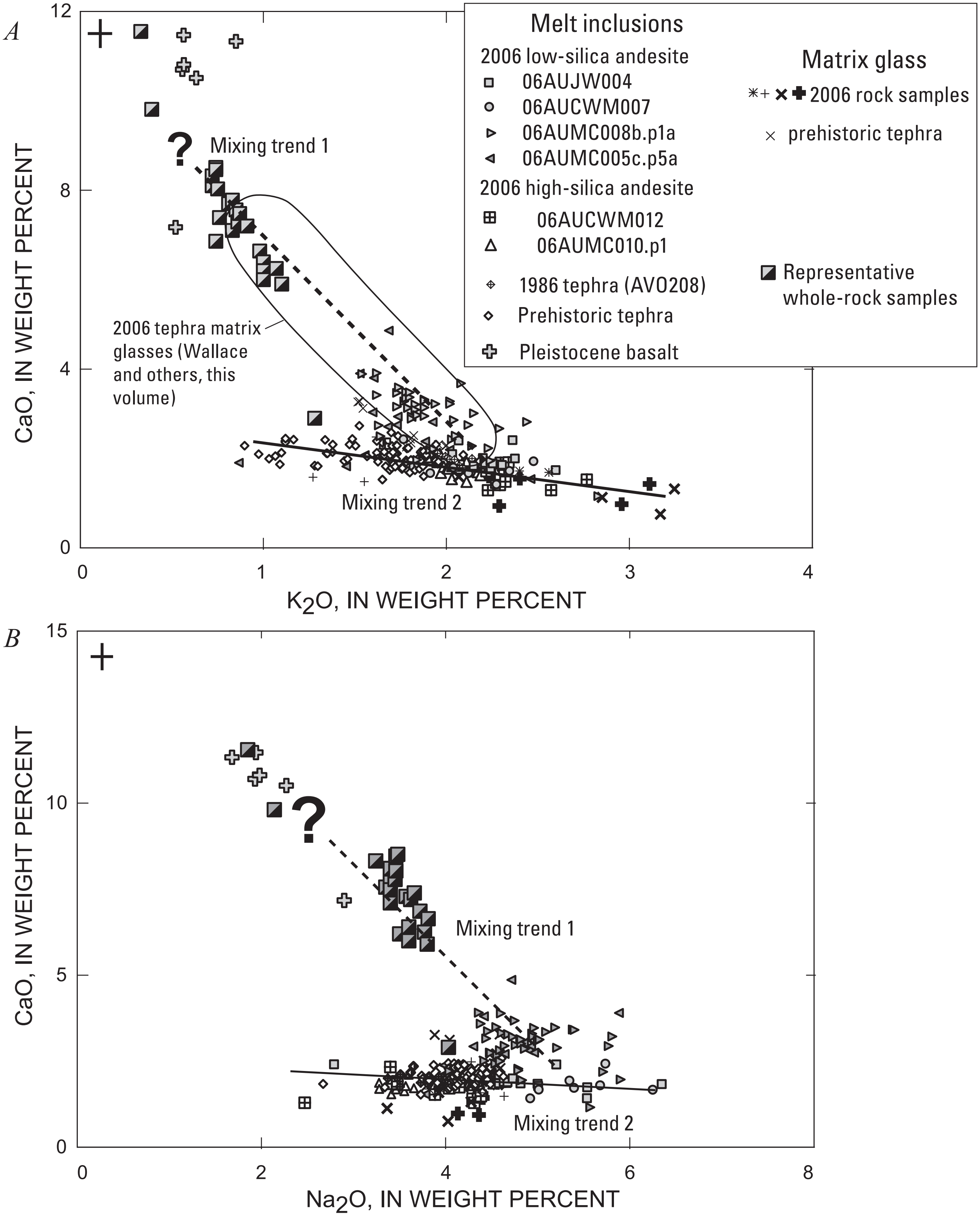
A
12
8
4
0
0
1
2
3
4
CaO, IN WEIGHT PERCENT
K_2O, IN WEIGHT PERCENT
?
Mixing trend 1
2006 tephra matrix glasses (Wallace and others, this volume)
Mixing trend 2
Melt inclusions
2006 low-silica andesite
06AUJW004
06AUCWM007
06AUMC008b.p1a
06AUMC005c.p5a
2006 high-silica andesite
06AUCWM012
06AUMC010.p1
1986 tephra (AVO208)
Prehistoric tephra
Pleistocene basalt
Matrix glass
2006 rock samples
prehistoric tephra
Representative whole-rock samples
B
15
10
5
0
0
2
4
6
8
CaO, IN WEIGHT PERCENT
Na_2O, IN WEIGHT PERCENT
?
Mixing trend 1
Mixing trend 2

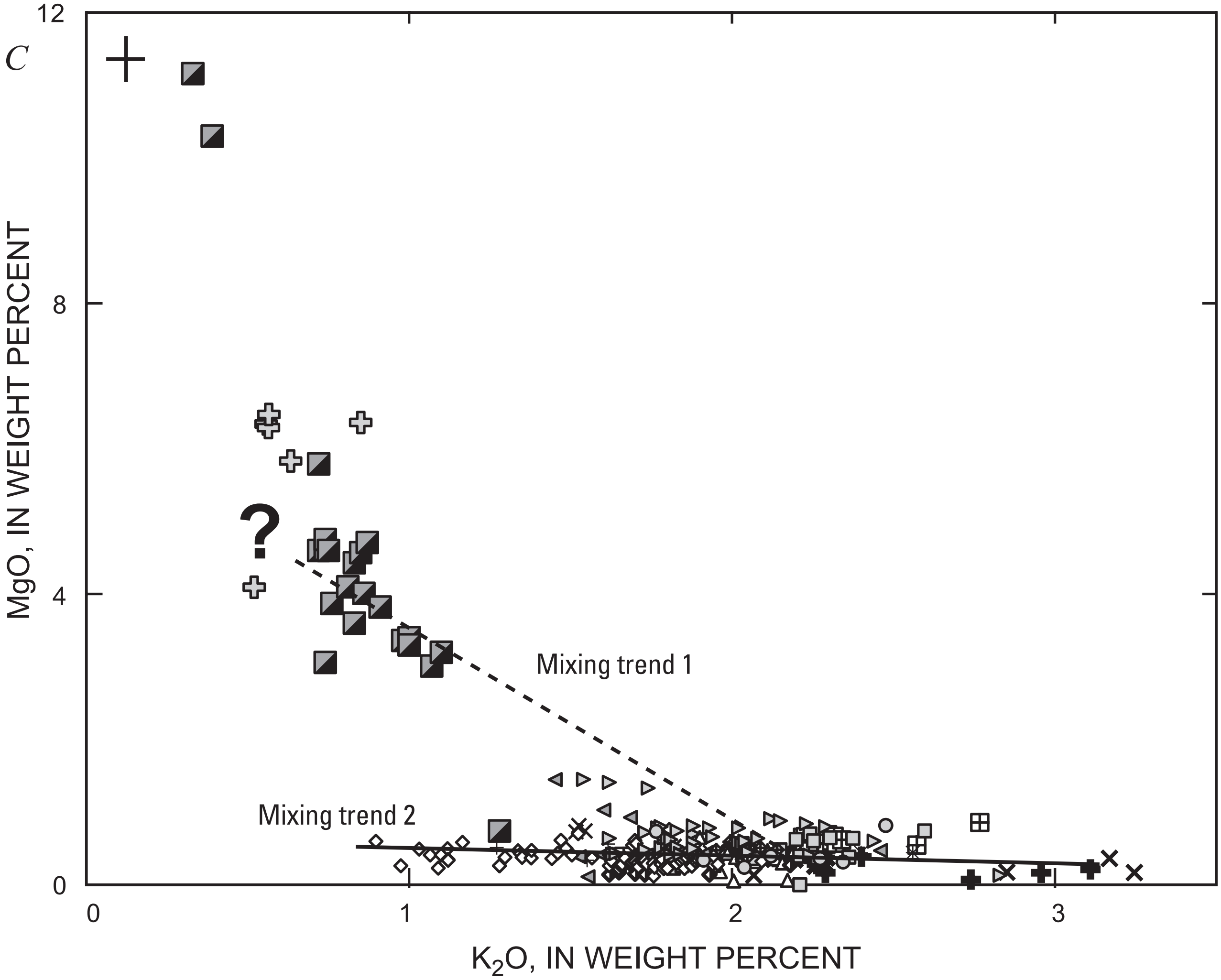

Figure 2. Plots of the relations between the concentrations of CaO and K_2O (*A*), CaO and Na_2O (*B*), and MgO and K_2O (*C*) for Augustine Volcano melt inclusions, matrix glasses, and whole-rock samples; the curves are schematic. Felsic melt inclusions from low-silica andesitic 2006 rock samples are shown with small gray-filled symbols and include 06AUJW004 (squares), 06AUCWM007 (circles), 06AUMC008b.p1A (right-pointing triangles), and 06AUMC005c.p5A (left-pointing triangles). Reheated melt inclusions from Pleistocene basalt sample (RBW91A137) represented by large filled crosses. Felsic melt inclusions from high-silica andesitic 2006 rock samples are shown with small clear-filled symbols and include 06AUCWM012 (gridded squares) and 06AUMC010.p1 (upward-pointing triangles). Other felsic melt inclusions from high-silica andesitic to dacitic rock samples are shown with small clear-filled symbols and include prehistoric tephra (open diamonds) (Tappen and others, 2009), our 1986 ignimbrite sample AVO 208 (gridded diamonds), other 1986 tephra (diamonds clear on one side and filled on right-hand side; sample 86E-63-2 of Roman and others, 2006). Our matrix glass analyses include samples 06AUCWM007 (bold X's), 06AUCMW014 (faint crosses), 06AUJW004 (bold crosses), 06AUJW001 (bold asterisks), 06AUMC008b.p1A (faint asterisks), and prehistoric tephra (faint X's). Elliptical field represents approximate range in CaO and K_2O for hundreds of matrix glass analyses from 2006 tephra (Wallace and others, this volume). Representative whole-rock samples shown as large, variably filled squares (Tappen and others, 2009; Keinle and Forbes, 1976; Daley, 1986; Harris, 1994). The data acquired from low-silica rock samples are consistent with upper curve (dashed line of mixing trend 1) and reflect consequences of magma mixing/mingling and other processes. Large question mark reflects unknown compositional characteristics of the basaltic mixing end member. Data from dominantly high-silica rock samples are consistent with the lower curve (solid line of mixing trend 2). This trend also reflects melt evolution dominated by magma mixing/mingling that apparently involved two high-silica magmas with varying K_2O and Na_2O concentrations and marginally varying CaO and SiO_2 concentrations. The silica content of nearly all of the latter melt inclusions, normalized to an H_2O-free basis, ranges from 71 to 78 weight percent. Representative and relative 1-σ precision for glass analyses is shown as cross in upper left corner. See text for discussion.

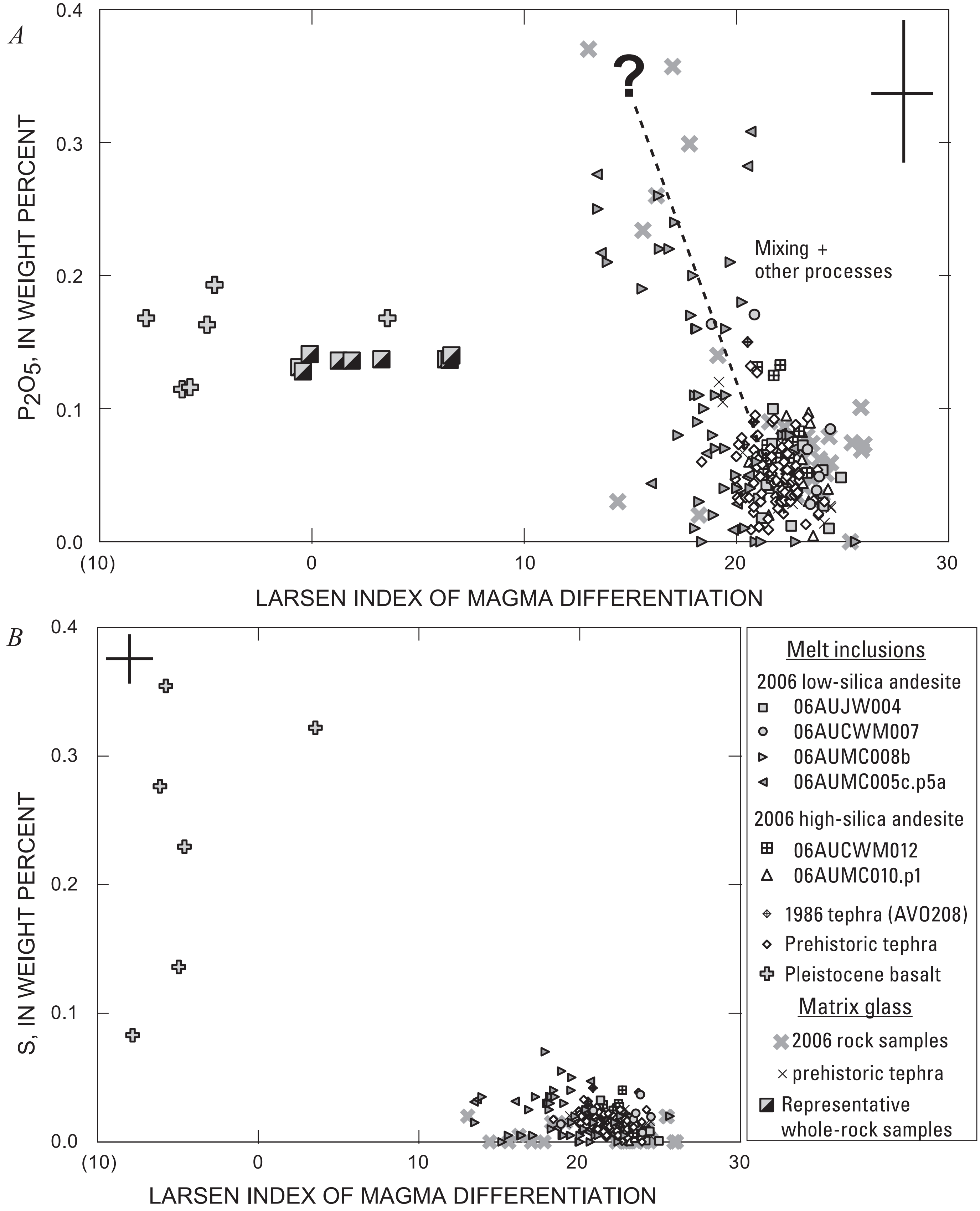
A
0.4
0.3
0.2
0.1
0.0
P_2O_5, IN WEIGHT PERCENT
?
Mixing +
other processes
(10)
0
10
20
30
LARSEN INDEX OF MAGMA DIFFERENTIATION
B
0.4
0.3
0.2
0.1
0.0
S, IN WEIGHT PERCENT
(10)
0
10
20
30
LARSEN INDEX OF MAGMA DIFFERENTIATION
Melt inclusions
2006 low-silica andesite
06AUJW004
06AUCWM007
06AUMC008b
06AUMC005c.p5a
2006 high-silica andesite
06AUCWM012
06AUMC010.p1
1986 tephra (AVO208)
Prehistoric tephra
Pleistocene basalt
Matrix glass
2006 rock samples
prehistoric tephra
Representative
whole-rock samples

mixing-based origin of these macroscopic features is further supported by microscopic-scale textural features in 2006 samples. These observations include the presence of numerous reversely zoned plagioclase phenocrysts, resorption-growth features in plagioclase, and partially resorbed and orthopyroxene-rimmed olivine phenocrysts. Moreover, the temperatures recorded by coexisting iron-titanium oxide minerals contained in the groundmass of 2006 rock samples (for example, 835 to 1,052°C) vary significantly (fig. 7), and they are consistent with the temperature ranges estimated for 2006 magmas by Larsen and others (this volume) and for temperature estimates of older Augustine magmas (Johnston, 1978; Johnson, 1986; Roman and others, 2006, Tappen and others, 2009). This observed dispersion in temperature for oxides within individual samples is a consequence of mixing processes (fig. 7). In fact, many of the plagioclase-hosted inclusions that occur within distinct resorption-growth zones are a result of and an indication of the interaction of extant plagioclase phenocrysts with younger aliquots of magma that were hotter and more H_2O enriched, and, therefore, they reflect the interaction of younger magma with phenocrysts of an older magma. The apparent method of entrapment of these inclusions (that is, heating through magma mixing) is consistent with their geochemical characteristics further supporting the occurrence of magma mingling and/or mixing.

The variety of mixing processes involving materials erupted in 2006 is complex; Larsen and others (this volume), for example, call for two stages of hybridization. In their model, the initial two-component mixing event involved a juvenile batch of hot, relatively volatile-rich, mafic magma that combined with cooler, crystal-rich, high-silica andesitic magma (that was likely residual from 1986 or older eruptive

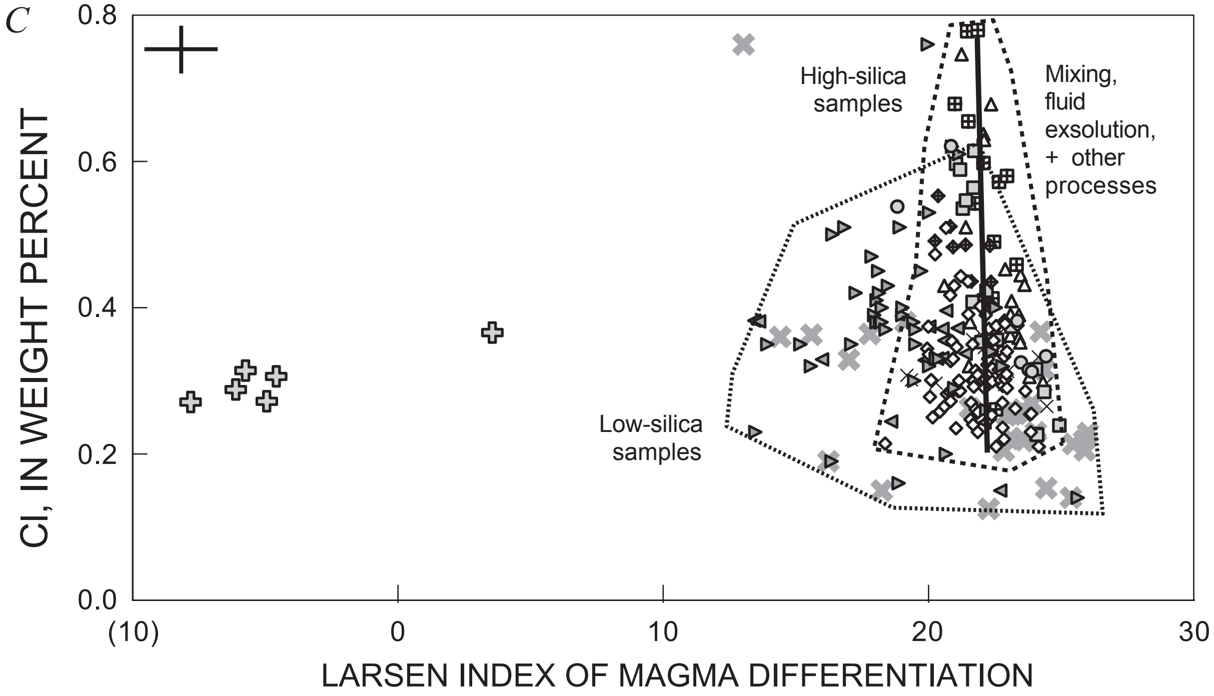

Figure 3. Plots of the relation between the concentrations of P_2O_5 (*A*), S (*B*), and Cl (*C*) and the Larsen differentiation index (for example, [[SiO_2x0.333] + K_2O] versus [CaO + MgO + FeO]] on a wt. percent basis) for melt inclusions and matrix glasses of Augustine Volcano rock samples; samples and symbols same as in figure 2, except all 2006 matrix glasses are shown as gray X's and those of prehistoric tephra shown as faint X's. Data express the changes in volatile- and fluxing-component concentrations in residual melt with progressive magma evolution assuming that basaltic-andesite melt inclusions (filled crosses) are geochemically representative of magmas parental to prehistoric, 1986, and 2006 magmas. *A*, Phosphorus concentrations generally decrease from Pleistocene andesitic melt inclusions and all whole rocks to that of the felsic melt inclusions from 2006, 1986, and prehistoric high-silica andesitic and dacitic rock samples and for most of the felsic melt inclusions of low-silica andesites of same eruptive units. However, the P_2O_5 contents of some felsic melt inclusions of low-silica andesites evolved to higher abundances with magma evolution. *B*, Sulfur concentrations of felsic melt inclusions of all Augustine rock samples are very low and reflect sulfide crystallization and/or exsolution of magmatic fluid(s). *C*, Chlorine concentrations of melt inclusions are highly variable; fields for low-SiO_2 andesitic rocks (dotted envelope) and high-SiO_2 andesitic rocks (dashed envelope) shown for comparison. Chlorine data reflect magma mixing, fractional crystallization, and fluid(s) exsolution as described in text. Representative and relative 1-σ precision for glass analyses is shown as cross in upper corners.

activities) to form the 2006 low-silica andesitic magma. The second mixing event that they observe involved syneruptive hybridization of low-silica and high-silica andesitic magma to form intermediate-silica andesitic rocks.

Our mixing trend 1 (fig. 2) is consistent with the first two-component mixing process of Larsen and others (this volume) that involved the combination of an unidentified mafic magma with older crystal-rich, high-silica andesitic residual magma. Interestingly, our analyses of glass compositions (figs. 2 and 3) allow us to provide some constraints on the composition of the melt in the high-silica andesitic magma that was involved in the mixing. Based on the curves shown in these figures, this melt contained ≤2 weight percent CaO, ≤1 weight percent MgO, ≥2.2 weight percent K_2O, ≥5 weight percent Na_2O, ≤0.05 weight percent P_2O_5, and ≤0.2 weight percent Cl. Close inspection of the most alkali-enriched melt inclusions of figures 2*A* and 2*B* also shows several data points representing more highly evolved glasses from the low-silica andesite samples, and it is important to note that these glass compositions are not compatible with the mixing trend 1 line because they imply a break-in-slope of the trend. These highly evolved samples of glass contain 3 or more weight percent K_2O and nearly 6 weight percent Na_2O, and we interpret them to reflect the consequences of fractional crystallization

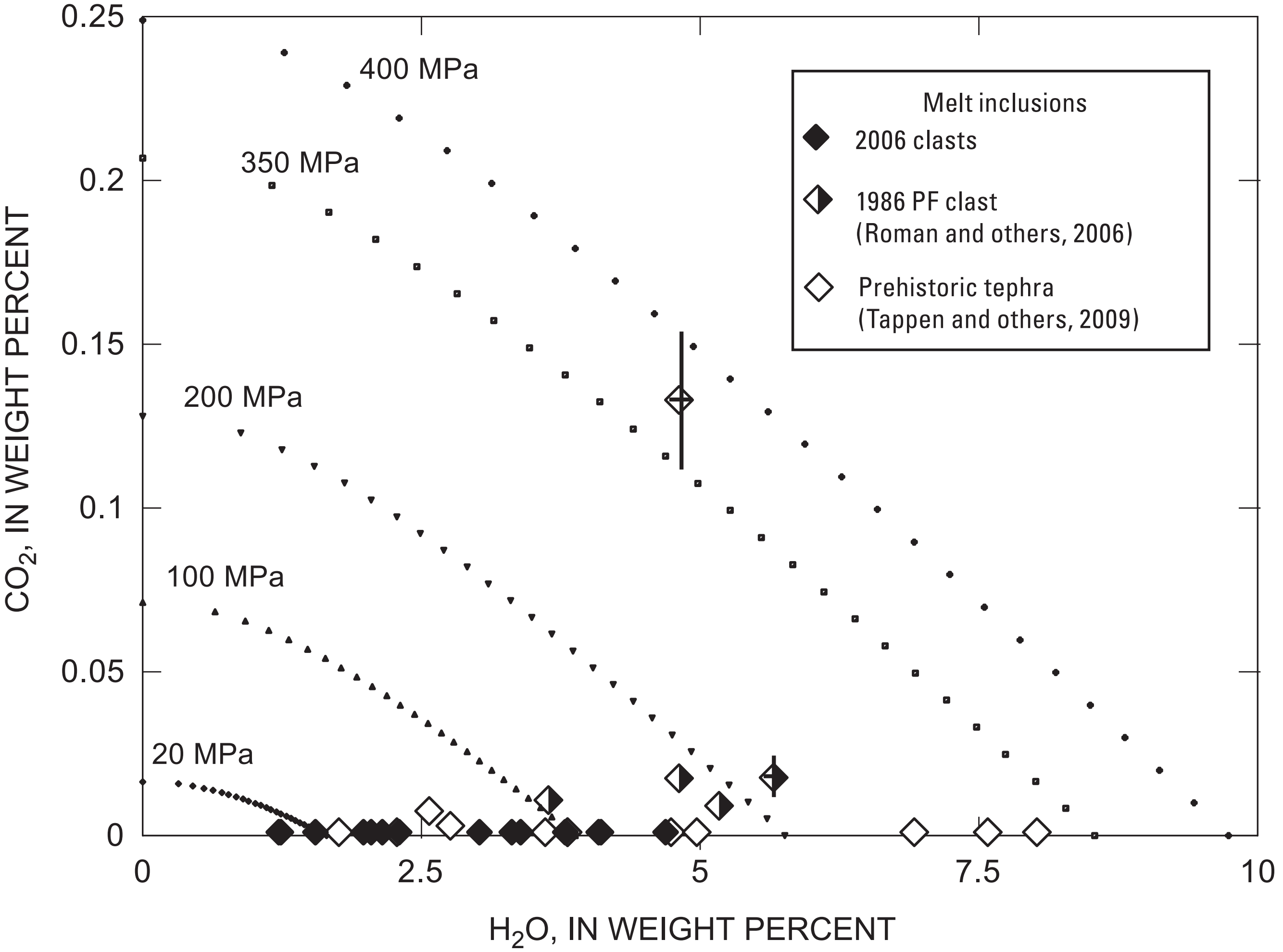

Figure 4. Plots of the relation between CO_2 and H_2O in 28 silicate melt inclusions from Augustine Volcano rock samples including prehistoric rocks (open diamonds; Tappen and others, 2009), 1986 tephra (diamonds filled on right side; sample 86E-63-2 of Roman and others, 2006), and our 2006 samples (filled diamonds). Data are plotted in reference to isobaric curves for rhyolitic melt saturated in CO_2- and H_2O-dominated fluid(s) using model of Newman and Lowenstern (2002). Melt inclusions in this plot reflect either minimum trapping pressure (given independent evidence that a melt inclusion represents fluid-saturated melt) or pressures at which a fluid-phase would have exsolved (if no such evidence is available). Prehistoric melt inclusions represent trapping or fluid-exsolution pressures ranging from 20 to >350 MPa, melt inclusions from 1986 samples represent trapping or fluid-exsolution pressures of about 10 to 220 MPa, and melt inclusions from 2006 samples reflect trapping or fluid-exsolution pressures of about 20 to 160 MPa. Estimated values for 1-σ precision for CO_2 and H_2O in glasses are shown as vertical and horizontal lines for two representative high- and low-CO_2 melt inclusions. See text for discussion.

of low-silica andesitic magma that occurred subsequent to mixing. Relatively late-stage fractionation, like this, is consistent with the presence of microlite-enriched groundmass in the low-silica andesitic rocks (Larsen and others, this volume).

Our mixing trend 2 is based on glass compositions, and it is inconsistent with the second hybridization process recognized by Larsen and others (this volume). Through their analysis of whole-rock data, Larsen and others described mixing of low- and high-silica andesitic magmas to generate hybrid andesitic magmas with intermediate silica contents. Compared with this second mixing trend of Larsen and others (this volume), our mixing trend 2 involves highly variable K_2O abundances that are not compatible with the bulk geochemistry of most of the andesites studied by Larsen and others (this volume). The origin of the felsic, low K_2O-end member is discussed in more detail below.

Fractional Crystallization in Magmas Erupted from Augustine in 2006

The 2006 rock samples contain normally zoned plagioclase and pyroxene phenocrysts, as well as highly evolved rhyolitic matrix glasses and silicate melt inclusions contained within andesitic to dacitic whole rocks. These features are normal products of fractional crystallization. The effects of fractional crystallization are also seen in the presence of fine-grained gabbroic inclusions, erupted in 2006, that are low in incompatible elements. These geochemical characteristics led Larsen and others (this volume) to interpret the gabbro to represent accumulated residual crystals. It is also noteworthy that the groundmass of the 2006 low-silica andesitic rocks contains abundant microlites and exhibits a felty texture; whereas, the matrix of high-silica andesitic rocks are microlite-poor and

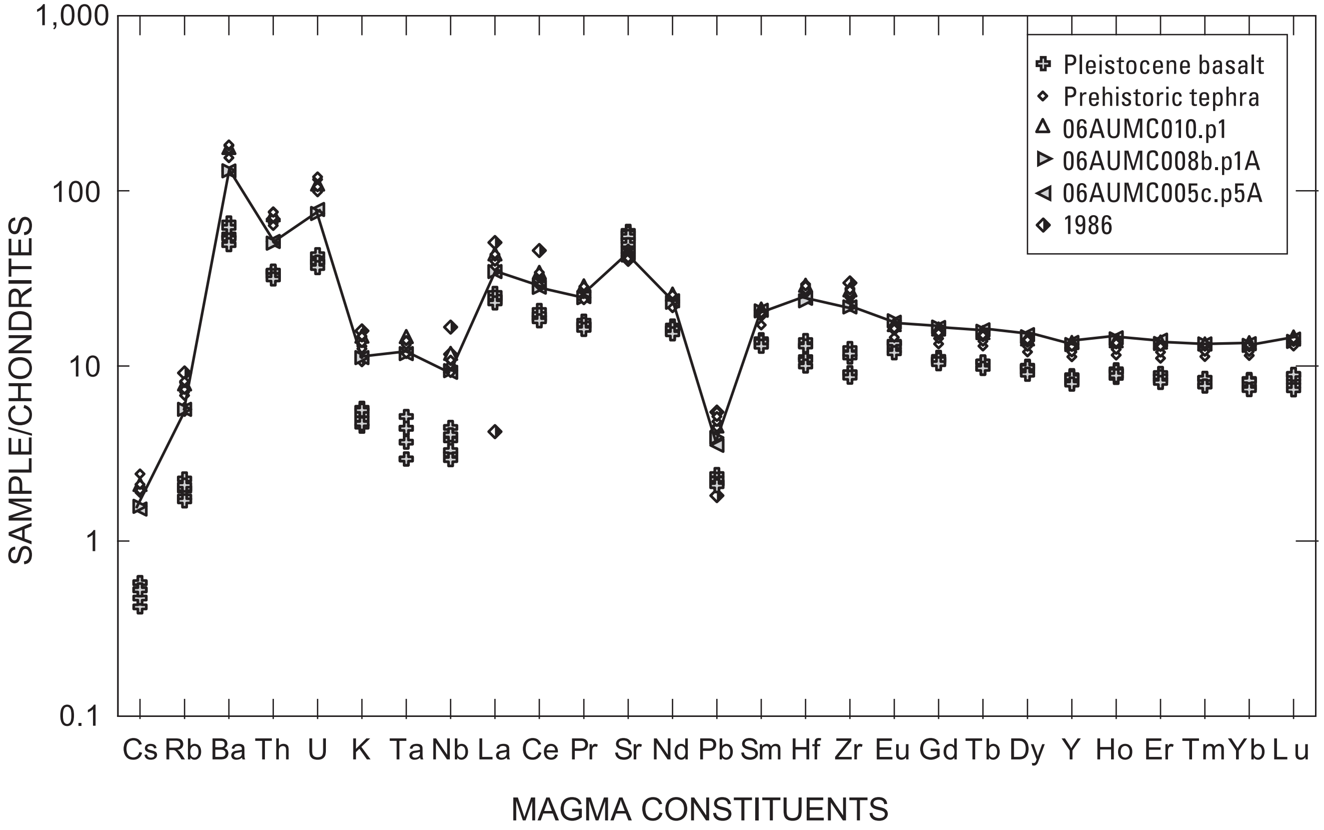

Figure 5. Plot of potassium and trace-element concentrations of Augustine Volcano whole-rock samples normalized to chondritic values (Sun and McDonough, 1995) for five prehistoric tephra (diamonds; from Tappen and others, 2009), six Pleistocene basalts (open crosses; Larsen and others, this volume), 06AUMC010.p1 (open upward-pointing triangles), 06AUMC008b.p1A (gray-filled right-pointing triangles), and 06AUMC005c.p5A (gray-filled left-pointing triangles), and 1986 tephra. Drawn line fitted to normalized data of sample 06AUMC005c.p5A as an example of 2006 eruptive materials relative to older eruptive materials. See text for discussion.

Figure 6. Photograph of large banded boulder within 2006 Augustine pyroclastic-flow deposit showing textural evidence of magma mingling. Bolder located on north slope of Augustine Volcano. One-half meter long rock hammer shown for scale.

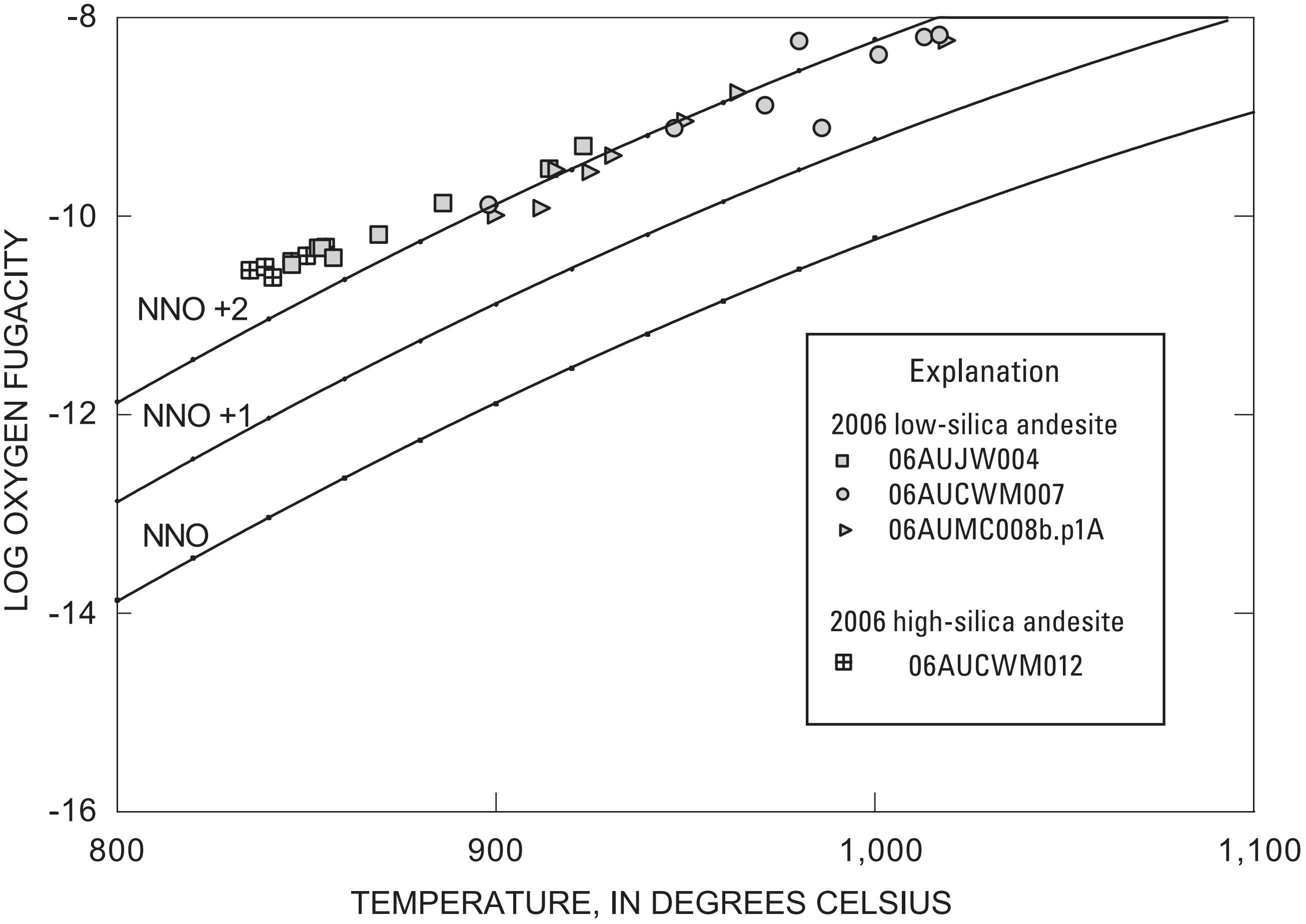

Figure 7. Plot of calculated equilibration temperature (°C) and log of oxygen fugacity (relative to nickel-nickel oxygen buffer = NNO) for coexisting (and "touching") pairs of ilmenite and titanomagnetite. Iron-titanium oxide minerals in 2006 rock samples: 06AUJW004 (gray-filled squares), 06AUCWM007 (gray-filled circles), 06AUCWM012 (gridded squares), and 06AUMC008b.p1A (gray-filled triangles). Data calculated using techniques of Andersen and others (1993) and evaluated using the method of Bacon and Hirshmann (1988), and corrected by reducing temperatures 30°C because these algorithms are not directly applicable to these oxide minerals at such elevated oxygen fugacities. See text for discussion of these methods.

contain glass suitable for microbeam analysis. This indicates that post-mixing, late-stage crystallization of magma forming the low-silica andesites influenced the composition of their near-final and final melts. As explained below and by Larsen and others (this volume), this stage of crystallization may have been facilitated by shallow magma ascent and decompression- and degassing-related processes.

A detailed trace-element analysis of whole-rock samples by Larsen and others (this volume), however, indicates that the high-silica andesites are not fractional crystallization-derived differentiates of the low-silica andesitic magmas that formed by magma mixing. In particular, the abundances of Cr and Ni of the high-silica andesites are too enriched and the concentrations of large-ion lithophile and some high-field strength elements are not sufficiently enriched to reflect an origin based solely on fractional crystallization.

The Behavior of Volatile Components in Evolving Augustine Magmas During the Previous 2,100 Years

Prior research indicates that some fractions of 1976, 1986, and 2006 magmas were fluid saturated during ascent (Johnston, 1978; Roman and others, 2006; Webster and others, 2006), so it is pertinent to consider the evidence and consequences of fluid exsolution on magma differentiation at Augustine. The analysis of volatile-component and fluid behavior in the most recently erupted Augustine magmas is challenging, however, due to the complex histories involving magma mixing, mingling, and fractional crystallization.

In discussion that follows, the compositions of silicate melt inclusions from our prehistoric, 1986, and 2006 eruptive materials are shown to provide distinct geochemical evidence of preeruptive fluids in some fractions of the corresponding magmas. Interpretation of the melt-inclusion data further suggests that initial volatile phase exsolution occurred prior to the entrapment of many of the melt inclusions. Specifically, the melt-inclusion data are compared with experimentally determined solubilities of volatile components in coexisting melt and fluid(s), but this approach can be problematic. Augustine magmas exsolve volatile phases that are variably enriched in the four principal volatile components H_2O, CO_2, S, and Cl (Symonds and others, 1990; McGee and others, this volume), and the sum of their partial pressures ($p_{H_2O} + p_{CO_2} + p_{S_{species}} + p_{Cl_{species}}$) must equal the total pressure of a fluid-saturated magma. It follows that all four components must be considered simultaneously in data treatments like this. For example, the presence of elevated S and/or Cl in a fluid phase will dilute the H_2O and CO_2 concentrations and alter the activity-composition mixing relationships (Botcharnikov and others, 2004; Webster and others, 2005) and, hence, change the larger behavior of H_2O and CO_2 in such fluids. Unfortunately, most experimental data are limited at present to pseudo-ternary systems including silicate melt-H_2O-CO_2, melt-H_2O-Cl, or melt-H_2O±S so we are forced to address the melt-inclusion data with individual pseudo-ternary systems in the discussion that follows.

H_2O in Augustine Magmas

The abundances of the components H_2O and K_2O, which are relatively incompatible in the phenocrysts and microlites in magmas like these, serve as a useful gauge of the extent of residual melt evolution (Anderson, 1976; Johnston, 1978; Roman and others, 2006). In particular, prior studies have interpreted negative correlations between K_2O and H_2O in silicate melt inclusions to represent the consequences of polybaric, decompression crystallization of fluid-saturated magma during ascent (Roman and others, 2006; Atlas and others, 2006). Therefore, we have plotted the concentrations of H_2O versus K_2O for a set of melt inclusions that were analyzed by FTIR and largely represent prehistoric, 1986, and 2006 high-silica andesitic and dacitic rock samples (fig. 8). Figure 8*A* includes 4 modeled trends that express the influence of (A) fluid-absent crystallization of 20 weight percent plagioclase, pyroxene, Fe-Ti oxides, and apatite (in modal abundances that are compatible with 2006 Augustine rocks), (B) complete degassing of an open magmatic system with no concurrent crystallization, (C) polybaric crystallization of 25 weight percent phenocrysts from this same mineral suite in a magma that also contains 4 weight percent exsolved aqueous fluid, and (D) mixing of magmas that may or may not be fluid saturated. The lengths of the arrows designating these trends are quantitative representations of the influence of these processes.

Trend A (fig. 8*A*) is consistent with the positive correlation involving the three most H_2O-enriched, prehistoric melt inclusions, and hence, may reflect the geochemical evolution of these and potentially other fractions of Augustine melts via fluid-absent fractional crystallization. Trend B is inconsistent with the negative correlation of H_2O versus. K_2O that is exhibited by most of the data. The slope of trend C is consistent with the general orientation of the melt-inclusion data field, but this trend requires 25 weight percent crystallization to generate the requisite increase in K_2O content and this degree of crystallization is problematic. It is too extensive for such felsic melts, because it would reduce the FeO, MgO, and CaO contents of the final residual melt to values near zero. Thus, we interpret these melt inclusions to reflect magma evolution dominated by magma mixing and/or mingling (symbolized by trend D) with associated fractional crystallization of fluid-saturated magmas because they are part of the clustered data of figure 2 best interpreted by linear mixing curves.

It should be noted that other processes influence magmatic systems like these. In a study of plagioclase-hosted, felsic melt inclusions in rocks produced during the April 10, 1980 to March 19, 1982, eruptions of Mount St. Helens, Blundy and Cashman (2005) noted a similar negative correlation involving H_2O and K_2O (fig. 8*B*). They computed temperatures of plagioclase-melt equilibrium and estimated the range in crystallization of the magmas involved. Their results showed distinct and robust correlations between magmatic temperature, water fugacity, crystallinity, and the compositions of residual fractions of melt in the Mount St. Helens magmas. Blundy and Cashman (2001, 2005) and Blundy and others (2006) concluded that the batches of magma represented by their melt inclusions underwent contemporaneous: (1) decompression crystallization, (2) loss of volatile components to magmatic vapor, and (3) associated release of latent heat within the magma due to phenocryst growth. They also concluded that the latent-heat effects may have increased temperatures in Mount St. Helens magmas locally by as much as 100°C, and that, in general, such latent-heat temperature increases are likely in any magma that decompresses slowly enough to undergo crystallization.

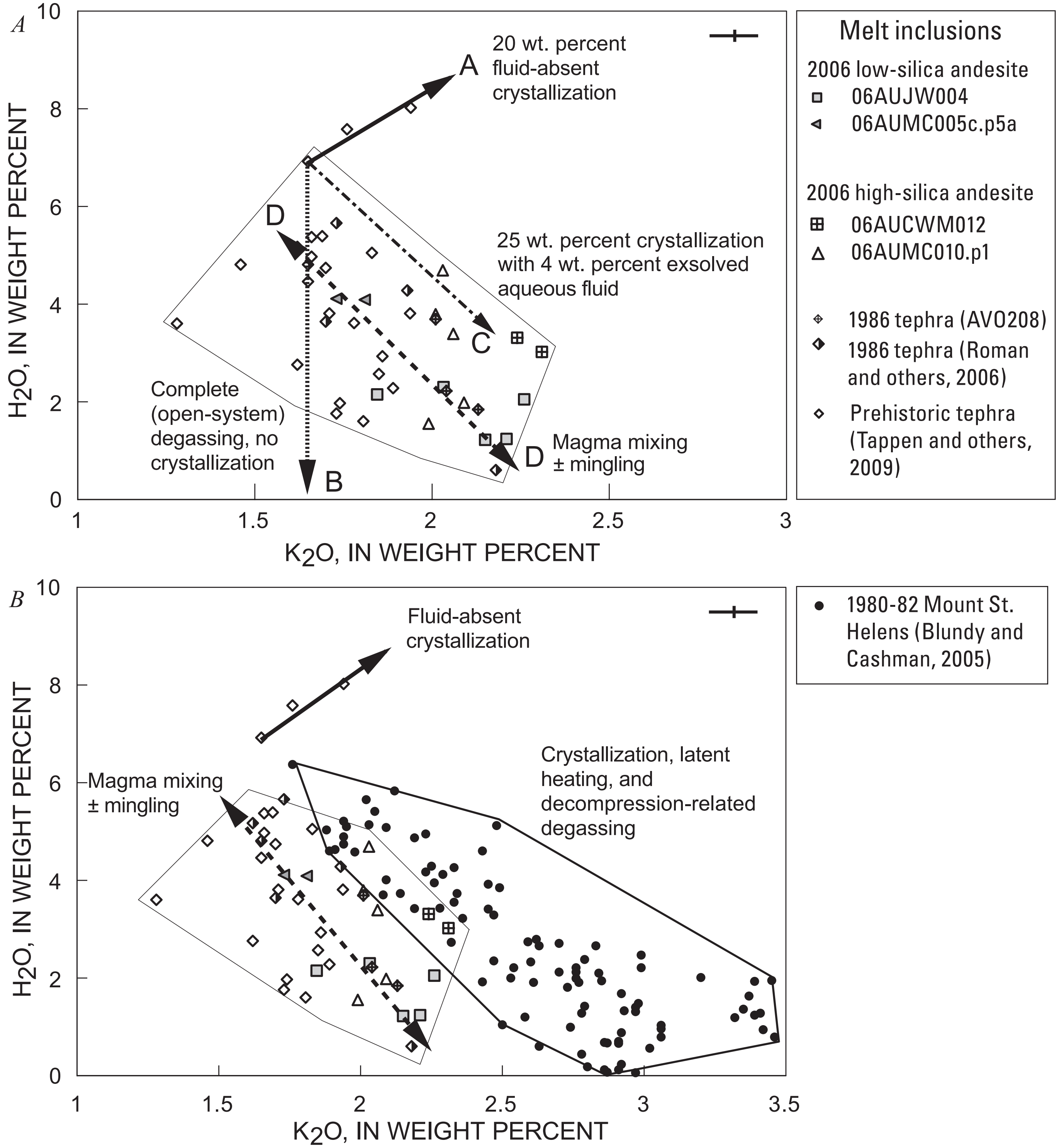

These Mount St. Helens magmas show little textural evidence of magma mixing or mingling which led the authors to note that these processes can account for some common textural features that would otherwise be attributed to preeruptive magma mixing. We conclude that reheating of Augustine magmas, by latent heat release, must also have occurred, but the effects of this process were likely subordinate to reheating caused by magma mixing and/or mingling, given the ample evidence of the latter process.

Sulfur and Chlorine in Augustine Magmas

The S concentrations of most of the rhyodacitic and rhyolitic Augustine melt inclusions are distinctly lower than those of the rehomogenized basaltic-andesite melt inclusions (fig. 3*B*) and the basaltic melt inclusions analyzed by Johnston (1978) and Zimmer and others (2004). These felsic melt inclusions also contain less S than the 0.2 to >0.3 weight percent reported for other subduction-related, calc-alkaline magmas (Anderson, 1982; Wade and others, 2006; Gurenko and others, 2005). The latter concentrations greatly exceed the measured average of 0.02 ± 0.01 weight percent S in all felsic melt inclusions of this study, and these differences indicate that some process of reducing S in the felsic melts occurs in Augustine magmas as they differentiate.

The behavior of S in magmatic systems varies with its oxidation state, and therefore the range in valence states of S in these magmas must be constrained. The 2006 magmas crystallized at f_{O_2} values of approximately NNO+1.5 to NNO+2.5 (fig. 7, table 5; Larsen and others, this volume). This range is similar to the range of circa NNO to NNO+2 reported for prehistoric (Tappen and others, 2009) and 1986 magmas (Roman and others, 2006). At these elevated values of f_{O_2}, the majority of sulfur present would be oxidized to S^{6+} (Carroll and Rutherford, 1988; Mandeville and others, 1998), so the magmatic fluids would contain a mixture of SO_4^{2-}, SO_2, H_2S, and S_2 at shallow crustal pressures (Luhr, 1990; Gerlach and others, 1996; Scaillet and Pichavant, 2003; Jugo and others, 2005; Burgisser and Scaillet, 2007). These theoretical constraints on magmatic SO_4^{2-} and SO_2 are compatible with the observation of significant SO_2 concentrations in volcanic vapor of the 2006 eruptive activities (McGee and others, this volume).

Sulfide and sulfate minerals have only rarely been observed at Augustine. For example, Johnston (1978) reported minor sulfides in 1976 rocks, Tappen and others (2009) observed very rare sulfide mineral inclusions in silicate phenocrysts of primitive prehistoric andesites, and anhydrite makes up less than 0.6 volume percent of some 2006 lithologies (Larsen and others, this volume). The presence of these crystalline phases during the early stages of evolution of the relatively primitive magmas, as evidenced by the depletion of S in the less-evolved melt inclusions (fig. 3*B*), would tend to deplete the S abundances of subsequent, residual melts. In fact, if pyrrhotite is included in the fluid-absent crystallization modeling, it would require 1 weight percent sulfide crystallization to generate a rhyolitic melt with only 200 ppm S (that is, a value that is similar to

◀ **Figure 8.** Plots of the relation between H_2O and K_2O in 45 silicate melt inclusions from 2006, 1986, and prehistoric rock samples from Augustine Volcano, Alaska. *A*, The enveloped area (fine, solid polygon) suggests that the K_2O concentrations correlate with H_2O for the data set, but melt inclusions from individual samples may variably reflect a variety of processes. (Trend A) The bold arrow quantitatively defines the influence of polybaric, 20 weight percent crystallization of Augustine felsic melt containing 6.9 and 1.65 wt. percent H_2O and K_2O, respectively, and is consistent with the three most H_2O-enriched melt inclusions that are also inconsistent with the other inclusions. (Trend B) The dotted arrow reflects the consequences of complete, open-system degassing of H_2O with no crystallization. (Trend C) The length of this dot-dash arrow quantitatively reflects the effect of 25 wt. percent crystallization of magma containing 4 wt. percent exsolved aqueous fluid during magma ascent and polybaric decompression. (Trend D) These melt inclusions also reflect consequences of mixing and/or mingling of multiple magmas, and the dashed arrow represents the differentiation of residual rhyolitic melts by mixing of relatively hydrous and Na_2O-, K_2O-, and Cl-deficient magma with relatively anhydrous magma. Mixing apparently occurred during contemporaneous crystallization and fluid exsolution. *B*, The H_2O and K_2O concentrations of silicate melt inclusions (filled circles) from Mount St. Helens eruptions of April, 10, 1980 to March 19, 1982, (Blundy and Cashman, 2005) are included with the Augustine melt inclusion data. Blundy and Cashman (2005) interpret this negative correlation, by the use of associated constraints on melt-plagioclase equilibration temperatures and modeling, to represent the consequences of decompression crystallization of fluid-saturated felsic magmas and the concurrent release of latent heat of crystallization. These Mount St. Helens magmas show little textural evidence of magma mixing or mingling, but they may have undergone loss of H_2O and other volatile components to magmatic vapor as they ascended and decompressed. The extent of crystallization increased, even though these magmas may have been heated by as much as 100°C by latent heating effects, because of the reduction in the fugacities of volatile components as they were sequestered by vapor. Blundy and others (2006) note that these processes can generate textural characteristics similar to those of magma mixing. Given the very similar nature of this relationship to that exhibited by the Augustine melt inclusions, this process may have also played a minor role in the evolution of Augustine magmas. Representative and relative 1-σ precision for glass analyses is shown in upper right corners. See text for discussion.

those of most of the felsic melt inclusions) from the basaltic-andesite melt inclusion compositions which is inconsistent with the lack of sulfide mineral inclusions in other phenocrysts of these rocks.

Mixing of magmas does not appear to be solely responsible for the trends involving S in most of the felsic melt inclusions. The apparent mixing trends expressed by the major constituents CaO, K_2O, and Na_2O (fig. 2) and some minor constituents P_2O_5 and Cl (fig. 3) in these inclusions exhibit strong variability in the abundances of these components as a result of varying degrees of mixing (that is, they show widely varying concentrations along the mixing lines). In contrast, the concentrations of S of the felsic melt inclusions are much more highly focused (that is, much less dispersed) at the average value of 0.01 weight percent, and, hence, they are inconsistent with this process. Mixing must have generated some variability in the mixed products, but other processes were apparently involved as well.

As sulfides are rare and only present in Augustine rocks at abundance levels well below that required to remove significant S from the residual melts and because magma mixing is not solely responsible for the strong reduction in S concentrations with melt evolution, the involvement of a fluid or fluid phases in S sequestration is required. The partition coefficient for S, D_S (weight percent S in fluid/weight percent S in melt) has been determined experimentally to range from approximately 10 to 80, 100 to 300, and 100 to 900 for basaltic (Scaillet and Pichavant, 2003), andesitic (Scaillet and Pichavant, 2003), and rhyodacitic (Botcharnikov and others, 2004) melts, respectively, at pressures of 100 to 300 MPa and temperatures and oxygen fugacities relevant to Augustine magmas (≤1,050°C and f_{O_2} of NNO to NNO+2) (fig. 7; Roman and others, 2006; Tappen and others, 2009). Thus, exsolved aqueous magmatic fluids would be highly efficient in stripping S from melts of the 2006, 1986, and prehistoric Augustine magmas. Importantly, values of D_S increase with reduced pressure (Scaillet and Pichavant, 2003), so the efficiency of this process would increase with the reduction in pressure that accompanies magma ascent. The differentiation of the residual fractions of melt to more felsic compositions would also enhance the efficiency of S sequestration given that D_S is greater for felsic as compared to mafic melts. Moreover, hydrothermal fluids are also capable of dissolving sulfide minerals not trapped as inclusions in other phenocrysts (Reed, 1997); so it is conceivable that any sulfide minerals that may have crystallized relatively early in these magmas were dissolved by fluids during later stages of fluid-saturated magma evolution.

The Cl concentrations of most felsic melt inclusions from the high-silica andesitic to dacitic rocks are variable, and yet, the Cl contents of many of them either equal or exceed those of the more primitive basaltic-andesite melt inclusions (fig. 3*C*). The Cl contents of melt inclusions from low-silica andesites studied are also variable, but in this case most of them are more equivalent to those of the basaltic-andesite melt inclusions (fig. 3*C*). In addition, the Cl concentrations of matrix glasses that we analyzed and those of Wallace and others (this volume) are quite similar to those of the melt inclusions from low-silica andesites. These comparisons indicate that the Cl concentration of some of the felsic melts represented by the melt inclusions from high-silica andesites increased to a limited extent during differentiation, and the trends apparently reflect the varied consequences of magma mixing, fluid(s) exsolution, and fractional crystallization as described below.

The Cl concentrations in the set of melt inclusions that were analyzed by FTIR (and largely represent prehistoric, 1986, and 2006 high-silica andesitic and dacitic rock samples; fig. 9*A*) correlate negatively with H_2O in general, but this is not true for the various subsets of data (distinguished by individual rock samples and stages of eruption) comprising this larger data set. This lack of correlation for melt inclusions from individual samples is the likely result of a variety of magmatic processes, and hence, the larger trend in this figure has been interpreted relative to a series of modeled trends expressing various processes of magma differentiation. For example, some subsets of these data may be consistent with the trend (A) that expresses fluid-absent, isobaric crystallization of 20 weight percent of a rhyolitic melt under closed-system conditions. Alternatively, some of these melt-inclusion data may be consistent with any of several polybaric, closed-system degassing trends that are shown and involve a reduction in pressure of 200 to 50 MPa. These degassing trends include: (B) 20 weight percent crystallization of a rhyolitic melt that is in equilibrium with a fluid containing 2 weight percent Cl (with an average value of D_{Cl} [concentration of Cl in fluid(s)/concentration of Cl in silicate melt] of 10 averaged for changing pressure) or (C) 20 weight percent crystallization of a rhyolitic melt that is in equilibrium with a fluid containing 1 weight percent Cl (with an average value of D_{Cl} of 5 averaged for changing pressure). These values of D_{Cl} are appropriate for this range of felsic melt compositions and this range in pressure (Webster and others, 1999). As magmatic processes do not necessarily occur at equilibrium, figure 9*A* includes a modeled trend (D) for the crystallization and degassing of magma that exsolves a Cl-free aqueous fluid under open-system conditions. Experimental research summarized by Baker and others (2005) demonstrates that H_2O diffuses more quickly than Cl through silicate melts, so (D) addresses magmatic degassing processes in which there is insufficient time for Cl to achieve an equilibrium distribution between melt and fluid(s). Trend D also involves preferential loss of H_2O with no loss of Cl to the fluid, such that the degassing magma has, in effect, a D_{Cl} value of 0, and some of these data appear consistent with this trend. Trend (E) appears more consistent with the larger, integrated data set, and it reflects the consequences of mixing two magmas that contain different H_2O and Cl contents. In summary, given the strong evidence for magma mixing as a dominant process of evolution of magmas erupted in 2006 and because of the relationships in figures 3C and 8, we suggest that the progressive evolution of late-stage, felsic Augustine melts of the high-silica andesitic magmas involved the mixing and/or mingling of relatively hydrous and K_2O-, Na_2O-, and Cl-deficient rhyolitic melt with relatively anhydrous, K_2O-, Na_2O-, and Cl-enriched rhyolitic melt.

To interpret these processes more fully, it is useful to apply empirically derived and modeled Cl and H_2O solubilities for geologically relevant melt compositions to the melt-inclusion data. Such comparisons provide key constraints on pressures of fluid phase exsolution and on the type of fluid phase(s) that exsolve. The curves in figure 9*B* express the solubilities of H_2O and Cl in rhyolitic melt for 3 pressure conditions, and they represent the exsolution of either a H_2O- (± CO_2) bearing vapor phase, a saline liquid, or vapor plus saline liquid as the (Cl/H_2O) ratio of the silicate melt progressively increases. In addition, the 20- and 200-MPa volatile component solubility curves for H_2O-deficient conditions involve a range in Cl concentrations. This range reflects the computed range in maximum Cl solubility for the corresponding range in glass compositions of the melt inclusions (Webster and De Vivo, 2002). It is crucial to account for the range in melt composition because Cl solubility in silicate melts varies strongly with bulk composition (Webster and De Vivo, 2002). These solubility curves also account for the influences of S and pressure on Cl solubility in silicate melts. Specifically, the solubility of Cl in melts that are saturated in S-bearing fluid(s) decreases dramatically with increasing S in the system (Botcharnikov and others, 2004; Webster and others, 2005). Chlorine solubility also decreases with decreasing pressure for silicate melts that are saturated in a saline liquid (Webster and others, 1999).

The compositions of the three, H_2O-enriched prehistoric melt inclusions that contain <0.33 weight percent Cl plot above but near the 200-MPa curve for vapor plus coexisting silicate melt, and hence, they imply pressures of volatile saturation that exceed 200 MPa and that the fluid would have been an aqueous (or potentially aqueous-carbonic) vapor when fluid saturation occurred. Unlike these three, most other melt inclusions are consistent with saturation of Augustine magmas in fluid(s) at lower pressures ranging from 20 to 200 MPa under closed-system conditions, and the latter data are inconsistent with magma storage and evolution at a single pressure (such as within a magma chamber). Interestingly, the compositions of melt inclusions from 2006 samples contain generally lower H_2O concentrations and exhibit larger (Cl/H_2O) ratios than melt inclusions from prehistoric or 1986 tephra. These relationships indicate that (1) the fluid(s) would have exsolved at generally lower pressures than those in the other, older magmas and (2) the compositions of the magmatic fluid phase(s) represented by the melt inclusions from 2006 samples would have been more highly saline. In fact, some aliquots of the fluids at the lower pressures included anhydrous saline liquids.

H_2O and CO_2 in Augustine Magmas

One can derive additional constraints on pressures of melt entrapment, the concentrations of CO_2 and H_2O in magmatic volatile phases, and applicable pressure-composition paths of magma ascent and degassing by comparing the concentrations of H_2O and CO_2 in felsic melt inclusions with experimentally determined and modeled solubilities of H_2O and CO_2 in rhyolite melt (Newman and Lowenstern, 2002; Moore, 2008). However, this procedure does not account for Cl or S species in the fluids. In the following discussion on fluid geochemistry and degassing processes, it must be recognized that the results of comparing the H_2O and CO_2 abundances of melt inclusions with theoretical H_2O and CO_2 solubilities in silicate melts can be interpreted in two ways. One interpretation is that the locations of the melt inclusion data, relative to the isobaric volatile-component solubility curves, determine pressures at which the corresponding aliquots of magma should have saturated in a H_2O- and CO_2-dominated fluid (vapor) phase as magma ascended toward the surface. Alternatively, if independent evidence—that the melt inclusions represent fluid-saturated magma at the time of melt entrapment—is available, then the locations of the melt-inclusion data relative to the isobaric volatile-component solubility curves constrain the pressure of melt inclusion entrapment. Note that the latter approach does not necessarily establish the initial pressures of or the corresponding maximum depths of magmatic volatile-phase exsolution, because the melt represented by a given melt inclusion could have exsolved a volatile phase at depths and pressures greater than those indicated and the melt inclusion simply represents fluid-saturated melt that was trapped in a growing phenocryst at some time well after the stage of initial magmatic fluid exsolution.

To this end, the H_2O and CO_2 abundances of melt inclusions from the 2006 rocks are plotted along with those collected from prehistoric tephra C (AVO 201), G (AVO 205), H (AVO 204), and I (AVO 203) and from several 1986 pumice samples (ours and those of Roman and others, 2006), and the concentrations of these volatile components are compared with the theoretical (Newman and Lowenstern, 2002) isobaric vapor-saturation curves for CO_2- and H_2O-bearing rhyolite melt (figs. 10*A* and 10*B*). This assessment indicates that the aliquots of rhyolite melt represented by most of these melt inclusions would saturate in H_2O- ± CO_2-bearing fluid(s) at pressures of 20 to 200 MPa. This observation is consistent with that detected previously in plots of H_2O versus Cl in that the Cl, CO_2, and H_2O data are inconsistent with magma storage and evolution at a single pressure (that is, within a magma chamber). It is noteworthy, however, that the compositions of 5 of these melt inclusions imply pressures of fluid phase saturation that exceed 200 MPa and that 1 inclusion indicates pressures that exceed 350 MPa. This is similar to that observed with H_2O versus Cl, and given that the bulk of the melt inclusions from these eruptions of Augustine Volcano provide roughly similar pressure estimates based on plots

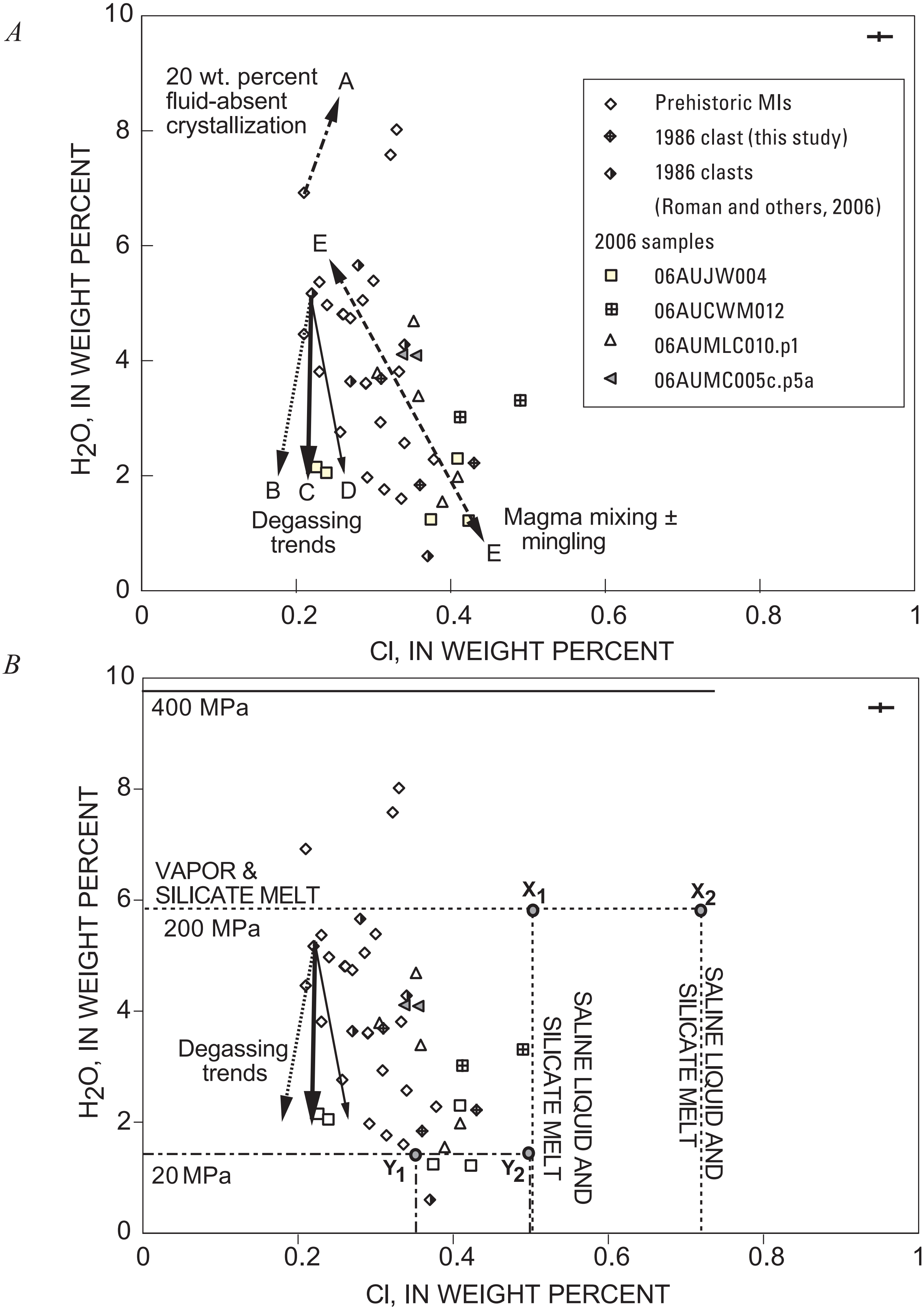
A
20 wt. percent fluid-absent crystallization
A
E
Degassing trends
B
C
D
Magma mixing ± mingling
E
◇ Prehistoric MIs
◈ 1986 clast (this study)
◆ 1986 clasts (Roman and others, 2006)
2006 samples
□ 06AUJW004
⊞ 06AUCWM012
△ 06AUMLC010.p1
◁ 06AUMC005c.p5a
H_2O, IN WEIGHT PERCENT
Cl, IN WEIGHT PERCENT
0
2
4
6
8
10
0
0.2
0.4
0.6
0.8
1
B
400 MPa
VAPOR & SILICATE MELT
200 MPa
X_1
X_2
Degassing trends
20 MPa
Y_1
Y_2
SALINE LIQUID AND SILICATE MELT
SALINE LIQUID AND SILICATE MELT
H_2O, IN WEIGHT PERCENT
Cl, IN WEIGHT PERCENT
0
2
4
6
8
10
0
0.2
0.4
0.6
0.8
1

involving two pseudo-ternary systems, we interpret this agreement to indicate that most of these melt inclusions represent magma that was fluid saturated at the time of entrapment and, therefore, that pre-eruptive saturation of Augustine magmas in fluid(s) was a common process.

The comparison of the melt-inclusion compositions with the volatile solubility curves indicates that many felsic fractions of Augustine magma would have coexisted with volatile phases comparatively enriched in H_2O over CO_2 (fig. 10*A*). In fact, the H_2O content of the fluid(s), not accounting for the influence of Cl and S, was ≥95 mole percent for most aliquots of 2006 and prehistoric magmas and ≥ 85 mole percent for most fractions of 1986 magma.

To establish potential pressure-composition paths of magma ascent and degassing for the recent Augustine magmas, we relate the melt-inclusion data to a series of theoretical curves that express the reduction in H_2O and CO_2 concentrations of residual rhyolitic melt in evolving magmas as they ascend from depths equivalent to pressures of ≥ 350 MPa (fig. 10*B*). The 2006 and prehistoric data are most consistent with the rise of magmas containing 1 weight percent of H_2O-enriched vapor under closed-system conditions. This modeled curve is based on initial conditions involving a fluid-saturated magma at 950°C and approximately 400 MPa; the rhyolitic melt in this magma contains 9.5 weight percent H_2O and 100 ppm CO_2 at the initiation of fluid-saturated ascent and crystallization. Of particular importance is that the pressures estimated from H_2O and CO_2 in melt inclusions in 2006 samples range from 150 to 20 MPa only. This pressure range is consistent with crystallization of 2006 magma from the depths indicated by geodetic measurements (that is, for magma storage at 4 to 6 km) up to depths near the surface (Cervelli and others, this volume). The melt inclusions from 1986 tephra are more compatible with the rise of a fluid-saturated magma that contains 3 weight percent of H_2O-enriched vapor under closed-system conditions; the rhyolitic melt contains 7 weight percent H_2O and 500 ppm CO_2 as it passes through the depth equivalent to 350 MPa. In both cases, the vapor-saturated magmas are assumed to be crystallizing at 950°C while at a depth of 14 km (about 350 MPa).

These magmatic fluids were stable in the presence of melt at pressures ranging from 350 MPa to values <20 MPa. This range of pressure corresponds to depths of magmatic degassing that extend over the range of 14 km to 800 m, and, clearly, degassing must have continued at more shallow conditions (that is, as magma ascended and breached the volcanic edifice). Moreover, the modeling based on relationships involving H_2O and CO_2 is consistent with closed-system magma ascent as polybaric crystallization and degassing progressed, and the computed initial mass of fluids, which ranges from 1 to 3 weight percent and represents minimum fluid quantities, is consistent with prior work on other calc-alkaline, subduction-related magmatic systems (Wallace and Anderson, 2000; Scaillet and Pichavant, 2003; Wallace, 2005).

◀ **Figure 9.** Plots of the relation between H_2O and Cl in 45 silicate melt inclusions from Augustine Volcano samples including prehistoric rocks (open diamonds; Tappen and others, 2009), 1986 tephra sample 86E-63-2 of Roman and others (2006) (diamonds filled on right side), our 1986 tephra (gridded diamonds), low-silica andesitic sample 06AUJW004 (open squares), and high-silica andesitic samples 06AUCWM012 (gridded squares) and 06AUMC010.p1 (upward-pointing triangles). *A,* Melt-inclusion compositions are compared with trends describing: (A, dot-dash arrow) the result of 20 weight percent isobaric crystallization of fluid-absent rhyolitic melt on H_2O and Cl concentrations of residual melt; (B) polybaric, 20 wt. percent crystallization and exsolution of 4 weight percent aqueous fluid (with an average fluid/melt $D_{Cl} = 10$); (C) polybaric, 20 weight percent crystallization and exsolution of 4 weight percent Cl-bearing aqueous fluid (with average $D_{Cl} = 5$); (D) 20 weight percent polybaric crystallization and exsolution of 4 weight percent H_2O and no loss of Cl to fluid (i.e., with $D_{Cl} = 0$); and (trend E) mixing and/or mingling of H_2O-enriched and Na_2O-, K_2O-, and Cl-deficient magma with H_2O-deficient magma. *B,* Melt inclusion data are plotted relative to modeled solubilities of H_2O in H_2O-rich vapor-saturated rhyolite melt at 400 (solid curve), 200 (dashed curve), and 20 (dot-dash curve) MPa and 900°C (after Newman and Lowenstern, 2002), and Cl solubility in rhyolitic melts saturated in Cl-rich, H_2O-poor saline liquid (after Webster and De Vivo, 2002; Webster and others, 1999; 2005). At X_1 and X_2 (200 MPa), and at Y_1 and Y_2 (20 MPa), silicate melt coexists with vapor plus saline liquid. The 20- and 200-MPa volatile component solubility curves for H_2O-deficient conditions involve a range in Cl concentrations. The differences in Cl concentration between X_2-X_1 and Y_2-Y_1 reflect the computed ranges in maximum Cl solubility for the corresponding range in composition for this set of melt inclusions for two pressure conditions (Webster and De Vivo, 2002). The curves also account for the influences of sulfur (Webster and others, 2005; Botcharnikov and others, 2004) and pressure (Webster and others, 1999) on Cl solubility in silicate melts. These data, in conjunction with observations of figure 3B, indicate that at relatively higher pressures >200 MPa the dominant fluid phase coexisting with residual fractions of silicate melt was H_2O- and (potentially CO_2-) enriched vapor; whereas with magma ascent to lower pressures (approaching 20 MPa) the dominant magmatic fluid phase coexisting with evolving silicate melt was saline Cl- (and presumably S-) enriched liquid. Representative and relative 1-σ precision for glass analyses is shown in upper right corners. See text for discussion.

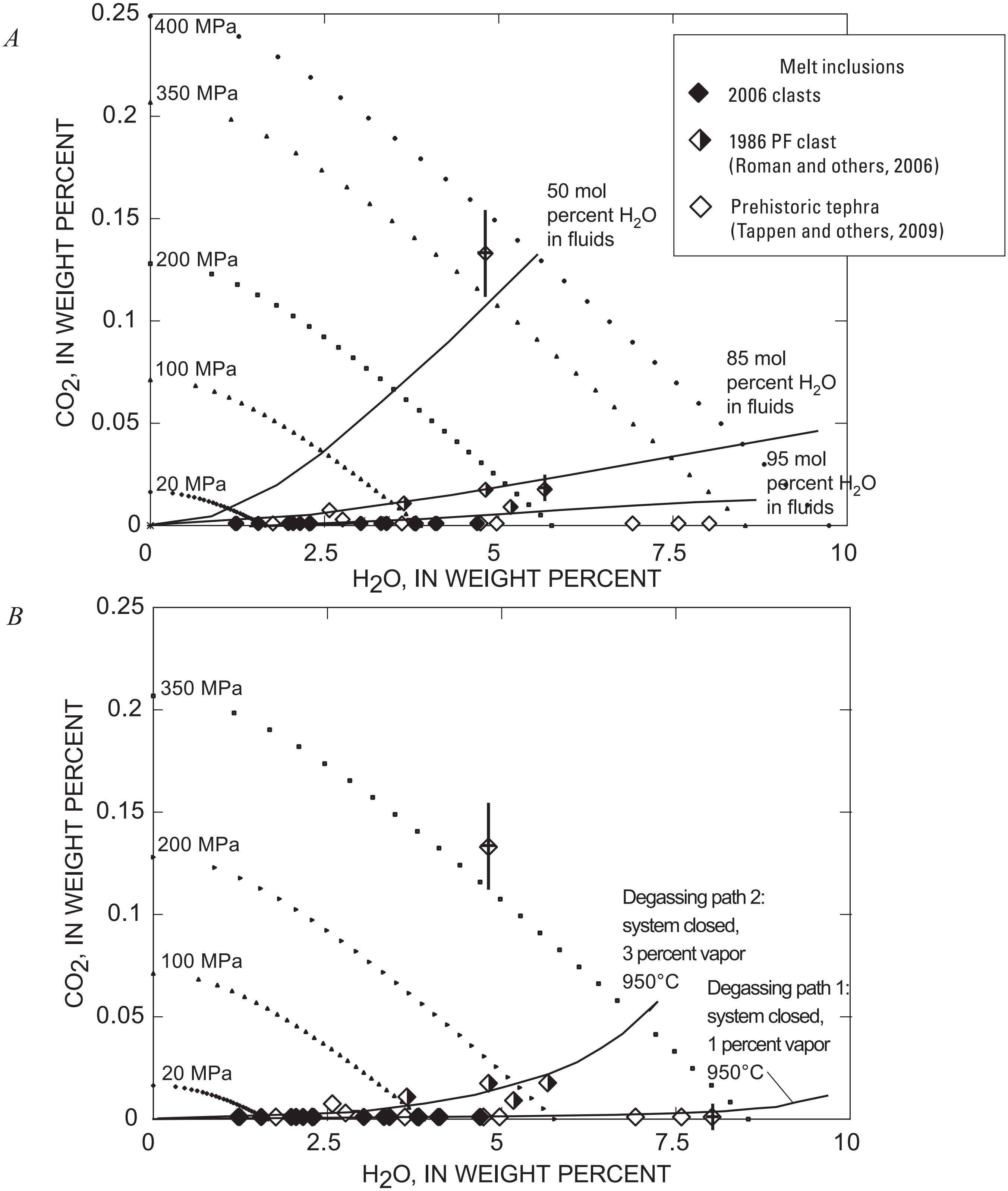
A
0.25
0.2
0.15
0.1
0.05
0
CO2, IN WEIGHT PERCENT
400 MPa
350 MPa
200 MPa
100 MPa
20 MPa
50 mol percent H2O in fluids
85 mol percent H2O in fluids
95 mol percent H2O in fluids
0
2.5
5
7.5
10
H2O, IN WEIGHT PERCENT
Melt inclusions
◆ 2006 clasts
◆ 1986 PF clast (Roman and others, 2006)
◇ Prehistoric tephra (Tappen and others, 2009)
B
0.25
0.2
0.15
0.1
0.05
0
CO2, IN WEIGHT PERCENT
350 MPa
200 MPa
100 MPa
20 MPa
Degassing path 2: system closed, 3 percent vapor 950°C
Degassing path 1: system closed, 1 percent vapor 950°C
0
2.5
5
7.5
10
H2O, IN WEIGHT PERCENT

Developing a Model for the Behavior of Fluid Phase(s) During Magma Ascent and Differentiation

The relationships involving H_2O, CO_2, Cl, and S in the integrated melt-inclusion data reveal that the 2006, 1986, and prehistoric magmas contained one or more fluid phases before eruption, which is consistent with the results of prior research on 1976 (Johnston, 1978) and 1986 (Roman and others, 2006) magmas. These data also indicate that volatile components were sequestered by magmatic fluids as magma mixing ± mingling and fractional crystallization occurred, and that the fluids were stable through an extended pressure range and depth of magma ascent. In this developing model, we focus primarily on shallow-crustal processes influencing magmas after the ascent of hot, volatile-enriched basaltic magma into the crust and after this mafic magma mixed (our mixing event 1) with other more-evolved magma that was residing in the Augustine conduit and reservoir system. This involvement of relatively hot basaltic magma likely represents a potential eruption-triggering mechanism, because of the input of additional thermal energy and volatile components by the basaltic magma (Larsen and others, this volume). Thus, we focus on the potential role of fluids that were present (1) after mixing event 1 (fig. 2) and (2) during and subsequent to mixing event 2 (fig. 2). This treatment is relevant to the 2006 and older eruptions.

The integration of phenocryst and melt-inclusion compositional data demonstrates that these magmas behaved as quasi-closed systems, with regard to volatile component escape, until the magmas reached very shallow crustal depths (that is, ≤800 m). The compositions and rim textures of amphiboles, for example, provide relevant constraints on depths of crystallization and rates of magma ascent, respectively. Comparison of the compositions of 2006 Augustine amphiboles with those grown during hydrothermal experiments on similar bulk compositions at pressure, temperature and f_{O_2} conditions pertinent to Augustine magmas allows us to constrain the more narrow range of magmatic conditions that bear on amphibole crystallization in these magmas. Experimental work on amphibole stability in Mount St. Helens dacite at 850 to 940°C and 70 to 260 MPa (Rutherford and Devine, 2008) indicates that amphiboles contain ≤11 weight percent Al_2O_3 if crystallized below 200 MPa (fig. 11). This is a result of the fact that the Al content of amphiboles is largely dependent on the pressure-sensitive Al-Tschermak [^{M}(Mg,Fe)+ ^{T}Si = ^{M}Al + ^{T}Al], temperature-dependent edenite [^{T}Si +^{A}vacancy = ^{T}Al + ^{A}(Na,K)], and Ti-Tschermak [2^{T}Ti + ^{M}Mn =2^{T}Al +^{M}Ti] substitution mechanisms. In related work, Moore and Carmichael (1998) conducted hydrothermal experiments involving calc-alkaline andesites and basaltic andesites from western Mexico that are strikingly similar in bulk composition and intrinsic f_{O_2} to the 2006 Augustine low-silica and high-silica andesites. Amphiboles generated in experiments on the calc-alkaline andesite at 101 to 285 MPa, 900 to 975°C, and log f_{O_2} of NNO +2 contain ≥10 weight percent Al_2O_3 and ≥15.6 weight percent MgO (fig. 11). In contrast, most Augustine 2006 amphiboles with similar MgO contents contain ≤9.5 weight percent Al_2O_3. In addition, amphibole was not stable in Moore and Carmichael's (1998) calc-alkaline andesite experiments at temperatures >970°C. Amphiboles in Moore and Carmichael's (1998) experiments on the basaltic andesite contain ≥11.9 weight percent Al_2O_3 and >16.0 weight percent MgO at 950° to 1,000°C and 222 to 303 MPa. Interestingly however, most Augustine 2006 amphiboles contain <16 weight percent MgO (as well as Al_2O_3 contents ≤9.5 weight percent; fig. 11), so it is likely that Augustine amphiboles crystallized at pressures <170 MPa, and the rarity of amphiboles also indicates that these magmas passed through the low-pressure portion of the amphibole stability field (~130 to 170 MPa) rapidly. In addition, the lack of decompression-driven reaction rims on many of these amphiboles may indicate rapid magma ascent from depths of 4 to 5 km (Rutherford and Hill, 1993) and/or lack of favorable reaction kinetics for amphibole breakdown (Browne and Gardner, 2006). Interestingly, one of the 2006 amphiboles analyzed (table 6) exhibits an ~ 7-fold increase in F content from core to rim, and Rutherford and Devine (2008) observed similar variations of F concentration in amphiboles from the 2004-2006 dacite of Mount St. Helens. The latter study

◀ **Figure 10.** Plots of the relation between CO_2 and H_2O in 35 silicate melt inclusions from 2006, 1986, and prehistoric Augustine Volcano rock samples; symbols same as in figure 4. *A*, Data are plotted relative to isopleths for compositions of fluids in equilibrium with rhyolitic melts (calculated using model of Newman and Lowenstern, 2002), with fluids ranging from 95 mole percent H_2O (and 5 mole percent CO_2) to 50 mole percent H_2O (and 50 mole percent CO_2). Most melt inclusions are consistent with fluids in 1986 magma(s) containing ≤15 mole percent CO_2 and 85 mole percent H_2O, and many melt inclusions from the 2006 and prehistoric samples indicate that those batches of magma represented by these samples contained only trace CO_2 and so the fluids were CO_2-deficient. *B,* Data are plotted relative to a calculated closed-system degassing paths (using Newman and Lowenstern, 2002). Degassing path 1 applies to rhyolite melt initially saturated with 1 wt. percent vapor containing ≥95 mole percent H_2O at 950°C; this path (and these conditions) are consistent with evolution of fluid-saturated 2006 magmas. Path 2 applies to rhyolite melt initially saturated with 3 weight percent vapor containing approximately 85 mole percent H_2O at 950°C. Estimated values for 1-σ precision for CO_2 and H_2O in glasses are shown as vertical and horizontal lines for two representative high- and low-CO_2 melt inclusions. See text for discussion.

demonstrated that these changes in F content near the rim preceded the formation of reaction rim products, and it attributed this feature to amphiboles that were not within the amphibole stability field during magma ascent.

As part of our working model, we suggest that some of the 2006 and 1986 melt inclusions from high-silica andesites (that is, those of mixing trend 2, fig. 2) represent aliquots of younger felsic magma that interacted with older felsic magma while passing through the volcanic conduit at shallow crustal levels. Indeed, it is clear that some of these melt inclusions reflect shallow pressures of entrapment (due to their low volatile component abundances) while also showing other geochemical differences that reflect varying stages of evolution resulting from mixing and fractional crystallization. Thus, some of these mixing/mingling processes occurred within the conduit system. This interpretation is consistent with the conclusion of Roman and others (2006) that some 1986 magma formed via differentiation within the dike network that comprises the volcanic conduit and not within a magma chamber. It is also compatible with the bulk geochemistry of the two felsic end-member type magmas that are consistent with mixing trend 2 (fig. 2).

Given these constraints on magma composition, what can one establish about the compositions of the dominant fluids involved? It has been demonstrated that some fractions of the 2006, 1986, 1976, and prehistoric magmas contained a Cl-bearing aqueous vapor and other fractions contained Cl-rich saline liquid. In this regard, the results of prior experimental and theoretical research indicate that Cl-bearing magmas, and Cl-enriched magmas in particular, may also contain two fluids (Cl-bearing aqueous or aqueous-carbonic vapor plus saline liquid) at the shallow crustal pressures and magmatic temperatures characterizing volcanic conduits (Shinohara, 1994; Webster and Mandeville, 2007). In such systems, HCl is the dominant chloride species in volcanic vapors at surface or near-surface pressures (Giggenbach, 1996; 1997; Edmonds and others, 2002), which is consistent with prior study of Augustine's volcanic emanations indicating that it releases H_2O-dominated vapors containing significant HCl (Symonds and others, 1990). Conversely, alkali chlorides and alkaline earth chlorides are the dominant Cl-bearing species in coexisting magmatic saline liquids (Giggenbach, 1995). It follows that magmatic vapor and saline liquid should tend to separate from one another because of their strongly differing densities. The vapor will tend to

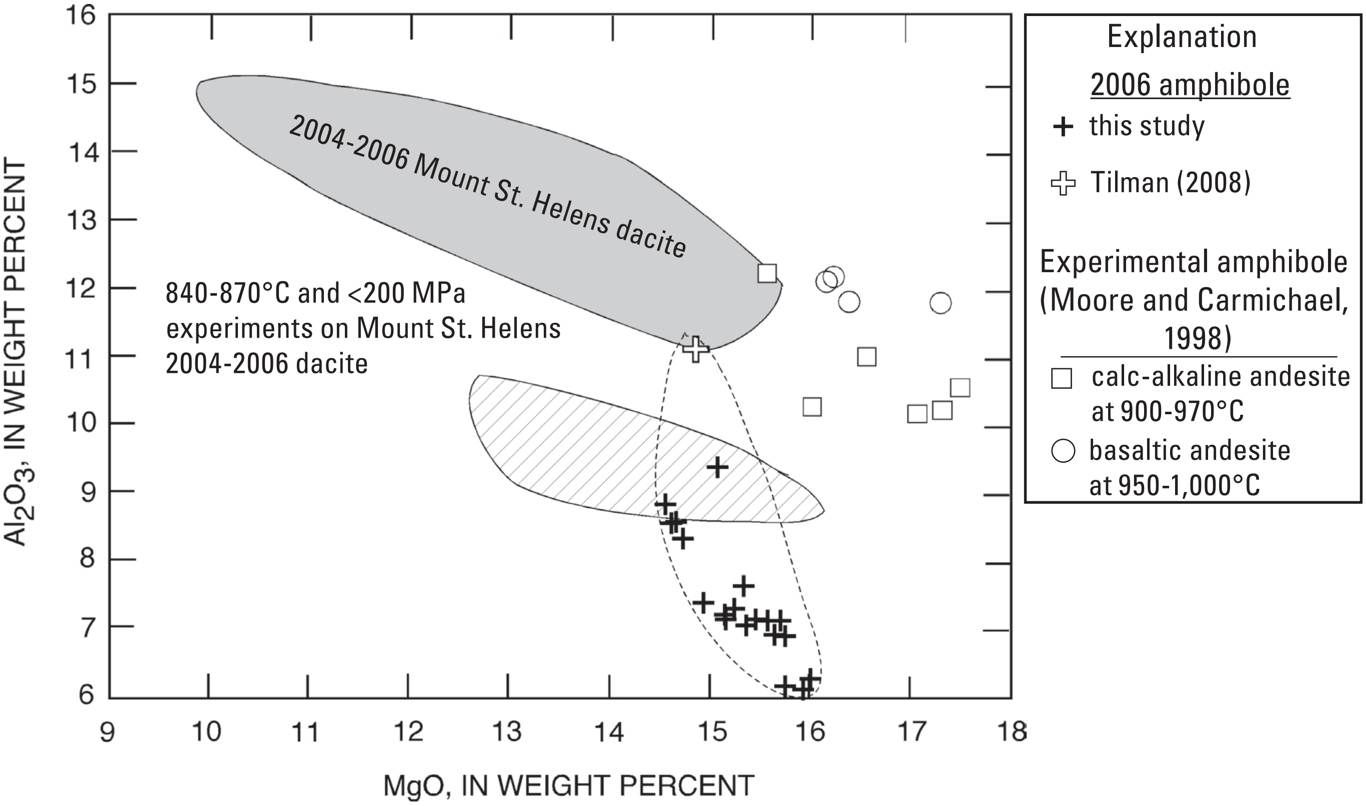

Figure 11. Plot of the relation between the concentrations of Al_2O_3 and MgO in amphiboles of Augustine Volcano rock samples compared to other natural and experimental amphibole compositions. Natural and experimental amphibole compositions from Mount St. Helens 2004–6 dacite from Rutherford and Devine (2008). Data from relatively rare Augustine 2006 amphiboles indicate they crystallized in the lower-pressure region of the amphibole stability field (~130 to 170 MPa).

ascend more rapidly through magma, and the saline liquid may either collect within a stratified “dryout” zone or horizon (Henley and McNabb, 1978) in the conduit (Hardee, 1982; Shmulovich and Churakov, 1998) or it may slowly ascend through the magma because its density is roughly half that of the encompassing silicate melt. In this regard, molten salt was observed flowing from fissures in the Vesuvius crater in the first decade following the 1944 eruption (Chiodini and others, 2001). Moreover, recent experimental studies have determined high solubilities of SO_4^{2-} in alkali chloride-enriched hydrothermal fluids at the pressures relevant to volcanism (Newton and Manning, 2005; Webster and others, 2007). Thus, the relatively oxidizing magmatic fluids at Augustine likely included H_2O-enriched and HCl-, H_2S-, S_2-, and SO_2- ± CO_2-bearing vapors; hydrosaline aqueous liquids largely enriched in Cl^-, SO_4^{2-}, alkalis, and H_2O; to moderately saline, H_2O-poor liquids containing Cl^-, SO_4^{2-}, and alkali elements.

The fluids at Augustine may also have played a significant role in the differentiation of evolved magma passing through shallowly located dikes. For example, one mechanism of forming a partially degassed and relatively anhydrous end-member melt composition that retains relatively high Cl contents during differentiation, that is, one similar to that involved in mixing/mingling at Augustine, involves the exsolution and loss of a saline liquid from felsic magma at low pressures. This is supported by close inspection of the volatile-component solubility relationships for H_2O and Cl that demonstrate that some fractions of felsic Augustine melt, represented by the most Cl-rich and H_2O-deficient melt inclusions, could exsolve a highly saline liquid (with or without coexisting vapor) and still contain moderate concentrations of H_2O at 20 MPa (at or near Y_1 and Y_2 in fig. 9*B*). This observation is a consequence of the strong deviations from ideal mixing behavior that occur in NaCl- and H_2O-bearing systems containing a saline liquid with or without vapor (Webster, 1992; Shinohara, 1994; Botcharnikov and others, 2004), and it is consistent with the modeled results of degassing trends B and C (fig. 9*A*). Even though the saline liquid is enriched in Cl, the exsolution of this phase does not reduce the Cl content of the melt significantly, because the activities of H_2O and chloride species are buffered at constant values in all phases present at equilibrium in a closed system (Shinohara, 1994; Webster and Mandeville, 2007). Thus, the subsequent separation and escape of a saline liquid from melt reduces the H_2O concentrations of the residual silicate melt, while maintaining elevated Cl levels in the melt.

Determining the origin of the low-K_2O end-member melt composition involved in mixing trend 2 is more of a challenge. It is difficult to envision how fractional crystallization could generate felsic melt compositions with such low K_2O concentrations like these without crystallizing alkali feldspar, which these rocks do not contain. This K_2O-enriched phase would have to have fractionated in significant quantities to generate the low K_2O values. Larsen and others (this volume) suggest that the low-K_2O matrix glasses may have formed by melting of low-K_2O, fine-grained gabbroic cumulate material, which follows the interpretation of Harris (1994) that mafic magma of the 1986 eruption mixed with magma residual from the 1976 eruption and also with low-K_2O, partially crystallized chamber residua. We suggest that the comparatively low concentrations of K, Na, Fe, S, and Cl in the melt inclusions representing this end-member composition are consistent with their mobilization in a fluid phase. Moreover, the elevated H_2O concentrations of this second “type” melt require that this style of fluid exsolution must have occurred at pressures greater than those bearing on the formation of the other end-member melt (for example, 100 to 200 MPa) because of the strong, positive relationship between pressure and water solubility in silicate melts. Experiments have demonstrated that the interaction of silicate melt with an HCl-bearing aqueous vapor tends to strip alkalis and Cl from the melt; in fact, some experiments have generated peraluminous melt compositions through the interaction of HCl-enriched vapors with melts that were initially subaluminous to metaluminous (Webster and Holloway, 1988; Williams and others, 1997; Frank and others, 2003). As discussed, the components in the vapor exsolved from Augustine magmas included HCl. Thus, it is plausible that the interaction of rhyolitic melt with HCl-bearing aqueous vapor at pressures of 100 to 200 MPa could have generated the observed geochemical characteristics of this second magma-mixing end member.

Relationships Involving Volatile Components, Fluids, and Eruptive Processes

Magma differentiation strongly influences volcanic activity, because the rate and style of eruptions vary directly with magma rheology, melt viscosity, and the concentrations of volatile components in late-stage magma as well as with temperature and pressure. Most melt inclusions chosen for this study represent silica-enriched residual melts with widely varying H_2O and Cl concentrations, and these parameters variably influence the viscosity of differentiated and fluid-saturated residual melts. We suggest that as the aliquots of younger and more hydrous felsic magma, which were variably depleted in Cl, Na_2O, K_2O, and FeO, ascended through the conduit system, they interacted at shallow depths with older and less hydrous felsic magma that had previously lost H_2O via degassing. The latter magma contained elevated concentrations of Cl, Na_2O, K_2O, and FeO that are more typical of evolved rhyolitic melts. The interaction of these magmas involved the exchange of heat as well as volatile components which played a critical role in subsequent eruptive processes.

Relationships involving H_2O, Cl, and CO_2 in some felsic melt inclusions, interpreted through experimental data from the corresponding melt-H_2O-CO_2 and melt-H_2O-Cl pseudoternaries provide independent indications (1) that the exsolution of fluid(s) from residual melt occurred at depths ≤14 km (that is, equivalent to approximately 350 MPa), (2) of the entrapment of fluid(s)-saturated melt at pressures as low as 20 MPa, and hence (3) that Augustine’s magmatic volatile phase(s) remained in equilibrium with the rhyolitic melts to depths of ≤800 m (that is, that closed-system behavior was maintained to quite shallow depths). Combination of these constraints with the observed lack of rimming or alteration of some amphibole phenocrysts (that crystallized in the 170 to 130 MPa range) suggests that the final ascent of amphibole-bearing magmas was also rapid.

It is noteworthy that before the 2006 eruption, precursory unrest in the form of increased seismicity, inflation, and pressurization at sea level began in mid-2005 (Cervelli and others, 2006; Power and Lalla, this volume). Similarly, seismic hypocenters preceding the 1986 eruption began to ascend from depths of 600 m to the crater just nine months before that eruptive phase began (Power, 1988; Roman, 2001; Power and Lalla, this volume), and similar seismic behavior was also observed before the 1976 eruption (Kienle, 1987). These seismic activities have been interpreted to signal hydraulic fracturing of overlying rock as magma (that is, fluid) pressure increased (Roman, 2001). This interpretation is consistent with observations from a similar study in which magmatic gas movement at Redoubt Volcano was called on as the source of some of its shallow seismic activity (Wolf and Eichelberger, 1997). We suggest these signals may also indicate that the fluid overpressures in Augustine magmas (with apparent fluid abundances of 1 to 3 weight percent) exceeded the confining rock strength and that they are indications of the separation of fluid(s) from magma at depths of 800 m or less. Augustine's crater rim is approximately 1.2 km in elevation, which means that some fluid-melt separation took place above sea level and well within the edifice. Interestingly, related modeling of the 2006 events by Coombs and others (this volume), based on average volumes of erupted material per explosion and the estimated conduit dimensions, determines that each Vulcanian explosion involved evacuation of the conduit to a depth of 1.9 km below the summit. In addition, they estimate an average evacuation depth, during eruptions, of 1 km. Thus, it is well supported that the separation and ascent of magmatic fluid at these quite shallow depths may have generated some of the recorded seismic behavior, while opening pathways for subsequent magma ascent.

Acknowledgments

We sincerely thank the staff of the Alaska Volcano Observatory for their considerable support and assistance during fieldwork on Augustine Island, and for subsequent collaborative assistance. We thank Dr. Richard B. Waitt of the USGS for providing the basalt sample (RBW-91A-137) and Dr. Chris Nye of the Alaska Division of Geological and Geophysical Surveys for sharing trace-element data for 6 Augustine basalt samples. Dr. George Harlow kindly shared his mineral recalculation program PRBDATNT. We thank Professor Jessica Larsen and Mariah Tilman of the University of Alaska at Fairbanks for providing data on amphiboles of 2006 rock samples. John Pallister, John Power, and Bruno Scaillet kindly provided detailed and thoughtful reviews of the manuscript. This research was supported by National Science Foundation award EAR-0308866 to J.D. Webster.

References Cited

Anderson, A.T., Jr., 1976, Magma mixing—petrological process and volcanological tool: Journal of Volcanology and Geothermal Research, v. 1, p. 3–33.

Anderson, A.T., Jr., 1982, Parental basalts in subduction zones—implications for continental evolution: Journal of Volcanology and Geothermal Research, v. 87, p. 7047–7060.

Anderson, A.T., Jr., 2003, An introduction to melt (glass ± crystals) inclusions, chap. 14 *in* Samson, I., Anderson, A., and Marshall, D., eds., Fluid inclusions—analysis and interpretation: Mineralogical Association of Canada, v. 32, p. 353–364.

Andersen, D.J., Lindsley, D.H., and Davidson, P.M., 1993, QUILF—A program to assess equilibria among Fe-Mg-Ti oxides, pyroxenes, olivine, and quartz: Computers and Geosciences, v. 19, p. 1333–1350.

Atlas, Z.D., Dixon, J.E., Sen, G., Finny, M., Pozzo, A.L.M.-D., 2006, Melt inclusions from Volcán Popocatépetl and Volcán de Colima, Mexico—Melt evolution due to vapor-saturated crystallization during ascent: Journal of Volcanology and Geothermal Research, v. 153, p. 221–240.

Bacon, C.R., and Hirshmann, M.M., 1988, Mg/Mn partitioning as a test for equilibrium between coexisting Fe-Ti oxides: American Mineralogist, v. 73, p. 57–61.

Bacon, C.R., Newman, S., and Stolper, D., 1992, Water, CO_2, Cl, and F in melt inclusions in phenocrysts from three Holocene explosive eruptions, Crater Lake, Oregon: American Mineralogist, v. 77, p. 1021–1030.

Baker, D.R., Freda, C., Brooker, R.A., and Scarlato, P., 2005, Volatile diffusion in silicate melts and its effects on melt inclusions: Annals of Geophysics, v. 48, p. 699–717.

Blundy, J., and Cashman, K., 2001, Ascent-driven crystallization of dacite magmas at Mount St. Helens, 1980-1986: Contributions to Mineralogy and Petrology, v. 140, p. 631–650.

Blundy, J., and Cashman, K., 2005, Rapid decompression-driven crystallization recorded by melt inclusions from Mount St. Helens volcano: Geology, v. 33, p. 793–796.

Blundy, J., Cashman, K., and Humphreys, M., 2006, Magma heating by decompression-driven crystallization beneath andesitic volcanoes: Nature, v. 443, p. 76–809.

Bodnar, R.J., and Student, J.J., 2006, Melt inclusions in plutonic rocks: petrography and microthermometry. chap. 1 *in* Webster, J., ed., Melt inclusions in plutonic rocks: Mineralogical Association of Canada v. 36, p. 165–188.

Botcharnikov, R.E., Behrens, H., Holtz, F., Koepke, J., and Sato, H., 2004, Sulfur and chlorine solubility in Mt. Unzen rhyodacitic melt at 850°C and 200 MPa: Chemical Geology, v. 213, p. 207–225.

Browne, B.L., and Gardner, J.E., 2006, The influence of magma ascent path on the texture, mineralogy, and formation of hornblende reaction rims: Earth and Planetary Science Letters, v. 246, p. 161–176.

Browne, B.L., Eichelberger, J.C., Patino, L.C., Vogel, T.A., Uto, K., and Hoshizumi, H., 2006, Magma mingling as indicated by texture and Sr/Ba ratios of plagioclase phenocrysts from Unzen volcano, SW Japan: Journal of Volcanology and Geothermal Research, v. 154, p. 103–116.

Burgisser, A., and Scaillet, B., 2007, Redox evolution of a degassing magma rising to the surface: Nature, v. 445, p. 194–197.

Carmichael, I.S., Turner, I., and Verhoogen, J., 1974. Igneous Petrology: McGraw-Hill, 739 p.

Carroll, M.R., and Rutherford, M.J., 1988, Sulfur speciation in hydrous experimental glasses of varying oxygen state—results from measured wavelength shifts of sulfur X-rays. American Mineralogist, v. 73, p. 845–849.

Cervelli, P.F., Fournier, T.J., Freymueller, J., and Power, J.A., 2006, Ground deformation associated with the precursory unrest and early phases of the January 2006 eruption of Augustine Volcano, Alaska: Geophysical Research Letters, v. 33, 5 p., doi: 10.1029/2006GL027219.

Cervelli, P.F., Fournier, T.J., Freymueller, J.T., Power, J.A., Lisowski, M., and Pauk, B.A., 2010, Geodetic constraints on magma movement and withdrawal during the 2006 eruption of Augustine Volcano, *in* Power, J.A., Coombs, M.L., and Freymueller, J.T., eds., The 2006 eruption of Augustine Volcano, Alaska: U.S. Geological Survey Professional Paper 1769 (this volume).

Chiodini, G., Marini, L., and Russo, M., 2001, Geochemical evidences of high-temperature hydrothermal brines at Vesuvio Volcano (Italy): Geochimica et Cosmochimica Acta, v. 65, p. 2129–2147.

Chou, I.-M., 1978, Calibration of oxygen buffers at elevated P and T using the hydrogen fugacity sensor: American Mineralogist, v. 63, p. 690–703.

Coombs, M.L., Bull, K.F., Vallance, J.W., Schneider, D.J., Thoms, E.E., Wessels, R.L., and McGimsey, R.G., 2010, Timing, distribution, and volume of proximal products of the 2006 eruption of Augustine Volcano, *in* Power, J.A., Coombs, M.L., and Freymueller, J.T., eds., The 2006 eruption of Augustine Volcano, Alaska: U.S. Geological Survey Professional Paper 1769 (this volume).

Daley, E.E., 1986. Petrology, geochemistry, and the evolution of magmas from Mt. St. Augustine volcano, Alaska: unpublished M.S. thesis, University of Alaska, Fairbanks, 106 p.

Danyushevsky, L.V., Della-Pasqua, F.N., and Sokolov, S., 2000, Re-equilibration of melt inclusions trapped by magnesian olivine phenocrysts from subduction-related magmas—petrological implications: Contributions to Mineralogy and Petrology, v. 138, p. 68–83.

Edmonds, M., Pyle, D., and Oppenheimer, C., 2002, HCl emissions at Soufriére Hills Volcano, Montserrat, West Indies, during a second phase of dome building: November 1999 to October 2000: Bulletin of Volcanology, v. 64, p. 21–30.

Evans, B.W., Scaillet, B., and Kuehner, S.M., 2006, Experimental determination of coexisting iron–titanium oxides in the systems FeTiAlO, FeTiAlMgO, FeTiAlMnO, and FeTiAlMgMnO at 800 and 900° C, 1–4 kbar, and relatively high oxygen fugacity: Contributions to Mineralogy and Petrology, v. 152, p. 149–167.

Frank, M.R., Candela, P.A., and Piccoli, P.M., 2003, Alkali exchange equilibria between a silicate melt and coexisting magmatic volatile phase—an experimental study at 800ºC and 100 MPa. Geochimica et Cosmochimica Acta, v. 67, p. 1415–1427.

Gerlach, T.M., Westrich, H.R., and Symonds, R.B., 1996, Pre-eruption vapor in magma of the climactic Mount Pinatubo eruption—source of the giant stratospheric sulfur dioxide cloud, *in* Newhall, C.G., and Punongbayan, R.S., eds., Fire and mud—eruptions and lahars of Mount Pinatubo, Philippines: PHIVOLCS and University of Washington Press, p. 415–433.

Giggenbach, W.R., 1997, The origin and evolution of fluids in magmatic-hydrothermal systems, chap. 15 *in* Barnes, H.L., ed., Geochemistry of hydrothermal ore deposits 3rd ed.: John Wiley and Sons Inc. New York, p. 737–796.

Giggenbach, W.R., 1996, Chemical composition of volcanic gases, *in* Scarpa, R., and Tilling, R., eds., Monitoring and mitigation of volcano hazards: Springer Berlin, p. 221–256

Giggenbach, W.R., 1995, Composition of magmatic components in hydrothermal fluids, chap. 11 *in* Thompson, J.F.H., ed., Magmas, fluids, and ore deposits, vol. 23: Mineralogical Association of Canada, p. 247–261.

Gurenko, A.A., Belousov, A.B., Trumbull, R.B., Sobolev, A.V., 2005, Explosive basaltic volcanism of the Chikurachki volcano (Kurile arc, Russia)—insights on pre-eruptive magmatic conditions and volatile budget revealed from phenocryst-hosted melt inclusions and groundmass glasses: Journal of Volcanology and Geothermal Research, v. 147, p. 203–232.

Hardee, H.C., 1982, Permeable convection above magma bodies: Tectonophysics, v. 84, p. 179–195.

Harlow, G.E., Murphy, A.R., Hozjan, D.J., de Mille, C.N., and Levinson, A.A., 2006, Pre-Columbian jadeite axes from Antigua, West Indies—description and possible sources: Canadian Mineralogist, v. 44, p. 305–321.

Harris, G., 1994. The petrology and petrography of lava from the 1986 eruption of Augustine volcano: University of Alaska, Fairbanks, unpub. M.S. thesis, 131 p.

Hawthorne, F.C., and Oberti, R., 2007, Classification of amphiboles: Reviews in Mineralogy and Geochemistry, v. 67, p. 55–88.

Henley, R.W., and McNabb, A., 1978, Magmatic vapor plumes and ground-water interaction in porphyry copper emplacement: Economic Geology, v. 73, p. 1–20.

Huebner, J.S., and Sato, M., 1970, The oxygen fugacity-temperature relationships of manganese oxide and nickel oxide buffers: American Mineralogist, v. 55, p. 934–952.

Izbekov, P., Wallace, K., Larsen, J., Nye, C., and Eichelberger, J., 2006, Variations of glass composition at the start of the 2006 eruption, Augustine Volcano, Alaska [abs.]: Geological Society of America Abstracts with Programs, v. 38, no. 5, p. 76–77.

Johnson, K.E., 1986, Isotope geochemistry of Augustine volcano, Alaska: Southern Methodist University, unpub. M.S. thesis, 144 p.

Johnson, K.E., Harmon, R.S., Richardson, J.M., Moorbath, S., and Strong, D.F., 1996, Isotope and trace-element geochemistry of Mt. St. Augustine volcano, Alaska—implications for magmatic evolution: Journal of Petrology, v. 37, p. 95–115.

Johnson, M.C., and Rutherford, M.J., 1989, Experimental calibration of the aluminum-in-magnesio-hornblende geobarometer with application to Long Valley caldera (California) volcanic rocks: Geology, v. 17, p. 837–841.

Johnston, D.A., 1978, Volatiles, magma mixing, and the mechanism of eruption of Mt. St. Augustine Volcano, Alaska: Seattle, Washington, University of Washington, unpub. Ph.D. dissertation, 177 p.

Johnston, D.A., 1979, Onset of volcanism at Mt. St. Augustine Volcano, Lower Cook Inlet: U.S. Geological Survey Circular 804-B, 78–80.

Jugo, P.J., Luth, R.W., and Richards, J.P., 2005, An experimental study of the sulfur content in basaltic melts saturated with immiscible sulfide or sulfate liquids at 1300°C and 1.0 GPa: Journal of Petrology, v. 46, p.783–798.

Kienle, J., 1987, Mt. St. Augustine works, but how?: Proceedings, Hawaii Symposium on How Volcanoes Work, p. 139.

Kienle, J., and Forbes, R.B., 1976, Augustine—evolution of a volcano: Geophysics Institute, University of Alaska Fairbanks, Annual Report 1975/76, p. 26–48.

Kienle, J., and Swanson, S.E., 1980, Volcanic hazards from future eruptions of Mt. St. Augustine volcano, Alaska: Geophysics Institute, University of Alaska, Fairbanks, Report UAG R-275, 122 p.

Larsen, J.F., Nye, C.J., Coombs, M.L., Tilman, M., Izbekov, P., and Cameron, C., 2010, Petrology and geochemistry of the 2006 eruption of Augustine Volcano, *in* Power, J.A., Coombs, M.L., and Freymueller, J.T., eds., The 2006 eruption of Augustine Volcano, Alaska: U.S. Geological Survey Professional Paper 1769 (this volume).

Lattard, D., Sauerzapf, U., and Kasemann, M., 2005, New calibration data for the Fe-Ti oxide thermo-oxybarometers from experiments in the Fe-Ti-O system at 1 bar, 1,000–1,300°C and a large range of oxygen fugacities: Contributions to Mineralogy and Petrology, v. 149, p. 735–754.

Leake, B.E., 1997, Nomenclature of amphiboles; Report of the Subcommittee on Amphiboles of the International Mineralogical Association Commission on New Minerals and Mineral Names: American Mineralogist, v. 82, p. 1019–1037.

Le Bas, M.J., Le Maitre, R.W., Streckeisen, A., and Zanettin, B., 1986, A chemical classification of volcanic rocks based on the total alkali-silica diagram: Journal of Petrology, v. 27, p. 745–750.

Lowenstern, J.B., 1995, Applications of silicate-melt inclusions to the study of magmatic volatiles. chap. 4 *in* Thompson, J.F.H., ed., Magmas, fluids, and ore deposits: Mineralogical Association of Canada, v. 23, p. 71–99.

Luhr, J.F., 1990, Experimental phase relations of water-and sulfur-saturated arc magmas and the 1982 eruptions of El Chichon Volcano: Journal of Petrology, v. 31, p. 1071–1114.

Mandeville, C.W., A. Sasaki, G. Saito, K. Faure, R. King and E. Hauri, 1998, Open-system degassing of sulfur from Krakatau 1883 magma: Earth and Planetary Science Letter*s*, v. 160, no. 3/4, p. 709–722.

Mandeville, C.W., Webster, J.D., Rutherford, M.J., Taylor, B.E., Timbal, A., and Faure, K., 2002, Determination of molar absorptivities for infrared absorption bands of H_2O in andesitic glasses: American Mineralogist, v. 87, p. 813–821.

Massare, D., Métrich, N., Clocchiatti, R., 2002, High-temperature experiments on silicate melt inclusions in olivine at 1 atm—inference on temperatures of homogenization and H_2O concentrations: Chemical Geology, v. 183, p. 87–98.

McGee, K.A., Doukas, M.P., McGimsey, R.G., Neal, C.A., and Wessels, R.L., 2010, Emission of SO_2, CO_2, and H_2S from Augustine Volcano, 2002–2008, *in* Power, J.A., Coombs, M.L., and Freymueller, J.T., eds., The 2006 eruption of Augustine Volcano, Alaska: U.S. Geological Survey Professional Paper 1769 (this volume).

Moore, G., 2008, Interpreting H_2O and CO_2 contents in melt inclusions—constraints from solubility experiments and modeling, chap. 9 *in* Putirka, K.D, and Tepley III, F.J., eds., Minerals, inclusions,, and volcanic processes: Reviews in Mineralogy and Geochemistry, v. 69, p. 333–361.

Moore, G., and Carmichael, I.S.E., 1998, The hydrous phase equilibria (to 3 kbar) of an andesite and basaltic andesite from western Mexico—constraints on water content and conditions of phenocryst growth: Contributions to Mineralogy and Petrology, v. 130, p. 304–319.

Newman, S., and Lowenstern, J.B., 2002, VOLATILE-CALC—a silicate melt-H_2O-CO_2 solution model written in

Visual Basic for excel: Computers and Geosciences, v. 28, p. 597–604.

Newman, S., Bacon, C.R., and Stolper, E., 1986, Measurement of water in rhyolitic glass—calibration of an infrared spectroscopic technique: American Mineralogist, v. 71, p. 1527–1541.

Newton, R.C., and Manning, C.E., 2005, Solubility of anhydrite, $CaSO_4$, in NaCl-H_2O solutions at high pressures and temperatures: Journal of Petrology, v. 46, p. 701–716.

Nye, C.J., 2006, The 2006 eruption of Augustine Volcano—overview [abs.]: Geological Society of America Abstracts with Programs, v.38, no. 5, p. 28.

Power, J.A., 1988, Seismicity associated with the 1986 eruption of Augustine Volcano, Alaska: University of Alaska, Fairbanks, unpub. Ph.D. dissertation, 142 p.

Power, J.A., Nye, C.J., Coombs, M.L., Wessels, R.L., Cervelli, P.F., Dehn, J., Wallace, K.L., Freymueller, J.T., and Doukas, M.P., 2006, The reawakening of Alaska's Augustine Volcano: Eos (American Geophysical Union Transactions), v. 87, no. 37, p. 373–377.

Power, J.A., and Lalla, D.J., 2010, Seismic observations of Augustine Volcano, 1970–2007, *in* Power, J.A., Coombs, M.L., and Freymueller, J.T., eds., The 2006 eruption of Augustine Volcano, Alaska: U.S. Geological Survey Professional Paper 1769 (this volume).

Reed, M.H., 1997, Hydrothermal alteration and its relationship to ore fluid composition. chap. 7 *in* Barnes, H.L., ed., Geochemistry of hydrothermal ore deposits, 3rd ed: John Wiley and Sons, p. 303–365.

Roedder, E., 1984, Fluid inclusions: Reviews in Mineralogy and Geochemistry, v. 12, 644 p.

Roman, D.C., 2001, The 1986 eruption of Mt. St. Augustine Volcano, Alaska—magma storage and ascent. The University of Oregon unpub. Ph.D. dissertation, 129 p.

Roman, D.C., Cashman, K.V., Gardner, C.A., Wallace, P.J., and Donovan, J.J., 2006, Storage and interaction of compositionally heterogeneous magmas from the 1986 eruption of Mt. St. Augustine Volcano, Alaska: Bulletin of Volcanology, v. 68, p. 240–254.

Rutherford, M.J., and Devine, J.D., III, 1996, Preeruption pressure-temperature conditions and volatiles in the 1991 dacitic magma of Mount Pinatubo, *in* Newhall, C.G., and Punongbayan, R.S., eds., Fire and Mud—Eruptions and lahars of Mount Pinatubo, Philippines: Seattle, University of Washington Press, p. 751–766.

Rutherford, M.J., and Devine, J.D., III, 2008, Magmatic conditions and processes in the storage zone of the 2004-2006 Mount St. Helens dacite, chap. 31 *in* Sherrod, D.R., Scott, W.E., and Stauffer, P.H., eds., A volcano rekindled—the renewed eruption of Mount St. Helens, 2004–2006: U.S. Geological Survey Professional Paper 1750.

Rutherford, M.J., and Hill, P.M., 1993, Magma ascent rates from amphibole breakdown—an experimental study applied to the 1980–1986 Mt. St. Helens eruptions: Journal of Geophysical Research, v. 93, p. 19,667–19,685.

Scaillet, B., and Pichavant, M., 2003, Experimental constraints on volatile abundances in arc magmas and their implications for degassing processes, chap. 2, *in* Oppenheimer, C., Pyle, D.M., and Barclay, J., eds., Volcanic degassing: Geological Society of London Special Publication, v. 213, p. 23–52.

Shinohara, H., 1994, Exsolution of immiscible vapor and liquid phases from a crystallizing silicate melt—implications for chlorine and metal transport: Geochimica et Cosmochimica Acta, v. 58, p. 5215–5221.

Shmulovich, K.I., and Churakov, S.V., 1998, Natural fluid phases at high temperatures and low pressures: Journal of Geochemical Exploration, v. 62, p. 183–191.

Stormer, J.C., 1983, The effects of recalculation on estimates of temperature and oxygen fugacity from analyses of multicomponent iron-titanium oxides: American Mineralogist, v. 68, p. 586–594.

Straub, S.M., and Layne, G.D., 2003, The systematics of chlorine, fluorine, and water in Izu arc front volcanic rocks—implications for volatile recycling in subduction zones: Geochimica et Cosmochimica Acta, v. 67, no. 21, p. 4179–4203.

Sun, S.-S., and McDonough, W.F., 1995, The composition of the Earth: Chemical Geology, v. 120, p. 223–253.

Symonds, R.B., Rose, W.I., Gerlach, T.M., Briggs, P.H., and Harmon, R.S., 1990, Evaluation of gases, condensates, and SO_2 emissions from Augustine volcano, Alaska—the degassing of a Cl-rich volcanic system: Bulletin of Volcanology, v. 52, p. 355–374.

Tappen, C., Webster, J.D., Mandeville, C.W., and Roderick, D., 2009, Petrology and geochemistry of ca. 2100–1000 a.B.P. magmas of Augustine Volcano, Alaska, based on analysis of prehistoric pumiceous tephra: Journal of Volcanology and Geothermal Research, v. 183, p. 42–62.

Tilman, M.R., 2008, An investigation of symplectite-rimmed olivine and magmatic processes during the 2006 eruption of Augustine Volcano, Alaska: University of Alaska, Fairbanks, unpub. M.S. thesis, 166 p.

Vallance, J.W., Bull, K.F., and Coombs, M.L., 2010, Pyroclastic flows, lahars, and mixed avalanches generated during the 2006 eruption of Augustine Volcano, *in* Power, J.A., Coombs, M.L., and Freymueller, J.T., eds., The 2006 eruption of Augustine Volcano, Alaska: U.S. Geological Survey Professional Paper 1769 (this volume).

Wade, J.A., Boudon, G., Nougrigat, S., Poteaux, S., and Michel, A., 2006, The volatile content of magmas from Arenal volcano, Costa Rica: Journal of Volcanology and Geothermal Research, v. 157, p. 94–120.

Waitt, R.B., and Begét, J.E., 2009, Volcanic processes and geology of Augustine Volcano, Alaska. USGS Professional Paper 1762, 78 p., 2 map plates [http://pubs.usgs.gov/pp/1762/].

Wallace, K.L., Neal, C.A., and McGimsey, R.G., 2010, Timing, distribution, and character of tephra fall from the 2005–2006 eruption of Augustine Volcano, *in* Power, J.A., Coombs, M.L., and Freymueller, J.T., eds., The 2006 eruption of Augustine Volcano, Alaska: U.S. Geological Survey Professional Paper 1769 (this volume).

Wallace, P.J., 2005, Volatiles in subduction zone magmas—concentrations and fluxes based on melt inclusion and volcanic gas data: Journal of Volcanology and Geothermal Research, v. 140, p. 217–240.

Wallace, P.J., and Anderson, A.T., Jr., 2000, Volatiles in magma, *in* Sigurdsson, H., ed., Encyclopedia of volcanoes: Academic Press, San Diego, p. 149–170.

Waythomas, C.F., and Waitt, R.B., 1998, Preliminary volcano-hazard assessment for Augustine volcano, Alaska: U.S. Geological Survey Open-File Report 98-106, 39 p.

Webster, J.D., 1992, Fluid-melt interactions involving Cl-rich granites—experimental study from 2 to 8 kbar: Geochimica et Cosmochimica Acta, v. 56, p. 679–687.

Webster, J.D., and DeVivo, B., 2002, Experimental and modeled solubilities of chlorine in aluminosilicate melts, consequences of magma evolution, and implications for exsolution of hydrous chloride melt at Mt. Somma-Vesuvius: American Mineralogist, v. 87, p. 1046–1061.

Webster, J.D., and Holloway, J.R., 1988, Experimental constraints on the partitioning of Cl between topaz rhyolite melt and H_2O and $H_2O + CO_2$ fluids—new implications for granitic differentiation and ore deposition: Geochimica et Cosmochimica Acta, v. 52, p. 2091–2105.

Webster, J.D., and Mandeville, C.W., 2007, Fluid immiscibility in volcanic environments, chap. 10 *in* Leibscher, A., Heinrich, C., eds., Fluid-fluid equilibria in the crust: Reviews in Mineralogy and Geochemistry, v. 65, p. 313–362.

Webster, J.D., Kinzler, R.J., and Mathez, E.A., 1999, Chloride and water solubility in basalt and andesite liquids and implications for magmatic degassing: Geochimica et Cosmochimica Acta, v. 63, p. 729–738.

Webster, J.D., Sintoni, M.F., and De Vivo, B., 2005, The role of sulfur in promoting magmatic degassing and volcanic eruption at Mt. Somma-Vesuvius, *in* De Vivo, B., ed., Volcanism in the Campania Plain—Vesuvius, Campi Flegrei and Ignimbrites: Elsevier, Developments in Volcanology, v. 9, p. 221–236.

Webster, J.D., Sintoni, M.F., De Vivo, B., Lima, A., 2007, Volatile solubilities in Mt. Somma-Vesuvius phonolite melt and new insights on degassing of sulfur, chlorine, and water [abs.]: Eos (American Geophysical Union Transactions), v. 88, V42B-03.

Webster, J.D., Mandeville, C.W., Gerard, T., Goldoff, B., and Coombs, M.L., 2006. Volatile abundances and magma geochemistry of recent (2006) through ancient eruptions (< 2100 a BP) of Augustine Volcano, Alaska [abs.]: Eos (American Geophysical Union Transactions), v. 87, V42B-05.

Williams, T.J., Candela, P.A., and Piccoli, P.M., 1997, Hydrogen-alkali exchange between silicate melts and two-phase aqueous mixtures—an experimental investigation: Contributions to Mineralogy and Petrology, v. 128, p. 114–126.

Wolf, K.J., and Eichelberger, J.C., 1997, Syneruptive mixing, degassing and crystallization at Redoubt Volcano, eruption of December, 1989 to May 1990: Journal of Volcanology and Geothermal Research, v. 75, p. 19–37.

Zimmer, M.M., Plank, T., Hauri, E.H., Faust Larsen, J., and Kelemen, P.B., 2004, Volatile contents in mafic magmas from two Aleutian volcanoes—Mts. St. Augustine and Makushin [abs.]: Eos (American Geophysical Union Transactions), v. 85 no. 46, V34A-01.

Appendix 1. Sample Descriptions

2006 Samples

06AUMC005C.p5a Low-silica andesite scoria. Petrographic description: the sample is a vesicular, porphyritic andesite with brownish felty matrix contains areas of trace glass and many microlites. Plagioclase shows remelting/reequilibration growth zones containing orthopyroxene needles and melt inclusions. Melt inclusions are pink to dark brown in color. Plagioclase phenocrysts show complex and variable growth zoning; some contain growth zones with dusty dark groundmass material entrained. Orthopyroxene and clinopyroxene phenocrysts are subequal in abundance. Pyroxenes do not appear, in general, to be as zoned as the plagioclase phenocrysts do but pyroxenes do show more incipient oxidation/alteration. Some glomerocrystic clots contain plagioclase, pyroxenes, and iron-titanium oxides. Minor embayed and altered olivine phenocrysts. Coexisting oxides (ilmenite and magnetite) occur in matrix and phenocrysts; ilmenite is typically rimmed by magnetite with no visible exsolution textures; 0.025 to 0.6 mm diameter for coexisting oxides. No amphibole or quartz observed. No anhydrite observed.

06AUMC008b.p1A Low-silica andesite scoria. Petrographic description: the sample is a porphyritic andesite with a plagioclase- and oxide-microlite-rich, brownish, felty groundmass. Plagioclase is dominant phenocryst; some show oscillatory zoning. Others have sieve-textured cores and others show dusty groundmass material in growth zones. Melt inclusions occur in some plagioclase remelting/reequilibration/growth zones; melt inclusions somewhat less abundant than in other 2006 samples. Plagioclase phenocrysts are as much as 2. 5 mm in length. Clinopyroxene phenocrysts more abundant than orthopyroxene phenocrysts. Orthopyroxene phenocrysts up to 1.2 mm in length. Some orthopyroxene rimmed by clinopyroxene. Some complex glomeroporphyritic clots have oxides, plagioclase, and pyroxenes. Several volume percent euhedral, some unaltered olivine phenocrysts (up to 2 mm in diameter). Olivine also present as microlites in groundmass. Minor amphibole; some unaltered but others show alteration. Coexisting oxides (ilmenite and magnetite) occur in matrix and phenocrysts; ilmenite is typically rimmed by magnetite with no visible exsolution textures; 0.025 to 0.6 mm diameter for coexisting oxides. No quartz observed.

06AUMC010p1 High-silica andesite. Petrographic description: the sample is a porphyritic andesite that contains plagioclase as dominant phenocryst. Many plagioclase phenocrysts appear skeletal with other mineral inclusions partially entrained in the skeletal plagioclase. Smaller plagioclase laths and glass shards appear aligned. Plagioclase phenocrysts show complex zoning and growth history; oscillatory zoning, remelting/re-equilibration/growth zones with melt inclusions. Other plagioclase phenocrysts appear quite clean of inclusions. Plagioclase phenocrysts up to 4.5 mm in length. Melt inclusions in plagioclase are relatively abundant and pink to brown in color. Orthopyroxene phenocrysts less abundant than clinopyroxene phenocrysts; some orthopyroxene appears replaced by clinopyroxene. Pyroxenes show less zoning than plagioclase, but some pyroxenes show oxidation. Orthopyroxene and clinopyroxene phenocrysts up to 1 mm in length. Minor olivine phenocrysts present. Coexisting oxides (ilmenite and magnetite) occur in matrix and phenocrysts; ilmenite is typically rimmed by magnetite with no visible exsolution textures; 0.025 to 0.15 mm diameter for coexisting oxides. We observed no amphibole. No quartz observed.

06AUCWM007 Low-silica andesite scoria. Petrographic description: porphyritic andesite with phenocryst abundances listed in order of decreasing modal abundance. Plagioclase is subhedral to euhedral and occurs as crystals 0.2 to 1.7 mm in diameter and also as glomeroporphyritic crystal clots in association with orthopyroxene, clinopyroxene, and Fe-Ti oxides. Some plagioclase phenocrysts contain melt inclusions in remelting/reequilibration growth zones and many other plagioclase phenocrysts contain dusty matrix-enriched growth zones. Orthopyroxene occurs as subhedral to euhedral phenocrysts from 0.1 to 0.6 mm in diameter and as part of glomeroporphyritic crystal clots in association with plagioclase, clinopyroxene, and Fe-Ti oxides. Orthopyroxene is more abundant than clinopyroxene phenocrysts by an approximate ratio of 2:1, and is also present in the groundmass glass as fine needles. Clinopyroxene occurs as phenocrysts from 0.1 to 0.3 mm in diam. and also as glomerocrysts in glomeroporphyritic crystal clots in association with plagioclase, orthopyroxene, and Fe-Ti oxides. Some orthopyroxene undergoing replacement by clinopyroxene. Titanomagnetite and ilmenite occur as phenocrysts ranging from 0.03 to 0.2 mm and present also in glomeroporphyritic crystal clots. There are touching oxide pairs in contact with matrix glass that exhibit no exsolution lamellae and these should be good for preeruptive temperature- f_{O_2} estimates. One very rare pyroxene-rimmed olivine grain was observed.

Groundmass glass is clear in color with abundant microlites of clinopyroxene, orthopyroxene, plagioclase, and oxides. Rough volumetric proportion of vesicularity 45 to 50 percent based on blue epoxy. Note no amphibole observed in thin section, however, 1 amphibole was handpicked from crushed rock crystal concentrate. No visible quartz.

06AUCWM012 High-silica andesite. Petrographic description: Porphyritic andesite with phenocrysts in order of decreasing abundance: plagioclase occurs as large subhedral to euhedral crystals from 0.2 to 2.0 mm. Plagioclase also present as glomerocrysts. Many contain good glassy melt inclusions in plagioclase. Some plagioclase phenocrysts contain melt inclusions in remelting/reequilibration growth zones and many other plagioclase phenocrysts contain dusty matrix-enriched growth zones. Orthopyroxene occurs as subhedral to euhedral crystals up to 1.0 mm and as part of glomeroporphyritic crystal clots. Orthopyroxene is more abundant than clinopyroxene by less than 2:1 (maybe 60/40). Orthopyroxene also contains good melt inclusions. Clinopyroxene occurs as subhedral to euhedral crystals from 0.2 to 0.7 mm and also in glomeroporphyritic clots associated with orthopyroxene, plagioclase, and Fe-Ti oxides. Pyroxenes show less zoning than plagioclase. Titanomagnetite and ilmenite occur as phenocrysts from 0.05 to 0.2 mm in diameter. Many touching oxide pairs in contact with glass with no exsolution lamellae that are good for temperature and oxygen fugacity estimation. Three amphibole grains were found in two thin sections and have the following occurrences: one small subhedral-embayed grain that has no reaction rim and is clean up to contact with matrix glass; one large 0.7 mm grain rimmed by pyroxene; one small amphibole inclusion in plagioclase. Groundmass glass is clear (rhyolitic) and in many areas is microlite-free and forms either thin stringers and wisps to more massive-texured glass near phenocryst clots. Despite high phenocryst abundance, matrix glass is highly vesiculated. No visible quartz.

06AUCWM014 Dense low-silica andesite. Petrographic description: Porphyritic andesite with phenocrysts in order of decreasing abundance: plagioclase occurs as large subhedral to euhedral crystals from 0.2 to 1.8 mm, some with partly resorbed/spongy cores and as part of glomeroporphyritic crystal clots in association with orthopyroxene, clinopyroxene, Fe-Ti oxides. Some plagioclase phenocrysts contain melt inclusions in remelting/reequilibration growth zones and many other plagioclase phenocrysts contain dusty matrix-enriched growth zones. Orthopyroxene occurs as large subhedral to euhedral crystals from 0.2 to 1.2 mm in diameter and is also present as part of glomeroporphyritic crystal clots associated with plagioclase, clinopyroxene, and oxides. Abundance of orthopyroxene is equivalent to that of clinopyroxene. Clinopyroxene occurs as subhedral to euhedral crystals ranging from 0.1 to 1.0 mm in diameter, and in glomeroporphyritic crystal clots. Some clinopyroxene replaces orthopyroxene. Olivine is common and occurs as isolated phenocrysts as much as 0.6 mm in diameter but it is always completely rimmed by orthopyroxene± clinopyroxene. All olivine phenocrysts contain small brown spinel inclusions. Groundmass glass is brown in color and has a felty texture as it is enriched in clinopyroxene, orthopyroxene, plagioclase, and Fe-Ti oxide microlites. Titanomagnetite and ilmenite occur as rare phenocrysts up to 0.2 mm in size, with most crystals < 0.05 mm. Titanomagnetite and ilmenite exhibit extensive exsolution lamellae, so won't be good for temperature and oxygen fugacity estimation. Groundmass vesicularity ~ 35 to 40 percent. No amphibole crystals or amphibole pseudomorphs were observed. No visible quartz.

06AUJW001 Oxidized dense low-silica andesite. Petrographic description: Sample is a vesicular and somewhat inflated rx; matrix contains large areas of apparently good glass undergoing spherulitic devitrification with numerous oxides and some (minor) microlites. Porphyritic andesite with phenocrysts in order of decreasing abundance: plagioclase-dominated rock with some in plagioclase as part of glomeroporphyritic crystal clots in association with orthopyroxene, clinopyroxene, and Fe-Ti oxides Some plagioclase contains melt inclusions in remelting/re-equilibration growth zones and other plagioclase phenos contain dusty matrix growth zones; also the plagioclase-hosted melt inclusions tend to be more crystallized than those in other samples. Plagioclase phenocrysts are 0.05 to 3.5 mm in length; some larger plagioclase phenocrysts show complex and variable growth histories in their patterns of zonation. Orthopyroxene phenocrysts 0.05 to 1 mm, and clinopyroxene phenocrysts are 0.1 to 2 mm in length; some orthopyroxene undergoing replacement by clinopyroxene. The pyroxenes do not appear, in general, to be as zoned as the plagioclase phenocrysts. Sample contains significant but small amphibole phenocrysts with strong red-brown color; their margins do not show typical reaction rims but some show embayment and/or filling or replacement by plagioclase. Minor altered/embayed olivine phenocrysts are as much as 0.6 mm in diameter. Coexisting oxides (ilmenite and magnetite) occur in matrix and phenocrysts; ilmenite is typically rimmed by magnetite; significant exsolution features present; 0.03 to 0.3 mm diameter for coexisting oxides. There are far fewer melt inclusions in this sample than in other samples, and many of the largest plagioclase phenocrysts and as part of glomerocrysts contain few to no melt inclusions. No visible quartz.

06AUJW004 Dense low-silica andesite. Petrographic description: porous, porphyritic andesite containing brownish microlite-rich felty groundmass that still contains minor glass. Phenocrysts in order of decreasing abundance, plagioclase is 0.05 to 3.4 mm in length. Most plagioclase phenocrysts are relatively clean of matrix or oxides, but many very large plagioclase phenocrysts or in glomerocrystic clots show extensive and complex zoning. Some plagioclase contains melt inclusions in remelting/reequilibration growth zones and sieve textured cores. The plagioclase phenocrysts tend to contain clear to generally brownish melt inclusions, but many of the largest unbroken plagiocase phenocrysts and glomerocrysts contain few to no melt inclusions. Pyroxenes are subequal in abundance with orthopyroxene phenocryst 0.05 to 1.8 mm in length, and clinopyroxene phenocrysts are 0.05 to 1 mm in length. Some evidence of plagioclase replacing pyroxene. Rare embayed and altered olivine phenocrysts are as much as 0.5 mm in diameter. Also contains amphibole phenocrysts which are rare and some appear to be undergoing replacement by pyroxene. Coexisting oxides (ilmenite and magnetite) occur in matrix and phenocrysts; ilmenite is typically rimmed by magnetite. Most oxides show no exsolution features; 0.025 to 0.5 mm diameter for coexisting oxides. No visible quartz.

06AUJW010 Dense low-silica andesite. Petrographic description: porphyritic rock containing brownish microlite-rich felty groundmass enriched in plagioclase and iron-titanium oxides. Plagioclase is the dominant phenocryst, phenocrysts are 0.05 to 4.8 mm in length; and it occurs as part of glomerocrystic clots containing pyroxenes and oxides. Approximately 20 to 25 percent of plagioclase phenocrysts contain sieve-textured cores, contain pyroxene inclusions, exhibit reheated growth zones that contain melt inclusions, and/or dusty growth zones that appear to have incorporated devitrified groundmass during late-stage plagioclase growth. Plagioclase phenocrysts contain clear to generally brownish melt inclusions, but the number of melt inclusions is not large. Zoning patterns in plagioclase show evidence of complex and variable growth histories. Orthopyroxene is more abundant than clinopyroxene. Orthopyroxene phenocrysts are 0.05 to 1.8 mm, and clinopyroxene phenocrysts are 0.05 to 0.8 mm in length; pyroxene phenocrysts show little optical evidence of zoning. Some pyroxene replaced by plagioclase. Minor altered (oxidized) and embayed olivine phenocrysts are as much as 0.4 mm in diameter. Coexisting oxides (ilmenite and magnetite) occur in matrix and phenocrysts; ilmenite is typically rimmed by magnetite. Significant exsolution features present; 0.025 to 0.4 mm diameter for coexisting oxides. No amphibole phenocrysts observed. No visible quartz.

Other samples

RBW-91A-137A Vesicular porphyritic olivine basalt. Petrographic description: porphyritic rock containing (in decreasing modal abundance) clinopyroxene, plagioclase, olivine, amphibole, and trace orthopyroxene. Clinopyroxene phenocrysts are oscillatory zoned and are as much as 3.5 mm in length; some show sieve-textured cores. Clinopyroxene phenocrysts are either euhedral or rounded (appearing partially resorbed); some clinopyroxene makes up most of glomeroporphyritic clots. Plagioclase phenocrysts are euhedral and are as much as 2.5 mm in length. Olivine phenocrysts are rounded, partially embayed, and bordered and apparently replaced by pyroxene. Olivine phenocrysts are as much as 1.5 mm in diameter. Groundmass is highly vesicular and holocrystalline, and contains pyroxene and tabular plagioclase microlites. Melt inclusions occur in olivine, pyroxene, and plagioclase; most inclusions are partially to fully crystallized but minor glassy inclusions are present.

AVO 208 Porphyritic pumiceous andesite. Petrographic description: porphyritic rock containing clear, highly vesicular, glassy groundmass containing few microlites of plagioclase, pyroxene, and iron-titanium oxides. Plagioclase is the dominant phenocryst and is as much as 2.5 mm in length. Plagioclase occurs as part of glomerocrystic clots containing pyroxenes and oxides. Some plagioclase phenocrysts contain clear to pinkish melt inclusions in remelting/re-equilibration growth zones, but unlike other samples few plagioclase phenocrysts contain dusty groundmass-bearing growth zones. Many oscillatory zoned plagioclase phenocrysts present. Orthopyroxene phenocrysts and clinopyroxene phenocrysts are subequal and far less abundant than plagioclase; pyroxene phenocrysts <1 mm in diameter. Pyroxene phenocrysts are not as strongly zoned as plagioclase. Trace olivine phenocrysts (<0.5 mm in diameter) appear resorbed, embayed, and replaced by pyroxene. Trace of amphibole observed. Melt inclusions are pink to clear to heavily crystallized and dark. Coexisting oxides (ilmenite and magnetite) occur in matrix and phenocrysts; ilmenite is typically rimmed by magnetite, with 0.025 to 0.4 mm diameter for coexisting oxides. No quartz observed.

Geodesy

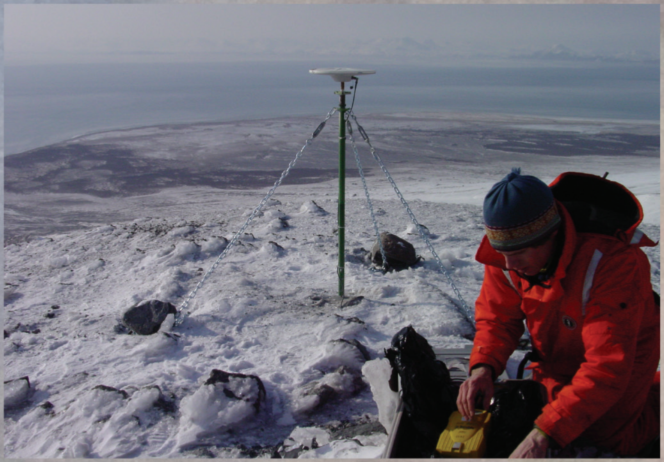

View of the north side of Augustine Volcano on August 7, 2006, showing the 2006 summit lava dome and north lava flow. Alaska Volcano Observatory photo by Michelle Coombs.

The 2006 Eruption of Augustine Volcano, Alaska
Power, J.A., Coombs, M.L., and Freymueller, J.T., editors
U.S. Geological Survey Professional Paper 1769

Chapter 17

Geodetic Constraints on Magma Movement and Withdrawal During the 2006 Eruption of Augustine Volcano

By Peter F. Cervelli[1], Thomas J. Fournier[2], Jeff T. Freymueller[3], John A. Power[4], Michael Lisowski[5], and Benjamin A. Pauk[5]

Abstract

For the first time in the United States, a modern geodetic network of continuously recording Global Positioning System (GPS) receivers has measured a complete eruption cycle at a stratovolcano, Augustine Volcano in Alaska, from the earliest precursory unrest through the return to background quiescence. The on-island network consisted of five continuously recording, telemetered GPS stations, four continuously recording, nontelemetered stations, and about 10 campaign bench marks. The continuous network recorded several distinct and conspicuous signals over the course of the unrest and eruption, starting with a months-long precursory inflation centered beneath the volcano at around sea level. Nearly coincident with the highest volumetric eruption rates, this inflation gave way to a more deep seated deflation that we interpret as a major withdrawal (approx. 25 million m^3 of compressed magma) from a nearly cylindrical magma reservoir centered about 5 km below sea level. Detailed analysis of the geodetic time series reveals additional nuance, including the probable upward propagation of a small dike into the edifice in the 60 days or so before the onset of large-scale explosive activity. Comparisons of the geodetic data and their resulting interpretations with other data, such as earthquake hypocenters and petrologically inferred magma-pressure histories, reveal a kinematic, if not mechanical, account of the 2006 eruption that details the shape and location of the magma source region, the means and velocity of magma transport, and the establishment of a short lived volume- (or pressure-) buffering capability held within the magma reservoir. The cumulative deformation over the course of the eruption shows a large signal close in and high on the edifice that decays rapidly with distance. This pattern indicates a small permanent increase in the edifice volume (beyond that added by the surficial lava dome) but also shows that without close-in (<2.5 km from the summit) stations, the eruption might have been invisible to campaign GPS stations alone.

Introduction

In this chapter we present a comprehensive account of the surface deformation that occurred before, during, and immediately after the 2006 eruption of Augustine Volcano. Following Coombs and others (this volume), we divide the eruption into five phases (table 1). The duration of the five phases, as well as the divisions between them, arises from basic geologic observations. Likewise, from a geodetic perspective, the phases make sense, although the timing of changes in deformation style do not always line up perfectly with the geologically established boundaries. Table 1 also lists, in one- or two-word summaries, general descriptions of the predominant geodetic observations during each phase, along with first-order interpretations. Organizationally, we largely follow this chronological sequence, bracketing the interpretative core of our report with a brief section on metadata at the start and, at the end, with discussions about the enduring changes at Augustine since the eruption.

---

[1] U.S. Geological Survey, 345 Middlefield Rd, Menlo Park, CA 94025.

[2] Rice University, Department of Earth Science, 6100 Main Street, Houston, TX 77005.

[3] Alaska Volcano Observatory, Geophysical Institute, University of Alaska Fairbanks, Fairbanks, AK 99775.

[4] Alaska Volcano Observatory, U.S. Geological Survey, 4200 University Drive, Anchorage, AK 99508.

[5] Cascades Volcano Observatory, U.S. Geological Survey, 1300 SE Cardinal Court, Vancouver, WA 98933.

Table 1. Phases of the 2006 Augustine Volcano eruption.

[BSL, below sea level; DRE, dense-rock equivalent]

Phase	Start	End	Deformation style	Deformation depth	Erupted volume (DRE; million m^3)[1]
Precursory	August 15	January 11	Slow inflation	Sea level	0
Explosive	January 11	January 28	Slow inflation	Sea level	30
Continuous	January 28	February 10	Rapid deflation	5–6 km BSL	19
Hiatus	February 10	March 3	Sluggish inflation	—	—
Effusive	March 3	March 16	Slow deflation	Shallow	23

[1] Data from Coombs and others (this volume).

In a section on the precursory phase, we revisit and refine the original analysis by Cervelli and others (2006), which treated the precursory deformation in detail but did not extend much beyond this interval. New data analyses, primarily petrologic geobarometry, provide constraints and insights that were not available at the time of Cervelli and others' report. In sections on the subsequent phases of the eruption, we focus on the three most conspicuous deformation signals: (1) the deformation immediately before the initial explosions of January 11, 2006, (2) the deflation approximately concurrent with the continuous phase of the eruption, and (3) the cumulative deformation that occurred over the course of the eruption. In addition to these conspicuous signals, we also present and, where possible, interpret several less distinct deformation features, including a minor inflation during the hiatus after the continuous phase and a small deflation that appears to accompany the effusion of early March 2006.

Each of the conspicuous deformation signals is remarkable it is own right. The precursory deformation before the explosions shows a stunning correlation with the seismic record (Power and Lalla, this volume) and provides strong corroborating evidence for the petrologic (Larsen and others, this volume) and mechanical (Coombs and others, this volume) accounts of the early eruptive processes. The deflation during the continuous phase also constrains petrologic analysis and, along with the petrology, provides insight into the shape and location of the midcrustal magma chamber, along with the timing of magma ascent. The cumulative (or net) deformation over the entire eruption indicates that a large part of the coeruptive deformation—nearly all of it, except for the near-field (<2.5 km from the summit) component—is transient and cannot be imaged without close-in continuously recording instruments or campaign bench marks.

Seeking a broader context, from a geodetic perspective we compare this eruption with eruptions elsewhere, particular at Mount St. Helens, 2004–8. These comparisons lead us to reflect on network design, station placement, the overall role of deformation measurements in volcano monitoring, and future opportunities for improved instrumentation and observation methodologies that promote a cross-disciplinary approach to the interpretation and modeling of volcanic processes. Finally, we emphasize the importance and underutilized potential of continuously recording GPS networks for volcano monitoring and short-term forecasts of volcanic hazard.

Metadata

Station and Observation History

Beginning in summer 2004, the National Science Foundation's Earthscope Project funded the installation of five continuously recording GPS instruments at Augustine Volcano, along with two nearby "backbone" stations (figs. 1, 2). As part of the Plate Boundary Observatory (PBO), these instruments were installed and are maintained by UNAVCO, Inc. (Pauk and others, this volume). Together with the Alaska Volcano Observatory (AVO)'s existing instrumentation and bench marks, these new GPS receivers formed a high-density, proximal geodetic network capable of recording the 2006 eruption and precursory unrest at an unprecedented level of detail. However, the Augustine GPS network had at least one shortcoming—an insufficient number of stations in the intermediate to far field. The size of the island imposes a basic constraint on the aperture size for any network on Augustine. Nonetheless, there was room for improvement, and so, in December 2005, we augmented the network with five additional continuously recording, though nontelemetered, receivers at campaign bench marks AUGB, AUGK, AUGS, A11, A5, (fig. 2), which we refer to below as the semipermanent network. Instrument and antenna information, installation history, and other relevant metadata, including the evolution of station nomenclature, for the permanent and semipermanent networks are listed in table 2.

The precise details of network design, though intended to provide the best possible geodetic coverage of the volcano, were largely constrained by external factors, including telemetry paths, scarce competent bedrock, budgetary limitations, and the inherent danger of working on an active volcano in a heightened state of unrest. The fact that the network in place at the beginning of the eruption was so comprehensive is entirely attributable to the judgment and effort of PBO and AVO engineers. In fact, mathematical deliberations about the strength of model-resolution kernels

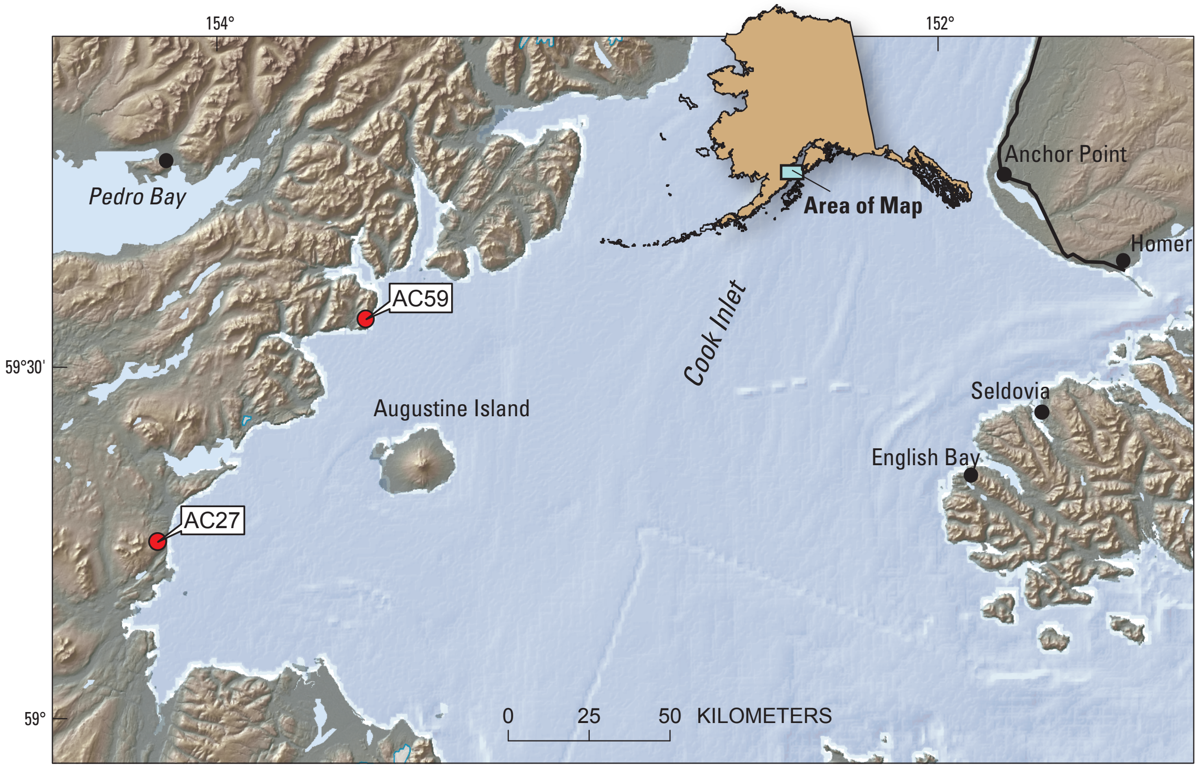

Figure 1. Cook Inlet, Alaska, showing Augustine Volcano, which is about 110 km west of Homer, and Plate Boundary Observatory backbone Global Positioning System (GPS) stations AC27 and AC59. Station AC59, which is used throughout this chapter as a reference station, is far enough away from Augustine to be insulated from volcanic deformation but close enough to measure approximately the same tectonic signal.

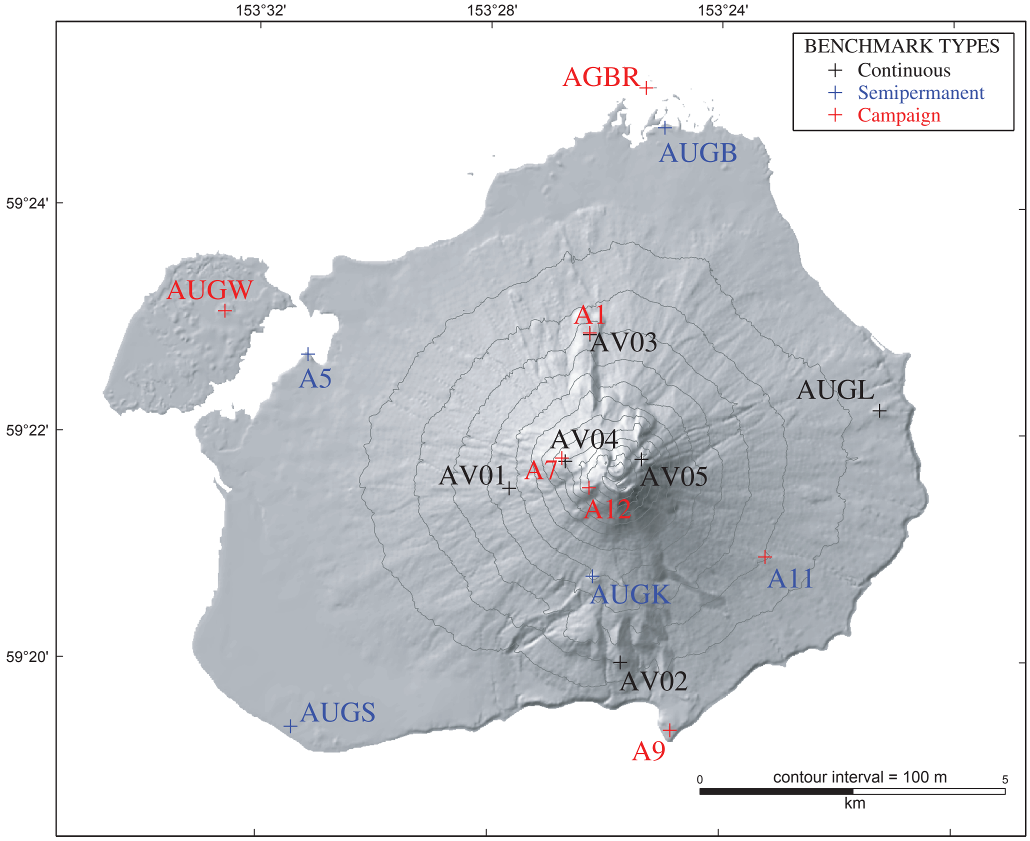

Figure 2. Augustine Island, showing locations of seismic stations in Global Positioning System (GPS) network as it existed in December 2005. Stations AV05, AV04, and AV03 were destroyed during the explosive and continuous phases of 2006 eruption.

Table 2. Instrument metadata and installation history, including station name aliases and other information.

Site Name	Site Name	Site Location			Measurement history			Type	Notes
	(Pauk and others, 2001)	Longitude (°W)	Latitude (°N)	Height (m)	2000	2004	2006		
A1	A1	153.437817	59.381555	355.2	•		•	Campaign	
A2	A2	153.424507	59.366622	879.3	•			Campaign	
A3	A3	153.424347	59.367624	865.2	•			Campaign	
A4	A4	153.423468	59.362369	1,055.8	•			Campaign	
A5	A5	153.519228	59.378120	28.9	•	•	•	Semipermanent	Reference station
A6	A6	153.437327	59.371180	677.1	•			Campaign	
A7	A7	153.445662	59.363068	900.6	•		•	Campaign	
A8	A8	153.433094	59.362447	1,218.6	•			Campaign	
A9	A9	153.413985	59.323001	40.9	•		•	Campaign	
A10	A10	153.432707	59.359329	1,243.2	•			Campaign	
A11	A11	153.386769	59.348648	216.9	•		•	Semipermanent	
A12	A12	153.437763	59.358693	1,100.6	•		•	Campaign	
A14	A14	153.425887	59.359396	1,179.9	•			Campaign	
A15	A15	153.428290	59.361713	1,224.1	•	•		Campaign	
A16	A16	153.427410	59.358774	1,219.1			•	Campaign	
A17	A17	153.422530	59.362799	1,038.3			•	Campaign	
A18	A18	153.587795	59.570064	394.9	•		•	Campaign	
AC27	N/A	154.162880	59.252508	417.5		•	•	Continuous	Off island, PBO
AC59	N/A	153.585200	59.567199	308.6		•	•	Continuous	Off island, PBO
AGBR	BURR	153.422443	59.417937	27.8	•		•	Campaign	
AGL1	LU01	153.427329	59.385923	246.2	•	•		Campaign	
AGL2	LU02	153.425045	59.371860	558.8	•			Campaign	
AGWD	N/A	153.437463	59.370604	683.6			•	Campaign	
AUGB	BUR2	153.416421	59.411877	27.5	•		•	Semipermanent	
AUGK	KAMISHAK	153.436557	59.345658	530.9	•		•	Semipermanent	
AUGL	N/A	153.353910	59.370299	104.0		•	•	Campaign	Renamed AV11 in January 2006
AUGM	MOUN	153.355060	59.370688	118.3	•		•	Campaign	80 m from AUGL, therefore excluded
AUGS	SAUG	153.523437	59.323203	28.7	•		•	Semipermanent	
AUGW	WAUG	153.543346	59.384420	44.0	•		•	Campaign	
AV01	N/A	153.460801	59.358531	487.2		•	•	Continuous	PBO
AV02	N/A	153.428391	59.332975	229.8		•	•	Continuous	PBO
AV03	N/A	153.437778	59.381297	360.2		•		Continuous	Destroyed, PBO
AV04	N/A	153.444672	59.362584	915.9		•		Continuous	Destroyed, PBO
AV05	N/A	153.422656	59.362933	1,036.6		•		Continuous	Destroyed, PBO
STEP	STEP	153.764839	59.434311	434.0	•		•	Campaign	Off island

or the degree of independence among the different stations of the network, though important, generally are only secondary considerations, given the logistical conditions in the field at the time of installation.

Previous geodetic field work at Augustine, consisting of electronic distance measurement (EDM) data and theodolite measurements, began in 1986. In 1988 and 1989, an island wide network of 19 trilateration bench marks was installed and measured in its entirety (Power and Iwatsubo, 1998). During 1992 and 1995, GPS surveys occupied parts of this network, but none of these surveys was complete. Additional measurements were made during the summers of 1993, 1994, and 1996. In 2000, a comprehensive GPS survey was undertaken (Pauk and others, 2001). Comparison of the 30 mark-to-mark slope distances measured in 1988 and 1989 with the results obtained from the 2000 GPS survey show differences of less than 5 cm along 24 of these distances. Of the six distances with greater than 5 cm of length change, three involved bench marks high on the 1964 and 1986 lava domes, both of which are known to be unstable and (or) subsiding. The remaining three anomalous distances involved bench marks believed to rest on stable parts of the island; however, no spatially coherent pattern of deformation among these three distances was evident. The locations of the campaign bench marks successfully reoccupied during the extensive geologic and geophysical fieldwork of summer 2006 are shown in figure 2.

Notes on Processing Methodology and Data Quality

Daily GPS solutions were processed with the GIPSY-OASIS software (Zumberge and others, 1997), release GOA4, in network mode, incorporating data from all continuous GPS sites in and around Alaska, using International Terrestrial Reference Frame station ALGO (located in Algonquin, Ontario, Canada) as a reference clock. We applied International Global Navigation Satellite System (GNSS) Service (IGS) 01 elevation-dependent phase-center models for each antenna, with an elevation mask of 10° (see http://www.ngs.noaa.gov/ANTCAL/), using the TPXO.2 ocean-tidal model, and estimated stochastic wet-tropospheric-path delays, using the Niell mapping function (Niell, 1996).

Subdaily solutions were calculated with the program RTD, version 3.0, from Geodetics Inc. (Bock and others, 2004). With RTD, each epoch of the LC (L3) ionospheric-free phase observation is processed independently in network mode to provide a position relative to a fixed master site. Station AUGB (fig. 2) served as the master site for the subdaily processing results presented here. Single-epoch data analysis with RTD is a multistep procedure that resolves integer-cycle phase ambiguities and estimates additional parameters, such as zenith troposphere delays. Our RTD solutions use IGS final orbits, National Geodetic Survey (NGS) elevation-dependent GPS antenna phase-center models, and all observations above 10°.

By late November 2005, enough snow and ice had accumulated at stations AV04 and AV05 (fig. 2) to seriously affect signal quality. Snow and ice accumulation on GPS antennas delays signal transmission along the path from the satellite to the antenna. This delay, unlike, for example, that due to the wet troposphere, is not easily modeled, especially if the size and shape of the obstructing snow and ice mass are unknown. The delays are azimuth and elevation dependent, because the transmission paths through the ice change as the satellites move, resulting in significantly degraded solution quality. However, because large and distinctive postfit phase residuals are diagnostic of unmodeled path delays, we can detect the presence and severity of ice problems without difficulty. At the beginning of each winter, phase residuals increase to more than 25 cm at station AV04, coincident with a large increase in scatter associated with the daily solutions. Phase residuals also increase at station AV05, though much less so—rarely more than 10 cm even at low elevation angles. Station AV05 was located in a higher, more windswept area than station AV04. Although both stations were exposed to similar temperatures and precipitation, higher winds at station AV05 frequently scoured the antenna clean. The net effect of the snow and ice was to make the data from station AV04 essentially unusable during the winter, while station AV05 by and large remained in working condition.

Observations, Interpretations, and Models

Precursory Phase

Though not detected until early autumn 2005, precursory deformation to the 2006 Augustine eruption began in mid-August 2005, as is evident from the baseline length between station AV02 and AV03 (fig. 2), which spans Augustine's summit from north to south (fig. 3). Seismicity began to increase somewhat earlier, at least by April 2005 and possibly as early as October 2004 (Power and Lalla, this volume). Cervelli and others (2006) divided the precursory deformation into three intervals on the basis of deformation style. We preserve these divisions here but rename them slightly for consistency with the rest of the volume. A three-component time series for the station AV05-to-AC59 baseline is plotted in figure 4. Three styles of deformation are evident, named here on the basis of their ultimate interpretations: (1) the inflation stage, (2) the dike-ascent stage, and (3) the preexplosive stage.

Inflation

The horizontal components of the velocity field measured during the early (before mid-November 2005) part of the precursory phase are mapped in figure 5 (black arrows). As noted by Cervelli and others (2006), the deformation pattern

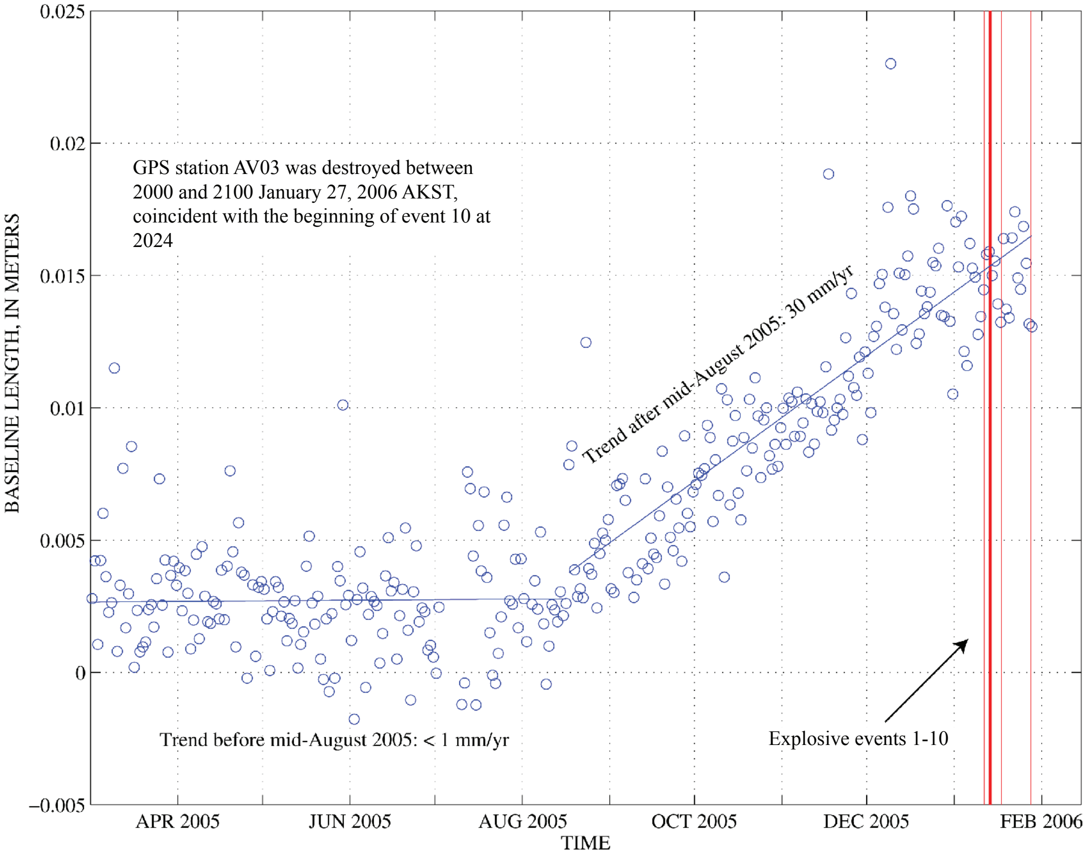

Figure 3. Time series of daily positions indicating distance change (baseline length) between stations AV02 (south of summit, fig. 2) and AV03 (north of summit) on Augustine Volcano between March 2005 and February 2006. Trends are shown before and after mid-August 2005. Vertical red lines denote times of explosive eruptions. These measurements proved extremely useful for forecasting volcanic hazard before destruction of station AV03 by pyroclastic flow on January 27, 2006.

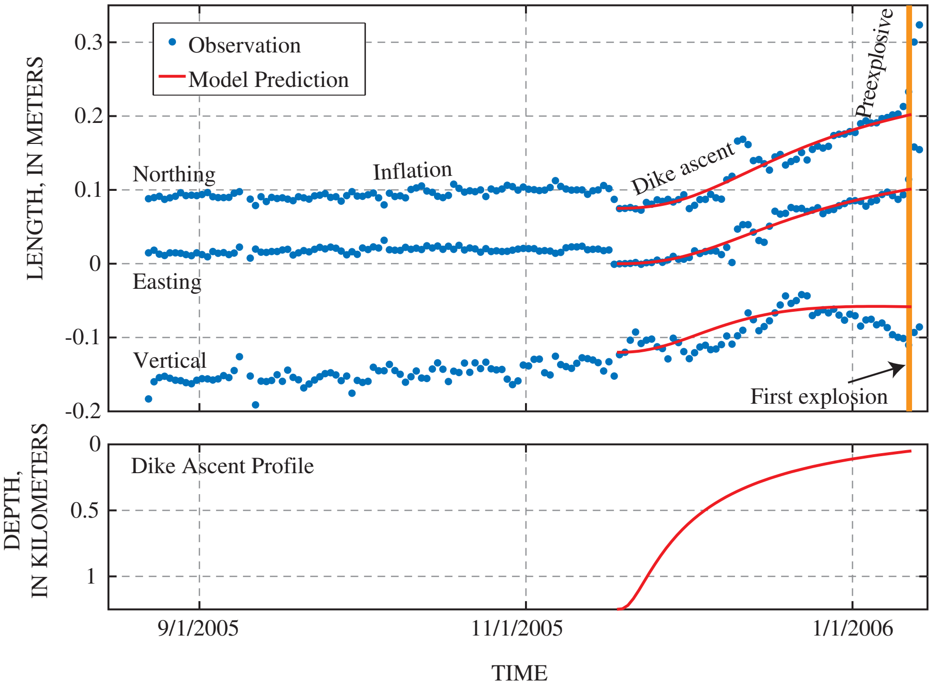

Figure 4. Observed (dots) and modeled (curves) deformation and inferred dike-ascent profile of Augustine Volcano between August 2005 and January 2006. The top panel, easting, northing, and vertical components of observed baseline between stations AV05 and AC59. A positive change in the y-axis direction indicates movement of AV05 eastward, northward, or upward relative to station AC59; a negative change indicates opposite movement. Bottom panel, inferred ascent history of model dike. Predicted deformation from this dike is shown by curves in top panel. Labels in top panel identify divisions of precursory phase. Modified from Cervelli and others (2006).

is clearly radial. The wavelength of the signal appears to demand a shallow source, although the absence of intermediate- and far-field stations introduces some ambiguity into this assessment. The semipermanent network had not yet been established. This deformation field can be modeled with a spherical point source (Anderson, 1936; Mogi, 1958) located approximately at sea level. Because the source depth appears to be shallow, the effect of topography becomes important, especially for comparing the modeled deformation source with other geophysical models on the same vertical datum. For this reason, we included a first-order correction for topography (Williams and Wadge, 1998). The velocities predicted by the model are mapped in figure 5 (red arrows). The predicted vertical velocities agree well with observations at the uppermost stations, AV04 and AV05 (fig. 2); however, the other stations show significantly more uplift than the model predicts. The volume-change rate of the point source is small—about 4×10^5 m^3/yr, or a total volume change of about 2×10^5 m^3. Volume accumulation at this rate would take nearly 200 years to account for the ~7.5×10^7 m^3 of material produced over the course of the eruption (Coombs and others, this volume), and so this small, initial pressurization was likely a slow buildup of volcanic gas beneath a mostly impermeable layer, such as the zeolitized Naknek formation (McClean, 1979).

As discussed below, other deformation models, such as a pressurizing vertical prolate ellipsoid (Bonaccorso and Davis, 1999), can also explain the observed, radial pattern of deformation during the early precursory phase. However, the spatial distribution of stations is insufficient to unambiguously discriminate among different models, especially in light of the high noise level at station AUGL (fig. 2). For this reason, we chose to use the simplest possible model—a spherical point source. Adding complexity will certainly improve data fit, but given that a point source already fits the data almost to within errors, a serious risk of “modeling” noise exists. Given the station distribution, the bottom of the pressurizing body cannot

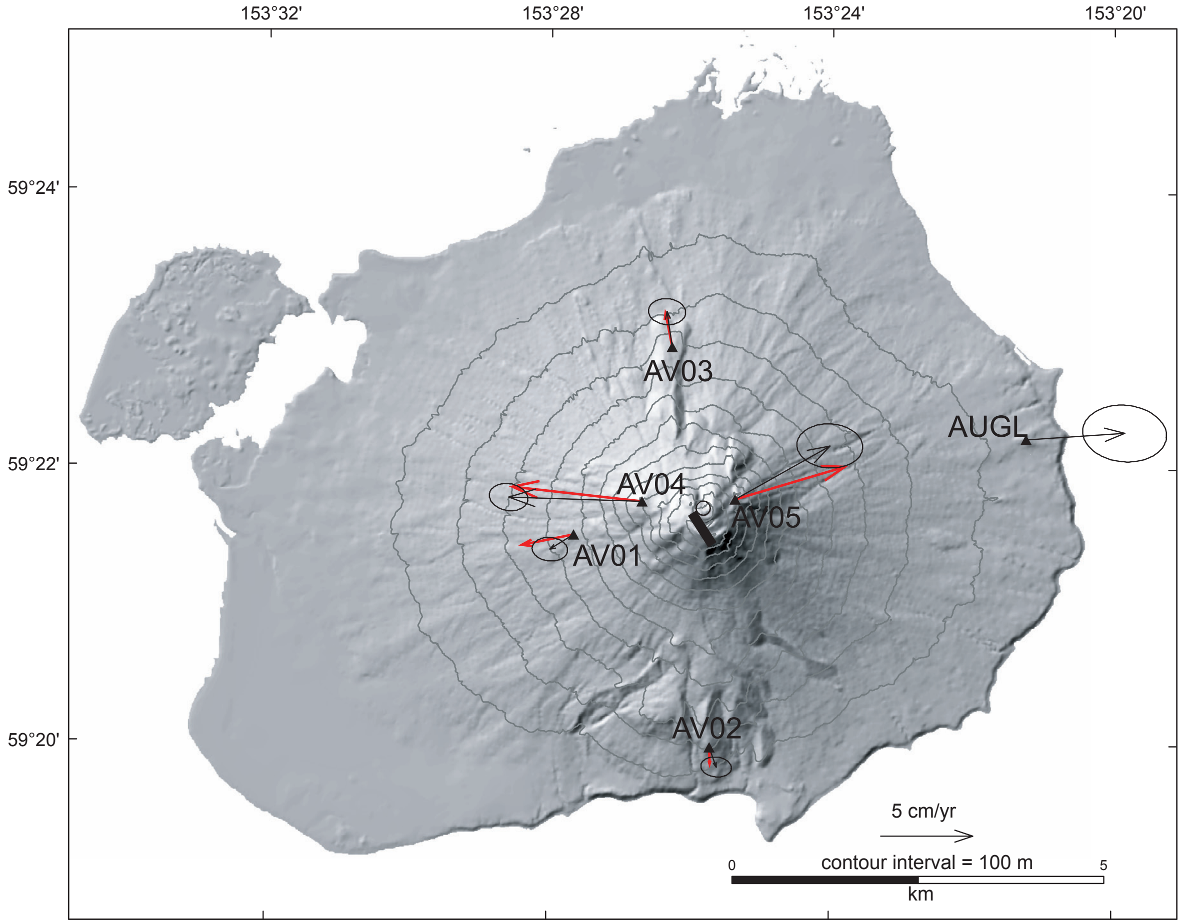

Figure 5. Augustine Volcano showing vectors of observed (black) and predicted (red) Global Positioning System (GPS) velocities relative to station AC59, located approx 24 km northwest (343°) of Augustine (fig. 1), during precursory phase in 2006. Error ellipses indicate 95 percent two-dimensional confidence regions. Predicted velocities are from a point source near sea level. Black circle, horizontal location of the modeled point source of pressurization active during precursory phase. Black bar near summit, surface projection of model dike that was active from mid-November 2005 through early January 2006. Predicted velocity at station AUGL is too small to show in this figure.

be easily constrained, whatever its geometry. The modeled depth of a point source, as mentioned above, probably reflects an impermeable layer rather than the top of a magma body.

Dike Ascent

An abrupt offset appeared in the GPS time series at stations AV04 and AV05 (fig. 2) around November 17, 2006 (fig. 4). By taking the difference between a 4-day mean position before and after November 17, we calculated a displacement of about 3.5 cm to the southwest and an uplift of about 3 cm at both stations. This offset did not appear elsewhere within the Augustine GPS network. Although we did not appreciate its significance at the time of its occurrence (or even its reality as a geologic signal), we now interpret this offset as the abrupt opening of a crack in the Naknek formation above the pressurizing region beneath the summit near sea level. This interpretation is somewhat speculative—there was no earthquake or other geophysical signal associated with the event—and requires that the opening occurred quickly enough to appear abrupt in the daily geodetic time series, but slowly enough (that is, at a low-enough strain rate) for the ductile and, therefore, aseismic failure.

Cervelli and others (2006) argued that magma likely ascended through the edifice in the weeks to months before the onset of the magmatic eruption. The only alternative interpretation is that an active magma column existed within the edifice before the start of unrest, reaching nearly to Augustine's summit. We rejected this interpretation on the basis of the 20-year interval since the latest extrusion and the relatively modest fumarolic temperatures at the summit. Temperatures after the 1986 eruption declined from 870°C in 1987 to about 95°C in the early 1990s. The question remaining, therefore, is whether the magma ascent occurred by the way of dike intrusion or through a diapiric process.

On the basis of the style of deformation observed at station AV05 (figs. 2, 4), we conclude that magma ascent occurred as a dike intrusion. Specifically, the observed change in the vertical component from uplift to subsidence (fig. 4) is characteristic of a shoaling dike, the subsidence arising from a Poisson effect as the rock above the dike is stretched. Further evidence for the dike hypothesis comes from geologic observations of the summit. Beginning in mid-December 2005, features interpretable as extensional became evident, including a new fissure that opened at the summit, striking approximately north (Wessels and others, this volume). Recently analyzed petrologic data (Larsen and others, this volume) indicate that glass compositions in the low-silica- content andesite, believed to be the initial magmatic component of the 2006 eruption, underwent shallow decompression-driven groundmass crystallization before it erupted, an interpretation consistent with the shallow magmatic storage entailed by a dike ascending through the edifice and stalling near the surface for several weeks.

To model the dike, we used rectangular dislocations (Okada, 1985) embedded in a linear, flat, elastic half-space. We then applied a linear least-squares analysis to estimate a dike-ascent history, assuming an exponential model for dike height as a function of time. We assumed an initial depth of 1.25 km and estimated a time constant (or "characteristic" time) for dike ascent and final height as time goes to infinity. We also tried other temporal models, including nonparametric, stochastic models, but observed that only a simple, well-constrained exponential equation fit the data as well as, or better than, any other. Likewise, we tried many different geometric models for the dike and determined that none of them permitted a dike-ascent history with a markedly different (for example, concave upward) ascent history than the one presented here.

The choice for an initial depth of 1.25 km below the top of the half-space was based on the distance between the summit and the location of the pressurizing region near sea level and on the excellent fit of the subsequent model. The dike could have propagated from greater depth, but given the size of the dike—at least when it was in the upper edifice—the existing geodetic network could probably not have detected its presence much below sea level. Thus, choice for initial depth represents an upper limit on the locus of initial dike ascent, rather than our best approximation of where that ascent began.

The estimated dike-ascent history as a function of time is plotted in figure 4. Dike ascent appears to have been begun rapidly, reaching a maximum ascent rate of nearly 100 m per day by November 25, 2005. If this ascent model is correct, the dike came within a few hundred meters of the surface by mid-December 2005, possibly explaining the onset of vigorous steaming and phreatic explosions on December 2, 2005, as well as the local deformation observed at the volcano's summit.

Coombs and others (this volume) argue that the explosions of January 11, 2006, were gas rich, with limited, if any, juvenile magma. They draw this conclusion from the absence of extensive hot flowage deposits and the scarcity of juvenile glassy clasts in tephra-fall deposits (Wallace and others, this volume). Deformation data alone, which are sensitive only to the displacement of the crack wall, cannot differentiate between upward propagation of a gas- versus magma-filled crack. However, given that after the explosions of January 11 no evident reversal of the accumulated deformation occurred, we can conclude that the crack did not close, suggesting that some material remained to keep it open and, in turn, that the observed deformation was, in fact, caused by the ascent of a magma-filled dike, possibly led by a volume of pressurized gas that violently exited in two stages on January 11. Other evidence, as discussed in detail in the next section, suggests that the partially degassed magma from the vanguard dike may have been slowly extruded in the form of a lava dome on January 12 and 13.

Explosive Phase

Average daily solutions, though accurate, are not especially useful for studying quickly evolving volcanic processes. In the hours before the first explosions on January 11, 2006, an energetic earthquake swarm rattled Augustine's summit

(Power and Lalla, this volume), prompting AVO to raise the level-of-concern color code to orange (Neal and others, this volume). Curious to see whether a deformation transient accompanied this swarm, we reprocessed the GPS data, solving for a position at each measurement epoch (every 30 s). We used the RTD processing software (Bock and others, 2004), which estimates each position independently—that is, no temporal smoothing is imposed on the solution time series. This processing methodology requires a stationary reference station, and the resulting solutions are the east, north, and up distances from this origin. Ideally, the reference station should be close enough to the stations of interest so that common error sources (troposphere, orbital errors, and so on) difference out, but far enough away to be outside the deforming area. We opted to use station AUGB (fig. 2), about 5.5 km away from Augustine's summit, as our reference station.

We examined the interval January 9–13, 2006 (UTC). Although the area of station AUGB was slowly deforming from the sea-level inflation source during this interval, the interval is sufficiently brief that the cumulative deformation is well below noise. The time series over the interval at station AV01 is plotted in figure 6. No deformation is evident over the interval on any of the three components, although we know from analysis of the daily solutions that station AUGB and AV01 (fig. 2) were slowly (centimeter per year) moving apart at this time (as primarily evident on the north component of this baseline). The absence of apparent deformation results only from the brevity of the interval under examination. Almost all other stations, except AV04 and AV05, have a similar "flatline" appearance. Icing introduced significant noise in the station AV04 time series. Although icing also affects the time series from station AV05, a signal is still clearly visible beginning around 12:00 a.m. January 11 (fig.7). After the initial explosions midday on January 11, the scatter in hourly median solutions increases, probably because the abundant ash in the air caused unmodeled path delays in the GPS transmissions. The last data were received

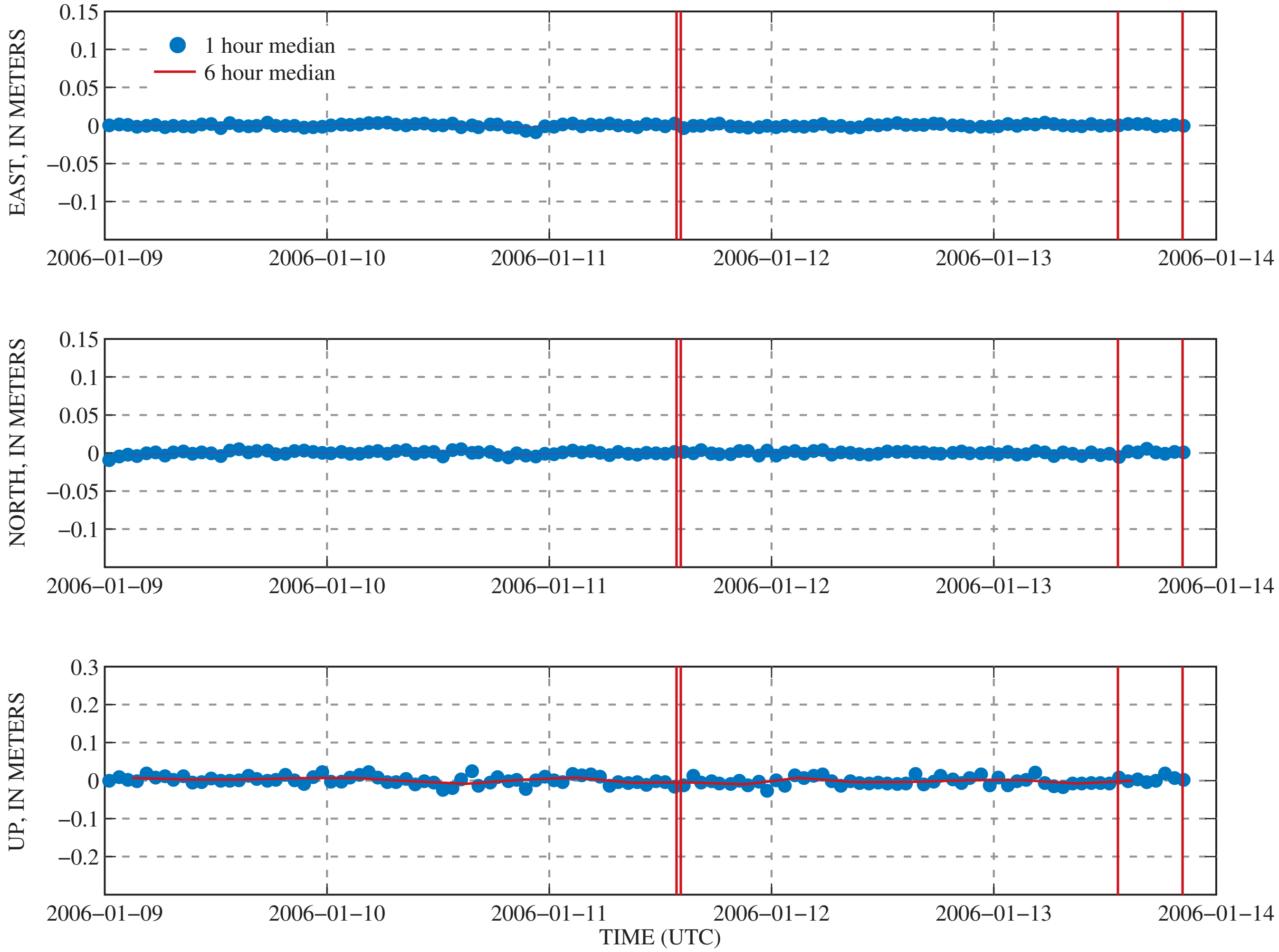

Figure 6. Time series of hourly solutions for distance of station AV01 from station AUGB (fig. 2) on Augustine Island in January 2006. Circles, 1-hour median solutions; curves, 6-hour medians. Note that scale for vertical component is twice that for horizontal components. Vertical red lines denote times of first four explosions. Deformation at station AV01 over this interval is negligible.

from station AV05 at 7 p.m. January 13, just before event 3 (Coombs and others, this volume), which presumably destroyed the station and (or) its telemetry. The signal—an acceleration in deformation—appears unambiguously in the east and north components and is directed northeastward. A vertical signal is difficult to resolve from the noise, but if one exists, it likely takes the form of subsidence.

Inferring a unique mechanical model from a short-lived signal that appears on the record from only a single station is impossible. Nonetheless, close examination of the signal, especially in comparison to seismic signals measured simultaneously, does lead to some interesting insights. The east component of the station AV05 time series, taken as 6-hour medians, is plotted on the same time scale as the Real-Time Seismic Amplitude (RSAM) system at broadband seismic station AU12 BHZ AV (fig. 8; located approx 850 m west of GPS station AV03, fig. 2). The first interesting observation is that the deformation transient begins almost concurrently with the energetic earthquake swarm early on January 11 (Power and Lalla, this volume). Both observations may be explained by upward propagation of a magma-filled crack into the highest part of the edifice. The absence of this signal on the record from nearby station AV01, which is 550 m below and 2,200 m west-southwest of station AV05, strongly suggests that the deformation source is close to station AV05 and, owing to the elevation difference, quite high.

The deformation transient appears to continue for many hours after the explosions of January 11, only to flatten out early on January 12 just as drumbeat earthquakes began to be recorded. Drumbeat earthquakes are commonly associated

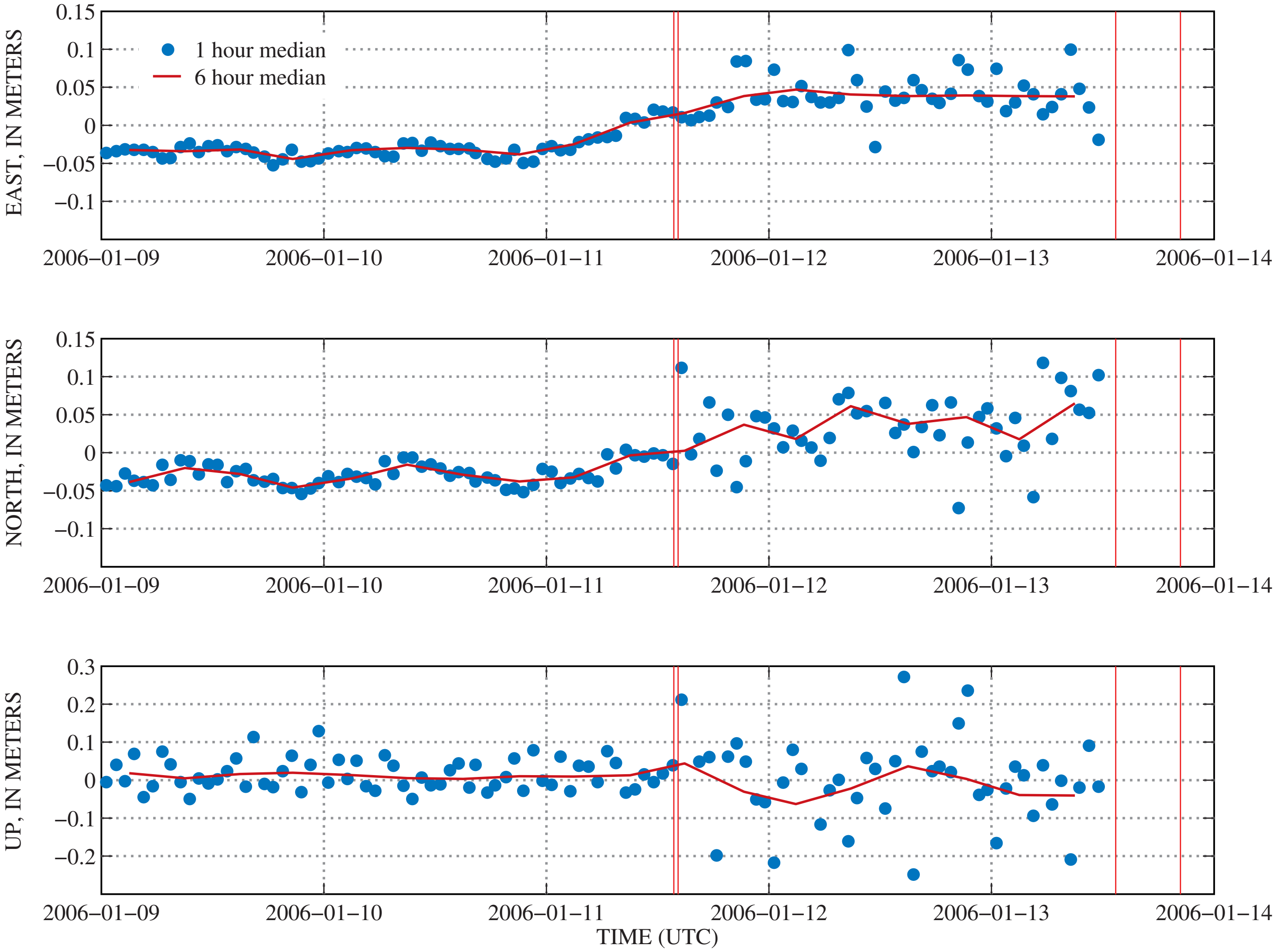

Figure 7. Time series of hourly solutions for distance of station AV05 from station AUGB (fig. 2) on Augustine Island in January 2006. Same scale as in figure 6. Circles, 1-hour median solutions; curves 6-hour median solutions. A clear acceleration in deformation occurs shortly after January 11 in east and north components. Overall noise level relative to station AV01-AUGB is higher, probably owing to a combination of factors, including antenna icing and presence of ash and volcanic gasses near summit. Noise level increases markedly after first explosions (vertical red lines), possibly owing to increased ash emission.

with the extrusion of lava (Moran and others, 2008; see Power and Lalla, this volume). During the period between the first explosions and the beginning of drumbeats, seismic activity declined markedly, in spite of the ongoing deformation. One explanation for this observation is that the explosions relieved the volatile pressure within the tip of ascending magma and removed the driving force behind much of the seismicity. Moreover, the explosions may have contributed to the physical erosion of a pathway for magma ascent. Deformation persisted as the walls of the pathway were pushed apart by the ascending magma. Finally, when lava extrusion began (as signaled by the drumbeats), a quasi-steady state (or open system) was established, and the deformation flattened.

Throughout the explosive phase, the baseline between stations AV02 and AV03 (fig. 2) continued to indicate slow, but unmistakable, extension (fig. 3). Indeed, the rate of extension seemed to remain steady to within measurement uncertainty, suggesting that explosions, individually and in aggregate, did little to relieve pressure within the shallow magmatic system.

Continuous Phase

The geodetic signal associated with the continuous phase of the eruption consisted of a sharp deflation from about January 28 through February 10, 2006. This pattern of deformation has two primary characteristics: it is directed radially inward, and it is uniformly downward. The radial direction of the deformation becomes particularly evident upon transformation to a cylindrical coordinate system. If each station coordinate is represented as a distance from Augustine's summit, then the

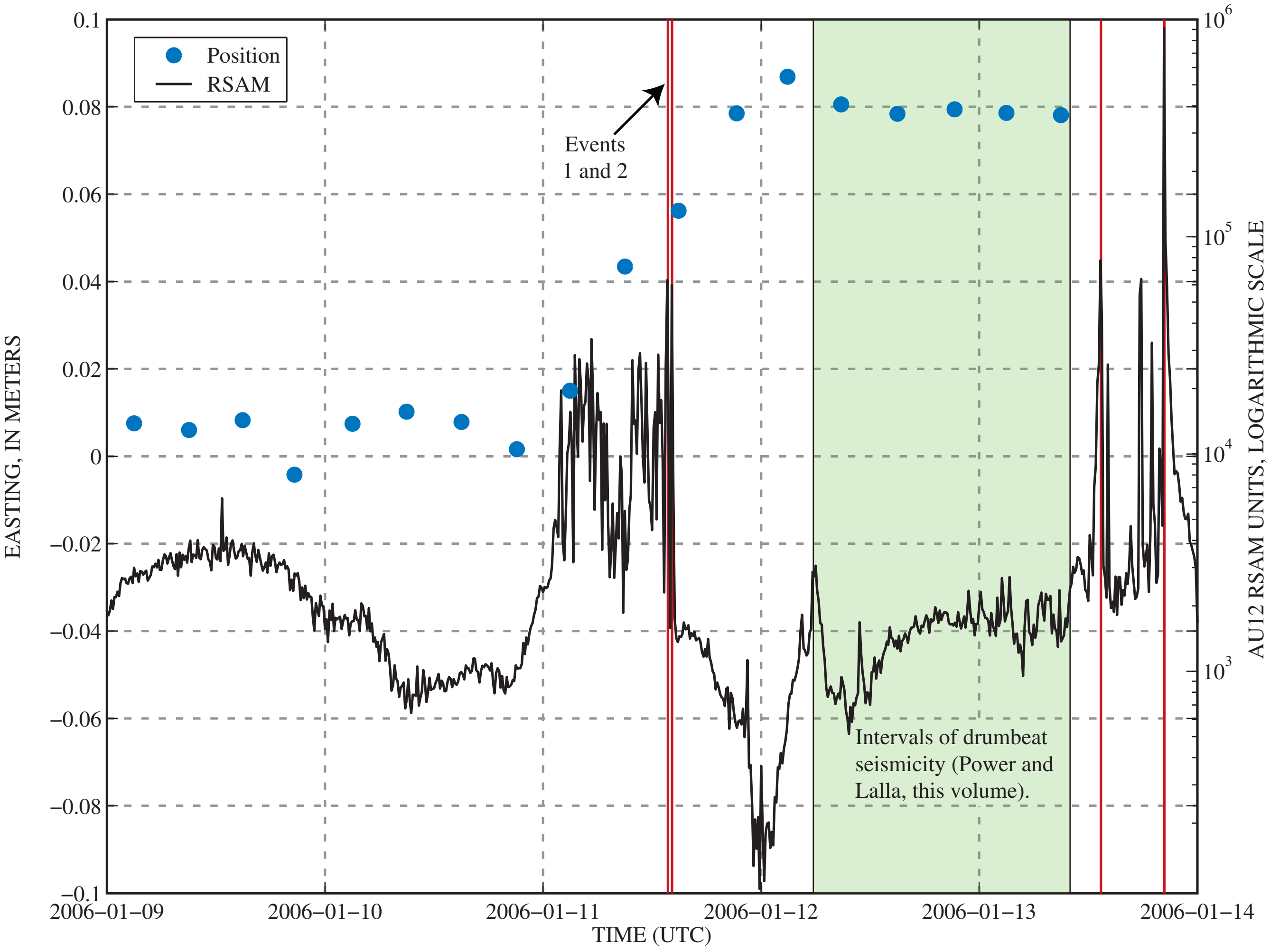

Figure 8. Preexplosive and postexplosive deformation at station AV05 compared to RSAM computed from broadband seismometer AU12. Circles, 6-hour median solutions for east component of baseline between stations AV05 and AUGB; curve, record from Real-time Seismic Amplitude (RSAM) at station AU12 BHZ AV, a broadband seismometer located about 850 m west of station AV03. Note that deformation accelerates suddenly at about midnight January 11, 2006, concurrently with increase in RSAM record corresponding to energetic earthquake swarm that preceded first explosions. Accelerated deformation continued for about 24 hours and then flattened at about the same time when drumbeat earthquakes were first observed (early on January 12).

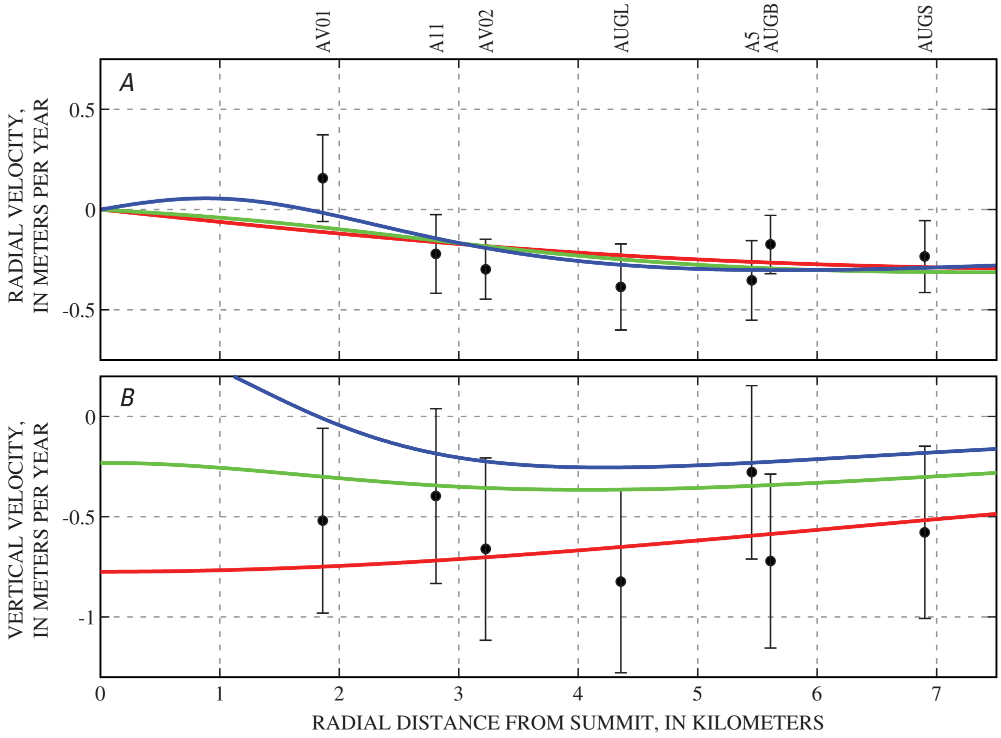

Figure 9. Summit deformation at Augustine Volcano during continuous phase in 2006. Observed velocities (circles) are shown rotated into radial (*A*) and vertical (*B*) components. Error bars are depicted at 95-percent confidence level. Radial component is in direction from observation site to summit. Model predictions over a range of 0 to 7.5 km are given for a spherical point source (red curve), closed pipe (green curve), and an open pipe (blue curve).

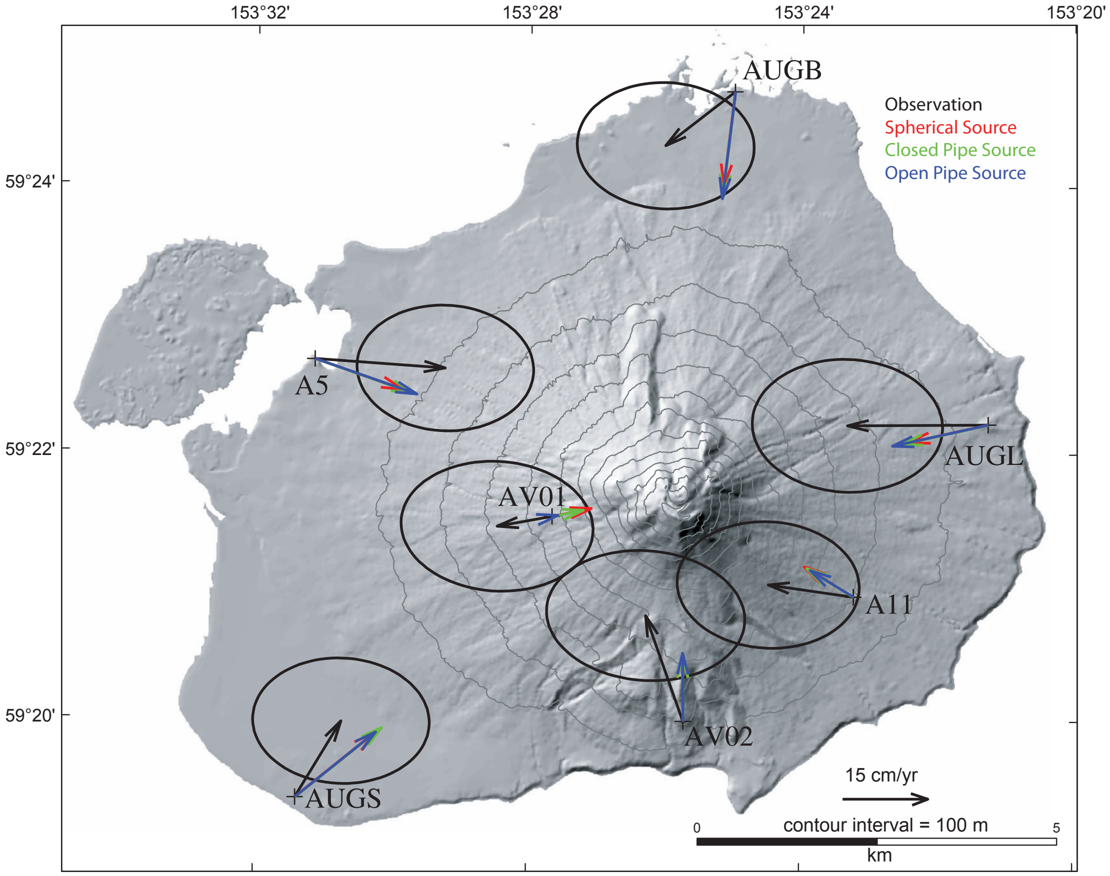

Figure 10. Augustine Volcano, showing vectors of continuous-phase deformation. Error ellipses of observations are scaled by (black vectors) scatter about mean velocity over interval and shown at 95-percent confidence level. Scaled signal-to-noise ratio (SNR) of data (including undepicted vertical components) is ~12; unscaled SNR is about double that. Model predictions are shown for a spherical point source (red vectors), a closed pipe (green vectors), and an open pipe (blue vectors).

three components of deformation can be expressed as (1) radial, motion toward or away from the summit; (2) tangential, motion perpendicular to the direction of the summit; and (3) vertical. In a "purely" radial deformation pattern, the second component will be zero. The estimated GPS velocities during the continuous phase, transformed into radial and vertical components, are plotted in figure 9 and mapped in figure 10. Within uncertainties, no single measurement of tangential deformation is distinguishable from zero, and the scatter about zero shows no obvious positive or negative tendency. The absence of any statistically significant tangential signal all but precludes modeling the deformation pattern with anything other than a radially symmetric source centered at the summit. Although the presence of a shear source, dike, or sill cannot be ruled out, if such a source was active during the continuous phase, it did not produce sufficient deformation for positive resolution.

Figures 9 and 10 also show that the radial deformation measured at the nearest station to the summit differs in sign from that measured at all other stations—station AV01 (fig. 2) actually appears to have moved away from the summit during the deflation of the continuous phase. Taken as an individual measurement, the previous observation is not decisive to within uncertainties; however, given that every other measurement is, within uncertainties, less than zero (directed toward the summit) the apparent sign difference is probably real. The overall trend of the radial deformation shows a gradual increase in motion after a sign change at around 2.5 km, reaching a maximum at about 4.5 km and flattening beyond that. Although the deformation almost certainly extends farther than the coastline, no measurements are available, except for the distal PBO backbone sites (stations AC27, AC59; fig. 1), where no volcanic deformation is visible.

The observed vertical deformation appears to be constant at all stations at about −0.55 ± 0.4 m/yr. Thus, the vertical deformation is distinguishable from zero, although no convincing trend in the magnitude of deformation as a function of radial distance is apparent. The uniformity of the vertical signal suggests a possible correlated noise source. For example, because the calculated velocities are relative to a stationary (over this short interval) station on the Alaska Peninsula, AC59 (fig. 1), position errors at that station can lead to correlated error across the network of remaining stations. The uniformity of the vertical signal, however, does not stretch to include the station AC27, 44 km southwest of Augustine (fig. 1), which, unlike the other seven stations, appeared to rise somewhat relative to station AC59 over the interval under consideration. Therefore, the uniformity—at least in sign if not in value—of the vertical signals probably reflects a volcanic process and not simply measurement error.

Given the abundance of erupted material, about 25 million m^3 each, during the explosive and continuous phases (Coombs and others, this volume), we conclude that the deflation imaged by the GPS network resulted from the withdrawal of magma out of a storage area, or chamber, at depth. Regarding this chamber, geodetic measurements can shed light on three main questions: (1) what is its shape? (2) how deep is it? and (3) how much did it contract?

Modeling Deformation During the Continuous Phase

The deformation observed during the continuous phase, though large when expressed as a rate, was quite small in terms of absolute displacement. Indeed, the signal-to-noise ratio (SNR), defined as the norm of the weighted data vector, of the geodetic measurements from the continuous phase was about a sixth that of the SNR of the precursory phase through mid-November 2005. Models of geodetic measurements with such modest SNRs are not likely to be well constrained or even unique. Nonetheless, modeling can be useful in ruling out interpretations that would otherwise remain plausible. Furthermore, although individual model types and their associated parameters are typically not well constrained with low SNR, constraints can be imposed on classes of models and ranges of model parameters, particularly when other corroborating data are available.

The first deformation source that we consider is a spherical point source (Anderson, 1936; Mogi, 1958), exactly the same source type as the one we used to model the precursory inflation. Maximum radial deformation from a spherical point source occurs at a distance of source depth over $\sqrt{2}$. Simply on the basis of inspection of the observed data in figure 5, a spherical point source must be at least 7 km deep to fit the observed horizontal deformation. Maximum vertical deformation from a point source occurs directly above the source and is inversely proportional to the square of source depth. The vertical deformation decays to half its maximum value at a distance of about 3/4 of a source depth. This fact, in combination with the large and uniform subsidence signal, suggests that a source depth greater than 10 km would be required to fit the data well.

In addition to a spherical point source, we also consider two additional deformation models—closed and open pipes (Bonaccorso and Davis, 1999). Both of these models share a similar geometry, although we model a closed pipe as a degenerate ellipsoid with equal semi minor axes, and an open pipe as a cylinder. Both models are parameterized similarly: (1) easting, (2) northing, (3) depth to the top of the pipe, (4) depth to the bottom of the pipe, (5) the pipe's semiminor axis (radius), and (6) a source strength. The two models differ with respect to the boundary conditions on the pipe walls. A closed pipe is characterized by constant pressure change on the pipe walls, while the conditions for a open pipe stipulate constant displacement on the pipe walls, along with zero pressure change at its top and bottom. The effect of this difference is that for an open pipe, no excess upward force (that is, force other than lithostatic) is exerted on the top of the pipe, hence the "openness." In an open pipe the source strength is a length change (a displacement), whereas in a closed pipe it is a pressure change.

Bonaccorso and Davis (1999) gave approximate expressions for surface deformation from both types of pipe, the approximation stemming from the fact that the boundary conditions on the cylinder walls are not met exactly. Results are accurate, however, if the cylinder radius is small relative to its height and depth. Mathematically, the level and characteristics of the approximation are similar to that of a spherical point source—an infinitesimal representation of a finite body. Indeed, a spherical point source, which approximates the deformation from a pressurized spherical cavity, also becomes more accurate as the ratio of the source depth to the source radius increases. Segall (2010) notes that the expressions of Bonaccorso and Davis (1999) are not general and apply only when Poisson's ratio equals 0.25. Segall (2010) provides the general expressions, which we employ here.

We derived the three-dimensional deformation fields (that is, deformation in the body as well as at the surface) for both pipe models, which permits the maximum displacement on the pipe walls to be calculated. This calculation, in turn, allows source strengths to be characterized as approximate volume changes rather than pressure or length changes. In the volume derivations that follow, for the sake of simplicity we use expressions for the internal deformation in an elastic full space (rather than a half-space). This simplification should yield satisfactory levels of approximation, provided that the tops of the pipes are well below (kilometers) the actual ground surface (that is, the top of the half-space).

In a closed pipe, the maximum displacement of the pipe wall, which occurs at the middle of the pipe along its height, is given by:

$$u_{max} = \frac{a\,p}{2\,\mu}\ ,$$

where a is the pipe's semi minor axis (radius), p is the pressure change, and μ is the shear modulus. Using the maximum-displacement term, a volume change can be estimated. For a closed pipe, the total volume is given by the formula for an ellipsoid:

$$V = \frac{4}{3}\,\pi a^2\,\frac{h}{2},$$

where V is total volume and $h/2$ is the semi major axis. Taking the first term of the Maclaurin Series of V as a function of a yields a simple approximation for volume change:

$$\Delta V = \frac{4}{3}\,\pi\;a\;h\;u_{max}\ .$$

Earlier, we referred to a "source strength" for closed and open pipes. We can extend this notion to a "potency," which is essentially a lumped parameter in the expressions for deformation that does not depend on the either the location of the observation coordinate or the source. In a closed pipe, the potency is given by:

$$P_{\mathrm{cp}} = \frac{a^2\rho}{4\,\mu}\,.$$

Substituting this term into the equation for volume change yields an expression for volume change that depends on only the potency term, thereby side stepping the necessity for estimating a source radius, pressure change, and shear modulus:

$$\Delta V = \frac{8}{3}\,\pi\;h\;P_{\mathrm{cp}}\,.$$

In an open pipe, the maximum displacement on the pipe walls is given by:

$$u_{max} = \frac{s}{2(1-\upsilon)},$$

where s is the displacement and υ is Poisson's ratio. Following an analysis similar to above, we can estimate the volume change for an open pipe as well. The total volume of an open pipe is given by the formula for a cylinder:

$$V = \pi a^2 h,$$

where V is total volume and h is the cylinder height. Again, taking the first term of the Maclaurin Series we get an approximation for volume change:

$$\Delta V = 2\;\pi\;a\;h\;u_{max}$$

The potency term for an open pipe is given by:

$$P_{\mathrm{op}} = \frac{a\;s}{8(\upsilon - 1)}\,,$$

which leads to an expression for volume change in terms of potency:

$$\Delta V = 8\;\pi\;h\;P_{\mathrm{op}}\ .$$

Again, because of this expression, we can focus on the volume change, side stepping the need to estimate the source radius and the displacement on the pipe wall. We note, however, that for our purposes, Poisson's ratio is not estimated but assumed. Through this analysis, we set Poisson's ratio equal to ¼.

Modeling Results and Discussion

In spite of our earlier remarks that a spherical point source must be quite deep to fit the data well, we nonetheless inverted for such a source, solving for depth and volume change. In contrast to the precursory source, near sea level, the potential source depths for the deflation observed during the continuous phase seem to be considerably deeper. Indeed, we surmise that they are large relative to the scale of regional topography, and so, for the sake of simplicity, we chose to dispense with a topographic correction. Imposing no constraints other than fixing the horizontal position of the point source to the coordinates of Augustine's summit, justified by the absence of deformation in the tangential direction, the inversion reduces to a simple search over a range of depths, linearly solving for the best-fitting volume—change rate at each iteration. The optimal model prediction is plotted in figure 9 and mapped in figure 10. The model both fails to predict the near-field sign change in the radial component and systematically underpredicts the vertical deformation but fits observations satisfactorily, given the low SNR of the data.

The results of our inversion for a spherical point source by depicting a "misfit" space for this model are plotted in figure 11. The solution that minimizes the misfit occurs at about 12.5-km depth, and corresponding to a volume loss of about 16.5 million m^3 over the interval of the continuous phase. Here and below, we quantify misfit as the difference between observation and prediction as measured by the mean squared error (MSE), a weighted L2 norm of the residual vector scaled by the number of data points less the number of free model parameters. The MSE for a best-fitting point source is approximately 2. We note that a substantial, diagonally trending region (dark blue area, fig. 11) of the graph also shows a relatively low misfit (MSE ≈ 2), indicating a significant correlation between volume loss and source depth and therefore some freedom to choose among precise pairs of these values.

Ideally, a quantitative statistical test could delineate a misfit boundary beyond which the observed data are violated. However, the non linearity of the inversion problem, exacerbated by the low SNR of the data in question, severely complicates such an analysis. For example, see Cervelli and others, 2000, for a discussion of applying an approximate *F*-test to non linear problems. Misfit graphs like that shown in figure 11 obviate these difficulties to a certain extent by presenting a quantitative account of how variations in the model parameters affect misfit when the parameters are considered both individually and together. We can then make qualitative assessments about ranges of plausible model parameters, although we still lack an objective, numerical criterion for when a certain set of model parameters is simply impermissible.

Because our data signal is weak, we cannot use the data alone to uniquely constrain a particular deformation source. We have just shown that the data can be fitted reasonably well by a spherical point source centered below the summit. The pipe sources considered below are geometrically more complex than the spherical source and should also fit the data well. The main questions, therefore, are: do the pipe models improve data fit in a statistically significant way? and, perhaps more importantly, are any of the models tested better suited to other (for example, petrologic, seismic) data?

The question arises as to whether to consider a closed pipe at all. We know that at least to a certain extent, the system was open during the continuous phase because the volcano was erupting throughout this interval. Yet we cannot simply dismiss closed models, including spherical and nondegenerate ellipsoidal sources (for example, Yang and others, 1988), both of which share the same pressure boundary conditions with a closed pipe, as useless. Eruptions necessitate a connection with an underground magma body; however, even in the event of continuous extrusion, the extrudate itself does exert some downward force or overpressure by way of its own mass (gravity), from internal friction, or from friction along the conduit walls. Likewise, the question whether

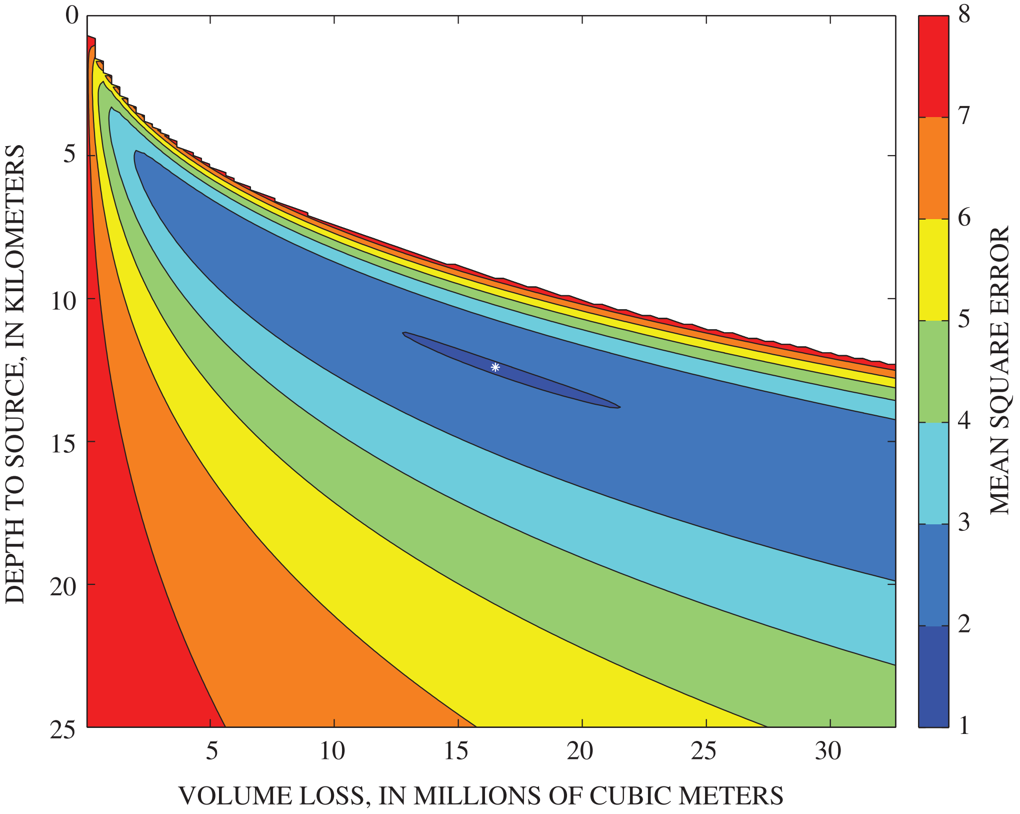

Figure 11. Model misfit for a point source. Colored regions depict misfit as a function of point source depth and volume loss based on measured velocities during continuous phase of 2006 eruption of Augustine Volcano (fig. 1). Model that minimizes misfit (white star) is about 12.5 km deep, with a volume loss of 16.5 million m^3 over interval.

an open pipe is a useful model also arises. What does it mean for a pipe to be “open” when it has a top depth of kilometers below sea level with a column of rock and magma above it? We note that both of these sources model not absolute pressures but changes in pressure over an interval. After deformation, an open pipe is not required to exert zero pressure at its top; instead, the net pressure change must be zero, and the total displacement on the pipe walls must be everywhere constant.

To evaluate data fit (that is, MSE) for both pipe models, we vary the pipe height and the depth to the pipe top over a wide range, using least squares to solve for the optimal potency parameter for each height/depth pair. As for a spherical point source, the horizontal positions of the pipes are constrained to lie directly at Augustine’s summit. The results of these analyses are plotted in figures 12 and 13, which depict the misfit space for closed-and open-pipe models, respectively. Also shown are the contours of volume change, so that for any point on the graph, misfit for a given set of the three parameters can be determined. The observed deformation from both the closed and open pipe models are plotted in figure 9 and mapped in figure 10. We note that in figure 10, all the predicted deformation vectors point in the same direction, although their magnitudes vary. This relation stems from the radial symmetry of the source models and the constraint that horizontal coordinates of the models lie at the origin (Augustine’s summit).

All of the tested model types—point source, open pipe, and closed pipe—fit the data adequately. Each model has a corresponding region in its misfit space bounded by an MSE of about 2, which is a reasonable fit to the data, given the 95-percent-confidence-level

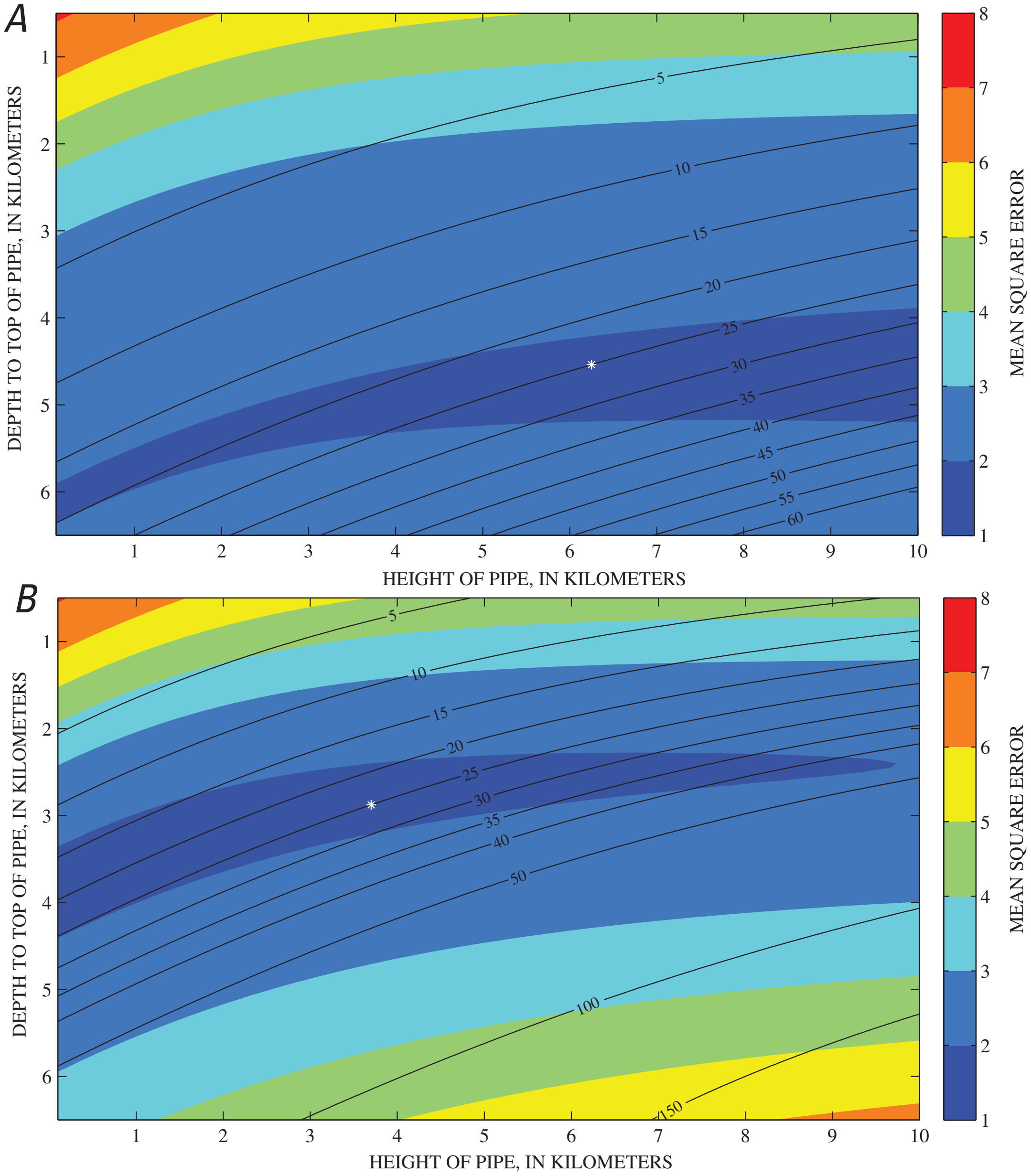

Figure 12. Model misfits for closed (*A*) and open (*B*) pipes. Colored regions depict misfit as a function of depth to pipe top, height of pipe, and volume loss (shown as contours). A substantial plausible region (MSE approx. 2) exists in misfit space, and so a precise set of model parameters is not mandated by data. However, by constraining volume loss to 25 million m^3, a specific top and height are entailed (white star).

uncertainty ellipses. The differences in misfit (that is, the difference between observations and predictions) among the models are not large and certainly not statistically significant. Misfit, therefore, cannot be a sole criterion for favoring one type of model over another. Each model type has different consequences that can be compared with other, nongeodetic data, enabling us to move beyond the mere satisfaction of a necessary condition—data fit—into the realm of sufficient conditions for determining which, if any, of our models is a useful approximation to a real geologic structure.

Petrologic analysis, including Al-hornblende geobarometry from Holocence fall deposits, indicates magma-storage pressures corresponding to no greater than 9-km depth (Tappen and others, 2009). Moreover, melt inclusions obtained from 1986 and older deposits suggest crystallization depths of less than 8 km (Roman and others, 2005; see Webster and others, this volume), and melt-inclusion volatile contents from 2006 high-silica andesite, erupted during the continuous phase, indicate pressures as high as 100 MPa, equivalent to depths of 3 to 4 km (Webster and others, this volume). All of these studies seem to contradict the 12.5-km depth of the point-source model. Indeed, even if we relax the data-fit requirement, figure 11 shows that to achieve a source depth consistent with the petrologic depth constraints, only a small volume loss (~ 5 million m^3) is needed. This value is only a tenth of the volume of magma erupted by the end of the continuous phase, a discrepancy that seems too large, even accounting for magma compressibility.

The geodetic data do not fully constrain the parameters for either a closed or an open pipe. “Plausible” regions bounded by the condition that MSE ≈ 2 are plotted in figures 12 and 13. These regions cover fairly extensive areas: 17 percent of the total graph for a closed pipe and 13 percent for an open pipe. Defining the plausible regions as bounded by MSE ≈ 2 is somewhat arbitrary, though not without justification. Sorted lists of MSE values for each pipe model, when plotted, show plateaus of MSE ≈ 2, with the values increasing sharply thereafter, implying that the plausible regions are, as well as being compatible with the data, well constrained, at least with respect to the total range of calculated misfits.

For a closed-pipe model, the plausible region extends to (and, though not plotted beyond) the right side of figure 12, corresponding to pipe heights of 10 km and greater. The data poorly constrain the height of a closed pipe or putting it another way, the depth to the pipe bottom. The only firm check on a closed pipe’s height is the absence of observed deformation at the far- field PBO site AC29, 44 km WSW of Augustine (fig. 1).

For both closed and open pipes, the contour corresponding to 25 million m^3 of volume change runs through the middle of the plausible regions. This contour also has the property—again, for both pipe models—of having a well-defined

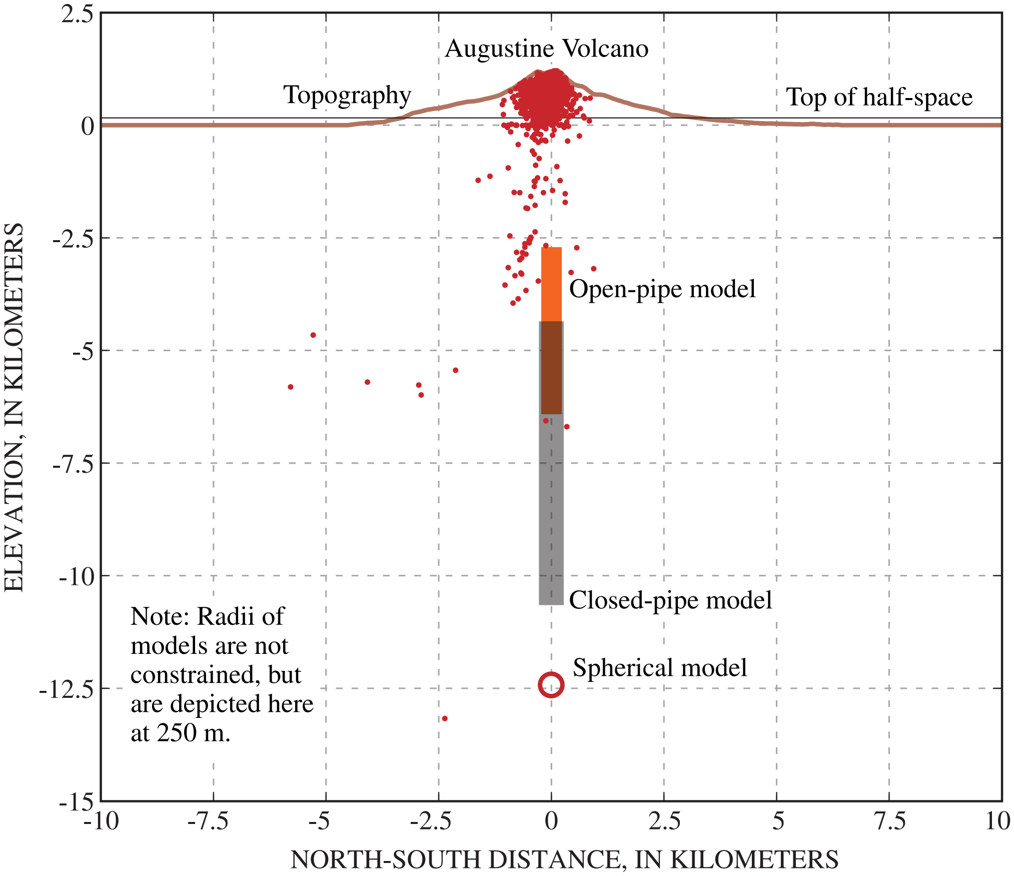

Figure 13. North-south cross section of Augustine Volcano (fig. 1), showing cross-sectional view of three source models under consideration for deflation during continuous phase, along with topography (brown curve), hypocenters (red dots), and top of elastic half-space (black horizontal line). Red circle, optimal point-source model; gray rectangle, favored closed-pipe model; orange rectangle, favored open-pipe model. Radii of pipes and sphere are conceptual and not constrained by data.

minimum MSE along its length, enabling us to focus on specific pipe depths and heights. In contrast, the misfit curves corresponding to the adjacent contours (20 million and 30 million m^3) do not exhibit such well-defined minimums. By this means, we choose our preferred parametrizations for open and closed pipes from among all possible values within the plausible regions. The preferred depths and heights for both pipe models are shown in figure 12 and 13 (white stars), and the models themselves are depicted in cross section in figure 13. Numeric descriptions of our preferred models are listed parametrically in table 2.

We note that the 25 million m^3 volume change value agrees well with the estimated eruptive output during the late explosive phase and continuous phase, and might then conclude that geodetic measurements are imaging a simple correspondence between magma withdrawal at intermediate depth and lava and tephra eruption at the surface. Several questions complicate this simple interpretation. Why, during the explosive phase, when 30 million m^3 of material was erupted, did no corresponding volume-loss signal occur in the geodetic data? Indeed almost half of this volume was erupted in the last 2 days of the explosive phase, and yet still no geodetic signal was observed. Second, why, during the hiatus, after the magmatic pathway had been thoroughly reamed out, was there another—albeit minor—episode of inflation? And third, why, during the effusive phase, was still another 25 million m^3 of lava extruded as a lava dome, with only a negligible deflation signal, much smaller than that observed during the continuous phase when a similar volume of lava was erupted?

Experience has shown that geodetic estimates of volume change are consistently too small relative to observed erupted volumes (for example, Owen and others, 2000). Mastin and others, (2008) addressed this discrepancy by noting that the ratio of the eruptive volume (dense-rock equivalent, or DRE) to the geodetically measured deflation volume depends on both the compressibility of the magma and the magma reservoir. Specifically:

$$\frac{V_e}{\Delta V} = -\left(1 + \frac{\kappa_m}{\kappa_c}\right),$$

where V_e is the erupted volume, ΔV is the geodetically inferred volume loss, κ_m is the magma compressibility and κ_c is the compressibility of the magma reservoir. For magma from the 2004-8 Mount St. Helens eruption, Mastin and others (2008) estimated that κ_m fell in the range 3×10^{-10} to 5×10^{-10} Pa^{-1}, whereas κ_c was about 1×10^{-10} to 1.5×10^{-10} Pa^{-1}, implying a $V_e / \Delta V$ ratio of about −4. Magma from the Mount St. Helens 2004–2008 eruption was notably degassed (Gerlach and others), resulting in an abnormally low compressibility. For the more gas- and bubble-rich magmas of Augustine, we estimate κ_m at about 1×10^{-9} Pa^{-1}. Because the P-wave velocity in the vicinity of the magma reservoir at Augustine is lower (~ 5.6 km/s; see Power and Lalla, this volume) than at Mount St. Helens, we estimate, using the methodology of Mastin and others (2008) and accounting for the differently shaped chamber geometries, κ_c at Augustine at about 5×10^{-10} Pa^{-1}. Together, these two compressibilities values yield a $V_e / \Delta V$ ratio of about −3.

Leaving aside for the time being the question whether the appropriate deformation model at Augustine is a closed or open pipe, we argue that the deflation observed geodetically during the continuous phase accounts for almost all the material erupted from Augustine in 2006. The 25-million m^3 volume, scaled by a $V_e / \Delta V$ ratio of about −3, amounts to a total volume loss of about 75 million m^3, quite close to the geologically estimated eruptive volume (Coombs and other, this volume). But how was 30 million m^3 of material erupted during the explosive phase before any geodetic deflation occurred? We suggest that during the explosive phase of the eruption, the gas-rich magma behaved as a "volume buffer." As the eruption proceeded, the pressure in the magma reservoir would instantaneously drop, leading to more bubble creation, which, in turn, kept the pressure (and volume) in a dynamic balance. Eventually, however, enough gas would exsolve and enough magma would erupt to overcome the buffering capacity of the reservoir, leading to a sharp pressure loss, a strong geodetic deflation signal, and the boilover characterizing the continuous phase. Left behind after all this activity would be a slug of relatively degassed magma high in the plumbing system, possibly in the edifice itself, which would eventually be extruded during the effusive phase, driven by a small excess pressure created as the main magma reservoir viscously reequilibrated.

The question remains of how to choose between the closed- and open-pipe models. A closed pipe is overall a deeper and more extensive magma reservoir model than an open pipe. Accounting for the difference between the top of the half-space and the top of the edifice, a closed pipe begins at about 4.5 km below Augustine's summit and extends for another 6 km. In contrast, an open pipe begins at about 2.6-km depth and continues for a little less than 4 km. Are these differences in depth sufficient to favor one model over another on the basis of the constraints from other data? Hypocentral locations of the relatively few earthquakes that occurred beneath Augustine cluster near 3.5 km below sea level (Power and Lalla, this volume), coinciding with the open-pipe-model position. Larsen and others (this volume) infer that most eruptive products during the continuous phase came from a depth of approximately 4 to 6 km below the summit and that melt-inclusion analysis suggests crystallization depths of less than 8 km (Roman and others, 2005; see Webster and others, this volume). Both the hypocenter data and the petrologic analysis seem to slightly favor an open-pipe model, but neither the data nor the analysis is absolutely determinative.

Careful examination of the predictions data from the two pipe models shows two potentially distinguishing characteristics: first, the closed-pipe model fails to capture the near-field curvature (sign change) in the radial deformation; and second, the open-pipe model systematically underpredicts the vertical deformation. These two shortcomings lead to speculation as to whether a hybrid, or "partially open," source may be at work. Indeed, distinguishing "open" from "closed" sources may not be just a simple choice of one over the other but, instead, the identification of a point on a continuum between a completely closed and a completely open magmatic system. Along with fitting the data better, a hybrid model might also be more physically realistic, in that it would capture the essential openness of an erupting system, while also accounting for the capacity of the extruding magma to sustain a pressure gradient over the height of its column.

Timing

Under ideal circumstances, GPS data can be used to precisely resolve the timing of changes in deformation style. Of particular interest for the continuous phase of the 2006 Augustine eruption is the moment when inflation gave way to deflation, which would be useful for estimating magma-ascent rates. We reprocessed the available GPS data into subdaily solutions, using the RTD software (Bock and others, 2004) as above, but the small SNR of the deflationary signal made our efforts ineffective. We are simply unable to identify the precise time when deflation began. Our best estimate, based on both daily and subdaily solutions, is that it began within 12 hours of 1200 January 29, 2006 UTC.

Hiatus and Effusive Phases

By the time of the hiatus and effusive phase, the deformation signal had begun to diminish. This fact, in combination with the loss of the three close-in GPS receivers due to explosions, pyroclastic flows, and ballistics, makes interpretation of the deformation during these periods difficult. The vertical signal from stations AV01 and AV02 (fig. 2) with respect to station AC59 are plotted in figure 14. Stations AV01 and AV02 were the only ones to show a deformation signal during the hiatus and effusive phase. Although subsidence (deflation) associated with the continuous phase is the most conspicuous signal, we also see a hint of uplift (inflation) during the hiatus. A generous interpretation of these data also shows a small subsidence (deflation) concurrent with the effusive phase, but the purported signal is not statistically significant. Indeed, no

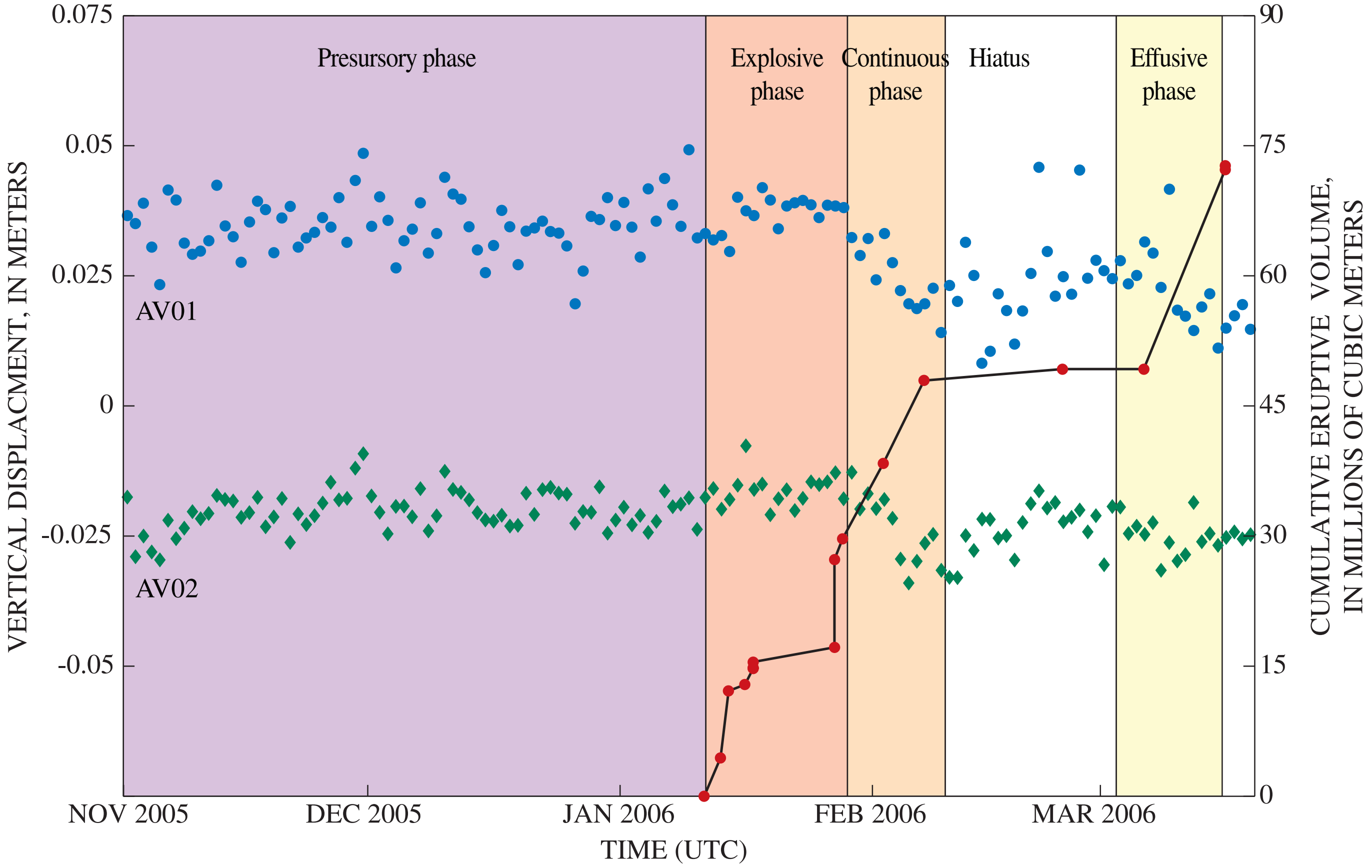

Figure 14. Long-term vertical time series from stations AV01 (top) and AV02 (bottom) with respect to AC59 (fig. 2). These close-in stations are the only two to have survived the course of the eruption intact. Cumulative eruptive volume from Coombs and others (this volume).

single velocity vector calculated from either the apparent hiatus uplift or effusive subsidence lies outside its error ellipse, although taken as whole, the deformation signal appears to slightly exceed the noise.

Modeling these data proved fruitless, although a few constraints on the dimensions and position of the magmatic sources operating over the hiatus and effusive phase can be imposed by the absence of an observed signal. A strong tradeoff exists, however, between source strength and depth that results in an insurmountable ambiguity. The same source that deflated during the continuous phase could have been repressurizing during the hiatus, although a weaker, shallower source is also consistent with the data. Another complicating factor, not considered so far, is the effect of viscoelastic relaxation of the hot material surrounding the subterranean magma. Newman and others (2006) showed that viscoelastic processes can have significant effects on observed deformation, although the short time scales characterizing the phases of the 2006 Augustine eruption probably minimized these effects.

Cumulative Deformation

The question of how much deformation remains after an eruption ends is important for several reasons. First, cumulative deformation is generally the only measurable variable of surface change, in the absence of a continuously recording network of geodetic instruments—a state of affairs characterizing nearly all of the world's volcanoes. Cumulative deformation also provides insight into volcanic processes occurring over the course of an eruption by providing at least partial answers to such questions as: (1) how does the overall shape of the edifice change during an eruption? (2) was there a net volume loss or gain to the edifice? (3) what proportion of the magma that passes through the shallow crust remains behind in comparison with the proportion that is erupted? and (4) what are the quantity, location, and orientation of the net stress change in the edifice after the eruption, and has the stress change contributed to flank instability? Finally, from a geodetic perspective, cumulative deformation amounts to a permanent record of an eruption. If the cumulative deformation is typically much smaller than, or even negligible relative to, coeruptive deformation, this difference will have important ramifications for the use of campaign versus continuous GPS stations for volcano monitoring and research.

To calculate cumulative deformation, we used both campaign and continuous GPS data, of which the campaign data consist of about a dozen bench marks on Augustine Island that were occupied in 2000 and then again after the eruption in summer 2006. Other bench marks exist that had been surveyed in 2000 but were not reoccupied in 2006, either because they could not be found or were inaccessible for logistical or safety reasons. Of interest is the net deformation that occurred over the course of the eruption. By necessity, we employ a proxy for this quantity consisting of the displacement from summer 2000 to summer 2006, subtracting out, to the extent possible, any nonvolcanic deformation (mainly plate motion) that occurred over this interval.

Ideally, a reference station would be located close enough to Augustine to undergo basiclly the same plate motion as the island but far enough away to be isolated from volcanic deformation. Several off-island stations meet this description (STEP, A18, AB22), but none of these stations were occupied throughout both the 2000 and 2006 campaigns. The reference station should be occupied simultaneously with other stations so that the subtraction needed to eliminate plate motion can be performed on each set of daily solutions. This procedure—differencing the daily solutions and then calculating the net displacement from the differences—is preferred over the converse because it (mostly) eliminates the effect of daily reference-frame errors. The only station occupied throughout both the 2000 and 2006 campaigns is A5, located on the northwest coast of Augustine Island (fig. 2). Because of its proximity to the volcano, this station would seem to be unsuitable for use as a reference station; however, calculating the average velocities between station A5 and the distal (15–20 km from Augustine) stations STEP and A18 over the 6-year interval in question reveals no motion distinguishable from zero. For this reason, we decided to use station A5 as a reference station in the following analysis.

The horizontal components of the permanent deformation that accumulated over the course of the 2006 Augustine eruption are mapped in figure 15. Though calculated over different intervals, the displacements from the campaign and continuous data should be comparable, assuming that little or no volcanic deformation occurred between summer 2000 and summer 2005. Lee and others (this volume) suggest island wide uplift from 1992 to 2005, but their results should have little effect on our analysis here because we focused on the intra island deformation gradients rather than the absolute deformation field.

The cumulative deformation at Augustine Volcano is plotted as a function of distance from the summit in figure 16. The horizontal component of the deformation, which is calculated by determining taking the magnitude of the east and north components of the displacement vector, should not be confused with the "radial" data plotted in figure 9, where the component of deformation is determined in the direction from individual stations to Augustine's summit.

Figures 15 and 16 show that the horizontal signal decays rapidly away from the summit, reaching zero by about 2.5-km distance. The vertical signal is negligible in comparison with the uncertainties in the data. Thus, in spite of the fact that three stations (A1, AV01, AV02, fig.2) show a statistically significant drop, we have little confidence of any overall vertical trend, although a slight tendency toward subsidence may exist.

The overall pattern of cumulative deformation resists straightforward modeling efforts. The large displacements close to the summit and the quick decay to zero suggest a shallow source of volumetric increase near the top of the edifice. We suspect that during the effusive phase of March 2006, the construction of a lava dome at the top of the edifice resulted in a permanent dilation of the magma conduit, along with the accumulation of a small amount of new eruptive material there. If so, we would expect some vertical signal (uplift) as well. However, the loading effect of the new lava dome would result in subsidence and potentially cancel or attenuate the uplift predicted by a dilated conduit. Modeling the expected deformation signal from the new lava dome would entail a fairly involved analysis, taking full account of the edifice topography and the shape and extent of the dome. A finite-element approach seems feasible and is an avenue for future research.

Regarding the question of stress changes within the edifice, we can speculate about a few possible consequences of the cumulative deformation. We are confident that at least a small permanent change occurred in the internal volume of the edifice during the 2006 eruption. Depending on where the volume was added, the competency of the new material, and the change in slope induced by the addition, the strength of the edifice might have been subverted and potentially brought closer to failure. Given Augustine's history of repeated sector collapse (Begét and Kienle, 1992), we expect that a tendency toward instability is the norm and that, on average, each new eruption is more likely to weaken than strengthen the edifice. Reinforcing this notion is the absence of deformation at the more distal stations, which implies that the largest stress changes were concentrated within the steep upper slopes of the volcano. Moreover, the magnitude of the displacements around the circumference of the summit is larger at higher elevation

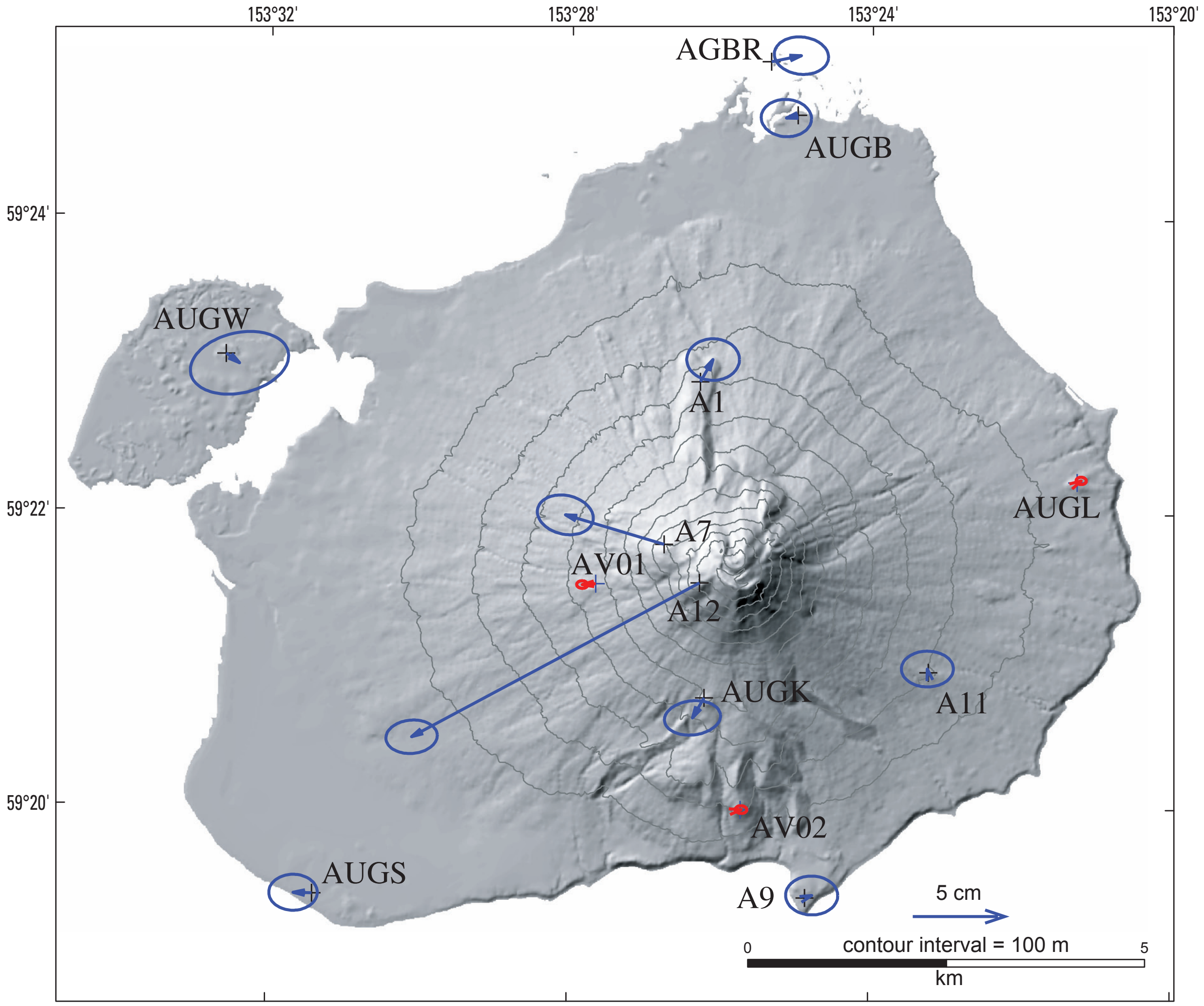

Figure 15. Augustine Volcano (fig.1), showing vectors of cumulative displacement from well before beginning of unrest to after eruption had decisively ended. Red, remaining intact Plate Boundary Observatory stations; blue, campaign bench marks. Only the four closest stations to Augustine's summit show significant deformation, with the maximum horizontal displacement at station A12 exceeding 20 cm.

(~20 cm at station A12, fig. 1) and declines downslope, also suggesting a trend toward steepening over time.

Discussion and Conclusions

Implications for Network Design

In our previous report on surface deformation at Augustine (Cervelli and others, 2006), we noted that the absence of evident precursory deformation at Mount St. Helens before its 2004–2008 eruption (Dzurisin and others, 2008; Lisowksi and others, 2008) prompted concern about whether continuous GPS was a useful monitoring tool on stratovolcanoes. We pointed out, however, that the only continuous GPS receiver operating immediately before the 2004 eruption was station JRO1, located approximately 8.5 km from the center of the crater. In contrast, the most distal Augustine GPS instrument, at station AUGL (fig. 2), was about half that distance from the summit. The total displacement at station AUGL during the precursory phase at Augustine was approximately 1 cm. If the depth of the source responsible for precursory pressurization was about 1.5 km (as we modeled it), then the corresponding displacement at a station 8.5 km laterally distant from the source (such as station JRO1 at Mount St. Helens) would be about 3 mm. Such displacement, emerging over 6 months, would be quite difficult to detect, especially without additional stations. What was needed before the 2004 Mount St. Helens eruption may well have been instrumentation and not signal. However, the magma composition at Mount St. Helens was much less gas rich than Augustine. Thus, at Mount St. Helens, little or no gas-driven precursory pressurization may have occurred, although at least some gas (mostly steam) was released in the initial explosion of the eruption on October 1, 2004 (Scott and others, 2008).

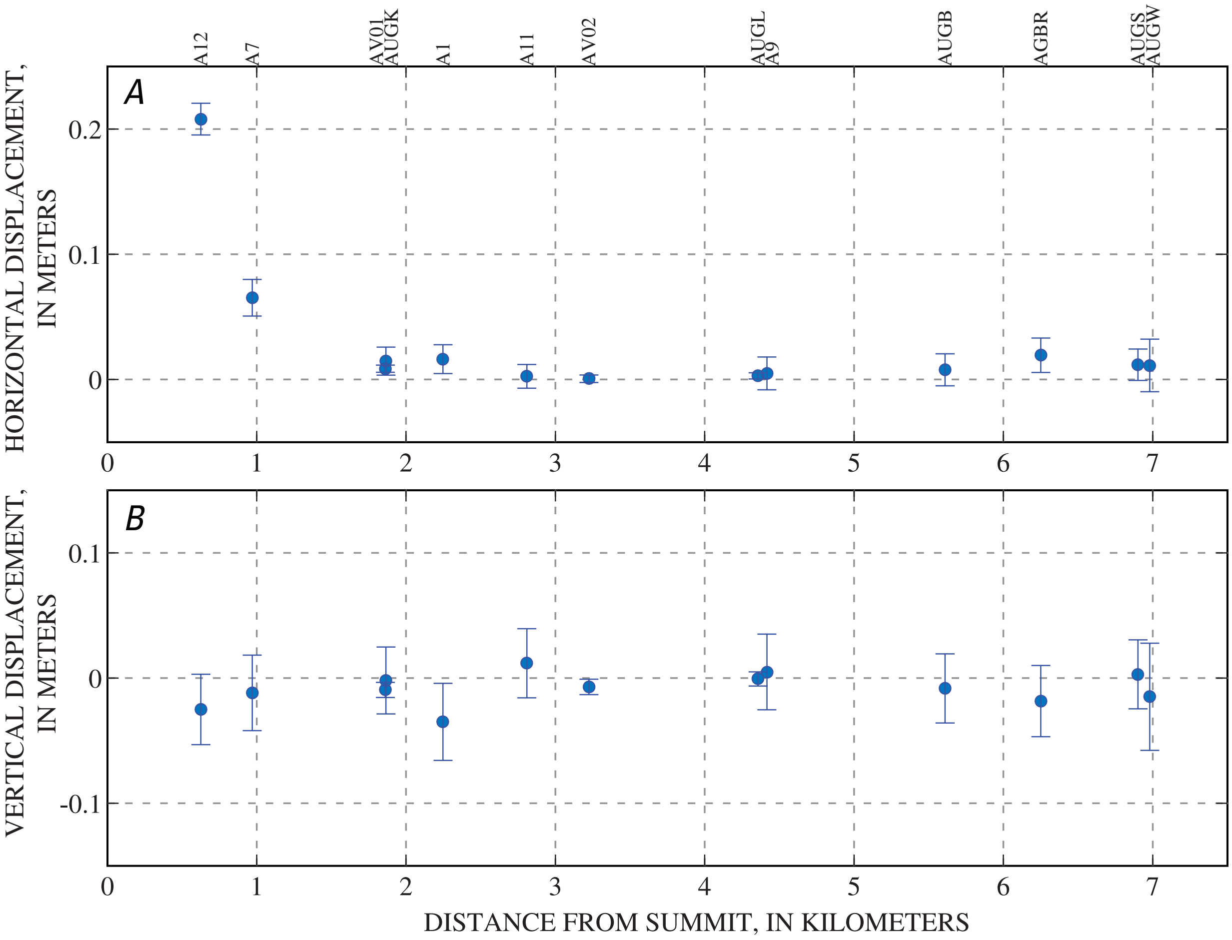

Figure 16. Horizontal (*A*) and vertical (*B*) sections of cumulative displacement over course of eruption 2006 of Augustine Volcano (fig. 1) as a function of distance from volcano's summit. Magnitude of horizontal displacement decreases drastically with distance, reaching zero about 2.5 km from summit. Vertical displacement is predominantly downward, although few individual measurements are statistically distinguishable from zero.

From the perspective of continuous GPS network design on stratovolcanoes, the main lesson of the 2006 Augustine eruption—especially in comparison with the 2004 Mount St. Helens eruption—is that close-in stations (<2 km from the summit) are extremely desirable for both volcano monitoring and research purposes. Installing stations this close to the summit presents many challenges, including steep slopes, friable rock, snow and ice at high latitudes, longer telemetry paths, and permitting issues; however, these challenges were overcome by UNAVCO (Pauk and others, this volume), and their efforts proved worthwhile. In addition to installation challenges, close-in stations are also prone to damage or destruction at even the earliest stages of precursory unrest; for example, several seismic stations became inoperable because of relatively minor phreatic explosions in early December 2005, and three GPS stations were lost in the initial explosive phase of the eruption. Mitigation strategies against station loss can take the form of hardened and (or) redundant installations. Neither strategy is likely to be completely effective, however, and both are expensive. The unavoidable fact is that the most interesting and important signals are commonly obtained in dangerous and inconvenient places. As volcanologists, we must accept this fact and explicitly acknowledge that a working instrument at risk of destruction is far more useful, and indeed, cost-effective than its undeployed counterpart resting safely on a shelf.

Because the cumulative, permanent deformation that accrued over the course of the eruption was concentrated quite close to (~2.5 km) the summit, in the absence of close-in bench marks the 2006 eruption would have been nearly invisible to campaign GPS. This fact reinforces our conclusion above that close is better when it comes to comprehensively imaging the deformation that occurs during unrest at stratovolcanoes, whether for continuously recording instruments or the establishment and occupation of campaign bench marks.

Deformation during the 2006 Augustine eruption arose from multiple sources, and our efforts to interpret these sources have several implications for network design. Two of the deformation sources (the precursory inflation and the deflation during the continuous phase) were clearly characterized by a radially symmetric deformation pattern. Distinguishing among different source types and depths requires a good distribution of stations over a range of distances from the summit. The station distribution at Augustine during the 2006 eruption was adequate, although it initially was hampered by a lack of intermediate (~5 km)-distance stations, which made it difficult to constrain source depths, particularly for sources deeper than a few kilometers. We improved the station distribution by adding temporary instruments at campaign bench marks AUGB, AUGK, AUGS, A5, and A11 (fig. 2). After the destruction of the summit sites, our ability to discriminate different deformation sources was significantly impaired—inflection or sign changes in near-field deformation can be tell tale indicators of deformation-source type.

Length measurements across the summit of a volcano have been used for decades for volcano monitoring (for example, Lipman and others, 1981). Summit-crossing baselines are easy to calculate, relatively insensitive to reference-frame error, and readily interpretable. The station pair AV02/AV03 (fig.2) proved especially useful for this purpose and played an important role in forecasting volcanic hazard. During the 10-day lull between the explosions of mid-January and those on January 27, considerable uncertainty existed about whether the quiescence represented the end of the eruption or only a brief pause. Not only had seismicity declined, but gas measurements were also showing the lowest levels of SO_2 flux since mid-December 2005 (McGee and others, this volume). During the lull, however, the baseline between stations AV02 and AV03 continued to indicate slow, but unmistakable, extension, indicating continued pressurization of the magma system and leading us to conclude that the eruption was not over. Explosions resumed on January 27, 2006, and the continuous phase began shortly thereafter.

One of the main shortcomings of continuous GPS is its relative insensitivity to high-frequency signals, particularly when sub daily solutions are sought in near-real time. This deficiency was felt acutely during the 2006 Augustine eruption, and in retrospect several important signals were clearly missed, at least from the perspective of short-term monitoring. For example, the deformation associated with the energetic earthquake swarm preceding the initial explosions would have been useful for forecasting purposes, had it been recognized at the time. Even after-the-fact post processing can be insufficient to resolve the level of temporal detail required to constrain such variables as the rate of magma ascent or dome growth. For these reasons, we strongly advocate that geodetic instruments with higher temporal precision, such as tiltmeters, be a part of any stratovolcano research and monitoring network. Tiltmeters are in routine use at other volcanoes and have repeatedly proved their usefulness (for example, Eaton, 1959; Dvorak and Okamura, 1987; Cervelli and Miklius, 2003), but nonetheless, instruments of this type remain far less common than continuous GPS. Another advantage of tiltmeters is that they are generally installed a few meters beneath the surface, making them considerably more resistant to damage than delicate GPS antennas. Even if their exposed telemetry system is swept away, tiltmeter data can still be retrieved after the end of the eruption, provided that those data are logged in the instrument and not at the surface and that the instrument is not buried beneath thick new deposits.

Summary

We have analyzed the geodetic data associated with the 2006 eruption of Augustine Volcano. Our main results are summarized as follows: (1) Deformation during the precursory phase of the eruption consisted of shallow (approx. sea level) inflation, probably attributable to volatile pressurization at the impermeable base of the edifice. The negligible volume change calculated during this phase, along with petrologic depth constraints, indicates that this source was not the primary magma body. (2) In the 60 days preceding the eruption, a dike probably propagated into the edifice, nearly reaching the surface by early January 2006. Evidence for this dike includes a characteristic, easily modeled geodetic signal, consistency with petrologic analysis, and large phreatic explosions on January 11, 2006. (3) In the 2 days before the explosions of January 13, 2006—the first explosions with a clearly juvenile product—the summit deformed rapidly, probably in response to the final ascent of the dike, followed by the initiation of dome growth. (4) During the eruption hiatus between January 17 and January 27, 2006, the edifice continued to inflate, suggesting that magma pressurization continued over this interval and that, from a hazard-forecasting perspective, the eruption was not over. (5) Beginning around January 29, 2006, deformation at Augustine abruptly switched from inflation to deflation. We interpret this deflation as partial draining of the primary magma reservoir, which we model as a cylindrical body starting from a top depth of 2.5 to 4.5 km below Augustine's summit and extending to between 6.5 to 10.5 km at its bottom. This model is consistent with petrologic analysis and earthquake locations. (6) After the end of the effusive phase, declining geodetic signal strength, in combination with the attrition of the GPS network, made quantitative interpretation difficult. Nonetheless, we argue that the geodetic data show a small inflation following the effusive phase, which gradually changes to deflation immediately before the dome building and lava flows of March 2006. Finally, (7) the total accumulated deformation over the course of the eruption is restricted to within about 2.5 km of the volcano's summit, although within this region the deformation is large and spatially coherent. This observation implies the permanent emplacement of new volume within the edifice. However, the absence of a cumulative deformation signal beyond the 2.5-km radius implies almost total recovery of the volume lost from the midcrustal chamber during the continuous and effusive phases. These implications suggest a magmatic system that over years to decades is relatively open from the lower crust to midcrust upward, but that closes at the summit after eruptions.

Acknowledgments

We thank the National Science Foundation's PBO and UNAVCO for constructing, maintaining, and operating the continuous GPS network on Augustine Volcano. USGS reviewers Larry Mastin and Michael Poland provided careful, thorough, and thoughtful reviews of the manuscript. We also thank David Schneider, Max Kaufmann, and Cyrus Read for their help in setting out and retrieving the campaign GPS sites. John Paskievitch, Guy Tytgat, Ed Clark, Tom Parker, Tim Plucinski, and Cyrus Read contributed considerable effort to keep the geophysical networks at Augustine running throughout the eruption. Finally, we are grateful to Michelle Coombs for her encouragement and patience while we were writing this manuscript.

References Cited

Anderson, E.M., 1936, Dynamics of the formation of cone-sheets, ring-dykes, and cauldron-subsidences: Royal Society of Edinburgh Proceedings, no. 56, p. 128–157.

Begét, J.E., and Kienle, J., 1992, Cyclic formation of debris avalanches at Mount St. Augustine volcano: Nature, v. 356, no. 6371, p. 701–704.

Bock, Y., Macdonald, T., Merts, J., Bock, L, and Fayman, J., 2004, Epoch-by-Epoch™ real-time GPS positioning in high dynamics and at extended ranges: ITEA Journal of Test and Evaluation, v. 25, no. 3, p. 37–45.

Bonaccorso, A., and Davis, P.M., 1999, Models of ground deformation from vertical volcanic conduits with application to eruptions of Mount St. Helens and Mount Etna: Journal of Geophysical Research, v. 104, p. 1053–10542.

Cervelli, P.F., and Miklius, A., 2003, The shallow magmatic system of Kilauea Volcano, *in* Heliker, C., Swanson, D.A., and Takahashi, T.J., eds., The Pu'u 'O'o-Kūpaianaha eruption of Kilauea Volcano, Hawai'i: U.S. Geological Survey Professional Paper 1676, p. 149–164.

Cervelli, P.F., Fournier, T., Freymueller, J.T., and Power, J.A., 2006, Ground deformation associated with the precursory unrest and early phases of the January 2006 eruption of Augustine Volcano, Alaska: Geophysical Research Letters, v. 33, 5 p., doi:10.1027/2006GL027219.

Cervelli, P.F., Murray, M.H., Segall, P., Aoki, Y., and Kato, T., 2001, Estimating source parameters from deformation data, with an application to the March 1997 earthquake swarm off the Izu Peninsula, Japan: Journal of Geophysical Research v. 106, no. B6, p. 11217–11237.

Coombs, M.L., Bull, K.F., Vallance, J.W., Schneider, D.J., Thoms, E.E., Wessels, R.L., and McGimsey, R.G., 2010, Timing, distribution, and volume of proximal products of the 2006 eruption of Augustine Volcano, *in* Power, J.A., Coombs, M.L., and Freymueller, J.T., eds., The 2006 eruption of Augustine Volcano, Alaska: U.S. Geological Survey Professional Paper 1769 (this volume).

Dvorak, J.J. and Okamura, A.T., 1987, A hydraulic model to explain variations in summit tilt rate at Kilauea and Mauna Loa volcanoes, *in* Decker, R.W., Wright, T.L., and Stauffer, P.H., eds., Volcanism in Hawaii: U.S. Geological Survey Professional Paper 1350, p. 1281–1296.

Dzurisin, D., Lisowski, M., Poland, M.P., Sherrod, D.R., and LaHusen, R.G., 2008, Constraints and conundrums resulting from ground-deformation measurements made during the 2004–2005 dome-building eruption of Mount St. Helens, Washington, chap. 14 *of* Sherrod, D.R., Scott, W.E., and Stauffer, P.H., eds., A volcano rekindled; the renewed eruption of Mount

St. Helens, 2004–2006: U.S. Geological Survey Professional Paper 1750, p. 281–300.

Eaton, J.P., 1959, A portable water-tube tiltmeter: Seismological Society of America Bulletin, v. 49, p. 177–206.

Gerlach, T.M., McGee, K.A., and Doukas, M.P., 2008, Emission rates of CO_2, SO_2, and H_2S, scrubbing, and preeruption excess volatiles at Mount St. Helens, 2004–2005, chap. 26 in Sherrod, D.R., Scott, W.E., and Stauffer, P.H., eds., A volcano rekindled; the renewed eruption of Mount St. Helens, 2004–2006: U.S. Geological Survey Professional Paper 1750, 543–571.

Larsen, J.F., Nye, C.J., Coombs, M.L., Tilman, M., Izbekov, P., and Cameron, C., 2010, Petrology and geochemistry of the 2006 eruption of Augustine Volcano, *in* Power, J.A., Coombs, M.L., and Freymueller, J.T., eds., The 2006 eruption of Augustine Volcano, Alaska: U.S. Geological Survey Professional Paper 1769 (this volume).

Lee, C.-W., Lu, Z., Jung, H.-S., Won, J.-S., and Dzurisin, D., 2010, Surface deformation of Augustine Volcano, 1992–2005, from multiple-interferogram processing using a refined small baseline subset (SBAS) interferometric synthetic aperture radar (InSAR) approach, in Power, J.A., Coombs, M.L., and Freymueller, J.T., eds., The 2006 eruption of Augustine Volcano, Alaska: U.S. Geological Survey Professional Paper 1769 (this volume).

Lipman, P.W., Moore, J.G., and Swanson, D.A., 1981, Bulging of the north flank before the May 18 eruption—geodetic data, *in* Lipman, P.W., and Mullineaux, eds., The 1980 eruptions of Mount St. Helens, Washington: U.S. Geological Survey Professional Paper 1250, p. 143–156.

Lisowski, M., Dzurisin, D., Denlinger, R.P., and Iwatsubo, E.Y., 2008, Analysis of GPS-measured deformation associated with the 2004–2006 dome-building eruption of Mount St. Helens, Washington, chap. 15 *of* Sherrod, D.R., Scott, W.E., and Stauffer, P.H., eds., A volcano rekindled; the renewed eruption of Mount St. Helens, 2004–2006: U.S. Geological Survey Professional Paper 1750, p. 301–333.

Mastin, L.G., Roeloffs, E., Beeler, N.M., and Quick, J.E., 2008, Constraints on the size, overpressure, and volatile content of the Mount St. Helens magma system from geodetic and dome-growth measurements during the 2004–2006 eruption, chap. 22 of Sherrod, D.R., Scott, W.E., and Stauffer, P.H., eds., A Volcano Rekindled; the renewed eruption of Mount St. Helens, 2004–2006. U.S. Geological Survey Professional Paper 1750, p. 461–492.

McGee, K.A., Doukas, M.P., McGimsey, R.G., Neal, C.A., and Wessels, R.L., 2010, Emission of SO_2, CO_2, and H_2S from Augustine Volcano, 1995–2006, in Power, J.A., Coombs, M.L., and Freymueller, J.T., eds., The 2006 eruption of Augustine Volcano, Alaska: U.S. Geological Survey Professional Paper 1769 (this volume).

McLean, H., 1979, Sandstone petrology; Upper Jurassic Naknek Formation of the Alaska Peninsula and coeval rocks on the Bering Shelf: Journal of Sedimentary Petrology, v. 49, p. 1263–1267.

Mogi, K., 1958, Relations between the eruptions of various volcanoes and the deformations of the ground surfaces around them: Univerity of Tokyo, Earthquake Research Institute Bulletin, v. 36, p. 111–123.

Moran, S.C., Malone, SD., Qamar, A.I., Thelen, W., Wright, A.K.,and Caplan-Auerbach, J., 2008, Seismicity associated with renewed dome-building at Mount St. Helens, 2004–2005, in Sherrod, D.R., Scott, W.E., and Stauffer, P.H., eds, A volcano rekindled; the renewed eruption of Mount St. Helens, 2004–2006: U.S. Geological Survey Professional Paper 1750, p. 27–60.

Neal, C.A., Murray, T.L., Power, J.A, Adleman, J.N., Whitmore, P.M., and Osiensky, J.M., 2010, Hazard information management, interagency coordination, and impacts of the 2005–2006 eruption of Augustine Volcano, *in* Power, J.A., Coombs, M.L., and Freymueller, J.T., eds., The 2006 eruption of Augustine Volcano, Alaska: U.S. Geological Survey Professional Paper 1769 (this volume).

Newman, A.V., Dixon, T.H., and Gourmelen, N., 2006, A four-dimensional viscoelastic deformation model for Long Valley Caldera, California, between 1995 and 2005: Journal of Volcanology and Geothermal Research, v. 150, p. 244–269.

Niell, A.E., 1996, Global mapping functions for the atmosphere delay at radio wavelengths: Journal of Geophysical Research v. 101, no. B2, p. 3227–3246.

Okada, Y., 1985, Surface deformation due to shear and tensile faults in a half-space: Seismological Society of America Bulletin, v. 75, p. 1135–1154.

Owen, S., Segall, P., Lisowski, M., Miklius, A., Murray, M., Bevis, M., and Foster, J., 2000, The January 30, 1997 eruptive event on Kilauea Volcano, Hawaii, as monitored by continuous GPS: Journal of Geophysical Research, v. 27, no. 17, p. 2757–2760.

Pauk, B.A., Power, J.A., Lisowski, M., Dzurisin, D., Iwatsubo, E.Y., and Melbourne, T., 2001, Global Positioning System (GPS) survey of Augustine Volcano, Alaska, August 3–8, 2000; data processing, geodetic coordinates and comparison with prior geodetic surveys: U.S. Geological Survey Open-File Report 01-0099, 20 p.

Pauk, B.A., Jackson, M., Feaux, K., Mencin, D., and Bohnenstiehl, K., 2010, The Plate Boundary Observatory permanent global positioning system network on Augustine Volcano before and after the 2006 eruption, *in* Power, J.A., Coombs, M.L., and Freymueller, J.T., eds., The 2006 eruption of Augustine Volcano, Alaska: U.S. Geological Survey Professional Paper 1769 (this volume).

Power, J.A., and Iwatsubo, E.Y. 1998, Measurements of slope distances and zenith angles at Augustine Volcano, Alaska, 1986, 1988, and 1989: U.S. Geological Survey Open-File Report 98-0145, 17 p.

Power, J.A., and Lalla, D.J., 2010, Seismic observations of Augustine Volcano, 1970–2007, *in* Power, J.A., Coombs, M.L., and Freymueller, J.T., eds., The 2006 eruption of Augustine Volcano, Alaska: U.S. Geological Survey Professional Paper 1769 (this volume).

Roman, D.C., Cashman, K.V., Gardner, C.A., Wallace, P., and Donovan, J., 2005, Storage and interaction of compositionally heterogeneous magmas from the 1986 eruption of Augustine Volcano, Alaska: Bulletin of Volcanology, v. 68, p. 240–254.

Scott, W.E., Sherrod, D.R., and Gardner, C.A., 2008, Overview of the 2004 to 2006, and continuing, eruption of Mount St. Helens, Washington, chap. 1 *of* Sherrod, D.R., Scott, W.E., and Stauffer, P.H., eds., A volcano rekindled; the renewed eruption of Mount St. Helens, 2004–2006: U.S. Geological Survey Professional Paper 1750, p. 3–26.

Segall, P., 2010, Earthquake and Volcano Deformation, Princeton, N.J., Princeton University Press, 458 p.

Tappen, C.M., Webster, J.D., Mandeville, C.W., and Roderick, D., 2009, Petrology and geochemistry of ca. 2100–1000 a.B.P. magmas of Augustine volcano, Alaska, based on analysis of prehistoric pumiceuous tephra: Journal of Volcanology and Geothermal Research, v. 183, p. 42–62.

Wallace, K.L., Neal, C.A., and McGimsey, R.G., 2010, Timing, distribution, and character of tephra fall from the 2005–2006 eruption of Augustine Volcano, *in* Power, J.A., Coombs, M.L., and Freymueller, J.T., eds., The 2006 eruption of Augustine Volcano, Alaska: U.S. Geological Survey Professional Paper 1769 (this volume).

Webster, J.D., Mandeville, C.W., Goldoff, B., Coombs, M.L., and Tappen, C., 2010, Augustine Volcano—The influence of volatile components in magmas erupted A.D. 2006 to 2,100 years before present, *in* Power, J.A., Coombs, M.L., and Freymueller, J.T., eds., The 2006 eruption of Augustine Volcano, Alaska: U.S. Geological Survey Professional Paper 1769 (this volume).

Wessels, R.L., Coombs, M.L., Schneider, D.J., Dehn, J., and Ramsey, M.S., 2010, High-resolution satellite and airborne thermal infrared imaging of the 2006 eruption of Augustine Volcano, in Power, J.A., Coombs, M.L., and Freymueller, J.T., eds., The 2006 eruption of Augustine Volcano, Alaska: U.S. Geological Survey Professional Paper 1769 (this volume).

Williams, C.A., and Wadge, G., 1998, The effects of topography on magma chamber deformation models; application to Mt. Etna and radar interferometry: Geophysical Research Letters, v. 25, p. 1549–1552.

Yang, X., Davis, P.M., and Dieterich, J.H., 1988, Deformation from inflation of a dipping finite prolate spheroid in an elastic half-space as a model for volcanic stressing: Journal of Geophysical Research, v. 93, no. B5, p. 4249–4258.

Zumberge, J.F., Heflin, M.B., Jefferson, D.C., Watkins, M.M., and Webb, F.H., 1997, Precise point positioning for the efficient and robust analysis of GPS data from large networks: Journal of Geophysical Research, v. 102, no. B3, p. 5005–5017.

The 2006 Eruption of Augustine Volcano, Alaska
Power, J.A., Coombs, M.L., and Freymueller, J.T., editors
U.S. Geological Survey Professional Paper 1769

Chapter 18

Surface Deformation of Augustine Volcano, 1992–2005, from Multiple-Interferogram Processing Using a Refined Small Baseline Subset (SBAS) Interferometric Synthetic Aperture Radar (InSAR) Approach

By Chang-Wook Lee[1], Zhong Lu[2], Hyung-Sup Jung[3], Joong-Sun Won[4], and Daniel Dzurisin[5]

Abstract

Augustine Volcano is an active stratovolcano located in southwestern Cook Inlet, about 280 kilometers southwest of Anchorage, Alaska. The volcano produced six significant explosive eruptions between 1812 and 1986. Augustine eruptions typically have an explosive onset followed by dome building. The most recent eruption began on January 11, 2006. We applied the small baseline subset (SBAS) interferometric synthetic aperture radar (InSAR) technique to measure ground surface deformation during 1992–2005 with the use of European Remote Sensing Satellites 1 and 2 (ERS–1 and ERS–2) radar imagery. Through a multiple-interferogram approach, atmospheric delay artifacts, which hinder conventional InSAR measurements, are significantly reduced by spatial and temporal filtering. This allows us to retrieve time-series deformation over coherent points at millimeter-scale accuracy. The deformation results from two independent satellite tracks agree with each other, suggesting 2 to 8 cm wholesale uplift of Augustine Volcano from 1992 to 2005. Global Positioning System (GPS) data acquired in September 2004 and October 2005 confirm the SBAS InSAR results. A preliminary model consisting of a contracting source at 2 to 4 km depth and an inflating source at 7 to 12 km depth fits the observed deformation reasonably well. We interpret the deeper source as a long-term magma storage zone and the shallower source as a subsidiary reservoir that was tapped during the 2006 eruption. The shallow source corresponds approximately to the location of the volcano-tectonic earthquakes that preceded and followed the 1976 and 2006 eruptions, respectively.

Introduction

Mapping volcanic deformation between eruptions can provide important clues to the magma plumbing system and magma supply rate (Dzurisin, 2007). Ground-based techniques, including Global Positioning System (GPS) observations, leveling, and tiltmeters, can measure subtle deformation with an accuracy of a few millimeters. Even though these ground-based techniques can provide accurate point-to-point deformation measurements, they are relatively expensive, logistically challenging, and often inadequate to characterize complex deformation patterns that sometimes are associated with eruptions (Dzurisin, 2007). Interferometric synthetic aperture radar (InSAR) is a satellite-based technique for mapping large-area surface deformation. InSAR has become an important tool for studying volcanoes in Alaska (Lu and others, 2007) and around the world (Zebker and others, 2000). In theory, InSAR can measure relative surface displacements with an accuracy of a few millimeters (Gabriel and others, 1989). In reality, however, atmospheric delay noise and other

---

[1] ASRC Research and Technology Solutions, contractor to USGS, 1300 SE Cardinal Court, Vancouver, WA 98683.

[2] U.S. Geological Survey, EROS Center and Cascades Volcano Observatory, 1300 SE Cardinal Court, Vancouver, WA 98683-9589.

[3] Department of Geoinfomatics, The University of Seoul, 90 Jeonnong-dong, Dongdaemun-gu, Seoul 130-743, Korea.

[4] Department of Earth System Sciences, Yonsei University, 134 Shinchon-dong, Seodaemun-gu, Seoul, 120-749, Korea.

[5] U.S. Geological Survey, Cascades Volcano Observatory, 1300 SE Cardinal Court, Vancouver, WA 98683-9589.

artifacts reduce the accuracy obtainable with InSAR to a few centimeters (Zebker and others, 1997).

Geodetic measurements began at Augustine Volcano starting in 1986 (Power and Iwatsubo, 1998), and GPS campaign surveys were conducted repeatedly in the early 1990s and in 2000 (Pauk and others, 2001). An initial analysis did not detect any surface deformation that could be attributed to magmatic activity for the period from 1988 to 2000 (Pauk and others, 2001). The campaign GPS data were reprocessed in late 2005 (J. Freymueller, written commun., December 14, 2005). Results indicated that a shallow source (depth less than a few kilometers) beneath the volcano's summit might have deflated at a rate of less than 5 mm/yr during 1988–2000. Five continuous GPS (CGPS) stations were established in September 2004 by the EarthScope Plate Boundary Observatory (Pauk and others, this volume), and detected shallow inflation of about 2 mm/month from June 2005 to January 2006 before the 2006 eruption (Cervelli and others, 2006).

Early results based on a limited number of InSAR images indicated subsidence of 1986 pyroclastic flows on the north flank of Augustine Volcano (Lu and others, 2003). Masterlark and others (2006) constructed a finite element model that simulated post-eruptive thermoelastic contraction of the initially hot and geometrically complex 1986 pyroclastic flow deposits. By combining a 1992–1993 InSAR image, the finite element model, and an adaptive mesh algorithm to iteratively optimize the geometry of the deposit, Masterlark and others (2006) determined an initial excess temperature for the pyroclastic flow unit of 640ºC and an average thickness of 9.3 m. Lee and others (2008) systematically processed all the available InSAR images for Augustine Volcano acquired during 1992–2005 and concluded that (1) typical summer-to-summer InSAR images maintain good coherence for only about 2 years, probably because most of the volcano is mantled by pyroclastic flows and other loose materials that are easily erodible and compactable; (2) atmospheric delay anomalies typically reached 2 to 3 cm in individual interferograms; and (3) stacking multiple InSAR images revealed no significant, centimeter-scale volcano-wide deformation during 1992–2005.

The first obstacle that prevented us from reaching millimeter-scale accuracy for InSAR measurements at Augustine Volcano is atmospheric path-delay anomalies, which are caused mainly by variation in the water vapor content of the atmosphere. Studies have shown that the apparent range change caused by atmospheric delays over Augustine (Lee and others, 2008) and other Aleutian volcanoes (Lu and others, 2007) can be as large as 10 cm. Averaging multiple InSAR images tends to reduce atmospheric noise, because water vapor patterns generally are not spatially correlated over time intervals spanned by interferograms. Nevertheless, the effectiveness of InSAR for monitoring Aleutian volcanoes has been hampered by the typical presence of large atmospheric path-delay anomalies, and theoretical accuracy of 2 to 3 mm for InSAR has not been achieved. A second factor affecting InSAR measurement at Augustine is the loss of InSAR coherence for InSAR images that span more than 2 years. This is because much of the volcano is covered by pyroclastic flows that do not maintain good coherence for C-band InSAR measurements.

Two techniques have been proposed to conduct time-series analysis of multiple interferograms to reduce atmospheric noise: (1) persistent scatterer InSAR (PSInSAR) (Ferretti and others, 2001) and (2) small baseline subset (SBAS) InSAR (Berardino and others, 2002). For PSInSAR, a single master image is used to construct all the interferograms for time-series analysis. This approach did not yield useful results for Augustine Volcano, owing to the problem with coherence loss that was mentioned previously. Instead, we used SBAS InSAR, which utilizes several master images to form interferograms with small baselines that span relatively short time intervals (and therefore tend to maintain coherence).

For this paper, we used all suitable SAR images of Augustine Volcano that were acquired from 1992 to 2005. Our objective was to detect and measure any subtle, small-scale deformation that might have occurred during the time of our investigation. We used SAR data from two independent satellite tracks to intercompare InSAR-derived deformation measurements. In addition, we compared InSAR measurements with continuous GPS measurements for the period September 2004 to October 2005. Finally, we used a two-source model to interpret the observed deformation pattern.

Historical Eruption of Augustine Volcano

Augustine Volcano is a 1,260-m-high and 90-km^2 island stratovolcano in the southwestern part of Cook Inlet, about 280 km southwest of Anchorage, Alaska (fig. 1). Augustine Island formed on Jurassic and Cretaceous sedimentary strata overlain by granitoid glacial erratics and volcanic hyaloclastites (Miller and others, 1998). Augustine Volcano is one of the youngest and most active volcanoes in Cook Inlet (Begét and Kowalik, 2006), with explosive eruptions in 1812, 1883, 1935, 1963, 1976, 1986, and most recently 2006. The most violent of these eruptions was in 1883, when a debris avalanche generated a small tsunami in Cook Inlet (Miller and others, 1998). This tsunami struck the eastern and western coasts of the southern part of Cook Inlet with 6 to 8 m waves (Begét and Kowalik, 2006). Ash clouds from the 1976 eruption were observed in eastern North America and drifted across the Atlantic Ocean (Kienle and Shaw, 1979). Most eruptions of Augustine began with an initial series of vent-clearing explosions with pyroclastic flows, surges, and lahars on the volcano flanks, followed by the extrusion of andesitic lava from the volcano's summit (Waythomas and Waitt, 1998). Proximal eruption hazards include pyroclastic flows and surges, debris avalanches, lahars, ballistics, and ash fallout. Tsunamis generated by debris avalanches can reach the Alaska mainland. Volcanic ash that can drift great distances poses a threat to airliners and to people with respiratory problems (Waythomas and Waitt, 1998).

InSAR Analysis

Data and Preprocessing

For our analysis, we chose SAR data that were acquired from two adjacent tracks by European Remote Sensing Satellites 1 and 2 (ERS–1 and ERS–2). From 1992 to 2005, there were 27 and 25 descending scenes acquired from tracks 229 and 501, respectively. To apply the SBAS InSAR algorithm, 25 and 27 InSAR images with perpendicular baselines of less than about 300 m were created. These were distributed in five and four small-baseline subsets as shown in figures 2*A* and 2*B*, respectively. As a result of the difference in satellite positions, SAR images between adjacent tracks cannot be combined to form interferograms. All the interferograms were obtained by using a complex multilook operation, with 2 looks in the range direction and 10 looks in the azimuth direction, resulting in a pixel dimension of about 40 m by 40 m. Topographic phase contributions in the original interferograms were removed by using the 1-arc-second Shuttle Radar Topography Mission (SRTM) digital elevation model (DEM; Farr and others, 2007).

Introduction to the SBAS InSAR Algorithm

The SBAS InSAR algorithm was recently proposed and demonstrated by Berardino and others (2002) as a means to mitigate atmospheric artifacts and topographic errors in time-sequential interferograms, and thus to obtain time-series deformation information. The algorithm uses only interferograms with small baselines that overlap in time in order to reduce spatial decorrelation.

The phase ($\Delta\phi$) of each interferogram is defined by

$$\Delta\phi(x,r) \approx \frac{4\pi}{\lambda}\Delta d(x,r) + \frac{4\pi}{\lambda}\frac{B_{\perp}}{r\sin\theta}\Delta z(x,r) + \Delta\phi_{atmo}(x,r) + \Delta\phi_{n}(x,r), \tag{1}$$

where x and r are the azimuth and slant-range pixel coordinates, λ is the radar wavelength, Δd is the surface displacement in the radar look direction, $B_{\perp}$ is the perpendicular baseline, θ is the SAR look angle, Δz is the topographic error, $\Delta\phi_{atmo}$ is the atmospheric phase-delay artifact, and $\Delta\phi_{n}$ is the phase due to other noise sources (Berardino and others, 2002).

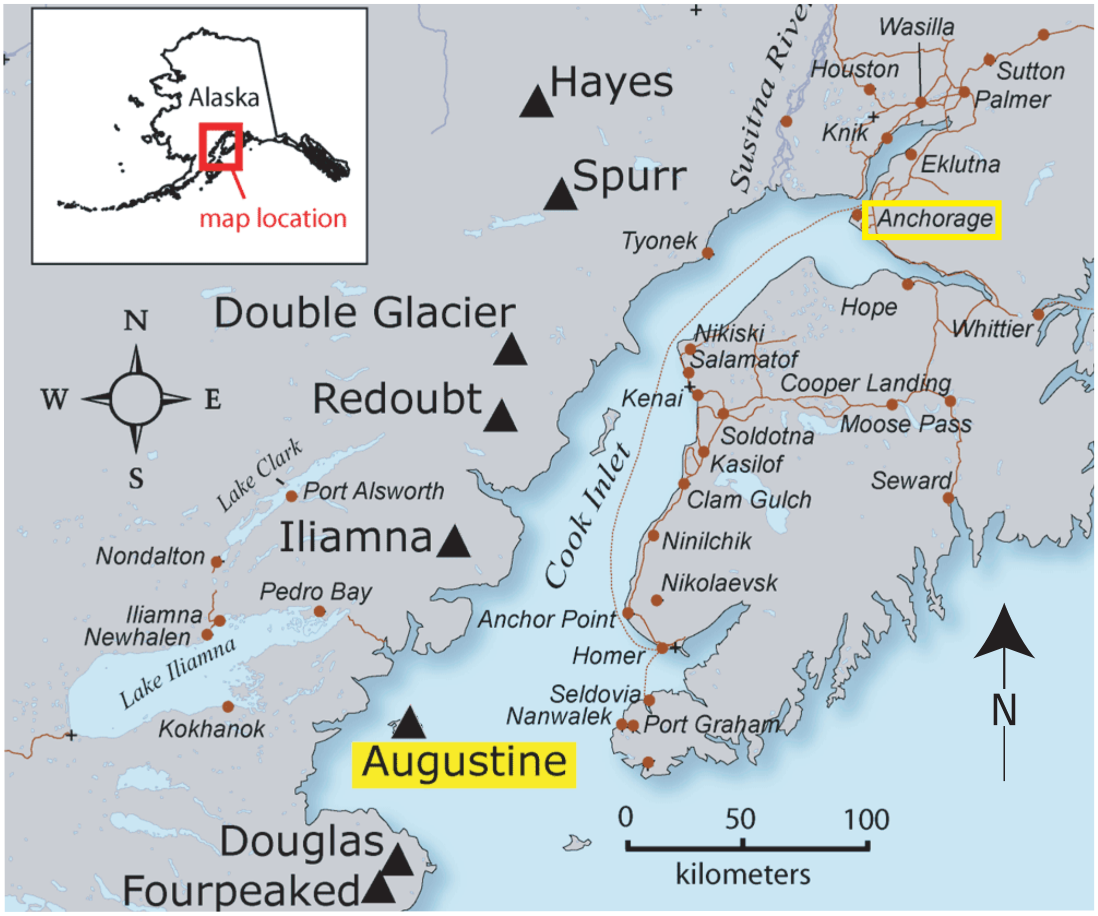

Figure 1. Location of Augustine Island in the southwestern part of Cook Inlet, Alaska. Triangles, volcanoes.

To achieve deformation time-series information from multiple interferograms, the SBAS algorithm estimates the mean deformation rate and the topographic error. The atmospheric artifacts are mitigated through temporal high-pass and spatial low-pass filtering of interferograms after the mean deformation rates have been removed. Because the interferograms are not adjacently linked (there may be temporal overlap or underlap between them), SBAS InSAR uses the singular value decomposition (SVD) approach based on a minimum-norm criterion of the deformation rate to derive time-series deformation measurements.

Although this algorithm is very effective for measuring time-series deformation, the suppression of errors caused by temporal decorrelation and other noise effects is not properly addressed. Linear deformation rates estimated by using interferograms having unwrapping errors commonly lead to misestimates of the actual deformation history. Estimates of atmospheric artifacts and topographic errors based on the assumption of linear deformation rate during the periods spanned by individual interferograms can further detract from the retrieval of accurate time-series deformation measurements. Moreover, the atmospheric artifact and orbital error at the reference point (a pixel location used to reference interferogram phase values at other pixels) have not been properly addressed, which can affect the deformation measurements.

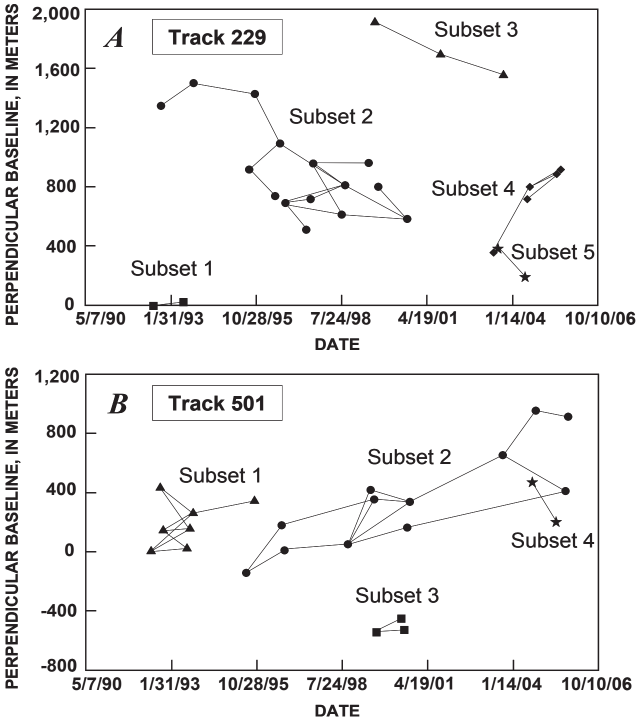

Figure 2. Perpendicular baselines used for small baseline subset (SBAS) interferometric synthetic aperture radar (InSAR) processing at Augustine Volcano, Alaska. *A*, Five different small baseline subsets from satellite track 229 were used for SBAS InSAR processing. *B,* Four different small baseline subsets from satellite track 501 were used for SBAS InSAR processing.

Refined SBAS InSAR Processing

Our refined SBAS InSAR algorithm improves estimates of time-series deformation in four respects. First, we correct phase unwrapping errors by distinguishing between high-quality (HQ) images in which no unwrapping errors could be found and low-quality (LQ) ones where phase jumps due to unwrapping errors are obvious. Second, we refine estimates of atmospheric artifacts, topographic errors, and time-series deformation measurements through an iteration procedure. Third, we further mitigate the temporal noise by the finite difference smoothing approach (Schmidt and Burgmann, 2003). Finally, we implement procedures to correct any possible phase bias at the reference point due to orbital and atmospheric phase artifacts. Specifically, the reference phase correction is based on the assumption that the mean of the unwrapped residual interferogram is approximately zero as given by

$$\frac{1}{N_{az}N_{rg}}\sum_{i=1}^{N_{az}}\sum_{j=1}^{N_{rg}}\left[\frac{4\pi}{\lambda}(\Delta d-\Delta\bar{d})+\frac{4\pi}{\lambda}\frac{B_{\perp}}{r\sin\theta}(\Delta z-\Delta\bar{z})+(\Delta\phi_{atmo}-\Delta\bar{\phi}_{atmo})+\Delta\phi_{n}\right]\approx 0, \tag{2}$$

where N_{az} and N_{rg} are total numbers of azimuth and range pixels; i and j are azimuth and range pixel coordinates; and $\Delta\bar{d}$, $\Delta\bar{z}$, and $\Delta\bar{\phi}_{atmo}$ are the estimated values of surface displacement, topographic error, and atmospheric phase delay. Equation 2 is used to correct phase values in each interferogram. The correct reference phase values should be such that the left term in equation 2 accurately represents the noise in a given interferogram (the residual phase values of the interferogram should be approximately zero after spatial averaging).

Figure 3 shows a block diagram of the refined SBAS InSAR processing algorithm. All the interferograms are classified as HQ or LQ, and the mean deformation rate ($\bar{v}$) is estimated from the HQ interferograms by using the relation

$$\bar{v}(x,r)=\frac{\lambda}{4\pi}\frac{\sum_{k=1}^{N_{hq}}\Delta\phi_{k}(x,r)}{\sum_{k=1}^{N_{hq}}\Delta t_{k}}\quad, \tag{3}$$

where k is the kth interferogram, N_{hq} is the total number of HQ interferograms and Δt is the time difference between master and slave images. This approach is better than deriving the mean deformation rate from linear regression of the deformation rates estimated from all interferograms, because atmospheric and orbital artifacts are, to a certain degree, mitigated

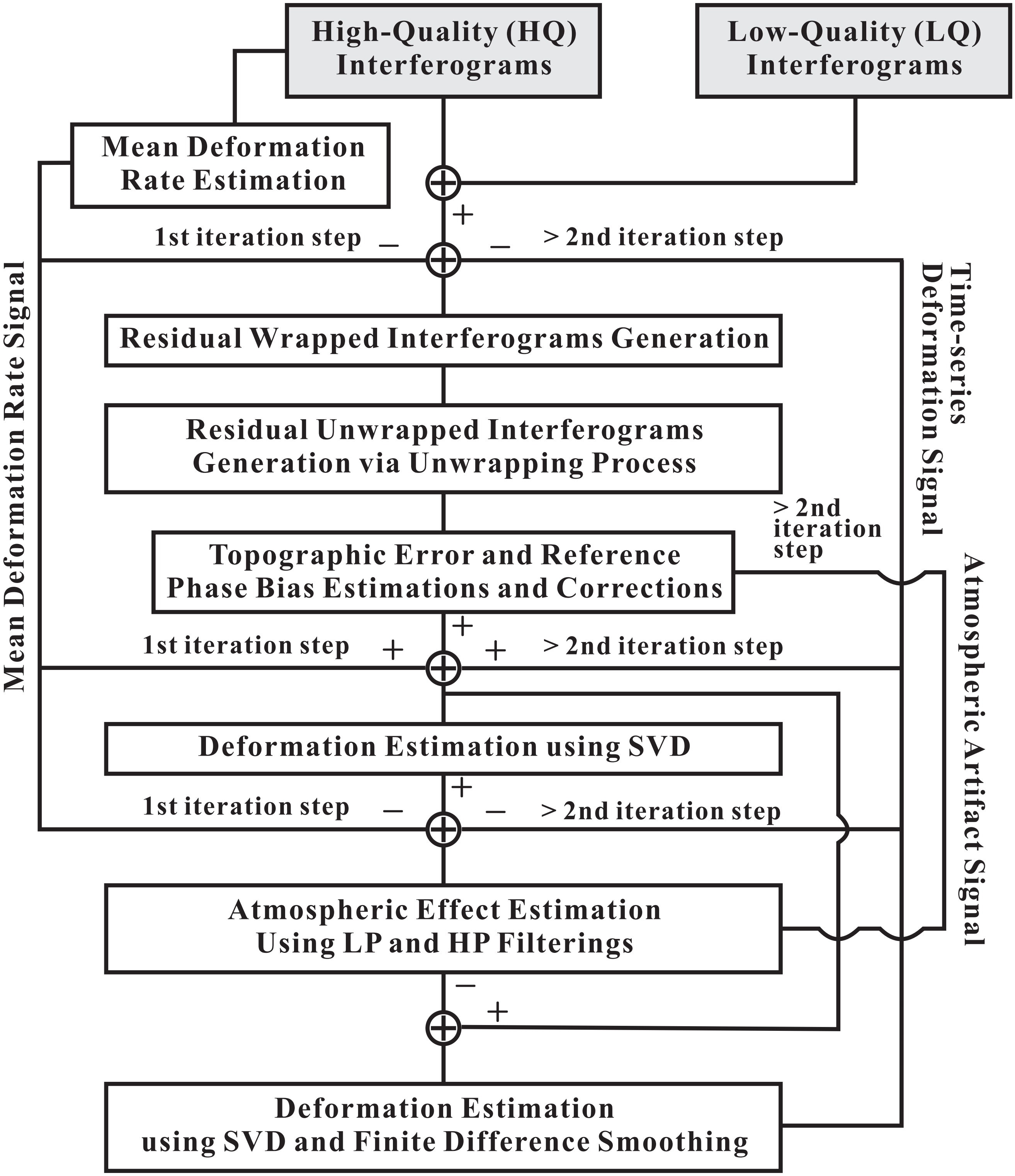

Figure 3. Block diagram of the refined small baseline subset (SBAS) interferometric synthetic aperture radar (InSAR) processing algorithm.

by eliminating LQ interferograms from the computation. New, wrapped residual interferograms are formed by subtracting the estimated linear deformation from each interferogram on a pixel-by-pixel basis. The residual interferograms are reunwrapped to create new unwrapped interferograms. This step essentially removes phase unwrapping errors from the LQ interferograms, because the fringe rates in the residual interferograms are much lower than those in the original interferograms.

The phase values in residual interferograms, ϕ_r, include topographic errors that depend on the perpendicular baselines. The topographic errors are estimated from all the residual interferograms as follows:

$$\Delta z(x,r) = \frac{\lambda}{4\pi} r \sin\theta \frac{\sum_{k=1}^{N_i} \left(\Delta\phi_r\right)_k (x,r)}{\sum_{k=1}^{N_i} \left(B_\perp\right)_k} \quad , \tag{4}$$

where N_i is the total number of interferograms. The residual interferograms after removing the topographic errors are defined by

$$\left(\Delta\phi_{rt}\right)_k (i,j) = \left(\Delta\phi_r\right)_i \ (i,j) - \frac{4\pi}{\lambda} \frac{\left(B_\perp\right)_k}{r\sin\theta} \Delta z(i,j)$$

$$\text{for } k = 1, 2, \ldots N_i \ , \tag{5}$$

where $(\Delta\phi_{rt})$ k is the k th residual interferogram corrected for topographic error, and the reference phase bias (ϕ_{ref}) for the k th interferogram is estimated from coherent pixels as follows:

$$\left(\phi_{ref}\right)_k = \frac{1}{N_{az}\ N_{rg}} \sum_{i=1}^{N_{az}} \sum_{j=1}^{N_{rg}} \left(\Delta\phi_{rt}\right)_k (i,j)$$

$$\text{for } k = 1, 2, \ldots N_i \ . \tag{6}$$

Next, the topography-corrected interferogram phase, $\Delta\phi_{rt}$ in equation 5, is further corrected by using the reference phase bias, ϕ_{ref} in equation 6. At this stage, the estimated linear deformation from equation 3 is added back to the topography-corrected interferograms, in which the reference phase bias has also been corrected by using equation 6. We call the resulting interferograms "corrected interferograms."

Our next objective is to estimate and remove atmospheric artifacts. To achieve this, we estimate the time-series deformation histories at each coherent pixel by using the SVD operation, and remove them from the corrected interferograms. The atmospheric artifacts are then removed by temporal high-pass (HP) and spatial low-pass (LP) filtering operations, because the atmospheric artifacts are spatially correlated and temporally random. After the atmospheric contributions are removed in this way, we recompute the time-series deformation by simultaneously applying the SVD approach and the finite difference smoothing method (Schmidt and Burgmann, 2003) in order to further suppress the noise contribution. This completes the first iteration of our refined SBAS InSAR processing, and results in time-series deformation estimates at each coherent pixel.

Parameter optimization and estimation in the above implementation of SBAS InSAR processing are based on the assumption of the linear deformation (equation 3). To get beyond the assumption of linearity, all processing steps are reapplied to the interferograms by using the estimated time-series deformation from the first SBAS InSAR iteration instead of the linear deformation estimated from equation 3. Our second iteration of SBAS InSAR processing corrects the topographic error, the reference phase bias, and the atmospheric artifact. Furthermore, the reference phase correction in equation 6 is refined by taking into account the estimated atmospheric artifact phase from the first iteration:

$$\left(\phi_{ref}\right)_k = \frac{1}{N_{az}\ N_{rg}} \sum_{i=1}^{N_{az}} \sum_{j=1}^{N_{rg}}$$

$$\left[\left(\Delta\phi_{rt}\right)_k \ (i,j) - \left(\Delta\overline{\phi}_{atmo}\right)_k \ (i,j)\right]$$

$$\text{for } k = 1, 2, \ldots N_i \ . \tag{7}$$

Refined SBAS InSAR Applied to Augustine Volcano

We investigated surface deformation of Augustine Volcano from 1992 to 2005 using a refined multiple-interferogram processing procedure. Our SBAS InSAR processing improves the original SBAS InSAR algorithm in the following aspects:

1. We divide all InSAR interferograms into HQ and LQ interferograms, and estimate the initial mean deformation rate by using the HQ interferograms only. This is critical because the topographic error, the atmospheric contribution, and the residual phase estimate largely depend on the estimated mean deformation rate. If the mean deformation rate is estimated poorly, the measured time-series deformation will be distorted. For this reason, the initial mean deformation rate is estimated by using only high-quality interferograms in which phase coherence is good and no phase unwrapping error exists.
2. The mean deformation rate is calculated under the assumption that the deformation rate is constant. Any departure from this assumption (such as time-variant deformation) will introduce significant errors in estimating the atmospheric contribution and the topographic error. To overcome this drawback in the original SBAS InSAR algorithm, an iterative approach was applied to our refined SBAS InSAR algorithm. In the first step, our SBAS InSAR algorithm estimates the atmospheric

contribution and the topographic error by using the initial mean deformation rate, and then calculates the time-series deformation. In the second step, our algorithm estimates the atmospheric contribution and the topographic error by using the time-series deformation from the first iteration instead of the initial mean deformation rate. This approach efficiently separates the atmospheric contribution and the topographic error from interferograms and improves the time-series deformation measurement. The original SBAS InSAR algorithm does not include the iteration step

3. We have incorporated the finite-difference noise compression approach (Schmidt and Burgmann, 2003) into the original SBAS InSAR algorithm.

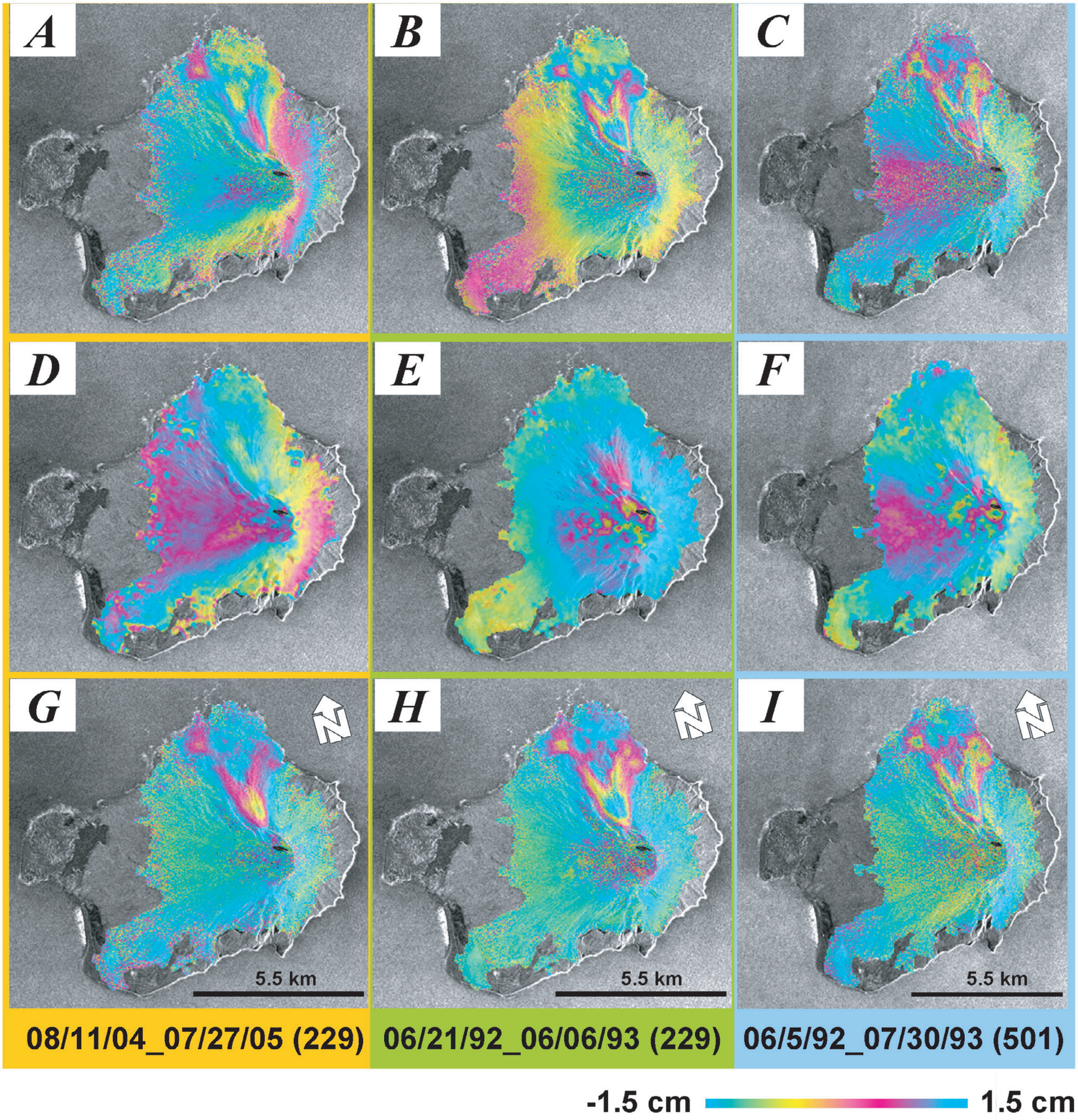

Figure 4. *A, B,* and *C,* Unwrapped interferograms of Augustine Volcano before small baseline subset (SBAS) interferometric synthetic aperture radar (InSAR) processing. *D, E,* and *F,* Atmospheric effects modeled using spatial low-pass filtering and temporal high-pass filtering. *G, H,* and *I,* Refined interferograms after removing atmospheric effects.

4. The reference phase correction procedure is a significant improvement in our refined SBAS InSAR algorithm. The reference phase is refined by several iteration steps. The initial reference phase correction is applied to the unwrapped residual interferograms. The correction is performed by removing the mean of the unwrapped residual interferograms and removing the bias caused by the atmospheric contribution. The initial phase correction can be slightly biased, but the bias is further corrected through iterations while the estimates of the atmospheric contribution and the topographic error are refined.

We applied the refined SBAS InSAR processing algorithm to 25 and 27 interferograms from satellite tracks 229 and 501, respectively. Among interferograms from track 229, there were 16 classified as HQ and 9 as LQ on the basis of the amount of phase unwrapping error. For track 501, there were 17 and 10 interferograms classified as HQ and LQ, respectively. A point near GPS station P2 (fig. 5) was selected as an initial reference point for SBAS InSAR processing.

Our processing procedures are briefly summarized here. During the first iteration of SBAS InSAR processing, unwrapped interferograms are corrected for the phase value at the reference point and the mean deformation rates are estimated in all coherent pixels from the HQ interferograms by using equation 3. The estimated mean deformation rates are then removed from all original wrapped interferograms (both HQ and LQ ones) to produce new wrapped residual interferograms. Then the phase unwrapping procedure is applied to the wrapped residual interferograms. We then estimate and remove topographic errors from the residual interferograms by using equation 4 and correct the reference phase bias by using equation 6. The corrected residual phase values are restored by adding back the linear deformation phase, and the initial time-series surface deformation histories are estimated from all interferograms by using the SVD approach. Spatial low-pass filtering and temporal high-pass filtering are then applied to estimate atmospheric artifacts. After the phase values due to the atmospheric contribution are removed from interferograms, the SVD approach and the finite difference smoothing method are applied simultaneously to further suppress the noise contribution. During the second iteration of SBAS InSAR processing, all processing steps are reapplied using the estimated time-series deformation histories from the first iteration. These final time-series deformation measurements are improved through iteratively refining the topographic error, the reference phase bias, and the atmospheric artifact.

Figure 4 shows three sets of interferograms, demonstrating the effectiveness of our refined SBAS InSAR algorithm in reducing atmospheric artifacts. Figures 4*A*–4*C* are three original InSAR images in which atmospheric anomalies amount to 3 to 5 cm.figures 4*D*–4*F* are primarily atmospheric artifacts modeled using spatial low-pass filtering and temporal high-pass filtering of multiple InSAR images. Figures 4*G*–4*I* are refined InSAR images in which atmospheric artifacts are mostly removed.

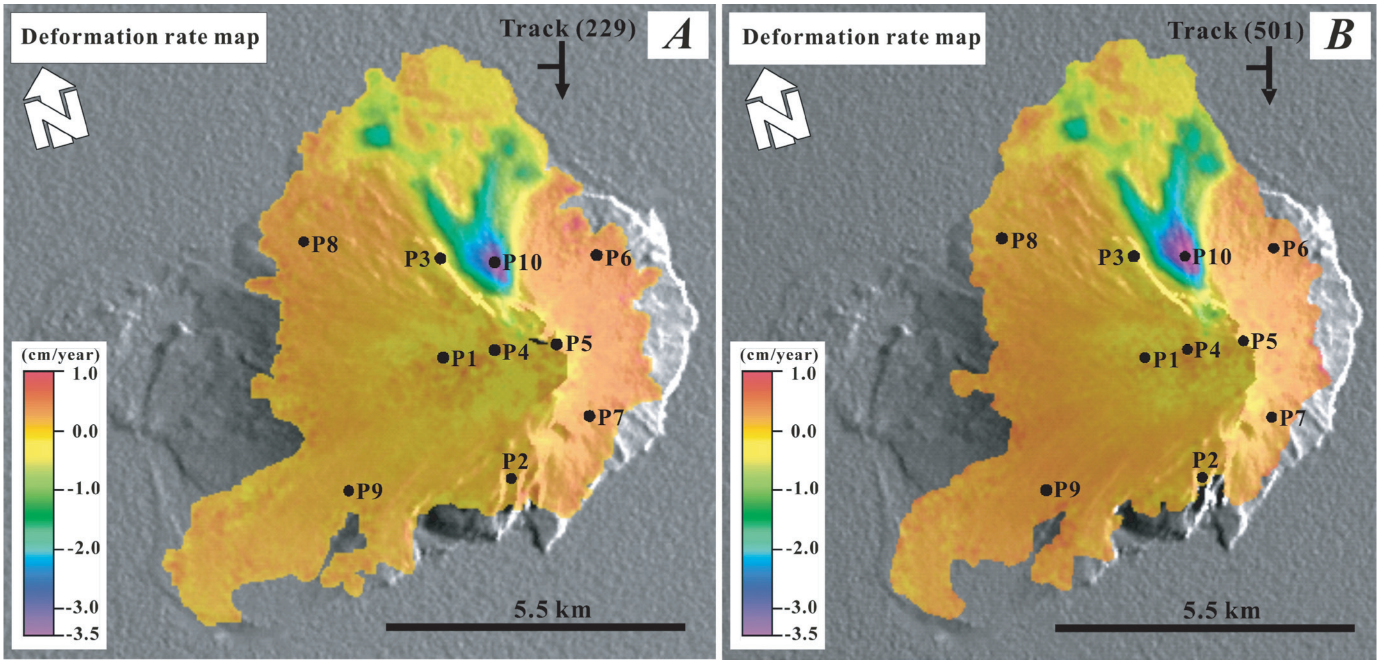

Figure 5. Maps of averaged deformation rate for Augustine Volcano from the refined small baseline subset (SBAS) technique for the period 1992–2005. *A,* Satellite track 229. *B,* Satellite track 501. Results from two independent tracks show similar results. Largest displacements are associated with subsidence of 1986 pyroclastic flow deposits in upper right quadrants of the maps.

Using our SBAS InSAR processing procedure, we conducted time-series analysis for interferograms from two independent satellite tracks: 229 and 501. We do not have other time-series deformation measurements during most of the time of investigation to compare with our results, so we compared results from two independent tracks for quality assurance. Figures 5*A* and 5*B* show mean deformation rate maps for Augustine Volcano from 1992 to 2005 that were created by using the refined SBAS InSAR technique. The mean deformation rates from the two independent tracks agree with each other well (figs. 5*A* and 5*B*). In general, we observe a wholesale uplift of Augustine Volcano, with slightly more uplift on the lower flanks.

Next, we show time-series deformation for several locations across the island. Figure 6 shows the corresponding time-series surface deformation histories at each point from tracks 229 and 501. Figures 6*A*–6*D* show surface displacement (uplift) of 4 to 6 cm for the lower flanks of Augustine

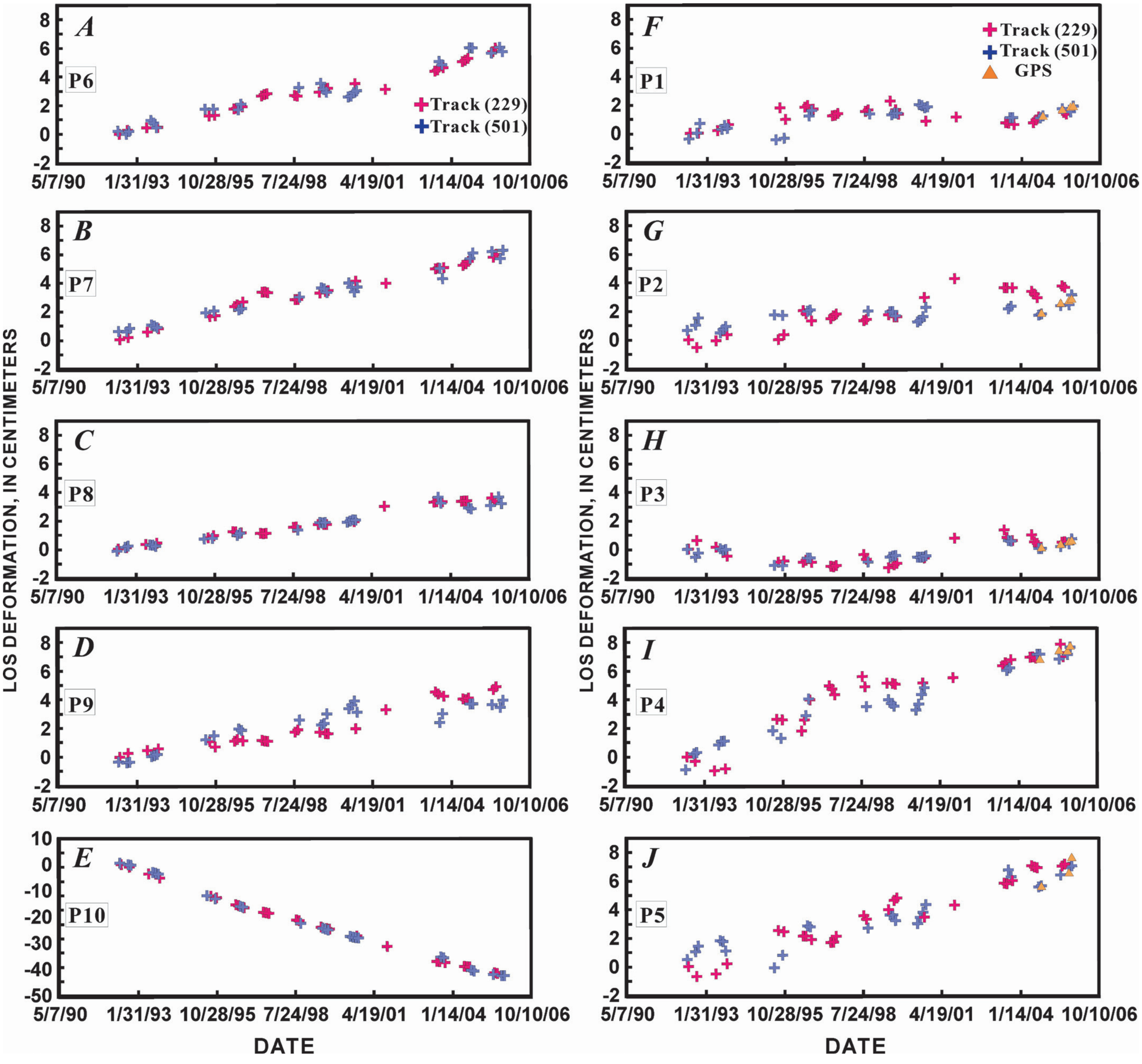

Figure 6. Line-of-sight (LOS) surface-displacement time-series for selected points (see fig. 5) on Augustine Volcano for the period 1992–2005. Red and blue symbols reflect satellite tracks 229 and 501, respectively. Continuous Global Positioning System (CGPS) measurements at five locations for 2004–2005 are also shown (triangles).

Volcano during the 13 years of the investigation. Figure 6*E* shows about 40 cm of subsidence for the 1986 pyroclastic flow deposit.

A network of continuous Global Positioning System (CGPS) receivers (P1–P5) was installed on the volcano by the Plate Boundary Observatory in fall 2004 (Pauk, this volume). We used the GPS data to validate InSAR measurements for the overlapping time interval between September 2004 and October 2005. All GPS data were converted into the InSAR line-of-sight (LOS) vector. Figures 6*F*–6*J* show time-series displacement at CGPS locations, comparing SBAS InSAR results and CGPS data from September 2004 to October 2005. The CGPS displacements were projected to the LOS vector by using the InSAR imaging geometry for track 501. About 3 to 8 cm of uplift is observed at five CGPS locations (figs. 6*F*–6*J*). In general, we find that the interferometric coherence on the upper part of Augustine Volcano, where CGPS stations are located, is worse than on the lower flanks (figs. 6*A*–6*E*). This is the main reason why SBAS InSAR time-series results look noisy (figs. 6*F*–6*J*). From September 2004 to October 2005, SBAS InSAR results indicate about 5 to 15 mm uplift at the five CGPS locations. These results agree with the CGPS observations that indicate Augustine Volcano had been inflated from early summer 2005 to the time of its eruption in January 2006 (Cervelli and others, 2006; Cervelli and others, this volume).

Deformation Modeling and Analysis

Our refined SBAS InSAR algorithm allows us to retrieve temporal surface deformation information while minimizing atmospheric artifacts, DEM errors, and phase unwrapping errors. We have processed InSAR images from two descending satellite tracks and found that the independent results indicate very similar trends, giving us confidence in our refined algorithm. CGPS observations during September 2004 to October 2005 further validate the refined SBAS InSAR processing algorithm.

Surface displacement at Augustine Volcano can be characterized as a wholesale uplift of the island by 2 to 8 cm during the 13 years of investigation. The amount of uplift of the upper flanks is slightly less than that of the lower flanks. To estimate the location of the source responsible for the observed surface displacement, we modeled the averaged deformation interferograms in figure 5 by using two point sources embedded in an elastic homogeneous half-space (Mogi, 1958). The four parameters used to describe a Mogi source are horizontal location (x, y), depth, and strength, which is related to a change in pressure, volume, or both. A nonlinear least squares inversion approach was used to optimize the source parameters. This approach minimizes a merit function defined as the chi-squared difference between the observed and synthetic interferograms. The Levenberg-Marquardt Method (Press and others, 1992) was used to iteratively improve the trial solution until the chi-squared effectively stopped decreasing. To account for topographic effects, we adopted a simple approach proposed by Williams and Wadge (1998) in which the elevation of the reference surface varies according to the elevation of each computation point in the model.

To model the deformation by using two Mogi sources, we first masked out the subsidence associated with the 1986 pyroclastic flow deposit, which was attributed to thermoelastic contraction (Masterlark and others, 2006). Next, we used a Mogi source to model the deformation of the upper part of the volcano by masking out the deformation over the lower half. In this case, we also included three ramping phase terms ($a+bx+cy$, where x and y are pixel coordinates) to account for the wholesale uplift of the volcano. The best source model is located 1.7 to 3.8 km below mean sea level, with an averaged contracting volume of about 0.2 million m^3/yr. Using the best-fit location for this first Mogi source, we generated a modeled deformation image (fig. 7*B*) and removed it from the observed deformation image (fig. 7*A*). The resulting deformation field over the lower part of the volcano was modeled with a second Mogi source. In this case, we did not include the three ramping phase terms in order to model the long-wavelength uplift, and we fixed the horizontal location of the second source to that of the first source (the second source is located directly beneath the first). The depth of the second Mogi source is poorly constrained. The best fit was obtained with a source 7 to 12 km below mean sea level inflating at about 2 million m^3/yr (fig. 7*C*). Figure 7*D* shows the modeled deformation from the use of two Mogi sources, which reproduce most aspects of the observed displacement field relatively well. We recognize that our modeling is preliminary and acknowledge that many alternative models can explain the observed deformation equally well.

A preliminary two-source model that reproduces the observed displacement field at Augustine Volcano during 1992–2005 consists of a contracting source 2 to 4 km below mean sea level and an inflating source 7 to 12 km below mean sea level. The shallower source might represent a shallow magma reservoir that fed the 1976 and 2006 eruptions, and was responsible for the volcano-tectonic earthquakes at depths of 2 to 5 km below sea level that preceded the 1976 eruptions and followed the 2006 eruptions (Power and Lalla, this volume). Petrologic evidence also suggests this as a source depth for 2006 magma (Larsen and others, this volume). The deeper source could be a long-term magma storage zone beneath the volcano.

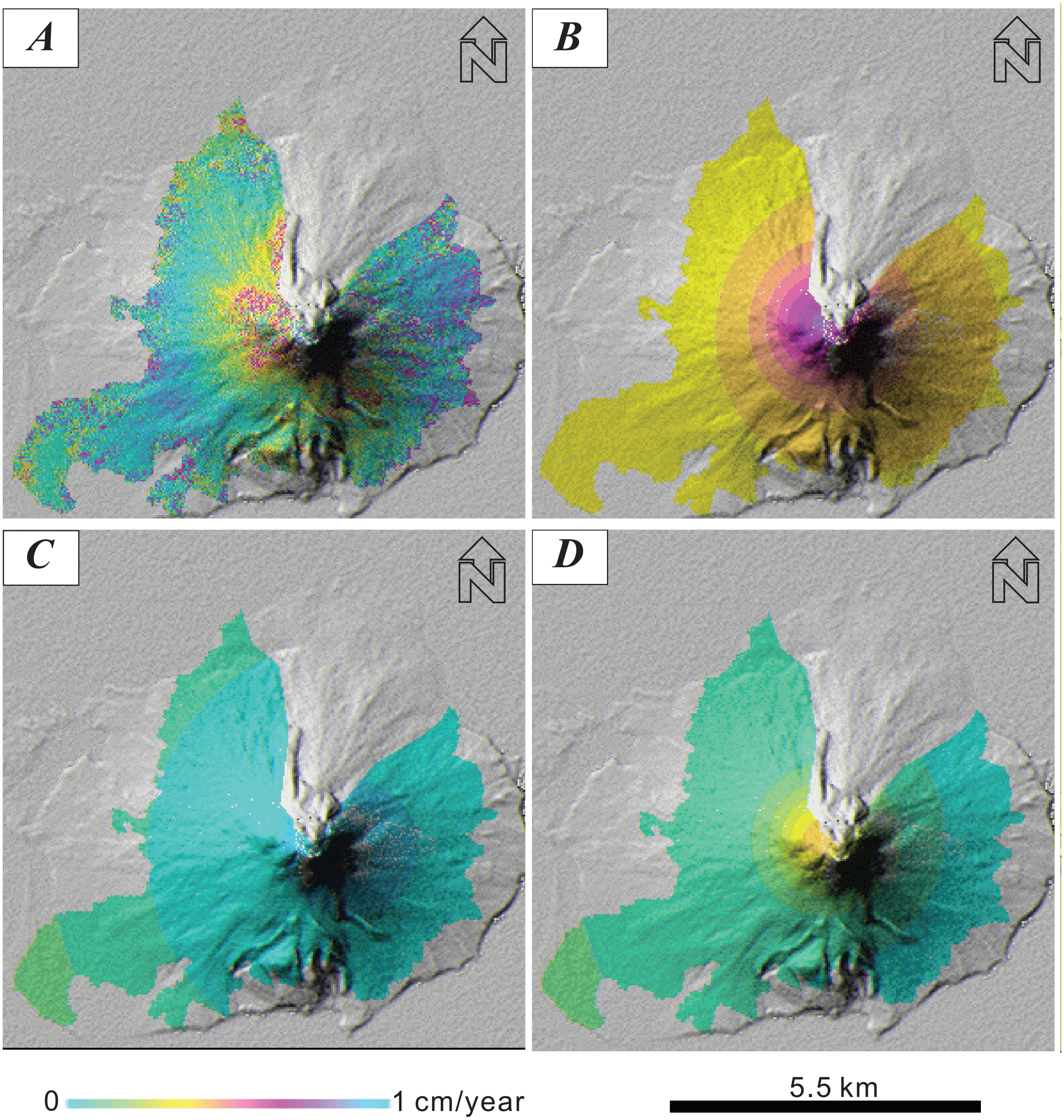

Figure 7. *A,* Observed averaged deformation rate of Augustine Volcano, 1992–2005. *B,* Modeled deformation from a contracting source 3.3 km below mean sea level. *C,* Modeled deformation from an expanding source 9.6 km below mean sea level. *D,* Modeled deformation from both Mogi sources (*B* and *C*).

Conclusions

We have developed a SBAS InSAR processing algorithm to study ground surface deformation by characterizing and removing atmospheric artifacts and DEM errors to improve surface deformation measurements through a multi-interferogram approach. The technique represents a significant advance and is particularly capable of retrieving subtle deformation over a long time interval. We applied the SBAS InSAR technique to Augustine Volcano by using SAR images from two independent datasets during 1992 and October 2005. Time-series deformation measurements from two satellite tracks agree with each other, both suggesting 2 to 8 cm uplift of the volcano during the time of investigation. The InSAR results also agree with CGPS observations at five stations that began operating in September 2004. A preliminary model consisting of a contracting Mogi source 2 to 4 km below mean level and an inflating Mogi source 7 to 12 km below mean sea level reproduces the observed displacement field reasonably well. The deeper source might represent a long-term magma storage zone beneath the volcano, and the shallower source a magma reservoir responsible for swarms of volcano-tectonic earthquakes that preceded and followed the 1976 and 2006 eruptions. Net contraction of the shallower source during a 13-year period leading up to the 2006 eruption might be a result of magma degassing or cooling. If so, both sources would seem to be long-term features of the magma plumbing system at Augustine. The shallower source, in particular, might be amenable to investigation by seismic tomography or other geophysical techniques.

Acknowledgments

SAR data used in this study are copyrighted by the European Space Agency (ESA) and were provided by the Alaska Satellite Facility. We thank Chuck Wicks for sharing his Matlab modeling codes, J. Power for sharing his insightful information about Augustine seismicity, and J. Power and R. Rykhus for technical review. This work is supported by the National Aeronautics and Space Administration (NASA) Earth Surface and Interior Program (05/0021), the U.S. Geological Survey (USGS) Volcano Hazards Program, and the USGS Land Remote Sensing Program.

References Cited

Begét, J.E., and Kowalik, Z., 2006, Confirmation and calibration of computer modeling of tsunamis produced by Augustine Volcano, Alaska: Science of Tsunami Hazards, v. 24, no. 4, p. 257–267.

Berardino, P., Fornaro, G., Lanari, R., and Sansoti, E., 2002, A new algorithm for surface deformation monitoring based on small baseline differential SAR interferograms: Institute of Electrical and Electronics Engineers Transactions on Geosciences and Remote Sensing, v. 40, no. 11, p. 2375–2383.

Cervelli, P., Fournier, T., Freymueller, J., and Power, J.A., 2006, Ground deformation associated with the precursory unrest and early phases of the January 2006 eruption of Augustine Volcano, Alaska: Geophysical Research Letters, v. 33, L18304, doi: 10.1029/2006GL027219.

Cervelli, P.F., Fournier, T.J., Freymueller, J.T., Power, J.A., Lisowski, M., and Pauk, B.A., 2010, Geodetic constraints on magma movement and withdrawal during the 2006 eruption of Augustine Volcano, *in* Power, J.A., Coombs, M.L., and Freymueller, J.T., eds., The 2006 eruption of Augustine Volcano, Alaska: U.S. Geological Survey Professional Paper 1769 (this volume).

Dzurisin, D., 2007, Volcano Deformation—Geodetic Monitoring Techniques: Springer Praxis Publishing Ltd., UK.

Farr, T., and 17 others, 2007, The Shuttle Radar Topography Mission: Reviews of Geophysics, 45, RG2004, doi:10.1029/2005RG000183.

Ferretti, A., Prati, C., and Rocca, F., 2001, Permanent scatterers in SAR interferometry: Institute of Electrical and Electronics Engineers Transactions on Geosciences and Remote Sensing, v. 39, p. 8–22.

Gabriel, A.K., Goldstein, R.M., and Zebker, H.A., 1989, Mapping small elevation changes over large areas—differential interferometry: Journal of Geophysical Research, v. 94, p. 9183–9191.

Kienle, J., and Shaw, G.E., 1979, Plume dynamics, thermal energy and long-distance transport of vulcanian eruption clouds from Augustine Volcano, Alaska: Journal of Volcanology and Geothermal Research, v. 6, no. 1-2, p. 139–164.

Larsen, J.F., Nye, C.J., Coombs, M.L., Tilman, M., Izbekov, P., and Cameron, C., 2010, Petrology and geochemistry of the 2006 eruption of Augustine Volcano, *in* Power, J.A., Coombs, M.L., and Freymueller, J.T., eds., The 2006 eruption of Augustine Volcano, Alaska: U.S. Geological Survey Professional Paper 1769 (this volume).

Lee, C., Lu, Z., Kwoun, O., and Won, J., 2008, Deformation of Augustine volcano, Alaska, 1992–2005, measured by ERS and ENVISAT SAR interferometry: Earth, Planets and Space, v. 60, 447–452.

Lu, Z., Wicks, C., Dzurisin, D., Power, J., Thatcher, W., and Masterlark, T., 2003, Interferometric synthetic aperture radar studies of Alaska volcanoes, Earth Observation Magazine , v. 12, no. 3, 8–18.

Lu, Z., Dzurisin, D., Wicks, C., Jr., Power, J., Kwoun, O., and Rykhus, R., 2007, Diverse deformation patterns of Aleutian volcanoes from satellite interferometric synthetic aperture radar (InSAR), *in* Eichelberger, J.C., Gordeev, E., Izbekov, P., Kasahara, M., and Lees, J.M., eds., Volcanism and tectonics of the Kamchatka Peninsula and adjacent arcs: American Geophysical Union Geophysical Monograph 172, p. 249–261.

Masterlark, T., Lu, Z., and Rykhus, R., 2006, Thickness distribution of a cooling pyroclastic flow deposit on Augustine Volcano, Alaska—optimization using InSAR, FEMs, and an adaptive mesh algorithm: Journal of Volcanology and Geothermal Research, v. 150, p. 186–201.

Miller, T.M., McGimsey, R.G., Richter, D.H., Riehle, J.R., Nye, C.J., Yount, M.E., and Dumoulin, J.A., 1998, Catalog of the historically active volcanoes of Alaska: U.S. Geological Survey Open-File Report 98-582, 104 p.

Mogi, K., 1958, Relations between the eruptions of various volcanoes and the deformations of the ground surface around them: Bulletin of the Earthquake Research Institute, University of Tokyo, v. 36, p. 99–134.

Pauk, B.A., Jackson, M., Feaux, K., Mencin, D., and Bohnenstiehl, K., 2010, The Plate Boundary Observatory permanent global positioning system network on Augustine Volcano before and after the 2006 eruption, *in* Power, J.A., Coombs, M.L., and Freymueller, J.T., eds., The 2006 eruption of Augustine Volcano, Alaska: U.S. Geological Survey Professional Paper 1769 (this volume).

Pauk, B.A., Power, J.A., Lisowski, M., Dzurisin, D., Iwatsubo, E.Y., and Melbourne, T., 2001, Global Positioning System (GPS) survey of Augustine Volcano, Alaska, August 3–8, 2000—data processing, geodetic coordinates and comparison with prior geodetic surveys: U.S. Geological Survey Open-File Report 01-099, 20 p.

Power, J.A., and Iwatsubo, E.Y., 1998, Measurements of slope distances and zenith angles at Augustine Volcano, Alaska, 1986, 1988, and 1989: U.S. Geological Survey Open-File Report 98-0145, 17 p.

Power, J.A., and Lalla, D.J., 2010, Seismic observations of Augustine Volcano, 1970–2007, *in* Power, J.A., Coombs, M.L., and Freymueller, J.T., eds., The 2006 eruption of Augustine Volcano, Alaska: U.S. Geological Survey Professional Paper 1769 (this volume).

Press, W., Teukolsky, S., Vetterling, W., and Flannery, B., 1992, Numerical recipes in C, the art of scientific computing: Cambridge University Press, 994 p.

Schmidt, D., and Burgmann, R., 2003, Time-dependent land uplift and subsidence in the Santa Clara Valley, California, from a large interferometric synthetic aperture radar data set: Journal of Geophysical Research v. 108, no. B9, 2416, doi:10.1029/2002JB002267.

Waythomas, C.F., and Waitt, R.B., 1998, Preliminary volcano-hazard assessment for Augustine Volcano, Alaska: U.S. Geological Survey Open-File Report 98-0106, 39 p.

Williams, C.A., and Wadge, G., 1998, The effects of topography on magma reservoir deformation models—application to Mt. Etna and radar interferometry: Geophysical Research Letters., v. 25, 1549–1552.

Zebker, H.A., Amelung, F., and Jonsson, S., 2000, Remote sensing of volcano surface and internal processes using radar interferometry, *in* Mouginis-Mark, P., ed., Remote sensing of active volcanism: American Geophysical Union Monograph, v. 116, p. 179–205.

Zebker, H., Rosen, P., and Hensley, S., 1997, Atmospheric effects in interferometric synthetic aperture radar surface deformation and topographic maps: Journal of Geophysical Research, v. 102, p. 7547–7563.

This page intentionally left blank

The 2006 Eruption of Augustine Volcano, Alaska
Power, J.A., Coombs, M.L., and Freymueller, J.T., editors
U.S. Geological Survey Professional Paper 1769

Chapter 19

The Plate Boundary Observatory Permanent Global Positioning System Network on Augustine Volcano Before and After the 2006 Eruption

By Benjamin A. Pauk[1], Michael Jackson[2], Karl Feaux[2], David Mencin[2], and Kyle Bohnenstiehl[2]

Abstract

In September of 2004, UNAVCO and the National Science Foundation (NSF) funded EarthScope Plate Boundary Observatory (PBO) installed five permanent Continuous Global Positioning System (CGPS) stations on Augustine Volcano, supplementing one existing CGPS station operated by the Alaska Volcano Observatory. All six CGPS stations proved crucial to scientists for detecting and monitoring the precursory deformation of the volcano beginning in early May 2005, as well as for monitoring the many subsequent small inflationary and deflationary episodes that characterized the 2006 eruption. Following the eruption, in September of 2006, PBO added six additional permanent CGPS stations. The 2006 eruption and its precursors were the first significant activity of the volcano in 20 years and the PBO CGPS network provided an unprecedented opportunity to monitor and detect volcanic ground deformation on an erupting Alaskan stratovolcano. Data from the new CGPS stations coupled with the existing seismic stations provided scientists with the first real opportunity to use geodetic data and real time seismic data to assess the volcanic hazards before, during, and after an Alaskan eruption.

Introduction

This paper describes the development and expansion of the Continuous Global Positioning System (CGPS) before and after the 2006 eruption of Augustine Volcano. In September of 2004, the EarthScope Plate Boundary Observatory (PBO) installed five permanent CGPS stations on Augustine Volcano. In planning for the installation of the stations, staff from the PBO Alaska regional office worked closely with staff from the Alaska Volcano Observatory (AVO) and the PBO Magmatic Systems Site Selection Committee to install CGPS stations at strategic locations around the volcano. The goal was to provide a good spatial distribution of stations to monitor and detect both short- and long-term volcanic deformation in response to magmatic intrusions at depth and magma migration through the volcanic edifice.

Owing to its frequent eruptive activity, Augustine was a relatively well instrumented volcano prior to the 2006 eruption (Power and others, 2006). In 1992, AVO installed a three-station GPS network on the volcano consisting of dual-frequency, high-power-consumption Ashtech LD-XII receivers (Murray and others, 1992). These receivers were located on the base of the volcano (station AUGL), on the flank of the volcano, and on the top of the 1986 volcanic dome. Due to the high power consumption of the receivers, they were operated for only a few hours a day. A telemetered network of tiltmeters was installed in 1993 and 1994 to extend the coverage of deformational monitoring on the volcano (Dzurisin and others, 1994). In 1996, the Ashtech LD-XII receivers were replaced with lower power L1-only Ashtech SCA-12 receivers (Murray and others, 1996). In 2000, AVO replaced station AUGL with a dual frequency Trimble 4700 GPS receiver and dual frequency choke ring antenna, and the remaining two stations were no longer maintained. The continuous instrumentation deployed in the 1990s and repeated Electronic Distance Measurement (EDM) and GPS measurements of the volcano for the period 1988 to 2000 suggested no discernible pattern of displacement that could be attributed to magmatic activity on Augustine Volcano (Power and others, 1998; Pauk and others,

---

[1] U.S. Geological Survey, Cascades Volcano Observatory, 1300 SE Cardinal Court, Vancouver, WA 98683.

[2] UNAVCO, 6350 Nautilus Drive, Boulder, CO 80301.

2001). Prior to the installation of the five PBO CGPS stations in 2004, AVO operated only the one dual frequency CGPS station (AUGL) located on the east quadrant of the volcano. AUGL was incorporated into the PBO network in 2006 and subsequently renamed AV21 to comply with the PBO volcanic station naming scheme.

All five of the PBO CGPS stations and the one AVO CGPS on the volcano were operating normally at the onset of the eruption, but half of the network went offline shortly thereafter due to volcanic activity. Pyroclastic flows generated by the eruption completely destroyed two of the original five PBO stations and severely damaged a third, but spared the remaining three CGPS stations. These stations continued to operate throughout the explosive and effusive phases of the 2006 eruption.

In 2006, PBO installed six additional CGPS stations on the volcano at the request of the PBO Magmatic Systems Site Selection Committee to improve ongoing geodetic monitoring of the volcano. The Committee requested new locations to strengthen the existing network geometry and to improve the detection of subtle ongoing volcanic deformation signals at the volcano. The new stations were installed on the lower western and northern flanks of the volcano, on the southwest flank of the volcano, and on the upper flanks on the north and south side of the volcano (fig. 1; table 1). The spatial distribution of the new stations was dictated by the availability of competent bedrock on the volcano, line of site between stations and the AVO data communication facility in Homer, and attempts to fill gaps in the original network geometry and strengthen the geodetic monitoring of the volcano.

2004 CGPS Station Installations

PBO installed short drilled-braced monuments (SDBM) as the primary monument type for all the PBO CGPS stations on Augustine during both the 2004 and 2006 installations (fig. 2). The SDBM is a very stable, inexpensive, and durable monument that can be installed in exposed competent bedrock with off-the-shelf construction tools. The monument is constructed of 1-inch diameter Type 316 stainless steel rods that are welded into a stable tripod structure. The SDBM consists of a vertical leg braced by three diagonal legs inclined at approximately 55 degrees to the ground. All the legs extend approximate 2 m into the bedrock and converge with the center leg approximately 1.5 m above the ground surface. An electric hand held drill is used to drill all four 3.5 cm holes into the rock and each leg is grouted in place and the angled legs are welded to the central leg. The UNAVCO Web site (http://facility.unavco.org/project_support/permanent/monumentation/sdbm.htm, accessed September 28, 2009) provides detailed instructions and equipment lists for the construction of the SDBM. A stainless steel leveling mount is welded onto a threaded adaptor on the top of the center leg. A dual-frequency choke ring GPS antenna is attached to the leveling mount and a protective radome is put over the antenna.

For the Augustine network, PBO used the Trimble NetRS geodetic grade GPS receiver, Trimble part number 48164, and a radome covered Trimble dual frequency (L1/L2) choke ring antenna, model number TRM 26959.00, at each station. The NetRS is a low-power (3 Watt) rugged GPS receiver that allows for remote operation, status monitoring, and programming using Internet Protocol (IP) (fig. 3). Utilizing a standard internet browser, a user can access NetRS data and change data recording parameters. This proved helpful during times of volcanic unrest when conditions prohibited site access. The choke ring antenna is a reliable, low-power, multipath-resistant geodetic antenna that maintains millimeter precision (fig. 4).

The five CPGS stations were installed in competent bedrock outcrops with excellent sky view and clear telemetry paths to the AVO communications facility in Homer (fig. 1 and appendix 1). Unfortunately, the lack of competent bedrock in each quadrant prevented an ideal distribution of the stations; however, the final station distribution was sufficient to capture deformation on the upper and lower flanks of the volcano prior to and after the eruption. The network was concentrated within 5 km of the volcano's summit to ensure detection of shallow magmatic sources.

Each CGPS station on Augustine consisted of a Plaschem fiberglass hut or enclosure that houses the GPS receiver, a charge controller, surge protector, and 24 rechargeable 12 volt, 110 amp hour, sealed lead-acid batteries (fig 2). The 24 battery bank provides sufficient continuous power to all equipment throughout the long winter when there is limited daylight and the solar panels are encased in ice or snow and are not charging the batteries. The fiberglass huts are 5 ft square, 5 ft high, and weigh approximately 650 lbs. Due to the size and weight of the hut, a helicopter is required to sling the hut from an established base of operations to the designated remote station location on the volcano. One 64-watt solar panel was mounted to the angled south face of the hut to recharge the batteries. Three additional solar panels are mounted to an aluminum solar panel mounting structure or “swing set” located adjacent to the hut. The swing set is constructed of 2-inch-diameter, schedule-80 aluminum pipe that is coupled to the ground on the corners with rock bolts cemented into the bedrock or set in cement when installed in soil (fig. 5). Solar panels on the swing set recharge the batteries that supply the primary power source for the GPS receiver and digital radio components at each station. The swing sets used at the Augustine stations are a modified version of the swing set developed and utilized by AVO at many seismic stations on other Alaskan volcanoes. Complete metadata information including all equipment types, equipment serial numbers, data products, and photos for each Augustine station can be found on the PBO Web site at (http://pboweb.unavco.org/shared/scripts/gmap/, accessed September 28, 2009).

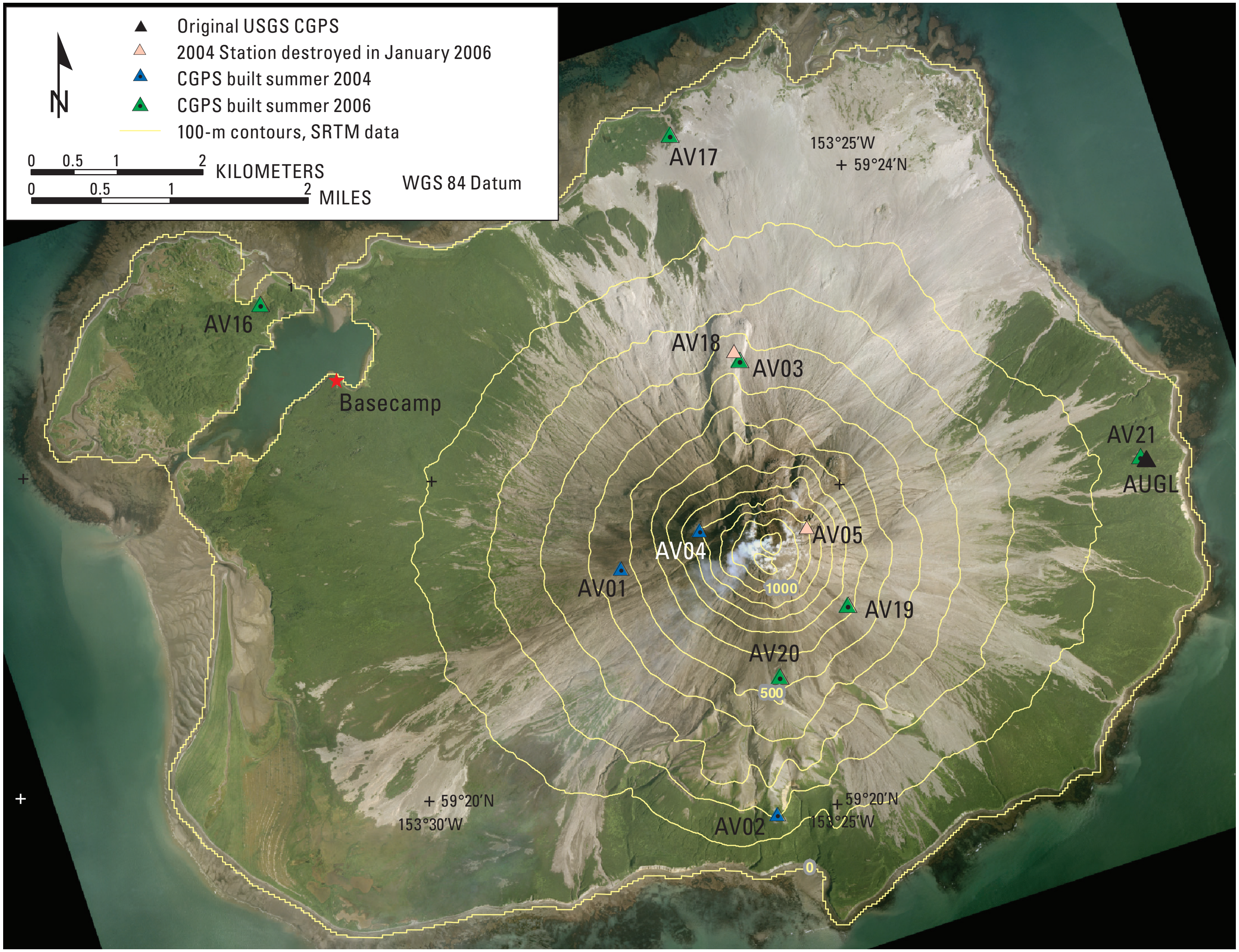

Figure 1. Map of Augustine Volcano showing Plate Boundary Observatory (PBO) Continuous Global Positioning System (CGPS) stations installed in 2004 and 2006, stations destroyed in the 2006 eruption, and Alaska Volcano Observatory (AVO) station on the volcano before the 2004 PBO installations. Note that station AV21 is in the same location as station AUGL. Base map from U.S. Geological Survey (USGS), orthophoto taken on July 12, 2006. Shuttle Radar Topography Mission (SRTM) contours.

Table 1. Geodetic coordinates of the Augustine GPS network and nearby regional Plate Boundary Observatory (PBO) GPS stations as of October 2006, including stations installed in 2004 and destroyed during the 2006 eruption of Augustine Volcano.

Station ID	PBO formal name	Longitude (degrees W)	Latitude (degrees N)	Elevation (meters)	Install date	Removal date
AC27	AC27MNEILAK2004	154.1630	59.2525	420.0	09/17/2004	Active
AC59	AC59URSUSAK2004	153.5852	59.5672	308.8	09/11/2004	Active
AUGL[1]	N/A	153.3539	59.3702	104.0	06/01/1996	01/09/2006
AV01	AV01AUGST_AK2004	153.4608	59.3585	47.9	09/10/2004	Active
AV02	AV02AUGST_AK2004	153.4284	59.3329	231.1	09/11/2004	Active
AV03	AV03AUGST_AK2004	153.4377	59.3812	360.2	09/08/2004	1/28/2006
AV04	AV04AUGST_AK2004	153.4447	59.3626	915.9	09/08/2004	Active
AV05	AV05AUGST_AK2004	153.2521	59.2146	1036.6	09/16/2004	1/13/2006
AV11	AUGS_MOUNAK2006	153.3546	59.3706	114.4	09/10/2006	Active
AV16	AUGLAGOONAK2006	153.5350	59.3859	26.5	09/04/2006	Active
AV17	AUGSTINNWAK2006	153.4510	59.4040	30.0	09/05/2006	Active
AV18	AUGVNORTHAK2006	153.4370	59.3800	370.0	09/03/2006	Active
AV19	AUGSTINSEAK2006	153.4140	59.3550	650.0	09/06/2006	Active
AV20	AUGS_SOUTHAK2006	153.4280	59.3470	540.0	09/11/2006	Active
AV21[1]	AV21AUGST_AK2006	153.3539	59.3702	104.0	01/09/2006	07/18/2008

[1] Sites AUGL and AV21 represent the same physical location. Only the name was changed.

2006 Augustine Eruption

All six CGPS stations on Augustine were operating prior to the 2006 eruption and proved useful in detecting inflation of the volcano before the eruption and subsequent deflation after the eruption (Cervelli and others, 2006; Cervelli and others, this volume). Unfortunately, pyroclastic flows damaged three of the stations early in the eruption. Station AV05 was destroyed on January 13 during the explosive stage of the eruption. Station AV04 was heavily damaged and stopped transmitting data on January 17 as the result of a large pyroclastic flow (fig. 6). Station AV03 continued to collect data until it was destroyed by a pyroclastic flow generated by an explosion on January 28 (fig. 7). Stations AV01, AV02, and AUGL were not damaged and remained operational throughout the entire eruption and subsequent debris flows generated on the volcano. Unfortunately, because of weather constraints and concern for crew safety, no attempt was made to repair AV04 until several months after the eruption had stopped and seismic activity had subsided. As a result of the station being offline, any deformation on the western flank of the volcano was not thoroughly recorded in the months that immediately followed the eruption.

2006 GPS Installations and Network Maintenance

In October of 2005, the PBO Magmatics Systems Site Selection Committee requested that the Alaska PBO regional office install an additional five to six permanent CGPS stations on Augustine in response to the precursory deformation of the volcano observed in the GPS data time series. The Alaska regional staff immediately began initial planning for the installation; however, severe winter conditions in Cook Inlet and concern about crew safety working on a restless volcano led to the decision to delay the installations until activity subsided and weather conditions were more favorable. However, in December of 2005, AVO staff upgraded the GPS station AUGL with a NSF-purchased NetRS GPS receiver, and the station was renamed AV21 and incorporated into the PBO network. Because of continued activity on the volcano after the 2006 eruption began, and because of other regional commitments, the Alaska regional office was unable to install the new stations until September of 2006.

During September of 2006, PBO installed an additional six new GPS stations on Augustine (fig. 1) and repaired AV04. At each new station, PBO built SDBM monuments and

Figure 2. Photo of Plate Boundary Observatory (PBO) station AV03, located on north side of Augustine Volcano. Station includes a standard PBO Short Drilled Braced Monument (SDBM) geodetic monument with GPS antenna enclosed in a plastic radome. Note that the original PBO style gray fiberglass enclosure and aluminum solar panel "swing set" installed in 2004. The station was completely destroyed by the 2006 eruption. Photo by Benjamin Pauk, September 12, 2004.

installed Trimble NetRS GPS receivers, Trimble choke ring antennas, and Intuicom digital radios. All data collected at the new stations were incorporated into the existing digital radio network telemetered to Homer.

The fiberglass enclosure huts deployed in 2006 are a larger and remodeled version of those installed in 2004. One key advantage of the new huts is that they were designed to accommodate two 64 watt solar panels (fig. 8). In addition, a new equipment mounting plate or back panel was developed and incorporated in the design for the interior of the enclosure. The new back panel is made of noncorrosive stainless steel and mounts to one of two sets of four bolts on either of the interior sides (east or west side) of the hut (fig. 9). The NetRS, Intuicom radio, charge controller, surge protector, and other associated equipment is mounted on to a single panel allowing rapid modular replacement of equipment.

The six stations installed in September of 2006 completed a robust network. Stations AV16 and AV17 were installed on the lower northwestern and western flanks of the volcano. Stations AV18 was installed within 300 m of the destroyed station AV03 on the north side of the volcano.

Figure 3. Photo of Trimble NetRS and Intuicom EB1 radio mounted inside an older style Plate Boundary Observatory (PBO) fiberglass enclosure installed on the volcano in 2004. Photo by Benjamin Pauk, September 9, 2004.

Station AV19 was installed on the southwestern flank of the volcano on a small spine of bedrock at an altitude of about 650 m. AV20 was installed in a bedrock outcrop approximately 1 km due north of station AV02 at a higher elevation on the volcano's southern flank. Due to concerns about the monumentation at AV21, a SDBM monument was built approximately 200 m west of AV21 and was designated as AV11, and AV21 was deactivated from the PBO network after the 2 stations recorded in parallel for almost two years. The heavily damaged station AV04 was repaired in 2006 and routine maintenance was performed at stations AV01, AV02, AC27, and AC59.

In addition to the 2006 hut modifications, a more rigid and durable swing set was designed and installed at three of the six new stations. No swing sets were needed at stations AV18, AV19, and AV20 as they have good southern exposure and are located on wind swept ridges where snow accumulations have historically been minimal. The new swing set was designed to withstand greater ice, snow, and wind loads commonly experienced by solar mounts on Augustine and other remote Alaskan volcanoes. Additional aluminum angled bar was bolted to the sides across the back of the panels to minimize flexure of the solar panels. The new hut and swing sets used the same 64-W solar panels deployed in 2004. As on the 2004 swing sets, all external connecting wires were enclosed in ½-inch-diameter Liquitite conduit, securely clamped to the aluminum poles and fed into the hut's power panel through a watertight plastic pass-through connection mounted to the side of the hut. In addition to the corners of the swing sets

Figure 5. Photo of solar panel "swing set" structure with three 64 watt panels installed in 2004 Plate Boundary Observatory (PBO) GPS stations on Augustine Volcano. Photo by Karl Feaux, September 11, 2004.

Figure 4. Photo of PBO station AV02 located on the south side of Augustine Volcano. Photo shows a Trimble L1/L2 choke ring dual frequency GPS antenna on a Plate Boundary Observatory (PBO) Short Drilled Braced Monument (SDBM). Plastic radome is removed to expose radome base, Southern California Integrated GPS Network (SCIGN) adapter and antenna. Monument is made of Type 316 1-inch diameter stainless steel rods. Photo by Karl Feaux, September 11, 2004.

Figure 6. Photo of damaged Continuous Global Positioning System (CGPS) station AV04, located on the upper west flank, after the 2006 eruption of Augustine volcano. The station was damaged by passing pyroclastic flow that ripped off the plastic radome, melted the coax antenna cable, conduit, and the middle of the L1/L2 choke ring antenna. Photo by Benjamin Pauk, September 2, 2006.

being set in concrete, it was further coupled to the ground using a minimum of four 3/16-inch diameter guy wires connected to 0.5×6 inch-long galvanized eyebolts on the swing set connected to another nongalvanized eyebolt cemented into available bedrock adjacent to the base of the swing set.

To minimize the time to install a complete station during the 2006 project, all swing sets were built at the base camp during weather delays and slung to each station by helicopter. Preconstruction of all equipment and programming of radios and receivers in the PBO warehouse before deployment to the island reduced the average site installation time from two days to one. During the 2006 installation period, Augustine was at Aviation Color Code Yellow and Volcano Alert Level Advisory indicating signs of elevated unrest and increased seismic activity at the volcano. Consequently, it was critical to minimize the amount of time spent working on the island in the event that volcanic activity increased, thereby necessitating a crew evacuation.

Network Installation Logistics

All operations for the 2004 and 2006 installations were based out of a camp established on the west side of the island adjacent to the informally named West Lagoon (fig.1). All gear, including huts, swing set materials, batteries, tools, and associated installation and camping equipment was transported to Augustine Island from Homer, Alaska, by the M/V *Maritime Maid* in 2004 and by the M/V *Kittiwake* in 2006. A Bell Long Ranger helicopter was used to sling all gear from the ships to the base camp staging area because no docks or landing areas are present on the island. Additional support, including equipment and crew transport to and from the island, was completed with float planes based in Homer. These support aircraft were able to take off and land in the lagoon. The lack of road and trails on the island required that a helicopter be used during both installations in order to provide logistical support and sling external loads of gear as well as transport internal loads of equipment and crew to and from each location on the island.

Figure 7. Photo of deformed and decapitated Continuous Global Positioning System (CGPS) monument AV03 after the 2006 eruption. Trimble antenna, plastic radome, and leveling mount were ripped off and monument was deformed in direction of pyroclastic flow that swept over the monument. The swing set and fiberglass enclosures were completely destroyed and buried by flow deposits. Photo by Benjamin Pauk, September 3, 2006.

Figure 8. Photo of modified fiberglass enclosure and solar panel structure deployed on Augustine Volcano during the 2006 installations. The new enclosure can accommodate two 64 watt solar panels, and both the enclosure and swing set use guy wires for added anchoring to the ground. Photo by Dave Mencin, September 4, 2006.

Current PBO Augustine Radio Network and Telemetry

Data from each existing GPS station in the Augustine network (except for AV20) are transmitted in real time through a point-to-multipoint, spread-spectrum 900 MHz ISM-band Ethernet radio network to a master radio located at the AVO communications facility in Homer (fig. 10). The radios are connected to an appropriate Yagi directional antenna mounted to vertical poles inside of each fiberglass hut. In some cases, an external mount on a 2-inch-diameter aluminum pole is used. The huts are transparent to frequencies in this 900 MHz range and protect the antenna from the elements. Stations AV04, AV16, AV17, and AV18 are stand-alone stations with only one slave radio located within the hut and transmit data to Homer through a repeater radio at PBO station AC59 16 km northwest of the volcano on the Alaska Peninsula at Ursus

Head. The slave radio connects to the NetRS GPS receiver through a standard CAT5 Ethernet patch cable. Station AV01, which serves as a slave repeater station, has two radios located in its hut. One is a slave radio that transmits data collected at AV01 to station AC59, whereas the second radio in the hut repeats data from AC27, located on the Alaskan Peninsula west of Augustine Island, to station AC59 and then to Homer (fig. 10). Data from stations AV02, AV11, and AV19 are routed directly to Homer. Station AV20 has no line of site to any other PBO station on the volcano or in the Cook Inlet region. As of this writing, the station is manually downloaded on a biannual basis and will be incorporated in to the existing radio telemetry at a later date.

PBO Augustine GPS Data Collection

The Trimble NetRS has 1 GB of internal memory for storing data and the standard operating procedures for all PBO CPGS is to split the data space on the receiver into two separate ring buffers, a 800 MB partition for data collection at 1 Hz to be used only during events such as a volcanic eruption, earthquakes, or other events of great scientific interest, and a 200 MB partition for daily data files with a 15 second data collection rate. The size of daily files sampled at the 15 seconds averages about 1 MB and it typically takes about six months to completely fill the 200 MB partition, at which point the receiver will overwrite older data.

Figure 9. Photo of stainless steel back panel mounting system developed for new huts deployed during the 2006 Augustine Volcano installations. Trimble NetRS and Intuicom EB1 spread spectrum radio mounted on to upper portion of panel. Photo by Benjamin Pauk, September 4, 2006.

Prior to the eruption, AVO requested PBO to set up three separate data partitions on each GPS receiver for simultaneous collection of three different sample rates. The three partitions stored daily and hourly files, both sampled at 15 seconds, and also hourly files sampled at 1 Hz. Prior to the eruption and request for additional sample rates, PBO only collected hourly and daily 15-second data files. Before, during, and after the eruption, all hourly 15-second data files were downloaded hourly whereas the 15-second daily files continued to be downloaded daily. During the explosive phase of the 2006 eruption, PBO collected and downloaded hourly 1-Hz data files from stations AV01 and AV02 on the volcano. Due to the large size of the 1-Hz data files and larger bandwidth requirements, the 1-Hz files were only collected for a few weeks during the explosive phases of the eruption and were no longer collected after the onset of the effusive phase of the eruption.

All raw data collected from the CGPS network on Augustine are available for download from the UNAVCO Data Archive Facility, with raw receiver files converted to standard Receiver Independent Exchange (RINEX) format for easy processing, analysis, and interpretation. In addition to raw data, PBO provides higher-level data products consisting of station position and velocity solutions in the Stable North America Reference Frame (SNARF), along with their related Solution Independent Exchange (SINEX) files. PBO's data analysis occurs at two analysis centers, one at the New Mexico Institute of Mining and Technology using the GAMIT processing package and the other at Central Washington University using the GIPSY processing package, with combined solutions generated at the Massachusetts Institute of Technology. These data products and the specific PBO Augustine data products collected before, during, and after the eruption can be accessed from the UNAVCO Archive Facility through the UNAVCO Web page at (http://www.unavco.org, accessed September 28, 2009) as well as directly from the PBO Web site at (http://pboweb.unavco.org, accessed September 28, 2009).

Conclusions

The original PBO CGPS network on Augustine Volcano was designed to follow the existing telemetry paths of the AVO seismic network, minimizing the need for extensive radio testing in the field. Extensive planning, organization, radio network development, and bench testing of the GPS and digital radio network in the laboratory prior to deployment proved extremely valuable in minimizing the amount of time spent in the field troubleshooting the radio network. Additionally, the original radio network design was implemented to allow for expansion. Consequently, the PBO engineers in 2006 were able to incorporate the radios for the new stations without having to significantly alter the existing radio telemetry paths.

The destruction of three of the original six stations early in the eruption severely affected AVO's ability to use GPS as a key monitoring tool during the entire eruption. Had field conditions permitted, PBO field crews could have redeployed new equipment shortly after the eruption began to ensure continued data collection. This would have provided invaluable information about flank deformation of the volcano after the onset of the eruption. Unfortunately, severe winter weather and hazardous conditions on the volcano prevented access and work during the eruption.

The interval between the original 2004 network deployment and the 2006 eruption response deployment provided PBO engineers ample experience to make marked improvements to GPS monument construction and enclosure and electronics design. One fundamental lesson learned from the 2004 installations was the need for well-defined logistics for this type of operation. The 2004 installations on Augustine were the first large-scale deployment for PBO field engineers in Alaska and many logistical items, such as scheduling of boats, helicopter contracts, and equipment transport, was conducted late in the planning process. As a result, additional float plane charters were required to bring some tools and equipment not available at time of shipping to the island after the 2004 installations began. In 2004, all construction, including assembly of the huts and swing sets, was done on site, adding significantly to construction time at a site. Logistics and construction of the 2006 installations were streamlined by effective planning that began in October of 2005 and included a thorough organization of equipment and materials, additional acquisition of tools, and construction of the enclosures in the warehouse prior to shipment to the volcano.

Another valuable lesson learned during the time between the two installations was the need for a larger enclosure with an accessible and standardized equipment panel for easy access and rapid replacement of equipment. Between the 2004 and 2006 installations, enclosures were redesigned to accommodate more solar panels, which in some cases during the 2006 installations, removed the need for swing sets in areas of good southern exposure and historically low snow accumulation. These modifications allowed for efficient installation of the new CGPS stations at the request of the PBO Magmatic Systems Site Selection Committee in 2006. As a result of the streamlined construction procedures, PBO field engineers were able to reduce site construction time by about 50 percent from two days to one. In the future, these procedures will allow for stations to be built quickly, efficiently, and safely in remote volcanic settings before the onset of volcanic unrest. The lessons learned from the 2004 and 2006 installations, combined with the hut and swing set improvements and streamlined construction procedures, proved extremely valuable to PBO volcanic network installations on Unimak Island in 2008 and contributed to their success.

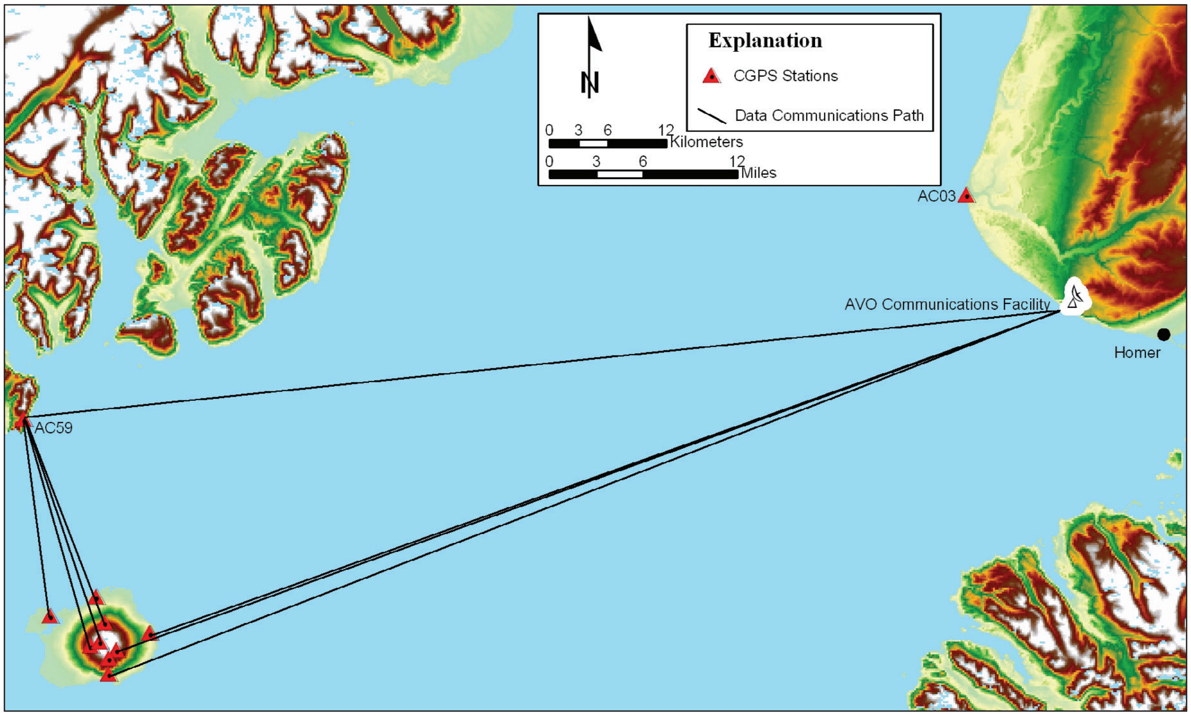

Figure 10. Regional map showing radio telemetry links of the Plate Boundary Observatory (PBO) Augustine Volcano GPS network. Map projection is Universal Transverse Mercator Projection, Zone 5, North American Datum of 1983 (NAD 83). CGPS, Continuous Global Positioning System.

Acknowledgments

The 2004 and 2006 GPS network installations on Augustine were both cooperative efforts involving personnel from UNAVCO, Inc., the Alaska Volcano Observatory, and the University of Alaska Fairbanks Geophysical Institute. Beluga Air, Kachemak Air Service, Maritime Helicopters, and Katmai Coastal Bear Tours provided safe, reliable, and efficient transportation of gear and crew to and from the island. The authors gratefully acknowledge all those who contributed to the success of both installations. We are also indebted to the support and advice from the Alaska Volcano Observatory for both installations; in particular we are grateful for the advice and assistance from Tom Murray, John Power, and John Paskievitch on permitting, logistics, and network operations. Material and results presented in this paper are based on data, equipment, and engineering services provided by the Plate Boundary Observatory operated by UNAVCO for EarthScope (http://www.earthscope.org, accessed September 28, 2009) and supported by the National Science Foundation (No. EAR-0323309).

References Cited

Cervelli, P.F., Fournier, T.J., Freymueller, J.T., Power, J.A., Lisowski, M., and Pauk, B.A., 2010, Geodetic constraints on magma movement and withdrawal during the 2006 eruption of Augustine Volcano, *in* Power, J.A., Coombs, M.L., and Freymueller, J.T., eds., The 2006 eruption of Augustine Volcano, Alaska: U.S. Geological Survey Professional Paper 1769 (this volume).

Cervelli, P.F., Fournier, T., Freymueller, J., and Power, J.A., 2006, Ground deformation associated with the precursory unrest and early phases of the January 2006 eruption of Augustine Volcano, Alaska: Geophysical Research Letters, v. 33, L18304, doi: 10.1029/2006GL027219.

Dzurisin, D., Iwatsubo, E.Y., Kleinman, J.W., Murray, T.L., Power, J.A., and Paskievitch, J.F., 1994, Deformation monitoring at Augustine Volcano, AK [abs.]: Eos, (American Geophysical Union Transactions), v. 75, n. 44, p. 166.

Murray, T.L., Endo, E.T., Iwatsubo, E.Y., and Dzursisin, D., 1996 A feasible real time radio-telemetered GPS network for short baseline applications [abs.]: Eos, (American Geophysical Union Transactions), v. 77 n. 46, p. 146.

Murray, T.L., Kleinman, J.W., Iwatsubo, E.Y., and Dzurisin, D, 1992 Establishment of a permanent radio-telemetered GPS network on Augustine Volcano, Cook Inlet, Alaska [abs.]: Eos, (American Geophysical Union Transactions), v. 73, n. 43, p. 124.

Pauk, B.A., Power, J. A., Lisowski, M., Dzurisin, D., Iwatsubo, E. Y., and Melbourne, T., 2001, Global Positioning System (GPS) survey of Augustine Volcano, Alaska, August 3–8, 2000—data processing, geodetic coordinates and comparison with prior geodetic survey: U.S. Geological Survey Open-File Report 01-0099, 20 p.

Power, J.A., and Iwatsubo, E.Y., 1998, Measurements of slope distances and zenith angles at Augustine Volcano, Alaska, 1986, 1988, and 1989: U.S. Geological Survey Open-File Report 98-145, 17 p.

Power, J.A., Nye, C.J., Coombs, M.L., Wessels, R.L., Cervelli, P.F., Dehn, J., Wallace, K.L., Freymueller, J.T., and Doukas, M.P., 2006, The reawakening of Alaska's Augustine Volcano: EOS, (American Geophysical Union), v. 87, no. 37, p. 373.

Appendix 1. Station and telemetry description of existing Plate Boundary Observatory (PBO) Augustine GPS network.

AV01: Station is located on the western flank of volcano on a prominent andesite outcrop. Radio telemetry path for the station is to PBO station AC59 located at Ursus Head, about 15 miles to the northwest, and is repeated to the AVO communications facility in Homer. AV01 also host a repeater radio that repeats data from PBO regional station AC27 located in McNeil River State Refuge. AV01 consists of an original style PBO fiberglass enclosure, swing set, and SDBM.

AV02: Station is located on the southern flank of the volcano on a prominent outcrop of sedimentary rock. The radio telemetry path is from the station directly to the AVO communications facility located in Homer. The station consists of an original style PBO fiberglass enclosure, swing set, and SDBM.

AV04: Station is located on the upper western flank of the volcano on a prominent flat spot. The radio telemetry path is to Homer through a radio repeater located at PBO station AC59. The station consists of an original style PBO fiberglass enclosure and SDBM.

AV11: Station is located in bedrock on the western end of a low lying east-west trending ridge on the northeastern side of the volcano. The radio telemetry path is directly to the AVO communications facility in Homer. The station is near the old AVO GPS station AUGL and consists of an older style AVO fiberglass enclosure, swing set, and SDBM.

AV16: Station is located on a large rock outcrop west of the main lagoon on the west side of the island. The radio telemetery path is to Homer through a repeater radio located at PBO station AC59. Station consists of a newer style fiberglass enclosure, newer style swing, set and SDBM.

AV17: Station is located on a 20 foot diameter rock outcrop on the northern base of the volcano. The radio telemetry path is to Homer through a repeater radio located at PBO station AC59. The station consists of a newer style fiberglass enclosure and SDBM.

AV18: Station is located in bedrock on the prominent lava flow on the north side of the volcano within 100 feet of location of the destroyed PBO station AV03. The radio telemetry path is to Homer through a repeater radio located at PBO station AC59. The station consists of a newer style fiberglass enclosure, newer style swing set, and SDBM.

AV19: Station is located on a bedrock spine on the southwest flank of volcano. The radio telemetry is directly to the AVO communications facility in Homer. The station consists of a newer style fiberglass enclosure and SDBM.

AV20: Station is located on the southern flank of the volcano about 0.5 miles north of station AV02. The station is manually downloaded once every three months and is not currently part of the existing telemetry network. The station consists of a newer style fiberglass enclosure and SDBM.

Remote Sensing and Volcanic Emissions

View of the east side of Augustine Island on January 24, 2006, with a strong steam and gas plume rising from the summit. Upper parts of the volcanic edifice are lightly coated with ash and minor lahar deposits can be seen in some drainages. Alaska Volcano Observatory photo by Cyrus Read.

The 2006 Eruption of Augustine Volcano, Alaska
Power, J.A., Coombs, M.L., and Freymueller, J.T., editors
U.S. Geological Survey Professional Paper 1769

Chapter 20

Integrated Satellite Observations of the 2006 Eruption of Augustine Volcano

By John E. Bailey[1,2], Kenneson G. Dean[1], Jonathan Dehn[1], and Peter W. Webley[1]

Abstract

Satellite observations played an important role in monitoring the 2006 eruption of Augustine Volcano. It represented the first opportunity for observers to use, in an operational setting, new Web-based tools and techniques developed by the Alaska Volcano Observatory remote sensing group. The "Okmok Algorithm" was used to analyze thermal infrared satellite data and highlight changes in the style and phases of activity. Temperature measurements were used to estimate ash cloud heights, which compared favorably to radar and ground-based observations, although larger discrepancies were seen when compared to pilot reports. Brightness temperature difference techniques were used to locate and track the 14 ash clouds produced during the explosive phase of the eruption. Stacking of these analyses allowed the creation of composite maps showing the distribution of airborne ash. The data from these maps were further combined with information from local reports and samples of ashfall to create a prototype of a concentration map that could be used to assess the potential hazard an eruption represents to aircraft, infrastructure and human health.

Introduction

The Alaska Volcano Observatory (AVO) monitors volcanoes in Alaska using a combination of geophysical, geological, and remote sensing data. AVO is responsible for providing both government authorities and the general public with information concerning hazards related to volcanoes that are currently in or showing increased potential for eruption. In particular, the detection of volcanic ash plumes and clouds is critical because of the potential of ash to damage machinery, adversely affect human health, and disrupt transportation infrastructure. AVO issues reports in conjunction with the National Weather Service (NWS) through the Anchorage Volcanic Ash Advisory Center (VAAC) and Federal Aviation Administration (FAA) to alert aircraft to the presence of potentially hazardous volcanic ash clouds.

The need for a volcanic hazards monitoring program in Alaska was highlighted during the December 1989 eruption of Redoubt Volcano (Dean and others, 1994; Miller and Chouet, 1994), when a Boeing 747 flew into the Redoubt ash cloud, causing all four engines to fail (Casadevall, 1994). A catastrophic loss of life was averted by the pilot restarting engines less than 2 minutes before impact. Damage to the aircraft was estimated at $80 million. Using a combination of satellite datasets and analysis methods, AVO is now able to track ash clouds similar to those from Redoubt and predict their probable dispersion patterns (Webley and others, this volume). In addition, other techniques using satellite data aid evaluation of precursory activity and assessment of the evolution in an eruption by considering the thermal output at the edifice.

Augustine Volcano is a small dome complex that forms an island near the mouth of Cook Inlet, Alaska (fig. 1). It erupted in January 2006 after a 20-year period of repose (Power and others, 2006). Seismic activity began increasing during May 2005, the first gas emissions began in September 2005, and steam plumes were first observed in satellite data on December 12, 2005. Between January 11 and 17, 2006, the volcano erupted explosively 13 times and then produced a continuous output of ash and gas from January 28 until February 2. After a hiatus, the volcano went into a two-week period of effusive eruption, which ended in mid-March. Located 280 km southeast of Anchorage International Airport, the volcano sits along the path of several local and international air traffic

---

[1] Alaska Volcano Observatory, Geophysical Institute, University of Alaska Fairbanks, 903 Koyukuk Drive, Fairbanks, AK 99775.

[2] Now at Scenarios Network for Alaska Planning, University of Alaska Geography Program, Fairbanks, AK 99775.

corridors (Power and others, 2006). To help prevent aircraft encounters with ash clouds, regional air traffic patterns were altered during the explosive phase of the eruption. Several nearby communities were affected by ashfall over this same period (Wallace and others, this volume).

Prior to 2006, there had been five known major historical eruptions (1883, 1935, 1963–64, 1976, 1986) of Augustine Volcano. Typically these events involved explosive eruptions followed by a period of lava effusion. Due to the relative repeatability of eruptions, the volcano was already well instrumented prior to the identification of precursory activity. As evidence increased that an eruption was likely to occur, the original instrumentation was greatly supplemented (Power and Lalla, this volume). The 2006 eruption of Augustine was the most intensely monitored eruption in AVO history, resulting in a multitude of datasets and providing an excellent opportunity to calibrate and validate satellite datasets. The range of activity displayed by the volcano provided a rich diversity of signals, with both explosive (of phreatic and magmatic origins) and effusive events occurring, and thus provided a robust test of AVO Remote Sensing (AVORS) group's operational capabilities.

This paper provides an overview of the observations made by AVORS using satellite data for all phases of the eruption. It highlights two areas of observation and analysis that are the primary capabilities of satellite-based volcano monitoring—thermal anomaly detection and ash cloud detection and tracking. On the basis of these datasets, we present discussions of the trends in the volcano's thermal output, discrepancies in the measurements of eruption cloud heights, and maps of the concentration and distribution of ash detected.

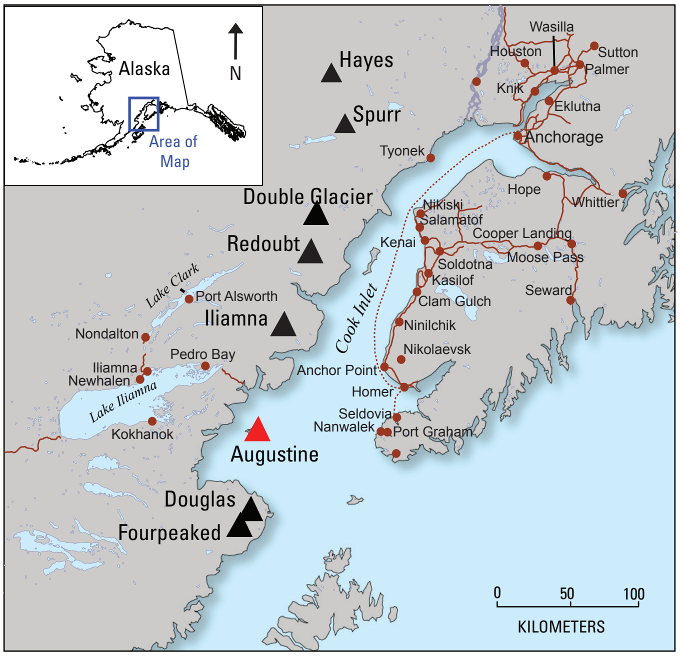

Figure 1. Map showing location of Augustine Volcano in Cook Inlet, Alaska. The area shown represents the Augustine sector that the Alaska Volcano Observatory remote sensing group creates from satellite data swaths to make large datasets more manageable during monitoring. Triangles indicate the location of volcanoes. Red lines show roads.

Background and Methodology

Satellite data provide quantitative information on volcanic clouds (Dean and others, 2002; Schneider and others, 2000) and elevated surface temperatures at volcanic edifices (Dehn and others, 2000; Harris and others, 1997, 2000). In recent years, new developments in satellite analysis have been implemented at AVO to harvest this information and make it available for operational monitoring purposes. These developments include systematic observation reporting using a dynamic database; Web-based imagery viewers; thermal anomaly detection and alarms; automated ash detection and compositing. Other tools, such as interfaces showing the detection of SO_2 using the Ozone Monitoring Instrument (OMI) and Atmospheric Infrared Sounder (AIRS) data have been developed through collaborations with other researchers. Satellite observations are supported by ground-based and airborne measurements (for example, use of a forward-looking infrared camera [FLIR]; Wessels and others, this volume); use of the Puff particle dispersion model (Searcy and others, 1998; Webley, this volume), ground-based aerosol samplers and LIDAR (Sasson and others, 2007; Webley and others, 2008), radar measurements (Schneider and others, 2006); webcam and pilot observations of activity. The operations of AVO combine all these measurements with those provided by seismology, geodesy and geology to create its best understanding of a volcanic event.

Satellite Datasets

The 2006 eruption of Augustine Volcano was the first operational test for many of the new remote sensing tools. They primarily analyze three satellite datasets: Advanced Very High Resolution Radiometer (AVHRR) data from the National Oceanic and Atmospheric Administration's (NOAA) Polar Orbiting Environmental Satellites (POES), Moderate Resolution Imaging Spectroradiometer (MODIS) data from the National Aeronautics and Space Administration's (NASA) Terra and Aqua satellites, and NOAA's Geostationary Operational Environmental Satellites (GOES) data. AVHRR and MODIS data are collected by receiving stations operated by the Geographic Information Network of Alaska (GINA) at the University of Alaska's Geophysical Institute. An additional AVHRR data feed is supplied by NOAA's Gilmore Creek satellite tracking station. GOES data are provided by the Naval Research Laboratory (NRL), Monterey Bay.

Data from these satellites/sensors are recorded in visible, mid-infrared, and thermal infrared wavelengths (table 1). AVHRR represents the "workhorse" for thermal anomaly and

Table 1. List of satellite data, wavelengths, and spatial and temporal resolution used to monitor volcanoes in Alaska.

[GOES, Geostationary Operational Environmental Satellites; NOAA, National Ocean and Atmospheric Administration; AVHRR, Advanced Very High Resolution Radiometer; MODIS, Moderate Resolution Imaging Spectroradiometer]

Satellite and Sensor[1]	Bands (B)	Wavelengths (µm)	Spatial Resolution (km)	Temporal Resolution (Repeat Coverage)
GOES Imager	1	0.52–0.72	8.0 at 60° N	0.5 hr
	4	10.5–11.5		
	5	11.5–12.5		
NOAA AVHRR (v3)	1	0.58–0.68	1.1 at nadir	Approx. every 1–2 hours at 60° N., due to large swath width and overlap
	2	0.73–1.00		
	3A (day)	1.58–1.64		
	3B (night)	3.55–3.93		
	4	10.3–11.3		
	5	11.5–12.5		
MODIS Terra/Aqua	28	7.175–7.475	1.0 at nadir	Approx. 2–4 passes per day
	29	8.4–8.7		
	31	10.78–11.28		
	32	11.77–12.27		

[1] All polar orbit except GOES (Geostationary).

ash detection. GOES is useful for tracking ash clouds because of its high temporal resolution. MODIS supplements the AVHRR thermal data and provides additional visible wavelength data allowing the creation of true color composites. Other data of opportunity (Landsat, Advanced Spaceborne Thermal Emission and Reflection Radiometer [ASTER]), which have high spatial resolution (<20 m/pixel) but infrequent repeat coverage (16+ days), can be used to corroborate observations made with AVHRR, MODIS, and GOES.

Detection Methodology

Dehn and others (2000) define a thermal anomaly (TA) as an unexpected increase in the radiant temperature value of a pixel in relation to its neighbors. For monitoring purposes, AVORS generally requires this difference (ΔT) to be >5°C to be of significance in any given dataset (AVHRR, MODIS, or GOES). However, in the early stages of activity at Augustine, observers were sensitive to smaller variations, especially when the anomalous pixels were located at the volcano's summit. Detection of thermal anomalies can be done either manually or using an automated algorithm. AVORS employs both methods, as there are a number of volcanological, environmental and technical explanations for TAs identified at a volcano, and not all are an indicator of volcanic activity. However, past history has shown that elevated radiant temperatures can often be a precursor to, or earlier indicators of, volcanic activity at Alaskan volcanoes, for example, Pavlof, 1996 (Roach and others, 2001), Okmok, 1997 (Patrick and others, 2003), Shishaldin, 1999 (Dehn and others, 2002), Cleveland, 2001 (Dean and others, 2004).

The 1996 eruption of Pavlof Volcano led to the creation of an algorithm that automatically processed images and identified thermal anomalies assessed to be of volcanic origin. This algorithm was successfully implemented during the 1997 eruption of Okmok and henceforth was known as the "Okmok Algorithm" (Dehn and others, 2000; Schneider and others, 2000; Dean and others, 2002). It has subsequently been updated (Okmok2) and augmented with a Web-based user interface that gives analysts access to a 15-year archive (1993+) of AVHRR images and Okmok Algorithm calculations for the North Pacific Region (fig. 2*A*). Additionally, if a thermal anomaly identified by the Okmok Algorithm meets certain criteria it generates warning emails and phone text messages that are sent to AVORS analysts. These alerts can also trigger a request for the acquisition of ASTER imagery at the volcano in question (Ramsey and Dehn, 2004).

Unfortunately it is difficult to create an algorithm that is 100 percent accurate in its identification of volcanic TAs, making manual checks an equally important part of regular monitoring activities. AVORS makes twice-daily manual checks of all acquisitions of AVHRR, MODIS, and GOES data and enters metrics for all identified thermal anomalies into a database using a Web-based interface. Reports that use a systematic template are then automatically generated and electronically distributed. The same database and electronic reports also include observations that are made of volcanic plumes and clouds.

The height and prediction of the movement of volcanic clouds are critical parameters required to assess their impact.

Satellite images offer a means to make these assessments, which would be difficult using only ground-based instruments and observations. Detection of these phenomena is complicated by the fact they might be composed of ash (of various size components), gas (of different species), or both. They might also assume different morphologies, related to atmospheric conditions, and whether they are a plume (generally used when the feature is still attached to the volcano) or a cloud (generally used when detached; that is, their volume is no longer being added to by the volcano). Although plumes will often have an elongated shape (due to regional wind effects) and higher ash density or steam content, volcanic clouds assume morphologies that can be hard to discriminate from surrounding meteoric clouds. Indeed all of these phenomena might not be seen on images if they are below higher altitude weather clouds.

As atmospheric winds carry volcanic clouds away from a volcano, diffusion and mixing cause them to spread, larger ash particles fall out, and their density is reduced. Thus an opaque cloud evolves into a translucent cloud. This evolution of volcanic clouds from opaque to translucent and the structure of the atmosphere both complicate and improve analyses (Schneider and others, 1995, 1999; Dean and others, 2004; Tupper and others, 2004). The identification of opaque versus translucent clouds requires the use of different bands in the satellite data. Opaque clouds appear as solid features, are colder than translucent clouds, and are usually visible in all bands. Translucent clouds by definition are less “solid” and often require a combination bands to be made visible.

Opaque clouds are needed to estimate height (table 2), where cloud-top temperatures measured from thermal IR band 4 (B4) satellite data are compared to atmosphere temperature profiles measured by sounders. This is referred to as the cloud temperature method. However, a major obstacle to the cloud temperature method is the tropopause, a position in the atmosphere where temperature does not decrease with height but stays about the same or, if above the tropopause, increases with height. An unambiguous height estimate can be derived only for clouds below the tropopause or larger umbrella clouds that reach into the stratosphere (Holasek and others, 1996; Tupper and others, 2007). For the 2006 Augustine eruption the lower tropopause boundary was at an altitude of approximately 8 km and upper boundary was at an altitude of approximately 16 km. Several of the 2006 Augustine eruptions were above the 8 km height.

Once a volcanic cloud becomes translucent valid cloud-top temperatures cannot be measured. However, a technique has been developed to detect translucent clouds that contain ash by subtracting long-wave thermal-infrared bands. This is referred to as the brightness temperature difference (BTD) or the split-window technique (Prata, 1989; Holasek and Rose, 1991). BTD values associated with volcanic ash have a negative signal between, 0 to −10 or lower, with the lowest value having the highest mass and presumably ash concentration for specific grain sizes (fig. 2*B*). Ash retrieval models have been developed to estimate ash particle size and total mass using BTD data (Wen and Rose, 1994; Schneider and others, 1999; Rose and Mayberry, 2000; Rose and others, 2001). Meteoric clouds can also exhibit negative BTD values, but the majority of these will not be more negative than −1.5. However, caution must be used when employing this technique, as volcanic clouds with ice-coated ash will not show a negative BTD signal (Prata 1989; Rose and others, 1995).

Ash Concentrations

One of the lessons learned from identifying and tracking the ash clouds produced by the Augustine eruptions was that it was easy to create a bottleneck in the flow of information being reported. This problem was caused by several factors: (1) six discrete eruptions occurred every few hours over a 20-hour period; (2) these events produced seven independently drifting ash clouds, visible in multiple datasets; (3) AVO reporting of ash clouds customarily involved text describing the position, direction of movement, and signal strength for each cloud on each image, a time consuming activity. In response to the bottleneck, a technique to produce composites of time-sequential BTD images was developed during post-eruption analysis. This method can act as a rapid visual summary of the previously cumbersome written descriptions.

There are three steps in the generation of the ash composites: (1) pixel values are extracted from selected images and compiled in a table, (2) BTD values are computed, and (3) values are displayed as an image. Three types of images are generated using the Most-Negative BTD values (Tupper and others, 2004), the Sum of BTD values, and Average BTD values. The Most-Negative image is generated such that the strongest BTD signal at each location is displayed and presumably includes the highest ash concentrations at that place. The Average image calculates average pixel values at each location and appears to identify signals that are related to the meteorological background, so it can be used to determine thresholds to differentiate weather from ash or other particulate signals. The Sum image is a simple summation of values at every location, but its usefulness is yet to be determined. Presently the Most-Negative images are automatically generated for each monitoring sector every 12 hours, with plans to implement updates in as near real-time as processing delays will allow. The images can viewed using a Web-based application, allowing multiple analysts to view the information simultaneously. These data have already proved to be a useful passive monitoring technique for small events at Cleveland (Alaska) and Bezymianny (Russia) volcanoes in 2007. However, as noted by Tupper and others (2004) some caution must be employed due to the failings of this technique for ice-coated ash.

Eruption Observations

The multitude of datasets collected during the eruption of Augustine permitted a detailed analysis of the events that

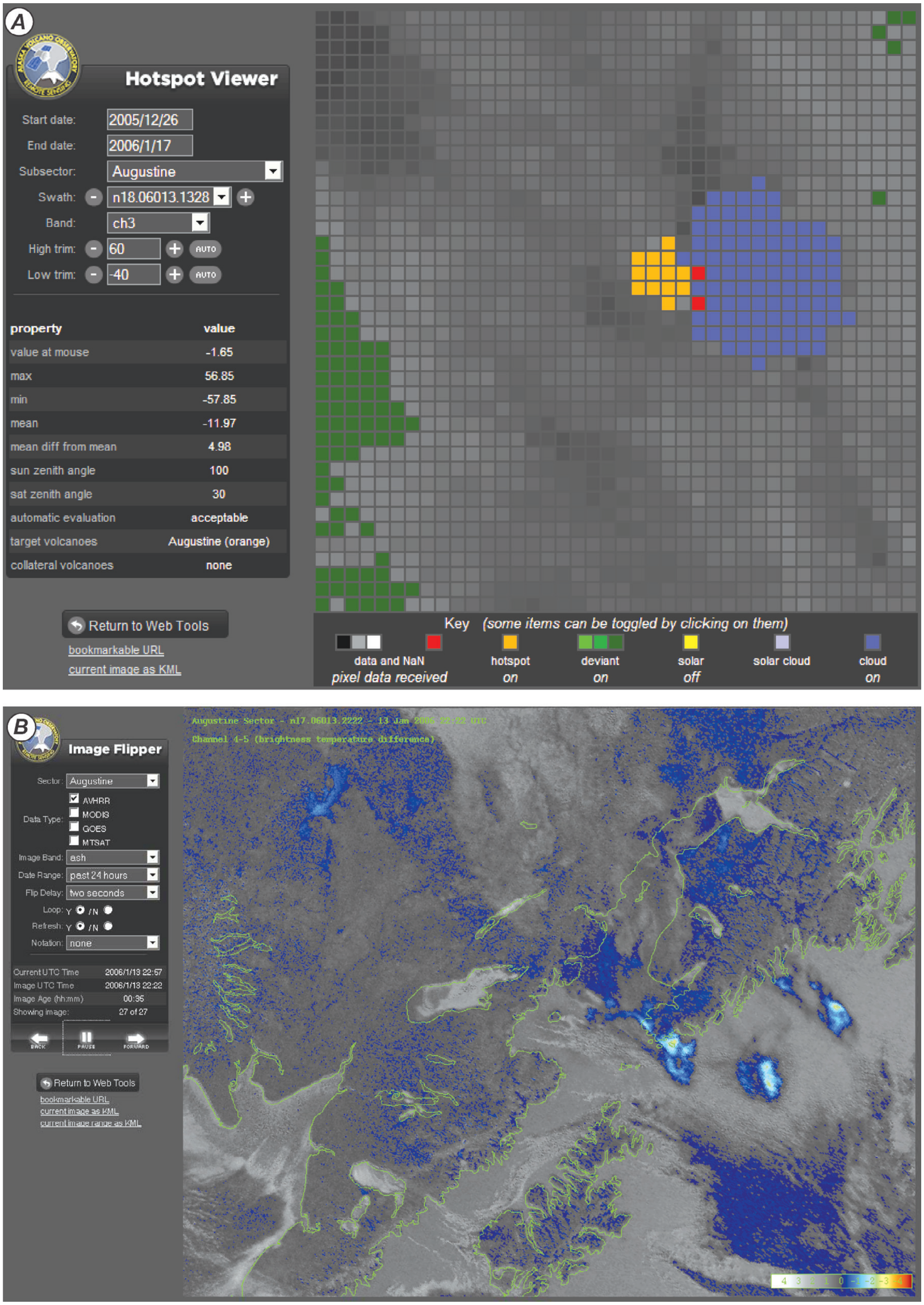

Start date: 2005/12/26
End date: 2006/1/17
Subsector: Augustine
Swath: n18.06013.1328
Band: ch3
High trim: 60
Low trim: -40

property	value
value at mouse	-1.65
max	56.85
min	-57.85
mean	-11.97
mean diff from mean	4.98
sun zenith angle	100
sat zenith angle	30
automatic evaluation	acceptable
target volcanoes	Augustine (orange)
collateral volcanoes	none

■□□	🟥	🟧	🟩	🟨	■	■

- ■□□ data and NaN — pixel data received
- 🟥 🟧 hotspot — on
- 🟩 deviant — on
- 🟨 solar — off
- ■ solar cloud
- ■ cloud — on

Sector: Augustine
Data Type: ☑ AVHRR ☐ MODIS ☐ GOES ☐ MTSAT
Image Band: ash
Date Range: past 24 hours
Flip Delay: two seconds
Loop: Y ● / N ○
Refresh: Y ● / N ○
Notation: none

Current UTC Time	2006/1/13 22:57
Image UTC Time	2006/1/13 22:22
Image Age (hh:mm)	00:35
Showing image:	27 of 27

Augustine Sector - n17.06013.2222 - 13 Jan 2006 22:22 UTC
Channel 4-5 (brightness temperature difference)

Figure 2. *A*, Web-based interface showing Okmok algorithm evaluation of an Advanced Very High Resolution Radiometer (AVHRR) image acquired at the start of Augustine Volcano's eruptive event 3 on January 13, 2006. *B*, Web-based interface showing a bright temperature difference evaluation of AVHRR bands 4 and 5 showing ash clouds from events 3, 4, and 5 at 1322 AKST (2222 UTC) on January 13, 2006.

Table 2. Augustine Volcano plume height observations.

[All satellite observations are based on AVHRR images unless noted. AKST, Alaska Standard Time; UTC, Coordinated Universal Time; NEXRAD, Next Generation Radar. See table 3 for dates of events]

Event	Satellite time (AKST/UTC)	Radar time (AKST/UTC)	Temperature based height (ft/km)	NEXRAD based height (ft/km)	Normalized difference wrt radar (%)	Comments
1	0456 1356	0449 1349	23,000 7.0	21,000 6.5	10	Tropopause (tropo) = 8.5 km., Plume < tropo.
2	0533 1433	0523 1423	28,900 8.8	33,500 10.2	−14	Tropo.= 8.5 km, Radar shows into tropo. Used 8.8 km for satellite.
3	0436 1336	0432 1332	29,500 9.0	33,500 10.2	−12	Tropo.= 8.5 km, Radar shows in tropo. Used 9 km for satellite.
4	1024 1924	0824 1749	NA	33,500 10.2	NA	Appears to be translucent cloud. Temperature values not valid.
5	1150 2050	1125 2025	29,500 9.0	34,500 10.5	−14	Tropo.= 9 km, Radar shows in tropo. Height 8 or 9 km for satellite.
6	1653 +0153	1642 +0142	32,000 10.0	34,000 10.5	−7	Tropo.= 9 km, Radar shows in tropo. Height 8 or 10 km for satellite.
7	1930 +0430	1930 +0430	36,000 11.0	34,500 10.5	4	Tropo.= 9 km, Radar shows in tropo. Height 7 or 11 km for satellite. GOES data.
8	0100 1000	0100 1000	23,000 7.0	20,000 6.1	15	Tropo.= 9 km, Radar < tropo. GOES data.
9	0838 1738	0801 1701	NA	45,000 13.7	NA	Tropo.= 9 km, Radar shows in tropo. Satellite temp. < meteoric cloud temp. suggests super cooling.
10	2042 +0542	2042 +0542	21,300 6.5	23,300 7.1	−9	Tropo. = 8 km, Radar shows < tropo.
11	NA	1140 +0840	NA	12,500 3.8	NA	No satellite data. Clouds translucent.
12	NA	0208 1108	NA	23,300 7.1	NA	No satellite data. Clouds translucent.
13	NA	0554 1654	NA	23,300 7.1	NA	Appears to be a translucent cloud.
14	NA	NA	NA	NA	NA	No satellite data.

occurred. The diversity of these datasets was further enriched by the range of activity displayed with explosive (of both phreatic and magmatic origins) and effusive events occurring. The evolution of the eruption was defined by four distinct phases, characterized by different styles of activity, and a hiatus (fig. 3; Coombs and others, this volume). The first phase was the precursory stage, which indicated increasing unrest at the volcano. Phase two saw the onset of explosive eruptions and culminated with a continuous eruption of material that defined phase three. This was followed by a hiatus during which the ash-cloud producing explosions stopped and the effusive activity that began sometime during phase two stalled. The fourth and final phase saw lava emplaced at the summit of the volcano.

The following sections describe the satellite observations for each phase of the eruption and give an overview of the events at the volcano. Other papers in this volume undertake a further exploration of these various aspects of the eruption using remote sensing techniques. McGee and others (this volume) describe the precursory and syn-eruption gas emissions at the volcano. Van Manen and others (this volume) combine satellite-derived thermal and seismic data to describe the activity beginning 10 days before the explosive phase. The distribution of tephra deposits produced during the eruption are defined by Wallace and others (this volume), whereas Webley and others (this volume) describe dispersion modeling of the plumes that produced these deposits. Ground-based imagery collected by time-lapse and infrared cameras is described in Sentman and others (this volume) and Paskievitch and others (this volume).

All times are given as Alaska Standard Time (AKST). In addition, times that relate to specific satellite images are also given in Universal Time (UTC) as the imagery UTC for its time/date identifier name. AKST is equal to UTC minus 9 hours.

Precursory Phase

The precursory phase began as an increase of microearthquakes beneath the volcano starting April 30, 2005 (Power and others, 2006). Initially occurring once or twice a day, the frequency steadily increased to 15 per day by mid-December (Jacobs and others, this volume). GPS measurements suggested pressurization of the volcano at sea level centered beneath the edifice (Cervelli and others, 2006). Starting in December small phreatic explosions were recorded by seismometers (McNutt and others, this volume), the largest of which occurred on the 10th, 12th and 15th. The December 12 event led to vigorous steaming and formation of a gas plume that was visible in AVHRR and MODIS data. Gas emissions started on December 12 at 1140 AKST (2040 UTC) and continued to at least 0442 AKST, December 13 (1342 UTC), although meteoric cloud cover prevented observations for the next 10 hours. The plumes were observed in visible and mid-infrared-band data. Most of the observed plumes were narrow and semi-translucent extending to 125 km or more, mostly to the south-east. No negative signal was detected in the BTD data, which combined visual observations by webcams on Augustine, suggested that there was little to no ash in these plumes. They were below 1,500 m altitude based on sounder data collected at 0000 UTC, December 6, 2005, at Kodiak. The best image showing this activity was recorded by the MODIS Aqua satellite at 1323 AKST (2223 UTC) (fig. 4). These events represented the first activity at Augustine that was visible in satellite data.

Explosive Phase

Generally cloudy conditions obscured views through December 2005 and early January 2006. On January 5, 2006, a break in the cloud cover allowed weak thermal anomalies (ΔT <3°C) to be detected at 2024 and 2119 AKST (0524 and 0619, January 6 UTC). Simultaneous webcam images collected at Homer showed clear views of a steaming edifice. Mostly cloudy weather returned and prevented further activity being seen in satellite images until 2245, January 10, AKST (0745 UTC, January 11) when a thermal anomaly (ΔT = 4.3°C) and a gas plume were detected. The plume was attached to the volcano indicating that material was still being emitted, and drifted to the southwest and west with the leading edge 74 km west of the summit of the volcano. It was only detected in band 3 data. No plume signal was detected in the longer TIR bands (B4 and B5) or in the split-window data, suggesting that little or no ash was in this emission.

January 11, 2006

Six hours later, two explosive eruptions occurred on at 0444 AKST (1344 UTC) and at 0512 AKST (1412 UTC) (table 3). Views of the edifice captured by AVHRR and MODIS in the hours after the eruptions showed a weak thermal anomaly located at the summit with low band 3 (B3) radiant temperatures (fig. 3). No thermal anomalies were observed immediately preceding the explosions, potentially suggesting that there was little or no fresh juvenile lava in the conduit

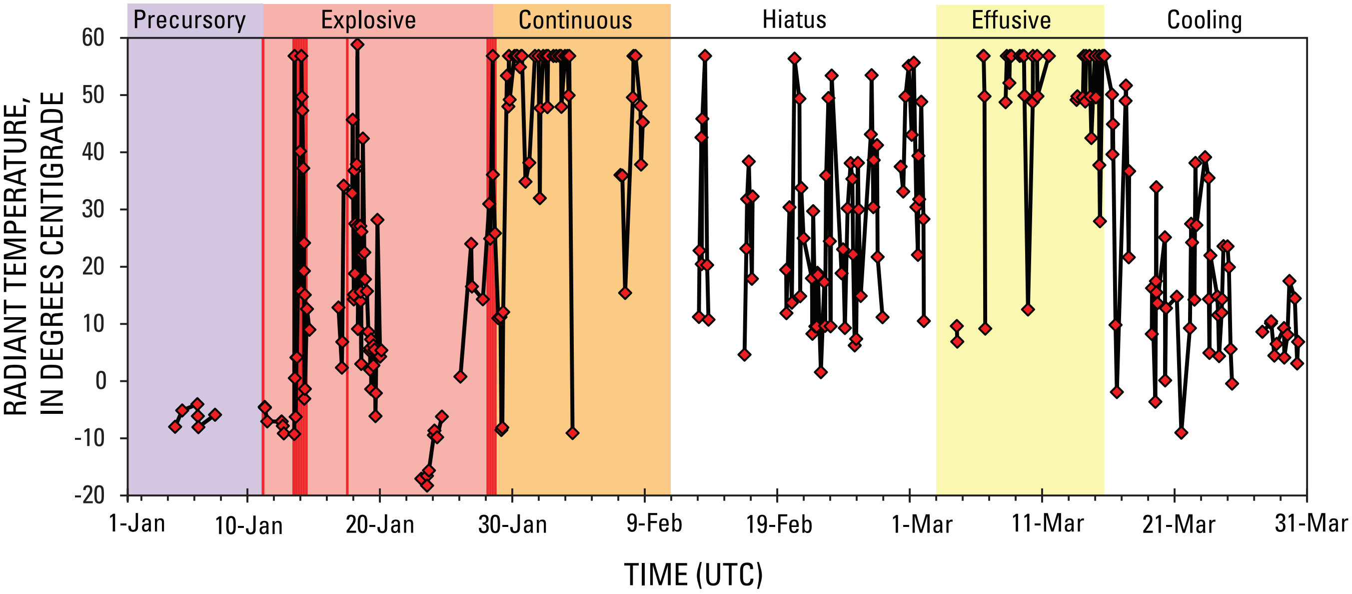

Figure 3. Plot of radiant temperatures of thermal anomalies seen at Augustine Volcano during the first 3 months of 2006 compared to eruption phases defined by geophysical measurements in Coombs and others (this volume). Vertical red lines represent explosive vents during the explosive phase.

that significantly contributed to the explosion. Analysis later confirmed that the ejected material was primarily older recycled debris (Wallace and others, this volume).

The material emitted by both of these eruptions was contained in a single opaque cloud although the curled tail of the second cloud may have been a remnant from the first eruption. The explosive eruptions were recorded on AVHRR satellite images within a few minutes of the start time of each event. The first image at 0448 AKST (1348 UTC) recorded the volcanic cloud 3 minutes after the explosive eruption ended (fig. 5*A*). This cloud was circular and directly over the volcano. The coldest volcanic cloud-top temperature was −46°C which corresponds to an altitude of approximately 7 km (23,000 ft) based on a dry atmosphere profile collected at Kodiak Island. Another image was recorded at 0525 AKST (1425 UTC), 10 minutes after the second eruption ended (fig. 5*B*). This cloud was also opaque and located over the volcano. It had a volcanic cloud-top temperature of −55°C, which corresponds to an altitude of approximately 8.5 km (28,000 ft) based on the same Kodiak atmospheric profile. Ground-based next generation radar (NEXRAD) estimates of volcanic cloud heights were similar for the first eruption with radar showing 6.5 km but were significantly different for the second with radar showing 10.5 km (Schneider and others, 2006). Wind directions suggested that the maximum cloud height was >8 km (~26,250 ft). The opaque cloud was observed in satellite images for 37 minutes, during which time the plume ascended 1.5 km (8,000 ft) at approximately 0.2 km/min (216 ft/min). On the basis of radar ascension rates were 0.108 km/min (355 ft/min).

GOES and AVHRR satellite passes recorded the movement, dispersion, and evolution of the plume. Images recorded

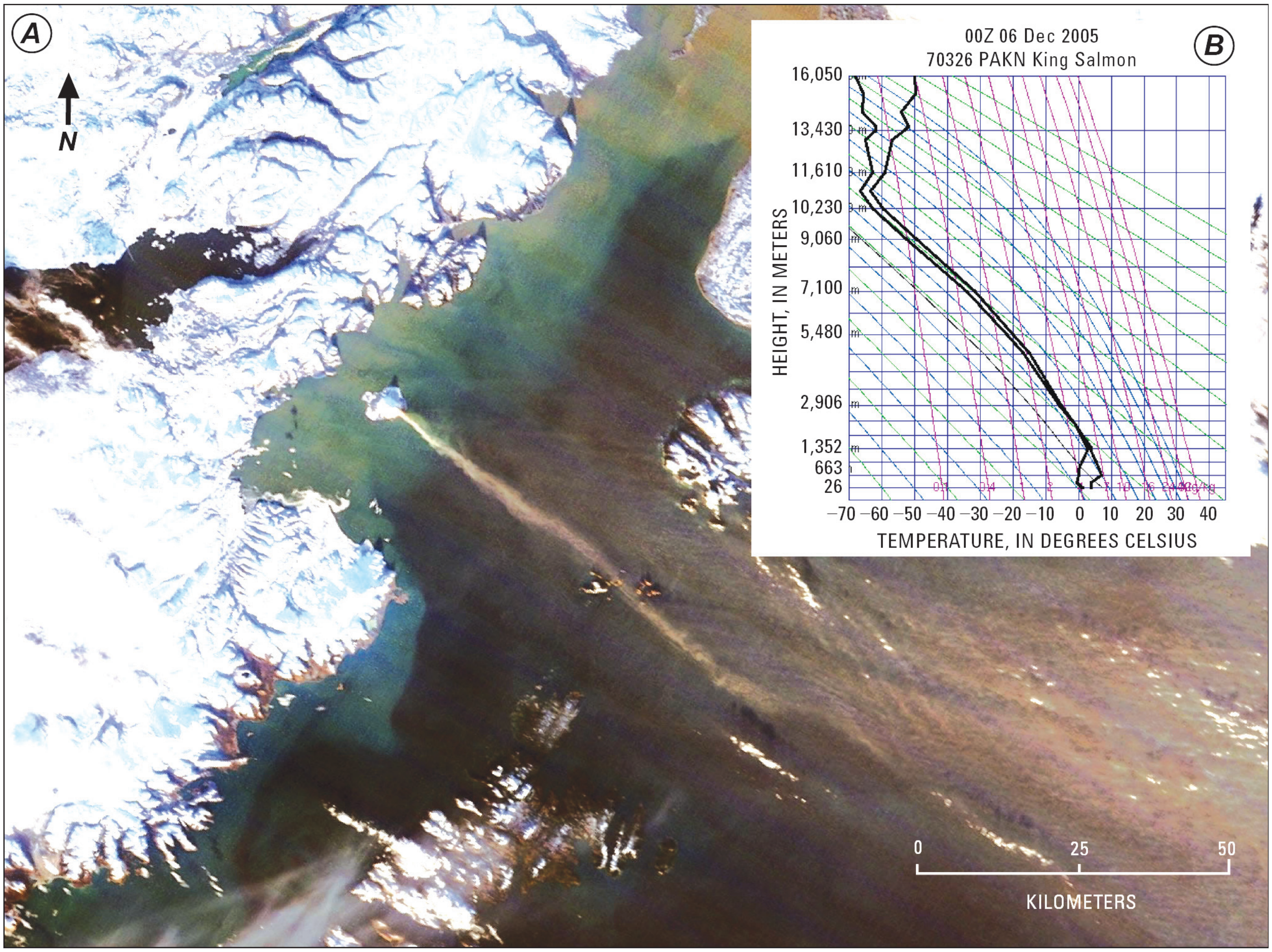

Figure 4. *A*, Moderate Resolution Imaging Spectroradiometer satellite true-color composite image showing a steam plume observed extending from Augustine Volcano for approximately 80 km (50 miles) to the southeast. There was no ash signal from the brightness temperature difference data indicating that this emission was most likely water vapor and SO_2. Image was acquired by the Terra satellite on 12 December 12, 2005 at 1216 AKST (2116 UTC) and processed by the Geographic Information Network of Alaska, University of Alaska Fairbanks. *B*, Regional radiosonde from the University of Wyoming's archive.

between 0530 and 0839 AKST (1430 to 1739 UTC) showed ash drifting to the northeast of the volcano, over Cook Inlet and the Alaska Peninsula. The opaque cloud began to disperse and become translucent at about 0530 AKST (1430 UTC), approximately 1 hour after the second explosion. These translucent clouds had BTD ash signals that ranged in value from −2.1 to −3.1, with the most negative values observed at 0730 AKST (1630 UTC; fig. 5). Data recorded after 0839 AKST (1739 UTC) had possible ash signals < −1, but these were not readily distinguishable from background noise. The cloud was mostly dispersed after 0930 AKST (1830 UTC). Generally, the strongest signals (< −3) were over water and within 20 km of the volcano. The majority of ash from these explosions probably fell into Cook Inlet. Very light ashfalls were reported approximately 100 km north-northwest at Lake Clark (Wallace and others, this volume) which is beyond the satellite-defined impact area. Most likely airborne ash in this region was at a concentration below the satellite detection threshold.

January 13–14, 2006

Six explosions (events 3 to 8) occurred on January 13 and 14 over a 25 hour period (fig. 6). Each explosion resulted in volcanic clouds that were tracked on 19 AVHRR satellite images, giving an average view of almost one image per hour. The first event for this period (event 3) occurred at 0424 AKST, January 13 (1324 UTC). An AVHRR image that was captured during the event (fig. 2*A*) showed an opaque cloud with a temperature of −54°C that reached an estimated altitude of 8.0 to 9.0 km based on sounder data collected at King Salmon. The cloud was still opaque when seen on a second image at 0456 AKST (1356 UTC), with a temperature of −52°C and was still at an altitude of approximately 8.0 to 9.5 km. NEXRAD radar reported a height of 34,000 ft (10.5 km). The cloud became translucent between images captured at 0637 and 0834 AKST (2 to 4 hours after the start of the eruption) with a BTD signal that weakened from −4.0 to −3.2 during this period. The volcanic cloud drifted east across Cook Inlet passing over the southern tip of the Kenai Peninsula. Ashfall was reported in the Homer, Seldovia, Port Graham, and Nanwalek areas between 0514 and 0850 AKST (Wallace and others, this volume). On the basis of satellite images, the ash cloud had moved east of Homer by 1024 AKST (1924 UTC) and by 1330 AKST (2230 UTC) the plume drifted over the coast near Seward, Alaska, and continued east across the Gulf of Alaska.

The second explosion (event 4) occurred at 0847 AKST (1747 UTC) and was recorded on an AVHRR image at 1024 AKST (1924 UTC). The image showed the cloud in transition from opaque to translucent and drifting east from the volcano. The cloud-top temperature of the opaque portion was −45°C, which suggested an altitude between 6.5 and 13.5 km based on sounder data collected at Kodiak. NEXRAD radar reported a height of 30,000 ft (9.1 km), and a pilot reported a height of 47,000 to 52,000 ft (14.3 to 15.8 km). The translucent portion of the cloud had a maximum BTD signal of −3.0 at the leading edge of the cloud that was approaching the Kenai Peninsula. This ash cloud passed over Seldovia and other towns at the southern tip of the Kenai Peninsula at 1130 AKST and then proceeded across the Gulf of Alaska. No ashfall was reported for this period from any towns in the area.

The third explosion (event 5) occurred at 1122 AKST (2022 UTC). Satellite images from 1130 to 1142 AKST (2030 to 2042 UTC) showed that the volcanic cloud was opaque with some translucent portions along its rim. The coldest cloud-top temperature of −54°C, observed at 1142 AKST (2042 UTC) translated to an altitude of 7.5 to 9.0 km based on sounder data collected at King Salmon. NEXRAD radar reported a height of 36,000 ft (11 km), and pilots reported a height of 52,000 ft (15.8 km). After 2042 UTC the cloud became more translucent as seen by an increase in cloud-top temperatures and increasing BTD signal strength. The ash cloud drifted east and passed over the lower Kenai Peninsula. It passed over towns in the vicinity of Seldovia from approximately 1322 to 1602 AKST and then continued across the Gulf of Alaska. No ashfall was reported for this period from any towns in the area.

The fourth explosion (event 6) occurred at 1640 AKST (0140 UTC, January 14). The first image recorded at 1645 AKST (0145 UTC, January 14) showed an opaque cloud with a translucent rim at the southern edge of Augustine Island that appeared to be still attached to the volcano. The minimum cloud-top temperature was −53°C, which corresponded to an altitude of 7.5 to 10.0 km based on the sounder at King Salmon. NEXRAD radar reported a height of 34,000 ft (10.4 km) and pilots reported a height of 30,000 to 35,000 ft (9.1 to 10.7 km). Images recorded around 1700 AKST (0200 UTC, 14 January) and later showed the cloud becoming translucent, as indicated by increasing cloud temperatures and increasing BTD signal strength. The most negative BTD signal of −4.0 was recorded at 1829 AKST (0329 UTC, 14 January). Unlike the previous events on this day, the ash cloud drifted to the south-east over Cook Inlet and the Gulf of Alaska. No ashfalls associated with this eruption were reported, and observations were unlikely because the cloud mostly drifted over the open ocean.

The fifth explosion (event 7) occurred at 1858 AKST (0358 UTC, January 14). GOES images recorded at 1900 AKST (0400 UTC, January 14) did not detect a volcanic cloud, probably due to its low spatial resolution at these latitudes, but the images at 1930 AKST (0430 UTC, January 14) and 2000 AKST (0500 UTC, January 14) showed an opaque cloud that was translucent along its periphery. The opaque cloud had a minimum temperature of −49°C on both of these images, which correlates to a height of 7 to 11 km based on the sounder at King Salmon. NEXRAD radar reported a height of 30,000 ft (9.1 km), and there were no pilot reports. The cloud became more translucent after 2000 AKST (0500 UTC, January 14), with the BTD-based ash signal reducing in strength over the next 3 hours. Time sequential GOES images

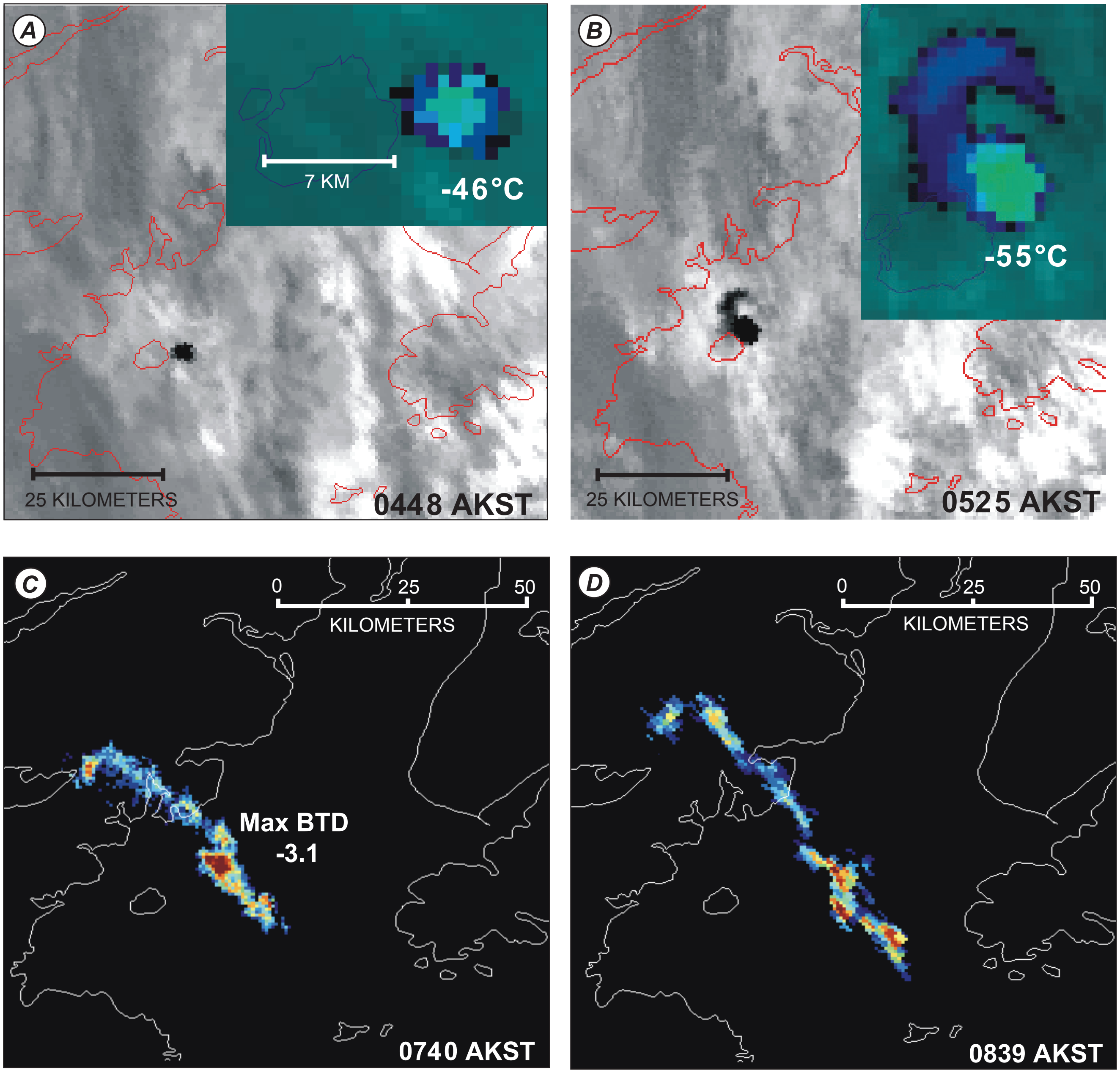

Figure 5. Advanced Very High Resolution Radiometer (AVHRR) satellite images of Augustine Volcano 2006 eruption event 1, the first explosive eruption. *A*, Band 4 thermal infrared image showing opaque cloud acquired at 0448 AKST (1348 UTC) on January 13, 2006. Insert shows enlarged view of the plume color-coded based on temperature. Coldest temperatures are indicated by light green pixels. *B*, Similar to *A*, acquired at 0525 AKST (1425 UTC). *C*, Brightness temperature difference (BTD) image showing the ash cloud drifting to the northeast over the Cook Inlet, acquired at 0740 AKST (1640 UTC). Most negative values of BTD are indicated by red pixels and indicate the highest concentration of ash. Moderate concentrations are shown by yellow and green pixels, with the blue pixels indicating the lowest concentrations of ash. *D*, Similar to *C*, acquired at 0839 AKST (1739 UTC).

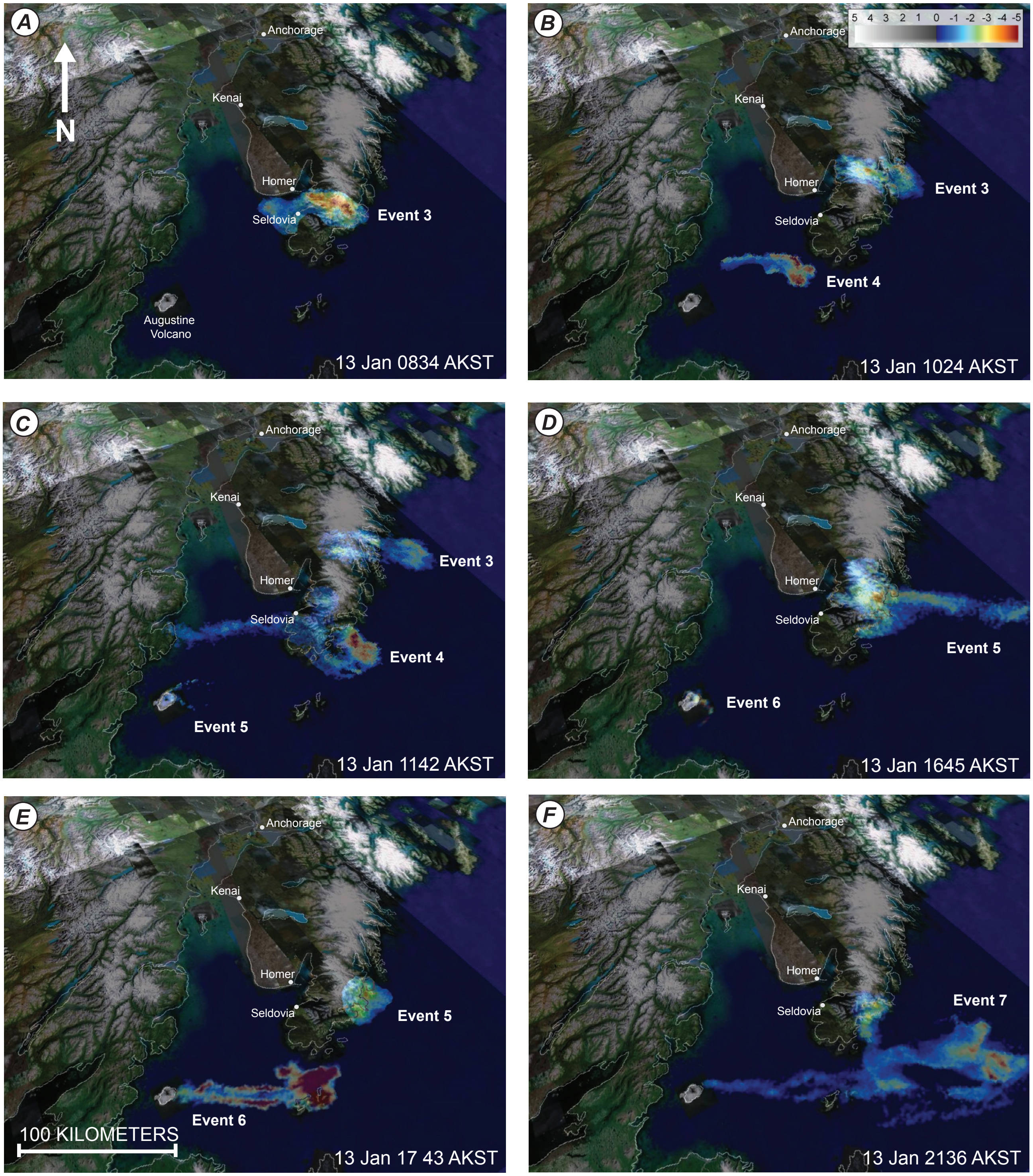

Figure 6. Advanced Very High Resolution Radiometer (AVHRR) data shown as brightness temperature difference images to detect ash clouds from the explosive events on January 13–14, 2006. The images are shown as overlays in Google Earth for geographic reference. Local time stamps are shown on images and equate to the following image UTC acquisition times: *A*, 1734, January 13; *B*, 1924, January 13; *C*, 2042, January 13, *D*, 0145, January 14; *E*, 0243, January 14; and *F*, 0636, January 14.

showed that the ash cloud drifted east over the lower Kenai Peninsula towns of Seldovia, Port Graham, and Nanwalek, but no ashfall was reported. Using just AVHRR data, it was difficult to distinguish event 7 ash clouds from previous ones in the general vicinity of the volcano. However, the high temporal resolution of time-sequential GOES data was sufficient to identify and track the movement of these ash clouds.

The sixth explosion (event 8) occurred on January 14 at 0014 AKST (0917 UTC). GOES satellite data recorded between 0030 and 200 AKST (0930 and 1100 UTC) showed an opaque cloud that became translucent as it dispersed. The opaque cloud had a minimum temperature of −50°C, which correlates to an altitude of 7.0 to 10.5 km. The translucent cloud had a maximum BTD signal strength of −3.2. The cloud moved east and north-east over the southern end of the Kenai Peninsula and the towns of Homer, Seldovia, Port Graham, and Nanwalek, then to the south-east across the Gulf of Alaska. No ashfalls were reported from this eruption.

Observations of thermal anomalies on January 13–14 were ambiguous due to the interaction of different effects. The maximum temperatures measured were a combined consequence of how long had passed since fresh, hot material was erupted and whether the volcanic cloud or steam at the volcano restricted views of the crater and surrounding deposits (fig. 3). In some images, solar reflection off the steam plumes also made the size of anomalies an uncertain parameter. In cases where images were collected with a clear view of the vent and/or fresh deposits around the edifice, AVHRR sensors reached their maximum calibration temperature (56.85°C) for band 3, and several pixels became saturated.

January 17, 2006

A further large explosion (event 9) occurred on January 17 at 0758 AKST (1658 UTC). GOES images recorded before the eruption showed a large weather cloud extending south-east and northwest from the volcano and approximately 200 miles long. The volcano erupted through this cloud. The GOES data recorded during and after the eruption did not show a distinct, coherent opaque volcanic cloud or definitive BTD ash signals that could be clearly distinguished from background weather signals. An AVHRR satellite pass at 0838 AKST (1738 UTC) did show a very distinct volcanic cloud in mid-infrared (B3) and thermal infrared (B4) wavelengths (fig. 7*B*). The B4 data showed minimum cloud-top temperatures of −56°C, which were colder than any height on the atmospheric temperature profiles collected at Kodiak. This suggested that the cloud was super-cooled, although this conclusion is tentative as the underlying meteoric cloud may have impacted the measured cloud temperature. The NEXRAD radar showed a maximum altitude of 45,000 ft (13.4 km), which indicated the ash cloud was well into the tropopause (Schneider and others, 2006).

Ashfall was reported from the Iliamna Lake and Lake Clark areas from 1200 to 1700 AKST (Wallace and others, this volume). A MODIS satellite image recorded on January 19, 2006 shows ash deposits on the snow-covered terrain west of Augustine Volcano beyond Iliamna Lake (fig. 7*A*). There was also a report of ashfall east of the volcano at Port Graham on the Kenai Peninsula. The AVHRR BTD data did not show the volcanic cloud extending to the east; however, Puff model predictions indicate that low level ash was predicted to pass over this area and thus the ash may have been below the detection limits of the satellite sensor (Webley and others, this volume). A similar situation occurred during the eruption of Cleveland Volcano in 2001, when a pilot reported the volcanic cloud well beyond the impacted area as defined by satellite data (Dean and others, 2004).

Similar to events on January 13–14, high radiant temperatures (>40°C) were only recorded in a few satellite passes following the explosion on January 17. The highest temperature measurement of 58.84°C was recorded at 2232 AKST (0732 UTC, January 18) in band 20b on Terra's MODIS sensor. Although values rapidly cooled from this peak, over the next 3 days elevated (above background) temperatures persisted (fig. 3). Poor weather conditions prevented observations January 20–23, but clear views on January 24 showed relatively weak thermal anomalies (ΔT = 10–15°C), with low radiant temperatures (<5°C).

Continuous Phase

Over the next 4 days the radiant temperatures increased rapidly, and activity moved into a phase that began with four more discrete explosions (events 10 to 14; table 3) that by 1430 AKST, (2330 UTC) January 28 transitioned into nearly continuous emission of gas and ash. Multiple ash clouds could be seen on most of the satellite data from this time until January 30 (fig. 8). The ash clouds drifted to the south on January 28 and 29 and then east after that time.

Eight minutes after the start of event 10, a satellite pass at 2042 AKST, January 27 (0542 UTC, January 28), showed an opaque cloud with a temperature of −45°C that correlated to estimated heights of 21,300, 31,200, or 47,600 ft (6.5, 9.5, or 14.5 km) based on atmospheric temperature profiles collected at King Salmon. Confusion in the true value was due to these heights being at or above the tropopause boundary. The maximum height recorded by radar was 34,500 ft (10.5 km), which puts the cloud top in the tropopause. The next satellite pass at 2115 AKST (0615 UTC, January 28) showed that the plume had become translucent with a BTD of −6.9 and was drifting south.

Events 11 and 12 were seen on four satellite passes between 2337 AKST, January 27 and 0745 AKST, January 28 (0837 to 1645 UTC, January 28). In the images translucent volcanic clouds with BTDs of −2.8 to −4.5, respectively, were seen drifting south over Kodiak Island. Event 13 was observed 34 minutes after the end of the eruption by a satellite pass at 819 AKST (1719 UTC) that showed a cloud which was part opaque and part translucent. The temperature of the opaque cloud was −45°C, which corresponded to an estimated height between 19,700 and 32,800 ft (6.0 to 10.0 km) based on an atmospheric profile collected at Kodiak. The tropopause was at 19,700 ft (6.0 km). NEXRAD gave heights of 25,000 ft, and pilot reported heights suggested 35,000 ft. The translucent portion of the cloud had BTD values of −2.4, and as the cloud drifted south the BTD signal strengthened to a minimum of −7.4.

During the continuous phase, radiant temperatures at the summit anomaly remained consistently high (>45°C) until February 3, after which time cloudy weather prevented satellite observations. Thermal anomalies were observed in most images during this period with many images showing saturated pixels (fig. 9*A*), and most recording maximum AVHRR sensor values. The anomalies were large (10+ pixels) and varied in morphology. In some cases they were roughly circular and located around the summit, but in several images they were elongated along the flanks of the volcano. In a few instances the changes in size and morphology could be accounted for by solar reflection off steam and large satellite viewing angles, but in most cases these observations suggested pyroclastic flow activity on the volcano. This hypothesis was supported by webcam views (fig. 9*B*) and the color and morphology of deposits shown by a high resolution ASTER images (fig. 9*C*). Field studies later confirmed that there had been pyroclastic flow activity on the north and east flanks (Vallance and others, this volume).

Clear views on February 7 and 8 showed thermal anomalies with relatively high temperatures, but the values were decreasing in magnitude through the 8th. The thermal anomalies were much smaller than those observed a week before, and the greater size seen in some anomalies could be accounted for by radiation from, and solar reflection off, steam plumes. Poor weather prevented satellite views of the volcano from February 9–12, during which time the activity transitioned out of the continuous phase and average temperatures dropped to 20 to 30°C. The volcano now entered an eruptive hiatus that lasted almost a month. Ground-based observations, seismology, and geodesy all suggest that from February 10 to March 3 no new material was extruded from the volcano (Coombs and others, this volume).

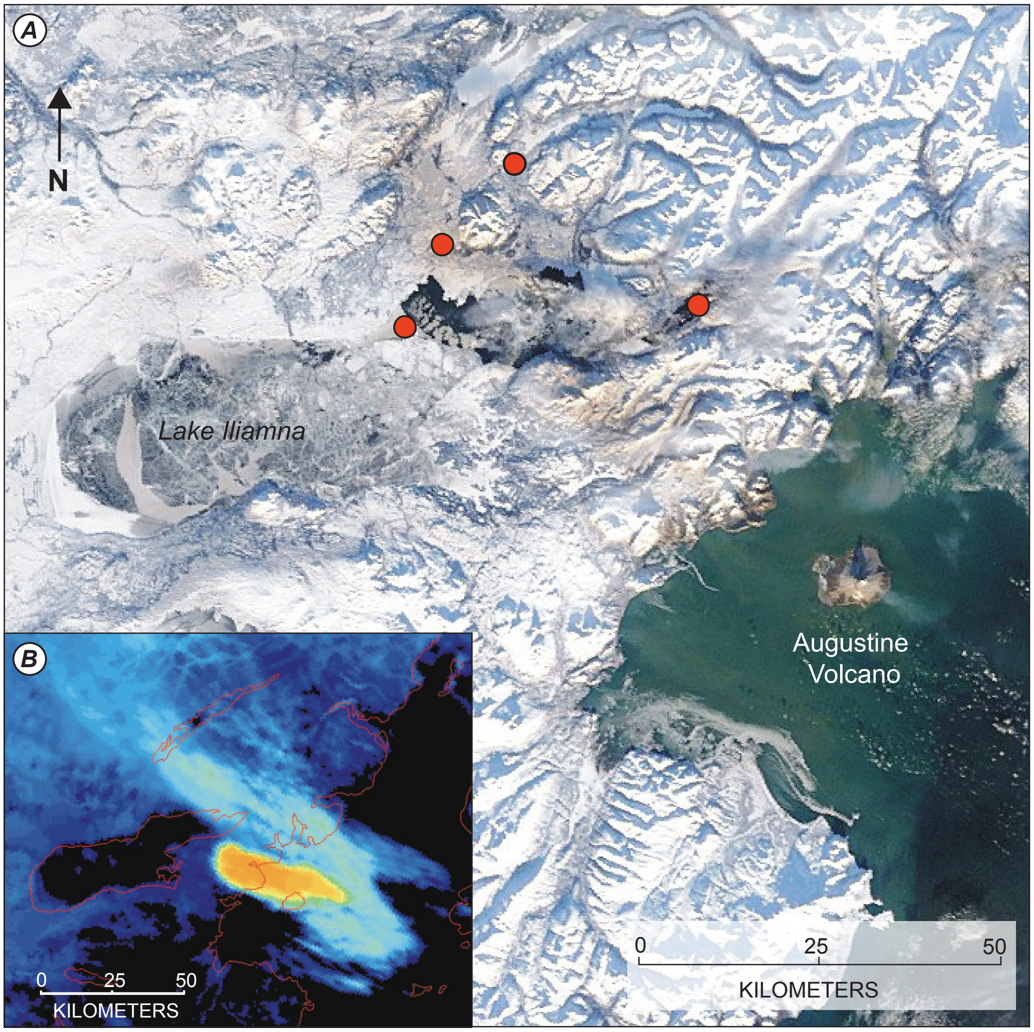

Figure 7. *A*, Moderate Resolution Imaging Spectroradiometer image showing ash fall from the eruption of Augustine Volcano on January 17, 2006. The ash cloud from the eruption drifted northwest from the volcano and dropped ash along a path that crossed the east end of Iliamna Lake, seen as brown tint in the snow. The red circles indicate (approximate) locations where light ash fall was reported or samples were collected. The image is a RGB color composite using visible bands 1, 4, and 3 acquired at 1240 AKST (2140 UTC) on January 19, 2006. *B*, Advanced Very High Resolution Radiometer band 4 view of the opaque ash cloud, acquired at 0838 AKST (1738 UTC) on January 17. Dense areas of ash are colored orange and yellow, with the distribution of finer ash shown in light blue.

Effusive Phase

During the 36 hours following the first explosions on January 11, several sequences of small, similar, regularly spaced volcano-tectonic earthquakes occurred, with rates as high as 3 to 4 per minute (Power and Lalla, this volume). Comparable sequences have been seen at other volcanoes, most notably Mount St. Helens (Dzurisin and others, 2005), in association with the emplacement of lava domes. During an over-flight on January 16, a new small dome was observed at the summit of Augustine Volcano. It was partly destroyed by the January 17 explosion, which blasted a 20 to 30 m crater in the dome. However, the lava dome continued to grow during January into early February and, after a period of hiatus, during March. The effusion of this final dome, and later two lava flows, defined the final phase of the activity (fig. 3).

The transition into the effusive phase was not observed by satellites due to cloudy weather that persisted from March 2–6. The radiant temperature values of two thermal anomalies that were observed on March 4 were greatly reduced by the cloud cover overhead. On the basis of seismic records, rockfalls increased on March 3 (Jacobs and McNutt, this volume), and on March 7 seismic activity once again became characterized by persistent, repetitive, and nearly identical earthquakes that increased in rate and size, forming a continuous signal by March 8 (Power and Lalla, this volume). Lava extrusion at the summit increased markedly in association with these signals (Power and others, 2006). As the volume of lava grew, two blocky lava flows moved down the volcano’s north and north-east flanks (fig. 10). These deposits were highly unstable and generated multiple block-and-ash flows through regular collapses of volumes of fresh lava (Sentman and others, this volume; Vallance and others, this volume; Wessels and others, this volume)

The repetitive earthquakes began a slow decline in frequency after March 14 and disappeared by March 16 (Power and Lalla, this volume). A similar transition was seen in satellite data as thermal anomalies exhibited persistently high radiant temperatures (>45°C) until March 15–16, when temperatures began to decrease. Despite the cessation of effusive activity, frequent collapses of the dome and flows continued due to the unstable nature of the new material, leading to hotter material being exposed and contributing to the scatter seen in the overall cooling curve shown by the radiant temperatures (fig. 3).

Discussion

The eruption of Augustine Volcano provided an opportunity to robustly test monitoring methods and techniques recently developed by the AVORS group. The measurements these improvements made possible led to notable insights in three areas of interest: the patterns of thermal activity, ash cloud heights, and ash concentration mapping.

Table 3. Explosive events that occurred at Augustine Volcano during the explosive and continuous phase of its 2006 eruption.

[Time measurements are based on monitoring by seismic instruments. AKST, Alaska Standard Time; UTC, Coordinated Universal Time]

Event	Local time (AKST)	Time (UTC)	Duration (min: sec)
1	0444 11-Jan-06	1344 11-Jan-06	1:18
2	0512 11-Jan-06	1412 11-Jan-06	3:18
3	0424 13-Jan-06	1324 13-Jan-06	11:00
4	0847 13-Jan-06	1747 13-Jan-06	4:17
5	1122 13-Jan-06	2022 13-Jan-06	3:24
6	1640 13-Jan-06	0140 14-Jan-06	4:00
7	1858 13-Jan-06	0358 14-Jan-06	3:00
8	0014 14-Jan-06	0914 14-Jan-06	3:00
9	0758 17-Jan-06	1658 17-Jan-06	4:11
10	2024 27-Jan-06	0524 28-Jan-06	9:00
11	2337 27-Jan-06	0837 28-Jan-06	1:02
12	0204 28-Jan-06	1104 28-Jan-06	2:06
13	0742 28-Jan-06	1642 28-Jan-06	3:00
14	1430 28-Jan-06	2330 28-Jan-06	continuous

Patterns of Thermal Activity

Thermal anomalies for the Augustine eruption were defined by a combination of manual methods and automated detection using the Okmok II algorithm. Measurements using thermal-infrared channels on the GOES, AVHRR and MODIS satellite sensors are integrated values for areas of 1 km^2 and higher for each pixel (table 1). This limited spatial resolution limits the use of these datasets to describe the details of volcanic activity at Augustine. However, the high frequency of repeatability does allow trends to be seen. As described in the observations section these trends can be correlated to styles of activity, providing further supporting evidence for the definition of phases (fig. 2). More detailed descriptions of the activity and erupted products’ thermal morphology require higher resolution thermal data (for example, ASTER), or use of ground-based thermal imaging (Sentman and others, this volume; Wessels and others, this volume). However, the satellite measurements can be used quantitatively to estimate erupted volumes and flux (Harris and others, 2007).

Ash Cloud Height Measurements

The 2006 Augustine eruption resulted in a large assortment of coincident observations that provided estimates or measurements of volcanic cloud heights, more so than any previous Alaskan eruption. Typical measurement methods include cloud-top temperatures, wind shear, and pilot reports. Additionally, for the Augustine eruption a new technique, the ground-based NEXRAD radar, was available (Schneider and others, 2006). Each method can produce very different estimates of ash cloud heights and the recent Augustine eruptions were no exception (table 2).

Pilot observations provide on-site, instant estimates of the ash cloud heights but are also the least quantitative and generally give values much greater than other techniques. Measurements made by NEXRAD radar and the satellite cloud-top temperature also have the advantage of being collected at coincident times, allowing direct comparison. A normalized difference in percentage using the radar as control was calculated for each event using:

$$[(\text{Cloud-top Height Estimate} - \text{Radar Height Estimate}) \,/\, \text{Radar Height Estimate}] \times 100 \qquad (1)$$

Radar is used as control because its radiometric response to the airborne particles is well known and the data were

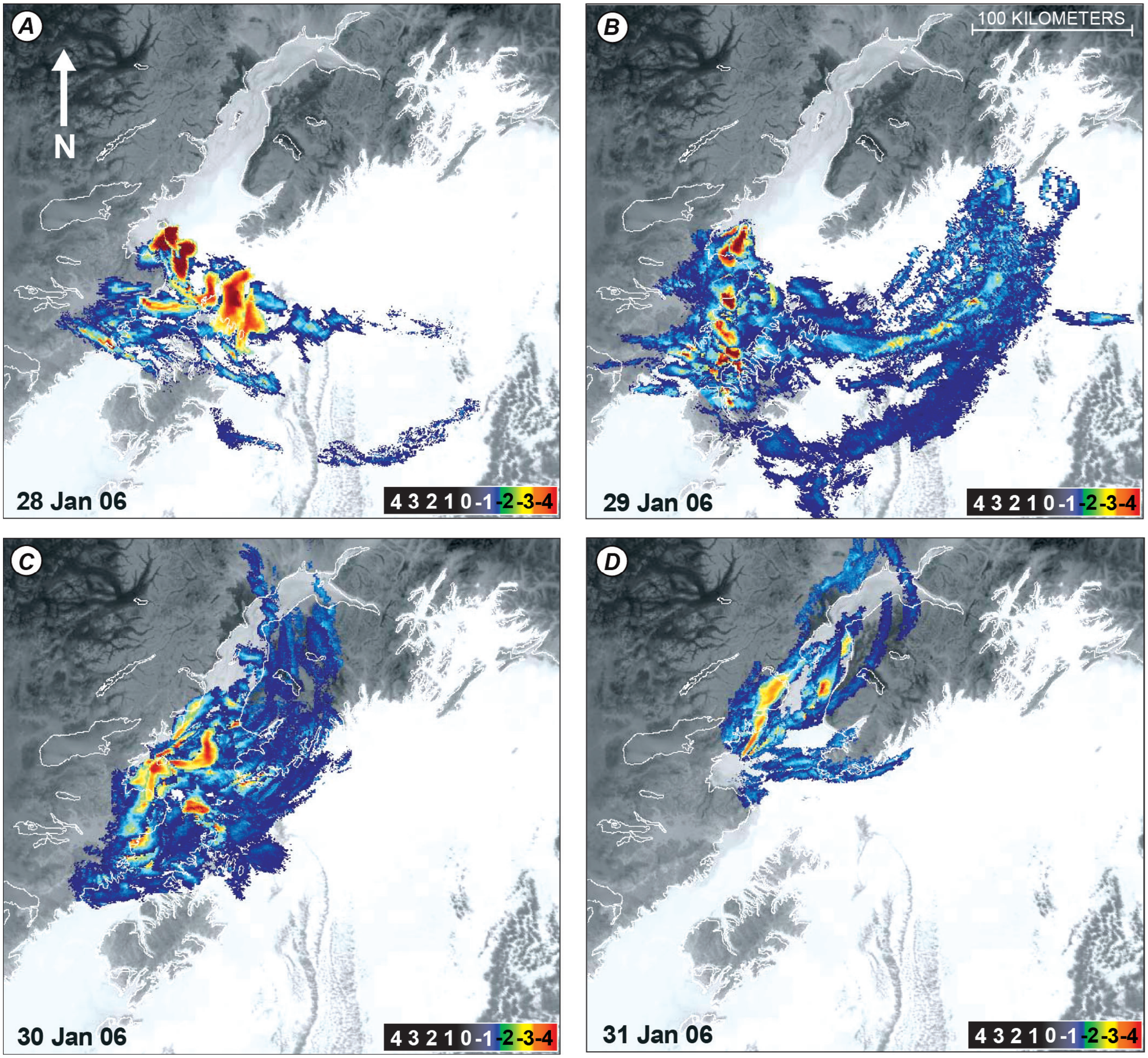

Figure 8. Composites of brightness temperature difference (BTD) data showing airborne ash distribution during the continuous phase of Augustine Volcano's 2006 eruption. Images show stacked data for one day's acquisitions on (*A*) January 28, (*B*) January 29, (*C*) January 30, and (*D*) January 31, 2006.

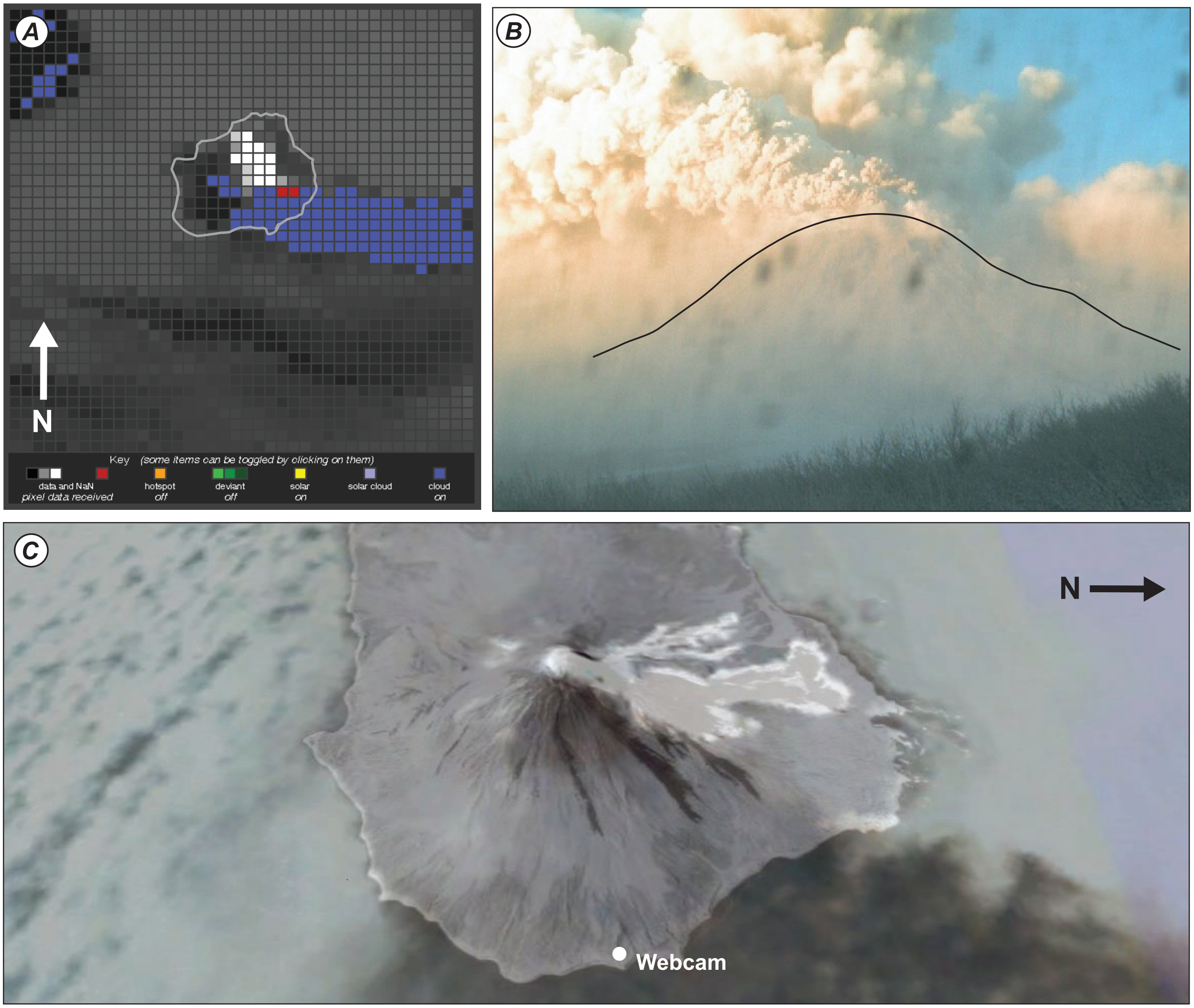

Figure 9. Views of ash clouds and pyroclastic flows generated during continuous phase of Augustine Volcano's 2006 eruption. *A*, Web viewer showing thermal anomaly (in white and shades of gray) in Advanced Very High Resolution Radiometer (AVHRR) image acquired 0829 AKST (1729 UTC) January 30. The white line defines Augustine Island. *B*, On island webcam view at 1016 AKST on January 29. The volcanic edifice is defined by a black line. *C*, Advanced Spaceborne Thermal Emission and Reflection Radiometer image acquired February 1, 2006, overlain on terrain in Google Earth. White areas show hot deposits. Views of hot deposits on east side of island are blocked by the ash cloud.

recorded consistently during the early stages of each eruption. Eight of the 14 events had sufficient satellite data to make this comparison. The comparison showed that all the cloud-temperature height estimates deviated by no more than 15 percent from the radar measurements (table 2).

However, there are some problems with the cloud-top temperature data. First, seven of the volcanic clouds were higher than 8.5 km, the approximate lower boundary for the tropopause, which means there are multiple heights that correlate to the cloud-top temperature. For these events it was assumed that the cloud ascended through the tropopause and reached natural buoyancy at the first height, which corresponded with the measured temperature. In reality, even if this was the case for the bulk of the cloud, there was likely some overshoot. Second, heights could not be estimated for six of the events due to missing data, because the cloud was translucent and valid temperatures could not be derived, or the cloud-top temperature was colder than the temperature of the atmosphere suggesting that this cloud was super-cooled and had not yet equilibrated to its surroundings (event 9).

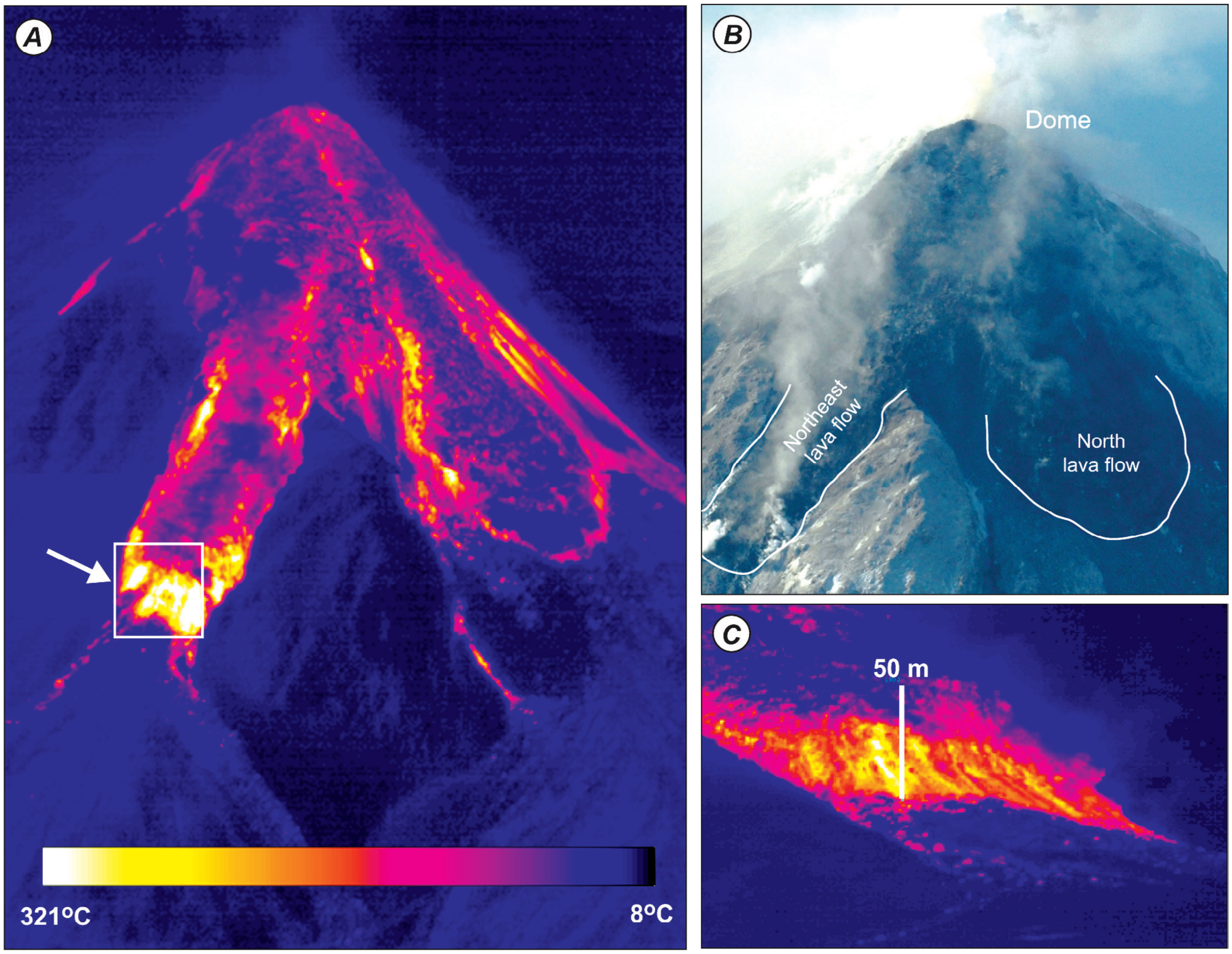

Figure 10. *A*, Forward looking infrared (FLIR) camera image showing Augustine Volcano summit lava dome and block flows on March 10, 2006 (FLIR images by Rick Wessels, AVO/USGS; Wessels and others, this volume). *B*, Photograph captured simultaneously with FLIR image (Photograph by Game McGimsey, AVO/USGS). *C*, Close-up of beveled front of the north-east lava flow. Location and angle of view shown by the white box and arrow in *A*.

Also, the comparisons for events 7 and 8 used GOES data, which has 8 km pixels, much larger than the 1.1 km pixels in AVHRR data. Thus GOES data are more likely to include a mixture of ground and cloud temperatures, resulting in a warmer reading and lower height estimate. Yet these still gave values to within the ±15 percent difference range.

Some of the variations in height estimates can be attributed to electromagnetic wavelengths used in detection. The NEXRAD method uses microwave energy and is sensitive to particle size and concentration. The cloud-top method uses thermal-infrared satellite data that detects smaller particles than radar does, and includes gaseous components (Schneider and others, 2006). Pilot reports are based on visual observations and are sensitive to water vapor and other gases appearing as the visible part of the cloud and are very qualitative (Simpson and others, 2001; Tupper and others, 2007). More quantitative visual measurements were made using oblique photography taken at the approximately the same time satellite images were acquired. These photos provided insight into the vertical structure of the eruption column and its relationship to the map view seen by satellites.

The eruption of event 6 provided an opportunity to compare and contrast these different techniques of cloud height measurement. Event 6 started at 1640 AKST on January 13. A satellite image at 1645 AKST (0145 UTC, January 14) showed a circular cloud over the volcano that was approximately 16 km across. A pilot reported a volcanic cloud up to 30,000 to 35,000 ft (9.1–10.7 km). The thermal-infrared image (fig. 11*A*) shows top-surface temperatures ranging from −15 to −30°C along its perimeter with much colder temperatures down to –53°C near the center, suggesting a height of 32,000 ft (10 km). Temperature differences in the cloud-top are usually related to variations in height (Tupper and others, 2004), although if portions of the volcanic cloud are translucent, then the signal from the warm ground combines with the cold cloud and increases the detected temperature values. NEXRAD gave values of 34,000 ft (10.5 km).

A ground-based photograph at 1650 AKST (0150 UTC) showed a profile view of the same eruption column (fig.11*A*). The photograph was taken from Lake Clark, west of the volcano (fig. 11*B*). It shows a relatively flat cloud-top along the perimeter with a thin outer edge that thickens inward. Away from the perimeter the cloud's bottom extends below the ridge in the foreground and it is unclear whether it is still attached to the volcanic vent, making "plume" the more correct terminology. Seismic records indicated that the event had ended and additional material was no longer being erupted, implying it was at this point a volcanic cloud. Comparing the satellite image to the photograph shows that the warmer cloud temperatures approximately coincide with the thinner and translucent (few kilometers thick) perimeter. The central core is colder and most opaque. Towards the center of the cloud-top a high peak can be observed that most likely coincides with the coldest temperature. On the basis of measurements using the photograph, this cloud-top was estimated to be at an altitude of 9 km (29,500 ft), a value at the lower end of estimates by the other techniques.

Ash Composite and Concentration Maps

The ash composite technique is useful in delineating areas impacted by airborne ash. To show the area impacted by the Augustine eruptions, the most-negative ash composites were generated for January 11 (events 1–2), January 13 and 14 (events 3–8), January 28 through 31 (events 10–14 and continuous ash emission; fig. 8), and one image that combined images from all these dates (fig. 12). The eruption on January 17 was not included because it did not produce a cloud that could be identified by BTD techniques in satellite data. The combined image showed that the areas most heavily impacted based on airborne ash detected on satellite data are north, east, and south of the volcano.

These ash composites were used to identify and delineate concentrations based on ash signal strength. Ash signals less than −3 were assumed to include areas with the highest concentrations and were restricted to the area within approximately 80 km of the volcano (fig. 13). The ash signals with strengths 0 to −3 were assumed to include areas with moderate ash concentrations and extended as far as approximately 400 km from the volcano (fig. 13). Most of the ground-based ash samples, observations of ash deposits, and ash falling in the Cook Inlet area were located within the moderate ash concentration map unit. The majority of these samples and reports indicated light ash fall.

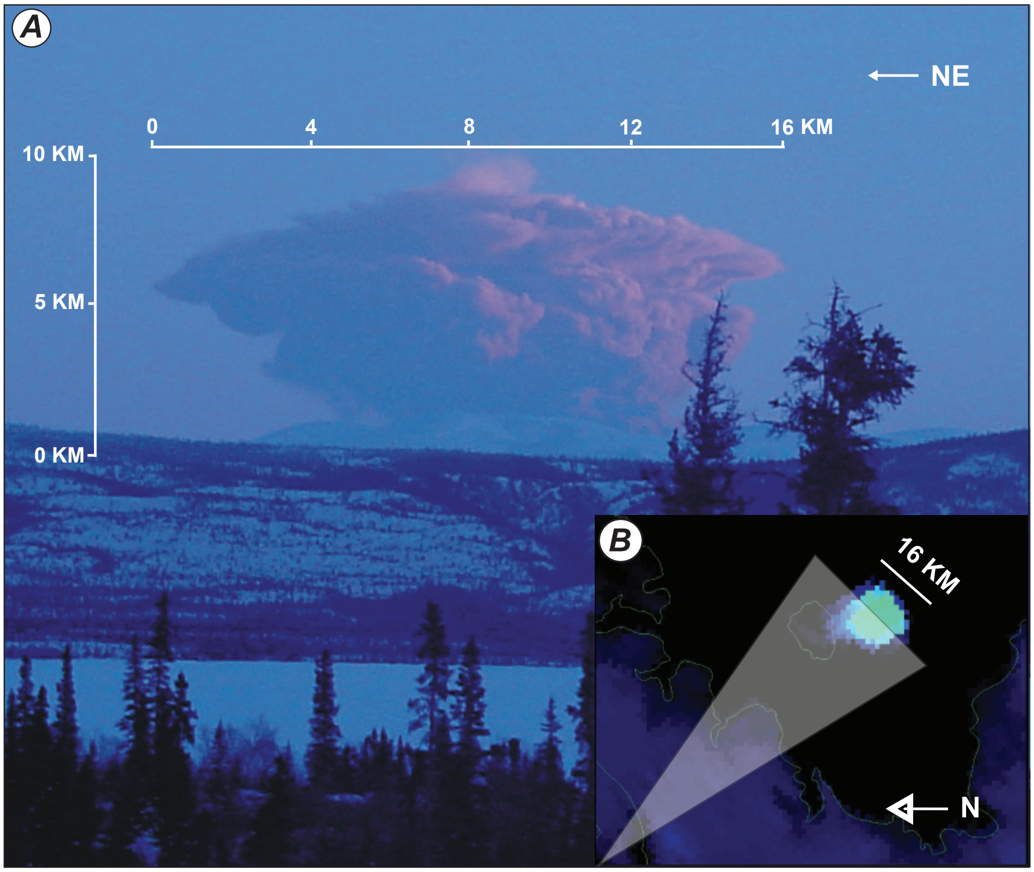

Figure 11. A comparison of an oblique photograph of an Augustine Volcano plume to a coincident satellite image. *A*, Oblique photograph of eruption cloud from event 6 on January 13, 2006 (Photograph by Leslie Beard). *B*, Advanced Very High Resolution Radiometer (AVHRR) band 4 image acquired at 1645 AKST, January 13, 2006 (0145 UTC, January 14).

The Puff dispersion model predicted the extent of ash beyond that observed on satellite data (Webley and others, this volume). These distal areas were north and east of the volcano and were considered to be the lowest concentrations (fig. 13). Measurements of airborne ash from ground-based LIDAR instruments at Fairbanks and Barrow (Sassen and others, 2007; Webley and others, 2008), aerosol samplers in Fairbanks and a snow sampler at Shasta, California (C. Cahill, written communication) validated the presence of the distal ash cloud. The Shasta ash was the most distant sample, at 1,800 miles (3,000 km) from the volcano. The distal portions of the plume presumably contained concentrations of ash below the detection limits of the satellite sensors and/or environmental conditions prevent detection by these sensors. It is likely that there were low airborne ash concentrations in these areas because no ash fall was reported by observers.

Conclusions

The 2006 eruption of Augustine Volcano provided an opportunity to test the robustness of several new tools that have been developed over the past few years by the AVORS group. It was also a catalyst for the development of new techniques and methodologies that have further complemented these primarily Web-based tools.

The thermal trends were observed at Augustine using satellite data in the 3 to 5 micron range. These data proved to be a good proxy for identifying the phases of eruption that were delineated using a range of geophysical measurements and visual observations. The success of the satellite data in defining the phases of eruption demonstrates the utility of remote sensing for monitoring Alaska's more remote but active volcanoes, such as Cleveland Volcano in the Aleutian Islands, which are not otherwise directly instrumented.

The multiple ash clouds erupted by Augustine allowed a comparison of multiple techniques that assessed the altitudes reached by these clouds. These methods included the use of satellite-based temperatures, ground-based radar, oblique photography, and pilot reports (PIREP). Instrument measurements proved to fairly consistent (table 2), but greater discrepancies occurred when comparisons were made to pilot's visual observations. These findings provide a cautionary tale for relying solely on one source for these data during monitoring operations.

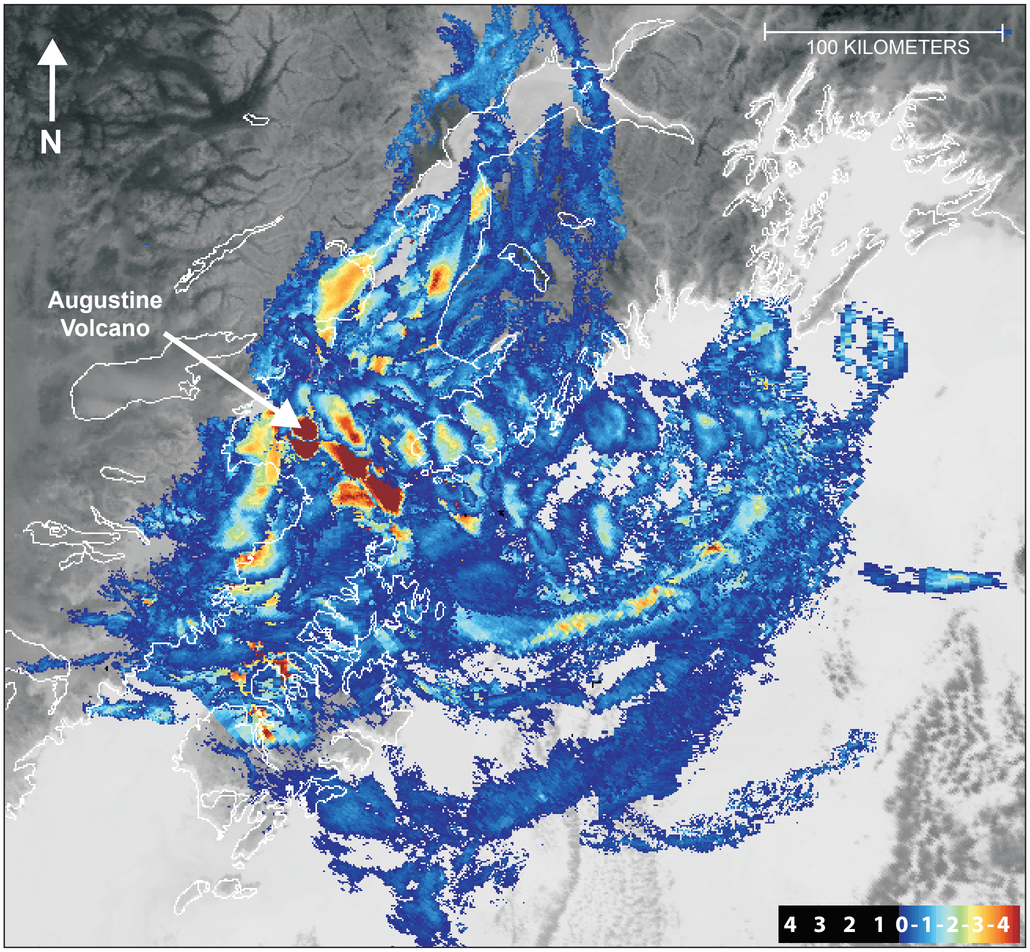

Figure 12. Brightness temperature difference (BTD) image showing combined airborne ash distributions from explosive Augustine Volcano eruptions. Image was created using Advanced Very High Resolution Radiometer (AVHRR) data showing the most negative ash composites for January 11 (events 1–2), January 13 and 14 (events 3–8), and January 28 through 31, 2006 (events 10–14 and continuous ash).

Airborne ash from the Augustine eruptions primarily impacted areas to the north, east, and south of the volcano, including Anchorage, Alaska's largest city, and towns on the Kenai and Alaska Peninsulas and Kodiak Island. Light ash fall was reported at many locations in the Cook Inlet region. Distal portions of the cloud drifted north over Fairbanks and Barrow, Alaska, and as far away as Mount Shasta, California. Various airlines cancelled multiple flights into the Ted Stevens International Airport, Anchorage, in response to this eruption.

A significant shortcoming of present hazard mitigation is the ability to detect or accurately predict the concentration of airborne ash. Quantitative ash concentrations are critical information to assess potential hazards to machinery (aircraft), transportation infrastructure, buildings and health (Blong, 1984; Horwell and Baxter, 2006). The U.S. military considers ash concentrations greater than 50 mg/m^3 dangerous to jet engines (Foreman, 1994). The concentration of ash that resulted in the failure of all four engines on the KLM 747 jet aircraft in Alaska in 1989 were estimated to be 2,000 mg/m^3 (Foreman, 1994), and ash concentrations based on those on the ground below the airspace of the encounter were estimated to be 500 g/m^2 with 75 percent of these particles smaller than 20 microns (Casadevall, 1994). The U.S. National Ambient Air Quality Standards (NAAQS) state that particles smaller than 10 microns are dangerous to human health, as they can enter and accumulate the respiratory system (U.S Environmental Protection Agency, 2007). Particles 2.5 microns and less are referred to as fine particles and can lodge deeply in the lungs. NAAQS, under the clean air act, requires particulate matter of 10 microns and smaller not to exceed 150 µg/m^3/24 hr, and particles 2.5 microns and smaller are limited to 35 µg/m^3/24 hr. These limits are based on values that protect public health, as well as damage to animals, crops, vegetation, and buildings.

The ash concentration map created using data from the Augustine eruption (fig. 13) is a prototype for the type of information that is required. One limitation of these data is

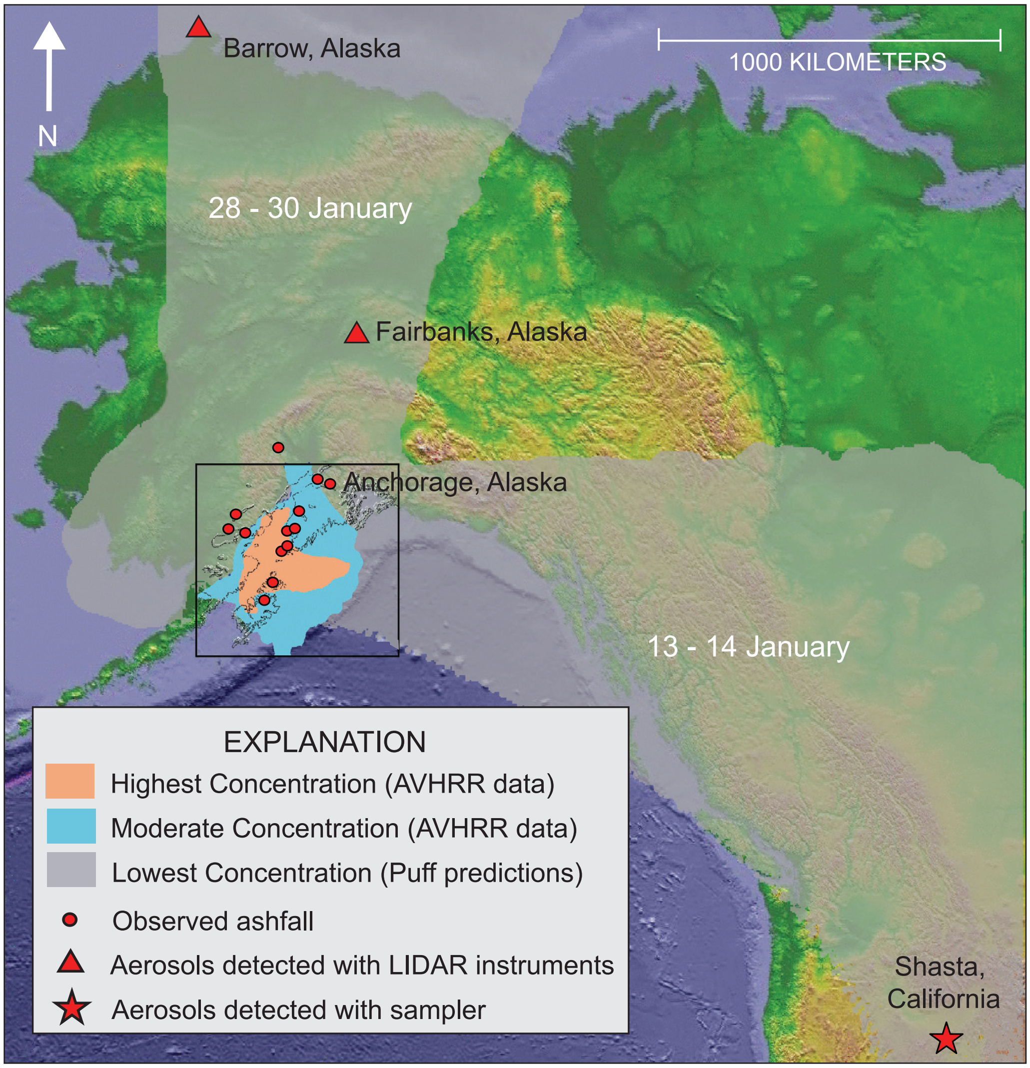

Figure 13. Map of relative ash concentrations from the eruptions of Augustine Volcano in January 2006. Based on combined airborne ash distributions (fig. 12), Puff model predictions (Webley and others, this volume), and ground-based observations and samples. AVHRR, Advanced Very High Resolution Radiometer; LIDAR, light detection and ranging.

that concentration assessments are based on relative quantities and do not give numerical values. The map units need to be calibrated so that they can be related to the hazard levels that can impact health and infrastructure, and to quantify the impact of a given event. This is an understanding that might prove crucial the next time Augustine or a similar volcano in the region erupts.

Acknowledgments

The authors would like to acknowledge the contributions of all the faculty, staff, and students that contributed to the AVORS's monitoring efforts during the eruption Augustine. In particular we thank Dave Schneider (AVO/U.S. Geological Survey) for his comments on cloud heights and William Ross (University of Alaska Fairbanks) and Joe Lovick (AVO/University of Alaska Fairbanks) for their contributions to the ash composite and distribution mapping.

References Cited

Blong, R.J., 1984, Volcanic Hazards—a sourcebook on the effects of eruptions: Sydney, Australia, Academic Press, 424 p.

Casadevall, T.J., 1994, The 1989–1990 eruption of Redoubt Volcano, Alaska—impacts on aircraft operations: Journal of Volcanology and Geothermal Research, v. 62,p. 301–316.

Cervelli, P.F., Fournier, T., Freymueller, J., and Power, J.A., 2006, Ground deformation associated with the precursory unrest and early phases of the January 2006 eruption of Augustine Volcano, Alaska: Geophysical Research Letters, v. 33, p. 5.

Coombs, M.L., Bull, K.F., Vallance, J.W, Schneider, D.J., Thoms, E.E., Wessels, R.L., and McGimsey, R.G., 2010, Timing, distribution, and volume of proximal products of the 2006 eruption of Augustine Volcano, *in* Power, J.A., Coombs, M.L., and Freymueller, J.T., eds., The 2006 eruption of Augustine Volcano, Alaska: U.S. Geological Survey Professional Paper 1769 (this volume).

Dean, K., Bowling, S.A., Shaw, G., and Tanaka, H., 1994, Satellite analyses of movement and characteristics of the Redoubt Volcano plume, January 8, 1990: Journal of Volcanology and Geothermal Research, v. 62, no. 1–4, p. 339–352.

Dean, K.G., Dehn, J., Engle, K., Izbekov, P., and Papp, K., 2002, Operational satellite monitoring of volcanoes at the Alaska Volcano Observatory, *in* Harris, A.J.H., Wooster, M., and Rothery, D.A., eds., Monitoring volcanic hotspots using thermal remote sensing: Advances in Environmental Monitoring and Modeling, v. 1, no. 3, p. 70–97.

Dean, K.G., Dehn, J., Papp, K.R., Smith, S., Izbekov, P., Peterson, R., Kearney, C., and Steffke, A., 2004, Integrated satellite observations of the 2001 eruption of Mt. Cleveland, Alaska: Journal of Volcanology and Geothermal Research, v. 135, no. 1–2, p. 51–73.

Dehn, J., Dean, K., and Engle, K., 2000, Thermal monitoring of North Pacific volcanoes from space: Geology, v. 28, no. 8, p. 755–758.

Dehn, J., Dean, K.G., Engle, K., and Izbekov, P., 2002, Thermal precursors in satellite images of the 1999 eruption of Shishaldin Volcano: Bulletin of Volcanology, v. 64, no. 8, p. 525–534.

Dzurisin, D., Vallance, J.W., Gerlach, T.M., Moran, S.C., and Malone, S.D., 2005, Mount St. Helens reawakens: EOS (American Geophysical Union Transactions), v. 86, no. 3, p. 25.

Foreman, P., 1994, Warning systems and pilot actions in ash and aviation safety, *in* Proceedings of the first international symposium on volcanic ash and aviation safety: U.S. Geological Survey Bulletin 2047, p. 163–168.

Harris, A.J.L., Blake, S., Rothery, D.A., and Stevens, N. F., 1997, A chronology of the 1991 to 1993 Mount Etna eruption using advanced very high resolution radiometer data—implications for real-time thermal volcano monitoring: Journal of Geophysical Research—Solid Earth, v. 102, no. B4, p. 7985–8003.

Harris, A.J.L., Dehn, J., Calvari, S., 2007, Lava effusion rate definition and measurement—a review: Bulletin of Volcanology, v. 70, p. 1–22.

Harris, A.J.L., Flynn, L.P., Dean, K., Pilger, E., Wooster, M. J., Okubo, C., Mouginis-Mark, P.J., Garbeil, H., Thornber, C., De la Cruz-Reyna, S., Rothery, D.A., and Wright, R., 2000, Real-time satellite monitoring of volcanic hot spots, *in* Mouginis-Mark, P.J., Crisp, J.A., and Fink, J.H., eds., remote sensing of active volcanism: Geophysical Monograph, American Geophysical Union, v. 116, p. 139–159.

Holasek, R.E., and Rose, W.I., 1991, Anatomy of 1986 Augustine volcano eruptions as recorded by multispectral image-processing of digital AVHRR weather-satellite data: Bulletin of Volcanology, v. 53, no. 6, p. 420–435.

Holasek, R.E., Self, S., and Woods, A.W., 1996, Satellite observations and interpretation of the 1991 Mount Pinatubo eruption plumes: Journal of Geophysical Research—Solid Earth, v. 101, no. B12, p. 27635–27665.

Horwell, C.J., and Baxter, P.J., 2006, The respiratory health hazards of volcanic ash—a review for volcanic risk mitigation: Bulletin of Volcanology, v. 69, p. 1–24.

Jacobs, K.M., and McNutt, S.R., 2010, Using seismic *b*-values to interpret seismicity rates and physical processes during the preeruptive earthquake swarm at Augustine Volcano 2005–2006, *in* Power, J.A., Coombs, M.L., and Freymueller, J.T., eds., The 2006 eruption of Augustine Volcano, Alaska: U.S. Geological Survey Professional Paper 1769 (this volume).

McGee, K.A., Doukas, M.P., McGimsey, R.G., Neal, C.A., and Wessels, R.L., 2010, Emission of SO_2, CO_2, and H_2S from Augustine Volcano, 2002–2008, *in* Power, J.A., Coombs, M.L., and Freymueller, J.T., eds., The 2006 eruption of Augustine Volcano, Alaska: U.S. Geological Survey Professional Paper 1769 (this volume).

McNutt, S.R., Tytgat, G., Estes, S.A., and Stihler, S.D., 2010, A parametric study of the January 2006 explosive eruptions of Augustine Volcano, using seismic, infrasonic, and lightning data, *in* Power, J.A., Coombs, M.L., and Freymueller, J.T., eds., The 2006 eruption of Augustine Volcano, Alaska: U.S. Geological Survey Professional Paper 1769 (this volume).

Miller, T.P., and Chouet, B.A., 1994, The 1989–1990 eruptions of Redoubt Volcano—an introduction: Journal of Volcanology and Geothermal Research, v. 62, p. 1–10.

Paskievitch, J., Read, C., and Parker, T., 2010, Remote telemetered and time-lapse cameras at Augustine Volcano, *in* Power, J.A., Coombs, M.L., and Freymueller, J.T., eds., The 2006 eruption of Augustine Volcano, Alaska: U.S. Geological Survey Professional Paper 1769 (this volume).

Patrick, M.R., Dehn, J., Papp, K.R., Lu, Z., Dean, K., Moxey, L., Izbekov, P., and Guritz, R., 2003, The 1997 eruption of Okmok Volcano, Alaska—a synthesis of remotely sensed imagery: Journal of Volcanology and Geothermal Research, v. 127, no. 1–2, p. 87–105.

Power, J.A., Nye, C.J., Coombs, M.L., Wessels, R.L., Cervelli, P.F., Dehn, J., Wallace, K.L., Freymueller, J.T., and Doukas, M.P., 2006, The reawakening of Alaska's Augustine Volcano: EOS (American Geophysical Union Transactions), v. 87, no. 37, p. 373.

Power, J.A., and Lalla, D.J., 2010, Seismic observations of Augustine Volcano, 1970–2007, *in* Power, J.A., Coombs, M.L., and Freymueller, J.T., eds., The 2006 eruption of Augustine Volcano, Alaska: U.S. Geological Survey Professional Paper 1769 (this volume).

Prata, A.J., 1989, Observations of volcanic ash clouds in the 10–12 um window using AVHRR/2 data: International Journal of Remote Sensing, v. 10, no. 4–5, p. 751–761.

Ramsey, M., and Dehn, J., 2004, Spaceborne observations of the 2000 Bezymianny, Kamchatka eruption—the integration of high-resolution ASTER data into near real-time monitoring using AVHRR: Journal of Volcanology and Geothermal Research, v. 135, no. 1–2, p. 127–146.

Roach, A.L., Benoit, J.P., Dean, K.G., and McNutt, S.R., 2001, The combined use of satellite and seismic monitoring during the 1996 eruption of Pavlof volcano, Alaska: Bulletin of Volcanology, v. 62, no. 6–7, p. 385–399.

Rose, W.I., Bluth, G.J.S., Schneider, D.J., Ernst, G.G.J., Riley, C.M., Henderson, L.J., and McGimsey, R. G., 2001, Observations of volcanic clouds in their first few days of atmospheric residence—the 1992 eruptions of Crater Peak, Mount Spurr volcano, Alaska: Journal of Geology, v. 109, no. 6, p. 677–694.

Rose, W.I., Delene, D.J., Schneider, D.J., Bluth, G.J.S., Krueger, A.J., Sprod, I., McKee, C., Davies, H.L. and Ernst, G.G.J., 1995, Ice in the 1994 Rabaul eruption cloud—implications for volcano hazard and atmospheric effects: Nature, v. 375, p. 477–479.

Rose, W.I., and Mayberry, G.C., 2000, Use of GOES thermal infrared imagery for eruption scale measurements, Soufriere Hills, Montserrat: Geophysical Research Letters, v. 27, no. 19, p. 3097–3100.

Sassen, K., Zhu, J., Webley, P., Dean, K., and Cobb, P., 2007, Volcanic ash plume identification using polarization lidar—Augustine eruption, Alaska: Geophysical Research Letters, L08803, v. 34, p. 1–4.

Schneider, D.J., Dean, K.G., Dehn, J., Miller, T.P., and Kirianov, V.Y., 2000, Monitoring and analyses of volcanic activity using remote sensing data at the Alaska Volcano Observatory; case study for Kamchatka, Russia, December 1997, *in* Mouginis-Mark, P.J., Crisp, J.A., and Fink, J.H., eds., Remote sensing of active volcanism: Geophysical Monograph, American Geophysical Union, v. 116, p. 65–85.

Schneider, D.J., Rose, W.I., and Kelley, L., 1995, Tracking of 1992 eruption clouds from Crater Peak vent of Mount Spurr Volcano, Alaska, using AVHRR, *in* Keith, T.E.C., ed., The 1992 eruptions of Crater Peak vent, Mount Spurr Volcano, Alaska: U.S. Geological Survey Bulletin 2139, p. 27–36.

Schneider, D.J., Rose, W.I., Coke, L.R., Bluth, G.J.S., Sprod, I.E., and Krueger, A.J., 1999, Early evolution of a stratospheric volcanic eruption cloud as observed with TOMS and AVHRR: Journal of Geophysical Research—Atmospheres, v. 104, no. D4, p. 4037–4050.

Schneider, D.J., Scott, C., Wood, J., Hall, T., 2006, NEXRAD weather radar observations of the 2006 Augustine Volcanic eruption clouds: Eos (American Geophysical Union Transactions), v. 87, no. 52, Fall Meet. Supplement, abstract V51C-1686.

Searcy, C., Dean, K., and Stringer, W., 1998, PUFF—a high-resolution volcanic ash tracking model: Journal of Volcanology and Geothermal Research, v. 80, no. 1–2, p. 1–16.

Sentman, D.D., McNutt, S.R., Stenbaek-Nielsen, H.C., Tytgat, G., and DeRoin, N., 2010, Imaging observations of thermal emissions from Augustine Volcano using a small astronomical camera, *in* Power, J.A., Coombs, M.L., and Freymueller, J.T., eds., The 2006 eruption of Augustine Volcano, Alaska: U.S. Geological Survey Professional Paper 1769 (this volume).

Simpson, J.J., Hufford G., Pieri D., and Berg J., 2001, Response to ‘‘Comments on ‘Failures in detecting volcanic ash from a satellite-based technique’”: Remote Sensing of Environment, v. 78, p. 347–357.

Tupper, A., Carn, S., Davey, J., Kamada, Y., Potts, R., Prata, F., and Tokuno, M., 2004, An evaluation of volcanic cloud detection techniques during recent significant eruptions in the western “Ring of Fire”: Remote Sensing of Environment, v. 91, no. 1, p. 27–46.

Tupper A., Itikarai I., Richards M., Prata F., Carn S., Rosenfeld D., 2007, Facing the Challenges of the international airways volcano watch—The 2004/05 Eruptions of Manam, Papua New Guinea: Weather and Forecasting, v. 22, no. 1, p. 175–191.

U.S. Environmental Protection Agency, 2007, Technology Transfer Network, National Ambient Air Quality Standards (NAAQS): [http://www.epa.gov/ttn/naaqs/pm/pm10_index.html].

van Manen, S.M., Dehn, J., West, M.E., Blake, S., and Rothery, D.A., 2010, The 2006 eruption of Augustine volcano—Combined analyses of thermal satellite data and reduced displacement, *in* Power, J.A., Coombs, M.L., and Freymueller, J.T., eds., The 2006 eruption of Augustine Volcano, Alaska: U.S. Geological Survey Professional Paper 1769 (this volume).

Vallance, J.W., Bull, K.F., and Coombs, M.L., 2010, Pyroclastic flows, lahars, and mixed avalanches generated during the 2006 eruption of Augustine Volcano, *in* Power, J.A., Coombs, M.L., and Freymueller, J.T., eds., The 2006 eruption of Augustine Volcano, Alaska: U.S. Geological Survey Professional Paper 1769 (this volume).

Wallace, K.L., Neal, C.A., and McGimsey, R.G., 2010, Timing, distribution and character of tephra fall from the 2005–2006 eruption of Augustine Volcano, *in* Power, J.A., Coombs, M.L., and Freymueller, J.T., eds., The 2006 eruption of Augustine Volcano, Alaska: U.S. Geological Survey Professional Paper 1769 (this volume).

Webley, P.W., Dean, K.G., Collins, R., Fochesatto, J., Sassen, K., Atkinson, D., Cahill, C., and Prata, A.J., 2008, Validation of a volcanic ash dispersion model during late January/early February 2006 eruption of Mount Augustine Volcano: Bulletin of American Meteorological Society, v. 89, p. 1647–1658.

Webley, P.W., Dean, K.G., Dehn, J., Bailey, J.E., and Peterson, R., 2010, Volcanic-ash dispersion modeling of the 2006 eruption of Augustine Volcano using the Puff model, *in* Power, J.A., Coombs, M.L., and Freymueller, J.T., eds., The 2006 eruption of Augustine Volcano, Alaska: U.S. Geological Survey Professional Paper 1769 (this volume).

Wen, S., and Rose, W., 1994, Retrieval of sizes and total masses of particles in volcanic clouds using AVHRR bands 4 and 5: Journal of Geophysical Research—Atmospheres, v. 99, no. D3, p. 5421–5431.

Wessels, R.L., Coombs, M.L., Schneider, D.J., Dehn, J., and Ramsey, M.S., 2010, High-resolution satellite and airborne thermal infrared imaging of the 2006 eruption of Augustine Volcano, *in* Power, J.A., Coombs, M.L., and Freymueller, J.T., eds., The 2006 eruption of Augustine Volcano, Alaska: U.S. Geological Survey Professional Paper 1769 (this volume).

Appendix 1. Satellite Observations

Table 4. Satellite observations of gas emissions from Augustine Volcano on 12–13 December 2005.

[AKST, Alaska Standard Time; UTC, Coordinated Universal Time; AVHRR, Advanced Very High Resolution Radiometer; MODIS, Moderate Resolution Imaging Spectroradiometer]

Satellite sensor	Time, date (AKST)	Time, date (UTC)	Length (km)	Direction	Comments
AVHRR	1310, 12-Dec	2210, 12-Dec	>110	SE	Visible in B2 and B3, no B4m5 signal
MODIS	1323, 12-Dec	2223, 12-Dec	125	SE	Very distinct plume
AVHRR	1356, 12-Dec	2256, 12-Dec	85	SE	Very faint steam plume, faint B4m5 signal
AVHRR	1423, 12-Dec	2323, 12-Dec	120	SE	Faint steam plume, no B4m5
AVHRR	1452, 12-Dec	2352, 12-Dec	30	SE	Very faint steam plume, faint B4m5
AVHRR	1605, 12-Dec	0105, 13-Dec	NA	E	Mysterious cloud, defined by a few pixels
AVHRR	0442, 13-Dec	1342, 13-Dec	100	ENE	Very distinct plume, with some B4m5 signal

Table 5. Satellite observations of volcanic clouds on January 11, 2006.

[Height measurements based on cloud temperatures. AKST, Alaska Standard Time; UTC, Coordinated Universal Time; BTD, Brightness Temperature Difference; GOES, Geostationary Operational Environmental Satellites; AVHRR, Advanced Very High Resolution Radiometer]

Satellite sensor	Time, date (AKST)	Time, date (UTC)	Plume temp (°C)	Max. BTD signal	Plume height (km)
AVHRR	0448, 11-Jan	1348, 11-Jan	−46	NA	7
AVHRR	0525, 11-Jan	1425, 11-Jan	−55	NA	8.5
GOES	0530, 11-Jan	1430, 11-Jan	NA	−2.1	NA
GOES	0600, 11-Jan	1500, 11-Jan	NA	−1.7	NA
GOES	0630, 11-Jan	1530, 11-Jan	NA	−2.2	NA
AVHRR	0659, 11-Jan	1559, 11-Jan	NA	−2.7	NA
GOES	0730, 11-Jan	1630, 11-Jan	NA	−3.1	NA
AVHRR	0740, 11-Jan	1640, 11-Jan	NA	−1.8	NA
AVHRR	0839, 11-Jan	1739, 11-Jan	NA	−1.2	NA

Table 6. Satellite observations of volcanic clouds on January 13–14, 2006.

[Height measurements based on cloud temperatures. AKST, Alaska Standard Time; UTC, Coordinated Universal Time; BTD, Brightness Temperature Difference; GOES, Geostationary Operational Environmental Satellites; AVHRR, Advanced Very High Resolution Radiometer]

Satellite sensor	Time, date (AKST)	Time, date (UTC)	Plume temp. (°C)	Max. BTD signal	Plume height (km)
AVHRR	0428, 13-Jan	1328, 13-Jan	−54[1]	NA	8 to 9
AVHRR	0456, 13-Jan	1356, 13-Jan	−52[1]	NA	8, 9.5
AVHRR	0637, 13-Jan	1537, 13-Jan	NA	−4.0	NA
AVHRR	0655, 13-Jan	1555, 13-Jan	NA	−4.0	NA
AVHRR	0749, 13-Jan	1649, 13-Jan	NA	−3.4	NA
AVHRR	0834, 13-Jan	1734, 13-Jan	NA	−3.2	NA
AVHRR	1024, 13-Jan	1924, 13-Jan	−45[1]	−3.0	6.5, 13.5
GOES	1130, 13-Jan	2030, 13-Jan	−41	−2.1	NA
AVHRR	1142, 13-Jan	2042, 13-Jan	−54	NA	8 to 9
GOES	1200, 13-Jan	2100, 13-Jan	−46	−2.1	NA
AVHRR	1203, 13-Jan	2103, 13-Jan	−51	NA	7.5
GOES	1230, 13-Jan	2130, 13-Jan	−45	−2.3	NA
AVHRR	1246, 13-Jan	2146, 13-Jan	−49	−2.2	NA
GOES	1300, 13-Jan	2200, 13-Jan	−44	−3.3	NA
AVHRR	1322, 13-Jan	2222, 13-Jan	−45	−2.3	NA
AVHRR	1437, 13-Jan	2337, 13-Jan	NA	−1.5	NA
AVHRR	1645, 13-Jan	0145, 14-Jan	−53	NA	7.5, 10
GOES	1700, 13-Jan	0200, 14-Jan	−44	2.1	NA
GOES	1730, 13-Jan	0230, 14-Jan	−44	−2.5	NA
AVHRR	1743, 13-Jan	0243, 14-Jan	−49	−3.9	NA
GOES	1800, 13-Jan	0300, 14-Jan	−39	−3.0	NA
AVHRR	1829, 13-Jan	0329, 14-Jan	NA	−4.0	NA
GOES	1830, 13-Jan	0330, 14-Jan	−36	−3.4	NA
GOES	1930, 13-Jan	0430, 14-Jan	−49	−2.4	7, 11
GOES	2000, 13-Jan	0500, 14-Jan	−49	−3.9	7, 11
GOES	2030, 13-Jan	0530, 14-Jan	−46	−3.0	NA
GOES	2100, 13-Jan	0600, 14-Jan	−43	−3.3	NA
AVHRR	2136, 13-Jan	0636, 14-Jan	NA	−2.6	NA
AVHRR	2204, 13-Jan	0704, 14-Jan	NA	−2.9	NA
AVHRR	2316, 13-Jan	0816, 14-Jan	NA	−0.3	NA
GOES	0030, 14-Jan	0930, 14-Jan	−47	−3.2	7, 10.5
GOES	0100, 14-Jan	1000, 14-Jan	−50	−3.0	7, 10.5
GOES	0130, 14-Jan	1030, 14-Jan	−50	−2.3	7, 10.5
GOES	0200, 14-Jan	1100, 14-Jan	−47	−3.1	7, 10.5

[1] Measurement uncertain.

Table 7. Satellite observations of volcanic clouds on January 17, 2006.

[Height measurements based on cloud temperatures. AKST, Alaska Standard Time; UTC, Coordinated Universal Time; BTD, Brightness Temperature Difference; GOES, Geostationary Operational Environmental Satellites; AVHRR, Advanced Very High Resolution Radiometer; MODIS, Moderate Resolution Imaging Spectroradiometer]

Satellite sensor	Time, date (AKST)	Time, date (UTC)	Plume temp. (°C)	Max. BTD signal	Plume height (km)
GOES	0830, 17-Jan	1730, 17-Jan	−51	NA	7.5, 9.1, 11
AVHRR	0838, 17-Jan	1738, 17-Jan	−56	NA	NA
GOES	0900, 17-Jan	1800, 17-Jan	−50	−2.2[1]	7.3
GOES	0930, 17-Jan	1830, 17-Jan	−47	−1.6[1]	NA
GOES	1200, 17-Jan to 1800, 17-Jan	2100, 17-Jan to 0300, 18-Jan	NA	NA	NA
MODIS	1240, 19-Jan	2140, 19-Jan	NA	NA	Ash fall on ground

[1] Measurement uncertain.

Table 8. Satellite observations of volcanic clouds on January 28–29, 2006.

[Height measurements based on cloud temperatures. AKST, Alaska Standard Time; UTC, Coordinated Universal Time; BTD, Brightness Temperature Difference; AVHRR, Advanced Very High Resolution Radiometer]

Satellite sensor	Time, date (AKST)	Time, date (UTC)	Plume temp. (°C)	Max. BTD signal	Plume height (km)
AVHRR	2042, 27-Jan	0542, 28-Jan	−45	NA	6.5, 9.5, 14.5
AVHRR	2115, 27-Jan	0615, 28-Jan	NA	−6.9	NA
AVHRR	0332, 28 Jan	1232, 28 Jan	NA	−4.5	NA
AVHRR	0349, 28-Jan	1249, 28-Jan	NA	−2.8	NA
AVHRR	0516, 28 Jan	1416, 28 Jan	NA	−3.6	NA
AVHRR	0819, 28-Jan	1719, 28-Jan	−45[1]	−2.4	6, 6.5, 10
AVHRR	0917, 28-Jan	1817, 28-Jan	NA	−7.4	NA
AVHRR	1211, 28-Jan	2111, 28-Jan	NA	−3.7	NA
AVHRR	1334, 28-Jan	2234, 28-Jan	NA	−4.3	NA
AVHRR	1516, 28-Jan	0016, 29-Jan	NA	−7.5	NA
AVHRR	1911, 28-Jan	0411, 29-Jan	NA	−6.8	NA
AVHRR	0709, 29-Jan	0709, 29-Jan	NA	−3.0	NA

[1] Measurement uncertain.

The 2006 Eruption of Augustine Volcano, Alaska
Power, J.A., Coombs, M.L., and Freymueller, J.T., editors
U.S. Geological Survey Professional Paper 1769

Chapter 21

Volcanic-Ash Dispersion Modeling of the 2006 Eruption of Augustine Volcano Using the Puff Model

By Peter W. Webley[1], Kenneson G. Dean[1], Jonathan Dehn[1], John E. Bailey[1,2], and Rorik Peterson[3]

Abstract

Volcanic ash is one of the major potential hazards from volcanic eruptions. It can have both short-range effects from proximal ashfall and long range impacts from volcanic ash clouds. The timely tracking and understanding of recently emitted volcanic ash clouds is important, because they can cause severe damage to jet aircraft engines and shut down major airports. Dispersion models play an important role in forecasting the movement of volcanic ash clouds by being the only means to predict a clouds' trajectory. Where available, comparisons are possible to both remote-sensing data and observations from the ground and aircraft. This was demonstrated in January 2006, when Augustine Volcano erupted after about a 20-year hiatus. From January 11 to 28, 2006, there were 13 explosive events, with some lasting as long as 11 minutes and producing ash clouds as high as 10–12 km (33,000–39,000 ft) above mean sea level (a.m.s.l). From January 28 to February 4, 2006, there was a more continuous phase, with ash clouds reaching 4–5 km a.m.s.l (13,000–16,000 ft). During the eruption, the Puff dispersion model was used by the Alaska Volcano Observatory for trajectory forecasting of the associated volcanic ash eruption clouds. The six explosive events on January 13 and 14, 2006, were the first time the "multiple eruptions" capability of the Puff model was used during an eruption response. Here we show the Puff model predictions made during the 2006 Augustine eruption and compare these predictions to satellite remote-sensing data, Next Generation Radar (NEXRAD) radar, and ashfall measurements. In addition, we discuss how automated predictions for volcanoes at elevated alert status provide a quicker assessment of the risk from the potential ash clouds.

Introduction

Volcanoes can inject large volumes of ash into the atmosphere, posing a threat to international and domestic aircraft as well as disrupting local communities. Ash clouds can cause severe damage to jet aircraft engines and fuel lines, abrade aircraft internal and external surfaces and shut down major airports (Blong, 1984; Casadevall, 1993; Casadevall and Krohn, 1995; Miller and Casadevall, 2000). The North Pacific (NOPAC) region is a vast expanse, 5,000 km by 2,500 km, containing numerous active volcanoes, most of which are located in uninhabited areas along the Aleutian Islands and Kamchatka Peninsula, Russia (fig. 1). From 1975 to 2006, there were more than 200 separate volcanic ash clouds that reached at least 6 km (20,000 ft) above mean sea level (a.m.s.l) and potentially jeopardized aircraft safety. Within the NOPAC region, the agencies responsible for monitoring volcanoes and their associated eruptions are: Alaska Volcano Observatory (AVO), Kamchatka Volcano Emergency Response Team (KVERT), and Sakhalin Volcanic Eruption Response Team (SVERT) who work together with the Tokyo, Washington and Anchorage Volcanic Ash Advisory Centers (VAAC) to provide advisories of airborne volcanic ash. These advisories are used by the local meteorological watch offices to provide a Significant Meteorological Information (SIGMET) warning to the aviation community and volcanic ashfall warnings to local communities.

Volcanic Ash Transport and Dispersion (VATD) models play an important role in forecasting the movement of volcanic ash clouds and provide information that is otherwise

---

[1] Alaska Volcano Observatory, Geophysical Institute, University of Alaska Fairbanks, 903 Koyukuk Drive, Fairbanks, AK 99775.

[2] Now at: Scenarios Network for Alaska Planning, University of Alaska Geography Program, Fairbanks, AK 99775.

[3] Department of Mechanical Engineering, University of Alaska Fairbanks, P.O. Box 755905, Fairbanks, AK 99775.

difficult or impossible to collect from other data sources. When remote-sensing data and observations from the ground and aircraft are available, these model predictions can be compared and validated. Before, and in the initial stages of volcanic eruptions, VATD models are invaluable in predicting the movement of volcanic ash clouds and ensuring aviation safety. A warning system should be capable of a 5-minute response time once an eruption has been detected (Hufford and others, 2000). During these initial minutes, predicting the movement of the ash cloud and the potential impacts on aircraft are critical. Within Alaska, AVO's level of response to remote volcanic activity varies depending on the source and content of the observation. After receiving a report of an eruption, AVO works with the National Weather Service (NWS) and Federal Aviation Administration (FAA) for corroboration and to solicit additional information. AVO itself is a joint program of the United States Geological Survey (USGS), the Geophysical Institute of the University of Alaska Fairbanks (UAF-GI) and the State of Alaska Division of Geological and Geophysical Surveys (ADGGS).

VATD models provide the only means to quantitatively predict an ash cloud's trajectory. There are three VATD models often used for forecasting ash cloud motion in the NOPAC region: Canadian Emergency Response Model (CanERM: Pudykiewicz, 1988, 1989), Hybrid Single-Particle Lagrangian Integrated Trajectories (HYSPLIT: Draxler and Hess, 1997, 1998), and Puff (Searcy and others, 1998). Peterson and others (2010) provide a detailed description

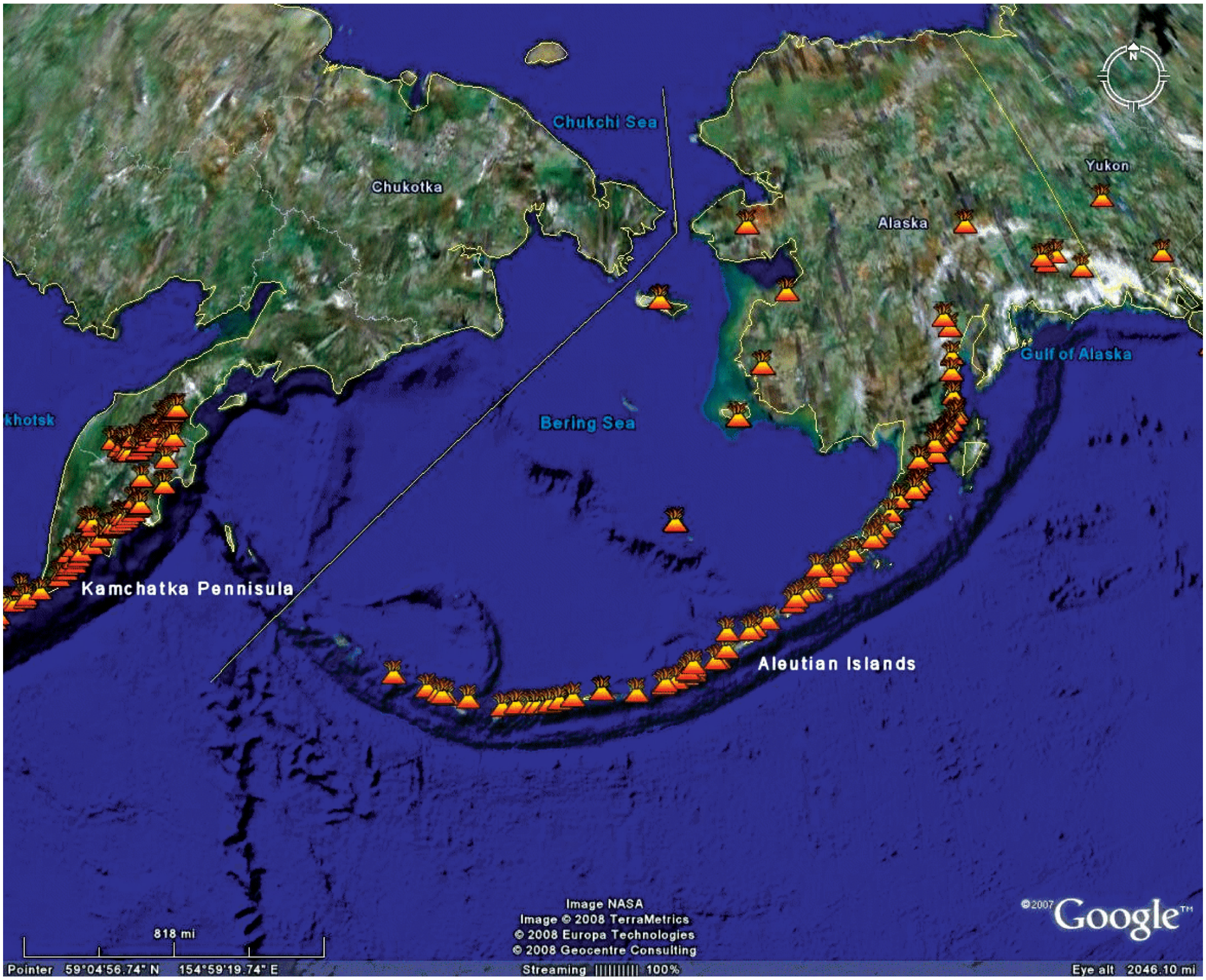

Figure 1. Map of North Pacific region, illustrating the numerous volcanoes (colored triangles) from Kamchatka in the west to the Alaska mainland and Canada in the east (image courtesy of Google Earth).

of all three models. Puff is primarily focused on forecasting volcanic ash transport and dispersion using an adjustable number of tracer particles to represent a volcanic ash cloud. The model is designed to rapidly predict the extent and movement of airborne ash particles during an eruption (Searcy and others, 1998). Model simulations place hypothetical particles above a selected volcano, release them into a gridded wind field and calculate their movement. Current numerical weather prediction (NWP) model forecasts are used for real-time predictions.

Puff is used at AVO, Anchorage and Washington VAACs, the Airforce Weather Agency (AFWA), and other national agencies and universities worldwide. The Puff model has been used as a VATD model for numerous volcanic eruptions in the North Pacific. The first use of the model was during the eruption of Redoubt Volcano in 1989–90 (Tanaka, 1994). Searcy and others (1998) demonstrated the model's use by comparing predictions to satellite images of the eruptions of Crater Peak at Mount Spurr in 1992 and of Klyuchevskoi Volcano in 1994. Dean and others (2002) predicted the movement of the ash cloud from the 2001 eruption of Cleveland Volcano and showed possible limitations of satellite data when compared to the model predictions, and Aloisi and others (2002) used the model to analyze the July 1998 eruption cloud from the Mount Etna paroxysm. Additionally, Papp and others (2005) investigated the probability of ash distribution in the NOPAC based on multiple, hypothetical eruptions over several years, and Peterson and others (2010) compared model predictions from Puff, HYSPLIT, and CanERM for selected eruptions in the NOPAC.

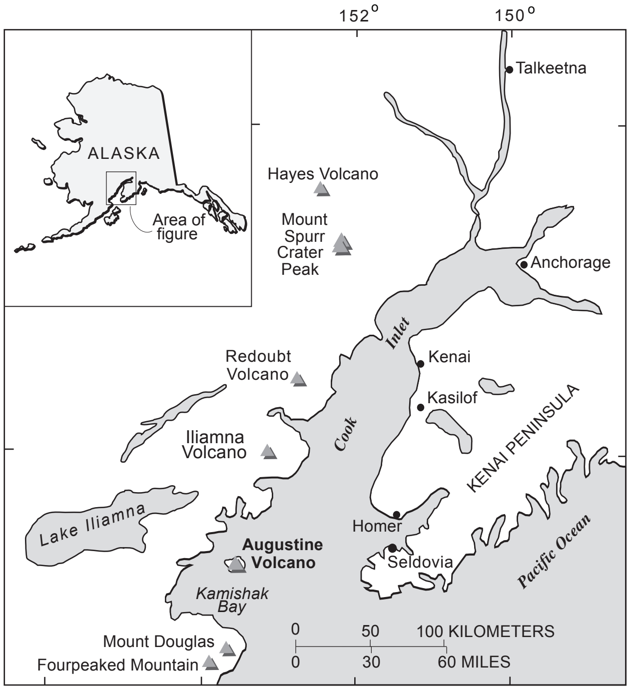

Figure 2. Map showing location of Augustine Volcano, in Cook Inlet, southwest of Anchorage, Alaska. Grey triangles show the locations of the volcanoes within this region of Alaska.

Most recently, the Puff model was used in January 2006, when Augustine Volcano (fig. 2) reawakened and over a period of 20 days produced 13 explosive eruptions, followed by a period of continuous ash emission. The 2006 eruption was preceded by approximately 8 months of increasing unrest that included escalating seismic activity, deformation of the volcanic edifice, gas emission, and small phreatic explosions (Power and others, 2006). The eruption progressed through four phases. In May 2005, the volcano started a precursory phase with increasing microearthquakes (Power and others, 2006). From January 11 to 28, 2006 the volcano was in an explosive phase characterized by 13 discrete explosions, followed by a more continuous phase of lesser explosivity and lava effusion from January 28 through February 10 and concluding with an effusive phase from March 3 to 15 (Coombs and others, this volume).

In this paper, we show the use of the Puff model during the 2006 eruption of Augustine Volcano. New modeling capabilities are introduced, many of which were used for the first time during an eruption response, with validation of these model simulations. Also shown is how the frequency of the explosive events at Augustine led to both new developments and new data-visualization tools. We compare the Puff model simulations to satellite data and ashfall measurements to assess the reliability of the eruption response predictions. We describe the Puff model's use by separating the explosive phase into three parts on the basis of the timings of the events: (1) January 11, (2) January 13 and 14, and (3) January 17, with the early part of the following continuous phase as one period, (4) January 28 to February 2, 2006.

The 2006 Eruption at Augustine Volcano

The 2006 eruption of Augustine Volcano was preceded by increased seismicity beginning in May 2005. By January 11, 2006, there were significant satellite detected thermal anomalies and strong seismic signals, and on that day two explosions occurred, each lasting less than 4 minutes (Power and others, 2006). The January 11 explosions produced ash plumes, reported by NWS to have reached heights greater than 9 km a.m.s.l. (approximately 30,000 ft), which moved slowly to the north and northeast (Power and others, 2006). On January 13, a third explosive event occurred, which lasted for 11 minutes and produced volcanic plumes/ash clouds detected to 10 km (33,000 ft) a.m.s.l. During January 13, there were five discrete events, followed by events on January 14 and 17 (see table 1). Figure 3*A* is a time-lapse camera image from Augustine Island that shows that the events on January 13 were ash rich, and by January 28, the continuous-phase eruptions were a mixture of steam, gases and some ash (fig. 3*B*).

In response to these explosive eruptions, the Puff model was used by AVO to track and predict the movement of the volcanic ash clouds. The model simulations were compared with all available satellite remote-sensing data. During the 2006 eruption, satellite data were available from the Advanced Very High Resolution Radiometer (AVHRR) on the National Oceanic and Atmospheric Administration (NOAA) satellites, the Moderate Resolution Imaging Spectroradiometer (MODIS) on National Aeronautics and Space Administration (NASA) Terra and Aqua satellites and the NOAA Geostationary Operational Environmental satellites (GOES). Bailey and others (this volume) provide a description of the data for both thermal monitoring and the detection of the volcanic ash clouds. On January 28, the volcano entered a period of more continuous eruptive activity that lasted until February 2. This phase began with four explosive eruptions that generated ash plumes up to 9 km (30,000 ft) a.m.s.l (Power and others, 2006). Ash plumes ascended to 4 km (~13,000 ft) a.m.s.l. frequently during the continuous phase. Winds carried ash to the south, depositing trace amounts on Kodiak Island and interrupting air traffic at the Kodiak Airport, and then carried ash north across Alaska (Webley and others, 2008).

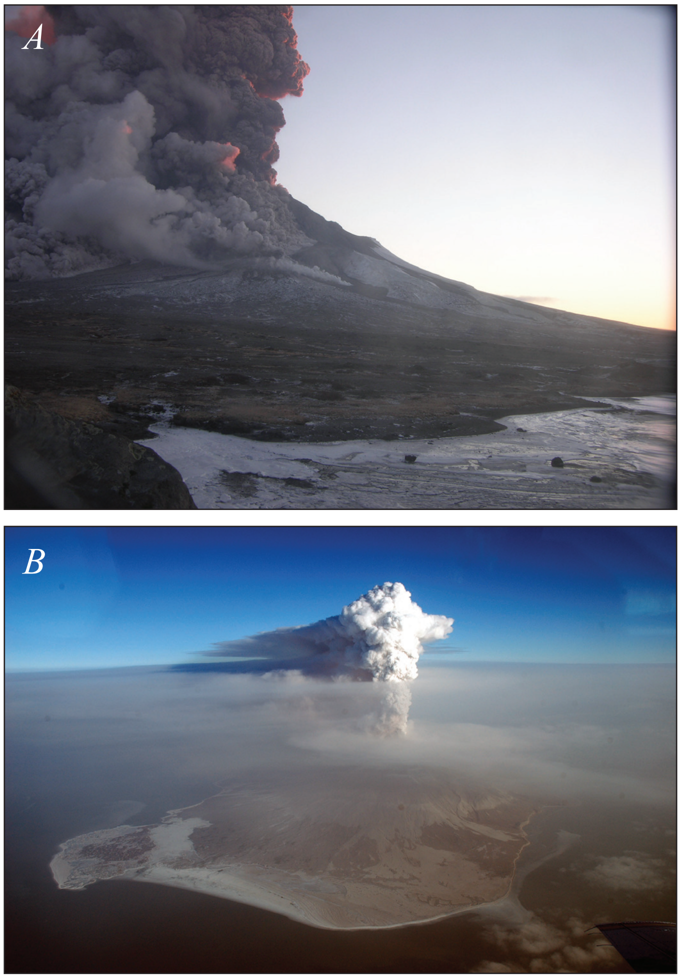

Figure 3. Photographs of Augustine Volcano's 2006 eruption. *A*, Time lapse camera image taken on January 13, 2006, from a site at Burr Point, 5 km north of Augustine's summit (Paskievitch and others, this volume). *B*, Oblique aerial photograph of a steam plume with minor ash, extending northeast from Augustine Volcano on January 30, 2006. The view is from southwest. AVO photo by R.G. McGimsey.

Puff Model Simulations

At AVO, once a volcanic event was confirmed, the Puff model was used to predict the movement of the subsequent ash cloud for the following 24-hour period. Initially, several assumptions were made for the plume height, eruption duration, particle-size distribution, and vertical distribution of the ash particles in the plume. As more information became available, the model prediction was updated to provide a better representation of the ash cloud movement. The Puff model uses numerical weather prediction (NWP) forecasts for its advective term when predicting the future movement of a volcanic cloud trajectory. During the Augustine eruption, the North American Mesoscale model (NAM) domain 216 was used; this is a 32-km spatial resolution data set. Additional NWP forecasts were available from the Weather Research Forecast (WRF) model at 1.67-km and 5-km spatial resolutions. However, this was an experimental data set and so was not used during the eruption response.

For this paper, AVHRR channel 4 (10.2–11.2 micron) and channel 5 (11.5–12.5 micron) data were used to detect ash clouds, including generating "split window" images, using the reverse absorption method, first noted by Prata (1989a, b). AVHRR channel 4 data are useful for detecting opaque ash clouds (Dean and others, 2002) and the reverse absorption method becomes a useful tool once the ash clouds are "semi-transparent". Here we use the reverse absorption method through a brightness temperature difference (BTD) of the infrared channels as stated by Prata (1989a). Eruption clouds early on in their development can fail to allow discrimination of ash, given that they are spectrally opaque (Wen and Rose, 1994; Krotkov and others, 1999; Simpson and others, 2000). Part of the ash cloud needs to be "translucent", which indicates a low optical depth, for the reverse absorption method to be successful. The ash signal can be affected by water vapor in the atmosphere, which can cause the signal sometimes to become slightly negative, even there is not ash present in the atmosphere (Simpson and others, 2000; Prata and others, 2001; Simpson and others, 2001). Additionally, ice within volcanic clouds can cause the reverse absorption method to be ineffective (Rose and others, 1995).

January 11, 2006

On January 11, 2006, Augustine Volcano had two explosive events at 0444 and 0512 Alaska Standard time (AKST; 1344 and 1412 UTC), as much as 3 minutes 13

Table 1. Volcanic eruption parameters for Augustine's 2006 explosive and continuous phases, as used by the Puff model.

[All heights a.m.s.l . UTC = coordinated universal time, AKST = Alaska Standard Time, Jan = January, Feb = February, km = kilometers, ft = feet, s = seconds, min= minutes. AKST = UTC – 9 hours. Note that the start and end times of the eruptive events were determined from AVO seismic stations]

Event No.	Date	Start Time (AKST)	End Time (AKST)	Duration	Plume Height[1]	Plume Height[2]
1	11 Jan 2006	04:44:00 (13:44:00 UTC)	04:45:18 (13:45:18 UTC)	1 min 18 s	30,000 ft (~9 km)	6.5 km
2	11 Jan 2006	05:12:00 (14:12:00 UTC)	05:15:18 (14:52:18 UTC)	3 min 18 s	28,000 ft (~8.5 km)	10.2 km
3	13 Jan 2006	04:24:00 (13:24:00 UTC)	04:35:00 (13:35:00 UTC)	11 min	34,000 ft (~ 10.4 km)	10.2 km
4	13 Jan 2006	08:47:00 (17:47:00 UTC)	08:51:17 (17:51:17 UTC)	4 min 17 s	30,000 ft + (~ 9 km+)	10.2 km
5	13 Jan 2006	11:22:00 (20:22:00 UTC)	11:25:24 (20:25:24 UTC)	3 min 24 s	36,000 ft + (~ 11 km+)	10.5 km
6	13 Jan 2006	16:40:00 (1/14 01:40:00 UTC)	16:44:00 (1/14 01:44:00 UTC)	4 min	34, 000 ft + (~ 10.4 km+)	10.5 km
7	13 Jan 2006	18:58:00 (1/14 03:58:00 UTC)	19:01:00 (1/14 04:01:00 UTC)	3 min	30,000 ft (~ 9 km)	13.5 km
8	14 Jan 2006	01:14:00 (09:14:00 UTC)	01:17:00 (09:17:00 UTC)	3 min	~ 30,000 ft (~ 9 km)	10.2 km
9	17 Jan 2006	07:58:00 (16:58:00 UTC)	08:02:11 (17:02:11 UTC)	4 min 11 s	45,000 ft (~ 13.7 km)	13.5 km
10	27 Jan 2006	20:24:00 (1/28 05:24:00 UTC)	20:33:00 (1/28 05:33:00 UTC)	9 min	30,000 ft (~ 9 km)	10.5 km
11	27 Jan 2006	22:37:21 (1/28 08:37:21 UTC)	22:38:45 (1/28 08:38:45 UTC)	1 min 2 s	< 10,000 ft (< 3 km)	3.8 km
12	28 Jan 2006	02:04:13 (11:04:13 UTC)	02:06:40 (11:06:40 UTC)	2 min 6 s	26,000 ft (~ 8 km)	7.3 km
13	28 Jan 2006	07:42:00 (16:42:00 UTC)	07:45:00 (16:45:00 UTC)	3 min	25,000 ft (~ 7.6 km)	7 km
continuous phase	28 Jan 2006	14:30:00 (23:30:00 UTC)	1 Feb 2006	4 days	10,000 – 14,000 ft[3] (~ 3 – 4.3 km)	3.8 km[4]

[1] Eruption response plume height from NWS.

[2] NEXRAD radar plume height.

[3] Discrete events to 30,000 ft.

[4] Discrete events to 7.2 km. 1 km = 3,280 ft.

seconds in duration, and that produced ash clouds of 8–9 km a.m.s.l. (26,000–30,000 ft) (table 1). Once the explosions were detected by the AVO seismic network, the Puff model was implemented to predict the movement of the emitted ash clouds using a default plume height of 16 km a.m.s.l (52,000 ft), to ensure that the full eruption column was included. For these two events, Puff predicted very similar patterns in both simulations (fig. 4): a spiral-shaped ash cloud with the ash above 6 km (20,000 ft) a.m.s.l drifting mostly east away from Augustine and across the Kenai Peninsula and the lower ash, < 6 km a.m.s.l, drifting mostly north. Initially, an opaque ash cloud was detected by satellite data (fig. 5*A*). Once translucent, this ash cloud was detectable by the reverse absorption method (fig. 5*B*), with

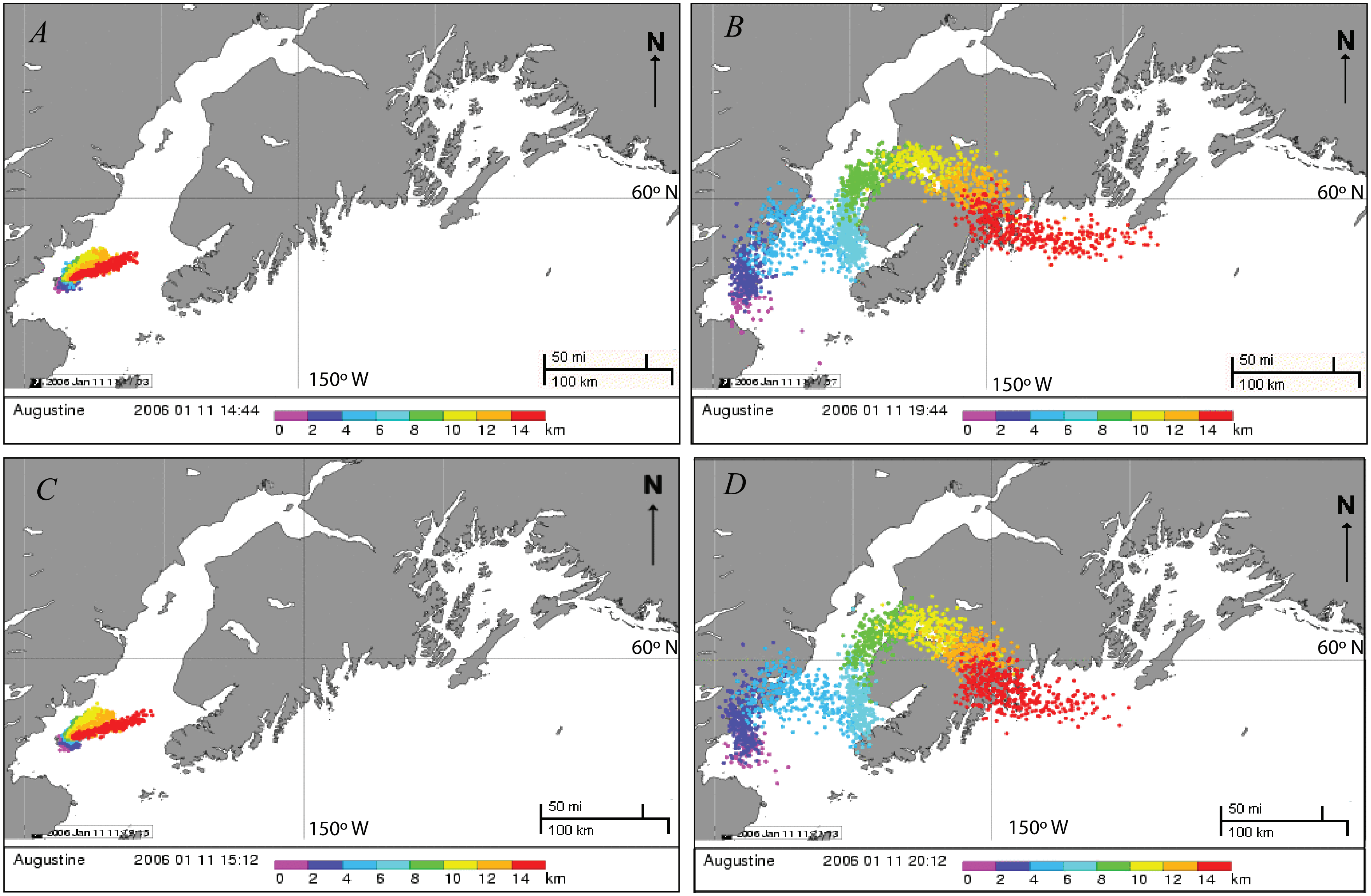

Figure 4. Puff eruption response simulations for the January 11, 2006 explosions. *A* and *B* for the first event at 0444 AKST (1344 UTC) eruptions at +1 and +6 hours. *C* and *D* are for the second event at 0512 AKST (1412 UTC) eruption at +1 and +6 hours. Times are in UTC, and particles are color-coded by elevation a.m.s.l.

a negative brightness temperature difference (BTD) signal. For these two events on January 11, the ash cloud was only detectable in a few satellite images. The NWS tracked the plume moving north towards the west side of Cook Inlet, corresponding to the low level sections of the Puff forecast below 6 km a.m.s.l. The explosive events on January 11 showed little ash in the satellite data, consistent with interpretation of seismic signals from the events, which suggest the explosions were mostly caused by gas release (McNutt and others, this volume).

January 13–14, 2006

Starting at 0424 AKST (1324 UTC) on January 13, Augustine Volcano had six further explosive events. On the basis of the AVHRR satellite sensor data, the events on January 13 and 14 (fig. 6) showed a stronger ash signal than seen for the second explosive event on January 11 (fig. 5). The first event on January 13 started at 0424 AKST (1324 UTC), had an 11-minute duration, and produced an ash cloud that ascended to approximately 10 km a.m.s.l (33,000 ft) (table 1). Within approximately 24 hours, there would be five more explosive events lasting around 3 to 4 minutes each, and producing ash columns from 9 to 11 km a.m.s.l (30,000–36,000 ft) (table 1). The movements of ash clouds from these events were predicted and simultaneously tracked using the “multiple eruption” option in the Puff model. This was the first time that this tool had been applied during an eruption response. The tool allows Puff to predict the movement of many volcanic ash clouds at one time. As each of the six events was confirmed, the model predictions were then updated. For each new prediction, the Puff model integrated the new and older ash clouds to track all of them together, so all six plumes’ movements were forecasted simultaneously. These forecasts were then compared to any additional data once available.

Figure 6 shows the volcanic ash plumes detected on several AVHRR satellite images during January 13–14. Figure 6*A* shows the first plume at 0609 AKST (1509 UTC) on January 13 drifting east across Cook Inlet towards the Kenai Peninsula. Figure 6*B* shows that there were two ash plumes detectable in the satellite data at 1024 AKST (1924 UTC). The first was over the Kenai Peninsula, with a weak ash signal, and the second was to the east of Augustine Volcano, in Cook Inlet. Figure 6*C* shows three detected ash clouds at 1203 AKST (2103 UTC) that moved in an east-northeast direction. By 2020 AKST on January 13 (0520 UTC on January 14), these first three plumes had dispersed and moved out into the Gulf of Alaska. Figure 6*D* shows the fourth and fifth plumes (events 6 and 7 in table 1), which moved in a more south-easterly direction, through the strait between the Kenai Peninsula and Kodiak Island and out into the Gulf of Alaska, with the strongest ash signal at the

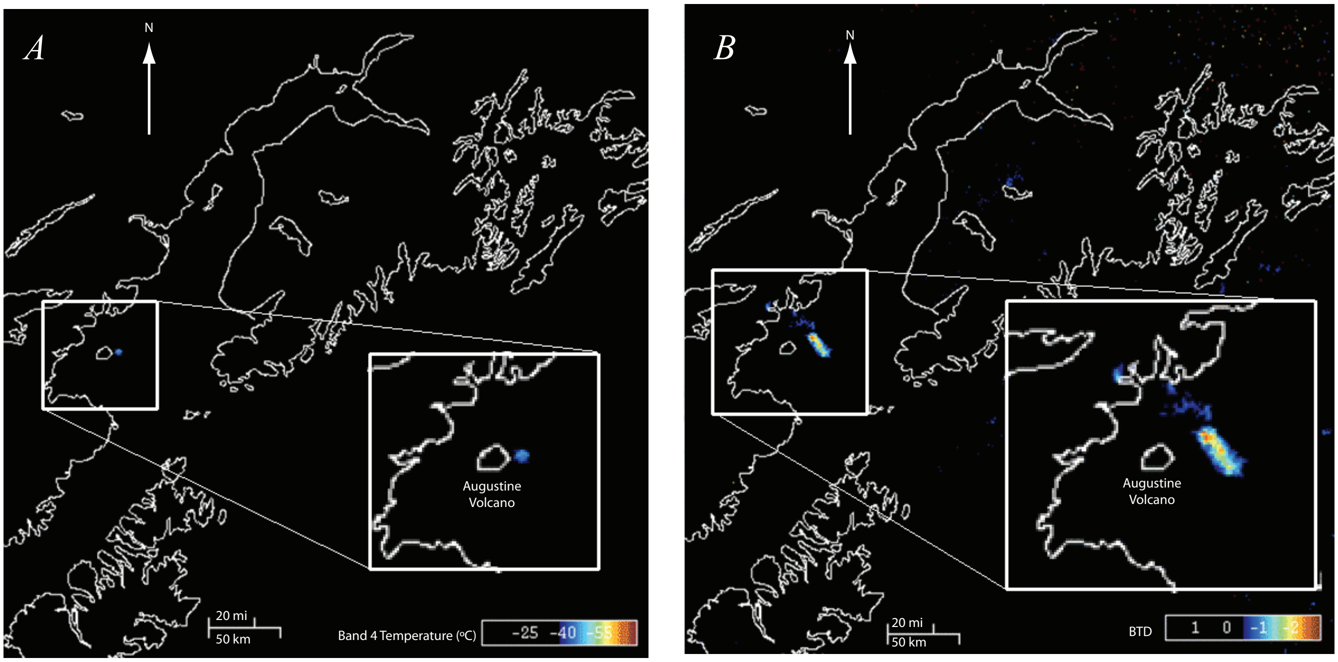

Figure 5. Advanced Very High Resolution Radiometer (AVHRR) satellite sensor data as images from January 11, 2006. *A*, Opaque ash cloud at 0448 AKST (1348 UTC). *B*, Ash signal, shown as brightness temperature differences (BTD), at 0659 AKST (1559 UTC). BTD scale is difference in AVHRR channels 4 and 5 using the reverse absorption method.

“head” of the ash clouds. Additional discussion of the satellite data collected on January 13–14 is included in Bailey and others (this volume). Figure 7 shows time-snapshots during the Puff model forecasts of the six plumes (events 3 to 8 in table 1) from January 13–14 as they drift across the Gulf of Alaska. The simultaneous forecast of the movement of these multiple ash clouds simplified a very complex geographic problem of displaying and accounting for all of the ash clouds at one given time and demonstrated that we can track and forecast all of them to make a hazard assessment.

Figure 8 shows a comparison of the Puff eruption response forecasts to the AVHRR satellite sensor data

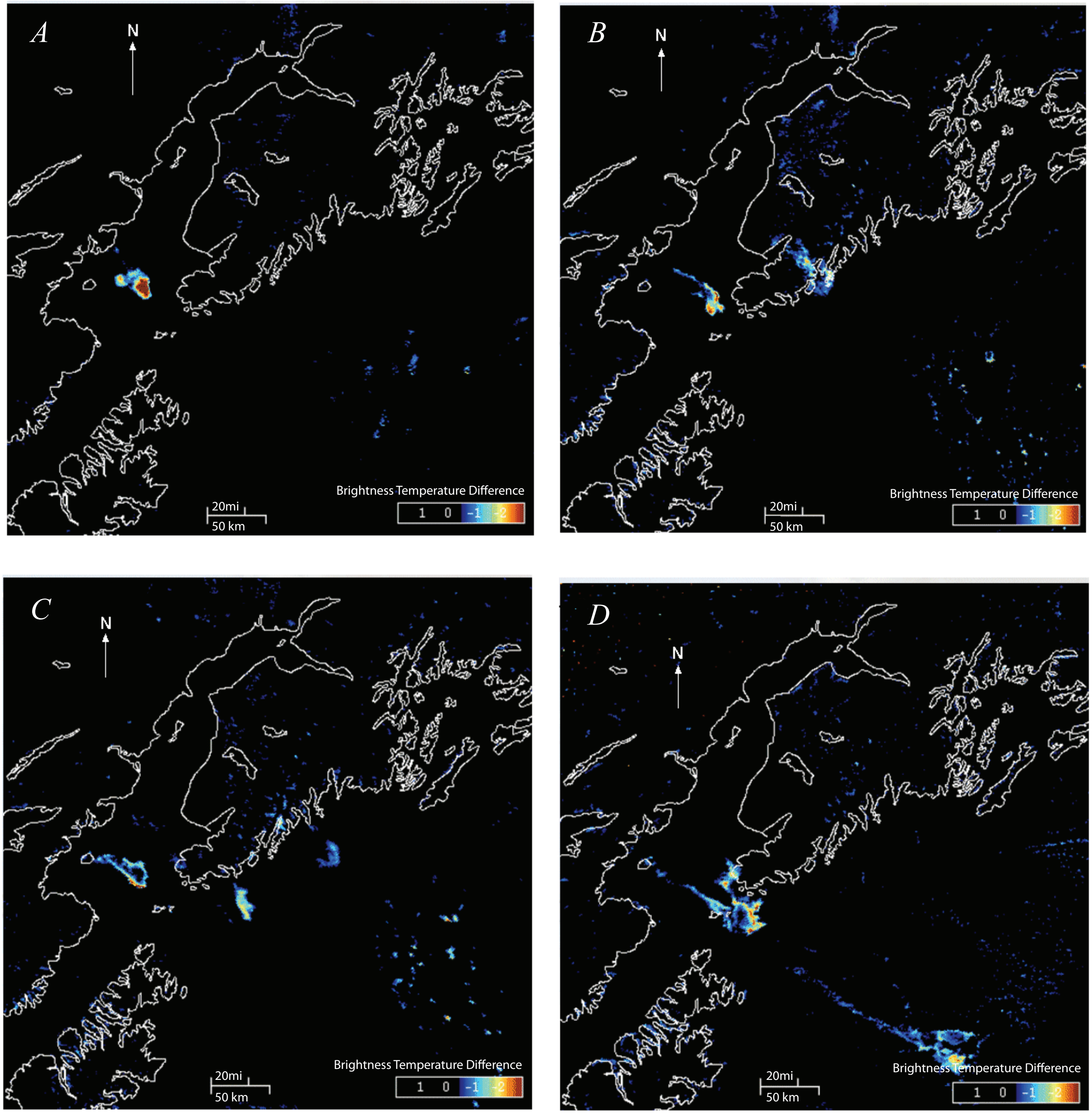

Figure 6. Time-snapshot series of the multiple plumes from Advanced Very High Resolution Radiometer sensor satellite data using reverse absorption method, BTD, on January 13, 2006. *A*, 0609 AKST (1509 UTC). *B*, 1024 AKST (1924 UTC). *C*, 1203 AKST (2103 UTC). *D*, 2020 AKST (0520 UTC on 14 January 2006). BTD scale is difference in AVHRR channels 4 and 5 using the reverse absorption method.

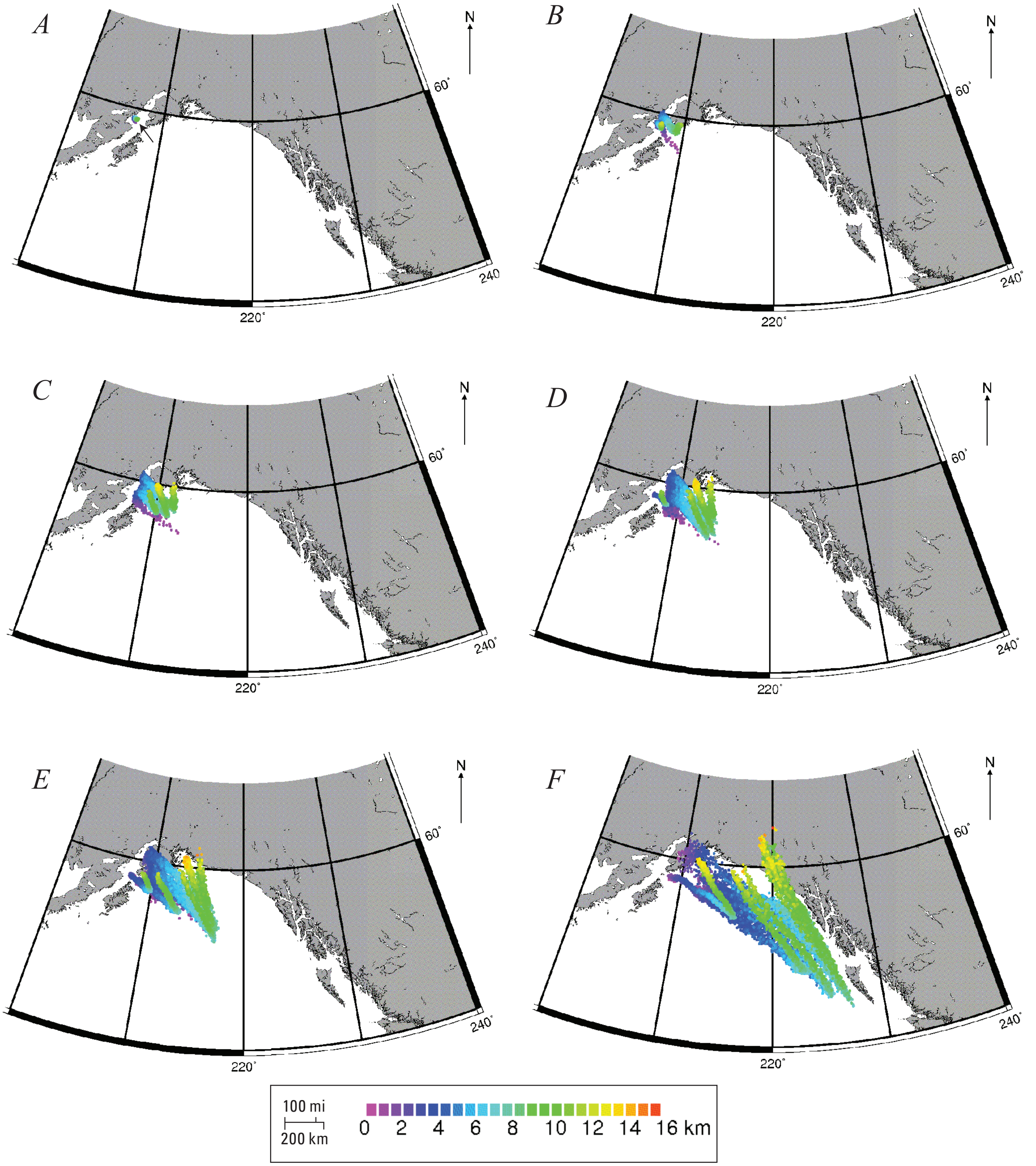

Figure 7. Time snapshots during the 24 hour Puff simulations from the six plumes during January 13–14, 2006. *A*, January 13 at 0520 AKST (1420 UTC). *B*, January 13 at 1020 AKST (1920 UTC). *C*, January 13 at 15:20 AKST (14 January at 0020 UTC). *D*, January 13 at 1820 AKST (14 January at 0320 UTC). *E,* January 13 at 2120 AKST (14 January at 0620 UTC). *F,* January 14 at 0720 AKST (1620 UTC). Date and times in Puff model forecasts are in UTC, and particles are color-coded by elevation a.m.s.l.

from the events on January 13 and 14. Figure 8*A* shows the AVHRR sensor satellite data at 1246 AKST (2146 UTC) on January 13. Here, the first three events from January 13, events 3–5 in table 1, are detected with the reverse absorption method in the satellite data, giving a negative BTD signal. Figure 8*B* shows the Puff forecast at 1250 AKST (2150 UTC), within 5 minutes of the satellite data. Figure 8*C* shows a comparison of the two data sets, by evaluating their spatial footprint. As we were unable to determine ash retrievals and then use the Puff model to predict airborne concentrations, a spatial comparison was the only possible method for data comparison. Here, the “footprint match” between the Puff predictions and the satellite data is emphasized by points labeled 1, 2 and 3 (fig. 8*C*). From the Puff forecasts, the modeled ash at altitudes from 8–10 km a.m.s.l. (26,000–33,000 ft) matches the satellite data. As the ash clouds were detectable in the satellite data using the reverse absorption method and a negative BTD signal, they were termed translucent. Determination of their altitude is only possible from this comparison method with Puff. The Puff

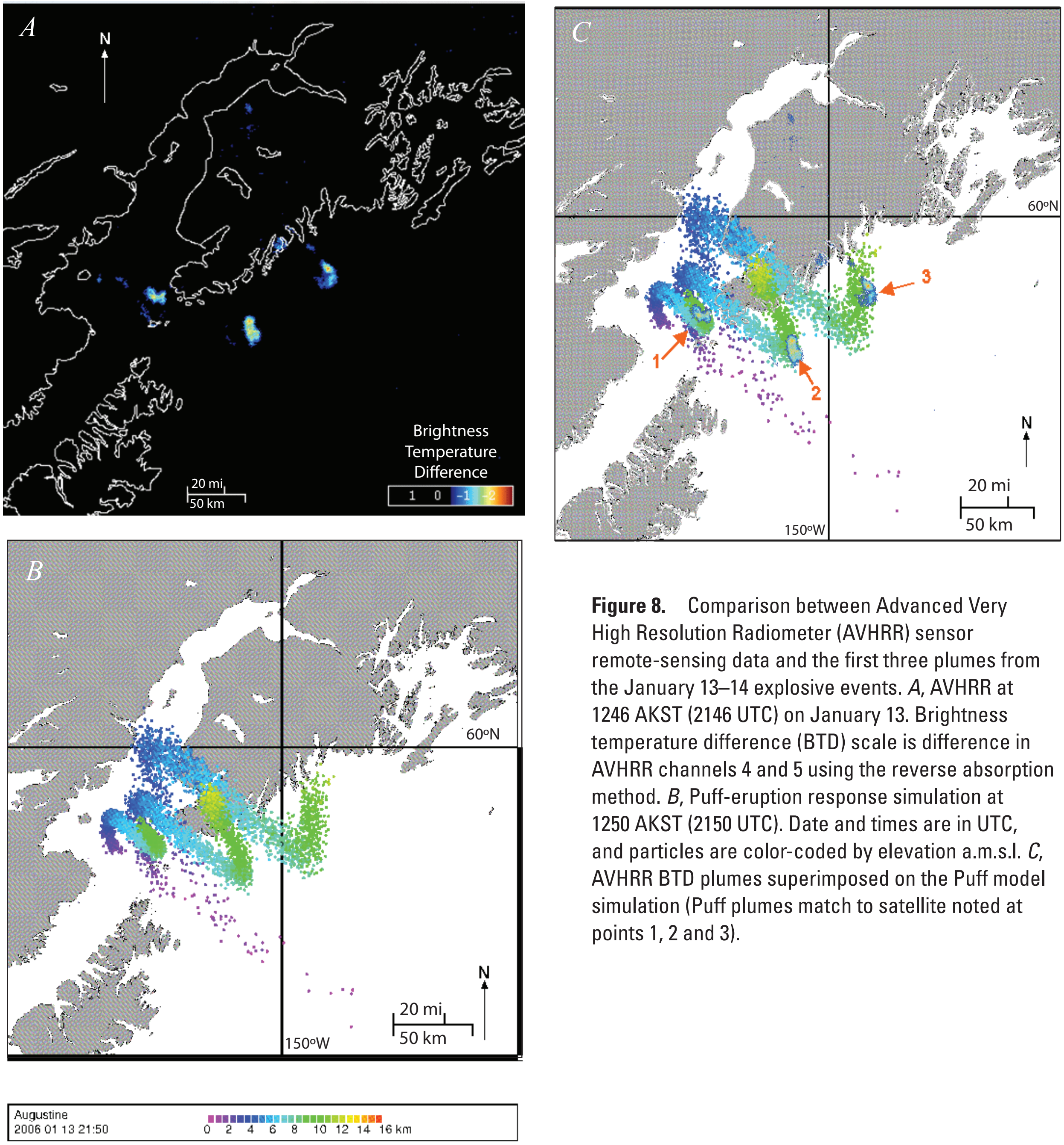

Figure 8. Comparison between Advanced Very High Resolution Radiometer (AVHRR) sensor remote-sensing data and the first three plumes from the January 13–14 explosive events. *A*, AVHRR at 1246 AKST (2146 UTC) on January 13. Brightness temperature difference (BTD) scale is difference in AVHRR channels 4 and 5 using the reverse absorption method. *B*, Puff-eruption response simulation at 1250 AKST (2150 UTC). Date and times are in UTC, and particles are color-coded by elevation a.m.s.l. *C*, AVHRR BTD plumes superimposed on the Puff model simulation (Puff plumes match to satellite noted at points 1, 2 and 3).

simulations were able to match the ash cloud movements, even though they showed a larger amount of dispersion. This increased dispersion could be a result of (1) the ash concentrations seen in the modeled cloud being below the detection limits of the reverse absorption technique or (2) in the model forecast, the dispersion factor being set too high.

In the past few years, virtual globes, specifically Google Earth™, have been used for displaying scientific data. They allow the Puff model predictions to be shown in their three-dimensional form. Figure 9 shows both a graphical representation of the Puff model forecast and a three-dimensional view of event 3 on January 13. Figure 9*A* shows the ash cloud's location in a graphical plan view, with no three-dimensional viewpoint. Here, the ash cloud altitudes are shown as color-coded particles from 0 to 16 km a.m.s.l (0 to 52,000 ft). Figure 9*B* shows a three-dimensional viewpoint of the same Puff prediction in Google Earth. Selecting each ash particle in Google Earth, the observer is provided with its location and altitude. In addition, there is a "time stamping option", highlighted within the box in figure 9*B*, which allows an animation of ash cloud movement. This three-dimensional viewpoint and interactive ability is a novel tool for analyzing the dispersion model forecasts, something that is not possible with the graphical map image.

Additional comparison data during the January 13–14 period included ashfall reports in Homer/Port Graham on January 13, as well as Shasta County, California, on January 16 (Wallace and others, this volume) and aerosol data collected in Homer on January 13 (Cahill and others, unpub. data). All reports indicate that ashfall was very light. Figure 8*B* shows the Puff simulation of the low level ash cloud moving towards Homer and the Kenai Pennisula, towards the ashfall reports in Port Graham and aerosol samplers in Homer. In addition, the Puff simulations of the six plumes (fig. 7*F*) show that the forecasted ash clouds could have passed over the northwestern contiguous United States,

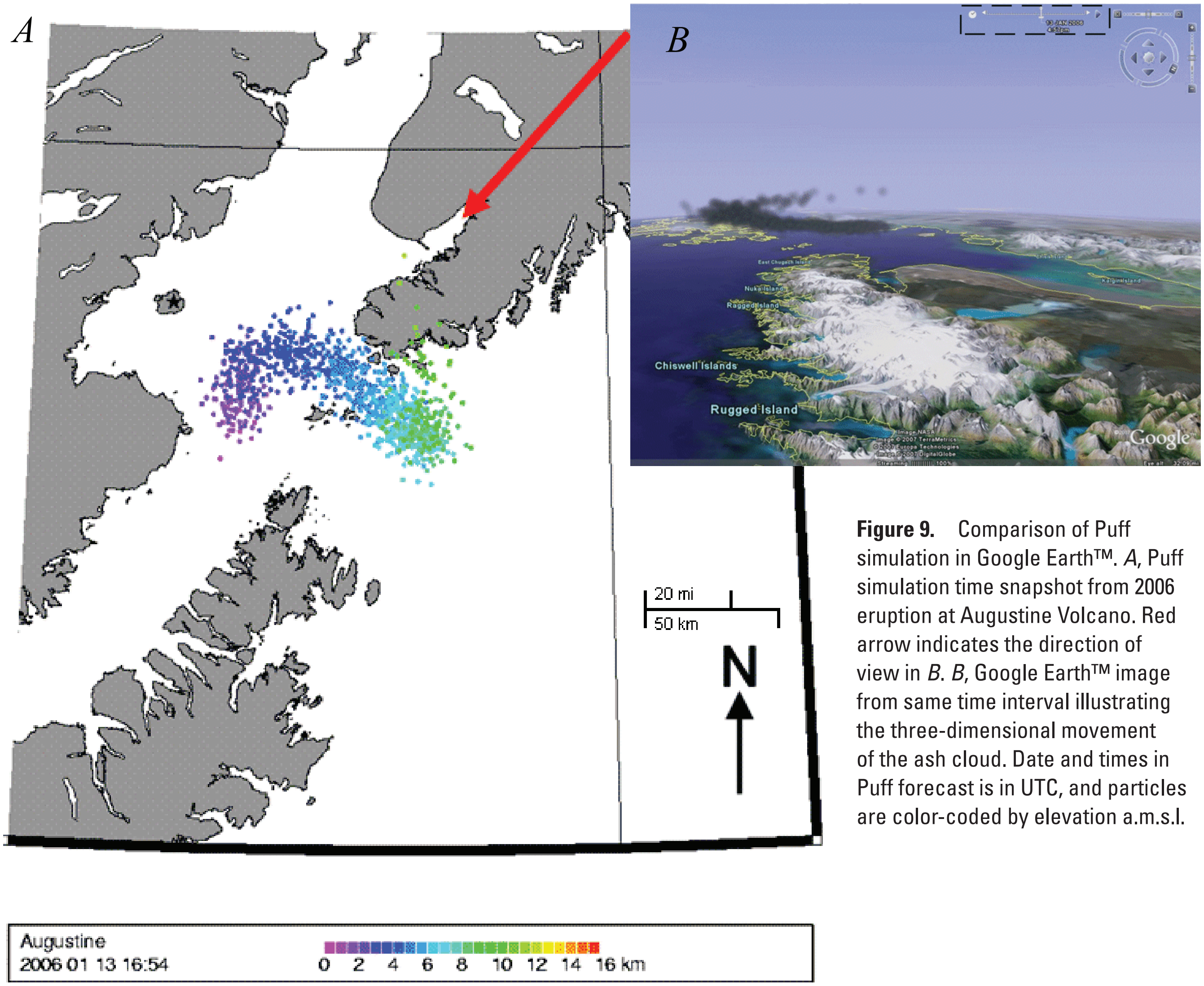

Figure 9. Comparison of Puff simulation in Google Earth™. *A*, Puff simulation time snapshot from 2006 eruption at Augustine Volcano. Red arrow indicates the direction of view in *B*. *B*, Google Earth™ image from same time interval illustrating the three-dimensional movement of the ash cloud. Date and times in Puff forecast is in UTC, and particles are color-coded by elevation a.m.s.l.

towards the reported ashfall in California. Peterson and others (2010) provide a comparison of the Puff simulations during the events on January 13–14 with those using the HYSPLIT and CanERM VATD models.

January 17, 2006

Following 3 days of relative quiescence, on January 17, 2006, Augustine had a single explosive event starting at 0758 AKST (1658 UTC), and lasting 4 minutes and 11 seconds, with a volcanic ash plume rising to an altitude of approximately 13 to 14 km a.m.s.l (43,000–46,000 ft) (event 9 in table 1). The ash cloud was only detected on 3 AVHRR satellite images (Bailey and others, this volume). Figure 10 shows the Puff model simulations in response to the detected eruption at 1 hour, 3 hours, and 6 hours after the start of the event. Here, the high altitude sections of the ash cloud travel north-northwest, and the low altitude sections travel to the southwest. Figure 11 shows a comparison between the Puff model simulations, the AVHRR satellite sensor data and the NWS Next Generation Radar (NEXRAD). Comparison between the Puff simulation (fig. 11*A*) and the satellite data (fig. 11*B*) show that the detected opaque ash cloud is at 8 to 10 km a.m.s.l (26,000–33,000 ft). The 0300 AKST January 17, 2006 radiosonde sounding collected from Kodiak, King Salmon, and Anchorage stations (http://weather.uwyo.edu/upperair/naconf.html), indicate that the −55.45°C temperature in figure 11*B* corresponds to approximately 8.5 to 9 km a.m.s.l (26,000-30,000 ft), using the altitude-temperature method of Sparks and others (1997) as developed from Kienle and Shaw (1979). NEXRAD, in clear air mode, shows very little reflectivity across Cook Inlet except for signals of +4 to +16 DBZ at Augustine (fig. 11*C*). The match in timing between the three datasets provides good agreement that (1) the radar was able to detect the ash cloud, (2) the Puff model results matched the satellite data, and (3) the ash cloud was at 8 to 10 km a.m.s.l. (26,000–33,000 ft).

In addition, a retrospective comparison between the Puff predictions and measured ashfall from the January 17 event was used to assess the Puff model's ability to reliably forecast ashfall (fig. 12). Figure 12*A*, adapted from Wallace and others (this volume), shows that ashfall occurred to the northwest of Augustine Volcano towards Lake Iliamna (location is shown in Figure 2). There are also ground observations of ashfall from Iliamna, Pedro Bay,

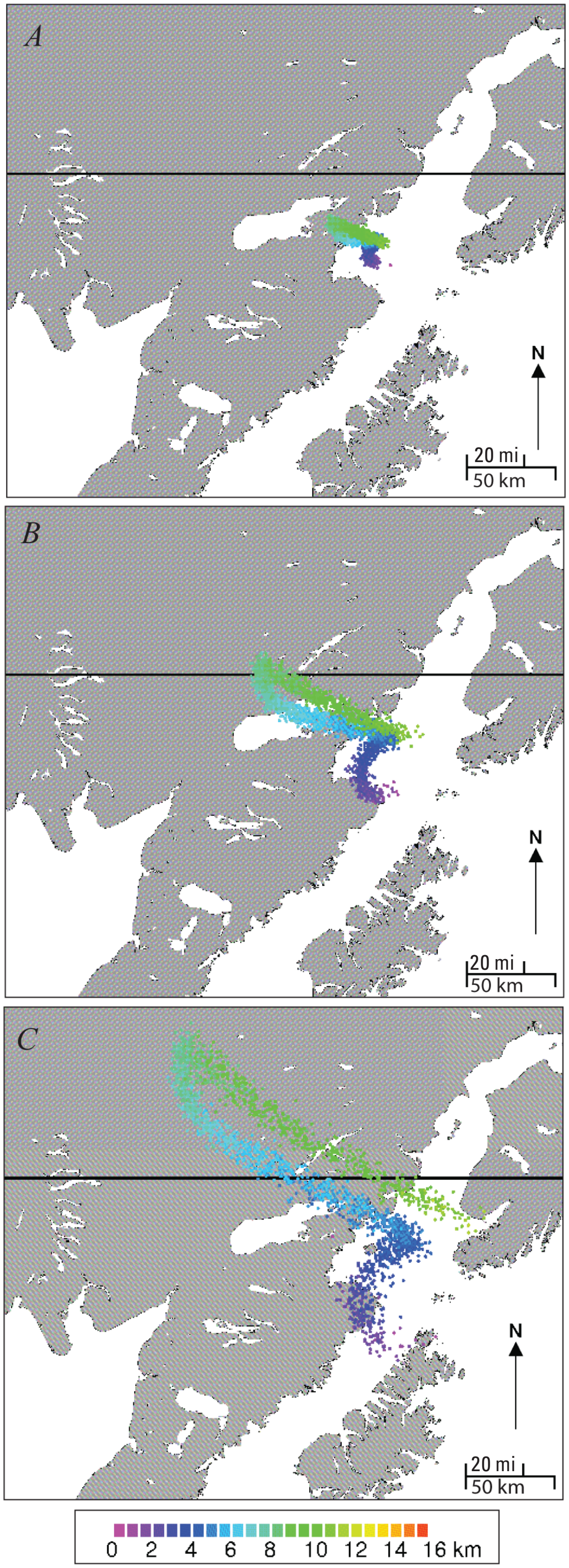

Figure 10. Puff time snapshots following simulation of January 17, 2006 explosive event. *A*, +1 hour or 0858 AKST (1758 UTC). *B*, +3 hours or 1058 AKST (1958 UTC). *C*, +6 hours or 1358 AKST (2258 UTC). Date and times are in UTC, and particles are color-coded by elevation a.m.s.l.

and Nondalton from local citizens. Figures 12*B*–12*D* show the Puff modeled ashfall predictions using three different wind-field datasets: National Centers for Environmental Prediction (NCEP) global reanalysis, WRF 5-km resolution and WRF 1.67-km resolution. For the reanalysis wind-field data (fig. 12*B*), the Puff-forecast ashfall occurs mostly over Cook Inlet. Although no ashfall samples were collected, there were ashfall reports at Port Graham, and the reanalysis forecast suggests that it could have been from this eruption, on the basis of a few predicted ashfall particles in the area. Because Puff is a tracer model, ashfall amounts can be simulated only relative to other locations, but light ashfall would be consistent with the model prediction.

Using the higher spatial resolution wind-field data from WRF, figures 12*C* and 12*D* show a very different ashfall pattern. Figure 12*C* predicts ashfall north of the volcano towards Pedro Bay and north-west towards Port Graham. Figure 12*D* predicts ashfall both southeast over the ocean and northwest towards Lake Iliamna (its location is shown in figure 2). This 1.67-km spatial resolution wind field was an experimental dataset used during the eruption, and as a result its spatial domain doesn't extend much beyond 20 km from the volcano. A larger domain at this finer spatial resolution could have resulted in a better match between the Puff model forecasts and the ashfall reports and measurements shown in figure 12*A*. The Puff model uses the wind field for its advection term, and the speed and direction for all particles is determined from the wind-field model data. A coarse resolution wind-field dataset requires interpolation to determine the wind field for each ash particle. Finer grids require less interpolation and hence more accurate representation of the actual atmospheric conditions.

This retrospective analysis suggests that an area like Cook Inlet, which has complex winds due to surrounding mountainous terrain and numerous valleys open to the ocean, requires higher resolution wind fields to better model the atmospheric boundary layer. This could result in more accurately modeled volcanic ashfall, an important factor for producing volcanic ashfall advisories in volcanic crises. Other factors, such as size distribution, aggregation, and deposition processes can also affect ashfall forecasts. However, a better representation of the wind field in the model's advective term will provide an improved forecast for both airborne ash movement and ashfall. Figures 10 through 12 have shown that the Puff model was able to match both the

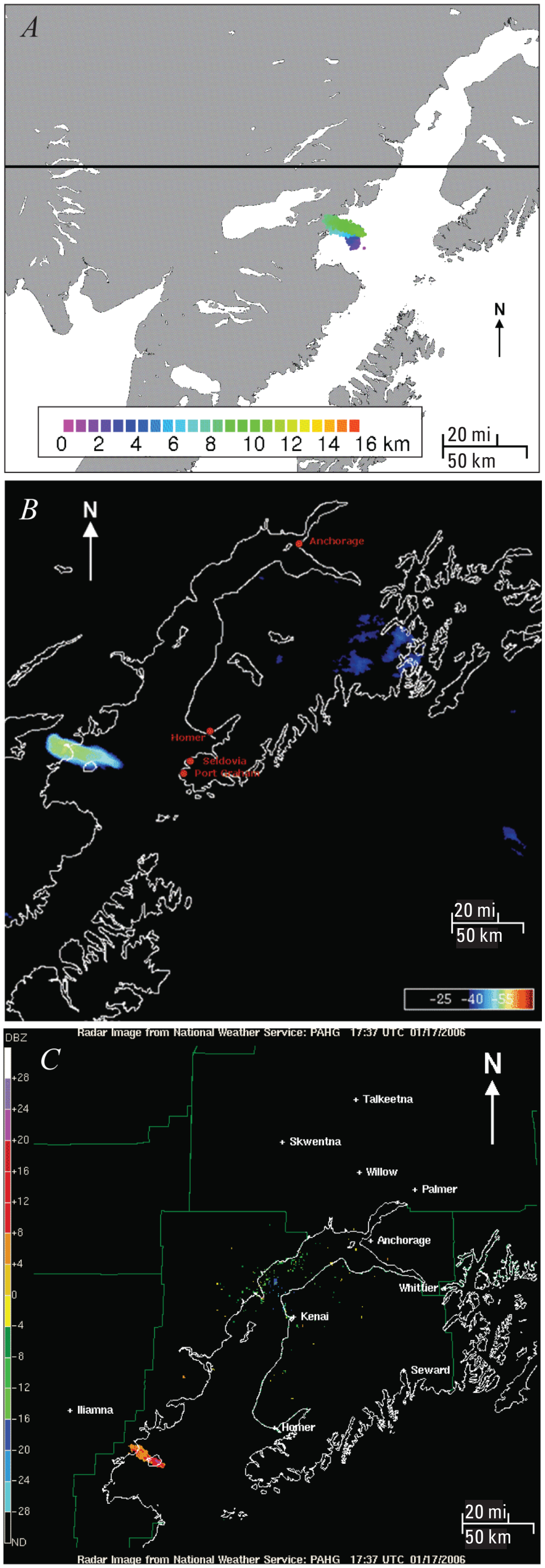

Figure 11. Three views of the January 17, 2006, explosive event. *A,* Puff model output from 0838 AKST (1738 UTC). Times are in UTC, and particles are color-coded by elevation a.m.s.l. *B,* Advanced Very High Resolution Radiometer single channel satellite data from 0838 AKST (1738 UTC), showing cold temperatures of the infrared spectrally opaque ash cloud. *C,* NEXRAD radar from 0837 AKST (1737 UTC).

radar and satellite data for the January 17 event, but they also show how higher resolution wind-field data are needed for the Puff model to provide reliable forecasts of ashfall. After this single event on January 17, the next events occurred on January 28 and led to the continuous eruptive phase from January 28 to February 10, 2006, with declining vigor from February 2 to 10.

January 28 to February 2, 2006

On January 27–28, 2006, at 2024 to 0742 AKST Augustine Volcano again produced several explosions (events 10–13 in table 1), lasting as long as 9 minutes with ash plumes varying from 3 to 9 km (10,000–30,000 ft) a.m.s.l. that dispersed to the southeast and south-southwest.

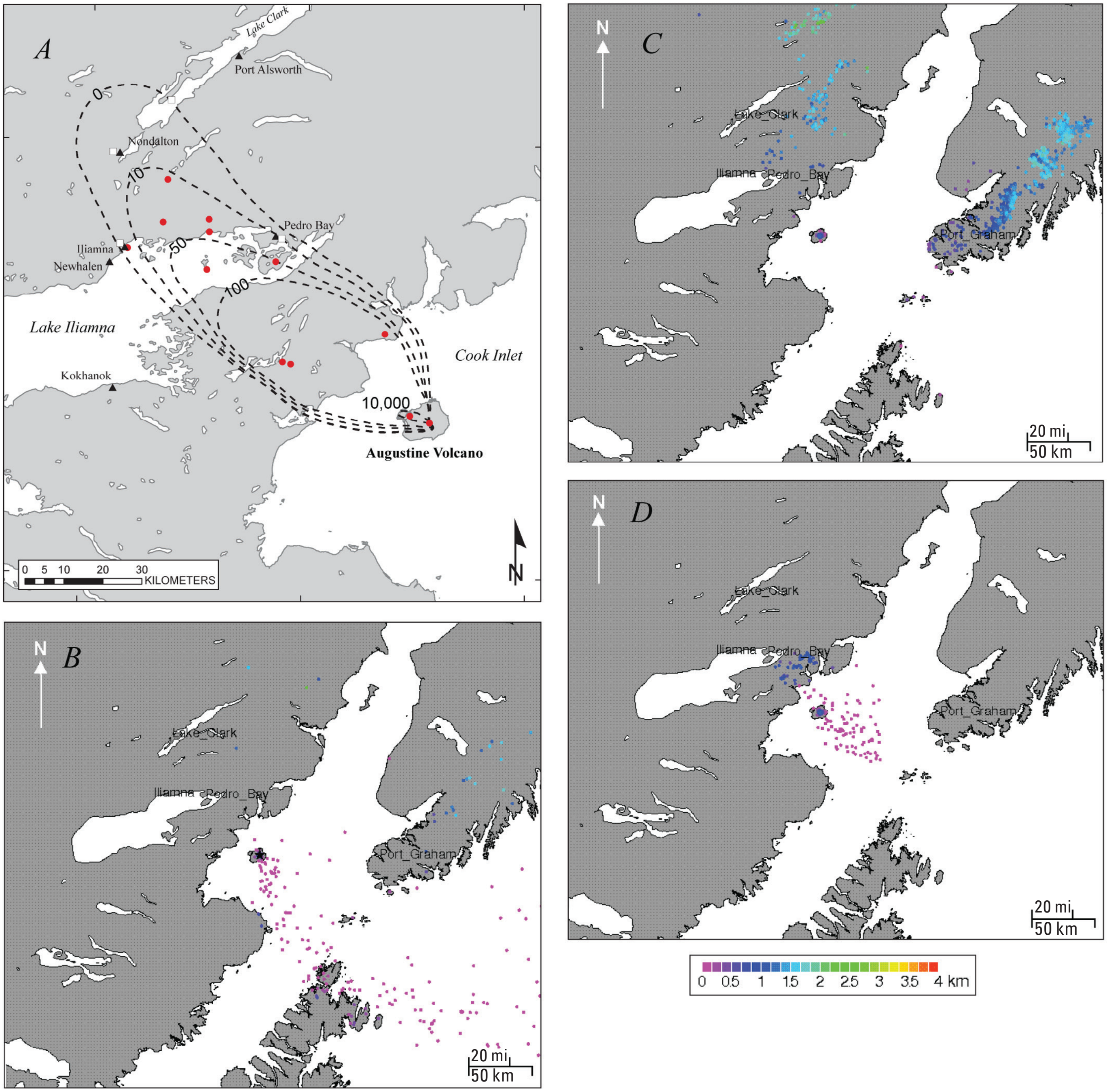

Figure 12. Measurements and simulations of ashfall from January 17, 2006 event. *A,* Ashfall isopach in g/m^2, (from Wallace and others, this volume). *B,* Puff model simulated ashfall from post event analysis with NCEP reanalysis wind field. *C,* Puff model simulated ashfall from post event analysis with WRF 5-km resolution wind field. *D*, Puff model simulated ashfall from post event analysis with WRF 1.67-km resolution wind field. Ashfall particles are color-coded by ground elevation a.m.s.l.

Then the volcano was relatively quiet for several hours from 0742 AKST (1642 UTC) until around 1430 AKST (2330 UTC), when seismicity began to increase. This led to the continuous phase as seen in the NEXRAD radar, which immediately started to detect a signal over the volcano, from ash emission, that continued for several days (D. Schneider, written communication (2006) and AVO Logs). Over the continuous phase, ash clouds reached approximately 3 to 4.5 km a.m.s.l (10,000–15,000 ft), with discrete events reaching 7.3 km (24,000 ft) (table 1). For the period from January 28, 2006, onwards, Puff used an initial 5 km (~16,500 ft) a.m.s.l ash plume and forecast wind fields from the NAM 216 model domain. To make the best use of the forecast data, the model was run for an initial 24 hours (from 1430 AKST/2330 UTC on January 28, 2006) and then restarted for another 24 hours, continuing in this way until February 2. Each new model run used the most recent forecast wind fields. Figure 13 is an example of the ash signal as detected from the BTD signal using the AVHRR satellite remote-sensing data on January 28 at 1731 AKST (January 29 at 0231 UTC). There is a very strong negative BTD signal to the south of the volcano across Kodiak Island. Additional discussion of the satellite data is included in Bailey and others (this volume).

At the beginning of the continuous phase, the synoptic conditions showed that volcanic material would initially move towards the southeast and then curve rapidly around with a northerly heading and be transported rapidly to the Alaska interior (Webley and others, 2008). Figure 14, adapted from Webley and others (2008), shows daily AVHRR and MODIS sensor data composites of the ash clouds from January 29 to 31. The movement of the ash clouds was initially in a southerly or south-easterly direction on January 28, shifting to a more southerly direction by January 29, then an easterly direction on January 30, and a northeasterly direction by January 31. These observations support Puff forecasts for this time period (fig. 15). Volcanic ash concentrations eventually receded to levels below the detection limits of the satellite data, with no ash clouds detected beyond the Cook Inlet area.

For the period from January 29 to February 1, the Puff predictions showed an ash-cloud trajectory towards Kodiak Island (fig. 15*A*) with a subsequent rotation to the northeast and across the Kenai Peninsula by the following day (fig. 15*B*). By the third day, predictions indicated a northeasterly trajectory (fig. 15*C*). Aerosol samples, from an eight stage impactor (described in Cahill, 2003) were collected at Homer, Alaska, and confirmed the presence of ash “at ground level there.” These provide ground-based verification to go with the airborne ash detection (fig. 14) of the ash within Cook Inlet. Lidar measurements from three distinct systems across Alaska were also used to aid in confirming the Puff-model-predicted volcanic ash clouds from the continuous period (Sassen and others, 2007; Webley and others, 2008). The lidar measurements at two sites were collected in response to the Augustine volcanic activity and Puff simulations. Lidar detected the ash cloud under both clear skies and partially cloudy conditions. The characteristics of the volcanic ash were distinct from those of the atmospheric clouds. Figure 16 shows the Puff model prediction at 1900 AKST, January 31 (0400 UTC, February 1), during the acquisition of the lidar data at one station, as described in Webley and others (2008).

The lidar data confirmed the presence of the volcanic cloud overhead at Fairbanks, Alaska, and also confirmed the independent motion of the upper and lower level ash clouds. The location of the ash cloud in figure 16 shows ash passing over Fairbanks (marked as “F”). Aerosol analysis showed that ratios of iron to calcium at both Homer and Fairbanks indicated to a similar source and under “normal conditions” such ratios would not have been recorded at Fairbanks (Cahill and others, unpub. data). Figures 15*C* and 16 show that Puff-predicted ash clouds would have passed over Homer and

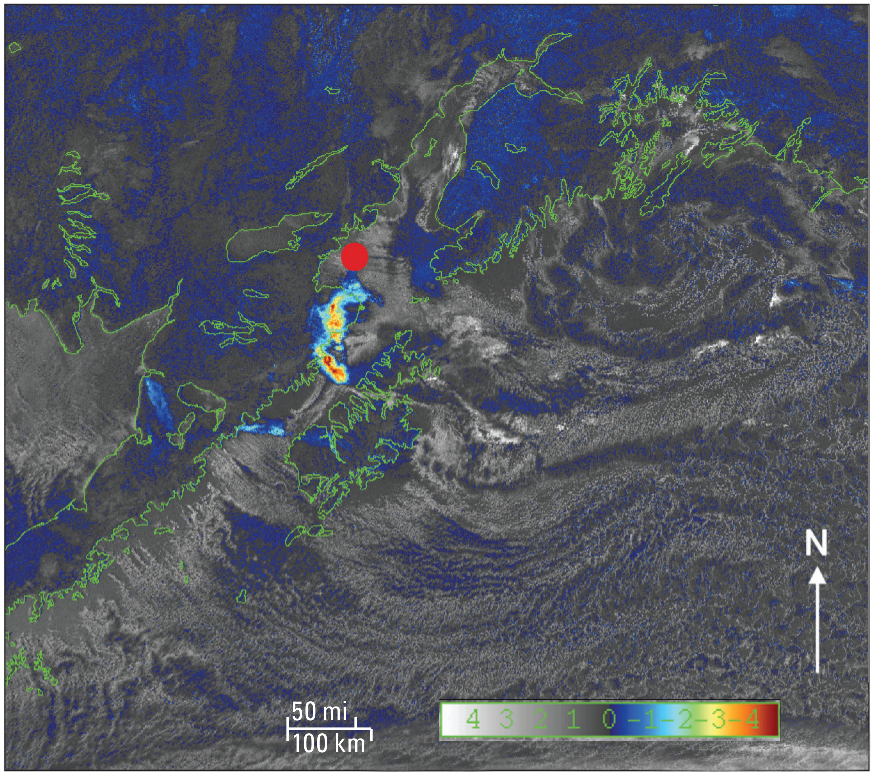

Figure 13. Advanced Very High Resolution Radiometer brightness temperature difference satellite data from January 28, 2006, at 1731 AKST (January 29, at 0231 UTC) showing the ash signal as detected through the reverse absorption method. Here, the ash is shown as a negative BTD signal. Location of the volcano is show by the red circle.

Fairbanks at the times the aerosol data were collected. The measurements of the aerosol signals in the lidar returns provided a unique confirmation tool to the Puff predictions.

The continuous phase of the eruption provided some unique validation opportunities for the Puff model predictions. Webley and others (2008) show the possibilities of lidar being used as a validation tool for volcanology. As shown by Sassen and others (2007), an autonomous lidar could be used by both the meteorological and volcanological communities for eruption crisis monitoring. Lidar measurements as an eruption response tool for volcano monitoring could be applied to known erupting volcanoes as well as the dispersed volcanic material from a much more distant eruption (Webley and others, 2008).

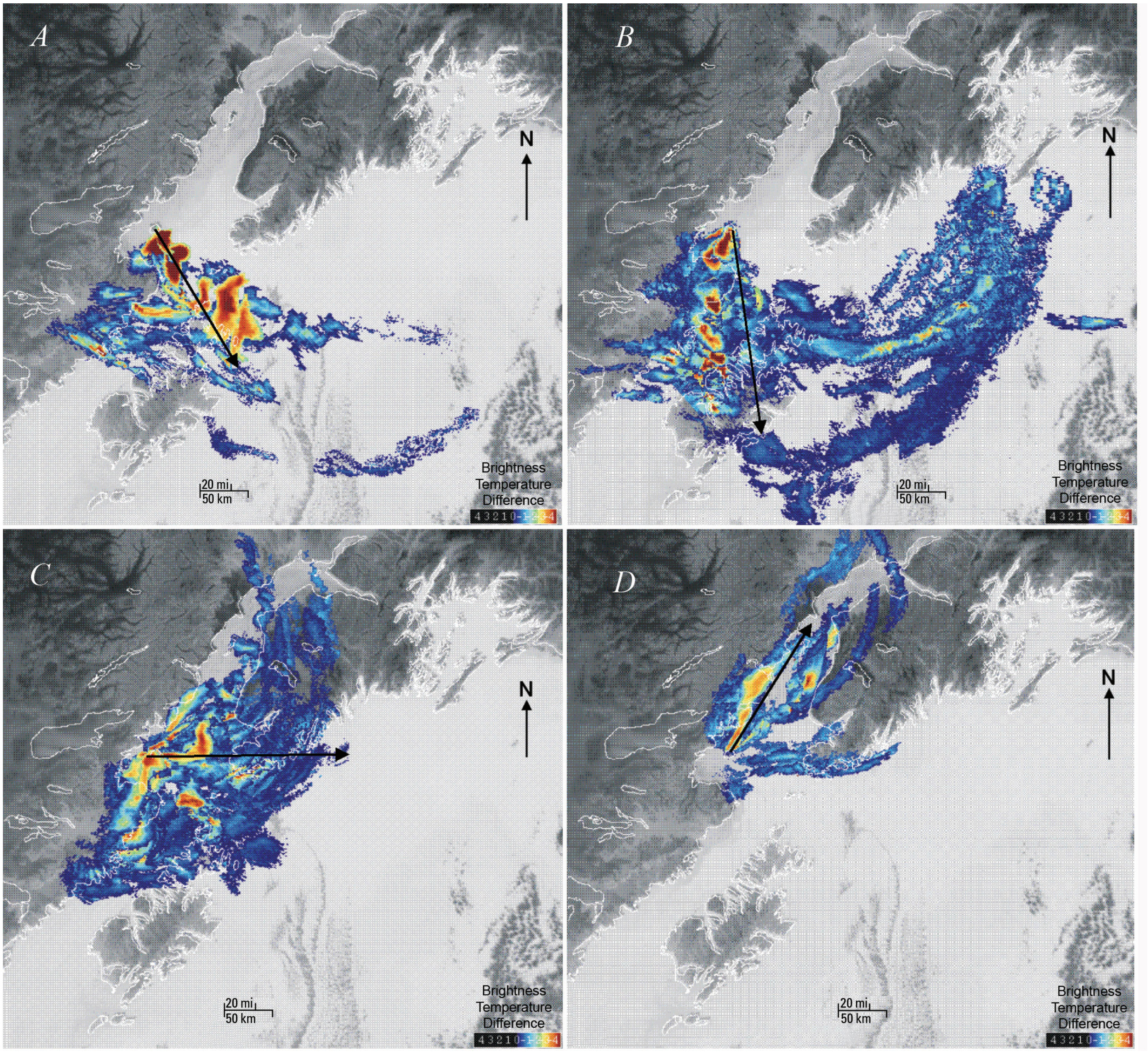

Figure 14 Moderate Resolution Infrared Spectrometer (MODIS) and Advanced Very High Resolution Radiometer data (AVHRR) ash-detection daily composites for (*A*), January 28, (*B*), January 29, (*C*), January 30 and ,(*D*), January 31 2006. Black arrows indicate general direction of ash cloud movement. Adapted from Webley and others (2008). Here, the ash is shown as a negative brightness temperature difference (BTD) signal.

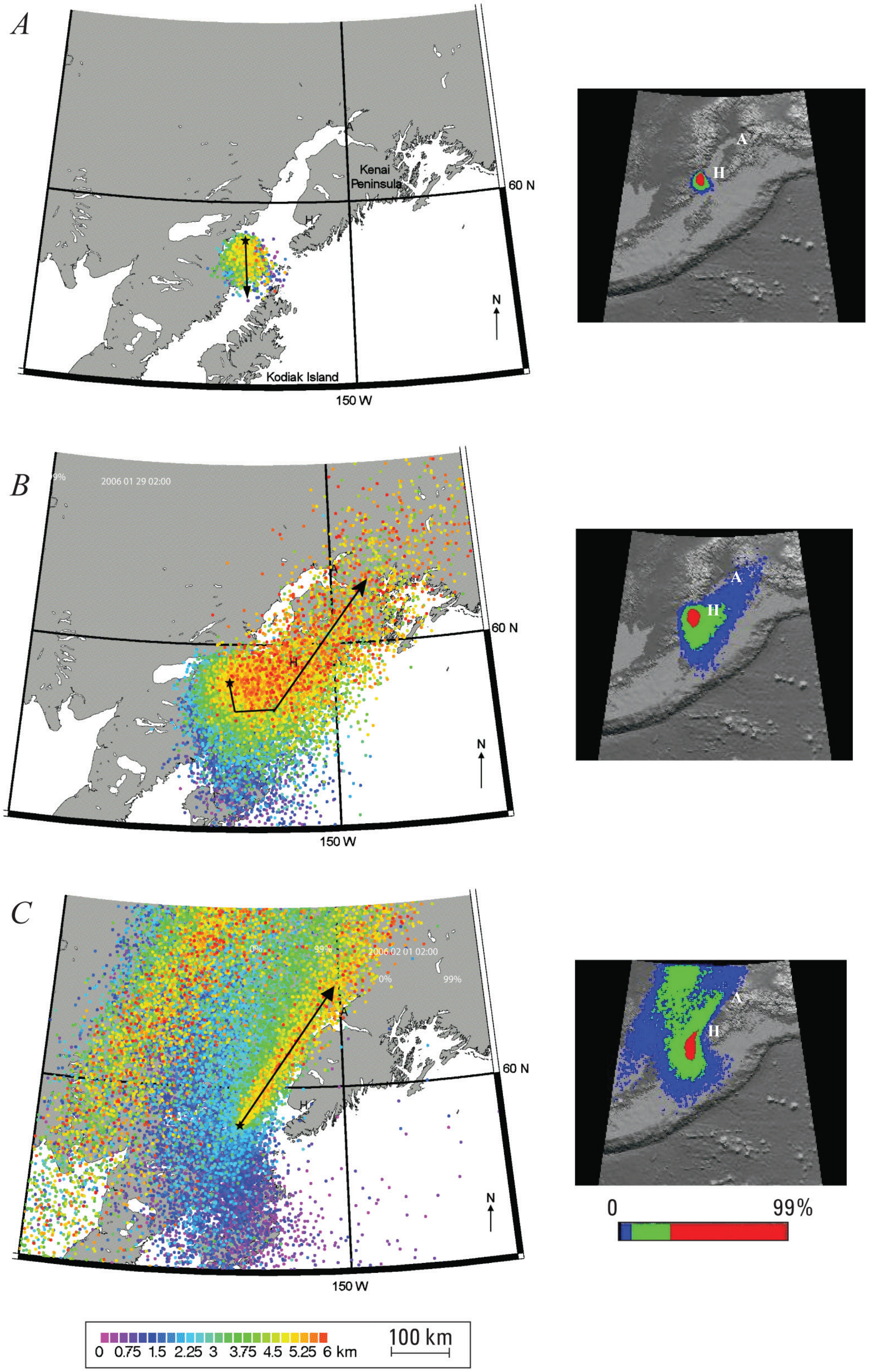

Figure 15. Puff model simulation of ash cloud movement in Cook Inlet during the continuous phase of the 2006 Augustine eruption, adapted from Webley and others (2008). Black arrows show general direction of the ash clouds movement. *A,* January 28 at 1700 AKST (January 29 at 0200 UTC). *B,* January 29 at 1700 AKST (January 30 at 0200 UTC). *C,* January 31 at 1700 AKST (February 1 at 0200 UTC). Date and times in Puff model forecasts are in UTC, and particles are color-coded by elevation. H, Homer; A, Anchorage. Thumbnail shows relative airborne concentration as a percentage of maximum predicted concentration.

Discussion and Conclusions

Volcanic ash clouds are a very real hazard during an eruption, even after the explosive/effusive activity has ended. They can pose a hazard to domestic and international air traffic and affect local communities. Also, they can be tracked over long distances for several days after the end of an eruptive period. The 2006 eruption of Augustine Volcano, Alaska, produced 13 explosive events over a 2-week period, followed by a continuous period of ash emission over several days.

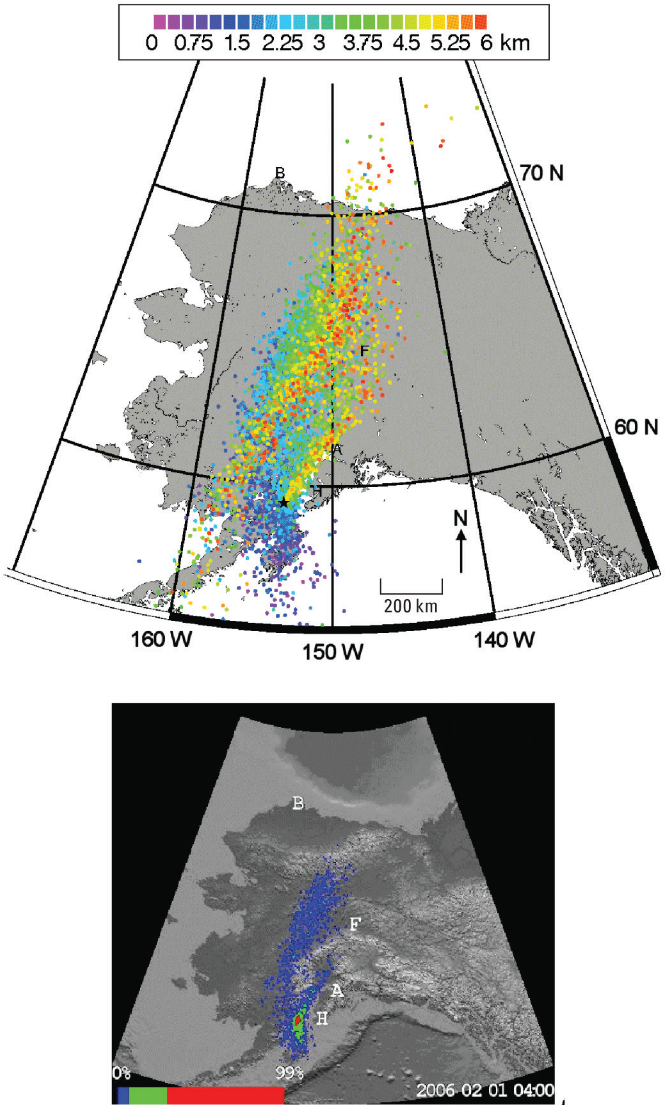

Figure 16. Puff model simulation snapshot on January 31, 2006 at 1900 AKST (February 1, 2006 at 0400 UTC) of ash cloud movement across Alaska mainland that coincided with lidar measurements, from Webley and others (2008). Particles are color-coded by elevation. Black star shows location of Augustine Volcano. H, Homer, A, Anchorage; F, Fairbanks. Lower panel shows relative airborne concentration as a percentage of maximum predicted concentration.

The Puff volcanic ash transport and dispersion model's ability to track multiple volcanic ash clouds was first used for an eruption response during this eruption. Its use was highly successful during the January 13–14 events and compared well with the satellite data (fig. 8). The NWS, with assistance from AVO, produced numerous volcanic ash advisories, and at one point Anchorage airport was affected, as airline flights were cancelled. Predicting the movements of these ash clouds from Augustine was critical to assess the impact they would have on their surroundings. The Puff model was able to provide forecasts of all the ash clouds from the events in table 1. The model's predictions were used during the eruption response by AVO and also the NWS to assess the cloud's movements and the impacts they would have on the aviation community and local residents.

As a result of the enormity of the data obtained during the Augustine eruption, the Google Maps™ application programming interface (API) is now used to display Puff automated predictions for potential eruptions at volcanoes of elevated alert status see Puff Web site (http://puff.images.alaska.edu). Webley and others (2009) provide a detailed description of the automated predictions and the API to all the Puff model predictions for these volcanoes. Virtual Globes are an excellent geographic frame of reference to display model results that can be easily understood. Figure 9 showed how displaying the data in a Virtual Globe provides (1) a better understanding of ash cloud movement and (2) an ability to visualize the data in three dimensions. Additional information, such as satellite and seismic data can be easily added to the Virtual Globe interface.

This paper illustrates the reliability of the Puff model airborne-ash predictions near Augustine Volcano and the distal ash plumes as compared to various other techniques, such as remote-sensing satellite data, aerosol samplers, and the lidar systems. Figure 11 for the January 17 event shows that use of higher spatial resolution wind fields would improve ashfall predictions, especially in a topographically diverse region such as Cook Inlet. Further work on the use of the WRF model for Puff predictions is required, both for airborne ash movement and for ashfall forecasts.

During the 2006 Augustine eruption, a large amount of information was provided by the model predictions. As a result, an improved tool to provide up-to-date analysis and allow quick assessments was required. The new automated predictions, now used by AVO, alleviated the requirement to initiate Puff model runs 24 hours a day, once an eruption was reported. The 5-minute assessment can be made from these automated Puff predictions and then "improved" once more information on the eruption is available. Since the 2006 eruption of Augustine, the Puff model predictions have been used for numerous volcanoes around the world (Webley and others, 2009). They are used by AVO, NWS, AFWA, and KVERT to determine the movement of volcanic eruption clouds in the NOPAC. Further developments for the Puff model will include determining reliable actual airborne volcanic ash cloud concentrations, through model initialization from satellite derived ash retrievals, and to work with the USGS-led eruption source parameters working group (Mastin and others, 2009) to provide improved volcanic ash forecasts by taking account of past eruption history.

Acknowledgments

The authors wish to thank the staff and students in the AVO remote-sensing group for their monitoring of Augustine Volcano and analysis of the remote-sensing satellite data during the eruption response. The authors would like to thank the Arctic Region Supercomputing Center (ARSC) for its support of Webley's and Bailey's postdoctoral fellowships during the eruption crisis. The authors also appreciate the Geophysical Institute at the University of Alaska Fairbanks for their support of the AVO remote-sensing team.

References Cited

Aloisi, M., D'Agostino, M., Dean, K.G., Mostaccio G., and Neri, A., 2002, Satellite analysis and PUFF simulation of the eruptive cloud generated by the Mount Etna paroxysm of 22 July 1998: Journal of Geophysical Research, v. 107, no. B12, doi:10.1029/2001JB000630.

Bailey, J.E., Dean, K.G., Dehn, J., and Webely, P.W., 2010, Integrated satellite observations of the 2006 eruption of Augustine Volcano, *in* Power, J.A., Coombs, M.L., and Freymueller, J.T., eds., The 2006 eruption of Augustine Volcano, Alaska: U.S. Geological Survey Professional Paper 1769 (this volume).

Blong, R.J., 1984, Volcanic hazards: A sourcebook on the effects of eruptions. Sydney. Academic Press, 424 p.

Cahill, C.F., 2003, Asian aerosol transport to Alaska during ACE-Asia: Journal of Geophysical Research, v. 108, no. D23, doi:10.1029/2002JD003271.

Casadevall, T.J., 1993, Volcanic hazards and aviation safety, lessons of the past decade: FAA Aviation Safety Journal, v. 2, p. 1–11.

Casadevall, T.J., and Krohn, D., 1995, Effects of the 1992 Crater Peak eruptions on airports and aviation operations in the United States and Canada: U.S. Geological Survey Bulletin 2139, p. 205–220.

Coombs, M.L., Bull, K.F., Vallance, J.W., Schneider, D.J., Thoms, E.E., Wessels, R.L., and McGimsey, R.G., 2010, Timing, distribution, and volume of proximal products of the 2006 eruption of Augustine Volcano, *in* Power, J.A., Coombs, M.L., and Freymueller, J.T., eds., The 2006 eruption of Augustine Volcano, Alaska: U.S. Geological Survey Professional Paper 1769 (this volume).

Dean, K., Dehn, J. Engle, K., Izbekov, P., Papp, K., and Patrick, M., 2002, Operational Satellite Monitoring of Volcanoes at the Alaska Volcano Observatory: Advances in Environmental Monitoring and Modelling, v. 1, no. 1, p. 3–35.

Draxler, R.R., and Hess, G.D., 1997, Description of the Hysplit-4 modeling system: NOAA Technical Memo ERL ARL-224, 24 p.

Draxler, R.R., and Hess, G.D., 1998, An overview of the Hysplit 4 modeling system for trajectories, dispersion and deposition: Australian Meteorological Magazine, v. 47, p. 295–308.

Hufford, G.L., Salinas, L.J, Simpson, J.J., Barske, E.G., and Pieri, D.C., 2000, Operational Implications of airborne volcanic ash: Bulletin of the American Meteorological Society, v. 81, no. 4, p. 745–755.

Kienle, J., and Shaw, G.E., 1979, Plume Dynamics, thermal energy and long distance transport of Vulcanian eruption clouds from Augustine Volcano, Alaska: Journal of Volcanology and Geothermal Research, v. 6, no.1–2, p. 139–164.

Krotkov, N.A., Torres, O., Seftor, C., Krueger, A.J., Kostinski, A., Rose, W.I., Bluth, G.J.S., Schneider, D. and Schaefer., S.J., 1999, Comparison of TOMS and AVHRR volcanic ash retrievals from the August 1992 eruption of Mt. Spurr: Geophysical Research Letters, v. 26, no. 4, p. 455–458.

Mastin, L.G., Guffanti, M., Servranckx, R., Webley, P.W, Barsotti, S., Dean, K., Denlinger, R., Durant, A., Ewert, J.W., Gardner, C.A., Holliday, C., Neri, A., Rose, W.I., Schneider, D., Siebert, L., Stunder, B., Swanson, G., Tupper, A., Volentik, A., and Waythomas, C.F., 2009, A multidisciplinary effort to assign realistic source parameters to model of volcanic ash-cloud transport and dispersion during eruptions Mastin, Larry, and Webley, Peter, eds., *in* Special Issue on Volcanic Ash Clouds: Journal of Volcanology and Geothermal Research, v. 186, no. 1–2, p. 10–21. doi:10.0116/j.volgeores.2009.01.008.

McNutt, S.R., Tytgat, G., Estes, S.A., and Stihler, S.D., 2010, A parametric study of the January 2006 explosive eruptions of Augustine Volcano, using seismic, infrasonic, and lightning data, *in* Power, J.A., Coombs, M.L., and Freymueller, J.T., eds., The 2006 eruption of Augustine Volcano, Alaska: U.S. Geological Survey Professional Paper 1769 (this volume).

Miller, T.P., and Casadevall, T.J., 2000, Volcanic ash hazards to aviation. In: Sigurdsson, H., ed., Encyclopedia of Volcanoes: San Diego, Academic Press, p. 915–930.

Papp, K.R., Dean, K.G., and Dehn, J., 2005, Predicting regions susceptible to high concentrations of airborne volcanic ash in the North Pacific region: Journal of Volcanology and Geothermal Research. v. 148, p. 295–314.

Paskievitch, J., Read, C., and Parker, T., 2010, Remote telemetered and time-lapse cameras at Augustine Volcano, *in* Power, J.A., Coombs, M.L., and Freymueller, J.T., eds., The 2006 eruption of Augustine Volcano, Alaska: U.S. Geological Survey Professional Paper 1769 (this volume).

Peterson, R., Webley, P.W., D'Amours, R., Servranckx, R., Stunder, R., and Papp, K., 2010, Volcanic ash transport and dispersion models, *in* Dean, K.G., and Dehn, J., eds., Monitoring volcanoes in the North Pacific—observations from space: Springer Praxis, London.

Power, J.A., Nye, C.J., Coombs, M.L., Wessels, R.L., Cervelli, P.F., Dehn, J., Wallace, K.L., Freymueller, J.T., and Doukas, M.P., 2006, The reawakening of Alaska's Augustine Volcano: Eos (American Geophysical Union Transactions), v. 87, no. 37, p. 373–377.

Prata, A.J., 1989a, Infrared radiative transfer calculations for volcanic ash clouds: Geophysical Research Letters, v. 16, p. 1293–1296.

Prata, A.J., 1989b, Observations of volcanic ash clouds in the 10-12 µm window using AVHRR/2 data: International Journal of Remote Sensing, v. 10, p. 751–761.

Prata, F., Bluth, G., Rose, W., Schneider, D., and Tupper, A., 2001, Comments on "Failures in detecting volcanic ash from a satellite-based technique": Remote Sensing of Environment, v. 78, p. 341–346.

Pudykiewicz, J., 1988, Numerical simulation of the transport of radioactive cloud from the Chernobyl nuclear accident: Tellus, v. 40B, p. 241–259.

Pudykiewicz, J., 1989, Simulation of the Chernobyl dispersion with a 3-D hemispheric tracer model: Tellus, v. 41B, p. 391–412.

Rose, W.I., Delene, D.J., Schneider, D.J., Bluth, G.J.S., Krueger, A.J., Sprod, I., McKee, C., Davies, H. L., and Ernst, G.G.J., 1995, Ice in the 1994 Rabaul eruption cloud; implications for volcano hazard and atmospheric effects: Nature, v. 375, p. 477–479.

Sassen, K., Zhu, J., Webley, P.W., Dean, K., and Cobb, P., 2007, Volcanic ash plume identification using polarization lidar; Augustine eruption, Alaska: Geophysical Research Letters. v. 34, no. 8, doi: 10.1029/2006GL027237.

Searcy, C., Dean, K.G., and Stringer, W., 1998, PUFF; A volcanic ash tracking and prediction model: Journal of Volcanology and Geothermal Research, v. 80, p. 1–16.

Simpson, J.J., Hufford, G., Pieri, D., and Berg, J., 2000, Failures in detecting volcanic ash from satellite based technique: Remote Sensing of Environment. v. 72, p. 191–217.

Simpson, J.J., Hufford, G., Pieri, D., and Berg, J., 2001, Response to Comments on "Failures in detecting volcanic ash from satellite based technique": Remote Sensing of Environment, v. 78, p. 347–357.

Sparks, R.S.J., Bursik, M.I., Carey, S. N., Gilbert, J.E., Glaze, L., Sigurdsson, H. and Woods, A. W., 1997, Volcanic Plumes: Chichester, Wiley, 589 p.

Tanaka, H.L., 1994, Development of a prediction scheme for volcanic ash fall from Redoubt Volcano, Alaska *in* Proceedings of the First International Symposium on Volcanic Ash and Aviation Safety: U.S. Geological Survey Bulletin, 2047, p. 283–291.

Wallace, K.L, Neal, C.A., and McGimsey, R.G., 2010, Timing, distribution, and character of tephra fall from the 2005–2006 eruption of Augustine Volcano, Alaska, *in* Power, J.A., Coombs, M.L., and Freymueller, J.T., eds., The 2006 eruption of Augustine Volcano, Alaska: U.S. Geological Survey Professional Paper 1769 (this volume).

Waythomas, C.F., Dorava, J. M., Miller, T. P., Neal, C. A., and McGimsey, R. G., 1998, Preliminary volcano-hazard assessment for Redoubt Volcano, Alaska: U.S. Geological Survey Open-File Report OF 98-0857, 40 p.

Webley, P.W., Dean, K., Collins, R., Fochesatto, J., Sassen, K., Atkinson, D., Cahill, C., and Prata, A., 2008, Predicting and validating the tracking of a volcanic ash cloud during the 2006 eruption of Mt. Augustine Volcano: Bulletin of American Meteorological Society. v. 89, no. 11, p. 1647–1658 doi: 10.1175/2008BAMS2579.1.

Webley, P.W., Dean, K., Bailey, J.E., Dehn, J., and Peterson, R., 2009, Volcanic ash modeling for North Pacific volcanoes automated operational monitoring and virtual globes, *in* Aviation Hazards from Volcanoes: Natural Hazards, special issue v. 51, no. 2, p. 345–361 doi:10.1007/s11069-008-9246-2.

Wen, S., and Rose, W.I., 1994, Retrieval of sizes and total masses of particles in volcanic clouds using AVHRR bands 4 and 5: Journal of Geophysical Research, v. 99, p. 542–5431.

The 2006 Eruption of Augustine Volcano, Alaska
Power, J.A., Coombs, M.L., and Freymueller, J.T., editors
U.S. Geological Survey Professional Paper 1769

Chapter 22

High-Resolution Satellite and Airborne Thermal Infrared Imaging of the 2006 Eruption of Augustine Volcano

By Rick L. Wessels[1], Michelle L. Coombs[1], David J. Schneider[1], Jonathan Dehn[2], and Michael S. Ramsey[3]

Abstract

Thermal infrared (TIR) images provided a timely pre- and syn-eruption record of summit changes, lava flow emplacement, and pyroclastic-flow-deposit distribution during the Alaska Volcano Observatory's (AVO) response to the 2006 eruption of Augustine Volcano. A series of images from both handheld and helicopter mounted forward looking infrared radiometers (FLIR) captured detailed views during a series of 13 overflights from December 2005 through August 2006. In conjunction with these images, data from the Advanced Spaceborne Thermal Emission and Reflection Radiometer (ASTER) provided frequent multispectral synoptic views of the eruption's emissions and deposits. The ASTER Urgent Request Protocol system also facilitated more frequent scheduling and faster data availability during the eruption. Airborne and satellite imaging provided 20 different days of TIR coverage over the 5-month eruptive period, with 4 of those days covered by both FLIR and ASTER. The high-resolution TIR images documented gradual pre-eruption heating of the summit, emplacement of pyroclastic-flow deposits, rapid temperature increase as the lava dome and flows formed, and slow cooling of the volcanic deposits that followed. The high-resolution data uniquely documented segmentation of the lava flows into hot areas of increased flow deformation and cooler, more stable crust on the active flows. In contrast, the satellite TIR data provided synoptic views of the areal distribution of volcanic products at Augustine including the extent and composition of the plumes.

Introduction

Thermal infrared (TIR) imaging of active volcanoes has increasingly become an important tool for monitoring and documenting dynamic volcanic processes. The Alaska Volcano Observatory (AVO) routinely monitors all volcanoes in the North Pacific using low-spatial-resolution (kilometer scale), high-temporal-resolution (multiple images per day) TIR data from the Advanced Very High Resolution Radiometer (AVHRR), Moderate Resolution Image Spectrometer (MODIS), and Geostationary Operational Environmental Satellites (GOES) (Harris and others, 1997; Dehn and others, 2002; Wright and others, 2002; see Bailey and others, this volume). Whereas these data work well for detecting gross thermal changes and large ash plumes that precede and accompany eruptions, higher-spatial-resolution data are commonly required to detect lower temperatures and the subtle changes that are common during ongoing volcanic phenomena (fig. 1). Satellite sensors, such as the Advanced Spaceborne Thermal Emission and Reflection Radiometer (ASTER) and the Thematic Mapper (TM)/Enhanced Thematic Mapper (ETM+) on Landsats 5 and 7, respectively, provide high-spatial-resolution (tens of meters), low-temporal-resolution (days to weeks) TIR data (Flynn and others, 2001; Ramsey and Dehn, 2004; Vaughan and Hook, 2006; Carter and others, 2008). Airborne or ground-based TIR imaging radiometers provide a very high spatial resolution (centimeters to meters) with a variable temporal resolution depending on the study (Harris and others, 2005; Ball and Pinkerton, 2006). High-resolution TIR images can document precursory changes in existing thermal features, such as fumaroles or hot springs, as well as track structural changes indicated by the formation of new fumaroles, hot fractures, and (or) the melting of snow and ice (Schneider and others, 2000; Andronico and others, 2005). Both satellite and airborne TIR images can also be used to effectively observe eruption plumes (see Bailey and others, this volume), to document lava dome and flow dynamics and effusion rates (Ramsey and Dehn, 2004; Harris and others, 2005), and to document pyroclastic flow emplacement (Carter and others, 2007).

---

[1] Alaska Volcano Observatory, U.S. Geological Survey, 4200 University Drive, Anchorage, AK 99508.

[2] Alaska Volcano Observatory, Geophysical Institute, University of Alaska Fairbanks, P.O. Box 755905, Fairbanks, AK 99775.

[3] Department of Geology and Planetary Science, University of Pittsburg, Pittsburg, PA 15260.

After more than 10 months of increasing seismicity, deformation, gas emission, and heat flow, Augustine Volcano, Alaska (fig. 1), explosively erupted on January 11, 2006. The volcano produced a total of 13 explosions during the last 3 weeks of January 2006. A new summit lava dome and two short, blocky lava flows were emplaced from February to March. A series of 13 forward looking infrared radiometer (FLIR) over-flights and 7 daytime and 15 nighttime Advanced Spaceborne Thermal Emission and Reflection Radiometer (ASTER) scenes were acquired in response to this activity. The FLIR and ASTER data provided several significant observations as part of a much larger suite of real-time or near-real-time data from other satellite (AVHRR, MODIS), airborne (visual, gas), and ground-based (seismometers, global positioning system [GPS], radiometers) sensors used at AVO (see Bailey and others, this volume; Cervelli and others, this volume, Coombs and others, this volume; McGee and others, this volume; Power and Lalla, this volume).

In this chapter, we summarize airborne FLIR observations acquired between December 2005 and August 2006 and the longer record of spaceborne ASTER observations acquired between December 2000 and May 2006. The high-resolution FLIR data document the gradual pre-eruption heating of the summit, the formation of pyroclastic-flow deposits, the rapid increase in temperature as the lava dome and flows formed, and the slow cooling of volcanic deposits after the eruption. In addition to these observations of the eruption, the ASTER data provide a baseline from which to examine temperature trends over several years leading up to and during the most recent volcanic unrest.

Instrumentation and Methodology

FLIR Surveys and Data Processing

The primary airborne imaging system used in this study consists of a FLIR Systems ThermaCAM PM595 infrared camera and a Sony EVI-370 NTSC video camera housed in a helicopter-mounted four-axis gyrostabilized gimbal (see Schneider and others, 2008, for system details). A handheld version of the PM595 camera was used for repeat ground-based time-lapse imaging. The infrared camera utilizes a 320×240 microbolometer detector array, which is sensitive from 7.5–13 µm, converting TIR emitted radiance into brightness temperature. The gimbal-mounted system has an integrated 12º lens with a horizontal field of view of 210 m and a pixel resolution of 65 cm at a distance of 1 km; the handheld system has an integrated 24º lens with a horizontal field of view of 420 m and a pixel resolution of 1.3 m at a distance of 1 km. The observation distance of each survey ranged from 0.5 to 5 km, averaging about 1.2 km. The measured FLIR brightness temperature is captured by using one of three ranges, −40 to 120ºC, 80 to 500ºC, and 350 to 1,500ºC. In the low

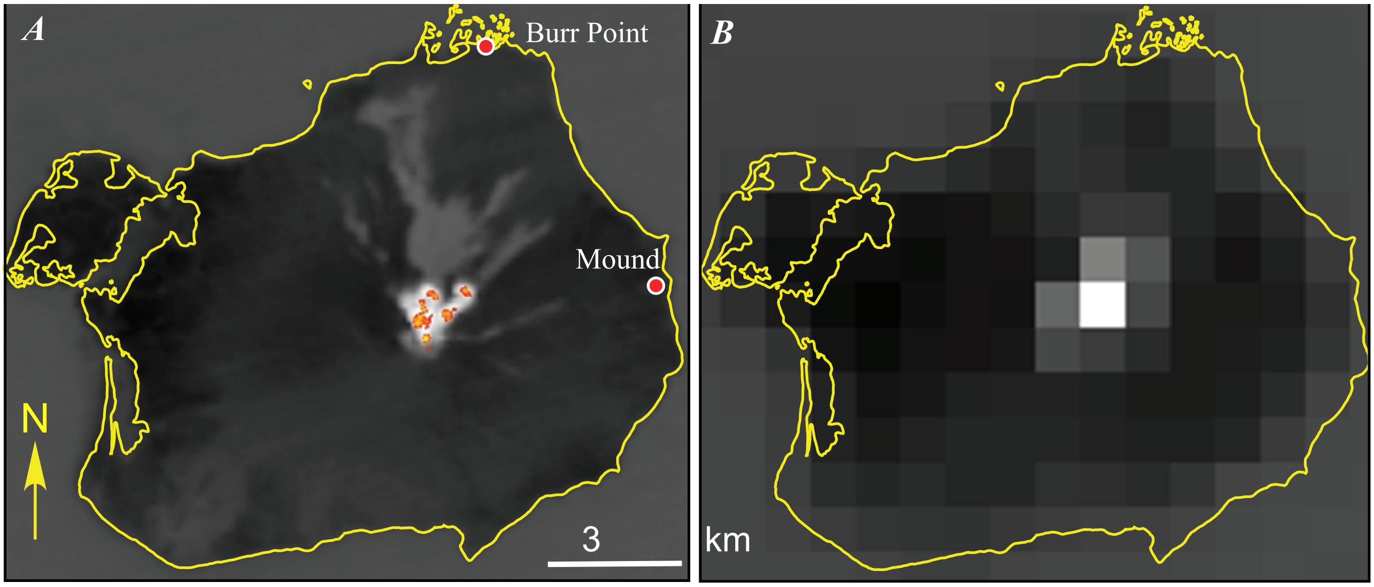

Figure 1. Nighttime 8.3-µm thermal infrared (TIR) images of Augustine Volcano acquired at 2245 AKST March 13, 2006, from the Terra spacecraft, oriented with north up. *A*, Advanced Spaceborne Thermal Emission and Reflection Radiometer (ASTER). *B*, Moderate Resolution Imaging Spectroradiometer (MODIS). Both MODIS and the Advanced Very High Resolution Radiometer (AVHRR) have ~1-km spatial resolution, which provides high-temporal-resolution views of North Pacific volcanic activity; however, these datasets lack sufficient spatial detail to capture persistent, low-level thermal features, smaller-scale activity, and eruptive deposits, are captured by ASTER TIR (90 m) and shortwave infrared (SWIR) (30 m) images.

range, the camera can record a maximum temperature of about 270ºC, but these measurements can be much less accurate because they fall outside the calibrated range. Because the temperatures measured at Augustine range from cool (ambient) to very hot (fumaroles/lava), no single PM595 gain setting covers the full range of possible temperatures, and so surveys were typically collected in at least the lower two dynamic ranges. For the FLIR temperatures reported here (see figs. 2, 5–12, 14–16), the color bar represents a linear scaling of most of the data, not the full temperature range; the lowest temperatures are clipped to black, and the highest are clipped to white.

Both the internal FLIR camera firmware (ThermaCAM PM595 Operator's Manual, 1999) and the FLIR desktop ThermaCAM Researcher software (ThermaCAM Researcher User's Manual, 2004) can convert the detected radiance to temperature-at-surface by making a first-order correction for atmospheric absorption and emission. The distance to target, ambient air temperature, relative humidity, and broadband emissivity of the surface must be inputted. Air temperature and humidity were measured onsite during each overflight. The distance to target was calculated from the difference between the time-synced GPS helicopter position and the estimated position of the feature being imaged. FLIR data were acquired during helicopter flights by several different flight crews as weather and volcanic activity permitted. For each flight, the track was recorded by using a hand-held GPS unit. The GPS tracking data provided the location and altitude at the time of the data collection, which allowed the distance to target to be calculated. The first flights conducted a general survey of the volcanic edifice and then focused on thermal changes at the summit. As the eruption progressed, later flights surveyed the fresh pyroclastic flow deposits and lava flows. Oblique aerial photographs and videos were acquired simultaneously for comparison with the TIR images. Although dates and times for geophysical data are typically recorded in UTC, we use Alaska standard time (AKST) (UTC+9) hours throughout this chapter (unless noted) to match other chapters in this volume. Alaska daylight time, which was in effect after March 21, is 1 hour later than AKST.

Satellite Data Acquisition and Processing

Visible and infrared satellite imaging of volcanoes needs to be frequent to record rapid changes in activity and to compensate for the obscuration by any heavy/recurring cloud cover. The primary high-resolution satellite-based TIR data used for this work were recorded by ASTER, which was launched in December 1999 onboard the Terra satellite. ASTER measures the top of atmosphere radiance in 14 spectral channels (Yamaguchi and others, 1998) that are collected by three subsystems, each at a different spatial resolution: the visible and near infrared (VNIR) sensor with three channels (0.56–0.81 µm) at 15-m spatial resolution, the shortwave infrared (SWIR) sensor with six channels (1.65–2.4 µm) at 30-m spatial resolution, and the TIR sensor with five channels (8.2–11.3 µm) at 90-m spatial resolution. ASTER TIR data saturate if the detected radiance exceeds a value that corresponds to a pixel-integrated brightness temperature of ~97°C. In these datasets, the at-sensor radiance from the higher-resolution SWIR channels was used to extract pixel-integrated brightness temperatures >100°C. We note that since January 2009, data from the SWIR sensor are no longer usable, owing to a failed cryocooler; however, the five TIR channels were used to extract most of the ASTER-derived temperatures presented in this chapter. Hot areas on active lava flows are typically smaller than the area covered by 90-m TIR pixels. As a result, the radiance measured is an area-weighted sum of the multiple-subpixel radiating components (Wright and Flynn, 2003). Depending on the magnitude difference of the measured temperatures, this averaging can produce a large underestimation or overestimation of the actual derived temperatures and errors in the surface emissivity (Rose and Ramsey, 2009). Therefore, the temperatures derived from mixed radiance data are commonly denoted as pixel-integrated temperatures.

The ASTER TIR data analyzed in this chapter are derived from the calibrated, at-sensor radiance. These data must first be corrected for atmospheric absorption/emission by using a standard atmospheric model with specific corrections for the image location and the time of year of acquisition (Thome and others, 1998). To then extract the pixel-integrated brightness temperatures from the atmospherically-corrected radiance, the downwelling sky radiance reflected off the surface must be removed, and the surface temperature separated from the emissivity in each pixel. These steps are applied in the temperature-emissivity separation (TES) standard data processing (Gillespie and others, 1998). The Level-2 Surface Kinetic Temperature product data distributed by the National Aeronautics and Space Administration (NASA) Land Processes Distributed Active Archive Center (LP DAAC) are presented here.

Observations and Results

Frequent FLIR missions before and during the 2006 eruption of Augustine Volcano provided detailed views of summit thermal features and fresh volcanic deposits (table 1). In this section we describe the key observations from FLIR TIR images acquired over 13 different overflights, as well as from ASTER data acquired before and during the eruption. A time series of FLIR images viewed from the same point north of the volcano show some of the changes to the volcanic edifice from January 9 to March 15, 2006 (fig. 2). For example, the January 9 images (figs. 2*A*, 2*B*) show the pre-eruption melting of the summit snow cover and warm air above caused by rising steam, and the February 24, images (figs. 2*C*, 2*D*) show the initial stages of the new summit lava dome and the north lava flow. These images also detect pyroclastic-flow deposits (unit Cpf, fig. 2) from late January, which are still warm. The March 10 (figs. 2*E*, 2*F*) and March 15 (figs. 2*G*, 2*H*) images detect a much larger lava dome and clear progression of the two lava flows.

Table 1. Summary of FLIR data for Augustine Volcano acquired 2005–2006.

Date	Time (AKST)[1]	FLIR: Tmax (°C)[2]	FLIR: Tbg (°C)[3]	FLIR: Tavg (°C)[4]	Observations (after Coombs and others, this volume)	Observation quality
December 22, 2005	1509	210	−3	5	Snow-covered summit and flanks; no flowage deposits; some increased heat flow and fumarole activity at summit	Summit partially obscured by steam
January 4, 2006	AM+PM	380	−5	0	Snow-covered flanks; no flowage deposits; maximum summit temperature at fumarole; overall heating of summit region	Summit partially obscured by steam
January 12, 2006	1204	121	−5	3	Ash from Events 1 and 2 on north flank; new vent visible through 1986 dome, just south of 1986 spine	Summit partially obscured by steam and ash plume
January 24, 2006	1229	140	−15	10	Fresh snow on summit and flanks, light ash on SE flank; dark, hot, steaming, levied flows on E, NE, and N flanks; ExD1 visible on east part of summit, Tmax 140°C	Summit mostly obscured by lenticular cloud
February 8, 2006	1149	120	−1	11	Dark Cpf and RPpf flows on north flank in high contrast to fresh white snow, range from 10−25°C with some bigger, hotter blocks.	Summit mostly obscured by lenticular cloud
February 20, 2006	AM+PM	277	0	40	Good views of Cpf, RPpf; EfLf dome and north flow visible especially in FLIR images	Summit mostly obscured by low cloud deck
February 24, 2006	1519	277	−13	38	Excellent views of summit, including north lava flow	Summit partially obscured by steam
March 10, 2006	AM+PM	700	−10	66	Clear views of both NE and N lava flows; active block-and-ash flows down East Chute and from front of NE lava flow	Summit partially obscured by light steam and ash
March 15, 2006	0953	335	−5	47	Both north and NE lava flows thickened and lengthened compared to March 10; rockfall activity and ash emission diminished	Summit partially obscured by steam
March 26, 2006	AM+PM	221	−2	16	No major changes from last observation; lava-flow fronts still hot, no significant temperature changes	Summit partially obscured by steam and clouds
April 6, 2006	AM+PM	652	−1	8	Lava-flow fronts cooler, flow tops similar as compared to previous surveys; lava-flow dimensions unchanged; Summit vent atop dome very hot (650°C)	Fresh snow has covered many deposits
May 13, 2006	0956	432	4	14	North-south linear trend of fumaroles and mineralization at summit; images of all flowage deposits; summit vent cooled to 432°C	Very clear summit views; rock sampling
August 7, 2006	1030	377	12	15	North-south linear trend of fumaroles and mineralization at summit; summit vent cooled to 377°C	Very clear summit views; rock sampling

[1] Overflight and field work typically span one-plus hours and are generally midday;

[2] (Tmax) maximum pixel-integrated temperature (a value of 277 indicates FLIR gain setting was saturated);

[3] (Tbg) FLIR-derived background temperature;

[4] (Tavg) average surface temperature of of warm ground or active lava areas.

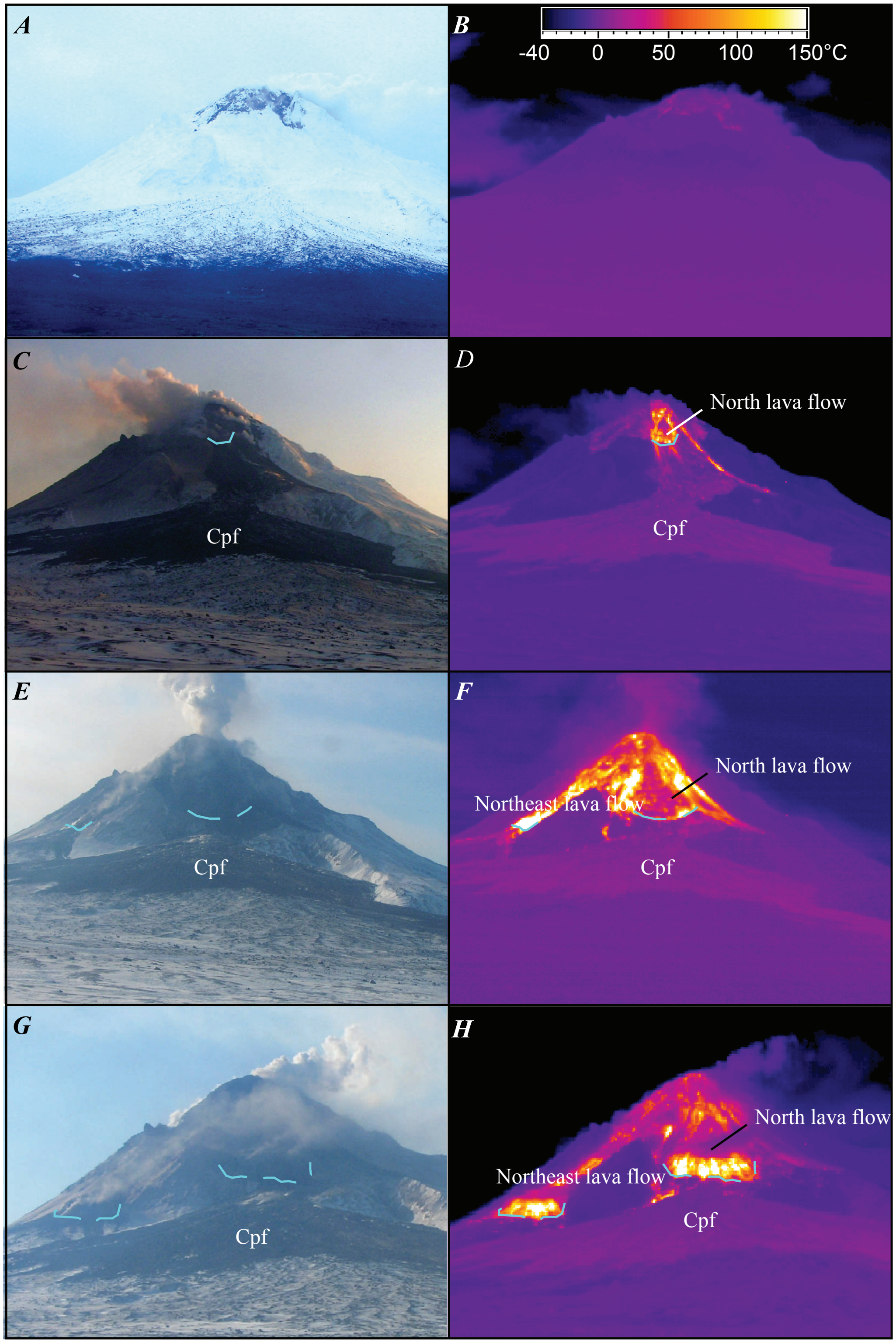

Figure 2. Photographs and Forward Looking Infrared Radiometer (FLIR) thermal infrared (TIR) images documenting growing thermal areas and new lava flows on Augustine Volcano. *A,B*, January 4, 2006. *C,D*, February 24, 2006. *E,F*, March 10, 2006. *G,H*, March 15, 2006. Images were acquired from Burr Point, which is on the coast 4.5 km north of summit (see fig. 1*A*). View southward. Cyan dashed lines denote approximate terminus of lava. Cpf pyroclastic-flow deposit.

Table 2. Summary of Advanced Spaceborne Thermal Emission and Reflection Radiometer (ASTER) data for Augustine Volcano acquired 2005–2006.

Date	Time (AKST)	Day/night[1]	SWIR-Tmax (°C)[2]	TIR-Tmax (°C)[2]	TIR: Tbg (°C)[3]	TIR: Tavg (°C)[4]	Observations (after Coombs and others, this volume)	Scene quality
December 20, 2005	12:37:00	day	NA	−8.8	−13	−9.5	Summit area warmed above background, snow-free areas	Thin clouds, but can see island.
January 12, 2006	12:42:44	day	NA	NA	NA	NA	Plume extending south from summit	Summit obscured by volcanic plume and thin clouds
January 24, 2006	22:44:25	night	95	3	−18	−4	TIR and SWIR thermal features at summit. Weaker TIR features on flanks	Mostly clear
January 31, 2006	22:50:44	night	408	98	−18	25.4	RPpf and smaller NW flank Cpfs visible; surface to east of RPpf obscured by plume	Summit and NE flank obscured by gas and ash plume
February 22, 2006	12:37:03	day		98	−13	25.8	Good views of new dome and pf deposits	
March 13, 2006	22:45:18	night	463.9	98	−7	63	Extents of two lava flows and hottest areas within them match up well with low-light camera images from the same night	Mostly clear
April 5, 2006	22:51:30	night	239.5	13	−11	−3.5	Summit and deposits warm, small SWIR anomaly still at summit	Mostly clear
April 27, 2006	12:37:30	day	NA	NA	NA	NA	Dark lava and pf flows on summit and north flank in high contrast to fresh white snow	Partly cloudy with high cirrus over east part of island
May 17, 2006	22:45:16	night	194.5	20	−3	5.7	Summit and pf deposits still warm, but no active lava	Clear view
May 29, 2006	12:37:25	day	NA	36.7	17	19	Summit and pf deposits still warm	Clear image
October 15, 2006	22:51:16	night	174.7	8.4	−5	1.2	Average flow temps cooler, though summit fumarole still hot	Clear image

[1] Day images have VNIR, SWIR, and TIR data, night images have on SWIR and TIR;

[2] (Tmax) maximum pixel-integrated temperature from SWIR and TIR;

[3] (Tbg) TIR-derived background temperature;

[4] (Tavg) average surface temperature of 2006 lava areas.

In addition to routine data acquisition by ASTER, the ASTER Urgent Request Protocol (URP) system (Ramsey and others, 2004) greatly improved the number of scheduled data acquisitions. A total of 25 ASTER scenes were acquired between October 30, 2005, and May 30, 2006 most during the height of activity from late January to mid-March. The volcano was clear to partly cloudy in 13 scenes, 10 of which were adequate for extracting TIR temperatures (fig. 3; table 2). During the 5 years preceding the 2006 eruption, ASTER averaged about one scene per month over the volcano.

Precursory Phase

Beginning in April 2005, an increase in the number of earthquakes below Augustine Volcano was detected by the on-island seismic network operated by AVO (see Jacobs and McNutt, this volume; Power and Lalla, this volume) and shallow inflation beneath the summit was first detected in June 2006 (Cervelli and others, 2006). By November 2005, summit GPS stations detected that this inflation had rapidly increased (Cervelli and others, 2006). In December 2005 and early

January 2006, increased seismicity and SO_2 output, as well as phreatic explosions, all suggested that volcanic unrest was intensifying (Power and others, 2006).

Of the 18 ASTER images acquired during 2005, a daytime image from December 20 (fig. 4) was the only partly clear TIR view of Augustine before the 2006 eruption. Thin cirrus-cloud cover prevented accurate TIR temperature retrievals from either the SWIR or TIR data. However, these data show a broad area of slightly elevated TIR radiance (fig. 4*C*), which corresponds to snow-free areas and fumaroles at the summit (figs. 3*A*, 4*A*). The two bright linear features visible in the SWIR image (fig. 4*B*) may represent the warmer, snow-free areas or fumarole plumes visible in the VNIR image (fig. 4*A*).

The first FLIR reconnaissance mission, which was conducted on December 22, 2005 (fig. 5), was the first of two flights during the precursory phase of the eruption. Several linear zones of warm bare rock were detected and active steaming was seen from several new fumaroles at the summit (figs. 5*A*, 5*B*). One warm (10ºC above background), snow-free area formed over a preexisting checkerboard pattern on the east side of the summit (figs. 5*C*, 5*D*). The maximum FLIR-derived temperature of a fumarole along the northeast edge of the 1986 dome was 80ºC, with a background temperature of −5ºC (figs. 5*E*, 5*F*). Fumaroles along the 1964 scarp ranged from 60 to 80ºC, and a vigorously jetting fumarole (informally referred to as Teapot) on the south flank below the summit at about 1,150-m elevation had a maximum temperature exceeding 210ºC (figs. 5*G*, 5*H*).

Photographs and FLIR images from January 4, 2006, show that the snow-free and steaming areas had expanded westward and covered more of the summit (figs. 6*A*, 6*B*). FLIR-derived pixel-integrated brightness temperatures of the snow-free areas ranged from 20 to 50ºC. The temperature of the fumarole along the northeast edge of the 1986 dome had increased to at least 380ºC, although thermal emission was likely attenuated somewhat by persistent steam (figs. 6*C*, 6*D*). The fumarole emissions had a yellow-green tint in the visible wavelengths, most likely due to reaction of SO_2 and H_2S to form native sulfur. Teapot was no longer jetting, and maximum temperatures had decreased significantly to 45ºC (figs. 6*E*, 6*F*).

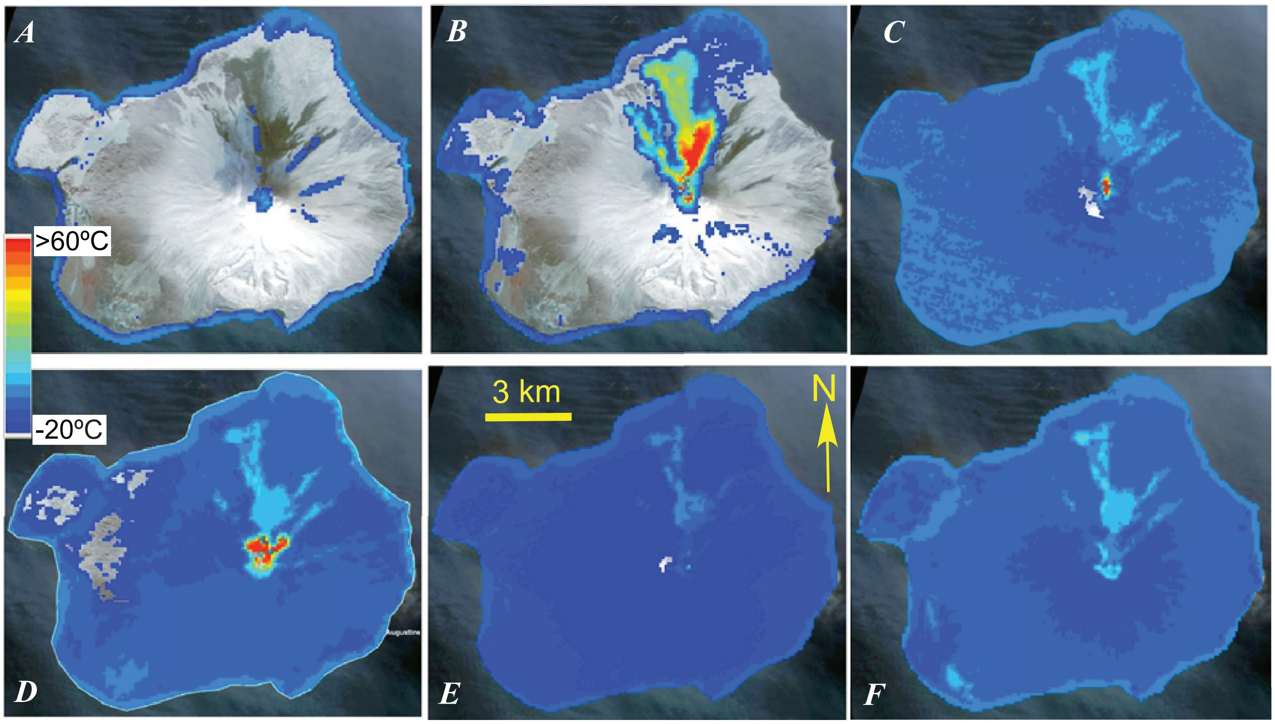

Figure 3. Advanced Spaceborne Thermal Emission and Reflection Radiometer (ASTER) pixel-integrated thermal infrared (TIR) temperatures higher than –20ºC on Augustine Volcano acquired between January 24 and May 6, 2006, showing the progression from heating of summit, through emplacement of initial pyroclastic-flow deposits after explosions in late January and early February, to effusion of first lava dome and subsequent flows as well as the gradual cooling of these volcanic deposits over time. *A*, 22:44:25 AKST January 24, 2006. *B*, 22:50:44 AKST January 31, 2006. *C*, 12:37:03 AKST February 22, 2006. *D*, 22:45:18 AKST March 13, 2006. *E*, 22:51:30 AKST April 5, 2006. F, 22:45:16 AKST May 17, 2006. Temperature data overlain on February 22, 2006, daytime ASTER visible and near-infrared (VNIR) image are visible in some images where temperatures below –20ºC were masked. North is at top of each image.

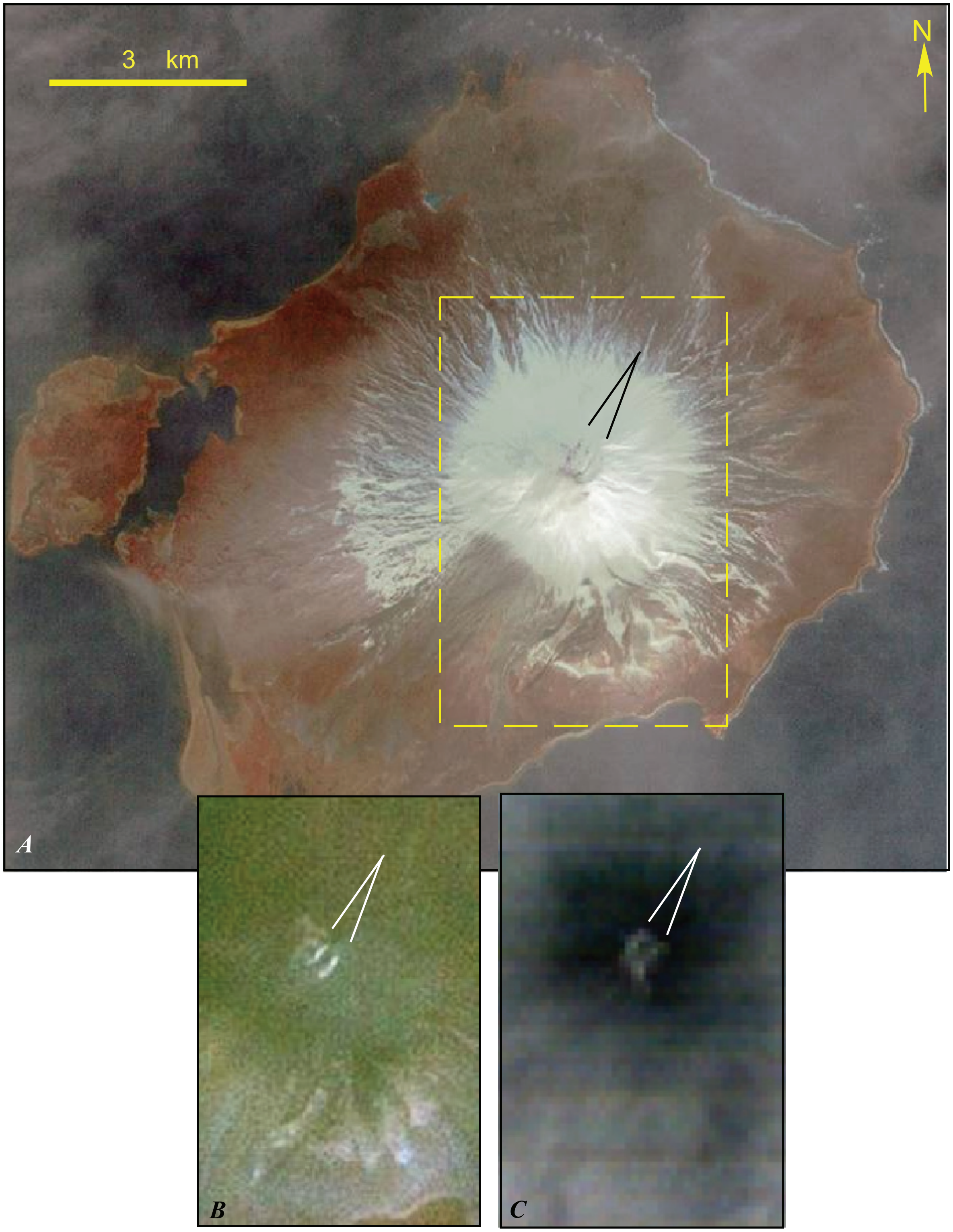

Figure 4. Partly cloudy Advanced Spaceborne Thermal Emission and Reflection Radiometer (ASTER) daytime data of Augustine Island acquired at 1235 AKST on December 20, 2005, which was only ASTER image acquired during precursory phase in late 2005 that was not completely obscured by clouds. *A*, 15 m visible and near-infrared (VNIR) image with channels 3,2,1 in R,G,B, respectively, showing the linear snow-free areas. Dashed yellow rectangle shows location of image subsets in *B* and *C*. *B*, Shortwave infrared (SWIR) image showing bright features trending same direction, likely from solar reflection off steam emanating from new fractures. *C*, Though partially obscured by thin clouds, thermal infrared (TIR) image showing elevated temperatures at the summit relative to summit temperatures in previous ASTER TIR winter observations.

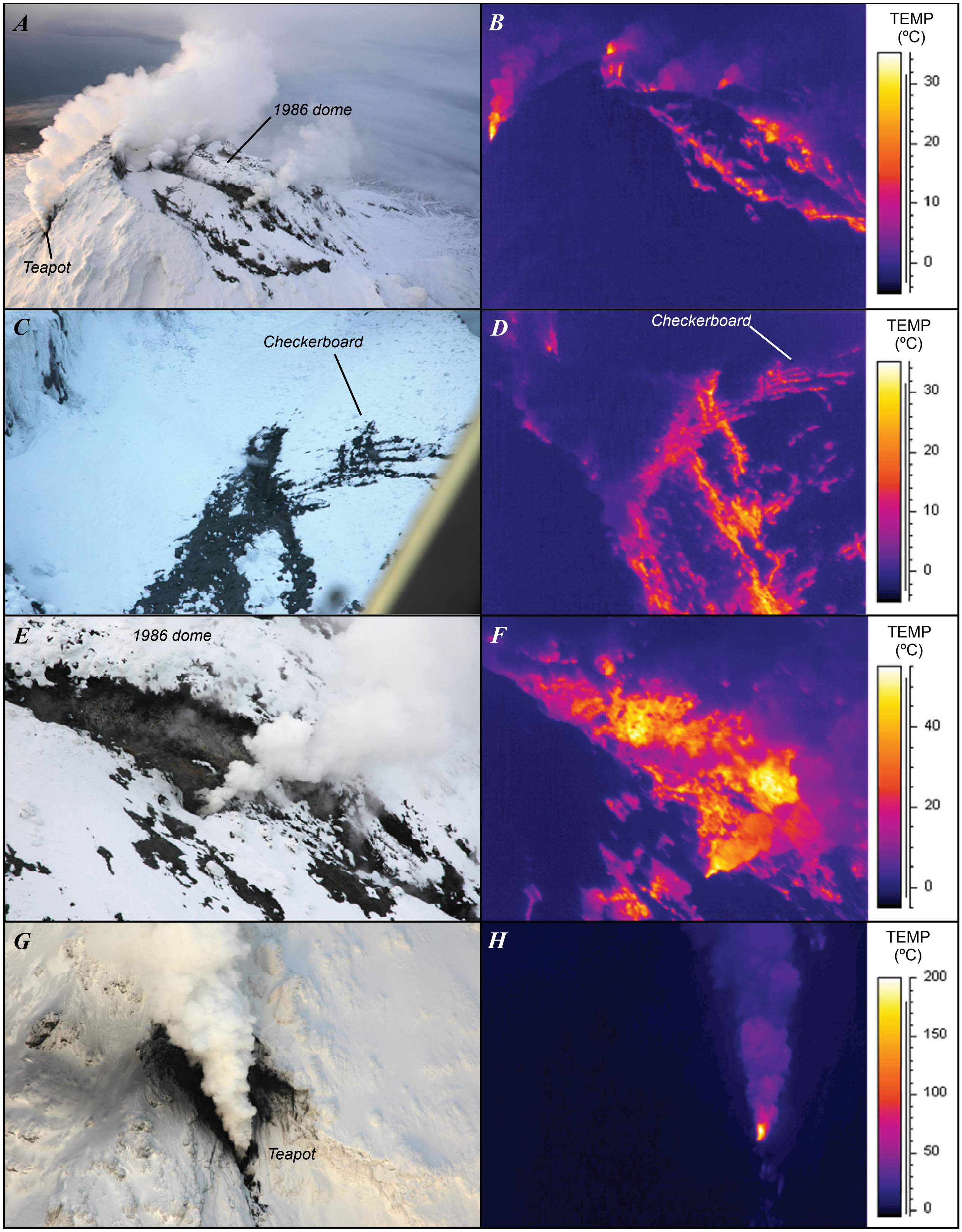

Figure 5. Photographs and thermal infrared (TIR) images of Augustine Volcano acquired during first Forward Looking Infrared Radiometer (FLIR) overflight on December 22, 2005, starting at 1509 AKST. *A,B*, Summit overview. View westward. *C,D*, “Checkerboard” pattern of snow-free fractures east of 1986 dome. *E,F*, New fumarole near edge of 1986 dome. View westward. *G,H*, Vigorously venting “teapot” fumarole on south flank.

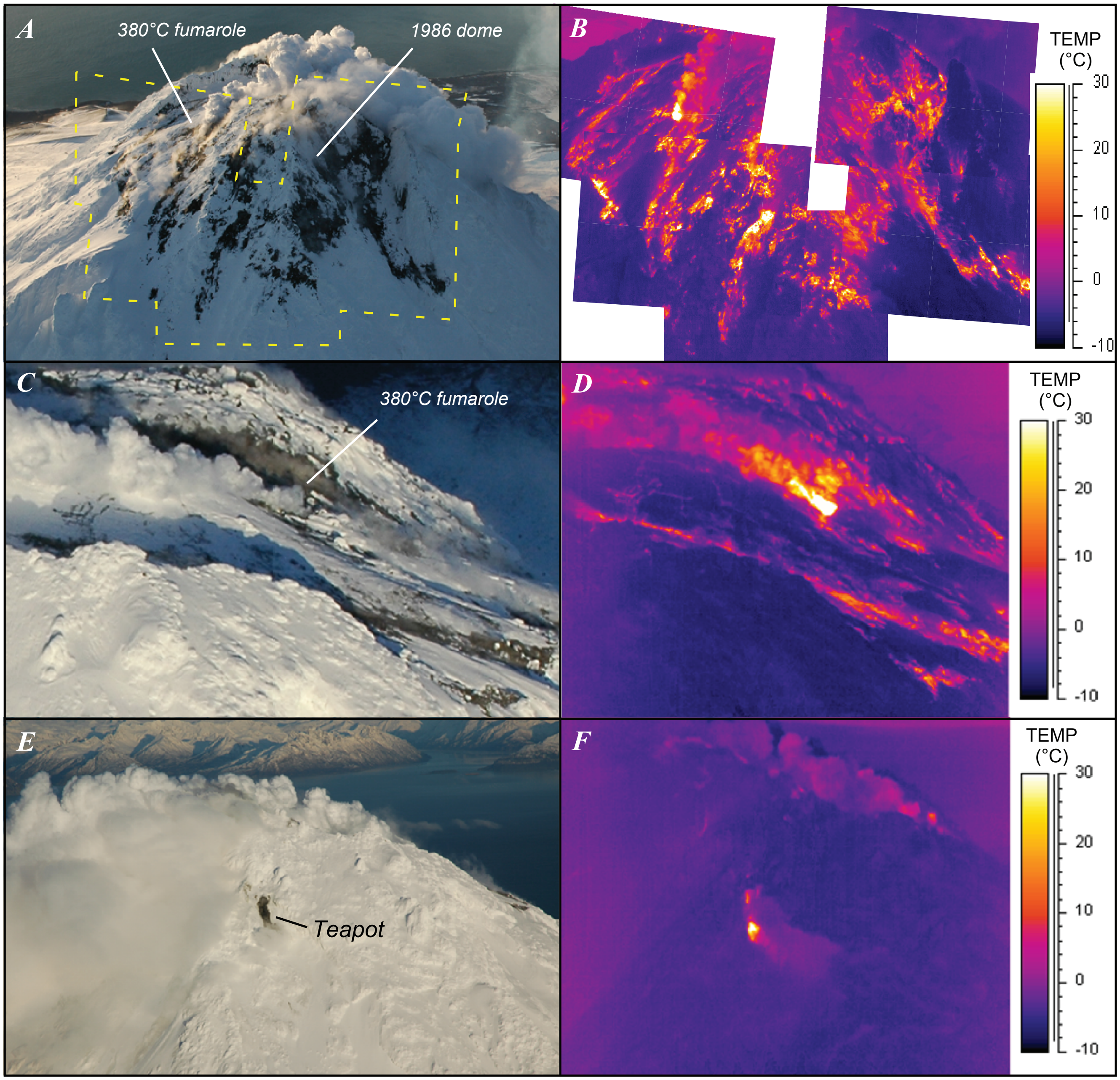

Figure 6. Photographs and thermal infrared (TIR) images of 1986 lava dome and upper flanks of Augustine Volcano acquired during Forward Looking Infrared Radiometer (FLIR) overflight on January 4, 2006. *A,B*, New warm snow-free areas extending from summit. Dashed yellow outline indicates approximate location of FLIR image mosaic shown in figure 6B. View westward. *C,D*, New fumarole along 1986 dome. View westward. *E,F*, Cooler, "Teapot" fumarole now showing only a thin steam plume. View northward.

Explosive Phase

Two explosions on the morning of January 11, 2006, heralded the beginning of the eruption's explosive phase. The explosions sent ash to 9 km above sea level (asl), but fall deposits appeared to lack juvenile material (see Wallace and others, this volume), and the explosions yielded no hot pyroclastic deposits on the island (see Coombs and others, this volume), suggesting that these explosions may have been primarily gas-release events. After about 48 hours of relative quiescence, seven more explosions on January 13 and 14 produced juvenile ash-rich clouds that rose to 14 km asl (Bailey and others, this volume; Wallace and others, this volume), hot pyroclastic flows, and secondary lahars and mixed avalanches, which were emplaced on most slopes of the volcano (see Coombs and others, this volume). Further explosions occurred on January 17, 27, and 28. A particularly explosive event on January 27 is believed to have emplaced the largest single pyroclastic-flow deposit of the entire eruption on the island's north flank (see Coombs and others, this volume). This deposit, known as the Rocky Point pyroclastic flow, approximately 4.8 km long and 17 million m^3 in volume, overran a small pond near its toe.

On January 12, 2006, 1 day after the first explosions, a FLIR helicopter mission observed that steam and ash emissions continued to reach a height of approximately 2,500 m asl and were moving southward (figs. 7*A*, 7*B*). Ash emissions waxed and waned during the time of the overflight, and a vigorous gas and ash plume emitting from a new vent, just south of the spine in the 1986 dome, was documented (figs. 7*C*, 7*D*). The maximum observed FLIR-derived brightness temperature was >275ºC, which was likely a minimum because the actual temperature exceeded the low gain setting on the FLIR. Further attempts to image this feature at a lower gain setting were unsuccessful because the vent was obscured by steam and ash emissions, which also obscured many of the elevated thermal regions visible in previous surveys, making them especially difficult to identify in images acquired from that day. Temperatures on the north face of the 1986 dome ranged from 20 to 40ºC, similar in intensity to the previous survey on January 4. Also, much less steam was observed in the south moat than during previous overflights. Drumbeat earthquakes (see Lalla

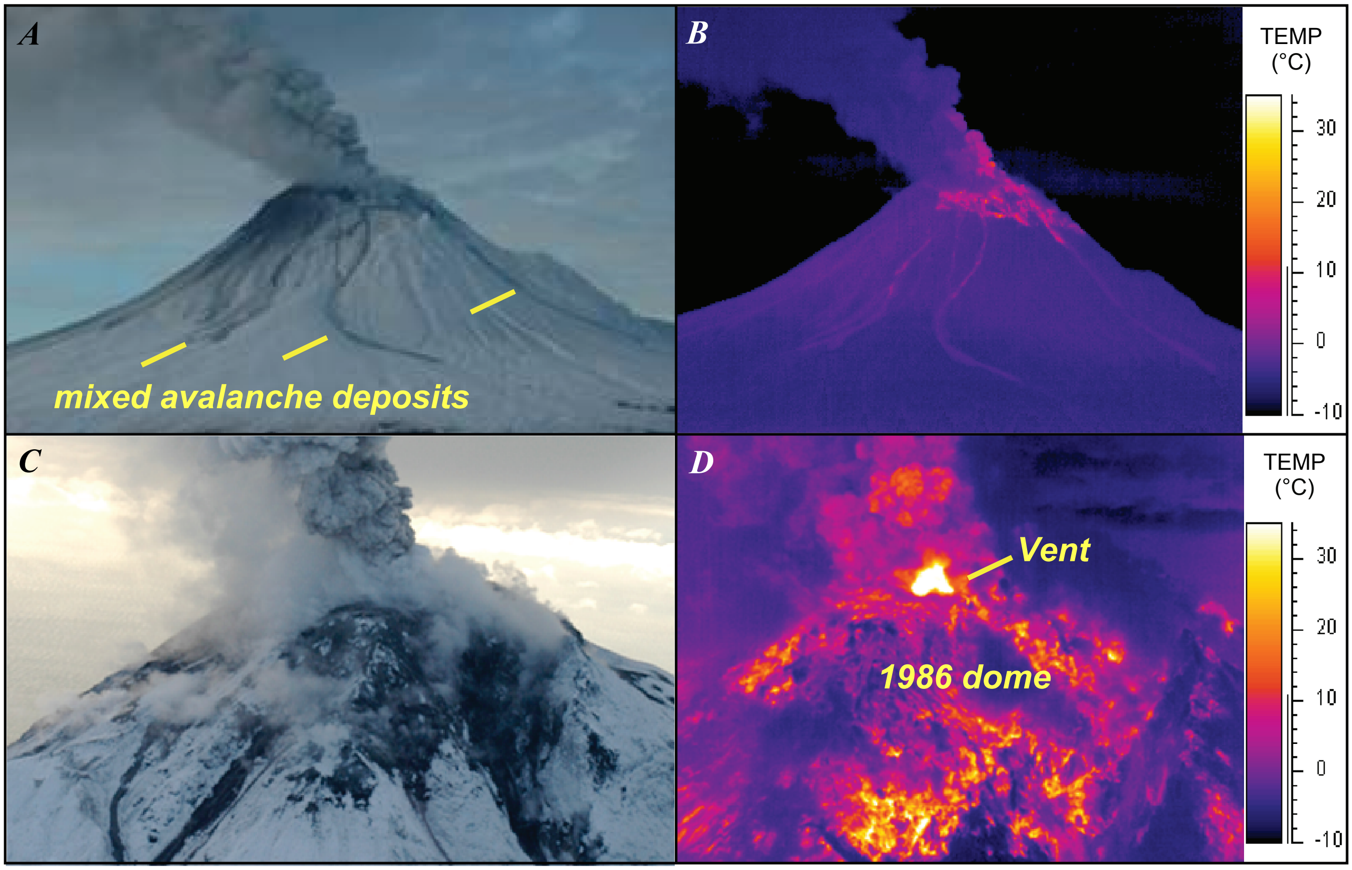

Figure 7. Photographs and thermal infrared (TIR) images of Augustine Volcano acquired during Forward Looking Infrared Radiometer (FLIR) overflight on January 12, 2006, starting at 1204 AKST. *A*,*B*, Gas and ash column venting from summit. Mixed avalanche deposits from explosions 1 and 2 on January 11, 2006, are visible on east flank. View northward. *C*,*D*, New vent (>275ºC) at top of 1986 dome. View southward.

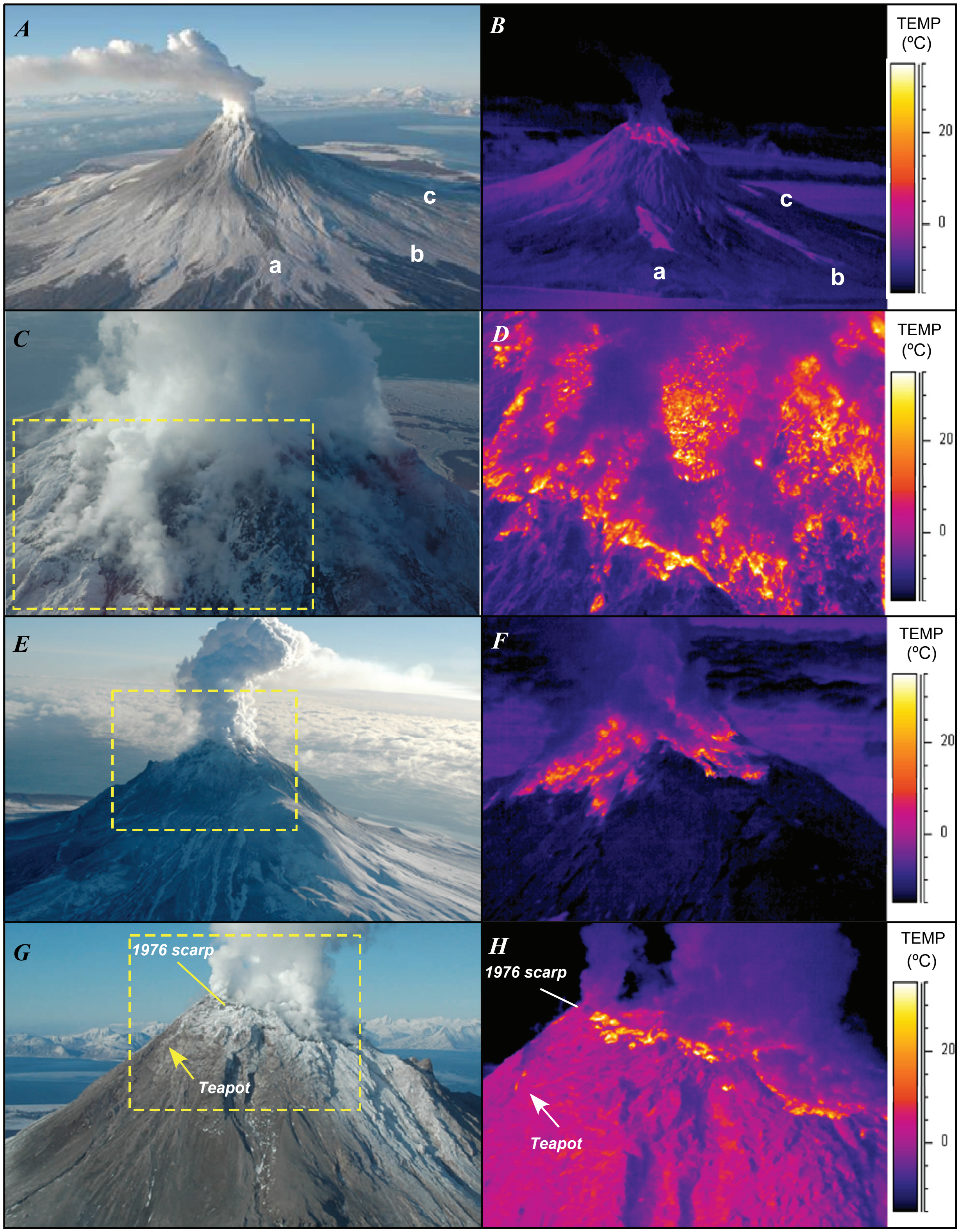

Figure 8. Photographs and thermal infrared (TIR) images of Augustine Volcano acquired during Forward Looking Infrared Radiometer (FLIR) overflight on January 24, 2006, starting at 1229 AKST. Dashed yellow boxes in *C*, *E*, and *G* indicate approximate locations of corresponding FLIR images to right. *A*,*B*, Cooling pyroclastic flows (a–c). View westward. *C*,*D*, Close-up of summit. View southwestward. *E*,*F*, Warming summit areas. View eastward. *G*,*H*, 1976 scarp at summit and "teapot" fumarole showing elevated temperatures. View westward.

and Power, this volume) and cessation of summit deformation (see Cervelli and others, this volume) suggest that lava effusion may have occurred on January 12. Saturated FLIR temperatures >275ºC were measured at the vent area through heavy steam and ash emissions, suggesting that new lava was likely present at or near the vent.

After the explosions on January 13, 14, and 17, 2006, photographs and FLIR images from January 24, showed no sign of magmatic temperatures at the summit. Cooling pyroclastic-flow deposits were observed on the east and north flanks, with surface temperatures ranging from 0 to 5ºC and a few large hot blocks, with temperatures of 30 to 40ºC (figs. 8*A*, 8*B*) were also visible. A maximum temperature of about 140ºC was observed near the new summit vent during brief views through the steam plume (figs. 8*C*, 8*D*). Steam plumes obscured much of the summit and were cold (figs. 8*E*–8*H*). Most of the summit region consisted of warm rubble, with temperatures ranging from 20 to 40ºC.

Nighttime ASTER TIR images from January 24, 2006, shows elevated summit temperatures and warm pyroclastic-flow deposits from the January 13–17 explosions on the northeast flanks (fig. 3*A*).

Continuous Phase

At about 1430 AKST on January 28, the volcano entered a period of more nearly continuous eruptive activity characterized by nearly constant ash-rich plume emissions to average heights of 3,600 m asl or less, as recorded by satellite data and radar (see Bailey and others, this volume). Occasional larger seismic signals, assumed to represent larger explosions, were associated with larger ash clouds up to 4,600 to 7,600 m asl. Subsequent observations showed that thick fans of pyroclastic material were deposited north and northeast of the summit during this period (see Coombs and others, this volume). This phase has been interpreted as the result of rapid effusion of lava at the summit, accompanied by nearly instantaneous collapse of parts of the growing lava dome to form numerous block-and-ash flows (see Coombs and others, this volume). Activity waned on February 3, and lower effusion rates produced a new lava dome and flow during the next week. Poor weather and low-lying ash obscured visual and satellite views during much of this period.

During the night of January 31, 2006, the ASTER URP system imaged an ash- and SO_2-rich plume and several large, hot pyroclastic-flow deposits on the volcano's north flank, including the Rocky Point pyroclastic flow that extends nearly to the north shoreline (fig. 3*B*). The 90-m ASTER TIR data show subtle temperature differences between the cooler distal ends of the pyroclastic-flow deposits and the warmer proximal areas. These temperature differences were likely controlled by both the age (hours) and thickness of the deposits. Multispectral TIR data also provide the means to identify silicate ash, ice, and SO_2 components in the plumes. ASTER SWIR (30 m) data from the same period show a ~700-m by 300-m region of hot pixels centered at the summit dome, with a maximum brightness temperature of 619°C.

A FLIR overflight on February 8, 2006, revealed several areas of cooling pyroclastic-flow deposits (fig. 9), the most extensive of which were in the northeast to northwest sectors. Smaller flows were deposited on the east flank (toward the Mound site), and a very small flow was observed on the southwest flank. Most of the pyroclastic-flow deposits had temperatures of 10–25°C, with numerous hotter large blocks (presumably dome fragments) with maximum temperatures >120°C. Pyroclastic-flow-deposit locations on the north and northwest flanks matched quite well with the warm features on the flanks observed in the nighttime TIR ASTER image of January 31 (fig. 3B). FLIR images of the summit were extremely difficult to acquire because of persistent steaming and cloud cover (fig. 9*A*). The maximum observed summit temperature of a contiguous area centered over the 1986 dome was ~50°C (fig. 9*B*); given the thick cloud cover, the actual temperature would have been much higher. Occasional photograph views through the steam and cloud showed a large black feature at the summit that was likely a new dome.

Eruptive Pause

From about February 10 through March 3, 2006, lava dome and flow effusion paused or at least slowed significantly (see Coombs and others, this volume). Limited thermal and visible views show little, if any, growth of the lava dome and flows during this period. FLIR and ASTER data spanning February 20–24 show a hot summit dome and rockfall deposits down the north flank and gradual cooling of the pyroclastic-flow deposits (figs. 3*C*, 10). FLIR images acquired on both February 20 and 24 detected maximum temperatures of 300°C at the edge of and below the active lava flow extending northward from the summit dome. The average surface temperature in mostly clear views of the summit dome was 40°C, whereas the average surface temperature of flows beneath the dome was 100°C. A wide area of steaming, bare rock surrounded the crater (figs. 10*C*, 10*E*), extending tens of meters down the flanks outside the 1976 crater (figs. 10*E*, 10*F*). The FLIR images, scaled for distance and pixel size, show that the warm north part of the dome was about 100 m wide and 115 m high. The slope distance from the top of the dome to the base of the 85-m-wide flow was approximately 390 m (275 m in plan view). Hot-rock deposits were also observed below the dome and along the lava flow in three distinct channels on the north flank (fig. 2*C*, 2*D*). The surfaces of the pyroclastic-flow deposits from late January had cooled to ~5°C.

Effusive Phase

After the apparent pause in eruptive activity throughout the second half of February, Augustine Volcano resumed

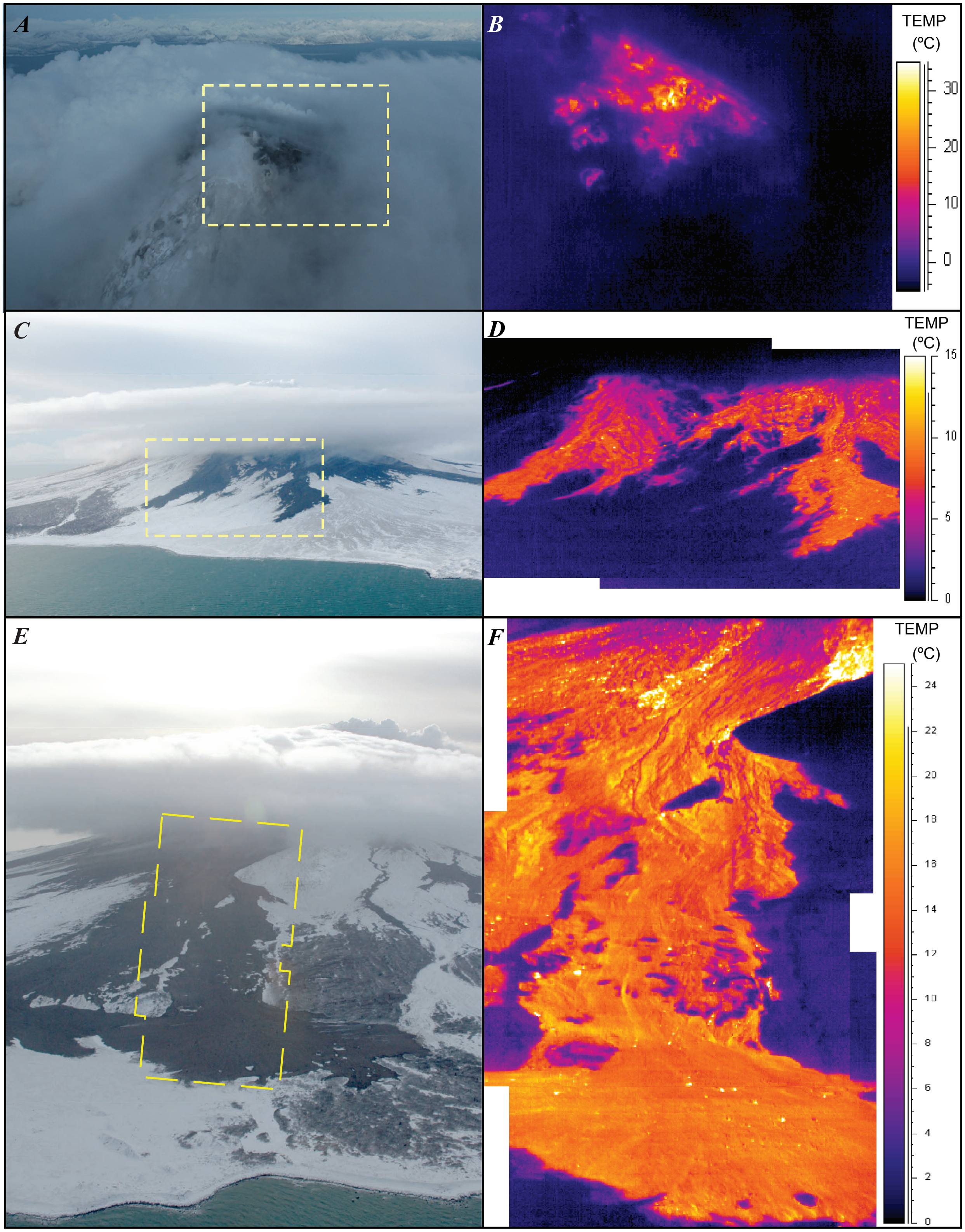

Figure 9. Photographs and thermal infrared (TIR) images of Augustine Volcano acquired during Forward Looking Infrared Radiometer (FLIR) overflight on February 8, 2006, starting at 1149 AKST. Dashed yellow boxes indicate approximate locations of corresponding FLIR image mosaics to right. *A*,*B*, Summit through thicker clouds. Dark, warm area might be obscured view of a new dome. View westward. *C*,*D*, Pyroclastic-flow deposits on northeast flank. View southwestward. *E*,*F*, Rocky Point pyroclastic-flow deposit. View southeastward.

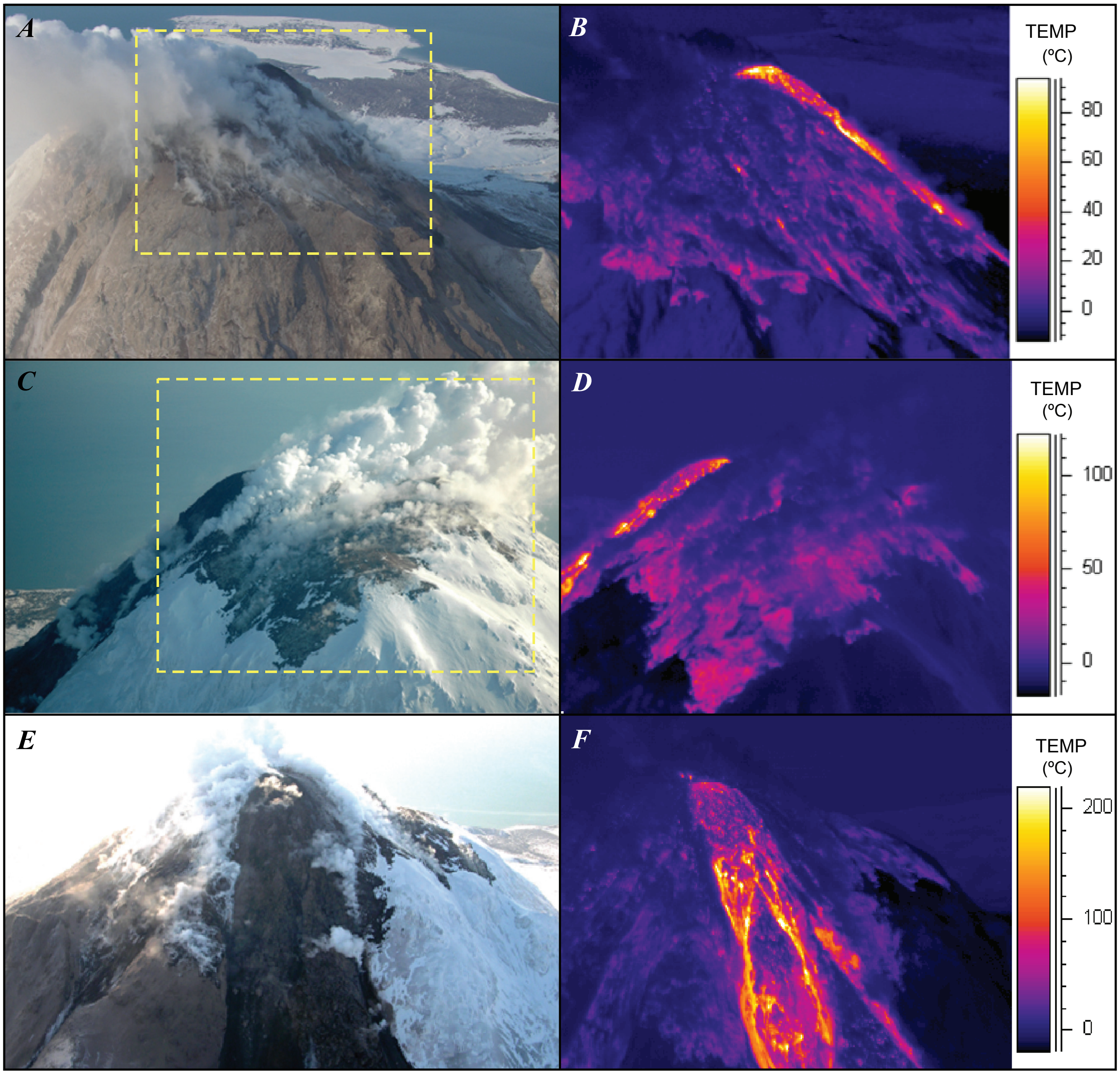

Figure 10. Photographs and thermal infrared (TIR) images of Augustine Volcano acquired during Forward Looking Infrared Radiometer (FLIR) overflight on February 24, 2006. Dashed yellow boxes in *A* and *C* indicate approximate locations of corresponding FLIR images to right. *A*,*B*, New summit lava dome, north lava flow, and hot rubble below flow, showing an expanded area of warm and steaming rock. View westward. *C*,*D*, Expanded area of warm and steaming rock at summit. View eastward. *E*,*F*, North lava flow and lava dome. View southward.

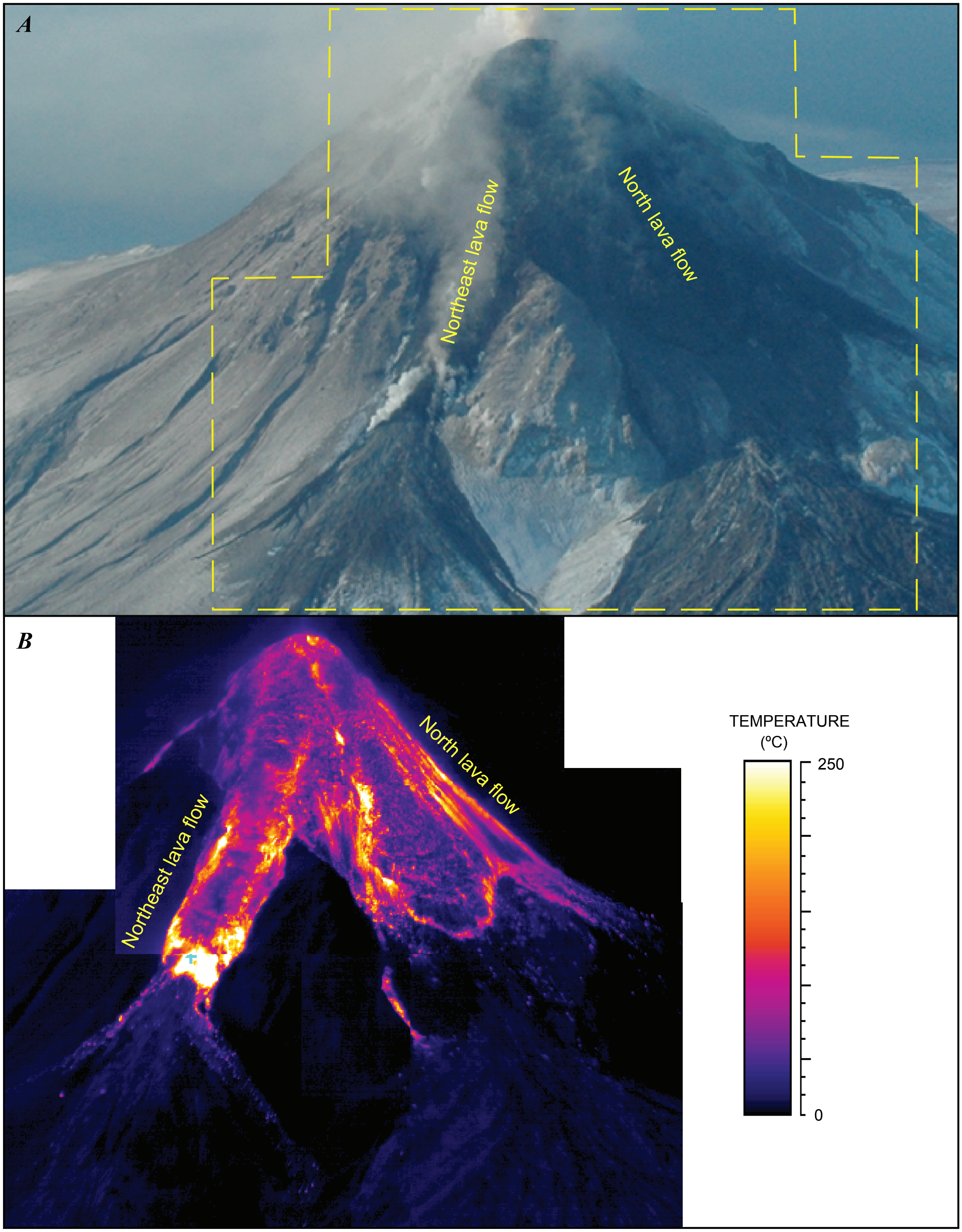

Figure 11. Photographs and thermal infrared (TIR) images of Augustine Volcano acquired 0959 AKST March 10, 2006, during Forward Looking Infrared Radiometer (FLIR) overflight. *A*,*B*, New summit lava dome and northeast and north lava flows. Summit and flows are partly obscured by dust and hot gas from frequent rockfalls from advancing flows, which are also visible in FLIR mosaic image. View southwestward.

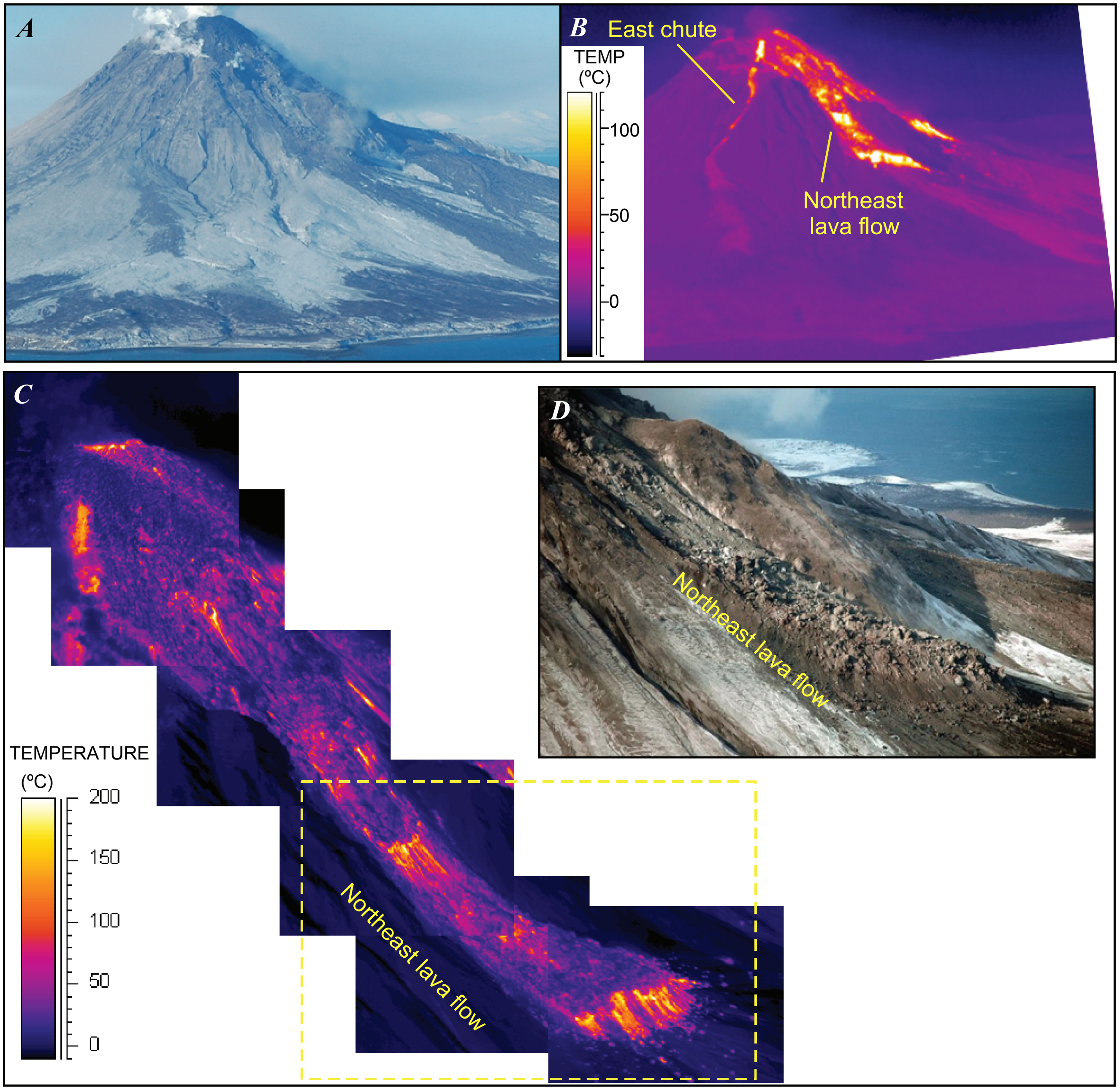

Figure 12. Photographs and thermal infrared (TIR) images of Augustine Volcano acquired during Forward Looking Infrared Radiometer (FLIR) overflight on March 15, 2006, starting at 0953 AKST. *A*,*B*, Entire volcano, with hot lava flows and small block-and-ash deposits extending down east chute below new summit lava dome. View westward. *C*,*D*, Mosaic of 6 close-up FLIR images of northeast lava flow and lava dome. Dashed yellow box indicates approximate location of figure 12*D*. View southeastward.

activity in March with the effusion of a larger summit dome, renewed growth of the north lava flow, and formation of a new lava flow confined to an erosional channel on the northeast side of the volcano, all accompanied by vigorous block-and-ash flows. This phase likely began on March 3 with an increase in the number of rockfall signals detected seismically, followed by a series of small explosions on March 4 (see Coombs and others, this volume; Power and Lalla, this volume). From March 8 to 16, seismic stations on the island recorded strong drumbeat earthquakes, indicative of lava effusion (see Power and Lalla, this volume), and incandescence was observed in Homer (see Sentman and others, this volume) and recorded by the Burr Point time-lapse camera (see Coombs and others, this volume). FLIR data acquired on March 10 and 15 provide some of the best information about growth of the new dome and flows (figs. 11, 12).

FLIR images from March 10, 2006, clearly show the larger dome and the two lava flows on the upper north and northeast flanks (figs. 2*E*, 2*F*, 11). A maximum temperature of 700°C was measured at the toe of the northeast lava flow, the highest temperature measured during the 2006 eruption. Mostly clear views of the summit dome revealed average surface temperatures of ~40°C; the average surface temperature of flows downslope from the dome was 100°C. The wide area of steaming, bare rock surrounding the crater that was observed in February persisted. The pyroclastic-flow deposits emplaced in late January had surface temperatures averaging 4°C, but were still steaming over the area of the now-buried pond.

On March 15, the north and northeast lava flows had both advanced and thickened since March 10. On the basis of scaled FLIR images from Burr Point (fig. 2*H*), the northeast flow advanced approximately 140 m to a total length of 930 m as measured from the base of the summit dome.

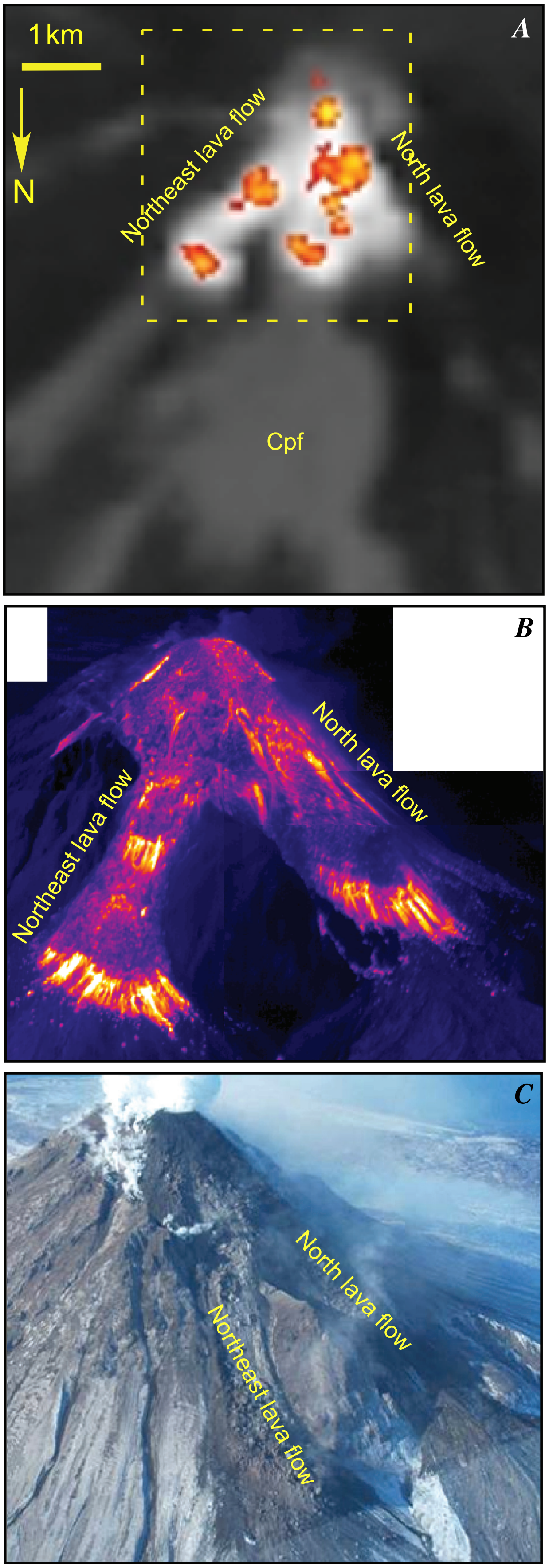

Figure 13. Comparison of multiscale, multispectral data of Augustine Volcano summit acquired March 13–15, 2006. *A*, March 13, 2006, Advanced Spaceborne Thermal Emission and Reflection Radiometer (ASTER) nighttime thermal infrared (TIR) image. *B*, Oblique airborne Forward Looking Infrared Radiometer (FLIR) image acquired 1.5 days later on March 15. *C*, Photograph taken at same time as FLIR image. ASTER image shows high temperature shortwave infrared (SWIR) (30 m) pixels in color over grayscale TIR (90 m) pixels. Map view in ASTER image is rotated with north at bottom to better match views in oblique photographs. Yellow dashed rectangle outlines approximate area of *B*. Combined TIR-SWIR ASTER image highlights benefit of having both datasets, with TIR image defining outline of active lava flows and SWIR image highlighting areas of exposed lava at surface. This SWIR image also reveals that both flows have zones of freshly exposed lava in areas of high extension-strain rate, as well as at summit and toes of flows.

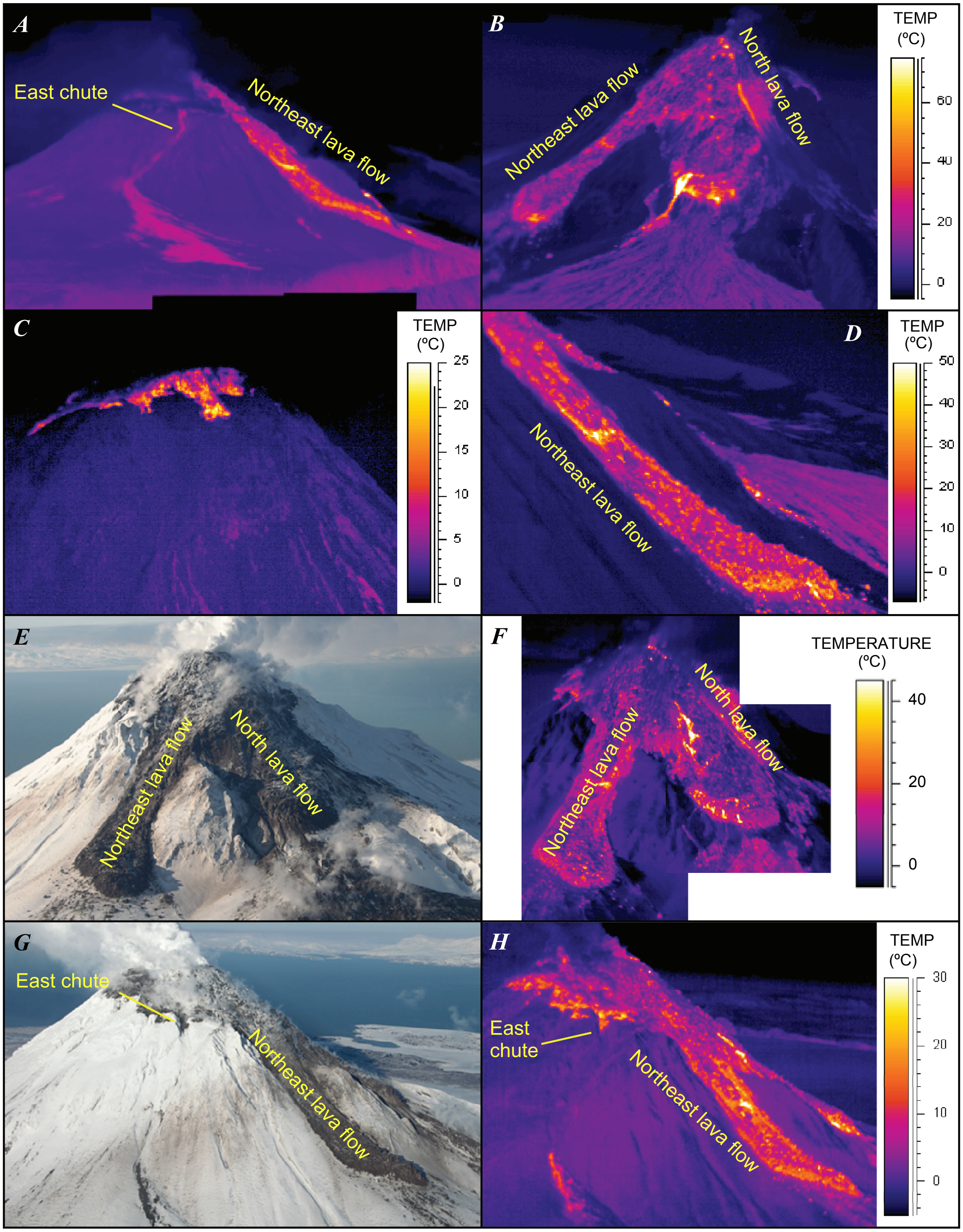

Figure 14. Photographs and thermal infrared (TIR) images of Augustine Volcano acquired during Forward Looking Infrared Radiometer (FLIR) overflights on March 26, 2006 (*A*–*D*), and April 6, 2006 (*E*–*H*). *A*, Northeast lava flow and warm, though apparently inactive, east chute (see fig. 12*C*). View westward. *B*, Northeast and north lava flows. Note active spalling along east side of north lava flow. View southward. *C*, Warm surface of summit scarp. View northeastward. *D*, Northeast lava flow. View westward. *E*,*F*, Lava flows. View southward. *G*,*H*, Northeast lava flow and east chute. View westward.

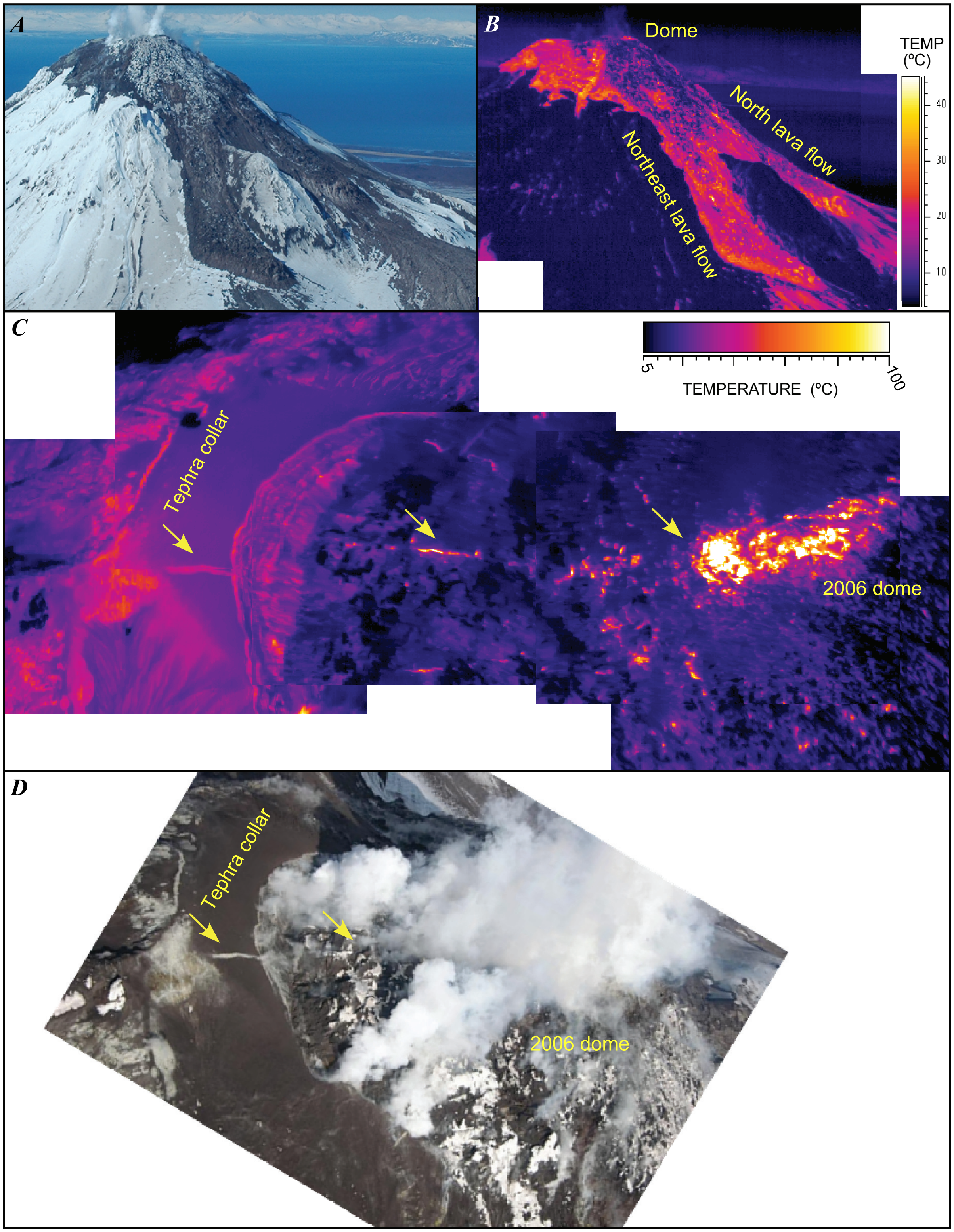

Figure 15. Photographs and thermal infrared (TIR) images of Augustine Volcano acquired during Forward Looking Infrared Radiometer (FLIR) overflight on May 13, 2006. *A*,*B*, Northeast and north lava flows, summit lava dome, and warm deposits on south side of summit. New dome rock is partly covered by a combination of snow, ice, and precipitates, whereas tephra deposits adjacent to dome remain snow free. View southward. *C*,*D*, Summit lava dome and tephra collar. Note elongate zone of high temperatures on dome and hot fractures extending southward from dome (arrows). South is to the left in both figures.

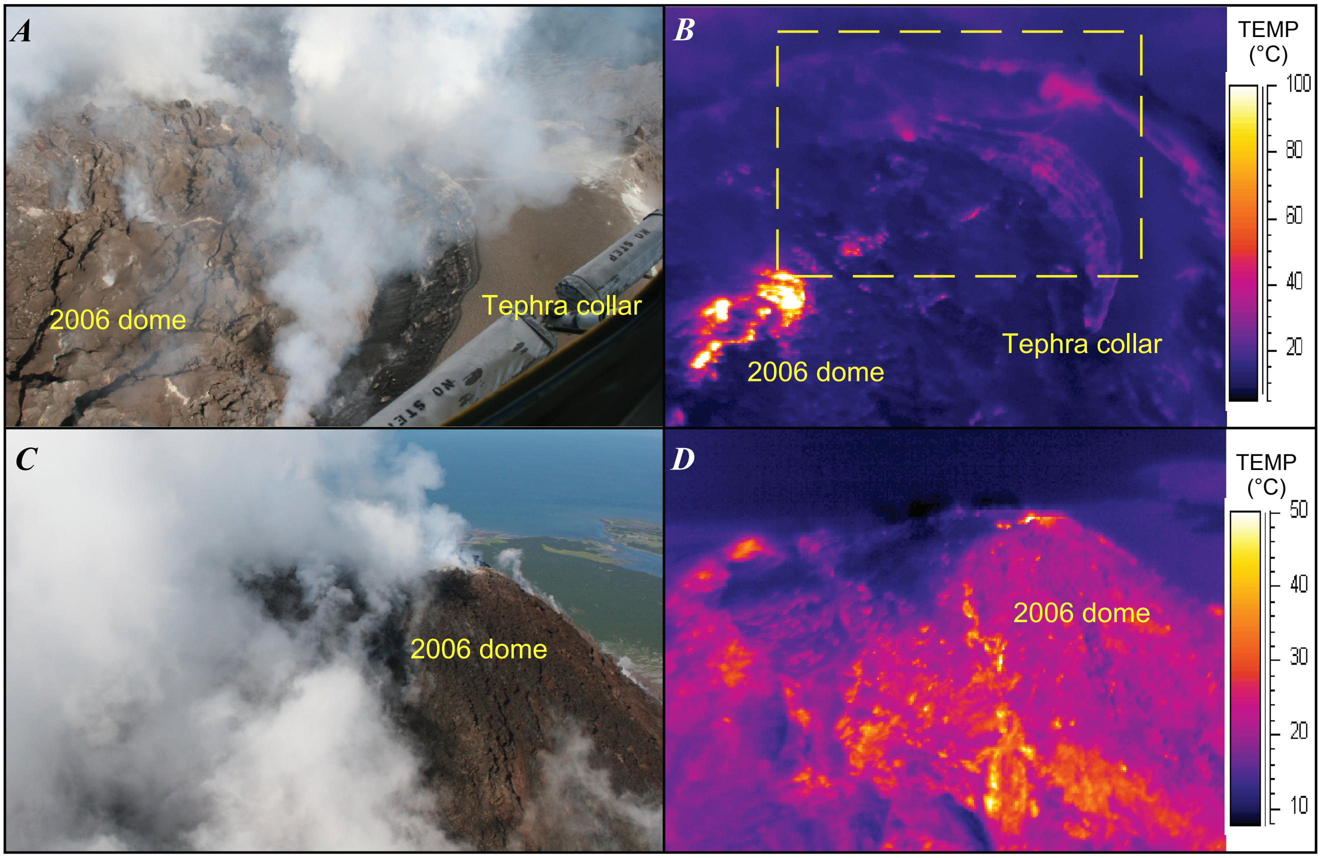

Figure 16. Comparisons between photographs and thermal infrared (TIR) images of Augustine Volcano acquired during final Forward Looking Infrared Radiometer (FLIR) overflight on August 7, 2006. *A–B*, Part of 2006 lava dome and 2006 tephra collar on south rim. Elongate zone of high temperatures on dome and hot fractures extending southward from dome persist. Dashed yellow box indicates approximate location of *A*. *C,D*, Summit lava dome, tephra collar, and remnants of east chute. View westward.

The north lava flow widened from by about 70 m to 410 m, but advanced downslope only approximately 20 m to a total length of 420 m. Most of the thermal energy was emitted from flow fronts and small windows through the rubble-covered carapace created by tensional fracturing as the flow advanced over steeper topography. This carapace was most notable on the east side of the dome, although no visible incandescence was observed anywhere along the flow edges (fig. 12*D*). Minimal rockfall activity suggested that the flows were generally advancing more slowly than on March 10. The average temperature measured on the flow and dome surfaces had decreased to ~40°C. The extent and temperatures of warm areas on the summit flanks were unchanged from March 10 and earlier.

FLIR data show the variation in temperature on the lava flow surfaces (fig. 12*E, 13B*). Both the lava flows and the dome edges have steeper areas of hotter material at the surface. The hot lava flows were observed about 34 hours before the FLIR survey by a nighttime ASTER image. The 90-m TIR image (figs. 3*D*, 13*A*) reveals the extent and temperature of the hot summit dome and flows as bright, sometimes saturated, pixels. The maximum pixel-integrated temperature extracted from ASTER 30-m SWIR (2.167 µm) radiance data was 463.9°C (fig. 13*A*).

Post Eruption

Seismic activity had dropped to pre-effusive-phase levels by March 20 (see Power and Lalla, this volume), and no new morphologic changes in the dome or lava flows were observed after March 15. Incandescence after this time was focused along the west margin of the north lava flow, where spalling and rockfalls continued to occur into May (see Coombs and others, this volume).

FLIR data from March 26 (figs. 14*A*–14*D*) showed that the average surface temperature was low, (~40°C). The lava flow fronts where fresh spalling had previously occurred had maximum temperatures of 180°C. Viewed at close range (500 m), one summit fumarole had a maximum temperature of 221°C. The southwest side of the summit had warm areas extending a short distance downward from the summit.

On April 6 (figs. 14*E*–14*H*) the north and northeast lava flows had not advanced notably since previous observations on March 15 and 26. The flow fronts also appeared to be cooler relative to the previous surveys, with little rockfall from their fronts. The north-lava-flow front and margins appeared to be more active than those of the northeast flow. The average temperature of the flow and dome surfaces was similar to that in previous surveys in March (~40°C), and the extent and temperatures of the warm areas on summit flanks appear to be unchanged from previous surveys.

The maximum temperature of ~650°C in a fumarole at the top of the dome was considerably higher than that recorded on March 26 (220°C), possibly owing to better viewing conditions on April 6, but also reflecting changes in the vent geometry since the previous survey. Although gas measurements by McGee and others (this volume) show a gradual decrease in SO_2 flux from late March through April, day-to-day averages vary somewhat during this period. The measured April 6 average SO_2 flux (~2 kt/d) was nearly double the flux for March 22 (~1 kt/d).

A FLIR survey of Augustine Volcano on May 13, 2006 (figs. 15*A*–15*D*) showed no obvious morphologic changes to domes or flows since April. The maximum temperature of 428°C recorded at the top center of the 2006 dome was lower than that recorded on April 6 (650°C). Warm areas persisted around the summit region, unchanged from previous surveys. The north- south-trending fractures first observed on the summit in December 2005 continued to persist as linear

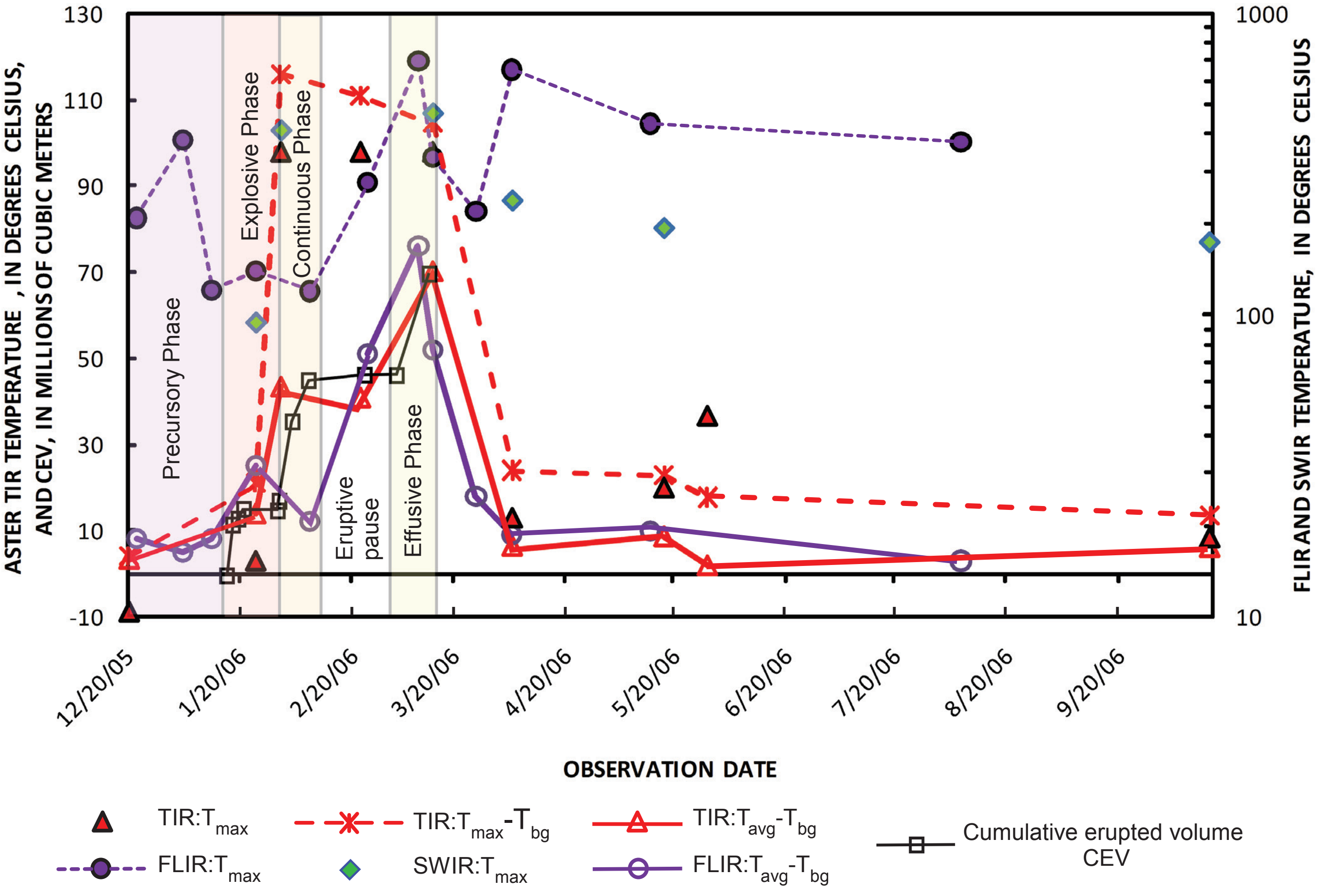

Figure 17. Advanced Spaceborne Thermal Emission and Reflection Radiometer (ASTER)- and Forward Looking Infrared Radiometer (FLIR)-derived temperatures (see tables 1, 2) and cumulative erupted volume (black squares; from Coombs and others, this volume) during each phase of 2006 eruption of Augustine Volcano versus date. Red solid triangles, maximum ASTER thermal infrared (TIR) temperatures at summit; red open triangles, ASTER TIR average lava-flow-surface temperature minus background temperature near summit elevation. Maximum ASTER TIR temperatures >100°C indicate data saturation during continuous and effusive phases. Green diamonds, maximum ASTER shortwave infrared (SWIR) brightness temperatures at summit; Purple dots, maximum temperature in multiple airborne FLIR images. Purple circles show average FLIR lava surface temperature minus FLIR background temperature.

warm areas atop the new dome and tephra collar with the same orientation.

The final FLIR survey of Augustine Volcano was conducted on August 7, 2006 (figs. 16*A–16D*). The summit lava dome surface and tephra collar had temperatures similar to those in the May survey. Corrected for background temperature, the flow surfaces had cooled ~7°C since May to ~3°C above background. FLIR data show that most of the new lava flow surfaces were barely above ambient temperature, although several areas of warm rubble had average surface temperatures of 30°C. Hot fumaroles persisted at the summit and in several parts of the new lava flows. The temperature of the 2006 summit dome fumarole was still ~370°C, and several fumaroles around the perimeter of the new flows had maximum temperatures of 150°C. The pyroclastic-flow deposits and the north and northeast lava flows were not imaged with FLIR during the final survey.

Summary and Conclusions

The combined near-real-time utilization of both airborne and satellite TIR images during the eruption of Augustine Volcano provided valuable insights into the eruption hazards and dynamics. The high-resolution TIR images documented gradual pre-eruption heating of the summit, growing pyroclastic-flow deposits, rapid temperature increases as the lava dome and flows formed, and slow cooling of the volcanic deposits after the eruption (fig. 17). These high-resolution images uniquely documented segmentation of the lava flows into hotter areas of increased flow deformation and cooler, more stable crust on the active flows.

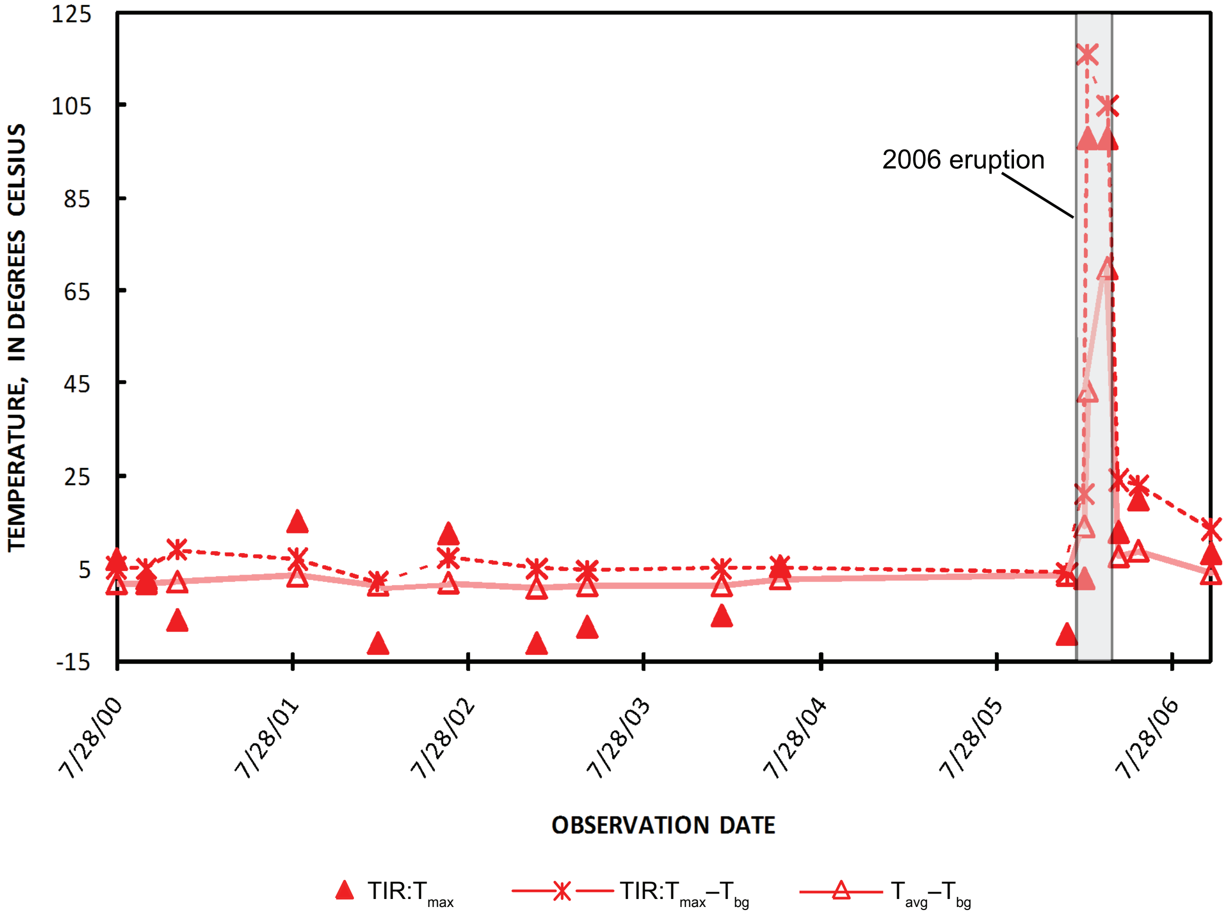

Figure 18. Advanced Spaceborne Thermal Emission and Reflection Radiometer (ASTER)-derived temperatures from July 28, 2000, to October 15, 2006. Red solid triangles, maximum ASTER thermal infrared (TIR) temperature at summit; red open triangles, average ASTER TIR surface temperature at summit minus background temperature near summit elevation; asterisks, maximum ASTER TIR temperature at summit minus background temperature near summit elevation.

The temperatures derived from FLIR and ASTER images are plotted against the cumulative erupted volume and eruptive phases (see Coombs and others, this volume) in figure 17. The widely varying maximum FLIR-derived temperatures (FLIR:T_{max}, fig. 17; table 1) for each overflight were from thermal features ranging from fumaroles at the summit during the precursory phase, through individual hot blocks in fresh pyroclastic-flow deposits during the explosive and continuous phases, to large incandescent fractures and spalling lava flow fronts and the summit vent during the effusive phase, back to fumaroles on the summit and cooling lava flows after the eruption ceased. The highest maximum FLIR-derived temperatures were recorded during the precursory (fumaroles) and effusive (lava) phases. Such results indicate that caution should be taken when using an average maximum temperature in models of effusion rates. Although these models can be highly accurate, they could be extracting temperatures from active lava flows, hot fumaroles, or simply exposed cracks. With lower-resolution satellite, discrimination of these features commonly becomes difficult.

To reduce the scatter and better assess overall temperature trends, the average surface temperatures of warm summit areas and, later, lava surfaces were measured (FLIR:T_{avg}, fig. 17; table 1). To further reduce meteorologic influences on FLIR-derived temperatures, the ambient background temperature near the summit (FLIR:T_{bg}, fig. 17; table 1) was subtracted from the average surface temperature (FLIR:T_{avg}). The resulting plot (FLIR:$T_{avg} – T_{bg}$, fig. 17) shows an increase in surface temperature during the precursory phase through the end of the effusive phase, with one anomalously low temperature likely due to poor observation conditions at the summit (February 8, 2006). The average surface temperature drops rapidly in late March, after the likely end of the effusive phase. Because the much larger ASTER pixels tend to integrate much of the variation in temperature documented by FLIR, maximum ASTER TIR (TIR:T_{max}, fig. 17; table 2) and ASTER SWIR (SWIR:T_{max}, fig. 17; table 2) -derived temperatures more closely follow the trend of FLIR:T_{avg} showing much elevated temperatures during the explosive through effusive phases. Deriving the average surface temperature from ASTER TIR (TIR:T_{avg}, table 2), the background-corrected plot (TIR:$T_{avg}–T_{bg}$, fig. 17) shows a steep rise in average surface temperature during the explosive and continuous phases, a slight decrease during the eruptive pause, an increase to the highest surface temperature during the effusive phase, and a steep drop in temperature after the eruption. The periods of rapid increase in ASTER-derived temperature appear to correlate with the higher effusion rates suggested by the cumulative erupted volumes estimated by Coombs and others (this volume).

Because Augustine Volcano is relatively close to communities in south-central Alaska, AVO was able to conduct many FLIR flights during the course of the eruption. However, most Alaskan eruptions occur in much more logistically difficult locations, making FLIR observations a rare occurrence outside the Cook Inlet region. high-resolution satellite TIR data from ASTER, in contrast, can be used to monitor any eruption no matter how remote. ASTER is well suited to volcanic observations because of its 15- to 90-m spatial resolution, its ability to be scheduled and point off-nadir, and its ability to collect multispectral data during both the day and the night. Aided by the high latitude of Augustine Volcano, ASTER was able to provide frequent repeat imaging as short as 1 day between scenes, with an average 6-day repeat during the height of eruptive activity in 2006 (fig. 17). A higher temporal resolution at ASTER TIR spatial resolution would be useful to more adequately establish volcano temperature trends, but owing to frequent clouds, volcanic emissions, and infrequent ASTER scheduling, better temporal coverage with high spatial resolution is not currently possible in Alaska for this type of detailed study.

Finally, ASTER also provides a means for reviewing volcano temperature trends since 2000. TES-derived kinetic temperature data extracted from 11 clear nighttime pre-eruption ASTER TIR images provide a timeline for low-temperature thermal activity at Augustine Volcano's summit (fig. 18). For the 6-year-period preceding the 2006 eruption, the background-adjusted ASTER TIR:T_{max} value averaged 5.4°C, with a standard deviation of 1.8°C. Over the same period, the background-adjusted ASTER TIR:T_{avg} averaged 1.9°C, with a standard deviation of 0.9°C. The sole pre-eruption ASTER TIR observation from December 20, 2005, 22 days before the first major explosions, had an ASTER TIR:T_{avg} value of 3.5°C at the summit, only about 1.6°C above the 6-year average but greater than 1σ.

Although ASTER did acquire another 3 daytime and 10 nighttime images during the year preceding the December 20 view, the volcano summit was obscured by clouds in all of them. The absence of cloud-free pre-eruption ASTER data demonstrates why future high-resolution satellite missions need to be designed to provide more frequent and regularly scheduled TIR acquisitions both day and night. The pre-eruption ASTER data, in combination with FLIR observations, suggest that if clear nighttime, high-resolution TIR data had been available days to weeks earlier, the anomalous summit temperatures might have been detected sooner than December 20, as occurred during both the 2005 and 2007 eruptions of Kliuchevskoi Volcano in Kamchatka, Russia (Ramsey and others, 2007; Rose and Ramsey, 2009).

Acknowledgments

We thank Matt Patrick and John Power for their timely reviews and suggestions. This research was supported by the USGS-AVO and NASA (grants NNG04GO69G and NNX-08AJ91G). ASTER data were obtained courtesy of NASA/GSFC/METI/ERSDAC/JAROS and U.S./Japan ASTER Science Team. We thank helicopter pilots Ken Deyoe and Rick Farish for safely and skillfully flying us to the volcano.

References Cited

Bailey, J.E., Dean, K.G., Dehn, J., and Webley, P.W., 2010, Integrated satellite observations of the 2006 eruption of Augustine Volcano, *in* Power, J.A., Coombs, M.L., and Freymueller, J.T., eds., The 2006 eruption of Augustine Volcano, Alaska: U.S. Geological Survey Professional Paper 1769 (this volume).

Ball, M., and Pinkerton, H., 2006, Factors affecting the accuracy of thermal imaging cameras in volcanology: Journal of Geophysical Research, v. 111, no. B11, p. 1–14.

Calvari, S., Spampinato, L., Lodato, L., Harris, A.J.L., Patrick, M.R., Dehn, J., Burton, M.R., and Andronico, D., 2005, Chronology and complex volcanic processes during the 2002–2003 flank eruption at Stromboli volcano (Italy) reconstructed from direct observations and surveys with a handheld thermal camera: Journal of Geophysical Research, v. 110, no. B2, p. 1–23.

Cervelli, P.F., Fournier, T., Freymueller, J.T., and Power, J.A., 2006, Ground deformation associated with the precursory unrest and early phases of the January 2006 eruption of Augustine Volcano, Alaska: Geophysical Research Letters, v. 33, L18304, doi: 10.1029/2006GL027219, 5 p.

Coombs, M.L., Bull, K.F., Vallance, J.W., Schneider, D.J., Thoms, E.E., Wessels, R.L., and McGimsey, R.G., 2010, Timing, distribution, and volume of proximal products of the 2006 eruption of Augustine Volcano, *in* Power, J.A., Coombs, M.L., and Freymueller, J.T., eds., The 2006 eruption of Augustine Volcano, Alaska: U.S. Geological Survey Professional Paper 1769 (this volume).

Dehn, J., Dean, K.G., Engle, K., and Izbekov, P., 2002, Thermal precursors in satellite images of the 1999 eruption of Shishaldin Volcano: Bulletin of Volcanology, v. 64, no. 8, p. 525–534.

Flynn, L.P., Harris, A.J.L., and Wright, R., 2001, Improved identification of volcanic features using Landsat 7 ETM+: Remote Sensing of Environment, v. 78, no. 1–2, p. 180–193.

Gillespie, A. R., Rokugawa, S., Matsunaga, T., Cothern, J. S., Hook, S. J., and Kahle, A. B. 1998, A temperature and emissivity separation algorithm for Advanced Spaceborne Thermal Emission and Reflection Radiometer (ASTER) images: Institute of Electrical and Electronics Engineers Transactions Geoscience Remote Sensing, v. 36, p. 1113–1126.

Harris, A.J.L., Dehn, J., and Calvari, S., 2007, Lava effusion rate definition and measurement; a review: Bulletin of Volcanology, v. 70, n. 1, p. 1–22.

Harris, A.J.L., Dehn, J., Patrick, M., Calvari, S., Ripepe, M., and Lodato, L., 2005, Lava effusion rates from hand-held thermal infrared imagery; an example from the June 2003 effusive activity at Stromboli: Bulletin of Volcanology, v. 68, p. 107–117.

Jacobs, K.M., and McNutt, S.R., 2010, Using seismic *b*-values to interpret seismicity rates and physical processes during the preeruptive earthquake swarm at Augustine Volcano 2005–2006, *in* Power, J.A., Coombs, M.L., and Freymueller, J.T., eds., The 2006 eruption of Augustine Volcano, Alaska: U.S. Geological Survey Professional Paper 1769 (this volume).

McGee, K.A., Doukas, M.P., McGimsey, R.G., Neal, C.A., and Wessels, R.L., 2010, Emission of SO_2, CO_2, and H_2S from Augustine Volcano, 2002–2008, *in* Power, J.A., Coombs, M.L., and Freymueller, J.T., eds., The 2006 eruption of Augustine Volcano, Alaska: U.S. Geological Survey Professional Paper 1769 (this volume).

Power, J.A., Nye, C., Coombs, M.L., Wessels, R.L., Cervelli, P.F., Dehn, J., Wallace, K.L., Freymueller, J.T., and Doukas, M., 2006, The reawakening of Augustine Volcano, Alaska: Eos, (American Geophysical Union Transactions), v. 87, p. 373–377.

Power, J.A., and Lalla, D.J., 2010, Seismic observations of Augustine Volcano, 1970–2007, *in* Power, J.A., Coombs, M.L., and Freymueller, J.T., eds., The 2006 eruption of Augustine Volcano, Alaska: U.S. Geological Survey Professional Paper 1769 (this volume).

Ramsey, M., and Dehn, J., 2004, Spaceborne observations of the 2000 Bezymianny, Kamchatka eruption; the integration of high-resolution ASTER data into near real-time monitoring using AVHRR: Journal of Volcanology and Geothermal Research, v. 135, no. 1–2, p. 127–146.

Ramsey, M.S., Dehn, J., Wessels, R.L., Byrnes, J., Duda, K., Maldonado, L., and Dwyer, J., 2004, The ASTER emergency scheduling system—A new project linking near-real-time satellite monitoring of disasters to the acquisition of high-resolution remote sensing data [abs.]: Eos (American Geophysical Union Transaction), v. 85, n. 47, Fall Meeting Supplement, Abstract SF23A-0026.

Ramsey, M.S., Duda, K., Dehn, J., Wessels, R., Skoog, R., and Rose, S., 2007, Application of the ASTER rapid response protocol for eruption detection and volcano monitoring: ASTER Science Workshop, p. 3–4.

Rose, S.R., and Ramsey, M.S., 2009, The 2005 eruption of Kliuchevskoi volcano; Chronology and processes derived from ASTER spaceborne and field-based data: Journal of Volcanology and Geothermal Research, v. 184, p. 367–380.

Schneider, D, Vallance, J., Wessels, R., Logan, M., and Ramsey, M., 2008, Use of thermal infrared imaging for monitoring renewed dome growth at Mount St. Helens, 2004, *in* Sherrod, D.R., Scott, W.E., and Stauffer, P.H. eds., A volcano rekindled; the renewed eruption of Mount St. Helens, 2004–2006: U.S. Geological Survey Professional Paper 1750, p. 347–359.

Thome, K., Palluconi, F., Takashima, T., and Masuda, K., 1998, Atmospheric correction of ASTER: IEEE Transactions on Geoscience and Remote Sensing, v. 36, no. 4, p. 1199–1211.

Vaughan, R.G., Hook, S.J., Ramsey, M.S., Realmuto, V.J., and Schneider, D.J., 2005, Monitoring eruptive activity at Mount St. Helens with TIR image data: Geophysical Research Letters, v. 32, L19305, doi:10.1029/2005GL024112.

Vaughan, R.G., and Hook, S.J., 2006, Using satellite data to characterize the temporal thermal behavior of an active volcano; Mount St. Helens, WA: Geophysical Research Letters, v. 33, L20303, doi:10.1029/2006GL027957.

Wright, R., and Flynn, L., 2003, On the retrieval of lava-flow surface temperatures from infrared satellite data: Geology, v. 31, p. 893–896.

Wallace, K.L., Neal, C.A., and McGimsey, R.G., 2010, Timing, distribution, and character of tephra fall from the 2005–2006 eruption of Augustine Volcano, *in* Power, J.A., Coombs, M.L., and Freymueller, J.T., eds., The 2006 eruption of Augustine Volcano, Alaska: U.S. Geological Survey Professional Paper 1769 (this volume).

Yamaguchi, Y., Kahle, A.B., Tsu, H., Kawakami, T., and Pniel, M., 1998, Overview of Advanced Spaceborne Thermal Emission and Reflection Radiometer (ASTER): Institute of Electrical and Electronics Engineers Transactions Geoscience Remote Sensing, v. 36, no. 4, p. 1062–1071.

The 2006 Eruption of Augustine Volcano, Alaska
Power, J.A., Coombs, M.L., and Freymueller, J T., editors
U.S. Geological Survey Professional Paper 1769

Chapter 23

The 2006 Eruption of Augustine Volcano—Combined Analyses of Thermal Satellite Data and Reduced Displacement

By Saskia M. van Manen[1], Jonathan Dehn[2], Michael E. West[2], Stephen Blake[1] and David A. Rothery[1]

Abstract

Augustine Volcano erupted explosively after 20 years of quiescence on January 11, 2006, followed by approximately 2 months of dome building and lava extrusion. This is the best monitored eruption in Alaska to date; the diverse complementary datasets gathered enable an interdisciplinary interpretation of volcanic activity. An analysis of reduced displacement (continuous measure of seismic tremor amplitude) and thermal energy output (from satellite imagery) observed between January 1 and April 30, 2006, shows relationships linked to the type of eruptive activity. Three different types of volcanic behavior can be identified as they show specific patterns in the combined data sets: (1) explosive activity, (2) lava extrusion (dome growth), and (3) cooling of erupted products. Explosive activity was characterized by high reduced displacement values but relatively low radiative thermal flux. Lava extrusion occurred in three distinct sequences characterized by increased values of reduced displacement and increased thermal emissions. Two periods of elevated thermal energy output and reduced displacement coincided with times of deflation, suggesting an increase in extrusion rate. Periods of cooling were marked by decreasing thermal emissions and reduced displacement. This work highlights the value of combined observations, which reveal more about the status of an active volcano than individual methods alone.

Introduction

Nearly 20 years after its last eruption, Augustine Volcano (59.361ºN, 153.426ºW; fig. 1) began to erupt on January 11, 2006 (Power and others, 2006). Augustine is an 8 by 11 km volcanic island located in the southern Cook Inlet, approximately 290 km southwest of Anchorage, Alaska. It has erupted 8 times since it was named in 1778 by Captain Cook (Miller and others, 1998). Its summit consists of an andesitic lava dome and lava flow complex, which has repeatedly collapsed resulting in debris avalanches, occasionally triggering tsunamis (Siebert and others, 1995). Currently, the primary hazard from Augustine arises from ash-rich plumes that traverse north Pacific air traffic routes (Miller and Casadevall, 1998). However, hazards also exist for nearby residents in the form of ashfall and tsunamis. An example of this is the 1883 eruption, which caused a tsunami that inundated large sections of Cook Inlet (Siebert and others, 1995; Waythomas and others, 2006).

The 2006 eruption was preceded by seismic unrest that started on April 30, 2005 (Jacobs and McNutt, this volume; Power and Lalla, this volume) and inflation of the edifice that started in July 2005 (Cervelli and others, this volume). Phreatic eruptions were reported throughout December 2005. In the 10 days preceding the first explosive event only three thermal anomalies were found by visual inspection in satellite data. However, more detailed changes in the thermal state of Augustine were observed in the higher resolution thermal camera (Forward Looking Infrared Radiometer, FLIR) data (Wessels and others, this volume). Explosive activity producing ash-rich plumes reaching up to 14 km above sea level (Petersen and others, 2006) started on January 11 and continued intermittently until January 28. Lava extrusion is thought to have commenced around January 13, as indicated by the presence of juvenile glass shards in ash samples (Wallace and

---

[1] Volcano Dynamics Group, Department of Earth and Environmental Sciences,The Open University, Walton Hall, Milton Keynes, MK7 6AA U.K.

[2] Alaska Volcano Observatory, Geophysical Institute, University of Alaska Fairbanks, 903 Koyukuk Drive, P.O. Box 757320, Fairbanks, AK 99775-7320.

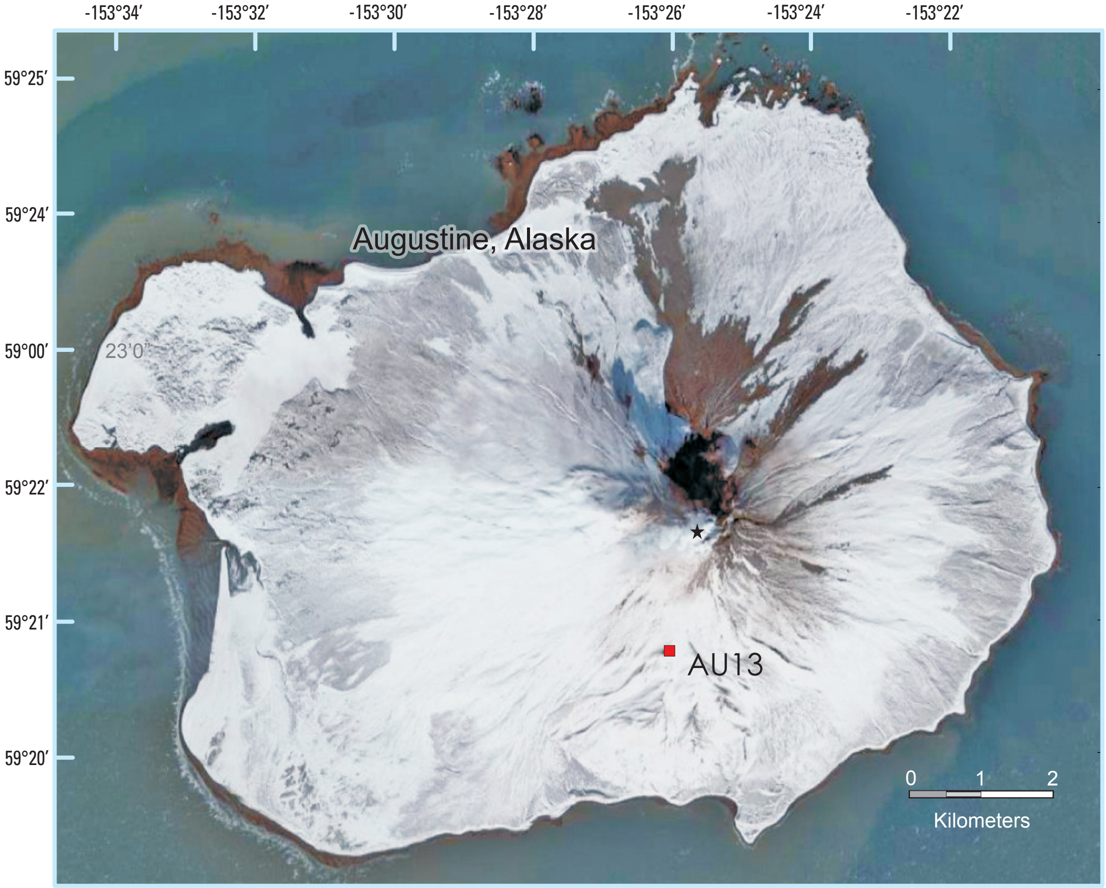

Figure 1. Location figure of Augustine Volcano. This Google Earth™ (DigitalGlobe) image of Augustine Volcano was taken after the 2006 eruption. The snow in the image highlights the location of the newly formed block and ash flows and pyroclastic deposits (all in black) on the north and northeastern slopes. Figure shows location of seismic station AU13, located 1.8 km from the summit of Augustine. This station is the source of the reduced displacement data.

others, this volume). Lava effusion continued until late March, resulting in a lava dome and two short (<1 km) blocky lava flows (Power and others, 2006). The exact date when lava effusion ceased is undocumented by field observations. During the course of the eruption Augustine went through three phases of inflation and two phases of deflation (Cervelli and others, this volume). In addition, numerous rock falls, pyroclastic flows, and block and ash flows were observed, likely related to the growth of the lava dome and flows (Coombs and others, this volume).

Lava dome emplacement is a nonlinear dynamic process accompanied by a wide range of phenomena, including the opening of fissures, increased fumarolic activity, extrusion of lava, earthquakes, dome collapse, explosions, and pyroclastic flows. In addition, phases of quiescence and violence often alternate depending on factors such as extrusion rate, magma rheology and thickness of the cooling top layer (Fink and Griffiths, 1998). Understanding the dynamics involved in the emplacement of lava domes is important because instability can result in collapses accompanied by pyroclastic flows, ash plumes and co-ignimbrite plumes that are capable of reaching air-traffic routes (Woods and Kienle, 1994; Miller and Casadevall, 1998).

This paper presents an interpretation of satellite and reduced displacement data obtained at Augustine Volcano between January 1 and April 30, 2006, spanning the entire eruption and part of the precursory phase, in order to form a more comprehensive understanding of how these signals relate to the observed volcanic activity. Relating thermal signatures to ground activity enhances remote-sensing and seismic monitoring capabilities, particularly in the Alaska-Aleutian-Kamchatka region where satellite data are often the only data source available.

Background

Satellite monitoring provides a means to characterize the thermal states of active volcanoes. Studying satellite-derived data in conjunction with ground-based data and visual observations may help to better understand the nature and significance of the thermal signals. This “ground truthing” permits improved interpretations of the satellite data, making it possible to better gauge volcanic activity at volcanoes monitored solely by remote sensing. Remote sensing of active volcanoes allows near real-time observation of a whole volcano in different parts of the electromagnetic spectrum (Mouginis-Mark and others, 2000). The temporal coverage depends on the satellite used. This study focuses on measurements of thermal flux and total radiated energy, other areas of remote sensing are discussed in other chapters in this volume (Webley and others, this volume; Lee and others, this volume).

This study uses Advanced Very High Resolution Radiometer (AVHRR) data. AVHRR is the primary instrument on the polar orbiting weather satellites operated by the National Oceanographic and Atmospheric Administration (NOAA). Each day, between 10 and 30 AVHRR images with a nadir pixel-size of 1.1 km, in five bands spanning the visible to the infrared, are acquired over the Augustine region. Not all of these images are of suitable quality for study; for example, images with a zenith angle greater than 55° are discarded, as data obtained from them is too geometrically distorted (Harris and others, 1997). The zenith angle is the angle between the local zenith and the line of sight to the satellite. This reduces the number of functional images to approximately half of those obtained. Drawbacks of AVHRR data include its coarse spatial resolution; however, this disadvantage is far outweighed by its high temporal coverage of the Alaska-Aleutian-Kamchatka area because of the polar convergence of the satellite orbits.

Seismology has long been a mainstay of volcano monitoring, as it provides one of the best means of assessing a volcano's state of activity. The central goal of volcano seismology is to understand the subsurface structure of volcanoes and track the movements of fluids, including gas and magma, through this structure. McNutt (2005) notes four main types of seismic signal that are observed at active volcanoes: (1) high-frequency events, also known as volcano-tectonic events (VT), (2) low-frequency events, also termed long-period (LP) events, (3) explosions and (4) volcanic tremor. These events can be divided into two groups based on the origin of their source energies: (1) those where fluid plays an active role in the source mechanism (Aki and others, 1977; Aki and Koyanagi, 1981) and (2) those where magmatic processes provide energy for rock failure (Shaw, 1980; Aki and Koyanagi, 1981; Weaver and others, 1981). The first group involves LP events and volcanic tremor, whereas the second category consists of VT earthquakes. Mixtures of the two types also occur, these are termed hybrid events (Shaw, 1980; Lahr and others, 1994).

Volcanic tremor is a common but poorly understood type of seismic signal that has been documented at more than 160 volcanoes (McNutt, 1994). Difficulty arises from the wide ranging definition of tremor, which covers many different types of behavior. A variety of source models have been proposed, including that it is a sustained sequence of LP events (Latter, 1979; Fehler, 1983; Malone and others, 1983). Others argue for a more continuous source formed by resonance in the conduit, possibly in conjunction with changing physical properties (Neuberg and O'Gorman, 2002; Benoit and others, 2003). Though the exact source of the tremor is debated and likely nonunique, all models associate tremor with the movement of fluids through the volcanic subsurface. Tremor often precedes and accompanies volcanic eruptions, although not all volcanic tremor culminates in eruptions (Julian, 1994).

Reduced displacement (D_r) is a continuous measure of tremor amplitude (Aki and Koyanagi, 1981). Tremor is a sustained phenomenon, because of this it dominates the seismic record when present. Reduced displacement is comparable to the RSAM (Real-time Seismic-Amplitude Measurement) method of Endo and Murray (1991), but it differs in that it adjusts the amplitude for a presumed source. Although this introduces a possible bias to the data, in practice it permits multiple seismic stations to be used together and allows comparisons between different eruptions on a common scale.

McNutt (1994) determined an empirical correlation between tremor amplitude and column height based on the analysis of 21 eruptions at 14 volcanoes. During the 1996 Pavlof (Alaska) eruption, a general relationship between plume height and tremor amplitude was observed by Roach and others (2001). In addition, the size of the observed thermal anomaly steadily increased before the eruption of the largest plumes, which reached an altitude of 10 km above sea level (Roach and others, 2001). However, Nye and others (2002) found that during the 1999 Shishaldin (Alaska) eruption there was a remarkable lack of correlation between reduced displacement and plume height. They also found that thermal anomalies often preceded volcanic tremor associated with strombolian outbursts. Galindo and Dominguez (2002) found good correlations between thermal and seismic data at Colima (Mexico) during 1997–2000. Using AVHRR and seismic data during precursory, effusive, and explosive stages of the eruption they recorded five seismic swarms, four of which coincided with periods of increased summit temperature and strong ash emissions. It is noteworthy that ash emissions were observed prior to the seismic swarms.

Data Acquisition

Thermal Imagery

Between January 1 and April 30, 2006, thermal anomalies centered over Augustine were identified in band 3 (3.55–3.93 µm) in 323 AVHRR images by the automated Okmok II algorithm. Thermally anomalous pixels are those that rise 5°C or more above the mean temperature of the surrounding eight pixels (AVO Remote Sensing Team, 2000). Okmok II improves upon its predecessor, Okmok (Dean and others, 1998; Dehn and others, 2000), by using a wider range of criteria to determine whether a pixel is a volcanic thermal anomaly or noise. The AVHRR images provide a snapshot of the thermal state of the volcano at that moment in time (fig. 2). The Okmok II algorithm automatically discards cloudy, daytime, and noisy images and then ascertains the apparent temperature of the hottest anomalous pixel in each image, as well as the accompanying background temperature. For the purposes of this paper it is assumed that the hottest pixel includes the summit of Augustine.

Thermally anomalous pixels were also manually identified in 526 images between January 1 and April 30, 2006, by the Alaska Volcano Observatory (AVO) as part of the twice-daily remote-sensing monitoring routine (Bailey and others, this volume). The number is much higher than determined by

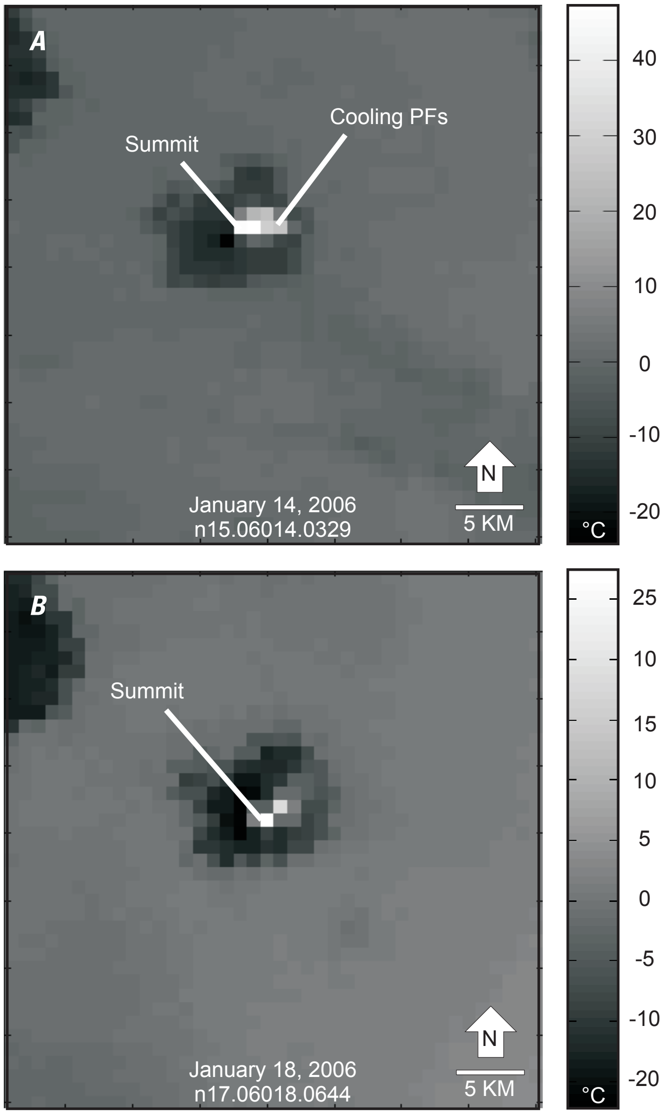

Figure 2. Selected band 3 (thermal infrared; 3.55-3.93 µm) AVHRR data over Augustine Volcano in January 2006 showing thermal anomalies at the summit of Augustine, as well as cooling pyroclastic flows. Both images are north oriented to the top, scalebar is in degrees Celsius (°C), the image identification numbers are noted on the bottom. *A*, January 14 at 03.29 UTC, zenith angle is 27°. *B*, January 18 at 0644 UTC, zenith angle is 42°.

the Okmok algorithm due to the fact that the Okmok algorithm excludes daytime, cloudy, or noisy images that an analyst can still use. For each of the images the number of hot pixels was recorded. This provides an indication of the activity that has occurred, taking into account the whole volcano. Small numbers of pixels with elevated temperatures generally suggest summit activity, whereas larger numbers can indicate cooling lava flows or pyroclastic deposits. However, increases in the number of hot pixels observed are only significant if they are large; with increasing zenith angle, pixels start to overlap, increasing the chance of a hotspot stretching across multiple pixels. In addition, even at lower zenith angles a hotspot can occasionally be on the border of two pixels, thus being reported in two or more pixels instead of one.

Radiative Thermal Flux and Total Radiated energy

The radiant temperature detected by AVHRR is a function of the sensor's field of view (FOV). It is integrated over the entire area of the pixel and can not directly reflect the temperature of the hottest volcanic material except in the highly unlikely event that such material homogenously occupies the whole pixel. This means that estimation of the volcanic temperature requires the simultaneous determination of the proportions of ground surface at various temperatures (Harris and others, 1997; Francis and Rothery, 2000). The radiance received will be affected by atmospheric attenuation and instrumental effects as well as by surface spectral emissivity. To calculate the thermal output from the summit at Augustine, the two-component method (Dozier, 1981; Rothery and others, 1988; Harris and others, 1997; Harris and others, 1998) was used in conjunction with the dataset gathered by the Okmok II algorithm. The manual data was only used to examine the number of hot pixels during the time period investigated. This was done as the Okmok II algorithm maintains constant criteria to determine whether or not a pixel is thermally elevated. This method assumes that a pixel with an elevated temperature (T_{int}) is composed of two parts; a subpixel hotspot at temperature (T_h), occupying a fractional area (p_h), while the remainder is at background temperature (T_{bg}) occupying ($1-p_h$). This assumption allows the temperature and the area covered by each component to be estimated using:

$$L(\lambda, T_{\text{int}}) = p_h L(\lambda, T_h) + (1-p_h)\, L(\lambda, T_{bg}) \qquad (1)$$

Where L is the Planck function for a blackbody at wavelength λ. This results in three unknowns: the fractional area, the temperature of the hot component, and the temperature of the background. Background temperature can be estimated using the temperatures of surrounding nonanomalous pixels, allowing the remaining two parameters to be calculated if one of them can be assumed or constrained. This work uses an integrated pixel temperature (T_{int}) determined from band 3 (3.55–3.93 µm) and a background temperature determined from band 4 (10.3–11.3 µm). This is done because the peak emittance of the background is closer to the central wavelength of band 4. The two component method is a simplification because a volcano consists of more than one hot and one cold component; however, it provides an accurate first order approximation of the radiative thermal flux. In order for it to work, the ratio of the hot to cold pixel fraction needs to be correct. The fractional area occupied by the hot component was estimated by determining the dome radius; visual observations indicate this was 110 m, this means approximately 3 percent of each pixel is considered to be at high temperature. Although the size and the shape of the dome changed throughout the course of the eruption, this size estimate provided a plausible ratio of the hot to cold pixel fraction because it is consistent with the satellite derived extrusion rates, which correspond to those observed in the field (Coombs and others, this volume). Having estimated the fractional area of the hot component allowed the temperature of the hot component (T_h) to be calculated. Consequently above-background summit radiative thermal flux (q_r) can be calculated using:

$$q_r = \varepsilon\sigma\tau p_h(T_h^4 - T_{bg}^4)\ , \tag{2}$$

where τ is the atmospheric transmissivity, σ is the Stefan-Boltzmann constant, and ε is the emissivity of the lava. Atmospheric transmissivity is difficult to account for as it is affected by the total transmissivity of the atmosphere as well as the concentration of volcanic gases above the vent (Dehn and others, 2002). However, due to the fact that the subarctic air is relatively dry, the effect of transmissivity only has a small effect on the absolute temperature values. Emissivity in the relevant wavelengths is assumed to be 0.9, an accepted value for andesitic lavas (Salisbury and D'Aria, 1992). The radiant thermal flux represents the average thermal flux integrated over the entire pixel. No correction for the pixel size is made, as the precise geometry of the edifice changes and the viewing geometry of the satellite is hard to constrain.

Using radiative thermal flux to monitor activity will result in underestimates of total energy flux at a volcano because other sources of heat loss such as convection, conduction, evaporation of rainfall, and hydrothermal circulation are ignored (Francis and Rothery, 2000). Radiative thermal flux is just one component of the total heat loss, however since it is the largest is provides a good proxy for the thermal state, and thus activity level, of a volcano. The total radiated energy was calculated by using the trapezoidal method of integration.

Seismic Tremor Data

Reduced displacement (D_r) is a low sample rate measure of seismic amplitude. It is widely used to normalize volcanic tremor recorded at varying distances from a volcano to a common scale and to allow comparisons between eruptions. It is a simple measure equal to the sustained root mean square (rms) ground displacement corrected for geometric spreading (Aki and Koyanagi, 1981). Site amplification can influence the results, but the order of magnitude scaling typically used with reduced displacement minimizes the influence of a constant scale factor.

For this study we use D_r calculated from channel HHZ (the vertical component) of station AU13 (59.3464ºN, 153.4341ºW). AU13 was chosen because it had a high signal-to-noise ratio, had few data gaps, remained on scale through the eruption, and was generally representative of D_r from other stations at Augustine. The sensor was a Guralp CMG-6TD (30 s) installed shortly before the eruption. This station was located 1.8 km from the summit (fig. 1). Because the station is within a few wavelengths of the source region beneath the summit, we use the body wave formulation of reduced displacement first presented by Aki and Koyanagi (1981). The original expression, formulated for paper records, is:

$$D_r = \frac{A}{2\sqrt{2}} \cdot \frac{r}{M} \tag{3}$$

where A is the peak-to-peak amplitude of the raw seismogram and the factor of estimates its root-mean-square value from the peak-to-peak measure. The source-to-receiver distance r, is the salient part of the expression which "reduces" the displacement to a common value. The magnification value, M, scales the seismogram from arbitrary units to true ground displacement. Although A is measured from raw seismic data, M, is frequency dependent. In this formulation M should be chosen at a frequency which best matches the tremor, thus introducing a frequency dependence to the reduced displacement expression.

The approach used in this study is true to the original definition of reduced displacement but benefits from digital processing techniques. In lieu of applying a frequency-dependent magnification factor, we use seismic data that have been corrected for instrument response and integrated from velocity to displacement. We calculate the root mean square of this signal directly. Although this is a more brute force approach, it can be written simply as:

$$D_r = RMS\ (X) \cdot r \tag{4}$$

where X is the instrument-corrected displacement record. In practice this is comparable to using the original formulation of Aki and Koyanagi (1981) without the frequency assumption introduced by the magnification factor. Here we calculate D_r on 30-minute windows of data, band-pass filtered for a frequency range of 0.5 to 8 Hz. The filter preserves the dominant frequencies of tremor, volcanic earthquakes, and rock falls while minimizing both the low-frequency microseism band and high-frequency wind noise. The wide frequency window is consistent with the use of reduced displacement in many monitoring environments.

It should be noted that this formulation for reduced displacement varies from a modified version used operationally by AVO (see McNutt and others, this volume). The operational version measures seismic amplitude in a narrow band around the dominant frequency of the signal. To make use of more distant stations, this approach also uses a geometric spreading term consistent with surface waves (Fehler, 1983). Because of the broader band approach, body wave decay term, and the use of stations close to the summit, values presented here are generally higher than those of McNutt and others (this volume). The discrepancy is inherent in the different approximations required to reduce complex seismic records to a simple metric, such as reduced displacement. However it is precisely such simplifications that allow quantitative comparisons between different eruptive episodes.

Analyses and Results

Thermal emissions and reduced displacement data plots were made using data spanning the entire eruption. The coeruptive data were examined in detail and additional analyses were performed on selected subsets.

Thermal Imagery

Summit Radiative Thermal Flux and Total Radiated Energy

The data show three broad peaks during which the summit radiative thermal flux rose above the average eruption background value of less than 10^8 W (figs. 3*A*, 4*A*). An additional minor spike is visible near the end of April. On the basis of the thermal imagery, the total energy output from the summit region of Augustine between January 1 and April 30, 2006, is 2.15×10^{16} J. The thermal flux increases appear to occur predominantly in three sequences as indicated by three time periods showing a distinct increase in slope on the cumulative energy output plot (fig. *5A*).

Although thermal anomalies (figs. *3A, 4A*) are observed prior to the start of the explosive activity on January 11, thermal flux then was lower, not exceeding $1\text{x}10^8$ W. The first main spike in thermal flux is not until January 13 at 13.27 h UTC, almost 48 hours after the initial explosions, when the summit thermal flux reaches 1.1×10^{10} W. This spike is then followed by two smaller but slightly broader spikes on January 14 and 17. On January 18 another large narrow spike of 8.2×10^9 W can be observed.

After January 20, radiative thermal flux again falls below $1\text{x}10^8$ W, until January 26 after which it quickly starts to rise. A small spike of 7.2×10^9 W can be seen on January 28, coincident with the four explosions that occurred during this phase. A spike of 1.6×10^{10} W is observed on February 3, after this the thermal flux tapers off quickly until February 13. Minor spikes of 1.3×10^{10} W and 6.8×10^9 W are seen on February 8 and 13.

Summit thermal flux starts to increase again on February 20, this time ramping up more slowly to a maximum of 1.7×10^{10} W on March 8. Numerous minor spikes are visible, including ones on February 26, March 1, and March 11, which reach 8.2×10^9 W, 1.5×10^{10} W, and 1.3×10^{10} W, respectively.

A small spike of 2.4×10^9 W, with some minor ramping up to this peak, can be seen on March 23. Another anomalous single spike with some minor increases beforehand can be observed in the radiative thermal flux towards the end of April, spiking on April 19 at 4.0×10^9 W.

Number of Hot Pixels

The number of hot pixels (N_{HP}) observed (fig. 3*B*) shows three sequences during which their number increases from a background value of approximately 2 during the eruption to more than 10. The timing of these sequences coincides with the spikes observed in the thermal data. There is also a remarkable correlation between N_{HP} and the reduced displacement values: the number of days that both are elevated is almost equal, whereas the radiative thermal flux increases have longer durations (broader peaks).

The number of hot pixels observed starts to increase on January 13, reaching an initial peak of 18 on January 14. N_{HP} then decreases again only to peak on January 19 at 10. The number of hot pixels does not exceed 2 between January 20 and January 28. After this a sharp increase can be observed, with the series maximum of 37 pixels observed on January 28 at 0615 h UTC. From January 29 onwards N_{HP} remains high, varying between 6 and 30 until February 7. Throughout the rest of February values remain between 1 and 9 pixels per image. March 1 sees an increase to 15 pixels; however, this value then drops to 2 pixels per image until March 5. After this N_{HP} observed increases again, although less sharply than during the previous phase of increases, only to peak at 35 on March 8. A slow decrease after this continues until March 30, after which values do not exceed 6, but most images only show 2 anomalous pixels.

Reduced Displacement

In general the reduced displacement (fig. *3C*) shows a trend similar to those for thermal emissions data and the number of hot pixels observed; there are three distinct intervals when reduced displacement rises above the average eruption background level of 10 cm^2.

Reduced displacement shows a number of minor peaks above background level before the explosions on January 11. On January 11 the peak value reached 417 cm^2. Levels then dropped back to background levels until January 13 when the highest reduced displacement value recorded at station AU13 during the eruption, 1,680 cm^2, was observed. Additional spikes are seen on January 14, but they do not exceed 500 cm^2. Another major spike is seen on January 17, this peaks at 1,034 cm^2. Each of these high reduced displacement values coincides with one of the 9 recorded explosions during this time. Cumulative reduced displacement values (fig. *5A*) show very sharp step-like increases in the values associated with the spikes observed in the 30 minute data.

After January 17 reduced displacement does not rise above 100 cm^2 until January 28. The cumulative values reflect this as a very shallow sloping increase. Four more explosions occurred on January 28; however, reduced displacement peaks at only 395 cm^2. Reduced displacement values remain high even after the explosions cease, peaking on January 30 and 31 and February 5 at 381 cm^2, 597 cm^2, and 536 cm^2,

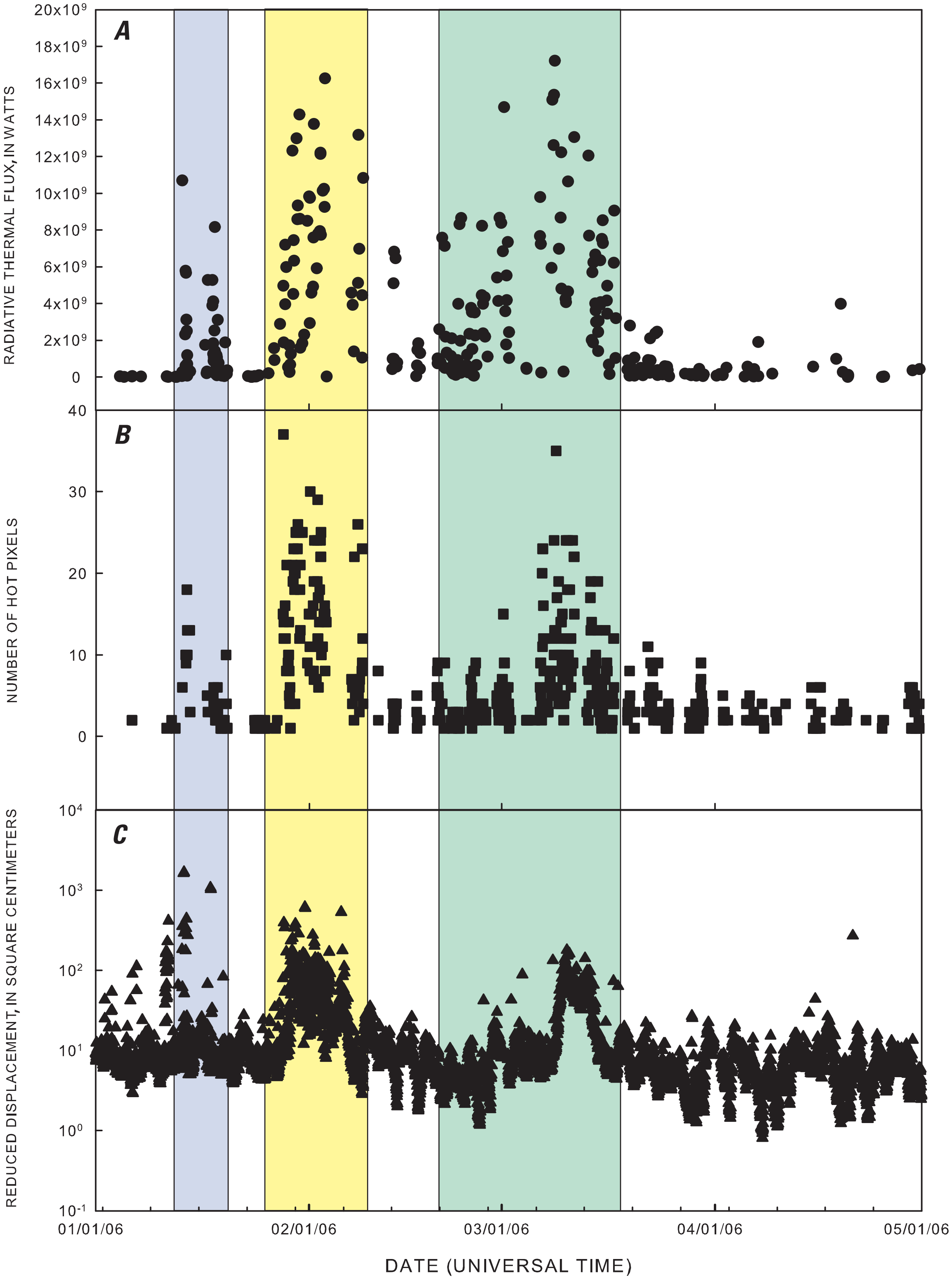

Figure 3. Summary of satellite thermal data collected from Augustine between January 1, 2006, and April 30, 2006. *A*, Summit thermal emissions; *B*, number of hot pixels per satellite image; and *C*, reduced displacement. All three data sets show three contemporaneous peaks. Please note the logarithmic scale on the y-axis of plot *C*. The colored bands indicate the three sequences of increased summit radiative thermal flux.

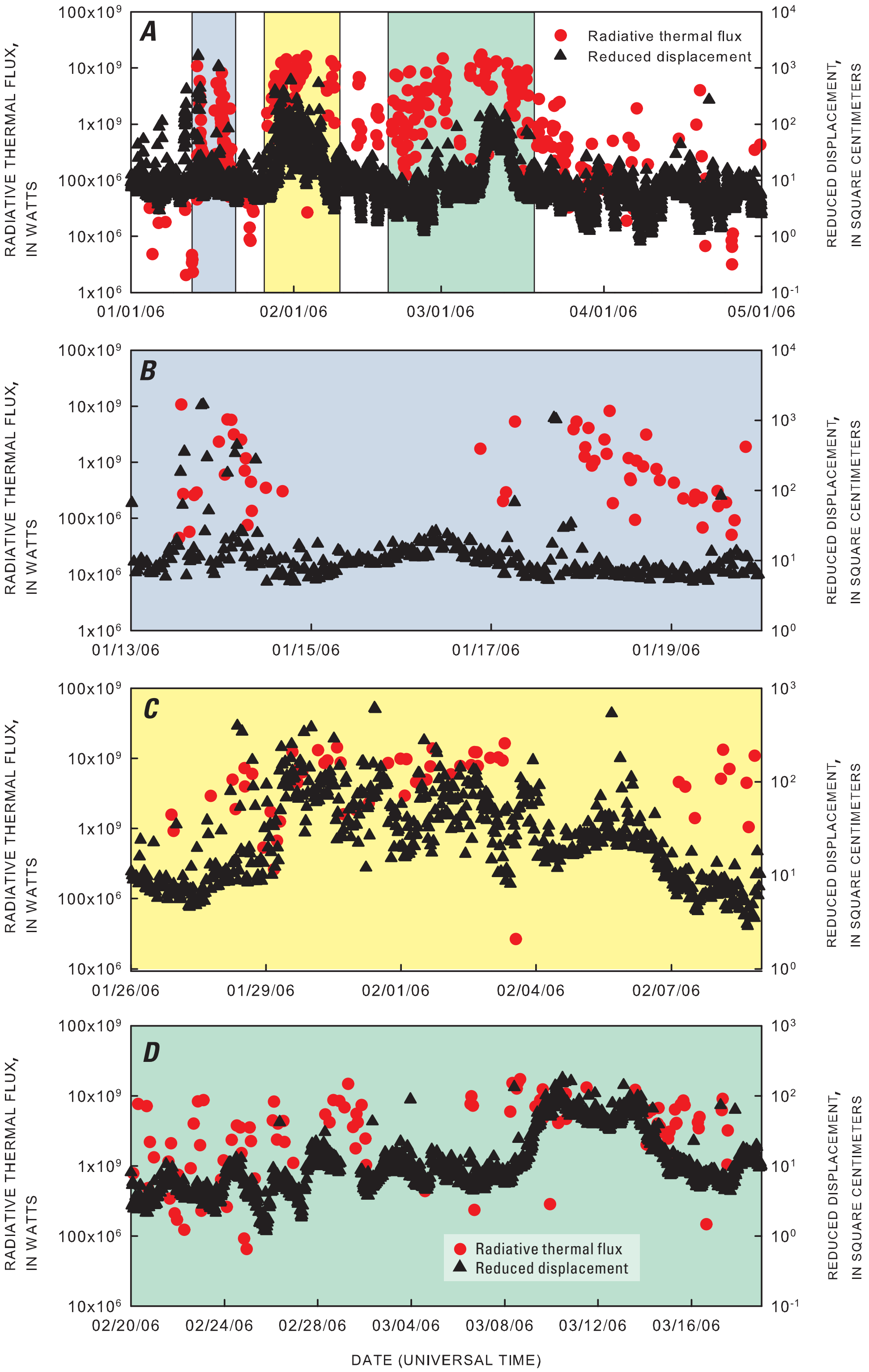

Figure 4. Summit thermal emissions (red) and reduced displacement (black) from Augustine Volcano as observed between January 1, 2006, and April 30, 2006. *A*, January 1, 2006, and April 30, 2006. The graph shows three areas where increases in thermal emissions and reduced displacement coincide. The colored bands indicate the three sequences of increased summit radiative thermal flux. *B*, First sequence of increased thermal emissions. *C*, Second sequence of increased thermal emissions. *D*, Third sequence of increased thermal emissions.

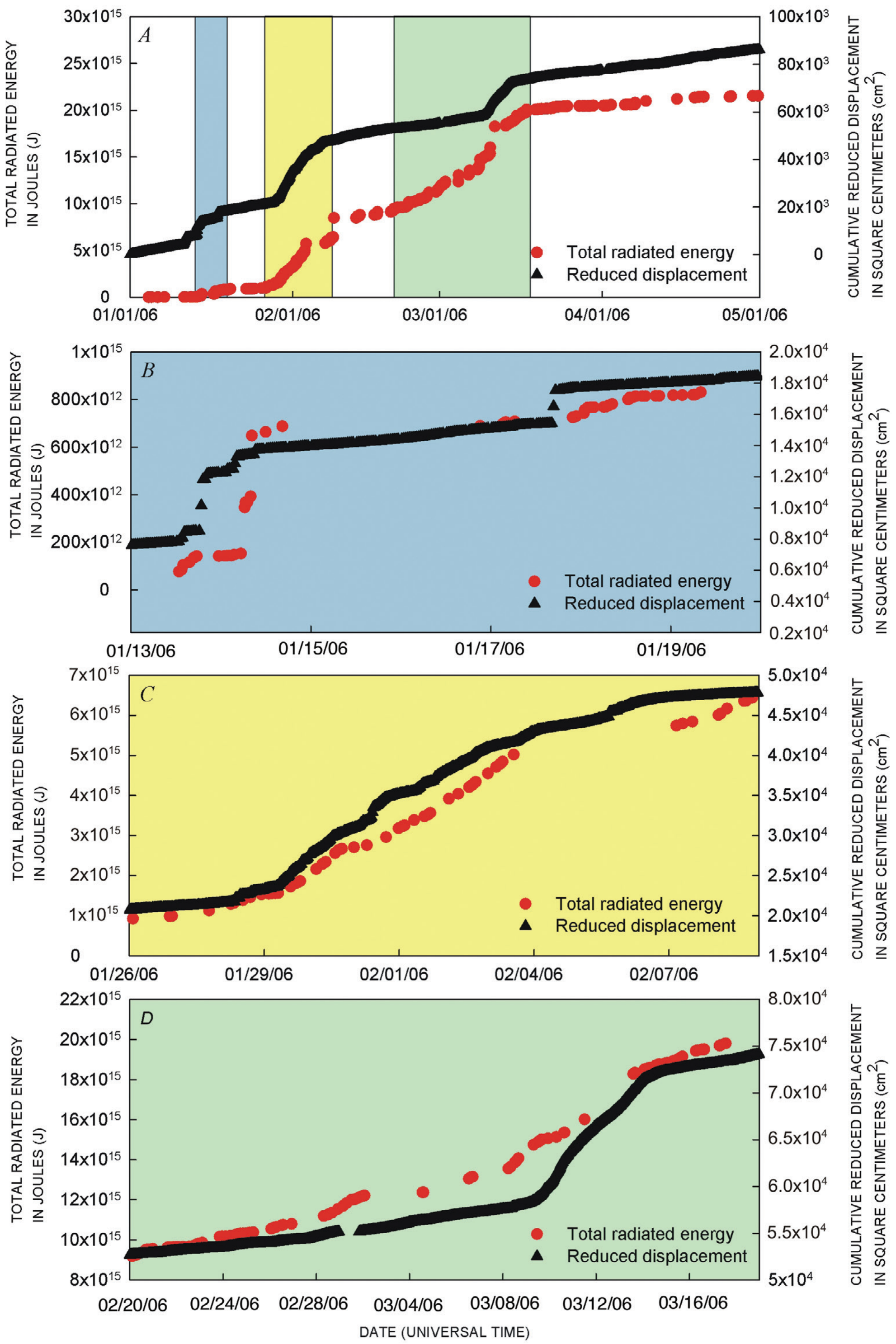

Figure 5. Total thermal energy output (red) and cumulative reduced displacement values (black) at Augustine Volcano between January 1, 2006, and April 30, 2006. *A*, January 1, 2006, until April 30, 2006. The graph shows the three phases as indicated by the colored bands. Note the differences in shape of the graph between phase 1 and 2 and phase 3. *B*, First sequence of increased thermal emissions; increases in thermal energy output postdate increases in reduced displacement. *C*, Second sequence of increased thermal emissions; increases in thermal energy output and reduced displacement occur almost contemporaneously. *D*, Third sequence of increased thermal emissions; increases in thermal energy output precede increases in reduced displacement.

respectively. This is reflected in the cumulative values in a steady increase in the slope.

Between February 7 and March 3 reduced displacement barely rose above background values, even at a maximum not exceeding 50 cm^2. Two minor peaks are visible on February 26 and March 2, but these do not rise to more than 42 cm^2. These background values are represented in the cumulative plot as a shallowly sloping line. Another single peak in the reduced displacement values is observed on March 8, reaching 133 cm^2. After this peak values drop to background levels only to slowly ramp up to a maximum of 179 cm^2 on March 10. Activity remains high, continuously exceeding 40 cm^2 with a minor peak on March 13 of 141 cm^2. The increase visible in the 30-minute reduced displacement values between March 8 and March 14 and is attributed to a continuous seismic tremor. After March 14 activity returns to background levels, manifested in the cumulative plot as a shallowly sloping line.

Combined Analysis of Thermal and Seismic Tremor Data

Two main types of behaviour are observed: (1) radiative thermal flux and reduced displacement have corresponding peaks, or (2) radiative thermal flux and reduced displacement do not have corresponding peaks (fig. 4). In general, peaks in the reduced displacement data and number of hotspots observed are much narrower in time than those of the radiative thermal flux.

The first explosions that occurred on January 11, 2006, did not produce a corresponding thermal signal (fig. 4*A*). The first time span that shows coincident increases in radiative thermal flux and reduced displacement is between January 13 and January 19. During this first peak in thermal output, high reduced displacement values coincide with the 9 recorded explosions (Petersen and others, 2006). The cumulative plot (figs. 5*A*, *B*) clearly shows that the total radiated energy did not increase until after the reduced displacement values had started to increase.

The second period when radiative thermal flux and reduced displacement display corresponding increases is between January 26 and February 6. In this case, the summit thermal flux started to increase coincident with the increase in reduced displacement (fig. 4*C*) and remained high after the reduced displacement has died down. High reduced displacement values do not correspond solely to explosions during this time, suggesting a contribution from other sources such as rockfalls.

During the third peak in summit radiative thermal flux, the rise of total radiated energy preceded increases in reduced displacement (figs. 4*D*, 5*D*). There is a very large jump in the total thermal energy output that coincides with the start of the increase in reduced displacement. Additional corresponding increases in thermal emissions and reduced displacement occur between March 8 and March 14. Reduced displacement increased at this time due to continuous seismic tremor. There are no directly corresponding peaks between the radiative thermal flux and the reduced displacement.

Interpretation

On the basis of the data there appear to be three sequences of increased summit radiative thermal flux—January 13–19 (figs. 4B, *5B*), January 26–February 8 (figs. 4*C*, 5*C*), and February 20–March 18 (figs. 4*D*, 5*D*). All three sequences are also characterized by increased numbers of hot pixels and increased reduced displacement; therefore, each of these three sequences has been interpreted as a period of lava extrusion (table 1). The first two sequences incorporate explosive activity whereas the last sequence is purely effusive. Figure 6 illustrates the changes occurring at the summit during these three sequences. There does not appear to be a correlation between the type of magma erupted (low and high silica andesite) as described in Coombs and others (this volume) and the seismic or thermal activity described here.

Sequence 1 (January 13–19)

The first sequence, which occurred during the explosive phase as identified by Coombs and others (this volume) and Power and Lalla (this volume), was characterized by high average reduced displacement values and low average thermal energy output compared to the other two sequences. However,

Table 1. Characteristics of each of the three sequences of increased thermal emissions.

Sequence	Dates	Duration (days)	Total radiated energy (x 10^{15} J)	Average radiated energy per day (x 10^{14} J)	Number of explosive events	Total reduced displacement (x 10^4 cm^2)	Average reduced displacement/day (x 10^3 cm^2)
1	01/13/06-01/19/06	7	0.82	1.3	7	1.09	1.57
2	01/26/06-02/08/06	14	5.53	4.01	4	2.71	1.98
3	02/20/06-03/18/06	27	10.60	4.18	0	2.14	0.75

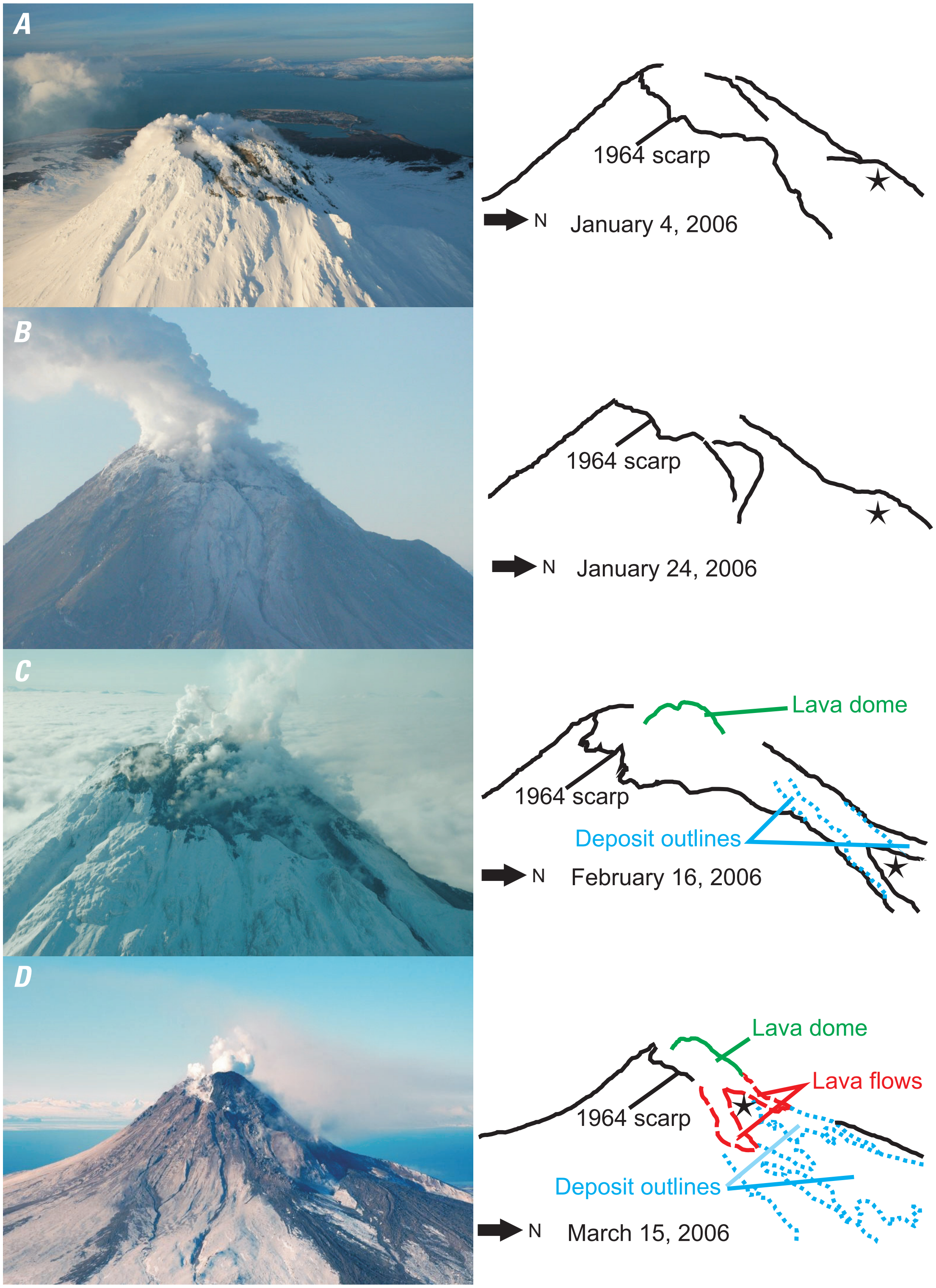

Figure 6. Pictorial time series of changes at the dome throughout the 2006 eruption of Augustine Volcano. The star in each image indicates the location of a feature known as "the Cleaver" for comparison purposes. *A*, The dome prior to magma extrusion, January 4, 2006 (AVO image by M. Coombs). *B*, January 24, 2006 (AVO image by J. Schaefer). *C*, The dome on February 16 after the second sequence of increased radiative thermal flux. (AVO image by R.G. McGimsey). *D*, The dome on March 15 2006, towards the end of the last phase of dome growth (AVO image by T. Plucinski).

the average thermal energy output still significantly exceeded background values. During this sequence a significant amount of mechanical energy was expended without bringing much hot material to the surface. In addition, the fact that increases in reduced displacement preceded increases in thermal energy output further suggests that this sequence was mainly conduit-clearing explosive activity accompanied by intermittent extrusion of lava and numerous pyroclastic flows. The number of hot pixels observed during this sequence did increase, suggesting both extrusion at the summit and the occurrence of pyroclastic flows. During this first sequence the volcano was still inflating, suggesting that the rate of magma accumulation at depth was greater than eruption rates. This interpretation is consistent with visual information obtained on overflights of the volcano; Coombs and others (this volume) reported a small new lava dome on January 16 (fig. 7) and fresh glass shards in ash samples on January 14. However, this small new dome was destroyed on January 17 by an explosion, so there was little change to the summit area compared to before the start of the sequence (figs. 6*A*, *B*). Coombs and others (this volume) list the explosive phase as the most voluminous at 30×10^6 m^3 dense rock equivalent; however, the majority of this was extruded towards the end during January 27–28, which in this study falls into sequence 2. A lot of the material extruded during sequence 1 was in the form of tephra, which being cold is not accounted for in this paper. Large amounts of tephra in the form of ash in a plume could attenuate the thermal signal, although we think that this is not the case here as even during the almost continuous ash emissions observed during the start of sequence 2 (Coombs and others, this volume) saturation of the sensors occurred.

Sequence 2 (January 26–February 8)

The second sequence was contemporaneous with the redefined continuous phase of the eruption (Coombs and others, this volume). High thermal energy output in combination with high reduced displacement values (table 1) during this sequence lead to the interpretation that this was a significant period of lava extrusion and dome growth. The absence of explosive activity after January 28 indicates that an open conduit to the surface had been established. The fact that reduced displacement values remained high after the explosive activity ceased on January 28 suggests that at this time there was also major migration of gas, fluid, and magma occurring within the edifice. This is confirmed by the thermal radiative flux which indicates significant dome growth and high extrusion rates. It is important to note that the high radiative flux is due to a combination of heat from the dome and from pyroclastic deposits, which are an indirect indicator of dome growth. This would suggest that there was significant movement of magma, as was also reflected in the reduced displacement values. The rapid dome growth would have resulted in oversteepening of the dome, resulting in rockfalls. These rockfalls also form a contribution to the reduced displacement signal. Figures 6*B* and *C* illustrate the visual changes that occurred at the summit during this sequence; the new dome is clearly visible, as

Figure 7. Augustine Volcano summit lava dome on January 16, 2006. Arrow points at the dome (AVO image by R.G. McGimsey).

are deposits from pyroclastic and block and ash flows. The emplacement of these deposits is reflected in the significant increase of the number of hot pixels recorded during this sequence. This sequence coincided with a period of deflation (Cervelli and others, this volume), also implying significant growth of the lava dome. It is likely that fresh magma was being erupted at this time, after the explosive behavior of both the first sequence and the January 28 explosions had cleared the vent.

Sequence 3 (February 20–March 18)

The third sequence, which occurred during the so-called hiatus and effusive phase (Coombs and others, this volume), was characterized by (1) high thermal energy output and (2) reduced displacement that was elevated but lower than during earlier eruptive phases (table 1). During the first part of this sequence little seismic energy was generated, suggesting that an open conduit to the surface had been established. The high radiative thermal flux values indicate there was significant extrusion of magma, not just to the dome but also to the two lava flows that formed to the north during this time. The peak thermal emissions during this sequence coincide with a period of deflation, which suggests that extrusion rates were greater than magma supply rates. This significant episode of dome growth would again have resulted in oversteepening of the dome and rockfalls, which are reflected in the reduced displacement signal. The radiative thermal flux peaks at the start of continuous tremor that occurred from March 8 until March 14. This suggests that towards the end of the eruption there was significant migration of gas, fluids, and magma, even though radiative thermal flux declines during this time. The movement of magma is reflected in the GPS data which indicate that at this time the edifice starts to inflate again (Cervelli and others, this volume). Visual observations (figs. 6*C*, *D*) show that during this sequence two short blocky lava flows were extruded and there were additional pyroclastic and block and ash flows. These lava flows and pyroclastic deposits are reflected in the number of hot pixels observed, which increased significantly during this time. Traditionally the end of lava effusion is estimated based on the time of the last image with saturated pixels in band 3; saturation generally occurs due to lava incandescence (Harris and others, 1997). Although this is a valid assumption for basaltic activity, dome growth can occur endogenously, thus not saturating the thermal signal. The last image with saturated pixels at Augustine was recorded on March 15; however, an image close to saturation was observed on March 17. Data were unavailable on March 18, whereas the temperatures observed on March 19 were significantly cooler. This suggested that extrusion of lava ceased between March 15 and 18; after this the thermal flux slowly decreased, indicating cooling of the extruded material. This is consistent with FLIR observations made on March 15 and March 26 (Wessels and others, this volume).

Implications for Future Monitoring

Although remote sensing data are important in the operational monitoring of active and potentially active volcanoes, there is a limit to the amount of information they can provide. To gain the most information regarding a volcanic system, thermal signatures need to be related to other observable activity. This will increase understanding of the processes occurring on the ground. This is particularly important for remote volcanoes that are monitored solely by remote techniques.

Analysis of the 2006 Augustine data has shown that summit thermal emissions and reduced displacement exhibit patterns that can be tied to specific types of volcanic behavior. It was found that high thermal energy output with corresponding high reduced displacement values indicate extrusion of magma whereas low thermal energy output values with correspondingly high reduced displacement values are associated with explosive behavior. The fact that most of the extrusion seemed to generate relatively little mechanical seismic energy suggests that after the explosive activity subsided an open conduit was established.

No reliable exploitable predictive trend that can be extrapolated to other dome building volcanoes has been found in the 2006 eruption Augustine radiative thermal flux. This is probably due to stochastic variations, as well as other factors such as the temporal coverage of the satellite data and local weather conditions.

This study highlights the importance of multiparametric synergistic studies. The joint analysis of both data sets is consistent with three sequences of lava dome extrusion. Interpretations of thermal emissions and correlations with other datasets can be optimized by monitoring thermal emissions at increased spatio-temporal resolution. Although AVHRR can be used to constrain the magnitude of the activity occurring at a volcano, it can not provide detailed data regarding the eruptive state of a volcano unless supplementary datasets (particularly continuous seismic data) are available. However, the temporal coverage in the Alaska-Aleutian-Kamchatka region makes AVHRR an invaluable tool for monitoring the gross behavior of hazardous volcanoes.

Acknowledgments

The authors would like to acknowledge the Alaska Volcano Observatory—a cooperative program between the U.S. Geological Survey Volcano Hazards Program, the Geophysical Institute at the University of Alaska Fairbanks, and the Alaska Division of Geological and Geophysical Surveys. A grant from the Geological Society of London funded Saskia M. van Manen's visit to AVO while the paper was being completed. In addition we would like to thank R. Wessels and M. Patrick for their helpful reviews.

References Cited

Aki, K., Christofferson, C., and Husebye, E.S., 1977, Determination of the three-dimensional seismic structure of the lithosphere: Journal of Geophysical Research, v. 82, p. 277–296.

Aki, K., and Koyanagi, R., 1981, Deep volcanic tremor and magma ascent mechanism under Kilauea, Hawaii: Journal of Geophysical Research, v. 86, no. NB8, p. 7095–7109.

AVO Remote Sensing Team, 2000, Manual for Satellite Monitoring of Volcanoes: Fairbanks, Alaska, Alaska Volcano Observatory, p. 47.

Bailey, J.E., Dean, K.G., Dehn, J., and Webley, P.W., 2010, Integrated satellite observations of the 2006 eruption of Augustine Volcano, *in* Power, J.A., Coombs, M.L., and Freymueller, J.T., eds., The 2006 eruption of Augustine Volcano, Alaska: U.S. Geological Survey Professional Paper 1769 (this volume).

Benoit, J.P., McNutt, S.R., and Barboza, V., 2003, Duration-amplitude distribution of volcanic tremor: Journal of Geophysical Research—Solid Earth, v. 108, no. B3, p. 15.

Cervelli, P.F., Fournier, T.J., Freymueller, J.T., Power, J.A., Lisowski, M., and Pauk, B.A., 2010, Geodetic constraints on magma movement and withdrawal during the 2006 eruption of Augustine Volcano, *in* Power, J.A., Coombs, M.L., and Freymueller, J.T., eds., The 2006 eruption of Augustine Volcano, Alaska: U.S. Geological Survey Professional Paper 1769 (this volume).

Coombs, M.L., Bull, K.F., Vallance, J.W., Schneider, D.J., Thoms, E.E., Wessels, R.L., and McGimsey, R.G., 2010, Timing, distribution, and volume of proximal products of the 2006 eruption of Augustine Volcano, *in* Power, J.A., Coombs, M.L., and Freymueller, J.T., eds., The 2006 eruption of Augustine Volcano, Alaska: U.S. Geological Survey Professional Paper 1769 (this volume).

Dean, K., Servilla, M., Roach, A., Foster, B., and Engle, K., 1998, Satellite monitoring of remote volcanoes improves study efforts in Alaska: Eos (Transactions American Geophysical Union), v. 75, no. 35, p. 413.

Dehn, J., Dean, K., and Engle, K., 2000, Thermal monitoring of North Pacific volcanoes from space: Geology, v. 28, no. 8, p. 755–758.

Dehn, J., Dean, K.G., Engle, K., and Izbekov, P., 2002, Thermal precursors in satellite images of the 1999 eruption of Shishaldin Volcano: Bulletin of Volcanology, v. 64, no. 8, p. 525–534.

Dozier, J., 1981, A method for satellite identification of surface temperature fields of subpixel resolution: Remote Sensing of Environment, v. 11, no. 3, p. 221–229.

Endo, E.T., and Murray, T., 1991, Real-time seismic amplitude measurement (RSAM)—A volcano monitoring and prediction tool: Bulletin of Volcanology, v. 53, no. 7, p. 533–545.

Fehler, M., 1983, Observations of volcanic tremor at Mount St Helens Volcano: Journal of Geophysical Research, v. 88, no. NB4, p. 3476–3484.

Fink, J.H., and Griffiths, R.W., 1998, Morphology, eruption rates, and rheology of lava domes—Insights from laboratory models: Journal of Geophysical Research—Solid Earth, v. 103, no. 1, p. 527–545.

Francis, P., and Rothery, D.A., 2000, Remote sensing of active volcanoes: Annual Review of Earth and Planetary Sciences, v. 28, p. 81–106.

Galindo, I., and Dominguez, T., 2002, Near real-time satellite monitoring during the 1997–2000 activity of Volcan de Colima (Mexico) and its relationship with seismic monitoring: Journal of Volcanology and Geothermal Research, v. 117, no. 1-2, p. 91–104.

Harris, A.J.L., Butterworth, A.L., Carlton, R.W., Downey, I., Miller, P., Navarro, P., and Rothery, D.A., 1997, Low-cost volcano surveillance from space—Case studies from Etna, Krafla, Cerro Negro, Fogo, Lascar and Erebus: Bulletin of Volcanology, v. 59, no. 1, p. 49–64.

Harris, A.J.L., Flynn, L.P., Keszthelyi, L., Mouginis-Mark, P.J., Rowland, S.K., and Resing, J.A., 1998, Calculation of lava effusion rates from Landsat TM data: Bulletin of Volcanology, v. 60, no. 1, p. 52–71.

Jacobs, K.M., and McNutt, S.R., 2010, Using seismic *b*-values to interpret seismicity rates and physical processes during the preeruptive earthquake swarm at Augustine Volcano 2005–2006, *in* Power, J.A., Coombs, M.L., and Freymueller, J.T., eds., The 2006 eruption of Augustine Volcano, Alaska: U.S. Geological Survey Professional Paper 1769 (this volume).

Julian, B.R., 1994, Volcanic tremor: nonlinear excitation by fluid-flow: Journal of Geophysical Research-Solid Earth, v. 99, no. B6, p. 11859–11877.

Lahr, J.C., Chouet, B.A., Stephens, C.D., Power, J.A., and Page, R.A., 1994, Earthquake classification, location and error analysis in a volcanic environment: implications for the magmatic system of the 1989–1990 eruptions of Redoubt volcano, Alaska: Journal of Volcanology and Geothermal Research, v. 62, no. 1–4, p. 137–152.

Larsen, J.F., Nye, C.J., Coombs, M.L., Tilman, M., Izbekov, P., and Cameron, C., 2010, Petrology and geochemistry of the 2006 eruption of Augustine Volcano, *in* Power, J.A., Coombs, M.L., and Freymueller, J.T., eds., The 2006 eruption of Augustine Volcano, Alaska: U.S. Geological Survey Professional Paper 1769 (this volume).

Latter, J.H., 1979, Volcanological observations at Tongariro National Park—2, Types and classification of volcanic earthquakes 1976–1978: New Zealand, Department of Scientific and Industral Research Geophics Division Report no. 150., p. 60.

Lee, C.-W., Lu, Z., Jung, H. S, Won, J.-S., and Dzurisin, D., 2010, Surface deformation of Augustine Volcano, 1992–2005, from multiple-interferogram processing using a refined small baseline subset (SBAS) interferometric synthetic aperture radar (InSAR) approach, *in* Power, J.A.,

Coombs, M.L., and Freymueller, J.T., eds., The 2006 eruption of Augustine Volcano, Alaska: U.S. Geological Survey Professional Paper 1769 (this volume).

Malone, S.D., Boyko, C., and Weaver, C.S., 1983, Seismic precursors to the Mount St. Helens—Eruptions in 1981 and 1982: Science, v. 221, no. 4618, p. 1376–1378.

McNutt, S.R., 1994, Volcanic tremor amplitude correlated with eruption explosivity and its potential use in determining ash hazards to aviation: U.S. Geological Survey Bulletin 2047, p. 377–385.

McNutt, S.R., 2005, Volcanic seismology: Annual Review of Earth and Planetary Sciences, v. 33, p. 461–491.

McNutt, S.R., Tytgat, G., Estes, S.A., and Stihler, S.D., 2010, A parametric study of the January 2006 explosive eruptions of Augustine Volcano, using seismic, infrasonic, and lightning data, *in* Power, J.A., Coombs, M.L., and Freymueller, J.T., eds., The 2006 eruption of Augustine Volcano, Alaska: U.S. Geological Survey Professional Paper 1769 (this volume).

Miller, T.P., and Casadevall, T.J., 1998, Volcanic Ash, Hazards to Aviation, *in* Sigurdsson, H., Houghton, B., McNutt, S.R., Rymer, H., and Stix, J., eds., Encyclopedia of Volcanoes: San Diego, Academic Press, p. 915–930.

Miller, T.P., McGimsey, R.G., Richter, D.H., Riehle, J.R., Nye, C.J., Yount, M.E., and Dumoulin, J.A., 1998, Catalog of the historically active volcanoes of Alaska: U.S. Geological Survey Open-File Report 98-582, p. 104.

Mouginis-Mark, P.J., Crisp, J.A., and Fink, J.H., 2000, Remote sensing of active volcanism: Washington, D.C., American Geophysical Union, 272 p.

Neuberg, J., and O'Gorman, C., 2002, A model of the seismic wavefield in gas-charged magma—Application to Soufriere Hills Volcano, Montserrat, *in* Druitt, T.H., and Kokelaar, B.P., eds., The Eruption of Soufriere Hills Volcano, Montserrat, from 1995 to 1999: Geological Society of London, p. 603–609.

Nye, C.J., Keith, T.E.C., Eichelberger, J.C., Miller, T.P., McNutt, S.R., Moran, S., Schneider, D.J., Dehn, J., and Schaefer, J.R., 2002, The 1999 eruption of Shishaldin Volcano, Alaska—Monitoring a distant eruption: Bulletin of Volcanology, v. 64, no. 8, p. 507–519.

Petersen, T., De Angelis, S., Tytgat, G., and McNutt, S.R., 2006, Local infrasound observations of large ash explosions at Augustine Volcano, Alaska, during January 11–28, 2006: Geophysical Research Letters, v. 33, no. 12, p. doi:10.1029/2006GLO26491.

Power, J.A., Nye, C.J., Coombs, M.L., Wessels, R.L., Cervelli, P.F., Dehn, J., Wallace, K., Freymueller, J.T., and Doukas, M.P., 2006, The Reawakening of Alaska's Augustine Volcano: Eos (Transactions American Geophysical Union), v. 87, no. 37, p. 373, 377.

Power, J.A., and Lalla, D.J., 2010, Seismic observations of Augustine Volcano, 1970–2007, *in* Power, J.A., Coombs, M.L., and Freymueller, J.T., eds., The 2006 eruption of Augustine Volcano, Alaska: U.S. Geological Survey Professional Paper 1769 (this volume).

Roach, A.L., Benoit, J.P., Dean, K.G., and McNutt, S.R., 2001, The combined use of satellite and seismic monitoring during the 1996 eruption of Pavlof volcano, Alaska: Bulletin of Volcanology, v. 62, no. 6-7, p. 385–399.

Rothery, D.A., Francis, P.W., and Wood, C.A., 1988, Volcano monitoring using short wavelength infrared data from satellites: Journal of Geophysical Research, v. 93, no. B7, p. 7993–8008.

Salisbury, J.W., and D'Aria, D.M., 1992, Emissivity of terrestrial materials in the 8-14 µm atmospheric window: Remote Sensing of Environment, v. 42, no. 2, p. 83–106.

Shaw, H.R., 1980, The fracture mechanisms of magma transport from the mantle to the surface, *in* Hargraves, R.B., ed., Physics of Magmatic Processes: Princeton, N.J., Princeton University Press, p. 201–264.

Siebert, L., Beget, J.E., and Glicken, H., 1995, The 1883 and late-prehistoric eruptions of Augustine volcano, Alaska: Journal of Volcanology and Geothermal Research, v. 66, no. 1, p. 367–395.

Wallace, K.L., Neal, C.A., and McGimsey, R.G., 2010, Timing, distribution, and character of tephra fall from the 2005–2006 eruption of Augustine Volcano, *in* Power, J.A., Coombs, M.L., and Freymueller, J.T., eds., The 2006 eruption of Augustine Volcano, Alaska: U.S. Geological Survey Professional Paper 1769 (this volume).

Waythomas, C.F., Watts, P., and Walder, J.S., 2006, Numerical simulation of tsunami generation by cold volcanic mass flows at Augustine Volcano, Alaska: Natural Hazards and Earth System Science, v. 6, no. 5, p. 671–685.

Weaver, C.S., Grant, W.C., Malone, S.D., and Endo, E.T., 1981, Post-May 18 seismicity—Volcanic and tectonic implications, *in* Lipman, P.W., and Mullineaux, D.R., eds., The 1980 Eruptions of Mount St. Helens, Washington: U.S. Geological Survey Professional Paper 1250, p. 109–121.

Webley, P.W., Dean, K.G., Dehn, J., Bailey, J.E., and Peterson, R., 2010, Volcanic-ash dispersion modeling of the 2006 eruption of Augustine Volcano using the Puff model, *in* Power, J.A., Coombs, M.L., and Freymueller, J.T., eds., The 2006 eruption of Augustine Volcano, Alaska: U.S. Geological Survey Professional Paper 1769 (this volume).

Wessels, R.L., Coombs, M.L., Schneider, D.J., Dehn, J., and Ramsey, M.S., 2010, High-resolution satellite and airborne thermal infrared imaging of the 2006 eruption of Augustine Volcano, *in* Power, J.A., Coombs, M.L., and Freymueller, J.T., eds., The 2006 eruption of Augustine Volcano, Alaska: U.S. Geological Survey Professional Paper 1769 (this volume).

Woods, A.W., and Kienle, J., 1994, The dynamics and thermodynamics of volcanic clouds—Theory and observations from the April 15 and April 21, 1990, eruptions of Redoubt volcano, Alaska: Journal of Volcanology and Geothermal Research, v. 62, no. 1–4, p. 273–299.

The 2006 Eruption of Augustine Volcano, Alaska
Power, J.A., Coombs, M.L., and Freymueller, J.T., editors
U.S. Geological Survey Professional Paper 1769

Chapter 24

Imaging Observations of Thermal Emissions from Augustine Volcano Using a Small Astronomical Camera

By Davis D. Sentman[1], Stephen R. McNutt[1], Hans C. Stenbaek-Nielsen[1], Guy Tytgat[2], and Nicole DeRoin[1]

Abstract

Long-exposure visible-light images of Augustine Volcano were obtained using a charge-coupled device (CCD) camera during several nights of the 2006 eruption. The camera was located 105 km away, at Homer, Alaska, yet showed persistent bright emissions from the north flank of the volcano corresponding to steam releases, pyroclastic flows, and rockfalls originating near the summit. The apparent brightness of the emissions substantially exceeded that of the background nighttime scene. The bright signatures in the images are shown to probably be thermal emissions detected near the long-wavelength limit (~1 μm) of the CCD. Modeling of the emissions as a black-body brightness yields an apparent temperature of 400 to 450°C that likely reflects an unresolved combination of emissions from hot ejecta and cooler material.

Introduction

Augustine Volcano is one of a chain of 80 Alaskan/Aleutian volcanoes of which 41 have been historically active (see Power and Lalla, this volume). Augustine, the most active of the Cook Inlet volcanoes, erupted previously in 1812, 1883, 1935, 1964, 1976, and 1986. Volcanic plumes, which are well known to be accompanied by lightning and other atmospheric electrical phenomena (James and others, 2008) have recently been the subject of several studies (McNutt and Davis, 2000; Williams and McNutt, 2005; McNutt and Williams, 2010). Recent volcanic activity has permitted a wide range of new studies to be undertaken, including volcanic lightning (Thomas and others, 2007 this volume), infrasound both locally (see McNutt and others, this volume) and at regional distances (Olson and others, 2006), and low-light nighttime imaging. Preliminary imaging observations of volcanic lightning that were attempted during the Augustine eruption in early 2006 are the subject of this chapter.

An increase in seismic activity beneath the mountain began on April 30, 2005 (see Jacobs and McNutt, this volume), eventually reaching high enough levels to lead to the Alaska Volcano Observatory issuing a color-code change to yellow in November 2005 and, finally, to a series of explosive eruptions beginning in January 2006 (see Power and Lalla, this volume). After the initial explosions on January 11, 13, and 14, a small astronomical camera was deployed with the intention of capturing images of lightning associated with the volcanic plume, such as those detected in radio emissions and described by Thomas and others (this volume). After the camera deployment on January 21, two large explosions occurred on January 27 and 28 that pushed ash plumes to at least 9 km above sea level, but adverse weather prevented observations of these explosions. No other large explosive eruptions occurred during the deployment interval of January 21 to April 15 that may have been accompanied by lightning, and no lightning was detected during our observations. However, faint nocturnal optical emissions associated with steam releases, rockfalls, and pyroclastic flows were unexpectedly observed with the imaging system that were associated with seismic activity measured from instruments on the island. Here we describe the imaging experiment that recorded these new data, with an analysis indicating that the detected emissions are most likely near-infrared (NIR) thermal emissions registered near the upper wavelength sensitivity limit (1.1 μm) of the camera charge-coupled device CCD.

---

[1] Geophysical Institute, 903 Koyukuk Drive, University of Alaska Fairbanks, Fairbanks, AK 99775.

[2] 2IRIS PASSCAL Instrument Center, New Mexico Tech, 100 East Road, Socorro, NM 87801.

Observations

Location and Geometry Relative to Augustine Volcano

Observations were made from the University of Alaska's Homer field site (lat 59.658° N., long 151.652° W.), which sits atop a 200-m-high bluff overlooking Cook Inlet to the west. During clear weather the location permits an unobstructed view of Augustine Volcano (lat 59.367° N., long 153.430° W.) at a distance of ~105 km west-southwestward across the open water of the inlet. Geophysical monitoring stations located on the island were described by DeRoin and others (2007), McNutt and others (this volume), and Power and Lalla (this volume).

Imaging System

The imaging observations were made using a monochrome Starlight Xpress model SXV-M7 16-bits/pixel integrating astronomical camera with a USB 2.0 external interface. The camera uses a 1/2 inch format Sony ICX429ALL monochrome 752- by 582-pixel CCD array, with pixel dimensions 8.6.by 8.3 µm, and a single stage of unregulated Peltier cooling to reduce thermal noise. The EXview Hole Accumulation Diode (HAD) technology used in this class of silicon sensors exhibits an extended wavelength response, with some sensitivity to 1.1 µm. This is in the near-infrared (NIR) wavelength range, slightly beyond the range of human eyesight (0.4–0.7 µm).

Various standard C-mount lenses were tested during the experiment, but the lenses used for most observations were a Tamron 35 mm f/2.4 CCTV (11.0° by 8.2° field of view, 26.6-m/pixel resolution at the observing distance of 105 km to Augustine Island) and a Sigma 135 mm f/1.8 (2.85° by 2.0° field-of-view, 6.89-m/pixel resolution at Augustine Volcano). Images were typically obtained at 10–20 s intervals, with a 5 to 15 s integration times, followed by 5 s image readout to a USB 2.0 disk drive and pause to wait for the next open-shutter synchronization command. Images were saved in 16-bit Flexible Image Transport System (FITS) format, which also recorded the start time of image integration. Camera operations were controlled using a custom script running within Cyanogen Inc.'s MaxIM DL/CCD v4 software operating under Microsoft Windows XP on an IBM notebook computer. The imaging system was connected to the Internet and remotely controlled from Fairbanks by way of Windows Remote Desktop operating over a virtual private network (VPN). System time was maintained accurate to ~100 ms by way of Network Time Protocol (NTP), which was deemed to be sufficiently accurate for correlation with other types of Augustine observations. Image collection commenced shortly after local sundown and continued uninterruptedly until sunrise the following morning, with 2,000 to 3,000 images typically recorded each night. The images were downloaded over the Internet each morning for archiving and offline analysis.

Sample Images

During the early part of the observing campaign (January 21 to February 12, 2006) a 35 mm f/2.4 wide-angle (11.0° by 8.2°) lens was used for the observations. In one scene, recorded the night of February 8 (UTC; fig. 1), Augustine is visible in the lower midcenter, with bright emissions emanating from along its north (right) flank.

Figure 1 records the broadband brightness detected by the monochrome camera at each pixel in the scene and has been colorized to aid interpretation. As shown below, the bright emissions labeled "NIR thermal emissions" appear to originate in the black-body emission spectrum of a hot source and are detectable because of the NIR sensitivity of the CCD. The other features in the image, such as cirrus haze, stars, reflected moonlight from the waters of Cook Inlet, and the foreground moonlit snowfield, provide the context needed to interpret the image, including the ability to spatially locate the source of the thermal emissions relative to Augustine Volcano and meteorological information needed to determine the quality of the viewing conditions (snow, fog, wind, and so on).

During most of the observing campaign (February 13 to April 15, 2006) a 135 mm f/1.8 lens with a narrow field of view (2.85° by 2.0°) was used for the observations. A second sample image, recorded on March 15 shortly after sunset, is shown in figure 2. Here, a steam plume is visible, along with several small thermal emissions near the summit and along the right (north) flank of the volcano.

Because thermal imaging of hot sources is commonly performed using infrared cameras with sensing elements optimized for the the most intense thermal emission wavelengths, we were surprised to see thermal-emissions with a silicon-based CCD. Imagers in satellite systems (Dehn and others, 2002) or in forward looking infrared (FLIR) cameras (Calvari and others, 2005; Harris and others, 2005; Patrick and others, 2007) for detecting the thermal activity associated with terrestrial volcanoes generally utilize non-silicon technology. However, CCD imaging has been used to investigate the active volcanism on Jupiter's moon Io (McEwen and others, 1997), and the CCD camera aboard the Galileo spacecraft was able to detect brightness temperatures down to ~700 K (430°C) in panchromatic images, although 1,000 K (730°C) was a more practical limit. Tighter temperature constraints came from images at different wavelengths, which allowed color temperatures to be computed (McEwen and others, 1998; Radebaugh and others, 2004; Milazzo and others, 2005; Keszthelyi and others, 2007). The coincidence of the transient, bright emission features recorded in our images with the seismic activity simultaneously recorded by instruments located on the volcanic island (DeRoin and others, 2007) strongly suggested that the bright features were thermal emissions

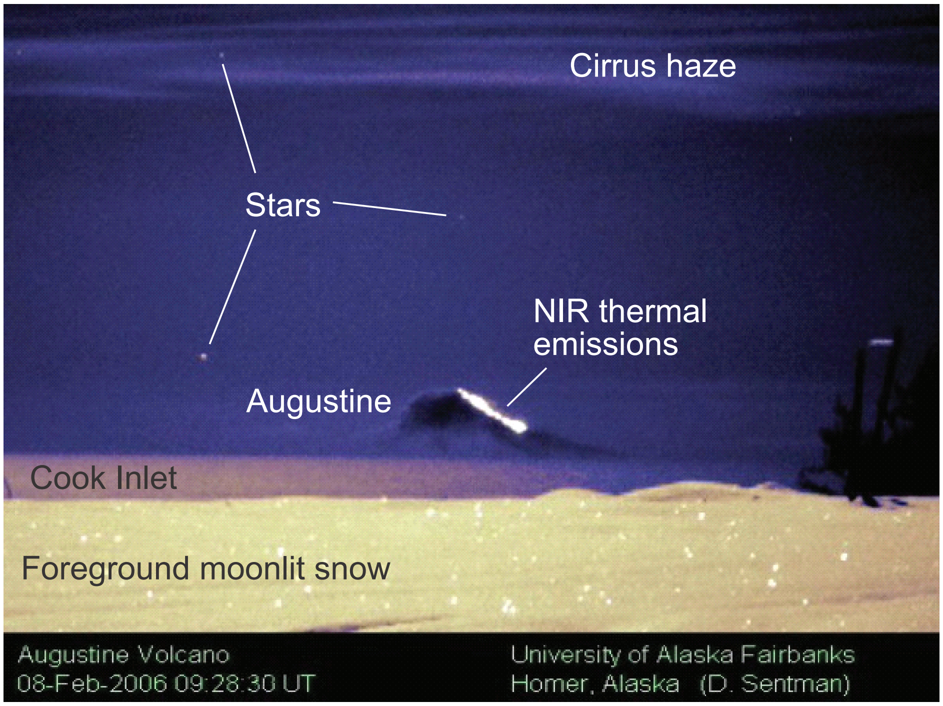

Figure 1. Augustine Volcano as observed the night of February 8, 2006 (UTC), from Homer, Alaska, when a bright moon illuminated the scene, including the steam from left (south) downwind side of the volcano. The image has been contrast stretched and colorized to facilitate feature identification.

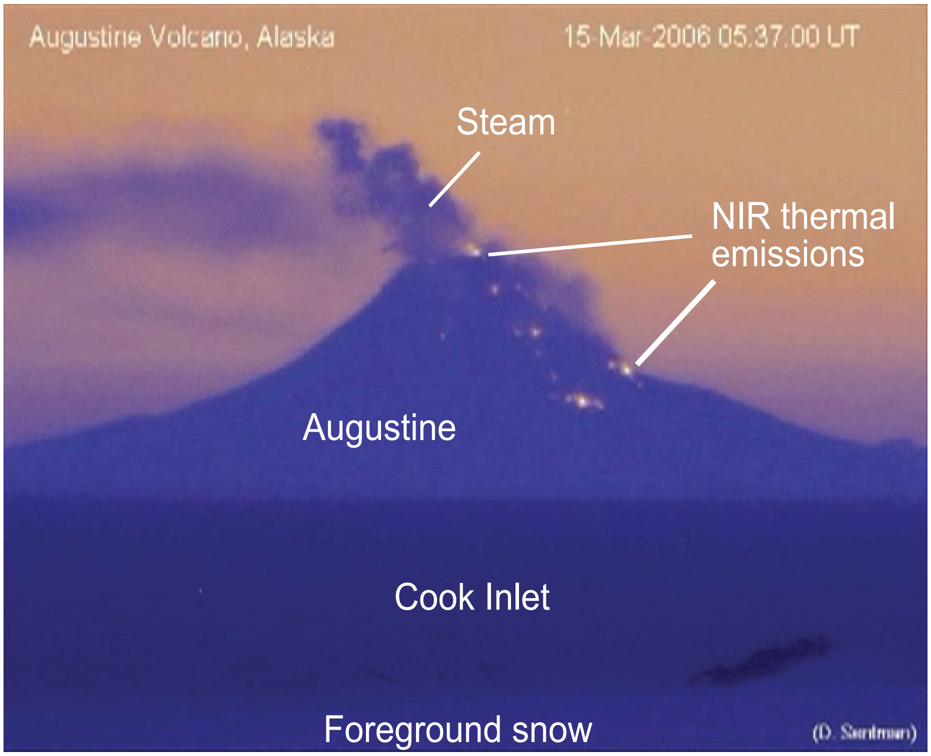

Figure 2. A zoomed image of Augustine obtained on March 15, 2006 (UTC), soon after local sunset using a 135 mm f/1.8 lens. As with figure 1, a false color palette has been used.

from pyroclastic flows or other hot ejecta. This prompted an analysis of the response of the camera to black-body thermal emissions with the aim of obtaining a general understanding of the various factors that enter into the analysis and ascertaining whether such observations might be useful as part of a more general program of volcano monitoring.

Analysis—Detectability of Thermal Emissions

The detectability of thermal emissions from a natural source depends on a combination of the source emission spectrum, the atmospheric radiative transfer characteristics between the source and the observer, the transfer function of the optical train in the sensor system, and the spectral response of the detector. For a silicon CCD detector, the measurements consist of the number of photons from the source emission spectrum that survive atmospheric absorption and losses in the optical train and within the sensor. To be a statistically meaningful observation, photon counts also must significantly exceed internal thermal and read noise associated with the sensor itself. Below we consider these factors in order.

Planck Black-body Emission Spectrum

Assuming that the bright emissions observed are black-body thermal emissions, Wien's displacement law relating the wavelength λ_{max} of peak emissions in the Planck radiation curve and the temperature T is $\lambda_{max}\, T = 2897\ \mu$m K, and so for a nominal temperature $T = 1{,}000$K we have $\lambda_{max} = 2.897\ \mu$m, which falls in the medium-wavelength infrared (MWIR) band. Thus, optical measurements of $\lambda < 1\ \mu$m using silicon sensors fall on the short-wavelength side of the Planck radiation curve. This curve falls off very steeply with decreasing wavelength below the peak of the thermal emissions, so the principal question to be addressed is whether enough energy from this part of the Planck curve intersects the sensor pass band to be detectable.

To understand the relation between camera sensitivity and wavelength in terms of a thermal emission spectrum, it is instructive to review the form of the Planck black-body radiation formula. The Planck formula for the spectral radiance $I(\lambda,T)$ of a black-body radiator in thermal equilibrium is (Rybicki and Lightman, 1979)

$$I(\lambda,T)=\frac{2hc^2}{\lambda^5}\frac{1}{e^{hc/\lambda k_B T}-1}, \tag{1}$$

where λ is the wavelength in meters, T is temperature in Kelvins, $h = 6.63 \times 10^{-34}$ [J s] is Planck's constant, and $k_B = 1.38 \times 10^{-23}$ [J/K] is Boltzmann's constant. For a small wavelength interval $d\,\lambda$, the dimensions of $I\,(\lambda,d\lambda)d\lambda$ are energy flux per unit solid angle (in joules per square meter per second per steradian).

The Planck formula describes the black-body emissions for any temperature and wavelength. Emission contours illustrating the general features of the Planck formula over wavelengths and temperatures of interest to our observations are plotted in figure 3. For the present problem of detecting thermal radiation using silicon-based optical sensors sensitive in the wavelength range 400 to 1100 nm, nominal temperatures of 500 to 1,000°C (773 to 1273 K) for hot volcanic ejecta (Larsen 1929) correspond to a sensor response on the very steep short-wavelength side of the Planck curve. Here, the thermal-emission spectrum changes rapidly with wavelength and so is very sensitively dependent on the temperature. For example, near the range of temperatures under consideration, on the short-wavelength side of the Planck radiation curve a 10-percent decrease in wavelength produces an ~50-percent decrease in the flux density, whereas a 10-percent decrease in absolute temperature (127°C) produces an ~80-percent decrease in the flux density. The emissions therefore depend extremely sensitively on the emission temperature and wavelength, such that small calibration uncertainties are correspondingly magnified.

Imaging-System Response to Thermal Radiation

Imaging sensors detect quantized packets of energy in the form of photons, and so the energy flux at a given wavelength must be converted to to the equivalent photon flux. The energy (in joules) carried by a single photon is $E=h\nu=hc/\lambda$, so the photon flux corresponding to equation 1 is

$$P(\lambda,T)\,d\lambda=(\lambda/hc)I(\lambda,T)d\lambda, \text{ or}$$

$$P(\lambda,T)d\lambda=\frac{2c}{\lambda^4}\frac{1}{e^{hc/\lambda k_B T}-1}d\lambda, \tag{2}$$

where $P(\lambda,T)d\lambda$ has the dimensions of photon flux per unit solid angle, (in protons per square meter per second per steradian).

The photon flux per unit wavelength incident on a pixel is then given by $N(\lambda,T)=P(\lambda,T)\,A\Omega$, where $N(\lambda,T)d\lambda$ is the number of photons per unit time in a small wavelength interval $d\lambda$ crossing a lens aperture of area A (in square meters) from a source region subtending a solid angle Ω (in steradians) as seen by an observer. The product $G=A\Omega$ (in square meters steradian) is the etendue (sometimes referred to as simply "A-omega") of the pixel-lens combination and is an important system element that determines the overall detected signal level.

For a circular lens of diameter D (in meters), the aperture area is $A=\pi D^2/4$ (in square meters). The aperture dimensions are not typically quoted for lenses used in imaging. Instead, this information is indirectly specified through the focal length L

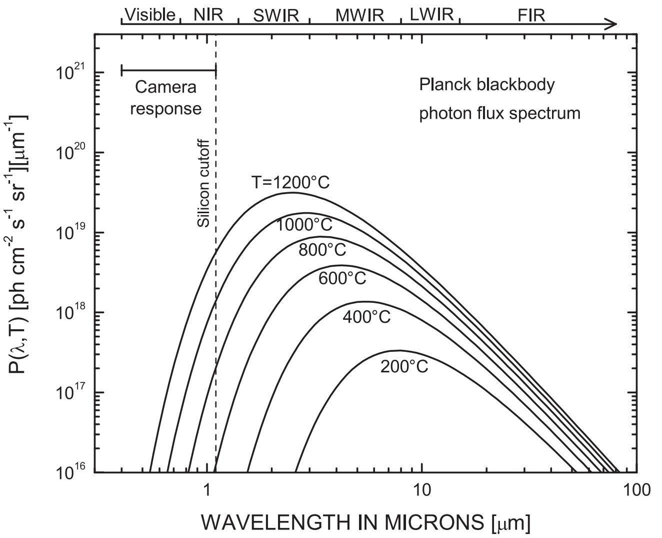

Figure 3. Photon flux spectrum $P(\lambda,T)$ for Planck blackbody radiation, expression (2) of the text. Note that here the unit area is expressed in cm^2 and the spectral density is in terms of mm^{-1}. The labels at the top refer to Near Infrared (NIR), Short Wavelength Infrared (SWIR), Medium Wavelength Infrared (MWIR), Long Wavelength Infrared (LWIR), and Far Infrared (FIR).

(commonly in mm), and the dimensionless speed (*f*-number) of the lens, where $f = L/D$, giving $A = \pi L^2/4f^2$.

For imagers where the focal plane of the lens is the CCD plane, the sensors are the individual pixels, and so the solid angle Ω subtended by the source is that of the field of view as seen by a single pixel. We assume that the source is of uniform brightness over the field of view of the pixel (diffuse-source approximation) and that the field of view is small, so angular apodization effects may be ignored. For a pixel of physical dimensions $p_x \times p_y$ (in square meters), the solid angle viewed by the pixel through a lens of focal length L is approximately $\Omega = p_x p_y / L^2$ (in sterdians).

Expressed in terms of the lens speed and pixel

dimensions, the etendue is $A\Omega = \frac{\pi}{4}\frac{p_x p_y}{f^2}$ (in square meters-steradians).

The number of blackbody photons per unit time incident on a pixel of dimensions $p_x \times p_y$ (in square meters) through a lens of speed f in a small wavelength interval $d\lambda$ centered on wavelength λ may then be written

$$N(\lambda,T)d\lambda = \frac{\pi c}{2\lambda^4}\frac{1}{(e^{hc/\lambda k_B T}-1)}\frac{p_x p_y}{f^2}\,d\lambda \, , \tag{3}$$

which shows that for bare CCD imaging of diffuse sources, large pixel sizes and fast (small *f*-number) lenses are advantageous. We note that as expressed in equation 3, the physical area of the lens aperture, the focal length of the lens, and the solid angle of the source viewed by a single pixel are all implicitly contained in the ratio $p_x p_y / f^2$.

Atmospheric Transmission

The transmission of optical emissions through the atmosphere is highly susceptible to Rayleigh scattering, wavelength-dependent absorption from such atmospheric molecular species as water vapor, and absorption and Mie scattering from rain, snow, fog, aerosols, and dust. For observations through a large number of air masses over long horizontal distances, such as Augustine Volcano from Homer, Alaska, the transmissivity can vary widely and, in the absence of active calibrations that continuously monitor changing conditions, it can only be specified approximately. Typically, good observations were possible only on optically clear nights, but even under ideal conditions noticeable shimmering was evident in many images, possibly owing to refraction effects due to temperature gradients in the boundary layer, as well as to variations in the transmissivity from changing amounts of water vapor and aerosols. The level of shimmer in the images provided a useful gauge of boundary-layer stability.

To estimate the transmissivity of the atmosphere for the given viewing geometry, we computed a nominal transmissivity spectrum $S(\lambda)$ for the NIR wavelength range 0.7-1.5 μm using the U.S. Air Force Moderate Spectral Atmospheric Radiance and Transmittance code (MOSART) program, version 1.7. A horizontal pathlength of 105 km, corresponding to ~15 air masses, was assumed, with clean air and marine boundary-layer conditions. The model parameters used to calculate the atmospheric parameters were pressure, 10,135 Pa; temperature, 257.2 K; water vapor, 1,405 ppm by volume (ppmv) CO_2, 330 ppmv; ozone, 0.018 ppmv, N_2O, 0.32 ppmv and maritime aerosol conditions (from table 35, Subarctic (60° N) latitude winter atmosphere, "MOSART Model Atmospheres," Photon Research Associates, Inc., May 1993.)

The results are plotted in figure 4. Severe atmospheric absorption/attenuation bands are evident near ~0.76, 0.95, and 1.13 μm, and across a wide band of wavelengths 1.3 to 1.5 μm, which correspond to molecular absorption by water, and vary widely, depending on the overall pathlength and the air humidity. A general degradation in transmissivity from Rayleigh scattering occurs at wavelengths shorter than 0.7 μm. We propose that the observed bright emissions are from black-body radiation from hot Augustine ejecta and that the emissions are transmitted to the observation site through the relatively narrow atmospheric transmission band 1.0 to 1.1 μm.

The assumptions used for the transmissivity calculation represent ideal viewing conditions and omit the effects of fog or other types of atmospheric contaminant that frequently compromise viewing. The variability in atmospheric transmissivity due to changing weather conditions is the largest uncertainty in the interpretation of observations. The effective brightness temperature based on these assumptions is of only limited accuracy and should therefore be treated with appropriate caution.

Transmission Through the Optical Elements

Wavelength-dependent losses occur in various elements of the optical system, including the plexiglass window through which the camera viewed Augustine Volcano, and the camera lens. Calibrations were unavailable for these elements, and so a constant transmissivity of 0.5 was assumed for the window/lens combination.

Detector Response

The quantum efficiency as a function of wavelength, $R(\lambda)$, for the Sony ICX429ALL CCD sensor used in the camera is plotted in figure 5, where the normalized scale on the left corresponds to a maximum quantum efficiency of 70 percent at a wavelength of 600 nm. The manufacturer's data sheet does not extend beyond 1,000 nm, as shown, but it may be assumed the response continues to decrease uniformly to zero at the silicon cutoff at 1.1 μm. Most of the scene information in figures 1 and 2, including reflection of moonlight, stars, and evening sky brightness, comes from the main part of the sensitivity curve 400–700 nm. It is believed that the bright thermal emissions are being detected from the far right portion of the curve, at $\lambda > 900$ nm, where the quantum efficiency is very small (<5 percent). In this wavelength region, slight uncertainties in sensitivity can lead to large effects in the observed signal and the inferred temperature.

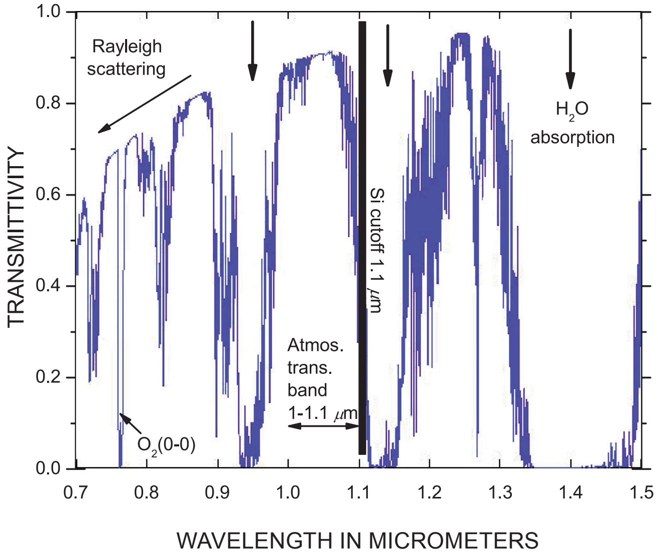

Figure 4. Atmospheric transmissivity versus wavelength 0.7-1.5 µm between Homer and Augustine volcano. The transmissivity was computed using MOSART code, assuming a horizontal path length looking through 15 air masses and marine boundary layer conditions. The heavy arrows at the top indicate major water- absoption bands, and the O_2(0-0) absorption line at 0.762 µm is also evident. The silicon cutoff wavelength at 1.1 µm is indicated. It is seen that there is a narrow transmission band between 1 and 1.1 µm.

End-to-End System Response Versus Black-Body Temperature

The photon counts from a thermal source accumulated over an integration interval of Δt is given by

$$N(T,\Delta t) = \Delta t \int_0^\infty N(\lambda,T) S(\lambda) R(\lambda) L(\lambda)\, d\lambda \ , \tag{4}$$

where, from equation 3, the Planck formula for photon flux is

$$N(\lambda,T) = \frac{\pi c}{2\lambda^4} \frac{1}{(e^{hc/\lambda k_B T} - 1)} \frac{p_x p_y}{f^2} \ , \tag{5}$$

in which we also include the etendue of the system. In equation 4, $S(\lambda)$ is the wavelength-dependent dimensionless atmospheric transmissivity function, and $R(\lambda)$ is the dimensionless CCD response function versus wavelength. Wavelength-dependent losses in the end-to-end transfer function of the optical train, given by $L(\lambda)$, include losses from lenses and filters, as well as from viewing ports such as glass or plexiglass windows. Additional factors that may be important for wide-angle scenes, but do not affect the present narrow field-of-view observations, include the apodization or obliquity factor needed to take into account the reduction in the apparent aperture area and pixel area for scene elements lying off the optical axis, and image vignetting that may occur if the physical size of the CCD detector is smaller than the image formed by the lens.

The photon counts into a pixel are given by the integral in equation 4, where the integrand is composed of four factors. On the short-wavelength side of the Planck spectrum near 1 μm the function $N(\lambda,T)$ increases rapidly with wavelength

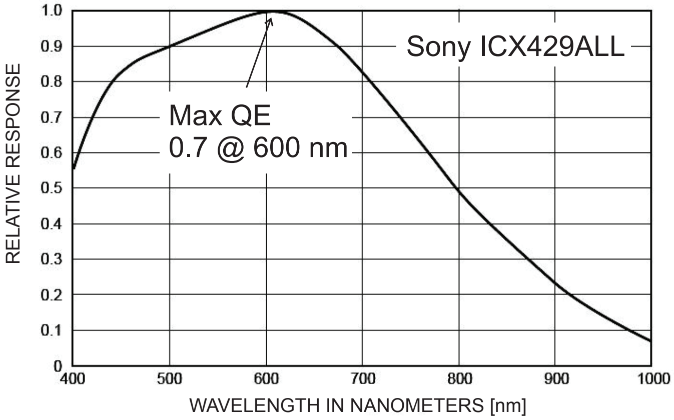

Figure 5. Relative response versus wavelength, normalized to the maximum quantum efficiency (QE), for the Sony model ICX429ALL CCD in the Starlight Xpress camera, per the Sony data sheet.

and temperature, while the sensor response $R(\lambda)$ decreases rapidly in this same wavelength region near the upper limits of its sensitivity. Their product, $P(\lambda,T)\ R(\lambda)$, is highly peaked around a wavelength of $\lambda\sim 1\ \mu$m and overlaps the atmospheric transmission window near 1 μm. The relations among these four factors are sketched in figure 6.

Given the overall uncertainties in the atmospheric transmissivity and detector sensitivity at wavelengths >1 μm, we use a crude approximation to estimate the value of the integral in equation 4. We assume that the integrand is highly peaked about some wavelength λ_0, as sketched in figure 6, that corresponds to transmission band λ_0 ~1 µm in figure 4. We further assume a width of the peaked function of $\Delta\lambda = 0.1$ µm, so that $\Delta\lambda << \lambda_0$. The integral may then be approximated using uniform response functions for $R(\lambda_0)$, $S(\lambda_0)$, and $L(\lambda_0)$. For a fixed geometry, the photon counts in a pixel as a function of source temperature and camera integration time is then

$$N(T,\Delta t) \approx \Delta t\, N(\lambda_0, T) R(\lambda_0) S(\lambda_0) L(\lambda_0) \Delta\lambda. \qquad (6)$$

Inserting system parameters for the present observations, we have: pixel dimensions of the Sony ICX429ALL CCD, 8.3 by 8.6 µm; relative response versus wavelength of the CCD (fig. 5), $\Delta\lambda = 0.1\ \mu$m at $\lambda_0 = 1\ \mu$m; quantum efficiency at $\lambda_0 = 1\ \mu$m is ~0.01; lens speed $f/2.4$; integration time $\Delta t = 5$ s; atmospheric transmissivity $S(\lambda_0) = 0.8$; wavelength-dependent losses $L(\lambda_0) = 0.5$, which includes losses in the lens and from window absorption. With these parameters the expected number of pixel counts versus temperature T [°C] from thermal emissions is plotted in figure 7, where the curve labeled “Ideal emission spectrum” shows the pixel counts versus black-body source temperature for the assumed system parameters, and the dashed curves labeled “50%” and “25%” show the effects of including additional inefficiencies in the system. The recorded pixel counts of ~6,000 correspond to an apparent thermal temperature of 400 to 450°C for bright emissions.

Discussion

The observed emissions are consistent with thermal emissions at an apparent temperature of 400 to 450°C. With the given pixel resolution of several tens of meters at the source, each pixel would likely have included the combined effects of a heterogeneous mixture of hot emitters and cooler surfaces (Keszthelyi and others, 2003).

Although the emissions reported here were invisible to the unaided eye when spot checks were made at the time of the observations, other researchers reported incandescence during the eruption period that was visible through binoculars or when using color digital cameras and telephoto lenses. The human eye is generally insensitive to wavelengths longer than ~700 µm, even under dark-adapted conditions

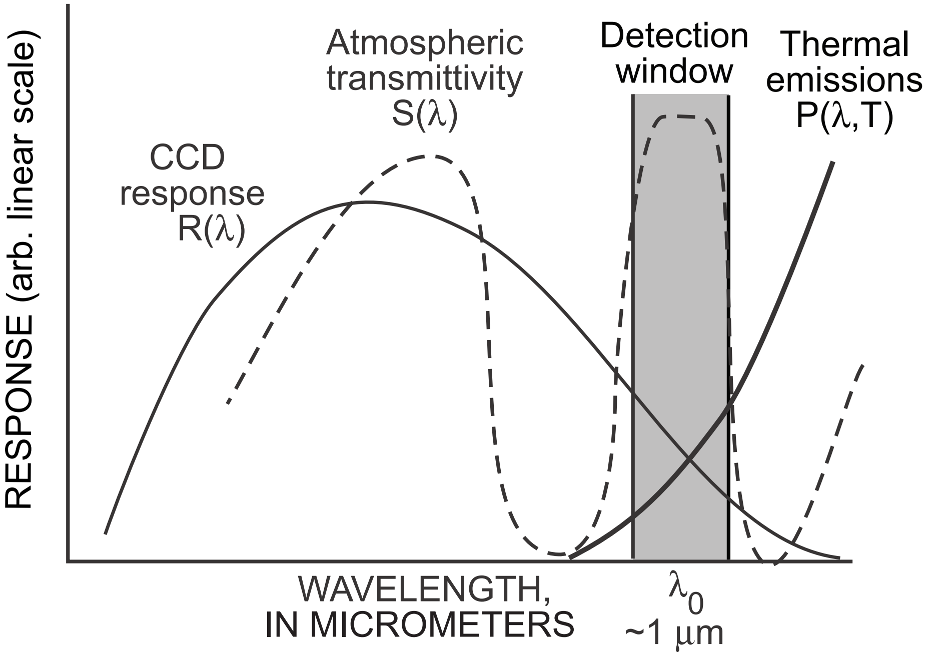

Figure 6. Sketch illustrating the various factors entering into the detectability of thermal emissions. The wavelength scale spans the general range of sensitivity of the camera CCD, from the blue on the left to the CCD cutoff wavelength slightly above 1 µm. The wavelength range believed detected in the images is indicated by the dark rectangle centered on λ_0 ~ 1 µm.

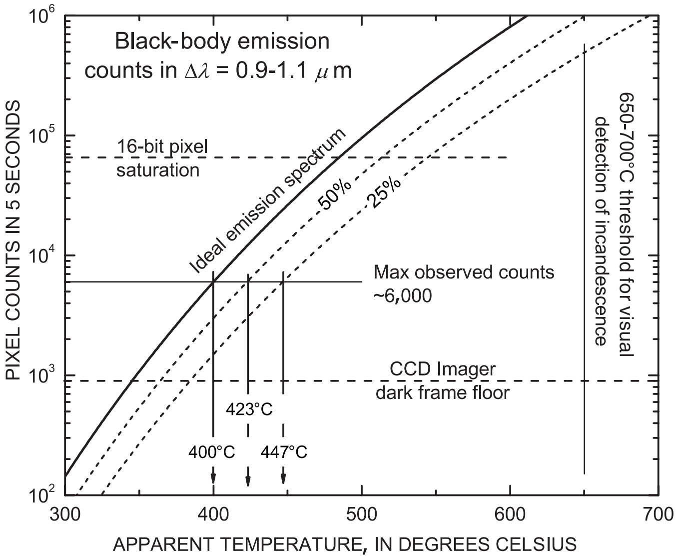

Figure 7. Number of counts in a 5 s integration interval for an f/2.4 lens and the system parameters given in the text. The heavy solid curve corresponds to the number of detector counts assuming an ideal black-body radiator at the given temperature on the abscissa. The effects on apparent temperature from departures from the ideal black-body due to additional inefficiencies beyond those assumed in the calculation are indicated by the dashed lines. The dark frame counts due to CCD thermal noise and bias are ~900 under typical operating conditions. The 16-bit saturation level is also shown. For the measured 6,000-count level shown, the apparent temperatures is ~400 to 450°C. The temperature threshold for visual detection of incandescence is indicated on the right.

(Kinney, 1958), so visual detection of incandescence implied that the temperatures at such times would have been at least ~650 to 700°C (see figure 7). We speculate that images of such visually detectable emissions made using the present camera system would have been much brighter than the examples presented here.

Conclusions

- Hot thermal emissions from steam releases, rockfalls, and pyroclastic flows from Augustine Volcano were detected in February to March 2006 using a small silicon-based astronomical camera. The observations were made over open water from a distance of ~105 km from Augustine.

- The emissions, which were quite bright in the optical images, were generally invisible to the dark-adapted human eye when spot checks were made, although informal observations of incandescence at other times were reported by other observers.

  Analysis of the emission brightness, taking into account the camera sensitivity versus wavelength and atmospheric transmissivity over the long distance between the volcano and the observing site, suggests that the detected emissions occurred within a narrow atmospheric-transmission window near the upper limit of the camera response at ~ 1 μm.

- The observed emissions are consistent with thermal emissions at an apparent temperature of 400 to 450°C. The uncertainties in this calculated apparent temperature are substantial because the observed emissions fall near the extreme limit of the camera response and the atmospheric transmissivity varies near this wavelength.

- Although silicon-based imagers are not optimal for detecting thermal emissions, the observations presented here suggest that they could provide a relatively inexpensive means to monitor some volcanoes for nocturnal thermal emissions.

Acknowledgments

We thank J. Dehn, J. Paskievitch, and K. Dean for useful discussions and D. Wilkinson for use of a camera lens. This work was supported by the Geophysical Institute University of Alaska Fairbanks, the Alaska Volcano Observatory, the U.S. Geological Survey as part of their Volcano Hazards Program, and by the State of Alaska.

References Cited

Calvari, S., Spampinato, L., Lodato, L., Harris, A.J.L., Patrick, M.R., Dehn, J., Burton, M.R., and Andronico, D., 2005, Chronology and complex volcanic processes during the 2002–2003 flank eruption at Stromboli volcano (Italy) reconstructed from direct observations and survey with a handheld infrared camera: Journal of Geophysical Research, v. 110, B02201, doi:10.1029/2004JB003129.

Dehn, J., Dean, K.G., Engle, K., and Izbekov, P., 2002. Thermal precursors in satellite images of the 1999 eruption of Shishaldin Volcano: Bulletin of Volcanology, v. 64, p. 507–519, doi:10.1007/s00445-002-0227-0.

DeRoin, N., McNutt, S.R., Reyes, C., and Sentman, D., 2007, Rockfalls at Augustine Volcano, Alaska—2003–2006: Eos (American Geophysical Union Transactions), v. 88, S43–1038.

Harris, A.J.L., Dehn, J., Patrick, M., Calvari, S., Ripepe, M., and Lodato, L., 2005, Lava effusion rates from handheld thermal infrared imagery; an example from the June 2003 effusive activity at Stromboli: Bulletin of Volcanology, v. 65, p. 101–117, doi: 10.1007/s00445-005-0425-7.

Jacobs, K.M., and McNutt, S.R., 2010, Using seismic *b*-values to interpret seismicity rates and physical processes during the preeruptive earthquake swarm at Augustine Volcano 2005–2006, *in* Power, J.A., Coombs, M.L., and Freymueller, J.T., eds., The 2006 eruption of Augustine Volcano, Alaska: U.S. Geological Survey Professional Paper 1769 (this volume).

James, M.R., Wilson, L., Lane, S.J., Gilbert, J.S., Mather, T.A., Harrison, R.G., and Martin, R.S., 2008, Electrical charging of volcanic plumes: Space Science Reviews, doi:10.1007/s11214-008-9362-z.

Keszthelyi, L., Harris, A.J.L., and Dehn, J., 2003, Observations of the effect of wind on the cooling of active lava flows: Geophysical Research Letters, v. 30, no. 19, p. 1989, doi:10.1029/2003GL017994.

Keszthelyi, L., Jaeger, W., Milazzo, M., Radebaugh, J., Davies, A.G., and Mitchell, K., 2007. New estimates for Io eruption temperatures—implications for the interior: Icarus, v. 192, p. 491–502.

Kinney, J.A.S., 1958, Comparison of scotopic, mesopic, and photopic spectral sensitivity curves: Journal of the Optical Society of America, v. 48, p. 185–190.

Larsen, E.S., 1929, The temperature of magmas: American Mineralogist, v. 14, p. 81–94.

McEwen, A.,Simonelli, D.P., Senske, D.R., Klaasen, K.P., Keszthelyi, L., Johnson, T.V., Geissler, P.E., Carr, M.H., and Belton, M.J.S., 1997. High-temperature hot spots on Io as seen by the Galileo Solid State Imaging (SSI) experiment: Geophysical Research Letters, v. 24, p. 2443–2446.

McEwen, A.S., Keszthelyi, L., Spencer, J.R., Schubert, G., Matson, D.L., Lopes-Gautier, R., Klaasen, K.P. , Johnson, T.V., Head, J.W., Geissler, P., Fagents, S., Davies, A.G., Carr, M.H., Breneman, H.H. and Belton, M.J.S., 1998, High-temperature silicate volcanism on Jupiter's moon Io: Science, v. 281, p. 87–90.

McNutt, S.R., and Davis, C.M., 2000, Lightning associated with the 1992 eruptions of Crater Peak, Mount Spurr Volcano, Alaska: Journal of Volcanology and Geothermal Research, v. 102, p. 45–65.

McNutt, S.R., and Williams, E.R., 2010, Volcanic lightning; global observations and constraints on source mechanisms: Bulletin of Volcanology, v. 72, p. 1153-1167, doi: 10.1007/s00445-010-0393-4.

Milazzo, M.P., Keszthelyi, L., Radebaugh, J., Davies, A.G., Turtle, E.P., Geissler, P., Klaasen, K.P., and McEwen, A.S., 2005, Volcanic activity at Tvashtar Catena, Io: Icarus, v. 179, p. 235–251.

Olson, J.V., Wilson, C.R., McNutt, S.R., and Tytgat, G., 2006, Infrasonic wave observations of the January 2006 Augustine Volcano eruptions: Eos (American Geophysical Union Transaction), v. 87, p. V51C–1685.

Patrick, M.R., Harris, A.J.L., Ripepe, M., Dehn, J., Rothery, D.A., and Calvari, S., 2007, Strombolian explosive styles and source conditions; insights from thermal (FLIR) video: Bulletin of Volcanology, v. 69, no. 7, p. 769–784, doi:10.1007/s00445-006-0107-0.

Power, J.A., and Lalla, D.J., 2010, Seismic observations of Augustine Volcano, 1970–2007, *in* Power, J.A., Coombs, M.L., and Freymueller, J.T., eds., The 2006 eruption of Augustine Volcano, Alaska: U.S. Geological Survey Professional Paper 1769 (this volume).

Radebaugh, J., McEwen, A.S., Milazzo, M.P., Keszthelyi, L.P., Davies, A.G., Turtle, E.P., and Dawson, D.D. , 2004, Observations and temperatures of Io's Pele Patera from Cassini and Galileo spacecraft images: Icarus, v. 169, p. 65–79.

Rybicki, G.B., and Lightman, A.P., 1979: Radiative processes in astrophysics: New York, Wiley-Interscience, 382 p.

Thomas, R.J., Krehbiel, P.R., Rison, W., Edens, H.E., Aulich, G.D., Winn, W.P., McNutt, S.R., Tytgat, G. and Clark, E. , 2007, Electrical activity during the 2006 Mount St. Augustine volcanic eruptions: Science, v. 315, no. 5815, p. 1097, doi:1126/science.1136091.

Thomas, R.J., McNutt, S.R., Krehbiel, P.R., Rison, W., Aulich, G., Edens, H.E., Tytgat, G, and Clark, E., 2010, Lightning and electrical activity during the 2006 eruption of Augustine Volcano, *in* Power, J.A., Coombs, M.L., and Freymueller, J.T., eds., The 2006 eruption of Augustine Volcano, Alaska: U.S. Geological Survey Professional Paper 1769 (this volume).

Williams, E.R., and McNutt, S.R., 2005, Total water contents in volcanic eruption clouds and implications for electrification and lightning, chap. 6 *of* Pontikis, C., ed., Recent progress in lightning physics: Kerala, India, Research Signpost Publishing, p. 81–93.

This page intentionally left blank

The 2006 Eruption of Augustine Volcano, Alaska
Power, J.A., Coombs, M.L., and Freymueller, J.T., editors
U.S. Geological Survey Professional Paper 1769

Chapter 25

Lightning and Electrical Activity during the 2006 Eruption of Augustine Volcano

By Ronald J. Thomas[1], Stephen R. McNutt[2], Paul R. Krehbiel[3], William Rison[1], Grayden Aulich[3], Harald E. Edens[3], Guy Tytgat[4], and Edward Clark[2]

Abstract

Lightning and other electrical activity were measured during the 2006 eruption of Augustine Volcano. We found two phases of the activity, the explosive phase corresponding to the explosive eruptions and the plume phase. We classified the lightning into three types, vent discharges, near-vent lightning, and plume lightning. Vent discharges are small, 10 to 100 m sparks, that occur at rate as great as 10,000 s^{-1} at the mouth of the volcano during the energetic explosive eruptions. The vent discharges were observed six different times. Near-vent lightning appears to develop upward from the volcanic cone into the developing column during explosions. This lightning is small, in the range of 1 to 7 km, and short, 0.01 to 0.1 s. The behavior of the near-vent lightning indicates an overall positive charge in the ejecta. The plume lightning resembled intracloud thunderstorm lightning. Often it was branched, spanned more than 10 km, and lasted more than 0.5 s.

Introduction

Throughout recorded history, spectacular lightning discharges have been observed in and from the ash clouds produced by large volcanic eruptions. Lightning has also been observed and photographed during much smaller eruptive activity. Early investigations of volcanic lightning were made during the Surtsey and Heimay eruptions in Iceland in 1963 and 1973 (Anderson and others, 1965, Brook and others, 1974). Lightning associated with eruption of Redoubt in 1989–90 (Hoblitt, 1994) and Spurr 1992 (McNutt and Davis, 2000) occurred in the ash cloud beginning 5 or more minutes after the explosion onsets. (This appears to represent only one type of volcanic lightning, referred to below as plume lightning.) The worldwide observations of volcanic lightning have recently been tabulated, encompassing more than 200 cases associated with 74 volcanoes (Mather and Harrison, 2006; McNutt and Williams, unpublished data), showing that lightning occurs for volcanoes with a wide variety of magma compositions, eruption types, and ash column heights. However, despite increasing interest and additional studies in recent years (reviewed in Mather and Harrison, 2006), volcanic lightning continues to be poorly understood.

Volcanic lightning is at the same time spectacular, dangerous, and interesting. It presents danger that most people close to the eruption will not be expecting. Its interests to science include its roll in the origin of life, similarities and difference to thunderstorms, and why the plume becomes electrified. Observing and monitoring lightning during an eruption opens many possibilities. First it could show where there may be danger to people and where fires could be started. The measurement techniques that we present, can detect lightning at a safe distance even when there is bad weather and visual observations are not possible. Thus, the occurrence of an eruption could be confirmed in remote locations or poor conditions if lightning signals were detected. The location of lightning in the drifting plume would show the location of the ash plume. Measurement of lightning and electrical activity can be another tool to help understand the processes occurring during the eruption.

Here we report observations of lightning during the 2006 eruption of Augustine Volcano, Alaska (Thomas and others, 2007), that have provided a much more detailed picture of volcanic lightning than heretofore available. The observations were obtained with a portable lightning mapping system that was recently developed at New Mexico Tech (NMT),

---

[1] Electrical Engineering Department, New Mexico Tech, Socorro, NM 87801.

[2] Alaska Volcano Observatory, Geophysical Institute, University of Alaska Fairbanks, 903 Koyukuk Drive, Fairbanks, AK 99775.

[3] Lagmuir Laboratory, New Mexico Tech, Socorro, NM 87601.

[4] IRIS Passcal Instrument Center, New Mexcio Tech, 100 East Road, Socorro, NM 87801.

and was deployed in cooperation with the Alaska Volcano Observatory (AVO).

We have designed and built a lightning mapping system which produces three-dimensional images of lightning discharges by measuring the arrival time of RF (radio frequency) radiation, at multiple ground stations (Rison and others, 1999; Thomas and others, 2004). The radiation is produced as the lightning channels form or are reionized. To make the system more versatile, we recently built a portable version for rapid deployment in field operations. In addition to studies of thunderstorm lightning, the portable version was built in anticipation of using it for studies of volcanic lightning. A few weeks after the construction of the first portable stations (December 2005), the recent eruption of Augustine began. After consultations about logistics between the New Mexico and Alaska groups, we moved quickly to deploy two stations to observe lightning from possible further explosive eruptions. These stations were installed on the east coast of Cook Inlet near Homer and Anchor Point (see fig. 1). Although more stations surrounding and closer to the volcano were desirable, the remoteness, the lack of power, and the winter conditions made this impossible in the short term. Installation of the two stations was completed only hours before the series of explosive eruptions that began on 27 January, 2006. In this paper, we report on the lightning observations made during these explosions.

In February of 2006, we installed two battery powered stations in remote locations, one on Augustine's informally named West Island (about 7 km from the vent) and one at Oil Point (520 m above Cook Inlet and about 34 km north of the volcano; see fig. 1). The stations operated automatically and unattended on battery power for a period of 1 to 1.5 months. Only a small amount of useful data from West Island was recorded, because the volcano went into a dome-building phase, with substantially decreased explosive activity. Also, due to an electronics problem, much of the data from the West Island station was unusable. On a few occasions during the effusive phase of the eruption, the remote systems recorded signals that were correlated to the signals received at the

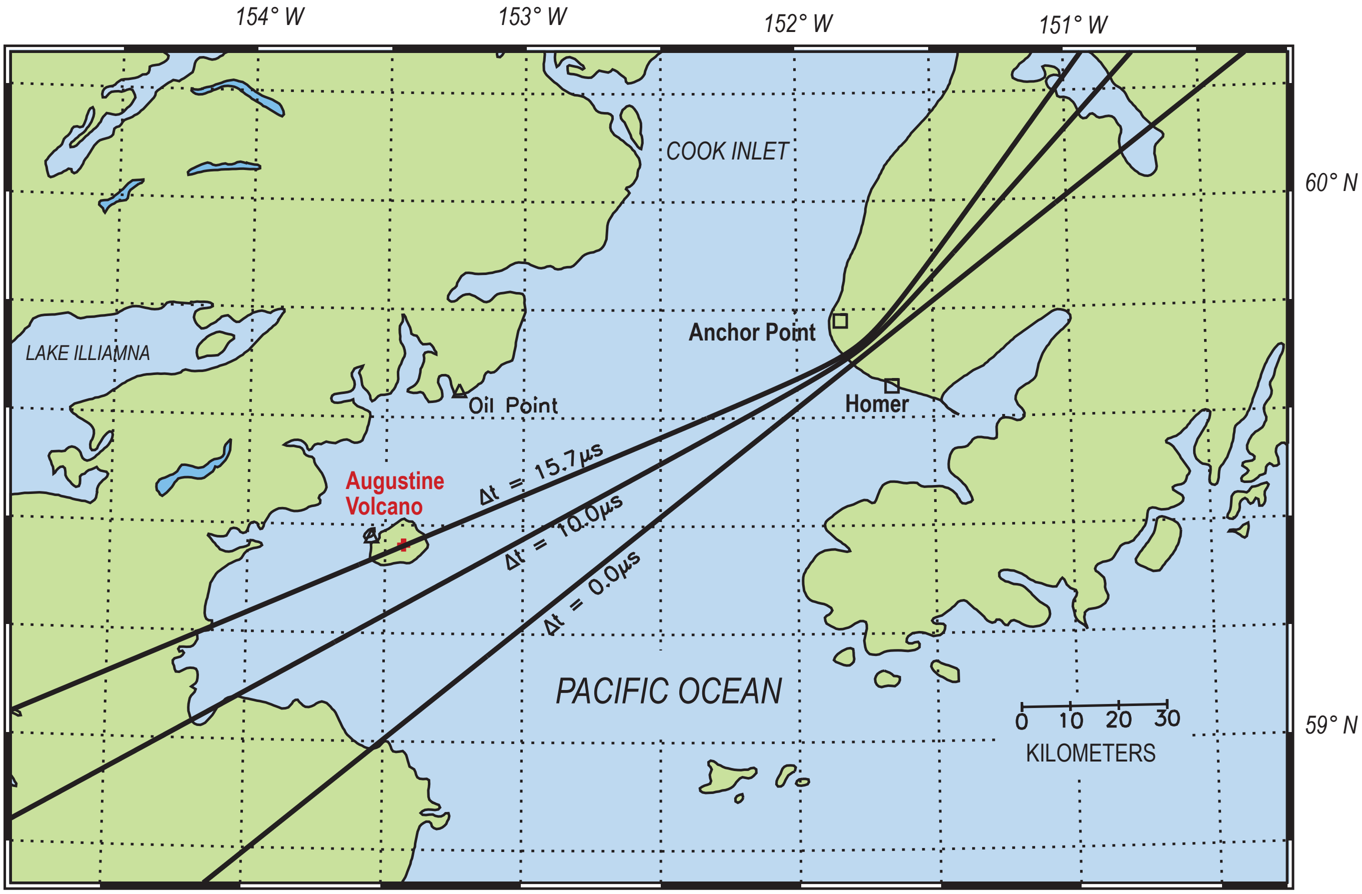

Figure 1. Map of the area surrounding Augustine Volcano and the locations of the lightning mapping stations. Anchor Point and Homer stations (squares) operated from January 27 to May 12, 2006. Oil Point station (triangle) operated from February 20 to March 16 and West Island (Augustine) station (triangle) operated from February 18 to April 2. The three hyperbola show the possible source location for different arrival time differences for the Homer and Anchor Point station pair.

Homer and Oil Point stations. These observations are also reported in this paper.

Other Observations of Lightning January 2006

Before the installation of the NMT Lightning Mapping Array (LMA) stations, lightning was observed accompanying 6 of the 9 explosions from January 11–17, 2006 (table 1). The data are from quite varied sources. A lightning detection system operated by the Bureau of Land Management (BLM) in central Alaska recorded two flashes during the January 13 explosions at 0424 AKST (1324 UTC) and one flash during the January 14 explosion at 0014 AKST (0914 UTC). As the primary use of the BLM system is to monitor summertime cloud-to-ground lightning, which may start forest fires, winter operation is not a high priority. Only four stations of the nine station network were operational during the Augustine eruption (T. Weatherby, written commun., 2006). Figure 3 of McNutt and Davis (2000) shows the locations of the BLM stations. The January 13 lightning flashes were both of positive polarity (as they transferred positive charge to ground) and occurred 10 and 12 minutes after the beginning of the explosion. This time difference is similar to intervals during the Redoubt eruption in 1990 (Hoblitt, 1994). One flash was cloud to ground (CG) and the other intracloud (IC) (T. Weatherby, written commun., 2006). The January 14 flash occurred 8 minutes after the explosion onset and was a CG flash with negative polarity. This event was also recorded on five seismic stations as an irregular spike, due to the interaction between the broadband lightning pulse and the seismic system electronics. The three Augustine flashes were the only lightning flashes recorded by the BLM system in all of Alaska for the first 2 weeks of January 2006.

The explosion on January 14 at 0847 AKST (1747 UTC) was observed by airline pilots flying 100 to 150 miles to the west. They state that they saw the eruption column rising “totally vertically, visibly growing as we watch it, probably 10–15 thousand feet above us now, static lightning discharges within the cloud, cloud is growing very fast…”

One other explosion on January 13 had lightning witnessed by ground observers within the radio station KDLG Dillingham listening area. We infer this to be the 1122 AKST (2022 UTC) explosion or the January 13 1858 AKST (January14 0358 UTC) explosion. Viewing conditions were favorable for both these explosions. The other report is from the January 17 explosion at 0758 AKST (1658 UTC).

During the explosions of January 27–29 there were no visual reports of lightning or detections by the BLM network.

Table 1. Observations of lightning during the Augustine Volcano, January 11-28, 2006, explosive eruption events.

[CG, cloud-to-ground; IC, Intarcloud; BLM, Bureau of Land Management; PIREP, Pilot Report; NMT, New Mexico Tech]

Event			Lightning	Data source	Plume Height (km)	Comments
Number	Date, 2006	Onset UT				
1	11-Jan	1344	No	-	6.5	
2	11-Jan	1412	No	-	10.2	
3	13-Jan	1324	Yes	BLM	10.2	2 flashes, positive polarity, 10 and 12 min after eruption onset, CG and IC
4	13-Jan	1747	Yes	PIREP	10.2	IC, viewed from aircraft 100-150 mi to the west
5	13-Jan	2022	Yes	Ground obs	10.5	telephone call from radio station KDLG Dillingham
6	14-Jan	0140	No	-	10.5	
7	14-Jan	0358	Yes	?	13.5	
8	14-Jan	0914	Yes	BLM	10.2	1 flash, negative polarity, 8 min after eruption onset, CG; also recorded on 5 seismic station
9	17-Jan	1658	Yes	?	13.5	
10	28-Jan	0524	Yes	NMT	10.5	365 flashes; 2 flashes showed up on pressure sensor at station AUE as interference with the pressure sensor electronics
11	28-Jan	0837	Yes	NMT	3.8	1 flash
12	28-Jan	1104	Yes	NMT	7.2	28 flashes
13	28-Jan	1642	Yes	NMT	7.0	6 flashes

Poor weather conditions at these times made for unfavorable viewing conditions.

Measurement Technique

The NMT LMA detects VHF (63 MHz) radio signals from electrical impulses that are produced by lightning and other sources. The arrival times of the signals are measured with 40 ns accuracy using a timing signal from a GPS receiver. With this timing accuracy a multistation LMA can determine the source location with 10-m horizontal error and 30-m vertical error, depending on the geometry of the station and source locations (Thomas and others, 2004). The system is a time-of-arrival system similar to the ones used to locate the source of seismic signals, except the radio signals travel at the speed of light in straight lines (as with light a clear path is needed between the source and receiver; however clouds will not block the signal but solid objects will). A system using eight or more stations spaced 10 to 20 km apart (fig. 2) can locate several thousand sources (in 3 dimensions; 3D) for a single lightning flash. Impulsive RF radiation is emitted as a lightning channel develops. A lightning channel develops in a bipolar manner, with negative breakdown at one end of the channel and positive breakdown at the other (Behnke and others, 2005). The radiation from the positive end of the channel is much weaker than that from the negative end, and the LMA detects primarily the breakdown associated with the extension of the negative end of the channel.

The LMA digitizes the log of the received power at a 25 MHz rate. If the peak amplitude in a short time interval exceeds the local noise level, the time and 8-bit amplitude of the strongest source is recorded. In this experiment this time interval (time window) was either 80 µs or 10 µs. Also, the number of events above the local noise threshold is recorded. This above threshold value will be between 1 and 2,000, with high value indicating continuous breakdown and a small value indicating that only one or a few impulsive events occurred in the 80 µs interval. The threshold is adjusted automatically so that during quiet periods background noise triggers the system about 10 percent of the time. If a source produces radiation strong enough to be detected by six or more stations, the 3D location of the source can be determined.

Figure 3 shows the LMA image of a lightning flash with a complex structure that is lower in altitude (2 to 6 km) and lasts a little longer (about 1 second) than a more typical discharge (6 to 10 km altitude with a duration of about half a second). This flash was selected because its characteristics are similar to the lightning in the Augustine plume after the initial explosion on January 27.

Due to time constraints and logistics, we were able to install only two receiving stations for the initial Augustine observations. The stations were located about 17.1 km apart and about 100 km north-northeast the volcano (see fig. 1). The line joining the stations was close to perpendicular to the direction to Augustine. The southern station was at the AVO field station north of Homer and the northern station was at the Anchor Point Public Library. The receiving antenna at the Homer station was located on the edge of a high (220 m) bluff overlooking Cook Inlet, with direct line of sight to Augustine. The Anchor Point station was located at 125 m altitude about 1.5 km inland from the coast and did not have a direct view of Augustine.

With this system we could determine the azimuthal direction to the radio source. Under these conditions it is a good approximation to assume that the arriving radio wave is a plane wave as shown in figure 4. The azimuthal direction θ to the source is given by $\sin(\theta) = c\,T_{13} / D$, where T_{13} is the difference in arrival times at the two stations, c is the speed of light, and D is the separation distance of the stations. An arrival time difference of 15.7 µs corresponded to signals arriving from the direction of Augustine's summit; signals originating in a southward direction from Augustine had decreased time differences as indicated in figure 1. The 40 ns resolution of the system

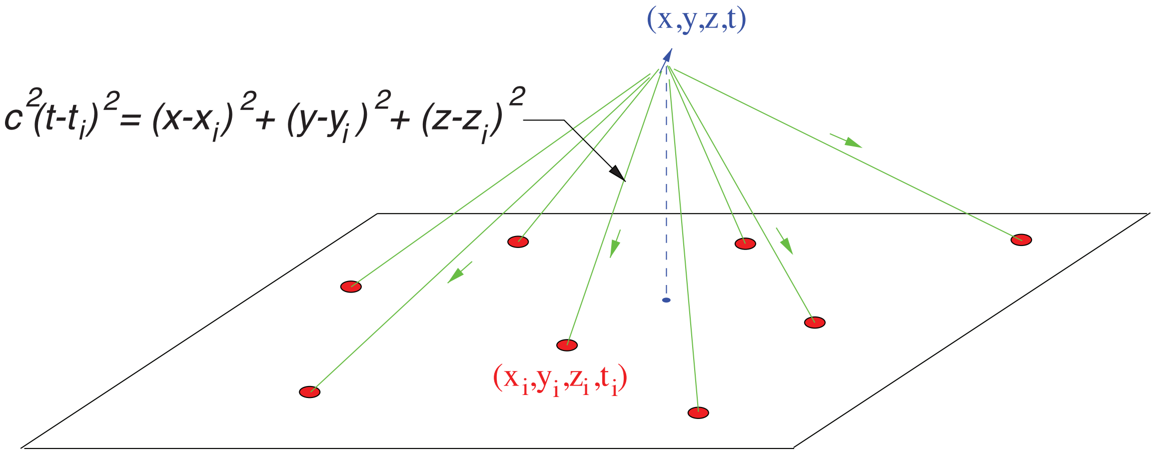

Figure 2. Diagram showing how lightning is located. The multiple station lightning mapping array locates the position of impulsive radio sources in three dimensions by carefully measuring the arrival times at each station.

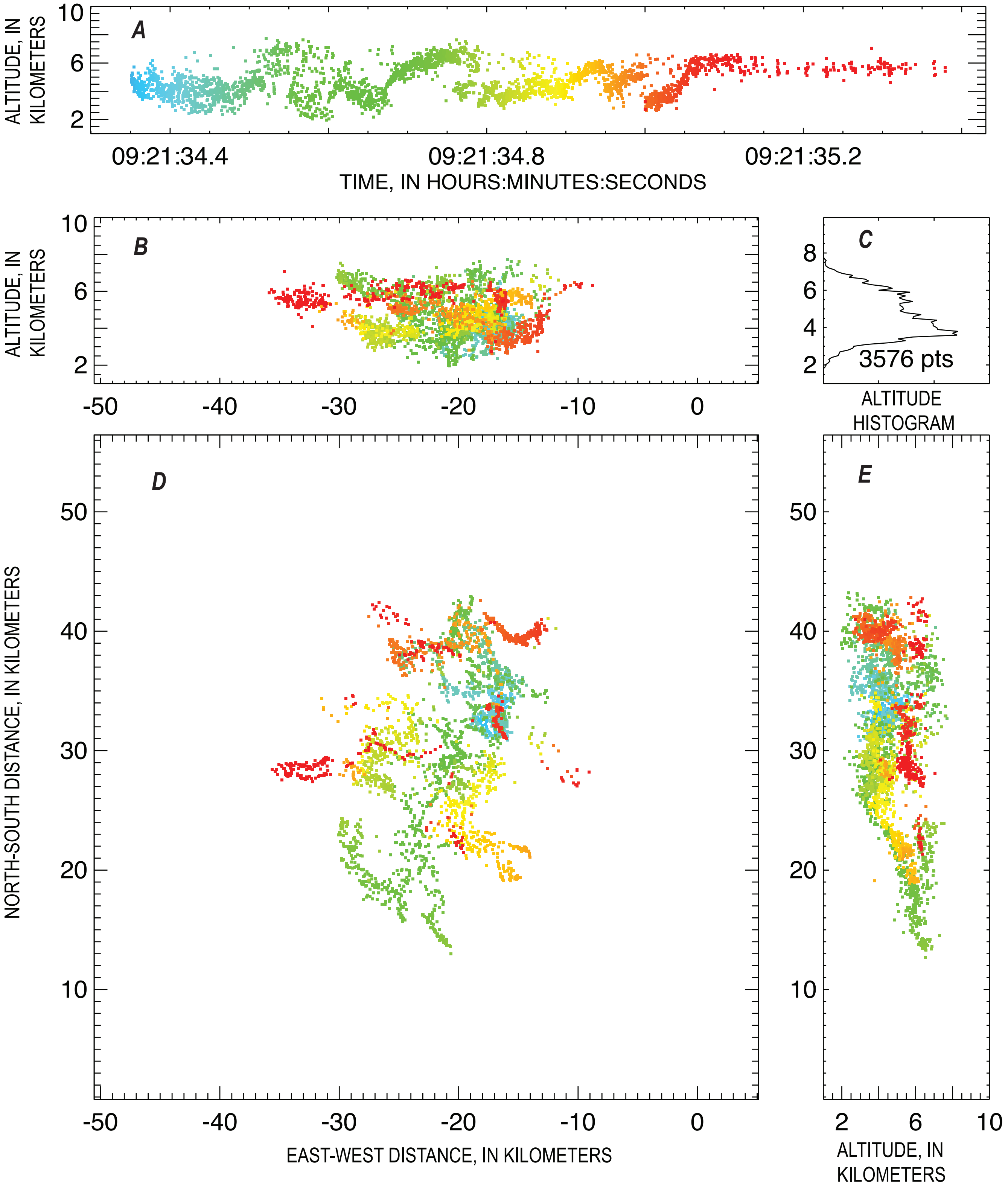

Figure 3. Three dimensional (3D) views of a low altitude intracloud lightning flash observed in eastern Colorado by the lightning mapping array (LMA). This flash was between a negative layer above 6 km and a positive layer below 6 km. The flash did not go to ground. *D* shows a plan view. Colors show the time development, beginning with blue and ending with red. *B* and *E* are vertical projections showing the altitude development. Part A shows the altitude versus time. *C* is an altitude histogram.

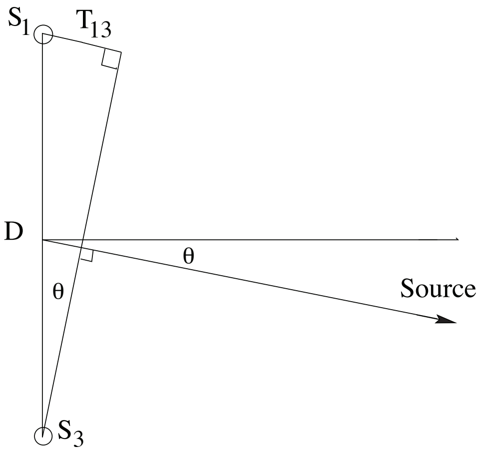

Figure 4. Diagram showing how the direction to a source is determined. Radio waves at an azimuth θ from the source in the distance arrive at station S_3 first and later at station S_1. T_{13} is the difference in arrival times at the two stations. *D* is the separation of the stations.

translates to 75 m (transverse distance, that is in a horizontal direction perpendicular to the line of sight, about north-south) resolution at the distance of the volcano. More precisely, using two stations, a measured time difference constrains the source to lie on a hyperbola (see fig. 1), and at large distances from the stations the azimuthal angle can be determined from the above relationship.

For comparison with the Augustine Volcano results, figure 5 shows the 3D locations of the thunderstorm lightning of figure 3 as they would be observed by a two station network. The top panel shows north-south position as a function of time as would be seen from the west or east. Branches that form continuously appear as lines; the slope can be used to determine the component of velocity perpendicular to the line between the stations and the lightning discharge. The second panel shows how the channels would look as observed from the north or south. The third panel shows the power emitted by the source in the 6 MHz bandwidth of the receivers. The fourth panel shows the number of points above threshold in

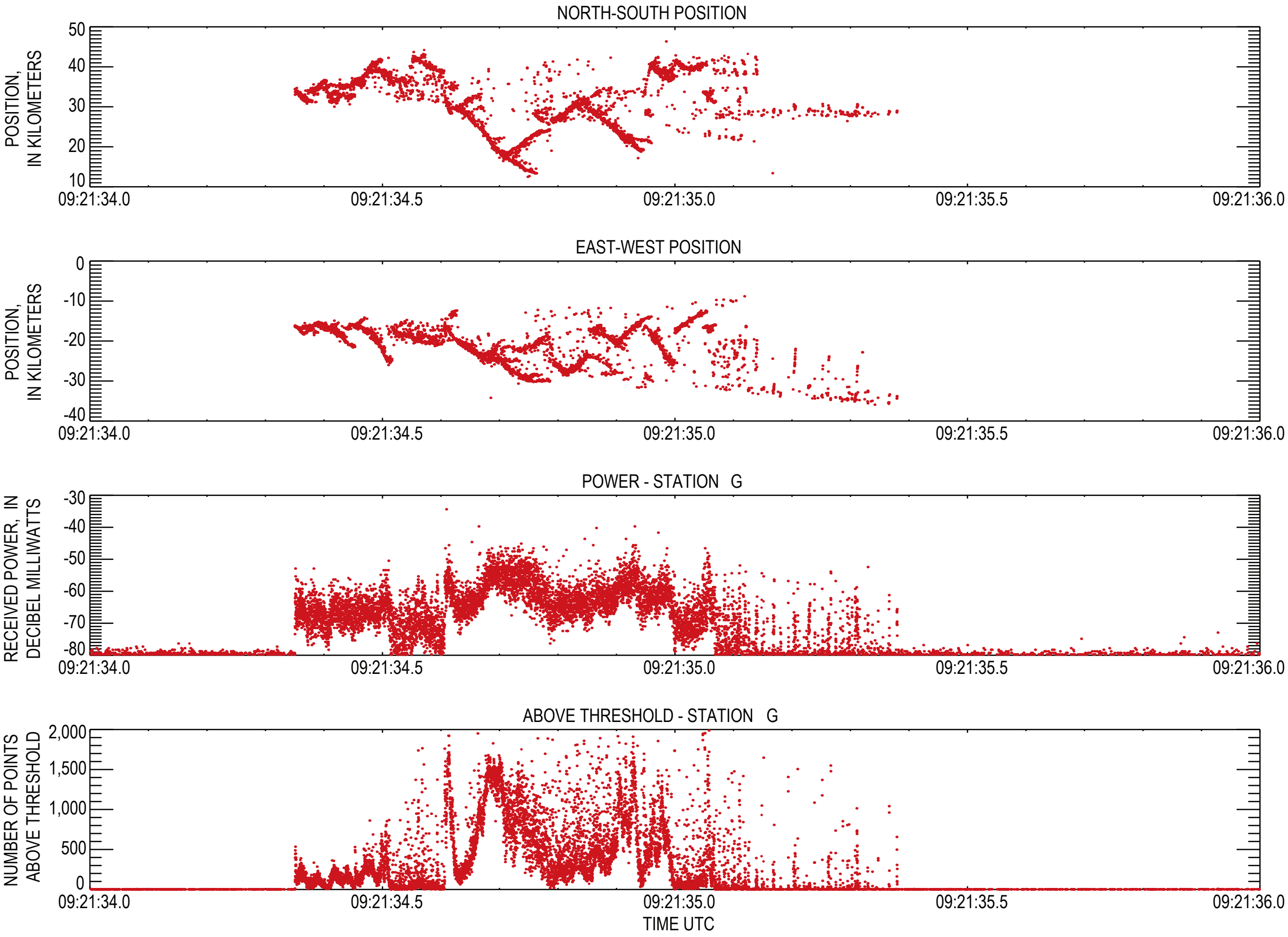

Figure 5. This set of plots show how the flash in figure 3 would appear to a two station network. The top two panels are the x and y positions versus time. The bottom two panels are raw data (power and number of points above threshold) from one station about 100 km from the flash. The times in this plot are in universal time (UTC).

each 10 μs window of the system. In this plot the flash divides into three parts of about equal lengths. During the middle phase of its development, RF radiation was mostly continuous (because the above threshold is near the maximum), and during the final phase, it consisted mostly of isolated impulses (since the above threshold is small).

Explosive Eruption at 2024 AKST on January 27, 2006

LMA Data

The raw data for the 2024 AKST (0524 UTC) explosion on January 27 (January 28 for UTC time) are shown in figure 6. The top panel shows the peak received power of the strongest event detected in each 80 μs interval (the time window was reduced to 10 μs at 1236 AKST (2136 UTC) for Homer and 1443 AKST (2343 UTC) for Anchor Point). In the top plot the color represents the relative density of the number of points at each power level. Several bands of background signals are observed. Most of these are due to local sources such as computers, other high speed electronics devices, motors, and transformers. The best way to identify signals caused by lightning is to correlate the signals from the two stations by looking for differences in arrival times consistent with sources near Augustine. (Peaks due to local sources will not correlate, because sources local to one station will not be detected at the other.) For this explosion we were interested only in time differences close to 15 μs (see fig. 1). Events we identify as correlated are marked with magenta in figure 7. We identified correlated points as groups of at least three points close in both time and arrival time difference.

The second panel shows number of points above threshold in each time window. The bottom panel displays the time between the strong events. During lightning flashes the rate increases and the time between events decreases. The three panels help to identify interesting events. Most of the events identified as correlated appear as vertical lines. Because lightning flashes generally last less than a second, have many high

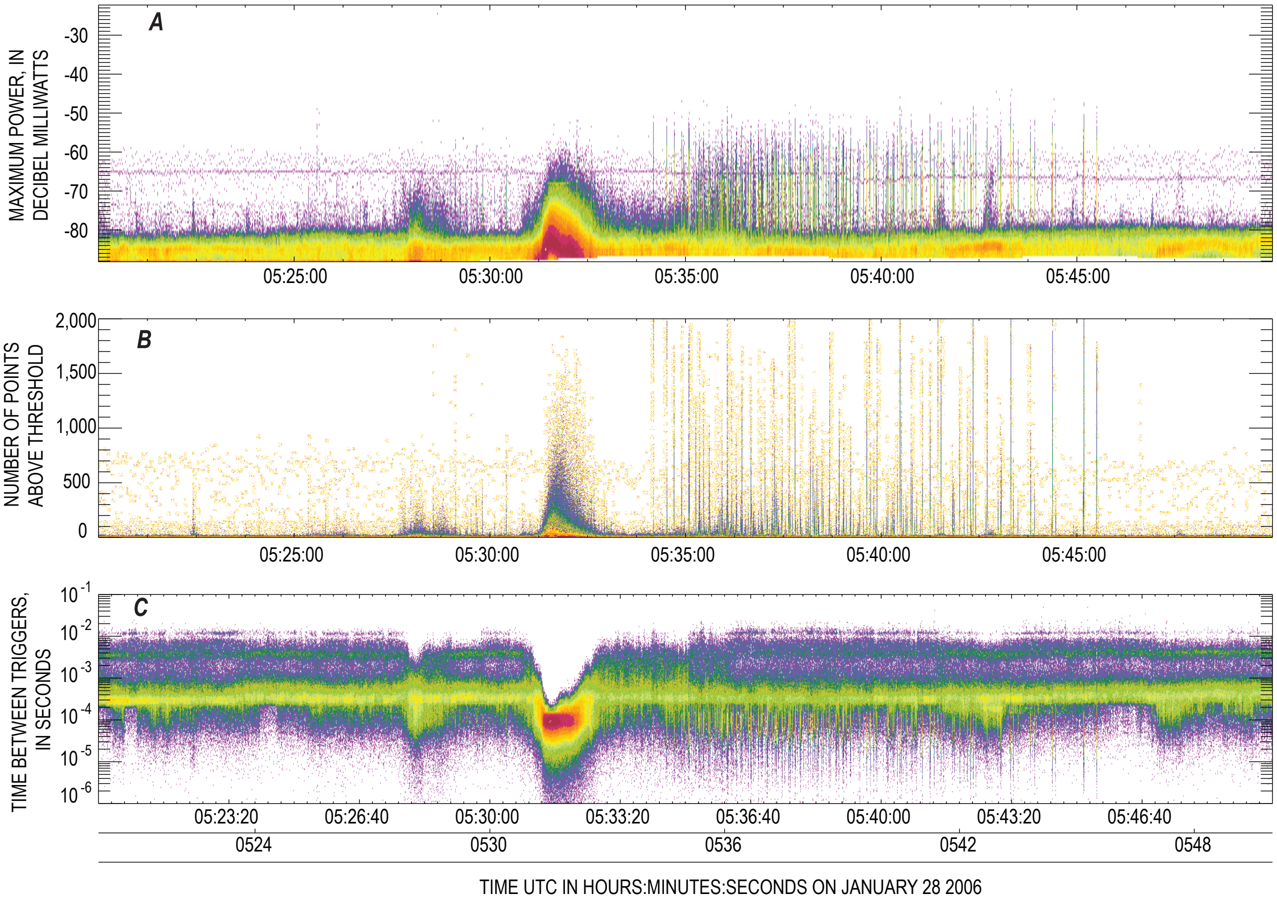

Figure 6. Plots of the raw lightning mapping data of the first explosive eruption on January 27 at 2031 AKST (January 28 at 0531 UTC) from the Homer station. The signature of the explosion is clearly visible as the bright red area. The power, the number of points above threshold, and the time between peaks are shown in the three panels as density plots; the color indicates the number of events with red being the most and blue-purple the least. The dates and times in this plot are in universal time (UTC).

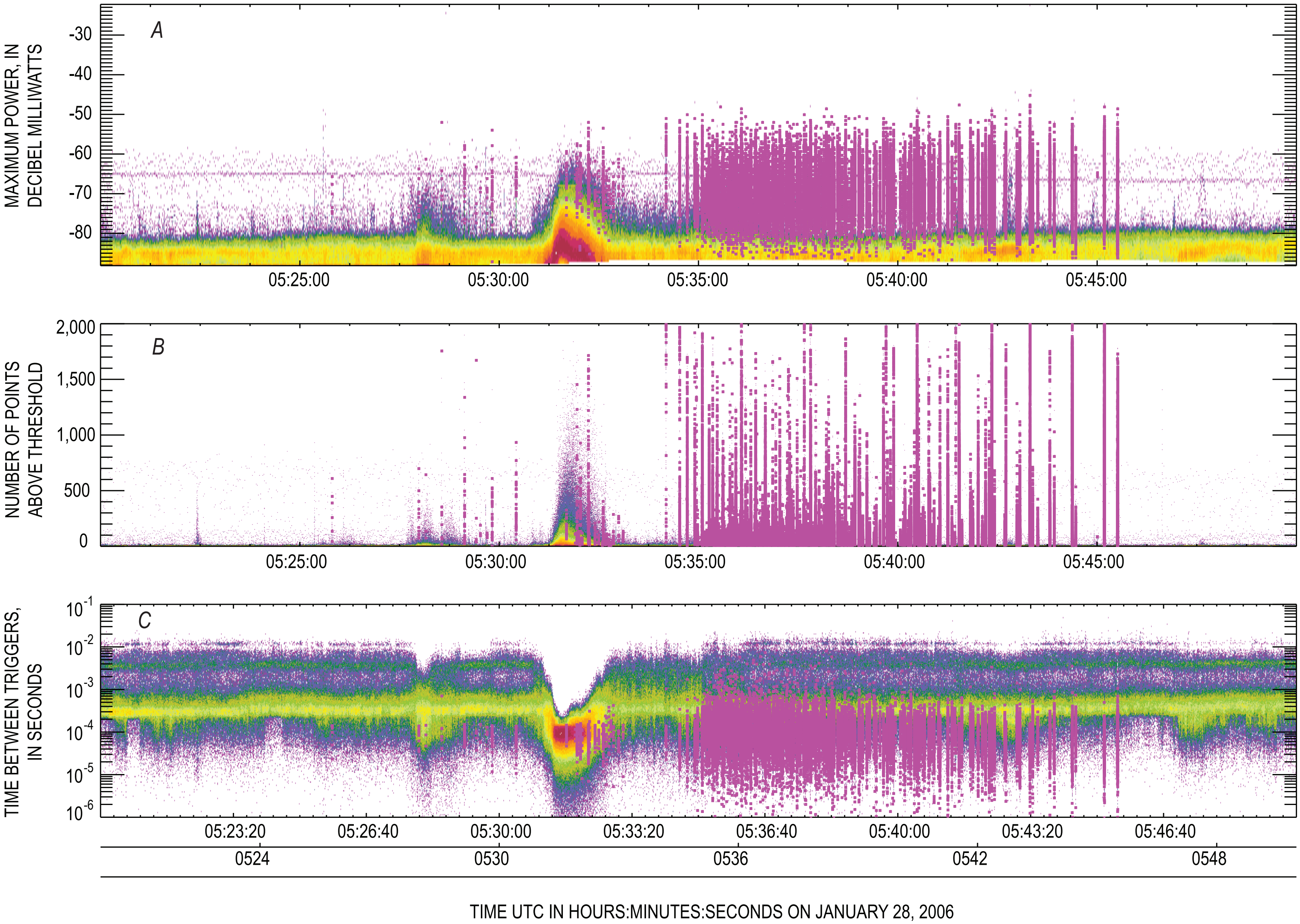

Figure 7. The raw data shown in figure 6 has been marked with magenta points to show events that are seen with both station and are correlated. The difference in the times of arrival show that these are from the volcano. The dates and times in this plot are in universal time (UTC).

power events, and many point above threshold, they should appear as vertical lines in plots with this time scale.

The explosion began at about 2024 AKST (0524 UTC), and was small at first. At 2027 AKST (0527 UTC) an increase in the energy of the explosion occurred, which can be seen as an increase in the LMA signal levels. At about 2031 AKST (0531 UTC) the largest eruptive pulse occurred as an enhancement lasting about two minutes and seen in all 3 panels of LMA data. This enhancement appears to have been caused by the explosion, as it is concurrent with the most intense part of the explosion based on seismic and infrasound data (see fig. 11 below) but is not correlated with data from Anchor Point. Because the station at Anchor Point was somewhat inland, was in a noisier radio frequency environment, and did not have line of sight to the Augustine summit, it was less sensitive to signals from Augustine than the Homer station. Although Anchor Point functioned well for higher-altitude events, it did not detect the noisy radiation during the explosive phases, even though the Homer data showed this radiation to be as strong as or stronger than that of more organized discharges. This indicates that the explosive-phase radiation originated at relatively low altitude at or slightly above Augustine's summit vent. The signals from the vent would have been more strongly attenuated at Anchor Point. The radiated source powers ranged from about 0 dBW up to 30 dBW (1 to 1,000 W) in the receiver passband, typical of values observed for ordinary lightning (Thomas and others, 2001). Because we saw similar enhancements during five other eruptive events (documented below), we conclude that the signals are due to electrical events at the vent during explosive eruptions. We will refer to these as vent discharges.

We have not observed similar electrical activity in thunderstorms (we have observed many thunderstorms with the same equipment and have not seen similar electrical signals). This type of electrical activity appears to be unique to volcanic explosions.

During the 2.2 minutes of enhanced signals starting at 2031 AKST (0531 UTC) there are 26 groups of events that correlate with Anchor Point. During this period only 573 events out of about 810,000 were correlated between the stations. The 810,000 events can be compared to the background of about 140,000 noise events in the same interval 10 minutes earlier. The correlated events are thought to be due to lightning higher up in the eruption column. The first lightning that is seen at both Homer and Anchor Point occurred much earlier, at 20:25:48.8 AKST (05:25:48.7 UTC), and was associated with the first phase of the explosion that began at 2024 AKST (0524 UTC). These lightning flashes have short durations (less than about 0.1 sec) and are few in number; we call these near-vent lightning.

Several minutes after the explosive phase signals ended (2033 AKST (0533 UTC)), there was a sequence of about 300 well-defined lightning discharges that continued for about 11 minutes (20:34:11 to 20:45:31 AKST (05:34:11 to 05:45:31 UTC); fig. 7). We believe that most of these were in the plume as the time differences slowly became smaller indicating a movement to the south in accordance with the wind direction and with radar images of the plume (Schneider and others, 2006). The transverse position of each source is shown in figure 8. The difference in the time of arrival of each correlated event gives the direction to the event, which can be translated to the distance from the summit of Augustine Volcano perpendicular to the

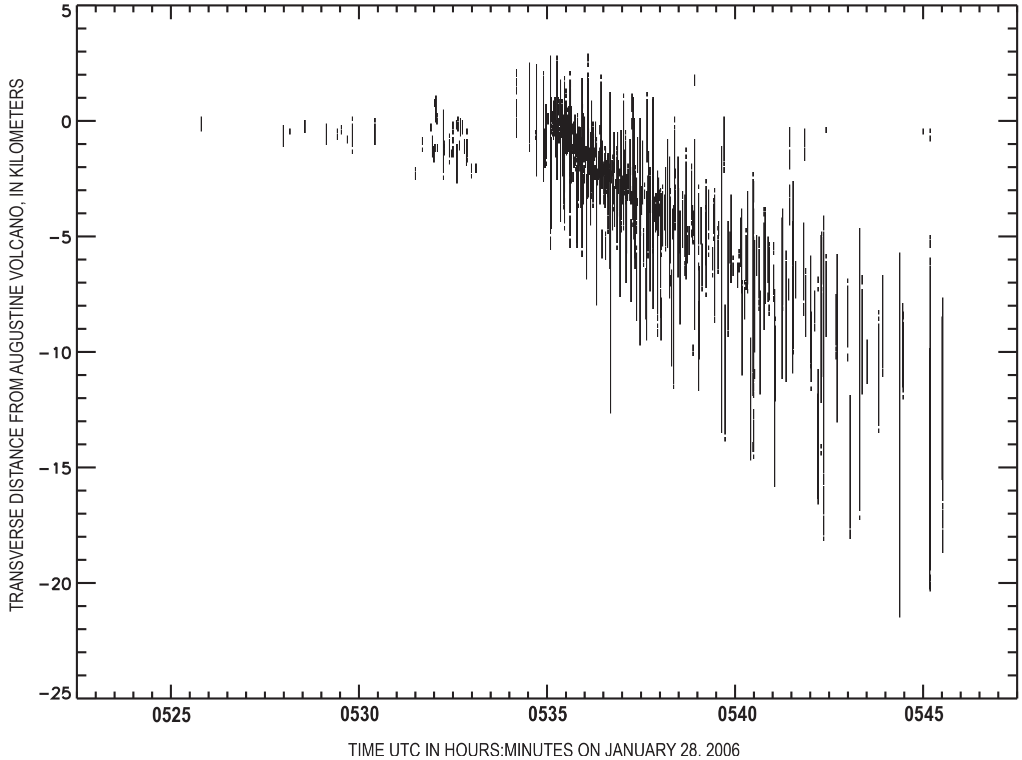

Figure 8. A plot of the transverse position of all the correlated points versus time. The position transverse to the line of sight at Augustine Volcano is found from the difference in the arrival times at the two stations and the distance to Augustine. During the explosion all the points are close to Augustine Volcano. After the explosion ended the location of the lightning drifted to the southeast. The transverse position is the distance from Augustine Volcano in a horizontal direction perpendicular to the line-of-sight from the station at Homer, about north-south. The dates and times in this plot are in universal time (UTC).

line of sight. It can be seen that during the explosion all the events are within 2 km of the volcano. After the explosion ended, the lightning is seen to drift to the south-east during this plume phase.

One of the final discharges lasted 650 ms and had a transverse extent of 15 km, extending to 22 km away from the volcano (fig. 9). The discharges undoubtedly occurred within the volcano's plume, which reached an altitude of 8 to 10 km. Hence we term this plume lightning. The lightning in both figures 8 and 9 undoubtedly also moved along the line of sight both toward and away from us. We were very fortunate that the movement of the plume and its elongation by the winds were mostly perpendicular to the line-of-sight.

The raw data for a plume lightning flash that occurred about a minute earlier are shown in figure 10. The format is similar to that of the thunderstorm flash of figure 5. Similar to the thunderstorm flash, numerous branches are observed, and both impulsive and continuous phases were present. The top panel of figure 10 shows the transverse source positions inferred from the differences in arrival times. The noisy background is a due to correlations which include a noise point at one of the stations which result in a time similar to the difference expected for events in the vicinity of Augustine. These noise correlations are easily removed, and the remaining points are assumed to be correlated.

Seismic and Acoustic Data

The relative timing between the signals from lightning (and other electrical activity) and the explosion as seen by the seismic and acoustic signals is key to understanding the mechanism for the production of lightning. In figure 11 lightning, seismic, and acoustic data are compared. The measured times are displayed, and signal propagation delays must be considered when comparing the two types of data. The lightning signals travel at the speed of light, which produces a delay of about 0.3 ms. The seismic signals travel at about 3 km/s, which produces delays of about 1.1 sec for the signals measured at Augustine Volcano and 6 sec for the signal measured at Oil Point (OPT). The acoustic signals travel more slowly in the air (about 330 m/s), resulting in a 10 s delay. All these delays are small compared to the time resolution of figure 11 and can be ignored here, but will be important for comparisons discussed later. The seismic signals from some of

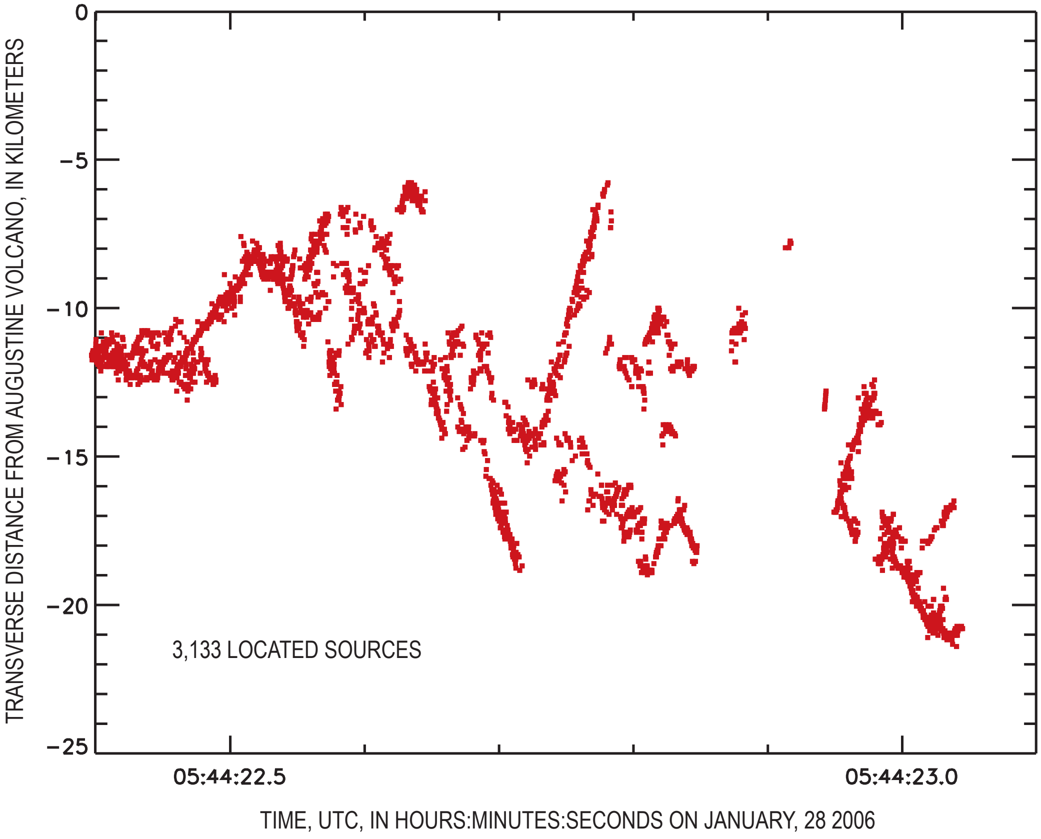

Figure 9. A plot showing the transverse position of the located points of single lightning flash near the end of the plume lightning on January, 27 AKST (January 28 UTC), 2006, during the eruption of Augustine Volcano. The transverse position shows it started about 12 km from Augustine and initially moves toward it. Later branches were as far as 21 km away from the volcano. The dates and times in this plot are in universal time (UTC).

the Augustine instruments saturated during the explosion. The seismic signal from Oil Point did not saturate, and making it suitable to compare seismic amplitudes with lightning signals throughout the explosion (Augustine station AU14 did not saturate and is very similar to that at OPT , see figure 4*B* in McNutt and others, this volume).

The seismic data indicate that the explosion lasted about 11 minutes, from 2025 to 2035 AKST (0524 to 0535 UTC), with a particularly energetic explosive pulse between 20:31 and 2033 AKST (0531 and 0533 UTC). A smaller explosive event occurred at about 2028 AKST (0528 UTC). An enhancement in the lightning background signal is observed at this time. These correlations in time and the similarities in the shapes in intensity are good evidence that the vent discharges are a result of small discharges occurring within the superheated ejecta as it exits the volcano. It also suggests that the number of discharges and their RF power is in some manner proportional to the explosion intensity. Further evidence of such vent discharges is shown by a spectacular photograph published in the September 2007 National Geographic (Grunewald, 2007). This time exposure of an eruption at Tavurvur Volcano, Papua New Guinea, shows about a dozen small electrical discharges that are spread throughout the ejecta. Most of these discharges are tens of meters long

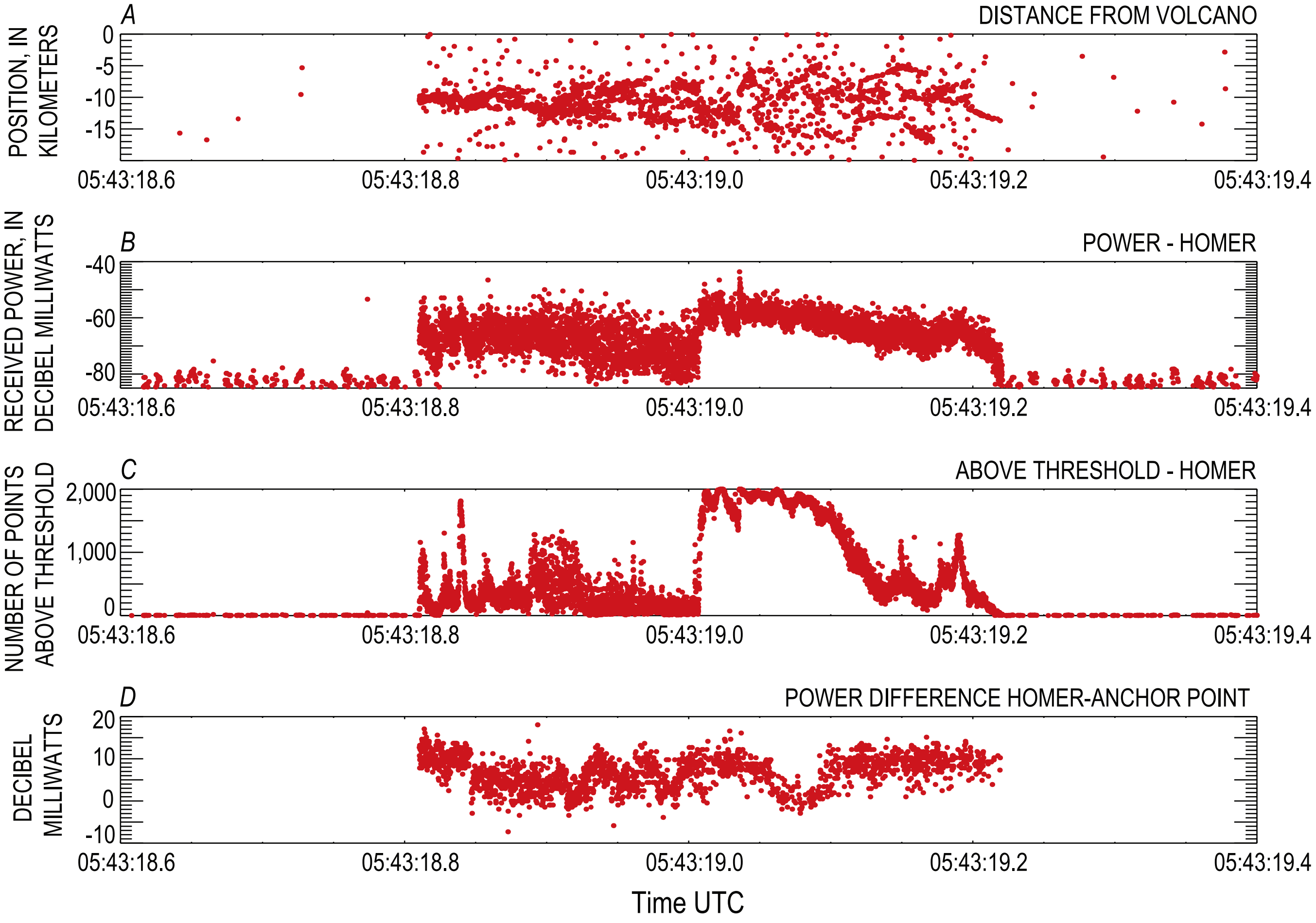

Figure 10. A set of plots showing how another flash from the plume phase evolves on January, 27 AKST (January 28 UTC), 2006, during the eruption of Augustine Volcano. It occurred about a minute before the one in figure 9. The format is similar to that of the thunderstorm lightning in figure 5. For the first 0.1 second the signals are just continuous enough to make the above threshold points reach values of several hundred. For the second 0.1 second the signals are more impulsive and the locations spread out. Beginning at 19.0 s the signals become very continuous and more powerful. In the top three panels all the raw data are included. The transverse positions (top panel) are a linear function of the arrival time differences at the two stations. The top panel also includes a noise background caused by one or both of the sources being a noise source. In the previous figure the noise points were removed by keeping only points that are in clusters. The lowest panel is the ratio of power measured in each station. Because the power is measured on a logarithmic scale the ratio is found by differencing the two measurements. The dates and times in this plot are in universal time (UTC).

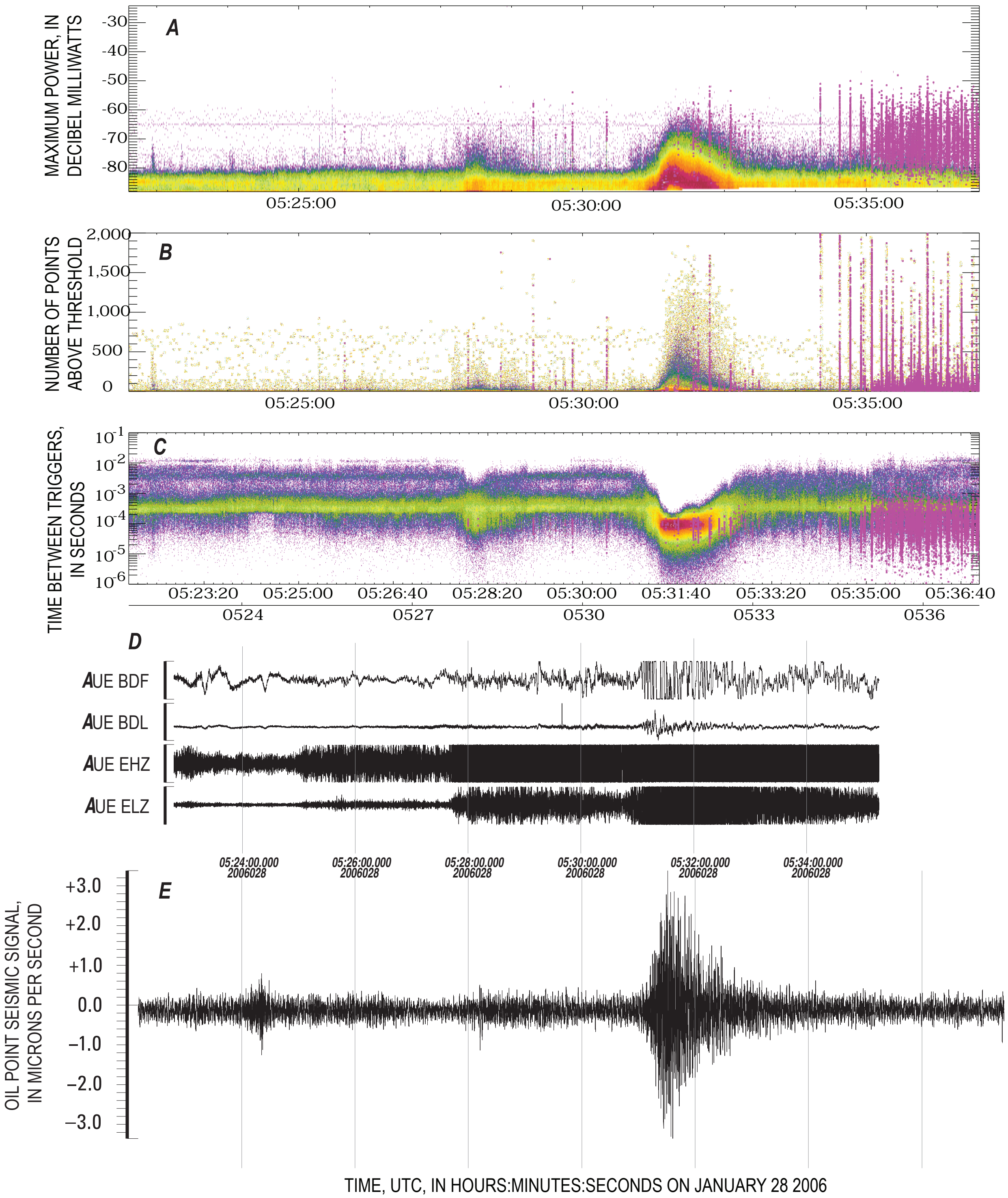

Figure 11. Seismic and acoustic data for the Augustine Volcano on January 27 AKST (January 28 UTC), 2006, are added to the plots of figure 7. The measured times for all the signals are aligned in this and following figures. Acoustic signals are from stations referred to as AUE BDF (high gain) and BDL (low gain). Seismic traces are from stations referred to as AUE EHZ (high gain) and ELZ (low gain). Station AUE is located 3.5 km east of Augustine Volcano's vent. The lowest trace is the seismic signal from Oil Point, about 34 km north of the volcano. The power, the number of points above threshold, and the time between peaks are shown in parts *A*, *B*, and *C* as density plots; the color indicates the number of events with red being the most and blue-purple the least. Units for acoustic and seismic data in part *D* are the same as shown in figure 17. The dates and times in this plot are in universal time (UTC).

and occur within a few tens of meters of the vent. Such small structures are compatible with our observations at Augustine, even though the details of the eruptions may differ.

LMA as an Interferometer

The station near Homer, on a bluff 220 m above the Cook Inlet, received radio signals directly from the lightning sources above the volcano and from their reflections off the sea surface. Because the reflected signal traveled slightly farther, the two signals were out of phase with each other when detected by the Homer station. Although we did not plan for or anticipate the effect, once recognized it allowed us to determine information about the altitudes of the sources. The same effect has been used by radio astronomers to infer the location and structure of astronomical radio sources (Bolton and Slee, 1953). Because the difference in path length varies with the altitude of the source, the interference pattern depends on source altitude. A path length difference that is exactly an integral number of wavelengths will result in constructive interference, whereas a path length difference of N + ½ (a phase change of π) will result in destructive interference. These effects were clearly present for a radiation burst at 20:32:14 AKST (05:32:14 UTC), during the main explosion.

Figure 12 shows how the Homer station functioned as a sea interferometer. The relatively simple discharge at 20:32:14 AKST (05:32:14 UTC) (a near-vent flash) produced received power values versus time that showed clear evidence of interference fringes. The raw data for this flash are shown in figure 13. Figure 13*A* shows the arrival time differences. The points due to the flash are tightly clustered while those associated with noise in one or both stations are scattered randomly, which illustrates how we identify our “correlated” events. Panels B and C show the received power of all points at the two stations.

While most of the high power points are from lightning, some of the high power points are due to weak local sources close to the station’s antenna. The correlation allows us to reject high power noise points and identify weak lightning events. To remove the effect of variations in the source power itself, the Homer power values were referenced to those of the same events at Anchor Point, which did not experience interference effects (fig. 14*C*). With the noise removed, the variations in the power ratio clearly show an interference effect.

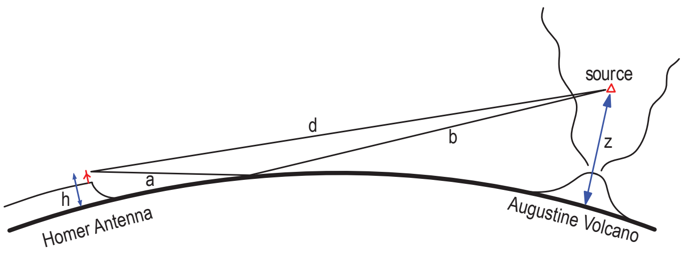

Figure 12. A diagram of the “sea-surface” interferometer. Signals could reach the antenna at the Homer station after bouncing off the water of Cook Inlet. Because the length of the two signal paths were slightly different the two signals interfered with each other depending on the altitude of the source. (From Thomas and others, 2007.)

The predicted interference pattern is shown in figure 14*D* along with the results of fitting the measurements to the predicted pattern. To obtain the predicted pattern it was necessary to take into account the curvature of the Earth, as well as the fact that seawater is a reasonably good conductor, with a phase shift close to π on reflection. Because of the extreme grazing nature of the reflections (the incidence angle varied between ~0.5 and 2.0 degrees from horizontal for the discharge of figure 12), the path length difference for the direct and reflected signals was only about 0.6λ for signals originating at Augustine's summit (1,260 m altitude) and increased at a rate of about 0.9λ per kilometer above Augustine. Thus, in going ~2 km upward, the discharge at 20:32:14 AKST (05:32:14 UTC) showed two complete interference fringes (fig. 14*D*).

Several steps were taken to fit the observed data to the predicted values. First, the logarithmic power differences needed to be shifted downward by 15 dB to compensate for the attenuation of the Anchor Point signals. Second, to match the depth of the interference minima, the reflection coefficient of the sea surface was adjusted to an effective value of 0.7 (versus 1.0 for an ideally smooth conducting surface). Finally, a piecewise-linear approach was used to map temporal intervals in the observed data to spatial intervals on the predicted interference fringes (figs. 14*A*, *C*). To accomplish this, a particular set of points in the temporal data was assumed to originate at heights that gave reasonable “eyeball” fits between the observed and predicted power values. The resulting time-height conversion (fig. 14*B*) was then used to convert the transverse distance versus time data of figure 14*A* to a 2-dimensional vertical projection plot.

Figure 15 shows the resulting vertical projection of the flash. The discharge appeared to begin about 250 m above Augustine’s summit and progressed upward and leftward (southward) along a single, 4-km long path. The average speed of progression was about 0.7×10^5 m sec^{-1} vertically and about 1×10^5 m sec^{-1} overall in the transverse plane. Such propagation speeds are characteristic of negative polarity breakdown propagating toward or through net positive charge (Behnke and others, 2005). Lightning emits radio frequency radiation primarily from developing negative-polarity breakdown, which propagates into positive charge regions, rather than from positive breakdown, which propagates into negative charge regions. The upward radiation sources of figure 15 are similar in character to the initial breakdown observed in intracloud discharges in thunderstorms, which are of negative polarity and propagate into and through regions of net positive charge (for example, Behnke and others, 2005). (The propagating radiation segments seen in figures 9 and 10 are also produced by negative breakdown through positive charge regions.)

The origin of the upward discharge in figure 15 is only an apparent location that corresponded to the time that the

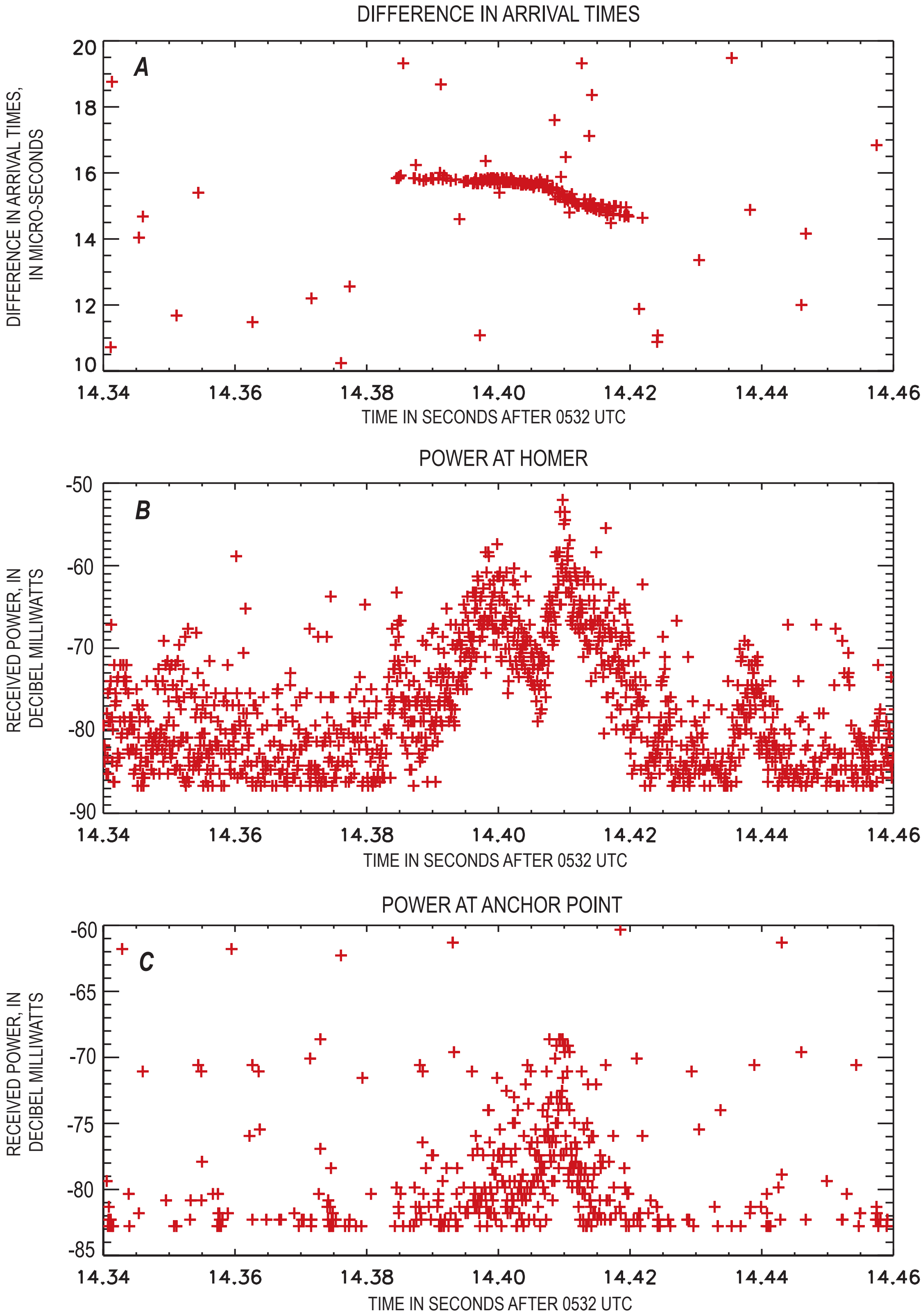

Figure 13. Plots of the raw data from a small lightning flash during the main explosion of the Augustine Volcano at 2032 AKST on January 27 AKST (0532 on January 28 UTC), 2006. All the measured power values are shown for the Homer and Anchor Point stations. The Anchor Point station is less sensitive as it is inland about 1.5 km. The power varies differently at each station. The dates and times in this plot are in universal time (UTC).

sources from the flash were strong enough to be detected by the Anchor Point station. The single-station power data from Homer show clear evidence of propagating breakdown prior to signals being detected at Anchor Point, indicating that the discharge began at lower altitude, almost certainly on the ground in the vicinity of the summit. Because the choice of the initial fringe is ambiguous, we cannot strictly rule out the possibility that the discharge began an integer number of fringes higher in altitude. However, this is considered unlikely in view of the above physical interpretation of the observations. There is also an ambiguity as to whether the discharge developed downward or upward, but this is readily resolved from the fact that downward development would give a physically incorrect picture of the discharge relative to the plume.

No cloud-to-ground discharges were detected by the BLM Alaska Lightning Detection System during the January 27–28 explosions. Upward-initiated discharges from the ground would not be detected by the BLM system because such networks locate the strong “sferic” produced by return strokes initiated by downward leader breakdown (Cummins and others, 1998). Low-frequency lightning location networks occasionally detect intra-cloud flashes, as the BLM network did for January 13 explosion. The BLM network detected cloud-to-ground discharges only during the early January explosions—one that

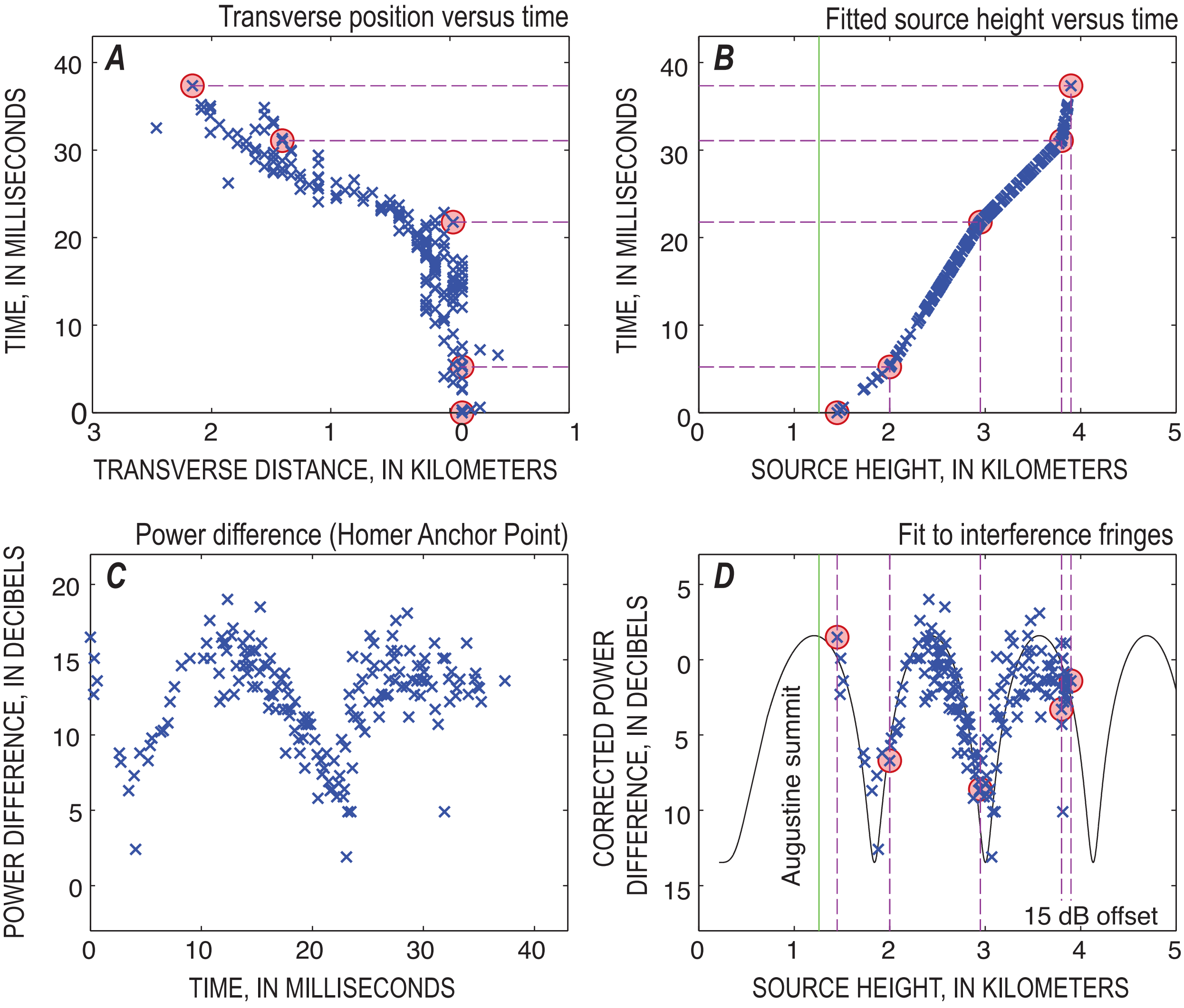

Figure 14. Four plots showing how the interference pattern is deciphered. This pattern is from a small lightning flash during the main explosion of the Augustine Volcano at 2032 AKST on January 27 AKST (0532 on January 28 UTC), 2006. *A,* Transverse distance versus time. *B,* Fitted source height versus time. *C,* Power difference between Homer and Anchor Point versus time. *D,* Corrected power difference versus height with interference fringes also shown. The pink circled points and dashed lines indicate breaks in the piecewise-linear fits. (from Thomas and others, 2007).

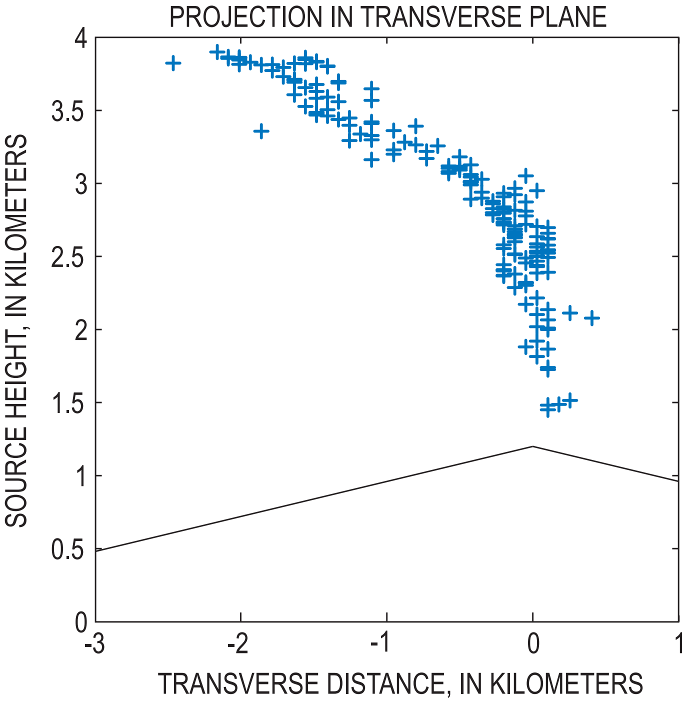

Figure 15. Plot showing the path of the lightning channel above Augustine Volcano. This lightning occured during the main explosion of the Augustine Volcano at 2032 AKST on January 27 AKST (0532 on January 28 UTC), 2006. The lightning began at the summit of Augustine and went up and then to the southeast where the wind was moving the plume. The volcano is represented by a simple line drawing. (from Thomas and others, 2007).

lowered positive charge to ground during the initial explosion (January 13 at 0424 AKST (1324 UTC); table 1), and one that lowered negative charge to ground during a later explosion (January 14 at 0014 AKST (0914 UTC)).

Flash Durations

Various aspects of the flash durations are plotted in figure 16. Initially the flashes lasted only a few milliseconds (fig. 16*A*); these are near-vent lightning discharges. During the explosion they increased in length to about 70 milliseconds. With a typical velocity of 10^5 m/s this implies a total length of less then 7 km. During the main eruptive phase, many of the flashes in the plume last several hundred milliseconds. During the initial part of this phase there are many fast small flashes, but their numbers decrease with time. figure 16*B* shows that most of the small flashes appear to be near the volcano vent, most likely in the rising plume column. Initially the flashes are separated by 10 or more seconds (fig. 16*C*), similar to what is seen in a small thunderstorm. As the plume lightning begins at about 2035 AKST (0535 UTC) the rate is more than 5 flashes per second. Such high rates are generally seen only in large thunderstorms, such as those produced by meos-scale systems in the Great Plains (MacGorman and Rust, 1998). At the end of the plume lightning phase the flash rate is typical of rates observed in similar sized thunderstorm in New Mexico. Interestingly, the number of points per millisecond seems to increase with the flash size (fig.16*D*).

Explosion at 2337 AKST on January 27, 2006

A very short and impulsive second explosion on this day occurred at 2337 AKST on January 27, 2006 (0837 UTC on January 28). Infrasound measurements show a short burst (20 s) with the highest peak acoustic pressure (105 Pa) for the entire eruption [Peterson and others, 2006]. The plume height was estimated to be 3.8 km (Schneider and others, 2006). Lightning, infrasound and seismic data are shown in figure 17. Both the signals from the electrical and acoustic sources begin very abruptly and last about 20 seconds. Because both the signals began so quickly their onsets can be determined to ±0.1 seconds. Using the time delay for the acoustic signal from Peterson and others (2006) of 9.4 s would indicate that the electrical activity began about a second before the acoustic signal. However, Peterson and others (2006) based their acoustic delay on an assumed atmospheric acoustic velocity of 340 m/s, which is velocity at room temperature. Correcting the velocity to a temperature of –10°C indicates that the onset of both signals was simultaneous within the measurement error of 0.1 s. This supports the argument that electrical activity is generated at the vent of the volcano and is produced by the high velocity ejecta. Both the electrical and acoustic signals indicate activity above ground. The strong seismic signal of the main event appears to begin several seconds before indicating the beginning of the explosion, deeper in the vent. A small seismic subevent began about 15 s before the main phase (fig. 17).

Plots of the electrical activity recorded at the Homer station (fig. 18) show about 10 vertical lines consistent with small lightning flashes. Only one of these flashes, a 10-ms-long flash at 23:38:19.36 AKST (08:38:19.36 UTC on January 28), correlated with signals at Anchor Point. Using an average velocity of lightning of about 10^5 m/s, we can estimate a length of 1 km for this flash. This indicates that the flash is near-vent lightning. It can be seen that there are very few vertical lines both before and after the minute of eruptive activity (fig. 18). Thus, it is very likely that the vertical lines during this period were produced by other small near-vent lightning flashes (lasting 5 to 10 ms).

A summary of parameters for the various types of lightning and electrical activity is given in table 2 for all the events in this study.

Table 2. Summary of lightning parameters measured by the Lightning Mapping Array for the Augustine Volcano eruptions in January 2006.

Date January 2006	Time UTC	Plume Height (km)	Vent Discharges		Near-Vent Lightning			Plume Lightning		
			Max power (dBm)	Duration (sec)	Number of flashes	Duration (min)	Delay (sec)	Number of flashes	Duration (min)	Delay (sec)
28	0524	10.5	-50	120	22	7.4	108	300+	11.4	10.5
28	0837	3.8	-70	20	1	-	42	0	-	-
28	1104	7.2	-65	30	28	1.2	60	0	-	-
28	1642	7.0	none	-	6	2	300	0	-	-
29	0040	3.8	none	-	35	18	n.a.	0	-	-
29	2019	7.2	-65	120	2	0.05	118	0	-	-
30	1228	7.2	-70	132	0	-	-	0	-	-
30	1522	7.2	-72	25	2	0.1	25	0	-	-

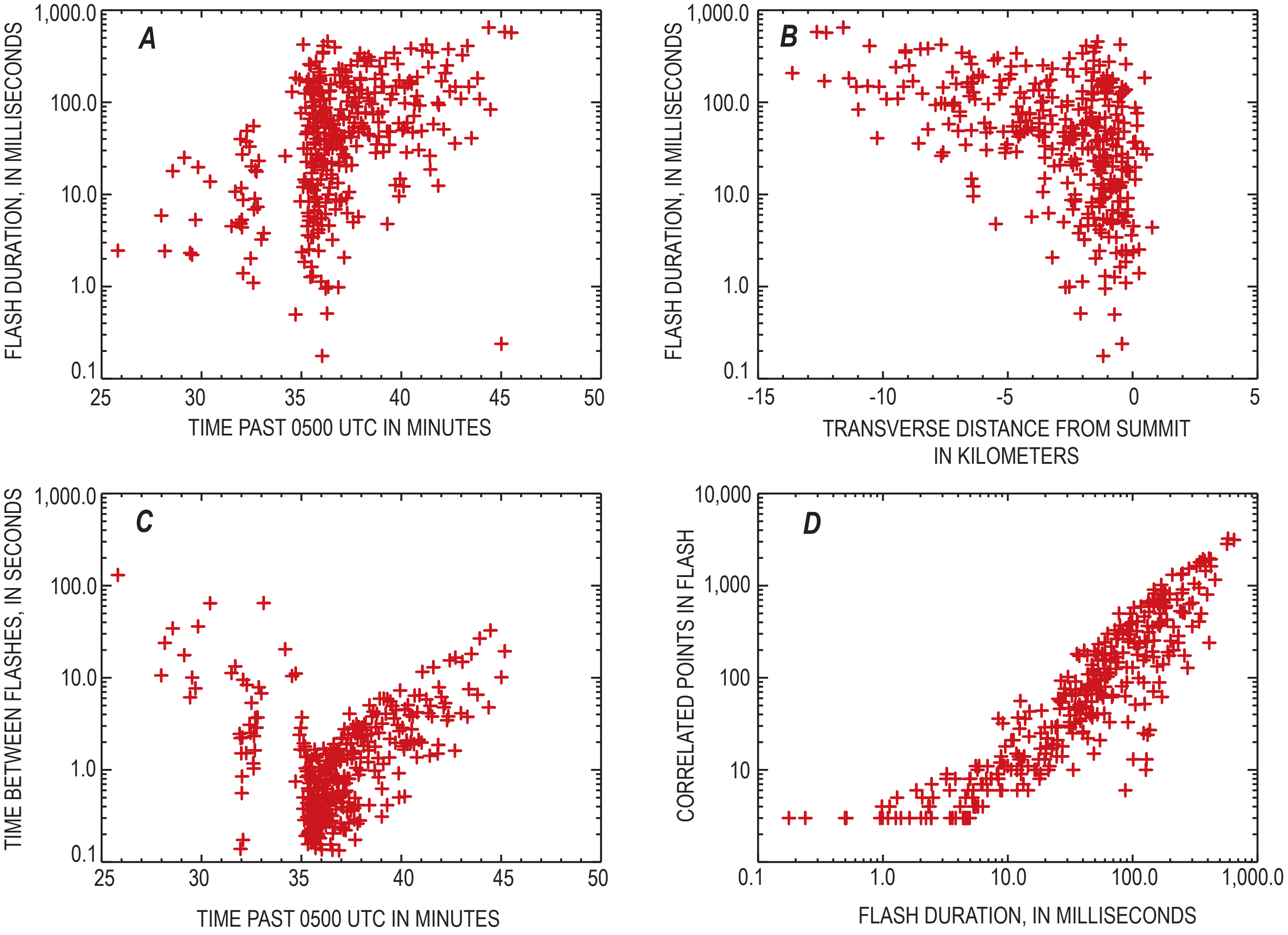

Figure 16. Plots showing the flash durations as a function of other parameters for the Augustine Volcano eruption on January 27 AKST (January 28 UTC), 2006. The panels show (*A*) the duration of each flash versus time, (*B*) the duration versus position, (*C*) the separation of flashes versus time, and (*D*) number of points in the flash versus duration. The dates and times in this plot are in universal time (UTC).

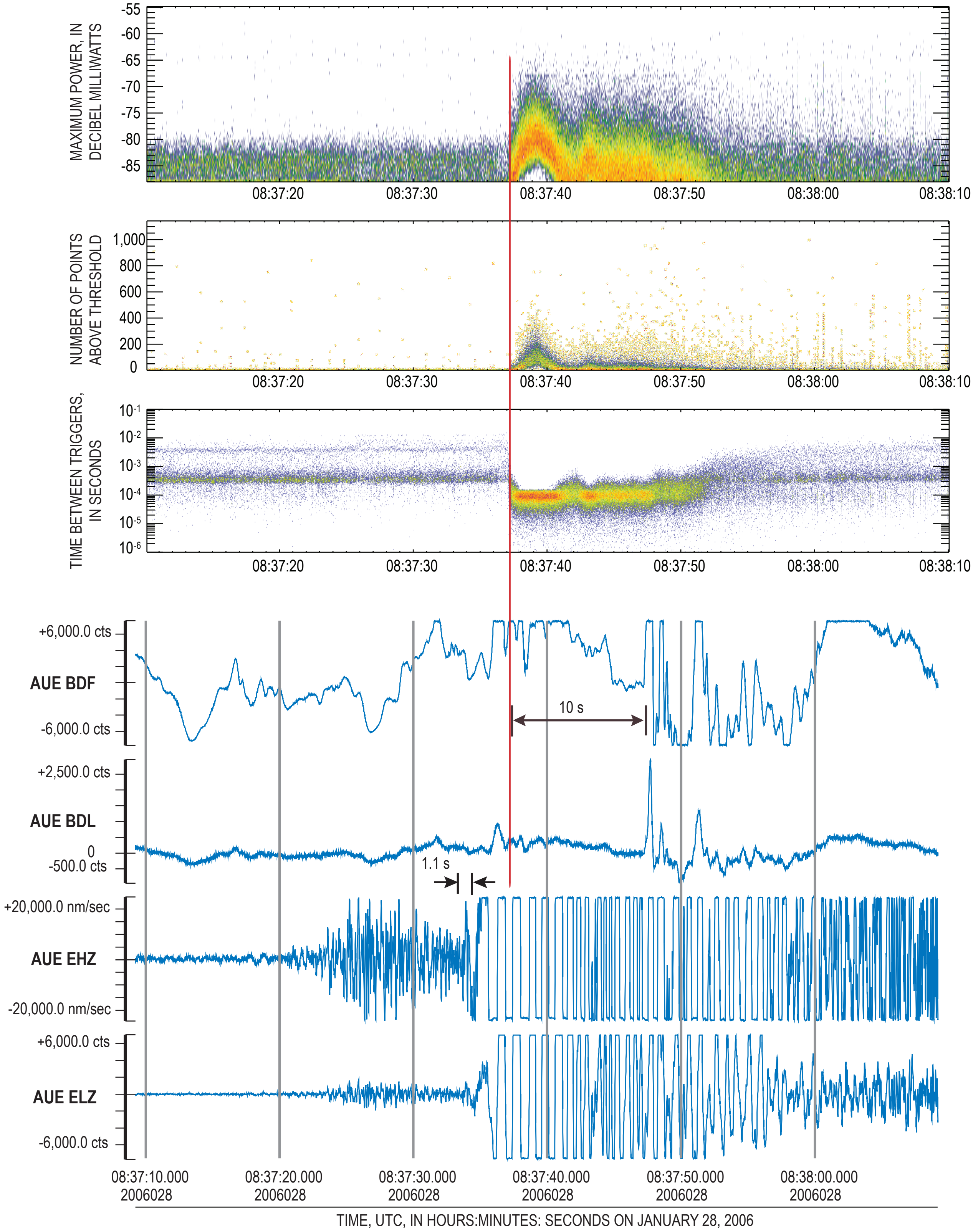

Figure 17. Plots of the data from Augustine Volcano's explosion at 2337 AKST on January 27 (0837 UTC on January 28), 2006 showing lightning mapping, seismic, and acoustic signals. When the acoustic travel time of 10 seconds is taken into account the beginning of the electrical and acoustic signals are coincident (vertical red line). Upper three panels show electrical data and lower four show acoustic and seismic data. See figure 11 caption for details. The dates and times in this plot are in universal time (UTC).

Explosion at 0204 AKST on January 28, 2006

The explosion at 0204 AKST (1104 UTC) on January 28, had smaller acoustic and seismic amplitudes than the previous two events. The peak acoustic pressure was 66 Pa and the plume height was 7.2 km. The seismic duration was longer than the 2337 AKST (0837 UTC) event but shorter than the 2024 AKST (0524 UTC) event (Petersen and others, 2006; McNutt and others, this volume). The data in figure 19 show similar behavior in the electrical, acoustic, and seismic signals. As in the previous explosions, we see both continuous background activity due to vent discharges and correlated signals indicating the development of lightning channels upward into the erupting column. All the correlated lightning appears to be near-vent lightning.

Figure 20 shows that most of the flashes lasted less than 10 ms and, therefore, had lengths of less than a km. A few could have been several km long. These are similar to the events in the first few minutes of the 2024 AKST (0524 UTC) explosion (fig. 16) that occurred before the plume lightning began at 2034 AKST (0534 UTC).

Explosion at 0742 AKST on January 28, 2006

The explosions at 0742 AKST (1642 UTC) on January 28, was smallest of the four explosive eruptions of this day in terms of the acoustic and seismic amplitudes (Petersen and others, 2006; McNutt and others, this volume). The duration (see fig. 21) was similar to the 0242 AKST (1104 UTC) event and was much longer than the earlier 2337 AKST (0837 UTC) event. This explosion began with a weak phase at 0742 AKST (1642 UTC), followed by a stronger phase starting at 0748 AKST (1648 UTC). We did not see the enhanced radiation

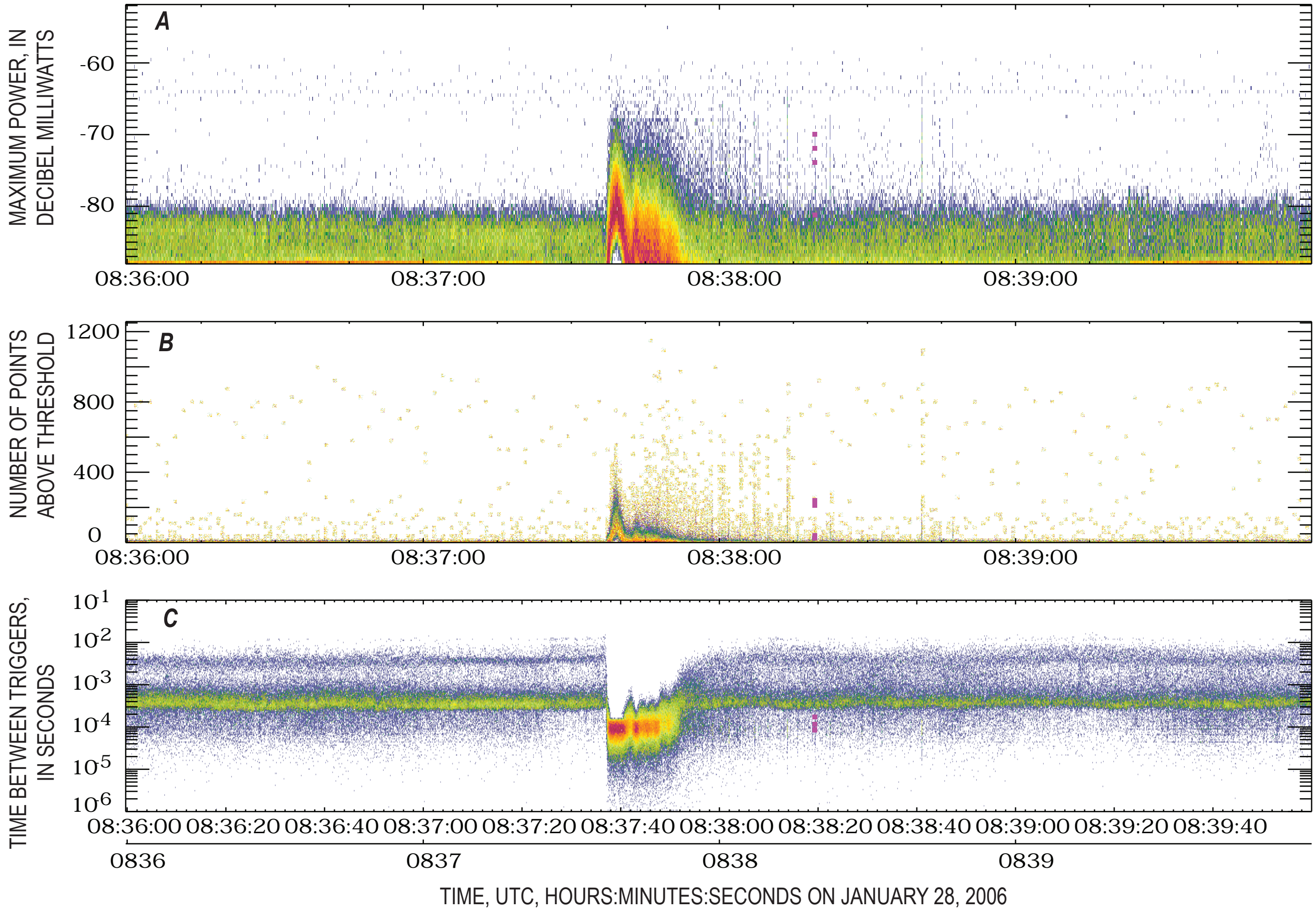

Figure 18. Data from Augustine Volcano's explosion at 2337 AKST on January 27 (0837 UTC on January 28), 2006. Because the background is small (easiest to see in panel *B*) both before and after the explosion, the vertical lines of signal points are probably small lightning flashes. See the captions of figures 6 and 7 for details. The dates and times in this plot are in universal time (UTC).

from electrical activity at the vent, but there were 6 small lightning flashes with correlated points. Most of the lightning occurs just before the major seismic event; this suggests it is near-vent lightning caused by the initial 0742 AKST (1642 UTC) event. It also implies that the large phase at 0748 AKST (1648 UTC) may have been mostly gas with little tephra. Figure 22 shows that all the flashes were very small and of short duration, similar to the near-vent lightning flashes associated with the other three explosions on January 28, 2006.

Lightning and Vent Discharges during the Continuous Phase on January 29 and 30, 2006

The explosive phase of the eruption ended with the event on January 28 at 0742 AKST (1642 UTC). This was followed by a transitional event that began at 1430 AKST (2330 UTC)

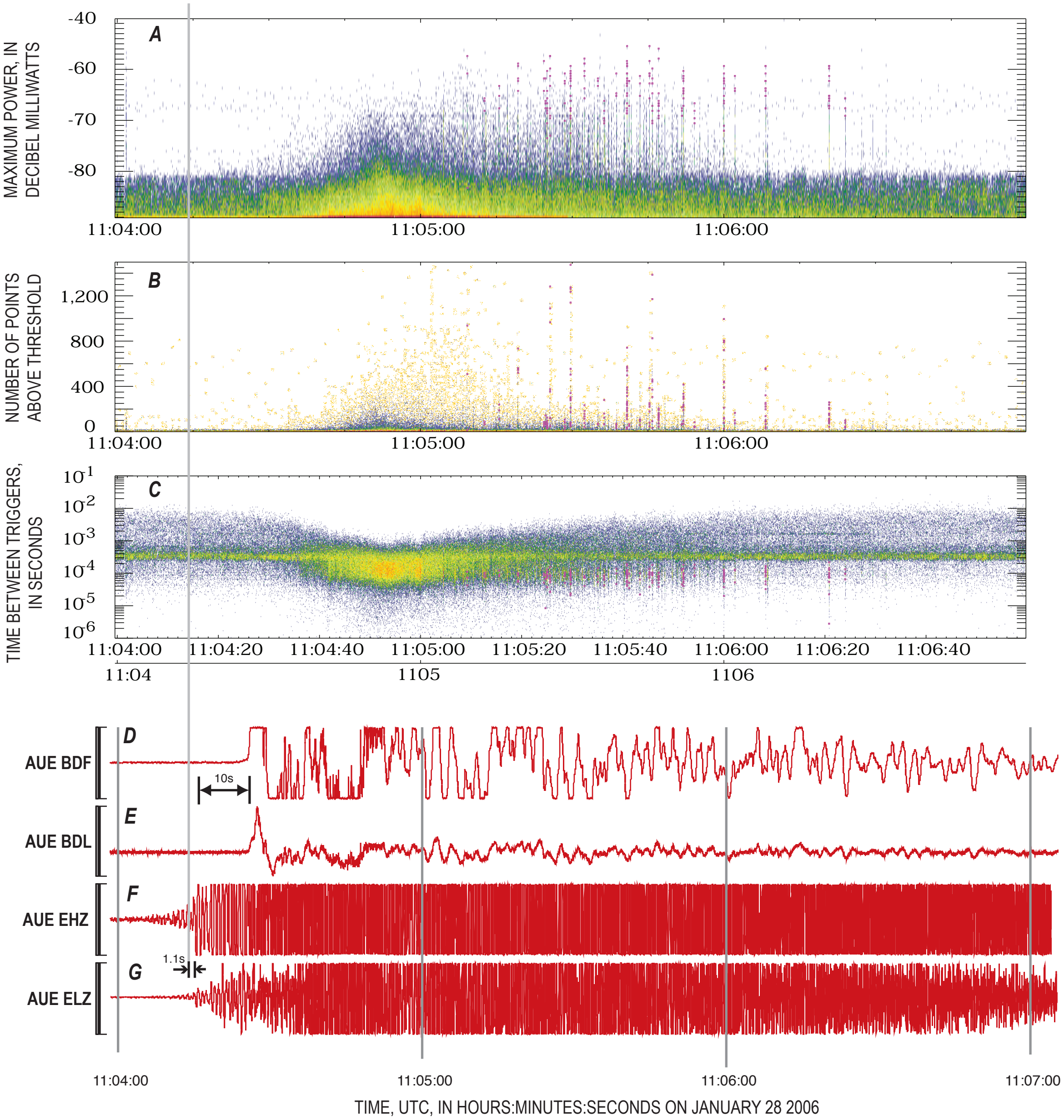

Figure 19. Data from Augustine Volcano's explosion at 0204 AKST (1104 UTC) on January 28, 2006. Panels *A* through *C* show electrical data, *D* and *E* acoustic data, and *F* and *G* seismic data. See figure 11 caption for details. Units for acoustic and seismic data in parts *D*, *E*, *F*, and *G* are the same as shown in figure 17. The dates and times in this plot are in universal time (UTC).

on January 28 (McNutt and others, this volume) and signaled the beginning of the continuous phase. The continuous phase was characterized by many small explosions that occurred a few minutes apart, so that ash was in the air continuously for several days. During this continuous phase, several larger explosions occurred. These were smaller than all 13 of the numbered explosive events (Petersen and others, 2006) but were larger than the small events that occurred every few minutes. Lightning was associated with several of these moderately large explosions.

Between 1540 and 1600 AKST on January 28 (0040 UTC and 0100 UTC on January 29), we saw electrical signals from about 28 lightning discharges (fig. 23). These occurred late during the transitional explosive event that began at 1530 AKST on January 27 (2330 UTC on January 28). This event had a seismic and acoustic duration of about 1 hr 45 min, and moderate amplitudes (McNutt and others, this volume). The lightning rate is much smaller here than in the previous events. Many of these flashes are as large as those in the big explosion at 2031 AKST on January 27 (0531 UTC on January 28), with 6 flashes lasting between 20 and 80 ms each (fig. 24). Several of these show interference patterns and altitude analysis may be possible. Thus, we interpret the lightning to be composed of upward propagating near-vent flashes. The total number of flashes was small presumably because the amount of tephra and height of the ash column were smaller than the 2031 AKST, January 27 (0531 UTC, January 28), explosion. Radar data indicate that the ash plume height was about 3.8 km during this event (Schneider and others, 2006).

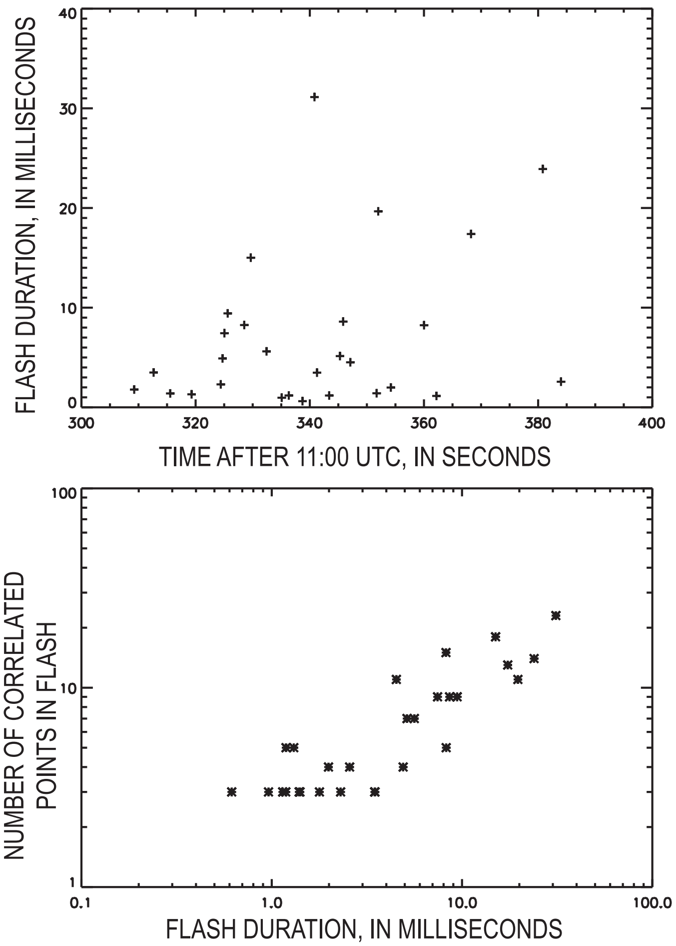

Figure 20. Durations of flashes during the 0204 AKST (1104 UTC) explosion of Augustine Volcano on January 28, 2006. The dates and times in this plot are in universal time (UTC).

On January 29 between 11:19:30 and 12:21:18 AKST (20:19:30 and 21:21:18 UTC) (fig. 25) there was an increased electrical background signal similar to that seen during the explosive eruptions. At the same time a large increase was seen in the radar reflectivity at 7.2 km, indicating an impulse of ash injected into the atmosphere (Schneider and others, 2006). Seismic and acoustic data indicate that a moderately strong explosive event began at 11:17:54 AKST (20:17:54 UTC) and lasted 340 s. The signals were strongest from 1119 to 1121 AKST (2019 to 2021 UTC), corresponding to the time of the continuous electrical signal. Two flashes of near-vent lightning occurred 2 minutes after the start of the continuous electrical signal. These were both short duration flashes. No plume lightning was observed.

On January 30 between 0128 and 0130 AKST (1228 and 1230 UTC) (fig. 26) there was an increased electrical background signal due to vent discharges, similar to that seen during the explosive eruptions. Seismic and acoustic data indicate an explosion starting at 1:25:18 AKST (12:25:18 UTC), strongest from 1:28:40 to 1:29:10 AKST (12:28:40 to 12:29:10 UTC), and lasting 340 s total. At the same time an increase was seen in the radar reflectivity at 7.2 km indicating an impulse of ash injected into the atmosphere (see Schneider and others, 2006). No near-vent or plume lightning occurred in association with this explosion.

On January 30 between 6:22:25 and 6:22:50 AKST (15:22:25 and 15:22:50 UTC) (fig. 27) there was another increased background signal similar to that seen during the explosive eruptions. Seismic and acoustic data show a moderate explosion beginning at 6:19:42 AKST (15:19:42 UTC) and lasting 290 s, strongest from 6:21:20 to 6:23:50 AKST (15:21:20 to 15:23:50 UTC). This event was less than half the amplitude of the 0128 (1228 UTC) event. At the same time an increase was seen in the radar reflectivity at 7.2 km indicating an impulse of ash injected into the atmosphere (Schneider and others, 2006). Two flashes of near-vent lightning occurred just after the continuous signal ended (table 2). No plume lightning was associated with this explosion.

Electrical Events in March 2006

During the dome building phase in March we had the two additional stations operating, one on West Island and one at Oil Point (fig. 1). During this time we found 6 periods where there were signals from two stations that were correlated. Almost all the correlations were between signals received at the Homer station and Oil Point. Figure 28 shows the possible

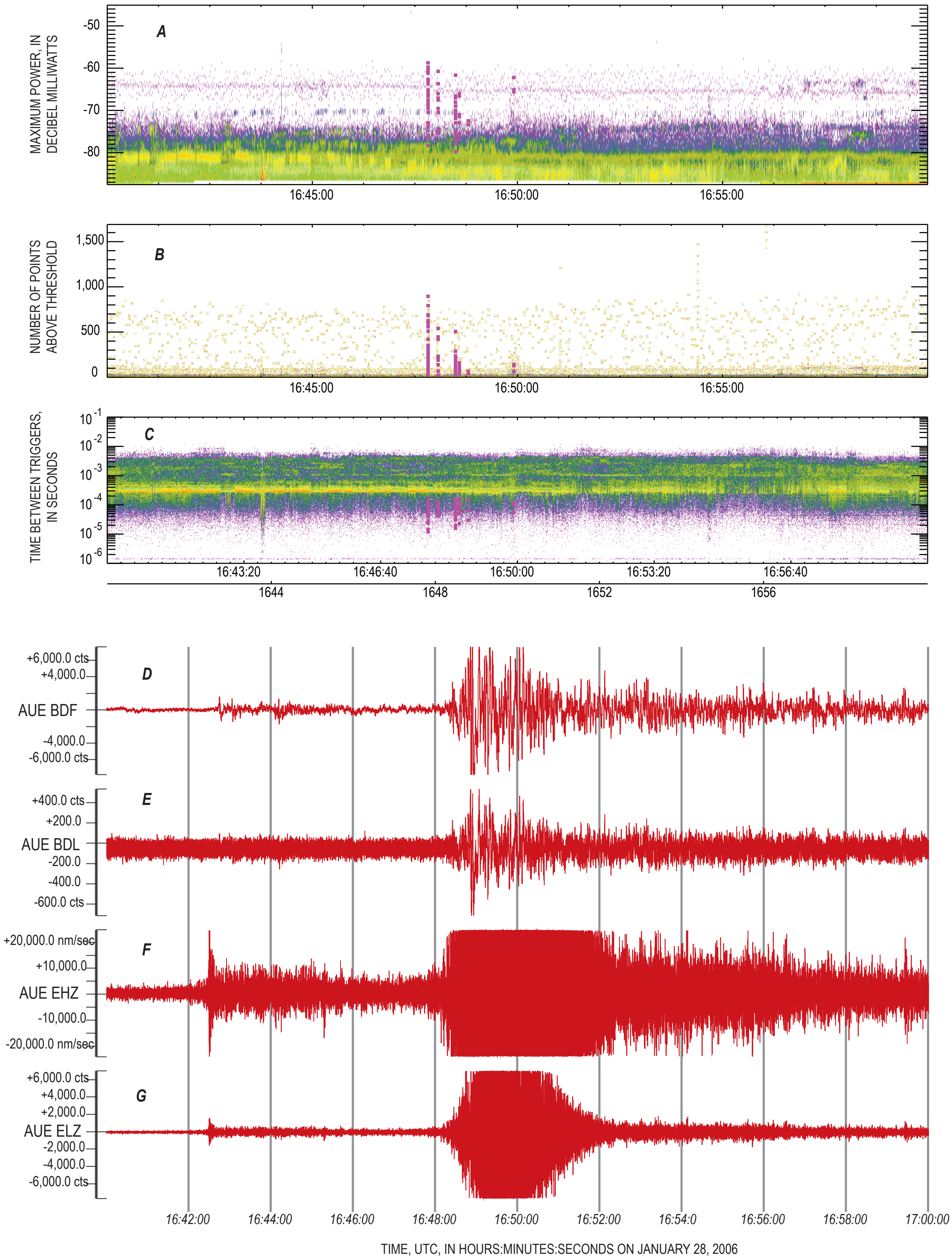

Figure 21. Data from Augustine Volcano's explosion at 0742 AKST (1642 UTC) on January 28, 2006. Panels *A* through *C* show electrical data, *D* and *E* acoustic data, and *F* and *G* seismic data. See figure 11 caption for details. The dates and times in this plot are in universal time (UTC).

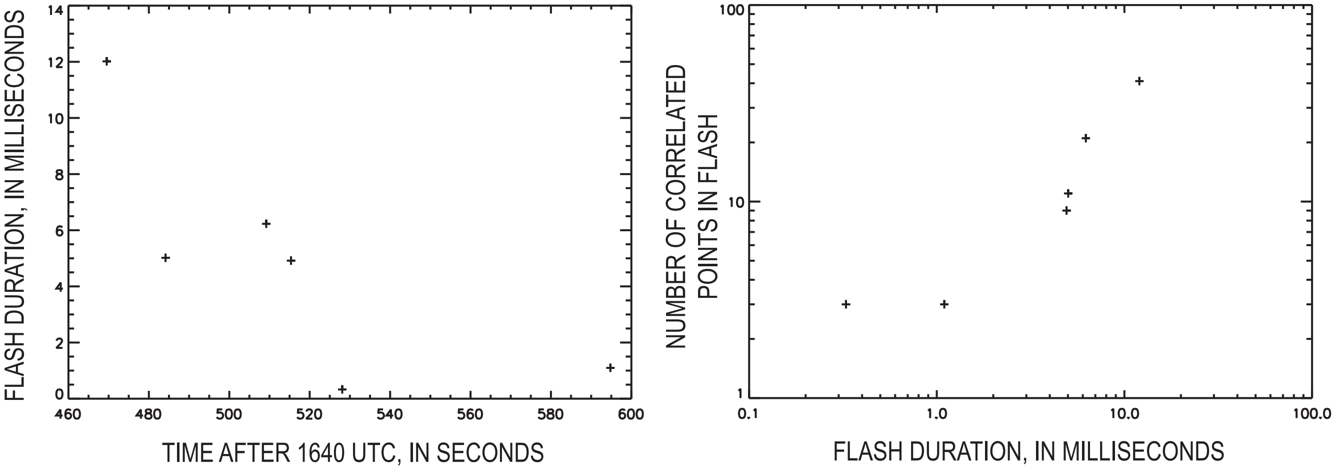

Figure 22. Durations of flashes during the 0742 AKST (1642 UTC) explosion of the Augustine Volcano on January 28, 2006. The dates and times in this plot are in universal time (UTC).

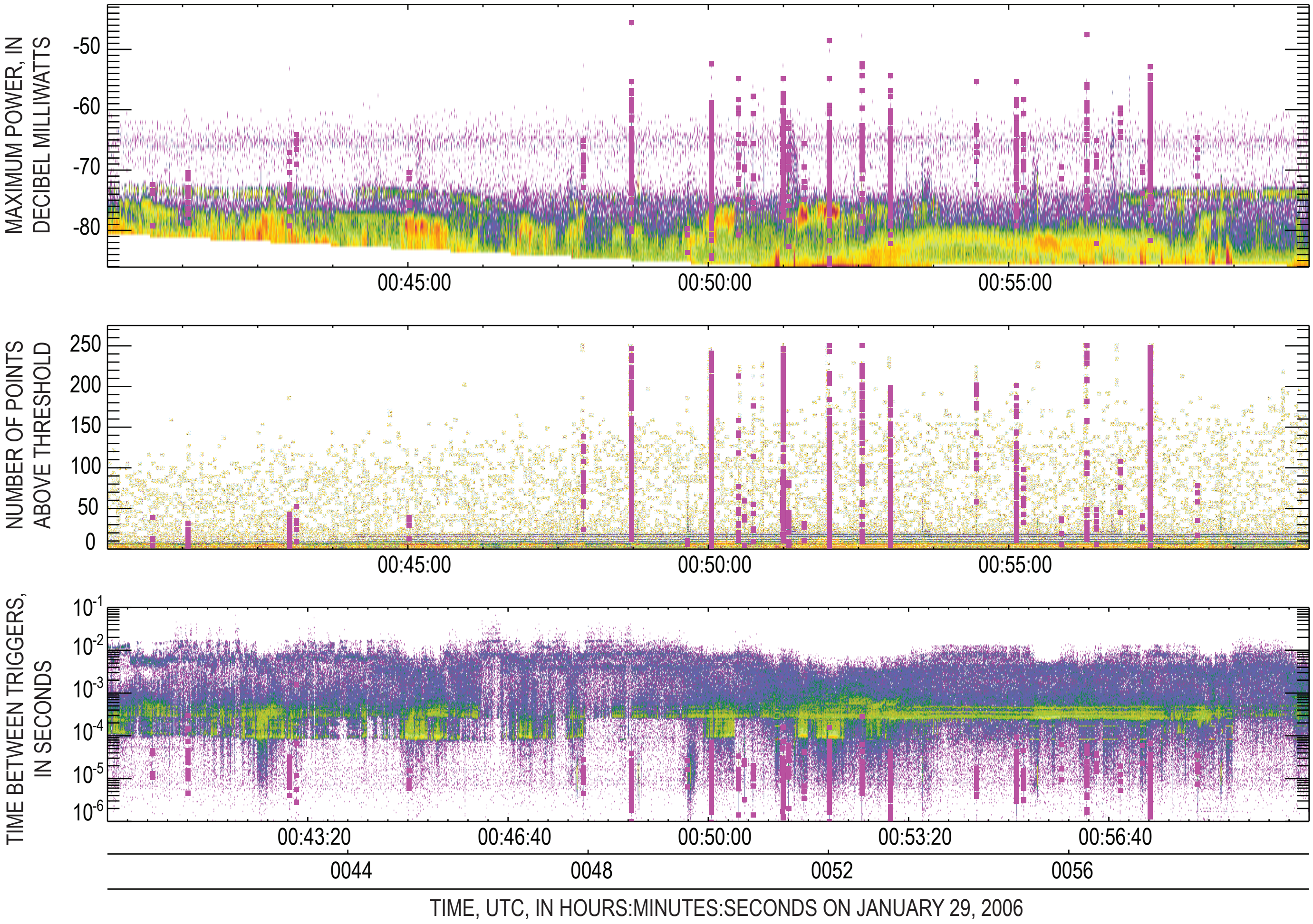

Figure 23. Lightning during Augustine Volcano's continuous eruptive phase, 1540 to 1600 AKST on January 28 (0040 to 0100 UTC on January 29). See the captions of figures 6 and 7 for details. The dates and times in this plot are in universal time (UTC).

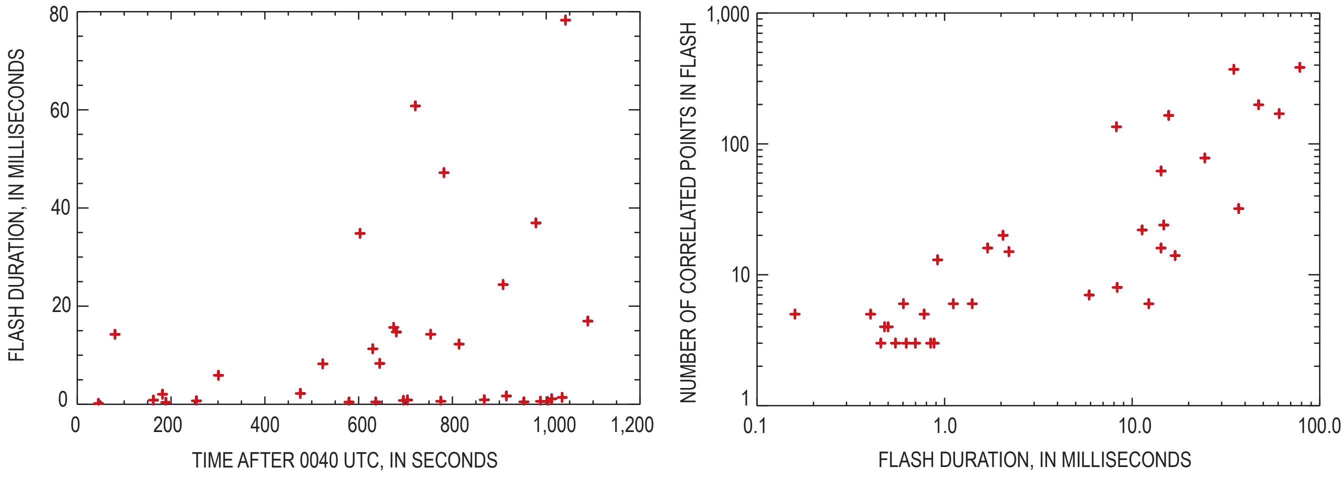

Figure 24. Durations of flashes between 1540 and 1600 AKST during Augustine Volcano's eruption on January 28 (0040 and 0100 UTC on January 29, 2006). The dates and times in this plot are in universal time (UTC).

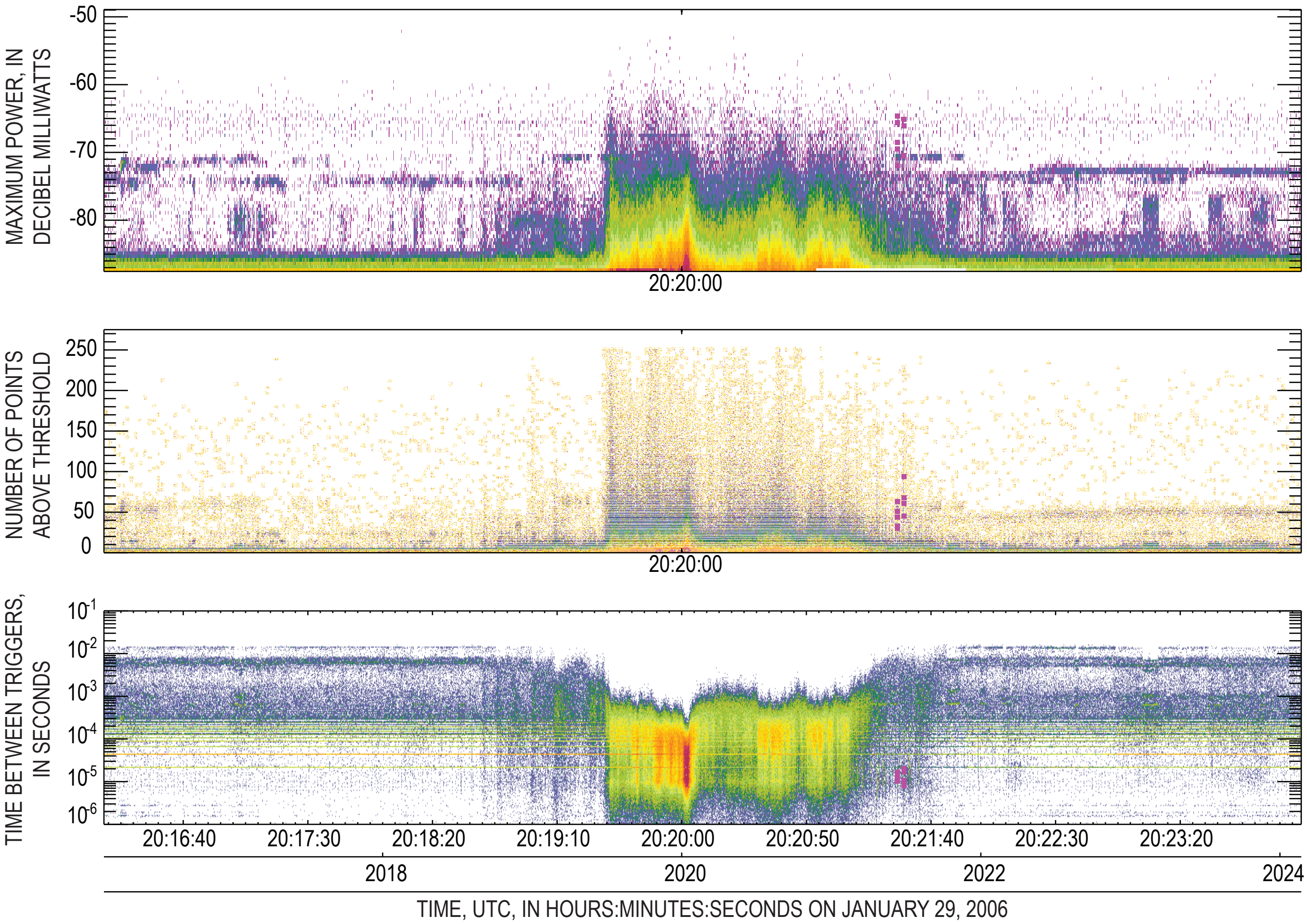

Figure 25. Lightning and electrical signals during Augustine Volcano's eruptive pulse at 1120 AKST (2020 UTC) on January 29, 2006. See the captions of figures 6 and 7 for details. The dates and times in this plot are in universal time (UTC).

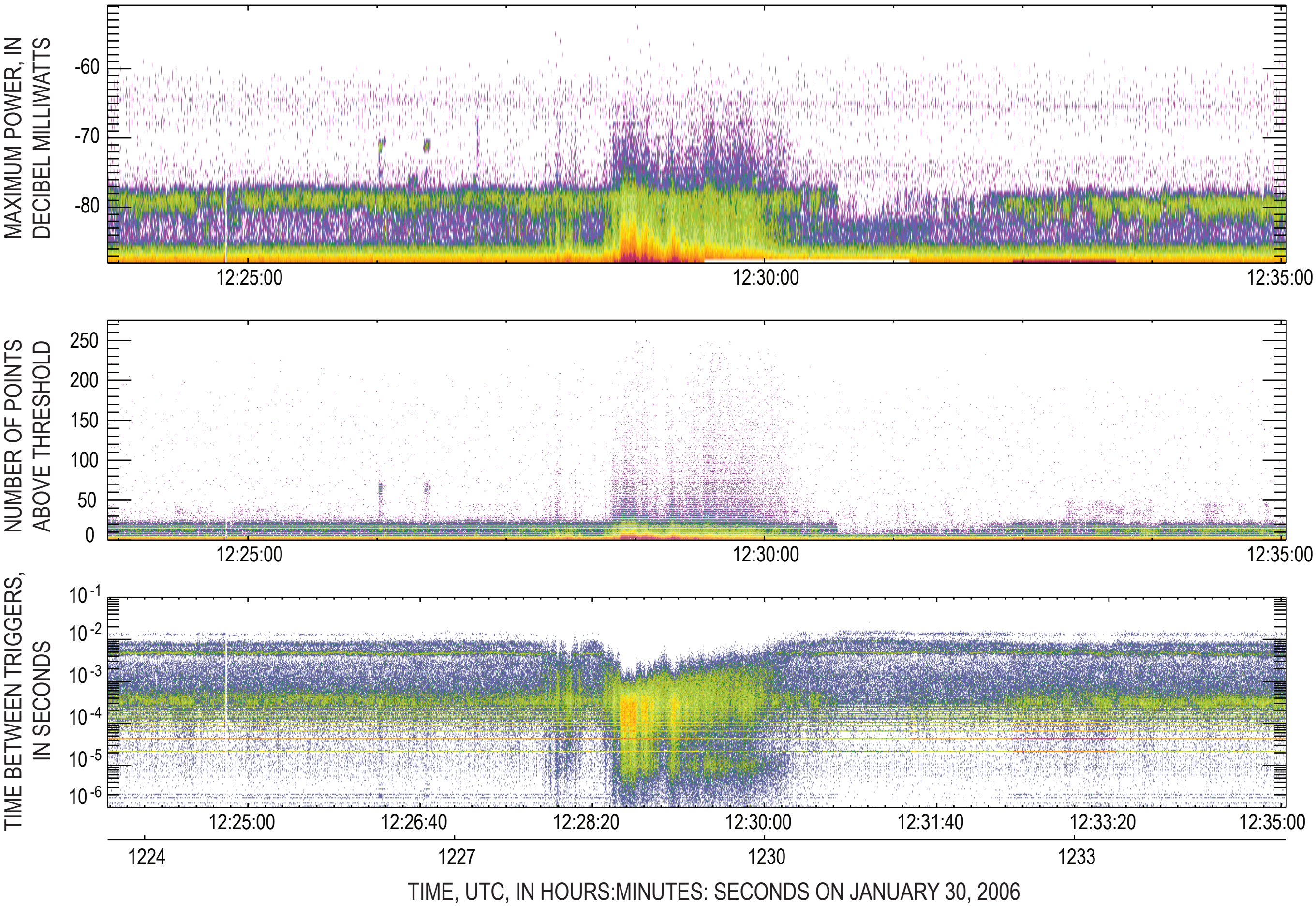

Figure 26. Lightning and electrical signals during Augustine Volcano's eruptive pulse at 0328 AKST (1228 UTC) on January 30, 2006. See the captions of figures 6 and 7 for details. The dates and times in this plot are in universal time (UTC).

location of sources for different time of arrival differences. Table 3 shows the time differences for the 6 periods. Because the signals were weak and coming from close to the volcano we would not expect to receive them at Anchor Point. The station at Oil Point was in a good location to observe signals arising from lava and pyroclastic flows on the north and east sides of Augustine. Because the station on West Island was very close (5 km), we expected to see many correlations in its data. However, we found correlations only during one period (table 3). There are two possible reasons for this. First we found a defective part in the antenna that could have intermittently blocked the signals, but we don't know when the part failed. Second, most of the other correlated signals seemed to come from the east side of Augustine Volcano and not visible to the station. Most of the ash and lava flows were also on the east side of the volcano (Coombs and others, this volume).

All these electrical emission are thought to be the result of charging of ash or gas during extrusion and flow of lava and pyroclastic materials. The breakup of material during pyroclastic flows can cause particles to become charged by fracto-emission (Hoblitt, 1994; Miura and others, 1996) (this mechanism will be discussed below). Additionally the interaction of hot volcanic material and water has been observed to produce charged particles (Vogfjörd and others, 2005).

For the event on March 5 there were several thousand correlated points received by the stations at Homer and Oil Point between 10:08:50 and 10:09:40 AKST (19:08:50 and 19:09:40 UTC). Their time difference were within a few tenths of a micro second of 240.0 μs. Figure 28 shows that these electrical signals came from the northeast side of Augustine Volcano along lava and ash flows. Neither the seismic data nor acoustic data give an indication that anything unusual occurred to give the electrical signals. Thus, it is likely they were associated with some sort of gravitationally driven flow event. Although the time difference could be due to events on the volcano's southwest side, neither station could have seen events occuring in this location.

On March 7 there was an event that produced a small number of correlated points between the Homer and West Island stations, with a duration of about 15 seconds. As this signal ended there were 10 seconds of correlated points between Homer and Oil Point. There were no points from Homer that correlated with both Oil Point and West Island. A possible explanation for this could be that initially the flow or eruptive material was near the summit and visible from both the east and the west but not the north. As the material came down the north east side it became visible from the north but not the west. This event was the only one which produced correlation between the West Island station and one of the other stations that we found. The locations of the events giving rise to these signals are close to the intersection of the 240 µs and 327 µs lines on figure 28.

Several more events were seen on March 9, 10, and 11 (see table 3). The time differences of 237.2 µs to 238.5 µs indicate that they came from the west or south faces of Augustine. The south face can be excluded as it would not be visible from Oil Point to the north. The most likely source is the avalanche channel on the northeast face.

Discussion and Conclusions

The electrical activity measured during the eruption of Augustine Volcano has given us a wealth of new information on volcanic lightning. We have classified the lightning and smaller discharges into two phases and three types. The phases are the explosive phase and the plume phase, and the types are (1) small and very short vent discharges, (2) small near-vent lightning, and (3) thunderstorm-like plume lightning. A continuous variation of phenomena spanning these three classifications is very likely. The three types are shown as simple drawings in figure 29.

The nearly continuous signals from the vent discharges do not consist of a continuous radio signal but of impulses that occur about every 10 to 100 µs. A developing lightning channel could emit a similar series of impulses, but the impulses would form a long channel in the process. The vent discharges appear to remain localized at the vent. If they went much

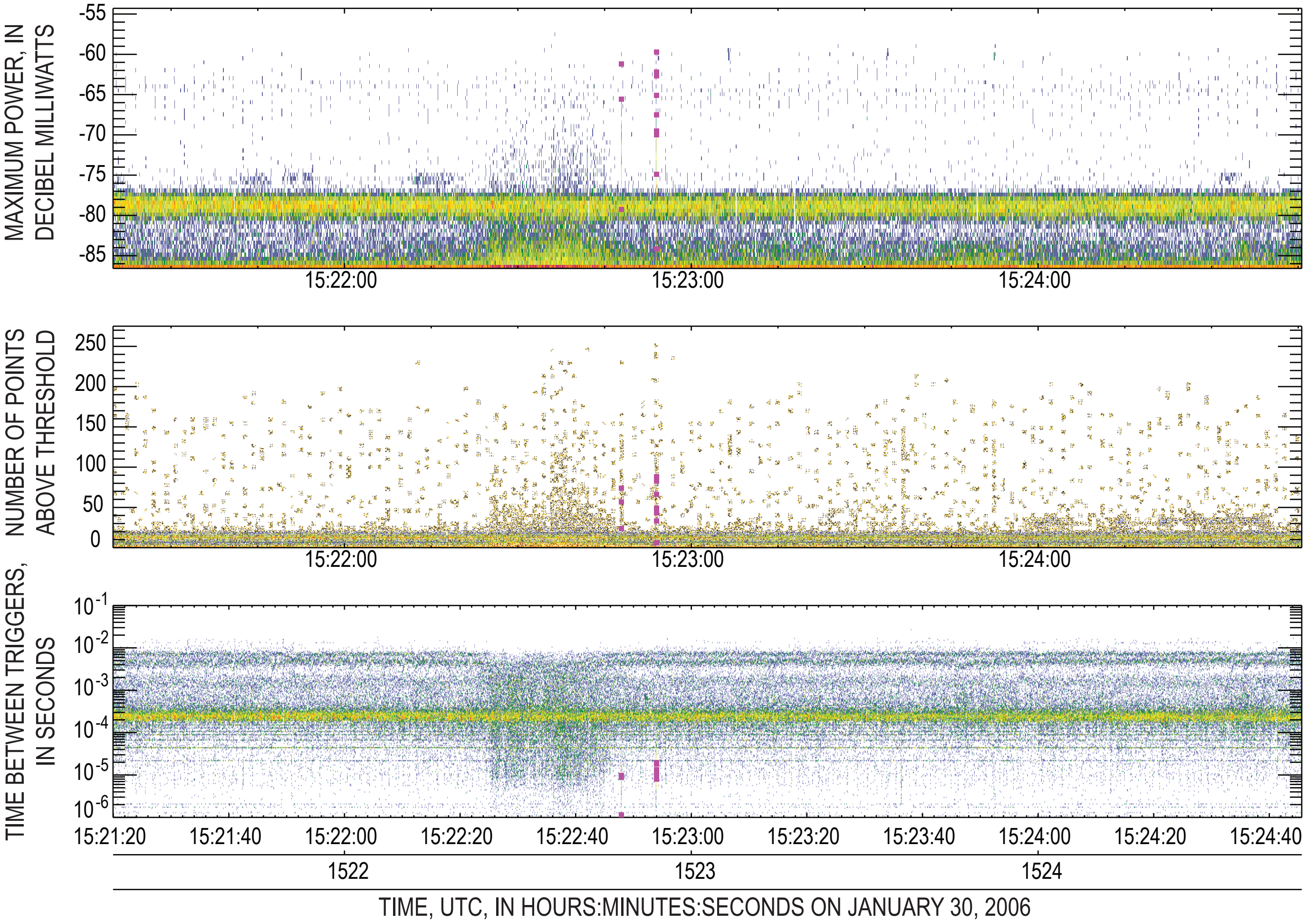

Figure 27. Lightning and electrical signals during Augustine Volcano's eruptive pulse at 0622 AKST (1522 UTC) on January 30, 2006. See the captions of figures 6 and 7 for details. The dates and times in this plot are in universal time (UTC).

Table 3. Electrical activity at Augustine Volcano detected during March 2006.

Date UTC	Time UTC	Homer-Oil Point Δt (arrival time difference) (µs)	Δt spread half-width (µs)	Duration (s)	Comments
March 5	1909	240.0	0.3	50	This correlation has the most points, also a suggestion of a Homer-Anchor Point correlation at 15.4 µs.
March 7	1241	240.0	0.3	10	Also a good 15 s of Homer-West Island correlations at 327.0 µs (0.3 µs wide).
March 9	2212	238.5	1.0	60	
March 10	0058	237.65	0.25	50	
	0059	237.7	0.1	10	
	0840	237.7	0.2	30	
March 11	0311	237.4	0.6	50	Time difference progressed from 237.8 to 237.2 µs.

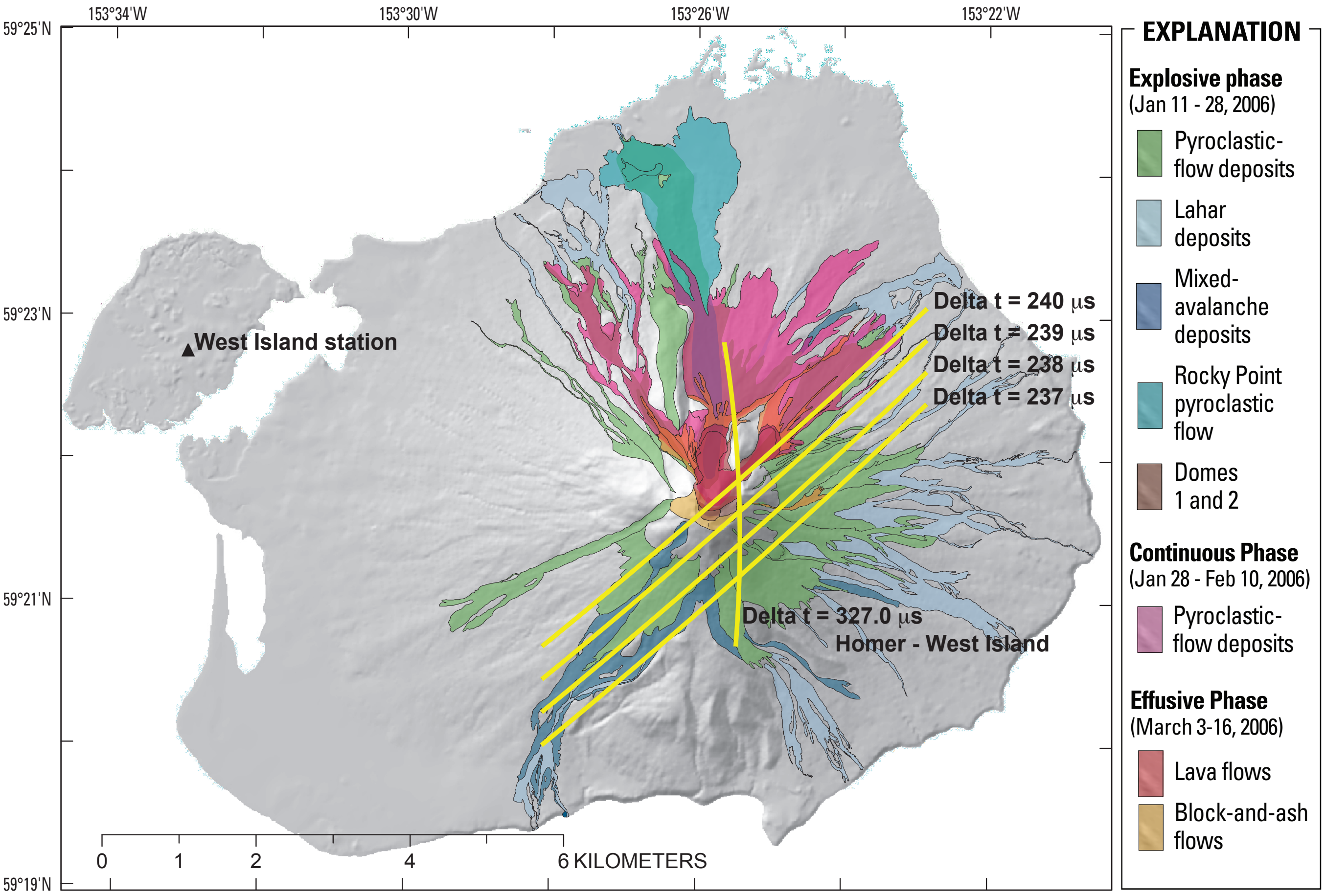

Figure 28. Simplified geologic map of Augustine Volcano deposits from the 2006 eruption with arrival time difference hyperbolas for March 2006. The time differences of 237 to 240 µs are for a combination of the Homer and Oil Point stations. Signal correlations were seen between Homer and West Island stations with a time difference of 327 µs. Base map courtesy of M.L. Coombs.

above the vent they would have been detected by the station at Anchor Point. In the large explosion on January 27 at 2031 AKST (January 28 at 0531 UTC) these impulses continued for 3 minutes. The discharges appear to be disconnected and independent. The RF power emitted by the impulses during vent lightning events is similar in magnitude to the power emitted during the formation of leader channels in thunderstorms (Thomas and others, 2001). This indicates that the sizes of the discharges that produce the RF are about the same as the steps during leader formation, about 10 to 100 m. The onset of the discharges coincided with the onset of the explosion indicating that the particle charging is due to processes associated with the explosion itself, rather than a delayed process such as particle interactions in a developing plume.

The charge is probably generated as the magma expands and fractures into ash particles in the volcanic conduit. The micro-physical properties of the ash and the other particles in the conduit will determine the sign of the charge transfer. This type of process is referred to as fracto-emission and leads to charged particles and emission of light in laboratory experiments. It was proposed by Lane and Gilbert (1992) as the mechanism charging ash rich plumes at Sakurajima Volcano in Japan. James and others (2000) conducted laboratory experiments fracturing pumice samples and found that charged particles were generated. Once the charged particles are generated in the conduit the positive and negative charge must be separated to produce the high electric field and discharges. In the upper part of the plume, as in thunderstorms, gravitational separation divides the particles by size and weight; however, in the conduit, jet flow dynamics could separate the particles. The observed vent discharges may be between different regions in the ejecta or between the ejecta and the vent of the volcano. Our observations of the upward development of the near-vent lightning indicate that the developing plume has a net positive charge. This indicates that much of the negative charge remains attached to the vent or is on large particles that fall back almost immediately. These vent discharges may be similar to the lightning photographed during Strombolian eruptions, such as those at Sakura-jima or Tavurvur. During the Augustine eruption there was probably much more ash, and these new-vent discharges could have been obscured by the ash cloud and would not have been visible even with good weather conditions.

During the explosions there were small near-vent lightning flashes that developed upward for several kilometers into the erupting column. These were observed as organized sets of impulses correlated between the Homer and Anchor Point stations. We were able to determine the altitude development of one of these near-vent discharges from the interference between the direct RF signal and the signal reflected from the sea surface received at the Homer station. Thunderstorm lightning that strikes the ground almost always begins in the cloud with a downward propagating leader channel forming a conducting path to ground, followed by a high current return stroke back up the channel. This return current pulse produces the bright flash as well as a low frequency electromagnetic pulse that can be used to locate the ground strike point by a network like the one operated by the BLM in Alaska. Occasionally lightning begins with a leader channel that develops from a tall tower and propagates upward into the thundercloud, with no associated return stroke. We suspect that most of the near-vent flashes begin at the summit and propagate upward into the developing column. This is consistent with the fact that no return strokes were detected by the BLM network during the explosions we observed. The near-vent lightning began 25 to 300 seconds after the onset of the explosion, during which time period an eruptive column formed (see table 2). The near-vent

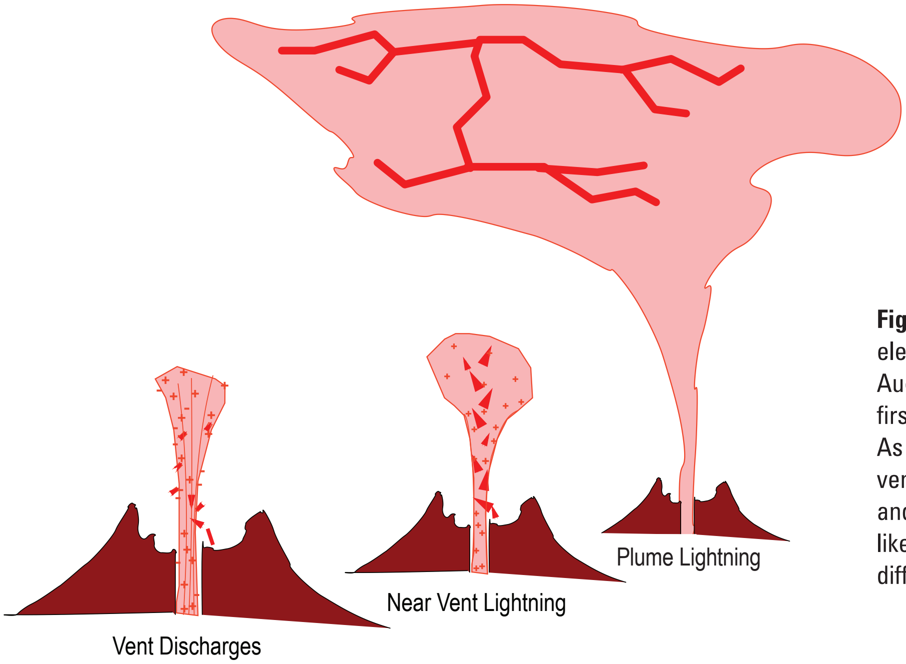

Figure 29. The three types of lightning or electrical discharges seen in the 2006 eruption of Augustine Volcano. The vent discharges are seen first, occurring as soon as the explosion begins. As the eruptive column develops upward near-vent lightning begins. After the plume develops and some charge separation occurs, thunderstorm like lightning begins; it is probably between two different charge regions at different altitudes.

lightning discharges ended several minutes after the end of the explosion. Charge generated by fracture in the conduit can account for these discharges. In other eruptions we would expect to see similar lightning discharges in or very close to the erupting column. The vent discharges indicate the electric field is the largest at the vent and this is where the near vent lightning would start and develop up into the plume.

One clear sequence of plume lightning was observed after the large explosion at 2031 AKST on January 27 (0531 UTC on January 28). The lightning began about 4 minutes after the onset of the large explosion and a minute after the explosion stopped. All the lightning during this period was intracloud (IC) lightning or upward lightning from the summit. There were no CG flashes detected by the BLM network. Data from the NEXRAD radars indicated that the plume extended to an altitude of 10.5 km (a typical height for thunderstorms) and drifted to the south east. It is very likely that the volcano injected a large volume of hot moist air into the cold winter atmosphere, producing conditions similar to those that exist in a small summertime thunderstorm (Williams and McNutt, 2004). As the buoyant air rises and mixes with surrounding air and cools, water droplets and ice are formed, that fall back through the rising air. This is the basis of the mechanism that is thought to produce charge separation in thunderstorms (Williams, 1985). A natural thunderstorm will typically last longer than this volcanic plume as it will have a much longer lasting source of rising warm moist air. A rough estimate of the amount of water injected into the atmosphere during the main explosion on January 28, 2006, can be made assuming that each cubic meter of magma had 100 kg of water (Williams and McNutt, 2005). About 17×10^6 m^3 of magma was erupted (Coombs and others, this volume). Thus there was about 1.7×10^9 kg of water vapor was injected into the atmosphere. Simulation of a small thunderstorm required about 10^9 kg (T. Mansell, oral commun., 2009). Thus all the components that generate and separate charge in a thunderstorm seem to be present in this plume.

After the ash, tephra, and gases have been injected into the plume by the initial velocity and buoyancy, the larger particles will settle out faster than the light ones. Cooled by entrained air, the particles will serve as condensation nuclei and the large quantities of water vapor will become coated with water or ice. The different sized particles falling at different speeds will collide, exchange charge, and separate. Because many of the particles are ice or water coated charge will be separated as in a thunderstorm. Volcanic plumes may have charge separation mechanisms not present in thunderstorms, because of collisions between different sizes and types of ash particles in the plume or collisions between ash particles and water droplets. If the large particles fall at 5 m s^{-1}, a plume could produce lightning for as long as 20 minutes as the particles fell 6 km.

Many of the particles were electrically charged during the ejection process (as evidenced by the vent discharges). If enough of these particles charged by fracturing in the conduit were not neutralized by the vent discharges and reach high altitudes and if the positive and negative charge were on different sized particles, subsequent settling could separate the charge and lead to lightning discharges. Lane and Gilbert (1992) proposed that electric fields (no lightning) observed during ash eruptions at Sakurajima were the result of this fracto-emission in the volcanic conduit and that the particles were charged negative and the positive charge was on gas. Our observations verify their idea that charged particles are generated in the explosion before they leave the vent of the volcano.

We can estimate the amount of charge needed if this mechanism was responsible for plume lightning we observed. A typical IC lightning flash discharges 10 to 40 C of charge. There were about 150 big flashes in the 10 minute sequence that would require 1,500 to 6,000 C. This implies a current of 2.5 to 10 A. The charging current produced by the settling of one type of charge particle is the charge density times the fall speed times the plume area. An 100 km^3 area (a square 10 km on a side) and a fall rate of 5 m s^{-1} indicates a charge density of 5 to 20 C km^{-3}. In thunderstorms charge densities are several C km^{-3} with a maximum of 10 C km^{-3} (MacGorman and Rust, 1998). Although this mechanism seems possible it is hard to understand why there was not charge separation and lightning during the period that the plume was forming.

It seems unlikely that gravitational separation of the different sized ash particles charged during the explosion could separate a sufficient amount of charge to produce the series of lightning flashes. Continued charge generation by a process such as the thunderstorm ice mechanism is needed for all but a brief series of flashes. More observations are needed to determine the roll of each charging mechanism in volcanic plumes.

Acknowledgments

We acknowledge important contributions by Nicholas O'Connor and Sandra Kieft in preparing for and conducting the field studies. This work was supported by the National Science Foundation under grants ATM-0536950 and ATM-0354218. Partial support was also provided by the Alaska Volcano Observatory, the University of Alaska Geophysical Institute, the U.S. Geological Survey, the State of Alaska, and NSF grant ATM-053831.

References Cited

Anderson, R., Bjornsson, S., Blanchard, D., Gathman, S., Hughes, J., Jonasson, S., Moore, C.B., Survilas, H.J., Vonnegut, B., 1965, Electricity in volcanic clouds: Science, v. 148, p. 1179–1189.

Behnke, S.A., Thomas, R.J., Krehbiel, P.R., and Rison, W., 2005, Initial leader velocities during intracloud lightning—possible evidence for a runaway breakdown effect: Journal Geophysical Research, v. 110, D10207, doi:10.1029/2004JD005312.

Bolton, J. G., and Slee, O.B., 1953, Galactic radiation at radio frequencies—V., The Sea Interferometer: Australian Journal of Physics, v. 6, p. 420–433.

Brook, M., Moore, C.B., and Sigurgeirsson, T. 1974, Lightning in volcanic clouds: Journal. Geophysical Research, v. 79, p. 472–475, Correction: Journal. Geophysical Research, v. 79, p. 3102.

Coombs, M.L., Bull, K.F., Vallance, J.W., Schneider, D.J., Thoms, E.E., Wessels, R.L., McGimsey, R.G., 2010, Timing, distribution, and volume of proximal products of the 2006 eruption of Augustine Volcano, Alaska, *in* Power, J., Coombs, M.L., and Freymueller, J.T., eds., The 2006 eruptions of Augustine Volcano, Alaska: U.S. Geological Survey Professional Paper 1769 (this volune).

Cummins, K.L., Murphy, M.J., Bardo, E.A., Hiscox, W.L., Pyle, R.B., and Pifer, A.E., 1998, A combined TOA/MDF technology upgrade of the U.S. National Lightning Detection Network: Journal Geophysical Research, v.103, p. 9035–9044.

Grunewald, O., 2007, Visions of earth (photograph of Tavurvur Volcano): National Geographic, v. 212, p. 14–15, September 2007.

Hoblitt, R.P., 1994, An experiment to detect and locate lightning associated with eruptions of Redoubt Volcano: Journal Volcanology and Geothermal Research, v. 62, p. 499–517.

James, M.R., Lane, S.J., and Gilbert, J.S., 2000, Volcanic plume electrification—experimental investigation of a fracture-charging mechanism: Journal Geophysical Research, v. 105, p. 16641–16649.

Lane, S.J., and Gilbert, J.S., 1992, Electric potential gradient changes during explosive activity at Sakurajima volcano, Japan: Bulletin of Volcanology, v. 54, p. 590–594.

McNutt, S.R., and Davis C.M., 2000, Lightning associated with the 1992 eruptions of Crater Peak Mount Spurr Volcano, Alaska: Journal Volcanology and Geothermal Research, v. 102, p. 45–65.

McNutt, S.R., Tytgat, G., Estes, S.A., and Stihler, S.D., 2010, A parametric study of the January 2006 explosive eruptions of Augustine Volcano, using seismic, infrasonic, and lightning data, *in* Power, J.A., Coombs, M.L., and Freymueller, J.T., eds., The 2006 eruption of Augustine Volcano, Alaska: U.S. Geological Survey Professional Paper 1769 (this volume).

Mather, T.A., and Harrison, R.G., 2006, Electrification of volcanic plumes: Surveys Geophysics, v. 27 p. 387–432, DOI 10.1007/s10712-006-9007-2.

Miura, T., Koyaguchi, T., and Yoshikazu, T., 1996, Atmospheric electric potential gradient measurements of ash clouds generated by pyroclastic flows at Unzen: Geophysical Research Letters, v. 23, p. 1789–1792.

MacGorman, D.R., and Rust, W.D., 1998, The electrical nature of storms: Oxford University Press.

Petersen, T., De Angelis, S., Tytgat, G., and McNutt, S.R., 2006, Local infrasound observations of large ash explosions at Augustine Volcano, Alaska, during January 11-28, 2006: Geophysical Research Letters, v. 33, L12303, doi:10.1029/2006GL026491.

Rison, W., Thomas, R.J., Krehbiel, P.R., Hamlin, T., and Harlin, J., 1999, A GPS-based three-dimensional lightning mapping system—initial observations: Geophysical Research Letters, v. 26, p. 3573–3576.

Schneider, D.J., Scott, C., Wood J., and Hall T., 2006, NEXRAD weather radar observations of the 2006 Augustine volcanic eruption clouds: Eos (American Geophysical Union Transactions), v. 87, abs. V51C-1686.

Thomas, R.J., Krehbiel, P.R., Rison, W., Edens, H.E., Aulich, G.D., Winn, W.P., McNutt, S.R., Tytgat, G., and Clark, E., 2007, Electrical activity during the 2006 Mount St. Augustine volcanic eruptions: Science, v. 315, p. 1097, doi: 10.1126/science.1136091.

Thomas R.J., Krehbiel, P.R., Rison, W., Hamlin, T., Harlin, J., and Shown, D., 2001, Observations of VHF source powers radiated by lightning: Geophysical Research Letters, v. 28, p. 143–146.

Thomas, R.J., Krehbiel, P.R., Rison, W., Hunyady, S.J., Winn, W.P., Hamlin, T., and Harlin, J., 2004, Accuracy of the lightning mapping array: Journal Geophysical Research, v. 109, no. D14, D14207, doi: 10.1029/2004JD004549.

Vogfjörd, K.S., Jakobsdóttir, S.S., Gudmundsson, G.B., Roberts, M.J., Ágústsson, K., Arason, T., Geirsson, H., Karlsdóttir, S., Hjaltadóttir, S., Ólafsdóttir, U., Thorbjarnardóttir, B., Skaftadóttir, T., Sturkell, E., Jónasdóttir, E.B., Hafsteinsson, G., Sveinbjörnsson, H., Stefánsson, R., and Jónsson, T.V., 2005, Forecasting and monitoring a subglacial eruption in Iceland: Eos (American Geophysical Union Transactions), v. 86, p. 245–248

Williams, E.R., 1985, Large scale charge separation in thunderclouds: Journal Geophysical Research v. 90, p. 6013–6025.

Williams E.R., and McNutt S.R., 2004, Are large volcanic eruptions just dirty thunderstorms?: Eos (American Geophysical Union Transactions), v. 85, Fall meeting. supp., Abstract AE23A-0842.

Williams, E.R., and McNutt, S.R., 2005, Total water contents in volcanic eruption clouds and implications for electrification and lightning, *in* Pontikis, Constantin, ed., Recent progress in lightning physics: Kerala, L\India, Research Signpost, p. 81–94.

The 2006 Eruption of Augustine Volcano, Alaska
Power, J.A., Coombs, M.L., and Freymueller, J.T., editors
U.S. Geological Survey Professional Paper 1769

Chapter 26

Emission of SO_2, CO_2, and H_2S from Augustine Volcano, 2002–2008

By Kenneth A. McGee[1], Michael P. Doukas[1], Robert G. McGimsey[2], Christina A. Neal[2], and Rick L. Wessels[2]

Abstract

Airborne surveillance of gas emissions from Augustine Volcano and other Cook Inlet volcanoes began in 1990 to identify baseline emission levels during noneruptive conditions. Gas measurements at Augustine for SO_2, CO_2, and H_2S showed essentially no evidence of anomalous degassing through spring 2005. Neither did a measurement on May 10, 2005, right after the onset of low level seismicity and inflation. The following measurement, on December 20, 2005, showed Augustine to be degassing about 600 metric tons per day (t/d) of SO_2, and by January 4, 2006, only 7 days before the first explosive event, SO_2 emissions had climbed to ten times that amount. Maximum emission rates measured during the subsequent eruption were: 8,930 t/d SO_2 (February 24, 2006), 1,800 t/d CO_2 (March 9, 2006), and 4.3 t/d H_2S (January 19, 2006). In total, 45 measurements for SO_2 were made from December 2005 through the end of 2008, with 19 each for CO_2 and H_2S during the same period. Molar CO_2/SO_2 ratios averaged about 1.6. In general, SO_2 emissions appeared to increase during inflation of the volcanic edifice, whereas CO_2 emissions were at their highest during the period of deflation associated with the vigorous effusive phase of the eruption in March. High SO_2 was probably associated with degassing of shallow magma, whereas high CO_2 likely reflected deep (>4 km) magma recharge of the sub-volcanic plumbing system, For the 2005–6 period, the volcano released a total of about 1.5×10^6 tons of CO_2 to the atmosphere, a level similar to the annual output of a medium-sized natural-gas-fired powerplant. Augustine also emitted about 8×10^5 tons of SO_2, similar to that produced by the 1976 and 1986 eruptions of the volcano.

Introduction

Augustine Volcano is located on an uninhabited island in the lower Cook Inlet of Alaska (fig. 1). It lies about 100 km west of Homer and 280 km southwest of Anchorage. The site of frequent explosive eruptions, Augustine Volcano is a young 1,250-m-high convergent plate boundary stratovolcano, lying about 100 km above the Benioff zone in the eastern portion of the Aleutian arc. It has had at least four periods of significant activity in the twentieth century in 1935, 1964–65, 1976, and 1986 before the most recent eruption in 2006 (Miller and others, 1998) and erupts mostly andesitic and dacitic lavas (Kienle and Swanson, 1983). Augustine Volcano consists of a broad apron of pyroclastic and debris-avalanche deposits surrounding a central vent and dome complex (Swanson and Kienle, 1988; Waitt and and Begét, 2009). When Augustine erupts, a number of volcanic hazards have the potential to threaten communities in south central Alaska and aviation, industrial facilities, petroleum and natural gas production, shipping, and other activities (Waythomas and Waitt, 1998).

Airborne gas measurements at Augustine Volcano are part of a systematic program to monitor baseline gas emissions at Cook Inlet volcanoes in order to recognize the beginning of unrest and to identify baseline values of gas emissions to which future measurements could be compared in the event of unrest (Doukas, 1995). In 1990, 4 years after the 1986 eruption, annual measurements were begun and have continued through 2008. This paper reports gas measurements made from 2002 to 2008 with special emphasis on precursory and eruptive activity during 2005–6.

Data from two earlier eruptions of Augustine allow comparisons with peak SO_2 emission rates measured during 2006. From February 8 through 18 during the 1976 eruption, Stith and others (1978) made a series of measurements using a Meloy flame photometric detector to determine total gaseous sulfur, which was assumed, by smell, to be all SO_2. They

---

[1] Cascades Volcano Observatory, U.S. Geological Survey, 1300 SE Cardinal Court, Vancouver, WA 98683.

[2] Alaska Volcano Observatory, U.S. Geological Survey, 4210 University Drive, Anchorage, AK 99508.

measured a peak value of 25,900 t/d of SO_2 on February 9, 1976, followed by 8,600 t/d on February 11, 13, and 18. Their lowest measured SO_2 emission rate was 173 t/d on February 12, 16, and 17. A little more than a year after the eruption, they returned to Augustine for an additional measurement and recorded a value of 26 t/d on April 22, 1977. Using a scrubber system attached to their instrument, they were also able to remove SO_2 and estimate an emission rate for H_2S of 3.5 t/d for the 1977 measurement. They estimated that Augustine emitted about 1×10^5 tons of SO_2 during the 1-year period surrounding the 1976 eruption. As this estimate neglects the paroxysmal emissions of April 1976, it is only a minimum value. They point out that a significant portion of the SO_2 emitted during the paroxysmal eruptions was attached to the surfaces of ash particles and fell out of the plume after a short time.

During the March–April 1986 eruption of Augustine, Rose and others (1988) successfully made airborne ultraviolet spectroscopic (COSPEC) plume measurements on April 3, 1986, and calculated a SO_2 emission rate of 24,000 t/d during active ash emission and under high wind conditions; gas emission rates were likely higher during the peak of the eruptive activity from March 27 to April 3. More than a year after the end of the eruption, additional measurements of 380 t/d (July 24, 1986) and 45 t/d (May 24, 1987) were made during a period of post-eruptive passive degassing (Symonds and others, 1990). Rose and others (1988) used ash leachate and emission data along with seismic information and other observations to scale up their SO_2 measurement of April 3, 1986, to an emission rate of 3.75×10^4 t/d that was likely achieved on more than one day during the peak phase of the eruption.

Before the 2005–6 eruption, fumarolic activity at Augustine was confined to scattered areas near the summit dome complex (fig. 2). As early as the summers of 1986 and 1987, Symonds and others (1990) observed that the 1986 lava dome produced >90 percent of the gas emitted from Augustine. Other sources were the solfataras located west of the 1986 dome along the high ridge between the remnants of the 1935 and 1964 lava domes and in unconsolidated pyroclastic flow deposits near the northern base of the volcano's dome complex. In 1987, at least one fumarole on the dome was as hot as 870°C, but by 1989 it

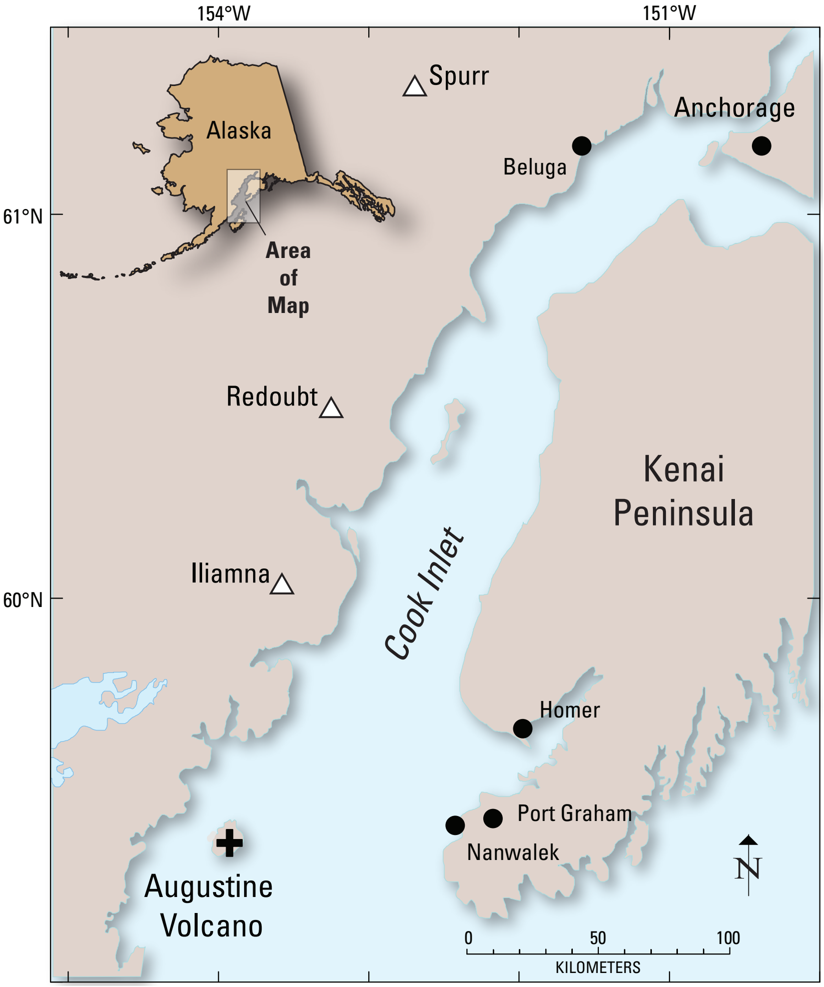

Figure 1. Location map for Augustine Volcano. Plus sign (+), Augustine Volcano; Open triangles, other volcanoes of Cook Inlet; Filled circles, cities and towns near Cook Inlet. Inset map of Alaska.

was only 640°C (Symonds and others, 1990). By 1992, fumarole temperatures had declined to about 97°C, boiling point for the summit elevation (Symonds and others, 2003).

Methods

Instrumentation

In this study, we used an instrument platform developed over the past 15 years at the Cascades Volcano Observatory (CVO). The platform is mounted on board an aircraft for transport to volcanic centers, usually in remote settings, and is capable of measuring volcanic CO_2, SO_2, and H_2S (Gerlach and others, 2008). For airborne emission measurements of the Augustine plume, a LI-COR Model LI-6252 nondispersive infrared analyzer and a Model LI-670 flow control unit were used to determine volcanic CO_2 (Gerlach and others, 1997; Gerlach and others, 1999). An Interscan Model 4170 analyzer with a 0 to 1 ppm range and an Interscan Model 4240 analyzer with a 0 to 2 ppm range were used for direct measurements of H_2S and SO_2 in the plume, respectively. These instruments consist of an electrochemical voltametric sensor coupled to a 1 -liter-per-minute sample-draw pump. The calibrated analog output of the instruments record gas concentrations as described in detail by McGee and others (2001) and Werner and others (2006).

The airborne instrument package also included a COSPEC for measuring SO_2 column abundance (units of parts per million-meter, or ppm·m) and a type-T thermocouple shielded from wind and direct sunlight for measuring ambient air temperature. Atmospheric pressure was measured in the unpressurized aircraft cabin by a pressure transducer mounted within the LI-COR analyzer. A GPS receiver was used to tag the precise latitude, longitude, and altitude of each measurement. Data from all of the instruments were recorded on a common 1/s time base. All gas readings were corrected for the actual pressure and temperature at the altitude at which the measurements were taken.

Procedure

Two different instrument configurations were used for the airborne measurements between 1995 and 2006 owing to funding limitations and instrumentation availability. In one configuration (24 of the 45 campaigns reported in table 1), only a COSPEC V and a Model 60CSX GPS were used to determine SO_2 emission rates. Typically, four to six traverses were flown under the downwind plume perpendicular to the direction of plume travel with the upward-looking COSPEC to determine an average column abundance of SO_2. GPS-registered wind circles (positions logged once per second) at the elevation of the plume were then flown in order to calculate the velocity of plume travel so that a SO_2 emission rate could

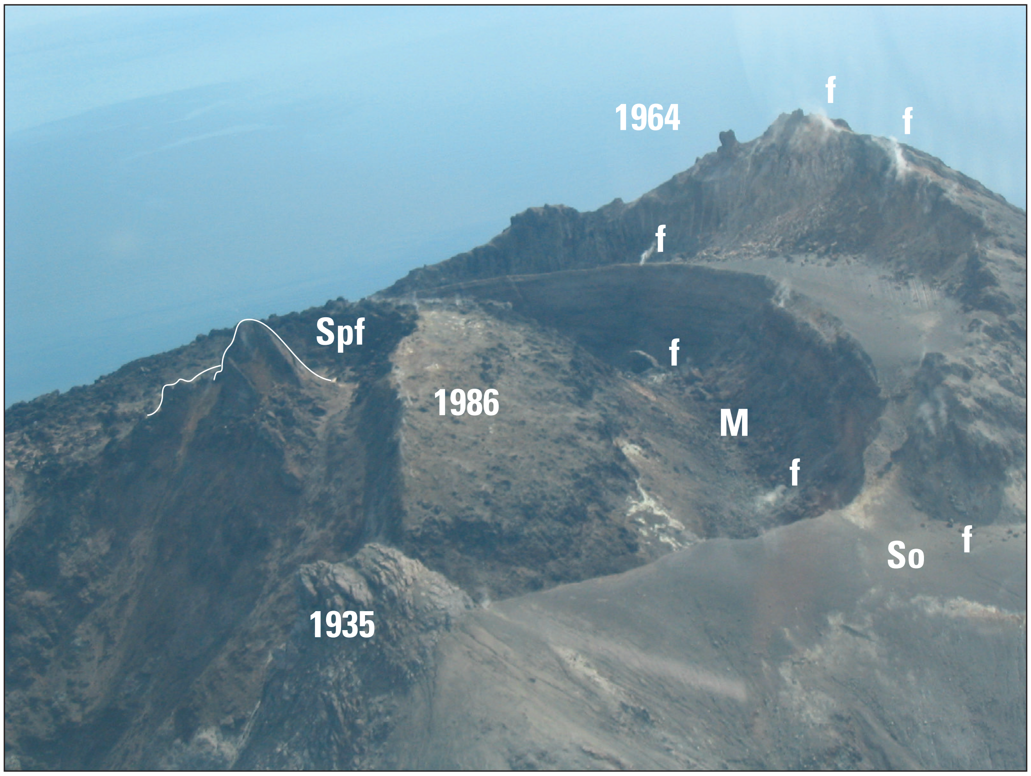

Figure 2. View of 2004 preeruptive summit of Augustine Volcano, as seen from the west. 1986, lava dome surrounded by moat (M) formed during the 1986 eruption. Spf, Spine fumarole located near base of spine (faint outline) (Symonds, and others, 1990). 1964, lava dome remnant forms collar on south summit. 1935, lava dome remnant lies north of the solfatara area (So). f, locations in 2004 wispy boiling-point fumaroles plumes (not sampled). Photo by M. Doukas.

be computed (Doukas, 2002). In the other configuration (21 of the 45 campaigns reported in table 1), the full instrument package for measuring CO_2, SO_2, and H_2S (LICOR, COSPEC, and Interscan) was mounted in a twin-engine aircraft configured for open-flow sampling of external air upstream of engine exhaust as described in Gerlach and others (1997) and Gerlach and others (1999). In addition to the traverses flown under the plume for the COSPEC measurements described above, a series of additional traverses were flown top to bottom through the plume at the same distance downwind of the vent in order to describe a vertical cross section of the plume.

To illustrate data collection techniques, figure 3 shows the reconstructed flight path from GPS data for a typical flight between 1400 and 1500 Alaska Standard Time (AKST) on January 19, 2006, with the full instrumentation package. Five traverses were made underneath the plume for the COSPEC measurements. Then, a series of 12 additional plume profile traverses were flown through the plume ranging from a top traverse at an altitude of 1,700 m above mean sea level (amsl) down to a bottom traverse of 780 m amsl based on aircraft altimeter readings and with an average vertical spacing of 80 m. Winds measured just after the flight by the wind circle method indicated winds out of the west-northwest at an average speed of 6.1 m/s. The plume from Augustine on this day was detected on all but the top and bottom traverses, and the characteristic smell of both H_2S and SO_2 was noticed by the aircrew on all of the traverses through the plume. Atmospheric pressure and temperature were nearly constant inside and outside the plume on each traverse and averaged 88.04 kPa and −9.8°C. No temperature anomaly was detected in the volcanic plume on any of the traverses.

Two representative COSPEC traverses from the January 19, 2006, example are presented in figure 4. The COSPEC SO_2 signal is processed in Peakfit v. 4.0 (AISN Software, Inc.) to determine the area under the signal curve in kilometers×ppm·m. The average ppm·m is then determined by dividing the area by the width in kilometers. The average signal is then reduced by the ratio of the calibration cells used during the flight. The reduction equation gives the SO_2 emission rate (E) in units of t/d:

$$E_{cospec}=0.00023(S_W \times \mathit{Plume\ width} \times \mathit{Ave\ ppm{\cdot}m}) \quad (1)$$

Where S_W is the average wind speed (m/s), Plume width in meters and *Ave ppm·m* is the resultant average ppm·m of the plume traverse. The constant reduces the concentration of the cross section to t/d.

Figure 5 shows a time-series plot of the January 19 CO_2, SO_2, and H_2S data series. The ambient CO_2 background measured on each traverse on either side of the CO_2 anomaly was fit using routines in PeakFit v. 4.0 (AISN Software, Inc.) and subtracted from each peak and zeroed to obtain the volcanic CO_2 gas signal. The resulting CO_2 plume anomaly on January 19, 2006, has a maximum concentration of nearly 5 ppm. A similar procedure was used for H_2S and SO_2 from the Interscan measurements, although no H_2S and SO_2 were present in the ambient

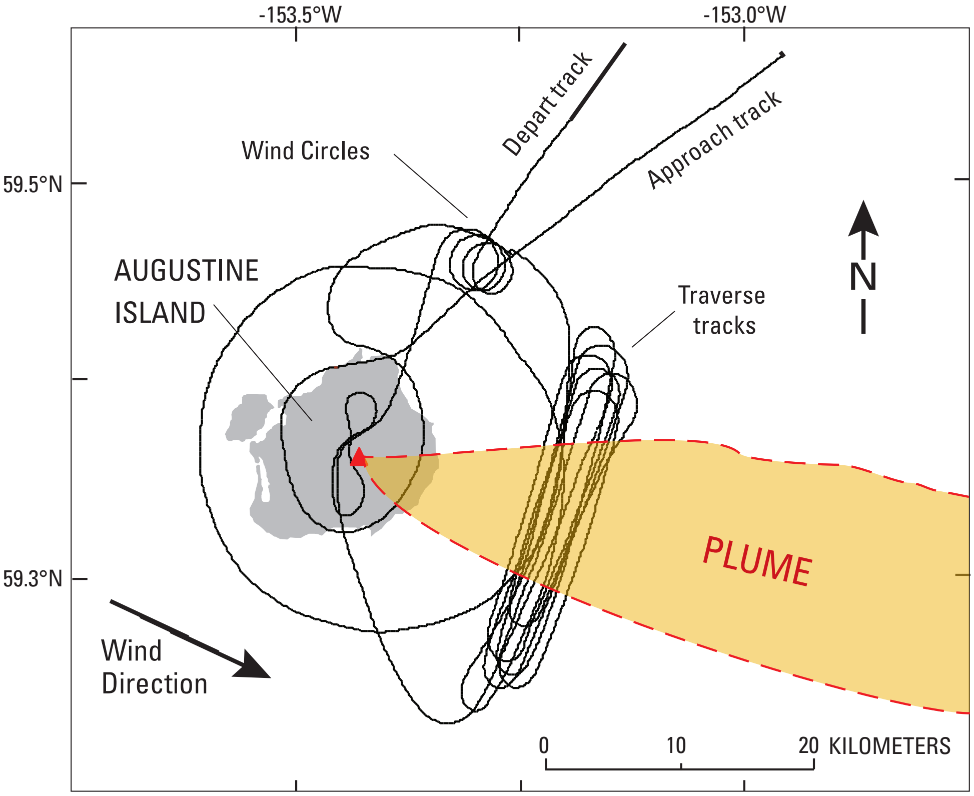

Figure 3. Map showing recorded GPS flight-track positions during the airborne survey at Augustine Volcano, Alaska, on January 19, 2006. Arrow shows determined wind direction, and the cluster of flights lines to the east of Augustine shows the NNE-SSW gas measurement traverses under and intersecting the volcanic plume downwind of the volcano. Red triangle locates the summit of the volcano. Flight tracks for wind circles to determine wind speed are shown northeast of Augustine and were flown at the altitude of the plume core.

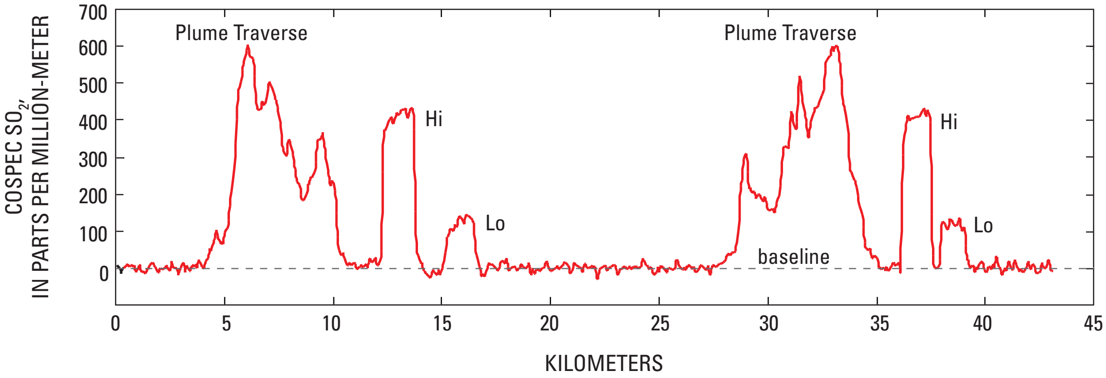

Figure 4. Data series from two of the five COSPEC traverses flown beneath the Augustine plume on January 19, 2006. High and low calibration-cell signals are labeled Hi and Lo and occur after the SO_2 peaks. The horizontal x-axis shows the cumulative flight distance for the two traverses in kilometers. Y-axis units are in parts per million-meter. Note the asymmetry of the SO_2 plume a result of flying in opposite directions.

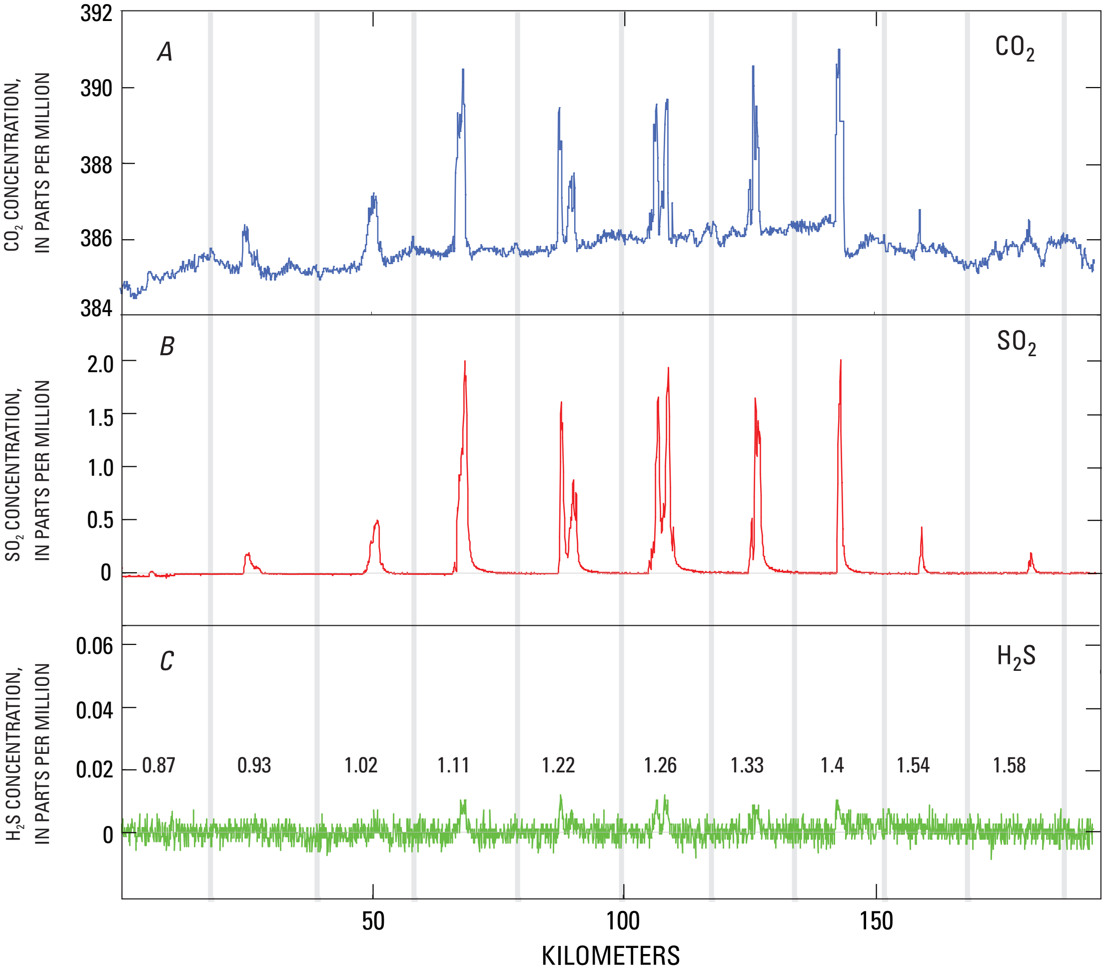

Figure 5. Time-series plots of concentration data (in ppm) for CO_2 (blue), SO_2 (red), and H_2S (green) during the series of traverses flown through the plume at Augustine Volcano on January 19, 2006. The horizontal x-axis is the cumulative flight distance during the traverses (kilometers). Elevation of each traverse indicated in kilometers in the H_2S box. Vertical gray lines locate turn-around point during flight.

(background) air. For the example shown, the maximum plume concentration was about 2 ppm for SO_2 and 0.01 ppm for H_2S.

The conventional airborne method for measuring CO_2 emission rates from passively degassing volcanoes is based on analysis of air sampled through the volcanic plume normal to wind direction. The emission rate is then calculated from the average plume pressure and temperature, wind speed, and the volcanic CO_2 concentration anomaly in cross section (Gerlach and others, 1997). This method was adapted further by using the location of H_2S peaks, when present, as a guide to resolving the boundary between volcanic CO_2 and ambient CO_2 (McGee and others, 2001). Further, anomalous CO_2 signals appear during flying maneuvers (fig. 5, between altitudes 1.26 and 1.33 km, CO_2 time series), but the absence of SO_2 and H_2S peaks confirmed the nonvolcanic nature of the gas. Because the measurement traverses at Augustine were flown in a back-and-forth fashion through the plume, every other traverse was inverted before processing so that all traverses start from a common latitude and longitude and extend in the same direction across the plume. This eliminates introducing potential offsets between traverses due to the travel time of gas in the sample tubing from intake to analyzer when importing the data into contouring and mapping software.

Equation (1) from Gerlach and others (1997) gives the CO_2 emission rate (E) in units of t/d:

$$E=0.457329\,(A\times S_W\times P_{CO_2})/\mathrm{T} \tag{2}$$

where A is the area of plume cross-section (m^2), S_W is the average wind speed (m/s), P_{CO_2} is the partial pressure of CO_2 (Pa) in the plume calculated from the product of average barometric pressure and the average molar concentration of CO_2 in the plume, and T is the average air temperature in the plume (K). The constant includes the formula weight of CO_2, the universal gas constant, and the number of seconds in a day. Average concentration of CO_2 in plume cross section was determined with kriging models for gridding and contouring the concentration measurements. A similar approach was used for computing emission rates for H_2S (constant = 0.354141) and SO_2 (constant = 0.665665).

Figure 6 shows resultant vertical plume cross sections for each of the three gases measured from the plume profile traverses on January 19, 2006, using contouring and mapping software (Surfer v. 8, Golden Software, Inc.). The cross-section for H_2S appears to show a smaller plume than those for CO_2 and SO_2 due to the very low concentration of H_2S and an Interscan detection limit of ~4 ppb for this type of measurement.

Standard deviation (s.d., table 1) for each day's COSPEC SO_2 emission rate calculation are based on the number of traverses flown and therefore represent the natural variation of the volcanic plume's SO_2. To decrease the standard deviation of the mean of our measurements by a factor of two would require that we acquire four times as many observations in our daily measurements. The distance to and from the volcano and aircraft fuel capacity limits time at the volcano and thus the number of traverses made.

With the full instrument configuration, comparison of COSPEC results and Interscan SO_2 emission rates (table 1) were not always in agreement. Variability of environmental conditions during measurement was usually the cause. For example, clouds at the summit or opaque (perhaps ash bearing) plumes may prevent traverses through the whole plume, resulting in higher COSPEC SO_2 emissions compared with Interscan contoured results. A higher concentration section of a plume may lie between traverses. For internal consistency, only the COSPEC results are used in this report.

2005–2006 Eruption Chronology and Gas Data

Before the onset of volcanic unrest in 2005, airborne measurements were usually made once per year. Flight frequency increased once the unrest started but varied considerably over the course of the eruption. From July 2002 through the end of 2008, 45 successful COSPEC measurements of SO_2 and 21 measurements of CO_2 and H_2S were made using the full instrument package.

Emission rates from airborne measurements for CO_2, SO_2, and H_2S at Augustine Volcano from 2002 through 2008 are given in table 1 (Doukas and McGee, 2007) and are shown plotted with other eruption parameters and eruptive phases in figure 7. CO_2 or SO_2 were not detected at Augustine from 2002 through May 2005 with the exception of a very small amount of CO_2 in May 1997. H_2S measurements were not begun until 2001, and no H_2S was detected through 2005. Not until December 20, 2005, was SO_2 detected during a COSPEC flight. CO_2 measurements were not attempted until January 16, 2006. Note that some data from the 2006 time period have been revised from those published in McGee and others (2008), owing to reprocessing using the contouring technique.

Precursory Phase (April 30, 2005–January 11, 2006)

The precursory phase (fig. 7) began with an increase in the number of microearthquakes in late April 2005 (fig. 8; Power and Lalla, this volume). The first airborne gas measurement during the unrest on May 10, 2005, detected no CO_2, SO_2, or H_2S. In mid-summer 2005, geodetic baselines began to lengthen suggesting inflation of the edifice throughout the last half of 2005 (Cervelli and others, this volume). The increasing seismicity continued until early December 2005 when a number of small phreatic explosions were recorded on seismometers (fig. 8; Power and Lalla, this volume). Sulfur smells had been reported in Nanwalek and Port Graham (fig. 1) on December 11, 2005, suggesting the arrival of significant sulfur-bearing gas at the surface at least by early December. On December 12, 2005, a vigorous gas and minor ash plume from the summit area was noted in MODIS satellite imagery and by observers, representing the most energetic of precursory phreatic explosions (fig. 9). The next measurement, for SO_2 only, was made on December 20, 2005, during the period of phreatic activity and showed a modest amount of SO_2 (660 t/d) in the plume. The emission rate was considered a minimum value owing to high wind speeds that pushed the plume to the ground, preventing the aircraft from flying below the plume (fig. 10). From early December 2005 through early January 2006, increased surface heating and snowmelt, phreatic explosions, and the energetic venting of gas and steam were recorded by the seismic network and observed on overflights (Power and Lalla, this volume; Power and others, 2006; Wessels and others, this volume). The following three measurements, taken on January 4, 9, and 10 near the end of the precursory phase, and just days prior to the first violent Vulcanian explosions, showed a significant rise in SO_2 emissions (6,700, 2,800, and 5,500 t/d, respectively; table 1; fig. 7).

Explosive Phase (January 11–28, 2006)

The explosive phase began with a vigorous swarm of volcano-tectonic (VT) earthquakes early on January 11, followed by two brief (1:18 and 3:18 minutes), ash-poor explosions (fig. 7; Power and Lalla, this volume). Additional explosions reamed a vent through the southern margin of the 1986 lava dome on January 13, 14, and 17. Ash clouds from these events deposited trace amounts of fine ash on communities to the northwest and east and disrupted air traffic (Wallace and others, this volume; Neal and others, this volume). Seismicity characteristic of lava effusion was recognized on January 12, 2006, (Power and others, 2006) and a small new lava dome was observed during a gas flight on January 16, 2006. Lava formed a second lava lobe between January 17 and 27, followed by more explosive events (Coombs and others, this volume).

Three gas-measurement flights with the full instrument package were conducted during the explosive phase (January 16, 19, and 24; table 1, fig. 7*A*). Sulfur dioxide emission rates were high (2,800, 3,000, and 730 t/d) but down somewhat

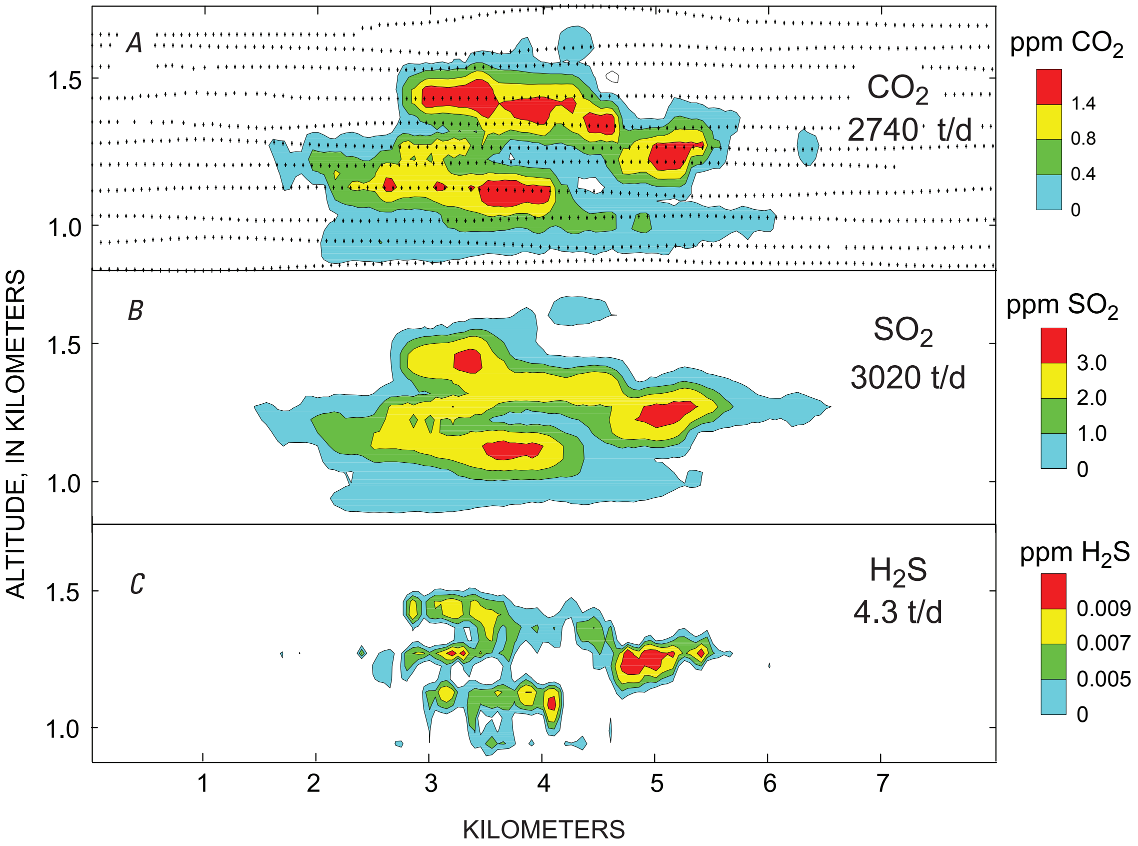

Figure 6. Concentration in a vertical cross-section for the CO_2 (*A*), SO_2 (*B*), and H_2S (*C*) components of the Augustine plume 5 km downwind from summit vent on January 19, 2006. View is upwind toward volcano. The x-axis is the flight distance during the traverses. Contours show concentration of each gas above background with color scale bars to the right. The CO_2 cross-section contains each data point of the traverses used to construct the contours (same points not shown in the SO_2 and H_2S contours). Cross-section of the 4 km-wide plume was constructed with contouring software (Surfer v.8) using exponential kriging models based on variograms fit to the concentration data for the plume. For the example shown, calculated emission rates are 2740 t/d of CO_2, 3,020 t/d of SO_2 and 4.3 t/d of H_2S.

Table 1. Augustine volcanic gas emission rates 2002 to 2008 (data from Doukas and McGee, 2007 and this report).

[Dates of eruption phases separate dates of measurements. Uncertainty derived primarily from wind speed measurements is estimated at plus or minus 19 percent (Doukas, 2002). n=number of traverses, s.d.=standard deviation, nm = not measured, tr = trace, below detection limit, nd = not determined m = minimum result]

Date	COSEC SO_2 t/d	n	s.d.	Interscan SO_2 t/d	LiCor CO_2 t/d	Interscan H_2S t/d	Molar ratio CO_2/SO_2	Distance Downwind km	Wind Speed m/s	Wind Error %	Wind Direction Degrees	T °C	P kpa	Plume Width km
07-01-02	0	5	0	0	0	0	0.0	3	8.8	6%	220	10.2	89.22	0
07-02-02	0	2	0	0	0	0	0.0	2	6.2	x	270	11.5	87.88	0
09-10-02	0	1	0	0	0	nm	0.0	2	nm	nd	180/270	1.4	85.64	0
09-10-02	0	7	0	0	0	nm	0.0	2	nm	nd		3.4	87.21	0
08-03-03	0	4	0	0	0	0	0.0	2	2.7	10%	270	7	88.02	0
08-07-04	0	2	0	0	0	0	0.0	2	3.4	38%	170	16.6	89.82	0
April 30, 2005			Precursory Phase											
05-10-05	0	5	0	0	0	0	0.0	1.5	4.6	26%	120	1.7	87.7	0
12-20-05^{m}	660	4	190	nm	nm	nm	nd	4.5	8.7	nd	90	nm	nm	2.1
01-04-06	6,700	4	790	nm	nm	nm	nd	4.5	13.4	nd	100	nm	nm	9.6
01-09-06	2,800	7	520	nm	nm	nm	nd	1.6	6.2	nd	90	nm	nm	3
01-10-06	5,500	2	200	nm	nm	nm	nd	13	10	19%	60	nm	nm	22
January 11, 2006			Explosive Phase											
01-16-06	2,800	4	500	836	1,470	tr	0.8	7	14.5	10%	0	0.9	96.08	2.6
01-19-06	3,000	5	620	1,516	2,700	4.3	1.3	15	6.1	31%	250	-9.8	88.04	7.5
01-24-06	730	5	80	280	500	1	1.0	15	2	80%	300	-21	80.1	8
January 28, 2006			Continuous Phase											
02-08-06	4,000	3	820	nm	nm	nm	nd	7	16.5	19%	110	nm	nm	10
02-13-06	3,400	3	700	nm	nm	nm	nd	8	5.3	28%	300	nm	nm	13.5
02-16-06	7,800	5	990	nm	nm	nm	nd	7	13	nd	230	nm	nm	4.1
February 24, 2006			Hiatus											
02-24-06	8,930	5	630	nm	nm	nm	nd	4.5	6.5	15%	320	nm	nm	2.3
03-01-06	8,650	8	1,130	nm	nm	nm	nd	4.5	5.6	18%	310	nm	nm	2
March 3, 2006			Effusive Phase											
03-09-06	1,130	4	200	340	1,800	0	2.3	13	17.3	4%	350	-12	89.78	2.8
03-10-06	3,200	4	430	390	1,200	0	0.5	10	7	.17%	30	-7.5	82.64	5.1
03-16-06	3,050	5	400	nm	nm	nm	nd	8	9.6	42%	80	nm	nm	8.2
March 16, 2006			Post-eruption Phase											
03-22-06	1,070	6	190	nm	nm	nm	nd	6.3	5.6	nd	50	nm	nm	2.5
03-29-06	1,270	6	190	nm	nm	nm	nd	10	5.5	11%	320	nm	nm	3.2
04-06-06	1,970	6	160	nm	nm	nm	nd	8	6	nd	45	nm	nm	3.9
04-11-06	1,220	5	90	nm	nm	nm	nd	5.8	7.7	13.7%	140	nm	nm	3
04-19-06	1,440	5	180	nm	nm	nm	nd	3.4	3.6	nd	220	nm	nm	5.2
04-27-06	750	5	210	860	660	1.3	1.3	10	18.6	2%	20	1.4	95.28	2.4
05-12-06	400	7	50	nm	nm	nm	nd	6	2.6	nd	40	nm	nm	6.3
05-23-06	230	5	30	nm	nm	nm	nd	11	7	21%	45	nm	nm	3.3
06-02-06	430	6	80	nm	nm	nm	nd	2.6	4.6	14%	330	nm	nm	1.8
07-12-06	500	7	90	nm	nm	nm	nd	4	7.3	3%	25	nm	nm	1.9
08-23-06	530	6	30	nm	nm	nm	nd	3.6	3.3	15%	330	nm	nm	5.4
09-24-06	250	3	56	180	280	1.3	1.6	6.5	4	13%	330	1.25	86.55	5.3
09-25-06	280	5	50	nd	nd	0	nd	7.1	7.8	12%	110	6.54	95.8	5
10-12-06	1,100	2	56	nm	nm	nm	nd	5	10.6	5%	120	nm	nm	7.65
10-23-06	100	2	3	nm	nm	nm	nd	4	16	nd	280	nm	nm	3.6
11-04-06	190	2	15	nm	nm	nm	nd	7.2	4.1	7%	280	nm	nm	4
11-16-06	170	2	43	0	0	0	nd	6.3	13	7%	45	-15.7	80.15	1.8
11-17-06	100	1	0	0	0	0	nd	5	4.3	6%	40	-9.3	84.5	2.8
11-18-06	220	1	0	0	0	0	nd	3	7.3	9%	40	-7.4	88.83	1.5
02-22-07	50	4	8	nm	nm	nm	nd	1.3	4.8	15%	280	nm	nm	1.3
05-18-07	30	4	6	80	94	0.0	4.3	2.8	3.7	8%	90	-4.9	85.88	2
03-14-08	Tr	4	14	nm	180	0		3	3.8	2%	270	-7	88.79	4.2
07-17-08	120	3	17	tr	tr	0	nd	2	5.4	18%	280	9.8	94.1	2.3

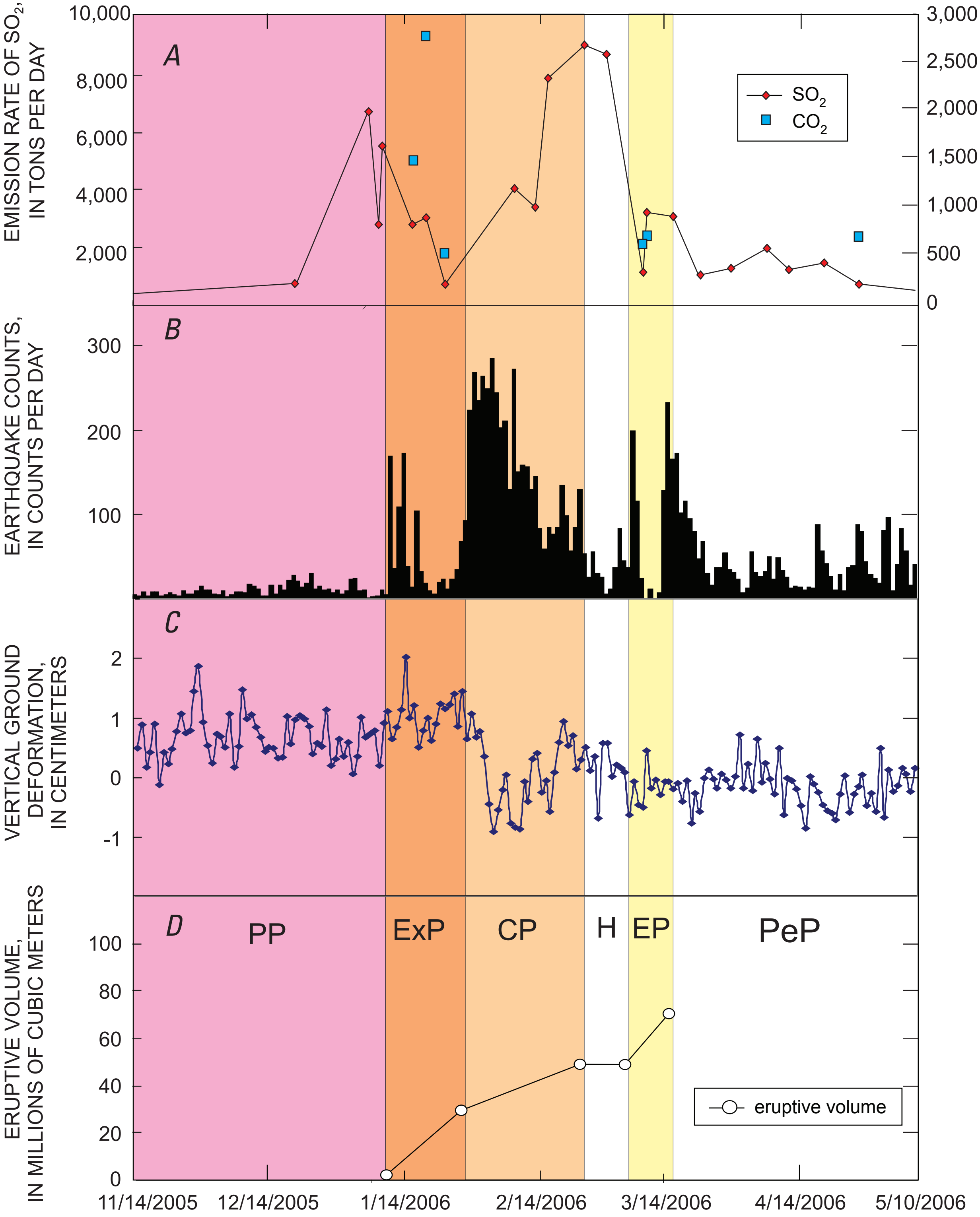

Figure 7. Time series from November 14, 2005, through May 10, 2006, showing: *A*, the measured SO$_2$ and CO$_2$ emission rates in tons per day, red diamonds are SO$_2$ and blue squares are CO$_2$; *B*, located earthquake counts per day (Power and others, this volume); *C*, the displacement in centimeters measured between CGPS stations A59 and AV02 (Cervelli and others, this volume), *D*, the erupted volume as determined by Coombs and others (this volume). Vertical colored segments in figure represent phases of the 2006 eruption (pre-November data not included). PP, precursory phase beginning April 30, 2005, to January 11, 2006; ExP, explosive phase January 11–28, 2006; CP, continuous phase January 28 to February 10, 2006; H, hiatus February 10 to March 3, 2006; EP, effusive phase March 3–16, 2006; PeP, post-eruption phase March 16, 2006 to July 17, 2008.

from the levels recorded during the precursory phase. CO_2 was measured for the first time since the beginning of the unrest (1,466, 2,740, and 500 t/d). The highest emission rate of H_2S during the eruption, 4.3 t/d, was recorded on January 19. We have no measurements of gas emissions during any of the 13 explosions that occurred between January 11 and 28.

Radar data and pilot reports suggest Augustine injected gases and ash into the stratosphere on as many as four different days during this period (January 11, 13, 17, and 27 (Collins, and others, 2007; Schneider and others, 2006). We estimate from meteorological data (NOAA, Air Resources Laboratory, www.arl.noaa.gov/ready.php, last accessed April 1, 2010) that the tropopause was at about 8.5 to 9.0 km asl above Augustine during this time period.

Infrared based Atmospheric Infrared Sounder (AIRS) satellite detected the SO_2 clouds during January 28 and 29, 2006. Prada (2006) reported that .0025 to .0041 Tg (2,500–4,100 t/d) were ejected into the atmosphere during the explosive events on these days. Early satellite measurements showed SO_2 eruption clouds represented equal to or above quiescent SO_2 emission rates (fig. 11). The AIRS satellite detected SO_2 in the stratosphere, so the values reported are probably minimums due to the missed SO_2 below 8 to 9 km. The first satellite measurements suggest measurements of the quiescent plumes with emission near 3,000 t/d (fig. 11). Later, measurements may represent syneruptive SO_2 plumes. These clouds did not contain the syneruptive amounts of SO_2 typical of explosive eruptions.

Ozone Monitoring Instrument (OMI) satellite determinations of SO_2 were unavailable during this time interval (Simon Carn, oral communication, 2008) owing to low winter UV levels. Not until March and at lower latitudes (Nevada) were OMI satellite results available.

Continuous Phase (January 28–February 10, 2006)

A continuous eruption phase began on January 28 and was characterized by nearly constant, low-altitude tephra emission and rapid andesitic dome extrusion, high rates of shallow seismicity, and steady deflation of the edifice. Repeated collapses of the growing dome and overlapping lobes of lava extending to the north beyond the margin of the 1986 lava dome produced block-and-ash flows intermittently through February 10, 2006 (Vallance and others, this volume; Coombs and others, this volume). Gas and ash plumes during this phase penetrated the tropopause on at least two days (January 28 and 29; Bailey and others, this volume); however, most ash plumes remained below 6,000 m asl. A gas measurement on February 8 (table 1, fig. 7*A*) during the continuous phase yielded an emission of 3,960 t/d SO_2, a value similar to those calculated during the late precursory and early explosive phases. SO_2 was detected (but no value derived) in the eruption cloud from January 29–30 by satellite (Dean and others, 2006). We have no CO_2 data from the continuous phase.

Hiatus (February 10–March 3, 2006)

Careful analysis of photography and other observations reveal no evidence of significant additional accumulation of lava in the summit crater from February 10 through March 3 (Coombs and others, this volume). Low levels of seismicity also suggest that the eruption was in a pause during this interval (Power and Lalla, this volume). Interestingly, of the four gas measurements made during the hiatus, three recorded the highest SO_2 emission rates of the eruption (7,800, 7,930, and 8,650 t/d; table 1; fig. 7*A*).

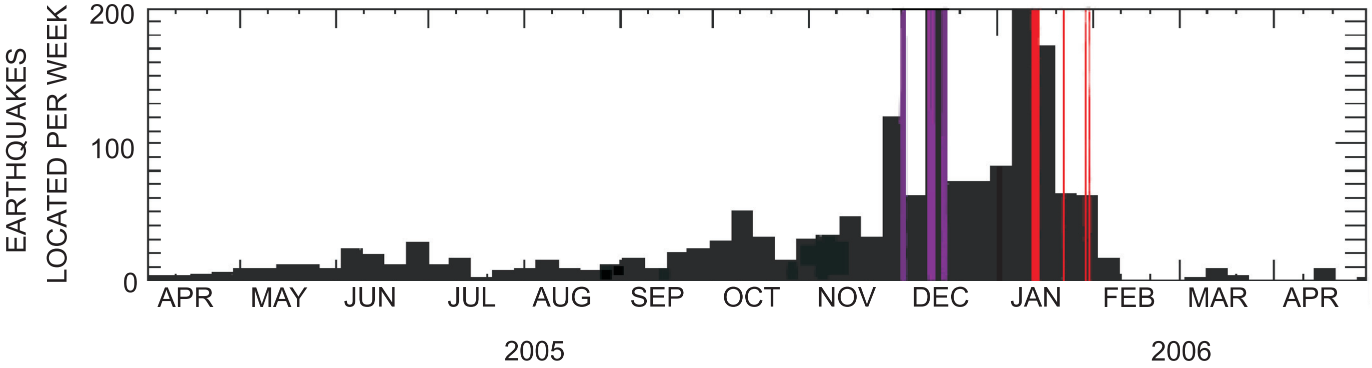

Figure 8. Earthquake counts from April 2005 through April 2006 showing the gradual increase of located earthquakes during 2005 (from Power and Lalla, this volume). Purple and red lines correspond to approximate times of phreatic and magmatic explosions, respectively (Power and Lalla, this volume).

Effusive Phase (March 3–16, 2006)

On March 3, increasingly frequent rockfall signals on seismometers suggested a return to active lava effusion and resulting instability of the dome as new material was added to the surface and lava flow fronts advanced. Over the next 2 weeks, more or less continuous eruption of lava from a single vent in the summit dome marked the final activity of the effusive phase of the eruption (EP, fig. 7*D*). The top of the growing dome eventually reached an elevation more than 100 m higher than the preeruption summit of the 1986 lava dome. Collapse of the fronts of two primary lava flow lobes produced block-and-ash flows down the north and northeast flank of Augustine especially during the early portion of the effusive phase. The end of the phase coincided with cessation of drumbeat earthquakes, which were recorded from March 7 to March 16 (Power and Lalla, this volume). Three SO_2 emission measurements during this period range from 1,130 t/d to 3,050 t/d, values in the low to moderate range for the eruption. Two emission rates for CO_2, however, were showing decline in the eruption sequence—590 and 680 t/d.

Post-eruption Phase (March 16, 2006–July 17, 2007)

Twenty-one additional gas measurement flights made from April 2006 to July 2008 show SO_2 emission rates declining from more 1000 t/d to less than or equal to 120 t/d (table 1). We define the end of the post-eruption phase as the date when SO_2 emissions reached levels of 50 t/d. A single helicopter-borne flight in July 2008 measured 120 t/d, revealing latent degassing was still possible at the volcano. These final low values of SO_2 emission are similar to those observed following the 1986 eruption of Augustine when, within 8 months of the end of the eruption, 45 t/d was measured (Symonds and others, 1990). Similarly, emission rates for CO_2 went from 660 t/d on April 27, 2006, to 94 t/d in May 2007. H_2S levels were typically very low (1.3 t/d) or not quantifiable through the last measurement in July 2008.

Discussion

Changing SO_2, CO_2, and H_2S emissions pre-, syn-, and post-eruption can be interpreted in the context of other monitoring and observational data to infer characteristics of changing magma supply and residence at shallow levels beneath and within the volcano (fig. 7). The following discussion is limited somewhat by the lack of equivalently detailed time series data for all three gas species, in addition to a paucity of gas output measurements by satellite or other means during individual explosive events.

Sulfur dioxide largely disappeared from the plume and fumarole gases of Augustine in the months following the 1986 eruption, indicating no further influx of fresh magma

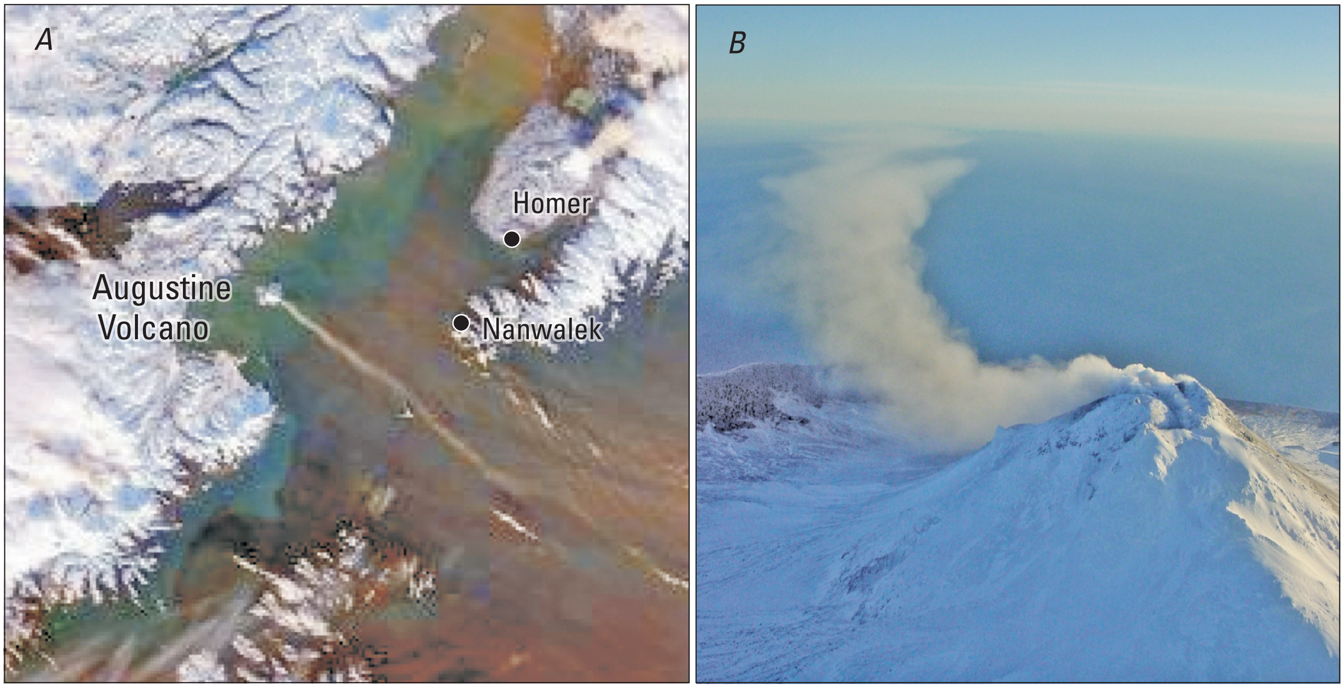

Figure 9. *A*, December 12, 2005, MODIS satellite view of lower Cook Inlet, Alaska, showing Augustine Volcano, as the source of a long narrow plume extending Southeast towards the southern portion of the Kenai Peninsula (image courtesy of the Geographic Information Network of Alaska (GINA)). *B*, December 12, 2005, photograph of an ashy plume extending from summit fumaroles to the southeast. Photo by R.G. McGimsey.

shallower than about 4 km below the summit (Doukas, 1995; Symonds and others, 1990; Symonds and others, 2003). Influx of water (both meteoric and seawater; Symonds and others, 1990) into the lower edifice likely consumed any residual SO_2 from the cooling 1986 magma by hydrolysis reactions. Indeed, annual airborne measurements at Augustine detected no SO_2 until December 2005, when precursory activity at Augustine was well advanced. It is notable that neither SO_2 nor CO_2 (CO_2 is a gas not easily scrubbed by water) were detected on a May 2005 flight during the earliest stage of the recent unrest. Cervelli and others (2006) suggest that a sea-level pressure source might have been present under the volcano by May 2005. If so, the lack of detected CO_2, which would have been significantly oversaturated in the magma at that shallow depth, suggests that the pressure source was not magmatic in origin but more likely resulted from an invigorated, expanding hydrothermal system being heated from below. Cervelli and others (this volume) conclude that this early deformation signal was not from a magma body. The corresponding lack of SO_2 is also consistent with no significant shallow (<4 km, sea level is approx 1.5 km) magma body at that time.

By late November 2005, magma likely rose to within several kilometers of the surface; shallow enough to degas SO_2 to the atmosphere and drive phreatic explosions. An airborne

Figure 10. Wind-depressed plume during the gas flight of December 20, 2005. Plumes from fumaroles were pushed down to the ground making COSPEC measurements difficult and minimizing the emission rate for that day. Photo by R.G. McGimsey.

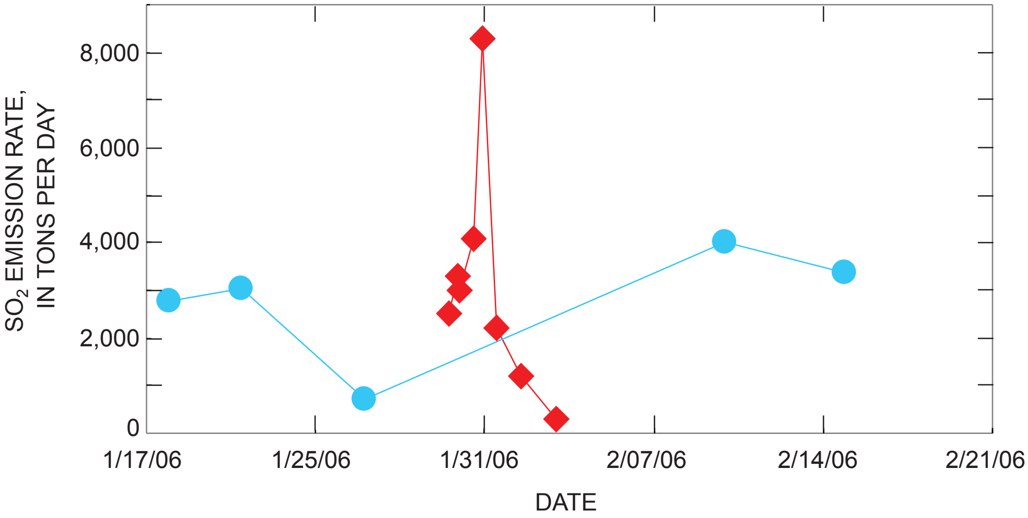

Figure 11. Airborne COSPEC emission rates (blue circles) and infrared AIRS satellite SO_2 determinations (red diamonds; F. Prada, written commun., 2009) during January 2006. AIRS satellite results are measurements of SO_2 in the stratosphere.

measurement on December 20, 2005, detected SO_2 at Augustine for the first time since 1987. A minimum emission rate of 660 t/d was measured on that flight (fig. 10, table 1; wind conditions prevented traverses completely beneath the plume, resulting in a minimum emission rate.). During December, observers also noted large white plumes that suggested the release of large amounts of water vapor from the volcano as it continued to heat up. ASTER thermal infrared (TIR) images of Augustine taken on December 20 showed a broad area of new snow-free ground and fumaroles at the summit, and forward-looking infrared (FLIR) surface-temperature measurements on December 22 indicated the temperature of a fumarole on the south flank was 210°C and the summit moat area at 80°C (Wessels and others, this volume). By January 4, 2006, the surface temperature of the moat area had increased to 390°C. Based on reports from residents in the village of Nanwalek on the lower Kenai Peninsula of strong “rotten egg” odors, it is likely that a significant portion of sulfur emissions from Augustine during the precursory stage were in the form of H_2S, consistent with earlier scrubbing of SO_2 by water and subsequent boiling of the fluid to create H_2S (Symonds and others, 2001). Further, during a FLIR flight on December 22, 2006, observers noted that fume emitted from a fumarole on the southeast base of the 1986 Augustine dome was distinctly pale yellow-green in color. We believe this was likely due to the transient presence of native sulfur in the plume produced by the reaction of H_2S and SO_2 (Symonds and others, 1994; Kodosky and others, 1991). Based on GPS measurements, dike propagation into the edifice started on November 17, 2005, a month earlier, and Cervelli and others (2006) conclude that magma was shallow enough by the time of the December 20, 2005, gas measurement to allow CO_2 and H_2S to escape, along with SO_2, and become incorporated into the plume. It is not possible, however, to confirm this because CO_2 and H_2S measurements were not made during this period.

By early January 2006, continued heating of the Augustine summit by the shallow magma had dried out the shallow hydrothermal system thereby limiting scrubbing effectiveness. The volcano was emitting SO_2 in large amounts with emission rates reaching 6,700 t/d (table 1; fig. 7*A*). On January 11, 2006, either the gas-filled dike tip arrived at the surface or a highly pressurized shallow hydrothermal system was breached, resulting in a series of explosions with little, if any, juvenile material ejected (Coombs and others, this volume; Wallace and others, this volume). SO_2 emission rates began to drop by more than half and finally to below 1,000 t/d near the end of the explosive period on January 28. This drop could reflect relative depletion in the volume of near-surface, SO_2-charged magma along with a temporary lack of replenishment. Similarly, CO_2 measurements during the explosive phase showed high CO_2 at the beginning (1,400–2,700 t/d) but dropping to 500 t/d by the end of the period. The continuing trend of inflation of the edifice throughout the explosive period (fig. 7*C*), however, suggests a net mass or pressure increase. An alternative explanation for the relatively low gas values during this time is a repetitive sealing of the shallow conduit system that prevented complete gas escape to the surface but contributed to pressurization seen as inflation.

Interestingly, on the gas-measurement flight of January 16, 2006, observers noticed a yellow-orange plume in the largely white vapor cloud enveloping the new lava dome within the summit crater (fig. 12). As noted earlier, the highest H_2S emission rate of the eruption was measured during this time (table 1). We believe the yellow-orange plume, like the colored plume observed on December 22, 2005, was native sulfur, produced at a single vent under just the right conditions of temperature and concentrations of gas streams rich in SO_2 and H_2S. This reaction possibly could reduce H_2S as seen in the trace amount measured that day. Production of native sulfur is achieved in industry using the Claus process ($2H_2S + O_2 \rightarrow S_2 + 2H_2O$) where gases rich in H_2S (>25%) at high temperatures burn to produce sulfur and water. An accompanying process with H_2S and SO_2 reacting together can reduce H_2S to native sulfur ($2H_2S + SO_2 \rightarrow 3S + 2H_2O$). The high-temperature fumarole at the base of the 1986 dome probably was a

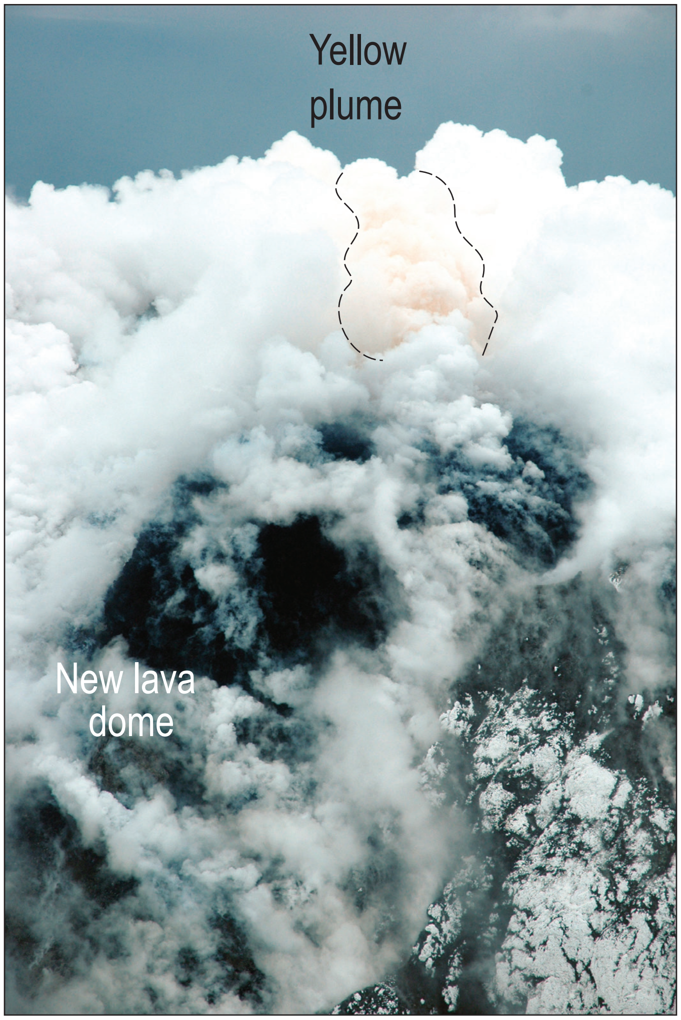

Figure 12. Yellow plume venting from summit of Augustine Volcano. View to the southwest. Dark mass below and left of yellow plume is first sighting of a lava dome mass (January 16, 2006). Dashed line outlines yellow part of plume. Photo by R.G. McGimsey.

source for this plume (Wessels and others, this volume). After January 19, 2006, H_2S emission rates declined and no further yellow plumes were observed during the eruption.

Moderate to high SO_2 emissions—similar in magnitude to those measured during the explosive phase—persisted during the continuous phase of the eruption and into the very early days of the hiatus as reflected in two airborne measurements on February 8 and 13 (table 1; fig. 7*A*). During the continuous phase, intense seismicity due to rapid extrusion and explosive disruption of blocky andesitic lava was accompanied by marked deflation of the volcano as magma was withdrawn to feed surface activity (Power and others, 2006; Coombs and others, this volume; Cervelli and others, this volume).

The onset of a hiatus in extrusion and a return to a very weak inflationary signal (Cervelli and others, this volume) on February 10 at first saw no significant change in SO_2 emission (fig. 7). However, SO_2 emission rates more than doubled on February 16 and remained high until the onset of rapid effusion (Coombs and others, this volume) and weak shallow deflation in early March (Cervelli and others, this volume). In fact, the highest SO_2 emission rates measured during the entire eruption occurred during this 3-week pause in extrusion, accompanied by low rates of seismicity and an overall weak inflationary trend (fig. 7). Several factors may have contributed to the high SO_2 during the hiatus. The high eruption rates and conduit drawdown of the continuous phase (fig. 7; Coombs and others, this volume) may have resulted in an open, hot, and dry pathway in the upper few kilometers of the conduit facilitating degassing of residual melt. Alternatively (or in addition), the inflationary signal during the hiatus may reflect recharge of the shallow conduit system with fresh, gas-rich melt that lacked sufficient time to reach the surface but was able to degas freely. Unfortunately, we have no CO_2 emission rate data for the hiatus.

The hiatus ceased on March 6 marked by the return of strong shallow seismicity and a deflationary signal as seen on GPS (fig. 7*C*). March 9 and 10 had relatively high CO_2 emission rates; at the same time, SO_2 emission rates were near the lower end of their range during the eruption. The plume was visually dramatic on these days (fig. 13). The high CO_2 probably reflected deep recharge of magma (see below) at depths below the SO_2 exsolution level. High CO_2 and heat flux could have been the response of the rapid extrusion of largely degassed lava in early March feeding the north and northeast lava flow lobes and associated block-and-ash flows (Coombs and others, this volume). The next measurement of CO_2 was at the end of April, by which time it had dropped to about 600 t/d, confirming that the influx of new magma had stopped.

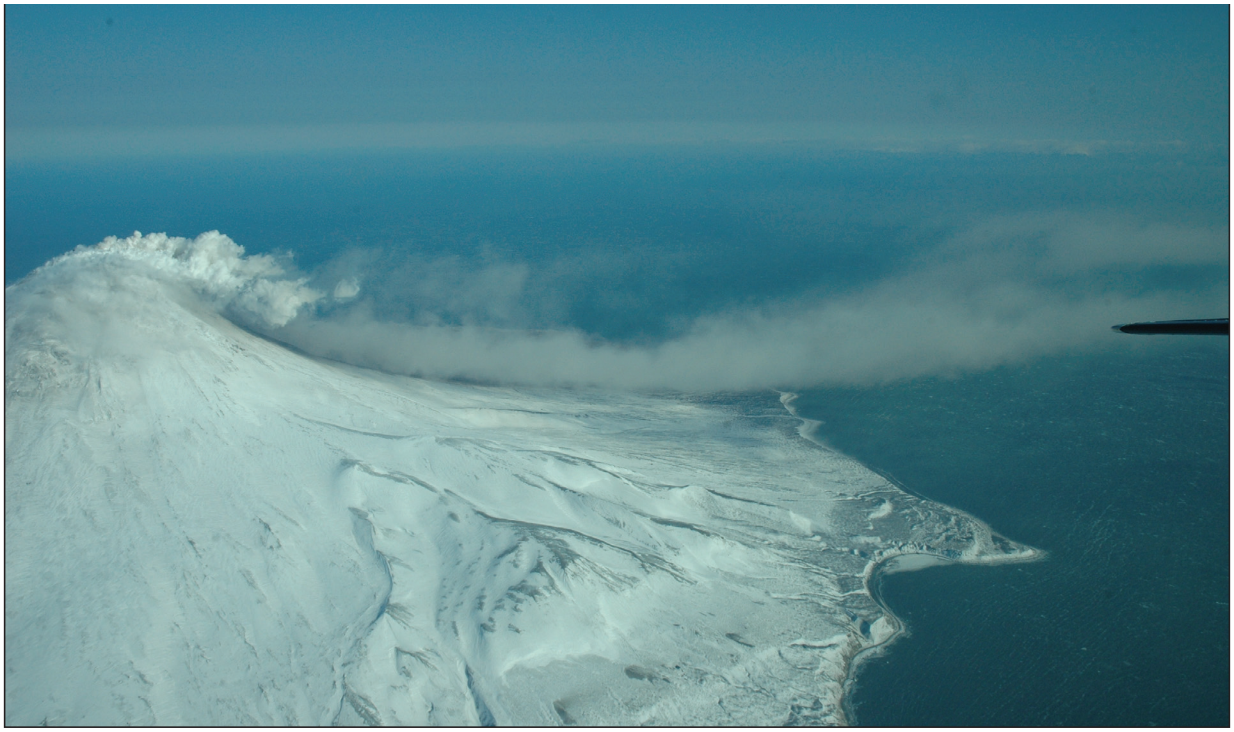

Figure 13. Gas plume from Augustine Volcano. White condensate plume is short lived, while gases and aerosols continue down wind. View to the east. Photo by R.G. McGimsey.

Evaluating CO_2/SO_2 Ratios

Seven instances of simultaneous airborne plume measurements of CO_2 and SO_2 during 2006 provide the opportunity to compute a CO_2/SO_2 ratio for those days (fig. 14). The mean molar ratio is 1.1 with a standard error of ±0.4.

The CO_2/SO_2 measured on March 9, 2006, (0.8 under a mean of 1.1) occurred during the effusive phase (EP), a period of intense seismicity that began in early March, increased to a nearly continuous signal by March 8, and lasted until March 14 (Power and others, this volume). This was also a period of weak deflation of the edifice (Cervelli and others, this volume) and partly reflects no new CO_2 or additional magma rising from depths up towards the surface to feed the eruption, and SO_2 being depleted from a shallower magma source. By May 2007 the molar ratio had climbed to 4.3, higher than the eruptive values (not used in the mean ratio calculation). Melting of the snow pack of winter 2006–7 added water to the shallow hydrothermal system in the summit, thus aiding in the scrubbing of residual sulfur gases and raising the ratio.

The mean molar CO_2/SO_2 value of 1.1 for Augustine during the eruption is not out of line with that of other active Cook Inlet volcanoes. Casadevall and others (1994) report an average CO_2/SO_2 of about 2 for the 1989–90 eruption of Redoubt Volcano. Molar CO_2/SO_2 values of 10 ranging to as great as 100 were noted for the gases produced by the 1992 eruption of Crater Peak, although the higher ratios were almost certainly due to the masking of SO_2 emissions by aqueous scrubbing (Doukas and Gerlach, 1995). During 1980–81 when CO_2 was measured at Mount St. Helens, CO_2/SO_2 ratios averaged about 8, while during 2004–5 the median CO_2/SO_2 was about 11; this difference was also attributed to scrubbing (Gerlach and others, 2008). In general, unless the magma is degassing through liquid or boiling water, it appears that CO_2/SO_2 values for convergent-plate volcanoes typically fall in the range 1 to 12 (Doukas and Gerlach, 1995; Marty and Le Cloarec, 1992; Williams and others, 1992).

SO_2 Emission Rates in Previous Augustine Eruptions

Two earlier eruptions of Augustine allow comparisons with peak SO_2 emission rates measured during 2006. Although the peak emission rates measured during the last three eruptions are different, other evidence suggests that the total SO_2 output for the Augustine eruptions in 1976, 1986, and 2006 were likely similar in magnitude.

During the 2006 unrest, the highest measured SO_2 emission rate was 8,930 t/d, only about one-third the peak values reported in 1976 and 1986. This could imply that the earlier eruptions were larger or more gas-rich events or simply reflect that during 2006 a measurement was not made on a day when SO_2 emissions were at their highest levels. Regardless, we believe total SO_2 emissions for the past three eruptions of Augustine are roughly similar. Eruptive volume estimates for the 1976, 1986, and 2005–6 eruptions of 0.39, 0.26, and 0.12×10^6 m^3, respectively (bulk volumes; Coombs and others, this volume) suggest that the recent event was smaller; however, limited gas data do not permit an in-depth comparison of total gas emissions from the three eruptions.

Comparison to Anthropogenic Emissions

Without quantitative emissions data it would be difficult to evaluate the volcanic contribution of greenhouse gases, such as CO_2, to the atmosphere. Augustine, even with its characteristically short interval between eruptions, illustrates that the volcanic contribution is likely not significant over time.

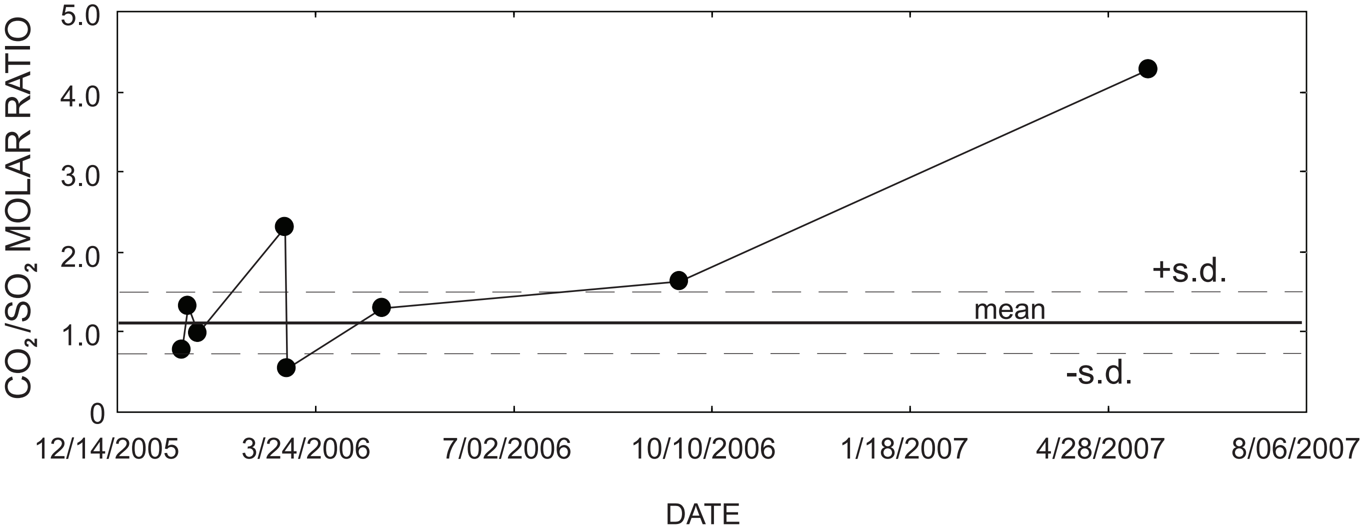

Figure 14. Molar CO_2/SO_2 for all the days when CO_2 and SO_2 were measured simultaneously. The mean molar ratio of the points (not counting the 4.3 ratio measured in 2007) is 1.3 (middle horizontal line) with a standard deviation of ±0.69.

Some volcanoes passively emit low levels of gases for decades or more (McGee, 2001). Others, like Augustine, become restless and emit gases for a few months and then become quiet again. In the case of Augustine, the repose periods between the five eruptions since the beginning of the twentieth century are 29, 11, 10, and 20 years. On the basis of CO_2 measurements reported here and using linear extrapolating to a full year, we estimate a total CO_2 output of 1.96×10^5 tons of CO_2 for Augustine in 2006, the year encompassing the majority of the most recent eruption. This is similar to the 1.2×10^6 tons of CO_2 emitted by the Beluga natural gas-fired powerplant on the west side of the Cook Inlet near Tyonek in 2004 (fig. 1) and significantly less than the output of most of the U.S. coal-fired power generation plants, some of which produce more than 20×10^6 million tons of CO_2 per year (U.S. Environmental Protection Agency, 2007). No CO_2 data exist for the earlier eruptions of Augustine. Even though Augustine erupts frequently, every 17.5 years on average since the beginning of the last century, it is clear that the greenhouse gas output of Augustine is negligible compared to the several hundred power plants of all fossil fuel types currently operating in the United States. Augustine's 2006 eruption might be considered a typical size for an average eruption worldwide (for example, volcanic explosivity index = 3, 0.01–0.1 km^3 of eruptive products; Simkin and Siebert, 1994). Using estimates from Casadevall and others (1994) for the total emission rate of SO_2 (1×10^6 tons) and the molar CO_2/SO_2 (~2) for the 1989–90 eruption of Redoubt Volcano, we can compute a total CO_2 emission rate of 1.4×10^6 tons for a similar-sized eruption of another Cook Inlet volcano.

From these data it is clear that even if several volcanoes like Augustine erupted continuously for a decade or even a century, they would still be negligible greenhouse gas contributors to the atmosphere compared to current anthropogenic sources of CO_2 emission. One of the largest continuous volcanic carbon dioxide sources on Earth is Kilauea Volcano, which emits about 9,000 tons of CO_2 a day (Gerlach and others, 2002). This amounts to 3.3×10^6 tons of CO_2 annually, still considerably less than the yearly output of a single large coal-fired powerplant (U.S. Environmental Protection Agency, 2007). Thus it appears that volcanoes are currently not significant contributors of greenhouse gases to the atmosphere compared to power generation plants.

We also estimate that Augustine emitted about 6.3×10^5 tons of SO_2 during 2006, slightly more than half the amount of CO_2 produced. Although not a greenhouse gas, SO_2 combines readily with water droplets to form aerosols and can fall as acid rain or cause cooling if injected into the upper atmosphere. The SO_2 output of Augustine during 2006 is equivalent to several coal-fired powerplants, but the short duration of the eruption insures that any impact from acid rain or acid-coated ash particles will be comparatively small. Further, given Augustine Volcano's island location and relatively low elevation, much of the gas from Augustine during 2006, with the exception of several days in January, was discharged at low elevation into the troposphere, and most of any resulting acid rain likely fell into the ocean or on sparsely inhabited land areas downwind. From early 2007 through the summer of 2008, the SO_2 output of Augustine was about 100 t/d and is expected to fall to near zero within several years as it has following the previous two eruptions.

Conclusions

1. The similar nature of recent Augustine eruptions points to generalizations regarding the timing and eruptive behavior of the volcano as well as to generalizations about the nature and magnitude of its gas emissions.

2. Geochemical surveillance of Augustine since the 1986 eruption indicates that degassing declines essentially to nil within 1 to 2 years after an eruption and does not resume to a measurable level until magma once again ascends toward the surface. This is likely due to abundant ground and hydrothermal waters available to scrub any acid gases released from remnant magma once the system cools down.

3. Although the number of plume measurements for SO_2 during the eruption is not large, the available evidence suggests that, in general, once magma is within hundreds of meters of the surface and an open pathway exists between magma and the surface, SO_2 emissions will increase. The measured SO_2 output decreased during the explosive and continuous phases but increased again during the hiatus phase of the activity prior to the final rapid effusion phase. The highest SO_2 emission rates were achieved during the early part of the hiatus, whereas the highest measured CO_2 emission rates were measured about 1 month earlier during inflation and explosive activity in January. This is in line with the idea that more SO_2 will be released as magma intrudes to shallow levels and lower pressures. High emission rates for CO_2 should be detected as deeper CO_2-rich magma moves toward the surface and discharges its load of CO_2 while still deep enough to inhibit SO_2 outgassing, although the scant CO_2 measurements do not conclusively illustrate this.

4. Emissions measurements yield an average molar CO_2/SO_2 value of about 1.3±0.7 for the 2006 eruption of Augustine, similar to typical values of 1 to 12 reported for other convergent plate boundary volcanoes.

5. Augustine is not a significant contributor to the atmospheric load of greenhouse gases compared to anthropogenic sources. In 2006, Augustine released about 1.9×10^5 tons of CO_2, a level similar to the output of a medium-sized natural-gas-fired powerplant. Augustine also released about 8×10^5 tons of SO_2 during the 2006 eruption. Evidence from other investigators suggests that the sulfur dioxide output in the 1976 and 1986 eruptions was of similar magnitude to that measured in 2006.

Acknowledgments

We would like to acknowledge the skilled and dedicated pilots and staff of Security Aviation in Anchorage for providing safe and effective air support. Comments by Tobias Fischer, Cynthia Werner, Michelle Coombs, and William Scott were appreciated in improvement of the manuscript.

References Cited

Bailey, J.E., Dean, K.G., Dehn, J., and Webley, P.W., 2010, Integrated satellite observations of the 2006 eruption of Augustine Volcano, *in* Power, J.A., Coombs, M.L., and Freymueller, J.T., eds., The 2006 eruption of Augustine Volcano, Alaska: U.S. Geological Survey Professional Paper 1769 (this volume).

Casadevall, T.J., Doukas, M.P., Neal, C.A., McGimsey, R.G., and Gardner, C.A., 1994, Emission rates of sulfur dioxide and carbon dioxide from Redoubt Volcano, Alaska, during the 1989–1990 eruptions, *in* Miller, T.P., and Chouet, B.A., eds., The 1989–1990 Eruptions of Redoubt Volcano, Alaska: Journal of Volcanology and Geothermal Research, v. 62, p. 519–530.

Cervelli, P.F., Fournier, T.J., Freymueller, J.T., and Power, J.A., 2006, Ground deformation associated with the precursory unrest and early phases of the January 2006 eruption of Augustine volcano, Alaska: Geophysical Research Letters, v. 33, p. 1–5, L18304 , doi: 10.1029/2006GL027219.

Cervelli, P.F., Fournier, T.J., Freymueller, J.T., Power, J.A., Lisowski, M., and Pauk, B.A., 2010, Geodetic constraints on magma movement and withdrawal during the 2006 eruption of Augustine Volcano, *in* Power, J.A., Coombs, M.L., and Freymueller, J.T., eds., The 2006 eruption of Augustine Volcano, Alaska: U.S. Geological Survey Professional Paper 1769 (this volume).

Collins, R.L., Fochesatto, J., Sassen, K., Webley, P.W., Atkinson, D.E., Dean, K.G., Cahill, C.F., and Kohei, M., 2007, Predicting and validating the motion of an ash cloud during the 2006 eruption of Mount Augustine Volcano, Alaska, USA: Journal of the National Institute of Information and Communications Technology, v. 54, no. 1/2, p. 17–28.

Coombs, M.L., Bull, K.F., Vallance, J.W., Schneider, D.J., Thoms, E.E., Wessels, R.L., and McGimsey, R.G., 2010, Timing, distribution, and volume of proximal products of the 2006 eruption of Augustine Volcano, *in* Power, J.A., Coombs, M.L., and Freymueller, J.T., eds., The 2006 eruption of Augustine Volcano, Alaska: U.S. Geological Survey Professional Paper 1769 (this volume).

Dean, K.G., Dehn, J., Wallace, K.L., Prata, F., and Cahill, C.F., 2006, The distribution and movement of volcanic ash and SO_2 observed in satellite data from the eruption of Augustine volcano, 2006 [abs]: Eos (American Geophysical Union Transactions), v. 87, no. 52, Fall Meeting Supplement, abstract V41F-05.

Doukas, M.P., 1995, a compilation of sulfur dioxide and carbon dioxide emission-rate data from Cook Inlet volcanoes (Redoubt, Spurr, Iliamna, and Augustine), Alaska, during the period from 1990 to 1994: U. S. Geological Survey Open-File Report 95-55, 15 p.

Doukas, M.P., 2002, A new method for GPS-based wind speed determinations during airborne volcanic plume measurements: U.S. Geological Survey Open-File Report 02-395, 13 p.

Doukas, M.P., and Gerlach, T.M., 1995, Sulfur dioxide scrubbing during the 1992 eruptions of Crater Peak, Mount Spurr Volcano, Alaska, *in* Keith, T.E.C., ed., The 1992 Eruptions of Crater Peak Vent, Mount Spurr Volcano, Alaska: U.S. Geological Survey Bulletin 2139, 220 p.

Doukas, M.P. and McGee, K.A., 2007, A compilation of gas emission-rate data from volcanoes of the Cook Inlet (Spurr, Crater Peak, Redoubt, Iliamna, and Augustine) and the Alaska Peninsula (Douglas, Fourpeaked, Griggs, Mageik, Martin, Peulik, Ukinrek Maars, and Veniaminof), Alaska from 1995–2006: U.S. Geological Survey Open-File Report 2007-1400, 13 p.

Gerlach, T.M., Delgado, H., McGee, K.A., Doukas, M.P., Venegas, J J., and Cardenas, L., 1997, Application of the LI-COR CO_2 analyzer to volcanic plumes; A case study, Volcán Popocateptl, Mexico, June 7 and 10, 1995: Journal of Geophysical Research, v. 102, p. 8005–8019.

Gerlach, T.M., Doukas, M.P., McGee, K.A., and Kessler, R., 1999, Airborne detection of diffuse carbon dioxide at Mammoth Mountain, California: Geophysical Research Letters, v. 26, p. 3661–3664.

Gerlach, T.M., McGee, K.A., Elias, T., Sutton, A.J., and Doukas, M.P., 2002, Carbon dioxide emission rate of Kilauea Volcano—Implications for primary magma and the summit reservoir: Journal of Geophysical Research, v. 107, no. B9, 2189–2204, doi:10.1029/2001JB000407.

Gerlach, T.M., McGee, K.A., and Doukas, M.P., 2008, Emission rates of CO_2, SO_2, and H_2S, scrubbing, and preeruption excess volatiles at Mount St. Helens, 2004–2005, chap. 26 *in* Sherrod, D.R., Scott, W.E., and Stauffer, P.H., eds., A volcano rekindled; the renewed eruption of Mount St. Helens, 2004–2006: U.S. Geological Survey Professional Paper 1750, p. 543-571.

Kienle, J., and Swanson, S.E., 1983, Volcanism in the eastern Aleutian arc; Late Quaternary and Holocene centers, tectonic setting and petrology: Journal of Volcanology and Geothermal Research, v. 17, p. 393–432.

Kodosky, L.G., Motyka, R.J., and Symonds, R.B., 1991, Fumarolic emissions from Mount St. Augustine, Alaska; 1979–1984 degassing trends, volatile sources and their possible role in eruptive style: Bulletin of Volcanology, v. 53, p. 381–394.

Marty, B., and Le Cloarec, M.-.F, 1992, Helium-3 and CO_2 fluxes from subaerial volcanoes estimated from polonium-210 emissions: Journal of Volcanology and Geothermal Research, v. 53, p. 67–72.

McGee, K.A., Doukas, M.P., and Gerlach, T.M., 2001, Quiescent hydrogen sulfide and carbon dioxide degassing from Mount Baker, Washington: Geophysical Research Letters, v. 28, p. 4479–4482.

McGee, K.A., Doukas, M.P., McGimsey, R.G., Neal, C.A., and Wessels, R.L., 2008, Atmospheric contribution of gas emissions from Augustine volcano, Alaska during the 2006 eruption: Geophysical Research Letters, v. 35, L03306, doi: 10.1029/2007GL032301, 5 p.

Miller, T.P., McGimsey, R.G., Richter, D.H., Riehle, J.R., Nye, C.J., Yount, M.E., and Dumoulin, J.A., 1998, Catalog of historically active volcanoes of Alaska: U.S. Geological Survey Open-File Report 98-582, 104 p.

Neal, C.A., Murray, T.L., Power, J.A, Adleman, J.N., Whitmore, P.M., and Osiensky, J.M., 2010, Hazard information management, interagency coordination, and impacts of the 2005–2006 eruption of Augustine Volcano, *in* Power, J.A., Coombs, M.L., and Freymueller, J.T., eds., The 2006 eruption of Augustine Volcano, Alaska: U.S. Geological Survey Professional Paper 1769 (this volume).

Power, J.A., and Lalla, D.J., 2010, Seismic observations of Augustine Volcano, 1970–2007, *in* Power, J.A., Coombs, M.L., and Freymueller, J.T., eds., The 2006 eruption of Augustine Volcano, Alaska: U.S. Geological Survey Professional Paper 1769 (this volume).

Power, J.A., Nye, C.J., Coombs, M.L., Wessels, R.L., Cervelli, P.F., Dehn, J., Wallace, K.L., Freymueller, J.Y., and Doukas, M.P., 2006, The reawakening of Alaska's Augustine volcano: Eos (American Geophysical Union Transactions), v. 87, no. 37, p. 373–377.

Prada, F., 2006, Augustine: Bulletin of the Global Volcanism Network v. 31, issue 01.

Rose, W.I., Heiken, G., Wohletz, K., Eppler, D., Barr, S., Miller, T., Chuan, R.L., and Symonds, R.B., 1988, Direct rate measurements of eruption plumes at Augustine volcano: A problem of scaling and uncontrolled variables: Journal of Geophysical Research, v. 93, p. 4485–4499.

Schneider, D.J., Scott, C., Wood J., and Hall T., 2006, NEXRAD weather radar observations of the 2006 Augustine volcanic eruption clouds [abs.]: Eos (American Geophysical Union Transactions), v. 87, abstract V51C-1686.

Simkin, T., and Siebert, L., 1994, Volcanoes of the World (2nd ed.): Tucson, Arizona, Geoscience Press, Inc., 349 p.

Stith, J.L., Hobbs, P.V., and Radke, L.F., 1978, Airborne particle and gas measurements in the emissions from six volcanoes: Journal of Geophysical Research, v. 83, p. 4009–4017.

Swanson, S.E., and Kienle, J., 1988, The 1986 eruption of Mount St. Augustine; Field test of a hazard evaluation: Journal of Geophysical Research, v. 93, p. 4500–4520.

Symonds, R.B., Rose, W.I., Gerlach, T.M., Briggs, P.H., and Harmon, R.S., 1990, Evaluation of gases, condensates, and SO_2 emissions from Augustine volcano, Alaska; The degassing of a Cl-rich volcanic system: Bulletin of Volcanology, v. 52, p. 355–374.

Symonds, R.B., Rose, W.I., Bluth, G.J.S., and Gerlach, T.M., 1994, Volcanic-gas studies: methods, results, and applications, *in* Carroll, M.R., and Holloway, J.R., eds., Volatiles in magmas: Reviews in Mineralogy, V. 30, p. 1–66.

Symonds, R.B., Gerlach, T.M., and Reed, M.H., 2001, Magmatic gas scrubbing; Implications for volcano monitoring: Journal of Volcanology and Geothermal Research, v. 108, p. 303–341.

Symonds, R.B., Janik, C.J., Evans, W.C., Ritchie, B.E., Counce, D., Poreda, R.J., and Iven, M., 2003, Scrubbing masks magmatic degassing during repose at Cascade-Range and Aleutian-Arc volcanoes: U.S. Geological Survey Open-File Report 03-435, 22 p.

U.S. Environmental Protection Agency, 2007, Emissions and Generation Resource Integrated Database (eGrid2006, Version 2.1): [http://www.epa.gov/cleanenergy/egrid/index.htm; last accessed April 12, 2007].

Vallance, J.W., Bull, K.F., and Coombs, M.L., 2010, Pyroclastic flows, lahars, and mixed avalanches generated during the 2006 eruption of Augustine Volcano, *in* Power, J.A., Coombs, M.L., and Freymueller, J.T., eds., The 2006 eruption of Augustine Volcano, Alaska: U.S. Geological Survey Professional Paper 1769 (this volume).

Waitt, R.B., and Begét, J.E., 2009, Volcanic processes and geology of Augustine Volcano, Alaska: U.S. Geological Survey Professional Paper 1762, 90 p, 2 plates.

Wallace, K.L., Neal, C.A., and McGimsey, R.G., 2010, Timing, distribution, and character of tephra fall from the 2005–2006 eruption of Augustine Volcano, *in* Power, J.A., Coombs, M.L., and Freymueller, J.T., eds., The 2006 eruption of Augustine Volcano, Alaska: U.S. Geological Survey Professional Paper 1769 (this volume).

Waythomas, C.F., and Waitt, R.B., 1998, Preliminary volcano-hazard assessment for Augustine volcano, Alaska: U.S. Geological Survey Open-File Report 98-106, 39 p.

Werner, C.A., Christenson, B.W., Hagerty, M., and Britten, K., 2006, Variability of volcanic gas emissions during a crater lake heating cycle at Ruapehu Volcano, New Zealand: Journal of Volcanology and Geothermal Research, v. 154, p. 291–302.

Wessels, R.L., Coombs, M.L., Schneider, D.J., Dehn, J., and Ramsey, M.S., 2010, High-resolution satellite and airborne thermal infrared imaging of the 2006 eruption of Augustine Volcano, *in* Power, J.A., Coombs, M.L., and Freymueller, J.T., eds., The 2006 eruption of Augustine Volcano, Alaska: U.S. Geological Survey Professional Paper 1769 (this volume).

Williams, S.N., Schaefer, S.J., Calvache, M.L., and Lopez, D., 1992, Global carbon dioxide emission to the atmosphere by volcanoes: Geochimica et Cosmochimica Acta, v. 56, p. 1765–1770.

Information Management

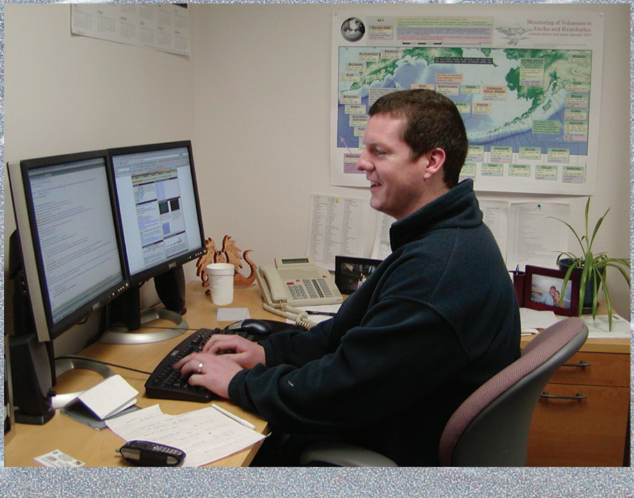

Oblique aerial view of Augustine Volcano's north flank on May 13, 2006, showing the light gray Rocky Point pyroclastic flow, emplaced during a single explosive event on January 27, 2006. Summit lava dome and flows are also visible. Alaska Volcano Observatory photo by Kate Bull.

The 2006 Eruption of Augustine Volcano, Alaska
Power, J.A., Coombs, M.L., and Freymueller, J.T., editors
U.S. Geological Survey Professional Paper 1769

Chapter 27

Public Outreach and Communications of the Alaska Volcano Observatory during the 2005–2006 Eruption of Augustine Volcano

By Jennifer N. Adleman[1,3], Cheryl E. Cameron[2], Seth F. Snedigar[2], Christina A. Neal[1],and Kristi L. Wallace[1]

Abstract

The 2005–6 eruption of Augustine Volcano in the Cook Inlet region, Alaska, greatly increased public desire for volcano hazard information, as this eruption was the most significant in Cook Inlet since 1992. In response to this heightened concern, the Alaska Volcano Observatory (AVO) increased ongoing efforts to deliver specific eruption-focused information to communities nearest to the volcano, created a public communications strategy to assist staff with managing requests, and used the recently upgraded AVO Web site as a primary information-delivery path. During the eruption, AVO responded to a minimum of ~1,700 individual requests for information from the media, the public, and other organizations with responsibilities associated with volcanic activity in Alaska; requests were received both as phone calls to the observatory and e-mail stemming from the AVO Web site. Staff also delivered approximately two dozen Augustine-specific presentations and gave nearly three dozen tours of the AVO Anchorage Operations Center in Anchorage. This intensity of public interaction was markedly higher than during noneruptive periods.

During the Augustine unrest and eruption, AVO also refined its internal communication procedures, instituted and maintained up-to-date and concise talking points concerning the most recent and relevant volcanic activity and hazards, and created a media management plan to assist staff in working with members of the media. These items aided staff in maintaining a consistent message concerning the eruption, potential hazards, and our response activities.

The AVO Web site, with its accompanying database, is the backbone of AVO's external and internal communications. This was the first Cook Inlet volcanic eruption with a public expectation of real-time access to data, updates, and hazards information over the Internet. In March 2005, AVO improved the Web site from individual static pages to a dynamic, database-driven site. This new system provided quick and straightforward access to the latest information for (1) staff within the observatory, (2) emergency managers from State and local governments and organizations, (3) the media, and (4) the public. From mid-December 2005 through April 2006, the AVO Web site served more than 45 million Web pages and about 5.5 terabytes of data.

Introduction

Augustine Volcano is located about 280 km (174 miles) southwest of Anchorage, Alaska, and within about 300 km (186 miles) of the major population centers of south-central Alaska (fig. 1). Eruptions and landslides at Augustine pose well-documented hazards to the region's citizens and economy (Waythomas and Waitt, 1998). Explosive eruptions of Augustine have occurred on at least six previous occasions since the early 1800s (1812, 1883, 1935, 1964–65, 1976, and 1986). Early during the 1883 eruption, a part of the summit collapsed and formed a debris avalanche that extended beyond the coast. This initiated a small tsunami reported at English Bay, 90 km (56 miles) east of the volcano (Waitt and Begét, 2009).

Each of the most recent eruptions of Augustine (1976 and 1986) were preceded by roughly nine months of precursory seismicity and sent airborne ash throughout south-central Alaska and beyond. In 1976, turbines at the Beluga Power Plant, the primary power supply for Anchorage, were damaged when airborne ash was ingested (Swanson and Kienle, 1988;

---

[1] Alaska Volcano Observatory, U.S. Geological Survey, 4210 University Drive, Anchorage, AK 99508.

[2] Alaska Volcano Observatory, Alaska Division of Geological and Geophysical Surveys, 3354 College Road, Fairbanks, AK 99709.

[3] Now at: Alaska Division of Homeland Security and Emergency Management, P.O. Box 5750, Fort Richardson, AK 99505-5750.

Waythomas and Waitt, 1998). Ash fall from the 1986 eruption of Augustine closed the Anchorage International Airport, and local military aircraft were moved to distant locations at the start of the 1986 eruptions (Kienle, 1994; Waythomas and Waitt, 1998).

Following Augustine's eruption in 1986, the Alaska Volcano Observatory (AVO) was founded in 1988 as a joint program of the U.S. Geological Survey (USGS), the Geophysical Institute of the University of Alaska Fairbanks (UAFGI), and the State of Alaska Division of Geological and Geophysical Surveys (ADGGS) in Fairbanks. AVO's primary missions are to conduct investigations to assess the likelihood and type of volcanic activity and to communicate timely warnings of volcanic unrest and eruptions of Alaska's volcanoes to local, State, and Federal officials and the public (Eichelberger and others, 1995). Since its inception, AVO has responded to a number of eruptions in Alaska, but the recent eruption of Augustine was the first in the Cook Inlet region since that of Mount Spurr's Crater Peak vent in 1992.

The 2005–6 Augustine eruption followed a similar pattern to previous historical eruptions of the volcano. After phreatic explosions on December 15, 2005, and January 11, 2006, Augustine began an explosive magmatic eruption on January 13 that tapered to effusive activity that lasted through March (Power and others, 2006). The eruption followed several months of precursory activity (increasing seismicity,

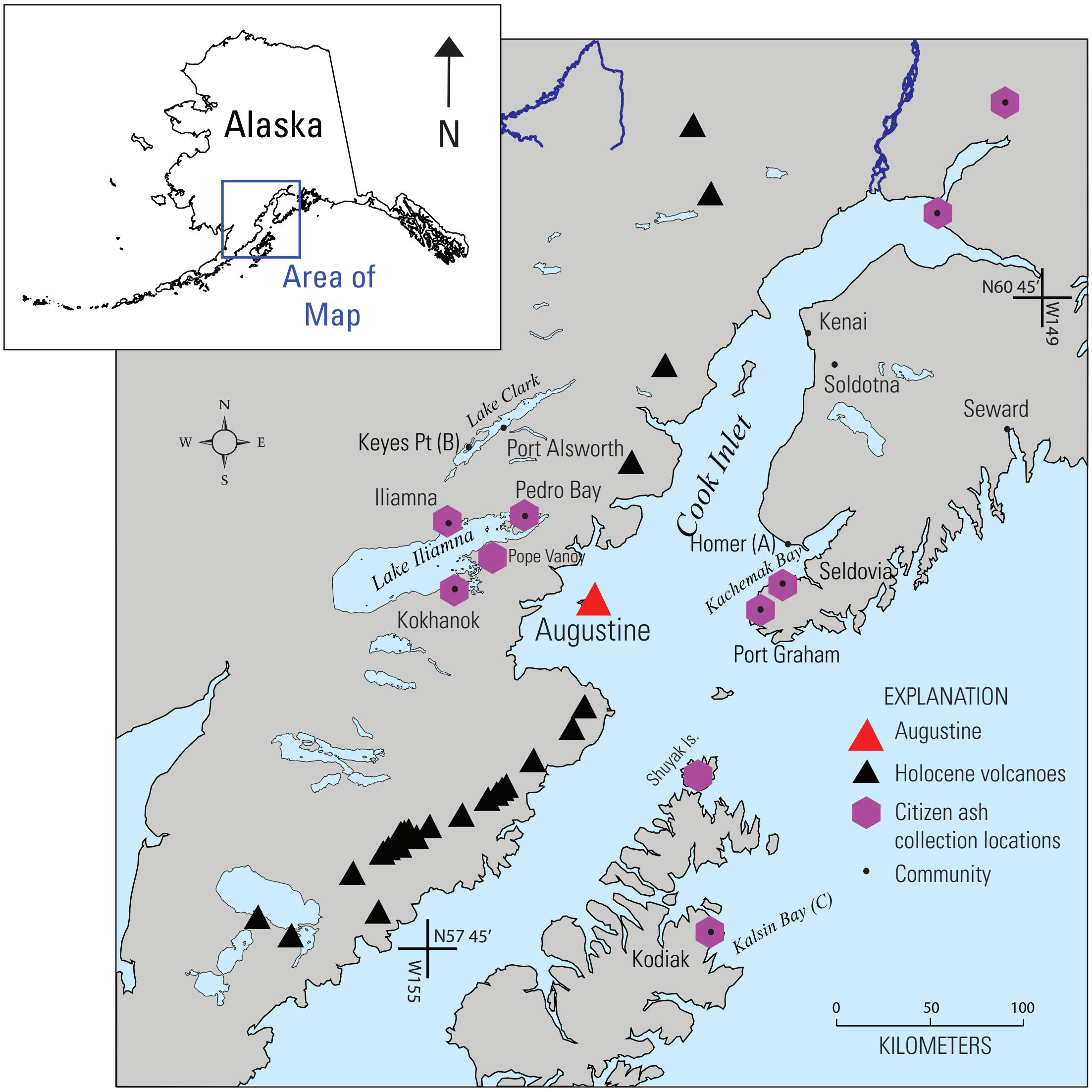

Figure 1. Cook Inlet and Kenai Peninsula region map including Augustine Volcano, surrounding Holocene volcanoes, and nearby communities. Communities from which volcanic ash was collected and submitted are indentified. The Alaska Volcano Observatory (AVO) also received volcanic ash collected from Castella, Calif.

deformation, and gas emission; Cervelli and others, this volume; Power and Lalla, this volume; Jacobs and McNutt, this volume; McGee and others, this volume).

Because of Augustine's prior historic eruptions and the more recent eruptions of Mount Spurr (1992) and Redoubt Volcano (1989–90), many longstanding Alaska residents are familiar with ash fall and other volcanic hazards. As Augustine began to exhibit unrest, however, questions raised at community meetings and e-mailed to the AVO Web site revealed gaps in residents' knowledge and may have reflected, in part, the increase in population since the last eruption in Cook Inlet. Keeping the public well-informed of volcanic hazards during eruptive and noneruptive periods is a central part of AVO's objectives. Operational roles and responsibilities among AVO and other agencies are outlined in the Alaska Interagency Operating Plan for Volcanic Ash Episodes (Madden and others, 2008) and are discussed further in Neal and others (this volume). This paper focuses on the preparation and application of AVO's communication tools and organization in response to public inquiries before and during the eruption.

Previous eruptions of Augustine occurred before the inception of AVO, and other recent eruptions in the Cook Inlet area predate widespread use of the Internet. The 2005–6 eruption of Augustine combined a greater population density in south-central Alaska with a public demand for 24/7 information through the Internet and television and radio newscasts, in addition to traditional daily print news. To meet these increased demands, AVO used an internal communications strategy that included three main parts—community education, internal strategies for external communication flow, and an improved Web site.

Laying a Foundation of Knowledge—Community Education and Involvement

Community Presentations and Outreach

When Augustine began showing signs of precursory unrest in late 2005, public interest in Cook Inlet volcanism was piqued. Beginning in May 2005, the AVO Education and Outreach (E and O) specialist led or coordinated about six presentations on the Kenai Peninsula in conjunction with the Kachemak Bay Environmental Education Alliance (KBEEA), a consortium of more than 15 natural resource organizations on the lower Kenai Peninsula. The majority of these were held during the summer and fall of 2005 at schools and community centers in Homer (pop. ~5,400), Kenai (pop. ~6,770), and Soldotna (pop. ~3,800) (Alaska Department of Labor and Workforce Development, 2010).

Although coordinated in mid-December 2005, on the morning of January 11, hours after the onset of the discrete, explosive eruptions at Augustine, staff from AVO and the Chief of the Homer Volunteer Fire Department participated in "Coffee Table," an hour-long radio call-in show on KBBI, Homer Public Radio. This radio show included live questions and answers about the volcanic activity and potential hazards, and advertised upcoming local presentations and an ash collection workshop scheduled in Homer for the following week (described below).

In December of 2005, KBEEA members requested AVO's participation in a public information meeting in Homer. They specifically sought information concerning the likely activity, impacts, and official response to an eruption of Augustine. With local input and assistance AVO staff developed a public presentation and discussion forum that were held in two back-to-back programs on January 19, 2006, at the interagency Islands and Ocean Visitor Center (appendix 1). Presenters from AVO, the West Coast and Alaska Tsunami Warning Center (WCATWC), the Kenai Peninsula Borough Office of Emergency Management, and the Kenai Peninsula Borough School District described the current volcanic unrest at Augustine and the preparedness and response activities of local, State, and Federal government organizations. A question and answer period followed the presentations. Additional representatives from the Federal Aviation Administration (FAA), the National Weather Service (NWS), Homer Fire Department, Homer Medical Center, South Peninsula Hospital, American Red Cross, and the U.S. Coast Guard were also available to answer questions. There were ~120 people in attendance at the programs.

From approximately January through August 2006, AVO staff gave about 25 presentations focused on Augustine at schools, museums, visitor centers, youth facilities, summer educational retreats, training venues (for example, National Park Service and FAA Anchorage Air Route Traffic Control Center), and professional society gatherings. During the same time frame, staff also gave about three dozen tours of the AVO Operations Center to a wide variety of groups ranging from nonprofit educational organizations, to public schools, media, and staff from other response agencies. For comparison, over the previous 7-month-long period (roughly May through December 2005), staff participated in approximately ten presentations (half of which were in Kenai and Homer) and more than 10 tours of the AVO Operations Center.

Citizen Ash-Fall Accounts and Sampling

AVO used civic speaking opportunities and other points of contact with the public to solicit information about ash-fall events, including sampling of ash fall, to assist AVO with scientific response to the eruption (Wallace and others, this volume). Staff also sought ash-fall observers and collectors from the NWS Cooperative Observer Program (Weather Spotters, http://www.weather.gov/os/coop/, last accessed February, 2008) and the State of Alaska Division of Community and Regional Affairs Community Database Online (http://www.commerce.state.ak.us/dca/commdb/CF_CONT.htm, last accessed February, 2008). Instructions and datasheets for making observations and collecting ash-fall samples were also prominently posted under the "Links" section on the AVO

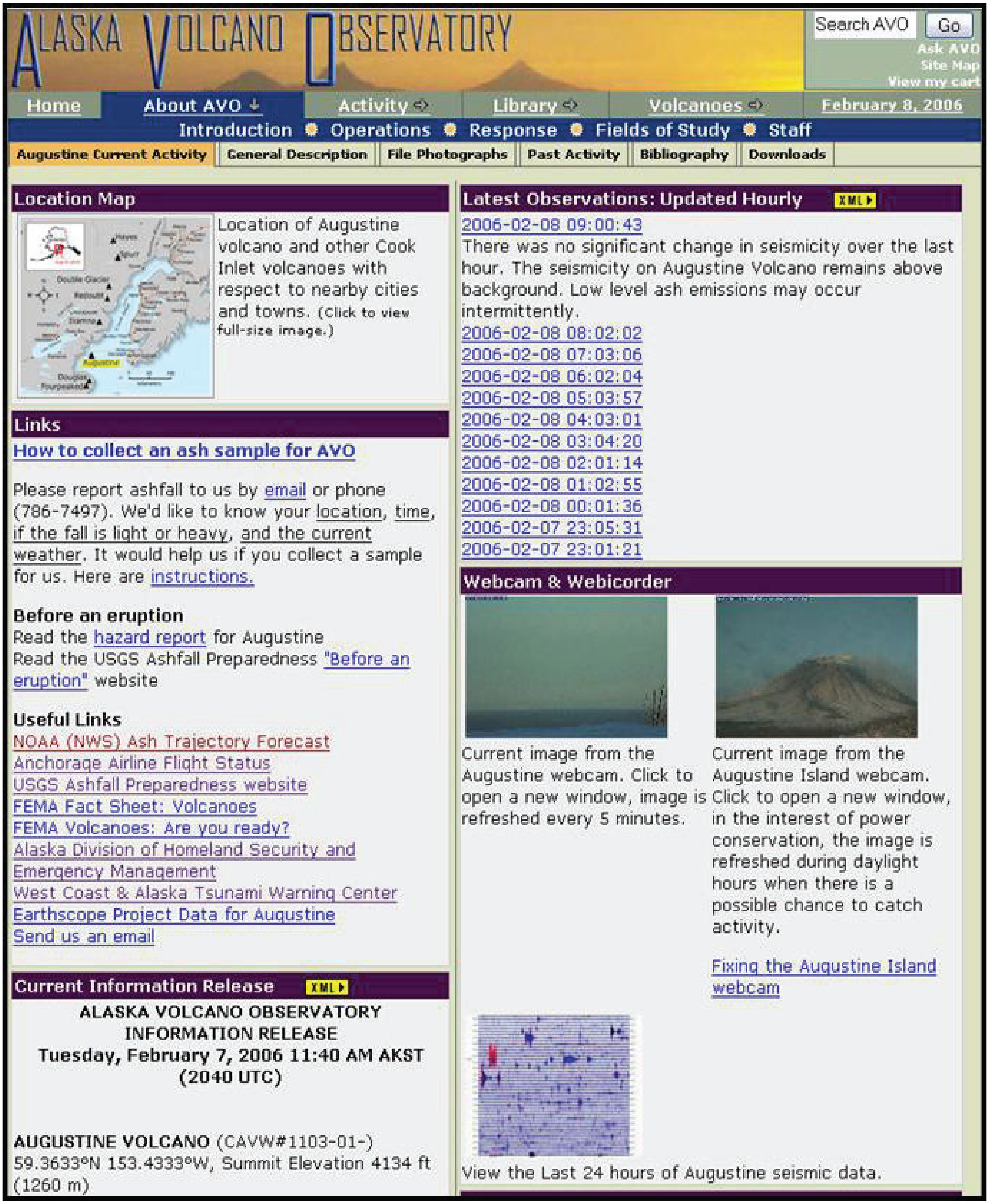

Location Map

Location of Augustine volcano and other Cook Inlet volcanoes with respect to nearby cities and towns. (Click to view full-size image.)

Links

How to collect an ash sample for AVO

Please report ashfall to us by email or phone (786-7497). We'd like to know your location, time, if the fall is light or heavy, and the current weather. It would help us if you collect a sample for us. Here are instructions.

Before an eruption
Read the hazard report for Augustine
Read the USGS Ashfall Preparedness "Before an eruption" website

Useful Links
NOAA (NWS) Ash Trajectory Forecast
Anchorage Airline Flight Status
USGS Ashfall Preparedness website
FEMA Fact Sheet: Volcanoes
FEMA Volcanoes: Are you ready?
Alaska Division of Homeland Security and Emergency Management
West Coast & Alaska Tsunami Warning Center
Earthscope Project Data for Augustine
Send us an email

Current Information Release

ALASKA VOLCANO OBSERVATORY
INFORMATION RELEASE
Tuesday, February 7, 2006 11:40 AM AKST
(2040 UTC)

AUGUSTINE VOLCANO (CAVW#1103-01-)
59.3633°N 153.4333°W, Summit Elevation 4134 ft (1260 m)

Latest Observations: Updated Hourly

2006-02-08 09:00:43
There was no significant change in seismicity over the last hour. The seismicity on Augustine Volcano remains above background. Low level ash emissions may occur intermittently.
2006-02-08 08:02:02
2006-02-08 07:03:06
2006-02-08 06:02:04
2006-02-08 05:03:57
2006-02-08 04:03:01
2006-02-08 03:04:20
2006-02-08 02:01:14
2006-02-08 01:02:55
2006-02-08 00:01:36
2006-02-07 23:05:31
2006-02-07 23:01:21

Webcam & Webicorder

Current image from the Augustine webcam. Click to open a new window, image is refreshed every 5 minutes.

Current image from the Augustine Island webcam. Click to open a new window, in the interest of power conservation, the image is refreshed during daylight hours when there is a possible chance to catch activity.

Fixing the Augustine Island webcam

View the Last 24 hours of Augustine seismic data.

Figure 2. Part of the Alaska Volcano Observatory (AVO) Augustine Current Activity Web page from February 8, 2006.

Augustine Current Activity Web page (fig. 2) and all contacts were directed to this Web page for information about how to sample ash. On January 19, 2006, staff also conducted an ash-collection workshop in conjunction with the public information meetings in Homer.

During the eruption, 30 volcanic ash-fall samples were collected by 15 citizens. These samples make up the majority of off-island samples of ash collected from this eruption and are an important part of its scientific documentation (fig. 1; Wallace and others, this volume).

During the eruption, more than 130 individual calls and e-mails to AVO included reports concerning ash fall. If reported by telephone, staff then filled out an internal ash-fall account worksheet (appendix 2). All ash-fall observations were reported immediately by phone to colleagues at the NWS Anchorage Weather Forecast Office because NWS has formal ash-fall warning responsibility (Wallace and others, this volume; Neal and others this volume).

Preeruption Interagency Press Conference

On December 22, 2005, staff from AVO, National Oceanic and Atmospheric Administration (NOAA), and the State of Alaska Department of Homeland Security and Emergency Management held a joint press conference at the Aviation Technology Center in Anchorage (appendix 3). Local media coverage of the event aided in reminding the public of Augustine's previous, ongoing, and likely future activity and the chief hazards—airborne volcanic ash and ash fall. The press conference also reestablished the ongoing relationships among State, local, and Federal agencies in the event of an eruption. This is the first time a formal, interagency press conference was held before the onset of a forecasted volcanic eruption in Alaska.

AVO's Public Website

In March 2005, AVO upgraded its existing Web site from thousands of static pages to a dynamic, database-driven design. This change gave the Web site greater flexibility, enabling more real-time data feeds and information analysis products. The 2005–6 eruption of Augustine was the first significant Alaskan eruption to take place since the Web site upgrade. With increasing Internet connectivity for Alaskans and the rest of the world, AVO's improved public site gained a greater eruption response role, and this was the first eruption where the AVO Web site became a primary source for the general public to get information. Because of increased capabilities, the internal part of the site also was used extensively for staff collaboration, eruption documentation, operational scheduling, and record keeping.

In 2005–6, the public part of the AVO Web site served as a digital distribution center for information on Alaskan volcanoes, including background information, bibliographic resources (including free downloadable papers), photographs and maps, and real-time data feeds of Web-camera images and webicorders (described below). The Web site also facilitated the distribution of formal information products such as "Status Reports" and "Information Statements" (Neal and others, this volume). Once posted to the AVO Web site, formal notices were automatically posted to the Disaster Management Interoperability Service (DMIS) network as well.

During the Augustine unrest and eruption, all Augustine-specific information was gathered on an Augustine Current Activity Web page, prominently linked from AVO's homepage (fig. 2). It included background information, maps, photographs, all of the formal information products (see Neal and others, this volume), links to Augustine's webcams and webicorders, information on located earthquakes, a chronology of major eruption and eruption response events, and links to useful Web sites.

During the eruption, AVO received feedback that people and organizations needed information more often than formal information products were released (typically twice a day at the height of the eruption). In response to that request, the "Latest Observations" section was added as a feature on the public Augustine Current Activity Web page on January 13, 2006 (fig. 2). This feature allowed Operations Center staff to use an internal Web form and post informal summaries of activity at hourly (or periodic) intervals to the public page (fig. 3*A*).

Novel Data Streams on the Web

This eruption of Augustine was the first Alaskan eruption to make extensive use of Web cameras, or webcams. Eventually four webcams were oriented towards Augustine (Paskievitch and others, this volume) and images were displayed on the AVO Web site (fig. 2). The webcams acquired images every few minutes (sometimes every hour or every few hours), and people viewing these images accounted for approximately 30 percent of the outgoing data from the Web site. Individual images in this suite of webcam images were viewed close to 20 million times during January–February 2006.

Another new feature to the AVO Web site during the Augustine eruption was the addition of webicorders that show data from selected AVO seismic stations (fig. 2). Webicorders display the past 24 hours of seismic data and update in near real time. Server logs show that webicorders were popular with site users, and they also generated hundreds of e-mails to the AVO webmaster. Webicorder displays were accompanied on the Web by brief text that described the main types of seismic signals displayed, including regional earthquakes and calibration pulses.

AVO's fledgling image database grew to contain nearly 5,000 images of Augustine, about 1,000 of which are viewable on the public Web site. The new image database also saw increased usage—2.5 million requests to view these images were made in January–February 2006, more than 20 times the normal usage in previous months. In contrast, AVO's old site contained only dozens of images per eruption. The dramatic growth and use of an image database occurred for several

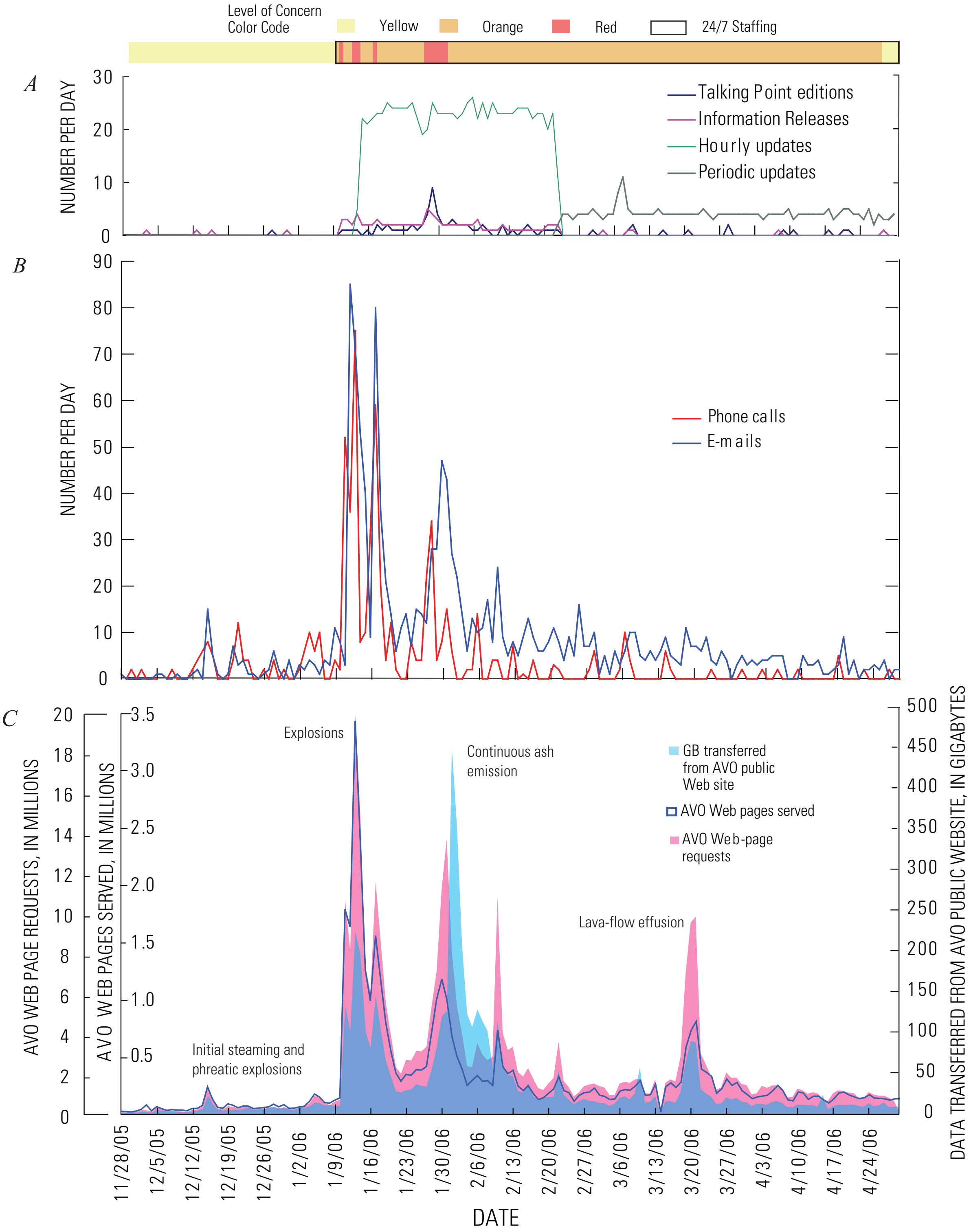

Figure 3. *A*, Daily totals of information items produced during the 2005–6 unrest and eruption at Augustine Volcano. Level of concern color code and period of 24/7 staffing at the Alaska Volcano Observatory (AVO) is shown along the top. *B*, Daily totals of recorded phone calls and e-mails received. *C*, AVO Web site statistics of gigabytes transferred, Web pages served and Web page requests. Each AVO Web page served consist of multiple objects (for example, pictures, style sheets, and javascript). Each individual object is counted as a request, thus the large difference in numbers between pages served and requests. Large spikes in the graph can be attributed to specific events during the unrest and eruption.

reasons. First, AVO now relies on digital cameras rather than film. Second, the image database made it relatively easy for staff to upload images and associated metadata (for example, photographer, date, and caption). Once in the database, scripting routines automatically create standardized thumbnail and screen-size resolution copies of the image, post them to public and internal Web sites, and generate unique and permanent Web-page addresses. Future placement and reference of the image on any AVO Web site can be done with just its database-assigned numerical identification number.

Web-usage Statistics

The 2006 eruption of Augustine created a huge increase in traffic to the AVO public Web site. During the eruption, the Web site was used heavily by agency responders and members of the public (fig. 3*C*), including visitors from 147 countries in January 2006. Each AVO Web page contains multiple objects (for example, pictures, style sheets, javascript) and each object is counted as a “request.” During the Augustine unrest and eruption, the Web site logged more than 345 million requests, served more than 45 million pages, and distributed about 5.5 terabytes of data (fig. 3*C*). This was nearly half the total amount of data served by the AVO public Web site since its inception in December 1994 through the end of 2005.

As observed during response to the 2004 eruption of Mount St. Helens, the number of Web requests (described as “hits” in Driedger and others, 2008), waxed and waned relative to the activity at the volcano (fig. 3*C*). The high peaks in AVO Web-site statistics correspond to time periods of AVO level of concern color code Red (see Neal and others, this volume, for discussion of the color code). The busiest day for the site during the Augustine eruption was January 13, 2006, correspondent with several consecutive explosions (Coombs and others, this volume; fig. 3*C*). Similar but smaller peaks in Web-site usage occurred coincident with continuous ash emission in late January–early February and lava effusion in mid-March.

Communication Strategies for Answering Public Queries

Since the observatory’s inception, AVO staff have engaged in communications with the media and the public during Cook Inlet volcanic eruptions. The demand for volcano information about the 1989–90 eruption of Redoubt Volcano quickly inundated AVO’s small staff. During that eruption, hazard information was distributed by AVO to government and industry officials through printed updates and briefings. Briefings were also given to the news media and the general public (Brantley, 1990). During the 1992 eruption of Mount Spurr, AVO’s use of updates, the level of concern color code, and direct personal communications worked well to inform the general public of anticipated eruptions and resultant hazards. AVO’s outreach was aided by intensive media coverage through local and national radio, television, and newspaper outlets (Eichelberger and others, 1995).

During the 2005–6 Augustine unrest and eruption, almost all observatory staff engaged in communicating with the public at various times. Along with round-the-clock monitoring duties, staff members took at least 338 phone calls from media, local residents, interested people from around the world, and other Augustine-responding State and Federal agencies (fig. 3*B*). Because the AVO operations center was staffed by a diverse group of scientists from AVO offices in Anchorage and Fairbanks, as well as by other staff of the USGS Volcano Hazards Team (VHT), it was important to have a defined protocol for handling media and public inquiries and to ensure that current information on the activity of Augustine was available to all staff.

Media Management Plan

In December 2005, staff began writing a Media Management Plan (MMP) to serve as a guide for handling current and likely increasing media attention. Many of the approaches incorporated into this plan were previously used by AVO and VHT staff assisting with media inquiries during eruption

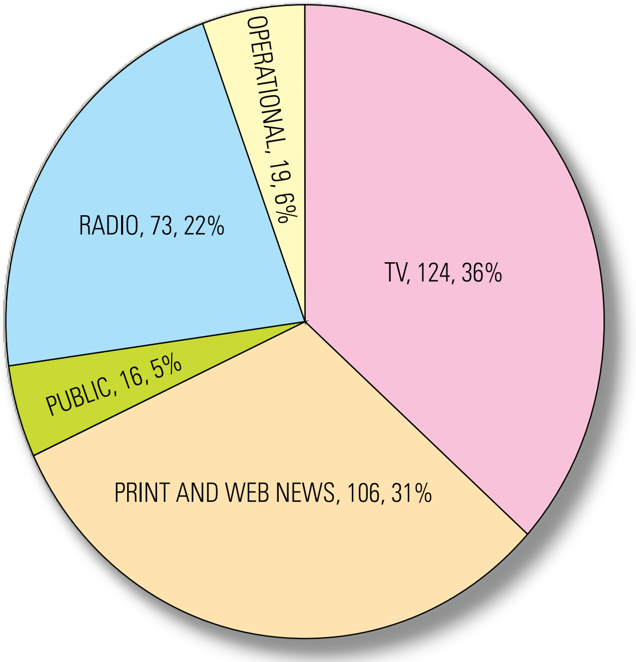

Figure 4. Sources of 338 reported phone calls made to the Alaska Volcano Observatory (AVO) from November 28, 2005, through May 16, 2006. Each wedge lists (1) source, (2) number of calls, and (3) percentage.

responses in Alaska and elsewhere. The MMP ensured message consistency and minimized disruption to scientists' other duties. The first MMP was implemented on December 27, 2005, and went through a few minor revisions as events at Augustine progressed. The MMP focused on (1) defining the roles of Media Coordinator and an Information Scientist, (2) providing information for interviews, (3) interview request guidelines, and (4) photo and video management guidelines.

The roles of the Media Coordinator and Information Scientist stemmed from the experience of staff and colleagues who participated in the Joint Information Center formed during the most recent eruption of Mount St. Helens in Washington (Driedger and others, 2008). The Media Coordinator, located in Anchorage, scheduled and organized venues, speakers, and graphical products (such as figures, video, and photos) for onsite and phone interviews. They also served as a point person for other staff with media needs, proactively coordinated local AVO press conferences, and coordinated the distribution of recent airborne observations and video imagery to media.

AVO and other U.S. volcano observatories have used the role of Information Scientist to orchestrate the release of information to the media and the public during earlier volcanic eruptions, including the 1989–90 eruptive sequence of Redoubt Volcano (Brantley, 1990). During the 2005–6 Augustine eruption, the Information Scientist, also located in Anchorage, was a week- to multi-week-long rotating position, working in conjunction with the Media Coordinator. The Information Scientist generated, updated, and distributed talking points (described below) and was often available for on-camera, radio, and phone interviews with the press. Members of both the AVO staff and the VHT outside of AVO served as Information Scientists during the Augustine eruption. Although the Information Scientist was usually tasked with meeting interview requests, those requests with a narrow focus on a particular subject were directed to the appropriate specialist(s). In total, AVO and VHT staff working in Alaska gave more than 350 on-camera, radio, phone and print media interviews from November 2005 through August 2006.

For the first few weeks following the January 11, 2006, onset of explosive magmatic activity at Augustine, press conferences were held almost daily in the AVO Operations Center. AVO representatives, principally the Information Scientist and the Media Coordinator, organized and attended these sessions and prepared new content, figures, and information with the explicit goal of meeting the 2:00 p.m. deadline for local television news stations.

Per the MMP, a single phone number for AVO—a longtime general phone number for the observatory—was publicized to the media. Calls to this number were answered by the Media Coordinator, the Information Scientist, and Operations Center staff. Callers were also reminded of AVO's up-to-date recorded information phone line and Web site as alternate primary sources for information.

On immediate return from observational and data-collection flights, scientists were asked to caption and upload digital photos in the AVO online image database and to notify the Web team to make these images available on the public Web site.

As the number of calls from the media and others increased (from a couple of calls per a day, to a record number of 75 reported calls on January 13), the range of question topics grew. AVO was asked about other agencies' information products, such as ash-fall and marine advisories, flight restrictions, restrictions of access to Augustine Island, and tsunami warning protocols, as well as general volcano hazard information and emergency preparedness guidelines. Later versions of the MMP, released in January 2006, included a list of public phone numbers and Web sites for use in redirecting public callers to the appropriate agency for questions about specific, non-AVO information products or announcements. An adaptation of this contact list was later included in the revised Interagency Operating Plan for Volcanic Ash Episodes (Madden and others, 2008). The entire MMP was updated (with new, local contacts and volcano-specific information) in response to the unrest and phreatic eruption of Fourpeaked volcano in September 2006 (Neal and others, 2009) and the eruption of Pavlof Volcano in the summer of 2007.

AVO's "Augustine Eruption Information" Files

Scientists must speak with a "single voice" to avoid confusion during hazardous events (Newhall and others, 1999). To ensure that AVO's information was authoritative and uniform, staff needed convenient access to consistent and up-to-date information. To this end, AVO staff compiled hard-copy talking points and other resources that were placed by each phone in the Anchorage Operations Center in "Augustine Eruption Information" binders. These items were available digitally to staff in Fairbanks and elsewhere through the internal AVO Web site and shared hard drive. Posting the information at all locations helped all AVO and VHT staff to provide accurate and specific information, and give similar accounts of current activity.

In late December 2005, AVO established the use of internal talking points pertinent to volcanic activity at Augustine. Talking points were typically generated and updated by the Information Scientist and summarized the most recent information pertaining to the eruption, possible hazards, and AVO response activities into concise bullets (Neal and others, this volume). AVO staff was encouraged to review the most recent talking points before each Operations Center shift, giving an interview, or answering a public question. From December 27, 2005, through April 30, 2006, there were about 80 editions of talking points (fig. 3*A*).

Other materials placed in the Augustine Eruption Information binders included (1) a set of brief facts regarding nearby populations, including community distances from Augustine; (2) talking points about the unlikely possibility of a volcanogenic tsunami from Augustine, compiled jointly by

AVO and the WCATWC; (3) a concise review Augustine's eruptive history and geology, gathered from the existing preliminary Augustine volcano-hazards assessment (Waythomas and Waitt, 1998).

As the eruption progressed, additional documents were added to the binders and appropriate electronic folders, including draft summaries of geophysical data time series, such as GPS data (Cervelli and others, this volume), a description of the deployment of ocean bottom seismometers (ten Brink, 2006), a description of Augustine's volcanic hazards and instrumentation (Ewert and others, 2005), and Augustine-related press releases from the USGS and UAF/GI.

Nature of Public Inquiries

Inquiries and observations from the media, the public, and cooperating agencies came to AVO by phone calls and e-mails. Users of the AVO public Web site were able to e-mail the AVO webmaster using a link on the footer of every Web page. Additional e-mail and phone calls were made directly to individual staff members. During the Augustine unrest and eruption, the AVO Web site also expanded its role as a proactive information provider—if interested parties could find the answer to their question on the Web site, they often didn't need to call or e-mail.

In an effort to evaluate the nature and effectiveness of AVO communications during the Augustine eruption, reported e-mails, phone calls, and Web traffic during the Augustine eruption were compiled, reviewed, and plotted relative to Augustine's level of concern color code. The greatest number of requests for information (phone calls, e-mails, and web traffic) correlate well with increased volcanic activity and elevated color codes (fig. 3). The volume of phone calls and e-mails roughly parallel each other, with a slight timing lag for e-mails.

Phone Calls to AVO

From November 28, 2005, through May 16, 2006, staff logged 338 phone calls, most regarding Augustine (fig. 3*B*; fig. 4). The highest numbers per day occurred when Augustine was at elevated color codes, a trend also noted in the number and timing of calls to the Joint Information Center during the 2004–6 eruption of Mount St. Helens (Driedger and others, 2008). Eighty-nine percent of the reported calls to AVO were from local, domestic, and international media, although media calls were likely overreported compared to calls from the public by Operations Center scientists. The majority of the media calls were from local and national television stations (36 percent) followed by local, national, and international print and Web-based press, such as Reuters and the Associated Press (31 percent; fig. 4). Local, national, and international radio contacts were responsible 22 percent of calls. Most media requests for a phone interview were fulfilled by the contacted staff member, but some calls from the media required coordination for onsite interviews or further response by a subject specialist.

Eleven percent of reported calls were from companies and agencies requesting information concerning their own hazards and preparedness operations (6 percent) and the general public (5 percent; fig. 4). The majority of calls regarding operational information concerned airborne volcanic ash, ash fall, the temporary flight restriction around Augustine, and calls from organizations asking if additional emergency response personnel from out of state were deployed or needed. Public callers sometimes gave informative eyewitness observations of volcanic activity (including the initial explosive onset on January 11, 2006) and reported ash fall. Observations were entered into the AVO internal logs. When appropriate, staff conveyed relevant public-reported observations to organizations such as the NWS.

During periods of inactivity as well as during eruptive activity, AVO maintains a phone line with a prerecorded message that repeats the most recent Information Release or Weekly Update. As stated at the beginning of the message, the number is not used to receive voice mail. Callers wishing to speak with someone are directed to call the AVO Anchorage public phone number. We have no way of determining the number of calls made to the AVO recorded information line.

The USGS Office of Communications staff in the Western Region (Seattle, Wash. and Menlo Park, Calif.) and at the USGS Headquarters (Reston, Va.) also reported receiving calls pertaining to the eruption (the number of calls received was not recorded), and they often referred callers to the AVO Web site or suggested individuals contact specific AVO staff (S. Hanna, L. Gordon, W. Lukas, and C. Ransom, written commun., 2008). The national "ASK USGS" phone service does not count the number or content of inquiries (K. Swanjord, oral commun., 2008). ADGGS staff did not receive a significant number of Augustine inquiries (J. Outten and P. Davis, written commun., 2008). The UAFGI Information Office did not count the number of calls it received about Augustine activity, but they did direct callers to appropriate UAFGI staff and use the AVO Web site to respond to general inquires (A. Hartley, oral commun., 2008).

E-mails to the AVO Webmaster

During this same period, from November 28, 2005, through May 31, 2006, staff logged and answered 1,336 e-mails to the AVO Web site (fig. 3*B*). During periods of low to no volcanic activity, the AVO Web site typically receives less than one e-mail per day. During the Augustine eruption, there were 676 e-mails in January 2006 alone—nearly 22 e-mails per day (fig. 3*B*). AVO staff rotated weekly in answering e-mail during the period of heaviest traffic (late December 2005 through January 2006). All e-mails (submissions and responses) are archived in a database, which allowed staff to (1) instantly determine if an e-mail had been answered, (2) cut and paste detailed and informative answers to commonly asked questions, (3) track correspondence with individuals, and (4) create a searchable archive of questions for later analysis of AVO's communications. In most cases staff assigned to Web e-mail duty answered questions; in some instances they sought answers from specialists.

A first-order categorization of the e-mails during the Augustine eruptive period consists of 429 e-mails (~32 percent) with positive feedback to AVO (about the Web site, information products, and flow of information), 896 e-mails (~67 percent) containing comments, questions or suggestions, and 11 e-mails (0.8 percent) containing negative comments about the Web cameras and the timeliness of online updates. Pertinent observations (for example, ash fall or sulfur smell) in e-mails were reported in the AVO internal log and conveyed directly to on-duty monitoring staff.

Although e-mails from people in the vicinity of Augustine were the most numerous during AVO's eruption response, people e-mailed the AVO webmaster from as far away as the East Coast of the United States and foreign countries. The Web site e-mail address provided a way for people to ask nonurgent questions of AVO without tying up limited phone resources. Such questions included queries like "Do you think my summer cruise to Alaska will be cancelled?" and "Where can I find information about hot spot volcanoes?" People living in far-flung time zones often wanted to know why the webcam was dark (typically due to the late-rising sun during arctic winters). Timely response to these e-mails helped AVO build a good relationship as a credible source of technical information, both for Alaskans and people around the globe.

Lessons Learned and Suggestions for Improvement

During times of significant volcanic activity, the demands on AVO's communication systems and education and outreach program are dramatically increased. To meet these increased needs during the 2005–6 Augustine eruption, AVO implemented an internal communications strategy that improved the efficiency, consistency, and timeliness of public information distribution and communication. This internal strategy included use of dedicated outreach personnel for community presentations, a Media Management Plan, distribution of talking points and other updated documents to all staff, and a growing, dynamic, database-backed Web site. Application of this plan and use of improved communication tools allowed AVO to respond to a high volume of information requests and to meet education and outreach opportunities before, during, and following the eruption with accurate and timely information.

Owing to population expansion in Alaska and the spread of global Internet use, Alaskan eruptions now possess a higher degree of visibility than previously. Improvements could be made to AVO's public outreach and communications efforts; these include (1) A toll-free version of the AVO recorded message line would be useful to the public and outside organizations (because the current number is not a local call outside of Anchorage); (2) ensuring the means to organize, archive, duplicate, and edit digital video would ease the crunch of media video requests during periods of volcanic crisis (currently no AVO staff members are specifically tasked with digital video duplication and editing, and AVO's video library remains largely inaccessible to both internal users and the media); (3) continued development and evolution of the AVO public Web site (the site has already completed two major revisions since the Augustine eruption, and should continue to evolve and become more interactive, as Web 2.0 technologies mature and become mainstream).

Acknowledgments

The authors wish to thank Steven Brantley, Michelle Coombs, and Carolyn Driedger for their thoughtful reviews, which greatly improved the content and utility of this paper.

References Cited

Alaska Department of Labor and Workforce Development, 2010, Table 4.3; Alaska Places by Borough and Census Area, 2000-2008; Kenai Peninsula Borough, *in* Alaska Population Overview 2007–2008 Estimates: p. 135 [http://www.labor.state.ak.us/research/pop/chap4.pdf; last accessed May, 2010].

Brantley, S.R., ed., 1990, The eruption of Redoubt Volcano, Alaska, December 14, 1989–August 31, 1990: U.S. Geological Survey Circular 1061.

Cervelli, P.F., Fournier, T.J., Freymueller, J.T., Power, J.A., Lisowski, M., and Pauk, B.A., 2010, Geodetic constraints on magma movement and withdrawal during the 2006 eruption of Augustine Volcano, *in* Power, J.A., Coombs, M.L., and Freymueller, J.T., eds., The 2006 eruption of Augustine Volcano, Alaska: U.S. Geological Survey Professional Paper 1769 (this volume).

Coombs, M.L., Bull, K.F., Vallance, J.W., Schneider, D.J., Thoms, E.E., Wessels, R.L., and McGimsey, R.G., 2010, Timing, distribution, and volume of proximal products of the 2006 eruption of Augustine Volcano, *in* Power, J.A., Coombs, M.L., and Freymueller, J.T., eds., The 2006 eruption of Augustine Volcano, Alaska: U.S. Geological Survey Professional Paper 1769 (this volume).

Driedger, C.L., and Neal, C.A., Knappenberger, T.H., Needham, D.H., Harper, R.B., and Steele, W.P., 2008, Hazard information management during the autumn 2004 reawaking of Mount St. Helen's Volcano, Washington, *in* Sherrod, D.R., Scott, W.E., and Stauffer, P.H., eds., A volcano rekindled; The renewed eruption of Mount St. Helens, 2004–2005, U.S. Geological Survey Professional Paper 1750, p. 505–519.

Eichelberger, J.C., Keith, T.E.C., Miller, T.P., and Nye, C. J., 1995, The 1992 Eruptions of Crater Peak Vent, Mount Spurr volcano, Alaska; chronology and summary, *in* Keith, T.E.C., ed., The 1992 eruptions of Crater Peak vent, Mount Spurr volcano, Alaska: U.S. Geological Survey Bulletin 2139, 220 p.

Ewert, J.W., Guffanti, Marianne, and Murray, T.L., 2005, An assessment of volcanic threat and monitoring capabilities in the United States; framework for a National Volcano Early Warning System (NVEWS): U.S. Geological Survey Open-File Report 2005-1164, 62 p.

Jacobs, K.M., and McNutt, S.R., 2010, Using seismic *b*-values to interpret seismicity rates and physical processes during the preeruptive earthquake swarm at Augustine Volcano 2005–2006, *in* Power, J.A., Coombs, M.L., and Freymueller, J.T., eds., The 2006 eruption of Augustine Volcano, Alaska: U.S. Geological Survey Professional Paper 1769 (this volume).

Kienle, J., 1994, Volcanic ash-aircraft incidents in Alaska prior to the Redoubt eruption on 15 December 1989, *in* Casadevall, T.J., ed., Volcanic ash and aviation safety; proceedings of the first international symposium on volcanic ash and aviation safety: U.S. Geological Survey Bulletin 2047, p. 119–123.

Madden, J., Murray, T.L., Carle, W.J., Cirillo, M.A., Furgione, L.K., Trimpert, M.T., and Hartig, L. (signatories), 2008, Alaska interagency operating plan for volcanic ash episodes: 52 p.

McGee, K.A., Doukas, M.P., McGimsey, R.G., Neal, C.A., and Wessels, R.L., 2010, Emission of SO_2, CO_2 and H_2S from Augustine Volcano, 2002–2008, *in* Power, J.A., Coombs, M.L., and Freymueller, J.T., eds., The 2006 eruption of Augustine Volcano, Alaska: U.S. Geological Survey Professional Paper 1769 (this volume).

Neal, C.A., McGimsey, R.G., Dixon, J.P., Manevich, A., and Rybin, A., 2009, 2006 Volcanic activity in Alaska, Kamchatka, and the Kurile Islands; Summary of events and response of the Alaska Volcano Observatory: U.S. Geological Survey Scientific Investigations Report 2008-5214, 102 p., [http://pubs.usgs.gov/sir/2008/5214/] .

Neal, C.A., Murray, T.L., Power, J.A, Adleman, J.N., Whitmore, P.M., and Osiensky, J.M., 2010, Hazard information management, interagency coordination, and impacts of the 2005–2006 eruption of Augustine Volcano, *in* Power, J.A., Coombs, M.L., and Freymueller, J.T., eds., The 2006 eruption of Augustine Volcano, Alaska: U.S. Geological Survey Professional Paper 1769 (this volume).

Newhall C., Aramaki, S., Barberi, F., Blong, R., Calvache, M., Cheminee, J.-L., Punongbayan, R., Siebe, C., Simkin, T., Sparks, S., and Tjetjep. W., 1999, IAVCEI Subcommittee for Crisis Protocols Professional conduct of scientists during volcanic crises: Bulletin of Volcanology, v. 60, p. 323–334.

Paskievitch, J., Read, C., and Parker, T., 2010, Remote telemetered and time-lapse cameras at Augustine Volcano, *in* Power, J.A., Coombs, M.L., and Freymueller, J.T., eds., The 2006 eruption of Augustine Volcano, Alaska: U.S. Geological Survey Professional Paper 1769 (this volume).

Power, J.A., and Lalla, D.J., 2010, Seismic observations of Augustine Volcano, 1970–2007, *in* Power, J.A., Coombs, M.L., and Freymueller, J.T., eds., The 2006 eruption of Augustine Volcano, Alaska: U.S. Geological Survey Professional Paper 1769 (this volume).

Power, J.A., Nye, C.J., Coombs, M.L., Wessels, R.L., Cervelli, P.F., Dehn, J., Wallace, K.L., Freymueller, J.T., and Doukas, M.P., 2006, The reawakening of Alaska's Augustine Volcano: Eos (American Geophysical Union Transactions), v. 87, n. 37, p. 373, 377.

Swanson, S.E., and Kienle, J., 1988, The 1986 eruption of Mount St. Augustine—field test of a hazard evaluation: Journal of Geophysical Research, v. 93, n. B5, p. 4500–4520.

ten Brink, U.S., 2006, Eruption of Augustine Volcano being monitored by state-of-the-art submarine seismometers: Sound Waves—Coastal Science and Research News from Across the USGS [http://soundwaves.usgs.gov/2006/03/].

Waitt, R.B., and Begét, J.E., 2009, Volcanic processes and geology of Augustine Volcano, Alaska: U.S. Geological Survey Professional Paper 1762, 78 p., 2 map plates [http://pubs.usgs.gov/pp/1762/].

Wallace, K.L., Neal, C.A., and McGimsey, R.G., 2010, Timing, distribution, and character of tephra fall from the 2005–2006 eruption of Augustine Volcano, *in* Power, J.A., Coombs, M.L., and Freymueller, J.T., eds., The 2006 eruption of Augustine Volcano, Alaska: U.S. Geological Survey Professional Paper 1769 (this volume).

Waythomas, C.F., and Waitt, R.B., 1998, Preliminary volcano-hazard assessment for Augustine Volcano, Alaska: U.S. Geological Survey Open-File Report 98-0106, 39 p., 1 plate, scale unknown.

Appendix 1. Handout for Homer Public Meetings

Current Unrest at Augustine Volcano and Public Safety Response
January 19, 2006

The purpose of this meeting is to review the current volcanic unrest at Augustine Volcano and the response plans of local, state and federal government agencies. A question and answer period will follow the presentations.

5:00pm - 6:30pm repeated 7:00pm – 8:30pm

Presentations

Welcome / Introduction	Alaska Volcano Observatory
Augustine Update	Alaska Volcano Observatory
Tsunami Hazard Review	NOAA's NWS West Coast and Alaska Tsunami Warning
Center Ash-fall Episode Plan	The Kenai Peninsula Borough Office of Emergency Management

Question and Answer Period

Panel participants from:

Alaska Volcano Observatory
West Coast and Alaska Tsunami Warning Center
Kenai Peninsula Borough
Federal Aviation Authority
National Weather Service

FOR MORE INFORMATION:

Please check the information tables in the lobby and visit the following websites:

Alaska Volcano Observatory	www.avo.alaska.edu/
West Coast and Alaska Tsunami Warning Center	http://wcatwc.arh.noaa.gov/
Kenai Peninsula Borough	http://www.borough.kenai.ak.us/emergency/default.htm
Federal Aviation Authority	http://www.alaska.faa.gov/
National Weather Service	http://www.arh.noaa.gov/ http://pafc.arh.noaa.gov/augustine.php

Appendix 2. Ash-fall Account Worksheet

ASH-FALL ACCOUNTS

WHAT TO ASK FOR*

*If caller is interested in collecting, refer to www.avo.alaska.edu/ashfall.php

DATE: ____
LOCATION: ____
TIME: ____
DURATION: ____
AMOUNT OF ASH COLLECTED: ___________________________________
WEATHER CONDITIONS AT TIME OF COLLECTION: __________________ _____________
____
NAME OF COLLECTOR: ____
CONTACT INFORMATION: ____

ON DUTY OPERATIONS ROOM STAFF

☐ Call or fax accounts to National Weather Service Anchorage Weather Forecast Office

☐ Enter ash-fall account into the Eruption Chronology

☐ Enter ash-fall details into Ash-fall Account Log

☐ Add to AVO internal website logs

☐ Archive

Any of these duties can be delegated so long as by the end of your duty shift all accounts are properly cataloged.

Appendix 3. Joint USGS-NOAA Media Advisory

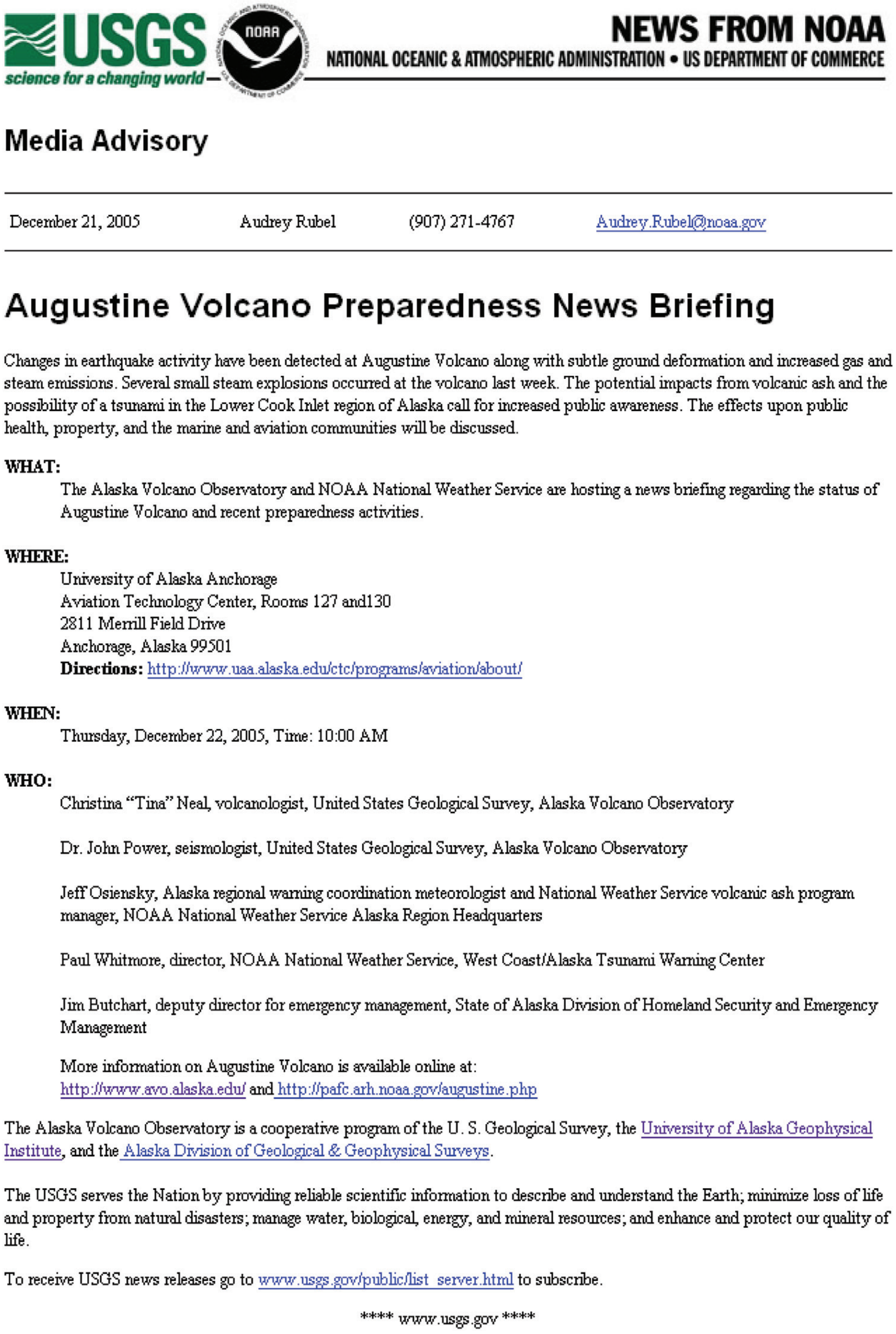

USGS
science for a changing world

NEWS FROM NOAA
NATIONAL OCEANIC & ATMOSPHERIC ADMINISTRATION • US DEPARTMENT OF COMMERCE

Media Advisory

December 21, 2005 Audrey Rubel (907) 271-4767 Audrey.Rubel@noaa.gov

---

Augustine Volcano Preparedness News Briefing

Changes in earthquake activity have been detected at Augustine Volcano along with subtle ground deformation and increased gas and steam emissions. Several small steam explosions occurred at the volcano last week. The potential impacts from volcanic ash and the possibility of a tsunami in the Lower Cook Inlet region of Alaska call for increased public awareness. The effects upon public health, property, and the marine and aviation communities will be discussed.

WHAT:

The Alaska Volcano Observatory and NOAA National Weather Service are hosting a news briefing regarding the status of Augustine Volcano and recent preparedness activities.

WHERE:

University of Alaska Anchorage
Aviation Technology Center, Rooms 127 and130
2811 Merrill Field Drive
Anchorage, Alaska 99501
Directions: http://www.uaa.alaska.edu/ctc/programs/aviation/about/

WHEN:

Thursday, December 22, 2005, Time: 10:00 AM

WHO:

Christina “Tina” Neal, volcanologist, United States Geological Survey, Alaska Volcano Observatory

Dr. John Power, seismologist, United States Geological Survey, Alaska Volcano Observatory

Jeff Osiensky, Alaska regional warning coordination meteorologist and National Weather Service volcanic ash program manager, NOAA National Weather Service Alaska Region Headquarters

Paul Whitmore, director, NOAA National Weather Service, West Coast/Alaska Tsunami Warning Center

Jim Butchart, deputy director for emergency management, State of Alaska Division of Homeland Security and Emergency Management

More information on Augustine Volcano is available online at:
http://www.avo.alaska.edu/ and http://pafc.arh.noaa.gov/augustine.php

The Alaska Volcano Observatory is a cooperative program of the U. S. Geological Survey, the University of Alaska Geophysical Institute, and the Alaska Division of Geological & Geophysical Surveys.

The USGS serves the Nation by providing reliable scientific information to describe and understand the Earth; minimize loss of life and property from natural disasters; manage water, biological, energy, and mineral resources; and enhance and protect our quality of life.

To receive USGS news releases go to www.usgs.gov/public/list_server.html to subscribe.

**** www.usgs.gov ****

The 2006 Eruption of Augustine Volcano, Alaska
Power, J.A., Coombs, M.L., and Freymueller, J.T., editors
U.S. Geological Survey Professional Paper 1769

Chapter 28

Hazard Information Management, Interagency Coordination, and Impacts of the 2005–2006 Eruption of Augustine Volcano

By Christina A. Neal[1], Thomas L. Murray[1], John A. Power[1], Jennifer N. Adleman[1, 4], Paul M. Whitmore[2], and Jeffery M. Osiensky[3]

Abstract

Dissemination of volcano-hazard information in coordination with other Federal, State, and local agencies is a primary responsibility of the Alaska Volcano Observatory (AVO). During the 2005–6 eruption of Augustine Volcano in Alaska, AVO used existing interagency relationships and written protocols to provide hazard guidance before, during, and after eruptive events. The 2005–6 eruption was notable because of the potential for volcanogenic tsunami, which required establishment of a new procedure for alerts of possible landslide-induced tsunami in Cook Inlet. Despite repeated ash-cloud generating explosions and far-traveled ash clouds, impacts from the event were relatively minor. Primary economic losses occurred when air carriers chose to avoid flights into potentially unsafe conditions. Post-eruption evaluations by agencies involved in the response indicated weaknesses in information centralization and availability of specific information regarding ash fall hazards in real time.

Introduction

The 2005–6 eruption of Augustine was the first significant volcanic event in mainland Alaska since the Crater Peak eruption of Mount Spurr Volcano in 1992 (Keith, 1995). Advances in communications technology and the explosive growth of Internet use have dramatically affected public and official expectations during volcanic eruptions, and this was reflected in the Alaska Volcano Observatory's (AVO) strategy of information management and interagency coordination during Augustine's recent eruption (Adleman and others, this volume). The importance of long-term, real-time instrumental monitoring, background geological studies, and hazard assessments at young volcanoes was underscored during the Augustine unrest, and the availability of this information profoundly influenced the accuracy of the AVO's hazard analysis before and during the eruption. Pre-event coordination among State, Federal, and local agencies was also critical in ensuring efficient flow of information during eruptive events and minimizing impacts of drifting ash clouds and ash fall.

This paper describes elements of AVO's management of volcano-hazard information during the 2005–6 Augustine eruption, as well as interagency coordination during the precursory and eruptive phases. We also summarize impacts of the Augustine eruption and key lessons learned during the post-eruption interagency after-action. This paper does not address in detail the hazard warning activities and messages of other agencies, particularly the large number of important aviation-specific warning messages issued by both the Federal Aviation Administration (FAA) and the National Weather Service (NWS).

Volcano Hazard Warning System in Alaska

Since its founding in 1988, AVO has been responsible for issuing hazard warnings pertaining to Alaska's active volcanoes. The three component agencies of AVO—the U.S. Geological Survey (USGS), the University of Alaska Fairbanks

---

[1] Alaska Volcano Observatory, U.S. Geological Survey, 4200 University Drive, Anchorage, Alaska, 99508.

[2] National Oceanic and Atmospheric Administration, West Coast and Alaska Tsunami Warning Center, 910 S. Felton Street, Palmer, Alaska 99645.

[3] National Oceanic and Atmospheric Administration, National Weather Service, 222 W. 7th Avenue, Anchorage, Alaska 99513.

[4] Now at: Alaska Division of Homeland Security and Emergency Management, P.O. Box 5750, Fort Richardson, AK 99505-5750.

Geophysical Institute (UAFGI), and the Alaska Division of Geological and Geophysical Surveys (ADGGS)—all have formal mandates to mitigate hazards posed by volcanic eruptions in Alaska. The USGS has national authority and responsibility to issue disaster warnings for earthquakes, volcanic eruptions, landslides, and other geologic events as directed under the Disaster Relief and Emergency Assistance Act of 1974 (Public Law 93-288; renamed the Robert T. Stafford Act). The UAFGI is tasked with the collection and storage of seismic data pertaining to volcanic activity in support of hazard assessment and risk reduction; the UAFGI coordinates its work with other agencies and organizations to inform the public, officials, industry and citizens about volcanic hazards and associated risk (Alaska Statute 14.40.075). Finally, the Alaska State Legislature has directed the ADGGS to conduct scientific investigations to assess geologic hazards including those posed by volcanic activity to infrastructure within the State (Alaska Statute 41.08.020).

Volcano Monitoring

To meet these responsibilities, AVO uses a variety of ground-based, aerial, and satellite-based methods to detect volcanic unrest and track activity once an eruption occurs. These include real-time seismic monitoring networks, satellite remote sensing using a variety of platforms, campaign GPS deformation surveys and real-time GPS networks, fixed-wing overflights and Web cameras, airborne and ground-based thermal imaging, and airborne gas measurements. Both satellite and seismic data are analyzed at least twice daily and more often during times of heightened volcanic activity. AVO is not staffed onsite at its observatory offices around the clock unless significant unrest or eruptive activity is in progress; most data streams can be monitored remotely using the Internet. During the Augustine eruption of 2005–6, AVO increased the frequency of offsite monitoring of data streams as unrest accelerated and began continuous around-the-clock staffing in both Fairbanks and Anchorage on January 10, 2006. Onsite 24/7 staffing was discontinued on May 19, 2006 (Adleman and others, this volume).

Because of its frequent activity and proximity to major population centers, Augustine was one of the most well-monitored volcanoes in Alaska at the start of the eruption. As of mid-2005, eight seismometers (Power and Lalla, this volume) and five continuous GPS receivers (Pauk and others, this volume) were operating on Augustine Island. Additional instrumentation was added during the precursory activity and over the course of the eruption to boost monitoring capacity, replace damaged equipment, and collect geophysical data for research purposes.

Alaska Interagency Operating Plan for Volcanic Ash Episodes

Although AVO is responsible for detecting volcanic unrest and issuing notification of hazardous activity, the complete public warning process involves communication among a number of other State and Federal agencies, each of which have their own warning and information dissemination responsibilities and products (table 1). This multiagency response to volcanic activity in Alaska is documented in “The Alaska Interagency Operating Plan for Volcanic Ash Episodes” (Madden and others, 2008). In the first iteration of the plan published in 1994 after the 1992 eruptions of Mount Spurr, signatory agencies include USGS, NWS, FAA, Alaska Department of Homeland Security and Emergency Management (ADHSEM; then called the Alaska Department of Emergency Services or ADES), and the U.S. Air Force (USAF). The U.S. Coast Guard (USCG) was added in 2004 and the Alaska Department of Environmental Conservation, Division of Air Quality (ADEC/DAQ), was added in 2008. By design, the plan is updated approximately every 2 years and the 2008 revision represents the 5th edition of the plan. The purpose of this document is to summarize each agency’s key responsibilities and procedures in alerting each other and the public regarding volcano hazards. The emphasis until 2008 had been on airborne ash hazards to aviation; following the Augustine eruption, it was expanded to include protocols related to ash-fall hazards on the ground, particularly as reflected in air quality and impacts on public health. As the 2005–6 Augustine unrest progressed, the Interagency Plan was a principal organizing document that guided agency preparedness and communications. This was the first time the plan was used in response to a significant event near Anchorage.

The Level of Concern Color Code

AVO has long used a level of concern color code system to concisely communicate the degree of unrest and severity of volcanic hazard at Alaskan volcanoes. The system in place during the 2005–6 Augustine unrest was a slightly modified version of the original color code scheme developed primarily to serve the aviation community during the Redoubt eruption of 1989–90 (Brantley, 1990). Colors change in progression of increasing volcanic unrest or severity of the hazard from Green to Yellow to Orange to Red (table 2). Decisions regarding changes in colors are based on monitoring data, direct observations, and an understanding of the eruptive style of a particular volcano and similar volcanoes worldwide. We discuss how AVO applied this color code the 2005–6 Augustine eruption in a later section.

Near-real-time Hazard Information Products from AVO

AVO uses telephone call downs, written information bulletins, a Web site, and recorded telephone lines to inform the public and others about volcanic unrest, eruption notices, and hazardous conditions (Adleman and others, this volume). The telephone notifications are the most time-critical means by which AVO informs other government agencies about changes in volcano hazard conditions; a formal call-down

Table 1. Official volcano warning products in Alaska.

[Primary warning agencies in Alaska involved in volcanic eruption hazard communication and the names of public warning products for events in south central Alaska. Some messages are very specific in their intended audience (for example Notices to Airmen [NOTAMs] and Urgent Pilot Reports [UUAs] are for aviation users) and others are of broader use (for example Ashfall Advisories, Air Quality Advisories, and Information Releases). Significant redundancy is inherent in this system and proactive coordination is necessary to ensure that messages are consistent. UUAs can be issued by either FAA or NWS personnel. Not all messages will be issued for every eruption or episode of volcanic unrest. More information about current protocols for each agency can be found in the Alaska Interagency Operating Plan for Volcanic Ash Episodes (Madden and others, 2008)]

Agency	Warning Products						
Alaska Volcano Observatory (AVO)	Information Release	Weekly Report	Daily Status Report				
National Weather Service (NWS)	SIGMET (Significant Meteorologic Information)	VAA (Volcanic Ash Advisory)	MIS (Meteorologic Impact Statement)	CWA (Center Weather Advisory)	Ashfall Advisory	Marine Advisory	Special Weather or Marine Statement
Federal Aviation Administration (FAA)	NOTAM (Notice to Airmen)	UUA (Urgent Pilot Report)					
Alaska Department of Homeland Security and Emergency Management (DSHEM)	SITREP (Situation Report)	Community Alert					
U.S. Coast Guard (USCG)	Notice to Mariners						
Alaska Department of Environmental Conservation, Division of Air Quality (DEC)	Air Quality Advisory						
Alaska Department of Public Health (DPH)	Public Service Announcement						
Municipality of Anchorage	Air Quality Advisory						

procedure is documented in the Alaska Interagency Plan for Volcanic Ash Episodes (Madden and others, 2008). Written AVO communication products in 2006 included (1) Daily Status Reports issued each day for any volcanoes at level of concern Yellow or higher; (2) Weekly Updates released each Friday summarizing the week's activity in Alaska; and (3) Information Releases issued when a significant volcanic event, change in eruption conditions, or information about AVO's operational status needed to be communicated. Examples of AVO Information Releases during the Augustine eruption are shown in appendix 1.

AVO's formal written products are disseminated using three primary communication pathways: e-mail, facsimile, and internet postings. All text products are generated using a graphical interface within the AVO internal Web site. Upon completion, messages are sent nearly simultaneously to a standing e-mail list, to others via an internet-based fax service, and to the AVO and USGS Volcano Hazards Program Web site for automatic posting. AVO messages are also available in an RSS (Really Simple Syndication) feed; users can subscribe to this electronic message feed using a variety of news aggregators available on the internet.

In addition to the AVO volcano hazard text messages, other State and Federal agencies such as NWS and FAA also produce formal notification and warning products pertinent to volcanic phenomena (table 1).

Table 2. Level of concern color code changes during the 2005–2006 unrest and eruption of Augustine Volcano, Alaska.

[Compiled from Alaska Volcano Observatory web site archives, internal logs, and master AVO chronology spreadsheet.]

Date	Time local[1]	Time UTC	Color Code Assignment[2]	Reason for Color Code Change
11/29/05	12:15 p.m. AKST	2115	Yellow	Months of slowly increasing seismicity, inflation of the edifice. No surface manifestation of unrest yet detected.
1/10/06	9:10 p.m. AKST	0610	Orange	Increased seismicity beginning ~3:00 p.m. AKST. Increased likelihood of explosive eruption in hours to days.
1/11/06	05:50 a.m. AKST	1450	Red	Explosive activity onset at 04:44 a.m. AKST.
1/12/06	08:25 a.m. AKST	1725	Orange	Decreased seismicity.
1/13/06	04:00 a.m. AKST	1300	Red	Seismicity increased suddenly suggesting renewed explosive activity imminent.
1/15/06	09:45 a.m. AKST	1845	Orange	Decreased seismicity.
1/17/06	08:00 a.m. AKST	1700	Red	Increasing seismicity and explosion at 07:58 a.m. AKST.
1/18/06	09:05 a.m. AKST	1805	Orange	Decreased seismicity.
1/27/06	8:35 p.m. AKST	0535	Red	Resumed vigorous ash emission at 8:01 p.m. AKST.
2/1/06	9:45 a.m. AKST	1845	Orange	Decreasing height of ash clouds during continuous eruption phase.
4/28/06	09:45 a.m. AKDT	1745	Yellow	Lava effusion significantly diminished or stopped.
8/9/06	3:00 p.m. AKDT	2300	Green	Seismicity at background and little surface change.

[1] Times listed are formal Alaska Standard Time (AKST) or Alaska Daylight Time (AKDT) time stamps on the header of Information Release documents; these times will differ slightly from those listed on our Web page. Announcements of color code changes via our telephone call down system typically occur tens of minutes to several hours before official release of the Information Release via email, fax, and Web-posting.

[2] Color Code definitions in use during the Augustine eruption (taken from the 2004 edition of the Alaska Interagency Operating Plan for Volcanic Ash Episodes):

Green: No eruption anticipated. Volcano is in quiet, “dormant” state.
Yellow: An eruption is possible in the next few weeks and may occur with little or no additional warning.
Small earthquakes detected locally and (or) increased levels of volcanic gas emissions.
Orange: Explosive eruption is possible within a few days and may occur with little or no warning.
Ash plume(s) not expected to reach 25,000 feet above sea level.
Increased numbers of local earthquakes. Extrusion of a lava dome or lava flows (non-explosive eruption) may be occurring.
Red: Major explosive eruption expected within 24 hours. Large ash plume(s) expected to reach at least 25,000 feet above sea level.
Strong earthquake activity detected even at distant monitoring stations.
Explosive eruption may be in progress.

Late 2005–Preparations for a Possible Magmatic Eruption at Augustine

Precursory activity was first noted at in the late spring of 2005 as the daily number of located volcano-tectonic earthquakes beneath Augustine Volcano began to increase (Power and Lalla, this volume). Beginning in July and continuing over the next several months, geodetic data detected a slow inflation of the volcanic edifice (Cervelli and others, 2006; Cervelli and others, this volume). Steadily increasing daily earthquake counts combined with acceleration in deformation in late November prompted AVO's first public announcement of unrest at Augustine on November 29, when the level of concern color code was changed from Green to Yellow (table 2.) The accompanying Information Release (appendix 1*A*) described changes detected at the volcano as a departure from background conditions but stated that an eruption was not necessarily imminent. The document reviewed the range of likely volcano hazards emphasizing that for most citizens the primary concern would be ash clouds and ash fall. AVO increased its frequency of seismic data analysis in response to the sustained unrest.

Visible changes in fumarolic activity near the summit of Augustine were noted by early December. On December 2, a seismically detected explosion followed by reports of sulfur odors on the Kenai Peninsula suggested an increased likelihood of magmatic eruption. A volcanic plume was reported by pilots and seen on satellite imagery on December 12, further intensifying public interest. Although the plume was predominantly volcanic gas and water vapor, a very minor ash fall had occurred on the upper flanks of Augustine. This prompted an additional AVO Information Release that described small explosions detected seismically and discussed the hazards of increased degassing (appendix 1*B*).

In response to increasing volcanic unrest, AVO initiated discussions with interagency partners at FAA and NWS regarding the possibility of a magmatic eruption, likely scenarios, and coordination regarding warning messages. AVO staff attended a meeting with NWS on December 13 to review procedures and anticipate challenges, particularly with regard to ash-fall warning messages. On December 22, 2005, NWS and AVO cohosted an interagency press conference on the status of Augustine Volcano at the Aviation Technology Center in Anchorage. Representatives from AVO, NWS, the West Coast and Alaska Tsunami Warning Center (WCATWC), and ADHSEM spoke about their agencies' preparations and plans to respond to an Augustine eruption (Adleman and others, this volume).

Into December, AVO received numerous calls and e-mails from the public and government agencies (city offices, fire departments, hospitals, schools) inquiring about potential volcanic activity at Augustine and recommended preparations (Adleman and others, this volume). Beginning in late December, AVO staff began to use talking points and developed contact lists to refer callers to appropriate primary resources on particular topics (for example, ash-fall hazard preparedness and aviation concerns). Tsunami-specific talking points and a media management plan were prepared on December 23 following press coverage on the topic of the tsunami threat from Augustine. AVO also spoke with facilities officials from the Ted Stevens Anchorage International Airport and the USCG office in Anchorage to ensure that lines of communication were open and any uncertainties about the developing unrest were clarified. Coordination with the Anchorage office of the USCG was the first of significance since the Mount Redoubt eruption in 1989–90 when lahars threatened the Drift River Oil Terminal (fig. 1) and vessel traffic in Cook Inlet (Dorava and Meyer, 1994). AVO and the USCG discussed potential impacts of the range of eruption scenarios, reviewed estimated hazard zones depicted in the hazard report, and discussed what kind of emergency messages the USCG would issue in the event of an eruption. AVO would later work with NWS and USCG to provide draft content for Notices to Mariners.

Preparedness activities took place in communities on the lower Kenai Peninsula. By mid-December, the village of Nanwalek, located about 80 km east of Augustine and noted site of a tsunami in 1883 (Kienle and Swanson, 1985), had taken steps to stockpile emergency supplies of food, water, and other provisions; check and review emergency siren operation; and ensure that residents knew evacuation routes to safety in the event of a tsunami (Scott Waldron, Kenai Borough Emergency Management Office, oral commun., 2006).

On January 10, 2006, as monitoring parameters continued to show elevated rates of change and unrest, AVO issued an expanded public Information Release summarizing observations to date and the range of possible outcomes including the most likely eruption scenario (appendix 1*C*). Such "scenario development"—used during previous eruptions by AVO—served to capture consensus interpretations of AVO scientists and lay out the range of possible unrest progressions and their associated hazards. Throughout the precursory period, public AVO communications emphasized these scenarios and associated impacts based on a thorough understanding of historical eruptions and the prehistoric geologic record at Augustine. Unlike many other volcanoes in Alaska, Augustine had erupted twice in 30 years during a time of significant scientific investigation and instrumental monitoring of the volcano. The volcano was, in fact, one of the most heavily instrumented in the Aleutian arc. Thus, AVO scientists had the advantage of a well-documented historic eruption record when discussing scenarios.

AVO organized an interagency public meeting in Homer on the southern Kenai Peninsula in mid-January (the meeting was supposed to have occurred preeruption and was perhaps more well-attended because of the onset of explosive activity on January 11). The purpose of the meeting was to directly address citizen concerns regarding volcanic activity and associated hazards. This meeting and other public outreach events are described more fully in Adleman and others (this volume).

Command Team

In December 2005 before the onset of magmatic eruption, the AVO Scientist-in-Charge (SIC), a USGS employee, formed

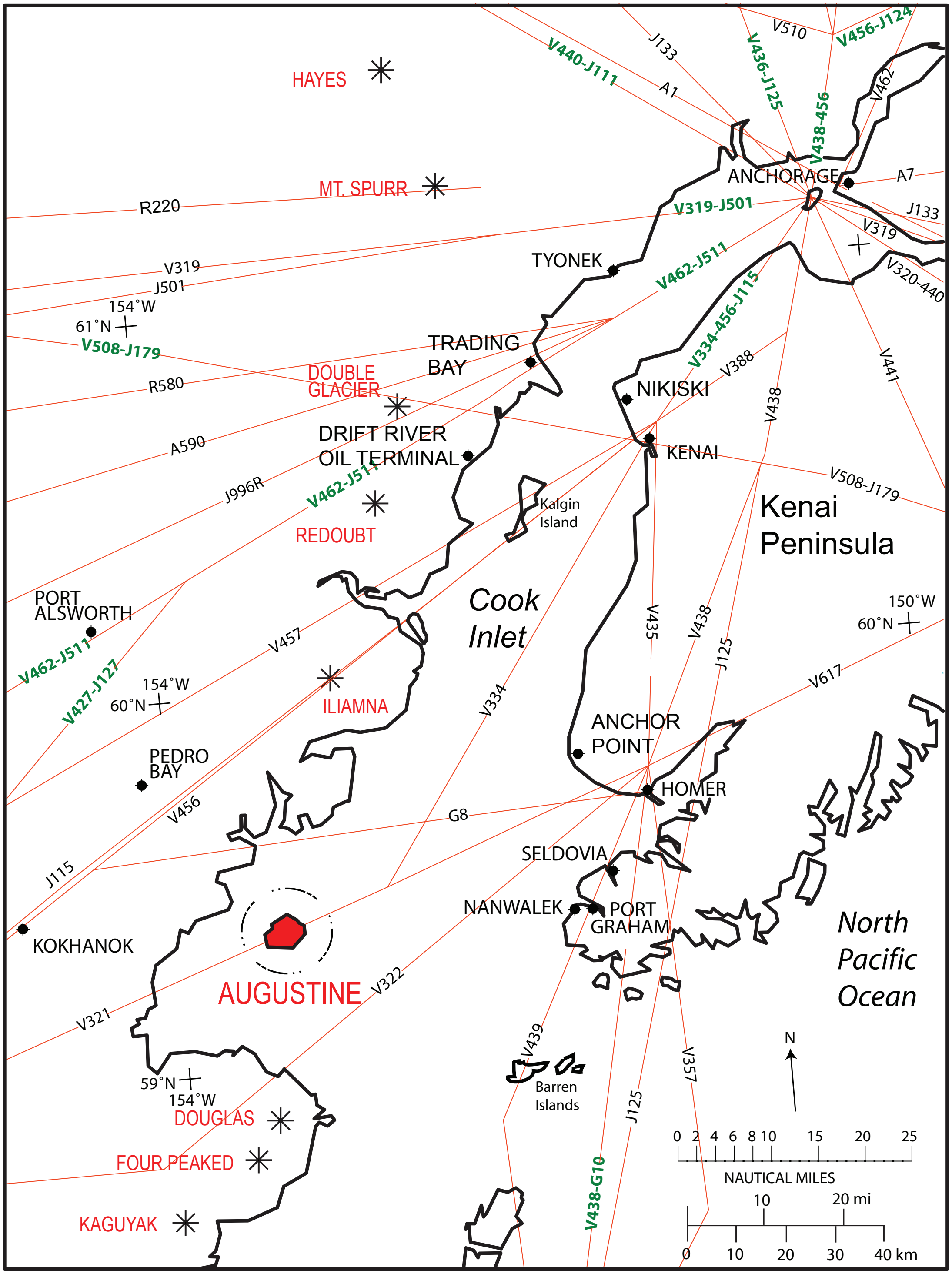

Figure 1. Map showing Cook Inlet area of south-central Alaska with principal fixed air routes (red lines). Volcanoes (asterisks), principal towns, cities, and facilities discussed in text are shown. V (victor) routes are for aircraft at and below 18,000 ft msl. All other routes are for aircraft at and above 18,000 ft. msl. Where two types of airways are superimposed, both airway labels are green. Augustine Volcano and island shown in red. The dashed circle surrounding the island is the approximate lateral extent of the Temporary Flight Restriction (TFR) put in place by the Federal Aviation Administration (FAA) on December 13, 2005. Base map (in Lambert Conformal projection) and aviation routes courtesy Walt Dotter, FAA.

a “Command Team” consisting of several AVO scientists in both the Anchorage and Fairbanks offices. The Command Team worked under the combined supervision and guidance of the SIC, the Coordinating Scientist from UAFGI, and the ADGGS Liaison. The purposes of this internal group were to clarify roles and responsibilities for managing the eruption response, to ensure adequate and coordinated operational and scientific responses, to facilitate scientific and logistical information flow within AVO, and to test a structure that could be used for all future eruption responses.

The team consisted nominally of five positions filled by AVO staff in Anchorage and Fairbanks. A “Chief of Operations” assumed responsibility for the overall response and was the primary manager of the Command Team meetings and task assignment. The Chief of Operations coordinated field and office aspects of the response including budgetary and personnel oversight in consultation with other AVO managers. In this case, the position was filled by the SIC. A “Science Coordinator” led technical discussions, maintained a synoptic view of scientific activities, data streams, analysis, and requirements to ensure accurate hazard assessment, forecasts of activity, and to maximize research opportunities. A “Media or Communications Coordinator” produced key graphics and briefing materials and oversaw the AVO Web page modifications during the eruption. This person would have been responsible for press release content development if needed. The “Information and Data Coordinator” ensured computer network health, continuity, and integration across the distributed AVO facilities. This person was also responsible for dealing with data security, data sharing protocols, and telecommunications needs. Finally, a “Hazards Information Coordinator” was responsible for developing hazard messages during the eruption. This person was the main AVO point of contact for other government agencies and addressed interagency coordination issues. Had a formal interagency Joint Information Center (JIC) been established during the eruption, the Hazards Information Coordinator would have been the primary AVO representative.

Volcano Hazard Reports for Augustine Volcano

Other important preeruption hazard resources were the published hazard reports for Augustine Volcano (Kienle and Swanson, 1985; Waythomas and Waitt, 1998). These documents, along with more dynamically updated internal talking points (see below and Adleman and others, this volume) formed the basis of the consistent public message regarding likely impacts and scenarios should an eruption occur at Augustine. As unrest progressed, AVO made frequent reference to the 1998 hazard report, which was available both on the AVO Web site and directly from the USGS. It is unknown how widely used this document was outside of AVO; an informal poll of interagency partners indicated that most knew of its existence as a key reference and many had examined it carefully. Web traffic statistics suggest at least several thousands of downloads of the 1998 hazard report in January 2006 alone (C. Cameron, ADGGS, written commun., 2007).

Hazard Information Management During the Eruption

Eruption Chronology

Following several months of precursory seismicity, deformation, increased fumarolic and degassing activity in the summit crater, and a series of small phreatic eruptions in December 2005, the main phase of the eruption began with a vent-clearing explosion on January 11 (Power and others, 2006; Cervelli and others, 2006; Neal and others, 2009). Over the next 20 days, 13 explosions sent ash between 4 and 15 km above sea level. Ash clouds drifted in all directions from the volcano, but predominantly to the northwest, northeast, east, and southeast, dusting several communities with less than 1 mm of ash (Wallace and others, this volume). On-island pyroclastic flows, surges, avalanches, ash fall, and ballistic showers impacted most of the volcano’s flanks. Interaction of hot pyroclastic debris with snow and ice on the volcano produced mixed avalanches and lahars, some of which reached the sea (Coombs and others, this volume; Vallance and others, this volume). A new lava dome was first sighted in the summit crater on January 16 (Coombs and others, this volume); however, seismicity reflective of dome growth was noted as early as January 12 (Power and others, 2006; Power and Lalla, this volume).

The eruption transitioned into a more continuous phase in late January, characterized by steady ash production and the generation of voluminous and pumiceous, high-silica andesite pyroclastic flows down the north flank of the volcano (Coombs and others, this volume). In early February, effusive activity became dominant and a new lava dome began to fill much of the summit crater. A hiatus in effusive activity occurred between about February 10 and March 3, but effusion resumed in early March with an especially vigorous period of lava effusion between March 8 and 14. Eventually, two lobes of blocky, low-silica andesite lava advanced north and northeast down the upper flank of the volcano. Intermittent shedding of hot debris from these flows produced an apron of block-and-ash avalanche deposits to the north (Vallance and others, this volume). The eruption waned by the end of March; however, the exact date effusion ceased is uncertain.

Talking Points and Expanded Information Releases

The rapid pace of information flow and intense demand that accompanies volcanic unrest and eruption are challenges for a distributed organization where any staff member may be called on to comment on hazard or status of the volcano. This is especially true as the number of real-time and near-real-time monitoring data streams increases and public expectation of current information becomes the norm. To keep AVO staff up to date on key observations, facts, and interpretations, a series of continually updated talking point documents were created in late December. Each version was shared widely within AVO (Adleman and others, this volume). Talking points were intended to be highlights of the current status of the volcano and contained key background information that staff members could use to guide response to media interviews or other outreach interactions. This was the first time during a protracted eruption that such a tool was used at AVO, although they have been used at other volcano observatories in the United States (for example, Driedger and others, 2008). Through time, talking point authors learned to anticipate media and public questions in the document which made them more useful and comprehensive. As learned during the 2004 unrest at Mount St. Helens (Driedger and others, 2008), the process of compiling such condensed statements of fact was in itself helpful in maintaining a synoptic view of the overall event. Further, the need for a sound-bite summary often helped drive science meeting discussion towards consensus interpretive statements.

On January 27, after nine explosive events, AVO issued an expanded Information Release that provided a chronologic and interpretive summary of the eruption to date, a synopsis of ongoing monitoring data and observations, and scenarios for the progression of the eruption. AVO concluded (correctly, it would turn out) that activity would likely follow the pattern of the last two historical eruptions with dome building and further explosive activity lasting months. These types of Information Releases serve two important purposes: (1) to present the consensus scientific interpretation of current and anticipated events and (2) to articulate the most important elements of ongoing volcano hazards for the public and other stakeholders.

Interagency Coordination Calls

As noted above, a number of agencies within Alaska are responsible for official response and warning messages during a volcanic event. To help ensure consistent hazard guidance to the public and keep agency representatives as up to date as possible on the state of the volcano, the ADHSEM organized and moderated frequent interagency telephone conferences during the most energetic phases of the eruption. AVO/USGS staff provided a quick update on the status of the volcano followed by NWS commentary on the day's weather, wind field, and likely ash trajectory. Additional participating agencies included FAA, Ted Stevens Anchorage International Airport, and the Alaska Department of Public Health, among others. Calls occurred with decreasing frequency as eruptive activity diminished in intensity.

Centralizing Information

Multiple messages distributed during volcanic events (table 1) can lead to confusion among the public and other entities about where to look for specific types of information. This is particularly true in the aviation and meteorology sectors where information about the status of the volcano, the presence of airborne ash, the trajectory of the cloud, ash-fall advisories, and pilot reports of ash cloud sightings are provided by different agencies in messages of varying format. To address this during the Augustine unrest, the Weather Forecast Office of the NWS in Anchorage centralized as much information as possible on an Augustine eruption coordination Web page. This page featured the full text of current ash fall warning messages, direct hyperlinks to AVO, the West Coast and Alaska Tsunami Warning Center, and the Alaska Aviation Weather Unit SIGMET pages as well as ash cloud forecast trajectory graphics produced by NOAA's Air Resources Laboratory. Had the event and associated impacts escalated (for instance, become a significantly larger, more continuous eruption or involved a tsunami-producing event), it is possible that a Joint Information Center (JIC) would have been created to help centralize and manage information flow. Discussions of such a JIC—a standard component of the Incident Command System—began in earnest on January 12 among AVO, NWS, and DHSEM; however, no firm plan was ever developed. This remains an important planning question for a future volcanic eruption (or other geologic disaster) of significance in Alaska.

Use of the Level of Concern Color Code

AVO made a total of twelve color changes during the Augustine eruption sequence as activity ramped up, became intermittently explosive, dominantly effusive, and then ceased (table 2; appendix 1*A–I*). Each color change followed internal discussion of monitoring trends and observational data in the context of what was known about the volcano's past eruptions. Some changes were urgent; for example, those following sharp accelerations in seismicity or a confirmed explosive ash producing event. Others were less time critical and were made after days of deliberation and careful crafting of accompanying language for an Information Release.

A decision to change colors always prompts a telephone call down to key agencies as outlined in the Interagency Operating Plan for Volcanic Ash Episodes (Madden and others, 2008). The call is followed by a written Information Release distributed by e-mail, fax, and Internet posting. Color codes are assigned following the generalized definitions for each color (table 2) but also take into account scientific understanding of the trend of unrest and the desired hazard message. No universal and specific data thresholds or criteria have been established for each color, in part to allow for the flexibility for each progression of volcanic unrest at individual volcanoes. These color codes are used as broad, intuitive signals reflecting the intensity of conditions at the volcano to encourage appropriate preparedness actions.

In light of this, how did AVO use the level of concern color code system to support hazard warnings during the Augustine unrest and eruption in 2005–6? The change to Yellow on November 29, 2005, was the first formal public notification of change at Augustine (appendix 1*A*). AVO had noticed and been discussing these changes internally for 4 months and, arguably, could have declared Yellow a number of weeks to several months earlier with the same impact. However, on the basis of the well-monitored status of Augustine and the precedents of the 1976 (Johnston, 1978; Kienle and Swanson 1985; Reeder and Lahr, 1987) and 1986 (Yount and others, 1987; Swanson and Kienle, 1988; Power, 1988) eruption timelines, AVO was confident that an eruption was not imminent and that further clear precursory changes would occur well in advance of actual eruption. We note that the weekly updates from AVO always include a caveat for volcanoes at the lowest level of alert "…some volcanoes may currently display anomalous behavior but are not considered to be at a dangerous level of unrest." The months of low-level unrest at Augustine could reasonably fall into this category.

AVO raised the color code to Orange in the evening of January 10, about 7 hours before the first significant explosion of the eruption, in response to a clear increase in seismicity (appendix 1*D*). Over the next 3 weeks, AVO assigned Red (table 2) just before or immediately following explosive events at Augustine, each time basing the decision primarily on interpretation of seismic signals with occasional corroborating evidence of high-altitude (greater than 30,000 ft asl) ash columns from radar (appendix 1*E*; Schneider and others, 2006) or pilot reports. The longest time period at Red was during the end of the explosive and beginning of the continuous eruption phase between January 27 and February 1, when the volcano was in an unstable pattern of nearly continuous ash emission and block-and-ash-flow production punctuated by explosions (appendix 1*F*). As ash cloud production decreased in intensity (and column heights became consistently below about 25,000 ft), AVO reverted to Orange and remained there for the duration of the eruption. We now know that this included a nearly one-month-long hiatus in effusion followed by a pulse of lava dome and flow activity that continued into mid-March (Coombs and others, this volume; appendix 1*G*).

As with many eruptive events, determining exactly when the eruption ended was difficult. AVO remained at Orange on the basis of continued or renewed lava extrusion and the potential for a sudden explosion or explosive collapse of the lava dome. The downgrade to Yellow on April 28 occurred nearly 7 weeks following the cessation of repetitive, shallow earthquakes and frequent rockfalls related to lava effusion (appendix 1*H*; Power and Lalla, this volume). The Information Release announcing Yellow, as well as subsequent weekly updates, continued to emphasize ongoing hazards from rockfalls, avalanches, and sudden explosions and also noted the possibility that eruptive activity could resume, although with likely precursory increases in seismicity, gas output, or deformation.

AVO ended 24-hour staffing of the Observatory on May 19, 2006, but remained at color code Yellow for Augustine until August 9. At that time, the consensus among AVO staff was that seismicity had returned to background levels and other monitoring data (deformation, gas, thermal) indicated a slowly stabilizing, post-eruptive system. No data suggested new magma ascent, decreasing the possibility that eruptive activity would resume. In addition, AVO field crews working on the volcano in early August observed no changes that would be indicative of renewed activity, further contributing to the decision to downgrade to Green. The Information Release accompanying this declaration emphasized again continuing hazards from sudden rockfalls, avalanches, and gas emissions (appendix 1*I*).

In the fall of 2006, the USGS instituted a new alert code system that retains Aviation Color Codes for aviation hazards but adds a parallel term—Volcano Alert Level—that integrates both aviation and ground-based hazards (Gardner and Guffanti, 2006). An important aspect of this new system is the ability of Volcano Observatories to decouple the Aviation Color Codes and the Volcano Alert Levels; for example, when a fluid lava flow eruption poses little threat to aviation but presents a significant threat on the ground. In such a case, the designation may be Yellow/Watch or even Orange/Warning. Evaluating the use of this new system retrospectively for the Augustine events of 2005–6, it is hard to see the need to decouple the two systems at any time. Even during the dominantly effusive phase of late February and March, 2006 when minimal ash was present in the atmosphere, the possibility of sudden explosive events remained high (an Orange/Watch situation). For Alaskan volcanoes, nearly all of which are capable of expelling ash into the atmosphere to altitudes of concern to aviation, it is likely the Aviation Color Codes and Volcano Alert Levels will always move together.

Tsunami Hazard and Protocols for Early Warning of Volcanogenic Tsunami

Augustine Volcano has a history of large debris avalanches that can produce tsunami in lower Cook Inlet (Begét and Kienle, 1992; Siebert and others, 1995; Waythomas and Waitt, 1998). In 1883, a 6 to 8 m wave associated with a large explosive eruption and sector collapse was reported at Port Graham (now called Nanwalek) and English Bay on the west shoreline of the lower Kenai Peninsula (Kienle and Swanson, 1985). Geologic evidence suggests that in the last few thousand years, about a dozen similar debris-avalanche events have occurred (Begét and Kienle, 1992; Siebert and others, 1995). Tsunamis associated with these events are not well understood, and geologic evidence for tsunami inundation is equivocal. Modeling studies of tsunami generation indicate that a moderate but potentially damaging wave is possible, with lead times of about 27 to 125 minutes for the shorelines of lower Cook Inlet from the Barren Islands to Kalgin Island (fig. 1; http://wcatwc.arh.noaa.gov/Augustine/AugustineWeb.htm, last accessed January 2008). Compared to other hazardous volcanic phenomena, the likelihood of a tsunami during a typical eruptive sequence and subsequent period of quiescence at Augustine is considered low (Waythomas and Waitt, 1998). Despite this, local consequences of such an event could be high, and, in 2006, the tsunami threat from Augustine was on the minds of many residents of the coastal portions of the Kenai Peninsula.

Before the first major explosions in January, AVO and the WCATWC developed a strategy to deal with potential volcanogenic tsunami and required public warnings. In the United States, tsunami warnings are the responsibility of the National Oceanic Atmospheric Administration's (NOAA) two regional Tsunami Warning Centers in Alaska and Hawaii. Tsunami warnings are issued via the Emergency Alert System, NOAA's Weather Radio, and other NOAA dissemination channels. In Alaska, warnings are also issued through State and local channels to key areas on the Kenai Peninsula and other communities and to civil authorities in Alaska. In addition, for isolated communities, such as Nanwalek and Port Graham, siren systems are activated by the issuance of an alert.

Historically, NOAA's primary responsibility has been to issue warnings for earthquake-induced tsunami. Tsunami initiated by volcanic processes (flank failure, flowage deposits, and others) require NOAA and volcano observatories to work together to effectively issue warning messages, and Augustine provided an opportunity to refine this cooperation.

The NOAA-AVO approach for Augustine took into account the most likely scenario for generation of tsunami from the volcano—a debris avalanche into Cook Inlet. Such an event was expected to be accompanied by a strong and unique seismic signal produced by a large-volume (0.1 to 0.5 km^3) flank failure and landslide event. If Augustine's level of concern color code was Orange or Red and a shallow earthquake occurred near Augustine Island with a magnitude greater than 4.5, a tsunami warning would have been issued immediately by the WCATWC for coastlines of the lower Cook Inlet. The WCATWC would then consult with AVO by phone to evaluate the event and other data streams (for example, WEB cameras, pressure sensors, on-island seismic network, their own regional seismic network) to refine or cancel the alert. In this way, given the short travel times, potentially affected communities would receive warnings with as much lead time as possible.

When the level of concern color code for Augustine reverted to Yellow or Green, WCATWC would call AVO before issuing any alert in order to evaluate the likelihood of a tsunami. The WCATWC was also added to the list of key government agencies on AVO's initial telephone call down list in the event of an explosive or significant event at Augustine. This would enable WCATWC staff to be on heightened alert for the possibility of tsunami following significant activity and production of pyroclastic flows or other flowage events that reached the sea.

Although the system was not tested during the 2005–6 eruption by earthquakes fitting the preestablished criteria, participants feel it was a successful approach to this difficult to forecast and confirm process. The many island volcanoes subject to flank failure in Alaska (Coombs and others, 2007) and other parts of the world (for example, the Marianas) suggests this approach, the first of its kind in the U.S., may be viable for other similarly situated volcanoes with sufficient seismic monitoring. Each volcano would require an independent analysis of flank failure scenarios, resultant wave travel time to vulnerable coastlines, and likely seismicity and detection thresholds for varying seismic station density. Interagency alert protocols for other volcanic phenomena such as pyroclastic flows, which can also produce tsunami, have yet to be discussed. Finally, although the emphasis of concern in this system has been on the coastal population centers, impacts of volcanically generated tsunami on marine vessel traffic and the required messaging to warn this constituency should also be considered. This will require close coordination with the USCG or other maritime authorities.

Impacts of the 2005–2006 Eruption

Impacts of this eruption were not rigorously tracked and much information presented here is anecdotal or collated from reports in the popular media.

General

According to news reports, preeruption publicity prompted a spike in local purchases of dust masks and automobile air filters and other emergency preparedness supplies throughout south-central Alaska. Both personal and institutional checking of disaster preparedness and plans was also widely reported. The Anchorage School District (ASD) administration reviewed emergency preparations in the event of an ash fall and sent information to parents outlining ASD preparedness, protocols for school closures, and other issues. Following the January 13 ash-producing events, Ninilchik elementary and Homer high schools closed early due to expected ash fall. Other closures occurred sporadically throughout January in anticipation of ash fallout. In Homor, the South Peninsula Hospital constructed a special prefilter apparatus for their building air intakes. Cancellation of Kodiak-based filming for a major motion picture was a significant economic blow to the Kodiak Borough.

In hindsight, some of these very proactive preparedness efforts were perhaps overly conservative given the magnitude of resulting ash fall and the severity of actual impacts. However, with no operational ash fall model in place and given the inherent uncertainty of an evolving eruptive event, it was difficult for AVO and NWS to provide specific guidance to emergency managers and the public regarding the amount of ash to expect. Further challenges are posed by the required style of NWS ash fall messages; these are highly formatted communications that are referenced to established zones that include large areas of Alaska. Thus, when ash fall was possible in a portion of a zone, the entire area is featured on warning graphics inadvertently depicting a much broader area of potential impact than is necessary.

In addition to limitations in accurate warning messages, incomplete public understanding of ash-fall events and likely impacts may have contributed to aggressive preparedness efforts. Residents of south-central Alaska had not experienced volcanic ash fall since the 1992 Mount Spurr eruption, and it is likely that many residents of the Kenai Peninsula were unacquainted with what to expect—the population of the Kenai Peninsula Borough increased by more than 25 percent (or 10,000 people) during the period 1990–2006 (http://www.borough.kenai.ak.us/econ/1S_P%20data/Demographics/PopulationOverview.htm, last accessed August 13, 2009). In addition, the last eruption to affect the Kenai Peninsula, the 1989–90 eruption of Redoubt Volcano, also occurred in midwinter and had significant impacts on the western Kenai on several occasions (Scott and McGimsey, 1994). Thus, a lack of experience with ash fall by some combined with others' memories of hardships during the last fallout event may have contributed to an extra-heightened sense of concern.

Aviation Sector

Significant interruptions of air travel into and out of Anchorage and other communities in south-central Alaska occurred during the explosive phase. Following several explosions, vulnerable air routes were modified or cancelled. Some airlines elected to bypass Anchorage or move aircraft out of concern for potential ash fall. Special Military Operations Areas were closed temporarily. One nondamaging encounter with an apparent volcanic gas cloud occurred on January 14 about 800 km downwind, and one other unconfirmed minor encounter on January 30 was reported. A summary of known aviation impacts is found in table 3.

To provide a safe operating environment for AVO field crews and to reinforce concerns about sudden explosive activity, a Temporary Flight Restriction (TFR) was put in place by FAA on December 13, 2005, following the December 12 plume and discussions with AVO about the possibility of further small explosions and minor ash falls near Augustine. This initial TFR—communicated to aviation interests through the national Notice to Airmen or NOTAM system—prohibited aircraft from flying within a 5-nm radius of the summit to 6,000 ft asl (fig. 1). The TFR also cautioned pilots operating near or downwind of the volcano. The TFR was expanded on January 11 following the first significant explosive event to include a cylinder with radius of 5 nm from the summit extending from sea-level up to but not including 50,000 ft asl. The TFR remained in effect until April 28, 2006, when AVO lowered the level of concern color code to Yellow.

Airport and Aviation Facility Closures

Kienle (1994) reviewed the impacts of the 1976 and 1986 eruptions of Augustine Volcano, which included damage to a number of aircraft due to ash encounters and many flight cancellations and diversions. While forecasting and communication of hazards to aircraft has vastly improved in the intervening decades, the number of aircraft at risk has grown immensely. By 2006, annual aircraft landings at Ted Stevens Anchorage International Airport had nearly tripled from 1976 levels to 100,496 landings and total passengers had almost doubled to 5,043,147 (http://dot.alaska.gov/anc/business/airServiceDevelopment/statistics/AnnualStats_1957-2007.pdf, last accessed August 21, 2009). Because of the very small amounts of ash fall on populated areas, there were no closures of any airfields or airports during the 2005–6 Augustine eruption, in contrast to the 1992 Spurr eruption (Casadevall and Krohn, 1995). The only known impact to an air traffic control facility was closure of the Homer Flight Service Station for part of January 13 due to concern for ash fall in the area. Anchorage International had no significant take-off or landing delays during January resulting from activity at Augustine (G. Howard, FAA, written commun., 2006).

Aircraft Encounters with Volcanic Clouds

We are aware of no damaging encounters between aircraft and volcanic ash from Augustine in 2005–6 despite more than a dozen explosive eruptions producing drifting ash clouds that traveled through air traffic corridors at night and in bad winter weather. This success can be attributed to a much broader awareness across the aviation sector regarding volcano hazards, a vastly improved warning network that links real-time volcano monitoring, ash-cloud detection, tracking, and forecasting across several Federal agencies, and clarified communication pathways. In addition, the short duration of the explosive events at Augustine meant that ash clouds were small and became rapidly diffuse downwind.

Two nondamaging encounters between aircraft and a volcanic cloud from Augustine came to the attention of AVO. The first and more costly occurred on January 14 about 800 km downwind of the volcano in the vicinity of Yakutat on the Gulf of Alaska coastline. A full Boeing 737 flying in daylight conditions from Anchorage to Seattle entered a suspicious cloud described as a brown-colored stratified layer at 31,000 ft. The crew noted a "dirty," musty odor lasting about 8 to 10 minutes. After climbing to 33,000 ft and deviating to the northeast into clear air, the layer was distinctly visible below the aircraft. On landing, the plane was taken out of service for 2 days and thoroughly inspected; no damage was found. Before this encounter, five discrete explosions at Augustine had produced small volume ash clouds to altitudes of greater than 30,000 ft estimated from both pilot reports and NWS radar (Schneider and others, 2006; Bailey and others, this volume). All clouds drifted southeast and then northeast over the Gulf of Alaska

Table 3. Summary of principle aviation impacts from the 2006 eruptive activity at Augustine Volcano.

[Data courtesy Greg Howard, Federal Aviation Administration, and Alaska Volcano Observatory records. ANC, Anchorage Ted Stevens International Airport; FAI, Fairbanks International Airport; PACOTS, Pacific Organized Track System; ATC, Air Traffic Control; ZAN, Anchorage Center; MOA, Military Operations Area; USAF, U.S. Air Force]

Date	Impact	Comment
11 Jan	Some flights from Anchorage to Homer cancelled or delayed until daylight allowed better visibility of ash cloud.	
11 Jan	Minor radio interference reported by one aircraft operating near the volcano.	
13 Jan	Six aircraft inbound to ANC from Asia choose to divert to FAI to avoid the risk of ash exposure on the ground.	This decision was made by individual air carriers based on forecast winds and ash trajectory models.
13 Jan	Air Cargo operators at ANC expedite turnaround to minimize ground time for aircraft.	
13 Jan	Westbound PACOTS moved to the south; 10 aircraft chose this route to avoid potential ash.	This action was done by Anchorage Center Traffic Management in consultation with Oakland Center.
13 Jan	Separation between aircraft inbound for Anchorage from Asia temporarily increased as a precaution.	
13 Jan	One westbound PACOTS track cancelled.	
14 Jan	PACOTS tracks moved south to avoid projected ash trajectory; this moved all eastbound PACOTS south of Alaska airspace.	Oakland ATC was advised to build tracks to remain south of 53N145W to avoid projected ash dispersion.
13–15 Jan	Several airlines cancelled or rescheduled a total of ~35 flights, primarily to avoid operations in the area of projected ash during hours of darkness.	
14 Jan	Boeing 737 briefly encounters volcanic cloud 800 km downwind.	Flight crew deviated to clear air; aircraft inspection shows no damage
14 Jan	Temporary ground-stop (no departures) in southeast Alaska due to pilot report of ash over Yakutat and ATC workload managing requests for reroutes.	
14–15 Jan	Route restrictions coordinated between Anchorage and Canadian Air Traffic Control Centers as the ash cloud entered Canada.	This action was based on forecast motion of the volcanic cloud into Canadian airspace.
14–15 Jan	Staffing at ZAN increased temporarily in anticipation of increased workload.	
17 Jan	PACOTS track moved to the south.	
17 Jan	Military exercises in NAKNEK and STONY MOAs delayed 5.5 hours due to ash cloud and need for a contingency air corridor in case inbound flights to ANC required diversion; USAF cancels 6 training sorties and 3.5 hours of flight training. Air National Guard moved 7 aircraft to Fairbanks.	Ash projected to move to the northeast from Augustine following significant explosive event.
17 Jan	Minor reroutes at pilot requests; one regional carrier flight from ANC to Kodiak returned to ANC after seeing brown haze.	
28–31 Jan	Low level ash emission January 28-31 resulted in numerous flight cancellations or re-routes based on SIGMET descriptions of ash cloud position and motion.	
30 Jan	Piper Cherokee encountered very fine ash in southwest Alaska; also reported a burning in nose and eyes.	No damage reported.

until they could no longer be seen on satellite. This aircraft may have entered an extremely ash-poor aerosol cloud from one or both of the last two explosions of January 13 (at 0140 and 0358 UTC, January 14) based on an analysis of PUFF model output with respect to the likely time and location of the encounter (P. Webley, written commun., 2007).

The second encounter on January 30 remains ambiguous, and we were not able to reach the pilot for careful followup. According to the original report, a Piper Cherokee aircraft flying between Togiak and Dillingham in southwest Alaska encountered very fine ash and possibly volcanic gas from the ground to an altitude of 7,000 ft. The report indicates fine ash accumulated on the windscreen—presumably when the plane was on the ground at Togiak—and the pilot reported a burning sensation in the nose and eyes. As the flight approached Dillingham, the pilot noted that the air cleared abruptly. Easterly winds did occur during the continuous phase of the eruption from January 28–31 and so a diffuse ash and gas cloud in the Togiak area is plausible (Wallace and others, this volume). Also on January 30, AVO received reports from St. George Island (1,000 km west-southwest of Augustine) of fine dust and an odd taste and smell in the air. This report was unsubstantiated by sampling or other means; however, it is consistent with forecast trajectories of the Augustine plume tracking to the west from the island and out over the Bering Sea. Both incidents occurred in areas where satellite imagery could no longer detect the fine ash and aerosol clouds from these short-lived explosions, illustrating current limitations on providing accurate tracking and long-term forecast of diffuse volcanic clouds. Two years later, several aircraft encounters with far-traveled, ash-poor volcanic clouds from Okmok and Kasatochi volcanoes again underscored the challenge of providing operationally helpful warnings and clear guidance on the severity of this hazard to the aviation sector (Osiensky and others, 2008).

Marine Sector

Cook Inlet surrounding Augustine Island is an economically important shipping corridor for cargo vessels to and from the Port of Anchorage, the Nikiski oil refinery and liquefied natural gas (LNG) facility on the west coast of the Kenai Peninsula, and petroleum production and storage sites at Trading Bay and Drift River on the west side of Cook Inlet (fig. 1). LNG-loaded tankers alone make about 40 round trip transits from Nikiski to Tokyo each year (http://www.kenailng.net/go/doc/1067/143609/). Sixteen oil and gas platforms are located in upper Cook Inlet between Kenai and Tyonek. Additionally, Cook Inlet is a rich commercial and subsistence fishing area and is also used mostly during summer months for recreational boating and fishing. According to the U.S. Coast Guard (USCG), most deep-draft vessels traveling north or south in Cook Inlet remain far to the east of Augustine Island to follow more direct, deep water routes, thus mitigating impacts from Augustine activity. Despite this, following discussions with AVO and after the onset of explosive activity, the USCG office in Anchorage took steps to ensure the safety of mariners in the vicinity of Augustine. First, a warning to mariners was issued describing activity at the volcano and possible hazards to boats including ash fall and debris in the water. Secondly, on January 18, the USCG issued a temporary safety zone around Augustine Island prohibiting vessel traffic within one nautical mile of the shoreline (Federal Register, 2006). This rule went into effect following a number of explosive events at Augustine and was to remain in effect until September 1, 2006, or until cancelled. We are not aware of any direct impacts on vessels from the eruption. Other than light ash fall and possible minor nearshore disturbance as lahars reach the coastline on a number of occasions, there would have been no significant harm to boat traffic during the 2005–6 activity. AVO did receive a number of inquiries from the fishing community about the state of the volcano and possible hazards at sea.

Ash Fall Impacts

The explosive and continuous phases of the eruption produced at least 13 drifting ash clouds. The majority of ash fallout occurred on Augustine Island and into Cook Inlet, but on a number of occasions, trace amounts of ash did fall on inhabited areas (Wallace and others, this volume). We are aware of no significant property damage or adverse health affects due to fallout, consistent with the very short duration and small volume of the individual ash falls. There were, as discussed above, indirect impacts and costs due to precautionary closures of schools and other facilities, effort expended to repeatedly cover computers and other sensitive electronics, and other actions taken out of concern for the potential of ash fall. Finally, a significant number of public inquiries to AVO and other agencies referred to ash fall likelihood and expected impacts (Adleman and others, this volume).

Eruption Interagency After Action and Lessons Learned

In April 2006, barely a month after the cessation of lava effusion at Augustine, AVO and NWS organized an interagency after-action review to gather lessons learned and identify ways to improve future eruption response efforts. Before the meeting, a questionnaire was sent to participants which included AVO, NWS, FAA, WCATWC, USCG, ADHSEM, the Alaska Department of Environmental Conservation, the U.S. Air Force, Kenai Borough Emergency Services, the Municipality of Anchorage, and contacts in several communities on the southern Kenai Peninsula (appendix 2). A similar questionnaire was also sent by e-mail to police, fire, and other officials in some affected communities to solicit feedback on the effectiveness of warning messages. A summary of the meeting was shared among the agency attendees. Many constructive suggestions contributed to the update of the Alaska

Interagency Plan in 2008 (Madden and others, 2008). Several key conclusions of the evaluation are below.

“Balkanization” of information—People expressed frustration at having to go to multiple Web sites for complete information on the status of the volcano and current warning messages. A one-stop Web page that includes current volcano hazard information and links to all formal warning messages—even more comprehensive than the National Weather Service Augustine coordination page developed during this eruption—is needed.

Joint Information Center (JIC)—A JIC formed under principles of incident command, although perhaps not required during this relatively low-impact eruption, may become necessary in the future. It is not clear how one will be created during a significant volcanic incident in the State of Alaska but a preliminary plan for JIC formation should be in place prior to such an event (Driedger and others, 2008).

Ash-fall hazard information—Initial public advisories were not specific enough in terms of the likely severity of impact (amounts and duration) and the areas where ash fall could be anticipated. Both the message content and dissemination pathways need improvement. More public health expertise is required in developing ash-fall warning guidance.

Conclusions

AVO applied experience gained during recent eruptions in Cook Inlet (Miller and Chouet, 1994; Keith, 1995), other parts of the Aleutian arc, and at Mount St. Helens, Washington (Driedger and others, 2008) to provide volcano hazard information during the 2005–6 unrest and eruption at Augustine Volcano. The Augustine activity occurred during an era of improved interagency coordination and advanced communications technology, both major contributors to effective response. The existence of an interagency coordination plan and well-established relationships among AVO and key Federal, State, and local agency representatives contributed to efficient and timely hazard messages before, during, and after the eruption. A lack of any significantly damaging aircraft encounter with ash, despite more than a dozen ash clouds in the greater Cook Inlet region, can be attributed in part to a properly functioning ash and aviation hazard mitigation network in Alaska and an informed aviation sector. Overall, eruption impacts were limited primarily to unknown economic losses due to flight cancellations and other decisions to avoid travel or other activities out of concern for potential impacts.

The Augustine eruption highlighted ongoing challenges to the interagency management of volcano hazard information. In particular, volcanology and meteorology communities have yet to make fully operational ash-fall forecasting and visualization tools to address fallout, one of the most important primary hazards of explosive volcanic eruptions. Similarly, hazards posed by ash-poor volcanic aerosol clouds to aircraft operations remain poorly understood. Effective operational guidance to the aviation sector regarding these distal cloud hazards remains an important goal.

References Cited

Adleman, J.N., Cameron, C.E., Snedigar, S.F., Neal, C.A., and Wallace, K.L., 2010, Public outreach and communications of the Alaska Volcano Observatory during the 2005–2006 eruption of Augustine Volcano, *in* Power, J.A., Coombs, M.L., and Freymueller, J.T., eds., The 2006 eruption of Augustine Volcano, Alaska: U.S. Geological Survey Professional Paper 1769 (this volume).

Bailey, J.E., Dean, K.G., Dehn, J., and Webley, P.W., 2010, Integrated satellite observations of the 2006 eruption of Augustine Volcano, *in* Power, J.A., Coombs, M.L., and Freymueller, J.T., eds., The 2006 eruption of Augustine Volcano, Alaska: U.S. Geological Survey Professional Paper 1769 (this volume).

Begét, J.E., and Kienle, J., 1992, Cyclic formation of debris avalanches at Mount St. Augustine volcano: Nature, v. 356.

Brantley, S.R., ed., 1990, The eruption of Redoubt volcano, Alaska, December 14, 1989–August 31, 1990: U.S. Geological Survey Circular 1061, 33 p.

Casadevall, T.J., and Krohn, M.D., 1995, Effects of the 1992 Crater Peak eruptions on airports and aviation operations in the United States and Canada, *in* Keith, T.E.C., ed., The 1992 eruptions of Crater Peak vent, Mount Spurr Volcano, Alaska, U.S. Geological Survey Bulletin 2139, p. 205–220.

Cervelli, P.F., Fournier, T.J., Freymueller, J.T., and Power, J.A., 2006, Ground deformation associated with the precursory unrest and early phases of the January 2006 eruption of Augustine Volcano, Alaska: Geophysical Research Letters, v. 33, 5 p., doi: 10.1029/2006GL027219.

Cervelli, P.F., Fournier, T.J., Freymueller, J.T., Power, J.A., Lisowski, M., and Pauk, B.A., 2010, Geodetic constraints on magma movement and withdrawal during the 2006 eruption of Augustine Volcano, *in* Power, J.A., Coombs, M.L., and Freymueller, J.T., eds., The 2006 eruption of Augustine Volcano, Alaska: U.S. Geological Survey Professional Paper 1769 (this volume).

Coombs, M.L., Bull, K.V., Vallance, J.W., Schneider, D.J., Thoms, E.E., Wessels, R.L., and McGimsey, R.G., 2010, Timing, distribution, and volume of proximal products of the 2006 eruption of Augustine Volcano, *in* Power, J.A., Coombs, M.L., and Freymueller, J.T., eds., The 2006 eruption of Augustine Volcano, Alaska: U.S. Geological Survey Professional Paper 1769 (this volume).

Coombs, M.L., White, S.M., and Scholl, D.W., 2007, Massive edifice failure at Aleutian arc volcanoes: Earth and Planetary Science Letters, v. 256, p. 403–418, doi: 10.1016/j.epsl.2007.01.030.

Dorava, J.M., and Meyer, D.F., 1994, Hydrologic hazards in the lower Drift River Basin associated with the 1989–1990 eruptions of Redoubt Volcano, Alaska, in Miller, T.P. and Chouet, B.A., eds., The 1989–1990 eruptions of Redoubt Volcano, Alaska: Journal of Volcanology and Geothermal Research, v. 62, n. 1, p. 387–407.

Driedger, C.L., Neal, C.A., Knappenberger, T.H., Needham, D.H., Harper, R.B., and Steele, W.P., 2008, Hazard information management during the autumn 2004 reawakening of Mount St. Helens volcano, Washington, in Sherrod, D.R., Scott, W.E., and Stauffer, P.H., eds., A volcano rekindled; the renewed eruption of Mount St. Helens, 2004–2006: U.S. Geological Survey Professional Paper 1750, p. 505–519.

Federal Register, 2006: vol. 71, no. 20, Tuesday January 31, 2006, p. 5010–5012.

Gardner, C.A., and Guffanti, M.C., 2006, U.S. Geological Survey's alert notification system for volcanic activity: U.S. Geological Survey Fact Sheet 2006-3139, 4 p. [http://pubs.usgs.gov/fs/2006/3139/].

Johnston, D.A., 1978, Volatiles, magma mixing, and the mechanism of eruption at Augustine volcano, Alaska: University of Washington, Ph.D. dissertation, 187 p., 20 plates, scale unknown.

Keith, T.E.C., (ed.), 1995, The 1992 eruptions of Crater Peak Vent, Mount Spurr volcano, Alaska: U.S. Geological Survey Bulletin 2139, 220 p.

Kienle, J., and Swanson, S.E., 1985, Volcanic hazards from future eruptions of Augustine volcano, Alaska, second edition: University of Alaska Fairbanks Geophysical Institute Report UAG-R 275, 122 p.

Kienle, J., 1994, Volcanic ash-aircraft incidents in Alaska prior to the Redoubt eruption on 15 December 1989, in Casadevall, T. J., ed., Volcanic ash and aviation safety; proceedings of the first international symposium on volcanic ash and aviation safety: U.S. Geological Survey Bulletin 2047, p. 119–12.

Madden, J., Murray, T.L., Carle, W.J., Cirillo, M.A., Furgione, L.K., Trimpert, M.T., and Hartig, Larry, signatories, 2008, Alaska interagency operating plan for volcanic ash episodes, 52 p.

Miller, T.P., and Chouet, B.A., 1994, The 1989–1990 eruptions of Redoubt volcano; an introduction, *in* Miller, T.P. and Chouet, B.A., eds., The 1989–1990 eruptions of Redoubt Volcano, Alaska: Journal of Volcanology and Geothermal Research, v. 62, n. 1, p. 1–10.

Neal, C.A., McGimsey, R.G., Dixon, J.P., Manevich, Alexander, and Rybin, Alexander, 2009, 2006 Volcanic activity in Alaska, Kamchatka, and the Kurile Islands—Summary of events and response of the Alaska Volcano Observatory: U.S. Geological Survey Scientific Investigations Report 2008-5214, 102 p. [http://pubs.usgs.gov/sir/2008/5214/].

Osiensky, J., and Hall, T., 2008, Detection and tracking of volcanic ash and SO_2 and its impact to aviation: Eos (American Geophysical Union Transactions), v. 89, no. 53, abs. A53B-0276.

Pauk, B.A., Jackson, M., Feaux, K., Mencin, D., and Bohnenstiehl, K., 2010, The Plate Boundary Observatory permanent global positioning system network on Augustine Volcano before and after the 2006 eruption, *in* Power, J.A., Coombs, M.L., and Freymueller, J.T., eds., The 2006 eruption of Augustine Volcano, Alaska: U.S. Geological Survey Professional Paper 1769 (this volume).

Power, J.A., Nye, C.J., Coombs, M.L., Wessels, R.L., Cervelli, P.F., Dehn, J., Wallace, K.L., Freymueller, J.T., and Doukas, M.P., 2006, The reawakening of Alaska's Augustine Volcano: Eos, v. 87, no. 37, p. 373, 377.

Power, J.A., and Lalla, D.J., 2010, Seismic observations of Augustine Volcano, 1970–2007, *in* Power, J.A., Coombs, M.L., and Freymueller, J.T., eds., The 2006 eruption of Augustine Volcano, Alaska: U.S. Geological Survey Professional Paper 1769 (this volume).

Power, John, 1988, Seismicity associated with the 1986 eruption of Augustine Volcano, Alaska: University of Alaska Fairbanks unpub. M.S. thesis, 142 p.

Reeder, J.W., and Lahr, J.C., 1987, Seismological aspects of the 1976 eruptions of Augustine volcano, Alaska: U.S. Geological Survey Bulletin 1768, p. 1–32.

Schneider, D.J., Scott, C., Wood, J., and Hall, T., 2006, NEXRAD weather radar observations of the 2006 Augustine volcanic eruption clouds: Eos (American Geophysical Union Transactions), v. 87, no. 52, Fall meet. supp., abs. V51C-1686.

Scott, W.E., and McGimsey, R.G., 1994, Character, mass, distribution, and origin of tephra-fall deposits of the 1989–1990 eruption of Redoubt volcano, south-central Alaska, *in* Miller, T.P. and Chouet, B.A., eds., The 1989–1990 eruptions of Redoubt Volcano, Alaska: Journal of Volcanology and Geothermal Research, v. 62, no. 1, p. 251–27.

Siebert, L., Begét, J.E., and Glicken, H., 1995, 1883 and late-prehistoric eruptions of Augustine volcano, Alaska: Journal of Volcanology and Geothermal Research, v. 66, p. 367–395.

Swanson, S.E., and Kienle, J., 1988, The 1986 eruption of Mount St. Augustine: field test of a hazard evaluation: Journal of Geophysical Research, v. 93, no. B5, p. 4500–4520.

Vallance, J.W., Bull, K.F., and Coombs, M.L., 2010, Pyroclastic flows, lahars, and mixed avalanches generated during the 2006 eruption of Augustine Volcano, *in* Power, J.A., Coombs, M.L., and Freymueller, J.T., eds., The 2006 eruption of Augustine Volcano, Alaska: U.S. Geological Survey Professional Paper 1769 (this volume).

Wallace, K.L., Neal, C.A., and McGimsey, R.G., 2010, Timing, distribution, and character of tephra fall from the 2005–2006 eruption of Augustine Volcano, *in* Power, J.A., Coombs, M.L., and Freymueller, J.T., eds., The 2006 eruption of Augustine Volcano, Alaska: U.S. Geological Survey Professional Paper 1769 (this volume).

Waythomas, C.F., and Waitt, R.B., 1998, Preliminary volcano-hazard assessment for Augustine Volcano, Alaska: U.S. Geological Survey Open-File Report 98-106.

Yount, E.M., Miller, T.P., and Gamble, B.M., 1987, The 1986 eruptions of Augustine Volcano, Alaska, hazards and effects, *in* Geologic studies in Alaska by the U.S. Geological Survey during 1986: U.S. Geological Survey Circular 998, p. 4–13.

Appendix 1. Excerpts from key Alaska Volcano Observatory Information Releases during the Augustine Volcano eruption on November 29, 2005, December 12, 2005, January 10, 2006, January 11, 2006, April 28, 2006, and August 9, 2006

[Some header and footer information has been deleted for brevity]

A. First announcement of significant unrest.

Tuesday, November 29, 2005 12:15 PM AKST (2115 UTC)

AUGUSTINE VOLCANO (CAVW#1103-01-)
59.3633°N 153.4333°W, Summit Elevation 4134 ft (1260 m)
Current Level of Concern Color Code: **YELLOW**
Previous Level of Concern Color Code: **GREEN**

AVO has detected important changes in earthquake activity and ground deformation at *Augustine* Volcano in southern Cook Inlet. These data are consistent with renewed volcanic unrest. AVO is therefore raising the level-of-concern color code from green to **YELLOW** and will continue to monitor activity closely. There is no indication that an eruption is imminent or certain.

Beginning in May 2005, there has been a slow increase in the number of earthquakes located under Augustine Volcano. The earthquakes are generally small (less than magnitude 1.0) and concentrate roughly 1 km below the volcano's summit. These earthquakes have slowly increased from 4-8 earthquakes/day to 20-35 earthquakes/day. Additionally, data from a 6-station Global Positioning System (GPS) network on Augustine Volcano indicate that a slow, steady inflation of the volcano started in mid-summer 2005 and continues at present. The GPS benchmark located nearest the summit has moved a total of 2.5 cm (1 inch). This motion is consistent with a source of inflation or pressure change centered under the volcano. This is the first such deformation detected at Augustine Volcano since measurements began just prior to the 1986 eruption.

No reports of increased steaming have been received by AVO, nor have satellite data shown increased thermal activity.

Historic eruptions of Augustine typically begin with explosive bursts that may send plumes of ash to 30,000-40,000 feet above sea level. The primary hazards to communities, aviation, and mariners in Cook Inlet and parts of south-central Alaska from an Augustine eruption are ash fall and drifting ash clouds. In 1986, 6 mm (0.25 inch) of ash fell in Homer, 120 km (75 mi) east of Augustine and light ashfall was recorded in Anchorage, 290 km (180 mi) away. Hot, ground-hugging flows of volcanic rock debris called pyroclastic flows may form during an eruption and could be hazardous to people, aircraft, or boats on or in the immediate vicinity of the island.

Island volcanoes can generate tsunamis by collapse into the sea. There is no evidence that conditions are developing that would lead to a major volcanic landslide or similar event at Augustine that, upon entering Cook Inlet, could generate a tsunami. No tsunami waves were generated during any of the last five eruptions of Augustine Volcano.

B. Discussion of first visible plumes and sulfur odors following explosions.

Monday, December 12, 2005 3:05 PM AKST (0005 UTC)

Current Level of Concern Color Code: **YELLOW**

A steam plume extending at least 75 km (45 mi) SE from *Augustine* Volcano is clearly visible by satellite and has also been reported by local pilots. Images in the web camera also show a plume. The plume appears to be primarily steam.

During the past several days, AVO has detected changes in the style of earthquake activity and received other information about gas emissions and steaming at Augustine Volcano. Two seismic events on Friday evening (12/9/05), and Sunday evening (12/11/05) may have perturbed the hydrothermal system, initiating steam explosions. These events are consistent with reports of steaming at the summit observed on Saturday (12/10/05), and distinct sulfur smell ("like from a sewer") in the air on Sunday evening (12/11/05) at Nanwalek and Port Graham, approximately 80 km (50 mi) east of the volcano. Collectively, these events are signs of continued and elevated level of volcanic unrest, but do not indicate that an eruption is imminent in the next few days to weeks. The level-of-concern color code remains at Yellow and AVO will continue to monitor activity closely.

Depending on the direction of the wind and the amount of gas emitted at the volcano, sulfur odors may persist. Periods of foul smelling air may accompany the present level of unrest at Augustine, but these periods should be relatively brief and are not expected to be a significant health concern. Humans can detect at very low concentrations the volcanic gases sulfur dioxide and hydrogen sulfide. At higher concentrations (or if a person has respiratory problems) the gases can irritate the eyes and respiratory system. People with respiratory problems should take reasonable precautions as they would for dealing with other types of slightly unhealthy air. See *http://www.ivhhn.org/* "guidelines and databases" for more information.

C. Expanded Information Release discussing possible outcomes and hazards.

Tuesday, January 10, 2006 1:05 PM AKST (2205 UTC)

Current Level of Concern Color Code: **YELLOW**

Since last spring, the Alaska Volcano Observatory (AVO) has detected increasing volcanic unrest at Augustine Volcano in lower Cook Inlet. Based on all available monitoring data AVO regards that an eruption similar to those in 1976 and 1986 is the most probable outcome. We expect such an eruption to occur within the next few weeks or months. There is currently no indication that an eruption will occur within the next few days and Augustine remains at color code **Yellow**.

Observations and Background:

Rates of earthquake occurrence increased slowly from an average rate of 1 to 2 per day in early May, to 3 to 4 per day in October and 15 per day in mid-December. These earthquakes are occurring directly beneath the mountain's summit at depths close to sea level. The largest event located to date is a magnitude 1.2. Concurrent with this increase, we have also detected a small uplift of the volcano using Global Positioning Systems (GPS) instruments permanently installed on the mountain. The total swelling to date is approximately 2 inches (5 cm). In early and mid December, a number of small steam explosions were recorded by seismic instruments on the volcano. Views of the summit following these explosions revealed new steaming cracks and localized deposits of debris. In addition, airborne gas measurements and thermal imaging measurements have shown an increase in the output of volcanic gas and heat at the summit of the volcano. The highest temperature recorded, on January 4, was 390 C (750 F). AVO interprets these changes as a sign that new magma is accumulating beneath the volcano's summit. Based on an analysis of past and current earthquake locations, GPS, gas, and heat data, this new magma may have risen to sea level or higher.

***C*.** Expanded Information Release discussing possible outcomes and hazards.—Continued

In response to this activity, AVO has deployed additional seismometers, GPS receivers, an infrasound sensor, and time lapse cameras on the flanks of the volcano, and established a web-based camera system. Further deployment of additional monitoring equipment is ongoing. We plan continued visual and infrared surveillance of the volcano's summit and frequent measurements of gas output.

The most recent eruptions of Augustine were characterized by an initial explosive phase lasting from 4 to 14 days. The explosive phase produces large ash plumes, that depending upon the prevailing winds and height of the eruptive column, can be carried hundreds to thousands of miles. Most communities in south-central Alaska experienced some ash fall with accumulations of several millimeters during both the 1976 and 1986 eruptions (Anchorage received 0.12 inches (3 mm) in 1976 and less than 0.04 inches (1 mm) in 1986; Homer received about 0.2 inches (5 mm) in 1976 and 1986). During the explosive phase of the eruption, many portions of Augustine Island are also overrun by pyroclastic flows (fast flowing mixtures of hot volcanic gasses, steam, rock and ash) and mud flows (fast moving mixtures of volcanic rock, ash and water). The explosive phase is generally followed by the extrusion of a lava dome which is generally accompanied by smaller explosions and pyroclastic flows. Communities in south-central Alaska may again experience minor ash fall during these later phases of the eruption.

Interpretation and Hazards:

Based on our current understanding of Augustine's past eruptions and our analysis of the current episode of unrest, AVO considers the following future scenarios as possible:

1) **Failed Eruption:** No eruption occurs as magma does not reach the surface. Earthquake activity, ground deformation, gas output, and steaming slowly decrease over several weeks or months.
2) **Eruption similar to those of 1976 and 1986:** Unrest continues to escalate culminating in an eruption that is similar to those that occurred in 1976 and 1986. An eruption such as this would likely spread volcanic ash throughout and perhaps beyond Cook Inlet depending upon the prevailing winds. Much of Augustine Island would be inundated by pyroclastic flows, mud flows, ash fall, and ballistic showers.
3) **Larger Explosive Eruption:** A significantly larger eruption could occur, perhaps similar to eruptions that are thought to have taken place prehistorically. Such an eruption might involve the production of larger ash plumes, significant modification of the island's summit, and large pyroclastic flows and mud flows on the island.
4) **Flank Collapse:** The intruding magma or other processes could destabilize a portion of the Augustine cone that could result in a large landslide. If this landslide entered Cook Inlet, a localized tsunami could be generated. Such a landslide and tsunami were associated with the 1883 eruption of Augustine Volcano. It is also likely that a landslide of this type would be accompanied by an eruption.

Based on all available monitoring data AVO, regards scenario number two, an eruption similar to those in 1976 and 1986, as the most probable outcome at this time. At this time scenarios one, three and four are considered less likely.

Comparing the time frame of pre-eruptive activity in 1976 and 1986 with the current unrest, we would expect such an eruption to occur within the next few weeks or months. There is currently no indication that an eruption will occur within the next few days. Both the 1986 and 1976 eruptions were preceded by short-term (hours to days) increases in seismic activity. Should earthquake activity or other monitoring data suggest that an eruption is expected within hours or days, AVO would move Augustine from its current level of concern color code Yellow to Orange or Red.

AVO will continue to monitor the volcano closely. We plan to add additional instrumentation on the volcano to help us better understand the nature of this unrest. New data and observations may lead us to change our assessment. Any changes would be announced in a subsequent Information Release.

Further information on Augustine Volcano and related hazards and response plans can be found at the following web sites:

C. Expanded Information Release discussing possible outcomes and hazards.—Continued

Alaska Volcano Observatory: Most recent information on Augustine Volcano
www.avo.alaska.edu

U.S. Geological Survey: Hazards associated with volcanic ash fall
http://volcanoes.usgs.gov/ash/

NOAA National Weather Service: Ash cloud trajectories and aviation warnings
http://pafc.arh.noaa.gov/augustine.php

NOAA West Coast and Alaska Tsunami Warning Center: Tsunami issues related to Augustine
http://wcatwc.arh.noaa.gov/Augustine/AugustineWeb.htm

Alaska Division of Homeland Security and Emergency Management: Community preparedness
http://www.ak-prepared.com/plans/mitigation/volcano.htm

D. Marked increase in seismicity and likelihood of explosive eruption.

Tuesday, January 10, 2006 9:10 PM AKST (610 UTC)

Current Level of Concern Color Code: **ORANGE**

The level of Concern Color Code for *Augustine* Volcano is now **ORANGE** .

Over the past six hours, earthquake activity beneath Augustine has increased markedly. AVO considers this activity indicative of a heightened possibility of an explosive eruption within hours to days.

AVO is monitoring the situation closely and will issue further updates as new information and analyses become available. Onsite staffing at AVO has now expanded to 24 hour operations.

E. Notice of first major explosive event.

Wednesday, January 11, 2006 5:50 AM AKST (1450 UTC)

Current Level of Concern Color Code: **ORANGE**
The level of Concern Color Code for *Augustine* Volcano is now **RED**

At 4:44 a.m. (AKST) this morning, AVO began recording seismic signals interpreted as explosions at the summit of Augustine Volcano that likely mark the onset of an eruption. The current activity may be emitting ash, steam, and volcanic gases.

If the volcano follows a pattern similar to the 1976 and 1986 eruptions, we would expect a further intensification of seismic activity prior to a larger explosive event. It is also possible that an explosive eruption could occur with little or no warning.

AVO is monitoring the situation closely and will issue further updates as new information and analyses become available.

F. Description of continuous phase.

Monday, January 30, 2006 9:15 AM AKST (1815 UTC)

Current Level of Concern Color Code: **RED**

Augustine volcano has been in a state of continuous eruption since 14:30 AKST (2330 UTC) January 28. Overflight observations on January 29 suggest that pyroclastic flows are being produced. Larger seismic signals were detected at 11:17 AKST (2017 UTC) on January 29, and 03:25 AKST (1225 UTC) and 06:21 AKST (1521 UTC) on January 30. National Weather Service radar indicates that ash clouds from these events rose to 25,000 feet above sea level. In general, other than during these three events, an ash-rich plume is rising to about 14,000 feet above sea level. For up-to-date Ashfall Advisories and wind trajectories, please refer to the latest National Weather Service website: *http://pafc.arh.noaa.gov/augustine.php*.

Thermal anomalies (measured by satellite-based instruments) persist, both at the summit of Augustine and on the northern flank, consistent with continuing eruption and hot pyroclastic flow deposits on the volcano.

G. Increased seismicity interpreted as increased extrusion rate.

Thursday, March 9, 2006 9:05 AM AKST (1805 UTC)

Current Level of Concern Color Code: **ORANGE**

Beginning at approximately 0530 AKST (1430 UTC) March 8, 2006, seismicity at *Augustine* Volcano increased markedly; as of about midnight AKST (0900 UTC) March 9, 2006 it became more or less continuous.. The amplitude of the seismicity is high, with the signal nearly saturating several instruments. Imagery from a low light camera in Homer show two distinct bright spots, the first at the summit, the second approximately midway down the north flank. Satellite imagery shows thermal anomalies at Augustine, as it has for the last several weeks. There are no indications of substantial ash emissions at this time.

Taken together, these data probably indicate accelerated rates of magma extrusion, in the form of increased dome growth, vigorous lava flows, or a combination of both. Extrusion of this kind creates local hazard, but is not likely to generate explosions, significant ash emissions, or a tsunami.

H. Downgrade to Yellow, first time at Yellow since January 10, 2006.

Friday, April 28, 2006 9:45 AM AKDT (1745 UTC)

Current Level of Concern Color Code: **YELLOW**
Previous Level of Concern Color Code: **ORANGE**

Based on the current level of activity at *Augustine*, we are lowering the Level of Concern Color Code from **ORANGE** to **YELLOW**.

Data and observations currently indicate that the growth of the summit lava dome and lava flows has stopped, or continues only at a very low rate. Seismic data show that rock fall and avalanche events are still occurring, but at a diminished level. Visual observations and satellite data show that there have not been any detectable changes at the summit over the last few weeks.

Despite the apparent cessation of lava dome growth, the new dome and lava flows are still highly unstable, and rock falls and avalanches are still occurring and may continue for several weeks or months. The north flank of the

H. Downgrade to Yellow, first time at Yellow since January 10, 2006—Continued

island is the area most susceptible to rock falls and avalanches, and the steep ends of the lava flows are also places where rock fall activity may continue. These areas are considered very hazardous. Small, dilute ash clouds produced by rock falls and avalanches may still develop, but these ash clouds are unlikely to extend beyond Augustine Island.

Some indicators suggest that magma is still present at shallow levels. AVO will continue to make volcanic gas measurements and recent measurements indicate that levels are still above background and likely indicate degassing of shallow magma. Weak thermal anomalies persist in satellite data, consistent with slow cooling of the lava dome and continued venting of hot gases.

Despite the volcano's current quiet state, renewed eruptive activity is possible. AVO expects that a renewal of explosive activity or lava extrusion would likely be preceded by increases in seismicity, gas output, and deformation.

Brief, unexpected explosions are still possible if hot gas and rocks interact with groundwater, but such explosions are unlikely to produce ash that would travel far beyond the island.

AVO continues to monitor Augustine closely and the observatory will remain staffed 24/7 until conditions at the volcano approach background levels.

I. Return to Green, normal, non-eruptive state.

ALASKA VOLCANO OBSERVATORY
Information Release
Wednesday, August 9, 2006 3:00 PM AKDT (2300 UTC)

AUGUSTINE VOLCANO (CAVW#1103-01-)
59°21'48"N 153°26'W , Summit Elevation 4134 ft (1260 m)
Current Level of Concern Color Code: **GREEN**
Previous Level of Concern Color Code: **YELLOW**

Based on the current level of activity at *Augustine* Volcano, we are lowering the Level of Concern Color Code from **YELLOW** to **GREEN**.

Seismic data and observations made by AVO geologists working on the volcano indicate that activity has decreased to background levels. Visual observations and satellite data show that there have been no detectable changes at the summit over the last few months.

Despite the cessation of lava dome growth, the new dome and lava flows are still unstable, and small rock falls and avalanches may occur for several months, especially on the north flank of the volcano. The steep ends of the lava flows are also places where rock fall activity may continue. These areas are still considered hazardous to anyone visiting the island.

The Augustine summit area continues to emit noxious volcanic gases. A gas-rich plume is often present and areas downwind of the summit may be engulfed by variable amounts of volcanic gas. Where the plume hugs the ground near the volcano, the gases can cause eye irritation and respiratory problems. Gases can accumulate in low-lying or confined areas of the summit and lava flows, and it is possible, but not likely, that the concentration of gases in these areas could reach levels dangerous to humans.

Though the volcano is currently quiet, renewed eruptive activity is possible. AVO expects that a renewal of explosive activity or lava extrusion would likely be preceded by increases in seismicity, gas output, and deformation.

Appendix 2. Interagency After-Action Premeeting Questionnaire

PRE-MEETING ASSIGNMENT TO PARTICIPANTS:

Please use the attached forms to submit the following information to no later than COB April 14. Responses will help guide the discussion and ensure we address key issues.

- **A. AGENCY GOALS FOR THE AFTERACTION**: what does your agency hope to get out of this meeting?
- **B. SUCCESSES**! What specific actions, policies, procedures, etc. were effective? These may be from your own agency or from any part of the interagency effort. What can we learn from this?
- **C. CHALLENGES!** What actions, policies, procedures, etc. were lacking in effectiveness and require improvement. How can we accomplish this?

PLEASE ANSWER THESE QUESTIONS prior to the meeting and be prepared to discuss:

- A. Did you or your agency make use of the published U.S. Geological Survey Volcano Hazard Assessment for Augustine Volcano? If not, why? If so, was it helpful?
- B. Were the daily coordination conference calls effective? How can they be improved?
- C. Was information about likely impacts of eruptive activity easy to obtain?
- D. Was there a good balance between Internet-based and other forms of communication?
- E. How did you receive the most critical information (phone? E-mail? Other?)
- F. Should a Joint Information Center have been established? If so, what would this look like, what is its purpose, and who would lead the JIC?
- G. What were the primary concerns of your agency and constituency and were these adequately addressed?

DO YOU HAVE ANY SPECIFIC QUESTIONS THAT YOU WOULD LIKE TO DISTRIBUTE TO THE GROUP PRIOR TO THE MEETING?

Produced in the Western Region, Menlo Park, California
Manuscript approved for publication, August 1, 2009
Edited by James W. Hendley II, Peter H. Stauffer, Jan Zigler, and George Havach
Layout and Design by Judy Weathers, David Jones, Jeanne DiLeo, Steve Scott, and Susan Mayfield

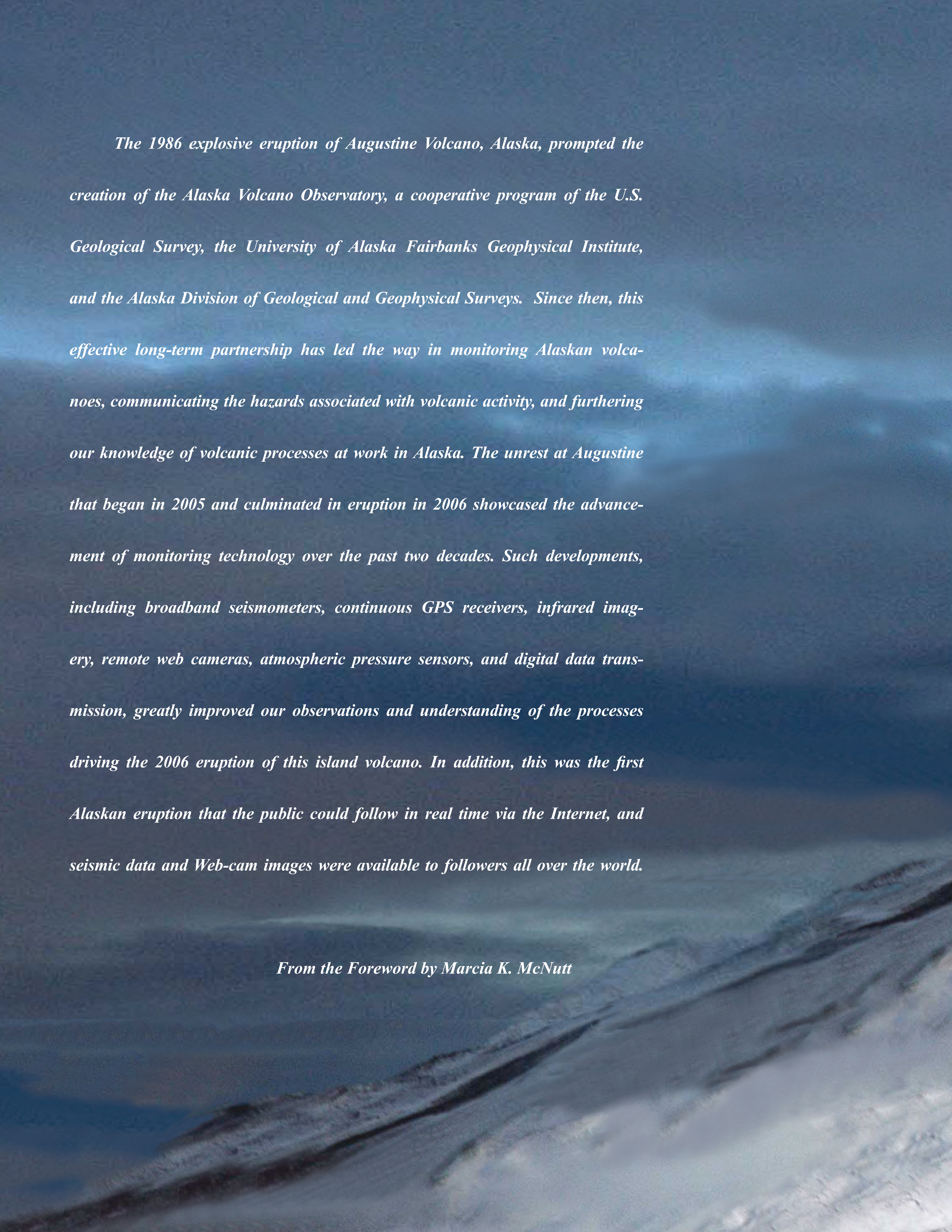

The 1986 explosive eruption of Augustine Volcano, Alaska, prompted the creation of the Alaska Volcano Observatory, a cooperative program of the U.S. Geological Survey, the University of Alaska Fairbanks Geophysical Institute, and the Alaska Division of Geological and Geophysical Surveys. Since then, this effective long-term partnership has led the way in monitoring Alaskan volcanoes, communicating the hazards associated with volcanic activity, and furthering our knowledge of volcanic processes at work in Alaska. The unrest at Augustine that began in 2005 and culminated in eruption in 2006 showcased the advancement of monitoring technology over the past two decades. Such developments, including broadband seismometers, continuous GPS receivers, infrared imagery, remote web cameras, atmospheric pressure sensors, and digital data transmission, greatly improved our observations and understanding of the processes driving the 2006 eruption of this island volcano. In addition, this was the first Alaskan eruption that the public could follow in real time via the Internet, and seismic data and Web-cam images were available to followers all over the world.

From the Foreword by Marcia K. McNutt